

Vasant Matsagar *Editor*

Advances in Structural Engineering

Dynamics, Volume Two

 Springer

Advances in Structural Engineering

Vasant Matsagar
Editor

Advances in Structural Engineering

Dynamics, Volume Two

 Springer

Editor
Vasant Matsagar
Department of Civil Engineering
Indian Institute of Technology (IIT) Delhi
New Delhi, Delhi
India

ISBN 978-81-322-2192-0 ISBN 978-81-322-2193-7 (eBook)
DOI 10.1007/978-81-322-2193-7

Library of Congress Control Number: 2014955611

Springer New Delhi Heidelberg New York Dordrecht London
© Springer India 2015

This work is subject to copyright. All rights are reserved by the Publisher, whether the whole or part of the material is concerned, specifically the rights of translation, reprinting, reuse of illustrations, recitation, broadcasting, reproduction on microfilms or in any other physical way, and transmission or information storage and retrieval, electronic adaptation, computer software, or by similar or dissimilar methodology now known or hereafter developed.

The use of general descriptive names, registered names, trademarks, service marks, etc. in this publication does not imply, even in the absence of a specific statement, that such names are exempt from the relevant protective laws and regulations and therefore free for general use.

The publisher, the authors and the editors are safe to assume that the advice and information in this book are believed to be true and accurate at the date of publication. Neither the publisher nor the authors or the editors give a warranty, express or implied, with respect to the material contained herein or for any errors or omissions that may have been made.

Printed on acid-free paper

Springer (India) Pvt. Ltd. is part of Springer Science+Business Media (www.springer.com)

Foreword

Earthquake Engineering and Structural Dynamics is a major subject of teaching and research in the present decade. This is evident from the size of publications taking place in different themes of the subject in recent years. The number of committees formed, the conferences organised and the special courses offered on the subject is also large. Therefore, it is natural that the number of papers received in this area is large for the Structural Engineering Convention (SEC 2014). As a result, a strict criterion has been adopted to review the papers for the inclusion in the conference proceeding to be published by Springer. The papers cover a wide range of topics, namely structural control, offshore dynamics, dynamic soil-structure interaction, seismic hazard analysis, retrofitting of structures for lateral loads, dynamic behaviour of structures and the like. The papers have been peer-reviewed for acceptance.

Like previous Structural Engineering Conventions, SEC 2014 has drawn the interest of all researchers in different academic institutes in India. It is heartening to see that a large number of researchers are working in the area of Structural Dynamics and Earthquake Engineering. Certainly, the conference venue will provide them an excellent platform to meet and exchange ideas on various topics of recent interest. The conference proceedings will be a good reference material for them. Further, the conference proceedings being published by an international publishing house will reach international readers. All these together make SEC 2014 an eventful congregation of researchers in the area of Structural Dynamics and Earthquake Engineering.

The trend of recent researches has numerical orientation because of the availability of standard software. Therefore, solution of application problems forms the core of majority of papers in the conference volume. In this context, the importance of the materials presented in this volume lies in exploring the response analysis of a variety of both models and prototypes of real-life structures. The excitations to the structures constitute a number of important dynamic loadings such as earthquakes, wind, wave, blast and moving loads. The structures include bridges, buildings, chimneys, offshore platforms, specialty structures, foundation structures and other types of civil amenity structures. The response analysis provides the values of

response parameters that describe the dynamic behaviour of structures. In certain cases, extensive parametric study is conducted to evaluate the effects of parameters that predominantly influence the response.

In earthquake engineering, a major thrust of the papers is on earthquake resistant design of structures. Both steel and concrete structures are considered. Post-yield or inelastic analysis is carried out in most cases to verify the adequacy of the earthquake resistant design. Performance-based design and seismic retrofitting form another set of interesting papers in which several issues related to the topics are thoroughly discussed. Some of the retrofitting strategies use a seismic design philosophy, e.g. they use structural control devices for retrofitting.

Two other areas of research are adequately covered in the conference volume, namely structural health monitoring and structural control. Both topics deal with a number of current research areas such as semi-active control, hybrid control and passive control applied to bridges and chimneys. Extensive parametric studies are presented to investigate the reliability and effectiveness of different control strategies. The effects of various uncertainties existing in the seismic structural control on the responses are brought out through interesting examples. In structural health monitoring, system identification including damage state evaluation forms the topics of discussion. Different types of health monitoring strategies are also presented in the papers.

This proceedings goes as a compendium of interesting research papers on topical themes on Structural Dynamics and Earthquake Engineering. Readers of the conference volume will find them useful for both profession and research. Certainly, it has the standard of an archive value.

Prof. T.K. Datta
Emeritus Professor
Department of Civil Engineering
Indian Institute of Technology (IIT)
Hauz Khas, New Delhi, India

Preface

I am delighted that the Department of Civil Engineering, Indian Institute of Technology (IIT) Delhi has hosted the eagerly awaited and much coveted 9th Structural Engineering Convention (SEC2014). The biennial convention has attracted a diverse range of civil and structural engineering practitioners, academicians, scholars and industry delegates, with the reception of abstracts including more than 1,500 authors from different parts of the world. This event is an exceptional platform that brings together a wide spectrum of structural engineering topics such as advanced structural materials, blast resistant design of structures, computational solid mechanics, concrete materials and structures, earthquake engineering, fire engineering, random vibrations, smart materials and structures, soil-structure interaction, steel structures, structural dynamics, structural health monitoring, structural stability, wind engineering, to name a few. More than 350 full-length papers have been received, among which a majority of the contributions are focused on theoretical and computer simulation-based research, whereas a few contributions are based on laboratory-scale experiments. Amongst these manuscripts, 205 papers have been included in the Springer proceedings after a thorough three-stage review and editing process. All the manuscripts submitted to the SEC2014 were peer-reviewed by at least three independent reviewers, who were provided with a detailed review proforma. The comments from the reviewers were communicated to the authors, who incorporated the suggestions in their revised manuscripts. The recommendations from three reviewers were taken into consideration while selecting a manuscript for inclusion in the proceedings. The exhaustiveness of the review process is evident, given the large number of articles received addressing a wide range of research areas. The stringent review process ensured that each published manuscript met the rigorous academic and scientific standards. It is an exalting experience to finally see these elite contributions materialise into three book volumes as SEC2014 proceedings by Springer entitled “Advances in Structural Engineering”. The articles are organised into three volumes in some broad categories covering subject matters on mechanics, dynamics and

materials, although given the diverse areas of research reported it might not have been always possible.

SEC2014 has ten plenary speakers, who are eminent researchers in structural engineering, from different parts of the world. In addition to the plenary sessions on each day of the convention, six concurrent technical sessions are held every day to assure the oral presentation of around 350 accepted papers. Keynote speakers and session chairmen for each of the concurrent sessions have been leading researchers from the thematic area of the session. The delegates are provided with a book of extended abstracts to quickly browse through the contents, participate in the presentations and provide access to a broad audience of educators.

A technical exhibition is held during all the 3 days of the convention, which has put on display the latest construction technologies, equipment for experimental investigations, etc. Interest has been shown by several companies to participate in the exhibition and contribute towards displaying state-of-the-art technologies in structural engineering. Moreover, a pre-convention international workshop organised on “Emerging Trends in Earthquake Engineering and Structural Dynamics” for 2 days has received an overwhelming response from a large number of delegates.

An international conference of such magnitude and release of the SEC2014 proceedings by Springer has been the remarkable outcome of the untiring efforts of the entire organising team. The success of an event undoubtedly involves the painstaking efforts of several contributors at different stages, dictated by their devotion and sincerity. Fortunately, since the beginning of its journey, SEC2014 has received support and contributions from every corner. I thank them all who have wished the best for SEC2014 and contributed by any means towards its success. The edited proceedings volumes by Springer would not have been possible without the perseverance of all the committee members.

All the contributing authors owe thanks from the organisers of SEC2014 for their interest and exceptional articles. I also thank the authors of the papers for adhering to the time schedule and for incorporating the review comments. I wish to extend my heartfelt acknowledgment to the authors, peer-reviewers, committee members and production staff whose diligent work put shape to the SEC2014 proceedings. I especially thank our dedicated team of peer-reviewers who volunteered for the arduous and tedious step of quality checking and critique on the submitted manuscripts. I am grateful to Prof. Tarun Kant, Prof. T.K. Datta and Dr. G.S. Benipal for penning the forewords for the three volumes of the conference proceedings. I wish to thank my faculty colleagues at the Department of Civil Engineering, Indian Institute of Technology (IIT) Delhi, and my Ph.D. Research Scholars for extending their enormous assistance during the reviewing and editing process of the conference proceedings. The time spent by all of them and the midnight oil burnt is greatly appreciated, for which I will ever remain indebted. The administrative and support staff of the department has always been extending their services whenever needed, for which I remain thankful to them. Computational

laboratory staff of the department had handled the online paper submission and review processes, which hardly had any glitch therein; thanks to their meticulous efforts.

Lastly, I would like to thank Springer for accepting our proposal for publishing the SEC2014 conference proceedings. Help received from Mr. Aninda Bose, the acquisition editor, in the process has been very useful.

Vasant Matsagar
Organising Secretary, SEC2014

About the Editor

Dr. Vasant Matsagar is currently serving as an Associate Professor in the Department of Civil Engineering at Indian Institute of Technology (IIT) Delhi. He obtained his doctorate degree from Indian Institute of Technology (IIT) Bombay in 2005 in the area of seismic base isolation of structures. He performed post-doctoral research at the Lawrence Technological University (LTU), USA in the area of carbon fibre reinforced polymers (CFRP) in bridge structures for more than 3 years. His current research interests include structural dynamics and vibration control; multi-hazard protection of structures from earthquake, blast, fire, and wind; finite element methods; fibre reinforced polymers (FRP) in prestressed concrete structures; and bridge engineering. He has guided students at both undergraduate and post-graduate levels in their bachelor's and master's projects and doctoral research. Besides student guidance, he is actively engaged in sponsored research and consultancy projects at national and international levels. He has published around 40 international journal papers, 60 international conference manuscripts, a book, and has filed for patents. He is also involved in teaching courses in structural engineering, e.g. structural analysis, finite element methods, numerical methods, structural stability, structural dynamics, design of steel and concrete structures, to name a few. He has organised several short- and long-term courses as quality improvement programme (QIP) and continuing education programme (CEP), and delivered invited lectures in different educational and research organisations.

Dr. Matsagar is the recipient of numerous national and international awards including "Erasmus Mundus Award" in 2013; "DST Young Scientist Award" by the Department of Science and Technology (DST) in 2012; "DAAD Awards" by the Deutscher Akademischer Austausch Dienst (DAAD) in 2009 and 2012; "DAE Young Scientist Award" by the Department of Atomic Energy (DAE) in 2011; "IBC Award for Excellence in Built Environment" by the Indian Buildings Congress (IBC) in 2010; "IEI Young Engineer Award" by the Institution of Engineers (India) in 2009; and "Outstanding Young Faculty Fellowship" by the Indian Institute of Technology (IIT) Delhi in 2009. He has also been appointed as "DAAD Research Ambassador" by the German Academic Exchange Programme since the academic session 2010.

About Structural Engineering Convention (SEC) 2014

The ninth structural engineering convention (SEC) 2014 is organised at Indian Institute of Technology (IIT) Delhi, for the first time in the capital city of India, Delhi. It is organised by the Department of Civil Engineering during Monday, 22nd December 2014 to Wednesday, 24th December 2014. The main aim towards organising SEC2014 has been to facilitate congregation of structural engineers of diverse expertise and interests at one place to discuss the latest advances made in structural engineering and allied disciplines. Further, a technical exhibition is held during all the 3 days of the convention, which facilitates the construction industry to exhibit state-of-the-art technologies and interact with researchers on contemporary innovations made in the field.

The convention was first organised in 1997 with the pioneering efforts of the CSIR-Structural Engineering Research Centre (CSIR-SERC), Council of Scientific and Industrial Research, Chennai and Indian Institute of Technology (IIT) Madras. It is a biennial event that attracts structural engineers from India and abroad, from both academia and industry. The convention, as much as it did in its history, is contributing to scientific developments in the field of structural engineering in a global sense. Over the years, SEC has evolved to be truly international with successive efforts from other premier institutes and organisations towards the development of this convention.

Apart from the 3 days of the convention, an international workshop is also organised on “Emerging Trends in Earthquake Engineering and Structural Dynamics” during Saturday, 20th December 2014 to Sunday, 21st December 2014. Eleven experts in the areas of earthquake engineering and structural dynamics delivered keynote lectures during the pre-convention workshop. The convention includes scholarly talks delivered by the delegates from academia and industry, cultural programmes presented by world-renowned artists, and visits to important sites around the historical National Capital Region (NCR) of Delhi.

Composition of Committees for SEC2014



Organizing Committee

Patron



R.K. Shevgaonkar
Director, IIT Delhi

Areas of Interest: Fiber Optic Communication, Photonics, Nonlinear Fiber Optics, Antennas, Image Processing, Radio Astronomy.

E-mail: rks@ee.iitd.ac.in
director@admin.iitd.ac.in
Phone: +91-11-2659-1701

(continued)

(continued)

Organizing Committee

Organizing
Chairman



A.K. Jain
Professor
Civil Engineering
Department,
IIT Delhi

Areas of Interest: Earthquake Resistant,
Analysis of Structures, Wind load,
Dynamic Behaviour of Offshore Structure.

E-mail: akjain@civil.iitd.ac.in
Phone: +91-11-2659-1202

Mentor



Tarun Kant
Institute Chair Professor
Civil Engineering
Department,
IIT Bombay, Mumbai

Areas of Interest: Solid Mechanics, Finite
Element and Other Numerical Methods,
Polymer Composites, Composite and
Computational Mechanics.

E-mail: tkant@civil.iitb.ac.in
Phone: +91-22-2576-7310

(continued)

(continued)

Organizing Committee

Members



A.K. Nagpal
Dogra Chair Professor
Civil Engineering
Department,
IIT Delhi

Areas of Interest: Structural Engineering, Tall Buildings, Bridges, Earthquake Engineering.

E-mail: aknagpal@civil.iitd.ac.in
Phone: +91-11-2659-1234



Abhijit Ganguli
Assistant Professor
Civil Engineering
Department,
IIT Delhi

Areas of Interest: Non-destructive Evaluation of Structures, Subsurface Imaging, Ultrasonics, Wave Scattering Problems, Structural Dynamics, Active Control of Structural Vibration Mechatronics.

E-mail: abhijit.ganguli@civil.iitd.ac.in
Phone: +91-11-2659-6426

(continued)

(continued)

Organizing Committee



Alok Madan
Professor
Civil Engineering
Department,
IIT Delhi

Areas of Interest: Structural Engineering, Nonlinear Structural Dynamics, Concrete Structures, Computing in Structural Engineering, Structural Masonry.

E-mail: madan@civil.iitd.ac.in
Phone: +91-11-2659-1237



Ashok Gupta
Professor
Civil Engineering
Department,
IIT Delhi

Areas of Interest: Structural Engineering, Artificial Intelligence, Technology Enhanced Learning, Web Based Courses.

E-mail: ashokg@civil.iitd.ac.in
Phone: +91-11-2659-1194

(continued)

(continued)

Organizing Committee



B. Bhattacharjee
Professor
Civil Engineering
Department,
IIT Delhi

Areas of Interest: Durability of Concrete,
Rebar Corrosion, Cement-Based Composites,
Construction Technology, Building Science.

E-mail: bishwa@civil.iitd.ac.in
Phone: +91-11-2659-1193



D.R. Sahoo
Assistant Professor
Civil Engineering
Department,
IIT Delhi

Areas of Interest: Earthquake Engineering,
Large-Scale Testing, Supplemental Damping
and Energy Dissipation Devices,
Performance-Based Seismic Design,
Steel-Fiber Reinforced Concrete.

E-mail: drsahoo@civil.iitd.ac.in
Phone: +91-11-2659-1203

(continued)

(continued)

Organizing Committee



G.S. Benipal
Associate Professor
Civil Engineering
Department,
IIT Delhi

Areas of Interest: Concrete Mechanics,
Constitutive Modeling, Nonlinear
Elasto-Dynamics and Stability.

E-mail: gurmail@civil.iitd.ac.in
Phone: +91-11-2659-1207



J. Uma Maheswari
Assistant Professor
Civil Engineering
Department,
IIT Delhi

Areas of Interest: Design Management,
Matrix-Based Design Techniques,
Construction Project Management,
Automation.

E-mail: umapaul@civil.iitd.ac.in
Phone: +91-11-2659-1189

(continued)

(continued)

Organizing Committee



K.C. Iyer
Professor
Civil Engineering
Department,
IIT Delhi

Areas of Interest: Financial Management, Project Risks, Legal Issues in Business, Infrastructure Project Management.

E-mail: kciyer@civil.iitd.ac.in
Phone: +91-11-2659-1209



K.N. Jha
Associate Professor
Civil Engineering
Department,
IIT Delhi

Areas of Interest: Construction Project Management, Project Success Factor, Asset Management, Schedule Cost Quality and Safety.

E-mail: knjha@civil.iitd.ac.in
Phone: +91-11-2659-6255

(continued)

(continued)

Organizing Committee



Shashank Bishnoi
Assistant Professor
Civil Engineering
Department,
IIT Delhi

Areas of Interest: Experimental and Numerical Studies into Hydration of Cement and Supplementary Cementitious Materials, Sustainability, Durability, Repairs and Life-Cycle Costs of Concrete Structures.

E-mail: shashank.bishnoi@civil.iitd.ac.in
Phone: +91-11-2659-1185



Supratic Gupta
Assistant Professor
Civil Engineering
Department,
IIT Delhi

Areas of Interest: Concrete Mechanics, Self-Compacting Concrete, Constitutive Modeling, Analytical and Experimental Research of RC and Prestressed Concrete Bridges, Bamboo Concrete Composites.

E-mail: supratic@civil.iitd.ac.in
Phone: +91-11-2659-6307

(continued)

(continued)

Organizing Committee



Suresh Bhalla
Associate Professor
Civil Engineering
Department,
IIT Delhi

Areas of Interest: Smart Material and Structures, Structural Health Monitoring, Non-destructive Evaluation, Biomechanics, Engineered Bamboo Structures.

E-mail: sbhalla@civil.iitd.ac.in
Phone: +91-11-2659-1040



T.K. Datta
Emeritus Professor
Civil Engineering
Department,
IIT Delhi

Areas of Interest: Earthquake Engineering, Wind Engineering, Offshore Dynamics, Structural Control.

E-mail: tkdatta@civil.iitd.ac.in
Phone: +91-11-2659-1184

(continued)

(continued)

Organizing Committee

Organizing
Secretary



Vasant Matsagar
Associate Professor
Civil Engineering
Department,
IIT Delhi

Areas of Interest: Multi-Hazard Protection of Structures, Earthquake, Wind, Blast and Fire Engineering, Fiber Reinforced Polymer Composites.

E-mail: matsagar@civil.iitd.ac.in

Phone: +91-11-2659-1225

Sub-Committee

Members



Arun Kumar
Assistant Professor
Civil Engineering
Department,
IIT Delhi

Areas of Interest: Human Health Risk Assessment, Nanoparticles, Water Treatment, Uncertainty Analysis.

E-mail: arunku@civil.iitd.ac.in
Phone: +91-11-2659-1166



Aravind K. Swamy
Assistant Professor
Civil Engineering
Department,
IIT Delhi

Areas of Interest: Modeling Behaviour of Asphaltic Material, Continuum Damage Modeling, Pavement Engineering, Rheology, Recycling of Pavement Materials.

E-mail: akswamy@civil.iitd.ac.in
Phone: +91-11-2659-1191

(continued)

(continued)

Sub-Committee



Bappaditya Manna
Assistant Professor
Civil Engineering
Department,
IIT Delhi

Areas of Interest: Dynamics Soil-Pile Interaction, Pile Foundation, Machine Foundation, Stability of Reinforced Slopes.

E-mail: bmanna@civil.iitd.ac.in
Phone: +91-11-2659-1211




C.T. Dhanya
Assistant Professor
Civil Engineering
Department,
IIT Delhi

Areas of Interest: Hydro-Climatological Modeling, Nonlinear Dynamics and Chaos Theory, Stochastic Hydrology, Optimization in Water Resource Systems, Data Mining in Hydrology, Water Resources Management.

E-mail: dhanya@civil.iitd.ac.in
Phone: +91-11-2659-7328

(continued)

(continued)

Sub-Committee	
	<p>Areas of Interest: Aerosol Monitoring Characterization and Modeling, Local Air Quality, Health and Climate Effects.</p> <p>E-mail: gazala@civil.iitd.ac.in Phone: +91-11-2659-1192</p>
<p>Gazala Habib Assistant Professor Civil Engineering Department, IIT Delhi</p>	<p>Areas of Interest: Soil Dynamics and Earthquake Engineering, Pile Foundations, Deep Excavations in Urban Areas, Problematic Soils and Ground Improvement.</p> <p>E-mail: araman@civil.iitd.ac.in Phone: +91-11-2659-1188</p>



R. Ayothiraman
Associate Professor
Civil Engineering
Department,
IIT Delhi

(continued)

(continued)

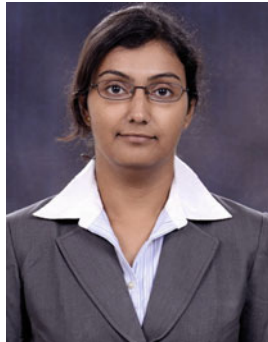
Sub-Committee



Sumedha Chakma
Assistant Professor
Civil Engineering
Department,
IIT Delhi

Areas of Interest: Settlement in Landfills, Gas Generation from Landfills, GIS Based Landfill Management, Bioreactor Landfill, Infiltration Characteristics of Different Vegetation and Land Use, Watershed Management, Water Contamination and Remediation, Open Channel Hydraulics, Contaminant Hydrology.

E-mail: chakma@civil.iitd.ac.in
Phone: +91-11-2659-1263



Tanusree Chakraborty
Assistant Professor
Civil Engineering
Department,
IIT Delhi

Areas of Interest: Foundation Engineering, Blast Loading in Soil, Soil Plasticity and Constitutive Modeling, Soil-Structure Interaction and Underground Construction in Soil and Rock.

E-mail: tanusree@civil.iitd.ac.in
Phone: +91-11-2659-1268

Contents

Volume 1

Part I Computational Solid/Structural Mechanics

On Accurate Analyses of Rectangular Plates Made of Functionally Graded Materials	3
D.K. Jha, Tarun Kant and R.K. Singh	
Static and Free Vibration Analysis of Functionally Graded Skew Plates Using a Four Node Quadrilateral Element	15
S.D. Kulkarni, C.J. Trivedi and R.G. Ishi	
Flexure Analysis of Functionally Graded (FG) Plates Using Reddy's Shear Deformation Theory	25
P.S. Lavate and Sandeep Shiyekar	
2D Stress Analysis of Functionally Graded Beam Under Static Loading Condition	35
Sandeep S. Pendhari, Tarun Kant and Yogesh Desai	
Equivalent Orthotropic Plate Model for Fibre Reinforced Plastic Sandwich Bridge Deck Panels with Various Core Configurations	43
Bibekananda Mandal and Anupam Chakrabarti	
Experimental and Numerical Modal Analysis of Laminated Composite Plates with GFRP	55
Dhiraj Biswas and Chaitali Ray	

Vibration Analysis of Laminated Composite Beam with Transverse Cracks	67
S. Behera, S.K. Sahu and A.V. Asha	
Non-linear Vibration Analysis of Isotropic Plate with Perpendicular Surface Cracks	77
Gangadhar S. Ramtekkar, N.K. Jain and Prasad V. Joshi	
Vibration and Dynamic Stability of Stiffened Plates with Cutout	95
A.K.L. Srivastava	
On Progressive Failure Study of Composite Hypar Shell Roofs	103
Arghya Ghosh and Dipankar Chakravorty	
First Ply Failure of Laminated Composite Conoidal Shell Roofs Using Geometric Linear and Nonlinear Formulations	113
Kaustav Bakshi and Dipankar Chakravorty	
Stochastic Buckling and First Ply Failure Analysis of Laminated Composite Plate	125
Appaso M. Gadade, Achchhe Lal and B.N. Singh	
Nonlinear Finite Element Bending Analysis of Composite Shell Panels	137
S.N. Patel	
 Part II Thermal Stress Analysis	
Thermal Stress Analysis of Laminated Composite Plates Using Third Order Shear Deformation Theory	149
Moumita Sit, Chaitali Ray and Dhiraj Biswas	
Effect of Degree of Orthotropy on Transverse Deflection of Composite Laminates Under Thermal Load	157
Sanjay Kantrao Kulkarni and Yuwaraj M. Ghugal	
An Accurate Prediction of Natural Frequencies of Sandwich Plates with Functionally Graded Material Core in Thermal Environment Using a Layerwise Theory	171
Shashank Pandey and S. Pradyumna	

Thermoelastic Stress Analysis Perfectly Clamped Metallic Rod Using Integral Transform Technique 181
 G.R. Gandhe, V.S. Kulkarni and Y.M. Ghugal

Part III Mathematical, Numerical, Optimization Techniques

The Emerging Solution for Partial Differential Problems 193
 P.V. Ramana and Vivek Singh

On Derivations of Stress Field in Bi-polar Coordinate Systems 205
 Payal Desai and Tarun Kant

Vibration of Multi-span Thin Walled Beam Due to Torque and Bending Moment 215
 Vinod Kumar Verma

A Convex Optimization Framework for Hybrid Simulation 221
 Mohit Verma, Aikaterini Stefanaki, Mettupalayam V. Sivaselvan, J. Rajasankar and Nagesh R. Iyer

Design Optimization of Steel Members Using Openstaad and Genetic Algorithm. 233
 Purva Mujumdar and Vasant Matsagar

Part IV Blast/Impact Mechanics

A Numerical Study of Ogive Shape Projectile Impact on Multilayered Plates 247
 M.D. Goel

Stochastic Finite Element Analysis of Composite Body Armor 259
 Shivdayal Patel, Suhail Ahmad and Puneet Mahajan

A Progressive Failure Study of E-glass/Epoxy Composite in Case of Low Velocity Impact 273
 Harpreet Singh, Puneet Mahajan and K.K. Namala

Capacity Estimation of RC Slab of a Nuclear Containment Structure Subject to Impact Loading 301
 Hrishikesh Sharma, Santanu Samanta, Katchalla Bala Kishore and R.K. Singh

Finite Element Analysis of Composite Hypar Shell Roof Due to Oblique Impact	313
Sanjoy Das Neogi, Amit Karmakar and Dipankar Chakravorty	
Analysis of Aluminum Foam for Protective Packaging	321
M.D. Goel	
Blast Response Studies on Laced Steel-Concrete Composite (LSCC) Slabs	331
A. Thirumalaiselvi, N. Anandavalli, J. Rajasankar and Nagesh R. Iyer	
Dynamic Analysis of Twin Tunnel Subjected to Internal Blast Loading	343
Rohit Tiwari, Tanusree Chakraborty and Vasant Matsagar	
Performance of Laced Reinforced Geopolymer Concrete (LRGPC) Beams Under Monotonic Loading	355
C.K. Madheswaran, G. Gnanasundar and N. Gopalakrishnan	
Dynamic Analysis of the Effect of an Air Blast Wave on Plate	369
S.V. Totekar and S.N. Madhekar	
Control of Blast-Induced Vibration of Building by Pole Placement and LQG Control Algorithm	381
Sanjukta Chakraborty and Samit Ray-Chaudhuri	
Performance Study of a SMA Bracing System for Control of Vibration Due to Underground Blast Induced Ground Motion	393
Rohan Majumder and Aparna (Dey) Ghosh	
Dynamic Analysis of Curved Tunnels Subjected to Internal Blast Loading	405
Rohit Tiwari, Tanusree Chakraborty and Vasant Matsagar	
Blast: Characteristics, Loading and Computation—An Overview	417
M.D. Goel	
Response of 45 Storey High Rise RCC Building Under Blast Load	435
Z.A.L. Qureshi and S.N. Madhekar	
Dynamic Response of Cable Stayed Bridge Pylon Subjected to Blast Loading	449
P.J. Shukla and C.D. Modhera	

Part V Strengthening and Retrofitting of Structures

Retrofitting of Seismically Damaged Open Ground Storey RCC Framed Building with Geopolymer Concrete 463
 Pinky Merin Philip, C.K. Madheswaran and Eapen Skaria

Evaluation of Shear Strength of RC Columns Strengthened by Concrete Jacketing 483
 M. Komathi and Amlan K. Sengupta

Steel Shear Panels as Retrofitting System of Existing Multi-story RC Buildings: Case Studies 495
 Antonio Formisano and Dipti Ranjan Sahoo

Softened Truss Model for FRP Strengthened RC Members Under Torsion Including Tension Stiffening Effect 513
 Mukesh Kumar Ramancha, T. Ghosh Mondal and S. Suriya Prakash

Part VI Joints/Connections and Structural Behaviour

A Strain Based Non-linear Finite Element Analysis of the Exterior Beam Column Joint. 529
 Shivaji T. Bidgar and Partha Bhattacharya

Numerical Modeling of Compound Element for Static Inelastic Analysis of Steel Frames with Semi-rigid Connections. 543
 M. Bandyopadhyay, A.K. Banik and T.K. Datta

Parallel Flange I-Beam Sections—Theoretical Study and Finite Element Analysis. 559
 Swati Ajay Kulkarni and Gaurang Vesmawala

A Novel Statistical Model for Link Overstrength. 567
 Jaya Prakash Vemuri

An Investigation of the Compressive Strength of Cold-Formed Steel Built up Channel Sections 577
 G. Beulah Gnana Ananthi, G.S. Palani and Nagesh R. Iyer

Shear Behavior of Rectangular Lean Duplex Stainless Steel (LDSS) Tubular Beams with Asymmetric Flanges—A Finite Element Study	587
J.K. Sonu and Konjengbam Darunkumar Singh	
Evaluation of Mean Wind Force Coefficients for High-Rise Building Models with Rectangular Cross-Sections and Aspect Ratio's of 6 and 8	597
A. Abraham, S. Chitra Ganapathi, G. Ramesh Babu, S. Saikumar, K.R.S. Harsha Kumar and K.V. Pratap	
Comparative Analysis of High Rise Building Subjected to Lateral Loads and Its Behavior	613
Deepak B. Suthar, H.S. Chore and P.A. Dode	
 Part VII Offshore Structures and Soil-Structure Interactions	
Variations of Water Particle Kinematics of Offshore TLPS with Perforated Members: Numerical Investigations	629
Srinivasan Chandrasekaran and N. Madhavi	
Force Reduction on Ocean Structures with Perforated Members	647
Srinivasan Chandrasekaran, N. Madhavi and Saravanakumar Sampath	
Influence of Pipeline Specifications and Support Conditions on Natural Frequency of Free Spanning Subsea Pipelines	663
Mrityunjoy Mandal and Pronab Roy	
Stochastic Dynamic Analysis of an Offshore Wind Turbine Considering Soil-Structure Interaction	673
Arundhuti Banerjee, Tanusree Chakraborty and Vasant Matsagar	
Numerical Modelling of Finite Deformation in Geotechnical Engineering	689
T. Gupta, T. Chakraborty, K. Abdel-Rahman and M. Achmus	
Effects of Soil-Structure Interaction on Multi Storey Buildings on Mat Foundation	703
Ankit Kumar Jha, Kumar Utkarsh and Rajesh Kumar	

Effect of Buoyancy on Stitched Raft of Building with Five Basements in Presence of Ground Anchors 717
 D.P. Bhaud and H.S. Chore

Influence of Soil-Structure Interaction on Pile-Supported Machine Foundations 731
 Karmegam Rajkumar, R. Ayothiraman and Vasant Matsagar

Author Index 743

Subject Index 745

Volume 2

Part VIII Seismology and Ground Motion Characteristics

Ground Motion Scenario for Hypothetical Earthquake (M_w 8.1) in Indo-Burmese Subduction at Imphal City 751
 Kumar Pallav, S.T.G. Raghukanth and Konjengbam Darunkumar Singh

Development of Surface Level Probabilistic Seismic Hazard Map of Himachal Pradesh 765
 Muthuganeisan Prabhu and S.T.G. Raghukanth

Simulation of Near Fault Ground Motion in Delhi Region 779
 Hemant Shrivastava, G.V. Ramana and A.K. Nagpal

Interaction Analysis of Space Frame-Shear Wall-Soil System to Investigate Forces in the Columns Under Seismic Loading 789
 D.K. Jain and M.S. Hora

Seismic Performance of Buildings Resting on Sloping Ground 803
 R.B. Khadiranaikar and Arif Masali

Part IX Earthquake Response of Steel, Concrete and Masonry Structures

Seismic Response Control of Piping System with Supplemental Devices 817
 Praveen Kumar and R.S. Jangid

A Case Study to Report the Advantage of Using Signed Response Quantities in Response Spectrum Analysis	831
Sanjib Das and Santanu Bhanja	
Performance of Medium-Rise Buckling-Restrained Braced Frame Under Near Field Earthquakes.	841
Ahmad Fayeque Ghowsi and Dipti Ranjan Sahoo	
Effect of Brace Configurations on Seismic Behaviour of SCBFs	855
P.C. Ashwin Kumar and Dipti Ranjan Sahoo	
Seismic Response of Moment Resisting Frame with Open Ground Storey Designed as per Code Provisions	869
Subzar Ahmad Bhat, Saraswati Setia and V.K. Sehgal	
Evaluation of Models for Joint Shear Strength of Beam–Column Subassemblages for Seismic Resistance	885
L. Vishnu Pradeesh, Saptarshi Sasmal, Kanchana Devi and K. Ramanjaneyulu	
Seismic Performance of Flat Slab Buildings	897
Subhajit Sen and Yogendra Singh	
Experimental Investigations on Seismic Performance of Gravity Load Designed and Corrosion Affected Beam Column Sub-assemblages	909
A. Kanchana Devi, Saptarshi Sasmal and K. Ramanjaneyulu	
Seismic Performance of Eccentrically Braced Frame (EBF) Buildings.	921
Abhishek Singhal and Yogendra Singh	
Influence of Joint Panel Zone on Seismic Behaviour of Beam-to-Column Connections	933
Arnav Anuj Kasar, Rupen Goswami, S.D. Bharti and M.K. Shrimali	
Performance Based Seismic Design of Reinforced Concrete Symmetrical Building	945
P.D. Pujari and S.N. Madhekar	
Response of R/C Asymmetric Community Structures Under Near-Fault Motion.	955
Subhayan Bhaumik and Prithwish Kumar Das	

Comparison of Seismic Vulnerability of Buildings Designed for Higher Force Versus Higher Ductility 963
 Chandu Smita and Ratnesh Kumar

Studies on Identifying Critical Joints in RC Framed Building Subjected to Seismic Loading 977
 Pradip Paul, Prithwish Kumar Das and Pradip Sarkar

Performance Based Seismic Design of Semi-rigid Steel Concrete Composite Multi-storey Frames 989
 R. Senthil Kumar and S.R. Satish Kumar

Seismic Performance of Stairs as Isolated and Built-in RC Frame Building 1001
 Zaid Mohammad, S.M. Talha and Abdul Baqi

Seismic Analysis of a 275 m Tall RCC Multi-flue Chimney: A Comparison of IS Code Provisions and Numerical Approaches 1015
 Rajib Sarkar, Devendra Shrimal and Sudhanshu Goyal

Finite Element Simulation of Earthquake Resistant Brick Masonry Building Under Shock Loading 1027
 A. Joshua Daniel and R.N. Dubey

Seismic Damage Evaluation of Unreinforced Masonry Buildings in High Seismic Zone Using the Nonlinear Static Method 1039
 Abhijit Sarkar, Lipika Halder and Richi Prasad Sharma

Design Guidelines for URM Infills and Effect of Construction Sequence on Seismic Performance of Code Compliant RC Frame Buildings 1055
 Putul Haldar, Yogendra Singh and D.K. Paul

Part X Seismic Pounding and Mitigation in Adjacent Structures

Experimental and Numerical Study on Pounding of Structures in Series 1073
 Saher El-Khoriby, Ayman Seleemah, Hytham Elwardany and Robert Jankowski

Dynamic Response of Adjacent Structures Coupled by Nonlinear Viscous Damper 1091
 C.C. Patel

Comparative Study of Seismically Excited Coupled Buildings with VF Damper and LR Bearing	1103
S.M. Dumne, S.D. Bharti and M.K. Shrimali	
Pounding in Bridges with Passive Isolation Systems Subjected to Earthquake Ground Acceleration	1117
Y. Girish Singh and Diptesh Das	
Random Response Analysis of Adjacent Structures Connected by Viscous Damper	1129
C.C. Patel	
 Part XI Hydro-Dynamics and Fluid-Structure Interaction	
Dynamic Analysis of a Mega-Float	1143
K.S. Arunraj and R. Panner Selvam	
Coupled Acoustic-Structure Interaction in Cylindrical Liquid Storage Tank Subjected to Bi-directional Excitation	1155
Aruna Rawat, Vasant Matsagar and A.K. Nagpal	
Behaviour of Elevated Water Storage Tanks Under Seismic Events	1167
M.V. Waghmare, S.N. Madhekar and Vasant Matsagar	
Assessing Seismic Base Isolation Systems for Liquid Storage Tanks using Fragility Analysis	1177
Sandip Kumar Saha, Vasant Matsagar and Arvind K. Jain	
Hydrodynamic Effects on a Ground Supported Structure	1193
Kuncharapu Shiva and V.S. Phanikanth	
Seismic Behaviour of R/C Elevated Water Tanks with Shaft Stagings: Effect of Biaxial Interaction and Ground Motion Characteristics	1205
Aparna Roy and Rana Roy	
 Part XII Dynamic Vibration Control of Structures	
Steel Hysteretic Damper Featuring Displacement Dependent Hardening for Seismic Protection of Structures	1219
Murat Dicleli and Ali Salem Milani	

Seismic Performance of Shear-Wall and Shear-Wall Core Buildings Designed for Indian Codes 1229
 Mitesh Surana, Yogendra Singh and Dominik H. Lang

A Study on the Design Parameters of the Compliant LCD for Structural Vibration Control Under Near Fault Earthquakes. 1243
 Achintya Kumar Roy and Aparna (Dey) Ghosh

Comparison of Performance of Different Tuned Liquid Column Dampers (TLCDs) 1257
 Meghana Kalva and Samit Ray-Chaudhuri

Seismic Control of Benchmark Cable-Stayed Bridges Using Variable Friction Pendulum Isolator. 1271
 Purnachandra Saha

Energy Assessment of Friction Damped Two Dimensional Frame Subjected to Seismic Load. 1283
 Ankit Bhardwaj, Vasant Matsagar and A.K. Nagpal

Seismic Response Control of Multi-story Asymmetric Building Installed with Dampers 1295
 Snehal V. Mevada

Seismic Protection of Soft Storey Buildings Using Energy Dissipation Device 1311
 Subhransu Sekhar Swain and Sanjaya K. Patro

Significance of Elastomeric Bearing on Seismic Response Reduction in Bridges 1339
 E.T. Abey, T.P. Somasundaran and A.S. Sajith

Performance of Seismic Base-Isolated Building for Secondary System Protection Under Real Earthquakes 1353
 P.V. Mallikarjun, Pravin Jagtap, Pardeep Kumar and Vasant Matsagar

Part XIII Bridge Engineering and Seismic Response Control

Nonstationary Response of Orthotropic Bridge Deck to Moving Vehicle 1367
 Prasenjit Paul and S. Talukdar

Seismic Performance of Benchmark Highway Bridge Installed with Passive Control Devices 1377
 Suhasini N. Madhekar

Estimation of Seismic Capacity of Reinforced Concrete Skew Bridge by Nonlinear Static Analysis 1391
 E. Praneet Reddy and Kaustubh Dasgupta

Part XIV Wind Induced Vibration Response of Structures

Shape Memory Alloy-Tuned Mass Damper (SMA-TMD) for Seismic Vibration Control 1405
 Sutanu Bhowmick and Sudib K. Mishra

Wind Analysis of Suspension and Cable Stayed Bridges Using Computational Fluid Dynamics. 1419
 B.G. Birajdar, A.D. Shingana and J.A. Jain

Improved ERA Based Identification of Flutter Derivatives of a Thin Plate 1431
 M. Keerthana and P. Harikrishna

Along and Across Wind Effects on Irregular Plan Shaped Tall Building 1445
 Biswarup Bhattacharyya and Sujit Kumar Dalui

Seismic and Wind Response Reduction of Benchmark Building Using Viscoelastic Damper 1461
 Praveen Kumar and Barun Gopal Pati

Optimum Tuned Mass Damper for Wind and Earthquake Response Control of High-Rise Building 1475
 Said Elias and Vasant Matsagar

Part XV Statistical, Probabilistic and Reliability Approaches in Structural Dynamics

Tuned Liquid Column Damper in Seismic Vibration Control Considering Random Parameters: A Reliability Based Approach. 1491
 Rama Debbarma and Subrata Chakraborty

Robust Design of TMD for Vibration Control of Uncertain Systems Using Adaptive Response Surface Method 1505
 Amit Kumar Rathi and Arunasis Chakraborty

A Hybrid Approach for Solution of Fokker-Planck Equation 1519
 Souvik Chakraborty and Rajib Chowdhury

On Parameter Estimation of Linear Time Invariant (LTI) Systems Using Bootstrap Filters 1529
 Anshul Goyal and Arunasis Chakraborty

Seismic Analysis of Weightless Sagging Elasto-flexible Cables 1543
 Pankaj Kumar, Abhijit Ganguli and Gurmail S. Benipal

Damage Detection in Beams Using Frequency Response Function Curvatures Near Resonating Frequencies 1563
 Subhajit Mondal, Bidyut Mondal, Anila Bhutia and Sushanta Chakraborty

Dynamic Response of Block Foundation Resting on Layered System Under Coupled Vibration 1575
 Renuka Darshyamkar, Bappaditya Manna and Ankesh Kumar

Interior Coupled Structural Acoustic Analysis in Rectangular Cabin Structures 1587
 Sreyashi Das (Pal), Sourav Chandra and Arup Guha Niyogi

Experimental and Numerical Analysis of Cracked Shaft in Viscous Medium at Finite Region 1601
 Adik R. Yadao and Dayal R. Parhi

Author Index 1611

Subject Index 1613

Volume 3

Part XVI Geopolymers

Mix Design of Fly Ash Based Geopolymer Concrete 1619
 Subhash V. Patankar, Yuwaraj M. Ghugal and Sanjay S. Jamkar

Effect of Delay Time and Duration of Steam Curing on Compressive Strength and Microstructure of Geopolymer Concrete	1635
Visalakshi Talakokula, R. Singh and K. Vysakh	
Behaviour of Geopolymer Concrete Under Static and Cyclic Loads . . .	1643
Sulaem Musaddiq Laskar, Ruhul Amin Mozumder and Biswajit Roy	
Biofibre Reinforced Concrete	1655
T. Manasa, T. Parvej, T. SambaSiva Rao, M. Hemambar Babu and Sunil Raiyani	
Experimental Investigation and Numerical Validation on the Effect of NaOH Concentration on GGBS Based Self-compacting Geopolymer Concrete	1673
J.S. Kalyana Rama, N. Reshmi, M.V.N. Sivakumar and A. Vasan	
Performance Studies on Geopolymer Based Solid Interlocking Masonry Blocks.	1687
M. Sudhakar, George M. Varghese and C. Natarajan	
 Part XVII Cement and Pozzolana	
A Review on Studies of Fracture Parameters of Self-compacting Concrete	1705
J. Sri Kalyana Rama, M.V.N. Sivakumar, A. Vasan, Chirag Garg and Shubham Walia	
Use of Marble Dust as Clinker Replacement in Cements	1717
Vineet Shah and Shashank Bishnoi	
High Level Clinker Replacement in Ternary Limestone-Calcined Clay-Clinker Cement.	1725
Sreejith Krishnan and Shashank Bishnoi	
Development of Mix Proportions for Different Grades of Metakaolin Based Self-compacting Concrete	1733
Vaishali G. Ghorpade, Koneru Venkata Subash and Lam Chaitanya Anand Kumar	
Evaluating the Efficiency Factor of Fly Ash for Predicting Compressive Strength of Fly Ash Concrete	1747
Khuito Murumi and Supratic Gupta	

Part XVIII Aggregates for Concrete

Use of Efficiency Factors in Mix Proportioning of Fly Ash Concrete 1761
Santanu Bhanja

Study on Some Engineering Properties of Recycled Aggregate Concrete with Flyash 1773
M. Surya, P. Lakshmy and V.V.L. Kanta Rao

Influence of Rubber on Mechanical Properties of Conventional and Self Compacting Concrete 1785
M. Mishra and K.C. Panda

Investigation of the Behaviour of Concrete Containing Waste Tire Crumb Rubber 1795
R. Bharathi Murugan and C. Natarajan

Study on the Properties of Cement Concrete Using Manufactured Sand 1803
M.R. Lokeswaran and C. Natarajan

Part XIX Concrete, Steel and Durability

Characterization of Recycled Aggregate Concrete 1813
S.R. Suryawanshi, Bhupinder Singh and Pradeep Bhargava

Durability of High Volume Flyash Concrete 1823
M. Vaishnavi and M. Kanta Rao

Numerical Estimation of Moisture Penetration Depth in Concrete Exposed to Rain—Towards the Rationalization of Guidelines for Durable Design of Reinforced Concrete in Tropics 1837
Kaustav Sarkar and Bishwajit Bhattacharjee

Acid, Alkali and Chloride Resistance of Early Age Cured Silica Fume Concrete 1849
A.P. Shetti and B.B. Das

Influence of Sea Water on Strength and Durability Properties of Concrete 1863
T. Jena and K.C. Panda

Corrosion Behavior of Reinforced Concrete Exposed to Sodium Chloride Solution and Composite Sodium Chloride-Sodium Sulfate Solution	1875
Bulu Pradhan	
Service Life Prediction Model for Reinforced Concrete Structures Due to Chloride Ingress	1883
D.R. Kamde, B. Kondraivendhan and S.N. Desai	
Electrochemical Behaviour of Steel in Contaminated Concrete Powder Solution Extracts	1895
Fouzia Shaheen and Bulu Pradhan	
 Part XX Fiber Reinforced Concrete (FRC)	
Parametric Study of Glass Fiber Reinforced Concrete	1909
Shirish Vinayak Deo	
An Experimental Approach to Investigate Effects of Curing Regimes on Mechanical Properties and Durability of Different Fibrous Mortars	1917
Damyanti Badagha and C.D. Modhera	
 Part XXI Low-Cost Housing	
A Scientific Approach to Bamboo-Concrete House Construction	1933
Ashish Kumar Dash and Supratic Gupta	
A Review of Low Cost Housing Technologies in India	1943
Vishal Puri, Pradipta Chakraborty and Swapan Majumdar	
 Part XXII Fiber Reinforced Polymer (FRP) in Structures	
Bond-Slip Response of FRP Sheets or Plates Bonded to Reinforced Concrete Beam Under Dynamic Loading	1959
Mohammad Makki Abbass, Vasant Matsagar and A.K. Nagpal	
Assessment of Debonding Load for RC Beam Strengthened with Pre-designed CFRP Strip Mechanism	1971
Mitali R. Patel, Tejendra G. Tank, S.A. Vasanwala and C.D. Modhera	

Performance Assessment of RC Beams with CFRP and GFRP Sheets 1987
Chennakesavula Venkateswarlu and Chidambarathanu Natarajan

Strain Analysis of RC T-beams Strengthened in Shear with Variation of U-wrapped GFRP Sheet and Transverse Steel 2001
K.C. Panda, S.K. Bhattacharyya and S.V. Barai

Structural Response of Thin-Walled FRP Laminated Mono-symmetrical I-Beams 2011
S.B. Singh and Himanshu Chawla

Performance of the FRPC Rehabilitated RC Beam-Column Joints Subjected to Cyclic Loading 2025
Abhijit Mukherjee and Kamal Kant Jain

Is GFRP Rebar a Potential Replacement for Steel Reinforcement in Concrete Structures? 2043
P. Gandhi, D.M. Pukazhendhi, S. Vishnuvardhan, M. Saravanan and G. Raghava

Flexural Behaviour of Damaged RC Beams Strengthened with Ultra High Performance Concrete. 2057
Prabhat Ranjan Prem, A. Ramachandra Murthy, G. Ramesh, B.H. Bharatkumar and Nagesh R. Iyer

Concrete Jacketing of Deficient Exterior Beam Column Joints with One Way Spiral Ties 2071
K.R. Bindhu, Mohana and S. Sivakumar

Part XXIII Concrete Filled Steel Tubes/Structures

Experimental Investigation on Uniaxial Compressive Behaviour of Square Concrete Filled Steel Tubular Columns. 2087
N. Umamaheswari and S. Arul Jayachandran

Comparative Study on Response of Boiler Supporting Structure Designed Using Structural Steel I-Columns and Concrete Filled Square Steel Tubular Columns 2103
T. Harikrishna and Kaliyamoorthy Baskar

Effect of Concrete Strength on Bending Capacity of Square and Rectangular CFST Elements 2117
 P.K. Gupta and S.K. Katariya

Effect of Tension Stiffening on Torsional Behaviour of Square RC Columns 2131
 T. Ghosh Mondal and S. Suriya Prakash

Part XXIV Concrete Structures

Estimation of Fundamental Natural Period of RC Frame Buildings with Structural Walls 2147
 Pratik Raj and Kaustubh Dasgupta

Enhancement of Lateral Capacity of Damaged Non-ductile RC Frame Using Combined-Yielding Metallic Damper 2157
 Romanbabu M. Oinam and Dipti Ranjan Sahoo

Comparative Modelling of Infilled Frames: A Descriptive Review and Analysis 2169
 Shujaat Hussain Buch and Dilawar Mohammad Bhat

Pushover Analysis of Symmetric and Asymmetric Reinforced Concrete Buildings 2185
 V.K. Sehgal and Ankush Mehta

Challenges Posed by Tall Buildings to Indian Codes 2197
 Ashok K. Jain

Influence of Openings on the Structural Response of Shear Wall 2209
 G. Muthukumar and Manoj Kumar

Ductility of Concrete Members Partially Prestressed with Unbonded and External Tendons 2241
 R. Manisekar

A Full Scale Fire Test on a Pre Damaged RC Framed Structure 2259
 Asif H. Shah, Umesh K. Sharma, Pradeep Bhargava, G.R. Reddy, Tarvinder Singh and Hitesh Lakhani

Effect of Temperature Load on Flat Slab Design in Thermal Analysis 2275
 Sanjay P. Shirke, H.S. Chore and P.A. Dode

Behaviour of Two Way Reinforced Concrete Slab at Elevated Temperature 2285
 N. Raveendra Babu, M.K. Haridharan and C. Natarajan

Experimental Investigations on Behaviour of Shear Deficient Reinforced Concrete Beams Under Monotonic and Fatigue Loading 2299
 Nawal Kishor Banjara, K. Ramanjaneyulu, Saptarshi Sasmal and V. Srinivas

Reverse Cyclic Tests on High Performance Cement Concrete Shear Walls with Barbells 2309
 N. Ganesan, P.V. Indira and P. Seenaa

Investigation of Shear Behaviour of Vertical Joints Between Precast Concrete Wall Panels. 2323
 Aparup Biswal, A. Meher Prasad and Amlan K. Sengupta

Experimental Evaluation of Performance of Dry Precast Beam Column Connection 2333
 Chintan B. Naik, Digesh D. Joshi and Paresh V. Patel

Behaviour of Precast Beam-Column Stiffened Short Dowel Connections Under Cyclic Loading. 2343
 R. Vidjeapriya, N. Mahamood ul Hasan and K.P. Jaya

Stability of Highly Damped Concrete Beam-Columns 2355
 Mamta R. Sharma, Arbind K. Singh and Gurmail S. Benipal

Part XXV Steel Structures

Ductility Demand on Reduced-Length Buckling Restrained Braces in Braced Frames 2373
 Muhamed Safeer Pandikkadavath and Dipti Ranjan Sahoo

Stress Concentration Factor in Tubular to a Girder Flange Joint: A Numerical and Experimental Study 2385
 Dikshant Singh Saini and Samit Ray-Chaudhuri

Studies on Fatigue Life of Typical Welded and Bolted Steel Structural Connections 2397
 G. Raghava, S. Vishnuvardhan, M. Saravanan and P. Gandhi

Effect of Gap on Strength of Fillet Weld Loaded in Out-of-Plane Bending 2409
 Pathipaka Sachin and A.Y. Vyavahare

Strength Comparison of Fixed Ended Square, Flat Oval and Circular Stub LDSS Columns 2417
 Khwairakpam Sachidananda and Konjengbam Darunkumar Singh

Part XXVI Masonry Structures

Non-linear Behavior of Weak Brick-Strong Mortar Masonry in Compression 2427
 Syed H. Basha and Hemant B. Kaushik

Performance of Hollow Concrete Block Masonry Under Lateral Loads 2435
 Shujaat Hussain Buch and Dilawar Mohammad Bhat

Feasibility of Using Compressed Earth Block as Partition Wall 2445
 Md. Kamruzzaman Shohug, Md. Jahangir Alam and Arif Ahmed

Structural Behavior of Rectangular Cement-Stabilized Rammed Earth Column Under Compression 2459
 Deb Dulal Tripura and Konjengbam Darunkumar Singh

Interaction Study on Interlocking Masonry Wall Under Simultaneous In-Plane and Out-of-Plane Loading 2471
 M. Sudhakar, M.P. Raj and C. Natarajan

Part XXVII Bridge Structures

Effect of Overweight Trucks on Fatigue Damage of a Bridge. 2483
 Vasvi Aggarwal and Lakshmy Parameswaran

Bending of FRP Bridge Deck Under the Combined Effect of Thermal and Vehicle Load. 2493
 Bibekananda Mandal and Chaitali Ray

Low Cycle Fatigue Effects in Integral Bridge Steel H-Piles Under Earthquake Induced Strain Reversals. 2505
 M. Dicleli and S. Erhan

Part XXVIII Reliability and Fragility

Confidence Bounds on Failure Probability Using MHDMMR 2515
 A.S. Balu and B.N. Rao

**Stochastic Simulation Based Reliability Analysis with
 Multiple Performance Objective Functions** 2525
 Sahil Bansal and Sai Hung Cheung

**Accident Modelling and Risk Assessment of Oil and Gas
 Industries** 2533
 Srinivasan Chandrasekaran and A. Kiran

**Review of Evaluation of Uncertainty in Soil Property Estimates
 from Geotechnical Investigation** 2545
 Ranjan Kumar and Kapilesh Bhargava

**Comparison of Damage Index and Fragility Curve of RC
 Structure Using Different Indian Standard Codes** 2551
 Tathagata Roy and Pankaj Agarwal

Part XXIX Non-Destructive Test (NDT) and Damage Detection

**Evaluation of Efficiency of Non-destructive Testing Methods
 for Determining the Strength of Concrete Damaged by Fire** 2567
 J.S. Kalyana Rama and B.S. Grewal

**Damage Detection in Structural Elements Through Wave
 Propagation Using Weighted RMS** 2579
 T. Jothi Saravanan, Karthick Hari, N. Prasad Rao and N. Gopalakrishnan

The Health Monitoring Prescription by Novel Method 2587
 P.V. Ramana, Surendra Nath Arigela and M.K. Srimali

**Structural Damage Identification Using Modal Strain
 Energy Method** 2599
 V.B. Dawari, P.P. Kamble and G.R. Vesmawala

**New Paradigms in Piezoelectric Energy Harvesting
 from Civil-Structures** 2609
 Naveet Kaur and Suresh Bhalla

Experimental Strain Sensitivity Investigations on Embedded PZT Patches in Varying Orientations 2615
Prateek Negi, Naveet Kaur, Suresh Bhalla and Tanusree Chakraborty

Fundamental Mode Shape to Localize Delamination in Cantilever Composite Plates Using Laser Doppler Vibrometer. 2621
Koushik Roy, Saurabh Agrawal, Bishakh Bhattacharya and Samit Ray-Chaudhuri

Efficiency of the Higher Mode Shapes in Structural Damage Localization. 2635
Gourab Ghosh and Samit Ray-Chaudhuri

Author Index 2649

Subject Index 2653

Part VIII
Seismology and Ground Motion
Characteristics

Ground Motion Scenario for Hypothetical Earthquake (M_w 8.1) in Indo-Burmese Subduction at Imphal City

Kumar Pallav, S.T.G. Raghukanth
and Konjengbam Darunkumar Singh

Abstract In this paper, variation of ground motion for Imphal city with respect to synthetically generated 10 samples of earthquake (M_w 8.1) that occurred in Indo-Burmese subduction zone (very near to Imphal) is presented based on finite-fault seismological model combined with equivalent linear site response analyses. For all 10 sample earthquake events, mean and standard deviation of surface level spectral ground acceleration at peak ground acceleration (PGA) and natural periods of 0.3 and 1 s have been reported in the form of contour maps. These maps can be used as first hand information for administration, engineers, and planners to identify vulnerable areas of Imphal city.

Keywords Ground acceleration · Earthquake · Seismology · Soil investigation · Faults · Site response · Stochastic

1 Introduction

The Imphal city ($24^\circ 48' N$, $93^\circ 56' E$), the capital of Manipur state, located in the Northeastern (NE) region of India, is considered as one of the most severe seismically active regions in the world (Fig. 1). In last 150 years, this region had experience more than 2,400 earthquakes of magnitude (M_w) greater than 4.0. The origin of these earthquakes owes to the crustal as well as the subduction zones, both of which are in the closer to (within a radius of 300 km) Imphal city. Oldham [23] and Nandy [21] has reported some of the past earthquakes that had caused massive

K. Pallav (✉)

Department of Civil Engineering, Motilal Nehru National Institute of Technology Allahabad, Allahabad, India

S.T.G. Raghukanth

Department of Civil Engineering, India Institute of Technology Madras, Chennai, India

K.D. Singh

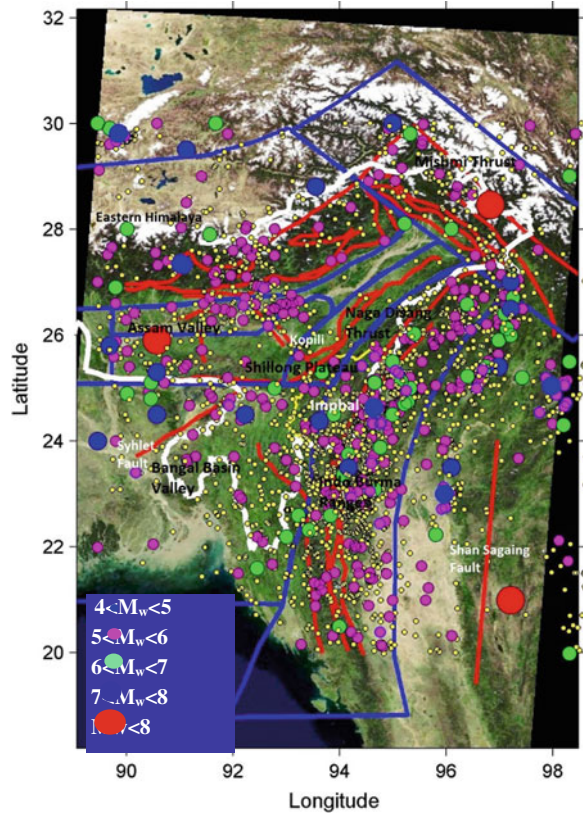
Department of Civil Engineering, Indian Institute of Technology Guwahati, Guwahati, India

© Springer India 2015

V. Matsagar (ed.), *Advances in Structural Engineering*,

DOI 10.1007/978-81-322-2193-7_59

Fig. 1 Seismotectonic map of NE India along with epicenters (1866–2013) geography of Imphal city



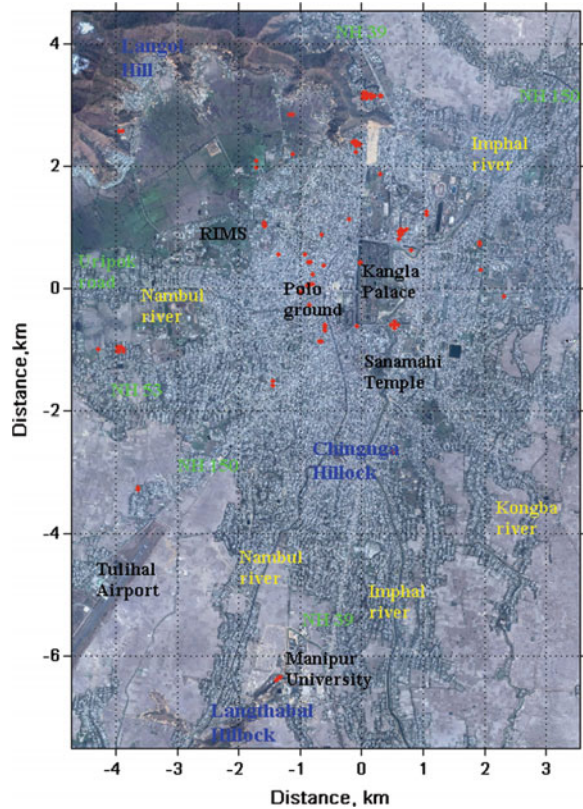
damages to life and property in this region. Unfortunately, the earthquake happened prior to 1869, there was no such documentation of damages for Imphal City. Sarangthem [27] had reported extensive details of 1869 earthquake for magnitude M_w 7.5 occurred at Kopili Fault. Manichandra (2007, Personal communication, Manipur University) has discussed about series of earthquakes that followed viz., 1947, 1950 and 1988 earthquake at Eastern Himalaya, Mishmi tectonic block and Indo-Burmese subduction zone respectively, damages were also observed in Imphal city. In the 1947 earthquake of magnitude M_w 7.9, there were reports of wall cracking, rolling of cooking pots, movements of bed etc. in Imphal city. Ningthoukhongjam [22] gives insight of 15th August 1950 earthquake (M_w 8.6), which occurred in the Mishmi tectonic block, wall cracks appeared in many buildings, temple bells rang due to vibrations, sloshing of Loktak (the biggest fresh water lake in eastern India) water surface was observed. In the 6th August 1988 earthquake (M_w 7.2) which occurred in the Indo-Burma Ranges (IBR), some four storied buildings in both Paona and Thangal markets tilted approximately at 1:240 slope, wall cracked, many doors and windows got jammed. The Indian Standard Code of practice for earthquake resistant design of structures, IS 1893 (2002), has identified

the NE region of India including Imphal city as a severe seismic hazard zone (i.e. zone V). In view of this, it would be of interest to estimate the ground motions due to hypothetical earthquake of M_w 8.1 in Indo-Burmese subduction zone near to Imphal city. It will be interesting for engineering purposes to know the variation of ground motion for such scenario earthquake.

The present work focuses on the estimation of mean and standard deviation the surface level spectral acceleration at Imphal city due to M_w 8.1 earthquake that may occur closer to Imphal city. The modified one-dimensional stochastic finite fault model proposed by Motazedian and Atkinson [20] is used for simulating the ground motion. Further inputs parameter viz., source, fault, and medium parameters are taken from previous work [16, 21, 26]. Then, using nonlinear site response analysis proposed by Idriss and Sun [11] the (de)amplification at the ground surface are obtained for all 122 sites. The estimated ground motion at surface are plotted in the form of mean and standard deviation of PGA and spectral acceleration contour maps for Imphal City for M_w 8.1 earthquake.

Imphal city is an integral part of Imphal Valley, which is also known as Imphal/Manipur basin located in the central part of the Manipur state. The valley has its width of about 30–35 km along east-west and a length of about 60–65 km along north-south direction and orients itself along NNW-SSE forms a oval shape valley. Physiographically, Imphal valley is a flat land surrounded by Patkai hills on the north and north-east and Manipur hills, Lushai hills, Naga hills and Chin hills on the south forming an integral part of Indo-Burma ranges [10, 17]. Agarwal and Shukla [1], based on geomorphological feature, had classified the valley into five units: (1) moderate to high structural cum denudational hills, which can be seen as the hills and mountains surrounding the valley, (2) residual hills composing of hillocks and hills which are scattered in the valley (e.g. Langol hill, Chingna hill, etc.), (3) piedmont plain features along the foothills, (4) older alluvial plains of alluvium deposits near foothills of Imphal valley, and (5) younger alluvial plains having lower elevation than the older alluvial plains and mostly flat in nature. The Disangs and Barails forms a major flysch basin in the tectonostratigraphy of Indo-Burma Ranges (IBR). Regarding the formation of Imphal valley, the hypothesis of Fluvio-lacustrine origin (with possible effects of subsequent earthquakes) is generally accepted (e.g. Ibotobmi [10]). As per author's knowledge the bed rock profile has not been mapped; however MESTEC (2007) report suggest that the average thickness of alluvium is at least ~ 100 –150 m. It is suggested that the basement more or less consists of Disang sediments. The extension of the basement faults guided to the growth of isolated hillocks, as remnants of horsts. This forms the basis of tectonic beginning and creation of Imphal valley [10]. However, this is in disparity to the erosional formation of valley, the valley was formed due to filling of river borne sediments in the Loktak lake, the original lake that engulfed the entire valley once. Laiba [17] as another theory suggested about the Fluvio-lacustrine origin of valley due subsequent earthquakes in the area. Due to the unavailability of adequate soil data for the entire Imphal city area, the scope of the present study is limited to a rectangular region of Imphal city of size 8.0 km \times 11.5 km for estimating the ground motion (Fig. 2).

Fig. 2 Imphal city (boreholes, transportation network and rivers)



Local soil plays an important role in soil amplification and it necessary to know the condition of soil of Imphal city. The main soil constituents of Imphal valley are sands, clays, silts etc. of fluvio-lacustrine origin, whereas ferruginous red soils are found near the isolated foothill region. The presence of alluvial type of soil can be found nearby important rivers like Nambul, Imphal and Kongba. Laiba [17] in his work explain in details about the type of soil.

Soils in valley areas are clayey type and are rich in humus. Soils in low-lying areas of Imphal city viz., Lamphelpat, Takyelpat, Prompat, Kakwapat (*pat* means lake) etc., are virgin soils like clayey loam, dark clayey, and boggy type. In present study for Imphal city is restricted with Standard Penetration Test (SPT)-N data as shear wave velocity profiles and Cone Penetration Test data are not available. Soil investigation reports of Imphal city has been obtained from various construction projects, which are through SPT at 122 different locations. These locations are scattered over an area of about $11.5 \text{ km} \times 8 \text{ km}$ along the NH-39 and NH-53 roads as shown in Fig. 2. It can be seen from the figure that location of boreholes are more around the Kangla palace area that houses several commercial and administrative establishments, in addition to the sides of NH-39, NH 53 and NH-150 roads. The SPT data observed are similar to the description given by Laiba [17]. These soils

are generally loose in density, which are typical of alluvial/fluvial deposits. Indeed the SPT data indicates that the SPT-N values even at 20–30 m depth below ground surface are very low, mostly of the order of 10–20, excluding few places where it is about 30–40. The subsurface soil condition and SPT-N profile at a typical borehole located to the east of Langol hill (near NH 39) are presented in Fig. 3. Site conditions have been classified based on average standard penetration resistance (\bar{N}) as shown [9].

$$\bar{N} = \frac{\sum_{i=1}^n d_i}{\sum_{i=1}^n (d_i/N_i)} \tag{1}$$

where, d_i and N_i are the thickness and SPT-N value of each layer, n is the total number of soil layers. Out of the 122 boreholes considered in the present analysis, 114 boreholes are classified as E-type ($\bar{N} < 15$), and the remaining 8 boreholes belong to D-type ($15 < \bar{N} < 50$). As per IBC [9], E-type sites are susceptible to liquefaction of soil. Therefore, it can be seen that most parts of Imphal city are vulnerable to liquefaction induced failure.

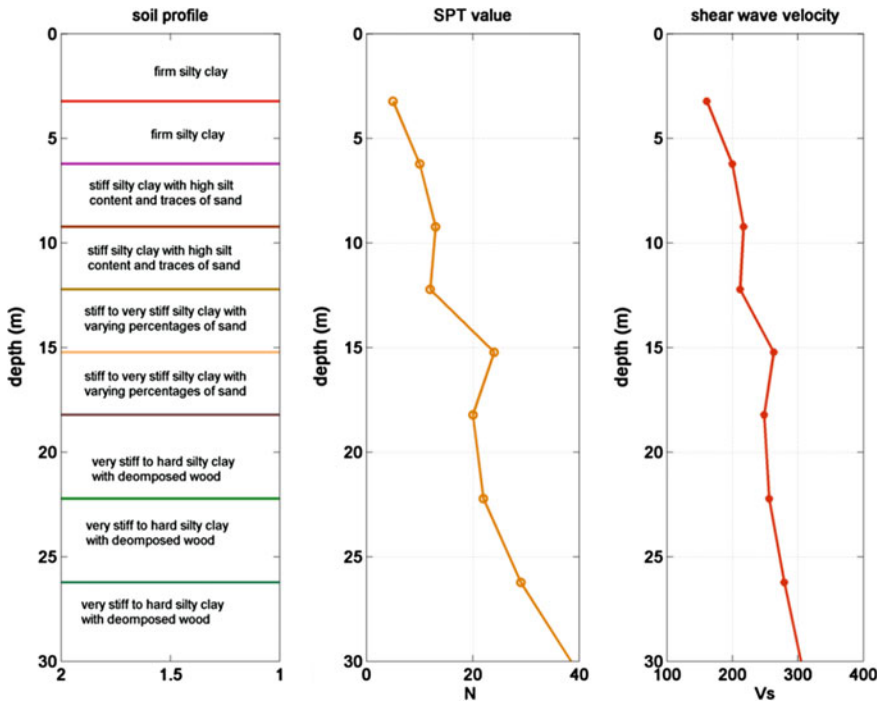


Fig. 3 Soil profile, SPT-N value and Shearwave velocity at a site near Langol hill

2 Estimation of Ground Motion

Figure 1 also shows the seismotectonic setup surrounding Imphal city [7]. Based on the seismotectonic features and geology, Goswami and Sarmah [5] and Nandy [21] have divided NE India into six broad seismic zones. These are IBR, Assam Valley, Shillong Plateau, Bengal basin, Eastern Himalaya and Mishmi Thrust. Among these tectonic blocks the IBR, Shillong Plateau and Bengal basin, are closer to Imphal, which makes the city more susceptible to the earthquakes originating in these seismic zones. In present work, the variation of ground motion has been estimated for Imphal city due to probable earthquake that may occur on IBR.

Earthquake ground motion is mostly represented by acceleration time-history. The parameters that affect the ground motion at a given site are generally grouped into source, path and site effects. In the site response analysis, the use of recorded acceleration time histories as inputs is appealing. Due to unavailability of strong motion records of past earthquakes that caused devastation to Imphal city, ground motions are simulated by an analytical model. In these models, features of the source and path are modelled as a large primary system and the effect of local topsoil condition is treated as a secondary modification. In this study first the rock level ground motion for the M_w 8.1 earthquakes is simulated by the stochastic finite fault approach of Motazedian and Atkinson [20] which is based on the concept of dynamic corner frequency and pulsing sub-faults. Finally, the generated ground motion is further modified by site response analysis to obtain the surface level time history. The application of stochastic finite-fault seismological model for estimating ground motion in NE India has been discussed in detail by Raghukanth and Dash [25].

In the present approach, the fault is divided into N number of sub-faults that are represented as point sources [8]. The rupture front spreads radially from the nucleation point and triggers the sub-faults when it reaches their center. The ground motion of sub-faults are estimated by stochastic point-source method, are summed with a suitable time delay in the time domain to obtain the ground-motion acceleration, $a(t)$, from the complete fault.

$$a(t) = \sum_{i=1}^{nl} \sum_{j=1}^{nw} a_{ij}(t + \Delta t_{ij}) \quad (2)$$

where, nl and nw are the number of subfaults along the length and width of main fault, respectively ($nl \times nw = N$), and Δt_{ij} is the relative delay time for the radiated wave from the ij th sub-fault to reach the observation point. The $a_{ij}(t)$ are each calculated by the stochastic point-source method is described by Boore [3].

Raghukanth and Somala [26] calibrated the above finite fault seismological model for NE India. The range of stress drop, pulsing percentage and the quality factor for Indo-Burma, Shillong plateau and Bengal basin tectonic blocks have been derived from the strong motion data of minor and moderate events in NE India. The

Quality factor, $Q(f)$, geometric spreading, and distance-dependent duration operators for northeast India are taken from Raghukanth and Somala [26].

The ground motion samples obtained are based on a given set of model parameters, which are themselves uncertain. Thus the sample ground motions from a suite of such simulations may still not reflect all the variability observed in real ground motion. To account for this, the slip distribution, stress drop and pulsing percentage are treated as random variables, distributed uniformly about a mean value. The variation of shear-wave velocity with depth for typical rock-type sites in NE India as reported by Mitra et al. [19] is shown in Table 1. Based on the average shear-wave velocity in the top 30 meters of the soil, the international building code [9] classifies sites as A ($V_{30} > 1.5$ km/s), B (0.76 km/s $< V_{30} < 1.5$ km/s), C (0.36 km/s $< V_{30} < 0.76$ km/s) and D (0.18 km/s $< V_{30} < 0.36$ km/s) type sites. Since the average shear velocity is 1.25 km/s (Table 1), the rock site in NE India (Table 1) can be classified as B-type site. Since modification between bedrock and A-type site is a linear problem in one dimension and hence for such sites amplification $[F(f)]$ can be found directly by the quarter-wavelength method of Boore and Joyner [4].

The input source and path parameters used in the finite fault seismological model, for simulating ground motion due to this event, are shown in Table 2. The

Table 1 Regional velocity model [19]

Depth (km)	V_s (km/s)
0.1	1.25
0.8	2.75
1.4	3.6
2.2	3.75

Table 2 Input parameters in the stochastic finite fault seismological model

Parameter	Hypothetical (Indo-Burma)
Magnitude, M_w	8.1
Location	
Latitude	27.1
Longitude	92.5
Depth to top of the fault (km)	60
Stress drop (bars)	50–100
Quality factor, $Q(f)$	$431f^{0.73}$
Site effects $[F(f)]$	Quarter wavelength
Kappa factor	0.03
Fault dimensions (km)	175×80
Fault orientation	
Strike($^\circ$)	55
Dip ($^\circ$)	58
Pulsing percentage	25–60
Rupture velocity	0.8β
Slip distribution	Random field

other parameter like magnitude, orientation, location of the fault and depth has been taken from Kayal [15]. The quality factor for Shillong plateau is taken as $431f^{0.73}$ [26]. The slip distribution, stress drop and pulsing area are treated as random field and random variables in the model. The stress drop is taken to vary between 50 and 100 bars [25]. The pulsing percentage is taken in the interval 25–60 %. The $175 \text{ km} \times 80 \text{ km}$ fault plane is divided into 14,000 subfaults of size $1 \text{ km} \times 1 \text{ km}$ respectively. Since the slip distribution on the rupture plane, stress drop and pulsing area percentage are modelled as random variables; one can generate an ensemble of time histories at the surface by numerical simulation.

By making use of latin hypercube sampling technique [13] 10 samples of random seismic parameter are generated with the help of three simulated seismic parameter. All ten simulated earthquakes are shown in Fig. 4. The PGA varies between 0.1 and 0.25 g The amplification as well as response spectra due to local site affect at Imphal city for one borehole are shown in Figs. 5 and 6.

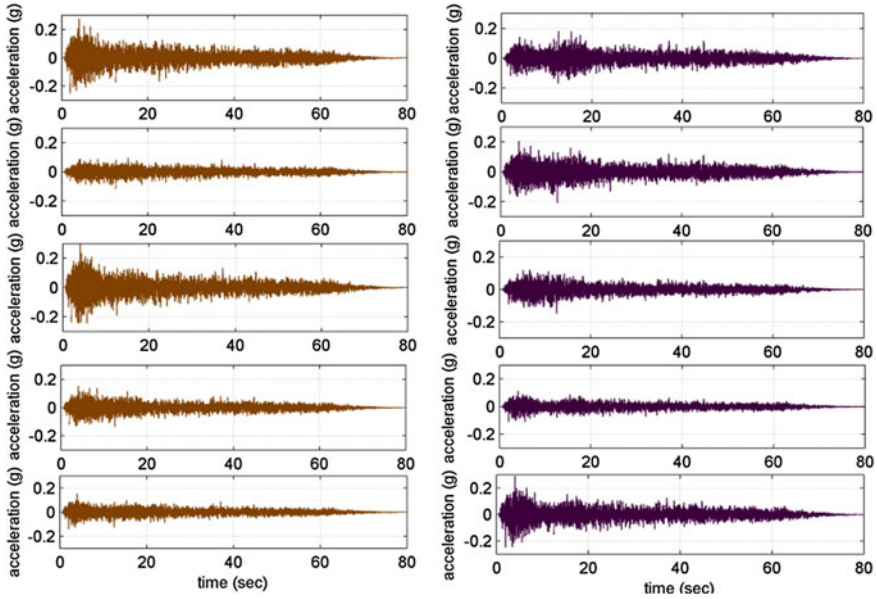


Fig. 4 Synthesis of ground motion due to a hypothetical earthquake (M_w 8.1) in the Indo-Burmese ranges

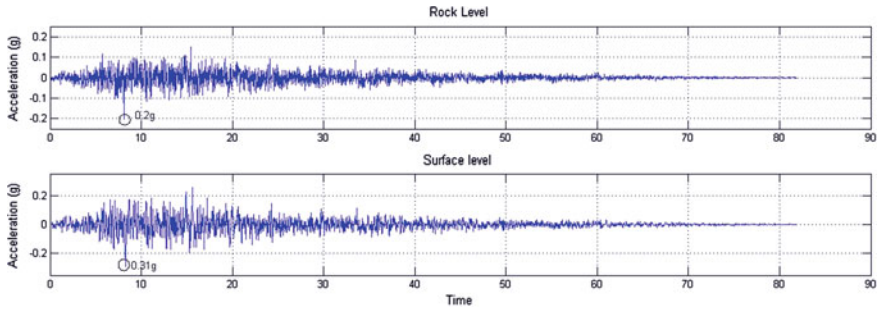


Fig. 5 Surface level ground motion for the borehole near Chingna hill (Fig. 1) in Imphal city

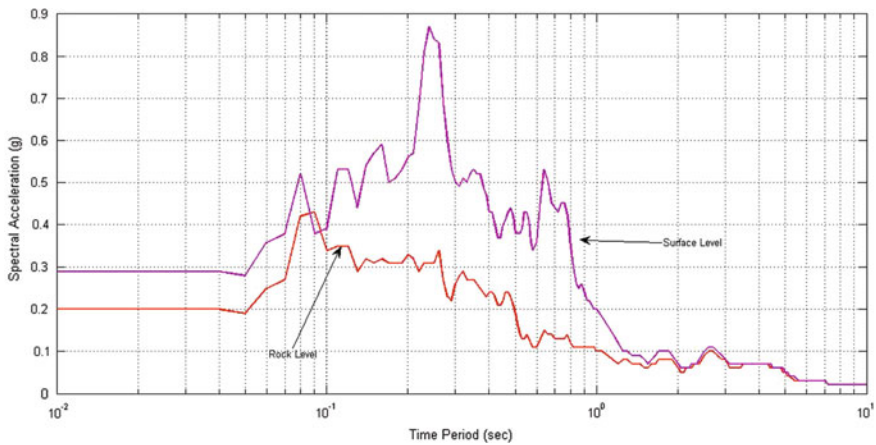


Fig. 6 Response spectra for one bore hole

3 Surface Level Ground Motion

Pallav et al. [24] shows that of IBR is the most active seismic zone in NE India that can affect to Imphal city (>100 km) and hence plays a significant role in seismic hazard analysis for this city. Some researchers have cogitated that there may be great earthquake in IBR after the 26th December 2004 Indonesian event. Hence possible ground motion due to a hypothetical earthquake in IBR has been considered in the study. Figure 7a shows the surface level PGA distribution for the M_w 8.1 hypothetical event in the IBA. Mean surface level PGA of 0.45 g has been observed in several areas surrounding the Kangla palace and to the east of Langol hill. The standard deviation around the central places viz., Kangla palace, polo ground and RIMS are 0.12, 0.1, and 0.14 respectively (Fig. 7b). For 0.3 s time period it can be seen that maximum mean surface level spectral acceleration of

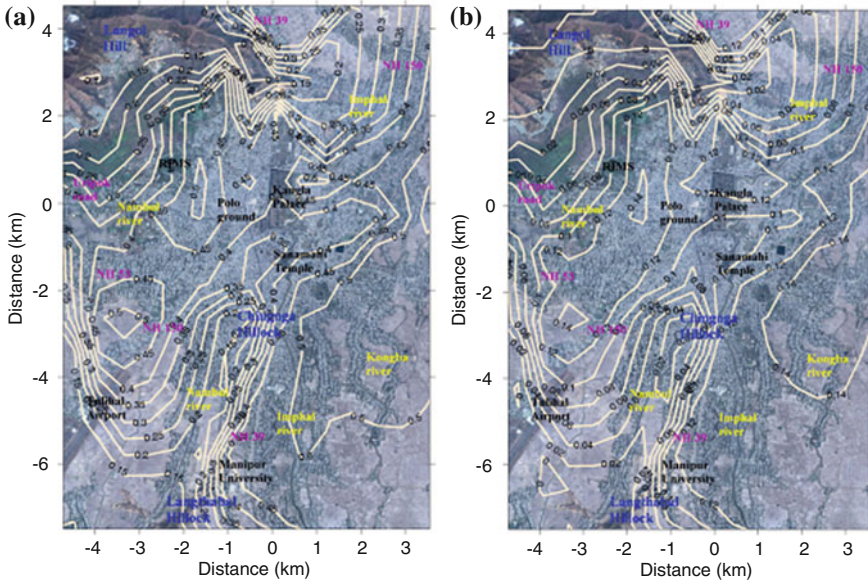


Fig. 7 a Mean surface level PGA (5 % damping). **b** Standard deviation of PGA (5 % damping)

0.27 g occurs to the east of Langol hill (Fig. 8a), whereas near Kangla palace, RIMS and Sanamahi temple area the mean spectra acceleration is around 0.175 g. The corresponding standard deviation at these locations is 0.05. Near Tulihal airport the spectral acceleration is 0.15 g with standard deviation of 0.04.

For 1.0 s natural period the maximum surface level spectral acceleration is found to be 0.055 g which occurs near Kangla palace area with standard deviation values at PGA being 0.14 (Fig. 9a, b). Further near RIMS, Tulihal airport, Manipur University and Sanamahi temple the mean spectral value is 0.035 g with standard deviation of 0.08 in all these locations. At 0.3 and 1.0 s period standard deviation are 0.04 and 0.016 near Kangla palace area and reduces towards Tulihal airport to 0.02 and 0.008 respectively (Figs. 8b and 9b). Surface level response spectra for M_w 8.1 (5 % damping) is shown in Fig. 10.

In comparison with the IS-1893: 2002 [12] response spectra. It can be seen that spectral acceleration for some of the sites the responses are underestimated by the code of practice for this particular hypothetical events. For design value spectral acceleration for all 122 sites the responses are underestimated by the code of practice.

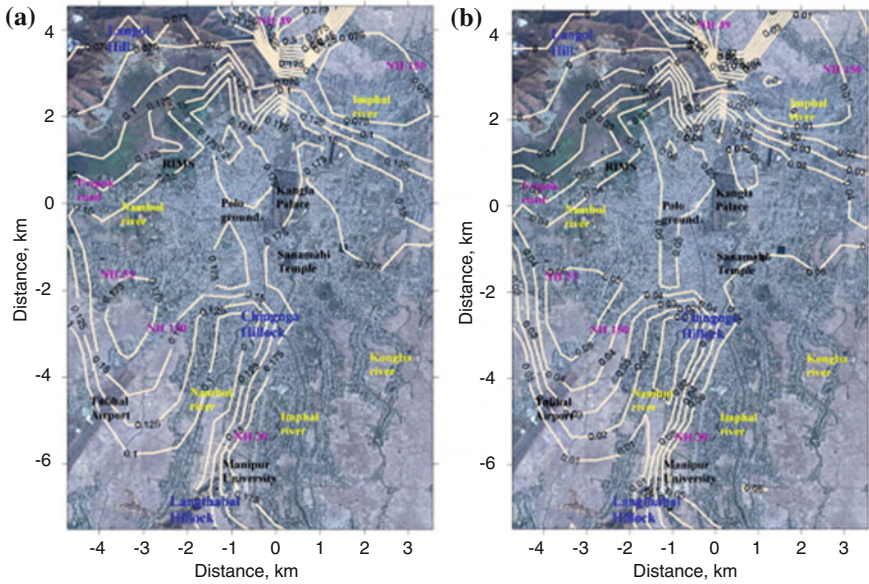


Fig. 8 **a** Mean surface level S_a at 0.3 s natural period (5 % damping). **b** Standard deviation at 0.3 s natural period (5 % damping)

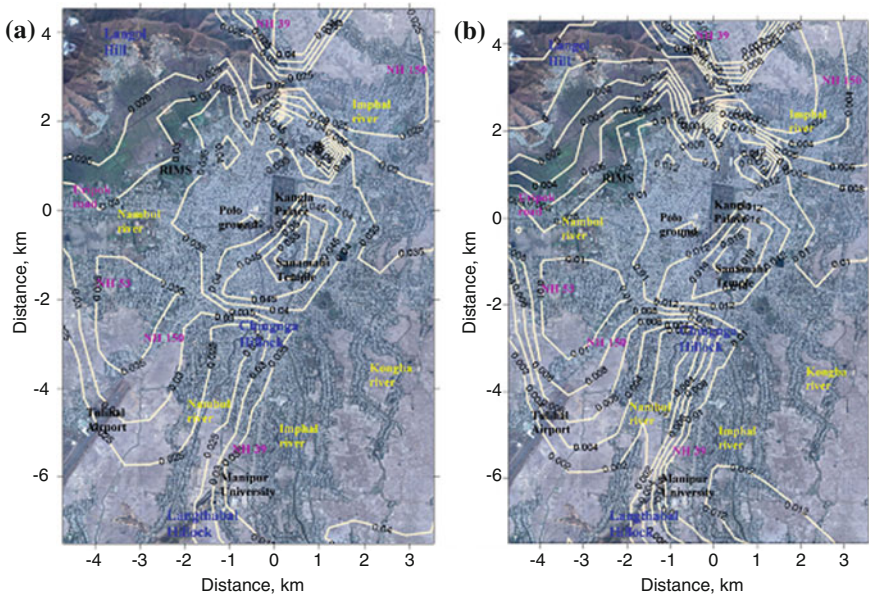


Fig. 9 **a** Mean surface level S_a at 1.0 s (5 % damping). **b** Standard deviation at 1.0 s (5 % damping)

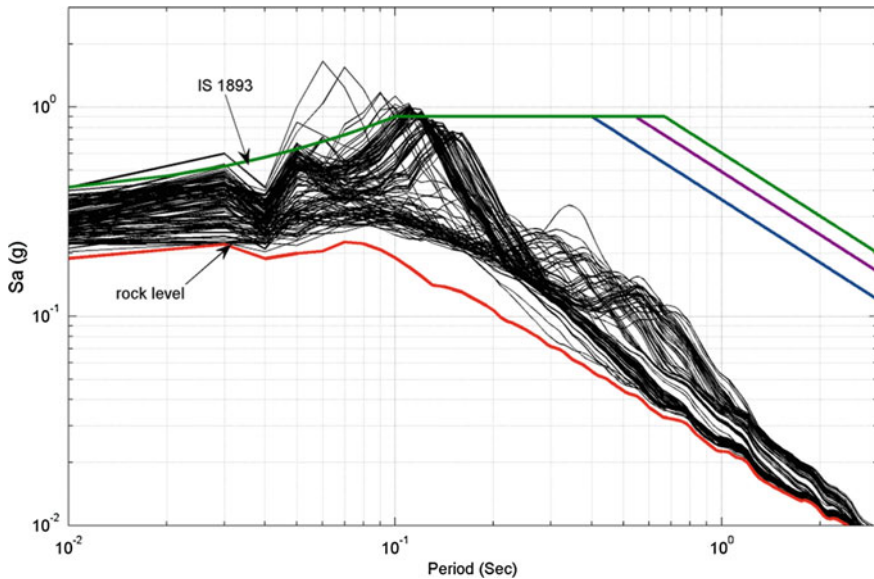


Fig. 10 Mean response spectra for all sites due to hypothetical earthquake in IBR (M_w 8.1) (5 % damping)

4 Summary and Conclusions

In this paper, mean ground motion and its standard deviation at Imphal city has been estimated for a possible future earthquake in the Indo-Burmese Subduction zone, using analytical approach. Stochastic finite-fault seismological model has been used for simulating rock level acceleration time histories. The input parameters have been taken from that reported in literature [7, 19, 21, 26]. Uncertainty in the slip field, stress drop and pulsing area has been considered for simulating rock level ground motion. The simulated rock level PGA at Imphal city due to Indo-Burmese Subduction earthquake of M_w 8.1 lies in between 0.1 and 0.25 g.

In order to know the effect of the underlying soil layers over the bed rock, nonlinear site response analysis has been accomplished at several locations in Imphal city, for ten sample rock level time history and using the local soil properties as inputs. Making use of empirical relation, proposed by Imai and Tonouchi [14], shear wave velocity has been computed from SPT-N value. The surface level ground motions have been computed by nonlinear site response analyses. The results obtained are presented in the form of contour maps for mean spectral acceleration and standard deviation at PGA, 0.3 and 1 s (Figs. 7, 8 and 9). It is observed that at important places around Kangla palace the amplification for PGA is of the order of 1.4–1.9. The contour maps show the significance of local site conditions and clearly reveal the non-uniform dispersion of spectral acceleration. To understand the frequency response functions, effect of soil layering and mean

surface level response spectra at 5 % damping are shown in Figs. 7, 8 and 9. The amplification and de-amplification are observed due to non-linear behavior of soil. Figure 10 shows comparison between the results obtained from this study with IS-1893 response spectra.

The results obtained from the present study will be of varied use in engineering constructions and design. The contour maps for the PGA can be useful in identifying vulnerable areas, thereby, facilitating planning, design and construction of new structures and strengthening of the existing structures in Imphal city.

It is well reported that complex local geometry (e.g. basin, undulated topography etc.) can significantly affect the local site responses due to ground motion reflection from the edges [2, 6]. As Imphal city is located on alluvial valley surrounded by hills and with sparse hillocks, it is speculated that a three dimensional model study may give more realistic insights into the behavior of soil response to obtain reliable surface accelerations.

References

1. Agarwal and Sukla (1996) Manipur: VIII 78—Imphal Valley. GSI, Special publication no. 4
2. Boore DM (1972) A note on the effect of simple topography on seismic SH waves. *Bull Seismol Soc Am* 62:275–284
3. Boore DM (1983) Stochastic simulation of high-frequency ground motions based on seismological models of the radiated spectra. *Bull Seismol Soc Am* 73:1865–1894
4. Boore DM, Joyner WB (1997) Site amplification for generic rock sites. *Bull Seismol Soc Am* 87(2):327–341
5. Goswami HC, Sarmah SK (1982) Probabilistic earthquake expectancy in the northeast Indian region. *Bull Seismol Soc Am* 72:999–1009
6. Geli L, Bard P, Jullien B (1988) The effect of topography on earthquake ground motion: a review and new results. *Bull Seismol Soc Am* 78:42–63
7. GSI (2000) Seismo-tectonic atlas of India and its environs. Geological Survey of India
8. Hartzell SH (1978) Earthquake aftershocks as Green's functions. *Geophys Res Lett* 5:1–4
9. IBC (2006) International building code. International code council
10. Ibotombi S (2000) Structural and tectonic framework of Manipur. Manipur Science Congress, Imphal
11. Idriss IM, Sun JI (1992) A computer program for conducting equivalent linear seismic response analysis of horizontally layered soil deposits. Users manual for SHAKE91
12. IS-1893 (2002) Indian standard, criteria for earthquake resistance design of structures. Fifth revision, Part-I. Bureau of Indian Standard, New Delhi
13. Iman RL, Conover WJ (1980) Small sample sensitivity analysis techniques for computer models, with an application to risk assessment. *Commun Stat Theory Methods* A9:1749–1874
14. Imai T, Tonouchi K (1982) Correlation of N-value with S-wave velocity and shear modulus. In Proceedings of 2nd European symposium on penetration testing, Amsterdam, pp 57–72
15. Kayal JR (2008) Microearthquake seismology and seismotectonics of South Asia. Capital Publishing Company, New Delhi
16. Kayal JR, Arefiev SS, Barua S, Hazarika D, Gogoi N, Kumar A, Chowdhury SN, Kalita S (2006) Shillong plateau earthquakes in northeast India region: complex tectonic model. *Curr Sci* 91:109–114
17. Laiba MT (1992) The geography of Manipur. Public Book Store, Imphal

18. MASTEC (2007) Final report on water harvesting and water conservation in Imphal East Block. www.mastec.nic.in/MASTEC
19. Mitra S, Priestley K, Bhattacharyya AK, Gaur VK (2005) Crustal structure and earthquake focal depths beneath northeastern India and Southern Tibet. *Geophys J Int* 160:227–248
20. Motazedian D, Atkinson GM (2005) Stochastic finite-fault modeling based on a dynamic corner frequency. *Bull Seismol Soc Am* 95:995–1010
21. Nandy DR (2001) *Geodynamics of Northeastern India and the adjoining region*. ACB Publications, Kolkata
22. Ningthoukhongjam KS (2005) *Cheitharol Kumpapa (in Manipuri)*. Manipur Sahitya Parisad, Imphal
23. Oldham T (1882) The Cachar earthquake of 10th January, 1869. *Mem Geol Surv India* 19:1–88
24. Pallav K, Raghukanth STG, Singh KD (2012) Liquefaction hazard scenario of Imphal city for 1869 Cachar and a hypothetical earthquake. *Int J Geotech Earthq Eng* 3(1):34–56
25. Raghukanth STG, Dash SK (2010) Deterministic seismic scenarios for North East India. *J Seismolog* 14:143–167
26. Raghukanth STG, Somala SN (2009) Modeling of strong motion data in Northeastern India: Q , stress drop and site amplification. *Bull Seismol Soc Am* 99:705–725
27. Sarangthem BS (2005) *Meetei Ningthourol*. Manipuri, Imphal

Development of Surface Level Probabilistic Seismic Hazard Map of Himachal Pradesh

Muthuganeisan Prabhu and S.T.G. Raghukanth

Abstract Himachal Pradesh has experienced several major earthquakes in the past and this high seismicity can be attributed to the under-thrusting of the Indian tectonic plate against the Asian plate. Multi-channel Analysis of Surface Waves tests (MASW) were carried out at 73 test sites, located in 22 important cities, which indicated that the test sites were of C and D types. The ground motion prediction equations capable of predicting the surface level ground motion for these site conditions have been developed in line with the Probabilistic Seismic Hazard Analysis (PSHA) methodology of NDMA report (2011) by incorporating the evaluated site response functions. The probable seismic sources were identified from the Seismotectonic Atlas of India published by GSI (2000) and the recurrence parameters were established from the earthquake catalogue of Raghukanth (Bull Earthq Eng 9:1361–1386, 2011). The surface level peak ground acceleration (PGA) was estimated by PSHA approach for a return period of 2,475 year that corresponds to a 2 % probability of exceedance during a design life of 50 years. Also, the uniform hazard response spectrum plots for some important test cities are presented. The predictions of the developed GMPE agrees well with the seismic events recorded in this region.

Keywords Seismic hazard · Seismic zones · Site response · MASW · Himachal Pradesh

M. Prabhu (✉) · S.T.G. Raghukanth
Department of Civil Engineering, Indian Institute of Technology Madras,
Chennai 600 036, India
e-mail: prabhu.muthuganeisan@gmail.com

S.T.G. Raghukanth
e-mail: raghukanth@iitm.ac.in

1 Introduction

Himachal Pradesh lies in a seismically active region and has experienced several major earthquakes in the past such as the Kangras (M_w 7.8, 1905), Uttarkashi (M_w 7, 1991), Killari (M_w 6.2, 1993), Chamoli (M_w 6.8, 1999). The seismicity can be attributed to the presence of several major faults in this region such as the Main central thrust (MCT), Main boundary thrust (MBT), etc. Due to high topographic variation and the presence of several perennial rivers (see Fig. 1), this region has immense hydro-electric potential that has drawn a considerable investment on infrastructures such as Dams, Tunnels, etc. Additionally, the touristic appeal of this region combined with the rugged terrain has resulted in clustered and unplanned developments across this region. Hence, it becomes necessary to judiciously evaluate the seismic hazard of this region and the risk it poses to human life and infrastructure. Several works have presented the hazard map of this region such as, Khattri et al. [13], Bhatia et al. [1], Parvez et al. [19], Mahajan et al. [15], report by the National Disaster Management Authority of India (NDMA) [17], Patil et al. [20]. It should be noted that these values are presented for bedrock level with a shear wave velocity exceeding 1,300 m/s. However, most of the population centers (such as Kangra, Shimla, Mandi, Una, Solan, Sundernagar, etc.) are located on the

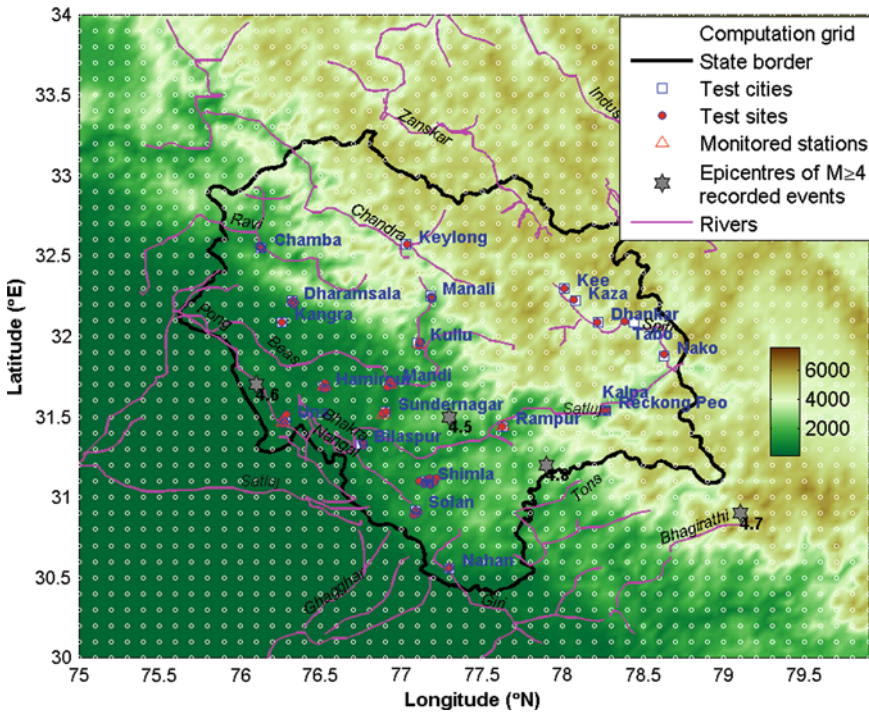


Fig. 1 Map of Himachal Pradesh: topography, location of the test sites, PSHA computation grid

lesser Himalayan region which are featured by thick Neogene Siwalik sediments with gravel and boulder beds [15] whose attenuation characteristics needs to be considered while estimating the hazard level. In such cases, the existing practice is to scale the design spectrum by a multiplying factor known as site coefficient. But, it has been well established that the local site conditions can significantly alter the ground motion by amplifying only certain frequencies depending on its dynamic characteristics. Instead, in this study, the site response function is incorporated in the procedure of PSHA to estimate the seismic hazard at surface level directly. However, this necessitates the characterisation of the site conditions at some of the important urban agglomerations in this study region.

As a result, Multi-channel Analysis of Surface Waves (MASW) tests were performed at 73 sites located in 22 important cities to characterise the dynamic properties of soil. Based on these tests, the site response functions have been evaluated using SHAKE91 [10] which were used to develop the surface level attenuation relation for the two geologic regions, viz., Himalayan and Indo-Gangetic region, observed within the test region. The developed attenuation relationships are integrated into the PSHA approach presented in NDMA report [17] to estimate the surface level hazard maps in terms of PGA values for MCE event with a return period of 2475 years that corresponds to a 2 % probability of exceedance in 50 years. The probable seismic sources have been identified from the Seismotectonic Atlas of India [8] whose seismogenic characteristics or recurrence parameters have been adopted from the NDMA report [17].

The methodology of developing the surface level attenuation relation and incorporating it into the PSHA methodology are briefly discussed further. The predictions of the attenuation relation are compared with actual events and the results of PSHA are presented in a simplified form that can be directly used for design purposes.

2 Geography of the Study Region

The state of Himachal Pradesh comprises of two geographically classified regions viz., Indo-Gangetic region in the South-West and the Himalayan region in the North. Remarkably, all the three geological divisions of Himalayas pass through the state with the altitudes varying from 320 m (Una district) at the low lying Siwalik regions in the South to 6,975 m (Kinnaur District) in the mountainous Greater Himalayas in the North. The altitude of the region increases from the South West towards North East (see Fig. 1). The district of Una and parts of the districts of Sirmaur, Solan, Bilaspur, Hamirpur and Kangra lie in the Indo-Gangetic plain. These regions are characterised either by the unconsolidated formations of the Siwalik sediments belonging to Quaternary era in the Southern parts to semi-consolidated formations of Tertiary era in the Northern parts with the presence of gravel or boulder embedded beds [22]. The district of Mandi, Shimla, Chamba, Kullu and parts of the districts of Bilaspur, Hamirpur, Kangra, Sirmaur and Solan are located in the lower hills of

Himalayas while the districts of Kinnaur and Lahaul and Spiti lie in the outer Himalayas [12]. The lower Himalayan regions are characterised by semi-consolidated formations of Tertiary, Mesozoic and Upper Paleozoic era [22]. The upper Himalayas are characterised by consolidated formations of Mesozoic, Paleozoic and Precambrian era and marked by highly weathered residuum of the Tethyan basin and fractured formations [22]. The districts of Bilaspur, Hamirpur, Kangra, Mandi, Sirmaur, Solan and Una generally have brown, alluvial and grey brown podzolic soils, the districts of Kullu and Shimla have grey-wooded podzolic soils, while Kinnaur, Lahaul and Spiti and some parts of Chamba have humus mountain speletal soils [5].

This extreme topographic and climatic conditions has resulted in the bunching of population in the favourable lower altitude regions such as Hamirpur, Bilaspur, Una, Kangra, etc. with population density of over 250 per sq.km. compared to the harsher higher altitude regions such as Kinnaur, Lahaul and Spiti, etc. with population density lesser than 15 per sq.km [7]. Additionally, the decadal population growth exceeding 12 % in the state highlights the elevated seismic risk level posed to these clustered population centers and reinforces the need to judiciously estimate the seismic hazard level of this region.

3 Seismotectonics and Seismicity of the Study Region

The identification of the probable potential sources is the initial step of the PSHA methodology. It can be observed from Fig. 2 that several prominent faults are situated in the study region. The locations of these faults, that lie within a 500 km radius of the study region, have been obtained from the Seismotectonic Atlas of India [8]. A total of 192 faults were identified to lie within 500 km around the state of Himachal Pradesh and were considered as probable sources in this study and are shown in Fig. 2. It can be seen that several major faults run across or close to some important cities, namely, Jwala Mukhi Thrust (JMT) across Hamirpur; Main Frontal Thrust (MFT) near Una; Drang Thrust near Nahan, Solan, Hamirpur, Mandi and Dhramshala; Main Boundary Thrust near Solan, Mandi and Dhramshala; Main Central Thrust (MCT) near Kullu, Manali, Kalpa, Keylong; Sundernagar Fault (SF) across Sundernagar.

Figure 2 also shows the past seismicity of this region between 1664 AD to 2011 AD taken from the available literature [17, 21]. It can be observed that the region had experienced some major earthquakes of magnitude exceeding 6 ($M_w > 6$) in the past. This high seismic activity of this region can be attributed to its location on the converging plate boundary between the Indian and the Asian tectonic plates. It can be seen that certain regions exhibit similar level of seismic activity and some of the past earthquakes can be associated with the identified faults. National Disaster Management Authority [17] has classified the Indian subcontinent into 32 seismogenic zones and estimated the recurrence parameters for these regions. Six of these seismogenic zones (1, 2, 3, 6, 21, 22, 28) that are present within 500 km distance of the study region have been considered in this study.

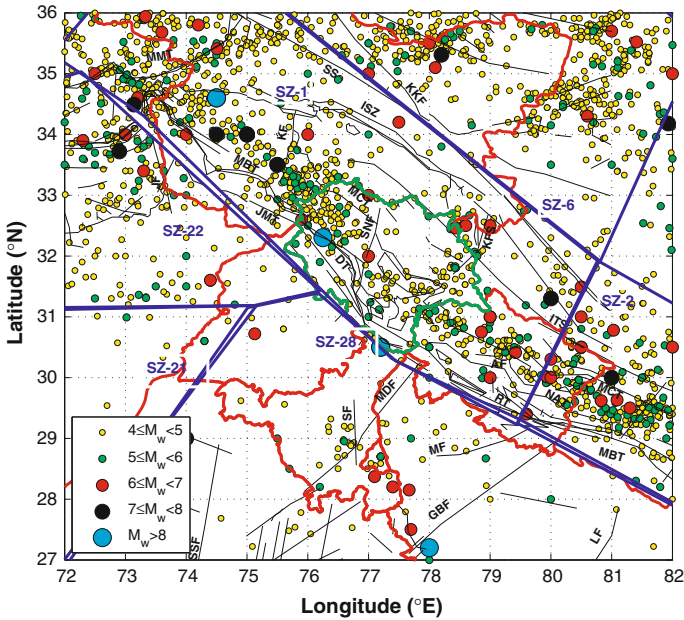


Fig. 2 Seismicity and fault map of HP. Also, showing the seismogenic zones of India considered for this study (*AF* Alaknanda Fault, *DT* Drang Thrust, *GBF* Great Boundary Fault, *ISZ* Indus Suture Zone, *ITS* Indus Tsangpo Suture, *JF* Jhelum Fault, *JWT* Jwala Mukhi Thrust, *KKF* Karakoram Fault, *KF* Kishtwar Fault, *KFS* Kaurik Fault Sytem, *LF* Lucknow Fault, *MBT* Main Boundary Thrust, *MCT* Main Central Thrust, *MDF* Mahendragarh-Dehradun Fault, *MF* Moradabad Fault, *MMT* Main Mantle Thrust, *NAT* North Amora Thrust, *RT* Ramgarh Thrust, *SF* Sohna Fault, *SNF* SunderNagar Fault, *SS* Shyok Suture, *SSF* Sardar Shahar Fault [8, 17, 21, 23])

4 Site Characterisation by MASW Test

The local soil conditions are known to significantly alter the ground motion and this becomes of engineering importance when the soil strata amplifies the ground motion across certain frequency ranges that are close to the structural frequency. It is widely accepted that the elastic response of the soil medium can be characterised by means of its shear wave velocity [9]. In this study, the shear wave velocity profiles of 73 sites located in 22 important cities, including all the 12 district headquarters, were estimated through Multichannel Analysis of Surface Waves (MASW) tests [18].

In short, an artificial source initiates the surface (Rayleigh) waves which will be recorded by multiple receivers spread along a survey line. Spectral analysis of these records will reveal the dispersion characteristics of the medium resulting in what is known as a dispersion curve, which indicates the variation in the wave velocity with depth. By inversion technique, the shear wave velocity profile is estimated by iterative comparison with the measured dispersion curve in a least-squares sense [18].

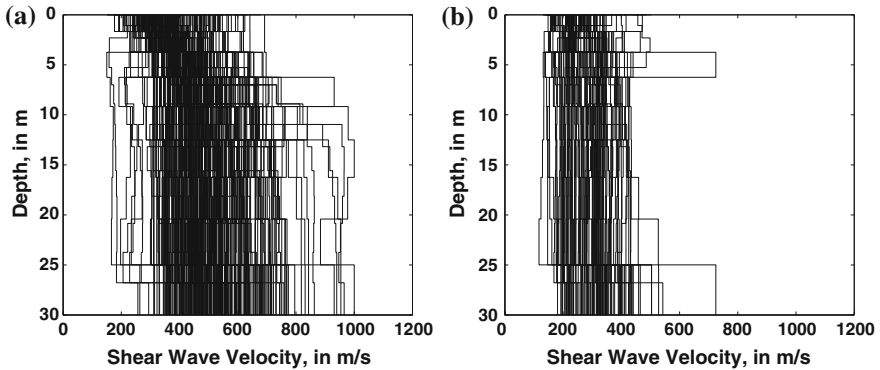


Fig. 3 Shear wave velocity profiles **a** C-Type sites, **b** D-Type sites

The active seismic source used was a 8 kg hammer, with an automatic trigger, struck against a metal plate which was always placed at a known offset from a equally spaced linear array of geophones or receivers (4.5 Hz frequency). The data was collected by a 24-channel Geode and stored in a laptop. A minimum of 3 shots were stacked at each source location to improve the Signal/Noise ratio.

The test locations at each of these cities were chosen based on their proximity to important structures, open area and low noise level. Based on the average shear-wave velocity in the top 30 m or $V_s,30$ values, these sites were classified according to IBC 2009 site classification. Among the 73 test sites, it was found that 2 were of B-type, 50 were of C-type and 21 were of D-type. Since the $V_s,30$ values of the two B-type sites were on the lower end, their V_s profiles were grouped along with the C-type sites for estimation of the site response coefficient. The shear wave velocity profiles for C and D-type sites are shown in Fig. 3a, b.

5 Site Response Function and Surface Level Ground Motion Simulations

From the MASW tests, it shows that the site conditions at the important cities were of either C or D type. The computed shear wave velocity profiles of these test sites indicate the variability in the soil layering within the top 30 m. Using these profiles, we perform a nonlinear site response analysis using SHAKE91 [10] to estimate the frequency response function of the site coefficient. For this analysis, 20 acceleration time histories were simulated using a finite source seismological model [3] for a A-type site or at bed rock level, simulated for both Himalayan and Indo-Gangetic regions, and were used as the input wave at the bedrock level. The frequency response function of the site coefficient or the site response function ' $F_s(f)$ ' is evaluated as the ratio of the spectral acceleration at the surface and the bedrock level. These site response functions were evaluated for all the 73 sites. Figure 4a, b

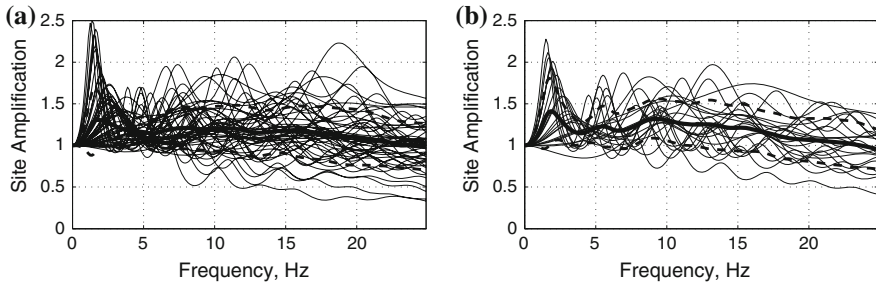


Fig. 4 Soil response function **a** C-Type sites, **b** D-Type sites

shows these functions grouped based on their site classification to evaluate the mean site response function and its standard deviation for both the site types.

In the absence of ground motion database with records complete for all magnitudes (M) and hypocentral distances (r), it has become acceptable to use a database of simulated ground motion [17]. In this study, the site response function, that were computed earlier, were used in the place of the site dependent function used in the stochastic finite fault approach of Boore [2] to simulate the synthetic ground motion time histories at the surface level. These ground motions were simulated for 10 values of M (ranging from 4 to 8 at 0.5 units), 20 values of R (ranging from 1 to 500 km), 8 azimuths (ranging from 0° to 315° at 45° interval) and 50 random combinations of 7 other uncertain seismic parameters such as: stress drop; focal depth; dip; radiation coefficient and pulsing percentage area, whose ranges were reported in the NDMA report [17] for the two geological regions. As a result, the synthetic database reflects the dynamic response of the local soil conditions observed in the study region. The intensity measures (such as PGA) of these surface level ground motions can be utilised to develop the region-specific attenuation relation described in the following section.

6 Surface Level Ground Motion Prediction Equations

The purpose of performing the site characterisation and developing a database of synthetic ground motion is to account for the uncertainty in the medium characteristics or the source-to-site path that causes the attenuation of the ground motion. The ground motion generated at a source attenuates as it travels through the medium and the extent of attenuation depends on several factors such as source-to-site distance (radiation damping), medium properties (anelastic damping), rupture characteristics, etc. Using the simulated database of surface level ground motion, region-specific surface level ground motion prediction equation (also known as attenuation relation), for C and D type sites in the two geological regions, have been

developed using the functional form proposed by the NDMA report [17] which is given as follows,

$$\ln\left(\frac{Y}{g}\right) = c_1 + c_2M + c_3M^2 + c_4r + c_5 \ln(r + c_6e^{c_7M}) + c_8 \log(r)f_0 + \ln(\varepsilon) \quad (1)$$

where, Y is the ground motion intensity measure (PGA), M is the magnitude, R is the hypocentral distance and $f_0 = \max(\ln(r/100), 0)$. The coefficients c_1, \dots, c_8 are determined by a two-step regression method proposed by Joyner and Boore [11] and the values are presented in Table 1. The term ε accounts for the aleatory uncertainty in the attenuation relation. The predictions of the developed GMPE compares agreeably with that of the response spectrum of measured events (35 Hz low-pass filtered data available [16]) as can be seen in Fig. 5a, b. For this comparison, the coefficients of the GMPE were evaluated for 28 natural periods and the values presented in Table 1 correspond to the S_a values at $T = 0s$.

With the development of these relations, it is now possible to estimate the surface level hazard at any site within the state of Himachal Pradesh due to any seismic activity at any of the 192 probable seismic sources.

7 Probabilistic Seismic Hazard Analysis

The PSHA methodology using Cornell-McGuire approach has been discussed widely in the literature [4, 14, 17] and was carried out using an in-house MATLAB[®] code. The aim of PSHA is to estimate the probability of the ground motion, at a site, to exceed certain intensity level due to earthquakes of any magnitude occurring at any or all of the probable seismic sources. If the earthquakes occurring at a fault are assumed to be independent then the number of earthquakes occurring at a fault follows a stationary Poisson process. Then, the probability of the ground motion at a site (Y) exceeding a certain level (y^*) in a time frame of T years will be,

$$P(Y > y^* \text{ in } T \text{ years}) = 1 - e^{-\mu_{y^*}T} \quad (2)$$

where, μ_{y^*} is the mean annual rate of exceedance and is determined by,

$$\mu_{y^*} = \sum_{i=1}^K N_i(m_0) \times \int_{m=m_0}^{m_u} \int_{r=r_{min}}^{r_{max}} P[Y > y^* | m, r] p_{R|M}(r|m) p_M(m) dr dm \quad (3)$$

where, $p_M(m)$ is the probability density function of the magnitude expressed as an exponential random variable and accounts for the magnitude uncertainty, $p_{R|M}(r|m)$ is the probability density function of the hypocentral distance computed numerically by the method of Der Kiureghian and Ang [6] and accounts for the uncertainty

Table 1 Coefficients of the attenuation relation in Eq. 1

Site class	c_1	c_2	c_3	c_4	c_5	c_6	c_7	c_8	$\sigma(k)$
<i>Himalayan region</i>									
C	-4.7738	1.5004	-0.0204	-0.0048	-1.4216	0.0465	0.8748	0.0912	0.3864
D	-4.5304	1.4623	-0.0175	-0.0049	-1.4392	0.0365	0.8948	0.0985	0.3881
<i>Indo-Gangetic region</i>									
C	-4.3477	1.2807	-0.0087	-0.0064	-1.2940	0.0084	1.0489	0.1234	0.3930
D	-4.3343	1.2847	-0.0090	-0.0064	-1.2983	0.0086	1.0439	0.1238	0.3941

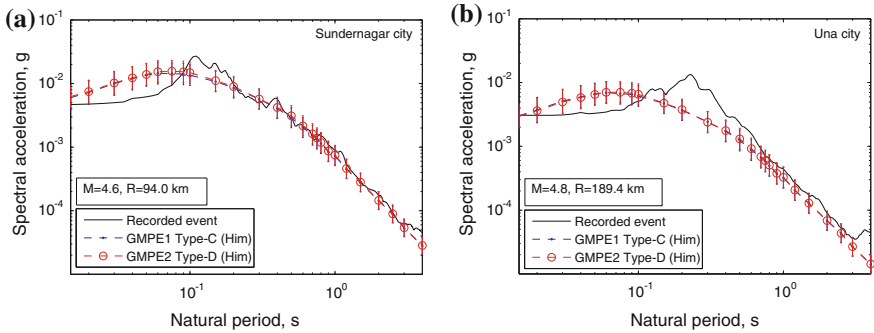


Fig. 5 Comparison the GMPE estimations with response spectrum of recorded events

in the hypocentral distance. $P[Y > y^* | m, r]$ is the conditional exceedance probability of y^* to be exceeded at the surface level, for a specified magnitude and hypocentral distance, and is determined using the developed GMPE. This accounts for the uncertainty in the medium characteristics and is expressed as a lognormal random variable.

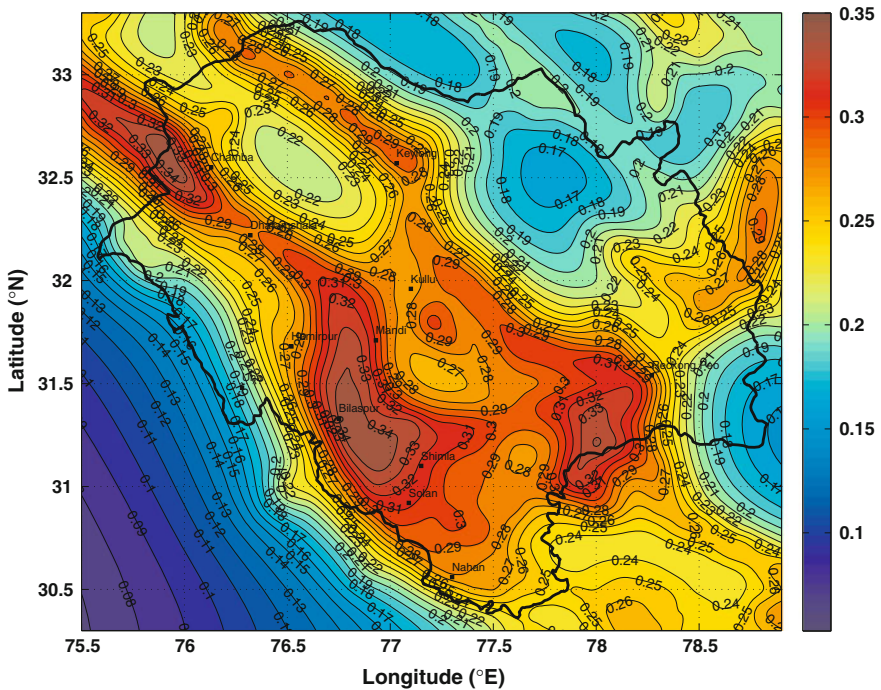


Fig. 6 PGA map for C-type sites for 2475 years return period

8 Results and Discussions

The region considered for this study spreads over $30^{\circ} 20'N$ to $33^{\circ} 15'N$ latitudes and $75^{\circ} 45'E$ to $79^{\circ} 00'E$ longitudes and encompasses the entire state of Himachal Pradesh and the surface level seismic hazard has been estimated at a $0.2^{\circ} \times 0.2^{\circ}$ grid level covering the entire study region as shown in Fig. 1. The MASW results indicate that the C and D type sites are prevalent at the populated regions of the state. B-type sites were detected at only 2 locations amongst all the tested locations and have been considered as C-type for conservative estimates, since their V_s30 values were bordering with that of C-type. Since, it is neither possible nor necessary to accurately determine the site condition at all location across the state, we have estimated the surface level hazard for this region considering it entirely to be of either C or D type. Thus, the surface level peak ground acceleration values were estimated for a return period of 2475 years, which corresponds to a 2 % probability of exceedance in 50 years, for these two site conditions and are shown in Figs. 6 and 7. It can be observed from these plots that the obtained PGA values are in the range of 0.16–0.35 g for C-type sites and 0.16–0.38 g for D-type sites. These values are higher than the values presented for A-type sites in NDMA [17] and Patil et al. [20] (with variable 'b') due to the consideration of the site effects.

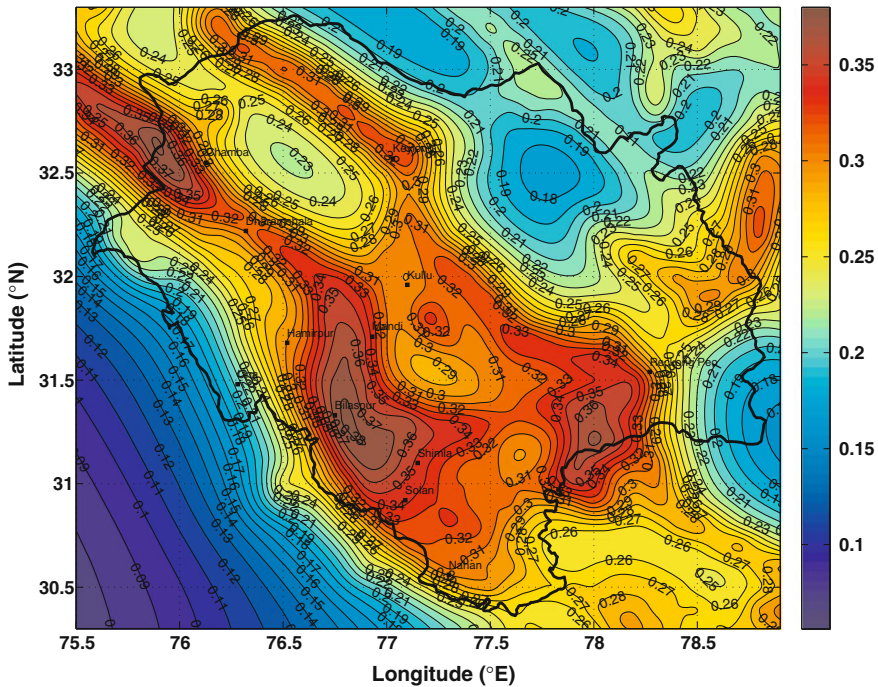


Fig. 7 PGA map for D-type sites for 2475 years return period

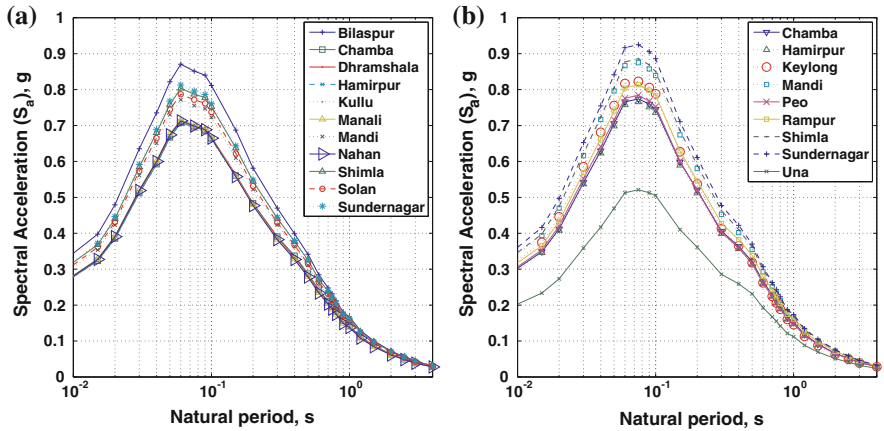


Fig. 8 Uniform hazard response spectrum for 2475 years return period. **a** C-type sites. **b** D-type sites. *Note* Some cities exhibit the same site type at all local test sites and UHRS is shown for that site type alone

Apart from the PGA contour maps, the Uniform Hazard Response Spectrum (UHRS) has also been estimated for all the district headquarters as shown in Fig. 8a, b. In order to obtain the UHRS curves, the ground motion prediction equations were developed using spectral acceleration values at 28 time periods. Each value in these response spectrums have uniform probability of exceedance for all the 28 spectral values. It can be observed from these plots that among all C-type cities, Bilaspur exhibits the highest hazard while Solan being the lowest. Also, Una being the only city in the Indo-Gangetic region exhibits the lowest hazard level among the D-type sites while the highest being Sundernagar. It can also be seen that for certain cities with both site types (e.g. Chamba, Sundernagar, etc.), the D-type sites exhibit higher hazard levels as expected.

9 Conclusions

In this study, MASW tests were conducted at 73 sites located in 22 important cities of Himachal Pradesh, to estimate the dynamic characteristics of these site conditions. Based on the evaluated site response functions, ground motion prediction equations have been developed to predict the surface level peak ground acceleration values for the widely prevalent C and D type sites in the two geological regions, viz., Himalayan and Indo-Gangetic regions. The predictions of the GMPE agrees with the measured values of actual events. Using these attenuation relations, the probabilistic seismic hazard analysis has been carried out for the state of Himachal Pradesh by adopting the framework proposed in the report of the National Disaster Management Authority [17]. The seismicity of 192 faults identified within a

500 km distance from this region have been considered while carrying out PSHA. The estimated surface level seismic hazard (PGA) of the Himachal Pradesh are presented for the both C and D site conditions. Also, Uniform Hazard Response Spectrum (UHRS) plots for some important cities are presented.

Acknowledgments The author's would like to thank the support of Dr. G.R. Dodagoudar and Mr. G. Maheshreddy while carrying out the MASW tests. The financial support received from the State Government of Himachal Pradesh and the assistance of TARU Leading Edge Pvt. Ltd. are gratefully acknowledged.

References

1. Bhatia SC, Kumar RM, Gupta HK (1999) A probabilistic seismic hazard map of India and adjoining regions. *Annali di Geophysica* 42:1153–1164
2. Boore DM (2009) Comparing stochastic point-source and finite-source ground motion simulations: SMSIM and EXSIM. *Bull Seismol Soc Am* 99:3202–3216
3. Boore DM, Joyner WB (1997) Site amplifications for generic rock sites. *Bull Seismol Soc Am* 87:327–341
4. Cornell CA (1968) Engineering seismic risk analysis. *Bull Seismol Soc Am* 58:1503–1606
5. Department of Planning (2003) An overview of planning in Himachal Pradesh. <http://hpplanning.nic.in/Reports.htm>
6. Der Kiureghian A, Ang A (1977) A fault-rupture model for seismic risk analysis. *Bull Seismol Soc Am* 67:1173–1194
7. Directorate of Census Operations (2001) Census of India: Himachal Pradesh. <http://www.censusindia.gov.in>
8. Geological Survey of India (GSI) (2000) Seismotectonic Atlas of India and its environs
9. IBC (2009) International building code. International code council
10. Idriss I, Sun J (1992) Users manual for SHAKE91: a computer program for conducting equivalent linear seismic response analyses of horizontally layered soil deposits
11. Joyner WB, Boore DM (1981) Peak horizontal acceleration and velocity from strong-motion records including records from the 1979 Imperial Valley, California, earthquake. *Bull Seismol Soc Am* 71:2011–2038
12. Karan P (1966) Geographic regions of the Himalayas. *Bull Tibetol* III:5–26
13. Khattri KN, Rogers AM, Perkins DM, Algermissen ST (1984) A seismic hazard map of India and adjacent area. *Tectonophysics* 108:93–134
14. Kramer SL (1996) Geotechnical earthquake engineering. Prentice Hall, Upper Saddle River, New Jersey
15. Mahajan A, Thakur V, Sharma M, Chauhan M (2010) Probabilistic seismic hazard map of NW Himalaya and its adjoining area, India. *Nat Hazards* 53:443–457
16. Mittal H, Kumar A, Rebecca (2012) Indian strong motion instrumentation network and its site characterization. *Int J Geosci* 3(6):1151–1167
17. NDMA (2011) Development of probabilistic seismic hazard map of India. A technical report of the working committee of experts (WCE) constituted by the National Disaster Management Authority (NDMA), Government of India, New Delhi
18. Park CB, Miller RD, Xia J (1997) Multi-channel analysis of surface waves. *Geophysics* 64(3):800–808
19. Parvez IA, Vaccari F, Panza GF (2003) A deterministic seismic hazard map of India and adjacent areas. *Geophys J Int* 155:489–508
20. Patil N, Das J, Kumar A, Rout MM, Das R (2014) Probabilistic seismic hazard assessment of Himachal Pradesh and adjoining regions. *J Earth Syst Sci* 123:49–62

21. Raghukanth STG (2011) Seismicity parameters for important urban agglomerations in India. *Bull Earthq Eng* 9:1361–1386
22. Ramakrishnan M, Vaidyanathan R (2010) *Geology of India*, vol 1. Geological Society of India, Bangalore
23. Valdiya KS (1976) Himalayan transverse faults and folds and their parallelism with subsurface structures of North Indian plains. *Tectonophysics* 32:353–386

Simulation of Near Fault Ground Motion in Delhi Region

Hemant Shrivastava, G.V. Ramana and A.K. Nagpal

Abstract Ground motions in the vicinity of the source caused severe damage to structures as evidenced during the past earthquakes (Loma Prieta 1989; Kobe 1995; Chi-Chi 1999). Near fault ground motions are characterized by long period velocity pulse as reported in literature (Somerville, 2005). This pulse type of motion is produced due to forward directivity where fault rupture propagates towards the site at a velocity close to shear wave velocity, causing most of the seismic energy to arrive at the site within a short time. Such impulsive motion subjects structures to high input seismic energy at the beginning of the record. In this study, near fault ground motion for M_w 6.0 has been simulated in Delhi region. The high frequency ground motion has been simulated using specific barrier model, combined with long period velocity pulse. As reported in literature, strong ground motion with long period pulse can increase the demand on medium and high rise structures.

Keywords Delhi region · Near fault · Long period velocity pulse

1 Introduction

Delhi, capital city, lies in the northern part of India. It is located between latitude $28^{\circ} 24' - 28^{\circ} 53'$ and longitude $76^{\circ} 50' - 77^{\circ} 20'$. It is centre of major economic and commercial activities with a very high density of infrastructure. It is situated at distance of 200–300 km from Himalayan arc region. Moderate/local earthquakes (M_w 6.0, 1960; M_w 2.6, 2002; M_w 3.4, 2004; M_w 4.1, 2007; M_w 5.0, 2012) were felt in the Delhi city. The earthquake that occurred on 27th August, 1960, has its epicentre near Sohna at a distance about 60 km from Delhi city and caused minor damage to buildings and left around about 50 persons injured [31]. Singh et al. [25] simulated ground motions in Delhi from possible future large/great earthquakes in

H. Shrivastava (✉) · G.V. Ramana · A.K. Nagpal
Department of Civil Engineering, Indian Institute of Technology Delhi, New Delhi, India
e-mail: hemant.shrivastava1986@gmail.com

the central seismic gap in Himalayan arc. They have generated ground motion for magnitude M_w 7.5, 8.0, and 8.5 using stochastic method (point source and finite source). Rao [23] simulated ground motion for M_w 6.0 and 6.5 earthquakes using specific barrier model. Bansal et al. [3] studied two local earthquakes (M_w 2.6, 2001; M_w 3.4, 2004) of Delhi and synthesized expected ground motions in the epicentre region for an M_w 5.0 earthquake in Delhi using EGF. Delhi earthquake of 25 November 2007 (M_w 4.1) was studied by Singh et al. [26] and they provided source parameters. They compared recorded PGA with attenuation relationship proposed by Iyengar and Ghosh [11]. The equation was found to overestimates the PGA for distances greater than 100 km. Kumar et al. [12] studied the effect of two hypothetical moderate earthquakes of M_w 5.5 and 6.0 for seismic hazard and risk in NCR (Delhi) region. They simulated earthquake ground motion using composite source technique at hard soil site and soft soil site. Manisha et al. [16] simulated strong ground motion at bedrock level in National capital (Delhi) region using semi empirical technique for M_w 5.5 and 6.0. Mittal et al. [18] simulated strong ground motion of a local earthquake (M_w 5.5) in Delhi using EGF at bedrock level and at different soil sites. However, none of the above studies incorporated long period velocity pulse which is important characteristic of near fault ground motion.

From past earthquakes (Loma Prieta 1989; Landers 1992; Kobe 1995; Chi-Chi 1999) it has been observed that stations located near fault recorded a ground motion with long period velocity pulse [29]. Bertero et al. [4] has been identified long period velocity pulse is critical in the design of structures. A coherent long period velocity pulse is generated by forward directivity effect. Forward directivity occurs when the fault rupture propagates towards the site at a velocity nearly equal to the propagation velocity of the shear waves and the direction of fault slip is aligned with the site and causes the wave front to arrive as a single large pulse [30]. The near fault pulses can cause very large inelastic deformation demands on a structure. The effect of long period ground motion on flexible structures has been extensively reported in the literature [28, 30]. The importance of near fault motions on structural performance has been reported in several studies [1, 9, 13–15]. The elastic and inelastic analysis of multi-degree of freedom systems indicates that amplitude and period of the pulse in the near fault earthquakes are key parameters that control the performance of structures [1, 4, 9, 24, 33]. A number of studies are available to characterize the amplitude and period of the pulse for long period ground motion in the near fault region [2, 7, 10, 17, 30]. The hybrid methodology, consisting of superimposition of high frequency ground motion and long period velocity pulse [6, 10, 17], is an efficient and effective method for the simulation of strong ground motion in near fault region [8, 10].

In the present study, the strong ground motion has been simulated using hybrid technique for near fault earthquake (M_w 6.0) in Delhi region from local sources. The specific barrier model has been used for simulating high frequency ground motion of M_w 6.0 earthquake and the long period velocity pulse model [17] is used for simulating the low frequency ground motion and these are then superimposed. This simulation method can be used to generate synthetic ground motion for scenario

earthquakes in Delhi region and it can further be used in the damage evaluation and seismic assessment of structures.

2 Simulation of High Frequency Ground Motion

For the simulation of strong ground motion, stochastic method described by Boore [5] is adopted here. The Fourier amplitude spectrum of S-wave portion of strong ground motion, $Y(M_o, r, f)$, at an distance R from an source, can be expressed as

$$Y(M_o, R, f) = E(M_o, f)G(R)A_n(f)P(f) \quad (1)$$

$$E(M_o, f) = c * S(M_o, f) \quad (2)$$

where, c is constant, $S(M_o, f)$ is source spectrum, $G(R)$ is path effects, $A_n(f)$ is path attenuation term, $P(f)$ is site terms, M_o is the seismic moment, f is the frequency and R represent distance in km.

The specific barrier model has been used to simulate the source spectrum [20, 21]. It composed of subevents that rupture randomly and independently in time. The subevents are modelled as identical circular cracks and the acceleration source spectrum [22] may be expressed as follows

$$S(M_o, f) = (2\pi f)^2 \left\{ N \left[1 + (N - 1) \left(\frac{\sin(\pi f T)}{(\pi f T)} \right)^2 \right] \right\}^{\frac{1}{2}} M_{oi}(f) \quad (3)$$

$$M_{oi}(f) = \frac{M_{oi}}{1 + \left(\frac{f}{f_2} \right)^2} \quad (4)$$

where, $M_{oi}(f)$ is the acceleration source spectrum of the individual subevent, N is the total number of subevents that compose the rupture.

3 Simulation of Long Period Velocity Pulse

In the case of near fault ground motion, most of the elastic energy arrives coherently in a single, intense, relatively long period pulse at the beginning of the record, representing the cumulative effect of almost all the seismic radiation from the fault. The phenomenon is even more pronounced when the direction of slip on the fault

plane points towards the site as well. Mavroeidis and Papageorgiou [17] proposed an analytical expression for near fault velocity pulse given as

$$v(t) = \begin{cases} \frac{A}{2} \left[1 + \cos\left(\frac{2\pi f_p}{\gamma}(t - t_0)\right) \cos[2\pi f_p(t - t_0) + v] \right], & t_0 - \frac{\gamma}{2f_p} \leq t \leq t_0 + \frac{\gamma}{2f_p} \quad \text{with } \gamma > 1 \\ 0, & \text{otherwise} \end{cases} \quad (5)$$

$$a(t) = \begin{cases} \frac{A\pi f_p}{\gamma} \left[\begin{array}{l} \sin\left(\frac{2\pi f_p}{\gamma}(t - t_0)\right) \cos[2\pi f_p(t - t_0) + v] \\ + \gamma \sin[2\pi f_p(t - t_0) + v] \left[1 + \cos\left(\frac{2\pi f_p}{\gamma}(t - t_0)\right) \right] \end{array} \right], & t - \frac{\gamma}{2f_p} \leq t \leq t_0 + \frac{\gamma}{2f_p} \quad \text{with } \gamma > 1 \\ 0, & \text{otherwise} \end{cases} \quad (6)$$

Here, parameter A controls amplitude of the signal, f_p is for prevailing frequency, v is phase of amplitude modulated harmonic, γ is a parameter that defines the oscillatory character of the signal and t_0 specifies the epoch of the envelope's peak. The pulse duration, pulse amplitude, as well as the number and phase of half cycles are the key parameters that define the waveform characteristics of near fault velocity pulses. The prevailing frequency ($f_p = 1/T_p$) of the signal is the inverse of the duration of the pulse. The pulse period and the moment magnitude are related through empirical relationship given by Mavroeidis and Papageorgiou [17].

$$\log T_p = -2.9 + 0.5M_w \quad (7)$$

4 Simulation of Near Fault Earthquake

Delhi region felt an earthquake of maximum M_w 6.0 till now. It occurred between Delhi cantonment and Gurgaon (epicentre within ~ 5 km of 28.47° N, 77.00° E) at a shallow depth [19, 27], however, no record of this earthquake is available. To generate M_w 6.0 earthquake, the fault location is assumed within ~ 5 km of 28.47° N, 77.00° E [27]. If site is located within distance of 15–25 km from fault and align in the direction of rupture and slip on the fault. It may cause large damage to site due to long period velocity pulse. The specific barrier model used for simulating high frequency ground motion for local sources of M_w 6.0 and the simulation parameters have been adopted from Rao [23] and are given in Table 1. These scenario earthquakes generated at the ridge observatory (Delhi).

The input parameters to simulate the long period velocity pulse are as following:

Table 1 Seismological source parameters for simulation of scenario earthquake

Input parameters	Values
Moment magnitude	6.0
Distance (km)	20
Crustal density (kN/m ³)	2.85
Rupture velocity (km/sec)	3.6
Path properties $Q(f) = Q_0 \exp(f)$	$800f^{0.42}$
Geometrical spreading	$G(R) = R^{-1}$ for $R \leq R_x$ $G(R) = (RR_x)^{-1/2}$ for $R > R_x$
Partition factor	0.71
Radiation factor	0.55
Free surface factor	2.0
f_{\max}	50
$\Delta\sigma_G, \Delta\sigma_L$ (bars)	60, 180

(a) Amplitude

For the amplitude of velocity pulse, the attenuation relationship developed by Somerville [28] between the peak ground velocity, moment magnitude and distance between fault and site has been adopted in present study. This relationship cannot be used for distance less than 3 km.

$$\log_{10} PGV = -1.0 + 0.5M_w - 0.5 \log_{10} R \quad (8)$$

where, R is the closest distance of the site to the fault and M_w is the moment magnitude.

(b) Number of Pulses

The number of significant pulses in the velocity time history is an important parameter for structural response. Multiple cycles of motion can dramatically increase the damage potential of the ground motions. The number of cycle of motion is defined as the number of half cycles. Somerville et al. [30] suggests that the number of half cycle sine pulse in the velocity time history might be associated with the number of asperities in a fault. From the point of view of ground motion prediction, this implies that prediction of number of significant velocity pulses in a given earthquake is associated with the determination of slip distribution in the causative fault. This is difficult to estimate a priori [6]. There are no models currently available for predicting the number of significant pulses in the velocity time history. For most, number of pulses will vary between 1 and 3, with number of pulse equal to 2 being a good general value to use in seismic evaluation [32]. In this work assumed number of significant pulse equal to 2 (i.e. one full cycle of pulse type ground motion).

(c) Phase Angle and Epoch of Envelope's Peak

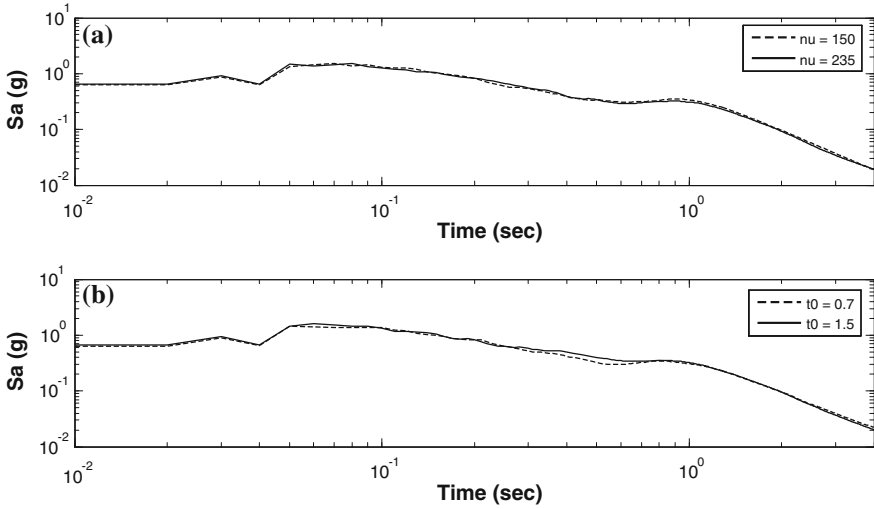


Fig. 1 Comparison of response spectra for **a** phase angle (ν) and **b** epoch of envelope's peak (t_0)

From literature, it is not clear that what value should be assumed for phase angle (ν) and epoch of envelope's peak (t_0) to simulate the long period velocity pulse. In order to study the effect of ν and t_0 a sensitivity analysis is carried out. The parameters amplitude, pulse period and number of pulse value kept constant in sensitivity analysis. The parameters values for ν and t_0 are taken as 150° , 235° and 0.7, 1.5 s respectively. Fifteen random time histories are generated for each ν and t_0 values and response spectrum is computed. The mean of response spectrum computed for each ν and t_0 value are shown in Fig. 1. It is found that the variation in response spectra for different t_0 and ν is negligible. From the analysis it is clear that t_0 and ν do not affect the simulation of ground motion with long period pulse.

To generate near fault ground motion, the high frequency ground motion is combined with long period velocity pulse. The input parameters for long period velocity pulse are given in Table 2. The procedure for combined the high frequency and low frequency ground motions adopted from Mavaroedis and Papageorgiou [17] are given below and shown in Fig. 2.

Table 2 Input parameters of long period velocity pulse

Parameters	Value
Magnitude	6.0
Amplitude (cm/s)	55.77
γ	1
ν	160
t_0	1.3

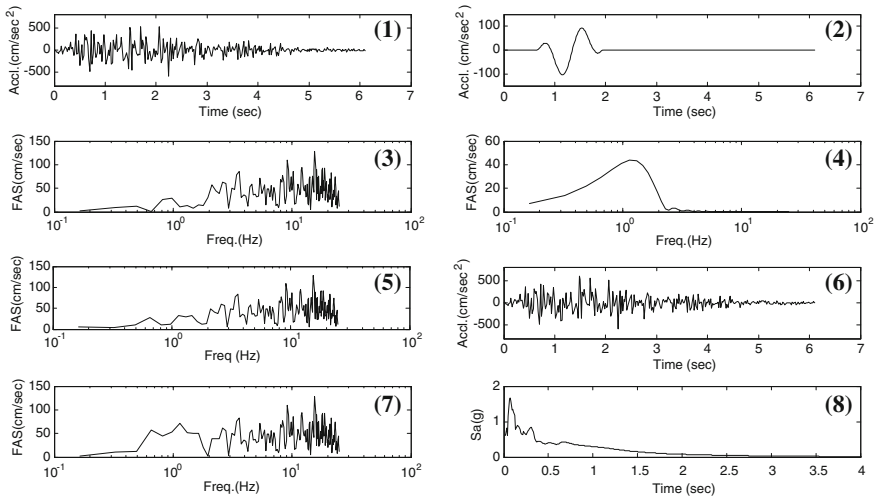


Fig. 2 Simulation of acceleration time history for M_w 6.0 earthquake with long period velocity pulse at bedrock level

1. Select the moment magnitude (M_w) of the potential earthquake and calculate the prevailing frequency (f_p). For selected values of the parameters A , γ and v , generate the long period component of acceleration time history.
2. For the selected fault-station geometry, generate the synthetic acceleration time histories for the moment magnitude, specified previously.
3. Calculate the Fourier transform of the synthetic acceleration time histories generated in steps 1 and 2.
4. Subtract the Fourier amplitude spectrum of the synthetic time history generated in step 1 from the Fourier amplitude spectrum of the synthetic time history produced in step 2.
5. Construct a synthetic acceleration time history so that (a) its Fourier amplitude spectrum is the difference of the Fourier amplitude spectra calculated in step 4; and (b) its phase coincides with the phase of the Fourier transform of the synthetic time history generated in step 2.
6. Superimpose the time histories generated in step 1 and 5. The near source pulse is shifted in time so that the peak of its envelope coincides with the time that the rupture front passes in front of the station.

Finally, the acceleration time history and response spectrum for 5 % damping with long period velocity pulse for M_w 6.0 are shown in Fig. 2 (6 and 8). In Fig. 3, response spectra (with and without long period pulse) are compared and the effect of long period pulse observed at 0.8–2.0 s. From literature [1, 4, 9, 13] it found that strong ground motion with long period pulse can increase the seismic demand (base shear, storey drift, ductility) on the medium and high rise building. The width of the

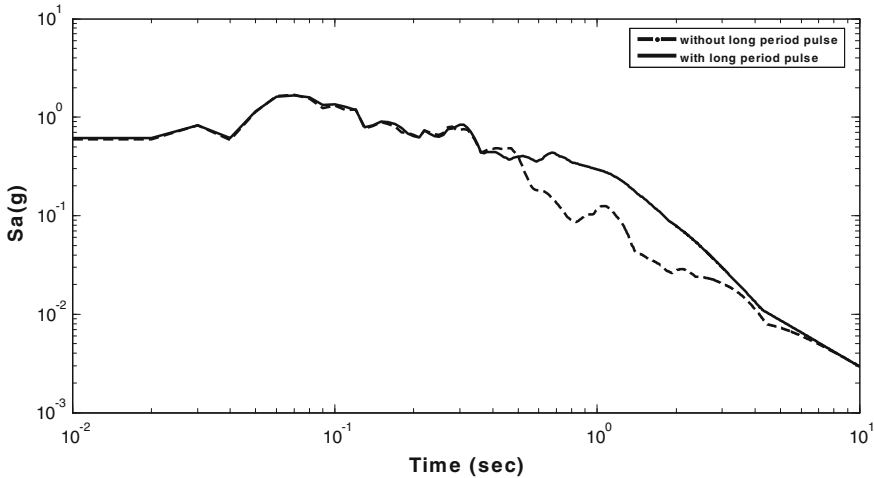


Fig. 3 Comparison of response spectra *with* and *without* long period pulse

pulse larger than the natural period of the structure can cause more damage. If building site lying along the direction of fault rupture then forward directivity will cause long period velocity motion which may lead to higher damage to building.

5 Conclusions

A methodology is proposed to simulate ground motion with long period velocity pulse in Delhi region. If the site lies along the forward directivity rupture direction then the ground motion with long period velocity pulse increases the seismic demand on the mid-rise and high rise building. The seismic demand from M_w 6.0 earthquake with long period pulse can affect the structure having time period range between 0.8 and 1.5 s at bedrock level. The earthquake of M_w 6.0 with long period velocity pulse from local sources is likely to be more destructive.

References

1. Anderson JC, Bertero VV (1987) Uncertainties in establishing design earthquakes. *J Struct Eng ASCE* 113(8):1709–1724
2. Alavi B, Krawinkler H (2000) Consideration of near fault ground motion effects in seismic design. In: 12th world conference on earthquake engineering
3. Bansal BK, Singh SK, Dharmaraju R, Pacheco JF, Ordaz M, Dattatrayam RS, Suresh G (2009) Source study of two small earthquakes of Delhi, India, and estimation of ground motion from future moderate, local events. *J Seismolog* 13:89–105

4. Bertero VV, Mahin SA, Herrera RA (1978) Aseismic design implications of near fault San Fernando earthquake records. *Earthq Eng Struct Dyn* 6:31–42
5. Boore DM (2003) Simulation of ground motion using the stochastic model. *Pure Appl Geophys* 160:635–676
6. Bray JD, Marek AR (2004) Characterization of forward directivity ground motions in the near fault regions. *Soil Dyn Earthq Eng* 24:815–828
7. Fu Q, Menun C (2004) Seismic environment based simulation of near fault ground motions. In: 13th world conference on earthquake engineering, paper no. 332
8. Halldorsson B, Mavroeidis GP, Papageorgiou AS (2011) Near fault and far fault strong ground motion simulation for earthquake engineering applications using the specific barrier model. *J Struct Eng ASCE* 137(3):433–444
9. Hall JF, Heaton TH, Halling MW, Wald DJ (1995) Near source ground motion and its effect on flexible buildings. *Earthq Spectra* 11(4):569–605
10. He WL, Agrawal AK (2008) Analytical model of ground motion pulses for the design and assessment of seismic protective systems. *J Struct Eng ASCE* 134(7):1177–1188
11. Iyengar RN, Ghosh S (2004) Microzonation of earthquake hazard in greater Delhi area. *Curr Sci* 87:1193–1202
12. Kumar D, Sarkar I, Sriram V, Teotia SS (2012) Evaluating the seismic hazard to the National capital (Delhi) region, India from moderate earthquakes using simulated accelerograms. *Nat Hazards* 61:481–500
13. Liao WI, Loh CH, Wan S (2001) Earthquake responses of RC moment frames subjected to near fault ground motions. *Struct Des Tall Spec Build* 10:219–229
14. MacRae GA, Morrow DV, Roeder CW (2001) Near fault ground motion effects on simple structures. *J Struct Eng ASCE* 127(9):996–1004
15. Malhotra PK (1999) Response of buildings to near fault pulse like ground motion. *Earthq Eng Struct Dyn* 28:1309–1326
16. Manisha, Kumar D, Teotia SS (2011) Seismic hazard based on simulated accelerograms due to moderate/strong earthquakes in National Capital (Delhi) region. *J Indian Geophys Union* 15 (2):77–84
17. Mavroeidis GP, Papageorgiou AS (2003) A mathematical representation of near fault ground motions. *Bull Seismol Soc Am* 93(3):1099–1131
18. Mittal H, Kumar A, Kamal (2012) Ground motion estimation in Delhi from postulated regional and local earthquakes. *J Seismolog* 17(2):593–605
19. Nath M, Narain K, Srivastava JP (1960) A report on the Delhi earthquake of 27 August 1960. Geological Survey of India, Northern Region, Lucknow, 1960
20. Papageorgiou AS, Aki K (1983a) A specific barrier model for the quantitative description on inhomogeneous faulting and the prediction of strong ground motion. Part I: description of the model. *Bull Seismol Soc Am* 73(3):693–722
21. Papageorgiou AS, Aki K (1983b) A specific barrier model for the quantitative description on inhomogeneous faulting and the prediction of strong ground motion. Part I: applications of the model. *Bull Seismol Soc Am* 73(3):693–722
22. Papageorgiou AS (1988) On two characteristics frequencies of acceleration spectra: patch corner frequency and f_{max} . *Bull Seismol Soc Am* 78:509–529
23. Rao HCh (2006) Ground response analyses and liquefaction studies for soils of Delhi. Ph.D. thesis, Indian Institute of Technology Delhi, New Delhi
24. Sasani M, Bertero V (2000) Importance of severe pulse-type ground motion in performance based engineering: historical and critical review. In: Proceedings of 12th world conference on earthquake engineering, Auckland, New Zealand
25. Singh SK, Mohanty WK, Bansal BK, Roonwal GS (2002) Ground motion in Delhi from future large/great earthquakes in the central seismic gap of the Himalayan arc. *Bull Seismol Soc Am* 92:555–569
26. Singh SK, Kumar A, Suresh G, Ordaz M, Pacheco JF, Sharma ML, Bansal BK, Dattatrayam RS, Reinoso E (2010) Delhi earthquake of 25 November 2007 (M_W 4.1): implications for seismic hazard. *Curr Sci* 29(7):939–947

27. Singh SK, Suresh G, Dattatrayam RS, Shukla HP, Martin S, Havskov J, Perez-Campos X, Iglesias A (2013) The Delhi 1960 earthquake: epicenter, depth and magnitude. *Curr Sci* 105 (8):1155–1165
28. Somerville PG (1998) Development of an improved representation of near fault ground motions. In: SMIP98 seminar on utilization of strong motion data, Oakland
29. Somerville PG (2005) Engineering characterization of near fault ground motions. In: NZSEE conference
30. Somerville PG, Smith NF, Graves RW, Abrahamson NA (1997) Modification of empirical strong ground motion attenuation relations to include the amplitude and duration effects of rupture directivity. *Seismol Res Lett* 68(1):199–222
31. Srivastava LS, Somayajulu JG (1966) The seismicity of the area around Delhi. In: 3rd symposium on earthquake engineering, University of Roorkee, Roorkee
32. Stewart JP, Chio SJ, Bray JD, Graves RW, Somerville PG, Abrahamson NA (2001) Ground motion evaluation procedures for performance based design. PEER report 2001/09, University of California, Berkeley
33. Zhang Y, Iwan WD (2002) Active interaction control of tall buildings subjected to near field ground motions. *J Struct Eng ASCE* 128:69–79

Interaction Analysis of Space Frame-Shear Wall-Soil System to Investigate Forces in the Columns Under Seismic Loading

D.K. Jain and M.S. Hora

Abstract The phenomenon of soil-structure interaction greatly affects the design of RC shear wall building frame resting on a deformable soil. In the present work, a G + 5 RC shear wall building frame (4×3 bays and 6 storeys) having open foundation (isolated footings) and resting on deformable soil is considered, to investigate axial force and bending moments in the columns. The 3-D interaction analysis is carried out using finite element software ANSYS. The superstructure and soil are considered to follow linear stress-strain relationship. The interaction analysis is carried out under various combinations of seismic loading as per IS-1893 (Part I): 2002. It is found that interaction phenomenon causes significant redistribution of forces in the superstructure. The governing bending moments in the bottom columns, along the direction of seismic loads, are increased many times as a result of soil-structure interaction as compared to the conventional non-interaction analysis.

Keywords Soil-structure interaction · Finite element analysis · ANSYS · Space frame · Shear wall · Linear elastic analysis · Column forces · RC framed building

1 Introduction

The conventional structural analysis of a RC space frame is carried out assuming foundation resting on unyielding supports. The analysis is carried out by considering bottom end of the columns fixed and neglecting the effect of soil deformations. In reality, deformations take place in soil, which are transferred to the

D.K. Jain (✉) · M.S. Hora
Department of Civil Engineering, Maulana Azad National Institute of Technology (NIT),
Bhopal, India
e-mail: dkjain63@gmail.com

M.S. Hora
e-mail: hora1961@gmail.com

structure due to soil-structure interaction, causing redistribution of forces and moments. In the present work, 3-D soil-structure interaction analysis has been carried out for a six storey RC framed building with isolated footings and shear walls (oriented along the direction of seismic loads) under normal as well as seismic loads using finite element software ANSYS. The analysis has been carried out considering superstructure and soil to follow linear stress-strain relationship. Various combinations of dead, live and seismic loads are considered as per IS-1893 (Part-I): 2002 [6]. The model is easily extendable to any configuration of space frame and shear wall as full 3-D space frame is considered for analysis. The results of linear interaction analysis (LIA), are evaluated to investigate the axial forces and moments in the columns.

2 Review of Literature

Several studies have been carried out in the past by many researchers to understand the soil-structure interaction effect on building frames and foundations and important conclusions have been drawn. The building frame as well as soils were approximated or idealised in various ways in most of the research work. Earlier research postulated 2-D idealisation of structure and soil, whereas, during recent few years, 3-D soil-structure interaction analysis with more realistic idealisation has been witnessed. Yet, the soil structure interaction effect has not widely been penetrated from research to design offices owing to modelling and analysis complexities involved.

Noorzai et al. [8] studied soil-structure interaction analysis of a plane frame-combined footing-soil system. Arlekar et al. [1] conducted an analytical study on moment resisting RC frame building, with open first storey and brick masonry in the upper storey, with isolated column footings resting on medium soil. Stavridis [10] presented simplified analysis approach for layered soil-structure analysis on an arbitrary structure. Dutta et al. [4] studied the response of low-rise buildings under seismic ground excitation incorporating soil-structure interaction. Natarajan and Vidivelli [7] examined the influence of column spacing on behaviour of a space frame raft foundation soil system under static loading using ANSYS software. Atefatdoost [9] examined the effect of soil structure interaction on torsional response of asymmetrical wall type systems. Hora [5] carried out interaction analysis of a three-bay three-storey RCC space frame-footing-strap beam-soil system using ANSYS finite element code.

Usually in design offices full 3-D analysis of structures is carried out for all important RC framed buildings. Likewise a full 3-dimensional soil-structure-interaction analysis is needed to capture the effect of interaction on the structure for directly incorporating the same into the design. Present study is an effort in that direction in which a full 3-D soil-structure interaction effect is investigated on axial forces and moments in the bottom columns of a 6-storey RC framed building with shear walls.

3 Problem Under Investigation

A six storey RCC framed building with shear walls and isolated footings resting on homogeneous soil mass has been considered in this study. The building consists of 4 bays in X-direction and 3 bays in Y-direction. For resisting lateral forces a dual system, consisting of special moment resisting frames (SMRF) and reinforced concrete shear walls, is considered. The shear walls are provided on outer frames along Y-direction i.e. the assumed direction of lateral seismic forces. The plinth beams are also provided. Such types of buildings are very common in urban areas. The space frame, shear walls and the soil mass are considered as a single compatible structural unit for the interaction analysis. The complete details of the problem under investigation are shown in Fig. 1a, b. The building is considered to be situated in seismic zone V of India. For the present analysis, super-structure, foundation, as well as soil are considered to behave in linear elastic manner.

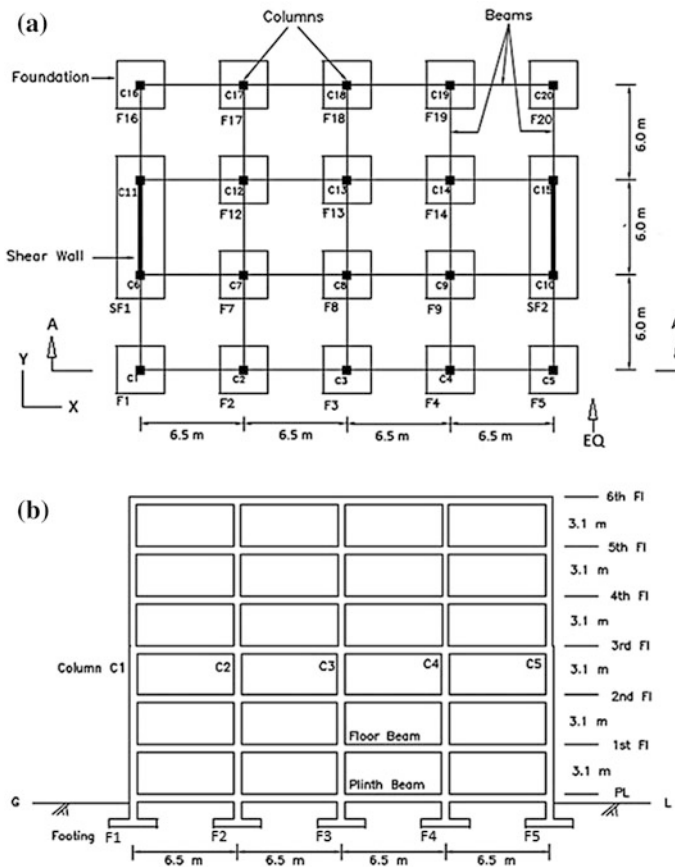


Fig. 1 a Plan of the Multi-Storeyed Space Frame with shear wall. b Sectional Elevation at section A-A

Table 1 Geometric parameters of space frame-shear wall-soil system

Parameter	Value
Slab thickness	200 mm
Beam size	300 × 500 mm
<i>Column sizes</i>	
(i) Foundation to 3rd floor	500 × 500 mm
(ii) 3rd floor to 6th floor	400 × 400 mm
Shear wall thickness	200 mm
Footing size below column	3 × 3 × 0.5 m
Footing size below shear wall	3 × 9 × 0.5 m
Semi-infinite extent of soil mass	100 × 100 × 25 m

Table 2 Material properties of concrete and soil

Property	Value
Grade of concrete for all structural elements	M25
Modulus of elasticity of concrete (N/mm ²)	$E_c = 5,000\sqrt{f_{ck}}$
Poisson's ratio of concrete	0.15
Density of concrete	25,000 N/m ³
Elastic Modulus of soil	14.78 N/mm ²
Poisson's ratio of soil	0.35

The geometrical properties of space frame-shear wall-soil system are provided in Table 1.

The elastic modulus of soil is taken as 14.78 N/mm² as per tri-axial test results reported in literature [3]. The material properties of concrete and soil are provided in Table 2.

The building is considered to be an institutional building. The live loads are considered as per IS 875 (Part II):1987. The live loads of 4 KN/m² on floors and 1.5 KN/m² on roof are considered. The brick masonry wall on outer periphery of the building and parapet wall on roof is also considered. Besides self-weight of various structural elements, dead load of floor finish is considered as 1 KN/m² and dead load of water proofing on roof is considered as 2.5 KN/m².

For seismic load calculations, equivalent static lateral force method is used as per IS 1893 (Part I): 2002. The parameters used for seismic load calculations are given in Table 3.

4 Finite Element Modelling

The finite element modelling and analysis of the problem is achieved using ANSYS software which has wide variety of elements and material models suited for the problem under consideration.

Table 3 Parameters for lateral seismic load calculation on the structure

Parameter	Value
Earthquake zone	V
Zone factor 'Z'	0.36
(Table 2 of IS 1893 (Part I): 2002)	
Importance factor 'I'	1.5
(Table 6 of IS 1893 (Part I): 2002)	
Response reduction factor 'R'	5.0
(Table 7 of IS 1893 (Part I): 2002) (Ductile shear wall with SMRF)	
Approximate fundamental natural period of vibration (T_a)	0.728 s
$T_a = 0.075 h^{0.75} = 0.075 (20.7)^{0.75} = 0.7278452$	
(as per clause 7.6.1 of IS 1893 (Part I): 2002)	
Average response acceleration coefficient (S_a/g)	1.8685
$S_a/g = 1.36/T_a$	
(for soil for 5 % damping, as given in Fig. 2 of IS 1893 (Part I): 2002, for the natural period T_a of 0.7278452 s)	

The beams and columns are modelled in ANSYS using its advanced line element Beam4 (3D Elastic Beam) having two nodes with 6 degrees of freedom at each node, slabs and shear walls are modelled using four node Shell63 (Elastic Shell) element having six degrees of freedom at each node, foundations and soil mass are modelled using SOLID45 (3D Structural Solid) element defined by eight nodes having three degrees of freedom at each node. Adopting same element type for foundation and soil mass enables better contact modeling between foundation and soil mass.

Surface to surface contact is established between foundation bottom area and soil using ANSYS surface to surface contact elements CONTA174 and TARGE170. The contact problems are highly nonlinear and require significant computer resources to solve. Except contact, the whole analysis of the structure and soil mass is considered linear elastic in the present problem. Under contact basic properties, behavior of contact surface is chosen as 'standard', which allows sliding as well as lifting of foundations. Coefficient of friction between concrete and soil is taken as 0.5.

4.1 Extent of Soil Mass

The soil mass is considered to be made up of homogeneous linear elastic isotropic material. Usually bed rock is encountered at most of the sites at varying depth from ground level. It is assumed that bed rock is encountered 25 m below top of soil in the present case. Horizontal stretch of 100 m × 100 m is kept for the soil mass which is achieved through numerous trial runs to ensure that the displacements and

stresses in the soil reduces to negligible values at the boundaries. Thus, soil participating volume of $100\text{ m} \times 100\text{ m} \times 25\text{ m}$ is kept, which is sufficient to capture the dominant effect of soil-structure-interaction of the problem under consideration.

4.2 Meshing and Mesh Optimization

The extensive mesh refinement is achieved for the superstructure as well as for the soil mass. Several trial analyses were conducted to observe the effect of increasing number of mesh division on the maximum deflection and the maximum stresses in the structure and the soil. Finer meshing consumes enormous amount of computing time and coarser meshing results in values far away from converged values. Optimised meshing is found to get converged results with minimum of computing time. Finally, the mesh size of 500 mm is adopted for beams, slabs and shear wall resulting in 12 divisions for beams and shear wall and 12×13 divisions for slabs. For the columns 12 mesh divisions are found appropriate. The foundation mesh size is kept as 500 mm. The mesh sizes of 500 mm is adopted below and around the building which maps the foundation and soil most efficiently and gives better converged results. The graded meshing is adopted beyond building area in increasing order of size and by several trial and error, mesh size giving optimized converged results with least processing time is achieved, as depicted in Fig. 2(a), (b).

The vertical displacement (U_z) is restrained on soil bottom as bed rock is assumed to be encountered at this location. The side boundaries of soil are considered to be restrained laterally (i.e. horizontal displacement (U_x) is restrained on boundaries perpendicular to X-direction and horizontal displacement (U_y) is restrained on boundaries perpendicular to Y-direction).

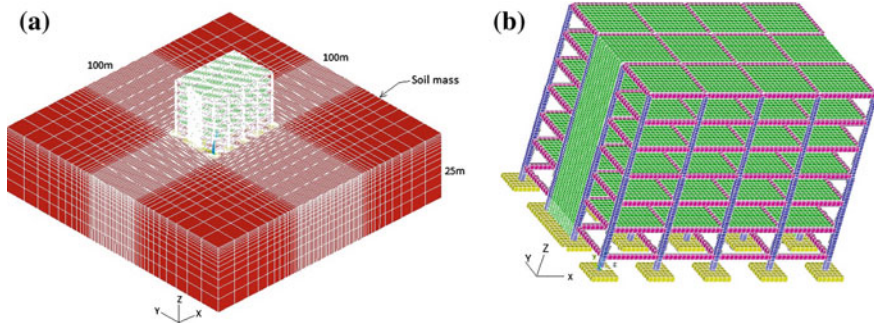


Fig. 2 Finite element discretization of space frame-shear wall- soil system. **a** Complete system **b** space frame-shear wall-system

Table 4 Load Combinations

Load case no.	Designation	Load combination
1	LC1	1.5(DL + LL)
2	LC2	1.2(DL + LL + EL)
3	LC3	1.2(DL + LL-EL)
4	LC4	1.5(DL + EL)
5	LC5	1.5(DL-EL)
6	LC6	0.9DL + 1.5EL
7	LC7	0.9DL-1.5EL

5 Linear Interaction Analysis

For the space frame-shear wall-soil system, the linear interaction analyses (LIA) is carried out assuming the structure, shear wall and soil to act as a single compatible structural unit and to behave in linear elastic manner. The non-interaction analysis (NIA) is also carried out for comparison of the results.

For each of the above analyses, following combinations (Table 4) of dead load (DL), live load (LL) and seismic load (EL) are considered as per Clause 6.3.1.2 of IS 1893 (Part I): 2002.

The seismic load (EL) is applied in the Y-direction. Positive sign of seismic load shows that it is applied from front and negative sign shows that it is applied from back i.e. from opposite direction.

6 Result and Discussion

The results of non-interaction analysis (NIA) and linear interaction analysis (LIA) are compared to investigate following forces and moments in the columns below plinth level;

- Axial force (F_z)
- Bending moment about X-axis (M_x) (i.e. along direction of seismic loads)

Results are tabulated for columns in one quarter portion of the structure (i.e. columns C1, C2, C3, C6, C7 and C8) owing to the symmetry.

6.1 Axial Force (F_z) in Columns Below Plinth Level

Table 5 shows the comparison of axial force F_z in columns for NIA and LIA systems. The load case LC1 causes decrease in axial force in the inner columns and increase in the outer columns, except for the shear wall boundary column C6, due to the interaction effect. In columns other than C6, the maximum increase of nearly 50 % is found in the column C1 and the maximum decrease of nearly 25 % is found

Table 5 Comparison of axial forces (F_z) in columns for NIA and LIA systems under various load cases

Column No.	Analysis	LC1	LC2	LC3	LC4	LC5	LC6	LC7
C1	NIA	1779.40	1209.80	1634.40	1231.40	1762.20	632.02	1162.80
	LIA	2668.40	1570.80	2693.50	1407.70	2811.40	562.42	1965.70
	% diff.	49.96	29.84	64.80	14.32	59.54	-11.01	69.05
C2	NIA	2907.70	2186.10	2465.20	2108.90	2457.90	1195.30	1544.20
	LIA	3089.40	2030.10	2911.30	1808.20	2909.40	858.35	1965.70
	% diff.	6.25	-7.14	18.10	-14.26	18.37	-28.19	27.30
C3	NIA	2865.90	2166.90	2418.50	2093.60	2408.10	1193.20	1507.70
	LIA	3232.60	2179.70	2991.50	1942.40	2956.90	956.28	1977.30
	% diff.	12.80	0.59	23.69	-7.22	22.79	-19.86	31.15
C6	NIA	944.91	1503.50 (T)	3015.00	2086.50 (T)	3561.50	2381.60 (T)	3266.40
	LIA	1731.10	1193.70	1573.30	1083.00	1562.40	575.48	990.33
	% diff.	83.20	**	-47.82	**	-56.13	**	-69.68
C7	NIA	4049.90	3183.40	3296.50	2734.00	2875.30	1612.20	1753.50
	LIA	3050.90	2327.50	2556.50	2053.00	2338.90	1171.30	1461.80
	% diff.	-24.67	-26.89	-22.45	-24.91	-18.66	-27.35	-16.64
C8	NIA	4168.60	3357.40	3312.50	2910.20	2854.00	1757.40	1701.20
	LIA	3269.30	2554.30	2679.70	2252.50	2408.80	1315.20	1479.50
	% diff.	-21.57	-23.92	-19.10	-22.60	-15.60	-25.16	-13.03

T Tension; ** reversal from tension to compression

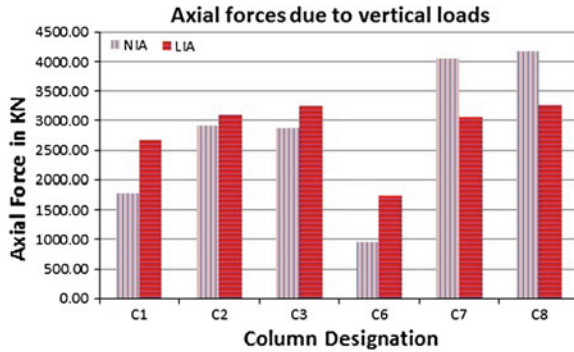


Fig. 3 Axial forces in columns below plinth level in space frame-shear wall-soil system under vertical loads (load case LC1) for NIA and LIA analyses

in the column C7. In the shear wall boundary column C6, an increase of nearly 83 % is found, below plinth level. Under various combinations of seismic loads, interaction effect causes decrease in axial forces in the inner columns and increase/decrease in axial forces in the outer columns. The maximum increase of nearly 70 % takes place in the corner column C1 and the maximum decrease of nearly 27 % takes place in the column C2.

Behaviour of the boundary columns of shear walls (C6) below plinth level is quite different under seismic loads. Non interaction analysis causes tension (lifting) in C6 under seismic loads and excessive compression when direction of seismic loads is reversed. The interaction effect significantly relieves these forces. The change in nature of forces from tension to compression is found. The maximum decrease of nearly 70 % is found in the compressive force.

Figures 3 and 4 shows axial forces in the columns below plinth level for vertical loads (load case LC1) and seismic loads (load cases LC4 and LC5) respectively, for the space frame-shear wall-soil system.

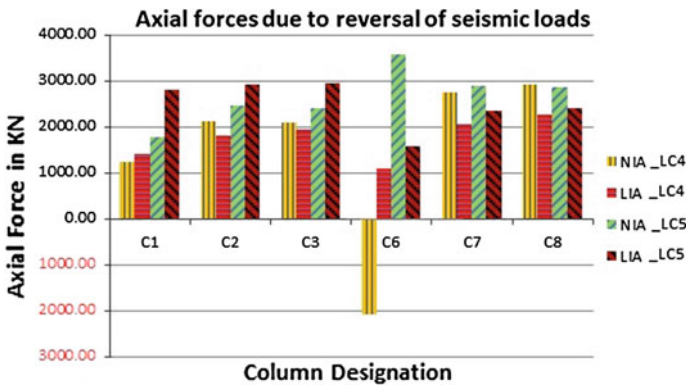


Fig. 4 Axial forces in columns below plinth level in space frame-shear wall-soil system under seismic loads (load case LC4 and LC5) for NIA and LIA analyses

Table 6 Comparison of bending moment M_x in columns below plinth level for NIA and LIA systems under various load cases

Bending moment M_x in columns under various load cases (KN-M)		LC1	LC2	LC3	LC4	LC5	LC6	LC7	
Column No.	Column End	Analysis							
C1	Lower	NIA	20.85	-39.44	72.26	-51.54	88.08	-58.98	80.64
		LIA	150.12	-337.26	597.84	-449.40	719.10	-444.48	674.65
		% diff.	620.03	755.19	727.35	771.93	716.41	653.57	736.63
C2	Upper	NIA	27.49	21.17	23.17	29.06	31.55	17.03	19.52
		LIA	147.97	121.08	147.97	122.38	129.04	106.60	76.38
		% diff.	438.19	471.89	538.77	321.09	308.95	526.10	291.37
C3	Lower	NIA	10.02	-30.61	46.65	-41.23	55.35	-44.05	52.53
		LIA	230.01	-242.94	608.21	-354.92	708.49	-422.67	648.49
		% diff.	2196.20	693.56	1203.83	760.91	1179.99	859.55	1134.56
C6	Upper	NIA	-5.79	7.72	-16.96	14.96	-15.89	15.15	-15.69
		LIA	159.73	231.46	22.49	246.26	-13.85	209.17	-64.43
		% diff.	2658.72*	2897.91	32.61*	1546.45	-12.81	1280.66	310.56
C3	Lower	NIA	10.10	-30.57	46.74	-41.24	55.40	-44.07	52.57
		LIA	248.16	-224.68	616.37	-338.16	712.56	-415.71	647.27
		% diff.	2356.79	634.87	1218.83	719.94	1186.30	843.25	1131.35
C6	Upper	NIA	-5.60	7.71	-16.69	14.84	-15.66	15.00	-15.50
		LIA	173.39	244.80	29.87	257.28	-10.21	215.81	-64.95
		% diff.	2996.25*	3074.23	78.97*	1633.23	-34.82	1338.54	318.98
C6	Lower	NIA	16.72	-97.37	124.05	-127.41	149.37	-131.82	144.96
		LIA	101.41	-1297.00	1457.90	-1646.50	1793.90	-1711.80	1795.30
		% diff.	506.48	1232.01	1075.25	1192.28	1100.98	1198.59	1138.48
C6	Upper	NIA	-30.65	-27.44	-21.93	-36.16	-29.27	-23.16	-16.26
		LIA	45.46	-74.33	144.09	-120.46	152.53	-136.18	146.16

(continued)

Table 6 (continued)

Bending moment Mx in columns under various load cases (KN-M)									
Column No.	Column End	Analysis	LC1	LC2	LC3	LC4	LC5	LC6	LC7
C7	Lower	% diff.	48.30*	170.87	557.20*	233.11	421.13*	488.10	798.67*
		NIA	7.39	-37.09	48.92	-49.66	57.86	-51.30	56.22
		LIA	33.01	-307.75	358.45	-390.41	439.80	-415.07	444.99
	Upper	% diff.	346.54	729.65	632.70	686.10	660.16	709.07	691.54
		NIA	9.16	10.96	3.71	9.69	0.64	7.63	-1.43
		LIA	85.35	187.65	-52.42	204.09	-96.06	183.34	-118.65
C8	Lower	% diff.	831.58	1612.76	1312.26*	2006.04	15024.47*	2303.54	8210.57
		NIA	7.43	-37.12	49.01	-49.69	57.97	-51.34	56.32
		LIA	29.18	-307.21	350.90	-389.55	430.37	-414.26	435.72
	Upper	% diff.	292.76	727.61	616.03	684.02	642.38	706.85	673.72
		NIA	8.87	10.83	3.35	9.68	0.33	7.68	-1.68
		LIA	88.62	183.27	-43.37	196.05	-87.35	174.64	-111.42
		% diff.	899.00	1592.24	1195.09*	1925.04	26406.54*	2175.29	6546.78

*with reversal of sign

6.2 Bending Moment M_x in Columns Below Plinth Level

Table 6 shows comparison of bending moment M_x in the columns below plinth level for NIA and LIA systems. Interaction effect results in increase of the governing values of M_x in the columns below plinth level under all the load cases. Under vertical loads i.e. load case LC1, this increase ranges from nearly 3 times (for columns C8 and C13) to nearly 24 times (for columns C3 and C18). Under various combinations of seismic loads, the increase ranges from nearly 6 times (for columns C8 and C13) to nearly 12.5 times (for column C6, C10, C11 and C15). Thus there is highly significant increase in the governing values of M_x due to the interaction effect.

7 Conclusions

Some significant research findings emerged from the study are summarised as follows;

1. The soil-structure interaction on deformable soil results in significant redistribution of forces and moments in the columns of the space frame-shear wall system. The design may not be realistic if this effect is overlooked.
Under vertical loads, interaction effect causes decrease in axial forces in the inner columns and increase in axial forces in the outer columns for columns below plinth level. Under various combinations of seismic loads, decrease in axial forces in the inner columns is found due to interaction effect. Other columns are subjected to increase as well as decrease in axial forces under different combinations of seismic loads.
2. The seismic forces cause compression/tensions in the columns below plinth level and reversal in the nature of forces is found when direction of seismic forces is reversed. Interaction reduces this effect significantly and provides more stability to the structure.
Seismic forces cause tension in one side boundary columns of the shear walls and excessive compression in the other side boundary columns under non-interaction analysis, for columns below plinth level. The interaction effect significantly relieves these forces. The change in nature of forces from tension to compression is found. Excessive compression is also decreased significantly.
3. The governing bending moments along the direction of seismic loads (M_x) are increased many times in all the bottom columns as a result of soil-structure interaction as compared to conventional non-interaction analysis. Columns of shear wall-space frame, designed on the basis of conventional analysis may, therefore, be vulnerable, on deformable soil. Interaction effect also causes reversal of sign of moments in various columns under many load cases.
4. The proposed methodology can be effectively used to evaluate the forces and moments in the superstructure for multi-storey space frame-shear wall-soil system for better and efficient building design.

References

1. Arlekar JN, Jain S, Murthy CVR (1997) Seismic response of R.C. frames buildings with soft first storeys. In: Proceedings of CBRI golden jubilee year conference, New Delhi, India, pp 13–14
2. ANSYS Inc. (2009) ANSYS structural analysis guide. ANSYS Inc., Southpointe, 275 Technology Drive, Canonsburg, PA 15317
3. Bishop AW and Henkel DJ (1962) The measurement of soil properties in the tri-axial test. Edward Arnold (Publishers) Ltd., London
4. Dutta SC, Bhattacharya K, Roy R (2004) Response of low-rise buildings under seismic ground excitation incorporating soil-structure interaction. *Soil Dyn Earthq Eng* 24:893–914
5. Vivek Garg, Hora MS (2012) Interaction effect of space frame-strap footing-soil system on forces in superstructure. *ARPJ Eng Appl Sci* 7(11):1402–1415
6. IS 1893 (Part I) (2002)—Criteria for earthquake resistant design of structures. (Part I : General provisions and buildings) (Fifth Revision)
7. Natarajan K, Vidivelli B (2009) Effect of column spacing on the behaviour of frame-raft and soil systems. *J Appl Sci* 9(20):3629–3640
8. Noorzai J, Viladkar MN, Godbole PN (1995) Elasto-plastic analysis for soil-structure interaction in framed structures. *Comput Struct* 55(5):797–807
9. Shakib H, Atefatdoost GR (2011) Effect of soil-structure interaction on torsional response of asymmetrical wall type systems. (Elsevier), *Procedia Eng* 14:1729–1736
10. Stavridis LT (2002) Simplified analysis of layered soil-structure interaction. *J. Struct. Eng. Div.,ASCE*, 128(2), pp 224–230

Seismic Performance of Buildings Resting on Sloping Ground

R.B. Khadiranaikar and Arif Masali

Abstract This study summarizes the knowledge in the seismic response of buildings on hill slopes. The dynamic response of the structure on hill slope has been discussed. A review of studies on the seismic behaviour of buildings resting on sloping ground has been presented. It is observed that the seismic behaviour of buildings on sloping ground differ from other buildings. The various floors of such buildings step backs towards hill slope and at the same time buildings may have setbacks also. Most of the studies agree that the buildings resting on sloping ground has higher displacement and base shear compared to buildings resting on plain ground and the shorter column attracts more forces and undergo damage when subjected to earthquake. Step back building could prove more vulnerable to seismic excitation.

Keywords Seismic performance · Sloping ground · Step back building · Step back set back building

1 Introduction

The scarcity of plain ground in hilly areas compels construction activity on sloping ground resulting in various important buildings such as reinforced concrete framed hospitals, colleges, hotels and offices resting on hilly slopes. The various floors of such buildings step back toward the hill slope and at the same time building may have setback also, as shown in Fig. 1. Due to the varied configurations of buildings in hilly areas, these buildings become highly irregular and asymmetric, due to variation in mass and stiffness distributions on different vertical axis at each floor. Such construction in seismically prone areas makes them exposed to greater shears and torsion as compared to conventional construction. Further, due to site conditions, buildings on hill slope are characterised by unequal column heights within a

R.B. Khadiranaikar (✉) · A. Masali
Civil Engineering Department, Basaveshwar Engineering College, Bagalkot 587102, India

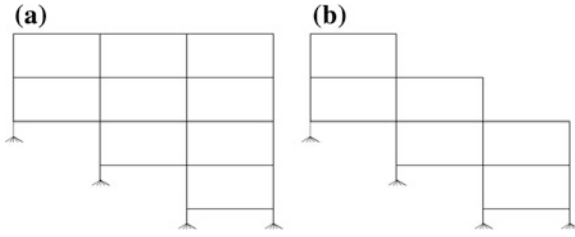


Fig. 1 a Step back building, b step back set back building

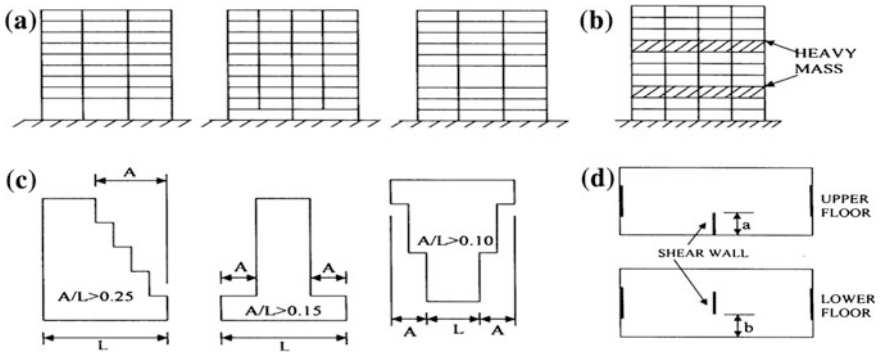


Fig. 2 a Stiffness/strength irregularity, b mass irregularity, c vertical geometric irregularity or set back, d in-plane discontinuity in vertical elements resisting lateral force when $b > a$

story, which results in drastic variation in stiffness of columns of the same storey. The short, stiff columns on uphill side attract much higher lateral forces and are prone to damage. As per IS 1893: (part 1) 2002, different vertical irregular configurations of buildings have been defined, as shown in Fig. 2. Which are stiffness irregularity (soft storey), mass irregularity, vertical irregularity (set back).

2 Review of Papers on Buildings Resting on Sloping Ground

Birajdar and Nalawade [1] studied seismic performance of buildings resting on sloping ground. They considered twenty four RC building frames with three different configurations as Step back building, Step back Set back building and Set back building situated at a slope of 27° with the Horizontal. They studied the seismic response of buildings with varying storey level ranging from 4 to 11 (15.75–40.25 m), consist of three bays along slope direction and one bay across slope, located in seismic zone III. They carried out 3D analysis including torsional effect by using Response spectrum method. They observed that there is a linear

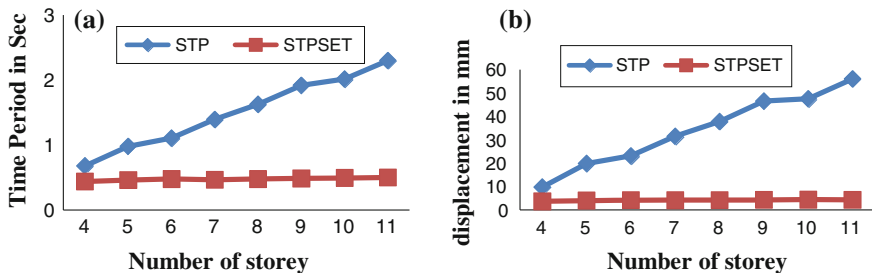


Fig. 3 a Variation of time period, b variation of displacement. Note STP Step back building; STEPSET Step back set back building

increase in the value of top storey displacement and fundamental time period as the height of building increases. From comparison they found that, this increase in top storey displacement and fundamental time period as the height of step back building increases is higher than step back set back building, as shown in Fig. 3a, b. From their study it is observed that the shear force in the column towards extreme left is significantly higher as compared to rest of the columns, in case of step back building it is found to be 55–250 % more than step back set back building. Thus they conclude that extreme left column at ground level, which are short are the worst affected and step back building could prove more vulnerable during seismic excitation than other type of configuration. They observed in step back buildings, the uneven distribution of shear force in the various frames suggests development of torsional moment due to static and accidental eccentricity.

Nagargoje and Sable [2] studied seismic performance of buildings on hill slope. They carried out 3D space frame analysis to study dynamic response of the buildings, in terms of base shear and top floor displacement. A parametric study was carried out on thirty six buildings with three configurations as step back, step back set back and set back buildings located in seismic zone III. Biradar and Nalawade [1] studied seismic performance of hill buildings by considering storey level up to 11, however in this paper the study is carried out by considering storey level ranging from 4 to 15 (15.2–52.6 m). They found that the storey displacement of step back buildings is quite high as compared to step back—set back buildings, as shown in Fig. 4. They observed that the base shear induced in step back set back buildings is higher in the range of 60 and 260 % than set back building. They suggested step back set back buildings may be favoured on sloping ground.

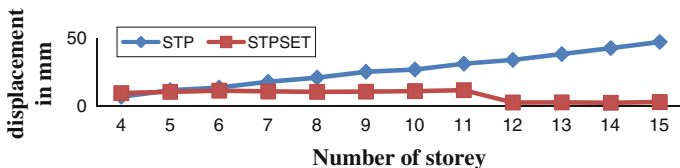


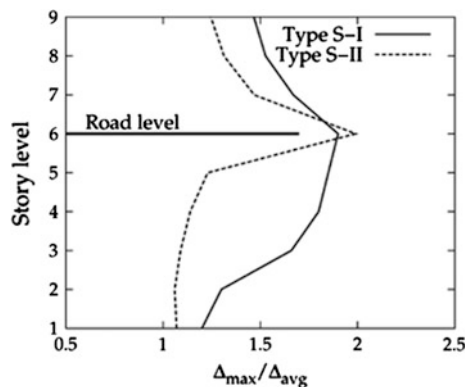
Fig. 4 Variation of displacement. Note STP Step back building; STEPSET Step back set back building

Singh et al. [3] studied seismic behaviour of buildings located on slopes. An analytical study is carried out on buildings considered, by using linear and non linear time history analysis. They considered 9 storey buildings, which include step back building at a slope of 45° with the horizontal, a RC frame located on steep slope/vertical cut which was not considered in previous studies, in which foundations are provided at two levels, at base downhill and at the road level, to compare the behaviour, they considered buildings resting on flat ground with 3 and 9 storeys. All buildings are located in seismic zone IV, consist of seven bays along slope and 3 bays across the slope. They have analysed buildings for a set of five ground motions, as shown in Table 1, which is taken from strong motion database of pacific Earthquake Engineering Research Centre. It is observed that, in all buildings on sloping ground, storey shear is resisted by short column. The effect of torsion irregularity in the building configuration can be represented by the ratio of maximum to average inter storey drifts ($\Delta_{max}/\Delta_{avg}$) in a storey. From which they observed that, in step back building torsion is observed in all storeys denoted as SI. Whereas torsion is observed in only top storeys of building located on vertical cut denoted as SII, as shown in Fig. 5. They conclude that the step back buildings are subjected to significant torsional effects under cross slope excitation. They also studied the inter storey drifts in the top three storeys of all buildings from which they observed that the inter storey drifts in the top three storey of hill building are quite close to those in the 3 storey regular building and the pattern of inter storey drifts of a storey building differs from other buildings.

Table 1 Earthquake records used in the analysis

S.no.	Event	Magnitude	PGA (g)	PGV (cm/s)	PGD (cm)
1.	1999 Chi-Chi	M7.6	0.266	38.331	38.331
2.	1979 Imperial Valley	M6.5	0.289	19.915	10.97
3.	1994 Northridge	M6.7	0.249	19.381	6.824
4.	1971 San Fernando	M6.6	0.33	56.35	60.017
5.	1995 Kobe	M7.2	0.28	16.369	8.067

Fig. 5 Variation of $\Delta_{max}/\Delta_{avg}$ along height in hill building configurations and due to seismic excitation in cross-slope direction. Note Type S-I Step back building



Farooque Patel et al. [4] focused on performance study and seismic evaluation of RC building on sloping ground. They studied the behaviour of RC frame on sloping ground with the presence of shear wall with different positions at centre and at corner and given the performance of structures with shear wall on sloping ground. A parametric study was carried out on eight storey building which includes a bare frame, building with shear wall at centre and at corner position located in seismic zone III. To give comparison they considered models on plane ground. All buildings consist of 5 bays in both directions. Seismic analysis has been done using linear static, Response spectrum analysis and evaluated using pushover analysis. Based on Equivalent static analysis, they found that the buildings with shear wall at centre and at corner have 41.4, 61.5 % respectively less displacement and based on Response spectrum analysis, these buildings have 23.6, 38.1 % less displacement as compared to the bare frame model on sloping ground. From which they conclude: as the buildings resting on sloping ground has higher displacement, the presence of shear wall reduces the lateral displacement considerably. Performance point determined from pushover analysis is the point at which the capacity of structure is exactly equal to the demand made on the structure by the seismic load. Based on state of structures at performance point, they observed that the spectral displacement of building on hill slopes have 114–179 % higher than building model on plain ground in longitudinal direction and also the plastic hinge formation is more in bare frame model, building with presence of shear wall on sloping ground when compared to the building on plain ground, which proves that the buildings on hill slopes are more vulnerable than other buildings. Hence, they conclude that the performance of buildings on hill slopes suggests an increased vulnerability of the structure with formation of column hinges at base level and beam hinges at each story level at performance point. Previous papers have not considered the presence of shear wall to study the seismic behaviour of hill slope buildings.

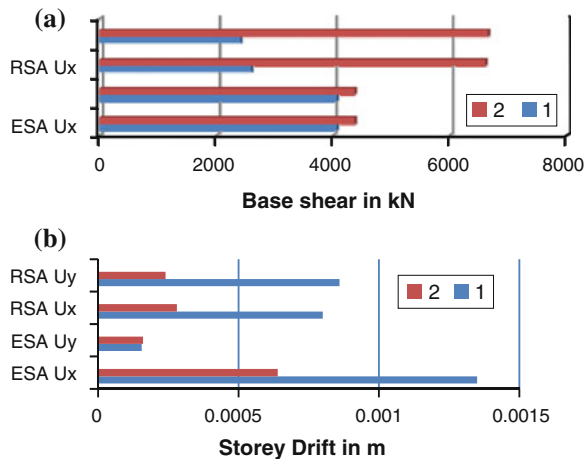
Prashant and Jagadish Kori [5] studied seismic response of one way slope RC frame building with soft storey. In this paper study is focused on the behaviour of buildings situated on sloping ground with and without infill wall, the influence of infill wall on buildings situated on sloping ground is presented. Non linear static pushover analysis is carried out on 10 storey buildings which include bare frame without infill wall and other model with infill wall including a soft storey building on sloping ground. All buildings consist of 5 bays along slope direction situated at a slope of 27° with the horizontal, located in seismic zone III. Building frame system considered is SMRF. They observed that the time period of bare frame model is found to be 1.975 s which is almost 96–135 % more than other models with presence of infill wall. Thus they conclude, this higher value of natural period in bare frame compared to infill frame ultimately results in underestimation of design base shear in bare frame model on sloping ground. The abrupt changes in the slope profile indicates stiffness irregularity, they observed that the displacement in bare frame model is found to be more because of reduced stiffness compared to other models with infill wall. They found that the base shear of infill models is almost 250 % more compared to bare frame. It is concluded that the formation of plastic hinges is more in bare frame model and soft storey building compared to fully

infilled frames. In this paper study is concentrated on variation of stiffness due to presence of infill wall and soft storey on sloping ground.

Siddiqui and Vidyadhara [6] carried out seismic analysis of earthquake resistance multi-storey multi bay RC frame. They studied the seismic behaviour of bare frame model, building with first soft storey (infill wall in upper storeys) with presence of both infill and shear wall at corner position for which they used 4 bay twelve storey building situated at a slope of 1:1/3 located in seismic zone V. These buildings have been analysed using Equivalent static, Response spectrum and Pushover analysis. Based on Equivalent analysis results they noted that there is reduction in displacement of models with infill and shear wall at corners with respect to bare frame model by almost 79.15 and 89.27 % respectively in longitudinal direction and from Response spectrum analysis which are almost 50.95 and 73.97 % respectively. Hence they conclude that the presence of brick infill and shear wall reduces lateral displacement considerably. It is observed that there is increased base shear in building with shear wall when compared to bare frame model, as shown in Fig. 6a. As per IS 1893 part (1) 2002 code, the permissible inter storey drift is limited to 0.004 times the storey height. In this study they found that all buildings considered are within permissible drifts, however the inter storey drifts of bare frame model on sloping ground found to be relatively higher compared to buildings with infill wall and shear wall, as shown in Fig. 6b. From pushover analysis, it is observed that the spectral displacement and Roof displacement of bare frame is higher than building with shear wall at corner. Thus they conclude that the presence of infill wall and shear wall influences the overall behaviour of structures when subjected to lateral forces by effectively reducing large joint displacements found in bare frame, which was also concluded in study done by Farooque Patel et al. [4].

Babu et al. [7] carried out pushover analysis of various symmetric and asymmetric structures constructed on plain as well as sloping ground subjected to various

Fig. 6 a Variation of base shear, **b** variation of storey drift. *Note 1* Bare frame building on sloping ground; *2* Building with shear wall



kinds of loads. They considered various structures in plan symmetry and also asymmetry with different in bay sizes in mutual direction. On sloping ground they considered a 4 storey building in which they have taken one storey above ground level which is situated at a slope of 30° with the horizontal. They found that the short column lies in the severity level beyond collapse prevention (CP) from pushover analysis, they obtained displacement and base shear for asymmetric sloping ground as 104×10^{-3} m and 2.77×10^3 kN respectively. Based on results they developed pushover curves with displacement on X-axis and Base shear on Y-axis and have given comparison between various cases they considered. They observed that the Base shear resisted for maximum displacement up to failure limit by symmetric structure is 70 % and by asymmetric sloped building is 24 % more than base shear resisted by asymmetric building on plain ground. They conclude that the structure with vertical irregularity is more critical than a structure with plain irregularity.

Ravikumar et al. [8] focused on the study of seismic performance of irregular configurations of RC buildings in which they studied vertical irregularities of buildings such as geometric irregularity and buildings resting on sloping for which two types of configurations were considered as buildings resting on sloped ground in X-direction and buildings resting on sloped ground in Y-direction. All buildings consist of 5 bays in X-direction and 4 bays in Y-direction with 3 storey located in severe zone V. The performance of these buildings was studied by linear analysis using code IS 1893 (part-1) 2002 and Nonlinear analysis using ATC 40. They observed that the vulnerability of sloping ground buildings was found to be remarkable which attracts large force to deform moderately. Base shear of building on hill slope was found to be 6019.2 kN, which was around 25–55 % more than other buildings and also displacement was found to be 83.4 mm which was moderately higher than other buildings. They found that the performance goal was not achieved of sloping ground buildings in X-direction and in Y-directions this was achieved after collapse point. Thus they conclude that the buildings resting on sloping ground are more vulnerable to earthquake than the buildings resting on plain ground.

Halkude et al. [9] focused on seismic analysis of buildings resting on sloping ground with varying number of bays and hill slopes. They studied the variation of time period, base shear and top storey displacement with respect to variation in number of bays along slope direction and hill slope angle. To study the seismic behaviour they considered different configurations, as step back building which are in the range of 4–11 storey and consist of varying bays of 3–6 in X-direction. They have not studied the seismic behaviour by varying bays along Y-direction, thus they considered one bay along Y-direction, situated at varying slopes of 16.32° , 21.58° , 26.56° and 31.50° with the horizontal located in seismic zone III. It is observed that, in all configurations, base shear increases with increase in number of storey, increases with increase in number of bay and decreases from lower angle to higher angle of slope as shown in Fig. 7a–c, when compared between different configurations, base shear of step back building is found to be higher than step set back building. They observed that the time period increases with increase in number of

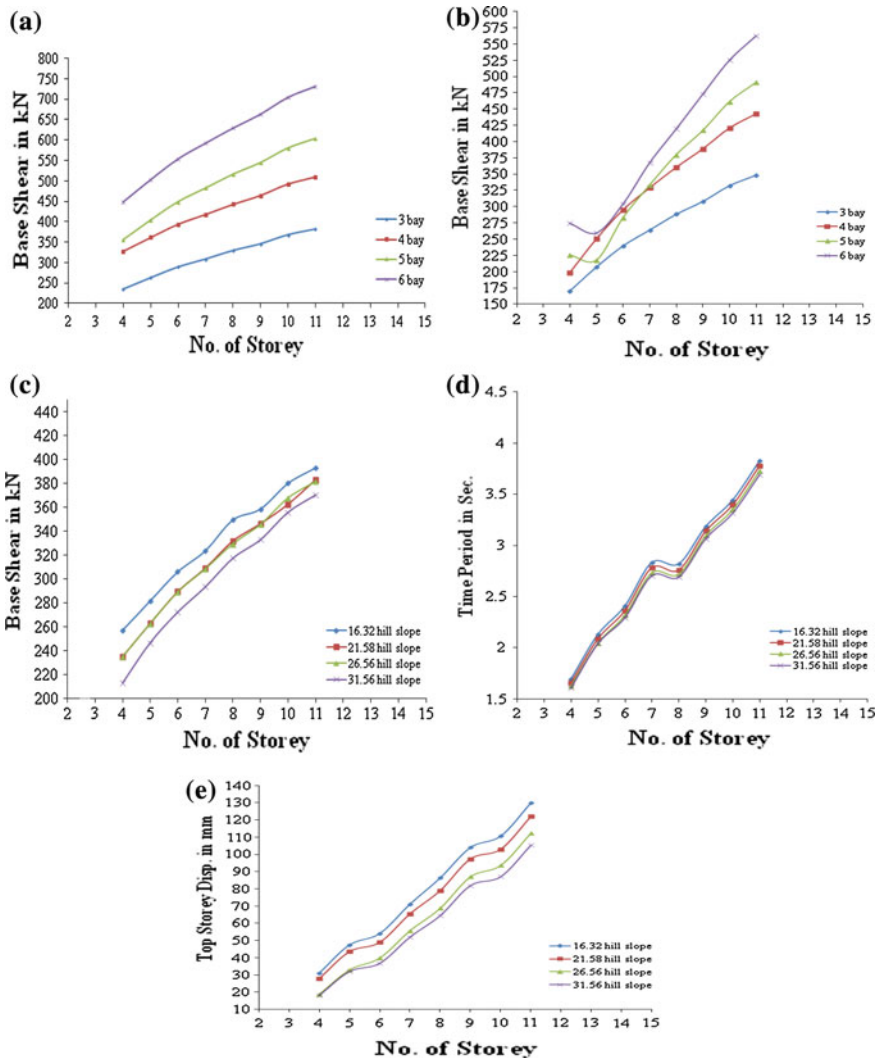


Fig. 7 a Variation of base shear for step back frame with respective to number of bays, b variation of base shear for step back set back frame, c variation of base shear for step back frame with respective to hill slope, d variation of time period for step back frame with respective to number of bays, e variation of top storey displacement for step back frame with respective to hill slope

storey in all configurations, in step back building time period increases with increase in number of bays, which is a reverse case in step back set back building in which time period decreases with increase in number of bay and in all configurations time period decreases with increase in hill slope showing minor change in time period as shown in Fig. 7d. In all configurations it is observed that the top story displacement increases with increase in number of storey, displacement is

nearly alike for 3 and 4 bays, But, it decreases considerably from 4 to 5 bays and further increases for 6 bay, as shown in Fig. 7e, with respective to hill slope, they found that the top storey displacement decreases with increase in hill slope showing lower value for higher slope. Thus they conclude that the step back frames produce higher base shear, higher value of time period and higher value of top storey displacement as compared to step back set back frames. Also they conclude that greater no of bays are observed to be better under seismic excitation, as number of bays increase time period and displacement decreases.

During the course of this Review, it is observed that very few researchers have studied the seismic behaviour of buildings situated on varying slopes and varying number of bays along slope direction. Some researchers have suggested suitable building configuration on sloping ground. Some researchers have studied the seismic behaviour of hill slope buildings by considering infill wall (soft storey) and Shear wall. A tabular summary of fundamental time period, Base shear and displacement given by various researchers is presented in Table 2.

3 Conclusions

From the above discussion following conclusions can be made.

1. Step back buildings produce higher base shear, higher value of time period, higher value of top storey displacement compared to step back set back building. During seismic excitation Step back building could prove more vulnerable than other configuration of buildings.
2. It is observed that, short columns attracts more forces and are worst affected during seismic excitation. From design point of view, special attention should be given to the size (strength), orientation (stiffness) and ductility demand of short column.
3. The hill slope buildings are subjected to significant torsional effects, due to uneven distribution of shear force in the various frames of building suggest development of torsional moment, which is found to be higher in step back building.
4. Many researchers suggested as step back set back buildings may be favoured on sloping ground.
5. From the study it is concluded that the presence of infill wall and shear wall influences the behaviour of structure by reducing storey displacement and storey drifts considerably, but may increase the base shear, hence special attention should be given in design to reduce base shear.
6. It is concluded that the greater number of bays are found to be better under seismic condition, as the number of bays increases, time period and top storey displacement decreases in hill slope buildings.

Table 2 Summary of fundamental time period, base shear and displacement given by various researchers

S.no	References	Type of building	Time period (in s)	Base shear (in kN)	Displacement (in mm)	Remarks
1	Birajdar and Nalawade [1]	STP 4-11	0.6782-2.2972	134-358	9.75-56.05	Step back 4-11 storey
		STPSET 4-11	0.437-0.499	86-103	3.61-4.28	Step back set back 4-11 storey
2	Nagargoje and Sable [2]	STP 4-15	-	398-290,25	7.27-47.07	Step back 4-15 storey
		STPSET 4-15	-	341.32-414.84	9.75-3.21	Step back set back 4-15 storey
3	Farooque Patel et al. [4]	8-storey	-	3111.72	13.10	Bare frame
		8-storey	-	7536.2	10	Building with shear wall at centre
		8-storey	-	13920.42	8.10	Building with shear wall at corner
4	Prashant and Jagadish Kori [5]	10-storey	1.975	6289,029	352.8	Bare frame
		10-storey	0.834	29034.46	117.6	Building with infill
5	Siddiqui and Vidhyadhar [6]	12-storey	-	2601.1	211	Bare frame
		12-storey	-	6508.9	103	Building with infill (soft storey)
		12-storey	-	6617.8	55	Building with infill and shear wall at corner

References

1. Birajdar BG, Nalawade SS (2004) Seismic analysis of buildings resting on sloping ground. In: 13th world conference on earthquake engineering, Vancouver, B.C., Canada, paper no. 1472
2. Nagargoje SM, Sable KS (2012) Seismic performance of multi-storeyed building on sloping ground. *Elixir Int J* 53: 11980–11982
3. Singh Y, Gade P, Lang DH, Erduran E (2012) Seismic behavior of buildings located on slopes—an analytical study and some observations from Sikkim earthquake of September 18, 2011. In: 15th world conference on earthquake engineering journal 2012
4. Farooque Patel MU, Kulkarni AV, Inamdar N (2014) A performance study and seismic evaluation of RC frame buildings on sloping ground. *IOSR J Mech Civil Eng* 51–58. e-ISSN:2278-1684, p-ISSN:2320-334X
5. Prashant D, Jagadish Kori G (2013) Seismic response of one way slope RC frame building with soft storey. *Int J Emerg Trends Eng Dev* 5(3)
6. Siddiqui RUH, Vidyadhara HS (2013) Seismic analysis of earthquake resistant multi bay multi storeyed 3D—RC frame. *Int J Eng Res Technol* 2(10). ISSN:2278-0181
7. Babu NJ, Balaji KYGD, Gopalaraju SSSV (2012) Pushover analysis of unsymmetrical framed structures on sloping ground. *Int J Civil Struct Environ Infrastruct Eng Res Dev* 2(4):45–54. ISSN:2249-6866
8. Ravikumar CM, Babu Narayan KS, Sujith BV, Venkat Reddy D (2012) Effect of irregular configurations on seismic vulnerability of RC buildings. *Archit Res* 2(3):20–26. doi:[10.5923/j.arch.20120203.01](https://doi.org/10.5923/j.arch.20120203.01)
9. Halkude SA, Kalyanshetti MG, Ingle VD (2013) Seismic analysis of buildings resting on sloping ground with varying number of bays and hill slopes. *Int J Eng Res Technol* 2(12). ISSN:2278-0181

Part IX
Earthquake Response of Steel, Concrete
and Masonry Structures

Seismic Response Control of Piping System with Supplemental Devices

Praveen Kumar and R.S. Jangid

Abstract Seismic loads on piping system due to an earthquake can cause excessive vibrations, which can lead to serious instability resulting in damage or complete failure. In this paper, passive and semi-active supplemental devices have been studied to mitigate seismic response and vibration control of piping system used in the process industries, fossil and fissile fuel power plant. A study is conducted on the performance of passive and semi-active supplemental devices due to variation in parameters of devices and/or with different control algorithms of the damper and subsequently optimum parameter of devices are obtained. The effectiveness of the passive and semi-active supplemental devices in terms of reduction in the responses, namely, displacements, accelerations and base shears of the piping system is investigated by comparing uncontrolled responses under four different artificial earthquake motions with increasing amplitudes. The analytical results obtained using Wen's model are compared with the corresponding experimental results available which indicated a good match with the proposed analytical procedure for the X-plate dampers. The analytical results demonstrate that the passive and semi-active supplemental devices under particular optimum parameters are very effective and practically implementable for the seismic response mitigation, vibration control, and seismic requalification of piping systems.

Keywords Seismic · Passive and semi-active supplemental devices · Stiffness ratio · Control law · Piping systems

P. Kumar

Architectural and Structural Engineering Division, Bhabha Atomic Research Centre,
Trombay, Mumbai 400 085, India

R.S. Jangid (✉)

Department of Civil Engineering, Indian Institute of Technology Bombay,
Powai, Mumbai 400 076, India
e-mail: rsjangid@civil.iitb.ac.in

1 Introduction

Piping systems are considered as the lifeline of industrial units such as process industries, fossil and fissile fuel power plant. Piping systems are normally installed on those structures in which acceleration at the location of piping support is higher than the ground acceleration. Seismic loads, generated in addition to normal load on piping systems due to earthquakes, can cause excessive vibrations, which can lead to high stresses resulting in damage or complete failure. Presently, piping system and mountings are supported by seismic support called snubbers. Moreover, snubbers are associated with operational problems like oil leakage, inadvertent locking-up, undesirable load on piping system due to malfunctioning of snubber and need frequent attention [1, 2]. At the same time, different structural control methods like passive, active, semi-active, and hybrid control devices also known as supplemental devices have been successfully implemented in vibrating systems to reduce structural response due to earthquake and wind loadings [3]. Researchers had extensively studied supplemental devices for buildings and bridges, but limited studies are available for possible use in the piping systems. However, simplified finite element analysis and systematic design procedures for optimal sizing and placement of these protective devices in 3-D piping system under tri-directional seismic excitation are needed and same has not been investigated so far.

The passive control of structures has initialized its applications in the lifeline structures in mid-eighties [4, 5]. In last few decades, special protective systems based on supplemental energy dissipation [3, 6] have been developed to enhance safety and reduce damage to the structures during strong ground motions. The passive supplemental devices [7, 8] consist of damping devices (friction, viscous or visco-elastic devices), yielding elements (X-plate or triangular metallic plates) or auxiliary oscillators (tuned mass damper—TMD or Multi-TMDs—MTMDs), placed strategically in the structural system to reduce its seismic response. Semi-active control devices do not inject energy into the controlled system, and their mechanical properties can be adjusted to improve their performance. Changes in the system's mechanical properties are based on feedback from measured responses and/or ground excitation. Since external power is only used to change device's properties such as damping or stiffness, and not to generate a control force, power requirements are very low in the order of tens of watts. Devices in this category include variable-orifice dampers, variable-stiffness control devices, semi-active tuned mass dampers, adjustable tuned liquid column dampers and controllable fluid dampers.

From the literature review, the X-plate damper, fluid viscous damper, visco-elastic damper, tuned mass damper, and multiple tuned mass dampers as passive devices and magneto-rheological MR damper, variable friction damper and variable stiffness damper as the semi-active devices can be used as supplemental devices to mitigate the seismic response of the piping systems. The performance of these devices for piping system is studied for four different artificial earthquake motions with increasing amplitudes. The main objective of the present study is to develop:

optimum design parameter of the piping system equipped with various supplemental devices; optimum parameter of control algorithms for semi-active dampers; investigate the hysteretic energy dissipation behaviour of the various supplemental devices; investigate numerically the feasibility and efficiency of supplemental devices in comparison to uncontrolled piping system; integrated computer program of the complex 3-D piping systems equipped with supplemental devices.

2 Modelling of Piping System with Damper

Experimental setup of 3-D piping system is shown in Fig. 1. Initially tests were conducted on 3-D piping system without and with X-plate damper under four different artificial earthquake motions with increasing amplitude (refer Table 1). Numerical investigations are then carried out for same piping system without and with different passive and semi-active supplemental devices and schematic of piping system with supplemental devices as shown in Fig. 2. Analysis is carried out using a computer code developed in the MATLAB[®] 7.0 R14, in which straight element in the piping system are modeled as 3-D beam and elbows as 3-D curved beams whose moment of inertia is modified as per American Society of Mechanical Engineers (ASME) codes and having six degrees-of-freedom at each node. The mass of each member is assumed to be distributed between its two nodes as a point mass. In addition to the mass of the piping system, the externally lumped masses are assumed to be effective in the three translational degrees-of-freedom. The dampers attached to the piping system in various combinations during analysis are: vertical, horizontal and both vertical and horizontal. Responses are obtained using Newmark's step-by-step time-integration technique. The responses evaluated are displacements, accelerations and support reactions/base shears of piping system. Seismic energy dissipation in the piping system was governed by the hysteretic characteristics of damper which is also evaluated. The fundamental frequency and model mass participation factor is also evaluated.

3 Governing Equations of Motion

The equations of motion of the piping system attached with supplemental devices, and subjected to earthquake motion, are expressed in the following matrix form:

$$[M]\{\ddot{u}\} + [C]\{\dot{u}\} + [K]\{u\} + [\Gamma]\{F\} = -[M]\{\Lambda\}\{\ddot{u}_g\} \quad (1)$$

$$\{u\} = \{x_1, y_1, z_1, \theta_{x1}, \theta_{y1}, \theta_{z1}, x_2, y_2, z_2, \theta_{x2}, \theta_{y2}, \theta_{z2}, \dots, x_N, y_N, z_N, \theta_{xN}, \theta_{yN}, \theta_{zN}\}^T \quad (2)$$

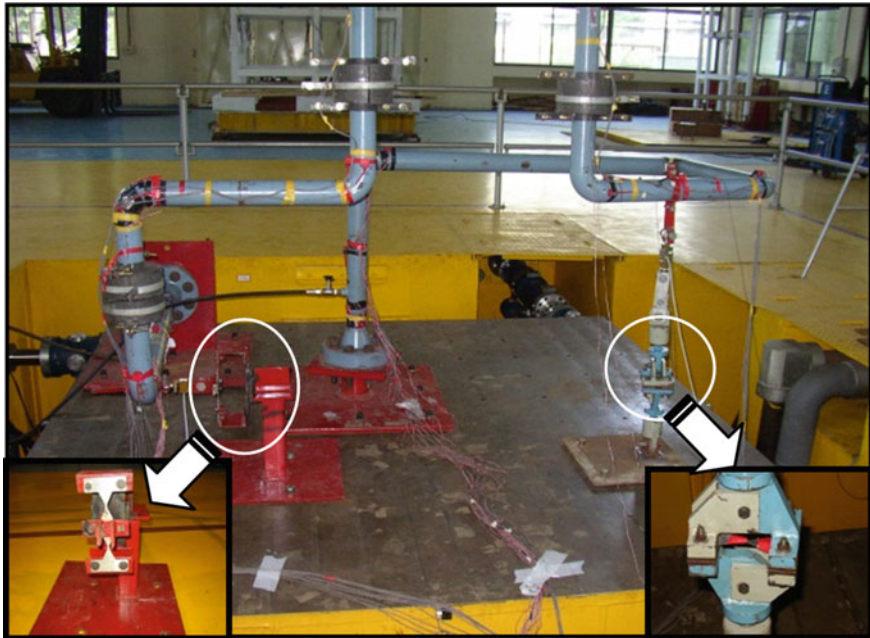


Fig. 1 Experimental setup of piping system with XPDs

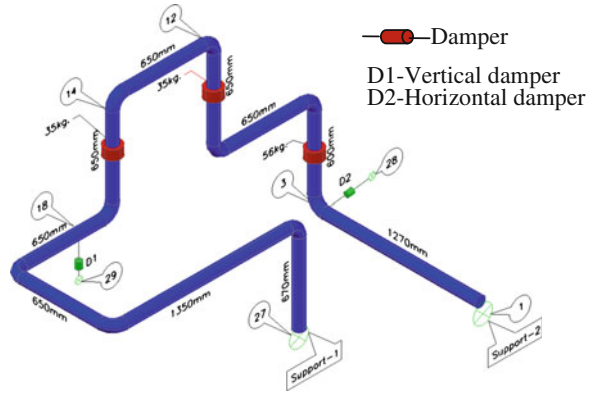
Table 1 Peak ground acceleration of different artificial earthquake motion

Artificial earthquake motions	Peak ground acceleration (m/s ²)			Earthquake duration (s)
	x-component	y-component	z-component	
TH10	2.38	2.15	1.88	33.50
TH20	4.85	4.15	3.22	33.64
TH30	7.17	6.31	4.91	33.68
TH40	10.01	8.65	6.25	33.89

$$\ddot{u}_g = [\ddot{x}_g \quad \ddot{y}_g \quad \ddot{z}_g]^T \tag{3}$$

where $[M]$, $[C]$, and $[K]$ represent the mass, damping, and stiffness matrix, respectively; $\{\ddot{u}\}$, $\{\dot{u}\}$, and $\{u\}$ represent acceleration, velocity, and displacement vectors, respectively; $[\Gamma]$ is the location matrix for the restoring force of damper; $\{F\}$ is the vector containing the restoring force of damper; $\{\Lambda\}$ is the influence coefficient vector; \ddot{u}_g is the vector of earthquake ground accelerations; \ddot{x}_g , \ddot{y}_g and \ddot{z}_g are the earthquake acceleration along X-, Y-, and Z-directions, respectively; x_i , y_i , z_i are the displacements and θ_{xi} , θ_{yi} , and θ_{zi} are the rotations of the i th node in the piping system in X-, Y-, and Z-directions, respectively.

Fig. 2 Schematic of piping system with passive dampers



4 Numerical Study of Piping System with Passive Devices

Passive supplemental devices investigated are X-plate damper (XPD), fluid viscous damper (VD), visco-elastic damper (VED), tuned mass damper (TMD), and multiple tuned mass dampers (MTMD). The fundamental frequencies of four modes with different location of XPD and without XPD in the piping system are listed in Table 2. The analytical results of XPDs are compared with those from experimental results and it is observed that they are in very close agreement. Later, it is observed from Fig. 5 that there are significant reduction in responses such as displacement, acceleration, and support reaction in the range of 47–67 %, 48–53 %, and 48–63 %, respectively for the piping system with XPDs in Z-direction at node 18. The energy dissipated in the hysteresis loops increases as the base acceleration increases from TH10 to TH40. The parametric study of damper parameters (i.e. height, width, and thickness of the XPD) is also investigated under the earthquake motions to find the optimum design XPDs.

The optimum design parameters of fluid viscous and visco-elastic dampers are obtained for the same the piping system attached with both vertical and horizontal dampers under tri-directional earthquake excitations. The seismic response of the piping system is investigated by comparing the response of the controlled piping system with the uncontrolled piping system. It is observed from Fig. 5 that there are significant reduction in responses such as displacement, acceleration and support reaction in the range of 45–50 %, 48–50 %, and 25–39 %, respectively for the piping system with VD in Z-direction at node 18. It is also observed from Fig. 5 that there are significant reduction in the displacement, acceleration and support reaction in the range of 53–57 %, 51–52 %, and 38–40 %, respectively for the piping system with VED in Z-direction at node 18. The inherent modal damping in the piping system in the fundamental mode, which was initially 1.2 %, is increased to 8.98 and 6.87 % in the piping system with fluid VD and VED, respectively. Response reduction in the VED is slightly better than VD this is because of the additional stiffness property in the VED.

Table 2 Free vibration characteristics of piping system with and without XPDs

Mode	Frequency (Hz)		Both vertical and horizontal XPDs		Horizontal XPD		Vertical XPD		Effective mass participation without XPD		
	Without XPD		horizontal XPDs		Horizontal XPD		Vertical XPD		X-dir (%)	Y-dir (%)	Z-dir (%)
	Anal.	Expt.	Anal.	Expt.	Anal.	Expt.	Anal.	Expt.	Anal.	Anal.	Anal.
1	4.03	4.06	4.51	4.25	4.03	4.00	4.40	4.25	9.58	17.79	42.82
2	4.54	4.45	6.05	5.75	4.71	4.50	5.85	5.75	32.24	34.41	0.42
3	7.73	*	8.60	*	7.93	*	8.60	8.75	5.24	1.34	0.19
4	8.96	8.90	9.81	9.50	9.30	9.25	9.42	-	27.58	11.61	35.35

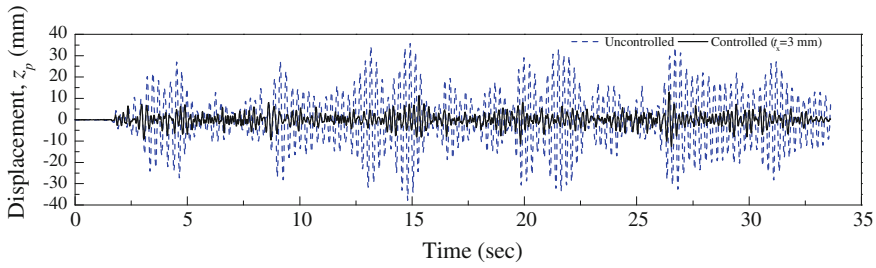


Fig. 3 Displacement-time variations at D1 for the piping system with vertical and horizontal XPD under earthquake motion, TH20

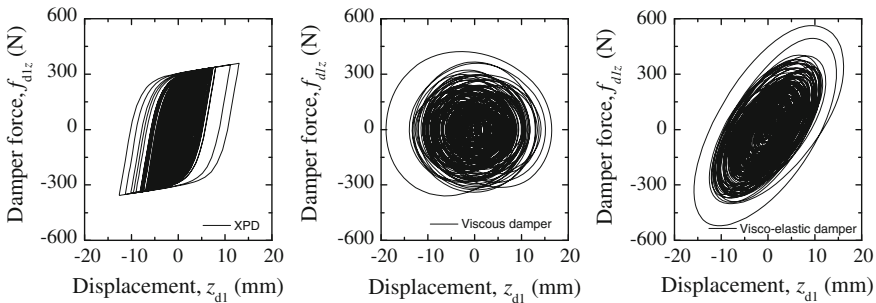


Fig. 4 Force-displacement variations at D1 for the piping system with both vertical and horizontal passive devices under earthquake motion, TH20

The effectiveness of auxiliary oscillators i.e. tuned mass damper and multiple tuned mass damper for response reduction of the piping system is investigated. It is observed that there exist design parameters or optimum parameters of the TMD and MTMD systems for which minimum response of the piping system is obtained. The design parameters of the TMD system [9] are obtained for seven values of damping ratios of the main system (i.e. $\xi_s = 0, 0.01, 0.02, 0.03, 0.05, 0.075, \text{ and } 0.1$) for different mass ratios in the range of 0.005–0.1 at an interval of 0.005. One TMD is designed for damping the first mode of the piping system, which has maximum mass participation. Similarly, number of TMDs in MTMD as 2, 4, and 7, and are designed for reducing the steady state responses in the piping system. It is observed that the inherent modal damping in the piping system in the fundamental mode, which was initially 1.2 %, is increased up to 6.14 %.

Figure 3 shows the displacement-time variation at D1 for the piping system with both vertical and horizontal XPD under earthquake motion, TH20. Figure 4 shows the force-deformation variation loops at D1 for the piping system with both vertical and horizontal passive devices under earthquake motion, TH20. It is observed from the loops that good amount of energy is absorbed by the dampers under earthquake motion. Further, it is observed from Fig. 5 that XPD, VD, and VED are very

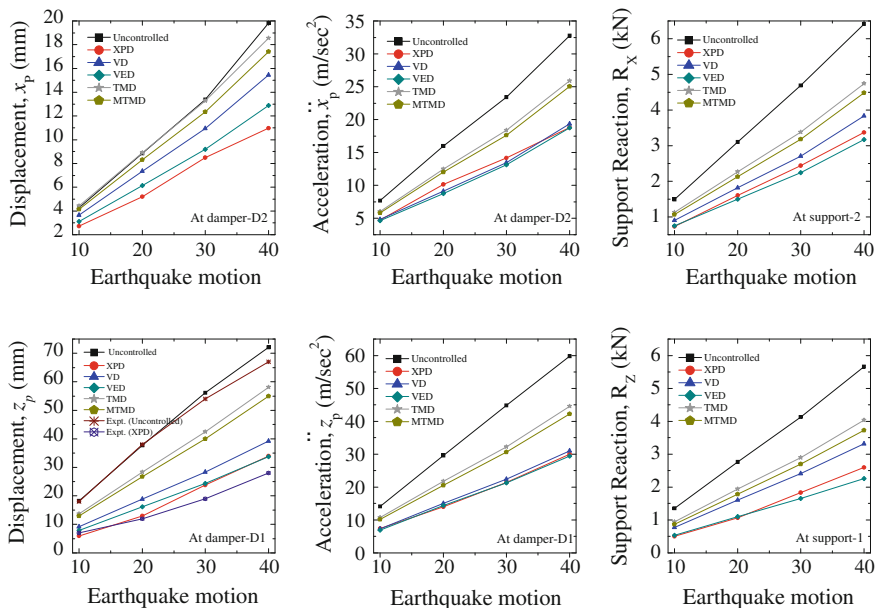


Fig. 5 Variation of displacement, acceleration and support reaction with earthquake motions of the piping system without and with passive devices

effective in reducing the seismic response of the piping system. However, TMD and MTMD are relatively less effective than above passive devices in reducing the seismic response of piping system.

5 Modeling, Control Law and Numerical Study of Piping System with Semi-active Devices

Semi-active supplemental devices investigated are MR damper, variable friction damper and variable stiffness damper. Semi-active control systems are typically highly non-linear. One of the main challenges in semi-active control is to develop an appropriate control algorithm. Also, modeling of the control devices is essential for the adequate prediction of the behavior of the piping system. The schematic of the piping system with semi-active supplemental devices and the mathematical models of semi-active dampers are shown in Figs. 6 and 7, respectively.

The modified Bouc-Wen model [10] is considered for the MR damper. Here, two versatile and effective control algorithms are selected in the current study and these are; the Bang-bang controller and the Lyapunov controller. The governing equation of the force predicted by this model is

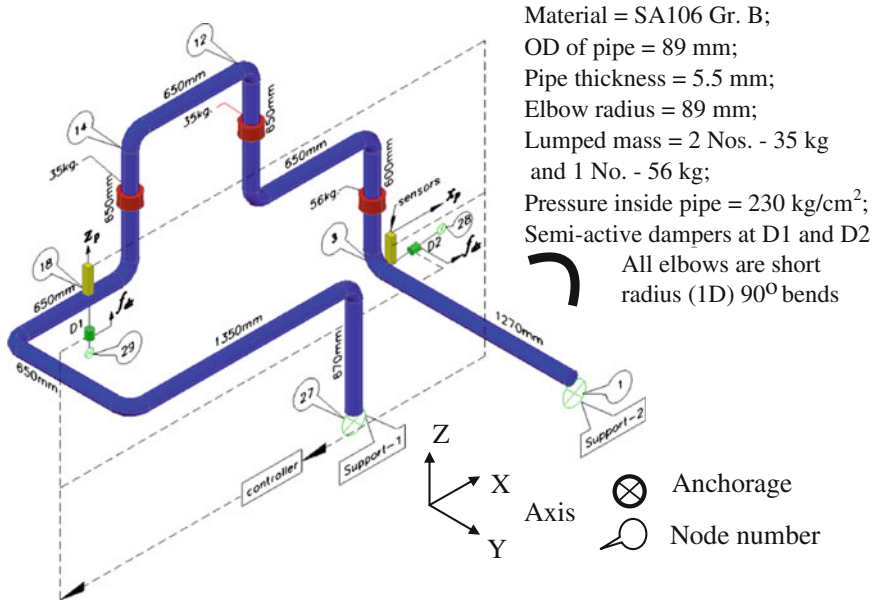


Fig. 6 Schematic diagram of piping system with semi-active dampers and control feedback system

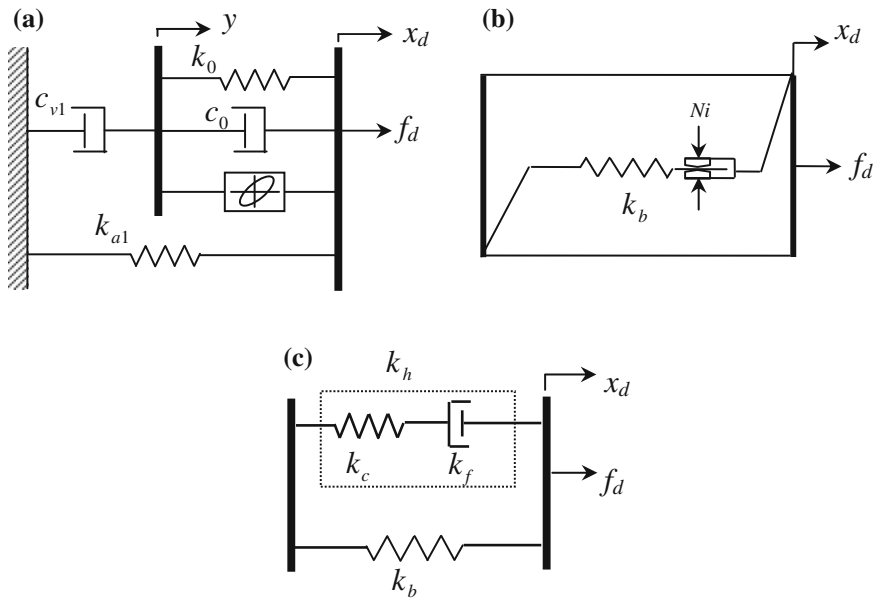


Fig. 7 Mathematical model of semi-active dampers (a) MR Damper, (b) Variable Friction Damper, (c) Variable Stiffness Damper

$$f_d = c_{vi}\dot{y} + k_{a1}(x_d - x_0) \quad (4)$$

where c_{vi} is viscous damping at lower velocity in the model to produce the roll-off; k_{a1} is the accumulator stiffness; x_d is the damper displacement; x_0 is the initial displacement of spring; \dot{y} is the velocity across the damper. The damper force increases with increasing magnetic field and depends on the input command voltage. The response of the MR damper depends on the local motion of the piping system and also on the maximum input command voltage to the current driver. Hence, it is important to know the optimum input command voltage, so that resulting MR damper force in a piping system causes optimum reduction in the piping responses. Kumar et al. [11], studied the response of piping system with the MR damper under tri-directional seismic excitation. To obtain the optimum input command voltage a parametric study is conducted in the range 0–2.25 V, keeping all other parameters of the MR damper constant. The variation of voltage is plotted with peak displacement, absolute acceleration, base shear, and peak control forces to obtain the optimum input command voltage under different earthquake motions. It is observed that, the command voltage plays an important role in the response of the piping system. It is observed from Fig. 10 that there are significant reduction in responses such as displacement, acceleration, and base shear in the range of 69–88 %, 57–73 %, and 39–45 %, respectively for the piping system with the MR dampers in Z-direction at node 18 under the different earthquake motions. Force-deformation, velocity-displacement, and FFT amplitude behaviours of the piping system with MR dampers under different control algorithms are also studied.

In semi-active variable friction damper (SAVFD), predictive control algorithm [12] with direct output feedback concept is considered. In predictive control algorithm, predicting the critical friction force is dependent on the optimal gain multiplier. Thus, the control force vector when all the dampers are brought into slip state is given by,

$$F[t] = \alpha(G_z z[t - 1] + G_u F[t - 1] + G_w \ddot{u}_g[t - 1]) \quad (5)$$

The factor α is a ratio of damper force to critical friction force and also α is treated as gain multiplier. The matrices G_z , G_u , and G_w are the control gains. A parametric study is conducted by variation of gain multiplier in the range 0–0.99. It is observed that, the gain multiplier plays an important role in the response of the piping system. It is observed from Fig. 10 that there are significant reduction in responses such as displacement, acceleration, and base shear in the range of 93.5–94 %, 89.3–90.4 %, and 61.4–66.5 %, respectively for the piping system with the SAVFD in Z-direction at node 18 under the different earthquake motion. Force-deformation, velocity-displacement, and FFT amplitude behaviours of SAVFD under control algorithms are also studied.

In semi-active variable stiffness damper (SAVSD), the recently proposed switching control law [13] is considered in which its performance is based on the information of structural displacement and velocity. As velocity sensors are not

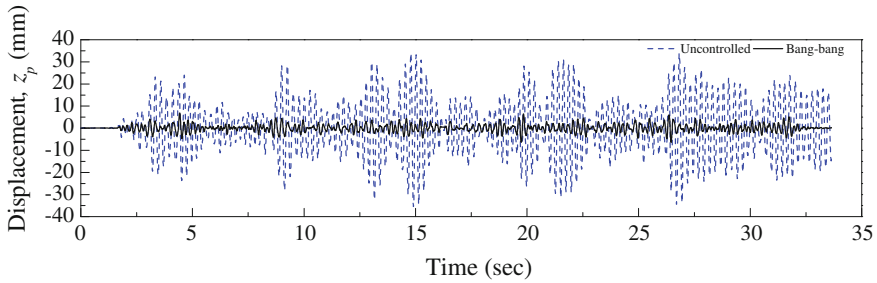


Fig. 8 Displacement-time variations at D1 for the piping system with vertical and horizontal MR damper under earthquake motion, TH20

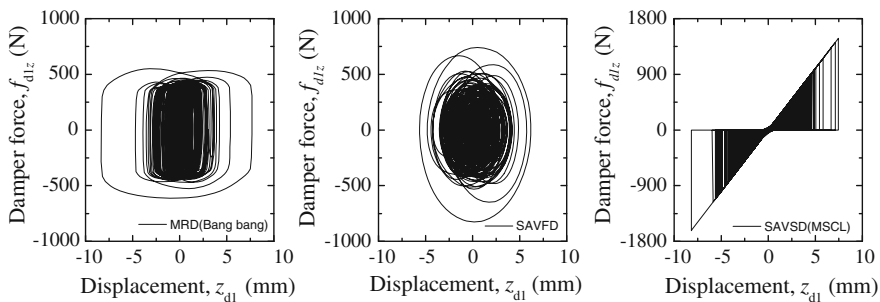


Fig. 9 Force-displacement variations at D1 for the piping system with vertical semi-active devices under earthquake motion, TH20

commonly used, it is difficult to implement this simple control logic. Hence, to overcome this problem, a modified switching control law is proposed. The damper force (f_{di}) at i th location is calculated as

$$f_{di} = K_{di}v_{si}\bar{x}_i \tag{6}$$

where K_{di} is the $(n \times n)$ effective stiffness matrix for SAVSD installed in the i th damper location, in which K_{di} is zero, except for $K_{di}(i - 1, i) = -k_{hi}$; \bar{x}_i is the drift at location of damper; and v_{si} is based on switching control law for the SAVSD installed in the i th location. Here, the effects of optimal damper stiffness ratio based on the different configurations of damper placement under different earthquake motions are investigated. The damper stiffness ratio, (α_k) is defined as the ratio of effective stiffness of damper device (k_{di}) to stiffness of pipe connected to the damper devices (k_{di}). Kumar et al. [14] studied the response of piping system with SAVSD under tri-directional seismic excitation. Parametric study is conducted for variation of α_k in the range 0–0.06 and it is observed that the parameter α_k plays an important role in the piping system responses. It is observed from Fig. 10 that there are significant reduction in responses such as displacement and base shear in the

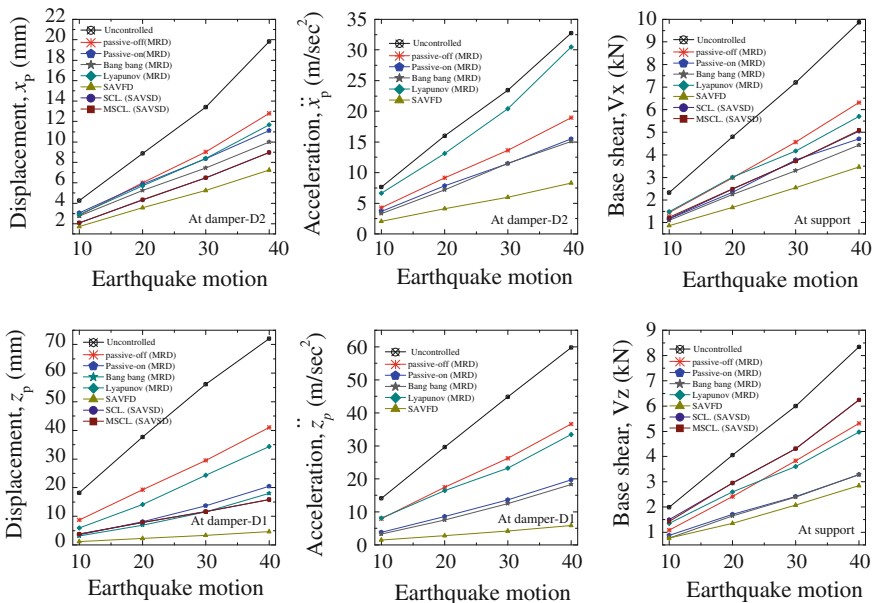


Fig. 10 Variation of displacement, acceleration, and base shear with earthquake motions of the piping system without and with semi-active devices

range of 78–79.2 % and 37.4–40.6 %, respectively for the piping system with the SAVSD in Z-direction at node 18 under the different earthquake motions. Force-deformation, velocity-displacement, and FFT amplitude behaviours of the SAVSD under different control algorithms are also studied.

Figure 8 shows the displacement-time variation at D1 for the piping system with both vertical and horizontal MR dampers under earthquake motion, TH20. Figure 9 shows the force-deformation variation loops at D1 for the piping system with both vertical and horizontal semi-active devices under earthquake motion, TH20. It is observed from the loops that good amount of energy is absorbed by the dampers under earthquake motion. Further, it is observed from Fig. 10 that semi-active dampers are very effective in reducing the seismic response of the piping system. However, semi-active variable friction dampers are relatively more effective than other two semi-active devices in reducing the seismic responses of piping system.

6 Conclusions

Based on the investigation carried out in this study on seismic control of the piping system, the following conclusions are drawn:

- (1) It is seen that passive and semi-active supplemental devices are very effective in reducing the seismic response of piping system.

- (2) Hysteresis loops indicate that good amount of seismic energy is absorbed by these supplemental devices.
- (3) There exist design parameters of the supplemental devices, which when adopted for designing the supplemental devices attached to the piping system produce minimum responses of the piping system.
- (4) Natural frequency of the piping system increases with XPD and VED whereas in case of the fluid viscous damper it is unaffected.
- (5) Inclusion of fluid viscous and visco-elastic dampers in the piping system significantly increases the modal damping of the piping system.
- (6) The response of the piping system decreases with increase in both, the mass ratio and the damping of the main system. For the same mass ratio and damping in the piping system, the MTMD is found to be more effective than single TMD.
- (7) From the parametric study, the peak displacements, accelerations, and base shear are reduced with increase in the input command voltage of the MR dampers. However, there exists an optimum value of the voltage input depending upon the damper locations.
- (8) The control algorithms considered for the MR damper, namely, the Bang-Bang and the Lyapunov impart reduction in piping system responses. But relatively, Bang-Bang control algorithm performed better than Lyapunov control algorithm.
- (9) The evaluated optimum parameter, α , in the range of 0.4–0.7 of the predictive control law for the SAVFD and α_k , of switching control law and modified switching control law for the SAVSD are found to be very effective in reducing the seismic responses for the piping system.
- (10) The SAVFD controlled by predictive control algorithm has elliptical hysteresis loop and the SAVSD controlled by switching control law and modified switching control law has triangular hysteresis loop.

References

1. Jonczyk J, Gruner P (1991) Loads of piping systems due to malfunctions of snubbers. *Nucl Eng Des* 130(3):411–433
2. Olson DE, Tang YK (1988) Decreasing snubber in service inspection costs through snubber reduction and improved test limits. *Nucl Eng Des* 107(1–2):183–199
3. Housner G, Bergman LA, Caughey TK, Chassiakos AG, Claus RO, Masri SF, Skelton RE, Soong TT, Spencer BF, Yao JTP (1997), Structural control: past, present, and future. *J Eng Mech ASCE* 123:897–971
4. Kunieda M, Chiba T, Kobayashi H (1987) Positive use of damping devices for piping systems-some experiences and new proposals. *Nucl Eng Des* 104(2):107–120
5. Keowen RS, Hueffmann G, Mays B, Remncher D (1993) Application of viscous dampers as pipe restraints. *Pressure vessels and piping division. ASME PVP* 256:135–147
6. Soong TT, Spencer BF Jr (2002) Supplemental energy dissipation: state-of-the-art and state-of-the-practice. *Eng Struct* 24(3):243–259

7. Mahmoodi P (1972) Structural dampers. *J Struct Div ASCE* 95(8):1661–1672
8. Soong TT, Dargush GF (1997) *Passive energy dissipation systems in structural engineering*, 1st edn Wiley, New York
9. Jangid RS (1999) Optimum multiple tuned mass dampers for base excited undamped system. *Earthq Eng Struct Dyn* 28(9):1041–1049
10. Spencer BF Jr, Dyke SJ, Sain MK, Carlson JD (1997) Phenomenological model of a magneto-rheological damper. *J Eng Mech ASCE* 123:230–238
11. Kumar P, Jangid RS, Reddy GR (2012) Response control of 3-D piping system with MR damper under tri-directional seismic excitation. *Int J Appl Sci Eng, ROC/USA* 10(2):99–111
12. Lu LY (2004) Predictive control of seismic structures with semi-active friction dampers. *Earthquake Eng Struct Dynam* 33:647–668
13. Yang JN, Kim JH, Agrawal AK (2000) Resetting semi-active stiffness damper for seismic response control. *J Struct Eng* 126(12):1427–1433
14. Kumar P, Jangid RS, Reddy GR (2013) Response of piping system with semi-active variable stiffness dampers under tri-directional seismic excitation. *Nucl Eng Des* 258:130–143

A Case Study to Report the Advantage of Using Signed Response Quantities in Response Spectrum Analysis

Sanjib Das and Santanu Bhanja

Abstract Static method of seismic analysis is based on the assumption that fundamental mode of vibration is predominant and there are no mass and stiffness irregularities in the structure. These assumptions of static analysis do not hold good for the irregular and/or tall structures. In such structures, Response Spectrum analysis is preferred as it provides an easy solution compared to Time History analysis. The results of Response Spectrum analysis are computed from modal responses obtained by performing modal analysis. Individual modal responses are combined using modal combination methods (SRSS, CQC etc.) to get maximum absolute responses. Modal combination process generates absolute response quantities. Unsigned member forces at the both ends of the members do not satisfy static equilibrium for the Response Spectrum load cases. Support Reaction of the supported nodes in Response Spectrum load case is also unsigned quantity. It does not allow understanding whether the supported node is subjected to uplift or not. Hence load combinations with these unsigned response quantities may lead to untenable and unrealistic support reaction. It may be observed that footing designed with such load combination is being subjected to huge uplift and requires unrealistic thickness. This problem can be easily eliminated if the sign of the responses of the dominant mode of vibration is considered. This has been clearly demonstrated in the present case study of a watch-tower constructed in seismic zone four in West Bengal where unsigned response quantities resulted in a huge uplift force in support reaction which resulted in unrealistic thickness of the foundation. It was observed that on using sign of the dominant mode, the supported nodes were not actually subjected to such huge uplift. It can be inferred from the present case study that the

S. Das (✉)

Department of Civil Engineering, National Institute of Technical Teachers' Training and Research, Kolkata, West Bengal, India

S. Das

Structural Group, Bentley Systems India Pvt. Ltd, 3rd Floor, Tower-A, DLF IT Park, 8 Major Arterial Road, Rajarhat, Kolkata 700 156, West Bengal, India

S. Bhanja

Department of Civil Engineering, National Institute of Technical Teachers' Training & Research, Block—FC, Sector—III, Kolkata, Salt Lake 700 106, West Bengal, India

responses obtained from modal combinations should be used for load combinations only with proper sign which is often not considered by the designers.

Keywords Response spectrum • Signed • Watch tower

1 Introduction

In the static method of seismic analysis, it is assumed that the fundamental mode of vibration dominates the response and mass and stiffness of the structure are evenly distributed thus giving a regular mode shape. In tall and/or irregular buildings, these assumptions are invalid and dynamic analysis needs to be performed. Dynamic analysis using Response Spectrum method is preferred as it is easy to use. Response spectrum analysis is a technique for performing an equivalent static lateral load analysis of structures for earthquake forces. It is useful in the approximate evaluation of the reliability and safety of structures under earthquake forces [1]. The major problem lies in the fact that the response quantities obtained from Response Spectrum analysis are absolute quantities as they are computed using modal combination methods like SRSS, CQC etc. The response quantities can be axial forces acting on a column, moment about its major axis or storey shear in a frame etc. The nature of the responses cannot be determined. The unsigned responses derived from a load combination involving a Response Spectrum load case may provide un-realistic results [2]. If they are used in the design of structural elements specifically columns, the results will be erroneous. Some special consideration is required in the Response Spectrum analysis by which the nature of the response quantities can be determined. A structural element is designed on the basis of the worst algebraic load combination that leads to maximum stress resultants [3]. Since member forces are expressed in local axes, unsigned member forces at the both ends of the members do not satisfy static equilibrium for the Response Spectrum load cases. Hence load combinations with these unsigned response quantities may lead to untenable and unrealistic member forces at the start and end of the member. The support reaction obtained in a Response Spectrum load also poses the same problem as the nature of the forces cannot be ascertained, only the magnitude is obtained. It becomes difficult to ascertain whether the reaction at a node is causing uplift or compression [4]. This problem can be easily eliminated if the sign of the responses of the dominant mode of vibration is considered. This has been clearly demonstrated in the present case study of a watch-tower situated in seismic zone IV in West Bengal where unsigned response quantities resulted in a huge uplift force at the foundation level. As a result of that the foundation for the structure had to be designed for high tensile force. The depth required for the foundation to stabilize this huge uplift was unrealistic. Considering the sign of the dominant mode, it was observed that the support reaction was not actually exhibiting that huge tension and a realistic depth of foundation could be obtained. It can be inferred from the present

case study that the responses obtained from modal combinations should be used for load combinations only with proper sign which is often not considered by the designers.

2 Objective of the Present Research Work

The objective of the present research work may be outlined as follows:

- To report in brief the analysis and design considerations adopted for the present case study
- To highlight how the unsigned response quantities in the in the response spectrum load cases may lead to unrealistic support reactions
- To discuss the methodology of using the sign of the dominant mode in the response quantities
- To demonstrate how the use of signed response quantities can resolve the problem

3 Introduction to the Case Study

The present case study consists of a watch-tower constructed at Jalpaiguri district of West Bengal, India. The typical administrative building plan is shown in Fig. 1.

Height of the tower was 15.05 m. The circular platform of the tower was at a height of 11.8 m from the ground level with a radius of 3.5 m. The entire model was supported by four circular columns which were tied at different levels. There were intermediate platforms at different levels. The main tower was made accessible by a series of stairs resting on a series of columns. These columns were not connected to the main tower model of the watch tower has been provided in Fig. 2.

The watch-tower was constructed in seismic zone IV and response spectrum analysis was proposed to capture the dynamic response of the watch-tower [5]. The watch-tower model was prepared in STAAD.Pro V8i software. Figure 3 shows the 3D structural model prepared using the software.

The model was analysed for dead load, live load and seismic forces. Response spectrum analysis was performed. The structural elements were designed with the maximum forces obtained with load combinations as per the relevant Indian standards code.

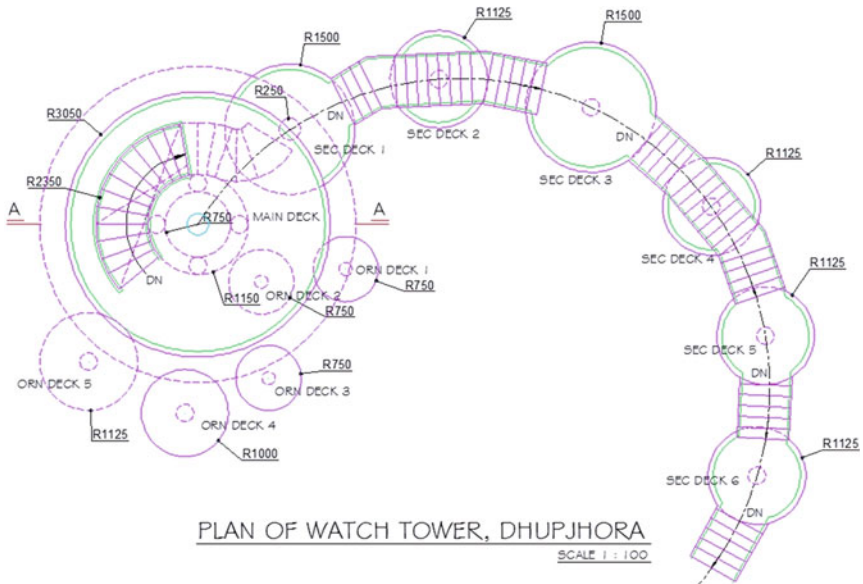


Fig. 1 Plan of watch tower

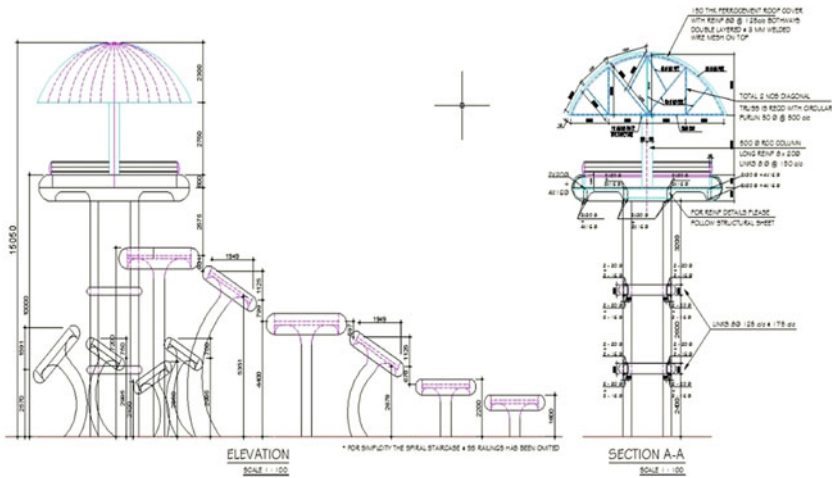
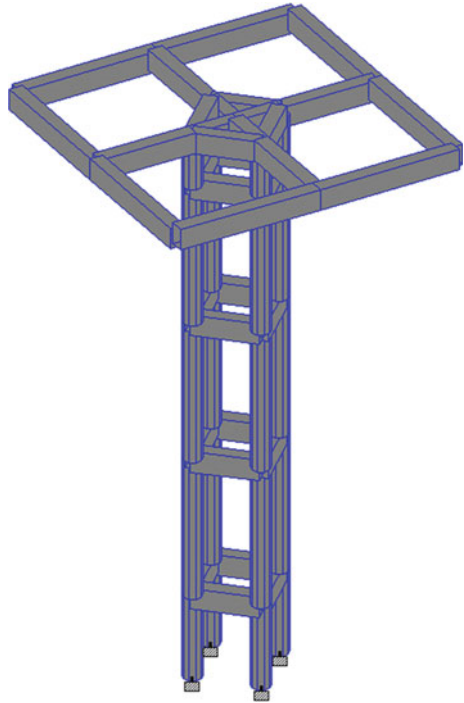


Fig. 2 3D Model of watch tower

Fig. 3 3D Structural model of watch tower prepared in software



4 Statement of the Actual Problem

The model was analysed for the primary load cases and load combinations created as per relevant Indian standards. Support reactions from the superstructure were obtained and they were adopted for the design of the foundation. A rectangular mat foundation having a size of $4.6 \text{ m} \times 4.5 \text{ m}$ was adopted. It was observed that 12 ms depth of foundation was required to stabilize this model for the uplift forces coming from the superstructure which was absurd and technically not feasible. It was observed that two supported nodes marked as node number 18 and 19 were experiencing very high uplift forces. The support reactions should be equal in magnitude but opposite in sign of the forces acting at the column connected to that node. Figure 4 indicates that if unsigned values of response spectrum quantities are used, the axial forces developing at the ends of the member for a load combination involving the gravity and Response spectrum loads fails to satisfy static equilibrium for that element.

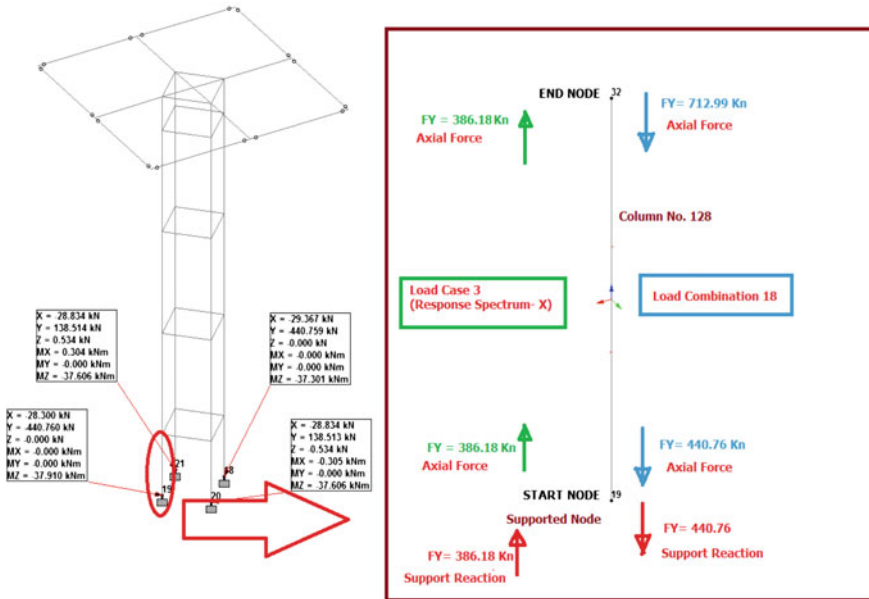


Fig. 4 Support reactions

5 Modifications Needed in the Analysis and Design

Considering the response spectrum load case i.e. Load case 3, the support reaction at node 19 was obtained as + 386.18 kN (i.e. acting upwards) and the axial force in the member 128 at that node was +386.16 kN (i.e. acting upwards) and at node 32 was 386.18 kN (i.e. acting upwards) as shown in Fig. 4. This clearly demonstrates that unsigned responses obtained in Response Spectrum load cases violates the conditions of static equilibrium. It was observed that load combination 18 [0.9 times dead load (Load case 1) +1.5 Response spectrum load case in X direction (Load case 3)] was the critical one for the foundation design. It was a tough task for the designers to find out a suitable depth for the mat foundation. Figure 5 shows the support reaction for the critical load combination 18.

At the supported node number 18 and 19 the support reactions in FY direction for load case 1 and 3 were 153.90 kN and 386.18 kN respectively. The support reaction in FY direction for the load combination 18 was computed as $(0.9 \times 153.910 - 1.5 \times 386.19) = -440.76$ kN. This has been shown in Fig. 6.

It can be inferred that the results of the Response spectrum load case being unsigned when added with other gravity load cases may lead to huge uplift forces in the foundation which is actually non-existent. This situation can be avoided by using signed Response Spectrum results. The mode having maximum mass participation is considered as the dominant mode and all the response quantities are assigned the sign of dominant mode [6]. On using the sign of the dominant mode,

SUPPORT REACTIONS -UNIT KN METE STRUCTURE TYPE = SPACE							
JOINT	LOAD	FORCE-X	FORCE-Y	FORCE-Z	MOM-X	MOM-Y	MOM Z
18	18	-29.37	-440.76	0.00	0.00	0.00	-37.30
19	18	-28.30	-440.76	0.00	0.00	0.00	-37.91
20	18	-28.83	138.51	-0.53	-0.30	0.00	-37.61
21	18	-28.83	138.51	0.53	0.30	0.00	-37.61

Fig. 5 Critical design forces

SUPPORT REACTIONS -UNIT KN METE STRUCTURE TYPE = SPACE							
JOINT	LOAD	FORCE-X	FORCE-Y	FORCE-Z	MOM-X	MOM-Y	MOM Z
18	1	-0.59	153.90	0.00	0.00	0.00	0.34
	3	19.22	386.18	0.00	0.00	0.00	25.07
	18	-29.37	-440.76	0.00	0.00	0.00	-37.30
19	1	0.59	153.90	0.00	0.00	0.00	-0.34
	3	19.22	386.18	0.00	0.00	0.00	25.07
	18	-28.30	-440.76	0.00	0.00	0.00	-37.91

Fig. 6 Support reactions for different load cases

the member forces/support reactions gets modified which also satisfies statical equilibrium for the different elements. The program is capable of finding out the dominant mode and use the sign of the responses from the dominant mode in the final result of response spectrum analysis.

It was found that support reaction for the supported node number 19 changed drastically on using the sign of dominant mode. Proper sign of the support reaction obtained from the dominant mode of vibration was assigned (Fig. 7). It was observed that the foundation was to be designed for uplift only for support number 18 and support 19 was not experiencing any uplift. Figure 8 shows the support reactions obtained after using the sign of dominant mode.

The mat foundation designed with these modified forces resulted in 0.9 m thickness which was quite a reasonable value. Figure 9 shows the finite element model created for mat foundation.

6 Findings from Present Case Study

Instead of using the unsigned numerical values of the responses, designers should use the signed response spectrum results. Designers can use the relevant command to instruct the program to use the sign of the member forces in Response Spectrum

MASS PARTICIPATION FACTORS IN PERCENT							BASE SHEAR IN KN			
MODE	X	Y	Z	SUMM-X	SUMM-Y	SUMM-Z	X	Y	Z	
1	0.00	0.00	0.00	0.000	0.000	0.000	0.00	0.00	0.00	
2	0.00	0.00	82.12	0.000	0.000	82.120	0.00	0.00	0.00	
3	82.12	0.00	0.00	82.120	0.000	82.120	50.90	0.00	0.00	
4	0.00	0.00	6.04	82.120	0.000	88.161	0.00	0.00	0.00	
5	6.04	0.00	0.00	88.161	0.000	88.161	4.72	0.00	0.00	
6	0.00	24.97	0.00	88.161	24.974	88.161	0.00	0.00	0.00	
7	0.00	0.00	0.00	88.161	24.974	88.161	0.00	0.00	0.00	
8	0.00	0.00	3.58	88.161	24.974	91.739	0.00	0.00	0.00	
9	3.58	0.00	0.00	91.739	24.974	91.739	2.80	0.00	0.00	
10	0.00	0.00	0.00	91.739	24.974	91.739	0.00	0.00	0.00	
11	0.00	0.00	0.00	91.739	24.974	91.739	0.00	0.00	0.00	
12	0.00	0.00	0.79	91.739	24.974	92.527	0.00	0.00	0.00	
13	0.79	0.00	0.00	92.527	24.974	92.527	0.56	0.00	0.00	
14	0.00	0.00	1.85	92.527	24.974	94.374	0.00	0.00	0.00	
15	1.85	0.00	0.00	94.374	24.974	94.374	1.08	0.00	0.00	
16	0.00	0.00	0.00	94.374	24.974	94.374	0.00	0.00	0.00	
17	0.00	0.00	0.00	94.374	24.974	94.374	0.00	0.00	0.00	
18	0.00	0.00	5.62	94.374	24.974	99.992	0.00	0.00	0.00	
19	5.62	0.00	0.00	99.992	24.974	99.992	2.75	0.00	0.00	
20	0.00	51.50	0.00	99.992	76.470	99.992	0.00	0.00	0.00	
ZPA	0.01	0.00	0.00	100.000	0.000	0.000	0.00	0.00	0.00	
							TOTAL SRSS SHEAR	51.28	0.00	0.00
							TOTAL 10PCT SHEAR	51.28	0.00	0.00
							TOTAL ABS SHEAR	62.82	0.00	0.00
							TOTAL CSM SHEAR	62.81	0.00	0.00
							TOTAL CQC SHEAR	51.34	0.00	0.00

USING THE DOMINANT MODE METHOD OF GIVING SIGNS TO THE RSA OUTPUT, THE DOMINANT MODE USED IS 3

Fig. 7 Dominant mode of vibration in X direction

SUPPORT REACTIONS -UNIT KN METE STRUCTURE TYPE = SPACE							
JOINT	LOAD	FORCE-X	FORCE-Y	FORCE-Z	MOM-X	MOM-Y	MOM Z
18	1	-0.59	153.90	0.00	0.00	0.00	0.34
	3	-19.22	386.18	0.00	0.00	0.00	25.07
	18	28.30	-440.76	0.00	0.00	0.00	-37.30
19	1	0.59	153.90	0.00	0.00	0.00	-0.34
	3	-19.22	-386.18	0.00	0.00	0.00	25.07
	18	29.37	717.79	0.00	0.00	0.00	-37.91

Fig. 8 Support reactions after using the sign of dominant mode

results for the most dominant mode—where the mass participation is the highest among all the considered modes in the analysis. If engineers use simple algebraic summation of the signed response spectrum quantities with the other load cases, the final result used for the design will have the proper sign. This can be easily understood from the output results of the present case study.

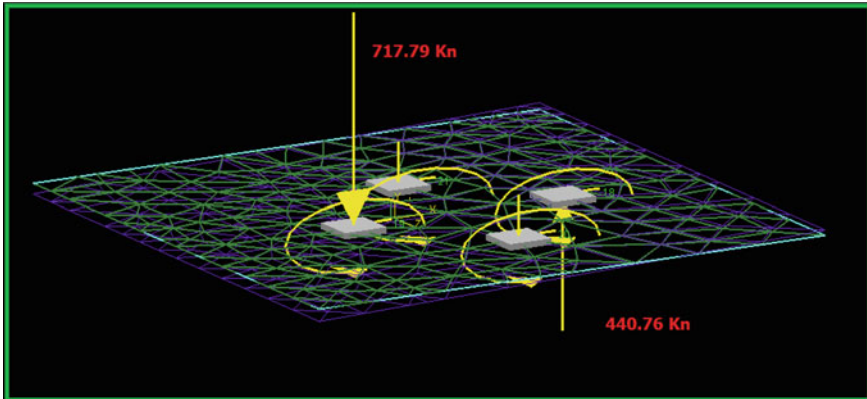


Fig. 9 Support reactions acting on the mat

7 Conclusion

Direct use of unsigned response spectrum analysis results in design sometimes may lead to an irrational/untenable situation. For example support reactions may yield very high tension arising from a load combination where the response spectrum load case is involved. It can be concluded from this case study that use of signed response spectrum results, where the sign of the response spectrum quantities obtained from the dominant mode, provides a realistic analysis result which can directly be used for proper design of structural elements.

References

1. Sen TK (2009) Fundamentals of seismic loading on structures, 2nd edn. Wiley, New York, pp 64–65
2. Wilson EL (2002) Three-dimensional static and dynamic analysis of structures, 1st edn Computers and Structures, Inc, pp 233–234
3. Dutta, TK (2010) Seismic analysis of structures, 1st edn. Wiley, Mississauga, pp 115–116
4. Housner GW, Jennings PC (1982) Earthquake design criteria. Earthquake Engineering Research Institute, Berkeley, pp 33–34
5. IS 1893(Part-I) (2002) Indian Standard. Criteria for earthquake resistant design of structures. General Provisions Buildings, Bureau of Indian Standards
6. Das S (2014) Use of signed response quantities in response spectrum analysis—a case study. National Institute of Technology, Durgapur, Innovation in Civil Engineering Structures

Performance of Medium-Rise Buckling-Restrained Braced Frame Under Near Field Earthquakes

Ahmad Fayeq Ghowsi and Dipti Ranjan Sahoo

Abstract Buckling-restrained braced frames (BRBFs) are generally used as lateral load-resisting systems in the seismically active regions. The better energy dissipation capacity and the absence of compressive buckling behaviour of braces in make the BRBFs a preferred alternative over the conventional concentrically braced frames. Most of the past studies focussed on the performance of BRBFs under the far-field earthquakes and concluded that BRBFs may suffer from the larger post-earthquake residual drift as compared to the other systems. This behaviour may be amplified in case of the near-fault earthquakes where long-period pulses and high-frequency contents. In this study, the seismic performance of a medium-rise building of 9-storey has been carried out analytically using SAP2000. The study frame has been designed as per the current seismic code AISC 341-2010 provisions. Forty near-fault ground motions are considered in the nonlinear dynamic (time-history) analysis. The main parameters investigated are inter storey drift response, residual drift response, sequence of hinge formations, and behaviour of beams and columns. The effect of brace configurations, i.e., Chevron and Split-X, are also studied under the same near-fault ground motions.

Keywords Split-X · Chevron · Braces · SAC · Near-fault · Earthquake · Interstorey · Drift

A.F. Ghowsi (✉) · D.R. Sahoo
Department of Civil Engineering, Indian Institute of Technology (IIT) Delhi,
New Delhi, India
e-mail: faieq.ghowsi@gmail.com

D.R. Sahoo
e-mail: drsahoo@civil.iitd.ac.in

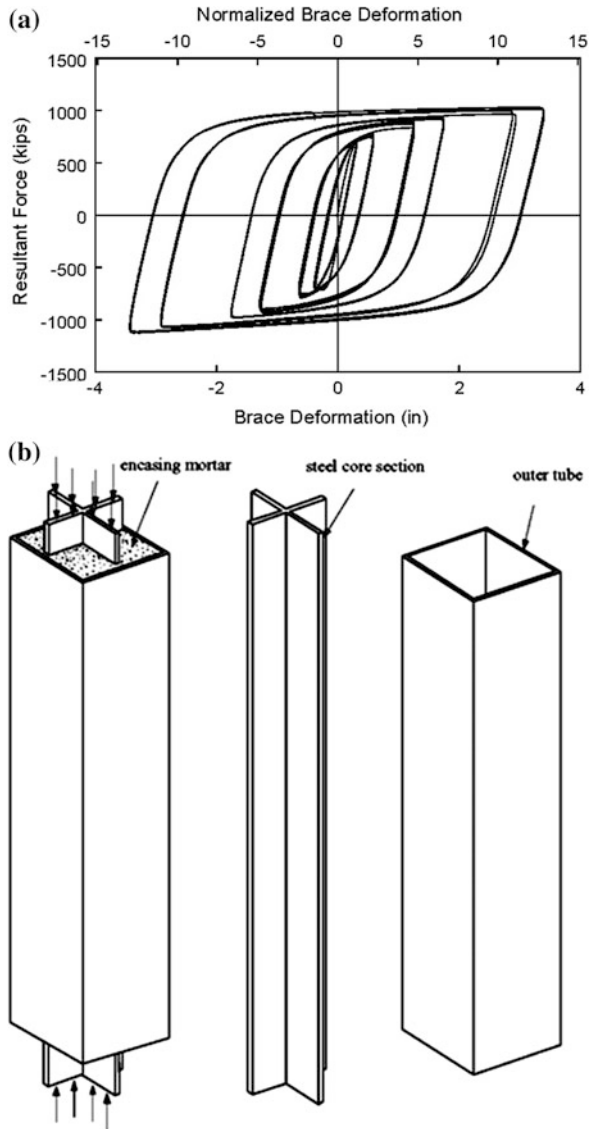
1 Introduction

Buckling-restrained braced frames (BRBFs) are usually used in active seismic regions for the purpose of lateral load resistance on the structure. Figure 1a shows the different components of a BRB element. Steel core plates of BRBs are separated by unbounded material from the restening parts and/or outer core, the yield of BRBs while tension and compression resulted in symmetric hysteretic response, high ductility level, and excellent energy dissipation as shown in Fig. 1b. A number of tests has been conducted by previous researcher for the component as well as the system level for seismic performance of BRBFs (e.g., [1, 5, 6, 8, 11, 14, 15, 18, 19]). The main parameters which has been studied are the displacement ductility and cumulative displacement ductility, energy dissipation potential, compression over-strength and strain-hardening factors, detailing of non-yielding segments and the end connections of BRBs. The type of beam-to-column connections has a visible impact on the seismic response of BRBFs [8, 9, 12].

Beam-to-column connections type can arrange with different braced configurations and also BRB can be arranged in single-diagonal, Chevron (inverted-V) or Double- storey-X configurations. A recent study by Ghowsi and Sahoo [10] concluded that Double- storey-X configuration of BRBs resulted in the relatively larger post-earthquake residual drift response of BRBFs as compared to those in Chevron configuration. Further, a huge studies have been done on seismic response of BRBFs far-field ground motions, but very limited studies carry out on the performance of BRBFs under the near-field ground motions (e.g. [4, 16]). The near-fault earthquakes has long period of pulses which can cause to permanent displacements of ground. The effect of such ground motions still not known to the international codes [3]. As the BRBFs recommendation is for the seismic active zone which can carry high load capacity [4]. Hereby, the near-fault ground motions can cause extensive structural damages as compared to the far-fault ground motions. Hence, there is a need of further study to investigate the performance of BRBFs under near-fault earthquakes.

In this study, the effect of brace configurations on the overall seismic response of a medium-rise BRBF under the near-field ground motions has been analytically evaluated. The main objective of this study is investigation of near fault earthquakes response of BRBFs equipped with both Chevron and Double- storey-X BRBs. Nonlinear dynamic analyses are carried out under the selected near-fault seismic excitations to understand the structural and ground motion characteristics that influence their seismic behavior of BRBFs. Inter- storey drift and residual- storey drift developed to investigation design of BRBFs under near fault ground motions.

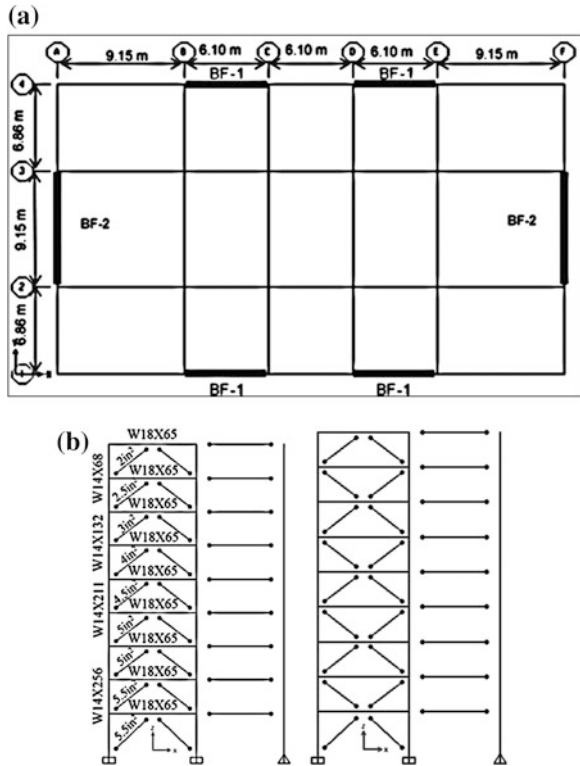
Fig. 1 **a** Components of an unbounded BRB [5]; **b** typical hysteretic response of BRBs under cyclic loading [14]



2 Modeling of Study Frames

A nine-storey steel building has been designed and considered as the study building in which the braced bays are lied on the exterior perimeters. The total height of the building is 32.31 m with a typical storey height of 3.51 m, except the first storey which has 4.27 m height. The building has been redesigned as per current code. The actual building geometry has been adopted from the seven storey which has been

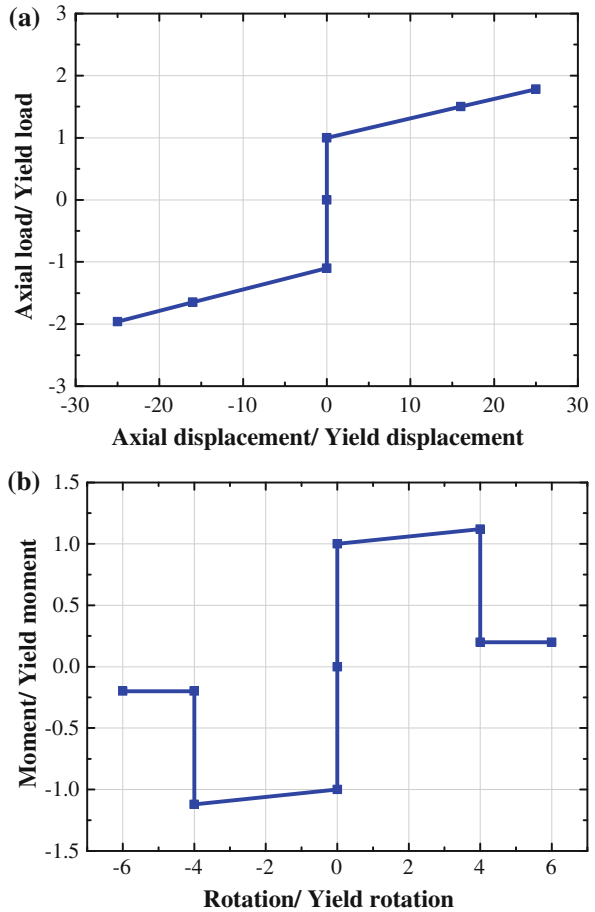
Fig. 2 **a** Plan view of the study building; **b** elevation of BRBFs considered in this study



designed elsewhere [13]. The braced bay (of width 9.15 m) along the wide of the building is considered as the study frame. Two types of brace configurations (i.e., Chevron and Double-X), designed as per ASCE/SEI 7-10 [3] provisions. Figure 2 shows the details of the study frame considered in this study. In order to study the effect of brace configurations, same structural sections are used as beams and columns in all BRBFs. All sections satisfy the seismic design requirements as per ANSI/AISC 341-05 [2] provisions. The beam to column connections has been considered to be rigid.

The nonlinear dynamic analysis has been done by computer software SAP2000 [7]. The beams and columns members are modelled as frame elements to be resisting the axial, shear, and bending actions. The elements are assigned the section and material properties. The value of tensile yield stress of steel used in BRBs, beams and columns is considered as 345 MPa. Material overstrength factor (R_y) for BRB is considered as unity. Compression overstrength (β) and strain-hardening (ω) factors of BRBs are assumed as 1.04 and 1.54, respectively. The nonlinear behaviour of frame members is considered in the models by using lumped plasticity concepts. Nonlinear moment-rotation ($M-\theta$) plastic hinges along with the axial load-bending moment ($P-M$) interaction properties are assigned to all the columns and beams. Both ($M-\theta$) and ($P-M$) plastic hinges are assigned at both end of the

Fig. 3 a Plastic hinge properties of BRBs; **b** plastic hinge properties of beam and column



columns, whereas these properties are assigned at the mid-lengths of beams in addition to the ends in case of RBC connections.

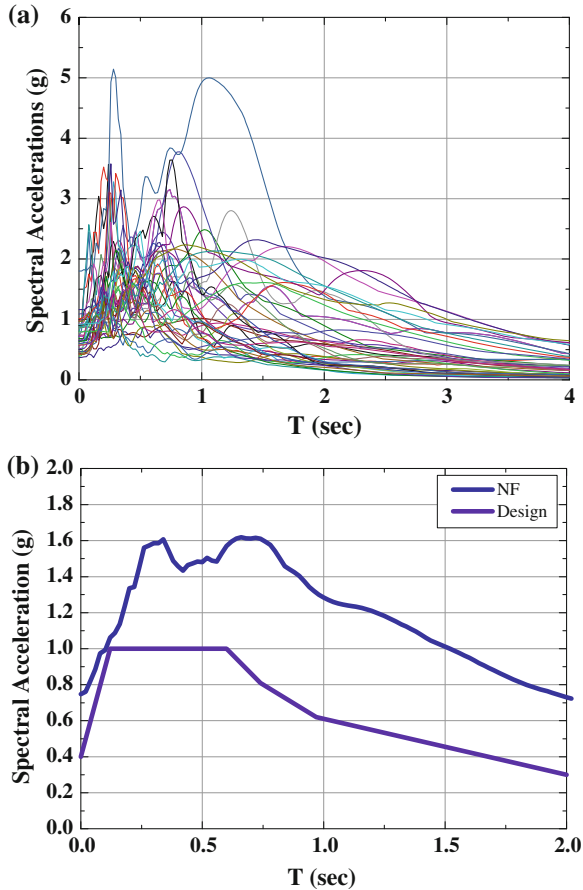
Figure 3b shows the nonlinear ($M-\theta$) plastic hinge properties used in the frame members. Both moment and rotation values are normalized with respect to their corresponding yield values. The ultimate resistance is assumed as 15 % of higher than the yield strengths. The post-peak residual strength is considered as 20 % of the yield strengths. Axial force-displacement plastic hinges, as shown in Fig. 3a, are used to model the nonlinear axial behaviour of BRBs. These plastic hinges are placed at the mid-lengths of BRBs. No post-peak descending behaviour is modelled for BRBs in this study. However, BRBs are assumed to have failed when the displacement ductility level exceeded a value of 25, the limit which most of the BRBs have exhibited in the past experimental studies (e.g., [8]). Kinematic hardening behaviour is assumed for all the elements of BRBFs. P-Delta effect due to gravity loads is considered by modelling a leaning column pinned at its base and

connected to the BRBFs through the rigid links at each floor level. The gravity loads contributing to the P-delta effect are applied to the nodes at each floor level of the leaning column. All the columns of BRBFs are assumed to be fixed at their bases.

3 Time History Analysis

An ensemble of forty SAC ground motions representing the near-fault records [17] are used in this study for the nonlinear dynamic analysis. Twenty ground motions (NF01-20) represent the recorded near-fault ground motions, whereas the remaining (NF21-40) ground motions are obtained by physical simulations considering the variations in the source-to-site distance (<20 km), fault rupture mechanism, soil medium, and earthquake magnitudes, etc., resembling the seismic characteristics in the near-fault region. Figure 4a show the elastic acceleration spectrum of the input

Fig. 4 a Elastic acceleration spectrum of the selected forty ground motions; **b** comparison of average elastic acceleration spectrum with the design spectrum

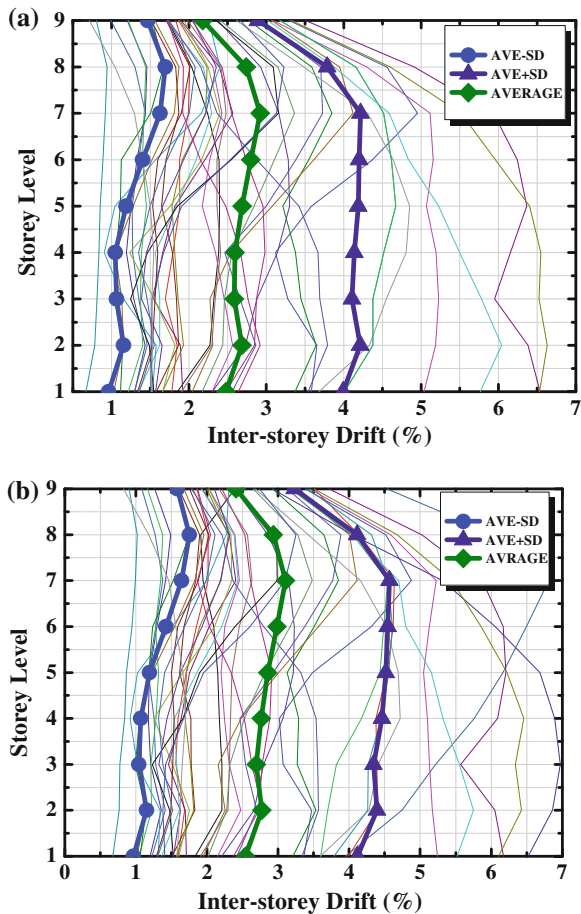


ground motions for 5 % damping which shows the pulse-like and long-period characteristics of the ground motions. Figure 4b shows a comparison of the average acceleration spectrum of all ground motions with the design spectrum as per ASCE/SEI 7-10 [3]. Except for the short period (<0.2 s), the average value of spectral acceleration of all ground motions lies well-above the design spectrum.

3.1 Inter Storey Drift Response

The inter storey drift ratio is computed from the ration inter storey displacement into high of that considered floor. Figure 5 shows the inter storey response of BRBF under near field ground motions. The statistical values, such as, mean and \pm standard deviation (SD) also shown in the figure. For both the cases of chevron and double-X,

Fig. 5 Inter-storey drift
a chevron b double-X



the average interstorey drift is higher in then limit of 2 % as per ASCE/SEI 7-10 [3] provisions. The distribution of inter storey drift is also uniform along the height of the frame with both cases.

In case of Chevron type of brace we have some ground motions (NF23, NF25, NF29) foully collapsed which the interstorey drift and residual storey drift is not taking into account, which the collapsed drift has extreme drift value, can change average of overall drifts. The maximum value of interstorey drift value of chevron and double-X is 6.6 and 7 %, respectively. Overall from both the cases, means are parallel along the height. The average of drift is more in 2nd and 7th floors compare to other floors.

As stated earlier, the design considerations should be different for Near Field ground motions as the drift value is much higher than the design value as per ASCE/SEI 7-10 [3] provisions. This shows that the current code-based design using the recommended as per far field ground motions is very conservative. Hence, a higher design consideration is required for the near field ground motions.

3.2 Residual Drift Response

Residual Inter storey drift ratio has been computed from the inter storey displacement at various storey level which is at last step of ground motion at each floor level height. Figure 6 shows the residual drift response of both cases of studied frames under near field earthquakes. For both chevron and double-X type of BRBFs seems same value of residual drift, except two cases of (NF31 and NF33) overall the maximum residual storey drift 1.9 and 2.2 % drift for Chevron type and double-X type, respectively. Although, in case chevron type of braces cases of NF23, NF25 and, NF29 has excepted. In cases of NF31 and 33 has collapse at the first floor level which is the reason for higher residual drift. Overall, the mean residual drift is equally parallel for both the cases, the average of residual drift is lesser at 8th and 9th floor levels also it shows higher value at first floor level.

3.3 Hinge Mechanisms

The plastic hinge deformation in various members which occurred for all near field ground motions has been monitored. As expected, the yielding occurred on the bracing members at most of the floor level especially the 1st–5th floors for all the cases. The minor yielding occurred at base ground floor column for all the cases for both case of brace configurations as it is expected. Except ground floor base column the rare cases plastic hinges formed into the columns at 6th, 7th and, 8th floors columns.

Fig. 6 Residual drift
a chevron b double-X

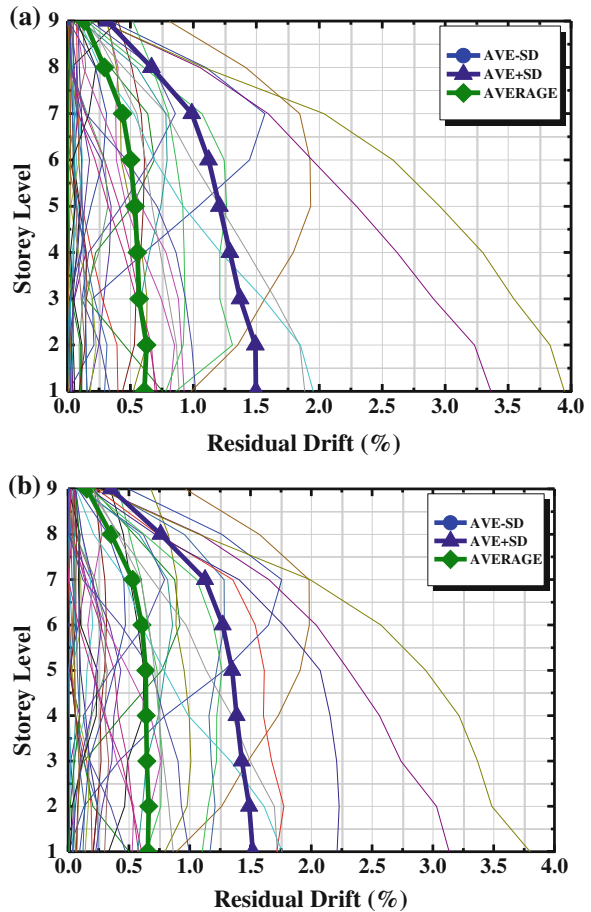


Table 1. Summarized the plastic hinges formed in the beams and columns of both cases of BRBFs. Some few extreme ground motions NF23, NF25 and, NF29 seems to be effected in case of chevron type of configuration which all the frame gone to collapse level. The minor hinges seem in the first 20 ground motions which are the real earthquakes compared to the last 20 ground motion which has been extracted from their physical simulations. A reduced number of plastic hinges are formed in alternative pairs of ground motions. Since the sever collapse is not recommended and the double-X configuration shows better capability of drift without and any series damages or collapse should be used in BRBFs to achieve a better seismic performance.

Table 1 Hinge mechanism

Near field ground motions				
	Chevron		Double X	
	Beam	Column	Beam	Column
NF01	1S2B, 2S2B, 3S2B	GF2B	1S2B, 2S2B	GF2B
NF02	1S2B	GF2B	1S1B	GF2B
NF03	1S1C, 1S1E, 2S2B, 3S2B, 5S2B, 6S2B, 7S2B, 8S2B	GF2B, 8S1B	1S2B, 2S2B, 3S2B, 5S2B, 6S2B, 7S2B, 8S1B	GF2E, 7S1B
NF04	1S2B, 2S2B, 3S2B	GF2B	1S2B, 2S2B, 3S2B	GF2B
NF05	1S2B, 2S2B, 3S2B, 5S2B, 6S2B, 7S2B	GF2B	1S2B, 2S2B, 3S2B, 5S2B, 6S2B, 7S2B	GF2B
NF06	NA	NA	NA	NA
NF07	1S2B, 2S2B, 3S2B, 5S2B, 6S2B	GF2B	1S2B, 2S1B, 3S2B, 5S2B, 6S1B, 7S1B	GF2B
NF08	1S2B	GF2B	1S1B	GF2B
NF09	NA	GF1B	NA	NA
NF10	1S2B	GF2	1S1B	GF1B
NF11	NA	NA	NA	NA
NF12	NA	NA	NA	NA
NF13	1S2B, 2S2B, 3S2B, 5S2B, 6S2B, 7S2B	GF2B	1S2B, 2S2B, 3S1B, 5S2B, 6S2B, 7S2B, 8S1B	GF2B
NF14	NA	NA	NA	NA
NF15	1S2B, 2S2B, 3S2B, 5S2B	GF2B	1S2B, 2S1B, 3S2B, 5S2B, 6S1B	GF2B
NF16	NA	NA	NA	NA
NF17	1S2B, 2S2B, 3S2B, 5S2B, 6S2B, 7S2B	GF2B	1S2B, 2S2B, 3S1B, 5S2B, 6S2B, 7S2B, 8S1B	GF2B
NF18	1S2B	GF2B	1S1B	GF2B
NF19	1S1C, 1S1B, 2S2B, 3S2B, 5S2B, 6S2B, 7S2B	GF1E, GF1C	1S1C, 1S1B, 2S2B, 3S2B, 5S2B, 6S2B, 7S2B	GF1E, GF1C
NF20	1S2B, 2S2B, 3S2B	GF2B	1S2B, 2S1B, 3S1B, 5S1B	GF2B
NF21	1S2B, 2S2B, 3S2B, 5S2B, 6S2B, 7S2B	GF2B	1S2B, 2S1B, 3S1B, 5S2B, 6S2B, 7S2B	GF2B
NF22	NA	GF1B	NA	NA
NF23	1- 9SE	1- 9SE	1S2B, 2S2B, 3S1C, 3S1B, 5S1C, 5S1B, 6S2B, 7S2B, 8S2B	GF1E, GF1B, 7S2B, 8S1B
NF24	6S2B, 7S2B	GF1B	6S1B, 7S2B	GF1B
NF25	1- 9SE	1- 9SE	1S2B, 2S2B, 3S2B, 5S2B, 6S2B, 7S2B, 8S1B	GF1E, GF1B
NF26	6S2B, 7S2B	GF1B	6S1B, 7S2B, 8S1B	NA
NF27	1S2E, 2S2E, 3S2E, 5S2C, 6S1C, 6S1B, 7S2B	GF2E	1S2E, 2S2C, 3S2B, 5S2B, 6S2B, 7S2B, 8S2B	GF2E, 1S1B, 7S1B

(continued)

Table 1 (continued)

Near field ground motions				
	Chevron		Double X	
	Beam	Column	Beam	Column
NF28	NA	NA	NA	NA
NF29	1– 9SE	1– 9SE	1S1E, 1S1C, 2S1E, 2S1B, 3S2B, 5S1C, 5S1B, 6S2B, 7S2B, 9S1B	GF2E, 7S1B, 8S2B
NF30	NA	GF1B	NA	GF1B
NF31	1S2E, 2S1E, 2S1B, 3S1E, 3S1B, 5S2B, 6S1E, 6S1B, 7S1C, 7S1B, 8S2B	GF2E, 7S1B	1S2E, 2S1C, 2S1B, 3S2C, 5S2B, 6S2B, 7S2B, 8S1B	GF2E, 7S1B
NF32	NA	NA	NA	NA
NF33	1S1E, 1S1B, 2S2C, 3S1C, 3S1B, 5S2B, 6S2B, 7S2B, 8S2B	GF2E, 7S1B	1S2E, 2S1C, 2S1B, 3S2C, 5S2B, 6S2B, 7S2B, 8S1B	GF1E, GF1C, 7S1B, 8S1B
NF34	NA	NA	NA	NA
NF35	1S2E, 2S2E, 3S2E, 5S1C, 5S1B, 6S1E, 6S1B, 7S2B, 8S1B	GF2E	1S2E, 2S2B, 3S2C, 5S2B, 6S2B, 7S2B, 8S1B	GF2E
NF36	NA	NA	NA	NA
NF37	1S1E, 1S1B, 2S1E, 2S1B, 3S2B, 5S2B, 6S2B, 7S2B	GF2E	1S2B, 2S2B, 3S2B, 5S2B, 6S2B, 7S2B, 8S1B	GF2E
NF38	1S2B, 2S2B, 3S2B	GF2B	1S2B, 2S1B, 3S2B	GF2B
NF39	1S1E, 1S1B, 2S1E, 2S1B, 3S1E, 3S1B, 5S2B, 6S2B, 7S2B	GF1E, GF1C	1S2B, 2S2B, 3S2B, 5S2B, 6S2B, 7S2B, 8S2B	GF1E, GF1C
NF40	1S2B, 2S2B, 3S2B, 5S2B	GF1C, GF1B	1S2B, 2S2B, 3S2B, 5S2B, 6S1B	GF2B

nSm m is number of plastic hinges at floor number n
mB is number of plastic hinges at yield level
mC, *mD* is number of plastic hinges at ultimate level
mE is number of plastic hinges at rapture point
NA is not available
GF ground floor base

3.4 Nonlinear Static Analyses

The static pushover analysis done to carried out the lateral strength and hinge mechanism of both study frames. The lateral displacement which used as lateral load distribution extract from the fundamental mode shape into pushover analysis. Figure 7 shows the comparison of capacity curves chevron and double-X braces. From the push over analysis can see the more number of hinges occurred at chevron type configurations compare to double-X braces. Hence, in order to have flexible

Fig. 7 Base shear capacity curves of chevron and double-X

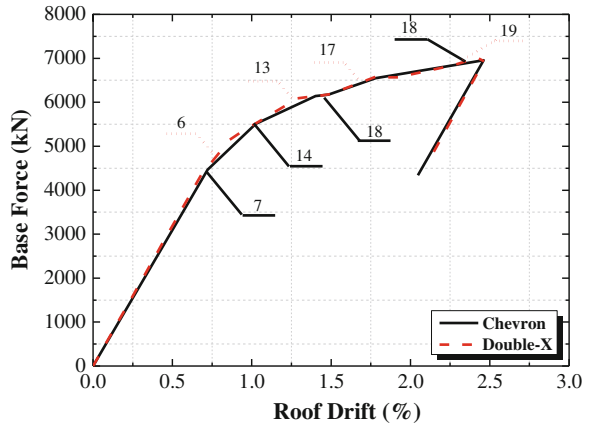
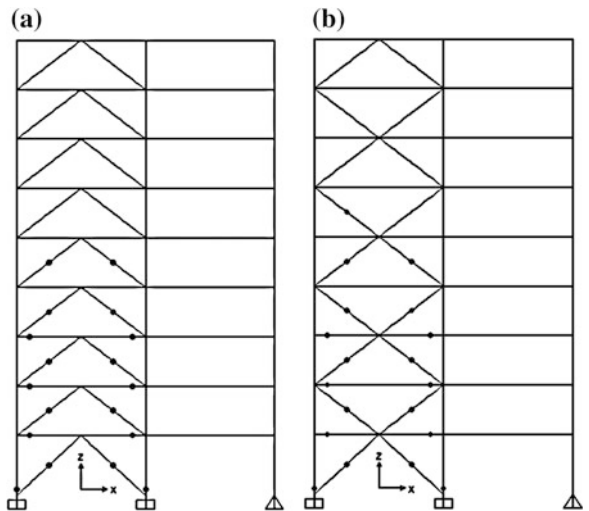


Fig. 8 Hinge mechanism at the stage of 2.42 % pushing of roof level **a** Chevron and **b** Double-X



BRBFs systems and desirable hinges forming in various stages of deforming is recommended to use double-X braces. Figure 8 shows the hinges formation drift at the last stage of 2.42 % of roof drift ratio.

4 Conclusions

Based on the analysis results, following conclusions can be drawn for medium-rise BRBFs:

- The new design consideration has to be provide for BRBFs under near field ground motions.

- The Double-X braced configurations has more flexibility compare to Chevron type configurations.
- The Chevron type of brace shows a stiffer which has brittle behavior, going under extreme collapse in some case of near field.
- The case of NF23, NF25 and, NF29 seems to be strong then all the ground motions, for the design evolution can be closed be checked for the structures.
- From the nonlinear static push over analysis it has found that most number of hinges occur for Chevron type compare to double-X type of brace configurations.
- The pairs of near fault ground motions one against the other is stronger, relatively.
- The behavior of Double-X configuration with BRBFs need be checked with various number of stories.

References

1. Aiken ID, Mahin SA, Uriz PR (2002) Large-scale testing of buckling restrained braced frames. In: Proceedings of Japan passive control symposium, Tokyo Institute of Technology, Japan
2. ANSI/AISC 341-05 (2005) Seismic provisions for structural steel buildings. American Institute of Steel Construction, Chicago
3. ASCE/SEI 7-10 (2010) Minimum design loads for buildings and other structures. American Society of Civil Engineers, Reston
4. Baghbanijavid Z, Jalali A, Yasrebinia Y (2010) Seismic response of buckling-restrained braced frames under near fault ground motions. *J Appl Sci* 10(23):2967–2977
5. Black CJ, Makris N, Aiken ID (2004) Component testing, seismic evaluation and characterization of buckling-restrained braces. *ASCE J Struct Eng* 130(6):880–894
6. Chou CC, Liu JH, Pham DH (2012) Steel buckling-restrained braced frames with single and dual corner gusset connections: seismic tests and analyses. *Earthq Eng Struct Dynam* 41 (7):1137–1156
7. CSI (2009) CSI analysis reference manual for SAP 2000. Computers and Structures Inc, Berkeley,
8. Fahnestock LA, Sause R, Ricles JM (2007) Seismic response and performance of buckling-restrained braced frames. *ASCE J Struct Eng* 133(9):1195–1204
9. Field C, Ko E (2004) Connection performance of buckling restrained braced frames. Paper No. 1321. In: Proceedings of thirteenth world conference on earthquake engineering, Vancouver, BC, Canada
10. Ghowsi AF, Sahoo DR (2013) Seismic performance of buckling-restrained braced frames with varying beam-column connections. *Int J Steel Struct* 13(4):607–621
11. Iwata M, Kato T, Wada A (2003) Performance evaluation of buckling-restrained braces in damage-controlled structures: behavior of steel structures in seismic area. In: Proceeding of fourth international conference STESSA, Naples, Italy
12. Lin ML, Tsai KC, Hsiao PC, Tsait CY (2005) Compressive behavior of buckling restrained braces gusset connections. In: First international conference on advanced experimental structural engineering, Nagoya, Japan
13. López WA, Sabelli R (2004) Seismic design of buckling-restrained braced frames. Structural Steel Education Council, Moraga

14. Merritt S, Uang CM, Benzoni G (2003) Subassemblage testing of core brace buckling-restrained braces, Report No. TR-2003/01, Department of Structural Engineering, University of California at San Diego, USA
15. Romero P, Reaveley L, Miller P, Okahashi T (2007) Report on full-scale testing of WC series buckling-restrained braces. Department of Civil and Environmental Engineering, University of Utah, USA
16. Shakib H, Safi R (2012) Behavior evaluation of the eccentric buckling-restrained braced frames under the near-fault ground motions. In: Proceedings of fifteenth world conference on earthquake engineering, Lisbon
17. Somerville PG, Smith M, Punyamurthula S, Sun J (1997) Development of ground motion time histories for phase 2 of the FEMA/SAC Steel Project, Report No. SAC/BD-97/04, SAC Joint Venture, Sacramento, CA
18. Tsai KC, Hsiao BC, Lai JW, Chen CH, Lin ML, Weng YT (2003) Pseudo-dynamic experimental response of a full-scale CFT-BRB composite frame. In: Proceedings of joint NCREE/JRC workshop on international collaboration on earthquake disaster mitigation research, Taipei, Taiwan
19. Watanabe A, Hitomi Y, Saeki E, Wada A, Fujimoto M (1988) Properties of brace encased in buckling-restrained concrete and steel tube. In: Proceedings of ninth world conference on earthquake engineering, Tokyo, Japan

Bibliography

20. FEMA 356 (2000) Prestandard and commentary for the seismic rehabilitation of buildings. Federal Emergency Management Agency, Washington, DC

Effect of Brace Configurations on Seismic Behaviour of SCBFs

P.C. Ashwin Kumar and Dipti Ranjan Sahoo

Abstract Special concentrically braced frames (SCBFs) are used as lateral force-resisting systems in steel structures located in the high seismic areas to resist lateral loads through the vertical concentric truss system. Through yielding in tension and buckling in compression, conventional braces allow the system as a whole to have ample drift capacity to resist the lateral forces without any failure of gravity load-resisting members with maximum damages to brace itself. AISC 341-2010 allows the selection of a proper brace configuration for SCBFs, but does not distinguish their individual performance. The code categorizes all configurations under the same label and provides similar values of response reduction factor, over strength factor and deflection amplification factor. This is questionable as the response of each configuration with respect to brace behaviour and its effect on the beams and columns are different for different configurations. Four different, number of storeys (3, 6, 9 and 18) were chosen for this study. The design of the braced frames were done as per the code based requirements with checks included for maintaining the compactness and slenderness ratio within limits. Two dimensional frame models for non-linear static and dynamic analysis were created using the computer package SAP 2000 “as reported by CSI (Analysis reference manual for SAP 2000, 2009)” environment. Nonlinear dynamic analyses has been carried out for near-field as well as design basis ground motions. A selection criteria has been obtained for different brace configuration depending on the number of storeys of the building.

Keywords Special concentric • Braced • Nonlinear • Dynamic

P.C.A. Kumar (✉) · D.R. Sahoo
Department of Civil Engineering, Indian Institute of Technology Delhi (IITD),
New Delhi, India
e-mail: ashwin85pc@yahoo.co.in

D.R. Sahoo
e-mail: drsahoo@civil.iitd.ac.in

1 Introduction

Special concentrically braced frames (SCBFs) are used as lateral force-resisting systems in steel structures located in the high seismic areas to resist lateral loads through the vertical concentric truss system. This system if compared to other lateral load resisting system can be cheaper and easier to build if proper care is taken in designing and detailing. The braces act as fuses which dissipate the input seismic energy through axial deformations in tension and compression loading cycles. Thus, through yielding in tension and buckling in compression the braces allows the system as a whole to have ample drift capacity to resist the lateral forces without any failure of gravity load-resisting members. From past research it is known that there are several parameters, such as, brace slenderness ratio, width-to-thickness ratio, size and detailing of gusset plate, brace configurations, brace cross section shapes, material property, loading history, loading rate, material infill inside brace etc. that control the response of SCBFs under earthquake loading (e.g., 1–3).

AISC 341-2010 [4] code and previous studies [5] specifies the use of single-V, inverted-V, single-X and split-X to be used in case of SCBF system. The code allows the selection of a proper brace configuration for SCBFs, but does not distinguish their individual performance. The values of response reduction factor, over-strength factor and ductility for all brace configurations are kept the same in the present international code inspite of the fact that their response to earthquake is different from one another. Comparative study on the seismic performance of SCBFs with different brace configurations has been carried out by previous researchers [6]. In most of the past research focus on the seismic response of SCBFs were made for far-field earthquakes. It is expected that the behaviour of SCBFs under the near-field ground motions will be different from those under the far-field earthquakes because of the different ground motion characteristics, such as, higher peak-ground accelerations, restricted frequency content in the higher frequencies, and the nature of ground motion pulses. High period pulse-like loading on the braced frame can intensify the ratcheting effect in the brace behaviour. This may result in the concentration of damages in few floor levels leading to the complete failure of the structural system. Hence, further study is warranted to understand each configurations response to near-field earthquake. Also, the design of building for earthquake, given in codes, focuses on designing the buildings for design basis earthquakes. So, to check the adequacy of the design methods and to compare the response of different configurations of braced frame, the system will also be subjected to design basis earthquakes.

The present study is focused on the evaluation of seismic response of low-to-high rise SCBF systems with different brace configurations. The main objectives of this study are (i) to investigate the effect of brace configuration on failure mechanism, drift response and lateral strength of SCBF systems under the near-field as well as design basis earthquake ground motions, and (ii) to evaluate the suitability of code design provisions for SCBFs as lateral force-resisting systems in the buildings located in high seismicity zones.

2 Description of Study Frames

2.1 Building Geometry

The plan of the building considered in this study in which all the braced bays were located at the perimeter of the building is as shown in Fig. 1a. The remaining interior frames are assumed as gravity frames. The width of each bay was kept as 9.2 m. The typical storey height was kept as 3.66 m except the ground storey which was 4.6 m in height as shown in Fig. 1b. Four low-to-high rise frames, i.e., 3-, 6-, 9- and 18-storey were investigated in this study. It can be seen from the figure that the building is symmetrical, horizontally and vertically. This explains the inclusion of 18-storey into the study as this would not have been possible for a building having either horizontal or vertical irregularity. All building parameters were kept same except the number of storey levels which were changed in the respective cases. The superimposed dead load on each floor was assumed as 3.65 kPa. The magnitude of

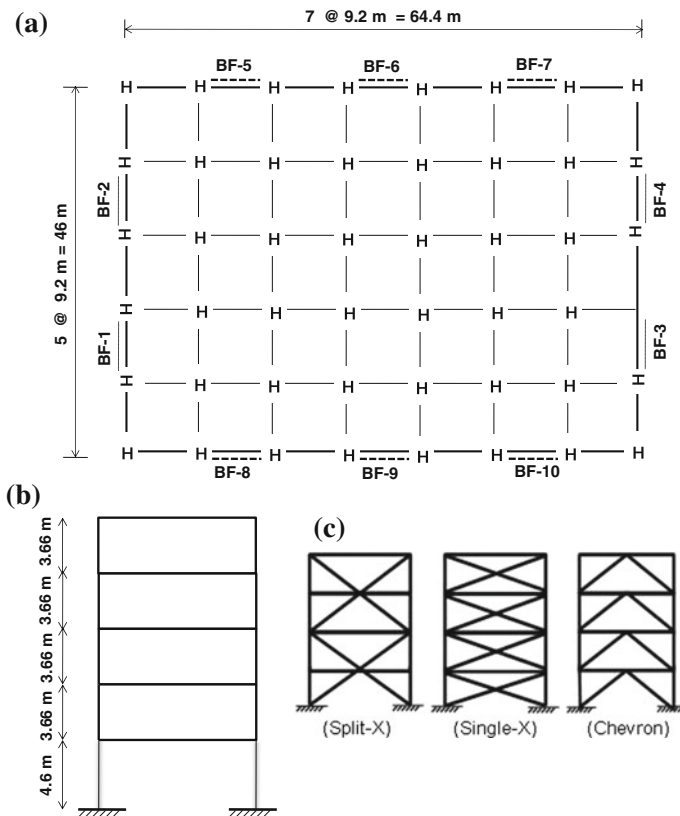


Fig. 1 a Building plan, b Elevation of 6-storey frame, c Brace configurations

live load on floor and roof levels was taken as 2.4 and 0.96 kPa, respectively. For the present study, the braced frame BF-2 was considered as the study frame. Three types of brace configurations, namely, Chevron, single-X, and split-X that was considered for this study is as shown in Fig. 1c.

2.2 Design of Study Frames

The designs of these braced frames were done based on the specifications given in ASCE 7-10 [7], AISC 341-2010 [4] and AISC 360-2010 [8]. Initially the base shear for the building was calculated using the parameters given in ASCE 7-10 [7] for the building geometry selected. Then with the storey forces the axial force magnitudes in the brace were found out for the basic seismic load combinations. Since for each floor there will be tension and compression for the braces, the compression force was chosen as the design value as for the chosen brace size the magnitude of tension capacity will be more than the demand. The opposite approach may result in a system with braces under designed for forces, basically the compression. The next phase of design involves the selection of beam and column sizes. The current code of practice suggests designing the beams and columns for two load conditions. First condition, assuming that the selected braces reaches their ultimate capacity in terms of compression and tension and second condition, when the brace reaches its ultimate capacity in tension and its post buckled capacity in compression. The post buckled state in compression leads to a capacity that is 0.3 times the initial buckling load capacity. In short the code assumes this system to form in all floor of the braced bay simultaneously. This may be true for low storeyed structure but may result in oversized stiff structure in case of taller buildings.

The design of beams has been done as a beam-column element as the braces transfer significant amount of axial load to the system. The columns have been designed for the axial load as well as the moment that is transferred from the beams. The demand versus capacity ratio of beams and columns have been kept above 0.9 for all floors but this approach needs to be further studied as for braced frames response the damage when initiated at a single floor continues to damage that floor continuously until failure occurs, leaving all other floors of braced frame partially unharmed. The frames were also checked for gravity load combinations since it is the priority or the objective of the design that all the damage is concentrated at the braces and no damage occurs to the gravity load resisting system. The value of response reduction factor (R) and over-strength factor (Ω) were considered as 5 and 2, respectively. It was assumed that A992 ($F_y = 345$ MPa) material was used for braces and A500 Gr-B42 ($F_y = 290$ MPa) was used for columns and beams in all the study frames. The design of beams in chevron configuration where an imbalance in load is produced during the post buckled stages of braces was given extra consideration during the design. The details of structural sections used in the study frames with different brace configurations are summarized in Table 1. In some cases built-up (BU) sections were used where the standard sections were not available or

Table 1 Design sections used in the study frames with different brace configurations

	Storey		Columns	Beams	18-storey	Chevron	Storey	Braces	Columns	Beams
	Braces	Beams								
3-storey	Chev.	3	HSS7.5 × 0.5	W10 × 45	W24 × 335		18	HSS6 × 6 × 0.625	W12 × 152	W27 × 368
		2	HSS9.625 × 0.5	W10 × 68	W24 × 335		17	HSS8 × 8 × 0.625	W12 × 152	W27 × 368
		1	HSS10.0 × 0.5	W12 × 120	W36 × 359		16	HSS10 × 10 × 0.625	W12 × 152	W27 × 368
	Spl-X	3	HSS8.75 × 0.375	W10 × 68	W24 × 306		15	HSS10 × 10 × 0.625	W12 × 152	W27 × 368
		2	HSS9.625 × 0.5	W10 × 112	W12 × 210		14	BU10 × 10 × 0.629	W12 × 210	W27 × 368
		1	HSS12.5 × 0.5	W12 × 96	W24 × 250		13	BU10 × 10 × 0.787	W12 × 305	W27 × 368
6-storey	Sin-X	3	HSS7.0 × 0.375	W10 × 68	W12 × 170	12	BU10 × 10 × 0.87	W14 × 370	W27 × 368	
		2	HSS8.75 × 0.375	W12 × 120	W12 × 170	11	BU10 × 10 × 0.98	W14 × 455	W27 × 368	
		1	HSS10.0 × 0.375	W12 × 152	W12 × 170	10	BU10 × 10 × 1.1	W14 × 550	W27 × 368	
	Chevron	6	HSS8.75 × 0.375	W10 × 88	W27 × 336	9	BU12 × 12 × 0.787	W14 × 665	W27 × 368	
		5	HS 10.75 × 0.5	W10 × 88	W27 × 336	8	BU12 × 12 × 0.87	W14 × 808	W27 × 368	
		4	HSS11.25 × 0.5	W12 × 96	W27 × 336	7	BU12 × 12 × 0.87	BU23.62 × 23.62 × 3.15	W27 × 368	
Split-X	3	HSS11.25 × 0.625	W12 × 170	W27 × 336	6	BU10 × 10 × 1.26	BU23.62 × 23.62 × 3.54	W27 × 368		
	2	HSS12.5 × 0.625	W12 × 230	W27 × 336	5	BU10 × 10 × 1.26	BU25.6 × 25.6 × 3.54	W27 × 368		
	1	BU12 × 12 × 0.629	W14 × 398	W21 × 201	4	BU10 × 10 × 1.26	BU27.6 × 27.6 × 3.54	W27 × 368		
	6	HSS8.75 × 0.375	W10 × 68	W12 × 120	3	BU10 × 10 × 1.26	BU29.53 × 29.53 × 3.54	W27 × 368		
	5	HSS10.75 × 0.5	W10 × 68	W12 × 120	2	BU10 × 10 × 1.26	BU31.5 × 31.5 × 3.54	W27 × 539		
	4	HSS11.25 × 0.625	W12 × 152	W12 × 120	1	BU12 × 12 × 0.87	BU43.3 × 43.3 × 3.93	W27 × 539		
Single-X	3	HSS12.5 × 0.625	W12 × 170	W12 × 120	Split-X	18	HSS6 × 6 × 0.625	W12 × 152	W12 × 210	
	2	BU10 × 10 × 0.629	W12 × 336	W12 × 120		17	HSS8 × 8 × 0.625	W12 × 152	W12 × 210	
	1	BU10 × 10 × 0.866	W14 × 342	W12 × 120		16	HSS10 × 10 × 0.625	W12 × 152	W12 × 210	
	6	HSS7.0 × 0.5	W10 × 68	W12 × 120		15	BU10 × 10 × 0.629	W12 × 152	W12 × 210	
	5	HSS10 × 0.375	W10 × 112	W12 × 120		14	BU10 × 10 × 0.787	W12 × 279	W12 × 210	
	4	HSS10.75 × 0.5	W12 × 210	W12 × 120		13	BU10 × 10 × 0.98	W12 × 305	W12 × 210	
3	HSS10.0 × 0.625	W12 × 252	W12 × 120	12	BU10 × 10 × 0.98	W14 × 455	W12 × 210			
2	HSS12.5 × 0.375	W14 × 500	W12 × 120	11	BU10 × 10 × 1.18	W14 × 455	W12 × 210			
1	HSS11.25 × 0.625	W14 × 500	W12 × 120	10	BU10 × 10 × 1.26	W14 × 665	W12 × 210			

(continued)

Table 1 (continued)

	Storey		Columns		Beams		Storey	Braces		Columns		Beams	
	9	8	W10 × 88	W27 × 368	W27 × 368	W27 × 368		BU12 × 12 × 0.87	W14 × 665	W12 × 210	W12 × 210		
Chevron	9	HSS7 × 7 × 0.5	W10 × 88	W27 × 368	W27 × 368	W27 × 368	BU12 × 12 × 0.87	W14 × 665	W12 × 210	W12 × 210			
	8	BU8 × 8 × 0.629	W10 × 100	W27 × 368	W27 × 368	W27 × 368	BU12 × 12 × 0.98	BU23.62 × 23.62 × 3.15	W12 × 210	W12 × 210			
	7	BU10 × 10 × 0.625	W10 × 112	W27 × 368	W27 × 368	W27 × 368	BU12 × 12 × 1.1	BU23.62 × 23.62 × 3.15	W12 × 210	W12 × 210			
	6	BU10 × 10 × 0.629	W12 × 170	W27 × 368	W27 × 368	W27 × 368	BU10 × 10 × 1.26	BU29.53 × 29.53 × 3.54	W12 × 210	W12 × 210			
	5	BU10 × 10 × 0.787	W12 × 252	W27 × 368	W27 × 368	W27 × 368	BU12 × 12 × 1.1	BU29.53 × 29.53 × 3.54	W12 × 210	W12 × 210			
	4	BU10 × 10 × 0.87	W12 × 336	W27 × 368	W27 × 368	W27 × 368	BU10 × 10 × 1.26	BU31.5 × 31.5 × 3.54	W12 × 210	W12 × 210			
	3	BU10 × 10 × 0.98	W14 × 426	W27 × 368	W27 × 368	W27 × 368	BU12 × 12 × 1.1	BU31.5 × 31.5 × 3.54	W12 × 210	W12 × 210			
	2	BU10 × 10 × 0.98	W14 × 550	W27 × 539	W27 × 539	W27 × 539	BU10 × 10 × 1.26	BU31.5 × 31.5 × 3.54	W12 × 210	W12 × 210			
	1	BU12 × 12 × 0.787	W14 × 808	W27 × 539	W27 × 539	W27 × 539	BU12 × 12 × 1.18	BU43.3 × 43.3 × 3.94	W12 × 210	W12 × 210			
	Split-X	9	BU10 × 10 × 0.98	W10 × 88	W12 × 210	W12 × 210	W12 × 210	HSS6 × 6 × 0.5	W12 × 136	W12 × 152	W12 × 152		
8		BU10 × 10 × 0.98	W10 × 100	W12 × 120	W12 × 120	W12 × 120	HSS7 × 7 × 0.5	W12 × 136	W12 × 152	W12 × 152			
7		BU10 × 10 × 0.98	W10 × 100	W12 × 210	W12 × 210	W12 × 210	HSS8 × 8 × 0.5	W12 × 136	W12 × 152	W12 × 152			
6		BU10 × 10 × 0.98	W12 × 252	W12 × 120	W12 × 120	W12 × 120	BU8 × 8 × 0.629	W12 × 170	W12 × 152	W12 × 152			
5		BU10 × 10 × 0.98	W12 × 252	W12 × 210	W12 × 210	W12 × 210	BU8 × 8 × 0.787	W12 × 279	W12 × 152	W12 × 152			
4		BU10 × 10 × 0.98	W14 × 426	W12 × 120	W12 × 120	W12 × 120	HSS10 × 10 × 0.625	W12 × 336	W12 × 152	W12 × 152			
3		BU10 × 10 × 0.98	W14 × 455	W12 × 210	W12 × 210	W12 × 210	BU8 × 8 × 0.98	W14 × 455	W12 × 152	W12 × 152			
2		BU10 × 10 × 0.98	W14 × 730	W12 × 120	W12 × 120	W12 × 120	BU10 × 10 × 0.709	W14 × 500	W12 × 152	W12 × 152			
1		BU12 × 12 × 0.79	W14 × 808	W12 × 210	W12 × 210	W12 × 210	BU10 × 10 × 0.787	W14 × 665	W12 × 152	W12 × 152			
Single-X		9	HSS7.0 × 0.5	W10 × 88	W12 × 106	W12 × 106	W12 × 106	BU10 × 10 × 0.787	W14 × 730	W12 × 152	W12 × 152		
	8	HSS9.625 × 0.5	W10 × 100	W12 × 106	W12 × 106	W12 × 106	BU10 × 10 × 0.87	BU23.62 × 23.62 × 3.15	W12 × 152	W12 × 152			
	7	HSS11.25 × 0.5	W12 × 210	W12 × 106	W12 × 106	W12 × 106	BU10 × 10 × 0.87	BU23.62 × 23.62 × 3.15	W12 × 152	W12 × 152			
	6	HSS12.5 × 0.5	W12 × 210	W12 × 106	W12 × 106	W12 × 106	BU10 × 10 × 0.98	BU29.53 × 29.53 × 3.54	W12 × 152	W12 × 152			
	5	HSS12.5 × 0.625	W12 × 305	W12 × 106	W12 × 106	W12 × 106	BU10 × 10 × 0.98	BU29.53 × 29.53 × 3.54	W12 × 152	W12 × 152			
	4	BU8 × 8 × 0.98	W14 × 398	W12 × 106	W12 × 106	W12 × 106	BU10 × 10 × 0.98	BU31.5 × 31.5 × 3.54	W12 × 152	W12 × 152			
	3	BU10 × 10 × 0.71	W14 × 455	W12 × 106	W12 × 106	W12 × 106	BU10 × 10 × 0.98	BU31.5 × 31.5 × 3.54	W12 × 152	W12 × 152			
	2	BU10 × 10 × 0.71	W14 × 730	W12 × 106	W12 × 106	W12 × 106	BU10 × 10 × 0.98	BU31.5 × 31.5 × 3.54	W12 × 152	W12 × 152			
	1	BU10 × 10 × 0.71	BU27.5 × 27.5 × 3	W12 × 106	W12 × 106	W12 × 106	BU10 × 10 × 0.98	BU47.24 × 47.24 × 3.94	W12 × 152	W12 × 152			

Note HSS Hollow Steel Section; BU Built-up section

for cost-effectiveness. Although the same structural sections have been used in few consecutive floors along the height, the sections were chosen based on the design requirements at the floor levels. Also for each section chosen the sectional properties like slenderness ratio and width to thickness ratio were checked to be complying with the codal provisions.

2.3 Modelling of Study Frames

Two-dimensional (2-D) models of all the present frames were modeled in SAP 2000 [9]. Beams, columns and braces were modelled as the frame elements. The support conditions for the columns were considered as fixed at their bases. The braces were modelled as having hinges at their ends. All beam-to-column connections were assumed as pinned in case of all the study frames. The rigid end zones at the beam-column connections were not explicitly modelled in this study. It needs to be mentioned that in real structures even if the beam column joint is designed as a pin connection then also due to the presence of gusset plate the beam gets additional rotational restraint. It has been observed in experiments done by previous researches that even after the brace undergoes fracture the gusset plate then also provides a diminished yet a significant amount of rigidity to the beam-column joint. P-delta effects due to gravity loads on the building were considered in the analysis. Since the past studies [6] showed that the floor mass have a significant effect on the dynamic response of the braced frames, the tributary floor mass at each floor level was also included in the analytical models. Nonlinear behaviour of the frame members was modelled by assigning the lumped plastic hinges at the potential hinge locations. The plastic hinge properties used for the modelling of inelastic properties of braces and frame members is as shown in Fig. 2. The plastic hinge parameters for the brace have been adopted from the results obtained from the parametric study of braces and also from past experimental studies. These values will vary for braces with different slenderness ratio and width to thickness ratio.

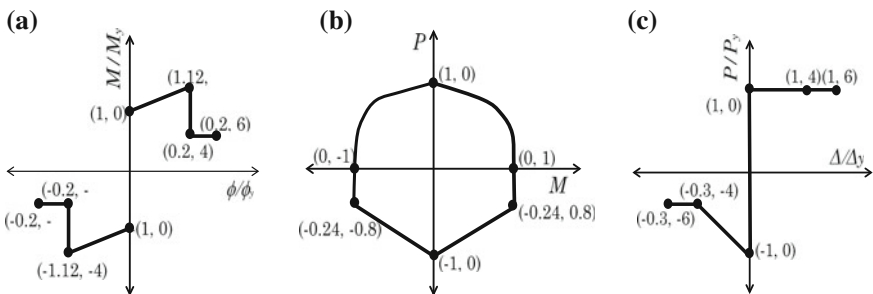


Fig. 2 a Nonlinear moment-rotation hinge, b P - M interaction hinge, c Force-displacement hinge of braces

Kinematic hardening was assumed for all elements. FEMA 356 [10] provisions were used for inputting various parameters of the moment-rotation plastic hinges adopted for this study. Since the presence of axial load reduces the plastic moment capacity of members, axial force-bending moment ($P-M$) interaction behaviour was included in the modelling. Twenty SAC ground motions representing near-field behaviour (i.e., NF01-20) and twenty more representing the design basis earthquake motion (i.e., LA01-20) [11] were considered for the nonlinear dynamic analysis in this study. Since the building locations and parameters have been based on Los Angeles, the ground motions selected for the analysis needs no further scaling.

3 Results

3.1 Nonlinear Static Analysis

To determine the lateral strength and failure mechanism of the study frames with different brace configurations push over analysis was carried out. Figure 3 shows the comparison of the capacity curves of the study frames up to 5 % storey drift

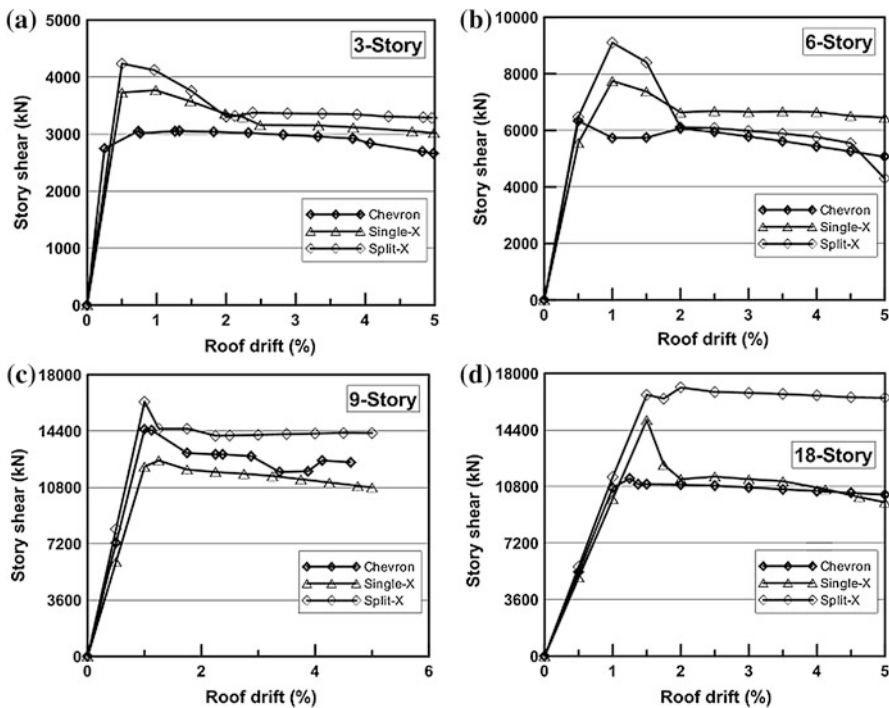


Fig. 3 Comparison of pushover curves: a 3-storey; b 6-storey; c 9-storey; d 18-storey

level, which can be considered as the maximum storey drift to be expected out of SCBF which gives perfect response. The split-X configuration had the highest lateral strength in comparison to all other configurations. Except the 9-storey frame results, the single-X configuration showed the next best performance in terms of lateral strength. The post-peak lateral strength behaviour of the braced frame showed that the split-X configuration showed deterioration in the lateral strength after reaching the peak value. However, for the 18-storey, there was no drop down and the structure attained a stable residual lateral strength in the post peak scenario. Even though there was a drop in the residual strength of the split-X configuration, the lateral strength value attained by the frame was comparable with the other two configurations for all storey heights. The performance of study frames with Chevron and single-X were not as conclusive as split-X configuration but varied with the frame height. The post-peak strength of Chevron configuration was stable for the 3- and 18-storey frames, whereas the single-X configuration showed relatively a better performance for the 6- and 9-storey frames.

The response of the structure in terms of the formation of hinges showed a similar trend for all three configurations. The onset of hinging started with the brace yielding followed by the yielding of columns. As the drift value was increased, the stresses in the braces started increasing and reached the ultimate values at few locations along the height of the structure. For the case of Chevron configuration, the yielding was observed in the case of beams. This was expected as the post-buckled stage of the brace resulted in the development of substantial unbalanced forces in the beams. In the case of 9- and 18-storey frames, the column or beam reaching their ultimate values was followed right after the brace reached its rupture strength. It was also seen that the brace reached its rupture value soon after the columns yielded. This was typical for 18-storey but this may also be related to the section sizes that were selected for this study. Also, a common feature noted was that for higher storeys as soon as the braces reached it ultimate value at any floor the rest of the damages or deformations were concentrated near that floor only. This is one of the drawbacks of using concentric braced frame i.e. there is concentration of damages and not a distribution or sharing of damages by the entire frame.

3.2 Nonlinear Dynamic Analysis for Design Basis Earthquake

Inter-storey drift ratio (IDR) at all storey level of the study frames was computed under the selected design basis ground motions. The mean (μ) and mean (μ) + standard deviation (σ) values of peak IDR response of the study frames are depicted in Fig. 4. The maximum values of mean (50th percentile) IDR were close to 1.5 % in all study frames, whereas the maximum value of ($\mu + \sigma$) IDR were 3 % for 18-storey, 3.5 % for the 6- and 9-storey, 4 % for 3-storey, respectively. The distribution of IDR response of the 3-, 6- and 9-storey was nearly uniform over their

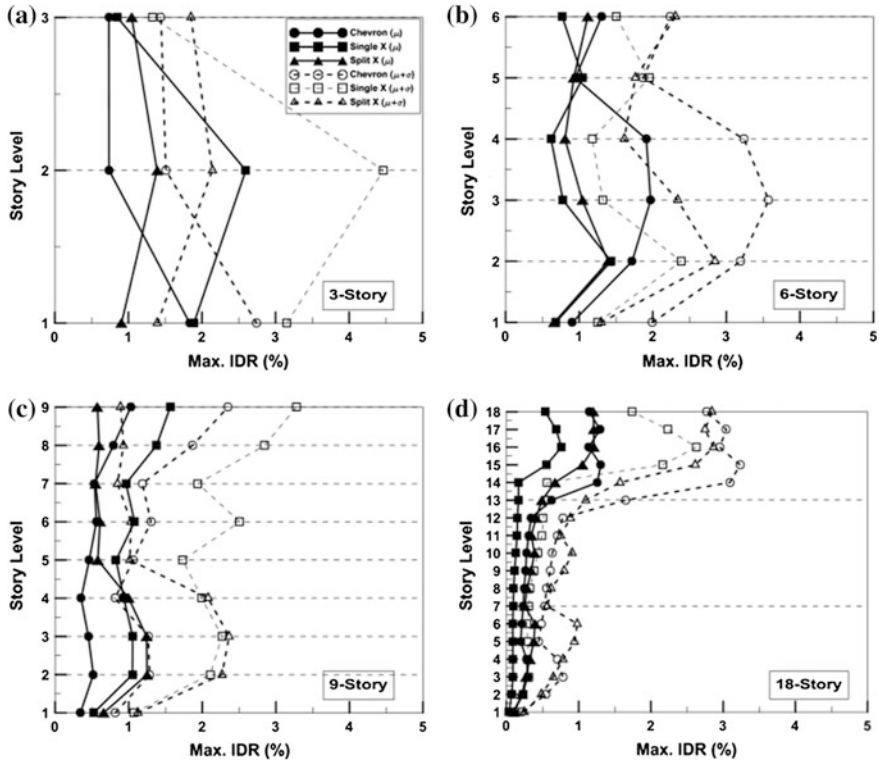


Fig. 4 Comparison of inter-storey drift response: a 3-story; b 6-story; c 9-story; d 18-story

heights. However, the larger IDR response was noted at the upper storey levels of the 18-storey as compared to the lower storey levels indicating that the column at the lower storey levels were little overdesigned. The reason for this over strength can be explained by understanding the current procedure of designing beams and columns in SCBFs, wherein, the code assumes mechanism in the brace to be formed in all storeys of the structure simultaneously. The mechanism here is the design procedure explained earlier, where two conditions of brace loadings are assumed for the design of beams and columns. It is worth mentioning that the member sizes used in the analysis satisfies the slenderness ratio as well the compactness ratio as specified in the codes. Results of 18-storey frame showed that the brace yielding was concentrated only at the top floors. Further, the analysis also showed that, in most cases, the upper level storeys showed higher drift response than the lower storeys. This may be attributed to the varied column sections along the height of the frames and also the beam-column connection which was kept as a simple shear connection thus reducing the stiffness of the structure. Although the response of all brace configurations showed comparable mean IDR response, it should be noted that in all cases complete collapse of the frames was noted during

Table 2 Instances of failures for different brace configurations

Storey	Instances of structural failure		
	Chevron	Split-X	Single-X
3	2	2	8
6	3	8	6
9	11	3	7
18	5	4	9

the analysis resulting in excessive IDR. Those ground motions were not considered in averaging the drift response.

The results of time history-analysis showed the complete collapse of the study frames for different configurations has been summarized in Table 2. It was noticed that except for the 9-storey Chevron and 6-storey split-X, both configurations showed better survivability under design basis earthquake. The single-X configuration underwent significant amount of failures under each storey level. The split-X configuration showed better response for 18-storey braced frame. This vindicates the response of present builders to adopt split-X configuration as it gives added advantage that it transfers forces from two floors, thus giving additional strength and redundancy.

These failures to different frames can also be attributed to the connection arrangement employed for the beam-column in this study. Even though the single-X configuration has lower material consumption as compared to other configuration, the number of failures showed its inadequacy to resist severe ground motions. Hence, the single-X brace configuration should be avoided in the mid-rise braced.

3.3 Nonlinear Dynamic Analysis for Near Field Earthquake

Similar to the study done for the design basis earthquake motion the Inter-storey drift ratio (IDR) at all storey level of the study frames was computed under the selected near-field ground motions. Figure 5 depicts the mean (μ) and mean (μ) + standard deviation (σ) values of peak IDR response of the study frames. The maximum values of mean (50th percentile) IDR were close to 2 % in all study frames, whereas the maximum value of ($\mu + \sigma$ IDR were 3 % for the 3- and 9-storey, and 4 % for 6- and 18-storey, respectively. The distribution of IDR response of the 3-, 6- and 9-storey was nearly uniform over their heights as was the case with the earlier study. The member sizes were kept same for all the studies in this paper so the response of 18-storey showed similar trait that all the inelastic response were concentrated in the upper storey, leaving all the below frame members intact. Although the response of all brace configurations showed comparable mean IDR response, it should be noted that in all cases complete collapse of the frames was noted during the analysis resulting in excessive IDR. Those ground motions were not considered in averaging the drift response.

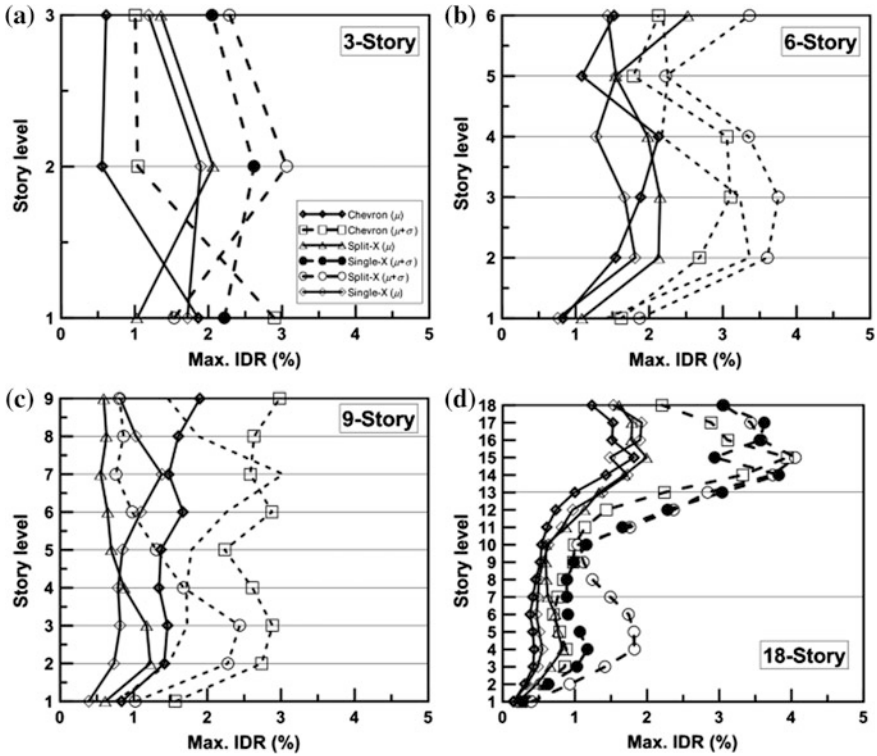


Fig. 5 Comparison of inter-storey drift response: a 3-storey; b 6-storey; c 9-storey; d 18-storey

The results of time history-analysis showed the complete collapse of the study frames for different configurations has been summarized in Table 3. It was noticed that in the 6- and 9-storey frames having single-X configurations, 50 % frames did not survive selected ground motions. However, in the case of 3- and 18-storey frame, the number of instances of collapse was relatively small as compared to the other frames considered in this study. In case of single-X brace configurations, the plastic hinges were formed at the mid-length of braces and the damage continued to develop in that brace leaving the other length of the brace nearly ineffective.

Table 3 Instances of failures for different brace configurations

Storey	Instances of structural failure		
	Chevron	Split-X	Single-X
3	3	4	5
6	5	8	10
9	6	8	11
18	5	2	4

The single-X configuration again showed poor performance, reiterating the fact that it should be avoided in special concentric braced frame unless proper investigation is done to improve the performance of single-X. It has to be asserted here that the selection of member sizes as well as the connection arrangement plays an important role in the response of the structure towards strong ground motions. This analysis also shows the inadequacy of the application of amplified seismic load combinations for designing beams and columns. The code specifications directs the design in such a way that the formation of plastic hinges is assumed to be formed at all storey levels simultaneously, this is contradictory to the analysis findings where the formation of hinges in the braces was limited to certain floors especially for high rise frames. This necessitates the use of applying performance based design concepts for ensuring predictable structural performance.

4 Conclusions

The following conclusions can be drawn from the present study:

- Single-X brace configuration should be avoided in the mid-rise braced frames, designed as per the code provisions in order to achieve better seismic performance under design basis and near-field ground motions.
- The design of high-rise braced frame as per the current code provisions resulted in oversized sections as columns at the lower storey levels. However, this margin of safety effectively helped in reducing the probability of complete collapse of the frames for both type of ground motions considered.
- Chevron brace configuration performed better as compared to the X-brace configurations in low-to-medium rise building frames, whereas in the case of the high-rise frame, the behaviour of split-X brace configuration was better for both type of ground motions considered.
- The lateral strength of braced frames was improved with the split-X brace configurations with better post-peak residual strength response as compared to other brace configurations.

References

1. Tang X, Goel S (1989) Brace fractures and analysis of phase I structure. *ASCE J Struct Eng* 115(8):1960–1976
2. Uriz P, Filippou FC, Mahin SA (2008) Model for cyclic inelastic buckling of steel braces. *ASCE J Struct Eng* 134(4):619–628
3. Roeder CW, Lehman DE, Clark K, Powell J, Yoo JH, Tsai KC, Lin CH, Wei CY (2010) Influence of gusset plate connections and braces on the seismic performance of X-braced frames. *Earthq Eng Struct Dynam* 40(4):355–374

4. ANSI/AISC 341-05 (2005) Seismic provisions for structural steel buildings. American Institute of Steel Construction, Chicago
5. Bruneau M, Uang CM, Sabeli (2011) Ductile design of steel structures, 2nd edn. McGraw Hill, New York
6. Khatib F, Mahin SA, Pister KS (1988) Seismic behavior of concentrically braced steel frames, Report No. UCB/EERC-88/01, Earthquake Engineering Research Center, Berkeley, CA
7. ASCE/SEI 7-10 (2010) Minimum design loads for buildings and other structures. American Society of Civil Engineers, VA.
8. ANSI/AISC 360-05 (2005) Specifications for structural steel buildings. American Institute of Steel Construction, Chicago
9. CSI (2009) Analysis reference manual for SAP 2000. Computers and Structures Inc, Berkeley, CA
10. FEMA 356 (2000) Prestandard and commentary for the seismic rehabilitation of buildings. Federal Emergency Management Agency, Washington, DC
11. Somerville PG, Smith M, Punyamurthula S, Sun J (1997) Development of ground motion time histories for phase 2 of the FEMA/SAC Steel Project, Report No. SAC/BD-97/04, Sacramento, CA

Seismic Response of Moment Resisting Frame with Open Ground Storey Designed as per Code Provisions

Subzar Ahmad Bhat, Saraswati Setia and V.K. Sehgal

Abstract Urbanization, functional requirements and paucity of space have led to multi-storey building having open ground storey. During the past earthquakes, open ground storey buildings have performed poorly due to the soft storey defect. Indian Standard 1893 Part 1 (Indian standard criteria for earthquake resistant design of structures, 2002) allows analysis of open ground storey buildings without considering infill stiffness but with a multiplication factor (MF) 2.5 in compensation for the stiffness discontinuity. The aim of this study is to check the applicability of the multiplication factor of 2.5 and study the behaviour and response of the structure. Investigations were carried on reference bare frame model without considering infill stiffness as suggested by IS 1893 (Indian standard criteria for earthquake resistant design of structures) using SAP 2000 (Version 14.0) by linear static analysis and response spectrum analysis. Total seven models were analysed and designed with multiplication factor ranging from 1.0 to 2.5. From the results, it is observed that the value of MF equal to 2.5 has been found on the higher side, resulting in increased dimension and percentage of reinforcement of ground storey columns without significant enhancement beyond a certain MF. The best possible rectification measure, when the stiffness of the infill is not considered, is to multiply the ground storey columns by 1.25 factor instead of codal value of 2.5. Using higher values of MF results in the introduction of soft storey effect in the upper storey.

Keywords Infill stiffness · Open ground storey · Response spectrum analysis · Stiffness irregularities · Soft storey effect

S.A. Bhat (✉)
GLA University Mathura, Mathura, UP, India
e-mail: subzarbhat@gmail.com

S. Setia · V.K. Sehgal
NIT Kurukshetra, Kurukshetra, Haryana, India

1 Introduction

Due to the availability of less space for the construction purposes in the developing countries, buildings are used for various purposes such as car parking, reception lobbies etc. Mostly, these buildings are irregular with different types of irregularity, such as plan irregularity, vertical irregularity etc. Among all the irregularities of the buildings, most vulnerable case is one having stiffness irregularity as observed during the past earthquakes. In some buildings, the ground storey is kept open, i.e. in the ground storey, there are no infills; instead having only columns. This type of construction is always vulnerable to the collapse during earthquake. Such type of open ground storey buildings in which stiffness of the ground storey is less the 70 % of the storey above are called soft storey buildings.

Buildings with open ground storey have performed poorly during the recent earthquake throughout the world. For example, during the 1999 Turkey, 1999 Taiwan, 2001 Bhuj, India, 2005 Jammu and Kashmir, India and 2003 Algeria earthquakes, maximum damaged buildings were found to have open ground storey. During earthquakes, such type of buildings behave as an inverted pendulum, as the upper portion of the building acts as a rigid mass and hence moves together as a single mass and the ground storey columns act as the pendulum rod. All the displacements are concentrated in the open ground storey columns alone, therefore causing large damage in the columns of the open ground storey during an earthquake. Soft storeys can also occur in the intermediate storeys of a building, and cause damage and collapse in those storeys too.

The seismic force experienced by the open ground storey buildings is distributed in accordance to the distribution of stiffness and mass along the height. As the buildings with open ground storey are having stiff upper storey, so there is small inter-storey drift in the upper storeys as compared to the open ground storey. Due to the large inter-storey drift in the ground storey, the strength demands of the columns in open ground storey moment resisting frame buildings are also large, as the shear in the first storey is maximum. For the upper storeys due to the uneven distribution of the stiffness along the height, columns forces are effectively reduced.

In the aftermath of the earthquake in Jabalpur, India, the vulnerability of open ground storey building to failure under seismic loads was experienced. The buildings which got badly damaged were partially open ground storey buildings having open ground storey on one side for parking, and brick infill walls on the other side. The maximum damage was caused in the columns of the open ground storey. Spalling of concrete cover, snapping of lateral ties, buckling of longitudinal reinforcement bars and crushing of core concrete took place in the columns of open ground storey columns [1]. After the collapses of open ground storey buildings in 2001 Bhuj, India earthquake, the Indian seismic code IS 1893 Part 1 [4] has included special design provisions related to soft storey buildings. As per the IS 1893 Part1 [4] clause 7.10.3, the forces in the columns, beams and shear walls under the action of seismic loads specified in the code, may be obtained by considering the bare frame building. After carrying out the earthquake analysis,

neglecting the effect of infill walls in other storeys; beams and columns in the open ground storey are required to be designed for 2.5 times the forces obtained from this bare frame analysis. These recommendations have met with some resistance in design and construction practice, due to the need for heavy reinforcement in ground storey columns, leading to congestion. Hence, the aim of this paper is to check the applicability of the multiplication factor of 2.5 in the ground storey beams and column when the building is to be designed as open ground storey framed building.

2 Past Studies

From the past earthquakes, it is observed that the soft storey irregularity is one of the main reasons of the building damage due to earthquakes. The open ground storey irregularity can't be eliminated, but some alternative measure can be adopted to compensate the situation. Arlekar et al. [1] adopted alternative measures to cater this problem by (i) provision of stiffer columns in the first storey, and (ii) provision of a concrete service core in the building. The former was found to be effective only in reducing the lateral drift demand on the first storey columns. However, the latter was found to be effective in reducing the drift as well as the strength demands on the first storey columns. The similar research was done by Dande and Kodag [2], in which strength and stiffness to the building frame was provided by modified soft storey provision in two ways, (i) by providing stiff column and (ii) by providing adjacent infill wall panel at each corner of building frame. Also, study has been carried out to compare modified soft storey provisions with complete infill wall frame and bare frame models. At the end it was concluded that the possible solution to cater this problem is in (a) increasing the stiffness of the first storey; (b) provide adequate lateral strength in the first storey. This was possible only by providing stiff column at open ground storey model or by providing adjacent infill wall provided at each corner of soft storey building model. This problem was also analyzed by Kaushaik et al. [7] by various strengthening options such as providing additional columns, diagonal bracings, and lateral buttresses for masonry infilled reinforced concrete frame buildings with an open ground storey. The strengthening schemes recommended in a few national codes were found to be ineffective in improving the lateral deformability of such frames because of the use of predetermined multiplying factors for increasing the lateral strength. In addition, it was observed that beams in the open first storey are not required to be designed for higher forces. Primary conclusion of the study was that the lateral load performance of the open first-storey RC frames cannot be improved by using code-specified strengthening schemes, i.e. by designing the first-storey members for higher forces; and the performance of such frames can be significantly improved by providing additional columns and lateral buttresses in the open first storey. Lamb and Londhe [8] carried out study on multi-storeyed buildings with soft first storey, located in seismic zone IV. Finally it was concluded that shear walls and cross bracings were very effective in reducing the stiffness irregularity and bending moment in the columns. Higher sizes of columns

are effective in reducing the drift, but it increases the shear force and bending moment in the first storey. Lightweight infill was found to be very effective in reducing the stiffness irregularity and storey drift. Saraswati and Vineet [10] carried out research on the influence of displacement, inter storey drift and storey shear on the behavior of a building with soft storey. In that study it was concluded that lateral displacement is largest in bare frame with soft storey defect both for earthquake force in x direction as well as in y direction for corner columns as well as for intermediate columns. In case of intermediate columns, displacement was minimum in buildings having masonry infill in upper floors and with increased column stiffness of bottom storey in comparison to the building with shear wall in x direction as well as in y direction. However, building with masonry infill in upper floors only showed a sudden change in slope of displacement in x direction as well as in y direction.

Design codes address this issue by permitting simplified analysis of soft storey buildings. Linear analysis of the 'bare frame' is allowed, but the storey shear and moments of the open ground storey need to be magnified by specified factors in design. For example, IS 1983 Part 1 [4] recommends a magnification factor of 2.5 to be applied on bending moments and shear forces calculated for the bare frame under seismic loads. The conservative nature of these empirical recommendations was first carried by Kanitkar and Kanitkar [6]. It was concluded that the existing provisions of IS 1983 Part 1 [4] appear inadequate to completely define the design parameters of buildings with soft storey although a scale factor of 2.5 is specified for moments and shears in the open storey members. It was also concluded that current code provisions do not account for the increase in column axial forces. Subramanian [11] concluded that the clause 7.10.3 (a) and (b) of IS 1893 Part 1 [4] were chosen arbitrarily without any scientific investigations. Davis et al. [3] attempted to estimate typical variations in multiplication factor. The results from response spectrum analysis indicated that multiplication factor values were in the range 1.04–1.13, for the four storied building and 1.11–2.39 for the seven storied building. However, the results of nonlinear dynamic analysis including hysteresis effects in frame and infill, suggest that there was no need for applying multiplication factor to low-rise building frames. In the case of the seven storied building frame, values of multiplication factor in the range 1.14–1.29 were observed, applicable to the base shear. However, this was not applicable to column bending moments, where multiplication factor values were found to be less than unity. Also, it was concluded by them that when large openings are present and thickness of infills are less, there is a reduction in multiplication factor.

In all the above literatures, open ground storey (OGS) buildings were strengthened by using various provisions, and also none of the literature talks about the effect of the multiplication factor on the seismic behavior of the structure. In this paper, the moment resisting frame with open ground storey is analyzed and designed for different ranges of multiplication factor without considering the infill stiffness. Then these models are analyzed to study the behavior of the structure in terms of displacement, storey drift and stiffness.

3 Analytical Modelling

During the analytical model development, various factors are taken into consideration. The most important factor, which was considered, is the representation of the building stock of India by the models that are considered. In present study, the soft storey effect was introduced by increasing the height of the storey and also keeping the ground storey open. In order to consider this, five storied (ground + four) structure with five bays in both directions is modelled. The span length for the bays in x direction was chosen as 5 and 3 m in y direction for both the models. The storey height in the models is chosen as 3.1 m for all the storeys except the ground storey, which is kept as 4.8 m. Figure 1 shows the plan and elevation of a typical structure considered in this study. The thickness of the external and internal wall is kept as 230 and 150 mm, respectively. The thickness of the slab is taken as 150 mm for all slabs. The height of the parapet wall is taken as 1.5 m. The structure is considered to be located in the zone V with medium soil conditions. The importance factor is taken as 1. The intensity of live load is taken as 3 and 1.5 kN/m² for all floors and roof, respectively. The intensity of the floor finish and roof treatment are taken as 1 and 1.5 kN/m² for all floors and roof respectively.

The load from the walls is distributed as uniformly distributed load and from the slab the load is distributed on the beams of the respective storeys as trapezoidal and triangular loads. The bare frame is considered for the model. In order to study the behaviour of the open ground storey building designed as per IS 1983 Part 1 [4], seven models are analysed and designed for range of multiplication factor.

Only the ground storey columns are designed for the multiplication factor as prescribed by the IS 1983 Part 1 [4]. In the design process the percentage of reinforcement and column dimensions are taken as variables.

To model and simulate the structure in geometry and behaviour, the modelled structure is taken as close to the real one as possible. Modelling is done in such a way that there is ideal distribution of mass, stiffness and strength of the structure. Different materials are used in the structural modelling. The grade of concrete and reinforcement used in the study of the models is taken as M 25 and Fe 415. The elastic properties of these materials are taken as the per the IS 456: [5]. As per clause 6.3.2.1 of the IS 456: [5] the modulus of elasticity of concrete is taken as $E_c = 5,000\sqrt{f_{ck}}$ N/mm² where, f_{ck} is the characteristic compressive strength of the concrete in N/mm² at 28 days. For present study, value of f_{ck} is 25. For the reinforcement, the yield stress (f_y) and modulus of elasticity (E_s) is taken as per IS 456: [5]. The material chosen for infill walls is masonry having compressive strength (f'_m) equal to 1.5 N/mm² and modulus of elasticity is taken equal to $E_m = 550f'_m$ as taken by Kaushaik et al. [7].

The beams as well as columns of the frames are modelled by 3D frame elements. All the beam-column joints are assumed to be rigid. Using [9] the beams and columns in the present study are modelled as frame elements with the centre lines joined at nodes. For the integral action of the floor slabs, all the slabs are

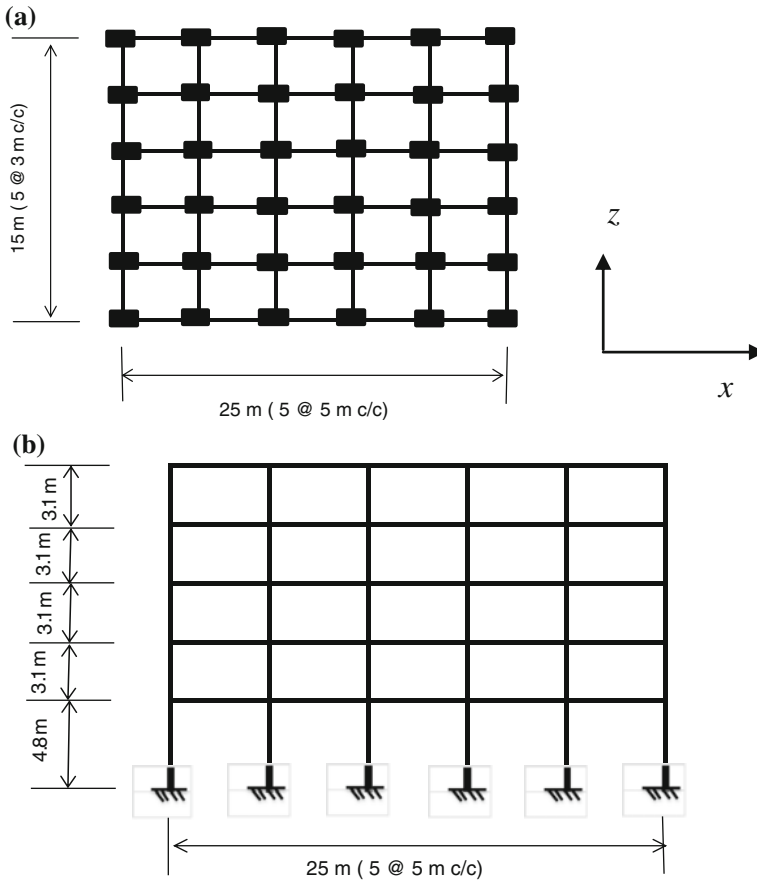


Fig. 1 Plan and the elevation of the structure. **a** Plan, **b** elevation

modelled as diaphragms. The selected structural models are assumed to be founded on the raft foundation. So all the supports of the structural are taken as fixed. Infill walls are usually considered as non-structural elements. Each model in this study is named according to the frame type and multiplication factor (MF). Model name BF 2.25 refers to the model in which bare frame is considered and 2.25 refers to the multiplication factor considered for the design of the columns of the open ground storey. The detailed nomenclature for the frame models considered is as given in Table 1.

4 Results from the Analysis

To investigate the response and behaviour of a MRF with soft storey defect, it is designed and analysed as per the IS code 1893 Part 1 [4]. The column size, stiffness and percentage of the reinforcement in the columns are the parameters

Table 1 Showing nomenclature of the different models

Bare frame reference	BF 1.0
Bare frame designed for the MF 1.25	BF 1.25
Bare frame designed for the MF 1.5	BF 1.5
Bare frame designed for the MF 1.75	BF 1.75
Bare frame designed for the MF 2.0	BF 2.0
Bare frame designed for the MF 2.25	BF 2.25
Bare frame designed for the MF 2.5	BF 2.5

for the evaluation. The parameters which are discussed include displacement, storey drift, time period and stiffness. In the analysis of the models, various load combinations are considered as given by IS 1893 Part 1 [4] clause 6.3.1.2. The most severe case was found to be 0.9 D.L. \pm 1.5 E.L. Equivalent static analysis and response spectrum analysis of these seven OGS MRF models are carried out to evaluate the effect and applicability of MF, which is applied to the OGS columns. Following sections presents the results obtained from these analyses.

4.1 Fundamental Time Period

The fundamental time period in both transverse and longitudinal direction being same for the models is given in Table 2. From Table 2 we can see that the periods calculated from the codal provisions are much less than those computed from [9]. For frame model BF 1.0 period of vibration is more as compared to other models, this is because of the stiffness. The stiffness of the frame BF 1.0 is much smaller than the other models. For the models BF 1.25, BF 1.5, BF 1.75, BF 2.0, BF 2.25 and BF 2.5, there is not much difference in the period of the vibration. For the model BF 1.5, percentage decrease in time period is 4.28 %. For the models designed for higher values of MF, maximum percentage reduction is 7.75 % only. Otherwise, there is large difference in the stiffness, cross-sectional area and the percentage of the reinforcement in the columns of the model BF 2.5 and BF 1.5.

Table 2 Time period of different bare frame models

Model	Period of vibration (seconds)	
	SAP 2000	Codal
BF 1.0	0.98	0.633
BF 1.25	0.97	0.633
BF 1.5	0.938	0.633
BF 1.75	0.934	0.633
BF 2.0	0.931	0.633
BF 2.25	0.909	0.633
BF 2.5	0.904	0.633

Table 4 displacement of bare frame models in y (or z) direction

Storey		Displacement in y direction (mm)						
Storey level	Storey no.	BF 1.0	BF 1.25	BF 1.5	BF 1.75	BF 2	BF 2.25	BF 2.5
Roof level	5	40.53	38.75	38.63	39.73	38.38	37.49	37.36
4th floor	4	37.56	35.85	35.56	36.71	35.29	34.34	34.19
3rd floor	3	31.42	29.77	29.13	30.38	28.82	27.73	27.54
2nd floor	2	22.28	20.98	19.86	21.23	19.49	18.25	18.00
First floor	1	10.89	9.95	8.41	9.78	8.02	6.77	6.49
Ground floor	0	0.00	0.00	0.00	0.00	0.00	0.00	0.00

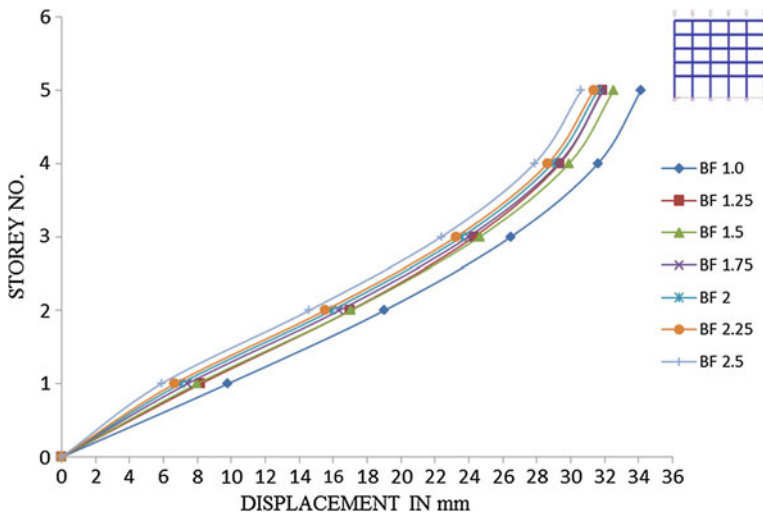


Fig. 3 Comparative graph of the displacement in x direction for bare frame models

model BF 2.5. The reason being the stiffness of the ground storey of the model BF 2.5 is very large compared to model BF 1.0. As the displacement is maximum for the model BF 1.0, the inter storey drift demand is also large. For the model BF 1.25, it is observed from the displacement profile that the percentage reduction in the displacement is 6.65 %. However this reduction in the displacement is achieved by increasing the stiffness and the area of cross section of the ground storey column for model BF 1.25 by 29 and 9 % respectively and keeping percentage of reinforcement same. For the model BF 1.5 the stiffness and area of cross section of the ground storey column is increased by 44.25 and 21.2 % and the percentage of reinforcement is kept same, reduction in the displacement is found to be 4.76 % only. For the models which are designed for the higher values of the MF, there is not much significant change in the displacement. For the model BF 2.5 the stiffness, area of

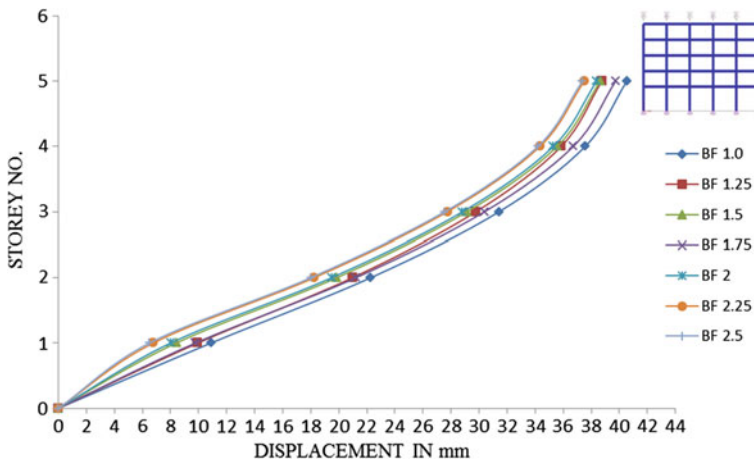


Fig. 4 Comparative graph showing the displacement in y direction for bare frame models

the ground storey column and percentage reinforcement is increased by 151, 55.5 and 66.67 % respectively and corresponding to this change the percentage decrease in the displacement is equal to 10.34 % only. Thus, it can be observed that when the stiffness is increased from 29 to 151 % and area of cross section is increased from 9 to 55.5 %, percentage decrease in the displacement is only 5.8 %. Thus, it is seen that by increasing the stiffness and the area of the cross section of the ground storey column above 29 and 9 % there is small decrease in the displacement values, which can be seen from Fig. 5. From the above results it is seen that the models which are designed for MF above 1.25, shows smaller decrease in displacement as compared to the increase in the stiffness and area of the column. Thus, model BF 1.25 gives the best results as compared to other models. That means there is no need to design the OGS columns for 2.5 MF, instead we can use 1.25 MF.

Figure 4 shows displacement graphs plotted for various bare frame models in y direction. The displacement in y direction is showing the same trend as is shown along x direction, only difference is in the percentage.

4.3 Storey Drift

The storey drift along x and y direction is shown in Tables 5 and 6, respectively.

From Figs. 5 and 6, it can be observed that the maximum storey drift is found in model BF 1.0 along the both x and y directions at first storey. For the other models the maximum storey drift is at 2nd floor but the value is within the limit. The reason for the maximum storey drift at first floor for model BF 1.0 is that the stiffness of the ground storey is about 73.3 % of the storey above. For other models the stiffness of the ground storey is increased, so the maximum storey drift shifts from first floor

Table 5 Storey drift in *x* direction for the bare frame models

Storey		Storey drift in <i>x</i> direction (mm)						
Storey level	Storey no.	BF 1.0	BF 1.25	BF 1.5	BF 1.75	BF 2	BF 2.25	BF 2.5
Roof level	5	2.55	2.52	2.63	2.66	2.68	2.71	2.76
4th floor	4	5.12	5.05	5.26	5.30	5.35	5.40	5.48
3rd floor	3	7.47	7.31	7.60	7.62	7.68	7.73	7.80
2nd floor	2	9.22	8.80	9.05	8.95	8.90	8.86	8.70
First floor	1	9.79	8.19	7.99	7.40	7.00	6.66	5.88
Ground floor	0	0.00	0.00	0.00	0.00	0.00	0.00	0.00

Table 6 Storey drift in *y* direction for the bare frame models

Storey		Storey drift in <i>y</i> direction (mm)						
Storey level	Storey no.	BF 1.0	BF 1.25	BF 1.5	BF 1.75	BF 2	BF 2.25	BF 2.5
Roof level	5	2.97	2.898	3.07	3.02	3.09	3.15	3.17
4th floor	4	6.14	6.079	6.43	6.33	6.48	6.60	6.65
3rd floor	3	9.14	8.79	9.27	9.15	9.33	9.49	9.55
2nd floor	2	11.39	11.04	11.45	11.45	11.47	11.48	11.50
First floor	1	10.89	9.95	8.41	9.78	8.02	6.76	6.49
Ground floor	0	0	0	0	0	0	0	0

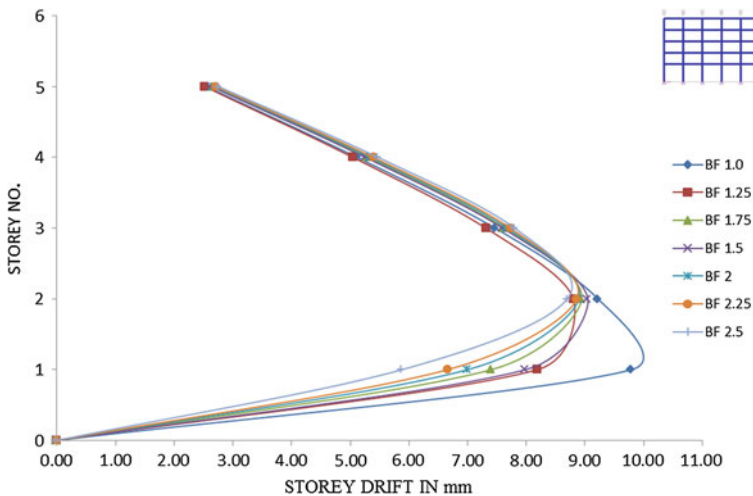


Fig. 5 Comparative graph for the storey drift of the bare frame models along *x* direction

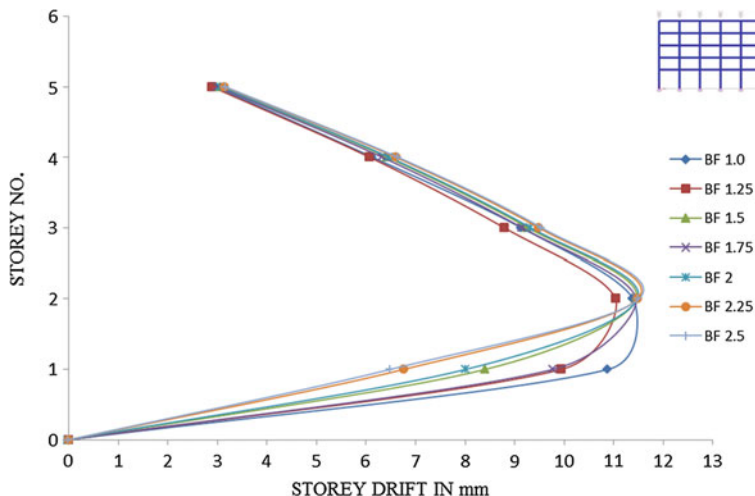


Fig. 6 Comparative graph for the storey drift of the bare frame models along y direction

to 2nd floor. As the stiffness and the area of cross section of the ground storey columns for the model BF 1.25 is increased by 29.8 and 9 % respectively, it can be observed from Fig. 5 that the storey drift of the model BF 1.25 in x direction is reduced by 16.34 % for first floor, 6.54 % for 2nd floor, but above the 2nd floor instead of the decrease in the storey drift there is increase in it. The same trend is followed by the frame BF 1.25 along the y direction. Along the x as well as y direction all the models follow the same trend only difference is in the percentage reduction in the storey drift at first floor. Maximum reduction in the storey drift at first floor is observed in case of the model BF 2.5,. For model BF 2.5, increasing the stiffness and area of cross sectional of the OGS columns in x direction by 151 and 55 % respectively, the reduction in the first floor storey drift is found to be 39.98 %. However, there is a slight increase in the storey drift at roof level. This slight increase in the upper storey drift may be because of the much increase in the stiffness of the ground storey. From the above results, it can be concluded that by increasing the stiffness and area above 29.8 and 9 % respectively, does not show the desirable change in the storey drift of the OGS structures. So when the stiffness of the infill is not considered, best possible rectification measure for the OGS columns is that the storey shear and moments should be increased by 1.25 MF. Same can be concluded from the Fig. 6 along the y direction.

4.4 Stiffness

Stiffness is one of the main parameter which predicts the soft storey behavior of the particular structure. In the present work as the models are designed for range of MF.

By using higher values of MF the stiffness of the ground storey increases in comparison to storey above. To evaluate the effect of the MF on the storey stiffness, various models are analysed by using [9]. The results obtained are discussed as under.

Table 7 shows the stiffness of the ground storey and first storey for bare frame models. The stiffness of the ground storey of the models BF 1.0 is 84 % of the first storey in *x* direction. As BF 1.25 is designed for 1.25 MF applied to the ground storey columns, the stiffness of the first storey becomes 104 and 83 % that of ground storey in *x* and *y* direction respectively. For the frame model BF 1.5 the stiffness of ground storey is increased so much that the stiffness of the first storey is 93 and 60 % in *x* and *y* directions respectively. That means instead of removing the soft storey effect, in this case soft storey have appeared at first storey in *y* direction as the stiffness of the first storey is less than 70 % that of the ground storey. For the models BF 1.75 and BF 2 same trend is seen in the stiffness. But for the models BF 2.25 and BF 2.5, the stiffness of the first storey in both directions becomes less than 70 %. So the models BF 2.25 and BF 2.5 are showing soft storey behaviour in both the directions. Thus the problem which arises here is that of the shifting of the soft storey effect from one storey to another storey. Now if the second storey columns are designed for 2.5 MF, then the soft storey effect will shift to the 3rd storey and so on. Thus by using 2.5 MF, instead of rectifying the soft storey effect, it creates soft storey above that level. From the above discussion it can be concluded that using the MF value higher than 1.25 for bare frame models, instead of rectifying the soft storey behaviour, one creates soft storey effect on storey above. Thus it is seen that most suitable rectification measure for the OGS structure, when the infill stiffness is not considered, is 1.25 MF. That means ground storey columns should be multiplied with 1.25 MF instead of 2.5.

Table 7 Storey stiffness for the bare frame models

Model	Lateral stiffness(kN/m)		Lateral stiffness (kN/m)	
	In <i>x</i> direction		In <i>y</i> direction	
	Ground storey	First storey	Ground storey	First storey
BF 1.0	4874267.6	6607028.97	3262939.45	2936457.32
BF 1.25	6328125.00	6607028.97	3559570.31	2936457.32
BF 1.5	7031250.00	6607028.97	4882812.50	2936457.32
BF 1.75	8045654.30	6607028.97	3856201.17	2936457.32
BF 2	8939615.89	6607028.97	5289713.54	2936457.32
BF 2.25	9833577.47	6607028.97	7040608.72	2936457.32
BF 2.5	12281901.04	6607028.97	7582194.01	2936457.32

5 Conclusions

From the above results, the main conclusions obtained from the present study are as follows:

- i. The value of MF equal to 2.5 has been found on the higher side, resulting in increased dimension and percentage of reinforcement without significant enhancement in the positive response beyond a certain MF.
- ii. The best possible rectification measure when the stiffness of the infill is not considered is to multiply the ground storey columns by 1.25 factor instead of codal value of 2.5.
- iii. When the building with OGS is designed for values of MF higher than 1.5 without considering infill stiffness, soft storey effect shifts from ground storey to first storey.

6 Recommendations

- i. It is found in the present study that the multiplication factor of 2.5 as given in IS 1893 Part 1 [4] is not justified.
- ii. In the present study, only the columns of the ground storey are designed for 2.5 factor. The analysis should be carried out to see the effect of both beams and columns when designed for 2.5 factor.
- iii. The infill wall stiffness is not considered in this study. Thus, the effect of infill should be considered in the analysis.
- iv. The non-linear analysis gives more accurate results than linear one. Thus, non-linear analysis should be used for the analysis.
- v. The same study should be carried out for different heights of the building, to check the applicability of 2.5 factor for high rise buildings.
- vi. The effect of the column orientation can be considered for the models, which will have great effect on the behaviour of the structure.
- vii. The effect of provision of shear wall at the periphery as far away as possible from the centre of the building should be studied.

References

1. Arlekar JN, Jain SK, Murty CVR (1997) Seismic response of RC frame buildings with soft first storeys. In: Proceedings of CBRI golden jubilee conference on natural hazards in Urban Habitat, New Delhi, India
2. Dande PS, Kodag PB (2013) Influence of provision of soft storey in RC frame building for earthquake resistance design. *Int J Eng Res Appl* 3(2):461–468
3. Davis R, Menon D, Prasad AM (2008) Evaluation of magnification factors for buildings using nonlinear analyses. In: The 14th world conference on earthquake engineering, Beijing, China

4. IS 1893 Part 1 (2002) Indian standard criteria for earthquake resistant design of structures. Bureau of Indian Standards, New Delhi
5. IS 456 (2000) Indian standard plain and reinforced concrete—code of practice. Bureau of Indian Standards, New Delhi
6. Kanitkar R, Kanitkar V (2004) Seismic performance of conventional multi-storey buildings with open ground storey floors for vehicular parking. *Indian Concr J* 78:99–104
7. Kaushaik HB, Rai DC, Jain SK (2009) Effectiveness of some strengthening options for masonry-infilled RC frames with open first story. *J Struct Eng* 135:925–937
8. Lamb PB, Londhe RS (2012) Seismic behaviour of soft first storey. *IOSR J Mech Civil Eng (IOSR-JMCE)* 4(5):28–33
9. SAP 2000 (Version 14.0) (2007) Integrated software for structural analysis and design. Computers & Structures Inc., Berkeley
10. Saraswati S, Vineet S (2012) Seismic response of RCC building with soft storey. *Int J Appl Eng Res* 7(11):1335–1339
11. Subramanian N (2004) Discussion on seismic performance of conventional multi-storey building with open ground floors for vehicular parking by Kanitkar and Kanitkar. *Indian Concr J* 78:11–13

Evaluation of Models for Joint Shear Strength of Beam–Column Subassemblages for Seismic Resistance

L. Vishnu Pradeesh, Saptarshi Sasmal, Kanchana Devi
and K. Ramanjaneyulu

Abstract Many parts of the world experienced devastating earthquakes in the recent past. It is observed that those collapsed reinforced concrete (RC) structures are decades old and not designed and detailed to resist seismic loads. Beam–column joints are the most affected structural components during earthquakes due to the discontinuous load path in the vicinity. Since, shear strength of beam column joint plays the major role on the performance of RC structures under earthquake, many models were proposed by researchers to predict the shear strength of beam–column joints using different idealizations, approaches and mechanisms. These can be categorized into plane stress-, explicit-, analytical- and empirical- models. In the present work, these models are critically reviewed and summarized. The concept, parameters considered, significant observations and their limitations of the most promising and robust models in predicting the joint shear behaviour are brought out in this paper.

Keywords Beam–column joint · Earthquake · Reinforced concrete · Shear strength

L. Vishnu Pradeesh (✉) · S. Sasmal · K. Devi · K. Ramanjaneyulu
Academy of Scientific and Innovative Research, Chennai, India
e-mail: pradeesh@serc.res.in

S. Sasmal
e-mail: saptarshi@serc.res.in

K. Devi
e-mail: kanchana@serc.res.in

K. Ramanjaneyulu
e-mail: rams@serc.res.in

S. Sasmal · K. Devi · K. Ramanjaneyulu
CSIR-Structural Engineering Research Centre, Chennai 600113, India

1 Introduction

Recent earthquakes have caused devastating effects on the infrastructures. Many parts of US, Italy, Japan, New Zealand, Iran, South east Asia including Himalayan region in India, etc. come under high seismicity zone which creates a large demand for adequate stiffness, strength, ductility, and stability of the structures to prevent collapse. Most of the existing reinforced concrete structures are decades old, and were designed and detailed for gravity loads only. Performance of these structures under seismic events is extremely vulnerable and needs to be assessed before taking any protective measure to improve human safety. It is evident from the previous earthquakes that the beam–column joint regions are the critical regions of reinforced concrete structures. Beam–column joint regions are the discontinuity regions where the load transfer mechanism becomes complex. During an earthquake, these joints are subjected to shear forces of large magnitude which make them to fail in brittle fashion. These joints play an important role in the stability and overall performance of a structure. There is an urgent need to evaluate the shear strength of these beam–column joints to ensure safety under seismic loading. Number of models such as empirical models, spring models, and analytical models were proposed by the researchers to evaluate the beam–column joints behaviour and to predict their shear strength. These models were developed, exploring the various mechanisms that are possible in a joint subjected to cyclic loads. In the present work, the models, which were reported in the literature, are critically reviewed and summarized.

2 Various Types of Analytical Models for Shear Strength Evaluation

2.1 Empirical Models

Empirical models were developed by many researchers by extracting some of the parameters that affect the joint shear strength. The basic assumption is that all the parameters are independent of each other.

2.1.1 Sarsam and Phipps Model

Sarsam and Phipps [7] suggested an empirical model for predicting the shear capacity of the beam–column joints, as given in Eqs. (1)–(3)

$$V_{cd} = 5.08(f_{cu} \rho_c)^{0.33} \left(\frac{d_c}{d_b}\right)^{1.33} b_c d_c \sqrt{1 + 0.29 \frac{N}{A_g}} \quad (1)$$

$$V_{sd} = 0.87f_{yv} A_{js} \tag{2}$$

$$V_{ud} = V_{cd} + V_{sd} \tag{3}$$

where, f_{cu} is the concrete cube strength (MPa) and ρ_c is the column reinforcement ratio, $\rho_c = \frac{A_{so}}{b_c d_c}$, where A_{so} is the area of the layer of steel reinforcement farthest from the maximum compression region in the column (mm^2), A_{js} is the area of the transverse reinforcement (mm^2) crossing the diagonal plane from corner to corner of the joint between the beam compression and tension reinforcements, N is the column axial load (in N), and f_{yv} is the tensile strength of the transverse reinforcement (MPa).

2.1.2 Scott et al. Model

Scott et al. [8] suggested a model based only on a single diagonal strut mechanism without the horizontal and vertical mechanisms. The formulae suggested are,

$$v_{crsh} = \frac{2\sqrt{f_{cu}}}{\left(\frac{z_{col}}{z_{bm}} + \frac{z_{bm}}{z_{col}}\right)} \tag{4}$$

$$V_{crsh} = v_{crsh} b_c d_c \tag{5}$$

where, f_{cu} is the concrete cube strength, $\frac{z_{bm}}{z_{col}}$ is the slope of the diagonal strut to the horizontal in which, z_{col} is the distance between the two centers of outer column reinforcement bars and z_{bm} is determined by section analysis.

2.1.3 Vollum Model

This model was proposed by Vollum [10] for exterior joints with or without the transverse reinforcements. Vollum and Newman [11] concluded that a realistic strut and tie model is difficult to construct due to its complexity. The difficulties lie in the determination of nodal sizes, column bar forces and the width of strut. The suggested equations of this model are,

$$V_c = 0.642\beta[1 + 0.552(2 - h_b/h_c)]b_c h_c \sqrt{f'_c} \tag{6}$$

$$\begin{aligned}
 V_j &= \max \left[(V_c - c h_c \sqrt{f'_c}) + A_{sj} f_y V_c \right] \\
 &\leq 0.97 b_c h_c \sqrt{f'_c} [1 + 0.552(2 - h_b/h_c)] \\
 &\leq 1.33 b_c h_c \sqrt{f'_c}
 \end{aligned} \tag{7}$$

The Eq. 6 is for joints without transverse reinforcement and Eq. 7 is for joints with transverse reinforcements. The β depends on the anchorage detail, $\beta = 1.0$ for type A, $\beta = 0.9$ for type C, α represents the effect of column axial load and concrete strength and is taken as 0.2, h_c and h_b are the depths of column and beam respectively, b_c is the width of column, f'_c is the concrete cylinder strength and f_y is the yield stress of reinforcement, A_{sj} is the area of the stirrups within the top two thirds of the beam in the joint depth below the main beam reinforcement.

2.1.4 Bakir and Bodurođlu Model

Bakir and Bodurođlu [1] proposed a model based on the regression analysis of available data reported by various researchers. In this model, the percentage of beam reinforcement and the aspect ratio of the joint are considered. The total joint shear strength is a sum of the strength contributed by the concrete and the steel.

$$V_c = \frac{0.71 \beta \gamma \rho_s^{0.4289}}{\left(\frac{h_b}{h_c}\right)^{0.61}} \left(\frac{b_c + b_b}{2}\right) h_c \sqrt{f'_c} \tag{8}$$

$$V_s = \alpha A_{sje} f_y. \tag{9}$$

The parameter β represents the anchorage detail where, $\beta = 1.0$ for anchorage type A, $\beta = 0.85$ for anchorage type C, $\gamma = 1.37$ for inclined bars in the joint and $\gamma = 1.0$ for others, $\alpha = 0.664$ for joints with less transverse reinforcement, 0.6 for medium reinforcements and 0.37 for higher reinforcements, A_{sje} represents the transverse reinforcement area in the joint, ρ_s is the percentage of tension steel in the beam, b_c and b_b are the widths of column and beam respectively, h_c and h_b are the depths of column and beam respectively, f'_c is the concrete cylinder strength and f_y is the yield stress of reinforcement.

2.1.5 Hegger et al. Model

Hegger et al. [4] developed a model which considers the column reinforcement ratio and joint aspect ratio in calculating the joint shear strength. The suggested relations for the model are given in Eqs. 10–12, as,

$$V_j = V_c + V_s \quad (10)$$

$$V_s = \alpha_2 A_{sj,eff} f_y \quad (11)$$

$$V_c = \alpha_1 ABC b_f h_c \quad (12)$$

where, α_1 represents the anchorage detail, $\alpha_1 = 0.95$ for type A, $\alpha_1 = 0.85$ for type C, A , B and C are the parameters representing the effect of aspect ratio, the effect of column reinforcement ratio and the ratio of concrete strength respectively, α_2 is the efficiency of transverse reinforcements, $A_{sj,eff}$ is the effective area of transverse reinforcements in the joint.

2.2 Comparison of Empirical Models

The shear strengths of the beam–column joints predicted by the empirical models are compared to understand the accuracy of the models (presented in Table 1). The specimen details reported in Fujii and Morita [3] (specimens K-B1, B4) is used to compare the models. The models which directly predict the shear strength of the joints are used to compare the results. The comparison is shown in Table 1.

From the above table, it is observed that the Vollum model predicts the shear strength of the joints with better accuracy but it overestimates the shear strength of the beam–column joints. Hegger et al. model and Scott et al. model are also observed to have good accuracy in predicting the joint shear strength.

2.3 Analytical Models

2.3.1 Softened Strut and Tie Model (SSAT)

Selection of the mechanism of the model is based on the load transfer mechanism within the joint. Usually, the strut-tie models are considered to satisfy only the equilibrium conditions. The satisfaction of other conditions like compatibility and constitutive relations can be achieved only through selection of a proper strut-tie and mechanisms based on force flow. Figure 1a shows how a strut is formed in an exterior joint from the load conditions, the joint experiences during an earthquake.

The principal stresses in the joint panel can be visualized through a linear finite element simulation model of a square joint sample (as shown in Fig. 1b). This figure can be used to validate the assumption that the principal direction of compression lies with the direction of diagonal strut, but is valid to some extent of the aspect ratio of the joint. The free body diagram of the strut and tie mechanism is shown in Fig. 2. The formulation of softened strut-tie model for the interior joint is same as the model for exterior joint.

Table 1 Comparison of empirical models

Specimen	$V_{jh, test}$ (kN)	Sarsam and Phipps		Scott et al.		Bakir and Bodurođlu		Hegger et al.		Vollum	
		V_{jh} (kN)	% diff	V_{jh} (kN)	% diff	V_{jh} (kN)	% diff	V_{jh} (kN)	% diff	V_{jh} (kN)	% diff
Fujii and Morita (K-B1)	246	170.02	-30.9	261.63	6.3	194.55	-20.9	240.63	-2.2	251.33	2.2
Fujii and Morita (K-B4)	287	226.73	-21.0	261.63	-8.8	218.67	-23.8	263.45	-8.2	296.08	3.1

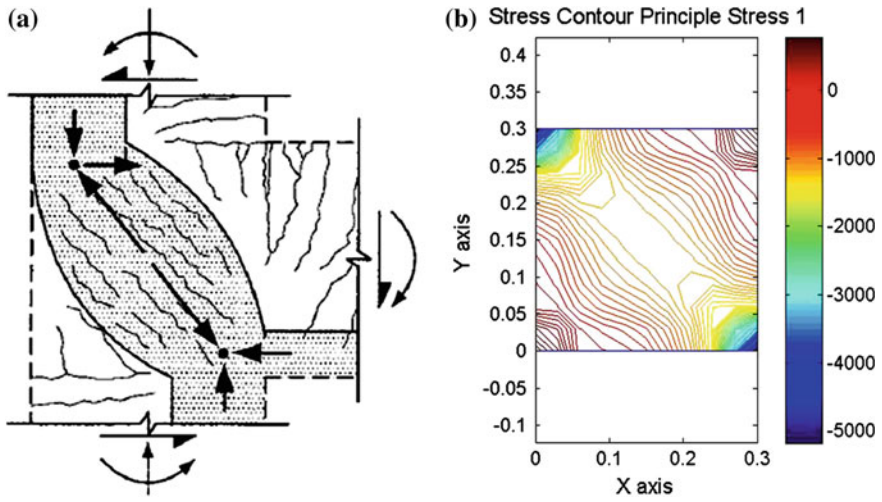
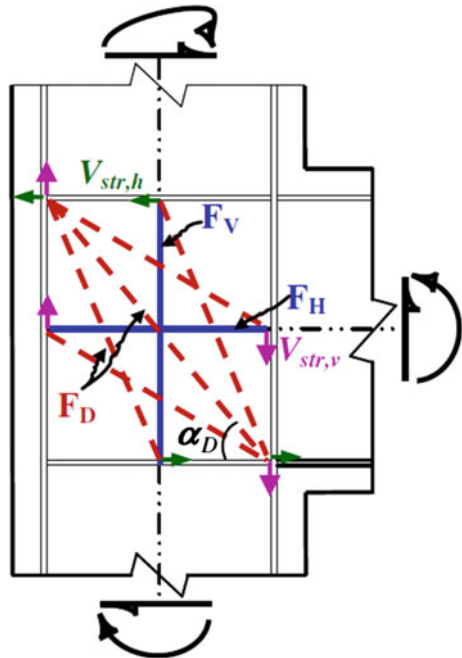


Fig. 1 a Diagonal strut mechanism, b force transfer obtained from finite element modelling

Fig. 2 Free body diagram of the strut-and-tie model in the joint



From the force equilibrium equations, the horizontal shear force acting in the joint can be determined by

$$V_{jh} = T_{b1} + C_{b2} - V_{c1} \quad (13)$$

where, C_{b2} is the compressive force resulting from the compression zone of beam. In reality, the tensile force T_{b1} do not necessarily coincide with the compressive force C_{b2} . For the sake of simplicity in computations, they are assumed to be coincidental.

The strain in the principal direction of tension can be calculated from the relation given by the two dimensional strain compatibility condition,

$$\varepsilon_r + \varepsilon_d = \varepsilon_h + \varepsilon_v. \quad (14)$$

Equation (14) is used to determine the principal strain value, which is used to calculate the softening coefficient of concrete at a given state of stress. The procedure needs an iterative technique (as proposed by Hwang and Lee [5]) for the evaluation of the strain in joint for carrying a particular amount shear.

2.3.2 Modified Rotating Angle Softened Truss Mechanism (MRA-STM)

In MRA-STM, the reinforced concrete beam–column joints are considered as reinforced concrete shear panels subjected to horizontal and vertical shear forces from the adjacent beams and columns. This model employs the deep beam analogy which represents the strut and truss actions in a typical beam–column joint by effective compression stresses and softened concrete truss mechanism. The model was derived from the Modified Compression Field Theory (MCFT) proposed by Vecchio and Collins [9] and Collins et al. [2]; and Rotating Angle-Softened Truss Model (RA-STM) where the contribution of concrete is adequately considered in cracked concrete membrane elements.

Relations for Average Stresses and Strains of Cracked Concrete

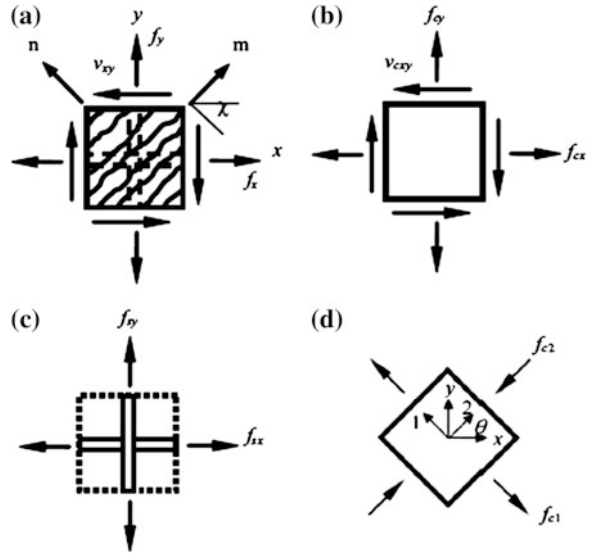
Average stresses of cracked concrete can be derived using the Mohr's circle (shown in Fig. 3) as:

$$f_{cx} = f_{c1} - v_{cxy} \cot \theta \quad (15)$$

$$f_{cy} = f_{c1} - v_{cxy} \tan \theta \quad (16)$$

$$v_{cxy} = \frac{f_{c1} - f_{c2}}{2} \sin 2\theta \quad (17)$$

Fig. 3 Stresses of cracked reinforced concrete membrane [12]



where, f_{cx} and f_{cy} are the average concrete stresses in x and y directions respectively, f_{c1} and f_{c2} are the average principal stresses of concrete in 1 and 2 directions, v_{cxy} is the average shear stress in x - y coordinate system, θ is the inclination of principal compressive stress in concrete.

Similarly, the average strains of the cracked concrete are derived from the Mohr's circle as:

$$\epsilon_{cx} = \frac{\epsilon_{c1} - \epsilon_{c2}}{2} (1 - \cos 2\theta) + \epsilon_{c2} \tag{18}$$

$$\epsilon_{cy} = \epsilon_{cx} + (\epsilon_{c1} - \epsilon_{c2}) \cos 2\theta \tag{19}$$

$$\gamma_{cxy} = 2(\epsilon_{cy} - \epsilon_{c2}) \tan \theta \tag{20}$$

where, ϵ_{cx} and ϵ_{cy} are the average concrete strains in x and y directions respectively, ϵ_{c1} and ϵ_{c2} are the average principal strains of concrete in 1 and 2 directions, γ_{cxy} is the average shear strain in x - y coordinate system.

To determine the steel stresses and check the stress equilibrium of the reinforced concrete membrane elements, the total strains should be determined. The total smeared strains in the x and y directions ϵ_x and ϵ_y are shown in the Fig. 4. The local strains at the cracks are calculated prior to obtaining total strains.

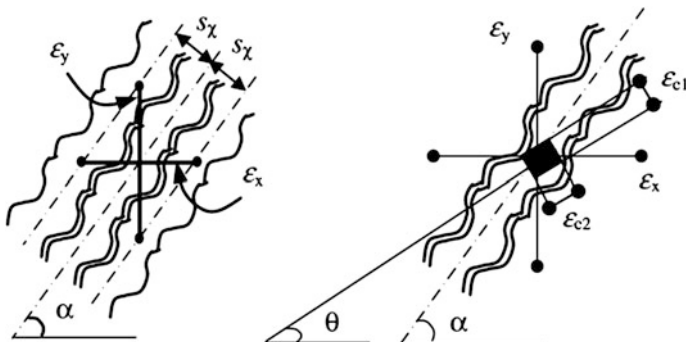


Fig. 4 Strain state of diagonal concrete strut

2.4 Comparison Between SSAT Model and MRA-STM

The two models discussed in the previous section are compared with the test results available in literature. The comparison is done with the same specimen details of Meinheit and Jirsa [6] which is used to validate both the softened strut and tie model and the modified rotating angle-softened truss model (as presented in Table 2). It is found that the predicted joint shear strength obtained from both the models is well corroborated with the reported test results. The percentage difference is evaluated against the experimental test results reported in the literature. The comparison is given in the table given below.

It is observed from the above table that both models predict the joint shear strength with good accuracy. The MRA-STM is found to have better results than the SSAT, but the model overestimates the shear strength of beam–column joints, whereas SSAT underestimates the shear strength in most cases. This is due to the consideration of post peak behaviour of the concrete stress–strain relationship in the MRA-STM.

Table 2 Comparison between SSAT and MRA-STM

Test results (kN)	V_{jh_SSAT} (kN)	% difference (SSAT)	V_{jh_MRA} (kN)	% difference (MRA-STM)
1,089.4	1,151	5.65	1,188.8	9.12
1,596.3	1,487	-6.85	1,691.2	5.94
1,227.2	1,167	-4.91	1,323.4	7.84
1,529.6	974	-36.32	1,612.2	5.4
1,645.2	1,595	-3.05	1,717.1	4.37
1,947.5	1,303	-33.09	1,995.7	2.47
1,556.2	1,564	0.5	1,661.4	6.76

3 Conclusion

The present study focuses on evaluation of the available models (both empirical and analytical) for joint shear strength evaluation. Among the empirical models, it is found that the Vollum model, Hegger et al. model and Scott et al. model predict the shear strength of the exterior beam–column joints with good accuracy. The softened strut and tie model is able to predict the mode of failure of the beam–column joint along with the joint shear strength. In softened strut and tie model, it is assumed that the principal plane angle and the crack angle are coincidental. Whereas, the modified rotating angle softened truss model assumes it non-coincidental, which is more realistic. The modified rotating angle softened truss model also predicts the shear strength of the beam–column joints with good accuracy. This model simulates the post peak behavior of the cracked concrete also. These two analytical models tend to have not only the shear strength of the beam–column joints but also give insight to the various force transfer and failure mechanisms in the joint region. It is significant to note that empirical models are too simplistic and based on few key parameters which vary from researchers to researchers. On the other hand, the analytical models are technically sound and combines the mechanics of material and structure. However, the analytical models differ from the stress state, assumption on crack formation, role of concrete after crack etc. that is evident from the present study.

Acknowledgment The paper is being published with the kind permission of the Director, CSIR-SERC, Chennai, India.

References

1. Bakir PG, Bodurođlu HM (2002) A new design equation for predicting the joint shear strength of monotonically loaded exterior beam–column joints. *Eng Struct* 24(8):1105–1117
2. Collins MP, Mitchell D, Adebar P, Vecchio FJ (1996) A general shear design method. *ACI Struct J* 93(1):36–45
3. Fujii S, Morita S (1991) Comparison between interior and exterior R/C beam–column joint behavior, vol 123. *ACI Special Publication*, Michigan, pp 145–165
4. Hegger J, Sherif A, Roeser W (2003) Nonseismic design of beam–column joints. *ACI Struct J* 100(5):654–664
5. Hwang SJ, Lee HJ (1999) Analytical model for predicting shear strengths of exterior reinforced concrete beam–column joints for seismic resistance. *ACI Struct J* 96(5):846–858
6. Meinheit DF, Jirsa JO (1977) The shear strength of reinforced concrete beam–column joints. Department of Civil Engineering, Structures Research Laboratory, the University of Texas at Austin, p 271
7. Sarsam KF, Phipps ME (1985) The shear design of in situ reinforced concrete beam–column joints subjected to monotonic loading. *Mag Concr Res* 37(130):16–24
8. Scott RH, Feltham I, Whittle RT (1994) Reinforced concrete beam–column connections and BS 8110. *Struct Eng* 72(4):55–60
9. Vecchio FJ, Collins MP (1993) Compression response of cracked reinforced concrete. *J Struct Eng* 119(12):3590–3610

10. Vollum RL (1998) Design and analysis of exterior beam–column connections, Ph.D. dissertation, Imperial College of Science, Technology and Medicine, University of London, London, UK
11. Vollum RL, Newman JB (1999) Strut and tie models for analysis/design of external beam–column joints. *Mag Concr Res* 51(6):415–425
12. Wong HF, Kuang JS (2014) Predicting shear strength of RC interior beam–column joints by modified rotating-angle softened-truss model. *Comput Struct* 133:12–17

Seismic Performance of Flat Slab Buildings

Subhajit Sen and Yogendra Singh

Abstract Flat slab system is becoming widely popular for multistorey buildings due to its several advantages. But performance of flat slab buildings under earthquake loading is unsatisfactory due to its vulnerability to punching shear failure. Several codes provide the guidelines for designing flat slab system under gravity load only. However flat slab buildings are also being constructed in high seismicity region which can cause collapse of the buildings under seismic loading. In this paper, performance of flat slab buildings designed as per existing code guidelines have been evaluated under earthquake loading. This study is carried out on a five and a ten storied buildings with identical plan. These buildings have been designed as per guidelines of Indian code, ACI code, Eurocode and New Zealand code. Nonlinear static analysis has been carried out to evaluate the performance of these buildings with and without considering the continuity of slab bottom reinforcement through column cages. Equivalent frame approach with transverse torsional members has been used to model these flat slab buildings. From the results of nonlinear analysis it is clear that most of the buildings are not ensuring CP performance for MCE level of hazard in high seismicity areas. Continuity of slab bottom reinforcement has an influence on performance of flat slab buildings. It improves the performance of the buildings. Maximum inter-storey drifts of the buildings at collapse have been compared with the limiting value of maximum inter-storey drifts corresponding to gravity shear ratio, given in literature. It is found that most of the buildings analyzed here are collapsing at an inter-storey drifts lower than that prescribed in literature.

Keywords Flat slab · Earthquake · Design · Code · Nonlinear analysis · Seismic performance

S. Sen (✉) · Y. Singh
Department of Earthquake Engineering, IIT Roorkee, Roorkee, Uttarakhand, India
e-mail: subha.sen.besu@gmail.com

Y. Singh
e-mail: yogenfeq@iitr.ac.in

1 Introduction

Flat slab is a reinforced concrete slab supported directly by columns without use of beams. Sometimes drop panels and capitals are also provided around and at the top of columns in flat slab buildings. Flat slab system is becoming widely popular for multistorey buildings due to its several advantages, e.g. easy to construct, economical, larger clear height and lesser building height. Though flat slab structures have several advantages, their performance under earthquake loading is doubtful. Flat slab buildings are very flexible and undergo large deflection under lateral load induced by earthquake. Flat slabs generally fail in punching shear mode which is a brittle mode of failure and reduces the ductility of the structures. In past earthquake, flat slab buildings face sudden collapse due to punching shear failure.

Most of the codes provide guidelines for designing flat slab buildings under gravity loads only. However flat slab buildings are also being constructed in high seismicity region which can cause collapse of the buildings under a major earthquake. In this study, guidelines of IS 456 [10], ACI 318 [1], EC 2 [6] and NZS 3101 (Part 1) [13] are used for design flat slab buildings. Performance of these buildings is evaluated using nonlinear static analysis for ground acceleration 0.36 g at rocky site.

2 Modelling of Flat Slabs

Two approaches, viz. finite element approach and equivalent frame method, are available for modelling flat slab buildings. In finite element approach, flat slabs can be modelled using plate bending elements or shell elements. For reasonably accurate results, large number of elements is required for meshing in finite element approach. This approach increases the cost of analysis for large buildings. The equivalent frame approach is relatively economical and easy to use for simulating seismic response of flat slab buildings. In this approach, flat slabs are modelled as beam members of equivalent width. Equivalent width (αl_2) of flat slab can be estimated using the following expression, proposed by Elwood et al. [5]:

$$\text{for interior supports} \quad \alpha l_2 = \left(2c_1 + \frac{l_1}{3} \right) \quad (1)$$

$$\text{for edge supports} \quad \alpha l_2 = \left(c_1 + \frac{l_1}{6} \right) \quad (2)$$

where, α is equivalent width factor, l_1 is length of slab panel (c/c of support) in the direction parallel to lateral load, l_2 is length of slab panel (c/c of support) in the direction transverse to lateral load, and c_1 is column dimension in the direction parallel of lateral loading.

Depth of beam members is kept same as thickness of flat slab. In this study, equivalent frame method proposed by Elwood et al. [5] has been used for modelling flat slab buildings. According to this method, the equivalent beams are connected to columns through ‘explicit’ torsional members. Torsional members represent the transfer of unbalanced moments, from slab to column, through torsion [4]. These members are modelled as rigid in all other degrees of freedom (DOFs), except for torsional DOF. To neutralize the additional moments due to offset between equivalent beams and column, two beam members, each having half the stiffness and strength of the equivalent beam, are connected to both sides of the column as shown in Fig. 1 Stiffness (K_t) of the torsional member under lateral loading [11] is estimated using equation Eq. (3). Effective stiffness factor (Table 1) for cracked slab section is taken as 0.33, and for column sections as recommended by ASCE/SEI 41 [3].

$$K_t = \sum \frac{6EC}{l_2[1 - (c_2/l_2)]^2} \tag{3}$$

$$C = \sum \left(1 - 0.63 \frac{x}{y} \right) \frac{x^3 y}{3} \tag{4}$$

where, c_2 is size of column in the direction transverse to the lateral load, x and y are the short and long dimensions of rectangular part of slab portion which transfers torsion (in flat slab x is depth of slab and y represents the column size in the direction of lateral loading).

Fig. 1 Equivalent frame modelling of flat slab systems

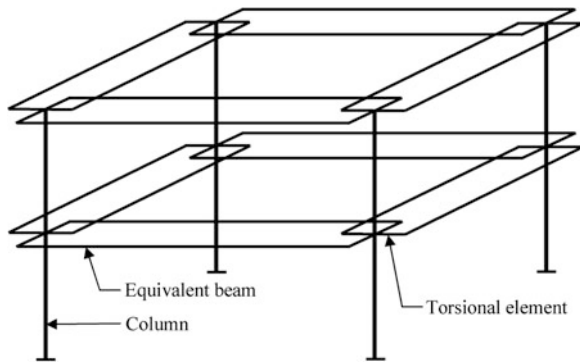


Table 1 Effective stiffness factor for modeling of different members [3, 5]

Member	Effective stiffness factor	
	Flexure rigidity	Shear rigidity
Equivalent beam	0.33	0.40
Column with compression due to gravity load $\geq 0.5 A_g f'_c$	0.70	0.40
Column with compression due to gravity load $\leq 0.3 A_g f'_c$ or with tension	0.50	0.40

For nonlinear analysis, three different types of plastic hinges are assigned to different members. Flexural hinges are assigned at the ends of the equivalent beam members. These represent the flexural capacity of flat slab near slab column connection. Punching shear capacity of slab-column connection is represented by torsional hinges assigned to fictitious torsional elements as per Hueste and Wight [7]. Torsional capacity (M_T) of these hinges is calculated using Eqs. (5) and (6). Rotational properties of torsional hinges are assigned as per Elwood et al. [5]. P–M–M interaction hinges are assigned at the ends of columns to represent the axial force-moment capacity of columns.

$$M_T = \min \left\{ \frac{M_f}{\gamma_f}; \frac{M_v}{\gamma_v} \right\} \quad (5)$$

$$v_n = \frac{V_g}{b_0 d} + \frac{M_f c}{J} \quad (6)$$

where, M_f is the capacity of moment transfer through flexure, and calculated based on transfer width of $c_2 + 5h$, h is overall depth of flat slab, M_v is capacity of moment transfer through eccentric shear, γ_f is factor used to determine the unbalanced moment transferred by flexure at slab–column connections, γ_v is factor used to determine the unbalanced moment transferred by torsion at slab-column connections, V_g is shear force due to gravity load, b_0 is perimeter of critical section, d is effective depth of slab, c is distance from the centroid of the critical section to the perimeter of the critical section, and J is polar moment of inertia of the critical section.

3 Seismic Performance

To study the seismic performance of flat slab buildings, designed for different codes, two sets of buildings, 5 storey and 10 storey tall, with identical plan shown in Fig. 2 have been considered. Each storey in the buildings is 2.8 m tall and consists of nine square slab panels having plan dimension 5 m × 5 m. The live load on floors has been considered as 2.5 kN/m². The buildings are designed for IS 456 [10], IS 13920 [8], ACI 318 [1], EC 2 [6] and NZS 3101 (Part 1) [13], Priestley et al. [12]. These codes provide the guideline for designing flat slabs for gravity load only. Two configurations of flat slab buildings are considered. In first case, no edge beam is considered and in second case edge beams are considered along perimeter of slab. In case of flat slab without edge beams, torsional portion of unbalance moment at the exterior support causes excessive punching shear stress, and design of flat slab is governed by punching shear failure at the exterior slab-column support. In flat slabs with edge beams, the unbalanced moment at exterior support is transferred through the edge beams, resulting in significant reduction in punching shear stress at slab column connection, which leads to reduction in thickness of slab. In the present study, design of flat slabs with edge beams is governed by deflection criteria. The characteristic

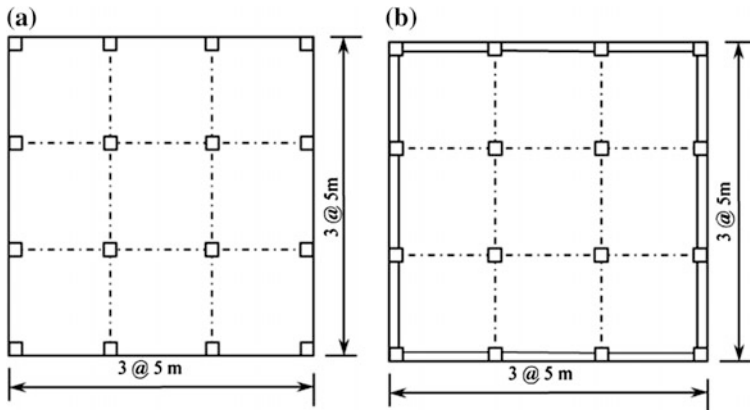


Fig. 2 Plan of the flat slab buildings: **a** without edge beams; **b** with edge beams

compressive strength of concrete (95 percentile cube compressive strength) and yield strength of reinforcing steel are considered as 30 and 415 MPa, respectively. Details of flat slab buildings with and without edge beams are shown in Tables 2 and 3. Among the different buildings without edge beams, the slab designed by EC 2 [6] has the maximum thickness, whereas for ACI 318 [1] the required thickness is minimum. All the flat slabs with edge beams have lower slab thickness as compared to flat slabs with perimeter beams.

Table 2 Section details for flat slab buildings without perimeter beams

Design code	5 storey building		10 storey building	
	Slab thickness (mm)	Column size (m × m)	Slab thickness (mm)	Column size (m × m)
IS 456:2000	270	0.4 × 0.4	275	0.5 × 0.5
ACI 318—08	225	0.4 × 0.4	200	0.5 × 0.5
EC 2:2004	325	0.4 × 0.4	325	0.5 × 0.5
NZS 3101 (Part 1)—2006	250	0.4 × 0.4	200	0.5 × 0.5

Table 3 Section details for flat slab buildings with perimeter beams

Design code	5 storey building			10 storey building		
	Slab thickness (mm)	Column size (m × m)	Edge beam (m × m)	Slab thickness (mm)	Column size (m × m)	Edge beam (m × m)
IS 456:2000	140	0.4 × 0.4	0.3 × 0.4	140	0.5 × 0.5	0.3 × 0.4
ACI 318—08	165	0.4 × 0.4	0.3 × 0.4	165	0.5 × 0.5	0.3 × 0.4
EC 2:2004	200	0.4 × 0.4	0.3 × 0.4	200	0.5 × 0.5	0.3 × 0.4
NZS 3101 (Part 1)—2006	175	0.4 × 0.4	0.3 × 0.4	175	0.5 × 0.5	0.3 × 0.4

Table 4 Gravity shear ratios at the slab column joints of flat slab buildings

Design code	Without perimeter beams		With perimeter beams	
	5 storey	10 storey	5 storey	10 storey
IS 456:2000	0.24	0.20	0.39	0.33
ACI 318—08	0.27	0.25	0.35	0.3
EC 2:2004	0.21	0.18	0.3	0.25
NZS 3101 (Part 1)—2006	0.26	0.25	0.33	0.3

Gravity shear ratio, the ratio of shear force due to gravity load at the slab-column connection and punching shear force capacity at critical section, has a very important role in failure of flat slab. Gravity shear ratios of all the considered buildings are shown in Table 4. Slabs designed for EC 2 [6] have the minimum gravity shear ratio.

Nonlinear static analysis has been carried out to evaluate the performance of these buildings with and without considering the continuity of slab bottom reinforcement through column cages. Hinge pattern for flat slab buildings with and without edge beams are shown in Figs. 3 and 4. All the flat slab buildings without edge beams and without continuity of slab bottom reinforcement fail in punching shear at the edge supports. In case of flat slab buildings with continuity of slab bottom reinforcement, the plastic rotation capacity in punching shear failure increases, and failure is governed by flexural capacity of the slab. All the buildings with edge beams also do not fail in punching shear, as the thicknesses of slabs in these buildings is governed by deflection criterion, resulting in significant over strength in punching shear. As these buildings are not failing in punching shear, continuity of slab bottom reinforcement does not influence behavior of these buildings and no separate analysis for continuity of slab bottom reinforcement has been carried out. Capacity curves obtained from nonlinear analysis of flat slab buildings without perimeter beams are plotted in Figs. 5, 6 and 7. From the plots, it is clear that flat slab buildings designed as per guidelines of EC 2 [6] have the maximum strength capacity. As the column sections of all the buildings of a particular height are identical, the strength capacity mainly depends on the thicknesses of the flat slabs. Capacity curves for 10 storey building without edge beams, designed for ACI 318 [1] and NZS 3101 (Part 1) [13] are identical as the thicknesses of slabs in the two buildings is same. Inelastic roof displacements of the buildings are calculated using the Displacement Modification Method (DMM) outlined in ASCE/SEI 41. Performance of the buildings, is evaluated for ground acceleration of 0.36 g (MCE in Indian seismic zone V as per IS 1893 [9]) at rocky site, and is summarized in Tables 5, 6 and 7. In case of flat slabs without perimeter beams, only 5 storey buildings designed for EC 2 [6] provide collapse prevention (CP) performance level without considering continuity of slab reinforcement through column cages. While considering continuity of slab reinforcement through column cages, all the 5 storey buildings and 10 storey buildings designed by EC 2 [6] provide CP performance level. This shows that continuity of slab reinforcement

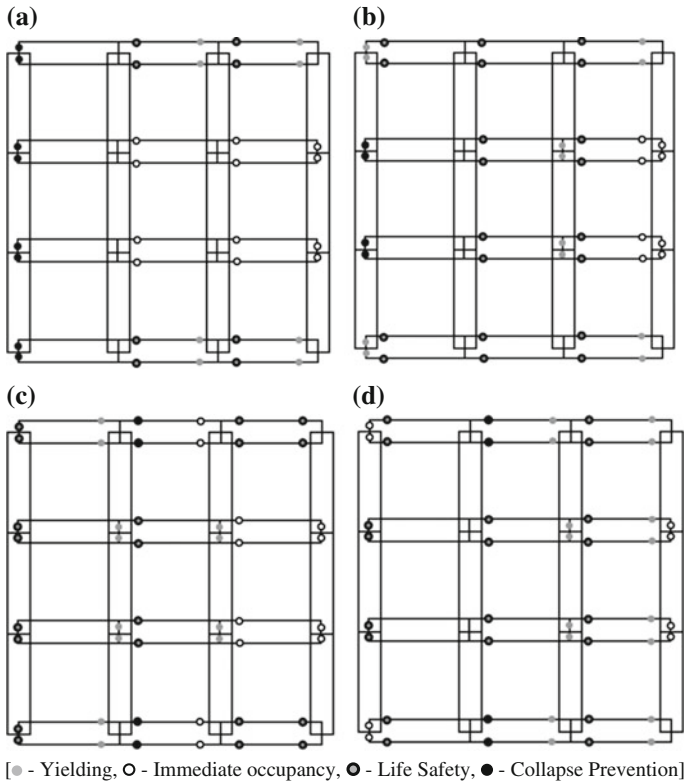


Fig. 3 Typical hinge patterns of flat slab buildings without edge beams: **a** 5 storey building without continuity of slab bottom reinforcement, **b** 10 storey building without continuity of slab bottom reinforcement, **c** 5 storey building with continuity of slab bottom reinforcement, **d** 10 storey building with continuity of slab bottom reinforcement

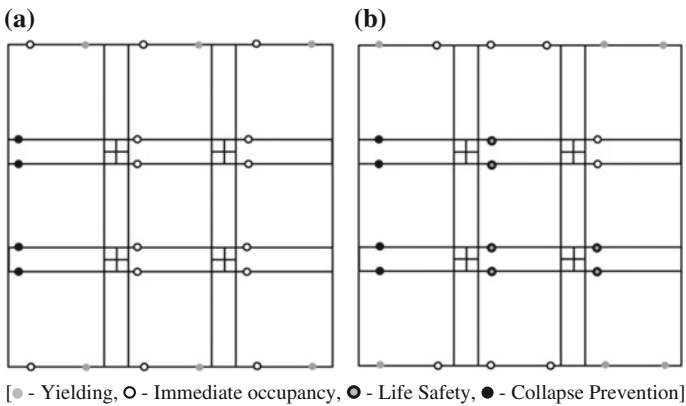


Fig. 4 Typical hinge patterns of flat slab buildings with edge beams: **a** 5 storey building, **b** 10 storey building

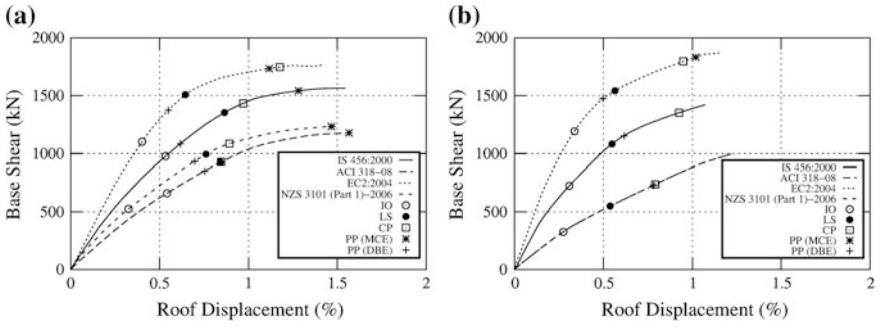


Fig. 5 Capacity curves for flat slab buildings without edge beams and without continuity of slab bottom reinforcement: **a** 5 storey buildings, **b** 10 storey buildings

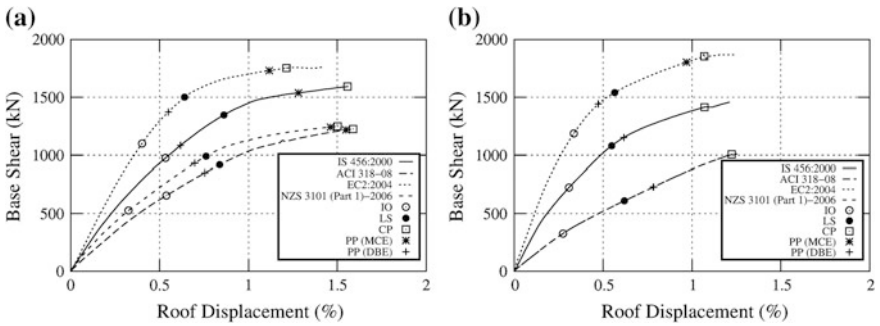


Fig. 6 Capacity curves for flat slab buildings without edge beams and with continuity of slab bottom reinforcement: **a** 5 storey buildings, **b** 10 storey buildings

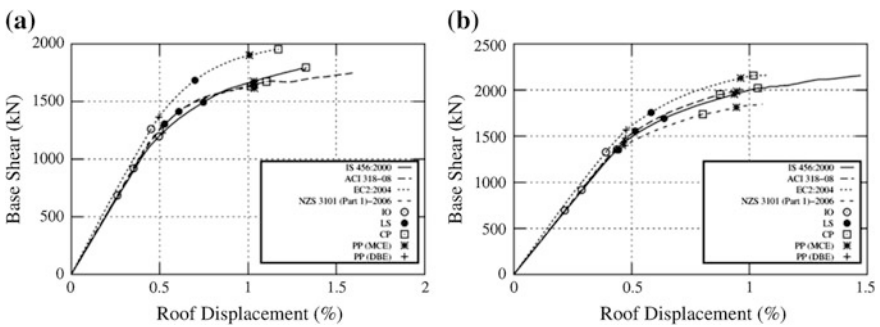


Fig. 7 Capacity curves for flat slab buildings with perimeter beams: **a** 5 storey buildings, **b** 10 storey buildings

Table 5 Estimated performance levels of flat slab buildings without continuity of slab reinforcements, at MCE

No. of storeys	Design code	Inelastic roof displacement (mm)	Maximum roof displacement for CP performance level (mm)	Performance level
5	IS 456: 2000	180	136	Collapse
	ACI 318—08	219	119	Collapse
	EC 2:2004	156	164	CP
	NZS 3101 (Part 1)—2006	205	125	Collapse
10	IS 456: 2000	356	260	Collapse
	ACI 318—08	450	222	Collapse
	EC 2:2004	285	266	Collapse
	NZS 3101 (Part 1)—2006	450	222	Collapse

Table 6 Estimated performance levels of flat slab buildings with continuity of slab reinforcements, at MCE

No. of storeys	Design code	Inelastic roof displacement (mm)	Maximum roof displacement for CP performance level (mm)	Performance level
5	IS 456: 2000	180	218	CP
	ACI 318—08	217	222	CP
	EC 2:2004	156	170	CP
	NZS 3101 (Part 1)—2006	204	210	CP
10	IS 456: 2000	359	300	Collapse
	ACI 318—08	450	343	Collapse
	EC 2:2004	275	302	CP
	NZS 3101 (Part 1)—2006	450	343	Collapse

Table 7 Estimated performance levels of flat slab buildings with perimeter beams, at MCE

No. of storeys	Design code	Inelastic roof displacement (mm)	Maximum roof displacement for CP performance level (mm)	Performance level
5	IS 456: 2000	144	186	CP
	ACI 318—08	145	155	CP
	EC 2:2004	141	164	CP
	NZS 3101 (Part 1)—2006	145	142	Collapse
10	IS 456: 2000	262	290	CP
	ACI 318—08	265	245	Collapse
	EC 2:2004	270	285	CP
	NZS 3101 (Part 1)—2006	264	225	Collapse

through column cages improves the performance of flat slab buildings, significantly. In case of flat slabs with edge beams, 10 storey building designed according to ACI 318 [1] and both 5 and 10 storey buildings designed according to NZS 3101 (Part 1) [13] do not ensure CP performance level.

Several plots for the limiting values of inter-storey drift corresponding to failure of flat slab buildings as a function of gravity shear ratio are available in literature. Among these, the limits prescribed in ACI 318 [2] are the most conservative. Figures 8 and 9 show the comparison of the maximum inter-storey drifts at failure of different flat slab buildings considered in this study, with the limiting values available in literature. Most of the buildings analyzed here collapsed at inter-storey drifts slightly lower than those prescribed in literature.

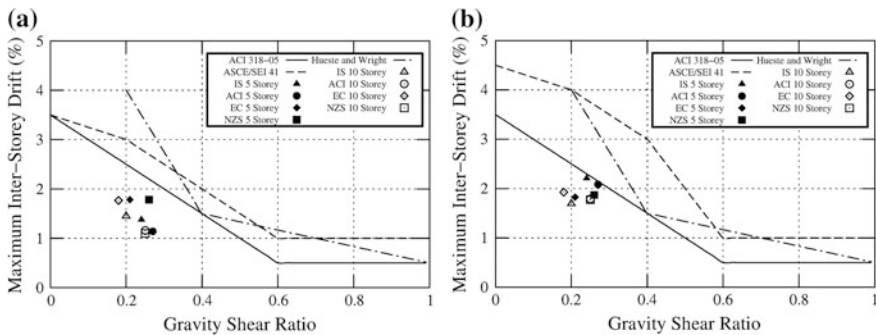
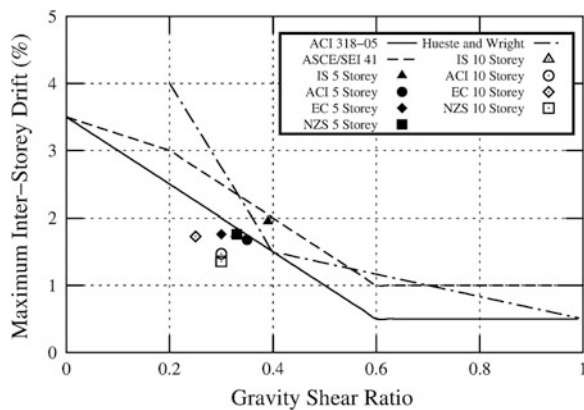


Fig. 8 Comparison of maximum inter storey drift for flat slab buildings, designed for different codes, with drift limits at failure, prescribed in literature: **a** without continuity of slab bottom reinforcement, **b** with continuity of slab bottom reinforcement

Fig. 9 Comparison of maximum inter storey drift for flat slab buildings with perimeter beam, designed for different codes, with drift limits at failure, prescribed in literature



4 Conclusions

Performance of most of the flat slab buildings without edge beams, considered in the present study, has been found to be unsatisfactory, except for 5 storey buildings with continuity of slab reinforcement. The failure of flat slab buildings is mostly governed by the punching shear failure at slab-column joints along the perimeter. Edge beams in flat slabs result in enhancement of punching shear capacity at these joints and avoid failure in punching shear. Continuity of slab bottom reinforcement also improves the performance of flat slab buildings, significantly. The analytically obtained ultimate drift capacity of all the flat slab buildings, considered in the present study, is slightly lower than the corresponding drift limits available in literature.

References

1. ACI 318—08 (2008) Building code requirements for structural concrete. ACI Committee 318, American Concrete Institute, Farmington Hills
2. ACI 318—05 (2005) Building code requirements for structural concrete. ACI Committee 318, American Concrete Institute, Farmington Hills
3. ASCE/SEI 41-06 (2007) Seismic rehabilitation of existing building. American Society of Civil Engineers, Reston
4. Beyer K, Dazio A, Priestley MJN (2008) Seismic design of torsionally eccentric buildings with U-shaped RC walls. IUSS Press, Pavia
5. Elwood KJ, Matamoros A, Wallace JW, Lehman D, Heintz J, Mitchell A, Moore M, Valley M, Lewoes LN, Comartin C, Mohele JP (2007) Update to ASCE/SEI 41 concrete provisions. http://peer.berkeley.edu/pdf/ASCE_41_update_PEER_Report_02.pdf-report
6. Eurocode 2 (2004) Design of concrete structures Part 1-1: general rules and rules for buildings. European Committee for Standardization, Brussels
7. Hueste MBD, Wight JK (1999) Nonlinear punching shear failure model for interior slab-column connections. *J Struct Eng ASCE* 125(9):997–1008
8. IS 13920 (1993) Indian standard ductile detailing of reinforced concrete structures subjected to seismic forces—code of practice. Bureau of Indian Standard, New Delhi
9. IS 1893 (2002) Indian standard criteria for earthquake resistant design of structures, part 1: general provisions and buildings. Bureau of Indian Standards, New Delhi
10. IS 456 (2000) Indian standard plain and reinforced concrete—code of practice. Bureau of Indian Standard, New Delhi
11. Park YM, Han SW, Kee SH (2009) A modified equivalent frame method for lateral load analysis. *Mag Concr Res* 61(5):359–370
12. Priestley MJN, Calvi GM, Kowalsky MJ (2007) Displacement-based seismic design of structures. IUSS Press, Pavia
13. NZS 3101: Part 1 (2006) Concrete structures standard part 1—the design of concrete structure. Standards New Zealand, Wellington

Experimental Investigations on Seismic Performance of Gravity Load Designed and Corrosion Affected Beam Column Sub-assemblages

A. Kanchana Devi, Saptarshi Sasmal and K. Ramanjaneyulu

Abstract Most of the reinforced concrete structures were designed only for gravity loads, even in the regions prone to high seismicity. Though these structures perform well under gravity load cases, their performance under seismic event is still a grey area. In RC structures, beam-column joints are crucial members, to dissipate the seismic energy imparted to the structure. It is evidenced that most of the reinforced concrete structures are severely affected by the corrosion and the performance of those structures under seismic events needs special attention. In view of this, investigations are carried out to evaluate the performance of the gravity load designed (GLD) uncorroded and corrosion affected beam-column sub-assemblages under reverse cyclic loading. The study not only brings out the extreme vulnerability of GLD structures under seismic events, but also points out the further detrimental situation due to corrosion in the RC structures. The findings of the present study will be helpful to formulate the adequate strengthening measures for improved seismic performance of the deficient- and degraded- structures to avoid catastrophic failures under seismic events.

Keywords Beam column · Corrosion effect · Gravity load design

1 Introduction

The catastrophic collapse of the existing structures experienced during past earthquakes necessitates the study of the performance of such old structures under the seismic activity. Moreover, most of the old reinforced concrete (RC) structures (built in pre 1960s) are gravity load designed and thereby exhibit extremely poor

A. Kanchana Devi (✉) · S. Sasmal · K. Ramanjaneyulu
Academy of Scientific and Innovative Research, Chennai, India
e-mail: kanchana@serc.res.in

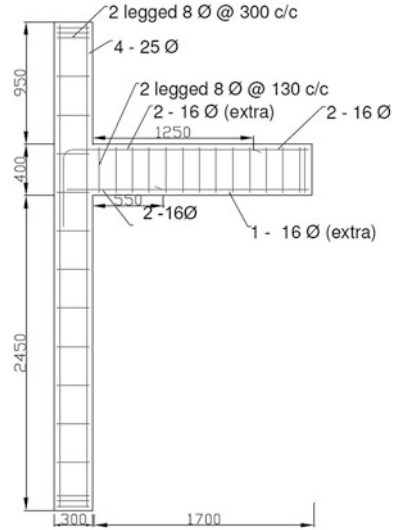
A. Kanchana Devi · S. Sasmal · K. Ramanjaneyulu
CSIR-Structural Engineering Research Centre, 600113 Chennai, India

seismic performance. In RC structures, beam-column joints are the crucial members, which are responsible to dissipate the seismic energy imparted to the structure. Hence, an investigation of joint behaviour under seismic type loading provides the insight on the seismic performance and thereby enabling to develop suitable, adequate and feasible upgradation schemes to improve its seismic performance. Numerous analytical and experimental investigations were reported to understand the seismic behavior of existing structures and to bring out the possible scopes for improvements in design and detailing for the structures in seismic prone zones. Aycardi et al. [3] studied the performance of Gravity load Designed (GLD) sub assemblages (according to ACI 318–389, 1989) under seismic loading and also attempted to analytically model the seismic behavior to identify the parameters which play the key role under seismic loading. Bracci et al. [4] conducted a series of tests to evaluate the seismic resistance of GLD structural frames (according to ACI 318–389, 1989) and found that the GLD structures mainly suffered from strong beam-weak column behavior with poor reinforcement detailing. El-Attar et al. [8] studied the behavior of GLD buildings (according to ACI 318–389, 1989) under seismic loading and observed that GLD RC buildings without walls would experience very large deformations associated with considerable stiffness degradation during a moderate earthquake.

A gravity load collapse mechanism of RC frames was investigated by Elwood and Moehle [9] using shake table test to observe the process of failure due to dynamic shear and axial load. The RC frame was characterized by low ductile columns with a predominant shear failure mode, which is found to accelerate the lateral strength degradation process. It was concluded that axial stress on the column influences the behavior of the column during shaking, particularly after shear failure. Dhakal et al. [6] carried out an experimental study on dynamic response of GLD RC connections (according to British Standard BS 8110–1985). It was observed that, the connection zones are most important parts in dissipating energy during earthquake, most of the GLD connections are weaker than the adjoining structure and failed in shear. Ramanjaneyulu et al. [12] evaluated the seismic performance of exterior beam-column sub-assemblages by considering different stages of Eurocode (EC) and Indian Standard (IS). It is found that the gravity load designed (GLD) structure is vulnerable to even medium intensity earthquake.

Corrosion of reinforcement in concrete is a serious problem. Corrosion causes three major effects in the RC structure (i) Induces the expansive force in the surrounding concrete (ii) Reduces the mechanical properties of the steel reinforcement (iii) Depletes the bond between steel and surrounding concrete. The effect of corrosion on mechanical properties of steel was studied by Maslehuddin et al. [10], Almusallam [1], Palsson and Mirza [11], Du et al. [7], Shin et al. [13], Cairns et al. [5], Apostolopoulos and Papadakis [2] and found that it reduces the ductility and energy absorption capacity of steel significantly. In present study, investigations are carried out to evaluate the performance of the gravity load designed (GLD) uncorroded and corroded beam-column sub-assemblages under reversed cycle loading.

Fig. 1 Reinforcement details of the gravity load designed specimen



2 Details of Gravity Load Designed (GLD) Specimen SP1

A typical three storied RC Framed building with 6 span and 3.5 m each floor height is taken up for the study. The building is analysed for combination of dead load, live load and designed for the same. The cross section dimension of 300 mm × 400 mm and 300 mm × 300 mm are arrived from the design for beam and column, respectively. The beams and columns are designed for critical shear force and bending moment. The reinforcement details arrived for SP1 specimens are given in Fig. 1. The length of the beam is adopted as 1.7 m. The lengths of the top and bottom segments of column are arrived based on proportion of moments at the joint and are found to be 0.950 and 2.450 m respectively Ramanjaneyulu et al. [12]. A mix proportion of 1 (cement): 2.25 (fine aggregate): 2.35 (coarse aggregate- 60 % 10 mm size, 40 % 20 mm size): 0.5 (w/c): 0.4 % (super plasticizer) was adopted for the present study. The reinforcement steel of grade Fe500D is used. The characteristic compressive strength of concrete cubes is found to be 36.17 N/mm². The test specimen was instrumented by affixing electrical resistance strain gages on beam and column reinforcements (main bars, ties, stirrups) to measure the strain. Linear variable differential transformer (LVDTs) were positioned at critical locations of beam and column portions of the sub-assembly to measure deformations and distortions.

3 Details of the Corrosion Damaged Specimen SP1-CR

The present study simulates the chloride induced corrosion on concrete structures that are subjected to marine exposure. Specimen SP1-CR is subjected to accelerated

corrosion by inducing impressed current. In the present study, beam reinforcements, stirrups and portion of joint adjoining the beam are corroded. This is done so by exposing the electrolyte in the region of interest. The main reinforcement (both top and bottom) are connected to the positive terminal of the DC pack there by acting as anode. The stainless plates are used as cathode and are connected to the negative terminal of the DC pack. The beam and adjoining joint region are immersed in solution of 3.5 % NaCl. A constant total impressed current of 5 A is applied to the reinforcement and a voltage of 11.6 V recorded on the DC Pack. The specimen is subjected to above condition for the period of 7 days until visible cracks appeared on the surface of the concrete.

4 Experimental Set Up

The test set-up was arranged so that the beam-column joint can be tested horizontally. The schematic diagram of test set-up and positioning of test specimen is shown in the Fig. 2a. An axial load of 300 kN is applied to the column by hydraulic jack at one end of the column against the reaction block at the other end. The level of axial load in column was arrived by analysis of the global system of the three storey four bay building. The axial load was kept constant during the test. The lateral load was applied on the beam tip in displacement control mode using 50 ton actuator, according to the load history shown in Fig. 2b. Reverse cyclic load is applied in terms of drift ratio (%) of the component where the drift is calculated as Eq. (1).

$$\text{Drift ratio (\%)} = (\Delta l / l_b) \tag{1}$$

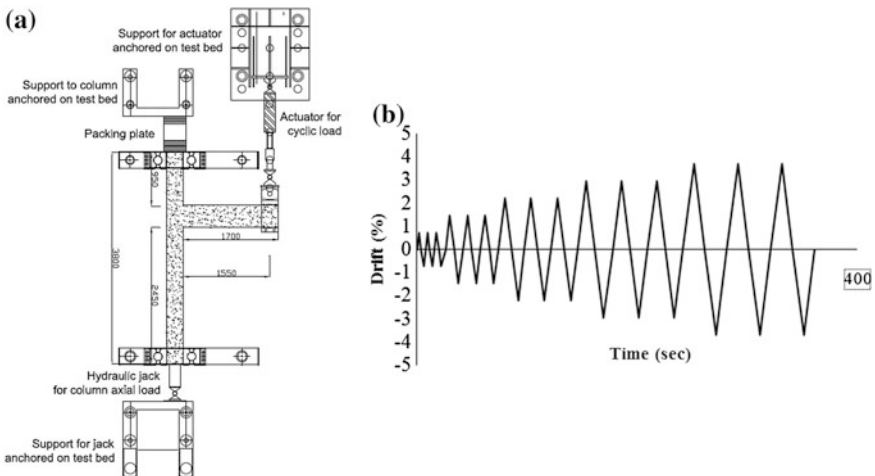


Fig. 2 a Test set up, b drift ratio versus time

where, Δl and l_b are the applied displacement at the beam tip and the length of the beam from column face to the application point of the displacement respectively. The lateral displacement increments have been applied in a quasi-static reverse cyclic manner. Three complete cycles are applied for each drift increment.

5 Experimental Investigation on Uncorroded (SP1) and Corrosion Affected (SP1-CR) Specimens

The specimen SP1 and SP-CR are experimentally investigated under reverse cyclic loading. The drift ratios are applied as displacement at the tip of the beam in the displacement control mode. Since the specimens are designed only for gravity loading, the beam bottom does not contain sufficient bottom reinforcement to resist the cyclic loading. Hence, flexure crack developed from the beam bottom in SP1 during upward loading as shown in the Fig. 3a. With the further increase in loading, diagonal cracks developed in the joint region. Upon further loading, the crack at beam-column junction is widened and wedging of concrete occurred in the joint region. A prominent crack along the joint line is observed at the failure stage (Fig. 3a). In specimen SP1-CR flexure cracks, similar to SP1, are found to be

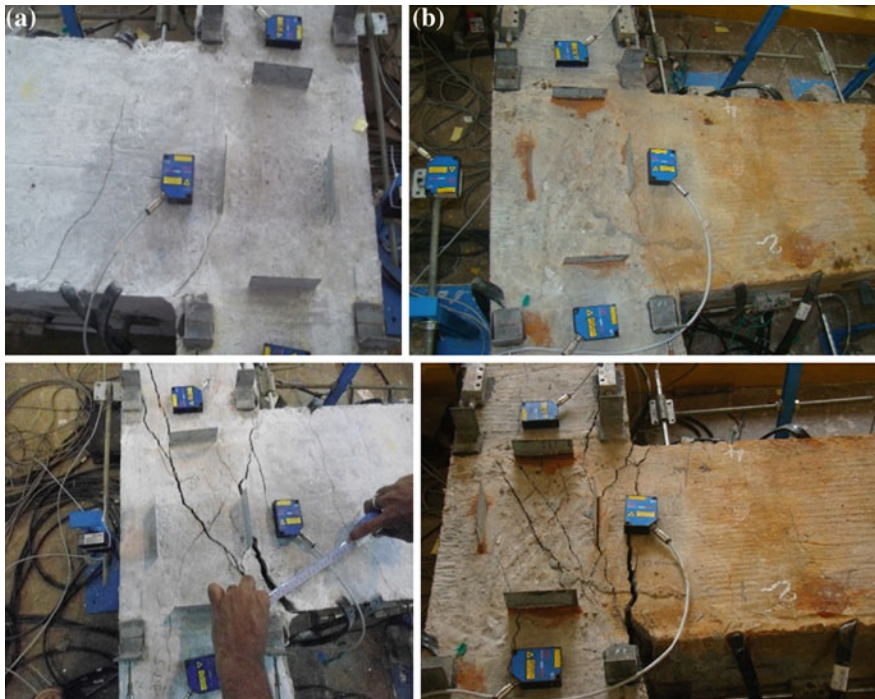


Fig. 3 a Crack pattern observed in Specimen-SP1. b Crack pattern observed in Specimen-SP1-CR

developed at the initial stage of loading (Fig. 3b). With the further loading, diagonal cracks developed in the joint region and propagated along the top and bottom portion of the column. The cracks formed are wider than that formed in the SP1. At final stage of loading, integrity of concrete was completely lost. Cover concrete from the inner faces of the column adjacent to the joint peeled off. The expansive forces exerted by the corrosion products damaged the surrounding concrete, which resulted in excessive peeling of cover concrete.

6 Level of Corrosion in SP1-CR

The level of corrosion is estimated by gravimetric weight loss measurement. After completion of tests on corrosion affected beam-column sub assemblage SP1-CR, the reinforcements of the specimen were exposed. It is found that corrosion on top and bottom beam reinforcement are found to be 2.1 and 5.37 % respectively.

7 Load-Displacement Hysteresis

The load displacement hysteresis obtained from the experiments are presented in Fig. 4. It could be observed that both SP1 and SP1-CR exhibit poor performance in reverse cyclic loading. Due to inadequate reinforcement in gravity load designed specimen SP1 and further damage due to corrosion in SP1-CR, the performance of both specimens are very poor which is clearly reflected through the load-displacement hysteresis. The load displacement envelope of the SP1 and SP-CR is shown in the Fig. 5. The maximum load carried by SP1-CR in the positive displacement cycle is decreased by 21 % compared to that of uncorroded specimen SP1. Corrosion of approximately 2 % in the top reinforcement did not produce significant reduction in the load carrying capacity of the member.

8 Energy Dissipation Capacity

The energy dissipation capacity is the key performance parameter as most of the energy imparted to system during earthquake is dissipated by the joint. The cumulative energy dissipation capacity of specimens (SP1 and SP1-CR) and energy dissipated in each cycle are shown in Fig. 6a, b respectively. The cumulative energy dissipation capacity of the specimens remain almost same till the drift ratio of 1.47 % i.e. till the appearance of shear cracks at the joint. After the drift level of 1.47 %, there is drop in the energy dissipation by SP1-CR as shown in Fig. 6a. At the drift ratio of 2.94 %, the cumulative energy dissipation capacity of the SP1-CR decreased by 34 % compared to that of specimen SP1. It is found that both specimens dissipate more energy in their first cycle but it depletes in subsequent two cycles for all drift ratios as shown in Fig. 6b. The energy dissipated by the first

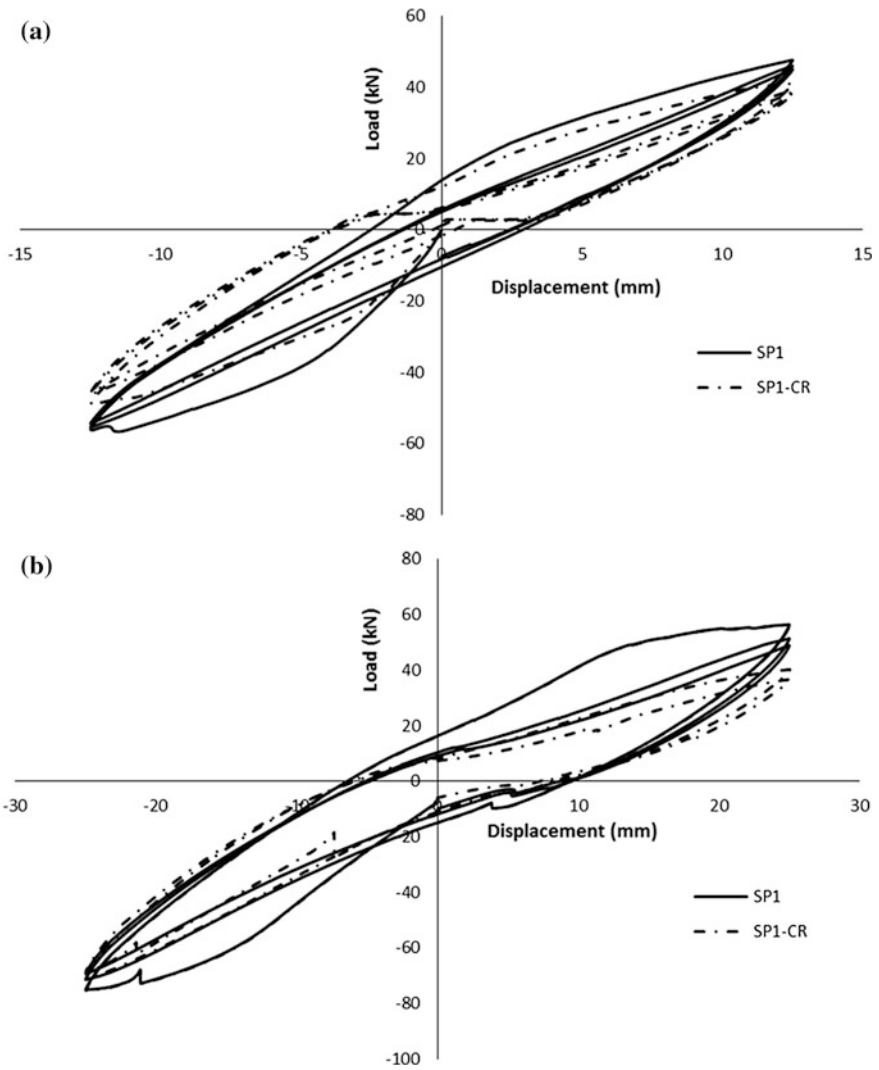


Fig. 4 Load-displacement hysteresis under reverse cyclic loading. **a** Load-displacement hysteresis for cycle 1. **b** Load-displacement hysteresis for cycle 2. **c** Load-displacement hysteresis for cycle 3. **d** Load-displacement hysteresis for cycle 4

cycle of SP1-CR is much lower than that of the SP1. At the drift ratio of 2.94 %, the energy dissipated by the first cycle of SP1-CR is 35 % lower than that of SP1.

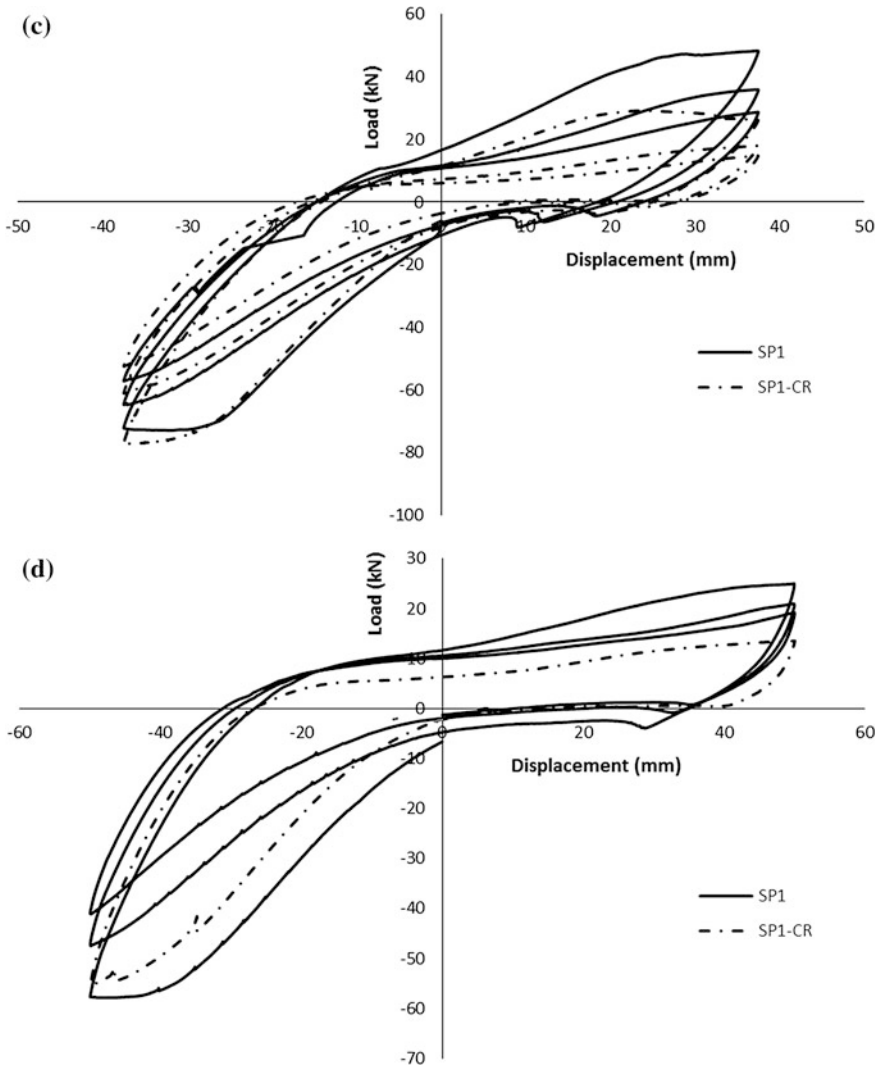


Fig. 4 (continued)

9 Stiffness Degradation

The stiffness degradation observed during the experiment is as shown in Fig. 7. At the drift ratio of +0.74 %, the stiffness degradation remains almost same for both specimens but after the drift ratio of +0.74 %, SP1-CR undergoes higher stiffness degradation compared to SP1 during the positive displacement cycle. In the negative drift cycles, with increase in the drift, stiffness degradation of the corroded

Fig. 5 Load-displacement envelope of specimens

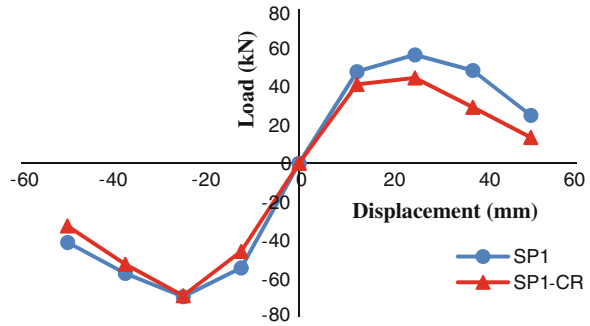
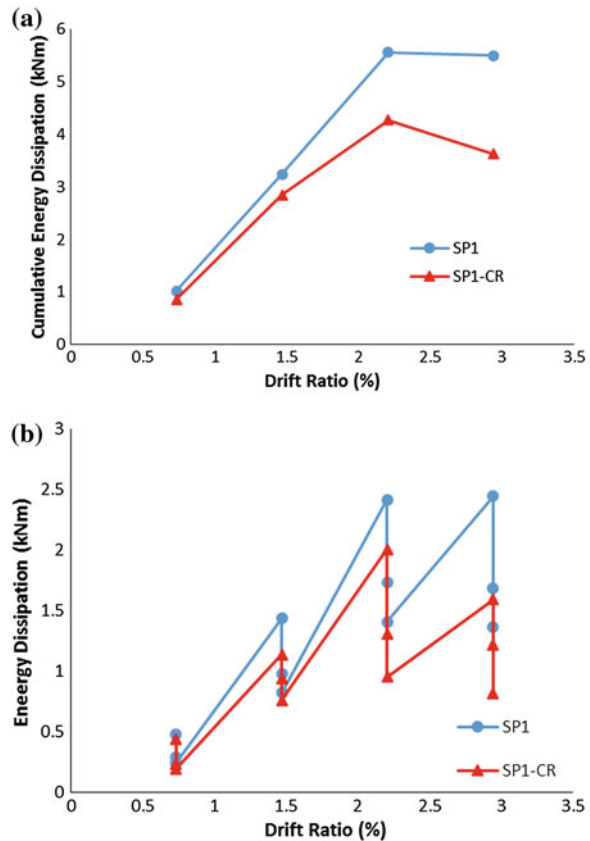


Fig. 6 a Cumulative energy dissipation capacity of the specimens. **b** Energy dissipation capacity of each cycle of specimens



specimen is lower than SP1. At the drift ratio of +2.94 %, the stiffness degradation of the first cycle of SP1-CR is 6 % higher than SP1. At the drift ratio of -2.94 %, the stiffness degradation of specimen SP1-CR is 3 % lower than SP1. The stiffness

Fig. 7 Stiffness degradation of the specimens

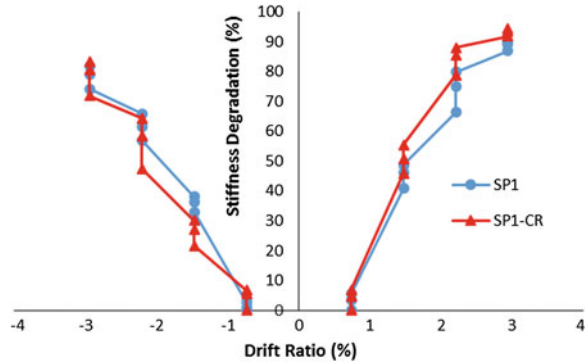


Table 1 Stiffness degradation (%)

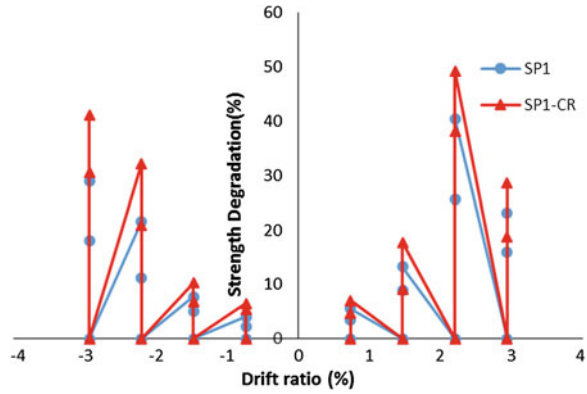
Drift ratio	Cycle	Stiffness degradation (%) for SP1		Stiffness degradation (%) for SP1-CR	
		+Drift cycle	-Drift cycle	+Drift cycle	-Drift cycle
0.73	1	0.0	0.0	0.0	0.0
	2	3.3	0.9	4.5	5.5
	3	5.5	2.8	6.9	6.7
1.47	1	40.8	32.9	45.8	21.6
	2	46.0	36.2	50.7	27.1
	3	48.6	38.0	55.4	30.1
2.2	1	66.3	56.9	78.7	47.4
	2	74.9	61.4	85.3	58.3
	3	79.9	65.9	88.0	64.3
2.94	1	86.9	74.2	91.8	71.8
	2	89.2	79.1	93.3	80.5
	3	89.9	81.7	94.2	83.4

degradation is large in positive drift cycle. The stiffness degradation observed in both the specimens is given in Table 1.

10 Strength Degradation

The strength degradation of specimens SP1 and SP1-CR obtained for each cycle is presented in Fig. 8. It is found that the strength degradation of specimen SP1-CR is slightly higher than that of specimen SP1 as shown in Fig. 8. The strength degradation percentage is higher during positive drift cycles compared to that of negative drift cycles. The strength degradation increases with the increase in drift

Fig. 8 Strength degradation of the specimens



(both positive and negative drift). At drift ratio of +2.2, the strength degradation between first and third cycles of SP1 and SP1-CR are 40 and 49 % respectively. At drift ratio of -2.2, the strength degradation between first and third cycles of SP1 and SP1-CR are 21 and 32 % respectively.

11 Concluding Remarks

The primary focus of the paper is to assess the seismic performance of GLD specimen and to evaluate the degree of degradation in the performance when such specimen is affected by corrosion. In the present study, the corrosion of the reinforcement is accelerated by inducing impressed current to the reinforcement. Both uncorded (SP1) and corrosion affected (SP1-CR) gravity load designed beam column sub-assemblages are tested under reverse cyclic loading. Important parameters such as load-displacement hysteresis, energy dissipation and strength and stiffness degradation are obtained for both the specimens. It is noted that the maximum load carried by SP1-CR in the positive cycle decreased by 21 % compared to that of SP-1. At the drift ratio of 2.94 % the cumulative energy dissipation capacity of the SP1-CR is found to be 34 % less than that of SP1. The study provides the insight into the seismic performance of deficient and deteriorated beam-column sub-assemblages. The findings of the present study would help to formulate the adequate strengthening measures for improved seismic performance of the deficient- and degraded- beam column sub-assemblages.

Acknowledgments This paper is being published with the kind permission of Director, CSIR-SERC, Chennai. The constant support and encouragement given by the Director, CSIR-SERC is gratefully acknowledged.

References

1. Almusallam AA (2001) Effect of degree of corrosion on the properties of reinforcing steel bars. *Constr Build Mater* 15:361–368
2. Apostolopoulos CA, Papadakis VG (2008) Consequences of steel corrosion on the ductility properties of reinforcement bar. *Constr Build Mater* 22:2316–2324
3. Aycardi LE, Mander JB, Reinhorn AM (1994) Seismic resistance of reinforced concrete frame structures designed only for gravity loads: experimental performance of sub assemblages. *ACI Struct J* 91(5):552–563
4. Bracci JM, Reinhorn AM, Mander JB (1995) Seismic resistance of reinforced concrete frame structures designed for gravity loads: performance of structural system. *ACI Struct J* 92(5):597–609
5. Cairns J, Plizzari GA, Du Y, Law DW, Franzoni C (2005) Mechanical properties of corrosion reinforcement. *ACI Mater J* 102(4):256–264
6. Dhakal RP, Pan T-C, Irawan P, Tsai K-C, Lin K-C, Chen C-H (2005) Experimental study on the dynamic response of gravity-designed reinforced concrete connections. *Eng Struct* 27(1):75–87
7. Du YG, Clark LA, Chan AHC (2005) Residual capacity of corroded reinforcing bars. *Mag Concr Res* 57(3):135–147
8. El-Attar AG, White RN, Gergely P (1997) Behaviour of gravity load designed reinforced concrete buildings subjected to earthquakes. *ACI Struct J* 94(2):133–145
9. Elwood KJ, Moehle JP (2002) Shake table tests on the gravity load collapse of reinforced concrete frames. In: Seventh US national conference on earthquake engineering, Earthquake Engineering Research Institute, Boston, MA, July 2002
10. Maslehuddin M, Allam IM, Al-Sulaimani GJ, Al-Mana AI, Abduljauwad SN (1990) Effect of rusting of reinforcing steel on its mechanical properties and bond with concrete. *ACI Mater J* 87:496–502
11. Palsson R, Mirza MS (2002) Mechanical response of corroded steel reinforcement of abandoned concrete bridge. *ACI Struct J* 99:157–162
12. Ramanjaneyulu K, Novák B, Sasmal S, Roehm C, Lakshmanan N, Iyer NR (2011) Seismic performance evaluation of exterior beam column sub-assemblages designed according to different codal recommendations. *Struct Infrastruct Eng* 37:1–17
13. Shin S, Kang I, Lee S, Lee H, Kyung J (2007) FEM analysis on the strength of RC members deteriorated by local part corrosion of tension main rebar. In: Proceeding of the international conference on sustainable buildings, Seoul, Korea., pp 1161–1166

Seismic Performance of Eccentrically Braced Frame (EBF) Buildings

Abhishek Singhal and Yogendra Singh

Abstract Eccentrically Braced Frames (EBF) have been researched upon and also implemented in practice worldwide, in the last three to four decades. However, the Indian Steel design code is still silent on this topic and does not provide any design provision for EBF. This paper is aimed to propose IS code compatible model design guidelines for EBF buildings. The guidelines are proposed after conducting a comparative study of design provisions from various national codes viz. American, European and New Zealand. The adequacy of proposed model guidelines is evaluated by modeling and designing suitable example buildings and subjecting them to non-linear pushover analysis. Suitable variations were introduced in examples by varying the number of storeys as five and ten; and designing the buildings as EBF with simple beam-column connections and moment resisting frame-EBF dual systems. The observations from analysis of different buildings are presented which indicate that EBF buildings demonstrated the 'Life Safety' performance level for the Design Basis Earthquake (DBE) but failed to achieve the desired 'Collapse Prevention' performance at the Maximum Considered Earthquake (MCE). Performance of buildings with dual lateral load resisting system, improved but was still not satisfactory along one direction at MCE hazard level. The paper discusses the efficacy of proposed model design guidelines for application of lateral loading and the potential issues in the satisfactory design of EBF buildings.

Keywords Eccentrically braced frames · Non-linear analysis · Seismic performance · Steel design code · Performance-based design

A. Singhal (✉) · Y. Singh
Department of Earthquake Engineering, Indian Institute of Technology Roorkee,
Roorkee 247667, Uttarakhand, India
e-mail: abhi.singhal.14@gmail.com

Y. Singh
e-mail: yogenfeq@iitr.ac.in

1 Introduction

Eccentrically Braced Frames (EBF) are relatively newer lateral load resisting building frame systems as compared to the Moment Resisting Frames (MRF) and Centrally Braced Frames (CBF). A typical EBF consists of beams, columns and diagonal braces provided such that the braces intersect at an eccentricity to isolate a part of the beam. This isolated part of beam is called a link, subjected to high levels of shear and flexure forces, plays an important role in EBF behavior. Hjelmstad and Popov [8] have demonstrated that for increase in link length to bay length ratio, the stiffness of EBF frame decreases. Popov and Engelhardt [12] have demonstrated that the link length decides whether the link will yield in shear or flexure. Thus, link length is an important parameter in EBF design. However, the optimum link length required for sound design of EBF is still an unresolved issue and is discussed in this study.

Major national seismic and steel design codes provide detailed design provisions for EBF buildings. The codes rely on force based design methodology and differ primarily on the recommended value of response reduction factor (R). This study is a step towards developing the model design guidelines for EBF buildings, compatible for Indian steel code, and examines their adequacy by designing and evaluating performance of suitable example buildings, using non-linear static analysis. The study also attempts to evaluate the adequacy for R factor value as prescribed by Indian seismic design code.

2 Design Provisions for EBF in Different Codes

This section provides a comparative study between design guidelines given in different codes, viz. American; European; and New Zealand. Wherever the relevant guidelines are provided in the Indian codes, these provisions are also included in the comparative study.

The different codes adopt different values of response reduction factor (R) or behavior modification factor (q) to obtain the design level forces in structure, accounting for the inelastic energy dissipation. The values of reduction factors recommended in different codes are given in Table 1 for buildings employing EBF system. The American and Indian code provide a constant value of reduction factor. In the European code, separate values are provided for various ductility classes. The New Zealand code gives exhaustive relations for reduction factor, given as (k_{μ}/S_p), which takes into account the structural ductility, μ , fundamental period of structure, T_l and site class (defined as per soil's unconfined compressive strength and shear wave velocity). The factor k_{μ} is given in Table 1 and S_p is structural performance factor, again a function of μ .

The common design philosophy adopted across all the codes is the capacity design approach in which all the inelastic activity of the EBF is concentrated in the

Table 1 Response reduction factors for EBF buildings

Code	Reduction factor
ASCE 7-10 [5]	8
EN 1998-1 [6]	4 for ductility class DCM, $5(\alpha_u/\alpha_1)$ for DCH where $(\alpha_u/\alpha_1) = 1.2$ for EBF
NZS 1170.5 [2]	For site class A, B, C, D $k_\mu = \mu$ For $T_1 \geq 0.7$ s
NZS 1170.0	For site class A, B, C, D $k_\mu = \left((\mu - 1) T_{1/0.7} \right) + 1$ for $T_1 < 0.7$ s.
	For site class E $k_\mu = \mu$ for $T_1 \geq 1$ s or $\mu < 1.5$
	For site class E $k_\mu = \left((\mu - 1.5) T_{1/0.7} \right) + 1.5$ for $T_1 < 1$ s and $\mu \geq 1.5$
IS 1893 (Part 1) [8]	5

link only; and rest all of the members in the frame remain essentially elastic under seismic loading. It is achieved by designing all the other members—braces, beams outside links, and columns for yielding forces in link, enhanced by an overstrength factor, as given in Table 2 for different codes. The American code includes material overstrength factor, R_y for defining overstrength factor while the New Zealand code gives a constant value. In the European code, material as well as any subjective overstrength (which is provided during design of link) is considered in overstrength factor. The subjective overstrength is given as a ratio of capacity of link section (V_p, M_p) to the design forces in the link (V_d, M_d), defined separately for shear or flexure links. Thus the capacity design procedure of European code can be considered as the most rational among all the three codes.

In an EBF, the link undergoes plastic deformations due to yielding in shear (in shear link) or in flexure (in flexure link). For a particular type of link—shear, intermediate or flexure, guidelines are available in different codes for link length and plastic rotation, which are presented in Table 3. It can be observed that the limits of maximum permissible inelastic rotation are fairly constant across all codes. Also, only a slight variation is seen in the limiting length values for different types of link. Based on this comparative study, a set of model design guidelines, are proposed and are presented in Table 4.

Table 2 Overstrength factor (for I-section links) in different codes

Frame components	AISC 341-10 [1]	EN 1998-1 (for shear links)	EN 1998-1 (for flexure links)	NZS 3404: part 1-1997 [4]
Diagonal braces and connections	1.25 R_y	1.65 (V_p/V_d) R_y	1.65 (M_p/M_d) R_y	1.4
Beams outside links	0.88 times of the forces for braces and columns	1.65 (V_p/V_d) R_y	1.65 (M_p/M_d) R_y	0.8 times of the forces for braces and columns
Columns	1.25 R_y	1.65 (V_p/V_d) R_y	1.65 (M_p/M_d) R_y	1.4

Table 3 Link length and rotation angle as per various codes

Type of link	AISC 341-10		EN 1998-1		NZS 3404: part 1-1997	
	Link length	γ_p (rad)	Link length	γ_p (rad)	Link length	γ_p (rad)
Shear links ^a (short links)	$e_s \leq 1.6M_p/V_p$	0.08	$e_s \leq 1.6M_p/V_p$	0.08	$e_s \leq 1.6M_p/V_p$	$0.08^b/0.03^b$
Intermediate links	$e_s < e < e_l$	Inter-polation	$e_s < e < e_l$	Inter-polation	$e_s < e < e_l$	Inter-polation
Flexural links ^a (long links)	$e_l \geq 2.6M_p/V_p$	0.02	$e_l \geq 3.0M_p/V_p$	0.02	$e_l \geq 3.0M_p/V_p$	0.03

^a e_s is the length of short links e_l is the length of long links

^b 0.08 rad for links attached to beam and column flanges and 0.03 for links attached to column webs

3 Role of Link Length

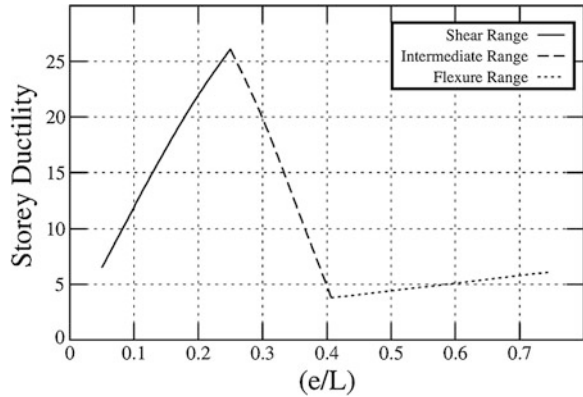
The literature review indicates that the link length influences the link yield mechanism and EBF stiffness. In this study, an exercise is conducted to study the variation of displacement ductility with link length in an EBF. The displacement ductility, μ can be estimated as the ratio of ultimate to yield storey drift. The yield drift, θ_y in an EBF storey is computed using approximate relationships provided by Priestley et al. [12].

The variation of estimated storey ductility is studied with respect to the ratio of (e/L). A hypothetical EBF is selected with length of bay as 3.6 m and height of frame as 3.3 m. The link cross-section is taken as Indian standard rolled section ISHB 450. The length of the link is increased so that it behaves first as shear link and then changes gradually to intermediate and finally as flexure link. The values of M_p and V_p are calculated as per the model design guidelines in Table 4. The variation between the storey ductility and (e/L) ratio is shown in Fig. 1. From the figure, it can be seen that the shear links provide the highest ductility. The storey ductility increases as the length of link increases within shear dominant range. As the link enters intermediate range, the storey ductility starts decreasing.

Table 4 Model design guidelines for EBF

Parameter	Proposed guidelines
Type of cross-section	Category-1 for links, beams outside the link, and columns; category-2 for braces.
Design capacity of link	Relationships as provided in IS 800:2007 [11] for beam design to be used.
Partial seismic load combination factor for members outside links	$\alpha 1.1\gamma_{ov}\Omega$ where: α = partial load combination factor used for links; γ_{ov} = material overstrength factor; Ω = minimum of $1.5(V_p/V_d)$ among all short links and $1.5(M_p/M_d)$ among all intermediate and long links.
Permissible plastic rotation in link	Maximum γ_p to be taken as 0.08 rad for link length less than $1.6(M_p/V_p)$ and equal to 0.03 rad for length greater than $2.6(M_p/V_p)$. For intermediate lengths, interpolation to be done between the two values.

Fig. 1 Variation of storey ductility with (e/L) ratio



This continues up to the limit of intermediate range of $2.6(M_p/V_p)$. After this limit, the storey ductility again starts increasing but the increase is much milder as compared to that for shear links. Thus, it can be inferred that to achieve the maximum storey ductility, shear links should be used with length as close to $1.6(M_p/V_p)$ as possible.

For optimum design of EBF buildings, the length of the links should be selected to maximize the ductility and to obtain uniformity in stiffness along the height. However, the optimum length of links also depends on the cross-sectional dimensions of links, in the form of the ratio of plastic moment to plastic shear capacity (M_p/V_p) . Selecting suitable sections for links to maintain utilisation ratio close to unity and simultaneously maximizing the storey ductility and maintaining uniformity of stiffness, is a challenging task.

4 Design of Example EBF Buildings

The proposed guidelines have been tested by designing two sets of 5 and 10 storey buildings. All the buildings have a common plan as shown in Fig. 2. Four eccentrically braced bays have been provided in both longitudinal and transverse directions. The two bays in transverse direction are separated by a corridor of 2 m span, and are connected only by floor slab. The eccentric braces are provided only in the exterior frames, whereas all the interior frames consist of only rectilinear beams and columns. Two types of lateral load resisting structural systems are considered in the present study. The first system consists of four bays of eccentrically braced frames and remaining bays of simply connected beam-columns. The second system is a dual framing system consisting of EBF as primary and MRF as secondary lateral load resisting elements. The buildings are assumed to be subjected to seismic intensity equivalent to Zone V with Type III soil as per the Indian code, IS 1893 (Part-1):2002, in addition to usual gravity loads as per relevant Indian

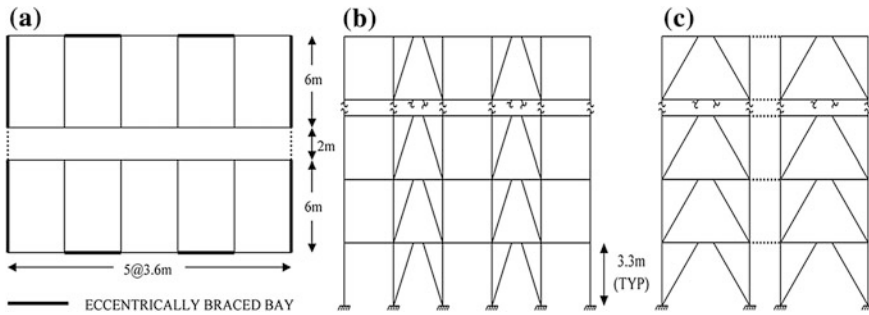


Fig. 2 Geometry of buildings considered in the study: **a** plan, **b** elevation along longitudinal direction, and **c** elevation along transverse direction

codes. The buildings are assumed to be having ordinary usage. The structural steel is considered to be having yield strength of 250 N/mm². A response reduction factor of 5.0 has been used in design, to test the adequacy of the magnitude prescribed in Indian seismic design code.

Cross-sections of all the link elements are chosen such that they act as shear links, and assumed to be provided with sufficient number of web stiffeners, so that they show the required ductility without any local web failure. To avoid subjective overstrength, all the members of the buildings are designed such that the utilization ratio of the cross-sections is close to unity. For the braces, columns, and the beams not part of EBF, built-up hollow square sections are employed for designing. For the links and the part of beams outside the links, two types of sections are used viz. Indian standard rolled I-sections from SP: 6 (1)—1964 [13] and hypothetical built-up I-sections. The built-up sections are used to achieve the maximum possible ductility. To design the built-up sections, standard thickness plates from IS 1730:1989 [10] are used. The beams outside the links, braces and columns are designed with an overstrength factor for seismic load as per model design guidelines. The material overstrength ratio is taken as 1.3 corresponding to the American A1043Gr.36 steel as per AISC 341-10, as the corresponding value for the Indian steel are unavailable. The overstrength factor has estimated as $1.1\gamma_{ov}\Omega$ ($= 1.1 \times 1.3 \times 1.5 \times 1.0 = 2.145$).

5 Performance Evaluation

To estimate the expected seismic performance of the designed buildings, static non-linear analysis is performed. Static pushover Analysis is performed according to the provisions of ASCE 41-06 [5].

The capacity curves for 5-storey buildings with different link sections are shown in Fig. 3 for the orthogonal directions. Out of the two buildings, the building with built-up I-section links has slightly higher yield base shear as well as yield displacement. This can be attributed to the longer and uniform links provided in all

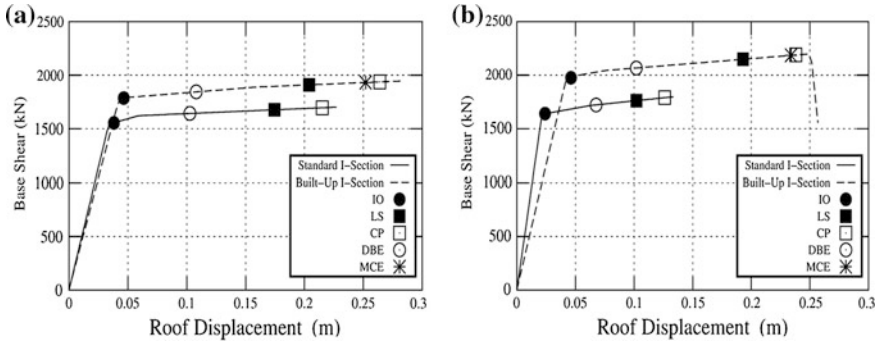


Fig. 3 Capacity curves for 5 storey EBF buildings, along: **a** longitudinal, and **b** transverse direction

the storeys as compared to the other building. The longer links reduced the stiffness and elongated the fundamental period of the building. In the longitudinal direction of the building with standard I-section links, the links in fourth storey have collapsed at Maximum Considered Earthquake (MCE). In the transverse direction, the top storey links failed to show any inelastic activity in shear, whereas the plastic hinges in the links of third storey reached Collapse level. The displacement ductility values of 4.97 and 5.91 are observed in the longitudinal and transverse directions, respectively, as shown in Table 5. However, even with this ductility, this building failed to achieve the desired CP performance at the MCE hazard level. The performance of the buildings with built-up I-section links improved, with no link reaching collapse in any direction. In the longitudinal direction, the shear hinges formed in links of third and fourth storey reached CP performance level under MCE. In the transverse direction, the links in the third storey reached CP performance level. With hypothetical built-up sections, the building achieved the intended LS performance at Design Basis Earthquake (DBE) level and CP performance at MCE level.

The capacity curves for the 10 storey buildings are presented in Fig. 4, for longitudinal and transverse directions. From the figure, it can be observed that both the buildings have yielded at almost equal level of base shear. However, the corresponding yield roof displacement differs in the two buildings. This can be attributed to high value of link to span length (e/L) ratio in building with built-up I-sections for links. The performance of the 10-storey building with standard I-sections has been unsatisfactory, with the building collapsing in both the directions even under DBE. In both the directions, the links only in the middle few storeys have yielded. In the longitudinal direction and transverse direction, the plastic hinges formed in links of the sixth storey and the fifth storey, respectively, are first to exceed the CP level. In both these storeys, there is a sudden decrease in the length of the links, as compared to the link length in the adjacent storeys. The displacement ductility demonstrated by this building is below 2.5.

The 10-storey building with built-up I-section links achieved the intended LS performance under DBE but failed to achieve CP performance under MCE.

Table 5 Seismic performance of different buildings designed as per proposed guidelines

Building model	Link section type	Direction of loading	Fundamental period	Displacement ductility observed	Average drift (%) at DBE	Average drift (%) at MCE	Estimated performance at DBE	Estimated performance at MCE
5 storey EBF	Standard I-section	Longitudinal	0.65	4.97	0.62	1.38 ^a	LS	Collapse
		Transverse	0.52	5.91	0.41	0.81 ^a	LS	Collapse
	Built-up I-section	Longitudinal	0.68	6.48	0.65	1.53	LS	CP
		Transverse	0.65	5.78	0.62	1.42	LS	CP
10 storey EBF	Standard I-section	Longitudinal	1.83	2.29	1.45 ^a	1.45 ^a	Collapse	Collapse
		Transverse	1.26	2.44	1.08 ^a	1.08 ^a	Collapse	Collapse
	Built-up I-section	Longitudinal	2.24	4.02	2.09	4.19	LS	Collapse
		Transverse	1.77	3.91	1.65	3.23 ^a	LS	Collapse
5 storey Dual Frame	Standard I-section	Longitudinal	0.60	7.45	0.54	1.33	LS	CP
		Transverse	0.52	7.21	0.40	0.94 ^a	LS	Collapse
	Built-up I-section	Longitudinal	0.61	6.77	0.54	1.30	LS	CP
		Transverse	0.57	7.37	0.47	1.14	LS	CP
10 storey Dual Frame	Standard I-section	Longitudinal	1.70	4.63	1.61	3.18	LS	CP
		Transverse	1.22	3.34	1.14	1.40 ^a	CP	Collapse
	Built-up I-section	Longitudinal	2.07	5.52	1.90	3.80	LS	LS
		Transverse	1.74	4.94	1.59	3.19	LS	CP

^a As the building reached collapse before demonstrating desired performance state, the average drift at collapse has been reported.

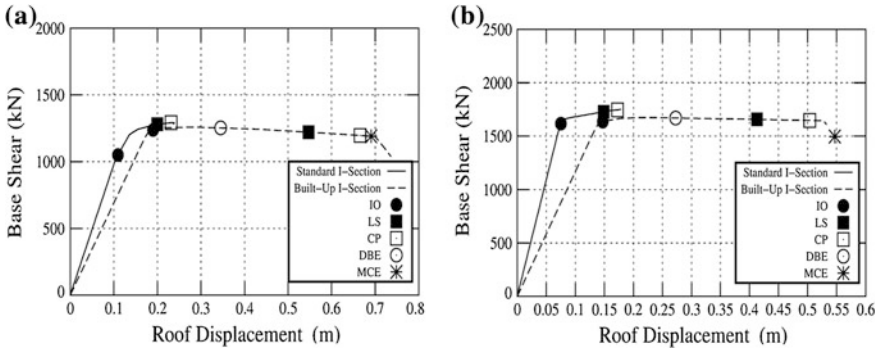


Fig. 4 Capacity curves for 10 storey EBF buildings, along: **a** longitudinal, and **b** transverse direction

The links in the top and the ground storeys did not participate in shear yielding. In both the directions, the plastic hinges formed in the links of sixth storey exceeded CP performance. Table 5 shows that the maximum displacement ductility achieved for this building is close to 4.0 in longitudinal direction and even lower in transverse direction. Thus, it can be inferred that the EBF with shear links do demonstrate good ductility within a storey, but fail to show desired performance if the links of all the storeys do not yield together.

The 5-storey dual framed buildings behaved in a similar manner (Fig. 5) as the corresponding EBF buildings, discussed earlier. For the building with standard I-section a displacement ductility of above 7.0 is observed from Table 5, in both the directions. However, under MCE, the building failed to achieve the CP performance level, in transverse direction. In the longitudinal direction also, the CP performance is just achieved with very little margin. Under MCE, the plastic hinges formed in links of only middle three storeys demonstrated CP performance. Some yielding in the moment resisting beams of interior frames has also observed. In the

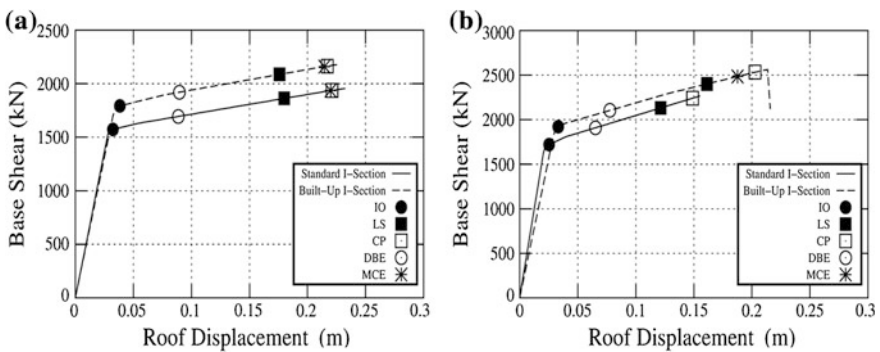


Fig. 5 Capacity curves for 5 storey dual frame buildings, along: **a** longitudinal, and **b** transverse direction

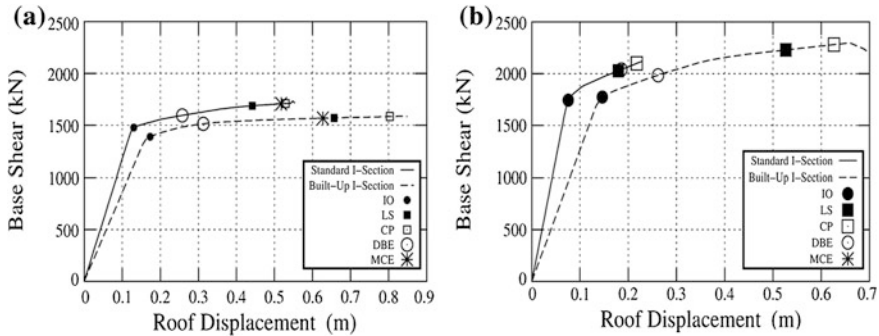


Fig. 6 Capacity curves for 10 storey dual frame buildings, along: **a** longitudinal, and **b** transverse direction

transverse direction, hinges formed in links of third and fourth storeys have crossed CP performance state. The links in these two storeys are shorter as compared to the links in storeys below. The interior beams in the transverse direction of this building, have not yielded. The building with built-up I-sections successfully achieved LS performance at DBE level and CP performance at MCE level of hazard. In the longitudinal direction, yielding in the moment resisting beams of interior frames is also observed.

The capacity curves for 10-storey dual frame buildings are shown in Fig. 6 with buildings behaving similar to 10-storey EBF buildings. The building with standard I-section links demonstrated the desired LS performance at DBE hazard level only in the longitudinal direction. In the transverse direction, the performance has deteriorated to CP at DBE hazard level. Similarly, at the MCE hazard level, the building just managed to reach CP performance in longitudinal direction. The building collapsed under MCE in transverse direction. In both the directions, the links in top storeys did not yield. As shown in Table 5, the displacement ductility capacity is around 4.6 in longitudinal direction and even below 3.5 in transverse direction. The 10-storey dual frame building with built-up I-section showed improved performance by achieving LS performance under DBE and CP performance under MCE. Some of the beams of the interior moment resisting frames have also yielded under flexure to reach IO performance level. The ductility of the buildings is also relatively high with values close to 5.0. The overall performance of this building is satisfactory.

6 Conclusions

Selection of suitable section and length for links in eccentrically braced frames is an important task, which governs the ductility capacity and hence expected performance of the building. For shear as well as flexure links, the storey ductility

increases with increase in link length, while increase in ductility of shear links is much steeper as compared to flexure links. Therefore, to achieve the maximum ductility in a storey, the link length should be kept close to the upper limit of shear critical range.

Model design guidelines for EBF buildings have been suggested based on comparison of different codes. However, the example buildings designed using the proposed guidelines in conjunction with the Indian code, could not yield satisfactory performance, particularly at MCE hazard level, indicating that the value of response reduction factor, prescribed by the Indian Code, needs to be reviewed. The buildings designed with built-up I-section links performed better than the buildings with rolled I-section links, because the flexibility in built-up sections allowed maximization of link length, while ensuring the shear critical behaviour and providing little subjective overstrength in links. The buildings having dual EBF—MRF system, provided improved performance as compared to buildings having only EBF system. Despite improvement over EBF, the performance of dual frame buildings has also not been satisfactory.

References

1. ANSI/AISC 341-10 (2010) Seismic provisions for structural steel buildings. American Institute of Steel Construction, Inc., Chicago
2. AS/NZS 1170.5-2004 (2004) Structural design actions-Part 5: earthquake actions—New Zealand. Standards Australia/Standards New Zealand, Wellington
3. AS/NZS 3404: Part 1-1997 (2007) Steel structures standard. Standards Australia/Standards New Zealand, Wellington
4. ASCE/SEI 41-06 (2006) Seismic rehabilitation of existing buildings. American Society of Civil Engineering, Inc., Reston
5. ASCE/SEI 7-10 (2010) Minimum design loads for buildings and other structures. American Society of Civil Engineering, Inc., Reston
6. EN 1998-1 (2004) Eurocode—design of structures for earthquake resistance-part 1: general rules, seismic actions and rules for buildings. European Committee for Standardization, Brussels
7. Hjelmstad KD, Popov EP (1984) Characteristics of eccentrically braced frames. *J Struct Eng Am Soc Civ Eng* 340-353
8. IS 1893 (Part 1):2002 (2002) Criteria for earthquake resistant design of structures part 1: general provisions and buildings. Bureau of Indian Standards, New Delhi
9. IS 1730:1989 (Reaffirmed 2004) (2004) Steel plates, sheets, strips and flats for structural and general engineering purposes—dimensions. Bureau of Indian Standards, New Delhi
10. IS 800-2007 (2007) General construction in steel—code of practice. Bureau of Indian Standards, New Delhi
11. Popov EP, Engelhardt MD (1988) Seismic eccentrically braced frames. *J Constr Steel Res* 321–354
12. Priestley MJN, Calvi GM, Kowalsky MJ (2007) Displacement-based seismic design of structures. IUSS Press, Pavia, Italy
13. SP-6 (Part 1):1964 (Reaffirmed 1998) (1998) Handbook for structural engineers no. 1, structural steel sections. Bureau of Indian Standards, New Delhi

Bibliography

1. AS/NZS 1170.0-2002 (2002) Structural design actions-part 0: general principles. Standards Australia/Standards New Zealand (Australian/ New Zealand Standard), Wellington
2. EN 1990 (2002) Eurocode—basis of structural design. European Committee for Standardization, Brussels
3. EN 1991-1-1 (2002) Eurocode—actions of structures-part 1-1: general actions—densities, self weights, imposed loads for buildings. European Committee for Standardization, Brussels
4. EN 1993-1-1 (2005) Eurocode—design of steel structures-part 1-1: general rules and rules for buildings. European Committee for Standardization, Brussels

Influence of Joint Panel Zone on Seismic Behaviour of Beam-to-Column Connections

Arnav Anuj Kasar, Rupen Goswami, S.D. Bharti and M.K. Shrimali

Abstract Steel structures, because of their inherent ductility, are considered to be suitable for construction in areas of high seismicity. To ensure a certain expected performance of a structure, concept of strong column weak beam design was introduced and became widely accepted. Effect of strength of joint panel zone (JPZ) on the overall behaviour of strong column weak beam interior beam-to-column strong axis connection is studied, to understand their contribution on the performance of such connections. Three dimensional non-linear finite element analysis of three typical interior beam column joint subassemblages is carried out to study inelastic behaviour of such joints with different column to beam strength ratio. The results indicates that there is significant JPZ deformation leading to the kinking of columns before plastic hinges are formed in the beams even when the beams are weaker than the columns. This is due to inadequate shear strength of the JPZ. Also, excessive kinking in columns may lead to brittle failure of connections far before flexural capacity of beam is reached, thereby causing complete collapse of the structure.

Keywords Panel zone shear strength · Beam-to-column connections · Deformation · Plastic hinges · Kinking of column

1 Introduction

In India, demands of steel construction (i.e., steel structures) have increased significantly in recent years. This is because steel, as a material, possesses high strength-to-weight ratio and material ductility, and is a common choice in countries

A.A. Kasar · S.D. Bharti · M.K. Shrimali (✉)

Department of Civil Engineering, Malaviya National Institute of Technology (MNIT) Jaipur, Jaipur 302017, Rajasthan, India
e-mail: mkshrimali@mnit.ac.in

R. Goswami

Department of Civil Engineering, Indian Institute of Technology (IIT) Madras, Chennai 600036, Tamil Nadu, India

like USA and Japan as construction material. Thus, steel structures are considered to be relatively more ductile than those constructed using any other material. However, performance of steel structures during Northridge Earthquake, 1994 and Kobe Earthquake, 1995 forced researchers to reinvestigate seismic design of steel structures for improved behaviour. The most popular connection scheme employed for beam-to-column strong-axis connection was bolted web welded flange (BWFF) connection. After 1994 Northridge earthquake, it was observed that, one of the key issues was failure in the form of brittle fractures in beam-to-column connection welds [14], which can be attributed to large inelastic strain demand on complete joint penetration (CJP) welds connecting beam flanges to column flanges. Some factors that cause large inelastic strain demand on CJP welds are unreinforced connections, defects in welds and welding procedure (size and shape of weld access holes, backing bar etc.), kinking of column flanges, and yielding of joint panel zone (JPZ). Of these, “controlled inelastic deformation” of JPZ was originally considered to be good structural response.

A number of experimental and analytical investigations have been carried out, since late 1960s, to understand the behaviour of JPZ [10, 13]. These studies suggest that, when subjected to repeated cyclic distortions, yielding of JPZ is a stable phenomenon, and can be helpful in dissipating the energy induced by these distortions. But, it is also evident from these studies that the overall frame stiffness is greatly influenced by the stiffness of the JPZ. Thus, a balanced JPZ design is adopted, which aims at simultaneous onset of flexural hinging in beams and shear yielding in JPZ [7]. Further, in cases where the column is not strong enough in comparison to the beam, weak JPZ, despite of having stable post-yield response, causes large inelastic drifts and loss of overall stiffness of frames, and often leads to kinking of column flanges at the level of beam flanges. This increases curvature and causes failure of welded connections. Indian specifications for design of steel structures needs to put emphasis on this important aspect related to design and detailing of JPZ in steel structures.

2 Background

Steel beam to column joint in moment frames [6] are generally assumed to be rigid when overall analysis or design is carried out of the structure [16]. But the actual behaviour of these joints can be most closely predicted by assuming them to behave in a semi-rigid manner. A critical part of the joint is the JPZ. The overall behaviour of the JPZ along with connections are often classified as rigid, semi-rigid or flexible [4, 9].

Classical seismic design of moment frames depend on inelastic energy dissipation by component elements. These components are the beam, the beam-to-column connections, the JPZ, the column outside the joint, or a combination of these [11].

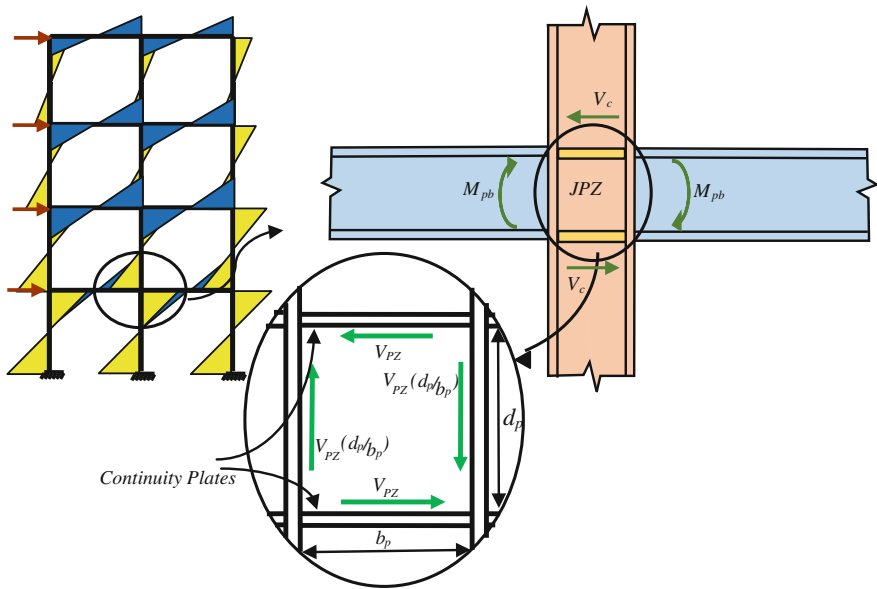


Fig. 1 Forces generated in JPZ in moment frame under lateral seismic actions

Concentration of inelastic action in the column outside the joint is not desired as it can prove to be detrimental to the overall stability of the structure. Similarly, concentration of inelastic action in the connections is detrimental may lead to brittle fractures as observed in past earthquakes. But, controlled ductile shear yielding of the JPZ may be allowed, and sometimes is beneficial to seismic response of the moment frame. However, too flexible JPZ causes secondary effects like kinking of column flange and high interstory drift; the later can cause severe non-structural damage [13]. Based on these, there are three distinct possible philosophies for design of the JPZs. These are, (i) *Strong Panel Zone Design* wherein the JPZ is supposed to remain elastic, forcing inelasticity in the beams; (ii) *Weak Panel Zone Design* wherein inelasticity is confined to the JPZ; and (iii) *Balanced Panel Zone Design* wherein the JPZ is designed such that inelasticity in the JPZ follows inelasticity in the beam [3, 5].

A typical interior beam column joint of a moment resisting frame along with the forces in JPZs is shown in Fig. 1; a JPZ is mostly subjected to pure shear, and produces stable hysteretic shear force-shear deformation response curves under reversed cyclic loading, as during seismic shaking. Controlled yielding of JPZ provides large energy dissipation capacity to the frame, but also leads to large overall deformation [13, 15]. Thus, weak panel zone design, though sometimes used in low-rise buildings, is not suitable for tall buildings.

3 Design of JPZ

The design shear strength (capacity) of JPZ is given by [1]

$$V_d = \phi_v 0.6 F_y d_c t_w, \text{ for } 0 < P \leq P_c \tag{1}$$

$$V_d = \phi_v 0.6 F_y d_c t_w \left(1.4 - \frac{P}{P_c} \right), \text{ for } 0.4 P_c < P \leq P_c \tag{2}$$

When frame stability including JPZ deformation is not considered. When frame stability including JPZ deformation is considered, the design strength is given by

$$V_d = \phi_v 0.6 F_y d_c t_w \left(1 + \frac{3 b_{cf} t_{cf}^2}{d_b d_c t_w} \right), \text{ for } 0; P \leq 0.75 \leq P_c, \text{ or} \tag{3}$$

$$V_d = \phi_v 0.6 F_y d_c t_w \left(1 + \frac{3 b_{cf} t_{cf}^2}{d_b d_c t_w} \right) \left(1.9 - \frac{1.2 P}{P_c} \right), \text{ for } 0.75 P_c < P \leq P_c, \tag{4}$$

Here, V_d is design shear capacity of JPZ, ϕ_v is resistance factor (in LRFD), F_y is minimum specified yield strength of column material, d_c is depth of column section, t_w is thickness of web of column section, P is factored axial load on the column, P_c is $0.6 P_y$ where P_y is the squash load of column, b_{cf} and t_{cf} are width and thickness of the column flange respectively, and d_b is the depth of deeper beam framing into the joint.

The shear force on a JPZ in an interior beam column joint of a moment frame, as shown in Fig. 1, is given by

$$V_{pz} = \frac{\sum M_{pb}}{(d_b - t_{bf})} \left(1 - \frac{(d_b - t_{bf})}{(H - d_b)} \right), \tag{5}$$

where, H is the height of column between two stories, $\sum M_{pb}$ is sum of resisting moments of beams framing in to the joint, and P_y is the squash load of the column. Thus, the minimum thickness t_{pz} of JPZ (including the thickness of doubler plates, if any) that is required to prevent yielding of JPZ is given by

$$t_{pz} \geq \frac{1}{F_y \left\{ 1 - \left(\frac{P}{P_c} \right)^2 \right\}^{1/2}} \frac{\sum M_{pb}}{(d_c - 2 t_{cf})(d_b - t_{bf})} \left(1 - \frac{(d_b - t_{bf})}{(H - d_b)} \right). \tag{6}$$

This assumes uniform distribution of shear stress within JPZ that is proved to be valid by many experimental investigations [2, 10, 11]. Also, this is the minimum thickness that will ensure that shear yielding in JPZ initiates only after flexural yielding of beams [12].

But, often design codes and guidelines directly prescribe minimum thickness of JPZ to be provided, instead of guidelines to design the JPZ. For instance, the required minimum thickness of JPZ for simultaneous shearyielding of panel zone and flexural yielding of beam is as

$$t = \frac{C_y M_c \left(\frac{H-d_b}{H} \right)}{(0.9)0.6F_y R_{yC} d_c (d_b - t_{bf})}, \quad (7)$$

where, R_{yC} is ratio of expected yield strength of column material to minimum specified yield strength, and M_c and C_y are coefficients to account for moment at column centreline resulting from moment amplification due to plastic hinging in beam and strain hardening of material of column, respectively. Alternatively, the required minimum thickness of the JPZ is given by

$$t \geq (d_p + b_p)/90, \quad (8)$$

where, d_p is panel zone depth between continuity plates, and b_p is the width of the panel zone between column flanges.

4 Structural Models and Analyses

Three different combinations of strong column weak beam (SCWB) strong-axis joint subassemblages are selected and analysed to illustrate JPZ behaviour; column to beam strength ratio $\sum M_{pc}/\sum M_{pb}$ considered are 1.1, 1.2 and 2.1. Each beam-column combination is used to model an interior beam column joint, as per specifications given in Indian Standard 800 [9], with continuity plates to reinforce the joints. The beams, columns and continuity plates are assumed to be of grade ASTM A36 steel with isotropic hardening model (yield stress of 250 MPa and ultimate stress of 415 MPa). The height of columns considered in the subassemblages is 3.8 m, which, in most cases, is the average storey height (Fig. 2). The distance considered between column centreline and the point of application of load on beams is 3.0 m, representing span of beam. AISC wide flange plastic sections are used for beams and columns. The thickness of continuity plates are considered to be equal to beam flange thickness, length equal to the clear distance between column flanges, and width equal to clear flange width of the column.

Nonlinear analyses are carried out on 3-dimensional solid models of the interior joint subassemblages using finite element analysis software ABAQUS [8]. A uniform mesh is developed for the models using eight noded linear brick element (C3D8R). SAC's standard loading protocol (Fig. 3) is used for analyses to obtain the differences in responses of these beam column joints. Axial compressive load is not considered on the columns, to reduce the number of parameters on which shear capacity of JPZ depends.

Fig. 2 Typical interior beam-column joint subassemblage

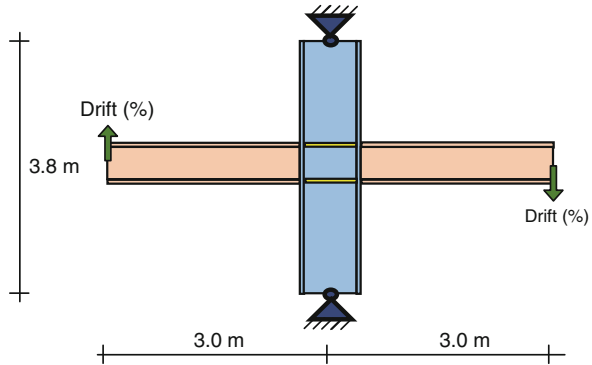
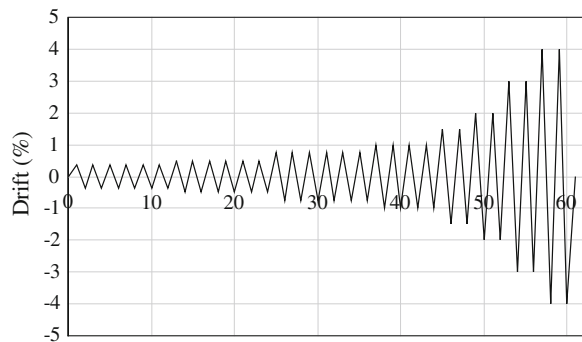


Fig. 3 Multi-cycle standard loading protocol



5 Results and Discussion

Results of nonlinear finite element analyses indicate that significant shear yielding occurs in panel zones in all three beam-column joint subassemblages without formation of flexural plastic hinge in beams. Yielding of JPZ occurs despite satisfying two key requirements of design codes, namely SCWB design and minimum thickness of JPZ, as listed in Table 1. This indicates that explicit design provisions are required to ensure plastic hinge formation in beam prior to shear yielding of JPZ. First yield in JPZ occurs at beam end drift of about 0.75 % (drift of 22.5 mm; rotation of 0.0075 rad).

Figure 4 shows the state of shear stress (in MPa) at 4 % drift level in the joint of the three subassemblages; complete yielding of JPZs in shear is seen (yield strength in shear being 145 MPa). Also, there is concentration of high (negative) shear at the beam flange levels, which are usually conceived to carry only flexure. Further, kinking of columns is evident due to shear distortion of the JPZ in all the three subassemblages, irrespective of the column to beam strength ratio.

Figure 5 shows von Mises stress (in MPa) at 4 % drift level in the joint of the three subassemblages; yielding of beam flanges is seen due to large normal stress.

Table 1 Performance of selected interior joint subassemblages

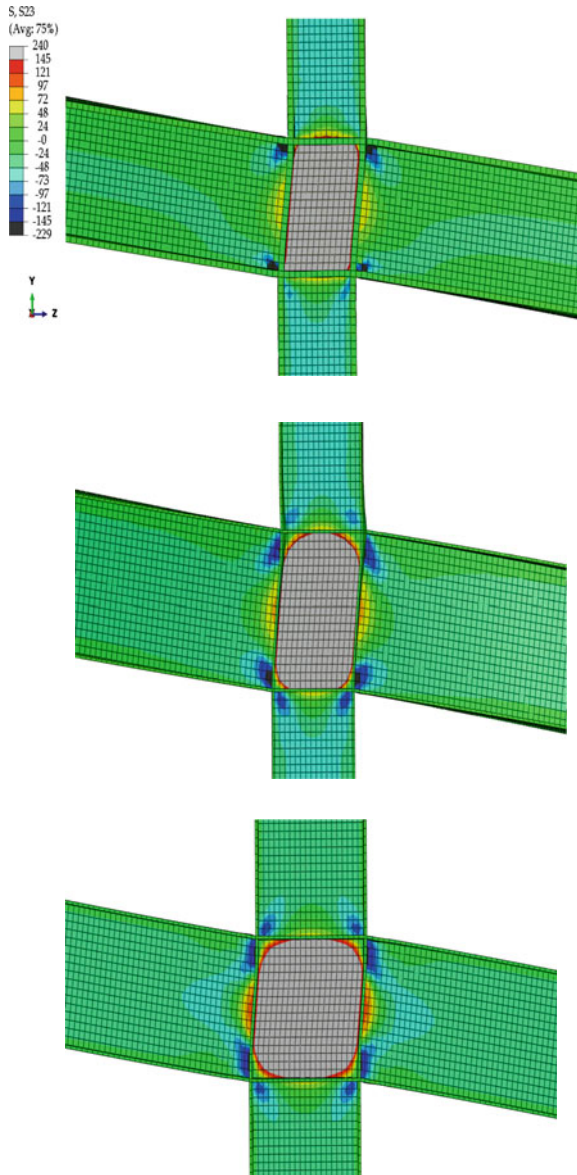
#	Column	Beam	$\frac{M_{cC}}{M_{cB}}$	$L_{JPZ, reqd}$ (mm)	$L_{JPZ, prov}$ (mm)	$V_{CAPACITY}$ (kN)	V_{DEMAND} (kN)	$\frac{V_{DEMAND}}{V_{CAPACITY}}$	Yielding of JPZ
1	W14×257	W18×192	1.1	9	48	1,877	6,537	3.5	Yes
2	W18×86	W24×62	1.2	11	20	841	1,744	2.1	Yes
3	W24×131	W21×73	2.1	12	24	1,400	2,281	1.6	Yes

But, the level of inelasticity in the beam is nominal in the subassemblages with column to beam strength ratios of 1.1. Yielding of flanges of the beams progressively increases with increase in column to beam strength ratio. But, the local yielding of columns is also seen, with least yielding of column in the subassemblage with column to beam strength ratio of 2.1. This indicates that higher column to beam strength ratio is required as yielding of column is not acceptable.

Further, it is also observed that large inelastic deformation JPZs causes large inelastic strain demand at weld regions in all the three subassemblages, irrespective of the value of column to beam strength ratio. This leads to brittle fracture of CJP welds connecting the beam flanges to the columns, as was observed in the Northridge and Kobe earthquakes. It is also pertinent to mention that premature yielding of JPZs in shear leading to kinking of column flanges at the beam flange levels restrains the beams in the joint region from developing their full flexural plastic capacity, thereby nullifying the whole SCWB design intent, although large amount of energy dissipation is possible due to inelastic shear deformation of JPZs.

The maximum shear demand to shear capacity of the three JPZs is in the range 1.6–3.5 at drift level of 4 %, as shown in Table 1. These results indicate that the shear strengths of JPZs are inadequate for all values of column to beam strength ratio. Thus, the minimum thickness of JPZ requirement given in IS 800 is not sufficient to prevent yielding of JPZs prior to formation of flexural plastic hinge in beams—JPZs need to be designed for the maximum expected demand as given by Eq. 5. Unless the JPZs are designed not to yield prior to yielding of beams, rigid connection behaviour is not realisable as envisaged by IS 800, particularly in special moment frames. Also, the criterion to ensure SCWB design alone does not ensure that plastic hinge will form in the beam before yielding of the JPZs.

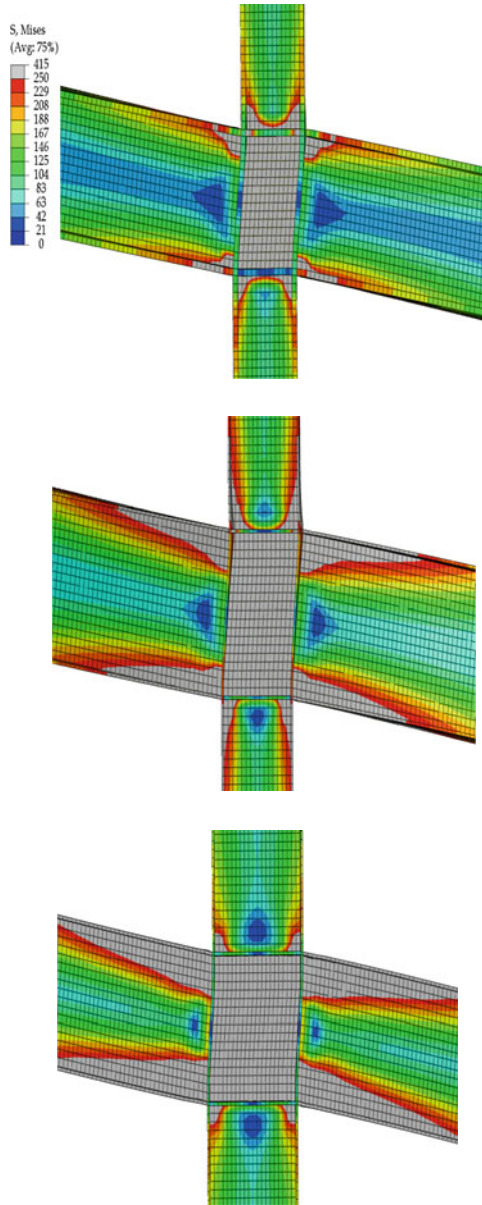
Figure 6 shows the variation of shear demand on JPZ normalized with shear capacity of JPZ attained as per SAC’s standard loading protocol; the hysteresis response curves corresponds to different values of column to beam strength ratio. The response curves show stable inelastic load deformation response in all three joint subassemblages, irrespective of the column to beam strength ratio. This is representative of stable yielding behaviour of JPZs in shear.



W18x192 Beam and W14x257 Column
W24x62 Beam and W18x86 Column
W21x73 Beam and W24x131 Column

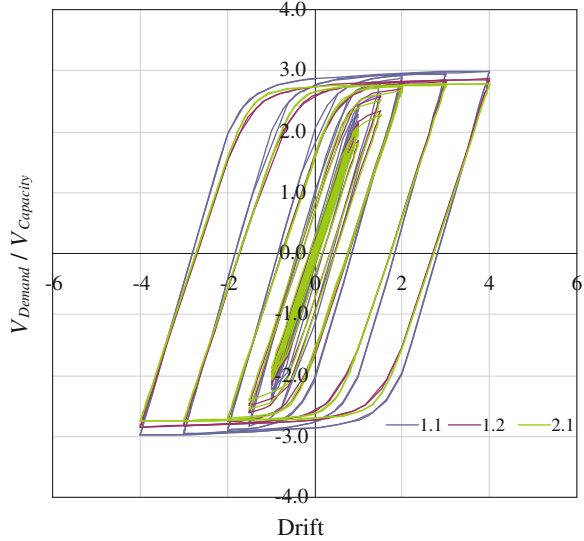
Fig. 4 Distribution of shear stress (in MPa) at 4 % drift

Fig. 5 Distribution of von Mises stress (in MPa) at 4 % drift



W18x192 Beam and W14x257 Column
W21x73 Beam x W24x131 Column
W24x62 Beam and W18x86 Column

Fig. 6 Hysteresis curves showing variation of normalised shear in JPZs under multi-cycle standard loading protocol



6 Conclusion

Premature yielding of JPZs limits formation of plastic flexural hinges in beams, even when SCWB design philosophy is employed. This indicates that JPZs need to be strengthened to resist the shear demand produced. Thus, it is concluded that the strength hierarchy between columns and beams is a necessary but not sufficient condition to ensure flexural yielding of beams. Design provisions in IS 800 need to include strength design of JPZs to avoid premature yielding of JPZs.

References

1. AISC 341-10 (2010) Seismic provisions for structural steel buildings, American Institute of Steel Construction, Chicago
2. Bertero VV, Popov EP, Krawinkler H (1973) Further studies on seismic behaviour of steel beam-column subassemblages. Report No. UCB/EERC-73/27, earthquake engineering research center, University of California, Berkeley
3. Bertero VV, Popov EP, Krawinkler H (1972) Beam-column subassemblages under repeated loading. *J Struct Eng ASCE* 98(ST5):1137–1159
4. Bjorhovde R, Colson A, Brozzetti J (1990) Classification system for beam-to-column connections. *J Struct Eng* 116(11):3059–3076
5. Englekirk RE (1999) Extant panel zone design procedures for steel frames are questioned. *Earthq Spectra EERI* 15(2):361–369
6. FEMA 350 (2000) Recommended seismic design criteria for new steel moment-frame buildings. Federal Emergency Management Agency, Washington
7. FEMA 355D (2000) State of the art report on connection performance. Federal Emergency Management Agency, Washington

8. HKS (2013) ABAQUS/Standard User's Manual. Hibbit, Karlsson and Sorensen, ABAQUS Inc., Pawtucket
9. IS 800:2007 (2007) General construction in steel: code of practice. Bureau of Indian Standards, New Delhi
10. Krawinkler H (1978) Shear in beam-column joints in seismic design of steel frames. Eng J AISC 15(3):82–91
11. Krawinkler H, Bertero VV, Popov EP (1971) Inelastic behaviour of steel beam-to-column subassemblages. Report No. UCB/EERC-71/7, earthquake engineering research center, University of California, Berkeley
12. Mazzolani FM, Piluso V (1996) Theory and design of seismic resistant steel frames. E and FN SPON 1996, ISBN: 0 419 18760 X
13. Popov EP (1988) Seismic moment connections for MRFs. J Constr Steel Res 10:163–198
14. Roeder CW, Foutch DA (1996) Experimental results for seismic resistant steel moment frame connections. J Struct Eng 122(6):581-588
15. Schneider SP, Roeder CW, Carpenter JE (1993) Seismic behavior of moment-resisting steel frames: experimental study. J Struct Eng ASCE 119(6):1885–1902
16. SP 6 (6) (1973) Handbook for structural engineers: application of plastic theory in design of steel structures. Bureau of Indian Standards, New Delhi

Bibliography

1. Nakashima M, Roeder CW, Maruoka Y (2000) Steel moment frames for earthquakes in United States and Japan. J Struct Eng 126(8):861–868
2. Tsai K, Popov EP (1988) Steel beam-column joints in seismic moment resisting frames. Report No. UCB/EERC-88/19, earthquake engineering research center, University of California, Berkeley

Performance Based Seismic Design of Reinforced Concrete Symmetrical Building

P.D. Pujari and S.N. Madhekar

Abstract One of the major developments in seismic design over the past decade has increased because of the continuing desire to limit excessive damage and maintain function of the structure after a moderate earthquake. Therefore, performance based seismic design and analysis is gaining popularity. The objective of performance-based analysis is to produce structures with predictable seismic performance. The prediction of ductility, capacity and demand is very important to understand the seismic performance and inelastic responses of a building subjected to earthquake ground motions. The nonlinear static analysis of a G+15 reinforced concrete building is carried out in SAP2000 software. The building is subjected to six different earthquake ground motions. Two models are considered for analysis as frame with infill walls and frame without infill walls effect. Infill walls are provided throughout the building frame except the ground storey to study the open ground storey effect. The comparison is done with respect to parameters as maximum base shear, drift ratios and top storey displacement for three different performance levels as immediate occupancy (IO), life safety (LS) and collapse prevention (CP). Analysis shows that due to open ground storey damage is localized to members in the ground storey alone, which is not captured by the bare frame analysis. Ductility requirement for frames without infill walls is higher than for frames with infill walls. The ductility requirement increases as we move towards lower performance objective (i.e. from IO to CP). Inelastic displacement demand ratio (IDDR) value for frame with infill is lower as compared to frame without infill walls. IDDR value increases from lower performance level to higher performance level. (i.e. from IO to CP). For frame without infill effect, the base shear is lower as compared with frame with infill walls and the displacement of storey is much higher for frame without infill walls as compared to frame with infill walls. The infill walls effect shows major change in the performance of building and the needs to be considered in the

P.D. Pujari (✉) · S.N. Madhekar
Department of Applied Mechanics, College of Engineering, Pune, India
e-mail: pujariPriya528@gmail.com

S.N. Madhekar
e-mail: snm.civil@coep.ac.in

analysis. Performance based design technique helps to determine how the building will perform under seismic effects; well in advance. Accordingly, one can undertake suitable measures to achieve the same.

Keywords Performance based · Pushover · FEMA · Capacity demand · Performance point · SAP2000

1 Introduction

Performance based seismic design came into existence after the Northridge earthquake (1994). It begins with the selection of design criteria stated in the form of one or more performance objective. The main objective of performance based design is to develop structures with predictable damage. An elastic analysis cannot predict failure mechanism and reasonable estimates of inelastic deformation or damage in structures. Inelastic procedures help in identifying modes of failure and the potential for progressive collapse. Nonlinear dynamic response history analysis is capable of providing the required information, but may be very time-consuming. For this purpose static pushover analysis is used to get the insight of nonlinear behavior of the structure.

Pushover analysis which is an iterative procedure is looked upon as an alternative for the conventional analysis procedures. The recent advent of performance based design has brought the non linear static push over analysis procedure to the forefront. Pushover analysis is a static nonlinear procedure in which the magnitude of the structural loading along the lateral direction of the structure is incrementally increased in accordance with a certain pre-defined pattern. It is generally assumed that the behavior of the structure is controlled by its fundamental mode and the predefined pattern is expressed either in terms of story shear or in terms of fundamental mode shape. With the increase in magnitude of lateral loading, the progressive nonlinear behavior of various structural elements is captured, and weak links and failure modes of the structure are identified. In addition, pushover analysis is also used to ascertain the capability of a structure to withstand a certain level of input motion defined in terms of a response spectrum.

2 Pushover Methodology

ATC 40, FEMA 273, FEMA 356 and FEMA 440 have described the pushover analysis procedure, modeling of different components and acceptable limits. Two methods, namely capacity spectrum method and displacement coefficient method are introduced in FEMA 440. This analysis procedure considers only first mode shape of the equivalent single degree-of-freedom system. This is the limitation of this method. Still it is very efficient analysis procedure because it gives insight of the nonlinear behavior of the structure. A key requirement of any meaningful

performance based analysis is the ability to assess seismic demands and capacities with a reasonable degree of certainty.

The overall capacity of a structure depends on the strength and deformation capacity of the individual components of the structure. In order to determine capacities beyond the elastic limits, some form of nonlinear analysis, such as the pushover procedure, is required. This procedure uses a series of sequential elastic analysis, superimposed to approximate a force displacement capacity diagram of the overall structure. A lateral force distribution is again applied until additional components yield. This process is continued until the structure becomes unstable or until a predetermined limit is reached.

Ground motion during an earthquake produces complex horizontal displacement patterns in the structure. It is impractical to trace this lateral displacement at each time-step to determine the structural design parameters. The traditional design methods use equivalent lateral forces to represent the design condition. For nonlinear methods it is easier and more direct to use a set of lateral displacements as the design condition. For a given structure and ground motion, the displacement demand is an estimate of the maximum expected response of the building during the ground motion. Once, a capacity curve and demand displacement, are defined, a performance check can be done.

3 Procedure to Get Capacity and Demand Curves by Capacity Spectrum Method

3.1 Capacity Curve

The overall capacity of a structure depends on the strength and deformation capacities of the individual components of the structure. This procedure uses sequential elastic analysis, superimposed to approximate force-displacement diagram of the overall structure. The mathematical model of the structure is modified to account for reduced resistance of yielding components. A lateral force distribution is again applied until additional components yield [1].

3.2 Demand Curve

Ground motion during an earthquake produces complex horizontal displacement patterns which may vary with time. Tracking this motion at every time step to determine structural design requirements is impractical. For a given structure and a ground motion, the displacement demands are estimated for the maximum expected response of the building during the ground motion. Demand curve is a representation of the earthquake ground motion [1].

3.3 Performance Point

Performance point can be obtained by superimposing capacity spectrum and demand spectrum. The intersection point of these two curves is the performance point.

4 Pushover Analysis in SAP2000

The analysis in SAP2000 involves the following steps:

A building frame is modeled in SAP2000. The member properties are assigned and the model is loaded based on the loading calculated. A gravity analysis is carried out. The lateral loads and their vertical distribution on each floor level are determined as per IS 1893 [2]. After assigning all properties to model, the gravity analysis is carried out. The model is then unlocked and push load is defined in the load case. Pushover hinges in terms of allowable plastic rotations are defined. The program includes several built-in default hinge properties that are based on average values from ATC 40 for concrete members and average values from FEMA-273 for steel members. In this analysis, P-M-M hinges have been defined at the column ends and M-3 hinges have been defined at both the ends. After the analysis different curves can be obtained and they are studied to get the required parameters.

5 Description of the Structure

The main objective of performance based design is to produce structures with predictable damage. An elastic analysis cannot predict failure mechanism and reasonable estimates of inelastic deformation or damage in structures. Inelastic procedures help in identifying modes of failure and the potential for progressive collapse. Nonlinear dynamic response history analysis is capable of providing the required information, but may be very time-consuming. For this purpose static pushover analysis is used to get the insight of nonlinear behavior of the structure.

The G+15 bare frame building is considered in this study. This structure is designed according to IS 456-2000 [3]. The material properties are M25 Grade concrete, Fe415 steel for the yield strength of the longitudinal and transverse reinforcement. The plan layout is shown in Fig. 1. The height of first storey is 4 m. The depth of foundation is assumed as 1.5 m. Remaining all storeys height is 3.5 m.

Normally, infill walls are considered as non-structural member, however, practically they provide significant stiffness under lateral load. If special provisions have not been followed in design, absence of infill at ground storey will lead to formation of soft ground storey. In addition to this, under lateral loading, lack of infill stiffness will lead to larger inter-storey drift concentrated to ground storey,

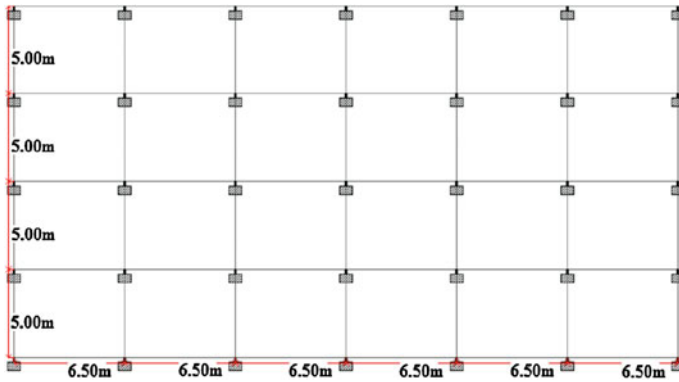


Fig. 1 Plan of building frame

leading to an early formation of plastic hinges, further impending collapse of structure. Therefore, for an RCC building considering infill wall effect a systemic nonlinear static analysis procedure is essential.

6 Modelling Considerations in SAP2000

In all the models, the support condition is assumed to be fixed. All the slabs are considered as shell element. The infill walls were provided below all the beams except the first floor beams. The thickness of wall considered is 230 mm. The material properties of masonry infill wall are modulus of elasticity: 13,800 MPa, Density: 20 kN/m³, Poisson's ratio 0.2.

Federal Emergency and Management Authority provide guidelines for how to generate infilled wall models in RC frame for analysis. The elastic in plane stiffness of a solid unreinforced masonry infill panel prior to cracking shall be presented with an equivalent diagonal compression strut of a width 'a'.

The equivalent strut shall have the same thickness and modulus of elasticity as the infill panel it represents.

7 Defining Hinge Properties for Strut

In this study, wall is considered as strut. If the lateral force is applied on building then the force is developed in strut which acts like a compression strut. Axial hinge is provided at the centre of the strut. Yield force is calculated based on formulae given in FEMA 356 [4].

Based on FEMA 356 [4] the values of acceptable criteria of hinge are calculated. Axial properties are defined based on nonlinear properties such as yield force, displacement control parameter and acceptance criteria.

8 Performance Verification Parameters

The seismic performance of a building can be evaluated in terms of pushover curve, performance point, displacement ductility, plastic hinge formation etc.

(1) Pushover Curve

The base shear versus roof displacement curve is obtained from the pushover analysis from which the maximum base shear capacity of structure can be obtained. This capacity curve is transformed into capacity spectrum ATC40 and demand or response spectrum is also determined for the structure for the required building performance level. The intersection of demand and capacity spectrum gives the performance point of the structure analyzed. At the performance point, the resulting responses of the building should then be checked using certain acceptability criteria.

From Fig. 2 it can be seen that the performance point is at location of base shear of 4603.602 kN and displacement at 0.076 m. It can be seen that the performance point lies well within elastic range and complete capacity of structure is not utilized. The inelastic capacity of structure needs to be taken into account to achieve better performance of building.

(2) Inter-storey drift

Inter-storey drift is defined as the ratio of relative horizontal displacement of two adjacent floors and corresponding storey height (h).

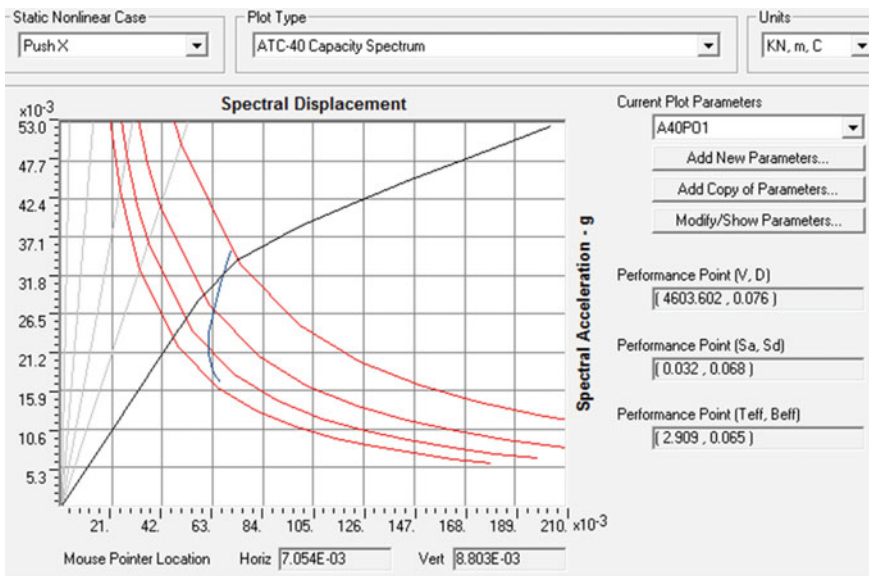


Fig. 2 Pushover curve as per ATC 40

(3) Ductility demands

Ductility demands of the structure for various levels of performance can be expressed in terms of Inelastic Displacement demand ratio (IDDR). IDDR represents the ratio of inelastic displacement demand over the ultimate inelastic displacement capacity.

(4) Pattern of hinge formation

The sequence of plastic hinge formation and state of hinge at various levels of building performance can be obtained from SAP2000 output. This gives the information about the weakest member and so the one which is to be strengthened in case of a building need to be retrofitted. Accordingly the detailing of the member can be done in order to achieve the desired pattern of failure of members in case of severe earthquakes. If the predefined performance objective is not satisfied then redefine the objective, else enhance the structures capacity to withstand the seismic damage achieve the objective.

Figure 3 shows the hinge formation pattern considering infill walls and Fig. 4 shows the hinge formation pattern considering without infill walls.

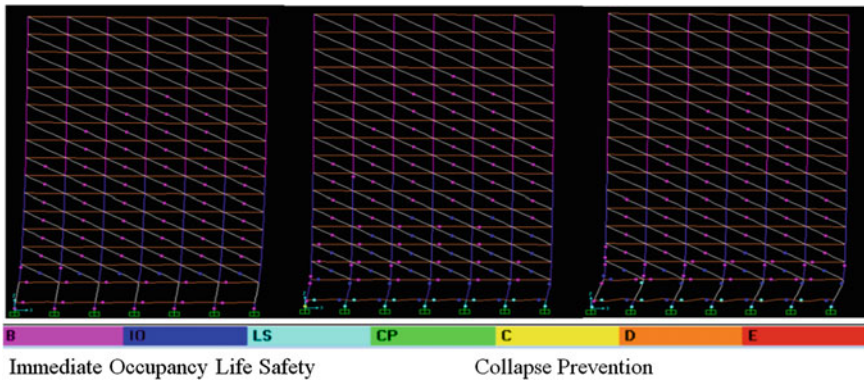


Fig. 3 Hinge Pattern for G+15 building subjected to Northridge time history (with infill)

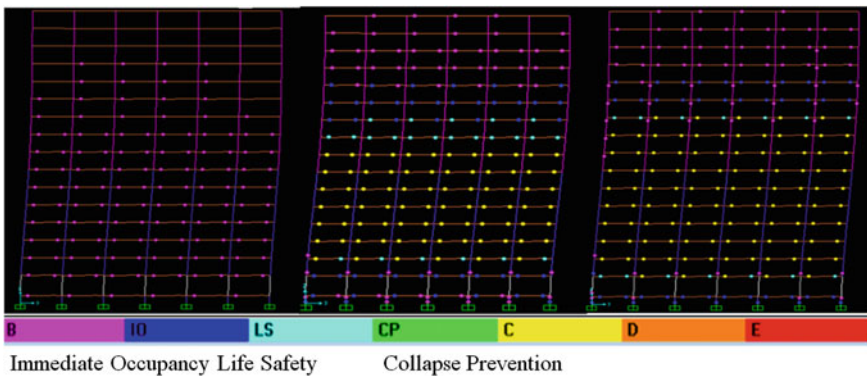


Fig. 4 Hinge Pattern for G+15 building subjected to Northridge time history (without Infill)

8.1 Observations from Hinge Formation Pattern (Fig. 3 to 4)

- (i) Pushover analysis results shows the pattern of hinges formed in the structure.
- (ii) For Immediate occupancy level, the hinges are in pink color at all floor levels in case of without infill wall.
- (iii) For with infill analysis, the open ground storey has crossed the Immediate occupancy level, rotations are maximum.
- (iv) Actual failure pattern due to open ground storey effect is seen.
- (v) Sequence of hinge formation and state of hinge shows the critical zone of failure which helps in necessary retrofitting techniques and detailing to reduce the damage.

9 Results

Pushover analysis G+15 framed building is carried out. The analysis is done for two cases i.e. one with bare frame and the other, considering the infill wall effect. For infill wall analysis the lower storey is kept open i.e. to consider the effect of open ground storey. Six different time histories are considered viz., Northridge (1994), Kobe (1995), El Centro (1940), Bhuj (2001), Koyana (1967) and Uttarkashi (1991). Three performance levels considered are Collapse Prevention (CP), Life Safety (LS) and Immediate Occupancy (IO). The comparison of performance parameters is done with respect to parameters like base shear, IDDR, IDR and ductility requirement.

- (i) The value of base shear for without infill wall is lower as compared to with infill wall. Infill walls increases the stiffness of the structure and attracts large force. Bare frame (without infill walls) are less stiff as compared to with infill frames and are flexible. Hence, bare frame structure attracts less force and value of base shear is less.
- (ii) The ductility requirement for without infill wall case is higher as compared to with infill case. The increase in lateral stiffness for infill wall building helps to resist more force. The capacity of structure is utilized completely for infill wall building. In case for without infill wall building because of less lateral stiffness the member capacity is not utilized completely. Hence ductility requirement increases.
- (iii) The inelastic displacement demand ratio (IDDR) values for without infill wall case is higher as compared to with infill case. IDDR depends on ductility requirement. The above explanation also holds well in case of IDDR.

The comparison of parameters is done and graphical representation of base shear versus displacement is done for six different earthquake ground motions. Each graph for a particular time history shows the variation of base shear vs. displacement for bare frame and infill frame with three performance levels (Collapse Prevention CP,

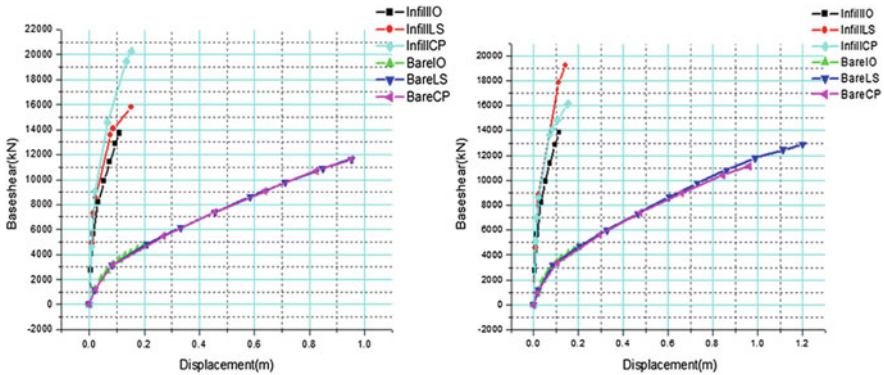


Fig. 5 Base shear versus displacement curves for G+15 building

Life Safety LS and Immediate Occupancy IO). Figure 5 shows the graphical representation of base shear versus displacement for different time histories.

10 Conclusions

In the present study, pushover analysis of G+15 reinforced concrete building is carried out. Further, two cases are considered, one is bare frame analysis (without infill) and another one is considering infill walls with open ground storey. The building models are subjected to six different earthquake ground motions viz., Northridge (1994), Kobe (1995), EI Centro (1940), Bhuj (2001), Koyana (1967) and Uttarkashi (1991). The comparison is made for three performance levels such as Collapse Prevention (CP), Life Safety (LS) and Immediate Occupancy (IO). A G +10 structure is analyzed with isolated base and the performance is compared with fixed base.

Based on the analysis results for all cases considered, following conclusions are drawn:

1. Due to inclusion of infills, behaviour and failure modes of buildings change. The results show the importance of considering infill walls in modeling, to get the real scenario of damage.
2. The IDDR values, ductility requirements and displacement are greater for bare frame. This leads to more consumption of material.
3. Pushover analysis result shows the effect of open ground storey and true failure mechanism. This effect is not captured in structural design and leads to catastrophic failure of structure.
4. From pushover analysis results the weak links in the structure are identified and the performance level achieved by structure is known. This helps to find the retrofiting location to achieve the performance objective.

5. Performance based seismic design helps to understand the behaviour of building well in advance and redesigning can help to improve the performance of structure. Non linear static analysis which is easy and requires less time as compared to time history analysis, provides the complete insight of structure in advance and design it accordingly to improve the performance of structure.

References

1. Applied Technology Council (ATC-40) (1996) Seismic evaluation and retrofit of concrete buildings, vol 1. California Seismic Safety Commission, California
2. IS 1893 (2002) Criteria for earthquake resistant design of structures. Part 1-General Provisions and Buildings Bureau of Indian Standards, New Delhi
3. IS 456 (2000) Code of practice for plain and reinforced concrete. Bureau of Indian Standards, New Delhi
4. American Society of Civil Engineers (ASCE) (2000) Prestandard and commentary for the seismic rehabilitation of buildings, FEMA-356. Washington, DC

Bibliography

1. Belejo A, Bento R, Maiode, Influence of modelling issues on nonlinear static seismic analysis of a regular 3D steel structure. ISSN:0871-7869
2. Mwafy AM, Elnashai AS (2001) Static pushover versus dynamic collapse analysis of RC building. Eng Struct 23:407–424
3. Applied Technology Council (ATC) (1997) NEHRP guidelines for the seismic rehabilitation of buildings, FEMA 273 report, Washington, DC
4. Computers and Structures SAP2000: three dimensional static and dynamic finite element analysis and design of structures. Computers and Structures Inc., Berkeley
5. Raju KR, Cinitha A, Nagesh RI (2012) Seismic performance evaluation of existing RC buildings designed as per past codes of practice, Sadhana, vol 37, Part 2. Indian Academy of Sciences
6. SEAOC (1995) Vision 2000: performance based seismic engineering of buildings. Structural Engineers Association of California, Sacramento

Response of R/C Asymmetric Community Structures Under Near-Fault Motion

Subhayan Bhaumik and Prithwish Kumar Das

Abstract Seismic vulnerability of asymmetric structures is repeatedly reported by different seismic damage surveys conducted all over the world. Moreover, it is also pointed out by a number of previous research efforts that such damage is more severe in R/C structures due to progressive strength and stiffness degradation of R/C structural elements. Community structures like auditoriums generally have load resisting elements distributed only near the boundary region of the structures leaving a large empty space at the central region. These types of structures are also having very small natural periods due to their comparatively less height than other type of residential or official building structures. Moreover, most of these auditorium structures generally have similar type of orientation in two opposite side whereas other two sides differs in orientation due to functional requirements which lead these types of structures having unidirectional asymmetry. Investigation of response of such systems under near-fault ground excitation are of great importance as there may be a huge gathering of people inside an auditoriums and amount of energy input to the structural systems will be much more in near-fault ground motions are than their far-field counter parts. On this aspect the present research effort investigates the responses of such uni-directionally asymmetric auditorium like community structural systems under a number of real earthquake ground excitation of near-fault nature and a general trend of behaviour is indicated along with comparison between responses of R/C and steel structures of these types.

Keywords Asymmetric structures • Earthquake • Near-fault motion • Reinforced concrete

S. Bhaumik (✉) · P.K. Das
Department of Aerospace Engineering and Applied Mechanics,
Indian Institute of Engineering Science and Technology,
Erstwhile Bengal Engineering and Science University,
Botanic Garden, Shibpur, West Bengal, India
e-mail: subhayan360@gmail.com

1 Introduction

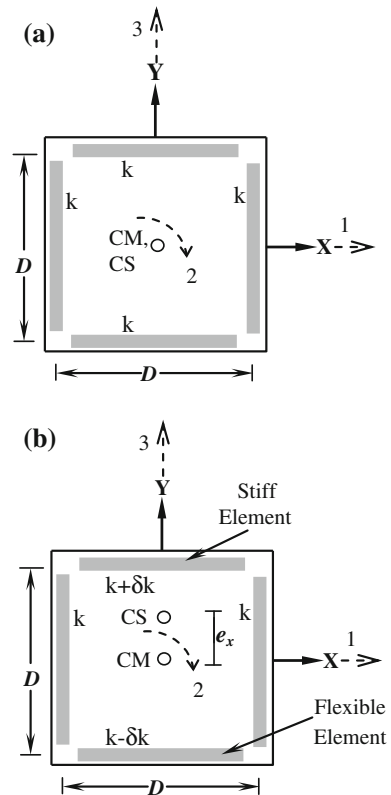
It is already well established all over the globe that asymmetric structures are more susceptible to seismic damage than the structures having symmetric configurations. Hence, over last few decades a large number of investigations have been conducted on elastic as well as inelastic range of seismic response for asymmetric structural systems to find out the cause as well as extent of seismic vulnerability of asymmetric structures. Majority of these investigations considered bi-linear elasto-plastic load-deformation behavior for lateral load resisting structural elements, which is suitable for steel-framed buildings constructed in advanced financially strong countries. But in most of the developing countries like ours buildings as well as community structures like auditoriums are constructed with reinforced concrete (R/C) structural elements to reduce the cost of construction. These R/C structural elements may undergo considerable amount of strength and stiffness degradation when subjected to inelastic range of reversible or repetitive loading during large earthquakes. These degrading features generally aggravate severely displacement demand as well as energy dissipation demand of R/C lateral load resisting structural elements in case of asymmetric structures. Few recent study investigated the effect of strength and stiffness degradation [2, 5, 6] on seismic response of idealized R/C structural system with unidirectional as well as bidirectional asymmetry. However, most of these investigations considered spectrum consistent as well as real earthquake data of far-field nature. Moreover, these investigations considered a general class of buildings having their lateral load resisting elements uniformly distributed over their plan areas. On the other hand, specialized structures like auditoriums have their lateral load resisting element distributed near the edge region of the structure. A previous study [4] investigated the response of such system in a limited form using only spectrum consistent simulated far field ground excitations. It is worthwhile to mention that these types of community structures are primarily made to accommodate huge gatherings. It is obvious that the energy input by near-fault ground excitations are much more than that of far-field ground motions due to proximity of epicenter in this type of seismic event. Hence, there remains a possibility of huge casualty due to collapse of R/C community structures with unavoidable plan-asymmetry under severe near-fault ground excitations. As most of these auditorium structures generally have similar type of orientation in two opposite side whereas other two sides differs in orientation due to functional requirements which lead these types of structures having unidirectional asymmetry. In this viewpoint, in the limited scope of the present research effort investigation of the response of such uni-directionally asymmetric structures under real near-fault ground excitations in a fruitful way.

2 Structural Systems and Method of Analysis

The idealized one-storied structural systems used in the present investigation are consist of single story rigid diaphragm model with three degrees of freedom, two translations in two mutually orthogonal directions and one in-plane rotation as shown in Fig. 1. Masses are assumed to be lumped at the floor, which is considered as rigid in its own plane as well as in flexure. Generally, in case of community structures like auditorium, lateral load-resisting structural members remain distributed near the boundary region of the structures. Thus, in the present study, to represent such a plan-wise distribution of the stiffness, structure has been idealized with four element system as also used in a previous investigation [4]. The total lateral stiffness in one direction is distributed between two edge elements in that direction. Figure 1a represents the schematic diagram of such idealized symmetric structural system.

The stipulated amount of eccentricity is introduced by increasing the stiffness of the lateral load-resisting element of one edge by a calculated amount and decreasing the same of the opposite edge element by the equal amount. The lateral load-resisting

Fig. 1 Idealized structural system



edge element with lesser stiffness is designated as flexible element and the opposite edge element having greater stiffness is referred to as stiff element. Three representative values of normalized eccentricities namely $e_x/D = 0.05$, $e_x/D = 0.1$, $e_x/D = 0.2$ are considered in this investigation where e_x is the eccentricity in x direction and D is distance between two edge element in x or y direction. In the limited scope of the present paper, some representative results of uni-directionally asymmetric systems (as presented in Fig. 1b) are presented.

The coupled equations of motion for considered the asymmetric structural system can be written by two translational as well as one rotational degrees of freedom as:

$$\begin{bmatrix} m & 0 & 0 \\ 0 & mr^2 & 0 \\ 0 & 0 & m \end{bmatrix} \begin{Bmatrix} \ddot{u}_x \\ \ddot{\theta} \\ \ddot{u}_y \end{Bmatrix} + [C] \begin{Bmatrix} \dot{u}_x \\ \dot{\theta} \\ \dot{u}_y \end{Bmatrix} + \{f_s\} = - \begin{bmatrix} m & 0 & 0 \\ 0 & mr^2 & 0 \\ 0 & 0 & m \end{bmatrix} \begin{Bmatrix} \ddot{u}_{gx}(t) \\ 0 \\ \ddot{u}_{gy}(t) \end{Bmatrix}$$

The equations of motion are numerically solved in the time domain by Newmark’s β - γ method likewise previous investigations. (e.g., [3, 5, 6] using modified Newton-Raphson technique. The Newmark’s parameters are chosen as $\gamma = 0.5$ and $\beta = 0.25$. The time step of integration is taken as $T_1/400$ s, where T_1 is the lateral natural period of asymmetric idealized system. This time step of integration is found to be sufficiently small from sample convergence studies.

The maximum displacement demand for extreme edge load resisting element of an asymmetric structural system is studied for a feasible range of dynamic characteristics of the system. Uncoupled lateral period T_1 and torsional to lateral period ratio τ are the two primary dynamic characteristic of that structural systems under seismic excitation. As most of the auditorium like community structures generally have low heights in comparison with multi-storeyed general residential or official buildings, systems with small uncoupled lateral time period namely T_1 equal to 0.1 s is used to represent natural period range of such low-rise stiff asymmetric structural system. The torsion to lateral time period ratio τ is varied within a range of 0.5–1.5 as torsional to lateral period ratio τ for most of low-rise buildings lies within this range.

3 Hysteresis Model and Ground Motion

In the present investigation two types of hysteresis models namely, (i) strength and stiffness degrading and (ii) elasto-plastic are considered. First type of hysteresis behavior may be considered for represent the characteristics of R/C structural members, while the second one represents the characteristics of steel frame structural members. The first types of hysteresis model are incorporated through the algorithm developed and explained as in [5]. These simplified hysteresis models are also used in some previous investigations [1, 3, 6].

Table 1

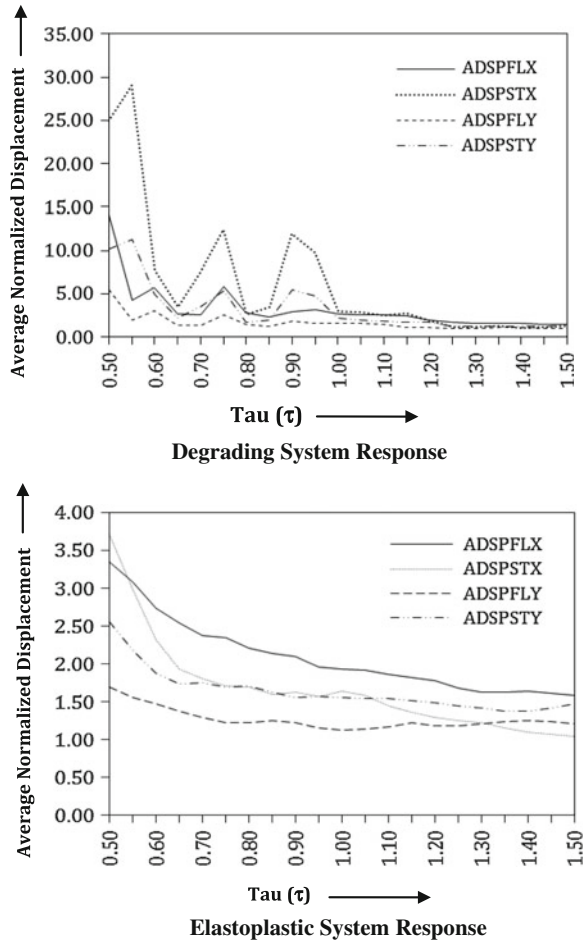
Sl. no	Seismic events	Station	Date	Magnitude in Richter	Distance from epicenter (km)	PGA
1	Chalfant Valley	Zack Brothers ranch	07.20.86	5.8	6.4	2.796
2	Coyote Lake	Gilroy Array #3	06.08.79	5.7	7.4	2.242
3	Imperial Valley	El Centro Array #3	10.15.79	6.5	12.9	3.714
4	Imperial Valley	Sahop Casa Flores	10.15.79	6.5	9.6	4.87
5	Loma Prieta	Saratoga—Aloha Ave	10.18.89	6.9	8.5	3.18
6	Mammoth Lakes	Convict Creek	05.25.80	6.1	6.6	4.332
7	Morgan Hill	Halls Valley	04.24.84	6.2	3.5	3.057
8	West of Westmorland	Westmorland Fire Sta.	04.26.81	5.9	6.5	4.896

Real ground motions of near-fault nature are considered in the present investigations are collected from strong motion data base available from PEER strong motion database (<http://www.peer.berkeley.edu>). The ground motions are selected in such a way that they are considered at measuring stations which are only few kilometers away from respective epicenters. In this present study an ensemble of eight set of real ground acceleration time history is considered and each set consists of two sets of ground acceleration data in two orthogonal directions in horizontal plane has been use as input ground motion. The main characteristics of the selected records are reported in Table 1. Out of these eight real earthquake ground acceleration data sets some are also used in a recent investigation [1].

4 Results and Conclusions

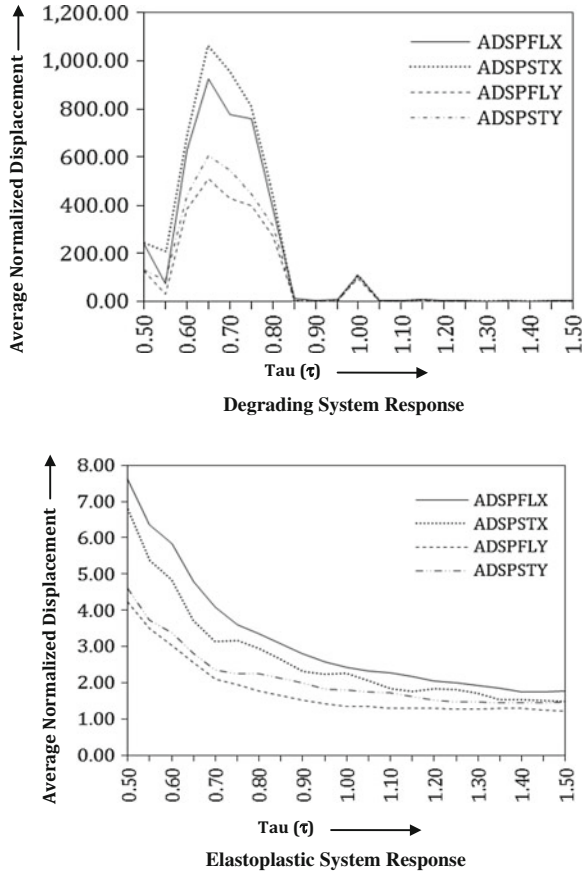
Maximum displacement responses of edge elements (flexible and stiff) of uni-directionally asymmetric structural systems with different values of eccentricities are computed in normalized form. Normalization is done by the maximum displacement responses of edge elements of similar but symmetric structural systems to investigate only the effect of asymmetry. Such normalized responses, computed for all eight real earthquake ground excitations of near-fault nature, are averaged and represented in Figs. 2 and 3. Each of these figures consist two set of graphs showing responses of degrading structures representing buildings with reinforced concrete structural elements and response of similar but elasto-plastic structural system representing buildings having steel structural elements. In each of

Fig. 2 Average normalized displacement response of uni-directionally asymmetric structural systems having $T_l = 0.1$ s, $e_x/D = 0.2$



the figure averaged normalized maximum displacement response is plotted against torsional to lateral period ratio τ (TAU). Four different curves in each figure represent averaged normalized maximum displacement response of (a) Flexible element in x direction (ADSPFLX), (b) Stiff element in x direction (ADSPSTX), (c) Flexible element in y direction (ADSPFLY) and (d) Stiff element in y direction (ADSPSTY). Careful comparison between two sets of graphs presented in each figures (Figs. 2 and 3) clearly reveal that though for the structural systems with elasto-plastic structural elements responses are magnified due to asymmetry but to a limited extent. On the other hand for strength and stiffness degrading structural systems representing R/C structures, the responses are magnified many more times than the elasto-plastic systems due to incorporation of asymmetry. Hence, comprehensive study of R/C asymmetric community structural systems under near-

Fig. 3 Average normalized displacement response of uni-directionally asymmetric structural systems having $T_l = 0.1$ s, $e_x/D = 0.1$



fault ground motions considering different aspect of such systems is the need of the hour.

References

1. Bhaumik S, Das PK (2013) Response of idealized R/C asymmetric structural systems under near-fault ground motion. In: Paper no.: 58-istam-sm-fp-43, 58th congress of the Indian society of theoretical and applied mechanics (ISTAM), an international meet, Bengal Engineering and Science University, Shibpur, West-Bengal, India, 18–21 Dec 2013
2. Das PK, Dutta SC (2002) Effect of strength and stiffness deterioration on seismic behaviour of R/C asymmetric buildings. *Int J Appl Mech Eng* 7(2):527–564
3. Das PK, Dutta SC (2003) Inelastic seismic behaviour of R/C structures with bi-directional asymmetry under near-fault motion. In: Proceedings of structural engineering convention (SEC 2003), an international meet, I.I.T. Kharagpur, India, pp 475–483, 12–14 Dec 2003
4. Dutta SC (2001) Effect of strength deterioration on inelastic seismic torsional behaviour of asymmetric RC buildings. *Build Environ* 36(10):1109–1118

5. Dutta SC, Das PK (2002) Validity and applicability of two simple hysteresis models to assess progressive seismic damage in R/C asymmetric buildings. *J Sound Vib* 257(4):753–777
6. Dutta SC, Das PK, Roy R (2005) Seismic behaviour of code-designed bi-directionally eccentric systems. *J Struct Eng ASCE* 131(10):1497–1514

Comparison of Seismic Vulnerability of Buildings Designed for Higher Force Versus Higher Ductility

Chande Smita and Ratnesh Kumar

Abstract Seismic vulnerability assessment is a complex problem involving input from various analyses. Pushover analysis is a commonly used method, which provides input for vulnerability analysis. Different level of ductility in a building can be considered by using different response reduction factor in linear analysis; however, the actual non-linear behavior of the building cannot be predicted on same basis. Therefore, response reduction factor (R) considered in designing, plays an important role in actual performance of building. The effect of different response reduction factors used in design on expected damage of building has been ascertained using vulnerability analysis. The seismic performance of low-rise and mid-rise RC buildings designed as per Indian codes with consideration of seismic forces (with two sets design levels SMRF and OMRF) and only gravity forces (designed for only gravity loadings) have been evaluated by fragility relationships. Nonlinear static analyses were performed to derive the fragility relationships. Based on nonlinear static procedure or pushover analysis the seismic performances in terms of ductility capacity and ductility demand have been obtained. The observations showed that the performance of buildings designed for higher ductility (R as 5) can be better relied than the buildings designed for higher forces (R as 3). The results showed that there is higher probability of damage in case of OMRF design buildings as compared to SMRF designed buildings.

Keywords Fragility function · Pushover analysis · RC frame buildings · Seismic performance · Vulnerability assessment

C. Smita (✉) · R. Kumar
Department of Applied Mechanics, Visvesvarya National Institute of Technology,
Nagpur 440010, Maharashtra, India
e-mail: smitchande@gmail.com

© Springer India 2015
V. Matsagar (ed.), *Advances in Structural Engineering*,
DOI 10.1007/978-81-322-2193-7_76

963

1 Introduction

In India, the majority of buildings are designed for gravity loads either without considering earthquake force or with a lower level of earthquake force. The consideration of lesser design force results in inadequate lateral strength of buildings. This may result in severe damage or even complete collapse. As in case of design practice the infill modelling effect is neglected by many structural designers while designing the building in software, resulting in more flexible structure than in real. The stiff structure produces more seismic forces than flexible one. This states that the wrong assessment of stiffness would consider lesser inadequate seismic forces for the design purpose. Designing the structure for lesser seismic forces may lead to complete damage or collapse of the structure in future earthquakes. However, if lesser seismic forces are taken while designing, then as per Indian Standard for ductile detailing IS 13920: [1], proper and sufficient ductile detailing has to be provided in the structural components.

Code design practices have been traditionally based on force based design (FBD) concept. In this method, the components of structure are proportioned for strength, such that structure can sustain the shocks of moderate intensities without structural damage and shocks of heavy intensities without total collapse. The internal forces are computed from elastic analysis. The inelastic behavior is accounted for by using a response reduction factor (R), which depends on ductility, redundancy and overstrength. The determination of R factor is based either on equal-displacement or equal-energy principles. The effect of ductility is accounted by providing proper detailing and proportioning of members. Ductility can be enhanced by facilitating plastic deformations and allowing failure of element/structure only in desirable ductile modes. This can be achieved by keeping sufficient strength differential between brittle and ductile modes of failure.

In past few decades, the losses caused by natural calamities have been increased dramatically. Increase in population, development of new cities located in high seismic zones etc. has increased such losses. Northridge (California, US) earthquake, 1994 has caused the highest ever insured earthquake loss at approximately US\$14 billion. The Kobe (Japan) earthquake, 1995 has caused the highest ever absolute earthquake loss of about US\$150 billion. It was mentioned in a report submitted in National Information Center of Earthquake Engineering (NICEE) by Jain and his group that the Bhuj earthquake of magnitude 7.9 caused a large loss of life and property. Over 18,600 persons were reported to be dead and over 167,000 injured; the estimated economic loss due to this quake was placed at around Rs. 22,000 Crores (\sim US\$5 billions). It was so, because in India buildings are normally designed for gravity loads only.

A significant component of a loss model is determination of vulnerability of the buildings stock. In simple words, seismic vulnerability is the degree of weakness in terms of damage to the building due to seismic ground motion. It can also be stated as the damage potential to a class of similar structures in a particular building stock subjected to a given seismic hazard. Vulnerability analysis tells the ability of

destruction of the structures under varying intensity or magnitudes of ground motion. The analysis defines the damage states of the building. This damage states are based on the applied base shear, which is stated as a function of the seismic demand. The damage states are defined from none to collapse with increasing levels of demand. The damage states are obtained by intersecting both building capacity and seismic demand curves. The roof displacement—base shear curve, also called the capacity curve, represents the nonlinear behavior of a building under increasing load or displacement demand. Intersection of the capacity and the demand curves represents the damage state likely to be experienced by the structure. The seismic performance obtained by the pushover analysis is for a particular structure or building in an area, whereas the seismic vulnerability assessment gives the probability of damage for a considered building type in that area representing whole stock of the buildings in that area.

Buildings constructed in India can be broadly categorized into three groups; buildings properly designed with ductile detailing as per seismic guidelines, buildings designed as per Indian codes but not detailed for ductility, and buildings designed for gravity loads without considering seismic forces. In order to simulate these three groups of buildings, three design levels have been considered for this study i.e. the building is designed as Special Moment Resisting Frame (SMRF); Ordinary Moment Resisting Frame (OMRF) and for gravity loads only. The response reduction factor (R) is based on ductility, over-strength and redundancy effects and thus requires the proper detailing of structure. Indian code on seismic forces IS 1893 (Part 1): [2], provides response reduction factor for SMRF as 5 and for OMRF as 3. Indian Standard code IS 13920: [1], provides the general guidelines for ductile detailing of RC structures and the same have been used in the present study for SMRF building. For the ‘gravity design’ level, the buildings have been designed only for gravity loads, and the seismic forces are not considered.

2 Parametric Study

2.1 *The Structural Modelling and Design*

The plan considered in the present study is of a hospital building located in Texas, USA [3]. The building plan is approximately regular, and is modelled in SAP2000 as a low-rise building having three storeys (G +2 model) and a mid-rise building having six storeys (G +5 model). The building plan is symmetrical in longitudinal direction and nominally asymmetric in transverse direction (Fig. 1).

The storey height is considered as 3.2 m. The building is assumed to be situated on medium soil strata (Type II) and is located in the seismic zone V as per Indian code (IS 1893(Part 1): [2] with Peak ground acceleration (PGA) as 0.36 g for Maximum Considered Earthquake (MCE). The slab thickness is assumed as 150 mm. The building is modelled in SAP 2000 as a 3D space frame structure. Dead and imposed loads have been computed using the Indian standard codes IS

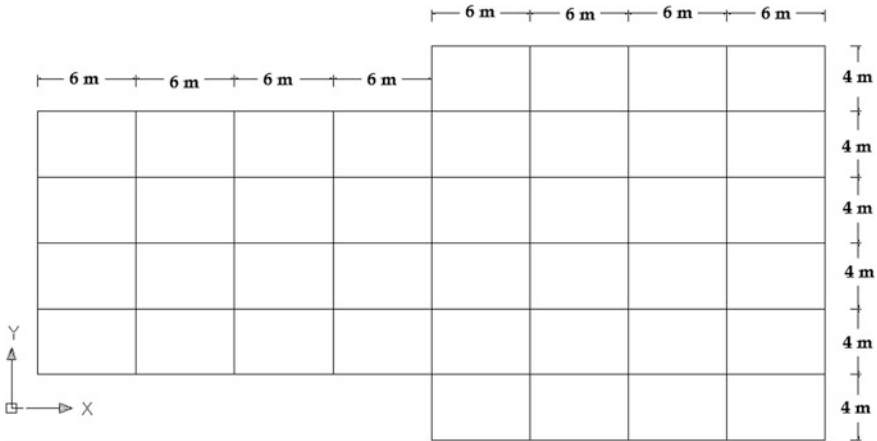


Fig. 1 Plan of building

875 (Part 1): [4] and IS 875 (Part 2): [5], respectively, and are assigned to the building. The seismic analysis and design has been performed considering the various load combinations mentioned in IS 1893 (Part 1): [2]. The preliminary sizes of beams and columns have been calculated based on the deflection criterion mentioned in IS 456: [6] and IS 13920: [1]. M25 grade of concrete and Fe415 grade of steel have been used for the design. RC slabs (Floor and Roof) act as rigid diaphragms, these are the horizontal elements that transfer earthquake induced inertial forces to the vertical elements of the lateral force resisting systems and therefore the building has been modelled with rigid diaphragms using diaphragm constraints. Response spectrum analysis of the building has been performed by considering seismic force combination as square root of the sum of squares (SRSS). The IS 1893 (Part 1): [2] defines two seismic levels as Maximum considered earthquake (MCE) and Design basis earthquake (DBE). The effective peak ground acceleration of MCE is considered as half of the effective peak ground acceleration of DBE. The building has been designed for the prescribed base shear as per IS 1893 (Part 1): [2] as given Eq. 1.

$$V_B = \frac{Z I S_a}{2 R g} W \tag{1}$$

where, Z represents the zone factor, R represents the response reduction factor, and I is the importance factor; S_a/g represents the response spectrum acceleration, based on the time period of building calculated as a function of height and plan of building and W is seismic weight of the building.

The building time period observed is much more than code specified period since the cracked sections (i.e. effective stiffness of frame members) is considered in the present study. The minimum base shear \bar{V}_B is calculated as per IS 1893 (Part 1): [2]. As per recommendation of code minimum base shear correction has been

applied by scaling up the recommended scaling of base shear by a factor \bar{V}_B/V_B , where V_B is the base shear calculated by using the response spectrum analysis and is the base shear obtained by using the time period analytically.

Minor cracking is expected in the RC frame members under the effect of service-gravity loading, however, the cracking will be significant under the seismic loading [7] and it is expected that either most of the members will yield or will reach near yielding, therefore it is necessary to use the realistic stiffness of RC frame members. It is also important to note that effective stiffness of column depends on level of axial load, however, axial load on column keeps changing during dynamic earthquake loading which is very difficult to account in design. Design axial load can be used as an approximation for axial load level for computation of effective stiffness. The simplified model for effective stiffness of normal-strength concrete flexural and compression members as proposed by Kumar and Singh [7] is used in the present study.

The different pushover curves obtained by performing the nonlinear static analysis on the 3 and 6 storey buildings designed as SMRF, OMRF and for gravity loads only, in SAP 2000 were compared. The nonlinear flexural hinge properties for beams and columns have been assigned as per FEMA 356 [8] guidelines. From capacity curve the yield and ultimate control points, and the ductility capacity are compared for the above mentioned models and tabulated in Table 1. The yield capacity control point is selected as the point where significant yielding is just beginning to occur (slope of capacity curve is essentially taken constant up to the yield point). Figures 2 and 3 compare the seismic performance of the 3-storey and 6-storey gravity designed buildings with those of the SMRF building and OMRF building for seismic zone V in longitudinal direction. In longitudinal direction for 3 storey building, the yield base shear of SMRF and OMRF building is 1.5 times and 2.15 times the gravity load designed building. In case of 6 storey building, the yield base shear of SMRF and OMRF building is 2.34 times and 4.25 times the gravity load designed building. Similar nature is observed in transverse direction.

2.2 Vulnerability Assessment

Seismic vulnerability gives the susceptibility of the structure to damage produced by a ground shaking of a given intensity. It is expressed in terms of intensity or Peak Ground Acceleration (PGA) or spectral displacement. The curve represents the lognormal continuous distribution showing the damage state distribution. Different approaches can be used to plot the vulnerability curves. The methods include the empirical data relationship based on previous earthquake damage data collection to analytical methods using the data from software analysis of structure to the judgmental data relationship, which is based on the expertise of researchers. The HAZUS methodology developed by FEMA document along with damage state models suggested by Giovinazzi and Lagomarsino [9] has been used in the present

Table 1 Pushover results considered building, δ_t indicates target displacement, μ_C indicates ductility capacity, μ_{DD} indicates ductility demand for DBE, μ_{DM} indicates ductility demand for MCE

Direction	Storey	Design level	Yield point		Ultimate point		δ_t MCE (m)	μ_C	μ_{DM}	μ_{DD}
			V (KN)	D (m)	V (KN)	D (m)				
Long.	3	Gravity designed	3,877	0.055	5,250	0.11	0.14	2	2,545	1.27
		SMRF	9,650	0.10	11,270	0.222	0.12	2.22	1.2	0.6
		OMRF	12,207	0.07	16,743	0.14	0.09	2	1.28	0.64
Trans.	3	Gravity designed	1,953	0.055	2,838	0.125	0.2	2.27	3.63	1.81
		SMRF	5,965	0.11	7,120	0.225	0.15	2.045	1.36	0.68
		OMRF	9,639	0.09	11,854	0.16	0.116	1.77	1.28	0.64
Long.	6	Gravity designed	4,273	0.225	5,337	0.4	0.19	1.778	0.84	0.42
		SMRF	14,400	0.14	17,574	0.54	0.42	3.85	3	1.5
		OMRF	22,450	0.13	28,950	0.35	0.16	2.69	1.23	0.615
Trans.	6	Gravity designed	2,281	0.16	3,031	0.42	0.48	2.625	3	1.5
		SMRF	7,487	0.14	10,501	0.498	0.2	3.55	1.42	0.71
		OMRF	18,619	0.109	22,707	0.15	0.16	1.37	1.46	0.73

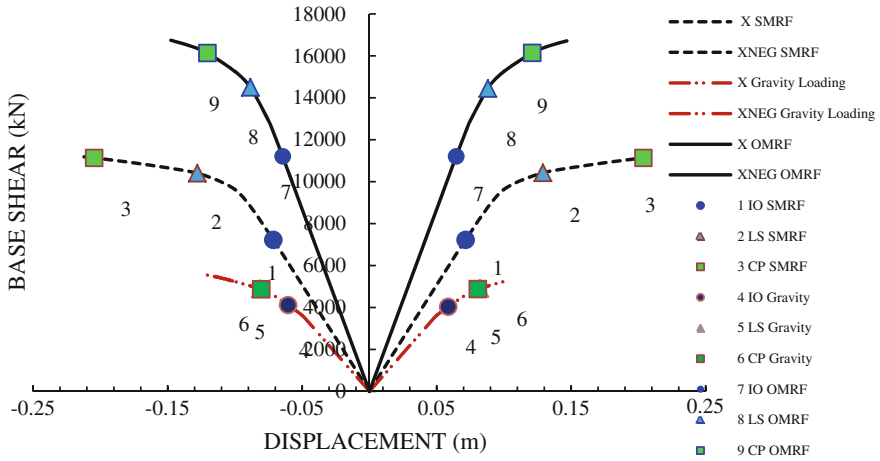


Fig. 2 Comparison of pushover curve for 3 storey building designed as SMRF, OMRF and for gravity loads in X direction

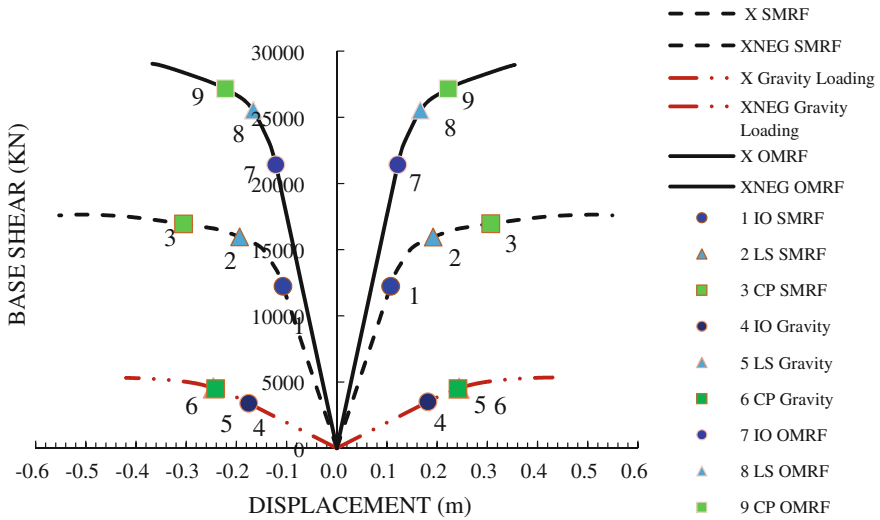


Fig. 3 Comparison of pushover curve for 6 storey building designed as SMRF, OMRF and for gravity loads in X direction

study to develop the vulnerability curves for RC buildings as per Indian standards. The methodology uses the data from the capacity curves, which have been used in this paper. This curve distributes damages in terms of slight, moderate, extensive and complete damage states. For a particular spectral response or displacement, the discrete damage state probability is calculated as the difference between cumulative probabilities of damage states. For example, for a given target displacement value,

Table 2 Damage state variability parameters considered for the buildings

	Design levels	Post-yield degradation (<i>k</i>)	Damage state variability (β_{Tds})	Capacity curve variability (β_c)	Damage state variability (β_{ds})
3 Storey	SMRF	Minor degradation (0.9)	Moderate (0.4)	Moderate (0.3)	0.8
	OMRF	Major degradation (0.1)	Moderate (0.4)	Moderate (0.3)	1.0
	Gravity-designed	Extreme degradation (0.1)	Moderate (0.4)	Moderate (0.3)	1.05
6 Storey	SMRF	Minor degradation (0.9)	Moderate (0.4)	Moderate (0.3)	0.75
	OMRF	Major degradation (0.1)	Moderate (0.4)	Moderate (0.3)	0.85
	Gravity-designed	Extreme degradation (0.1)	Moderate (0.4)	Moderate (0.3)	1

the probability of moderate damage will be difference of probability of moderate damage state and the probability of extensive damage state.

$$P[ds|S_d] = \Phi \left[\frac{1}{\beta_{ds}} \ln \left(\frac{S_d}{S_{d,ds}} \right) \right] \tag{2}$$

where, S_d is spectral displacement defining the threshold of a particular damage state; $S_{d,ds}$ is median value of spectral displacement at which the building reaches the threshold of damage states or damage state medians, can be calculated by various damage state models; β_{ds} is standard deviation of natural logarithm of S_d for damage states; Φ is standard normal cumulative distribution function. Fragility curve defines various damage states. HAZUS defines two-criteria approach based on the performance levels of the individual members. The damage state thresholds are defined using the model proposed by Giovinazzi and Lagomarsino [9] (see Table 2) based on the capacity spectrum of the buildings, and the same approach has been used in the present study.

2.3 Development of Damage State Variability

The lognormal beta or standard deviation describes the total variability of the damage states as shown in Table 2. The variability associated with the capacity curve, β_C , demand spectrum, β_D , and the variability associated with the discrete threshold of each damage state, β_{Tds} , are to be accounted while calculating the total variability. The demand spectrum is developed from 5 % damped elastic response (input) spectrum in terms of Spectral Acceleration versus Spectral Displacement and the Capacity curve is the plot of force-deformation in terms of Spectral Acceleration versus Spectral Displacement. Thus, the demand spectrum and capacity curves are inter dependent, the variability accounted by both are combined by convolution process. The third component β_{Tds} is mutually independent from the first two variability components and its effect is considered by combining it with the results of CONV process using SRSS method [10].

$$\beta_{ds} = \sqrt{(CONV[\beta_C, \beta_D])^2 + (\beta_{Tds})^2} \quad (3)$$

where, β_{Tds} is the lognormal standard deviation parameter that describes total variability associated with the discrete threshold of each damage state, β_C is the lognormal standard deviation parameter that describes variability associated with the capacity curve, β_D is the lognormal standard deviation parameter that describes variability associated with the demand spectrum, ($\beta_D = 0.45$ at short periods and $\beta_D = 0.5$ at long periods).

The median spectral displacements can be determined analytically. Estimation of variability is a difficult process requiring statistical data for local conditions. Therefore, variability parameters are directly used from HAZUS [10]. For Indian buildings, such data is not available. The damage state thresholds presented by Giovinazzi and Lagomarsino [9] as being on conservative side, have been used in the present study. As discussed earlier, in the cases of ‘gravity-designed building’, extreme degradation has been considered as there is no conforming transverse reinforcement provided in the structure. In case of special moment resisting frame, the conforming transverse reinforcement has been provided, therefore minor degradation case is considered. The fragility curves of the gravity designed and SMRF buildings have been compared for all the damage states—slight, moderate, extensive and complete damage states. Figures 4, 5, 6 and 7 show the fragility curves for different design levels of 3-storey and 6-storey as discussed earlier.

It can be observed that the fragility curves of OMRF and SMRF buildings are crossing each other in some cases, indicating different damage patterns and damage variabilities for the considered types of buildings. The slope of fragility curve depends on the standard deviation of the natural logarithm of spectral displacement β_{ds} , which as discussed earlier is assumed to be different in all the types of building depending on the considered degree of degradation. It can be observed that the slope of any damage state of considered design level building such as OMRF and SMRF buildings and gravity loading designed buildings are same.

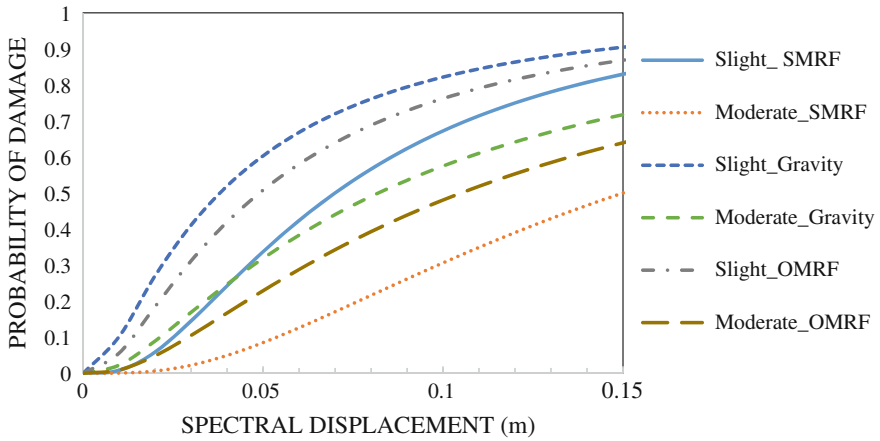


Fig. 4 Comparison of fragility curves for slight and moderate damage states for 3 storey building designed as SMRF, OMRF and for gravity loads in X direction

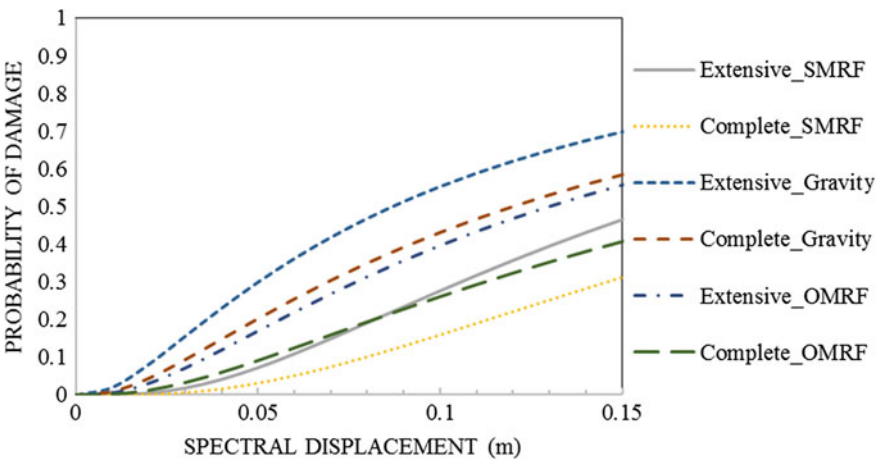


Fig. 5 Comparison of fragility curves for extensive and complete damage states for 3 storey building designed as SMRF, OMRF and for gravity loads in X direction

Tables 3 and 4 show the probabilities of damage being greater than or equal to a particular grade for the 3-storey and 6-storey buildings, respectively, and this values obtained from fragility curves correspond to the target displacement at Maximum Considered Earthquake MCE levels for seismic zone V. It can be noted from those tables that the probability of damage for building designed as SMRF at the target displacement is lesser than that of the buildings designed as OMRF and for gravity loading only.

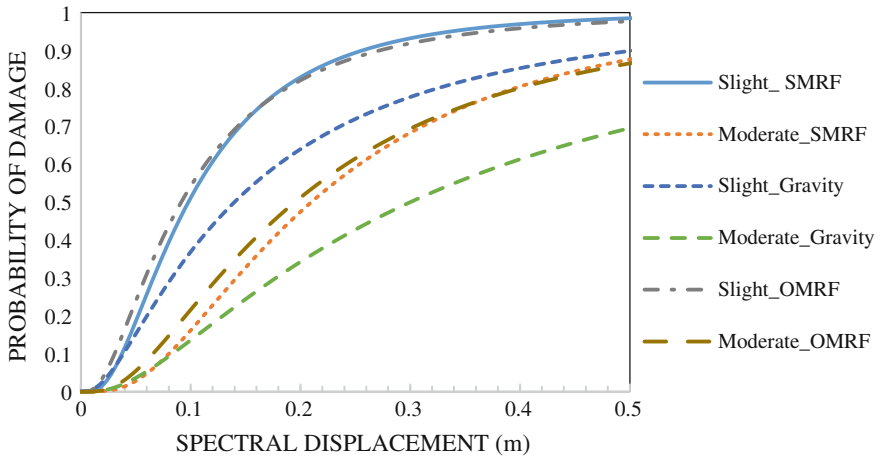


Fig. 6 Comparison of fragility curves for slight and moderate damage states for 6 storey building designed as SMRF, OMRF and for gravity loads in X direction

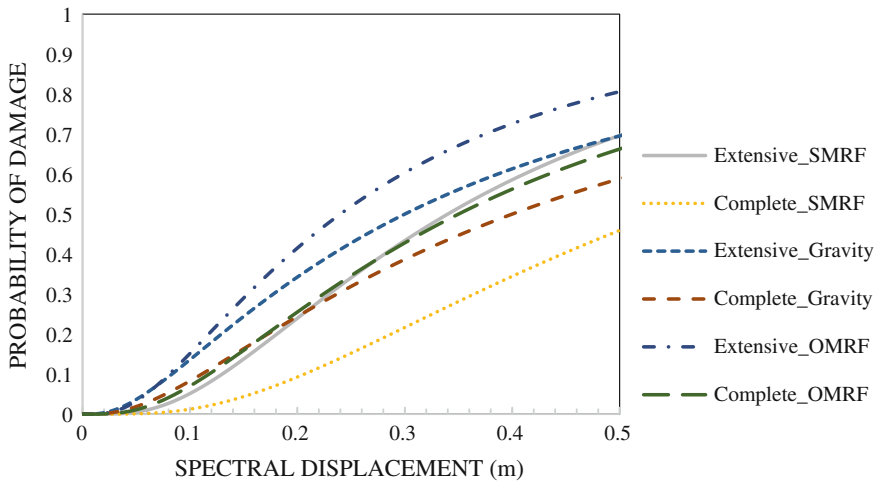


Fig. 7 Comparison of fragility curves for extensive and complete damage states for 6 storey building designed as SMRF, OMRF and for gravity loads in X direction

Table 3 Damage probabilities (%) for the 3 storey and 6 storey buildings in longitudinal (X) direction

Design level	P (slight)	P (moderate)	P (extensive)	P (complete)
3 Storey SMRF	71.39	34.9	31.6	19
3 Storey OMRF	72.8	43.8	36.65	22.7
3 Storey gravity designed	88.9	69.18	67.19	55.78
6 Storey SMRF	81	44.69	21.89	8.18
6 Storey OMRF	74.44	40.79	31.66	17.78
6 Storey gravity designed	86.4	63.17	63.17	51.9

Table 4 Damage probabilities (%) for the 3 storey and 6 storey buildings in transverse direction

Design level	P (slight)	P (moderate)	P (extensive)	P (complete)
3 Storey SMRF	79.77	45.25	39.5	24.2
3 Storey OMRF	74	45.3	39.7	27
3 Storey gravity designed	91.17	73.5	70.8	59.28
6 Storey SMRF	82.9	47.4	26.8	11.199
6 Storey OMRF	80.9	48.98	42.7	27.6
6 Storey gravity designed	92.65	75.58	69.28	55.4

3 Conclusions

The seismic performance of low-rise and mid-rise RC buildings designed according to Indian codes with consideration of seismic forces (with two sets design levels—SMRF and OMRF) and only gravity forces (designed for only gravity loadings) were evaluated using fragility functions. Nonlinear static analyses were performed to provide input to fragility relationships. The nonlinear static procedure or push-over analysis provides the seismic performances in terms of ductility capacity, ductility demand and performance levels.

Even though the design base shear observed for OMRF building was higher than the SMRF building, the ductility capacity was observed higher in case of SMRF building. The ductility capacity of building designed as SMRF was observed 30 % more than that of building designed as OMRF. Also, it was observed that ductility capacity of building designed as SMRF was 54 % more than that obtained from the building designed for gravity loads only. Thus, buildings designed as SMRF offered more ductility than the buildings designed for the gravity loadings and designed as OMRF.

For six storied building, the ultimate displacement of SMRF has been observed to be 35 % higher than that of OMRF and 26 % higher than the building designed for gravity loads only.

From fragility analysis of the considered six storied building, it has been observed that the building designed for gravity load only has 66 % higher probability of complete damage than the building designed as SMRF. Also, the results

showed that there is 59 % higher probability of complete damage in the buildings designed for gravity loads only than the buildings designed as OMRF.

From fragility analysis for the considered building in transverse direction, the results showed that there is 80 % higher probability of complete damage in the buildings designed for gravity loads only than the buildings designed as SMRF. Also, the results showed that there is 51 % higher probability of complete damage in the buildings designed for gravity loads only than the buildings designed as OMRF.

References

1. IS 13920 (1993) Ductile detailing of reinforced concrete structures subjected to seismic forces-code of practice. BIS, New Delhi
2. IS 1893 (Part 1) (2002) Criteria for earthquake resistant design of structures, Part 1 general provision and buildings (fifth revision), BIS, New Delhi
3. Plan Link. http://www.cc.gatech.edu/ai/robotlab/tmr/floor_1autocad_format.htm. Accessed 5 Aug 2013
4. IS 875 (Part 1) (1987) Code of practice for design loads (other than earthquake) for buildings and structures (second revision). BIS, New Delhi
5. IS 875 (Part 2) (1987) Code of practice for design loads (other than earthquake) for buildings and structures (second revision). BIS, New Delhi
6. IS 456 (2000) Plain and reinforced concrete-code of practice (fourth revision). BIS, New Delhi
7. Kumar R, Singh Y (2010) Stiffness of Reinforced concrete frame members for seismic analysis. *ACI Struct J* 107(5):60
8. FEMA 356 (2000) Prestandard and commentary for the seismic rehabilitation of buildings, Report FEMA 356. Federal Emergency Management Agency (FEMA), Washington, DC
9. Giovinazzi S, Lagomarsino S (2006) Macro-seismic and mechanical models for the vulnerability and damage assessment of current buildings. *Bull Earthq Eng* 4:415–443
10. NIBS (2003) Multi-hazard loss estimation methodology, earthquake model-HAZUS-MH: technical manual, report prepared for the Federal Emergency Management Agency (FEMA). National Institute of Building Sciences, Washington, DC

Studies on Identifying Critical Joints in RC Framed Building Subjected to Seismic Loading

Pradip Paul, Prithwish Kumar Das and Pradip Sarkar

Abstract A beam-column joint is very critical element in reinforced concrete (RC) framed structure where the elements intersect in all three orthogonal directions. In normal design practice for gravity loads, the design check for joints is not usually critical in reinforced concrete (RC) frames and hence not warranted in general. However, failures of RC frames during recent earthquakes have revealed heavy distress in the joints and resulted in the collapse of several structures due to joint shear failure. Despite the critical role of joints in sustaining large deformations and forces during earthquakes, specific guidelines are not explicitly included in current Indian codes of practice IS 1893:[1], IS 13920:[2] and IS 456:[3]. On account of this, it is tacitly assumed in practice that adequate lapping of the main reinforcement and provision of transverse ties satisfies the integrity and strength of joints. However, the kind of reinforcement detailing given in the design codes is not consistent with the Indian practice of construction in terms of implementation. This paper aims to study the behaviour of beam-column joints in multi-storeyed RC framed structure with an objective to identify the location of deficient joints and developing alternative design scheme suitable for Indian construction industry. A family of multi-storeyed building of 2 bay \times 2 bay (at 5 m) frames from 3 storey (10.5 m height) to 10 storey (35 m height) is studied. Shear force demand in the joint is estimated from the concept of capacity design. The shear capacity is calculated for the interior joints at different height (i.e., at different floor level) of the buildings as per selected international building codes and other methods available in literature. This result shows that the maximum joint demand occurs not in the lowest storey level of the building but somewhere in the second, third or fourth storey level. The maximum joint shear demand found to be more than the corresponding capacity for all building above 5 storeys (i.e., 17.5 m height) studied here. An effort has been

P. Paul (✉) · P.K. Das

Department of Aerospace Engineering & Applied Mechanics, Indian Institute of Engineering Science and Technology, Shibpur, India
e-mail: getpradip@yahoo.com

P. Sarkar

Department of Civil Engineering, National Institute of Technology, Rourkela, India

made for correlating the joint shear demand in any interior joint with the height of the joint. This will be helpful for identifying the critical joint location in a building.

Keywords Beam-column joint · Reinforced concrete · Joint shear · Critical joint · Seismic loading

1 Introduction

A beam-column joint is very critical element in reinforced concrete (RC) framed structure where the elements intersect in all three orthogonal directions. Joints ensure continuity of a structure and transfer forces that are present at the ends of the members. Beam-column joints in moment resisting frames are crucial zones that control the effective transmission of forces in the structure. In normal design practice for gravity loads, the design check for joints is not usually critical in reinforced concrete (RC) frames and hence not warranted in general. However, failures of RC frames during recent earthquakes have revealed heavy distress in the joints and resulted in the collapse of several structures due to joint shear failure.

Despite the critical role of joints in sustaining large deformations and forces during earthquakes, specific guidelines are not explicitly included in current Indian codes of practice IS 1893:[1], IS 13920:[2] and IS 456:[3]. On account of this, it is tacitly assumed in practice that adequate lapping of the main reinforcement and provision of transverse ties satisfies the integrity and strength of joints. However, the kind of reinforcement detailing given in the design codes is not consistent with the Indian practice of construction in terms of implementation. Therefore, in practice, joint reinforcement detailing prescribed in the design codes is not followed.

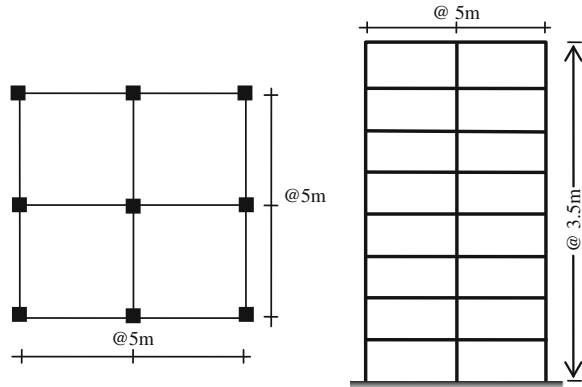
This research effort aims to study the behaviour of beam-column joints in multi-storeyed RC framed structure with an objective to identify the location of deficient joints and developing alternative design scheme suitable for Indian construction industry.

2 Building Geometry and Modelling

The study in this paper is based on analysis of a family of RC multi-storeyed framed buildings. This section presents a summary of various parameters defining the computational models, the basic assumptions and the building geometries considered for this study.

The study is based on 3D building frames which are orthogonal with storey heights and bay widths. Uniform bay width of 5 m was considered for this study. It should be noted that bay width of 4–6 m is the usual case, especially in Indian and

Fig. 1 Typical structural models used in the present study



European practice. Eight different height categories were considered for the study, ranging from 3 to 10 storeys, with a uniform storey height of 3.5 m. The structures are modelled by using standard computer software made for the purpose and designed for dead load, live load in combination with seismic load as per prevailing Indian Standards. Moderate seismic region, Zone-III (PGA = 0.16 g) is considered for the special moment resisting frame design. Figure 1 presents typical structural models used in the present study.

Modelling a building involves the modelling and assemblage of its various load-carrying elements. The model must ideally represent the mass distribution, strength, stiffness and deformability. Modelling of the material properties and structural elements used in the present study is discussed below.

M-20 grade of concrete and Fe-415 grade of reinforcing steel are used for all the frame models used in this study. Elastic material properties of these materials are taken as per Indian Standard IS 456 [3]. The short-term modulus of elasticity (E_c) of concrete is taken as:

$$E_c = 5000\sqrt{f_{ck}}\text{MPa} \tag{1}$$

where $f_{ck} \equiv$ characteristic compressive strength of concrete cube in MPa at 28-days (20 MPa in this case). For the steel rebar, yield stress (f_y) and modulus of elasticity (E_s) is taken as per IS 456 [3].

Beams and columns are modelled by 2D frame elements. In the primitive stage the beam-column joints are assumed to be rigid. The column end at foundation was considered as fixed for all the models in this study. The structural effect of slabs due to their in-plane stiffness is taken into account by assigning ‘diaphragm’ action at each floor level. The mass/weight contribution of slab is modelled separately on the supporting beams.

3 Evaluation of Joint Shear Demand and Capacity

A family of multi-storeyed building of 2×2 (@ 5 m) frame from 3 storey (10.5 m height) to 10 storey (35 m height) is studied. The interior joint is marked as Si-INT-j; where i represent total number of storeys in the building frame whereas j represents storey level for the joint under consideration. For example S3-INT1 means an interior joint at 1st floor level of a 3 storey building (refer Fig. 2). Shear force demand in the joint is estimated from the concept of capacity design.

Joint shear demand at any interior joint is calculated considering the ultimate moment capacity of adjoining beams. Free body diagram of interior joint# S3-INT-1 in equilibrium is given in Fig. 3 along with the forces from adjoining beam# S3B1 at ultimate failure.

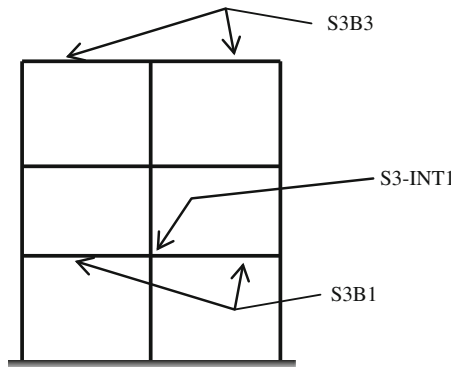


Fig. 2 Typical designation of joints and beams used in the study

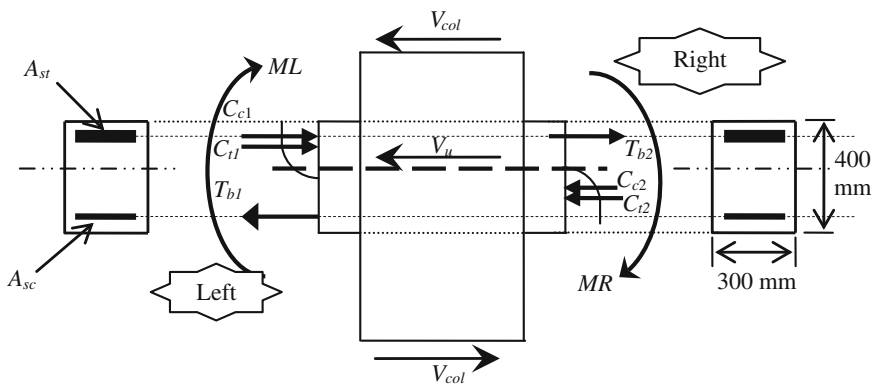


Fig. 3 Forces associated with estimation of Joint shear demand

Considering lateral loads from either direction the section designed are identical in either side of joint. The section properties as obtained by general design methodology are as follows: Top reinforcement, A_{st} : $1,549 \text{ mm}^2$, Bottom reinforcement, A_{sc} : 455 mm^2 .

Though the section is designed based on the critical negative moment at support, i.e., tension at top but in reality when the frame will be subjected to lateral load with combination of dead and live load the negative moment will be generated at one side and in the other side positive moment will be generated. The corresponding stress block diagram is shown in Fig. 3.

At left side of the joint, though the beam is designed as tension reinforcement at top, but due to generation of positive moment the A_{st} will act as compression reinforcement and A_{sc} will act as tension reinforcement. Considering equilibrium of the beam section at left side we have

$$T_{b1} = C_{c1} + C_{t1} \quad (2)$$

As in the ultimate state the reinforcement at tension side should reach at maximum stress before failure;

$$T_{b1} = 1.25f_y \times A_{sc} = 1.25 \times 415 \times 455 = 236,000 \text{ N} = 236 \text{ kN} \quad (3)$$

Similarly at right side of joint

$$T_{b2} = 1.25f_y \times A_{st} = 1.25 \times 415 \times 1549 = 803,500 \text{ N} = 803.5 \text{ kN} \quad (4)$$

The column shear V_{col} is obtained for critical case as $V_{col} = 74 \text{ kN}$

$$V_u = (C_{t1} + C_{c1}) + T_{b2} - V_{col} = T_{b1} + T_{b2} - V_{col} \quad (5)$$

Therefore, $V_u = 236 + 803.5 - 74 \text{ kN} = 965.6 \text{ kN}$.

Thus joint shear has been calculated for a typical interior joint at different heights using the above principle. Table 1 summarizes the results.

Joint shear capacity of beam-column joints primarily depends on (a) characteristic strength of concrete, (b) geometric details or Joint aspect ratio, (c) existence of transverse beams and slabs, and (d) column to beam strength ratio.

The typical interior beam-column joints considered here is laterally confined by beams of dimension $300 \times 400 \text{ mm}$ from both the horizontal axes and by continuous column of size $550 \times 550 \text{ mm}$. The shear capacity is calculated for the interior joints at different height (i.e., at different floor level) of the buildings as per selected international building codes and other methods available in literature. Figure 4 presents the joint shear capacity versus the joint height as per different methods. This figure shows that ACI and NZS do not consider the effect of column axial force in the joint capacity. Although the Eurocode and Muhsen and Umemura [7] consider the effect of column axial force for calculation of joint shear capacity the trend is reverse.

Table 1 Summary of joint shear

Frame type	Joint ID	Joint height (m)	Beam ID	Design reinforcement		T _{b1} (kN)	T _{b2} (kN)	Col. shear V _{col} (kN)	Joint shear V _u (kN)
				A _{sc} (mm ²)	A _{st} (mm ²)				
3 Storey (S3)	S3-INT 1	3.5	S3B1	455	1,549	236	804	74	966
	S3-INT 2	7.0	S3B2	390	1,659	202	860	40	1,022
	S3-INT 3	10.5	S3B3	227	1,324	118	687		805
4 Storey(S4)	S4-INT 1	3.5	S4B1	559	1,825	290	947	85	1,152
	S4-INT 2	7.0	S4B2	569	1,865	295	968	69	1,194
	S4-INT 3	10.5	S4B3	398	1,666	206	864	34	1,037
	S4-INT 4	14.0	S4B4	227	1,293	118	671		789
5 Storey (S5)	S5-INT 1	3.5	S5B1	577	1,873	299	972	92	1,179
	S5-INT 2	7.0	S5B2	798	2,066	414	1,072	82	1,403
	S5-INT 3	10.5	S5B3	619	1,905	321	988	63	1,246
	S5-INT 4	14.0	S5B4	336	1,616	175	838	29	984
	S5-INT 5	17.5	S5B5	227	1,191	118	618		736
6 Storey (S6)	S6-INT 1	3.5	S6B1	663	1,949	344	1,011	97	1,258
	S6-INT 2	7.0	S6B2	921	2,186	478	1,134	91	1,521
	S6-INT 3	10.5	S6B3	830	2,101	431	1,090	79	1,441
	S6-INT 4	14.0	S6B4	567	1,864	294	967	59	1,203
	S6-INT 5	17.5	S6B5	243	1,546	126	802	25	903
	S6-INT 6	21.0	S6B6	227	1,140	118	591		709

(continued)

Table 1 (continued)

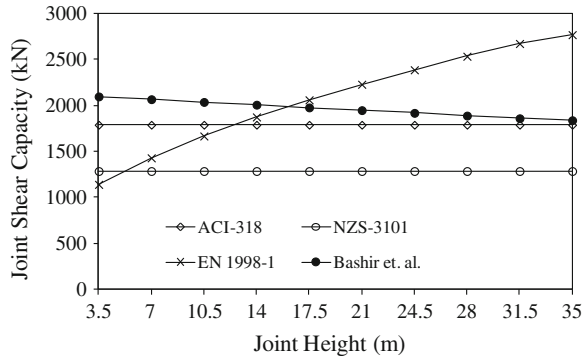
Frame type	Joint ID	Joint height (m)	Beam ID	Design reinforcement		T _{b1} (kN)	T _{b2} (kN)	Col. shear V _{col} (kN)	Joint shear V _u (kN)
				A _{sc} (mm ²)	A _{st} (mm ²)				
7 Storey (S7)	S7-INT 1	3.5	S7B1	803	2,054	416	1,065	102	1,380
	S7-INT 2	7.0	S7B2	997	2,261	517	1,173	97	1,593
	S7-INT 3	10.5	S7B3	1,040	2,280	540	1,183	89	1,633
	S7-INT 4	14.0	S7B4	832	2,099	431	1,089	75	1,445
	S7-INT 5	17.5	S7B5	520	1,817	270	943	54	1,158
	S7-INT 6	21.0	S7B6	227	1,498	118	777	22	872
	S7-INT 7	24.5	S7B7	227	1,122	118	582		700
8 Storey (S8)	S8-INT1	3.5	S8B1	810	2,078	420	1,078	106	1,392
	S8-INT2	7.0	S8B2	1,074	2,335	557	1,211	102	1,667
	S8-INT3	10.5	S8B3	1,082	2,343	561	1,216	96	1,681
	S8-INT4	14.0	S8B4	1,035	2,274	537	1,180	86	1,630
	S8-INT5	17.5	S8B5	791	2,060	411	1,069	72	1,407
	S8-INT6	21.0	S8B6	540	1,806	280	937	51	1,167
	S8-INT7	24.5	S8B7	227	1,473	118	764	20	862
	S8-INT8	28.0	S8B8	227	1,468	118	761		879
9 Storey(S9)	S9-INT1	3.5	S9B1	831	2,102	431	1,090	110	1,412
	S9-INT2	7.0	S9B2	1,141	2,399	592	1,245	106	1,730
	S9-INT3	10.5	S9B3	1,167	2,425	606	1,258	101	1,762
	S9-INT4	14.0	S9B4	1,103	2,361	572	1,225	94	1,702
	S9-INT5	17.5	S9B5	935	2,202	485	1,142	84	1,543
	S9-INT6	21.0	S9B6	783	2,034	406	1,055	69	1,393
	S9-INT7	24.5	S9B7	486	1,753	252	909	47	1,114
	S9-INT8	28.0	S9B8	227	1,437	118	745	19	844
	S9-INT9	31.5	S9B9	227	1,041	118	540		658

(continued)

Table 1 (continued)

Frame type	Joint ID	Joint height (m)	Beam ID	Design reinforcement		T _{b1} (kN)	T _{b2} (kN)	Col. shear V _{col} (kN)	Joint shear V _u (kN)
				A _{sc} (mm ²)	A _{st} (mm ²)				
10 Storey (S10)	S10-INT1	3.5	S10B1	893	2,158	463	1,120	113	1,470
	S10-INT2	7.0	S10B2	1,192	2,449	618	1,270	109	1,779
	S10-INT3	10.5	S10B3	1,169	2,443	606	1,267	106	1,768
	S10-INT4	14.0	S10B4	1,176	2,434	610	1,263	100	1,772
	S10-INT5	17.5	S10B5	1,046	2,310	543	1,198	92	1,649
	S10-INT6	21.0	S10B6	910	2,175	472	1,128	81	1,519
	S10-INT7	24.5	S10B7	660	1,944	342	1,008	65	1,285
	S10-INT8	28.0	S10B8	436	1,704	226	884	45	1,065
	S10-INT9	31.5	S10B9	227	1,396	118	724	17	825
	S10-INT10	35.0	S10B10	227	981	118	509		627

Fig. 4 Joint shear capacity versus the joint height as per different methods



ACI and Eurocode require a stringent ductility detailing for the joint reinforcement and this reflects in the higher estimation of joint shear capacity as per these two codes. Figure 4 shows that the NZS give the most conservative estimate of the joint shear capacity. In absence of any method to calculate joint shear capacity in Indian Standard, the procedure outlined in New Zealand code is used for comparing the demand to capacity of the selected interior joints. The reason behind selecting this is the tradition of poor ductile detailing in construction practice in India. Figure 5 presents Variation of joint shear demand with respect to joint height for different height of buildings. This figure found to be interesting as it shows that the maximum joint demand occurs not in the lowest storey level but somewhere in the second, third or fourth storey level. This result is consistent for all the building analyzed in the present study. It is also clear from this figure that a joint shear demand for many joints is more than the capacity for every building above 5 storey (i.e., 17.5 m height).

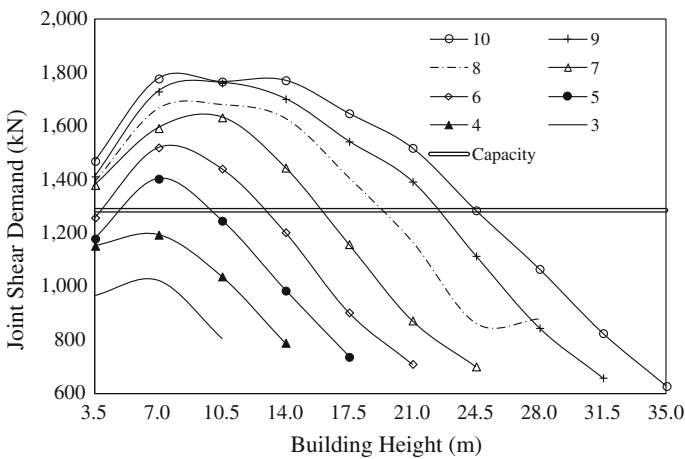
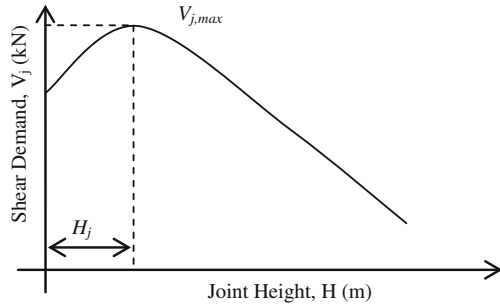


Fig. 5 Variation of joint shear demand with respect to joint height for different height of buildings

Fig. 6 Joint shear demand as a function of joint height in a typical building



An effort has been made for correlating the joint shear demand in any interior joint with the height of the joint. This will be helpful for identifying the critical joint location in a building. The above each curve can be represented by simple third order polynomial equation. If building height is represented by H and joint shear demand is represented by V_j then V_j can be expressed as:

$$V_j = aH^3 + bH^2 + cH + d \tag{6}$$

For, V_j to be maximum, $\frac{d(V_j)}{dH} = 0$.

Therefore,

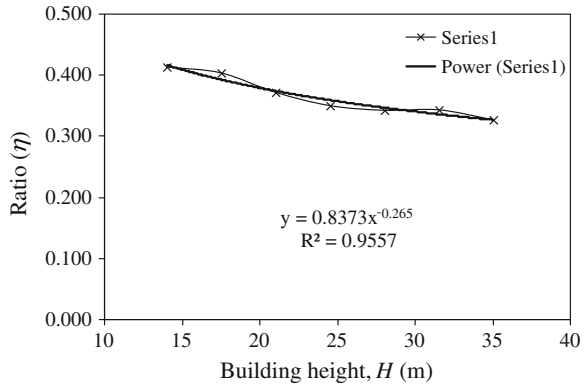
$$3aH^2 + 2bH + c = 0 \tag{7}$$

Figure 6 shows joint shear demand as a function of joint height in a typical building. Eq. (6) is a second order polynomial of H . By solving the above equation we can easily obtained the height of joint H_j where shear demand will be maximum. Though the location of joint in the frame is spread in discrete way, we can predict the location of joint with maximum shear demand in proximity of H_j . The set of H_j and $V_{j,max}$ is obtained for each building. The results are tabulated in Table 2. Ratio (η) of joint height with maximum shear demand to the total building height is also presented.

Table 2 The set of H_j and $V_{j,max}$ is obtained for selected building

Height of building frame (H)	H_j (m) at $V_{j, \max}$	Ratio, $\eta = H_j/H$
10.5	5.97	0.569
14.0	5.79	0.413
17.5	7.06	0.404
21.0	7.81	0.372
24.5	8.58	0.350
28.0	9.59	0.342
31.5	10.81	0.343
35.0	11.45	0.327

Fig. 7 Correlation between the building height and ratio η



The equation of joint shear for 3 storied building (10.5 m) was obtained as 2nd order polynomial and other were best fit to 3rd degree polynomial. Thus, building frame of 10.5 m height is excluded from co-relation. Otherwise, a very good co-relation exists between H and η is obtained as,

$$\eta = 0.8373H^{-0.265} \tag{8}$$

Figure 7 shows the correlation between the building height and ratio (η) of joint height with maximum shear demand to the total building height. This figure shows that the R-square value is very close to unity for Eq. (8).

Now we can determine the probable height of the beam-column joint with maximum horizontal shear demand in any building with the following simple equation as a function of total building height. This equation can be used as a simple quick check for evaluation of beam to column joints against seismic force.

$$H_j = \eta \times H \tag{9}$$

Example: If a building of height H = 50 m with uniform storey height of 3.5 m is designed as per capacity design principle then from the Eqs. (8) and (9) we get $H_j = 14.8$ m. Hence beam-column joints at floor# 4 (at 14 m) and floor# 5 (at 17.5 m) will have highest joint shear demand.

4 Summary and Conclusions

A family of multi-storeyed building of 2 bay \times 2 bay (at 5 m) frames from 3 storey (10.5 m height) to 10 Storey (35 m height) is studied for their behaviour under lateral load in combination with the gravity load in order to identify the location of deficient beam-to-column joints in the frame. Shear force demand in the joint is estimated from the concept of capacity design. The shear capacity is calculated for

the interior joints at different height (i.e., at different floor level) of the buildings as per selected international building codes and other methods available in literature. This result shows that the maximum joint demand occurs not in the lowest storey level of the building but somewhere in the second, third or fourth storey level. The maximum joint shear demand found to be more than the corresponding capacity for all building above 5 storeys (i.e., 17.5 m height) studied here. A correlation between the joint shear demands in any interior joint with its height is developed. This will be helpful for identifying the critical joint locations in a building and design the joints accordingly.

References

1. IS 1893:2002 (Part-1) (2002) Indian standard code of practice for criteria for earthquake resistant design of structures. Bureau of Indian Standards, New Delhi
2. IS 13920:1993(1993) Indian standard code of practice for ductile detailing of reinforced concrete structures subjected to seismic forces. Bureau of Indian Standards, New Delhi
3. IS 456:2000 Indian standard code for practice for plain reinforced concrete for general building construction. Bureau of Indian Standards, New Delhi
4. ACI 318-02 (2002) Building code requirements for structural concrete (ACI 318 M-02) and commentary (ACI 318RM-02), american concrete institute. ACI Committee 318, Farmington Hills, MI
5. NZS 3101: Part 1:1995 (1995) Concrete structures standard, Part 1: the design of concrete structures. New Zealand Standard, New Zealand
6. EN 1998-1-3:2003 (2003) Design provisions for earthquake resistant structures-Part 1: general rules, seismic actions and rules for building, Brussels
7. Muhsen BA, Umemura H (2011) New model for estimation of shear strength of reinforced concrete interior beam-column joints *Procedia Engineering*, Vol.14, pp 2151–2159

Performance Based Seismic Design of Semi-rigid Steel Concrete Composite Multi-storey Frames

R. Senthil Kumar and S.R. Satish Kumar

Abstract Steel-concrete composite frames offer several advantages such as efficient sections in terms of strength and stiffness, economy and speed of construction. Semi-rigid connections can also be easily achieved by providing additional rebars in the slab to resist hogging moments at beam ends. However, design of these frames is a complex problem as the minimum connection stiffness and strength required to satisfy seismic drift limitations are not easy to determine. Hence a comprehensive study is being undertaken with the objective of determining the most optimum connection properties for frames with various configurations such as spans and storey heights located in different seismic zones of India. In this study, regular plane frames of two, four and eight storeys are analysed under equivalent static and non-linear static pushover analysis. The linear response of semi-rigid frames is characterised in the form of ratios of roof drifts and time periods taken with respect to equivalent rigid frames. The moment-rotation curves for the semi-rigid connection are obtained from the results of an earlier study conducted by Smitha and Kumar (J Constr Steel Res 82:164–176, 2013) on stiffened flange plate composite connections. The variation of roof drifts and time periods with respect to connection stiffness is obtained. The roof drifts under equivalent static loads and time periods decrease exponentially with increase in connection stiffness. The analyses results showed that significant reduction in design base shears can be achieved for practical semi-rigid frames as the time periods of these frames are higher than that of rigid frames. A design procedure is proposed to ensure that the frames satisfy code stipulated drift limitations. The seismic performance of a rigid and semi-rigid frame designed to satisfy current codal provisions are compared by carrying out non-linear static pushover analysis. The comparison indicates that, in low (zone II) to moderate (zone III) seismic areas, frames with semi-rigid connections can be designed to perform satisfactorily thereby reducing the overall cost of the structure.

Keywords Composite · Frame · Semi-rigid · Performance · Seismic

R. Senthil Kumar (✉) · S.R. Satish Kumar
Department of Civil Engineering, Indian Institute of Technology (IIT) Madras,
Chennai 600036, India

© Springer India 2015
V. Matsagar (ed.), *Advances in Structural Engineering*,
DOI 10.1007/978-81-322-2193-7_78

989

1 Introduction

The use of moment frames incorporating composite steel-concrete floor systems offers several behavioural and practical advantages over bare steel or reinforced concrete alternatives. The increase of stiffness and capacity due to composite action enables the use of larger beam spans under the same loading conditions. Accordingly, the demand for larger and more flexible usable space, coupled with the need for faster optimised construction processes, has led to an increased utilisation of composite frames in recent years [5]. Composite framed construction is suitable for earthquake resistant design as compared to pure steel and reinforced concrete constructions since it offers large stiffness and load bearing capacity. However, the number of detailed studies carried out on the seismic response of composite frames, in comparison with other counter-parts is limited.

Composite connections are defined as regions where the composite beam frames into a steel column. Frames with semi-rigid beam-to-column connections have many economical and constructional advantages over frames with rigid connections. It is well known that semi-rigid connections provide economical options for designing steel moment frames subjected to gravity loads, essentially due to the reduced moment transfer from the beams to the columns. Semi-rigid connections could be used with great advantage to resist earthquake loads, provided they satisfy the seismic design requirements. Due to their inherent flexibility, semi-rigid connections take less moment and also accommodate large rotations without severe stress concentration effects [7]. This means that semi-rigid connections are less susceptible to failure by brittle fracture modes such as those observed in the Northridge and Kobe earthquakes. The more flexible characteristic of semi-rigid connections also lead to a reduction in the seismic loads. In regions of low to moderate seismicity, semi-rigid connections may provide a more economical and aesthetic alternative to braced frames or frames with other lateral load resisting systems such as shear walls.

Performance based seismic design (PBSD) method is a rapidly growing design methodology based on the probable performance of the building under different ground motions. The structures designed by current codes undergo large inelastic deformations during major earthquakes. The current seismic design approach is generally based on elastic analysis and accounts for inelastic behaviour in an indirect manner. The inelastic behaviour, which may include severe yielding and buckling of structural members and connections, can be unevenly and widely distributed in the structure.

From the above discussions, it is clear that use of semi-rigid connections will be advantageous in steel-concrete composite frames. Also, the PBSD concept needs to be extended to composite frames with semi-rigid connections where failure will occur in the connections rather than in the beams. This will also eliminate the need to use Reduced Beam Sections to develop plastic hinges in the beams. Further, PBSD design of semi-rigid frames will have great economic advantage over that of rigid frames especially in the low to moderate seismic zones of India.

2 Literature Review

A major part of the research on composite connections has been done by Ammerman and Leon [3], Leon et al. [14] and Leon [13] who have tested connections with top, seat and web angles under monotonic and cyclic loads. They developed the concept of semi-rigid composite connections and observed from the tests that significant increase in strength and stiffness of “simple” connections can be achieved by making the steel beam act composite with the slab and by providing some supplementary slab reinforcement in the hogging regions. The seat and web angle connection didn't have symmetric moment-rotation behaviour because of the lower stiffness resulting from opening up of seat angle under sagging moments. To overcome this failure, Smitha and Kumar [16] investigated the behaviour of flanged plate semi-rigid connection and stiffened flange plate semi-rigid connection under cyclic loading experimentally and analytically. The parameters affecting moment-rotation characteristics of connection were discussed and various moment-rotation curves corresponding to variations in parameters like rebar area to flange area, depth of web angle to depth of beam were presented. They were found to perform equally well under hogging and sagging moments. The energy dissipation capacity and ductility were found to be adequate for use in seismic resistant frames.

Requirements for seismic qualification of semi-rigid connections are adequate stiffness under serviceable limit, elastic response under moderate earthquake (strength) and prevent collapse under severe earthquake (ductility). Kumar and Rao [7] have given requirements of stiffness, yield and ultimate strengths, ductility and energy dissipation capacity for use in seismic resistant frames. The requirement is that rotation of the connection, at a moment equal to the first yield moment of the connected beam, does not exceed 0.02 radians. Energy efficiency index of connection should have a minimum value of 20 % for use in seismic areas. In all the semi-rigid frames analyzed, plastic hinges are formed in both connections as well as at the column base. Connections are provided with substantial ductility and stable hysteretic behavior to eliminate the need for imposing column-to-beam over strength factors in the presence of partial strength connections [6]. Instead column-to-connection over strength factors need to be imposed, which allows the use of smaller sections provided all other code requirements are met. This would also imply a possible relaxation on the beam cross section slenderness limitations, and thus significant economies can be achieved in the frame.

Research on semi-rigid frames by Ahsan et al. [1] indicated that instead of ultimate strength, serviceability limit on lateral drift is most likely to govern the design. The important role of the connection rigidity becomes apparent with the increase in frame height. Frames with very flexible connections and greater number of stories have collapsed even under the working load. Semi-rigid frames with appropriate connection stiffness meet the serviceable roof drift limit of 1/300 times the height of the frame. Pavan Kumar [15] analysed the semi-rigid steel frames of various connection stiffness and formulated the procedure to find the minimum stiffness to satisfy the drift limits under design earthquake.

Connection rotation depends on the restraints the connection is subjected to and the lateral shear on frame at the level of the connection. The maximum level of connection rotations of medium-rise semi-rigid frames will seldom exceed the initial and middle portions of the tri-linearised moment rotation curves. The use of semi-rigid connections resulted in reduction in the stiffness of the frame, but the displacements did not increase proportionally. The stiffness degradation and pinching effects in the connection behaviour increased the story drifts. Therefore, while designing the semi-rigid frames, connections having kinematic hardening behaviour with minimal pinching should be utilized, to limit the connection rotations. The codes also require that the moment capacity of the connections should be more than 50 % of the beam capacity [2].

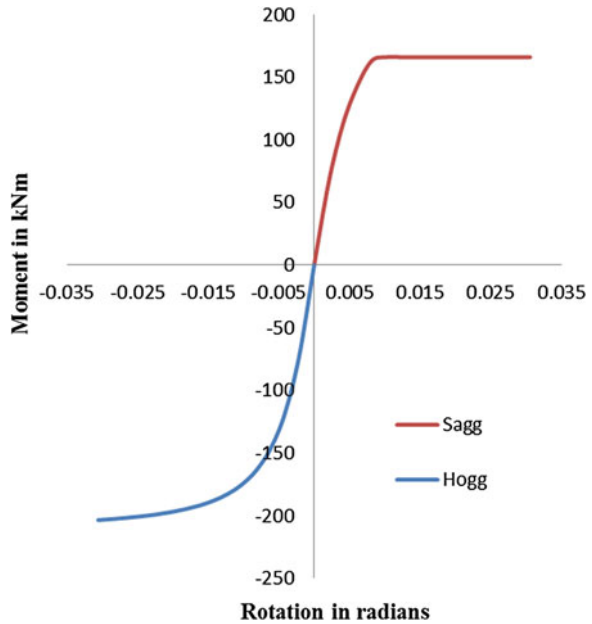
The sagging rotation capacity of composite beams consisting of a concrete slab attached to a steel beam by a shear connection was studied by Ansourian [4]. He proposed the expressions for the minimum inelastic rotation and deflection available at collapse.

Performance based seismic design procedure for steel moment frames based on pre-selected yield mechanism and target drift was proposed by Lee et al. [12]. The design base shear was derived from a modified energy balance equation incorporating the concept of seismic force reduction factor and the displacement amplification factor. A new seismic lateral force distribution based on nonlinear dynamic analyses was also presented. Three steel moment frames were designed using the proposed lateral force distribution and the performance of plastic design methodology with specified pre-selected target drifts were studied. Analysis results showed that the proposed design method produced structures that met the preselected performance objectives.

3 Modelling and Analysis of Frames

Nonlinear Static Pushover analysis was carried out on rigid and semi-rigid steel concrete composite frames to evaluate their seismic performance using SAP2000 NL. Regular two storey rigid and semi-rigid steel concrete composite plane frames were considered for this study. Composite beams were designed as per IS 11384:1985, columns as per IS 800:2007 and seismic loads calculated as per IS 1893:2002. Bay width and storey height of the frames were taken as 8 and 4 m, respectively. The frames were assumed to be spaced 4 m apart and supporting reinforced concrete slab of thickness 100 mm, for calculating the dead and imposed loads which were considered as per IS: 875–1987. The floor masses were obtained as 136 and 102 kN for the ground and top floor respectively. The frames were assumed to be located in zone III on medium soil strata. A damping ratio of 5 % was assumed for the steel-concrete composite frames. The frames were designed to satisfy the load combinations stipulated in IS800:2007. Connection moment-rotation curve was modelled as linear rotational spring for linear static and eigenvalue analysis and nonlinear spring for Nonlinear Static Pushover analysis. Moment–rotation (M- θ)

Fig. 1 Moment-rotation curve of semi-rigid connection ($J = 6$)



curves for semi rigid steel concrete composite stiffened plate connection given by Smitha and Kumar [16] were used to develop $M-\theta$ of the connections. In SAP2000, linear spring was modelled as linear link element and nonlinear spring as Multi-linear Plastic link element. Connections were designed as full strength and they were classified as semi rigid connections by stiffness criteria as per Bjorhovde classification (IS 800–2007). Connection rotation capacity was taken as lesser of the sagging and hogging rotation capacities. Composite beam’s plastic hinge and connection’s moment-rotation curve modeled as single link. Moment-rotation curve of the connection was bifurcated by composite beam’s plastic moment when beam’s moment capacity was lesser than connection’s (Fig. 1). Moment-rotation curve of composite beam was developed from expressions given by Ansourian [4]. $M-\theta$ model given by FEMA 356 was used for steel columns.

4 Parametric Study of Semi-rigid Steel-Concrete Composite Frames

4.1 Linear Static and Eigen Value Analysis

Connections should have adequate stiffness to satisfy the drift limitations under serviceable loads. The usual procedure for ensuring compliance with drift limitations is to apply the seismic load as an equivalent static load on the frame and carry out a linear static structural analysis to calculate the storey and roof drifts (IS: 1893,

2002). IS: 1893 (2002) imposes a limit on storey and roof drifts as 0.4 % of the storey height and total height, respectively. For regular frames with uniform storey heights, and subjected to a prescribed pattern of loading the two drifts will be related and so in the present study only the roof drift is considered.

Semi-rigid frames are characterised by two parameters J and α . The ratio of connection stiffness to the composite beam flexural stiffness is called the ‘joint factor (J)’,

$$J = \frac{K_o}{(EI/L)_{beam}} \quad (1)$$

where,

K_o initial tangent rotational stiffness of the connection

E Young’s modulus

I moment of inertia

L span of the beam.

The other parameter α is defined as the ratio of the flexural stiffness of beam to the flexural stiffness of the column. Mathematically,

$$\alpha = \frac{(EI/L)_{beam}}{(EI/h)_{column}} \quad (2)$$

where h is the height of the column.

In the present study, α is varied from 0.5 to 2 for all storeys while joint factor (J) is varied from 2 to 10. The response parameters of interest are the variation of roof displacements and time periods with connection stiffness. The static drift factor (SDF) of the semi-rigid composite frame is defined as the ratio of roof displacement of semi-rigid composite frame to that of corresponding rigid frame under the same equivalent static lateral loads. Similarly, the time period factor (TF) of semi-rigid composite frame is defined as the ratio of the fundamental natural time period of the semi-rigid composite frame to that of the corresponding rigid frame. The variation of SDF and TF with J will be similar and the fact is verified by plotting the graphs.

4.2 Nonlinear Static Pushover Analysis

Pushover analysis is frequently used in practice to study the ductility and performance of the buildings under earthquake loading. ATC-40 capacity spectrum is used to find the performance point of the capacity curve under DBE (Design Basis Earthquake) and MCE (Maximum Considered Earthquake) response spectrums. Response spectrum of MCE is taken as twice that of DBE. The important response parameter for performance based seismic design is inter-storey drift index (IDI). IDI is defined as the difference in displacement of two consecutive floors divided by the storey height.

5 Results and Discussions

5.1 Variation of Static Drift Factor (SDF) with Joint Factor (J)

The variation of SDF with J is important since it enables the calculation of semi-rigid frame drifts from the corresponding rigid frame drifts. Variation of SDF with joint factor (J) and α has been studied for the two storey frames. α can be varied by changing either the moment of inertia or the lengths of beams and columns. In the present study, α is varied from 0.5 to 2 by changing the moment of inertia of column (I_c). Although the roof displacement depends on the absolute values of member geometric properties, SDF is almost independent of the absolute values for same value of α . Thus, variations in member geometric properties such as member length and section moment of inertia can be accounted for by using the simple parameter α . Table 1 gives the sectional properties of the frames analysed. The variation of SDF with J for the two storey frame for four different α values is shown in Fig. 2. Figure 2 shows that SDF decreases exponentially with increase in J. Since, frame lateral stiffness increase with increase in J, frame drifts will decrease. From the Fig. 2 it can also be observed that the variation of SDF with α is relatively small compared to its variation with J.

Fig. 2 Variation of static drift factor (SDF) with joint factor (J)

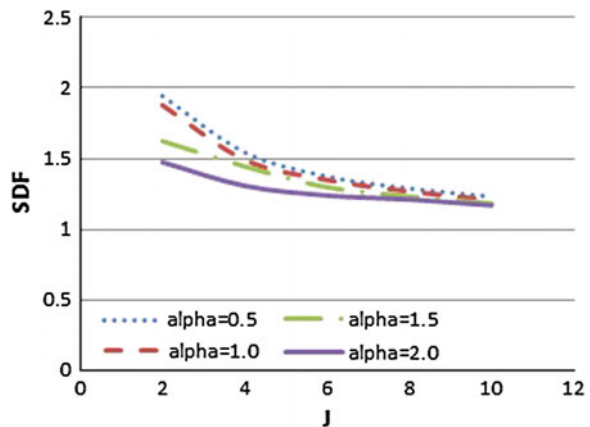


Table 1 Sectional properties of frames analysed for linear static and eigen analysis

α	$I_b \times 10^{-5} \text{ m}^4$	$I_c \times 10^{-5} \text{ m}^4$
0.5	39.39	38.60
1.0	38.67	19.30
1.5	38.67	13.20
2.0	38.67	9.87

5.2 Variation of Time Period Factor (TF) with Joint Factor (J)

Figure 3 shows that TF decreases with increase in J similar to SDF. Since, stiffness increase with increase in J, flexibility of the frame will decrease. As per IS1893–2002, for longer periods base shear is inversely proportional to the time period. Base shear will increase with increase in stiffness. Flexible frame attracts less seismic force compared to stiffer frame and should be taken advantage of in the design of semi-rigid composite frames for seismic loading.

5.3 Variation of Inter-storey Drift Index (IDI) with Joint Factor (J)

Figures 4 and 5 show that IDI increase with decrease in J. Story drifts and roof drifts were inversely proportional to the frame stiffness. From Figs. 4 and 5 it can be observed that not much difference is there between joint factors 6, 8 and 10. In push over analysis, hinges are formed in upper storeys and also in joint factor 10. It means, if connection stiffness increases, column size should be increased to avoid hinges in columns (Strong Column-Weak Beam Concept). The fitted curves of the Static Drift Factor (SDF) and Time Period Factor (TF) are shown in Figs. 6 and 7, respectively.

Fig. 3 Variation of time period factor (TF) with joint factor (J)

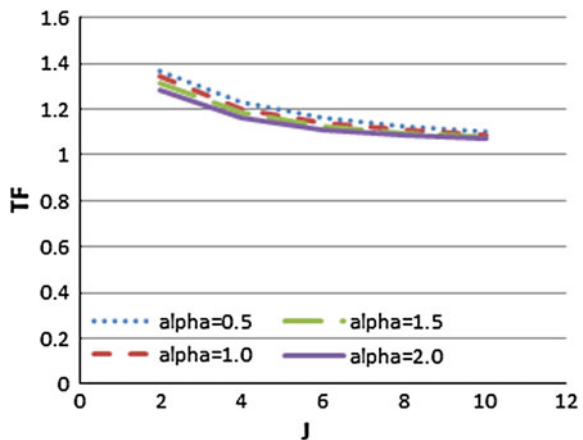


Fig. 4 Variation of IDI with joint factor (J) under DBE

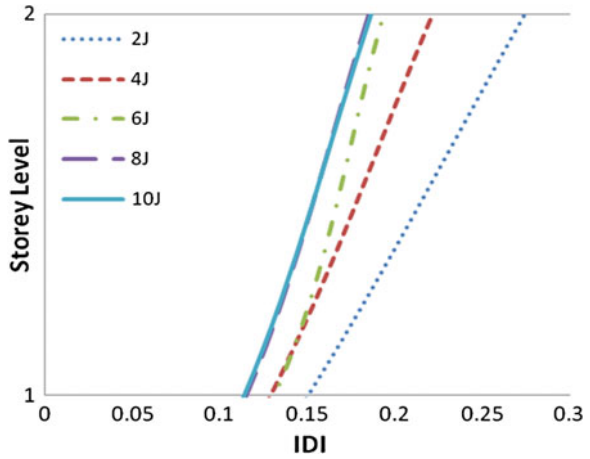


Fig. 5 Variation of IDI with joint factor (J) under MCE

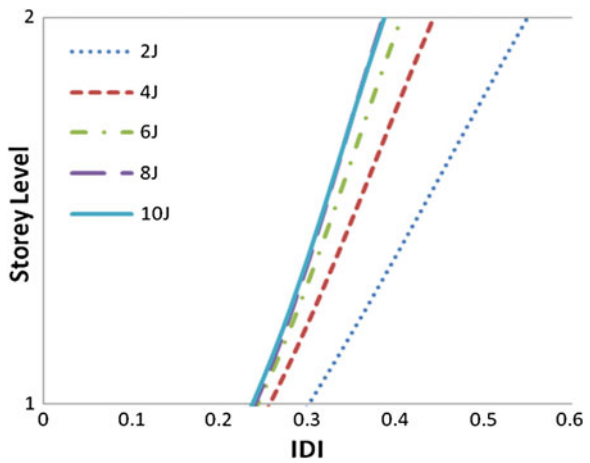


Fig. 6 Curve fitting of SDF with J

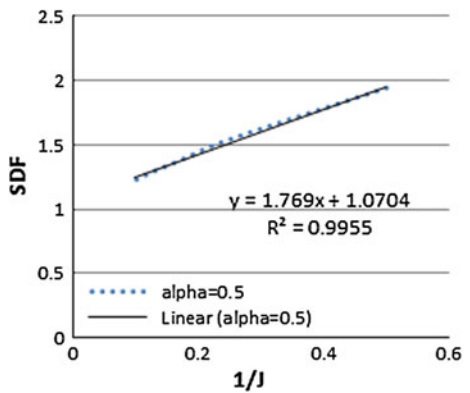
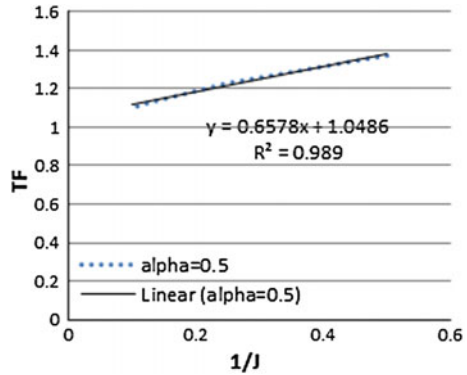


Fig. 7 Curve fitting of TF with J



6 Design Recommendations

The flexibility of semi rigid composite frame improves the seismic performance but it increases the storey and roof drifts drastically. So, connection should have adequate minimum stiffness to satisfy the drift limits under design earthquake given as per IS 1893–2002. A design procedure is proposed here to find the minimum connection stiffness (J_{min}) for a composite frame so as to satisfy the drift limitations under design earthquake.

The equations relating SDF and TF with J can be formulated by using curve-fitting for the case of two-storey frame with value of α as 0.5. The relations are

$$SDF = (A_1/J) + A_2 \tag{3}$$

$$TF = (A_3/J) + A_4 \tag{4}$$

where A_1, A_2, A_3 and A_4 are constants given in Tables 2 and 3

Table 2 A_1 and A_2 values for Eq. (3)

α	A_1	A_2
0.5	1.8187	1.0575
1	1.5865	1.0571
1.5	1.0804	1.1165
2	0.6906	1.1268

Table 3 A_3 and A_4 values for Eq. (4)

α	A_3	A_4
0.5	0.6578	1.0486
1	0.6279	1.0322
1.5	0.5894	1.0275
2	0.5409	1.0203

6.1 Steps to Predict J_{min} for Semi-rigid Composite Frames (Pavan Kumar [10])

The equations or graphs given above can be used to reduce the number of iterations in design. A convenient design procedure is proposed as follows:

1. Obtain the number of storeys from the frame geometry.
2. Calculate the α value for the frame.
3. Select appropriate design curve or equation, for corresponding α and number of storeys. Linear interpolation can be done for A1 and A2 values for the intermediate α values.
4. Assume $\Delta_{SR} = 0.004H$, where H = Total height of the frame
5. Δ_R can be calculated using any structural analysis program for the design seismic load corresponding to TR.
6. Calculate $SDF_i = \Delta_{SR}/\Delta_R$
7. Calculate J_i from the corresponding design curve or Eq. (3)
8. Find corresponding TF for J_i using design curve or Eq. (4)
9. Find $T_{SR} = TF \times T_R$
10. Calculate the seismic base shear V_{BSR} corresponding to T_{SR}
11. Update
12. $\Delta_R = \frac{V_{BSR}}{V_{BR}} \times \Delta_R$

Repeat the steps 6–11 till updated value of Δ_R is close to the previous Δ_R obtained in step 5. The corresponding J is the minimum value which will satisfy drift limits.

7 Conclusions

- Plots of SDF and TF as a function of the joint factor J can be used to calculate the time period and drift of the semi-rigid composite frames corresponding values of rigid composite frames. The values of SDF and TF were exponentially decreased with increase in J.
- Significant reduction in seismic base shears of semi-rigid frames could be obtained for lower connection stiffness.
- The proposed design procedure can be used to ensure that the semi-rigid composite frames satisfy drift limitations under design seismic loads.
- Inter-storey Drift Index (IDI) decreased with increase in Joint Factor (J) and also observed that not much difference between joint factors 6, 8 and 10. Hence, we can get same performance with joint factor equals to 6 economically.
- If connection stiffness increases, column size should be increased to avoid hinges in columns.

References

1. Ahsan R, Ahmed I, Ahemed B (2003) Lateral drift of semi-rigid steel frames-I. *J Civil Eng CE* 31(2):177–189
2. Aksoylar ND, Elnashai AS, Mahmoud H (2012) Seismic performance of semi-rigid moment resisting frames under far and near field records. *J Struct Eng* 138(2):157–169
3. Ammerman DJ, Leon RT (1987) Behaviour of semi-rigid composite construction. *AISC Eng J* 24:53–61
4. Ansourian P (1982) Olastic rotation of composite beams. *J Struct Div ASCE* 108:643–659
5. Elghazouli AY, Castro JM, Izzuddin BA (2008) Seismic performance of composite moment resisting frames. *Eng Struct* 30:1802–1819
6. Elnashai AS, Elghazouli AY, Denesh FA (1998) Response of semi-rigid steel frames to cyclic and earthquake loads. *J Struct Eng (ASCE)* 124(8):857–867
7. IS 11384:1985 (1985) Code of practice for composite construction in steel and concrete. Bureau of Indian Standards, New Delhi
8. IS 875:1987 (1987) Code of Practice for Design Loads (other than Earthquake) for Buildings and Structures. Bureau of Indian Standards, New Delhi, India
9. IS 1893:2002 (2002) Criteria for Earthquake Resistant Design of Structures. Part 1-General Provisions and Buildings. Bureau of Indian Standards, New Delhi, India.
10. IS 800:2007 (2007) Code of Practice for General Construction in Steel. Bureau of Indian Standards, New Delhi, India
11. Kumar SRS, Rao DVP (2004) Seismic qualification of semi-rigid connections in steel frames. In: 13th World conference on earthquake engineering, Paper No: 2149, Canada
12. Lee SS, Goel SC, Chao SH (2004) Performance based seismic design of steel moment frames using target drift and yield mechanism. In: 13th world conference on Earthquake Engineering, vol 266, Canada
13. Leon RT (1990) Semi-rigid composite construction. *J Constr Steel Res* 15:99–120
14. Leon RT, Ammerman DJ, Lin J, McCauley RD (1987) Semi-rigid composite steel frames. *AISC Eng J* 24:147–55
15. Pavan Kumar VR (2006) Seismic analysis and design of semi-rigid steel frames. MS thesis, IIT Madras, India
16. Smitha MS, Kumar SRS (2013) Semi-rigid composite flange plate connections-finite element modeling and parametric studies. *J Constr Steel Res* 82:164–176

Seismic Performance of Stairs as Isolated and Built-in RC Frame Building

Zaid Mohammad, S.M. Talha and Abdul Baqi

Abstract Stairs are vulnerable part of buildings subjected to earthquakes while stair elements have low ductile capacity and may be subjected to brittle failure. Also in analysing a RC building for gravity and seismic loads, its presence is not considered due to modelling complexity instead its weight is transferred to supporting beams or walls. Thus, design of stairs is of keen interest. Normally stair slabs are supported on wall or cast monolithic with the floor beam provided along or across the direction of flight. These supports provide rigidity in the stair slabs and impart hogging moments at corners and near supports. Also, as part of building frame, the loads are transferred from the stair slab to the supporting beams, hence a considerable reduction in the deflection and moments in the stair slabs. The behaviour of stair slab is further changed when subjected to seismic loads. Presently, the behaviour of reinforced concrete stair slab is investigated considering different support arrangements with and without seismic effects, and values of moments are compared as obtained in conventional design methods based on specifications of standard codes of practices.

Keywords Staircase · Reinforce concrete · Earthquake · Building frame · Monolithic

1 Introduction

Stairs are vulnerable part of structures subjected to earthquakes, while stair elements have low ductile capacity and may be subjected to brittle failure. However, while analysing a RC building for gravity and seismic loads, its presence is

Z. Mohammad (✉) · A. Baqi
Department of Civil Engineering, Aligarh Muslim University,
Aligarh 202002, India

S.M. Talha
University Polytechnic, Aligarh Muslim University,
Aligarh 202002, India

© Springer India 2015
V. Matsagar (ed.), *Advances in Structural Engineering*,
DOI 10.1007/978-81-322-2193-7_79

1001

not considered due to modelling complexity and its weight is transferred to supporting beams or walls. Normally stair slabs are supported on wall or cast monolithic with the floor beam provided along or across the direction of flight. These supports provide rigidity in the stair slabs imparting hogging moments at corners and near supports. Also, due to fixed support action there is significant reduction in the deflection and moments in the stair slabs. But in practice, such behaviour of stair slabs is normally ignored. The true behaviour of stairs in building with varying support arrangements is still not well understood and need be studied thoroughly. Seismic forces acting on stairs further complicate the behaviour and a comprehensive test study is required. The present work is however limited to a theoretical study on selected models to incorporate varying support arrangements.

2 Literature Review

To predict the real behaviour of stair slabs a 3D modelling of the same is an apt choice, though researchers have initially attempted to idealize the stair slabs as a 2D planar structures supported on walls or beams. It is seen that the behaviour is changed with the support arrangements as claimed by Ahmed et al. [1, 2] and Baqi and Mohammad [3]. Normally, the design of such stair slabs is done assuming it as one way slab with effective span assumed as a horizontal distance between the end supports. Sometimes the landing portions in a U-turn stair slabs are supported on the sides and for such case the Indian Code of Practice (IS 456: 2000) [4] suggests a reduced horizontal span. British Code of Standards (BS 8110 Part 1: 1985) [5] also suggests a reduced effective span for typical support conditions which, if incorporated in the design, may results in some saving in the material as compared to the conventional design. The American Code of Practice (ACI 318-05) [6], however, does not provide any recommendation regarding the restraining effect due to inherent support conditions. Stair slab with different boundary condition was also analysed as two-dimensional beam model, representing a strip of unit width [7] and found that results are comparable with that obtained by F.E. analysis. Hakan and Ergin [7] also observed considerable axial forces develop in the stair slab with side supported landings, due to its two dimensional behaviour, though bending moment, shear and axial forces in transverse direction were almost constant. Also, it was observed that such stair slabs when supported with edges on the walls behave similar to the simply supported floor slab except at the junction of the inclined portion of the slab and landing and the corners of landings where stresses were abruptly increased as reported by Baqi and Mohammad [3]. The conventional method of design, however, does not incorporate such changes in the behaviour.

During earthquakes stairs are considered to be the weakest and most vulnerable elements in the building. Few researches have, therefore, attempted to investigate its performance with in the existing RC building [8] and found that the stair slabs transfer bending and axial forces to the supporting beams but attract additional shear forces. A similar study by Zhang and Yuan [9] proved that the stair slabs are

affected with seismic forces and may cause serious damage to the supporting beams and columns. Stair slabs existed within RC frame structures are also found to contribute to the global stiffness of the structure framework to its 'K' shaped bracing [9, 10] and thus effecting the net deformation of the framework. It may be concluded that the seismic effect on the stair slab needs special attention of the researchers to give a basis for rational design of this complex structure.

Further, the behaviour of such stair slabs as part of beam-column frame system may change due to transfer of forces from stair slab to adjoining beam/slab elements and also due to inherent deflection of supporting beams. Specially, during earthquakes, transfer of forces may affect the behaviour considerably. This aspect may be investigated by comparing the results of individual stair slab and a stair slab incorporated in building frame. For this, in present study, the behaviour of multi-flight stair slab with landings on both the sides supported at the ends has been investigated theoretically with few type of models i.e. isolated stair slab with different support arrangements and the stair case incorporated within RC framed building. These models have been tested subjected to gravity and seismic forces to give the idea about its behaviour as isolated structure and as contained in RC framed building.

3 F.E. Modelling and Analysis

3.1 Model Formation

The behaviour of multi-storied stair slab with landings has been investigated theoretically using four types of finite element models as below and described in Fig. 1.

Model 1: Simply supported at edges parallel to risers

Model 2: Simply supported at edges similar to frame configuration

Model 3: Multi-flight staircase built in isolated RC frame

Model 4: Multi-flight staircase built in RC framed building

In the first model (Model 1, Fig. 1a) the stair slab with landings on both sides and supported on walls at the ends has been idealized as 2D plate bending elements and subjected to gravity loads i.e. the dead weight of the material and uniform distributed live load over its complete area. The behaviour of such stair slab is also investigated for its floor landing supported on its sides (Model 2, Fig. 1b). To predict the behaviour of stairs in RC frames where the supporting beams are free to sag under applied loads, a six storey staircase has been tested both as isolated staircase building as well as a staircase included in a RC building frame. For this, two different models (Models 3 and 4, Fig. 1c, d respectively) have been tested under gravity loads and seismic effects acting in two orthogonal directions i.e. along and across going in stairs.

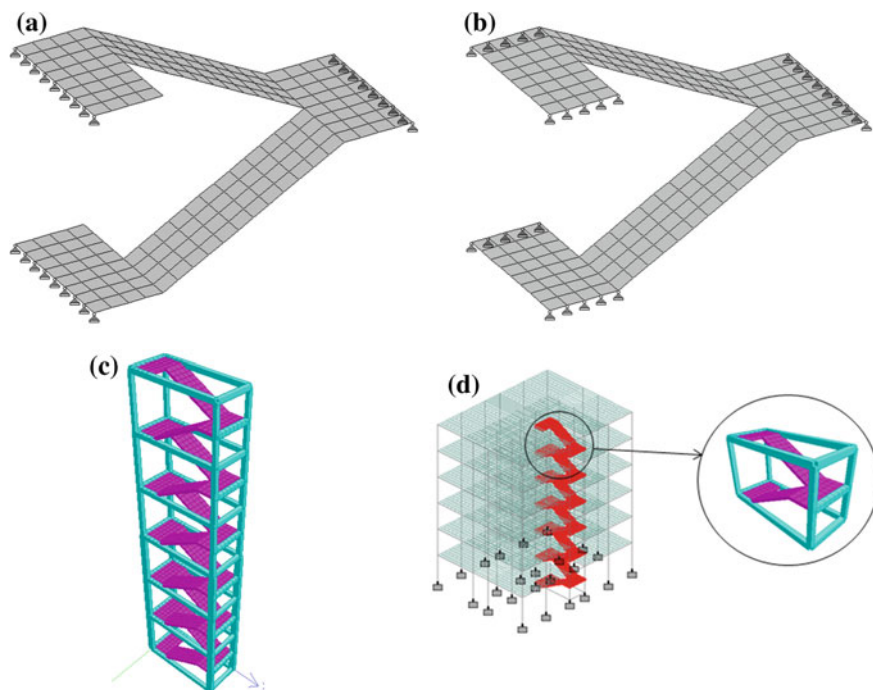


Fig. 1 Types of models. **a** Model 1. **b** Model 2. **c** Model 3. **d** Model 4

To compare the behaviour of a stair slab in four different models, a uniform size of the stair slab i.e. each flight of 1.25 m wide, 1.8 m high (half of the floor height), 150 mm thick slab with inclined waist-slab of 3.75 and 1.25 m wide landings at both the sides, has been chosen for modelling (see Fig. 2). The supports in Models 1 and 2 are assumed as simply supported where as in Models 3 and 4 the stair slab is assumed as rigidly fixed with beam of RC frame buildings. These RC buildings consist of 0.4×0.5 m sized column and 0.3×0.4 m beams with each storey height of 3.6 m. In Model 4 the staircase is assumed to be incorporated near the middle of building plan as per the normal practice. The material used in RC frame building and stair slabs in all the four models is assumed as M20 mix concrete and Fe 415 grade steel. For a simplest finite element analysis, the slab is divided into four node plate elements of size 0.3×0.3 m approximately.

3.2 Method of Analysis

The models constitute two node elements for beams and columns and four node plates for stair slabs. Beams and column elements are subjected to gravity loads whereas the plates are subjected to both gravity and live loads. In addition to the

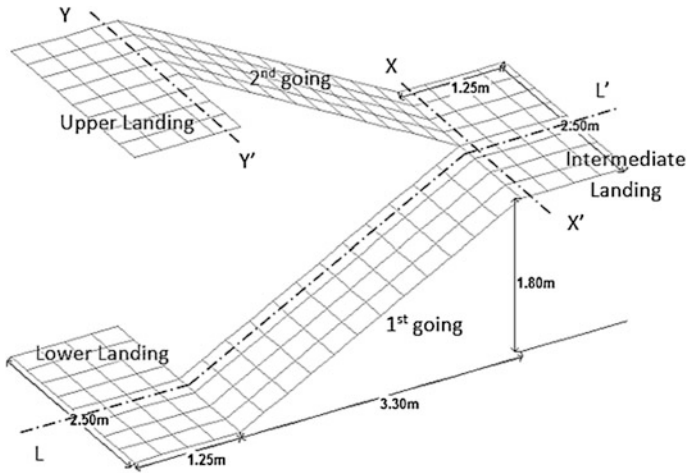


Fig. 2 Finite element mesh of staircase

static loads, Models 3 and 4 are also analysed for seismic loads, adopting Linear Response Spectrum method of analysis as per IS: 1893(Part I)-2002 with SRSS combination. The different combinations of loads (as per IS 456: 2000) considered in the analysis are given as:

- i. LC (i): $1.5 * (DL + LL)$
- ii. LC (ii): $1.2 * (DL + LL \pm EQ \text{ IN } X)$
 - (a) $1.2 * (DL + LL + EQ \text{ IN } X)$
 - (b) $1.2 * (DL + LL - EQ \text{ IN } X)$
- iii. LC (iii): $1.2 * (DL + LL \pm EQ \text{ IN } Z)$
- iv. LC (iv): $0.9 * DL \pm 1.5 * EQ \text{ IN } X$
- v. LC (v): $0.9 * DL \pm 1.5 * EQ \text{ IN } X$

The gravity loads are undertaken as self-weight; dead weight due to stair steps which is 2.875 kN/m^2 and floor finish as 1.0 kN/m^2 . Whereas, the live load is assumed to be 3.0 kN/m^2 on floors and 5.0 kN/m^2 on stair slabs.

4 Seismic Parameters (as Per IS 1893 (Part 1): 2002)

In the present study, for dynamic analysis both Models 3 and 4 are subjected to peak ground acceleration (PGA) of 0.16 g i.e. Zone III. To increase the seismic effect on the structures, importance factor (I) has been taken as 1.5, also the structures are assumed to be ordinary moment resisting frames having response reduction factor

(*R*) of 3. The soil condition of the site is taken to be medium strata and the damping coefficient is assumed as 5 %.

The analysis is based on following assumptions

1. Material is taken as homogenous, isotropic and elastic.
2. The values of modulus of elasticity and Poisson’s ratio are 22,360 N/mm² and 0.2.
3. The floor diaphragms are taken as rigid in their plane.
4. Degree of freedom per node is 6 i.e. 3 translational and 3 rotational.
5. Torsional effect is considered as per IS 1893 (Part 1): 2002.

5 Results and Discussion

In the present study, different staircase models as discussed above have been analysed for different load cases and for different support conditions. In each of these cases the applied load is assumed as uniformly distributed over the complete area of stair slabs including landings. In the Models 1 and 2, the landings are assumed to be supported on walls whereas in case of Models 3 and 4, landings are supported on beams of the framed structure of building. Thus, sagging of supporting beams along its span will also allow the deflection of the supported landings.

Though, the analytical results for deflection and bending moments were available at every node of plate, for convenience, the values have been compared along suitably chosen sections (see Fig. 2) to describe the true behaviour. The values of deflection of stair slabs are taken at inner edge of going and average values of moment M_x and M_y , are taken at centre of plates. The graphical representations of values of deflection and bending moments M_x along critical sections i.e. section LL’ at first going, and M_y along XX’ and YY’ at intermediate landing and upper landing respectively, for different load combinations are shown in Figs. 3, 4, 5, 6, 7, 8 and 9. The results obtained from static and dynamic analysis of the models are discussed separately for better comparison. The result values at critical positions are also discussed.

Fig. 3 Deflection variation for static load case LC (i)

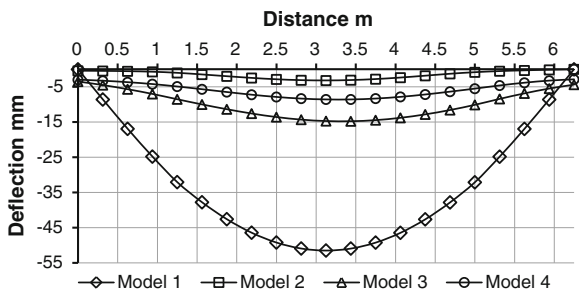


Fig. 4 Bending moment M_x variation at LL' for static load case LC (i)

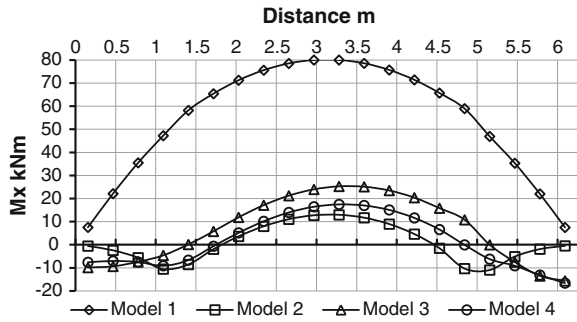


Fig. 5 Bending moment M_y variation at XX' for static load case LC (i)

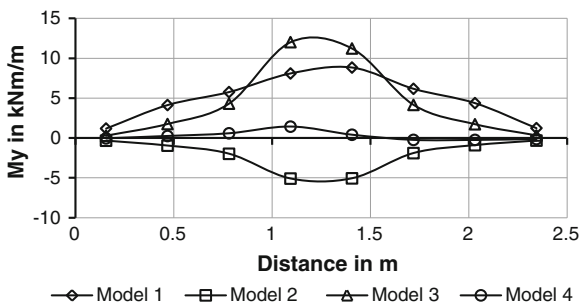


Fig. 6 Bending moment M_y variation at YY' for static load case LC (i)

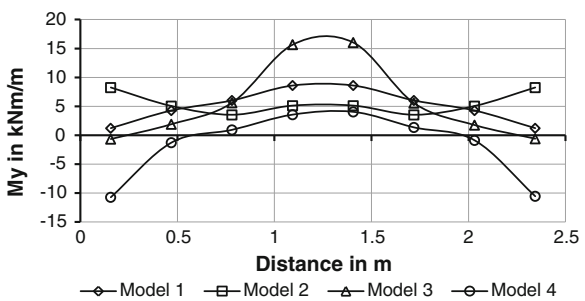


Fig. 7 Comparison of bending moment M_x variation at LL' for dynamic load case

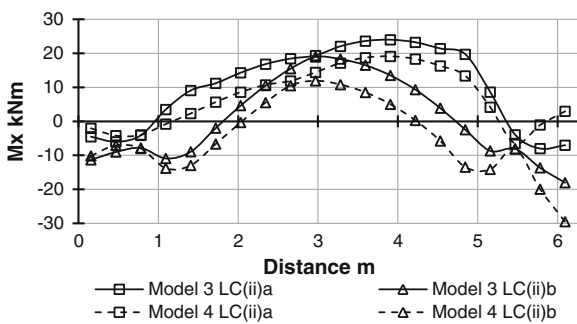


Fig. 8 Comparison of bending moment M_y variation at XX' for dynamic load case

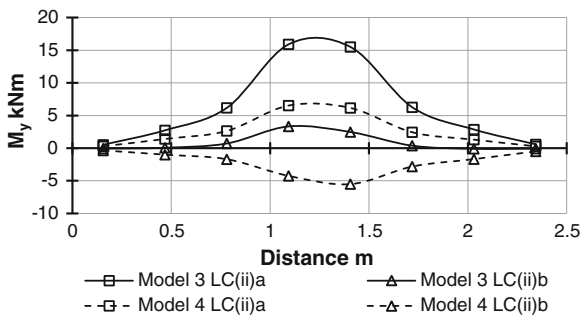
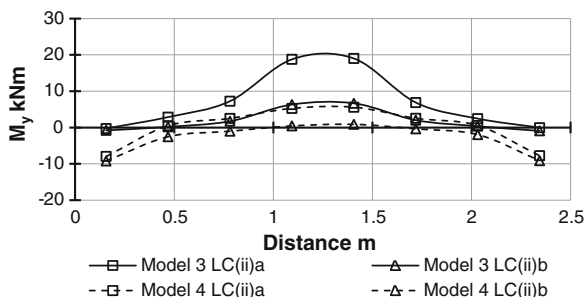


Fig. 9 Comparison of bending moment M_y variation at YY' for dynamic load case



6 Static Analysis

6.1 Variation of Deflection

Each of the models has been separately analysed for static gravity loads i.e. $1.5 * (DL + LL)$, here described as load combination LC (i). Since each of these models has different support arrangements, the critical position of maximum deflection changes in each case. Also, the values of deflection at mid-span vary due to side support conditions and it is increased from supported edges towards the free (inner) edge of stair slab. For the purpose of comparison of maximum deflection anywhere in the stair slab, the values are taken at inner edge of going to obtain higher deflections in each model. Figure 3 shows the variation of deflection along going in all the models, where it is seen that the maximum deflection is obtained at mid-span. Values of maximum deflection for Models 1 and 2 are seen to be about 52 and 3 mm respectively. A reduced value of the deflection in Model 2 explains the reduction in effective span due to side supports of the landings. This is further verified by reduction of moments in Model 2 as compared of that in Model 1 (Fig. 4). The maximum deflection in Models 3 and 4 i.e. 15 and 7 mm respectively, is also found to be reduced as compared to Model 2. This is due to rigidity provided by supporting beams of frame; where as in Model 4 value of deflection further reduces due to continuity of the floor slab in landing. For glance study, the values at critical locations are given in Table 1.

Table 1 Comparison of static analysis results

Particulars	Model 1	Model 2	Model 3	Model 4	% ratio			
					1-2	2-3	2-4	
Max. deflection (mm)	51.48 ^m	3.18 ^m	14.76 ^m	8.56 ^m	6.17	464.15	269.18	
M_x at LL'	+ve	80.00 ^m	12.94 ^m	25.26 ^m	17.48 ^m	16.18	195.21	135.08
	-ve	-	10.95 ^k	15.66 ^{ls}	16.59 ^{fs}	-	143.01	151.5
M_y at XX'	+ve	8.84 ^m	-	12.56 ^m	1.43 ^m			
	-ve	-	5.10 ^m	-	0.13 ^s			
M_y at YY'	+ve	8.65 ^m	5.12 ^m	17.56 ^m	4.04 ^m			
	-ve	-	-	0.61 ^s	10.73 ^s			

6.2 Variation of Bending Moment M_x , Along Going of Stairs

The values of longitudinal bending moment M_x for load case LC (i), for different models as compared in Table 1 and represented in graphical form (Fig. 4), are seen to be critical near mid-span, kink (junction of going and landing) and in the vicinity of the corners of landing. It is to be noted here that the critical position of the moments are mostly undefined in conventional methods. To study the true behaviour, the critical section along going is chosen suitably near the middle of stair slabs i.e. LL', and the values have been plotted for Models 1, 2, 3 and 4 in Fig. 4. It is seen that at the mid-span, sagging moment is maximum in case of Model 1, whereas hogging moments as seen in other models is found to be maximum near the kinks and at continuous edges of landing. In case of Model 2 the maximum sagging moment is reduced to 16.15 % as compared to that of Model 1, where as in Models 3 and 4 this value is reduced to 31.57 and 21.85 % respectively. This increased bending moment in Models 3 and 4 as compared to Model 2 is due to additional deflection of the edges of landings supported on beams of building frame. The maximum hogging moment of 16.6 kNm in Model 4 as obtained at edge of landing supported on beam, is comparable to the maximum sagging moment near mid-span. This hogging moment is never observed in Models 1 and 2 due to simple supports. Further, Models 2, 3 and 4 have less sagging moments as compared to Model 1 which is either due to the side supports provided below the landings or due to extra rigidity provided by continuous floors casted monolithically with the supporting beams.

6.3 Variation of Transverse Bending Moment M_y in Landings

Bending moments in transverse direction mostly does not vary if the edges of stair slabs are unsupported. However, due side support conditions as well as continuity

of material at landings in two directions, this moment, sometimes becomes critical and hence need to be considered in a rational design. The results for bending moments were available throughout the surface of stair slab including landing, but for convenience, the values are plotted only along critical sections, suitably chosen in landing portion i.e. XX' and YY' (Fig. 1) at intermediate and upper floor level landings respectively. Figures 5 and 6 give the variation of transverse bending moment M_y in landings, which show the location of critical moments i.e. near the kink and corners of landings. At intermediate landing in Models 2 and 3, the maximum bending moment M_y is observed near the kink as +12.56 kNm (sagging) and -5.1 kNm (hogging) respectively (Fig. 5). This change in behaviour may be due to different support arrangements, as the landings in the Model 3 are supported on beam whereas in case of Model 2, it is supported on wall. The presence of supporting beam and corner columns provide partial fixity to the landing, hence, developing localized stress concentration at junctions of the columns and landing. On the other hand, the bending moment M_y at floor landing (Fig. 6) varies differently as compared to intermediate one. In this case, the critical position of moment changes and shows concentrated sagging moment of +17.56 kNm near kink in Model 3 and hogging moment of -10.73 kNm near supporting beams in Model 4. But, the reason behind the development of sagging moment near support in Model 2 is still unknown.

6.4 Von Mises Stress Distribution Under Static Loads

For a better idea of stress distribution over complete area of stair slabs including landings, the results were obtained for Von Mises stress in contour form. For maximum applied static loads i.e. LC (i) the results are shown for all models in Fig. 10. It is seen that in Model 1, the deflection and moment increase from support to mid-section of going, and the Von Mises stress varies from 0.73 N/mm² at supports to 21.8 N/mm² at mid-going (Fig. 10a). However, in the case of Model 2, the values are dramatically decreased to 0.046 N/mm² at supports and about 5.91 N/mm² at mid-going, because of landings supported at sides. In this case, the maximum value of 8.57 N/mm², is obtained at kink of floor landing. In Model 3, the maximum value of stress is shown at corners of the intermediate landing which is 15.6 N/mm². This is due to the partial rigidity provided by the beam. Also, the value at mid-going increases and found to be 8 N/mm² (approx.), showing same variation as of M_x . On the other hand, Model 4 shows different variation from the Model 3. The value of stress at corners of intermediate landing is reduced to 8.95 N/mm². This may be due to presence of adjacent floors in the building which provide extra restraining effect to supporting beams and hence to the going slab. This can be proved by the reduction of stresses shown at the mid going, which is found to be 5.61 N/mm² (approx.).

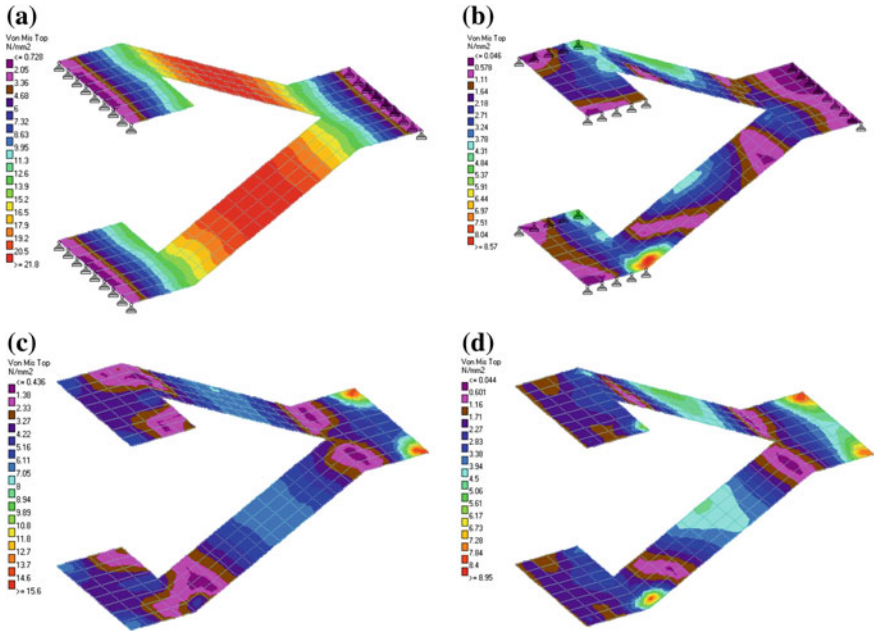


Fig. 10 Von Mises stresses in models under LC (i). **a** Von Mises stresses in Model 1. **b** Von Mises stresses in Model 2. **c** Von Mises stresses in Model 3. **d** Von Mises stresses in Model 4

7 Dynamic Analysis

7.1 Variation of Bending Moment M_x

As mentioned earlier, Models 3 and 4 are analysed for static loads as well as dynamic response spectrum analysis for SRSS combination. The results of the dynamic analyses are compared in Table 2. For evaluating critical values, seismic response of all models are observed in X direction (along going of stairs) in both +ve and -ve X directions under load cases LC (ii)a and LC (ii)b, respectively. The results obtained for longitudinal bending moment M_x i.e. along section LL' are

Table 2 Comparison of dynamic analysis results

Particulars		Model 3		Model 4	
		LC (ii)a	LC (ii)b	LC (ii)a	LC (ii)b
M_x at LL'	+ve	23.98 ^m	18.96 ^m	19.12 ^m	11.92 ^m
	-ve	8.02 ^{ls}	18.04 ^{ls}	6.48 ^k	29.51 ^{ls}
M_y at XX'	+ve	16.46 ^m	3.33 ^m	6.53 ^m	–
	-ve	–	0.07 ^s	–	5.53 ^m
M_y at YY'	+ve	20.03 ^m	6.78 ^m	5.58 ^m	0.88 ^m
	-ve	0.29 ^s	0.776 ^s	7.96 ^s	9.22 ^s

shown in Fig. 7. It is observed that the maximum sagging moment is found (23.98 kNm) in case of Model 3 under LC (ii)a and is comparable to that obtained in static analysis of same model. However, in case of Model 4, the sagging moment reduces to 11.92 kNm only under LC (ii)b, showing the minimum value in all cases. Further, it is seen that due to seismic loads, there is development of hogging moment at new location i.e. at kink, in addition to the junction of landing and supporting beams where the stresses were critical under static loads. The maximum value of hogging moment is found to be -14.11 kNm at kink on intermediate landing of Model 4 under the load case LC (ii)b, whereas, the value at supports gets increased to -29.51 kNm which is nearly equal to the sagging moment at mid-span of the going in Model 3. This requires special attention to the designers to provide extra reinforcement either or both at top and bottom faces near kinks and the corners of landings.

7.2 Variation of Bending Moment M_y

When the models are subjected to seismic loads, the values of M_y are found to be changed as compared to that in case of Model 2. The reason behind this behaviour may be due to change in support configuration i.e. landing supporting on beams. At intermediate landing, an increase of 31.1 % in the bending moment M_y in Model 3 at kink is observed, when it is subjected to earthquake load in +X direction i.e. LC (ii)a (Fig. 8). In the case of Model 4, the bending moment values are found to be +6.53 and -5.53 kNm under LC (ii)a and LC (ii)b respectively.

The values of bending moment at floor landing of Model 3, (Fig. 9) shows 16.8 % increase in the value of sagging moment near kink under LC (ii)a from static analysis. Whereas, when the structure is subjected to seismic load in $-X$ direction, this value decreases to 60.4 %. Apart from that, in Model 4, there is not much increase is observed at kink; however, there is development of hogging moment of about 10.73 kNm at supporting beams, which is due to rigidity provided by the adjacent floor slab to the landing. Thus area at kink, near to supporting beams and columns are of great importance.

7.3 Variation of Von Mises Stresses Under Dynamic Loads

Models 3 and 4 are subjected to dynamic lateral loads in X (both +ve and -ve) direction (along going) i.e. LC (ii)a and LC (ii)b. Both the Models 3 and 4 show different variation under seismic loading (Fig. 11). When these models are subjected to seismic load in +ve X direction, the values are found to be less than that observed in static analysis. However, the places of critical moments obtained under dynamic loads are same as in earlier load case. But there is significant increase in the values from LC (i), when Models 3 and 4 are subjected to lateral

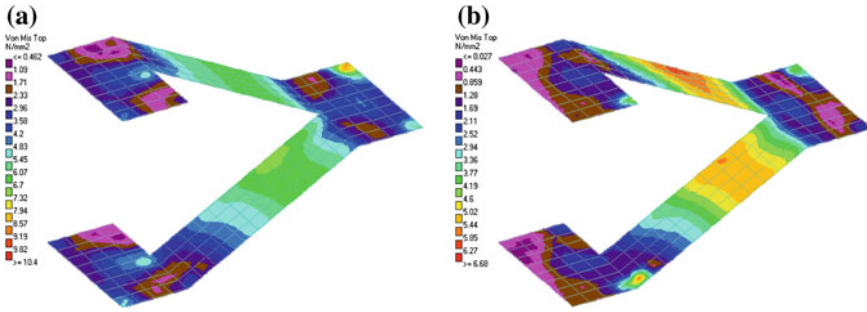


Fig. 11 Von Mises stresses in models under LC (ii)a. **a** Von Mises stresses in Model 3. **b** Von Mises stresses in Model 4

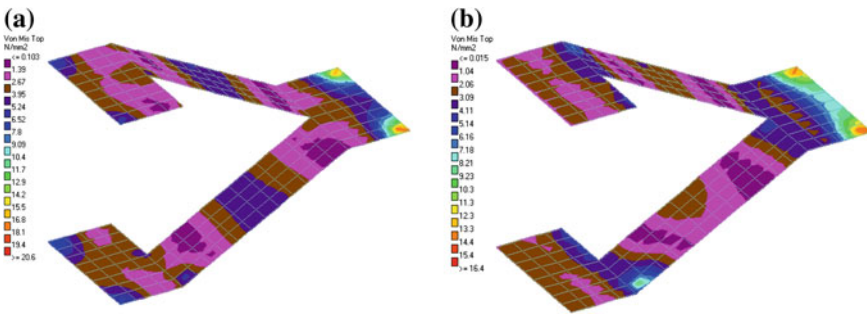


Fig. 12 Von Mises stresses in models under LC (ii)b. **a** Von Mises stresses in Model 3. **b** Von Mises stresses in Model 4

load in $-ve$ X direction i.e. LC (ii)b. The values are found to be 20.6 N/mm^2 at intermediate landing (Fig. 12) in Model 3 and 16.4 N/mm^2 in the case of Model 4. The reduction in the value of Model 4 is due to extra stiffness provided by the building frame against lateral loads, which is not present in the case of Model 3. Apart from this, there is also development of stress at kink position (about 6 N/mm^2), which is of keen interest. The Von Mises Stress Distribution is presented in Table 3.

Table 3 Von Mises stress distribution

Models	Von Mises stress N/mm^2		
	LC (i)	LC (ii)a	LC (ii)b
1	21.8^m	–	–
2	8.57^{fs}	–	–
3	15.6^{ls}	10.4^{ls}	20.6^{ls}
4	$8.95^{ls, fs}$	$6.68^{m, fs}$	16.4^{ls}

Note LC Load Case; *m* critical value at mid-span; *s* critical value at support; *k* critical value at kink (junction of going and landing); *fs* critical value at floor landing support; *ls* critical value at intermediate landing support

8 Concluding Remarks

Stair slabs are conventionally analysed and designed as per recommendations of standard codes of practice adopted in the country. These codes normally describe the methods for calculating maximum moments for given support conditions. However, critical moments and deflection developed due to different support arrangements, such as waist slab and/or landings supported on their sides either on walls or beams as a part of building frames, are not considered in conventional method of design. The present analysis considering support arrangements, as discussed above, clearly indicates that the maximum bending moment and its location in stair slab do change with landing supported on their sides on walls or beams of a building frame. As described earlier, in Model 1 the stair slab is supported on the extreme edges of landing whereas in Model 2, side supports are provided on landings. The maximum sagging moments along the going i.e. M_x , at mid-span are reduced to only 16 % by providing side supports at floor landing. The hogging moment up to a maximum value of 10.95 kNm is observed in the vicinity of kinks. This shows that the moments are redistributed on the surface due to the effect of side supports at floor landings as well as continuity of material in the adjoining landings.

References

1. Ahmed I, Muqtadir A, Ahmed S (1995) A design basis for stair slabs supported at landing level. *J Struct Eng ASCE* 121(7):1051–1057
2. Ahmed I, Muqtadir A, Ahmed S (1996) Design provisions for stair slabs in the Bangladesh building code. *J Struct Eng ASCE* 122(3):262–266
3. Baqi A, Mohammad Z (2013) Effect of U-turn in RC dog-legged stair slabs. In: Proceedings of the ICCSEE 2013: international conference on civil, structural and earthquake engineering, Istanbul, Turkey, 20–21 June 2013. Article no 180 and World Academy of Science, Engineering and Technology, vol 7, No 6, pp 1060–1065
4. Indian Standard: Plain and Reinforced Concrete-Code of practice (IS-456: 2000) (2000) Bureau of Indian Standards, New Delhi, July, 2000
5. British Standard: Structural use of Concrete Part-I (Code of Practice for Design and Construction), BS 8110 Part 1: 1985 (1989) British Standards Institution, May, 1989
6. Building Code Requirement for Structural Concrete (ACI-318-05) (2005) American Concrete Institute
7. Hakan K, Ergin C (1997) Discussion on design provisions for stair slabs in the Bangladesh building code, A technical note. *J Struct Eng ASCE* 123:1115–1116
8. Cosenza E, Verderame GM, Zembrano A (2008) Seismic performance of stairs in existing reinforced concrete buildings. In: 14th world conference on earthquake engineering, Beijing, China, 12–13 Oct 2008
9. Zhang PC, Yuan Q (2012) The seismic design of stair in frame structure. *Adv Mater Res* 368–373:865–868 (Trans Tech Publications, Switzerland)
10. Cheng Y, Du H, Zhang S, Xu L (2011) Seismic designs of R.C stairs in masonry structures. *Adv Mater Res* 163–167:4133–4137 (Trans Tech Publications, Switzerland)

Seismic Analysis of a 275 m Tall RCC Multi-flue Chimney: A Comparison of IS Code Provisions and Numerical Approaches

Rajib Sarkar, Devendra Shrimal and Sudhanshu Goyal

Abstract Tall chimneys play pivotal role in proper functioning of many industrial facilities like thermal, nuclear power plants, petrochemical and steel industry. Because of the non-uniformity of the diameter along the height of the chimney and also the variation of dead weights at different levels, seismic analyses of chimney have become critical and the design values need to be recommended with caution. In this paper, a RCC multi-flue chimney of 275 m height has been considered for study. Design forces in the chimney were obtained in accordance with the stipulated recommendations of IS 1893 (Part 4) 2005 for based on equivalent static lateral force method. Then dynamic response spectrum modal analyses were carried out for calculating the seismic forces developed in the chimney. The results from the response spectrum method were compared with the values obtained from the codal procedures for different base conditions viz. fixed base, circular raft resting on soil and annular raft resting on piles. Next, spectrum compatible time history for the particular project site has been considered and detailed dynamic analyses using time history were carried out for the chimney structure. The variations in the design force values as compared to the simplified methods are discussed and the importance of the proper dynamic analyses in designing of multi-flue RCC chimney is highlighted.

Keywords IS code · Multi-flue chimney · Seismic analysis

1 Introduction

Tall chimney structures require special attention for structural analysis and design activities. As the ratio of base dimension to chimney height is nearly one tenth (1/10), chimney behaves like a slender structure and detail dynamic analysis is

R. Sarkar (✉) · D. Shrimal · S. Goyal
Department of Civil Engineering, MNIT Jaipur, Jaipur 302017, India
e-mail: rajibdeq@gmail.com

© Springer India 2015
V. Matsagar (ed.), *Advances in Structural Engineering*,
DOI 10.1007/978-81-322-2193-7_80

1015

absolutely necessary for assessment of seismic forces. IS 1893 (Part 4): 2005 [2] stipulated provisions for seismic analysis of RC chimney considering equivalent lateral force method. But, the code also mentioned the importance of detail seismic analysis of chimney by response spectrum method of analysis and also time history method of analysis. In the present paper, study has been carried out for a tall RCC chimney with different methods of seismic analyses and comparison of the design forces is being presented for different foundation conditions.

2 Details of the Chimney Considered

2.1 Chimney Profile

A RCC chimney is now being constructed at a thermal power plant in Haldia, West Bengal, India. The details of this chimney are adopted for the study. Salient features of the chimney profile are provided in Table 1. Overall, seven access/restraint platforms at different elevations have been considered. Two flues are provided and the flues are made up of mild steel and for its thermal insulation mineral wool of thickness 100 mm is used.

2.2 Material Properties

Material properties assumed in the analyses and design are tabulated in Table 2.

Table 1 Salient features of chimney profile

Height of the chimney: (above FGL considered at level 0.00)	275.0 m
Height of the wind shield	269.3 m
External diameter of the chimney at base	32.0 m
External diameter of the chimney at top	15.3 m
Concrete shell thickness at base	0.85 m
Concrete shell thickness at top	0.40 m
Internal diameter of each flue	5.0 m
No. of flue	2
Thickness of each flue	10.0 mm (for mild steel)

Table 2 Material properties considered in the analyses

Grade of concrete	M30
Elastic modulus of concrete	33.5 GPa
Poisson's ratio of concrete	0.17
Density of concrete	2,500 kg/m ³
Grade of steel	Fe 415

Table 3 Generalized soil profile and the soil parameters

Strata no.	Basic description	Thickness (m)	Unit weight γ (kN/m ³)	Cohesion C_u (kPa)	Friction angle ϕ° (degree)
I	Soft silty clay	2	19.1	40	–
II	Soft clayey silt	5	18.2	23	–
IIIA	loose sandy silt	12.5	18.0	–	28
IIIB	Medium dense silty sand	3	19.0	–	30
IV	Stiff clayey silt	2.5	18.4	49	–
V	Medium dense silty sand	1.5	19.0	–	32

3 Soil Profile Considered for the Study

As stated earlier, the present study has been carried out for a project site at Haldia in West Bengal, India. The site is very near to a river and the ground conditions at the site comprise superficial deposits underlain by the clay formation. The parameters of the soil profile considered in the study are provided in Table 3.

4 Types of Foundation

Though pile foundations are ideal foundation type for the prevalent soil conditions at the particular site and high loading on the chimney, following types foundation are considered for the analyses as per IS 1893 (Part 4): 2005 [2]. For example,

- i. Fixed base or raft on hard soil,
- ii. Circular raft on soil,
- iii. Annular raft on pile foundations.

Raft on soil and annular raft on pile foundations are considered with the translational and rotational spring stiffness attached to the base of the structure. The stiffness values are computed as per the recommendation of IS 1893 (Part 1): 2002 [3] considering the foundation to be resting on strata IIIA as shown in Table 4. Following parameters of soil were adopted: Poisson's ratio $\nu = 0.3$ and shear wave velocity, $V_s = 160$ m/s. For annular raft on pile foundations, total 436 numbers of 600 mm diameter piles with 1,250 kN vertical capacity (IS 2911 (Part 1): 1979 [4]) are employed for calculation of stiffness values with outer diameter of raft as 51.2 m and inner diameter 18.2 m. The detail pile calculation is out of scope of the present paper.

Table 4 Major inputs for seismic analyses

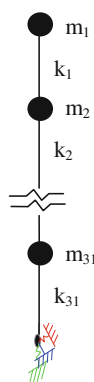
Input parameter	Input dependence	Input value
Zone factor (Z)	Location of the project site	0.24
Importance factor (I)	Structure type	1.75
Response reduction factor (R)	Seismic damage performance of the structure	3
Damping as a fraction of critical damping, ξ	Dynamic property of the structure	3 % of critical damping
Soil sites	Soil type of the project site	Medium

In practice, fixed base condition is generally assumed for the analyses of the chimney structures and the foundation compliance is generally not taken into cognizance [1]. In the subsequent sections, the changes in design forces in the chimney for various foundation conditions are discussed.

5 Computer Model Adopted for Analyses

STAAD.Pro (V8i) software package has been used for modeling and analysis purpose. Tall chimney with ratio of base dimension to chimney height approximately 1/10 is a highly slender structure and behaves like a pure cantilever beam element in response to the horizontal earthquake or wind load action. Hence, this 275 m tall RCC chimney was modeled with beam element as available in STAAD. Total thirty two nodes are considered for the full height of the chimney. Thirty one beam elements are formed connecting the consecutive nodal points. Self-weight is distributed all over the height of the chimney. Other permanent loads are applied at the corresponding levels. Total weight of the chimney considering was calculated to be 267,840 kN. Springs were attached at the base node according to the foundation type. This model is shown in Fig. 1.

Fig. 1 Conceptualized chimney model with beam element



6 Inputs for the Seismic Analyses

The inputs for the seismic analyses are mentioned in the Table 4.

7 Types of Seismic Analyses

Following types of analyses were performed for the chimney

- i. **Simplified Analysis (IS Code):** IS 1893 (Part 4) recommends simplified analysis by equivalent static lateral force method and provides the formulae for calculating the design bending moment and the shear force by utilising moment and shear distribution factors. The analysis is carried out in MS-Excel (2010) spreadsheet.
- ii. **Response Spectrum Analysis:** The code also recommends dynamic response spectrum analysis for stack like structures. For this IS 1893 (Part 1): 2002 [3] is referred. Overall 10 nos. of modes were considered and SRSS rule of modal combination is employed in the analysis. This analysis is carried out in STAAD.
- iii. **Time History Analysis:** Detail dynamic analysis using time history was carried out using spectrum compatible time history generated for the site Haldia. Analysis is carried out in STAAD.

8 Spectrum Compatible Time History for Haldia Site

Sarkar et al. [6] has generated spectrum compatible time history for Haldia site since no strong motion records are available. Based on the expected PGA at the site, the recorded earthquake motion data from the September 20, 1999 Chi-Chi Earthquake having a magnitude of 7.6 with PGA of 0.25 g from TCU122 station was selected. This time history was then modified to obtain the spectrum compatible time history to be used for the study. The target spectrum was considered as per IS 1893 (Part 1: 2002) [3] with medium soil condition. The comparison of different spectra is shown in Fig. 2a, b shows the spectrum compatible acceleration time history for the particular site. Damping of 5 % was adopted for input earthquake time history.

In nutshell, three types of analyses were carried out for the RCC chimney with different three types of foundations and the design forces in the chimney section were then compared.

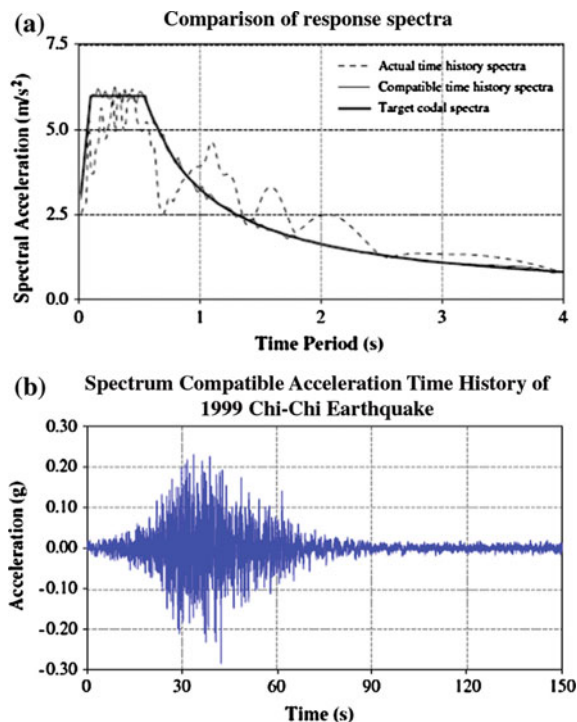


Fig. 2 **a** Comparison of target and compatible response spectrum of Chi–Chi Earthquake time-history. **b** Spectrum compatible acceleration time history (*Courtesy Sarkar et al. [6]*)

9 Results and Discussion

9.1 Design Forces for Different Foundation Conditions as Per Codal Provisions

Figure 3 presents the comparison of shear force and bending moment profiles of the chimney for different foundation types as per the stipulation of IS code. It was observed that the shear force along the chimney sections for fixed base conditions is higher than the values obtained by considering other two types of foundations. But the base shear forces are identical for all the cases. Bending Moment in case of raft foundation on soil is higher than that of for piled and fixed base conditions because of lower rigidity. But the variation is not very significant. Hence, it may be said that the foundation type plays an important role in determining the shear force in the chimney sections but not that extent in case of bending moment. Again, the variation of shear force may be pivotal in designing the wind shield under earthquake conditions.

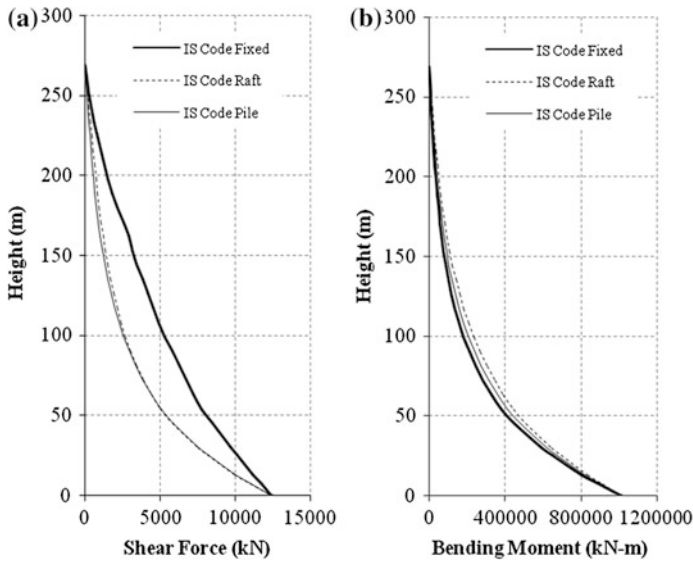


Fig. 3 Design forces as per codal provisions: a shear force b bending moment

9.2 Design Forces from Response Spectrum Analyses

The RCC chimney with different foundations was then analyzed with response spectrum method of analysis. Figure 4 compares the shear force and bending moment profile for different types of foundations. Unlike the codal provisions, the shear force and bending moment profile have steep change in gradient at about the elevation of 250 m. It may be noted that the flues were hung from that elevation and due to the sudden increase in weight at that elevation the design forces changed at that location. Therefore, from Figs. 3 and 4, it is clear that IS code provision could not capture the sudden increase in forces but response spectrum analyses were more precise than the codal provisions. Again, it may be observed that the shear force and bending moment profiles are almost similar for different types of foundations though the chimney with raft foundation yield more force than the other two types of foundations due to lower rigidity of the overall system. Also, base moment and shear forces for fixed base condition are lowest compared to the other two foundation conditions. So assuming chimney structure as fixed base condition and analyzing it for design may not be safe in terms of design forces. Hence, adoption of proper foundation condition is absolutely necessary for designing structures as important as chimney.

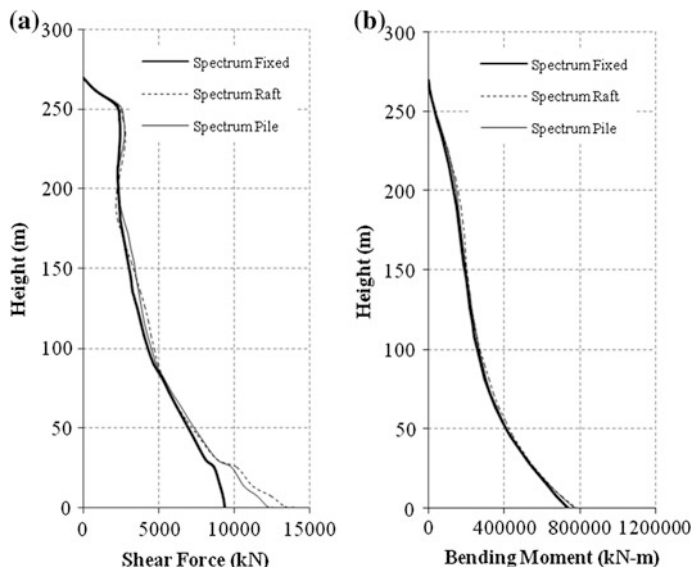


Fig. 4 Design forces with response spectrum analyses: **a** shear force **b** bending moment

9.3 Design Forces from Time History Analyses

Time history analyses were then carried out to obtain the design forces in the chimney sections. The spectrum compatible time history generated for Haldia site was then employed as the base motion for the chimney with different foundations. The maximum design forces along the chimney height obtained from time history analyses are presented in Fig. 5. It may be observed from Fig. 5 that the design forces changes its gradient at the elevation from where flues were hung. It was similar as observed in response spectrum method analyses. Again like response spectrum analyses, the forces for chimney with raft foundation are on the higher side compared to the values for other two types of foundations. However, the forces predicted by the time history analyses are on the higher side in comparison to that of the response spectrum analyses. So it may be stated that time history analyses captured the essential characteristics the design forces and also predicting higher values of the design forces.

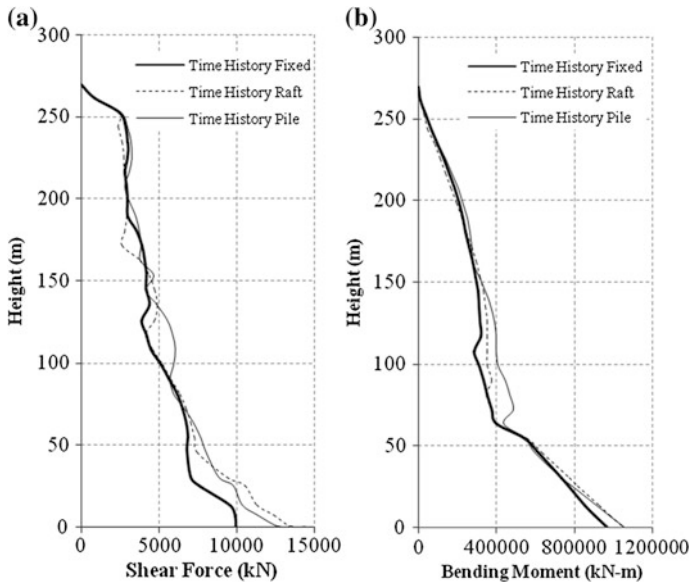


Fig. 5 Design forces with time history analyses: a shear force b bending moment

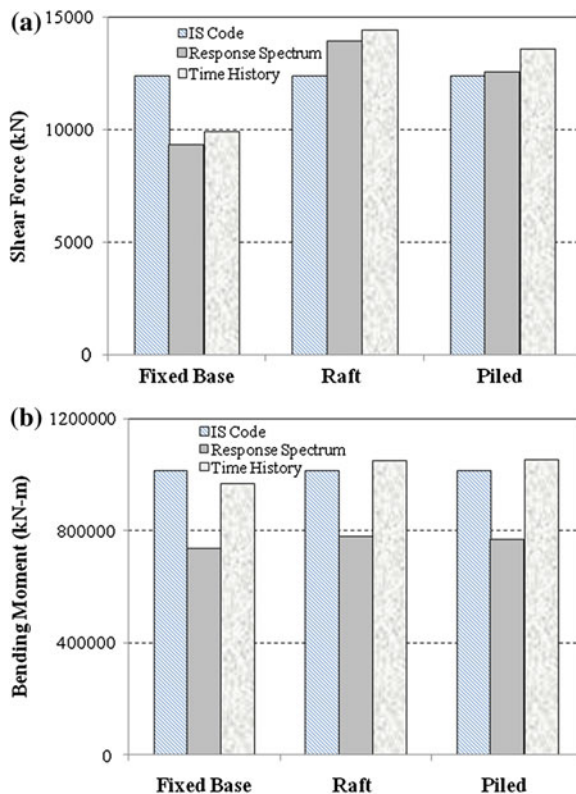
9.4 Comparison of Design Forces from Different Methods of Analyses

This section discusses, in detail, the comparison of design forces obtained from different methods of analyses and for different types of foundations. The comparison of base shear forces and base moments are presented in Fig. 6. For fixed base condition, it was observed that time history analysis yields higher design forces for height more than 150 m but the base forces are higher from the codal stipulations. Jain et al. [5] also concluded that IS codal stipulation over estimates the base forces for fixed base situation.

When the foundation is raft on soil, the design forces obtained from time history analyses are higher. The base shear is about 16 % higher and the base moment is 3.5 % higher than the value obtained from codal procedure. From response spectrum analysis, the base shear is 12 % higher than the codal values.

When the foundation type is annular raft on piles, the time history analyses yield 9.4 % higher base shear and 3.8 % higher base moment than that obtained from IS code of practice. From response spectrum analysis, the base shear is just about 1 % higher than the IS code values. It may be mentioned that the response spectrum analyses yielded lesser base moment than the other two analysis procedures.

Fig. 6 Comparison of design forces from different methods of analyses: **a** comparison of base shear force **b** comparison of base moment



10 Conclusion

A comparative study has been carried out for 275 m tall multi-flue RCC chimney for design forces in the chimney sections with different foundation types. The study may be summarized as following.

- i. Types of foundation have significant influence on the design forces in the chimney section.
- ii. Though base moment and shear for fixed base conditions are higher with IS codal procedure, the moment and shear at higher elevations of the chimney are critical with detail dynamic analysis.
- iii. Detail dynamic analysis with time history yields critical values of design moment and shear for foundation types of raft on soil and annular raft on piles.
- iv. Based on the observations, detail dynamic analysis with time history is recommended for analysis and design of tall RCC chimney.

Acknowledgments Authors would like to thank Prof. M.K. Shrimali and Dr. S.D. Bharti, Dept. of Civil Engineering, MNIT Jaipur for extending every possible help in carrying out the research work presented here.

References

1. Chowdhury I, Singh JP, Tilak R (2012) Seismic response of self supported stacks- considering foundation compliance. In: Proceedings of 15th world conference on earthquake engineering, Lisbon, Portugal
2. IS 1893 (Part 4): 2005. Criteria for earthquake resistant design of structures: part 4—Industrial structures including stack like structures, Bureau of Indian Standards (BIS), New Delhi, India
3. IS 1893 (Part 1): 2002. Criteria for earthquake resistant design of structures: part 4—General provisions and buildings, Bureau of Indian Standards (BIS), New Delhi, India
4. IS 2911 (Part-I/ Sec-1): 1979. Code of practice for design and construction of pile foundations, Bureau of Indian Standards (BIS), New Delhi, India
5. Jain SK, Singh BP, Gupta BK (1900) I.S. code provisions for seismic design of tall chimneys. *Int J Struct* 10(2):103–111
6. Sarkar R, Bhattacharya S, Maheshwari BK (2014) Seismic requalification of pile foundations in liquefiable soils. *Indian Geotech J (Springer)* 44(2):183–195

Finite Element Simulation of Earthquake Resistant Brick Masonry Building Under Shock Loading

A. Joshua Daniel and R.N. Dubey

Abstract Modelling and analysis of a brick masonry building involves uncertainties like modelling assumptions and properties of local material. Therefore, it is necessary to perform a calibration to evaluate the dynamic properties of the structure. The response of the finite element model is improved, predicting the parameter by performing a linear dynamic analysis on experimental data by comparing the acceleration. Further, a nonlinear dynamic analysis was also performed comparing the roof acceleration and damage pattern of the structure obtained analytically with the test findings. The roof accelerations obtained analytically were in good agreement with experimental roof accelerations. The damage patterns observed analytically after every shock were almost similar to that of experimental observations.

Keywords Brick masonry building · Finite element model · Dynamic analysis · Shock loading · Experimental data

1 Introduction

Masonry is mainly a composite, anisotropic and a non-homogeneous material. The brickwork is a combination of bricks and mortar joints. The response of masonry subjected to loading depends on the properties of its brick, mortar and their interaction. Further, the response of masonry depends on the layout of bond and their interaction with other structural members. Modelling of masonry is a highly challenging process. Normally a high computation cost is associated with the intrinsic complexity of masonry that requires a large number of degrees of freedom [5],

A. Joshua Daniel (✉) · R.N. Dubey
Department of Earthquake Engineering,
Indian Institute of Technology, Roorkee (IITR), Roorkee, Uttarakhand, India
e-mail: ajoshdani@gmail.com

R.N. Dubey
e-mail: rndubey84@gmail.com

which usually excludes simplifications like rigid diaphragms and ideal connections which is applied in modelling of other kind of structures. Another reason for the complexity is that the material constitutive models are not well defined, especially in the non-linear range.

As of now, numerical models have mainly been validated for an individual structural component. However, the validation of the entire building is still not available. Development of adequate techniques, which authenticate the numerical models, can be a major contribution to provide a powerful tool to assess and predict the performance of brick masonry structures. Until now, only a few studies refer to the analysis of masonry structures [1, 14]. Based on the previous literature reviews it was revealed that the modulus of elasticity plays a vital role in representing the actual experimental behaviour of masonry. Further, the modulus of elasticity depends on other parameters like workmanship, quality of brick, quality of the mortar, thickness of the mortar joint, ambient condition and type of curing. So, for an effective analysis, parametric study on Young's modulus will have to be carried out. During cyclic loading the masonry walls will be subjected to simultaneous in-plane and out-of-plane load [16]. Individual validation on in-plane behaviour and out-of-plane behaviour of the material constitutive law, concrete damage plasticity (CDP) shows that it will be extremely effective under combined loading scenario. The same concrete damage plasticity (CDP) used by Rai et al. [16] to study the non-linear behaviour of un-reinforced masonry walls subjected to cyclic loading is used for this study. Further, a nonlinear dynamic analysis was also performed on the earthquake resistant brick masonry building. The problem statement of this study requires the explicit technique for analysis. This explicit technique does not require a fully assembled system's stiffness matrix; rather it solves the problem using the theory of dynamic wave propagation in solids. As iterations are not performed, much smaller increments of the applied load are required for the explicit technique to provide acceptable results and thus can simulate highly nonlinear events [3].

Dubey [4] performed an experiment on earthquake resistant brick masonry building on shock table facility available at the Department of Earthquake Engineering, IIT Roorkee. A total of eight shocks with intensity varying from 0.53 to 4.52 g were applied at the base of the model. The corresponding acceleration obtained at roof after every shock was also recorded. In this study the first shock and its corresponding roof acceleration are being considered to calibrate of the model. We expect that this study will contribute to the improvement of calibration for analysis of the brick masonry building. Further, the effectiveness of this calibration will be verified by performing a non-linear dynamic analysis on earthquake resistant brick masonry building by applying the base shock recorded during experimentation and by comparing the analytical roof acceleration and damage pattern with that of the test findings.

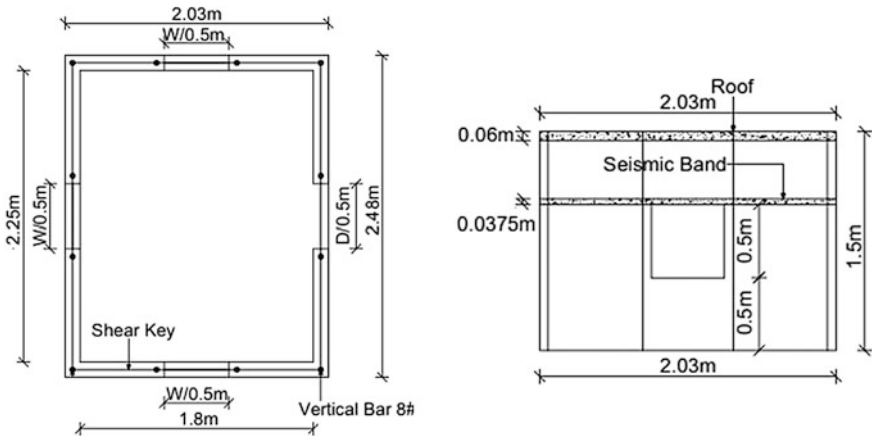


Fig. 1 Plan and elevation of half scale earthquake resistant brick masonry model

2 Model Descriptions

The earthquake resistant brick masonry building, constructed on the shock table [4] was tested under the increasing intensity of the shock loading. The base acceleration as well as the roof acceleration was recorded. The plan and the elevation of the earthquake resistant brick masonry building are shown in Fig. 1.

3 Structural Modelling

The physical model constructed on the shock table is modelled in ABAQUS. Masonry with mortar is modelled as a homogeneous material. The walls, roof and lintel are modelled using a solid 8-nodded linear hexahedral element with incompatible modes (C3D8I) [14]. Tie constrains are used to connect different structural

Fig. 2 Meshed finite element model of earthquake resistant brick masonry building

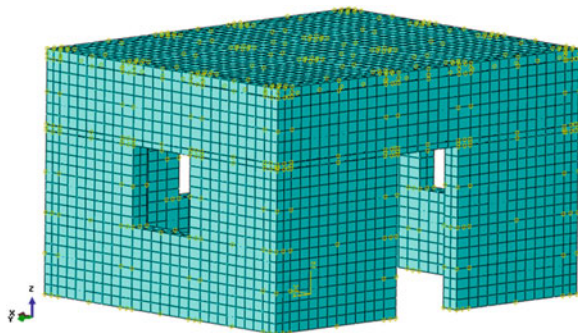


Table 1 Detail of parametric analysis for the earthquake resistant brick masonry building

Material	Trial	Young's modulus ^a	Base acceleration	Experimental roof acceleration	Analytical roof acceleration
		N/m ²	g	g	g
Masonry	1	2.3×10^9	0.53	0.61	0.57
	2	2.3×10^9	0.53	0.61	0.60

^a Density of concrete = 2,400 kg/m³; Young's modulus of concrete = 1.94×10^{10} N/m²; Poisson ratio of concrete = 0.2; Density of steel = 7,850 kg/m³; Young's modulus of steel = 2.00×10^{11} N/m²; Poisson ratio of steel = 0.3; Density of masonry = 1,920 kg/m³; Poisson ratio of masonry = 0.2

members. The reinforcement is modelled using 2-noded, linear truss element (T3D2) and is embedded inside the respective material [12]. Displacement is unrestrained along the direction of shock loading and is restrained in all other directions. Figure 2 shows the meshed finite element model of earthquake resistant brick masonry building.

4 Result on Parametric Study

Masonry, Concrete and Steel are the materials used in the model. Density, Poisson ratio and Young's modulus were the properties used in this parametric study. It is assumed that for the first shock the materials will be within the elastic limit. So, by applying the shock 1 at the base and by retaining constant value for all the materials except the Young's modulus of masonry, the roof acceleration obtained was compared with the experimental roof acceleration. A linear dynamic analysis was performed and Table 1 shows the detail of parametric analysis.

5 Material Modelling

The seismic response is a cyclic process on all materials. The cyclic load has the influence on the material behaviour. Masonry is a brittle material with very low tensile stress. During uni-axial compression or tension test, modulus of elasticity is constant up to the yield. The non-linear material properties help in understanding the material behaviour beyond the elastic range.

Concrete, masonry and rebar are the materials used in the actual physical model. The metal plasticity in ABAQUS is used for recreating the nonlinear material response of rebar [17]. The CDP in ABAQUS is used for replicating the nonlinear behaviour of concrete [17, 6, 10]. Same as concrete, masonry is a brittle material with very low tensile strength. Therefore, CDP used for concrete is adopted for recreating the nonlinear behaviour of masonry.

5.1 Masonry

The compressive strength of masonry prism used in this study is 4.1 MPa [11]. The stress-strain curve for masonry in compression developed using tri-linear model [11] has been used in this study. The tensile strength of masonry used in this study is 0.28 MPa [13]. The stress-strain curve for masonry in tension used by Chen et al. [2] is adopted for this model. Figure 3 shows the stress strain curve for masonry in compression and tension. The other parameters are used for masonry by CDP are density = 1,920 kg/m³, modulus of elasticity = 2.8 × 10⁹ N/m², Poisson’s ratio = 0.2, dilation angle = 30°, flow potential eccentricity = 0.1, ratio of initial equi-biaxial compressive yield stress to initial uni-axial compressive yield stress = 1.16, ratio of second stress invariant = 0.667, viscosity parameter = 0 [11].

5.2 Rebar

The steel of Fe 250 grade is used for reinforcement. Figure 4 shows the stress-strain graph for rebar [15]. The other parameters used for steel are density = 7,850 kg/m³, modulus of elasticity = 2 × 10¹¹ N/m², Poisson’s ratio = 0.3 [9, 9, 15].

5.3 Concrete

The concrete used for lintel and RC slab is of grade M15. Therefore, the characteristic compressive strength [8] for M15 grade is 15 MPa. The stress-strain curve for concrete in compression is developed from an empirical relation used by Hu et al. [7] is adopted for this study. The maximum stress will be reached at a strain approximately equal to 0.002. The strain at which the failure of concrete occurs is taken as 0.005 [15]. The stress-strain curve for concrete in tension developed from an empirical relation used by Vecchio. Vecchio [18] is adopted for this study.

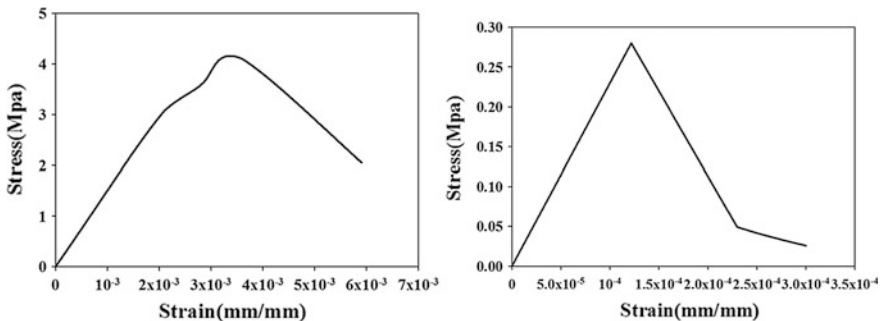


Fig. 3 Stress-strain curve for masonry in compression and tension

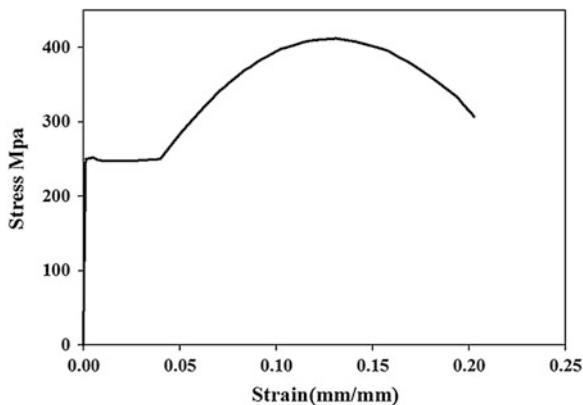


Fig. 4 Stress-strain curve for steel

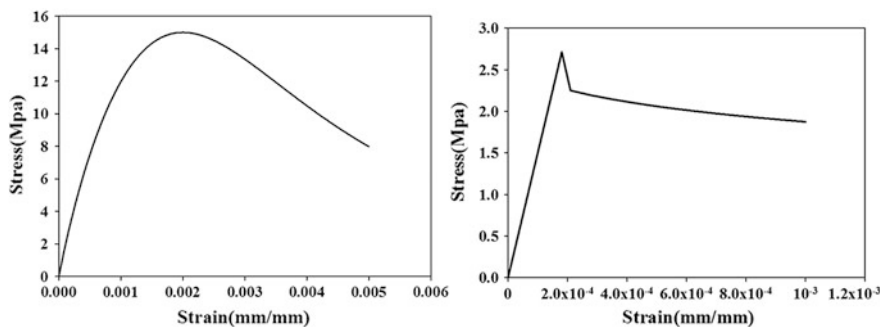


Fig. 5 Stress-strain curve for concrete in compression and tension

Flexural strength of concrete is calculated based on the formula given in Indian code of practice IS: 456-2000 [8]. The limiting tensile strain of concrete is 0.0001 [15]. Figure 5 shows the stress-strain curve for concrete in compression and tension. The other parameters used for concrete by CDP are density = 2,400 kg/m³, modulus of elasticity = 1.94×10^{10} N/m², Poisson’s ratio = 0.2, dilation angle = 38°, flow potential eccentricity = 0.1, ratio of initial equi-biaxial compressive yield stress to initial uni-axial compressive yield stress = 1.16, ratio of second stress invariant = 0.667, viscosity parameter = 0 [10].

6 Observation

The earthquake resistant brick masonry building modelled in ABAQUS was subjected to a gradually increasing intensity of shock loading and a nonlinear dynamic analysis was performed. During experimentation on the actual physical model, a total of eight shocks were being applied.

6.1 Acceleration

The acceleration recorded at the base during actual physical testing is applied at the base of the analytical model. The roof acceleration thus obtained is compared with the experimental roof acceleration. Figures 6, 7, 8, 9, 10, 11, 12, and 13 show the comparison of base acceleration applied at the base of the model recorded during experiment, with the corresponding analytically obtained roof acceleration. Table 2 shows the base acceleration of each shock with corresponding experimental as well as analytical roof acceleration.

6.2 Damage

During the experiment, the shock was applied along east west direction. The same is being simulated analytically, and it was observed that until third shock, there was no visible damage on masonry model. The same situation has also been observed

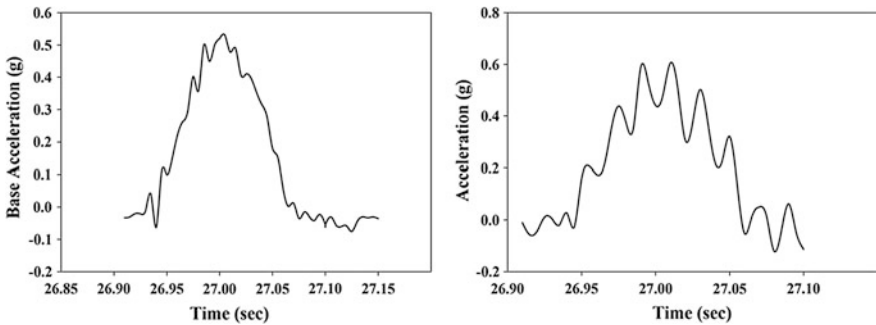


Fig. 6 Input acceleration at base and estimated response at roof of shock 1

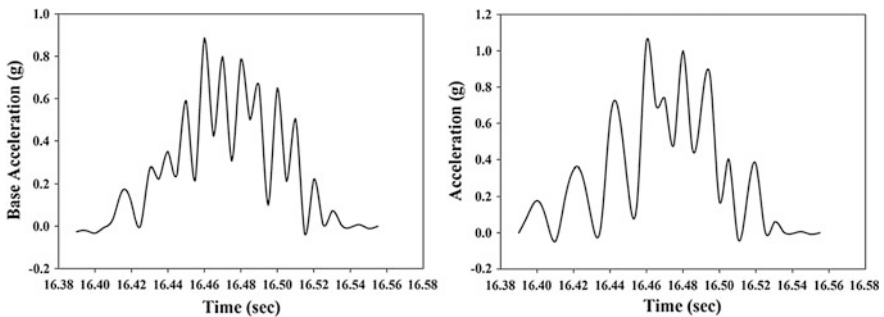


Fig. 7 Input acceleration at base and estimated response at roof of shock 2

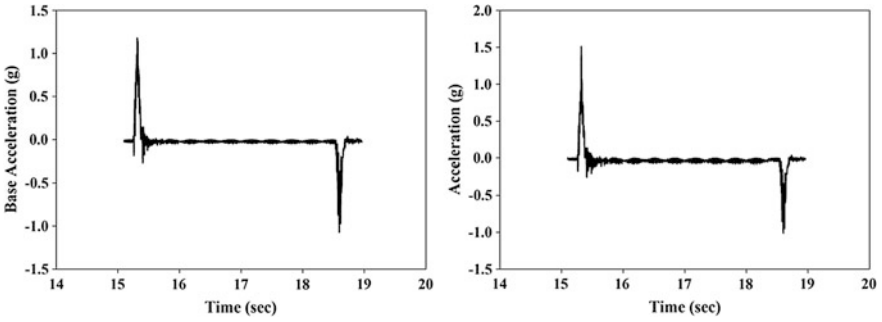


Fig. 8 Input acceleration at base and estimated response at roof of shock 3

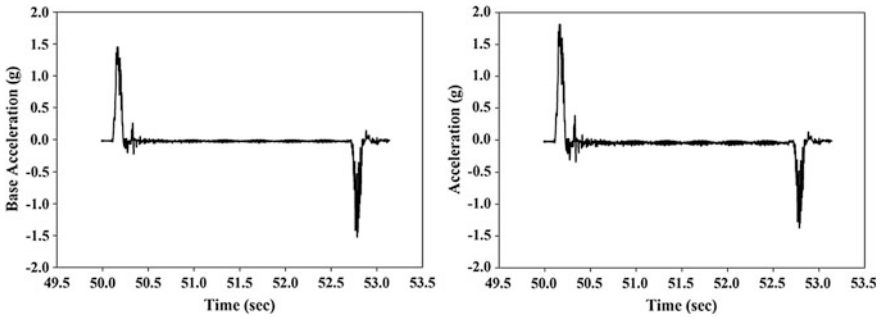


Fig. 9 Input acceleration at base and estimated response at roof of shock 4

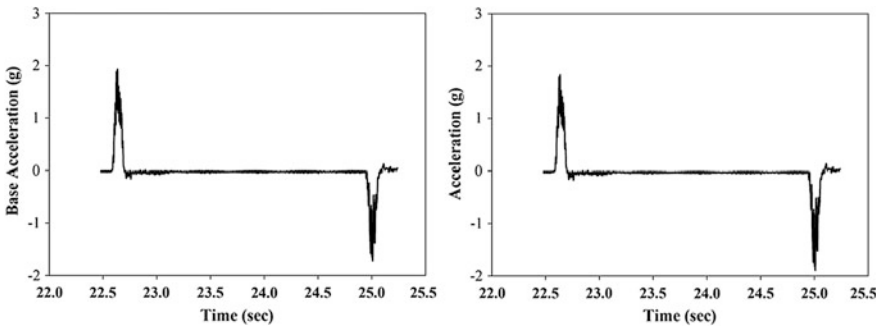


Fig. 10 Input acceleration at base and estimated response at roof of shock 5

during experimentation. Figure 14 shows the minor damage to the south shear wall after sixth shock. Figure 15 shows the damage of north south shear wall after seventh shock. Figure 16 shows the damages in the north shear wall after eighth

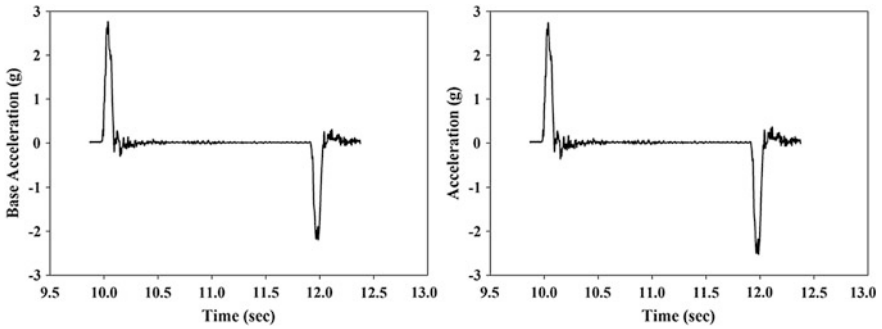


Fig. 11 Input acceleration at base and estimated response at roof of shock 6

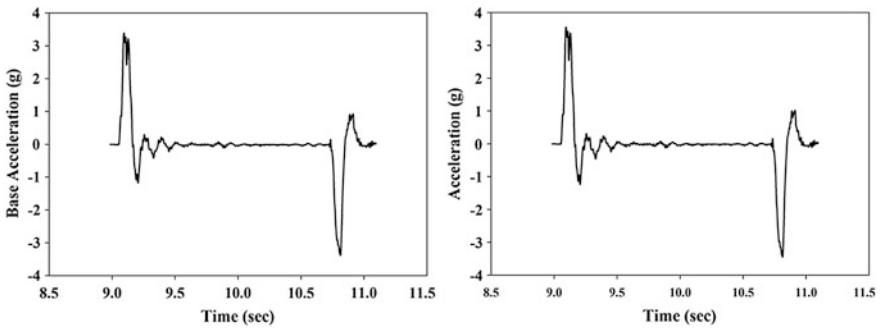


Fig. 12 Input acceleration at base and estimated response at roof of shock 7

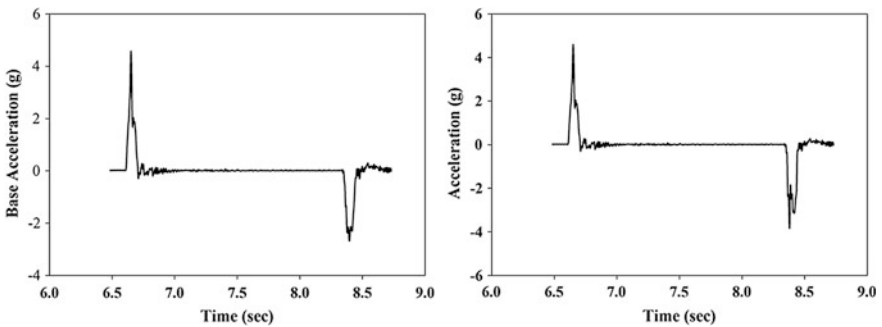


Fig. 13 Input acceleration at base and estimated response at roof of shock 8

shock. The earthquake resistant brick masonry model withstood all the eight shock. The damage pattern obtained analytically were quiet similar to that of the experiment.

Table 2 Comparison of roof acceleration for earthquake resistant model

Shock	Base acceleration		Experimental roof acceleration		Analytical roof acceleration	
	Loading pulse (g)	Rebound pulse (g)	Loading pulse (g)	Rebound pulse (g)	Loading pulse (g)	Rebound pulse (g)
Shock 1	0.53	–	0.61	–	0.60	–
Shock 2	0.88	–	1.09	–	1.05	–
Shock 3	1.18	1.05	1.55	1.03	1.51	0.99
Shock 4	1.45	1.51	1.88	1.44	1.81	1.35
Shock 5	1.93	1.62	2.02	1.84	1.83	1.75
Shock 6	2.73	2.18	2.90	2.62	2.70	2.51
Shock 7	3.38	3.35	3.85	3.62	3.55	3.42
Shock 8	4.52	4.05	4.59	4.14	4.50	3.79

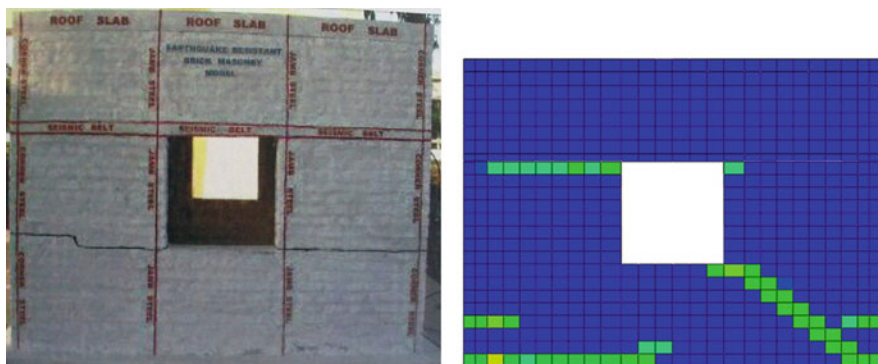


Fig. 14 Comparison of experimental and analytical damage of south shear wall after shock 6

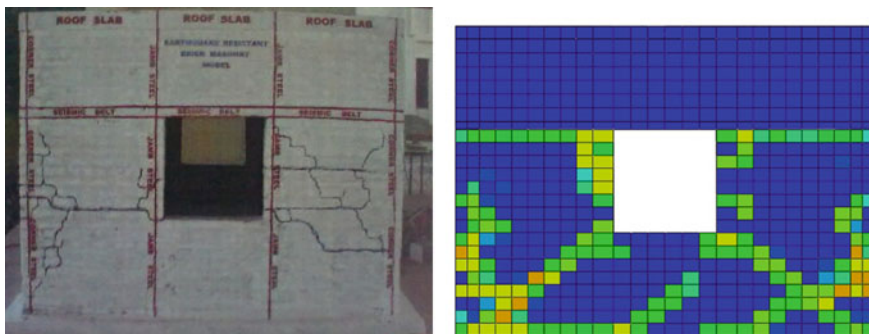


Fig. 15 Comparison of experimental and analytical damage of south shear wall after shock 7

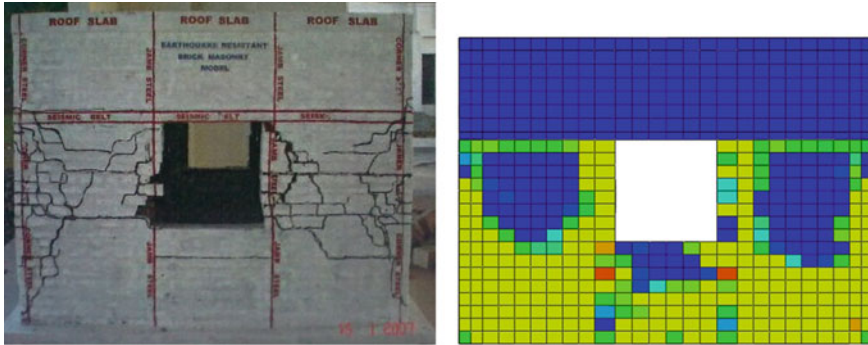


Fig. 16 Comparison of experimental and analytical damage of south shear wall after shock 8

7 Conclusion

The modelling and analysis of brick masonry building involves uncertainties like modelling assumptions and the properties of local material. The properties of local material include numerous other parameters like workmanship, quality of brick, quality of the mortar, thickness of the mortar joint, ambient condition and type of curing. To overcome these uncertainties a parametric study was performed to estimate the dynamic property comparing the acceleration of the first shock. Further a nonlinear dynamic analysis was performed comparing the roof acceleration and damage pattern of the structure obtained analytically with the experimental observation. The conclusion drawn from the above study are summarized below

- The roof accelerations obtained analytically were in good agreement with experimental roof accelerations. The variation in the roof accelerations is nearly 13 %.
- No damage was observed both in analytical model as well as during experimentation till fifth shock.
- The crack propagation and the damage pattern observed analytically in earthquake resistant brick masonry model after every shock were almost similar to that of experimental observation.

References

1. Chavez M, Meli R (2011) Shaking table testing and numerical simulation of the seismic response of a typical Mexican colonial temple. *Earthq Eng Struct Dyn* 41:233–253
2. Chen Y, Ashour AF, Garrity SW (2008) Moment/thrust interaction diagrams for reinforced masonry sections. *Constr Build Mater* 22:763–770
3. Dhanasekar M, Haider W (2007) Explicit finite element analysis of lightly reinforced masonry shear wall. *Comput Struct* 86:15–26

4. Dubey R (2011) Experimental studies to verify the efficacy of earthquake resistance measure in masonry structures. Ph. D. thesis, Earthquake Engineering Dept, Indian Institute of Technology Roorkee, Roorkee, India
5. Giordano A, Mele E, De Luca A (2002) Modelling of historical masonry structures: comparison of different approaches through a case study. *Eng Struct* 24:1057–1069
6. Grecchi G (2010) Material and structural behavior of masonry: simulation with a commercial code. Laurea Thesis, University of Pavia, Lombardy, Italy
7. Hu TH, Lin FM, Jan YY (2004) Nonlinear finite element analysis of reinforced concrete beams strengthened by fiber-reinforced plastics. *Compos Struct* 63:271–281
8. IS: 456 (2000) Plain and reinforced concrete—code of practice. Bureau of Indian Standard, New Delhi, India
9. IS: 875 (Part 1) (1987) Code of practice for design loads (other than earthquake) for building and structures. Bureau of Indian Standard, New Delhi, India
10. Jankowiak T, Lodygowski T (2005) Identification of parameters of concrete damage plasticity constitutive model. *Found Civil Environ Eng* 6:53–69
11. Kaushik HB, Rai DC, Jain SK (2007) Stress-strain characteristics of clay brick masonry under uniaxial compression. *J Struct Eng ASCE* 19:728–739
12. Lee HK, Kin BR, Ha SK (2007) Numerical evaluation of shear strengthening performance of CFRP sheets/strips and sprayed epoxy coating repair systems. *Compos Part B: Eng* 39:851–862
13. Nateghi AF, Alemi F (2008) Experimental study of seismic behaviour of typical Iranian URM brick walls. In: *The 14th world conference on earthquake engineering*, Beijing, China
14. Oyarzo-Vera C, Abdul Razak AK, Chouw N (2009) Modal testing of an unreinforced masonry house. In: *International operational modal analysis conference*, Portonovo, Ancona, Italy
15. Pillai SU, Menon D (2010) Reinforced concrete design. Tata McGraw-Hill Education Private Limited, New Delhi
16. Rai DC, Agnihotri P, Singhal, V (2011) Out-of-plane strength of damaged unreinforced masonry walls. In: *12th North American masonry conference*, Minneapolis, Minnesota, USA
17. Simulia (2011) Abaqus/CAE user's manual. Providence, RI
18. Vecchio FJ (1990) Reinforced concrete membrane element formulation. *J Struct Eng, ASCE* 116:730–750

Seismic Damage Evaluation of Unreinforced Masonry Buildings in High Seismic Zone Using the Nonlinear Static Method

Abhijit Sarkar, Lipika Halder and Richi Prasad Sharma

Abstract Seismotectonic features of northeast India signify a very high probability of occurrence of major earthquake in future. However, a considerable portion of the building stock of this region is unreinforced masonry buildings. These buildings possess very little displacement capacity and consequently a devastating effect may be observed during a future earthquake. Therefore, potential seismic evaluation of unreinforced masonry buildings in these areas is very essential in order to implement any kind of seismic hazard mitigation strategy. In this study, seismic evaluation of representative masonry building models is carried out by performing pushover analysis using available computer program SAP2000. In this method the masonry walls are modeled as equivalent frame made of vertical (pier) and horizontal (spandrels) elements with rigid intersecting joint elements and lumped plastic hinge concept. The model simulates nonlinear in-plane behaviour of the wall panels. The shear failure of spandrel is addressed by shear hinge at the middle and a combined failure of pier is addressed by two P-M interaction hinges at either end of the pier. However, combined failure is governed by the minimum failure envelope of P-M interaction curves to ensure the effect of vertical load on the failure of pier. Lastly, fragility curves which express the expected damage as a function of spectral displacement were developed based on the capacity curve.

Keywords Masonry · Capacity curve · In-plane behaviour · Damage · Fragility curve

A. Sarkar · L. Halder (✉) · R.P. Sharma
Department of Civil Engineering, National Institute of Technology, Agartala,
Barjala, Jirania 799055, India
e-mail: erlhalder@yahoo.co.in

A. Sarkar
e-mail: srkr.avijit@gmail.com

R.P. Sharma
e-mail: rps.civil@nita.ac.in

1 Introduction

In the past, northeastern region of India experienced several destructive earthquakes such as the 1897 Shillong earthquake (M_w 8.1); the 1918 Srimangal earthquake (M_s 7.6); the 1947 Arunachal earthquake (M 7.5); the 1950 Assam earthquake (M_w 8.7) etc. This region of India is divided into five seismotectonic zones as Eastern Himalayan collision zone, Indo-Myanmar subduction zone, Syntax is zone of Himalayan arc and Burmese arc (Mishmi Hills), Plate boundary zone of Shillong Plateau and Assam Valley and Bengal Basin and Plate Boundary Zone of Tripura Mizoram Fold belt based on the distribution of epicentres, fault plane solution and geotectonic features. This region is also reported as the most severe seismic zone of India in Indian seismic code (IS 1893 2002). Hence, there is a very high probability of occurrence of major earthquake in this region in future. However, these earthquakes caused a damaging effect in life and property of this region. A considerable portion of housing in this region is unreinforced masonry (URM) buildings due to its lower cost of construction, availability of materials and ease of construction. However, these buildings are very vulnerable during earthquake since they possess very little nonlinear deformation capacity in contrast to the newly built structures based on new earthquake resistant design codes. So, failure of these buildings extends damages to a great extent. Therefore, potential seismic evaluation of URM buildings is to be carried out before implementing any kind of effective seismic hazard mitigation strategy for this region.

Finite element (FE) approach is powerful tool for seismic evaluation of URM building but it is time consuming and requires a large amount of data. Moreover, high computational cost, more significantly high analytical skill required for this approach as these models are based on isotropic-orthotropic homogeneous nonlinear material, or even heterogeneous nonlinear material assumptions. In addition, discrete element formulations based on the nonlinear behavior of joints between masonry units are also consider in this approach. Instead of the more refined FE approach, now-a-days equivalent frame analysis approach is widely used for idealization of URM buildings (e.g. [2, 12, 13, 15, 16, 19, 20, 23]). In this approach, the URM building is idealized as an assemblage of one-dimensional elastic beam elements consisting of piers (vertical components) and spandrels (coupling horizontal structural components), which are characterised by concentrated plastic hinges in the well-specified cross-sections.

It has been observed in the past earthquake and also reported in the literatures that seismic response of masonry buildings with flexible roof is governed by out-of-plane action of wall, while in the case of buildings with rigid roof the response is governed by the in-plane failure of the walls [14, 24]. The main aim of the present study reported in this paper is seismic vulnerability assessment of residential unreinforced masonry buildings with flat rigid roofs/floors, simulating the in-plane behavior. Equivalent frame approach is used for idealization of the URM buildings. It is found in the literature that the capacity curve obtained from nonlinear static analysis is used for developing fragility curves [7, 21, 23]. In this study the fragility

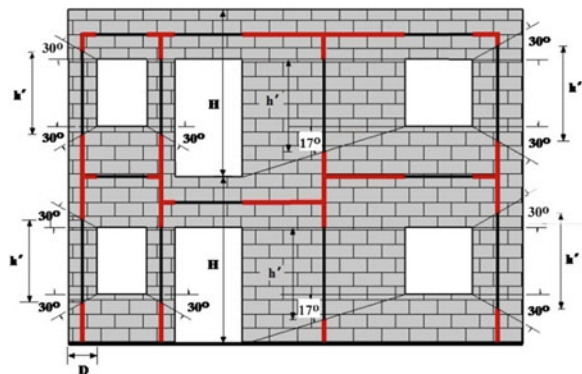
curves that are used to predict the level of damage that a building may experience based on probable ground acceleration level are also derived for those buildings.

2 Nonlinear Static Analysis (Pushover) on Equivalent Frame Model

Nonlinear static analysis or pushover analysis is very familiar in performance based evaluation methodology in order to estimate nonlinear lateral deformation capacity. It has the advantage over linear analysis as the latter cannot sufficiently simulate the seismic response of the masonry buildings [17] and over dynamic analysis as well. The nonlinear modeling of the structure is prepared using equivalent frame modeling approach in SAP2000. The material is assumed to be homogeneous and isotropic and consequently, the complex nature of masonry will not be highly influential in the simulation and thus it is saving of time, memory and economy. In equivalent frame modeling approach, the structure is idealized as a frame-like structure of one-dimensional elastic beam elements. An equivalent frame model (EFM) of a wall with opening has three components such as vertical elements which are modeled as piers, horizontal elements that are modeled as spandrels and rigid end offsets modeled pier-spandrel intersections which are supposed to be stiffer than joining piers and spandrels [13]. In order to consider coupling effect between pier and spandrel, the effective height of the pier is taken as per Dolce [6] and effective length of the spandrel is taken as the length equal to the length of the opening [22]. An EFM of a typical perforated masonry wall with identification of h' , D , H used in the calculation of the effective height of the piers as per Dolce [6] is shown in Fig. 1 and the effective height of the pier as per Dolce [6] can be expressed as such:

$$H_{eff} = h' + \frac{D \cdot (H - h')}{3 \cdot h'} \tag{1}$$

Fig. 1 Equivalent frame modeling of a typical masonry wall plane with identifications of h' used in the calculation of effective height of piers as per Dolce [6]



The model so produced is elastic and nonlinear behavior is introduced in the model by assigning plastic hinges at the appropriate locations. The plastic hinges are to be well-characterised by the constitutive relationships as these govern the accuracy of the simulation to the actual structural problem. In the model, a single shear hinge is provided at the middle of the horizontal element and this is governed by the shear-deformation relationship of the element. On the other hand, P-M interaction hinges are provided at either end of the vertical element to simulate the combined behavior of piers in rocking and shear [23]. The influence of the axial stress is taken into account considering the following principal failure modes as found in Magenes and Calvi [14].

- (1) Rocking: With increase in horizontal load, formation of tensile cracking at both ends of masonry pier leads to a rigid body rotation about its compressed toe and final failure is obtained by crushing of diagonally opposite compressed corners of the piers. Tensile strength of masonry is not considered. This failure is prevalent in slender piers. The governing equation describing rocking failure is expressed as:

$$V_r = \frac{D^2 t p}{2H_0} \left(1 - \frac{p}{K f_u} \right) \quad (2)$$

where p is the mean vertical stress, D is the pier width, t is the pier thickness, H_0 is the effective pier height, f_u is the compressive strength of masonry, K is a coefficient which takes into account the vertical stress distribution at the compressed toe (a common assumption is an equivalent rectangular stress block with $K = 0.85$).

- (2) Diagonal tension: This is a very common damage during earthquake in the form of diagonal cracks in the walls. It occurs due to less tensile strength of masonry. When principle tensile stress exceeds tensile strength of masonry for a given mean compressive axial stress and peak shear stress, diagonal cracks form at the centre and propagate towards the ends of the piers. As earthquakes are reversed seismic action, generally double diagonal (X) shear cracks are observed. However, the path of crack formation is highly dependent on relative strength of masonry components. The governing equation describing diagonal tension failure is expressed as:

$$V_d = \frac{f_{tu} D t}{b} \sqrt{1 + \frac{p}{f_{tu}}} \quad (3)$$

where f_{tu} is the tensile strength of masonry, b is a coefficient related to the pier aspect ratio and accounts for the distribution of shear stress at the centre of the wall

($b = 1$ for aspect ratio ≤ 1 , $b =$ value of aspect ratio for $1 <$ aspect ratio < 1.5 , $b = 1.5$ for aspect ratio ≥ 1.5).

- (3) Sliding: As name suggests, relative sliding occurs between upper part and lower part of wall. Due to reversed seismic action, horizontal tensile crack forms in the bed-joints and this can act as a potential sliding plane along which sliding can occur. This failure is generally occurred for low levels of vertical loads or low friction coefficients. The governing equation describing sliding failure is expressed as:

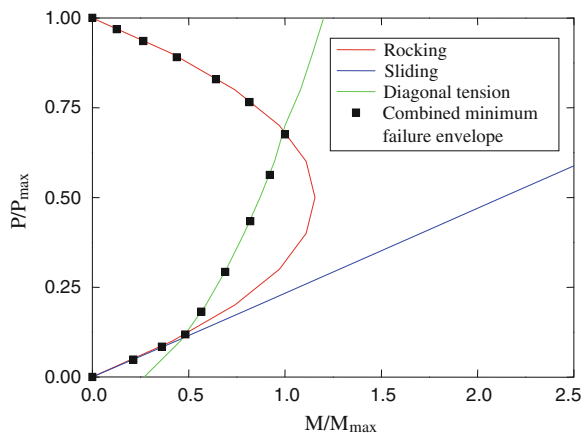
$$V_s = Dt \left(\frac{1.5c + \mu p}{1 + 3 \frac{c\alpha_v}{p}} \right) \tag{4}$$

where $\alpha_v (= \frac{M}{VD} = \frac{H_0}{D})$ is the shear ratio, c is the masonry shear strength with zero vertical stress, and μ is the coefficient of sliding friction of the masonry joints.

The shear capacities of a pier under three principal failure modes can be calculated using Eqs. 2–4. It is clear from these equations that shear capacities are influenced by the mean vertical stress acting on the pier. Therefore, changes in vertical stress will affect the failure mode. This effect can be addressed by the inclusion of a P-V interaction in the hinge definition. However, P-V interaction is not available in the SAP2000. But P-M interaction can be opted by converting shear capacity multiplied by effective pier height into moment capacity. The locus of the minimum shear capacities out of three principal failure modes at different levels of axial stresses forms minimum failure envelope. The failure envelope is normalised by maximum axial compressive force under pure compression ($P_{max} = P_u = Kf_uDt$) and maximum moment capacity as shown in Fig. 2.

The constitutive relationship for defining plastic hinges are taken from Petrovčič and Kilar [18] which were determined as per Eurocode 8 [5], in which the structural

Fig. 2 Normalised P-M interaction curve (minimum failure envelope formed by combination of all the principal failure modes)



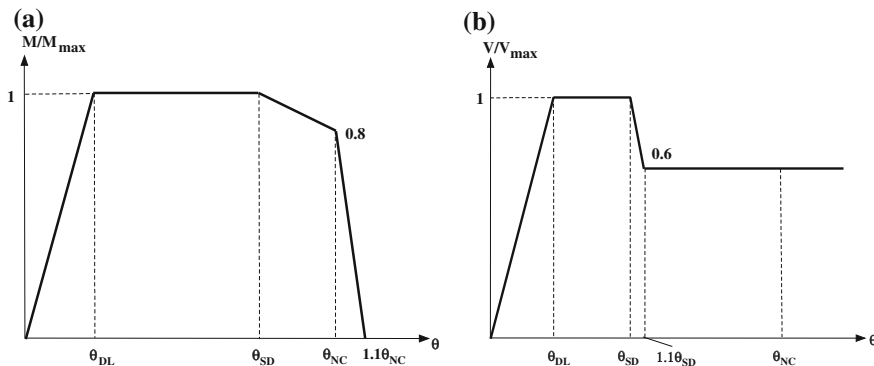


Fig. 3 Constitutive relationships of the plastic hinges, **a** moment-rotation relationship for pier, **b** shear-displacement (given in terms of chord rotation) relationship for spandrel

performance are represented by three limit states which are damage limitation (DL), significant damage (SD) and near collapse (NC). The adopted constitutive relationships are given in Fig. 3.

The pushover analysis is carried out on the model under constant gravity loads and gradually increasing lateral load conforming to an inverted triangular force distribution pattern in the desired horizontal direction. For simplification of the problem, the predominant dynamic response of the building is assumed to be governed by fundamental mode of vibration. And the response of the structure is obtained in the form of pushover curve (base shear as a function of top displacement).

3 Analysis of Existing Masonry Buildings

The low rise URM and RCC buildings are adequately found in Agartala. Among these buildings, URM buildings are considered in this present study as these buildings are primarily designed to resist vertical loads and there are lacks of earthquake resistant features which lead to failure of the buildings under inertial lateral loads generated during earthquake. All the buildings of a building class are to be analysed in order to obtain a comprehensive damage scenario of an area. However, the entire process of analysis of all the buildings consumes a huge time and it is cumbersome as well. Therefore, it is better to group the buildings based on some parameter and then find out the representative building of these groups for further analysis. In this study, grouping of the buildings is done based on the total floor area of the buildings which may indicates the socio-economic levels of this city Agartala. Three groups as, Group-I (Gr-I) for total floor area less than 600 sq. ft (~ 56 sq. m.), Group-II (Gr-II) for total floor area between 600 and 1,200 sq. ft. (~ 56 – 112 sq. m.) and Group-III (Gr-III) for total floor area greater than 1,200 sq. ft. (~ 112 sq. m.) are

considered here. The responses of the representative buildings of each building group are studied by conducting nonlinear static analysis. Since construction practice and material properties of the buildings of same class of an area are more or less similar, representative buildings are sorted out from the available building plans

Table 1 Grouping and distribution parameters of the URM buildings

Plan sl. no.	No. of storey	Total floor area (sq.m.)	Wall density (%)		Group
			x-direction	y-direction	
1	1	54.04	7.94	9.28	Gr-I
2	1	43.98	6.29	9.77	
3	1	48.15	7.97	7.31	
4	1	52.21	6.50	9.49	
5	1	52.74	7.88	10.25	
6	1	47.71	6.67	7.64	
7	1	65.91	7.40	9.70	Gr-II
8	1	85.81	2.77	4.40	
9	1	69.86	8.58	5.99	
10	1	83.41	5.55	7.05	
11	2	87.97	6.29	9.77	
12	2	105.48	7.88	10.25	
13	2	95.42	6.67	7.64	
14	2	96.31	7.97	7.31	
15	2	104.44	6.5	9.49	
16	2	136.08	6.31	6.90	Gr-III
17	2	146.34	7.07	7.68	
18	2	150.01	7.24	8.49	
19	2	182.81	5.84	6.81	
20	2	207.18	6.65	6.64	
21	2	147.02	6.73	8.37	
22	2	164.00	6.35	7.85	
23	2	159.08	6.44	5.45	
24	2	136.65	7.59	7.55	
25	2	173.20	9.07	6.67	
26	2	154.99	5.97	7.96	
27	2	136.43	8.50	7.85	
28	2	169.69	6.71	7.64	
29	2	194.07	7.93	6.93	
30	2	135.81	7.33	9.58	
31	2	141.74	8.55	7.44	
32	2	149.67	6.65	9.20	
33	2	116.88	6.30	7.87	
34	2	155.28	5.39	7.85	

based on the parameter, which is expected to influence the resistance of the building, such as wall densities (amount of cross-sectional wall area per total floor area in each direction). Table 1 shows the grouping and distribution of parameters of 34 nos URM buildings.

The building plans are very much irregular in plan; eccentricities (distance between centre of mass and centre of rigidity, as a ratio of the dimension of the building, in the direction of earthquake) are excluded for the selection of representative buildings. To this end, mean and standard deviation for wall densities of all the buildings of three groups are calculated and these are listed in Table 2. The building plans whose values are nearer to the mean values of each group are considered as a representative building plan for the pertinent group and their parameters are listed in Table 3. The plan view of the ground floor of the representative buildings are shown in Fig. 4. The particulars of the four representative buildings of three groups (Gr-II has two representative buildings as one single storey designated as Gr-IISS and another double storey named as Gr-IIIDS) are tabulated in Table 4. The material properties used in the analysis are taken from the Manual of Indian Society for Earthquake Technology [11] with 1:6 cement-sand mortars. The property like shear modulus is taken as 0.35E; friction coefficient is taken as the maximum limit and self-weight is taken from IS 875 [3] and these are listed in Table 5. These four representative buildings are modeled by EFM to simulate seismic behavior. The 3D EFMs of two representative buildings are shown in Fig. 5. The nonlinear static analysis has been carried out by using the FEM based software SAP2000 to develop capacity curve for all the four buildings. Pushover curves are then converted into bilinear capacity curve as suggested by FEMA 356 [8]. Bilinear capacity curves of the representative buildings are shown in Fig. 6. It is

Table 2 Mean and standard deviation of the wall densities

Group	Wall density in x-direction (%)		Wall density in y-direction (%)	
	Mean	Standard deviation	Mean	Standard deviation
Group-I	7.21	0.80	8.96	1.19
Group-IISS	6.07	2.53	6.78	2.22
Group-IIIDS	7.05	0.80	3.23	1.33
Group-III	6.98	0.98	7.62	0.95

Table 3 Parameters of selected representative buildings of three groups

Group	Selected plan sl. no.	Fundamental frequency (Hz)	Wall density (%) in x-direction	Wall density (%) in y-direction
Gr-I	4	7.70	6.50	9.49
Gr-IISS	10	10.00	5.55	7.06
Gr-IIIDS	15	4.20	6.50	9.49
Gr-III	21	4.80	6.73	8.37

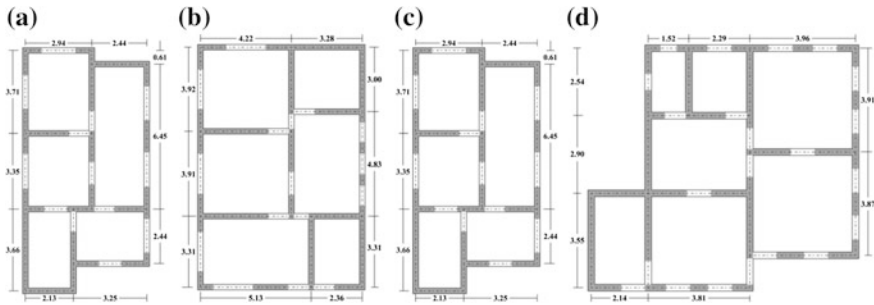


Fig. 4 Plan view of the ground floor of the representative buildings of **a** Gr-I, **b** Grp-IISS, **c** Gr-IIDS, and **d** Gr-III

Table 4 Description of the representative buildings

Particulars	Gr-I	Gr-IISS	Gr-IIDS	Gr-III
Building storey	G + 0	G + 0	G + 1	G + 1
Storey height (m)	3.2	3.202	3.2	3.2
Structural wall thickness (m)	0.25	0.254	0.25	0.25
Slab thickness (m)	0.11	0.127	0.11	0.11
Height of opening (m)	Door-2.1 Window-1.2	Door-2.118 Window-1.22	Door-2.1 Window-1.2	Door-2.1 Window-1.2
Walls in x-direction	6	5	6	6
Total piers per storey in x-direction	11	10	11	20
Walls in y-direction	4	6	4	5
Total piers per storey in y-direction	16	16	16	16
Seismic weights (kN)	1158.8	1453.733	981.45 (2nd) 1173.24 (1st)	1143 (2nd) 1445 (1st)
Centre of mass (x, y) (in m)	2.57, 5.39	4.06, 5.56	2.57, 5.39	4.05, 4.2
Centre of rigidity (x, y) (in m)	2.58, 5.39	3.72, 5.64	2.42, 5.4	3.8, 3.99

observed from the Fig. 6 that the yield displacement of the building under Gr-III is less than the Gr-IIDS building, which signifies that the effective lateral stiffness is more for Gr-III building. Table 3 also justifies this behaviour as the frequency of Gr-III building is more than Gr-IIDS.

Table 5 Material properties considered for representative buildings

Parameter	Value	Parameter	Value
Self-weight (γ)	18.85 kN/m ³	Young's modulus (E)	2,000 MPa
Compressive strength (f_u)	6 MPa	Shear modulus (G)	700 MPa
Tensile strength (f_{tu})	0.25 MPa	Friction coefficient (μ)	0.8
Shearing strength (c)	0.39 MPa		

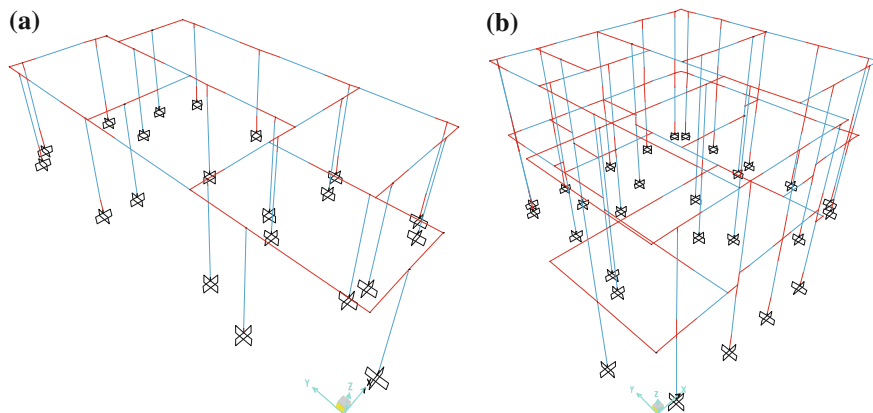
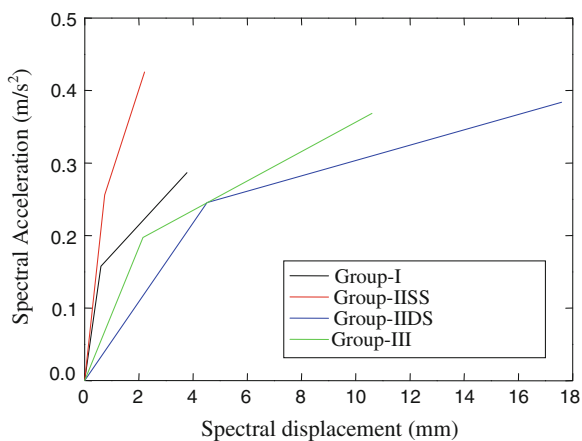


Fig. 5 3D EFM of the representative buildings of **a** Gr-I, and **b** Gr-III

Fig. 6 Bilinear capacity curves of the representative buildings



4 Derivation of Fragility Curves

Fragility curves are a set of cumulative distribution curves which represent exceedance probability of certain damage states as a function of seismic ground motion intensity. Ground motion intensity is represented in terms of spectral displacement at a certain period. Four states of damage are listed in HAZUS [9] as slight, moderate, extensive and complete. It is not easy to identify damage states in the nonlinear pushover curves. However, damage state thresholds which are given in terms of yield and ultimate displacement (S_{dy} and S_{du}) can be identified in the bilinear capacity curves and such damage state thresholds as per Giovinazzi [10] are used in the present study and listed in Table 6.

Fragility curve follows the form of lognormal cumulative distribution function with median value and a logarithmic standard deviation or dispersion of seismic ground motion corresponding to a particular damage state [1].

Therefore, probability of exceedance of damage state ds , given the spectral displacement S_d , is described by the following expression [9]:

$$P[ds|S_d] = \phi \left[\frac{1}{\beta_{ds}} \ln \left(\frac{S_d}{\bar{S}_{d,ds}} \right) \right] \tag{5}$$

$$\beta_{ds} = \sqrt{(CONV[\beta_c, \beta_D])^2 + (\beta_{T,ds})^2}$$

where $\bar{S}_{d,ds}$ is the median value of spectral displacement at which the building reaches the damage state threshold, ds ; β_{ds} is the standard deviation of the natural logarithm of spectral displacement for damage state, ds ; ϕ is the standard normal cumulative distribution function; β_C is the uncertainty related with building capacity; β_D is the uncertainty related with earthquake demand and $\beta_{T,ds}$ is the uncertainty related with damage state threshold. Total variability is influenced by the $\beta_{T,ds}$ and the combined uncertainty of capacity and demand, $CONV[\beta_C, \beta_D]$ and it is calculated by convolution process. In order to minimise the difficulty level of convolution process, the pre-calculated values of damage-state beta from ‘Advanced Engineering Building Module’ (Table 6.5, [9]) are used. The values are already used by Singh et al. [23] and also suggested that minor degradation corresponds to slight damage, major degradation corresponds to moderate damage, and extreme degradation corresponds to extensive and complete damage. Considering moderate conditions, the values corresponding to $\beta_C = 0.3$ and $\beta_{T,ds} = 0.4$ is taken for values of β_{ds} which are tabulated in Table 7.

Table 6 Damage state thresholds for URM structures

Damage state	Giovinazzi [10]
Slight	$0.7S_{dy}$
Moderate	$1.5S_{dy}$
Extensive	$0.5(S_{dy} + S_{du})$
Complete	S_{du}

Table 7 Values of standard deviations (β_{ds}) for damage states [9]

Damage states	Slight	Moderate	Extensive	Complete
For $\beta_C = 0.3$ and $\beta_{T,ds} = 0.4$	0.80	0.95	1.05	1.05

5 Establishment of Fragility Relationships of the URM Buildings

Fragility curves are prepared for the groups of the buildings using the capacity curve parameters of the single representative buildings pertinent to the groups. In this regard, analytical fragility curves are developed using median spectral displacements for the damage states equal to the spectral displacements estimated using relationships of Table 6 and standard deviation listed in the Table 7.

In IS 1893 [4], two earthquake levels are considered as maximum considered earthquake (MCE) and design basis earthquake (DBE). For zone V, MCE is considered for peak ground acceleration of 0.36 g whereas DBE is considered for 0.18 g. In the present study, demand spectrum (5 % damping) corresponding to 0.36 g for medium soil site proposed in the IS 1893 [4] is used to calculate the spectral displacement demand by using FEMA 356 [8] displacement coefficient method. These bilinearised capacity curve parameters corresponding to MCE level are listed in Table 8. As per this table the ultimate spectral displacement of the first storey buildings groups (group I and II) are less and will undergo higher damages in the lesser spectral displacement demands. However, the other groups will experience complete damage state at comparatively higher spectral displacement.

Fragility curves for the representative buildings are shown in Fig. 7. The spectral displacement demands for the buildings corresponding to the MCE level are identified in the fragility curves (MCE demand is shown in fragility curves by the blue dashed line). The discrete damage state probabilities can be calculated by taking the difference of the cumulative exceedance probabilities of successive damage states for a given spectral displacement demand. The fragility curves show that at MCE, the probability of exceeding complete damage state is nearly 50 % for all the groups of buildings. More than 60 and 80 % probability is there that the building will cross the extensive and moderate damage states. However, the probability of exceeding slight damage state is nearly 100 % for all the group.

Table 8 Bilinearised capacity curve parameters for the analyzed models of the representative buildings

Damage state	Fundamental period (T) (s)	S_{dy} (mm)	S_{ay} (g)	S_{du} (mm)	S_{au} (g)
Gr-I	0.13	0.60	0.16	3.77	0.29
Gr-IISS	0.10	0.74	0.26	2.21	0.43
Gr-IIIS	0.24	4.52	0.25	17.59	0.38
Gr-III	0.21	2.15	0.19	10.59	0.37

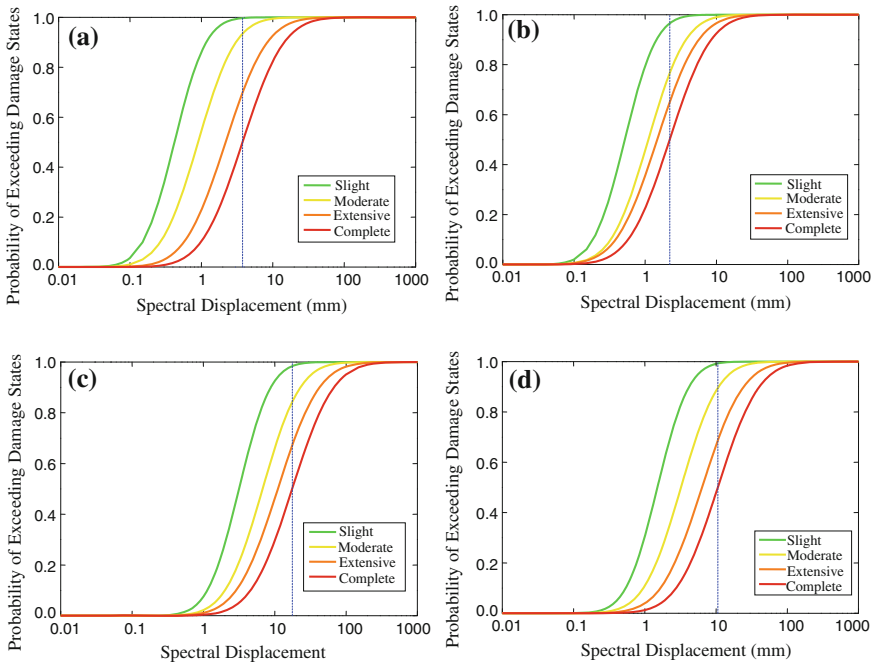


Fig. 7 Fragility curves for buildings under **a** Gr-I, **b** Gr-IISS, **c** Gr-IIIDS and **d** Gr-III

6 Conclusions

URM buildings occupied a large portion of the housing stocks in India and the seismic evaluation of this kind of building is very essential especially for high seismic region like northeast India. In this present study, four URM buildings of Agartala are considered for the seismic damage evaluation and nonlinear static analysis is performed considering inverted triangular distribution of lateral loading along the height of the buildings. The analysis of these buildings is restricted up to the in-plane mechanisms of the walls. The nonlinear modeling has been carried out by equivalent frame modeling approach. In this modeling approach piers and spandrels are modeled as one dimensional elastic beam elements with concentrated plastic hinges at the well-defined locations and junctions are modeled as rigid end offsets. The axial force effect in the piers is also considered in the P-M interaction hinges. The minimum failure envelope considering three possible principal failure modes is fed into the P-M interaction hinges and due to this the variation of failure modes with different levels of axial forces can be obtained. Since damage states cannot be easily marked on the nonlinear capacity curves, the obtained nonlinear capacity curves are bilinearised as per FEMA 356 displacement coefficient method. Consequently, convenient damage state thresholds proposed by various literatures are easily identified on these bilinearised capacity curves. Displacement based

analytical fragility curves are generated using the spectral displacement demands of the representative buildings at various damage states as median values and dispersion taken from expert opinion based values for the URM buildings suggested by the HAZUS technical manuals. The fragility curves represent the damage scenarios of the building groups. Present study reveals that for URM buildings, probability of exceeding complete damage state under MCE level is 50 % and a very high probability is there that the building may suffer moderate to extensive damage state.

References

1. ATC (2011) ATC-58-1: seismic performance assessment of buildings. Applied Technology Council, Redwood City
2. Belmouden Y, Lestuzzi P (2009) An equivalent frame model for seismic analysis of masonry and reinforced concrete buildings. *Constr Build Mater* 23:40–53
3. BIS (1987) IS-875 (Part1): code of practice for design loads (other than earthquake) for buildings and structures. Bureau of Indian Standards, New Delhi
4. BIS (2002) IS-1893: Indian standard criteria for earthquake resistant design of structures, part 1-general provisions and buildings. Bureau of Indian Standards, New Delhi
5. CEN (2005) Eurocode 8: design of structures for earthquake resistance—part 3: assessment and retrofitting of buildings. European Committee for standardisation, Brussels
6. Dolce M (1989) Models for in-plane loading of masonry walls. *Corso sul consolidamento degli edifici in muratura in zona sismica. Ordine degli Ingegneri* (in Italian). (quoted in Simões et al. 2012)
7. Duan X, Pappin JW (2008) A procedure for establishing fragility functions for seismic loss estimate of existing buildings based on nonlinear pushover analysis. In: *Proceedings of the 14th world conference on earthquake engineering*, Beijing, China, 12–17 Oct 2008
8. FEMA (2000) FEMA 356: Prestandard and commentary for the seismic rehabilitation of buildings. American Society of Civil Engineers and Federal Emergency Management Agency, Washington, DC
9. FEMA (2002) Earthquake loss estimation methodology-HAZUS®-MH MR5. Advanced engineering building module-technical and user's manual. Federal Emergency Management Agency, Washington, DC
10. Giovinazzi S (2005) The vulnerability assessment and the damage scenario in seismic risk analysis. Doctoral Thesis, Technical University Carolo-Wilhelmina and University of Florence
11. ISET (2001) A manual of earthquake resistant non-engineered construction. Indian Society of Earthquake Technology, Indian Institute of Technology, Roorkee, India
12. Kappos A, Penelis G, Drakopoulos C (2002) Evaluation of simplified models for lateral load analysis of unreinforced masonry buildings. *J Struct Eng ASCE* 128(7):890–897
13. Magenes G (2000) A method for pushover analysis in seismic assessment of masonry buildings. In: *Proceedings of the 12th world conference on earthquake engineering*, Auckland, New Zealand, 30 Jan–4 Feb 2000
14. Magenes G, Calvi GM (1997) In-plane seismic response of brick masonry walls. *Earthq Eng Struct Dyn* 26:1091–1112
15. Magenes G, Della Fontana A (1998) Simplified non-linear seismic analysis of masonry buildings. In: *Proceedings of the British masonry society*, London, UK 13–15 Oct 1998
16. Milani G, Beyer K, Dazio A (2009) Upper bound limit analysis of meso-mechanical spandrel models for the pushover analysis of 2D masonry frames. *Eng Struct* 31:2696–2710

17. Parisi F, Augenti N (2013) Seismic capacity of irregular unreinforced masonry walls with openings. *Earthq Eng Struct Dyn* 42:101–121
18. Petrovčić S, Kilar V (2013) Seismic failure mode interaction for the equivalent frame modeling of unreinforced masonry structures. *Eng Struct* 54:9–22
19. Roca P, Molins C, Mari´ AR (2005) Strength capacity of masonry wall structures by the equivalent frame method. *J Struct Eng ASCE* 131(10):1601–1610
20. Salonikios T, Karakostas C, Lekidis V, Anthoine A (2003) Comparative inelastic pushover analysis of masonry frames. *Eng Struct* 25:1515–1523
21. Shinozuka M, Feng MQ, Kim HK, Kim SH (2000) Nonlinear static procedure for fragility curve development. *J Eng Mech* 126(12):1287–1295
22. Simões A, Bento R, Gago A, Lopes M (2012) Seismic vulnerability of old masonry ‘Gaioleiro’ buildings in Lisbon. In: *Proceedings of the 15th world conference on earthquake engineering*, Lisbon, Portugal, 24–28 Sept 2012
23. Singh Y, Lang DH, Prasad JSR, Deoliya R (2013) An analytical study on the seismic vulnerability of masonry buildings in India. *J Earthq Eng* 17:399–422
24. Tomaževič M, Lutman M, Petkovič L (1996) Seismic behaviour of masonry walls: experimental simulation. *J Struct Eng ASCE* 122(9):1040–1047

Design Guidelines for URM Infills and Effect of Construction Sequence on Seismic Performance of Code Compliant RC Frame Buildings

Putul Haldar, Yogendra Singh and D.K. Paul

Abstract Un-reinforced masonry (URM) infilled RC framed buildings are the most common construction practice for modern multi-storey buildings in India like many other parts of the world. Although the behavior and failure pattern of the global structure changes significantly due to infill-frame interaction, the general design practice is to treat them as non-structural elements and their stiffness, strength and interaction with frame is often ignored, as it is difficult to simulate. Indian Standard, like many other major national codes, does not provide any explicit guideline for modeling of infills. This paper takes a stock of controlling design provisions in some of the major national seismic design codes to ensure the desired seismic performance of infilled frame. Most of the national codes on seismic design of buildings still lack in adequate guidelines on modelling and design of URM infilled frames results in variable assumption in analysis and design. This paper, using nonlinear pushover analysis, also presents the effect of one of such assumptions of conventional ‘simultaneous’ analysis procedure of infilled frame on the seismic performance of URM infilled RC frame buildings.

Keywords Construction sequence · Infilled frame · RC frame · Seismic design codes · URM infills

1 Introduction

Reinforced concrete buildings constitute the majority of the multi-storey buildings throughout the world, especially in developing countries like India. The typical construction in urban India consists of Reinforced Concrete (RC) moment-resisting

P. Haldar (✉)

Department of Civil Engineering, MNIT Jaipur, Jaipur 302017, India
e-mail: reach2putul@gmail.com; phaldar.ce@gmail.com

Y. Singh · D.K. Paul

Department of Earthquake Engineering, IIT Roorkee, Roorkee 247667, India

frame structures with Un-Reinforced Masonry (URM) infills, especially because of ease in construction and cost effectiveness. Past earthquakes have shown [1–5] that the degree of infill-frame interaction changes the behavior of the RC structure and consequent damaging action of infills mostly leads to undesired structural performance. Modeling RC frame structure with URM infills still remains a challenging task due to the inherent uncertainty in infill-frame interaction leading complex failure mechanism of infilled frames when compared to bare RC frames, either at member level (e.g. shear failure in columns, Fig. 1a; damage to joint region, Fig. 1b) or the global behavior (e.g. soft storey mechanism, Fig. 2).

The complex infill-frame interaction makes the modeling and analysis of infilled frame difficult for designers. Particularly in absence of computation and time inexpensive modeling guidelines of infills for all practical purposes, URM infills are treated as non-structural elements and their stiffness, strength, and interaction with

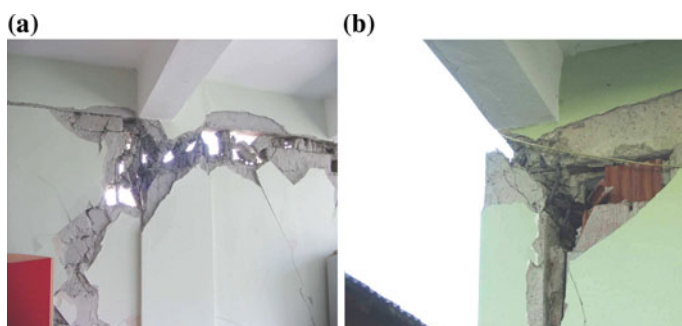


Fig. 1 a Shear failure of column; b Shear failure of beam-column joint due to strut action of infill in 2003 Bingöl earthquake [5]

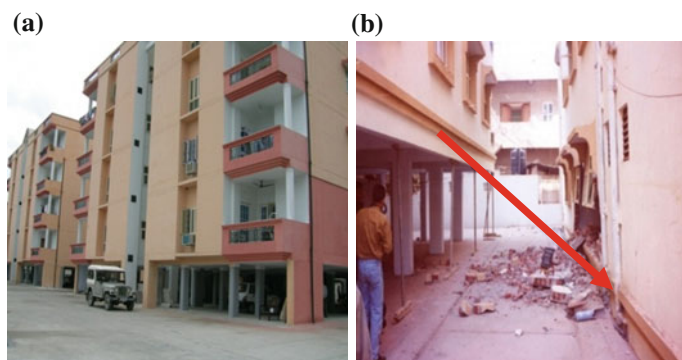


Fig. 2 a Typical Indian multi-storey buildings with ground storey kept open for parking; b failure due to soft/weak storey phenomenon in an open ground storey building during 2001 Bhuj earthquake

frames are often ignored in general design practice. Indian Standard, like many national standards is silent about the modeling guidelines of infilled frame, leaving free the designer to assume suitably. These variable assumptions make the retrofitting of huge stock of such vulnerable buildings even more difficult. For the purpose of consensus, an attempt has been made in this paper to compare the controlling design provisions of some of the major national seismic design codes [6–9] to ensure the desired seismic performance of infilled frame. Further, using nonlinear pushover analysis, this paper also presents the effect of one of the most common assumptions of conventional ‘simultaneous’ analysis procedure of infilled frame on the seismic performance of URM infilled RC frame buildings.

2 Provisions for URM Infilled RC Frames in Seismic Design Codes

Despite scrupulous research on infilled frames, infill panels in frame buildings are traditionally not designed as structural components, mostly because of the absence of adequate modeling guidelines in national standards. None of the national standards, except NZS-4230 [8], provide any modeling guidelines for infills. Some of the national codes [7, 8] recognize the need of considering the effect of infills in the seismic response evaluation of infilled frames and prescribe some precautionary checks, whereas other codes [6, 9] are silent on this issue. The control on design parameters to obtain the desired safety against possible considered earthquakes in some major seismic design codes are discussed below.

2.1 Seismic Design Guidelines for URM Infilled RC Frames in Indian Seismic Code

Indian Standard [6] exercises three types of controls in the design to ensure the desired seismic performance [10]. The code prescribes effective Response Reduction Factor to control ductility demand on the structure, imposes minimum design base shear by providing capping on the design period (Eq. 1) for calculation of design base shear, and controls flexibility by limiting inter-storey drift. The empirical expression for design period for URM infilled RC frame buildings, is given as

$$T_a = \frac{0.09h}{\sqrt{d}} \quad (1)$$

where, T_a (s) is the design natural period of a building having height equal to h (m) and base dimension d (m) along the direction of the vibration. The capping is

implemented by scaling all the design member forces due to earthquake by a factor equal to $\frac{\bar{V}_B}{V_B}$, where \bar{V}_B is the base shear calculated using the empirical design period, and V_B is the base shear obtained analytically. However, Indian codes are silent about Response Reduction Factor and permissible allowable inter-storey drift of frame with infill panels.

Again, it is commonly found that the ground storey is kept open in these multi-storey buildings for parking purposes, leading to soft ground storey failure under earthquake loading. According to BIS [6] guidelines, these open ground storey buildings should be designed for 2.5 times the base shear obtained from bare frame analysis.

In addition to the above provisions, the design of URM infilled RC buildings is governed by the general design provisions of Indian Standard BIS [11]. The provisions most relevant to the present study are the control of beam deflections for Serviceability Limit State and minimum reinforcement requirements. In some cases, these criteria, govern the size and reinforcement of the members.

2.2 Seismic Design Guidelines for URM Infilled RC Frames in European Seismic Code

European code of practice [7] well recognizes the significant contribution of infills to the lateral stiffness and resistance of building and recommends considering the effect of increased strength and stiffness due to presence of infills in an indirect way. Without recommending any particular model, the codes emphasizes on the use of a reliable model, CEN [7] specifies that in absence of a precise model, the design period to be used to evaluate the seismic base shear should be taken as the average of that for the bare frame and for the elastic infilled frames (Eq. 2). Seismic demand on frame members can then be determined by modeling the frame structure without the infills.

$$T_a = C_t H^{(0.75)} \quad (2)$$

where,

$$C_t = \frac{0.075}{\sqrt{A_c}} \quad (3)$$

and

$$A_c = \sum A_i \left(0.2 + \frac{l_{wi}}{h} \right)^2; \quad \frac{l_{wi}}{h} \leq 0.9 \quad (4)$$

H is the height of the building; A_c is the total effective area of the masonry infills in the first storey of the building; A_i is the effective cross-sectional area of infill i in the direction considered in the first storey of the building; and l_{wi} is the length of infill i in the first storey, in the direction parallel to the applied forces.

The influence of the irregular distribution of infill panels, in plan or in elevation, is also addressed in Eurocode-8 (2004). It suggests increasing the effects of the accidental eccentricity by a factor of 2 when masonry infill panels are irregularly distributed but not constitute a severe irregularity in the plan. In case of severe plan irregularities, sensitivity analysis regarding the position and the properties of the infills is recommended, whereas, non-uniform distribution of infills in elevation can be catered by amplifying the seismic action effects on columns through a magnification factor ($\eta > 1.1$), given as

$$\eta = \left(1 + \frac{\Delta V_{RW}}{\sum V_{Ed}} \right) \leq q \quad (5)$$

where, ΔV_{RW} is the total reduction in the resistance of masonry walls in the storey concerned, compared to the more infilled storey above it; $\sum V_{Ed}$ is the sum of the seismic shear forces acting on all vertical primary seismic members of the storey concerned; and q is the behavior factor.

2.3 Seismic Design Guidelines for URM Infilled RC Frames in New Zealand Seismic Code

The New Zealand code, NZS-4230 [8], deals with infilled frames in a much detailed manner. It is the only code providing modeling guidelines for the infills. The code clearly acknowledges that infill panels modify the structural behavior and have an adverse effect on the seismic performance of frame unless complete separation from the surrounding frame is provided. The design provisions of this code are governed by the reduced period of vibration resulting in increased seismic load and ductility demand on the frame members of the infilled frame. For the purpose of force distribution, the code idealizes infilled frame as an equivalent diagonally braced frame having the width of the masonry infill diagonal as one quarter of its length. Possible failure modes i.e., shear failure of infill panels, crushing of the diagonal strut, tension failure of infill panels, flexural or shear failure of columns, soft storey mechanism after failure of infill panels, have been identified, though not quantified, as these are difficult to predict with accuracy. Therefore, to avoid shear failure of the supporting columns, NZS-4230 [8] recommends designing infilled frames for higher structural type factors unless the infills are properly tied with the surrounding frames to act together in full composite action. To ensure satisfactory performance of infilled frame after the shear failure of the infills at a level, NZS-4230 [8] suggests ductility demand at any storey level should not be more than two. Thus maximum storey ductility μ , for building of equal story height can be expressed as

$$\eta = \frac{n+1}{n} \quad (6)$$

where, n is the number of storeys.

2.4 Seismic Design Guidelines for URM Infilled RC Frames in American Seismic Code

Unlike the design code for new buildings, the American code for rehabilitation of existing buildings [9] and FEMA guidelines [12–14] clearly explain the procedure to assess the seismic response of infilled frames. According to these documents, the effect of masonry infill panels can be replicated by introducing one or more concentrically or eccentrically placed equivalent diagonal struts. The thickness and modulus of elasticity are kept same as that of the infill panel, whereas the equivalent width of the infill panel prior to cracking is defined as

$$a = 0.175(\lambda_1 h_{col})^{-0.4} r_{inf} \quad (7)$$

where,

$$\lambda_1 = \left[\frac{E_{me} t_{inf} \sin 2\theta}{4E_{fe} I_{col} h_{inf}} \right]^{\frac{1}{3}}$$

h_{col}	column height between centerlines of beams
h_{inf}	height of infill panel
E_{fe}	expected modulus of elasticity of frame material (concrete)
E_{me}	expected modulus of elasticity of infill material
I_{col}	moment of inertia of column
L_{inf}	length of infill panel
r_{inf}	diagonal length of infill panel
t_{inf}	thickness of infill panel and equivalent strut

3 Construction Sequence of Infilled Frames

Traditionally, infill panels in framed buildings are provided after construction of the frame is completed, at least for a few storeys. The construction sequence of infill panels relative to RC frame followed in India is shown in Fig. 3.



Fig. 3 Photographs showing typical construction sequence of an infilled frame building: **a** intermediate stage, **b** final stage of construction, **c** gap between infills and beam due to construction sequence of infilled frames

Figure 3a, c show intermediate stages of construction of infill panels in RC frames, whereas Fig. 3b show the final stage. The construction sequence of infilled frames leads to a gap between the infill panel and the beam above (Fig. 3c). This gap spares the infill panels from resisting any gravity load coming to the frame. Even relatively small initial gap can have significant effect on the structural behavior of infilled frames [15, 16]. According to [17], parameters like initial lack of fit between infill and frame, and workmanship may have even higher impact on the strength of infilled frame than the parameters like strength and stiffness of infills, though these are difficult to be quantified and generalized. Contrary to the actual sequence of construction, in the conventional ‘simultaneous’ analysis procedure, the infills and the frame are considered to come to existence instantaneously, and the infills are also subjected to vertical as well as lateral loads, along with the frame members. The application of this fictitious vertical load in the infills may significantly affect their behavior, simulated in a simultaneous analysis.

4 Parametric Study

In order to study the effect of conventional assumption of ‘simultaneous’ construction of infilled frame in analysis, on the realistic seismic behavior of infilled frames, a parametric study has been carried out on a set of multi-storey RC frame buildings with solid uniform infill panels, considering the generic building plan shown in Fig. 4 for mid-rise (four storey) and high-rise (ten storey) buildings. The thickness of solid infill panels are considered as 115 and 230 mm for interior and exterior partitions, respectively, as per the prevailing practice in India. As there are large number of existing buildings designed only for gravity loads even in high seismic zones (III, IV and V), the present study considers both the set of mid and high-rise buildings designed for gravity loads only, considering relevant Indian Standards BIS [11, 18, 19]. The two sets of four and ten storey uniformly infilled RC frame buildings have been assumed to be situated on hard soil [6] in seismic zone IV (Effective Peak Ground Acceleration, EPGA = 0.24 g for Maximum Considered Earthquake, MCE).

4.1 Modelling of Infilled Frame

Three dimensional space frame models of the buildings have been developed using structural nonlinear analysis software SAP2000 [20]. Beams and columns have been modeled as 3D frame elements. The floor/roof slabs are modelled as rigid diaphragms and the rigidity of beam-column joints is simulated using the guidelines of ASCE/SEI-41 Supplement-1 [21]. Realistic idealization of infill panels is the most crucial issue in simulating the behavior of URM infilled RC frame buildings.

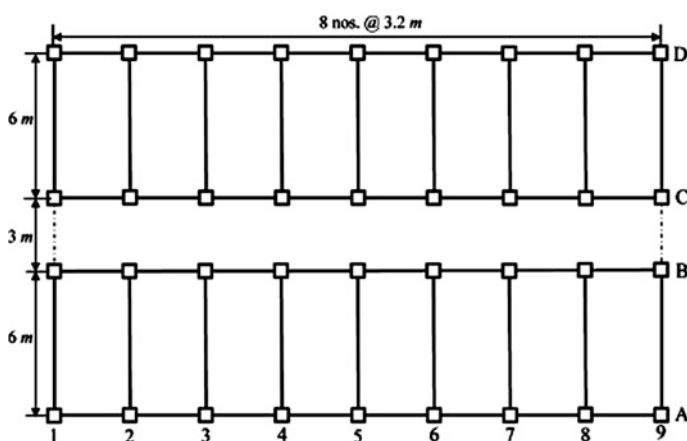


Fig. 4 Plan of the generic building

Infill panels are modelled as equivalent diagonal struts as this most commonly used approach for simulating the action of infills, and can realistically predict the failure modes in infilled frames [22].

The seismic behaviour of the considered buildings has been estimated using Nonlinear Static pushover analysis according to ASCE-41 [9]. For this purpose lumped plasticity models of the buildings are developed, in which flexural (M) hinges are assigned at both ends of beams, whereas axial force-bi-axial moment interaction hinges (P-M-M) are assigned to columns. Axial plastic hinges, with strength capacity estimated based on all the possible failure modes, have been assigned at mid-length of the equivalent diagonal struts simulating infills. Non-conforming, 'NC' and conforming, 'C' type of transverse reinforcement has been considered for gravity designed and SMRF infilled frames, respectively, to assign the plastic rotations for beams and columns as per ASCE-41 [9].

The construction sequence of infilled frames results in another important issue in modelling of infills, as no vertical load is transferred through infills. To avoid transfer of vertical load to equivalent struts, the construction sequence has been simulated in the analysis by defining the model in two stages. In the first stage, the bare frame is modelled and subjected to gravity loads, and in the second stage, the infills are added to the already loaded bare frame and the whole structure is subjected to seismic loads. Further, 'gap' elements have been used to de-activate the struts in tension. Since the 'gap' element is active in nonlinear analysis only, the stiffness of the gap elements has been assigned in such a way that stiffness of the infilled frame is simulated realistically in both linear and nonlinear analyses [23].

4.2 Effect of Construction Sequence of Infills on Seismic Behavior of RC Frame Buildings

Figures 5 and 6 show the yielding pattern of the infill panels in the four and ten storey gravity load designed buildings, respectively, subjected to gravity load alone, when the initial gap between infill and frame is not considered in the modeling. It can be observed from the figures that some of the infill panels in the longitudinal direction, in the bottom storey of the four storey building have yielded under the gravity load itself. In case of the ten storey building, the effect is even more pronounced, where all the infill panels in the bottom three storeys in longitudinal direction, and the bottom two storeys in transverse direction, have crossed "Immediate Occupancy" (IO) performance level [9]. Similarly, Figs. 7 and 8 show the yield pattern of the infill panels in the four and ten storey buildings, respectively, designed for earthquake loads. The buildings are subjected to gravity load alone and the construction sequence has not been considered. Similar behavior is observed in this case also, except that the number of panels yielding under gravity load reduces due to relative increase in the size of frame members in case of buildings designed for earthquake forces. This behavior is contradictory to the

Fig. 5 Hinge pattern under gravity load for the four storey uniformly infilled frame building, designed for gravity loads only, when construction sequence is not considered in analysis:

a typical longitudinal frame;
b typical transverse frame

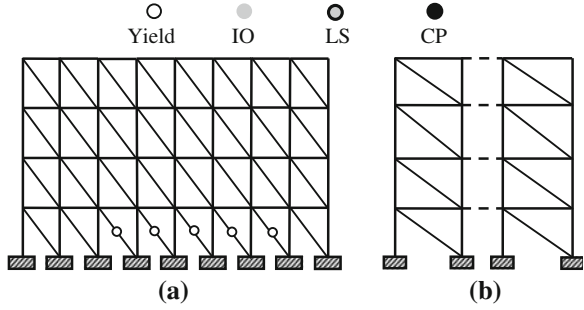


Fig. 6 Hinge pattern under gravity load, for the ten storey uniformly infilled frame building, designed for gravity loads only, when construction sequence is not considered in analysis: **a** typical longitudinal frame; **b** typical transverse frame

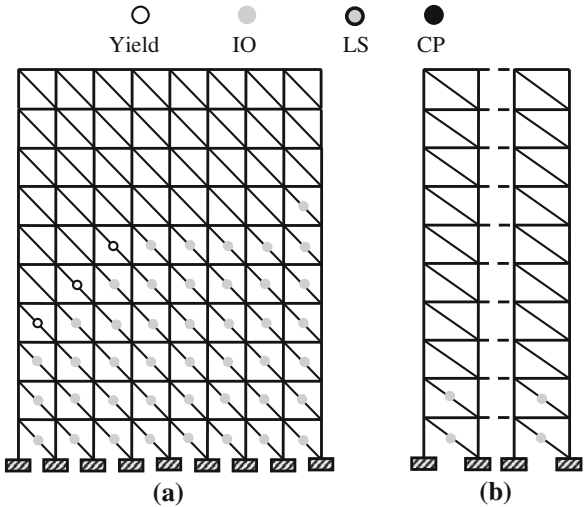
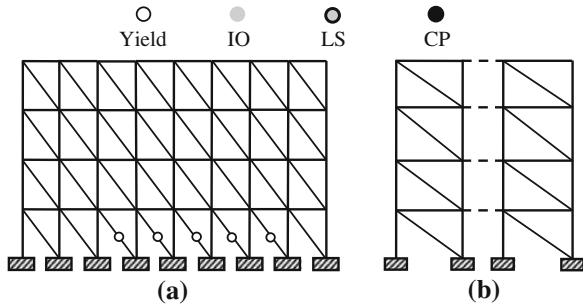
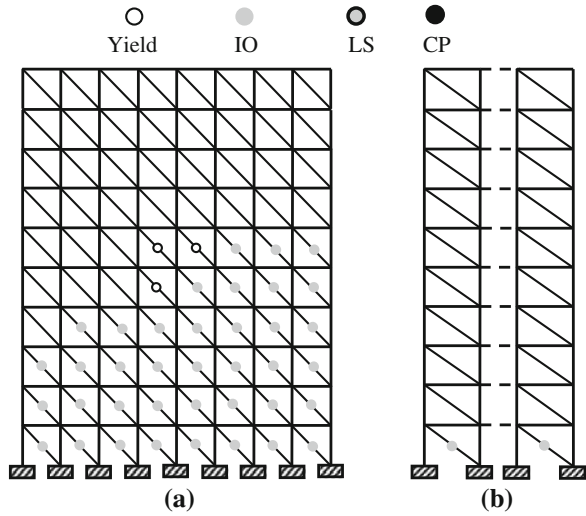


Fig. 7 Hinge pattern under gravity load for the four storey uniformly infilled SMRF building, when construction sequence is not considered in analysis: **a** typical longitudinal frame; **b** typical transverse frame



common observation and understanding that the infills do not share gravity loads. Therefore, there is need to simulate the construction sequence in the analysis of infilled frames to get realistic results.

Fig. 8 Hinge pattern under gravity load for the ten storey uniformly infilled SMRF building, when construction sequence is not considered in analysis: **a** typical longitudinal frame; **b** typical transverse frame



Past studies [9, 24–26] have shown that the equivalent strut models provide sufficiently accurate results for frame infills. Accordingly, in this present study, an equivalent concentric diagonal compressive strut element has been used to simulate the infill panels. To simulate the effect of initial lack of fit between infield panel and beam, ‘gap’ elements have been used. In presence of gap elements, the struts are active in compression only. Since the ‘gap’ element is active in nonlinear analysis only, the stiffness of the gap elements has been assigned in such a way that it will not affect the linear and nonlinear stiffness of the infilled frame. In linear analysis, one brace is inactive due to zero stiffness of gap element. Similarly, in nonlinear analysis the gap element is in-effective in tension.

Figures 9 and 10 compare the capacity curves of the four storey and ten storey gravity designed bare and uniformly infilled frames with and without considering the construction sequence. It can be observed that the infills have very significant effect on capacity curves of the buildings. The stiffness of the building increases 130 times and 68 times and strength increases 5.2 times and 3.3 times in the longitudinal and transverse directions, respectively, in case of the four storey building. In case of the ten storey building, the increase in stiffness is 14.6 times and 36.7 times, and increase in strength is 4.7 times and 2.5 times, in the longitudinal and transverse directions, respectively. However, the inelastic deformation capacity of the infilled frame decreases drastically. The sharp saw-tooth curve in case of ten storey infilled frame building shows the sudden drop in the lateral force due to failure of a set of infills, and quick re-gains in lateral force with displacement, due to high stiffness of the infills.

The effect of construction sequence of infill panels on the capacity curves of four and ten storey infilled frames can also be observed from the Figs. 11 and 12, respectively.

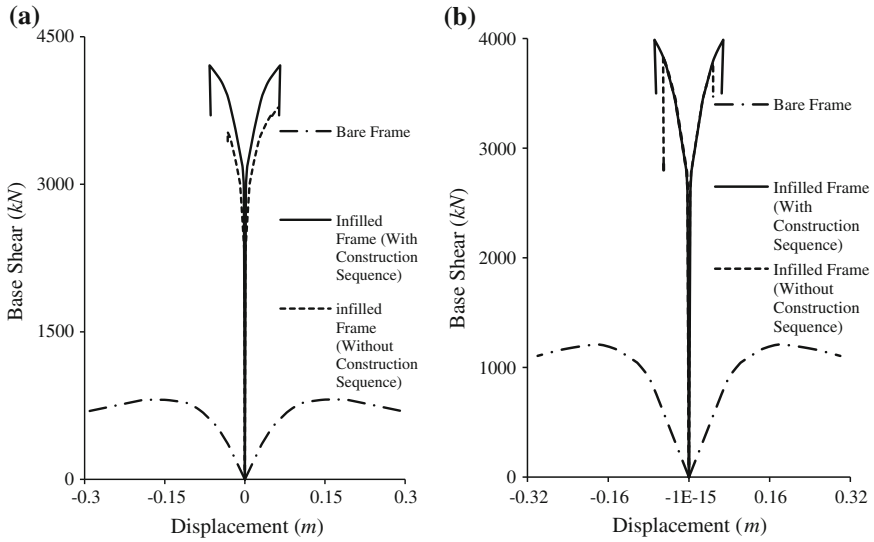


Fig. 9 Comparison of capacity curves of bare frame and uniformly infilled frame for the four storey building designed for gravity load only: **a** longitudinal direction; **b** transverse direction

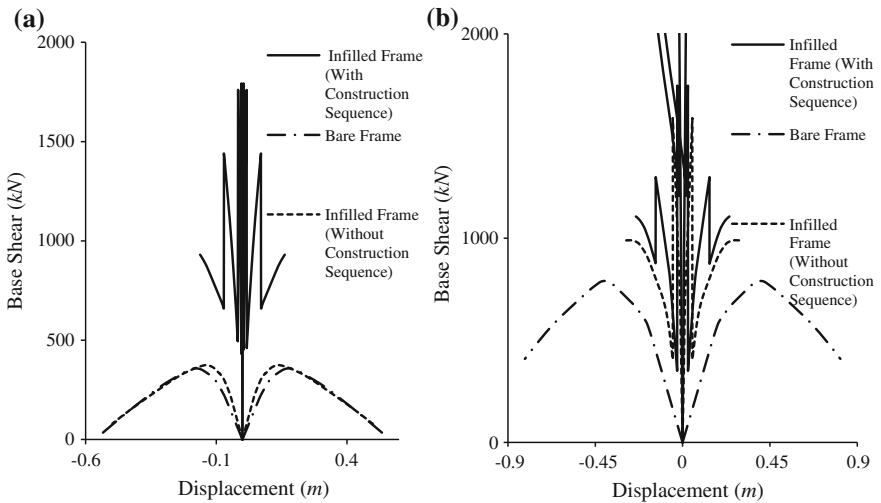


Fig. 10 Comparison of capacity curves of bare frame and uniformly infilled frame for the ten storey building designed for gravity load only: **a** longitudinal direction; **b** transverse direction

In case of the four storey gravity designed buildings, the effect of construction sequence is relatively small and the capacity curve is close to the case when construction sequence is ignored, whereas in case of the ten storey building, the

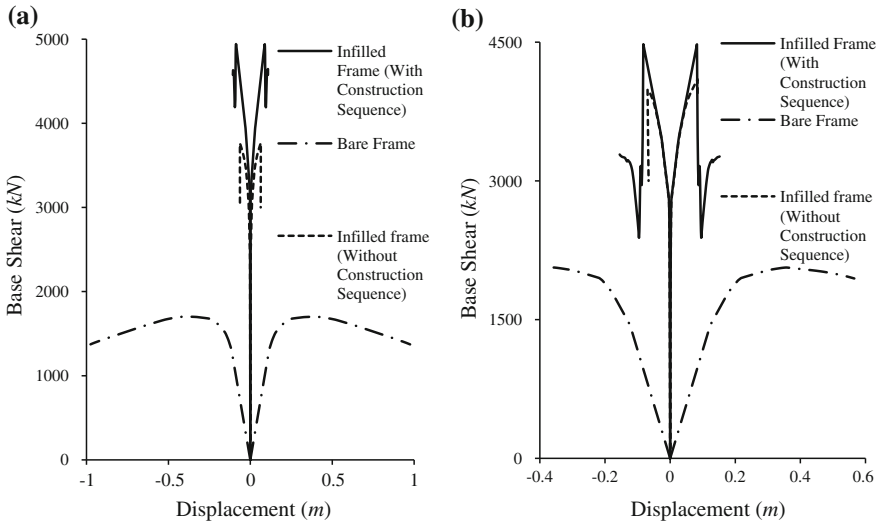


Fig. 11 Comparison of capacity curves of bare frame and uniformly infilled frame for the four storey building designed as SMRF as per relevant Indian Standards: **a** longitudinal direction; **b** transverse direction

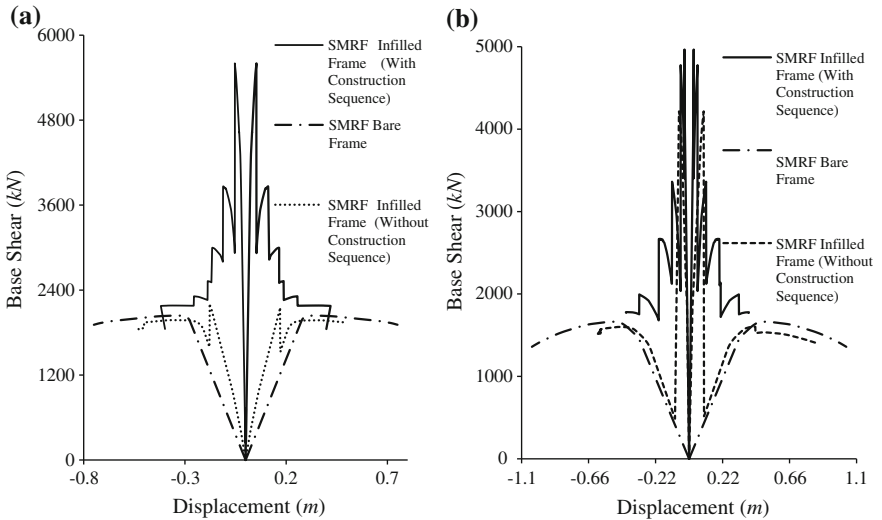


Fig. 12 Comparison of capacity curves of bare frame and uniformly infilled frame for the ten storey building designed as SMRF as per relevant Indian Standards: **a** longitudinal direction; **b** transverse direction

effect of construction sequence is so dramatic that the capacity curve in the longitudinal direction is close to that of the bare frame. This is because in case of four storey building, no infill panel in transverse direction and a very few infill panels in

longitudinal direction (Fig. 5), yielded under gravity load, whereas in case of the ten storey buildings, a large number of infill panels (particularly in the longitudinal direction) yielded under gravity load itself (Fig. 6).

The comparison of capacity curves of the four and ten storey SMRF buildings is presented in Figs. 11 and 12, respectively. As the buildings are designed for earthquake forces also, the strength and ductility increases as compared to the gravity load designed buildings. Further, as the stiffness and strength of the frame members increases relative to the infills, the effect of infills on capacity curve reduces. In this case, the stiffness and strength of the infilled frame is 149 times and 2.9 times, respectively of the bare frame in the longitudinal direction, and 111 times and 2.2 times, respectively, in the transverse direction, for the four storey building. In case of the ten storey building, these values are 14.6 times and 2.8 times, respectively in longitudinal direction and 37 times and 2.9 times, respectively in the transverse direction. The effect of construction sequence of infill panels on the capacity curves of the four and ten storey SMRF buildings is similar as in case of the corresponding gravity load designed buildings.

5 Conclusions

Infills have drastic effect on capacity curves of the infilled frames and their stiffness and strength has been found to increase up to 149 times and 5.2 times, respectively as compared to the bare frames for the studied buildings. The effect of construction sequence on seismic performance of URM infilled RC frame buildings has been studied with the help of an analytical study carried out on four and ten storey buildings with different design levels. It has been observed that simulation of construction sequence of infills relative to frame has a drastic impact on the estimated capacity curve of the infilled frames and this effect increases with the height of the building. The conventional simultaneous analysis ignoring the construction sequence may be highly erroneous in some cases, and it has been found to almost nullify the effect of infills in longitudinal direction of the ten storey building considered in the present study.

References

1. GSI (1995) Report on Uttarkashi earthquake of 20th October 1991. Geological Society of India (GSI), Memoir 30, Bangalore, India
2. DEQ (1999) A report on Chamoli earthquake of March 29, 1999. Department of Earthquake Engineering, University of Roorkee, Roorkee, India
3. GSI (2003) Kutch (Bhuj) earthquake 26 January 2001. Geological Survey of India Lucknow, India
4. EERI (2002) Bhuj, India earthquake of January 26, 2001, reconnaissance report. Earthquake Engineering Research Institute

5. Özcebe G, Ramirez J, Wasti ST, Yakut A (2003) Bingöl earthquake of 1 May 2003 engineering report. <http://www.seru.metu.edu.tr/archives.html>, <http://www.anatolianquake.org>
6. BIS (2002) IS 1893 (Part 1) Indian standard criteria for earthquake resistant design of structures. Bureau of Indian Standards, New Delhi
7. CEN (2004) EN 1998-1, Eurocode 8: design for structures for earthquake resistance, Part 1: general rules, seismic actions and rules for buildings. European Committee for Standardization (CEN), Brussels, Belgium
8. NZS-4230 (2004) Design of reinforced concrete masonry structures. Standards Association of New Zealand, Wellington, New Zealand
9. ASCE-41 (2007) Seismic rehabilitation of existing buildings (ASCE/SEI 41-06). American Society of Civil Engineers Reston, Virginia
10. Haldar P, Singh Y (2009) Seismic performance and vulnerability of Indian code designed RC frame buildings. *ISET J Earthq Eng* 46:29–45
11. BIS (2000) IS 456 Indian standard plain and reinforced concrete-code of practice (Fourth Revision). Bureau of Indian Standards, New Delhi
12. FEMA-273 (1997) NEHRP guidelines for the seismic rehabilitation of buildings. Federal Emergency Management Agency, Washington, DC
13. FEMA-306 (1998) Evaluation of earthquake damaged concrete and masonry wall buildings. Federal Emergency Management Agency, Washington, DC
14. FEMA-356 (1998) Prestandard and commentary for the seismic rehabilitation of buildings. Federal Emergency Management Agency, Washington, DC
15. Riddington JR (1984) The influence of initial gaps on infilled frame behavior. *Proc Inst Civ Eng Part 2* 77:295–310
16. Saneinejad A, Hobbs B (1995) Inelastic design of infilled frames. *J Struct Eng (ASCE)* 121:634–650
17. Moghaddam HA, Dowling PJ (1987) The state of the art in infilled frames. ESEE research report no 87-2, Civil Engineering Department, Imperial College, London
18. BIS (1987a) IS: 875 (part 1) Indian standard code of practice for design loads (other than earthquake) for buildings and structures. Bureau of Indian Standards, New Delhi
19. BIS (1987b) IS: 875 (part 2) Indian standard code of practice for design loads (other than earthquake) for buildings and structures. Bureau of Indian Standards, New Delhi
20. SAP2000 (2010) CSI analysis reference manual for SAP2000. Computers and Structures Inc., Berkeley, California
21. ASCE/SEI-41 (2007) Supplement-1, update to ASCE/SEI 41 concrete provisions. American Society of Civil Engineers Reston, Virginia
22. Haldar P, Singh Y, Paul DK (2013) Identification of seismic failure modes of URM infilled RC frame buildings. *Eng Fail Anal* 33:97–118
23. Haldar P, Singh Y (2012) Modelling of URM infills and their effect on seismic behaviour of RC frame buildings. *Open Constr Build Technol J* 6(Suppl 1-M1):35–41 (Bentham Science Publishers)
24. Smith BS (1962) Lateral stiffness of infilled frames. *ASCE J Struct Div* 88:183–199
25. Madan A, Reinhorn AM, Mander JB, Valles RE (1997) Modeling of masonry infill panels for structural analysis. *J Struct Eng (ASCE)* 123:1295–1302
26. Asteris PG (2003) Lateral stiffness of brick masonry infilled plane frames. *J Struct Eng ASCE* 129:1071–1079

Part X
Seismic Pounding and Mitigation in
Adjacent Structures

Experimental and Numerical Study on Pounding of Structures in Series

Saher El-Khoriby, Ayman Seleemah, Hytham Elwardany and Robert Jankowski

Abstract Pounding between structures in series during earthquakes may cause serious damage in the structural elements. The aim of this paper is to show the results of an experimental and numerical study that is focused on pounding between more than two structures which may be described as “structures in series”. In this study, the shaking table experiments, as well as the numerical analyses, were performed using three tower models including rigid and flexible structures with different configurations and different gap distances under several earthquake excitations. The results show that pounding may affect the behaviour of the structures significantly. They also indicate that the rigid towers are more influenced by pounding than the flexible ones. Moreover, increasing or decreasing the gap distance may lead to increase or decrease in the response under different earthquakes with no specific trend. Furthermore, the optimal gap size has been found to be either the distance which prevents pounding or the zero gap.

Keywords Structural pounding · Numerical analysis · Series of structures · Earthquakes · Contact surfaces

1 Introduction

Due to the high costs of land in the urban areas, buildings are constructed in contact with each other. Such a problem may induce the reciprocal pounding between buildings in series during earthquakes. The surveys on damage during past ground

S. El-Khoriby (✉) · A. Seleemah · H. Elwardany
Faculty of Engineering, Structural Engineering Department,
Tanta University, Tanta, Egypt

R. Jankowski
Faculty of Civil and Environmental Engineering,
Gdansk University of Technology, Gdansk, Poland

motions show that interactions between insufficiently separated buildings, or bridge segments, may result in substantial damage or even contribute to total structural collapse [1].

Numerical simulations concerning pounding phenomenon were carried out using different structural models. The fundamental study on pounding between buildings in series, modelled as single-degree-of-freedom systems with linear viscoelastic model of impact force, was conducted by Anagnostopoulos [2]. More detailed analyses were carried out on discrete multi-degree-of-freedom structural models with the mass of each storey lumped on the floor level. Anagnostopoulos and Spiliopoulos [3], for example, studied the effect of the mutual pounding during earthquakes on 5 and 10-storey buildings. The buildings were idealized as lumped-mass, shear beam type, multi-degree-of-freedom systems with bilinear force-deformation characteristics and with bases supported on translational and rocking spring-dashpots. The main conclusion of the study is that pounding may increase or reduce the response of a given building in a block, depending primarily upon its period and mass, in relation to the period and mass of the building (or buildings) next to it, and on whether the collisions are at one or two sides. It has also been concluded that, when the masses of two interacting buildings are similar, the response of the stiffer building may be amplified because of pounding. Moreover, if there are large differences in the masses of the colliding buildings, then pounding can cause high over stresses in the structure with smaller mass. Discrete multi-degree-of-freedom structural models, with the mass of each storey lumped on the floor level, were also used by other researchers [4–7]. Further studies were conducted using more accurate structural models. Abdel Raheem [8] studied the effect of impact between two adjacent steel moment resistant frame buildings of 8 and 13 storeys. Such study used contact force-based model with both linear and nonlinear springs. In addition, a nonlinear contact model accounting for energy dissipation was also utilized to model impact. Finite element (FE) models of colliding buildings were employed in the analysis carried out by Papadrakakis et al. [9], in which floors of structures were modelled by single four-node plane stress elements and walls by four linear beam-column elements. The detailed non-linear analysis of interactions between two buildings using finite element method (FEM) was also conducted in [10–12].

On the contrary to numerical analyses, the results of experimental studies on pounding under earthquake excitations are very limited. Most of the experimental studies were conducted between two adjacent buildings only. For example, Chau et al. [13] carried out a shaking table experiment to investigate the pounding phenomena between two steel towers with equal height of 2.0 m with different natural frequencies and damping ratios. The towers were subjected to sinusoidal waves of various magnitudes and frequencies as well as the ground acceleration of the 1940 El Centro earthquake. The results of the study indicate that whether periodic or chaotic pounding occurs depends non-linearly on the changes in parameters of the two adjacent towers and the ground motion characteristics. It has also been concluded that pounding amplifies the response of stiffer structures but suppresses the response of more flexible ones. More recently, an experimental work

has been conducted using small shaking table to study the effect of pounding between two small towers with different frequencies, damping ratios and masses under the NS component of the El Centro earthquake for different gap sizes between the towers [14]. The main conclusion of the experiment is that pounding may lead to considerable amplification of the response as well as it may also play a positive role by reducing vibrations in some cases.

The studies for the reciprocal pounding between adjacent buildings in series have received little attention by researchers. Detailed numerical analyses have been conducted by Anagnostopoulos and others [2, 3]. On the other hand, according to the author's knowledge, the experimental study on pounding between structures in series has not been conducted so far (compare [15]). The aim of the current paper is to present results of a study concerning pounding between three structures. Two configurations were tested experimentally on a shaking table using three tower models in one row to investigate the behaviour of structures in series when subjected to different earthquake excitations. Configuration (1) studies the behaviour of pounding between the three towers with different gap distances considering the more rigid tower in the middle. On the other hand, Configuration (2), considers the behaviour of pounding between the three towers with different gap distances considering the more flexible tower in the middle.

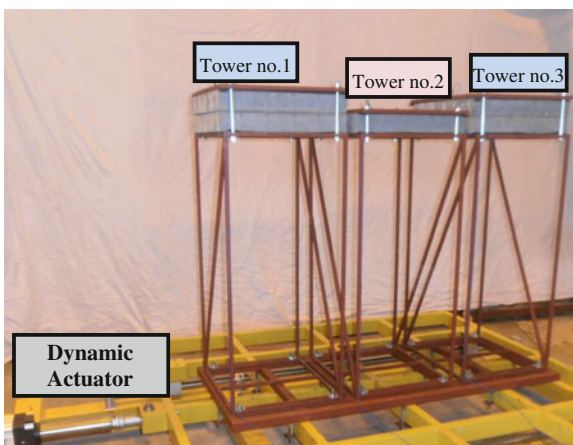
2 Shaking Table Experiments

A unidirectional shaking table with platform dimensions 2.0×2.0 m (see Fig. 1), located at the Gdansk University of Technology (Poland), was used in the experimental study. Three tower models with 1.0 m height and different properties (Figs. 2 and 3) were mounted on the platform of the shaking table. Each tower was constructed out of four steel columns and additional skew bracings to avoid torsional vibration behaviour. The columns were constructed from box section $15 \times 15 \times 1.5$ mm with a rectangular shape arrangement and a spacing of 480 mm in the longitudinal direction and 571 mm in the transversal one. The bracing elements for the three towers were constructed from the same cross section as the vertical elements and the total weight of the supporting columns of each tower, including the horizontal members and bracings, was 10.72 kg. Concrete plates with dimensions $500 \times 500 \times 70$ mm and weight of 42.2 kg were mounted at the top of each tower (see Figs. 2 and 3). In the experiment, two configurations were tested. In the first configuration, two concrete plates were mounted on the external towers, and only one concrete plate was located on the middle tower (Fig. 2). In the second configuration, two concrete plates were mounted on the middle tower and only one concrete plate was located on the external towers, as shown in Fig. 3. In the experiment, five different earthquake records and one mining ground motion (see Table 1) were used with gap distances varying between the zero gap up to the gap size large enough to prevent pounding. Four accelerometers recorded the results of the experiments, three of them (A1, A2 and A3) were mounted on the left,

Fig. 1 Setup of the experiment



Fig. 2 Configuration (1)—rigid tower in the *middle*



the middle and the right tower, respectively, and the fourth one was attached to the shaking table platform. The natural properties of the towers, determined from the free vibration tests, are summarized in Table 2.

In this paper, the detailed results for the cases of zero and 40 mm gap distances in addition to the case of independent vibrations (gap distance large enough to prevent pounding), under the NS component of El Centro 1940 earthquake, are presented. The peak absolute accelerations under other ground motions are also shown.

Fig. 3 Configuration (2)—flexible tower in the *middle*

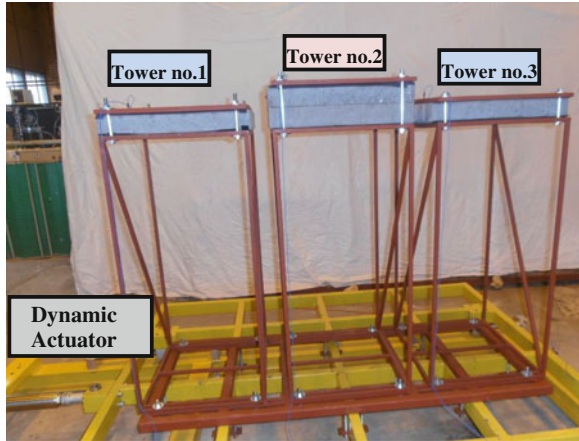


Table 1 Ground motion excitations used in the experiments

Excitation	Amplification (%)	Original PGA (m/s ²)
1940 El Centro, NS	100	3.070
1995 Kobe, NS (JMA station)	25	8.057
1989 Loma Prieta (Corralitos station, NS component)	50	6.315
1994 Northridge, EW (Santa Monica station)	75	8.660
1971 San Fernando, N74E (Pacoima Dam station)	25	11.375
2002 Polkowice ^a , Poland, NS	100	1.634

^a Mining ground motion

Table 2 Natural properties of different towers extracted from the free vibration tests

	Configuration (1)			Configuration (2)		
	1	2	3	1	2	3
Tower no.	1	2	3	1	2	3
Frequency (Hz)	2.40	3.38	2.26	3.19	2.45	3.12
Damping ratio (%)	0.34	0.25	0.38	0.37	0.34	0.28

The experimental results are shown in Figs. 4 and 5 for the case of zero gap distance, in Figs. 6 and 7 for the case of 40 mm gap distance and in Figs. 8 and 9 for the case of a gap distance large enough to prevent pounding between the model structures. In particular, Figs. 4 and 5 show the experimental acceleration time histories of the three towers for Configuration (1) and Configuration (2), respectively. The general shape of acceleration time history for each configuration is more or less similar except for the region around 5th sec. This suggests that the three towers acted more or less as one structure. Calculating the natural frequencies of the

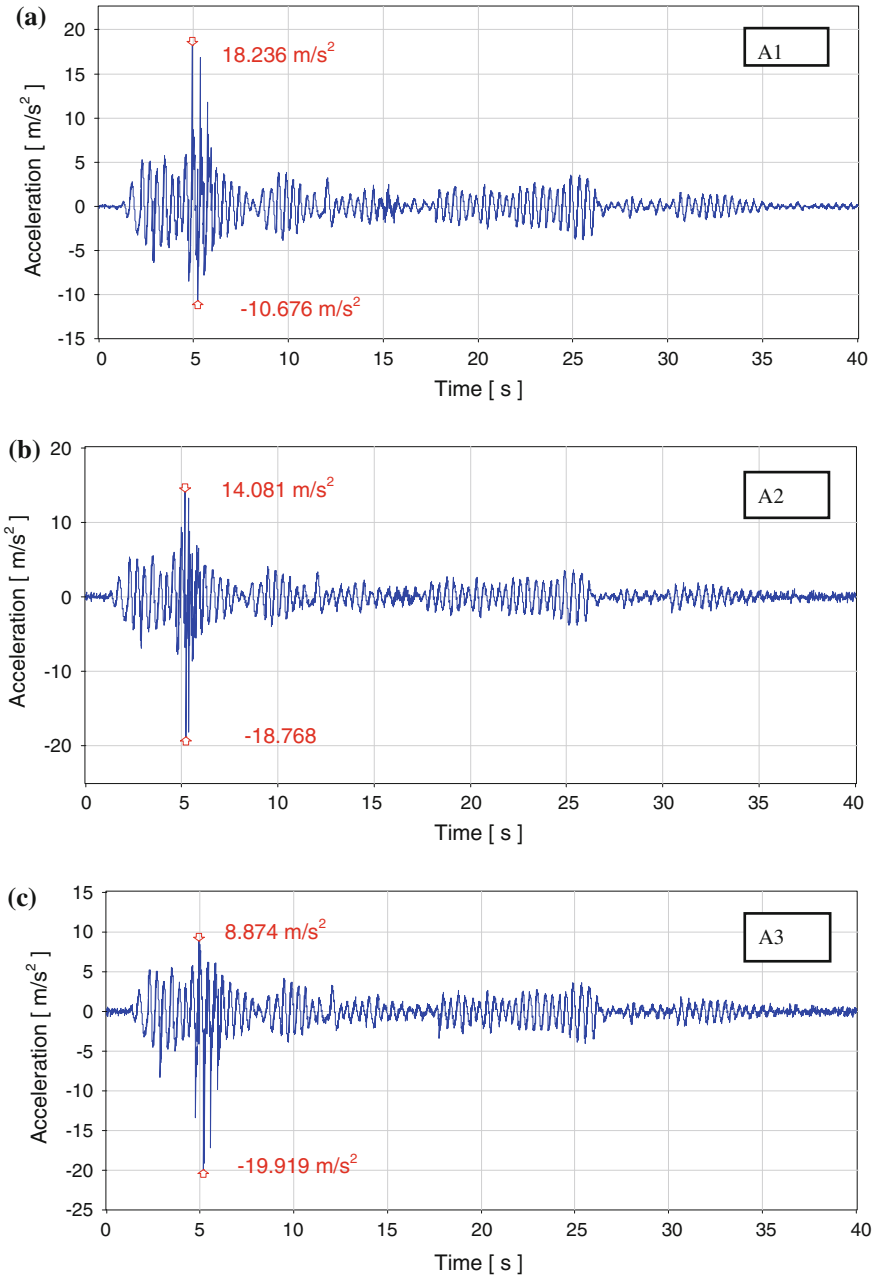


Fig. 4 Acceleration time histories of different towers when subjected to El Centro earthquake. [Configuration (1); zero gap distance]

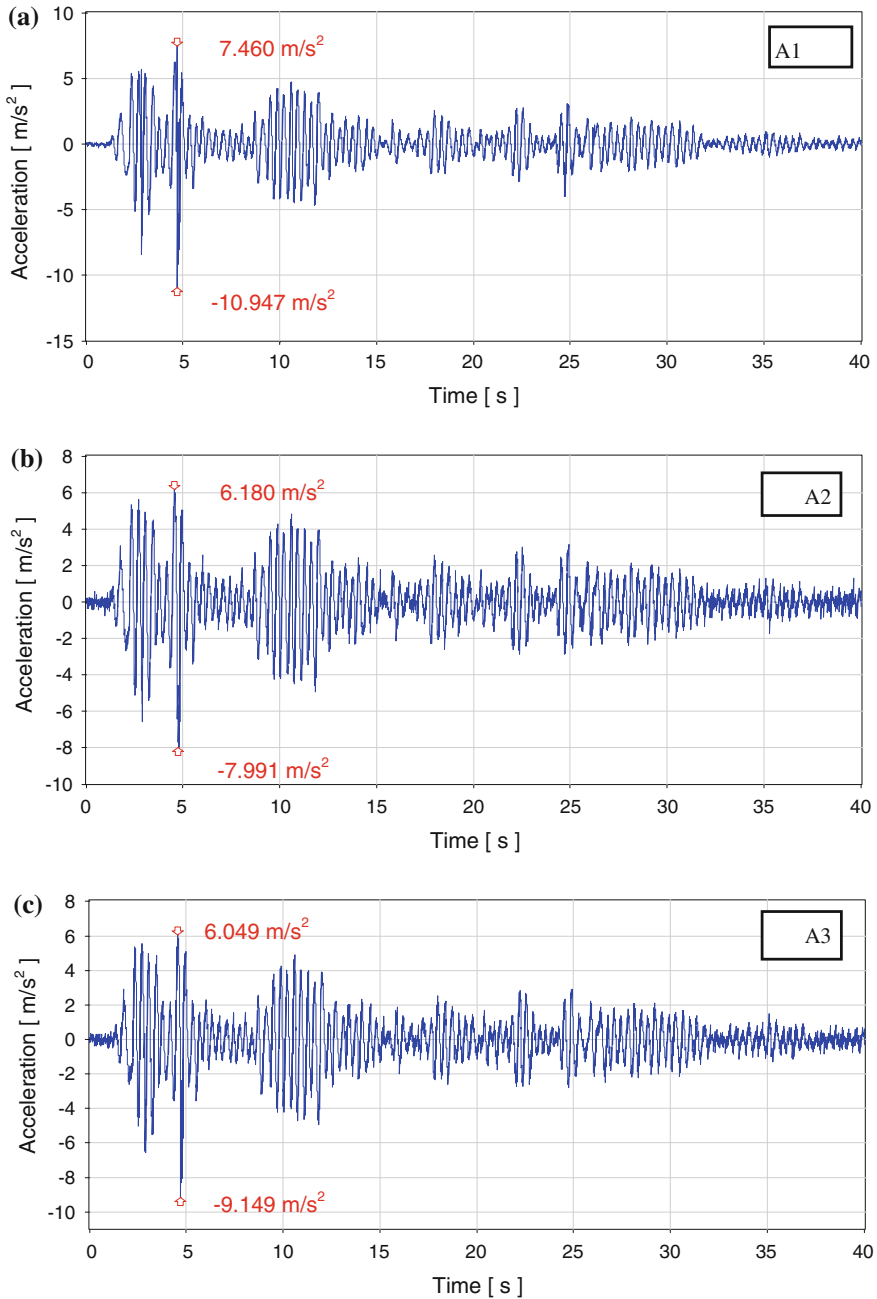


Fig. 5 Acceleration time histories of different towers when subjected to El Centro earthquake. [Configuration (2); zero gap distance]

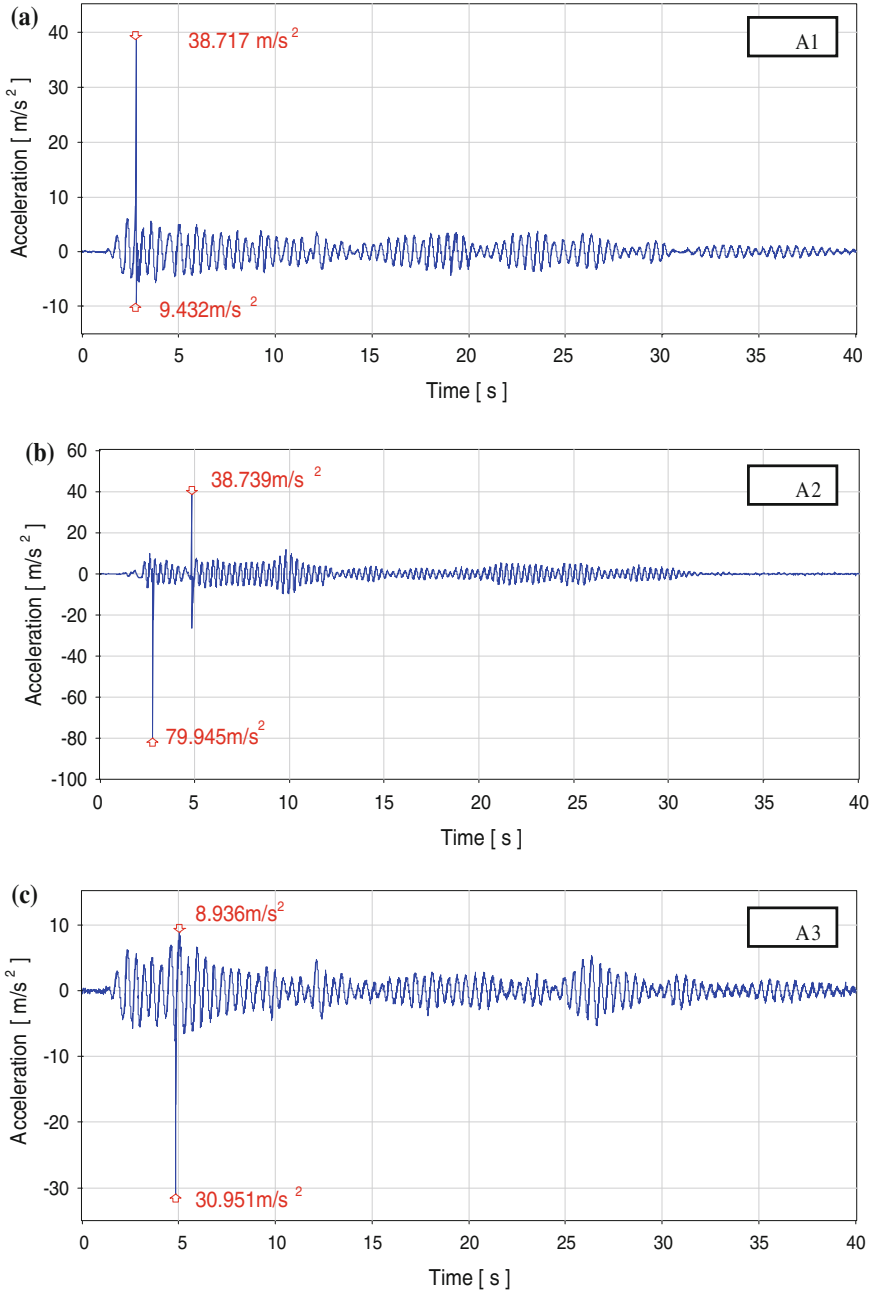


Fig. 6 Acceleration time histories of different towers when subjected to El Centro earthquake. [Configuration (1); 40 mm gap distance]

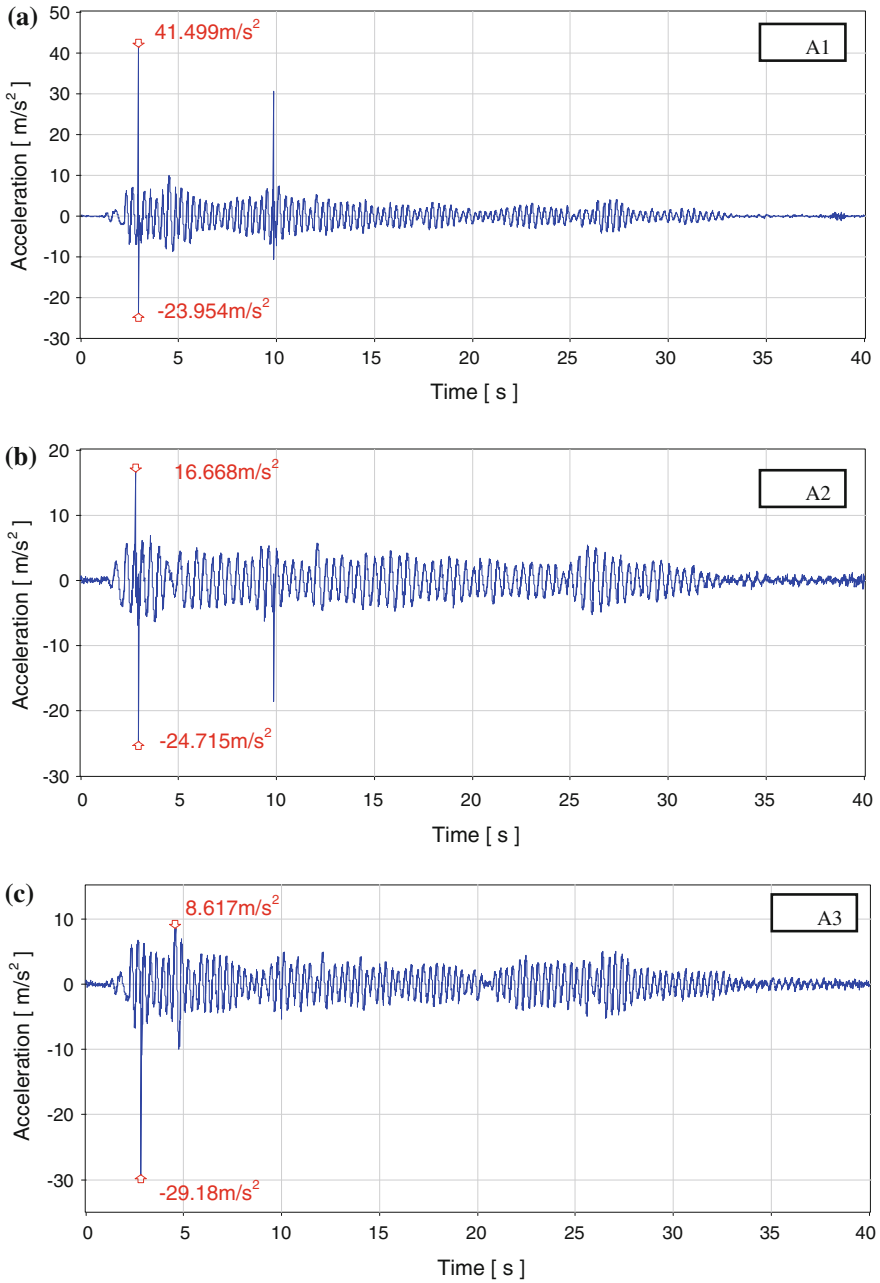


Fig. 7 Acceleration time histories of different towers when subjected to El Centro earthquake. [Configuration (2); 40 mm gap distance]

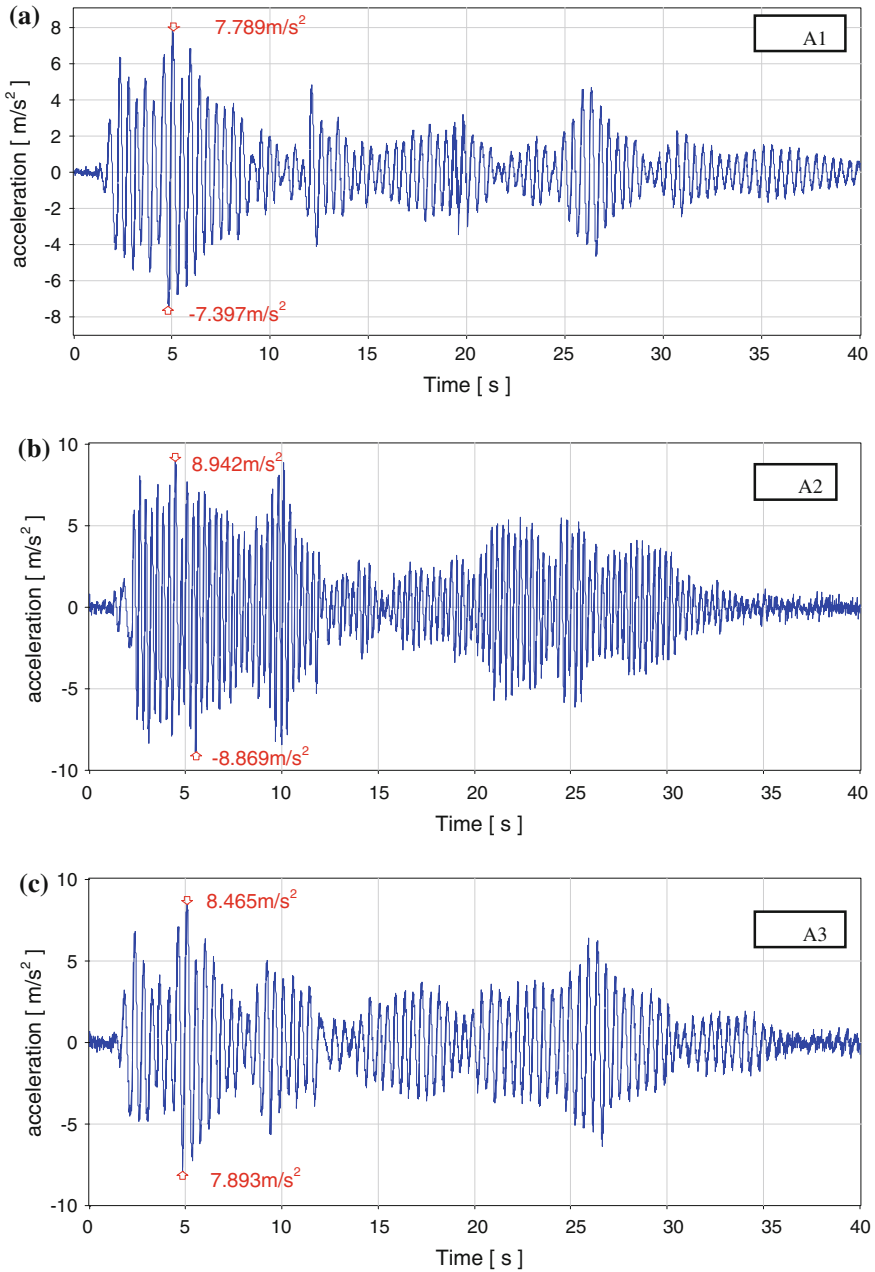


Fig. 8 Acceleration time histories of different towers when subjected to El Centro earthquake. [Configuration (1); large gap distance]

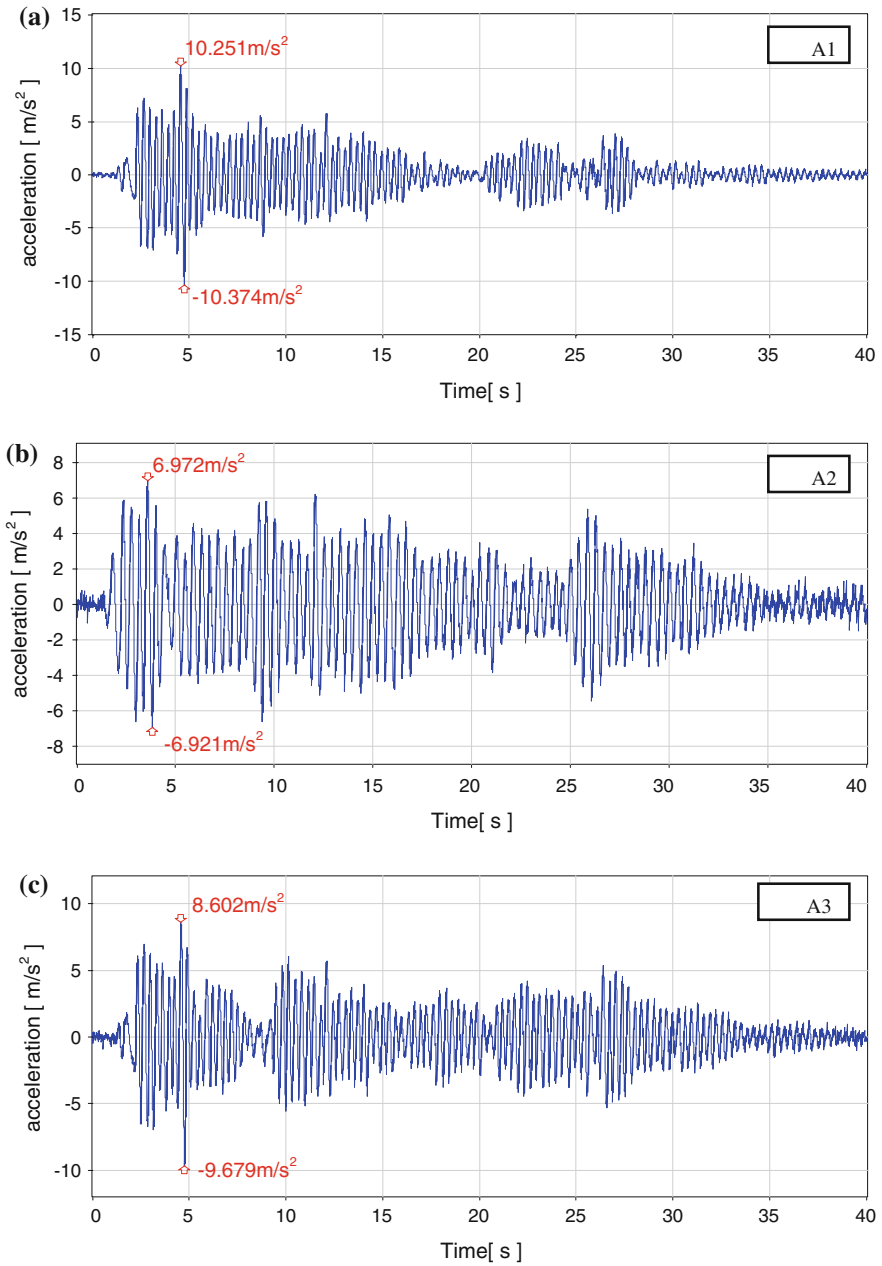


Fig. 9 Acceleration time histories of different towers when subjected to El Centro earthquake. [Configuration (2); large gap distance]

towers, assuming that they are connected, results in frequencies of 2.60 and 2.86 Hz for Configurations (1) and (2), respectively. Counting a number of cycles per second gives frequencies of nearly 2.50 and 2.90 Hz, for Configuration (1) and (2), respectively. This close matching indicates that, for the case of zero gap distance, the towers mostly behave as they are one unit with combined stiffness and mass. However, the existence of some pounding is due to the fact that, the towers are not fully connected and so little separation may occur at the time of peak seismic excitation.

For Configuration (1), comparing the maximum absolute acceleration values shown in Fig. 4 with the corresponding values obtained for the case of independent vibrations (see Fig. 8) indicates that pounding increases the maximum absolute acceleration of the towers by factors reaching 135 %. On the other hand for Configuration (2), comparing the maximum absolute acceleration values shown in Fig. 5 with the corresponding values obtained for the case of independent vibrations (see Fig. 9) indicates that minor change in the accelerations due to pounding (between 5 and 15 %) has been obtained. This behaviour can be explained. For Configuration (1), at the instant of separation between the towers, existence of the flexible towers on the left and right sides gave them the chance to vibrate more freely in the out-word direction gaining in displacement and velocity. In their way back they collided with the rigid tower in the middle which acted as a stopper for them. While, for Configuration (2), at the instant of separation, existence of the rigid towers on the left and right sides caused them to vibrate in the out-word direction with small displacements, and hence, small velocities. Existence of the flexible tower in the middle didn't give it a chance to gain more displacement or velocity since the rigid towers in the left and the right sides acted as stoppers and confined the middle tower.

For gap distance of 40 mm, comparing the maximum absolute acceleration values shown in Figs. 6 and 7 for Configuration (1) and Configuration (2), respectively, with the corresponding values obtained for the case of independent vibrations (see Figs. 8 and 9) indicate that, for both configurations, pounding may considerably affect the response of the structures during earthquakes. For Configuration (1), pounding caused a very high increase in the impact acceleration of the rigid tower, reaching 794 %, as compared to the no pounding case. It also caused a moderate increase in the impact acceleration of the flexible towers, reaching 397 and 265 % for the left and right tower, respectively. On the other hand for Configuration (2), pounding caused a moderate to minor increase in the impact acceleration of the rigid towers, reaching 300 and 202 % for the left and right tower, respectively. It also caused a moderate increase in the impact acceleration of the middle flexible tower, reaching 254 %. This behaviour can be explained in the same way as previously mentioned for the case of zero gap distance at instant of separation between towers.

Figures 10 and 11 show the experimental results of the maximum absolute acceleration versus the gap distance for different ground motions (see Table 1) for the three towers for both configurations. As mentioned earlier, symbols A1, A2 and A3 denote the accelerometers mounted on the left, middle and the right tower, respectively. It can be observed from the figures that the flexible and the rigid towers are substantially influenced by pounding phenomena. It can be observed that

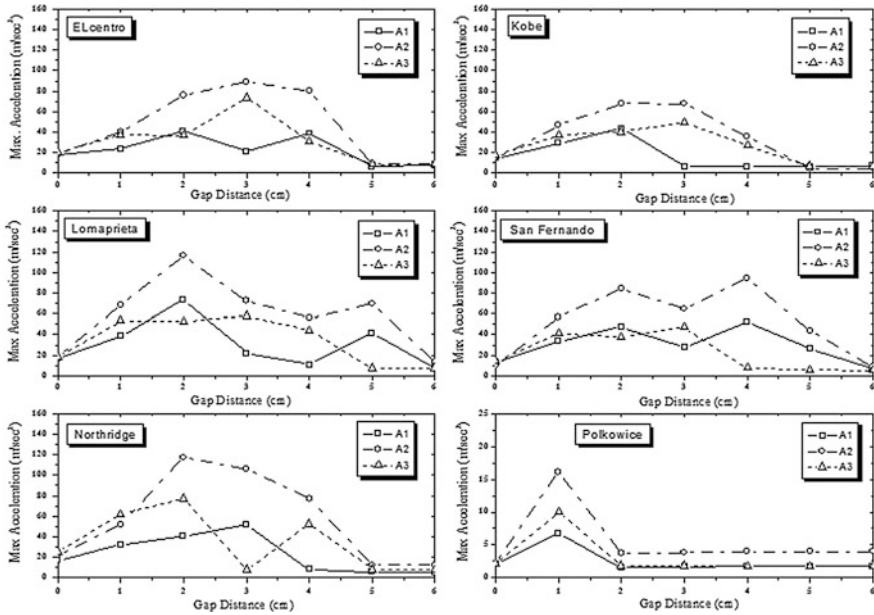


Fig. 10 Experimental results of the maximum absolute acceleration versus the gap distance. [Configuration (1)]

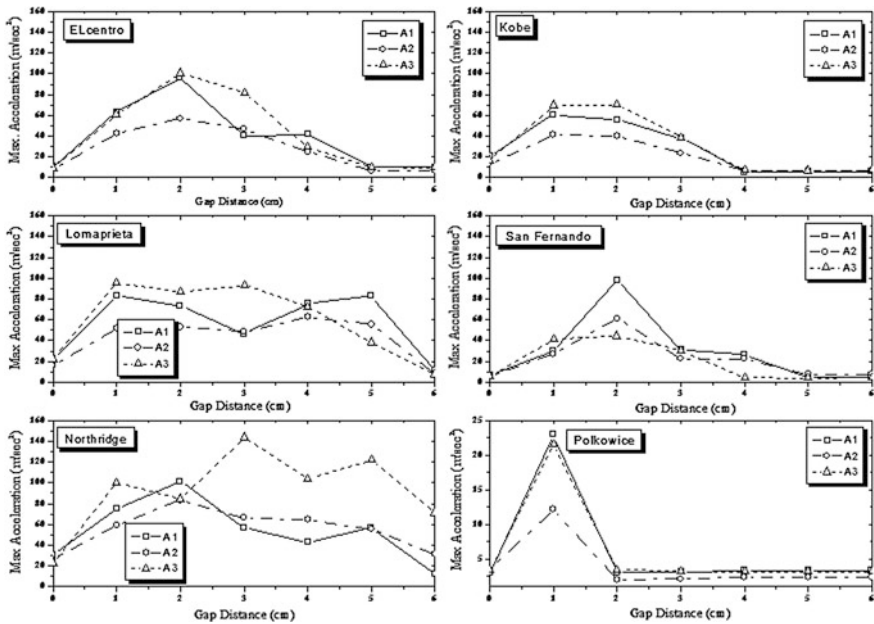


Fig. 11 Experimental results of the maximum absolute acceleration versus the gap distance. [Configuration (2)]

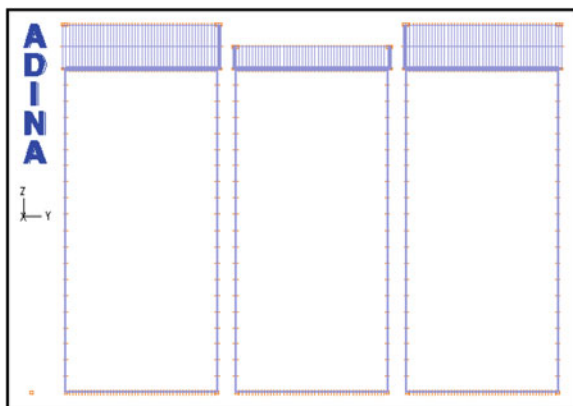
for gap distances not large enough to prevent pounding, the acceleration of the rigid towers increased 2–23 times, as compared to the no pounding case. On the other hand, the acceleration of the flexible towers increased 2–12 times, as compared to the no pounding case.

It is obvious, as a general trend, that the rigid towers are more influenced by pounding for the two configurations than the flexible ones because they act as stoppers for the flexible structures. These results are in agreement with the numerical results of Anagnostopoulos and Spiliopoulos [3]. The current experimental results indicate that increasing or decreasing the gap distance may lead to the increase or decrease in the response under different earthquakes with no specific trend. It is also clear from Figs. 10 and 11 that the optimal gap size is either the distance large enough to prevent pounding or the zero gap distance. These results are consistent with other findings of the numerical simulations previously conducted (see [16], for example).

3 Finite Element Analysis

In the second stage of the study, a numerical analysis, using ADINA [17] software, was conducted. A dynamic contact analysis of two-dimensional (2D) finite element models of the frames with the direct integration method under 1940 El Centro earthquake (NS component) was performed. The large displacement formulation was used, so the P- Δ effect is included in the analysis. The contact surface model was applied in the analysis without any connecting elements between the adjacent structures. In such a numerical model, both target and contactor surfaces were only defined. The contact surface calculation [18] enables the transmission of the pressure and friction forces at the points of contact with no force at the separation phase between the two adjacent segments. Figure 12 shows the 2D finite element model of the three towers for Configuration (1). Examples of the results in the form of

Fig. 12 Finite element model of the three towers for Configuration (1)



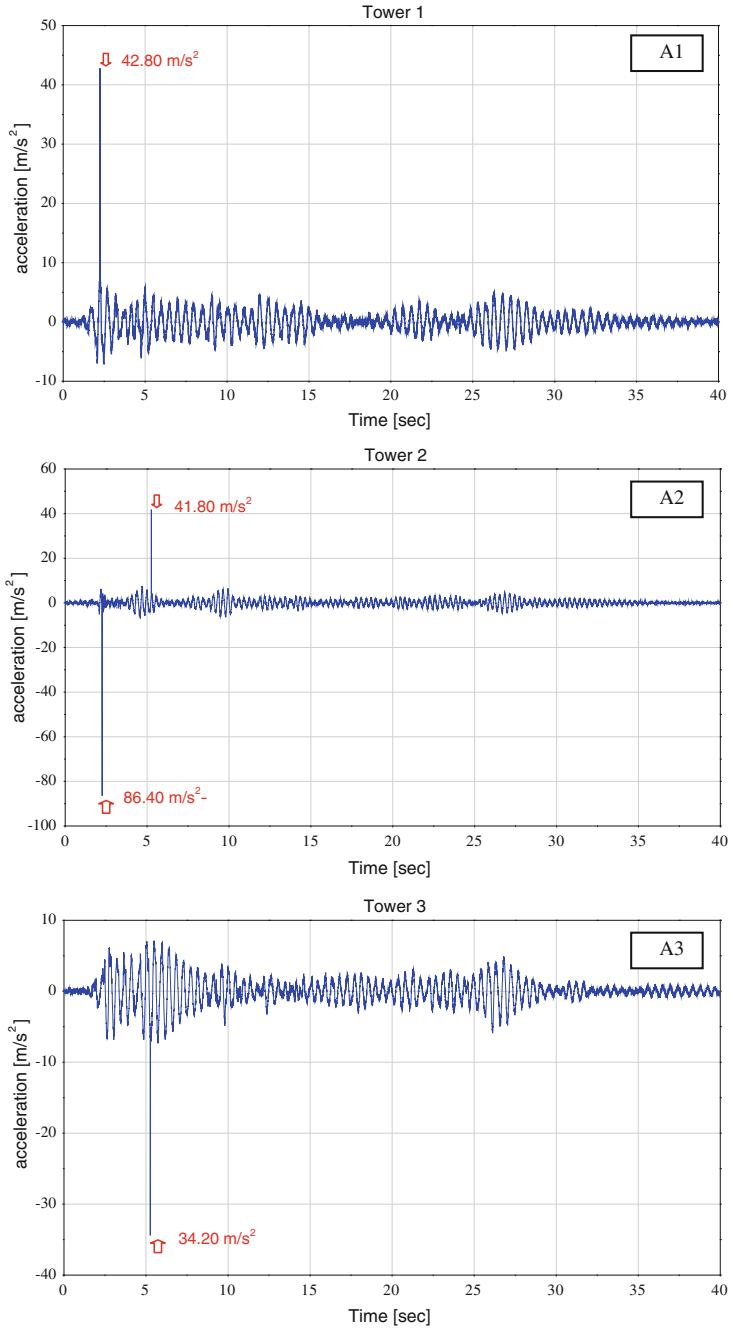


Fig. 13 Acceleration time histories as predicted by the finite element analysis for different towers when subjected to El Centro earthquake. [Configuration (1); 40 mm gap distance]

acceleration time histories obtained from the finite element analysis for the left, the middle and the right towers for the case of 40 mm gap distance are shown in Fig. 13. The results of the finite element analysis are compared with the experimental results shown in Fig. 6. It can be seen that the finite element analysis gives quite good prediction of the experimental results in terms of both time and magnitude of the impact. The correlation coefficient has been calculated as equal to 10.5 %. It is observed that impact between the external towers and the middle one occurred during the first 5 s of the earthquake, what is consistent with the experimental results.

4 Conclusions

In this paper, the results of an experimental and numerical study for pounding phenomena between structures in series have been presented. The study was performed using three tower models with different frequencies and different gap distances, under six different ground motion excitations. Two configurations of the towers were tested. The first configuration included a rigid tower located in the middle between two flexible structures, while the second case concerned a flexible tower located in the middle between two rigid structures.

The results of the experimental study clearly indicate that pounding may affect the behaviour of the structures significantly. They also show that the rigid towers are more influenced by pounding than the flexible ones because they act as stoppers for the flexible structures. Moreover, increasing or decreasing the gap distance may lead to increase or decrease in the response under different earthquakes with no specific trend. Furthermore, the results confirm that the optimal gap size is either the distance large enough to prevent pounding or the zero gap distance.

The results of the finite element analysis show relatively good agreement with the experimental results in terms of both time and magnitude of the impact.

Further research is needed to study pounding between structures with different dynamic properties which are constructed one close to another. This concern in particular the case of more than three structures in series, which was not considered in the study described in this paper.

Acknowledgments The authors would like to thank Ms. Barbara Sołtysik and Mr. Henryk Michniewicz for their help in conducting experiments.

References

1. Kasai K, Maison BF (1997) Building pounding damage during the 1989 Loma Prieta earthquake. *Eng Struct* 19:195–207
2. Anagnostopoulos SA (1988) Pounding of buildings in series during earthquakes. *Earthq Eng Struct Dyn* 16:443–456

3. Anagnostopoulos SA, Spiliopoulos KV (1992) An investigation of earthquake induced pounding between adjacent buildings. *Earthq Eng Struct Dyn* 21:289–302
4. Maison BF, Kasai K (1992) Dynamics of pounding when two buildings collide. *Earthq Eng Struct Dyn* 21(9):771–786
5. Karayannis CG, Favvata MJ (2005) Earthquake-induced interaction between adjacent reinforced concrete structures with non-equal heights. *Earthq Eng Struct Dyn* 34(1):1–20
6. Mahmoud S, Jankowski R (2010) Pounding-involved response of isolated and non-isolated buildings under earthquake excitation. *Earthq Struct* 1(3):231–252
7. Mahmoud S, Abd-Elhamed A, Jankowski R (2013) Earthquake-induced pounding between equal height multi-storey buildings considering soil-structure interaction. *Bull Earthq Eng* 11 (4):1021–1048
8. Abdel Raheem SE (2006) Seismic pounding between adjacent building structures. *Electr J Struct Eng* 6:66–74
9. Papadrakakis M, Apostolopoulou C, Zacharopoulos A, Bitzarakis S (1996) Three-dimensional simulation of structural pounding during earthquakes. *J Eng Mech* 122:31–423
10. Jankowski R (2007) Assessment of damage due to earthquake-induced pounding between the main building and the stairway tower. *Key Eng Mater* 347:339–344
11. Jankowski R (2009) Non-linear FEM analysis of earthquake-induced pounding between the main building and the stairway tower of the Olive View Hospital. *Eng Struct* 31(8):1851–1864
12. Jankowski R (2012) Non-linear FEM analysis of pounding-involved response of buildings under non-uniform earthquake excitation. *Eng Struct* 37:99–105
13. Chau KT, Wei XX, Guo X, Shen CY (2003) Experimental and theoretical simulations of seismic poundings between two adjacent structures. *Earthq Eng Struct Dyn* 32:537–554
14. Jankowski R (2010) Experimental study on earthquake-induced pounding between structural elements made of different building materials. *Earthq Eng Struct Dyn* 39:343–354
15. Jankowski R, Seelemah A, El-Khoriby S, Elwardany H (2014) Experimental study on pounding between structures during damaging earthquakes. In: *Proceedings of 13th international conference on fracture and damage mechanics, Sao Miguel Island, Azores, Portugal, 23–25 Sept 2014*
16. Jankowski R, Wilde K, Fujino Y (2000) Reduction of pounding effects in elevated bridges during earthquakes. *Earthq Eng Struct Dyn* 29:195–212
17. ADINA R&D, Inc. *Automatic Dynamic Incremental Nonlinear Analysis* (2010) Reference manual June 2010
18. Bathe KJ, Chaudhary A (1985) A solution method for planar and axisymmetric contact problems. *Int J Numer Meth Eng* 21:65–88

Dynamic Response of Adjacent Structures Coupled by Nonlinear Viscous Damper

C.C. Patel

Abstract The response of two adjacent single degree-of-freedom (SDOF) structures connected by nonlinear viscous damper under base excitation, modeled as stationary white-noise random process is investigated. Considering nonlinear force-deformation phenomenon of nonlinear viscous damper, the dynamic response of connected structures is obtained using the equivalent linearization technique. A parametric study is carried out to examine the influence of system parameters such as mass ratio and frequency ratio on optimum damping of damper and corresponding response. It is found that frequency ratio affects the performance of damper and corresponding response significantly, whereas, the effect of mass ratio is marginal.

Keywords Adjacent structures · Dynamic response · Viscous damper · Passive control · Seismic effect

1 Introduction

Various energy dissipation devices and control systems have been developed to protect the structures against natural disturbances. Significant efforts have been given for design of engineering structures with different control strategies to increase their safety and reliability. The control mechanism termed as protective system for the new structures and the existing structures can be retrofitted effectively for future seismic activity, as control mechanism can modify dynamically the response of structure in a desirable manner. The mechanics and working principle of various passive energy dissipation devices like viscous dampers, friction dampers, metallic yielding dampers, tuned mass dampers, tuned liquid dampers (dynamic absorbers) etc. can be found in reference Soong and Dargush [18]. Past

C.C. Patel (✉)

Department of Civil Engineering, Sir Padampat Singhanian University,
Udaipur 313601, India
e-mail: drccmpatel@gmail.com

studies confirm that the passive control devices are found to be effective for seismic response control of structures Housner et al. [5], Kasai et al. [7–9] and many others.

Amongst the various structural control techniques, connecting adjacent structures by passive energy dissipation device when possible, is one of the developing control mechanism to reduce the excessive structural vibration due to natural disturbances and it also minimize the chances of pounding. The concept to couple adjacent structure is to allow exerting control forces upon one another to reduce the overall response of the system. The free space available between adjacent structures can be effectively utilized for installation of control devices. The concept of coupling adjacent tall buildings was proposed by Klein et al. [10] in United States. Kunieda [11] proposed coupling multiple structures in Japan. The concept of linking adjacent structures has been introduced and verified analytically and experimentally by number of researchers, Westermo [19] have introduced the concept of linking adjacent fixed-base buildings and verified analytically and experimentally to avoid pounding damages during earthquakes; Maison and Kasai [13] have presented a analysis for types of structural pounding; Luco and De Barros [12] have studied connecting low to medium rise structures with passive devices; Zhu and Iemura [20] proposed a new structure-vibration-control approach using passive coupling element between two parallel structures to reduce the seismic response of a system due to earthquake excitation; Ni et al. [14] developed a method for analyzing the random seismic response of a structural system consisting of two adjacent buildings interconnected by non-linear hysteretic damping devices. Iemura et al. [6] have studied passive, active and semi-active control of two low-rise structures and have conducted full-scale tests on three and five storey building connected at third floor, to verify the concept at the Disaster Prevention Research Institute (DPRI) in Kyoto, Japan. The coupling parallel structures also studied by Bhaskararao and Jangid [1] presented the dynamic behavior of two adjacent SDOF structures connected with a friction damper under harmonic ground acceleration. Bhaskararao and Jangid [2] presented the optimum linear viscous damping for adjacent coupled structures under harmonic as well as stationary white-noise random excitation; Patel and Jangid [16] presented the seismic response analysis of adjacent structures connected by viscous damper considering Maxwell model; Patel and Jangid [17] studied the dynamic response of adjacent structures connected by friction damper subjected presented stationary white-noise random excitations, and many others.

The present study is aimed to investigate the dynamic response of two adjacent SDOF structures connected by nonlinear viscous damper under base excitation modeled as stationary white-noise excitation. The objectives of the present study are (i) to derive the dynamic response of adjacent SDOF structures connected by nonlinear viscous damper, (ii) to ascertain the optimum value of damper damping, (iii) to derive the close-form expression for the optimum damping and (iv) to examine the effect of important parameters such as frequency ratio and mass ratio on the optimum damper damping.

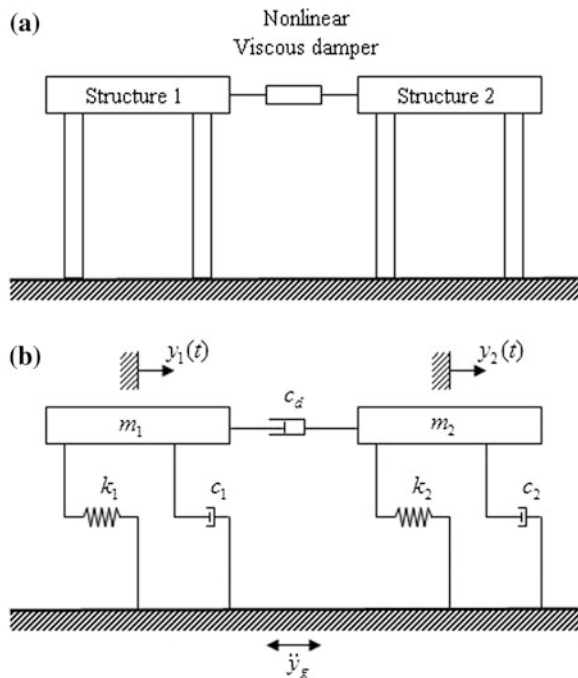
2 Adjacent Structures Connected by Nonlinear Viscous Damper

Consider two adjacent SDOF structures connected by a nonlinear viscous damper as shown in Fig. 1. The two structures are assumed to be remains linearly elastic and effect due to soil-structure interaction is neglected. Both structures are assumed to be subjected to the same ground acceleration. The adjacent structures are idealized as two SDOF coupled system and referred as Structures 1 and 2, respectively.

Let m_1, c_1, k_1 and m_2, c_2, k_2 be the mass, damping coefficient and stiffness of the Structure 1 and 2, respectively. Let $\omega_1 = \sqrt{k_1/m_1}$ and $\omega_2 = \sqrt{k_2/m_2}$ be the natural frequencies and $\zeta_1 = c_1/2m_1\omega_1$ and $\zeta_2 = c_2/2m_2\omega_2$ be the damping ratios of Structures 1 and 2, respectively. The inertia force generated due to ground motion is related with mass of the structure, and the damper force depends on the relative velocity of the damper ends, which is also related with fundamental natural frequency of the connected structures. Let η and λ be the mass and frequency ratio of two structures, respectively, expressed as

$$\eta = \frac{m_1}{m_2} \tag{1}$$

Fig. 1 Structural model of two SDOF adjacent coupled structures. **a** Adjacent structures connected by non-linear viscous damper. **b** Mathematical model



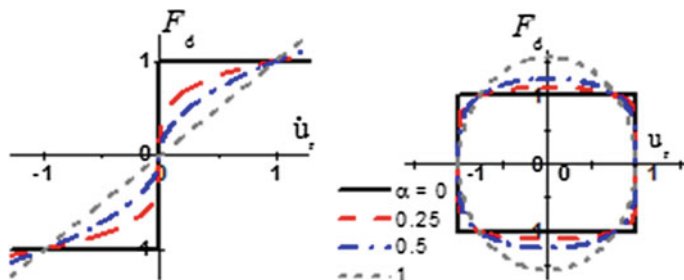


Fig. 2 Damper force-velocity and force-displacement relation for nonlinear viscous damper for various value of α

$$\lambda = \frac{\omega_2}{\omega_1} \tag{2}$$

The force in the viscous damper F_d is assumed to be proportional to the relative velocity of the damper ends, is given by

$$F_d = c_d |\dot{y}_r|^\alpha \text{sgn}(\dot{y}_r) \tag{3}$$

The damper force-velocity and damper force-displacement relationship for various value of α is shown in Fig. 2. From the figure, $\alpha = 1$ represent the linear damper (linear viscous damper) and the force-displacement plot is an ellipse shape, while $\alpha = 0$ represent the constitutive law of pure friction device is restored and the force-displacement plot is rectangle shape. For α , any value between 0 and 1 the damper force is given by Eq. (3). For seismic application the value of α ranging between 0 and 1. Damper with α larger than unity have not been seen often in seismic practical application Soong and Dargush [18]. The damping coefficient of damper c_d , which is expressed in the normalized form as

$$\zeta_d = \frac{c_d}{2m_1\omega_1} \tag{4}$$

where $\dot{y}_r = \dot{y}_1 - \dot{y}_2$ is relative velocity of the damper ends, ζ_d is the normalized damping coefficient of damper and sgn denotes the signum function. The governing equation of motion for the damper connected system can be written as

$$m_1 \ddot{y}_1(t) + c_1 \dot{y}_1(t) + k_1 y_1(t) + c_d |\dot{y}_r|^\alpha \text{sgn}(\dot{y}_r) = -m_1 \ddot{y}_g(t) \tag{5}$$

$$m_2 \ddot{y}_2(t) + c_2 \dot{y}_2(t) + k_2 y_2(t) - c_d |\dot{y}_r|^\alpha \text{sgn}(\dot{y}_r) = -m_2 \ddot{y}_g(t) \tag{6}$$

where $y_1(t)$ and $y_2(t)$ are the displacement response, relative to the ground, of Structures 1 and 2, respectively; and $\ddot{y}_g(t)$ is the ground acceleration. Considering nonlinear force-velocity relationship of the damper device, although the couple structure behaves linearly, the whole damper connected adjacent structural system

has nonlinear properties. Thus, the equations of motion of nonlinear viscous damper connected system is nonlinear and the corresponding equivalent linearized equations are given by

$$m_1\ddot{y}_1(t) + c_1\dot{y}_1(t) + k_1y_1(t) + c_e\dot{y}_r(t) = -m\ddot{y}_g(t) \tag{7}$$

$$m_2\ddot{y}_1(t) + c_2\dot{y}_2(t) + k_2y_2(t) - c_e\dot{y}_r(t) = -m_2\ddot{y}_g(t) \tag{8}$$

where c_e is equivalent constant. The equivalent constant c_e is expressed in the normalized form as

$$\xi_e = \frac{c_e}{2m_1\omega_1} \tag{9}$$

where ξ_e is the equivalent normalized constant. The parameter c_e is chosen in such a way that the mean square error made in linear and nonlinear term of Eqs. (5) and (7) is minimum with respect to ξ_e , that is

$$\mathbf{E} \left[(c_d|\dot{y}_r|^{\alpha} \text{sgn}(\dot{y}_r) - c_e\dot{y}_r)^2 \right] = \min_{\xi_e} \tag{10a}$$

further can be simplified as

$$\mathbf{E} \left[(2\xi_d\omega_1m_1|\dot{y}_r|^{\alpha} \text{sgn}(\dot{y}_r) - 2\xi_e\omega_1m_1\dot{y}_r)^2 \right] = \min_{\xi_e} \tag{10b}$$

where $\mathbf{E}[\cdot]$ means ensemble average. By performing the minimum we obtain

$$\xi_e = \xi_d \frac{\mathbf{E} \left[|\dot{y}_r|^{\alpha+1} \right]}{\mathbf{E} \left[(\dot{y}_r)^2 \right]} \tag{11}$$

The nonlinear system represented by Eqs. (5) and (6) has been replaced by the linear one, then the responses of Eqs. (7) and (8) is Gaussian [3]; it follows

$$\mathbf{E} \left[|\dot{y}|^{\beta} \right] = \frac{2}{\sigma_{\dot{y}}\sqrt{2\pi}} \int_0^{\infty} \exp \left(-\frac{\dot{y}^2}{2\sigma_{\dot{y}}^2} \right) \dot{y}^{\beta} d\dot{y} = \frac{2^{(\frac{\beta+1}{2})} \Gamma \left(\frac{\beta+1}{2} \right)}{\sqrt{2\pi}} \sigma_{\dot{y}}^{\beta}; \tag{12}$$

$$(\beta = \alpha + 1, \beta = 2)$$

where $\Gamma(\cdot)$ is Gamma function and $\sigma_{\dot{y}} = \sqrt{E[\dot{y}^2]}$ is standard deviation of the relative velocity of damper ends. The dependence of equivalent normalized damping coefficient of damper ξ_e on the velocity response of the system $\sigma_{\dot{y}}$, represent the existence of nonlinear phenomenon of the damper connecting two adjacent structures.

From Eqs. (7) and (8) the absolute acceleration responses of the Structure 1 and 2 respectively are expressed as

$$\begin{aligned}\ddot{y}_{a_1} &= \ddot{y}_1(t) + \ddot{y}_g(t) \\ &= -(c_1/m_1)\dot{y}_1(t) - (c_e/m_1)(\dot{y}_1(t) - \dot{y}_2(t)) - (k_1/m_1)y_1(t)\end{aligned}\quad (13)$$

$$\begin{aligned}\ddot{y}_{a_2} &= \ddot{y}_2(t) + \ddot{y}_g(t) \\ &= -(c_2/m_2)\dot{y}_2(t) + (c_e/m_2)(\dot{y}_1(t) - \dot{y}_2(t)) - (k_2/m_2)y_2(t)\end{aligned}\quad (14)$$

The structural control criteria depend on the nature of dynamic loads and the response quantities of interest. Flexible structures are displacement sensitive, whereas stiff structures are acceleration sensitive, which generates higher inertia force in structures. Minimizing the relative displacement and absolute acceleration of the system are always been considered as the control objectives. In view of this, the study aims for optimum parameters of damper for minimizing exclusively displacement as well as acceleration responses.

3 Response to Stationary White-Noise Excitation

Let the coupled system with equal structural damping ratio, $\zeta_1 = \zeta_2 = \zeta$ be subjected to the base acceleration \ddot{y}_g , modeled as Gaussian white-noise random process with constant power spectral density S_0 . The mean square displacement, ($\sigma_{y_1}^2$ and $\sigma_{y_2}^2$) of Structure 1 and 2 respectively are expressed as Nigam [15]

$$\sigma_{y_1}^2 = \int_{-\infty}^{\infty} |y_1(i\omega)|^2 S_0 d\omega \quad \text{and} \quad \sigma_{y_2}^2 = \int_{-\infty}^{\infty} |y_2(i\omega)|^2 S_0 d\omega \quad (15a, b)$$

The $y_1(i\omega)$ and $y_2(i\omega)$ are the frequency response function for displacement responses $y_1(t)$ and $y_2(t)$, respectively, obtained by solving Eqs. (7) and (8). The mean square displacement responses are obtained by solving the integral of Eq. (15a, b) and using the technique given by Cremer and Heckl [4]. The solution of the integrals are given by the following close form expressions

$$\sigma_{y_1}^2 = 2\pi S_0 \left[\frac{(\Delta_2 + \Delta_e)^2(\Delta_1 + \Delta_2 + \Delta_e)\omega_1^2 + ((\Delta_e + \Delta_1 + \Delta_2)(\Delta_2\Delta_{e1} + \Delta_1(\Delta_{e2} + \Delta_2)) - 2(\Delta_{e2} + \Delta_2)\omega_1^2)\omega_2^2 + (\Delta_{e2} + \Delta_2)\omega_1^4 + (\Delta_{e2} + \Delta_2)\omega_2^4}{2\omega_1^2((\Delta_{e1} + \Delta_1)(\Delta_{e2} + \Delta_2)\omega_1^4 + (\Delta_{e2} + \Delta_2)\omega_1^2((\Delta_e + \Delta_1 + \Delta_2)(\Delta_2(\Delta_{e1} + \Delta_1) + \Delta_{e2}\Delta_1) - 2(\Delta_{e1} + \Delta_1)\omega_2^2) + (\Delta_{e1} + \Delta_1)\omega_2^2((\Delta_e + \Delta_1 + \Delta_2)(\Delta_2(\Delta_{e1} + \Delta_1) + \Delta_{e2}\Delta_1) + (\Delta_{e2} + \Delta_2)\omega_2^2))} \right] \quad (16)$$

$$\sigma_{y_2}^2 = 2\pi S_0 \left[\frac{(\Delta_e + \Delta_1)^2(\Delta_e + \Delta_1 + \Delta_2)\omega_2^2 + ((\Delta_e + \Delta_1 + \Delta_2)(\Delta_1\Delta_{e2} + \Delta_2(\Delta_{e1} + \Delta_1)) - 2(\Delta_{e1} + \Delta_1)\omega_2^2)\omega_1^2 + (\Delta_{e1} + \Delta_1)\omega_2^4 + (\Delta_{e1} + \Delta_1)\omega_1^4}{2\omega_2^2((\Delta_{e1} + \Delta_1)(\Delta_{e2} + \Delta_2)\omega_1^4 + (\Delta_{e2} + \Delta_2)\omega_1^2((\Delta_e + \Delta_1 + \Delta_2)(\Delta_2(\Delta_{e1} + \Delta_1) + \Delta_{e2}\Delta_1) - 2(\Delta_{e1} + \Delta_1)\omega_2^2) + (\Delta_{e1} + \Delta_1)\omega_2^2((\Delta_e + \Delta_1 + \Delta_2)(\Delta_2(\Delta_{e1} + \Delta_1) + \Delta_{e2}\Delta_1) + (\Delta_{e2} + \Delta_2)\omega_2^2))} \right] \quad (17)$$

The mean square accelerations ($\sigma_{a_1}^2$ and $\sigma_{a_2}^2$) of Structure 1 and 2, respectively, under stationary white-noise random excitation are given by Nigam [15]

$$\sigma_{a_1}^2 = \int_{-\infty}^{\infty} |\ddot{y}_{a_1}(i\omega)|^2 S_0 d\omega \quad \text{and} \quad \sigma_{a_2}^2 = \int_{-\infty}^{\infty} |\ddot{y}_{a_2}(i\omega)|^2 S_0 d\omega \quad (18a, b)$$

The $\ddot{y}_{a_1}(i\omega)$ and $\ddot{y}_{a_2}(i\omega)$ are the frequency response function for acceleration responses, obtained by solving Eqs. (13) and (14). The mean square displacement responses are obtained by solving the integral of Eq. (18a, b) and using the technique given in Cremer and Heckl [4]. The solution of the integrals are given by the following expressions

$$\sigma_{a_1}^2 = 2\pi S_0 \left[\begin{aligned} & (\Delta_{e_2} + \Delta_2)\omega_1^6 \\ & + (\Delta_{e_2} + \Delta_2)\omega_1^4(\Delta_1^2 + \Delta_1\Delta_2 + \Delta_2^2 + 3\Delta_{e_1}\Delta_2 \\ & \quad + (\Delta_{e_1} + \Delta_1 + 2\Delta_2)\Delta_{e_2} + \Delta_{e_2}^2 - 2\omega_2^2) \\ & + (\Delta_{e_1} + \Delta_1)\omega_2^2((\Delta_{e_1}\Delta_2 + \Delta_1(\Delta_{e_2} + \Delta_2))(\Delta_1^2 + \Delta_{e_1}\Delta_2 + \Delta_1(\Delta_{e_2} + \Delta_2)) \\ & \quad + (\Delta_1(\Delta_{e_2} + \Delta_2) + \Delta_{e_1}(\Delta_{e_2} + \Delta_2))\omega_2^2) \\ & + \omega_1^2((\Delta_{e_2} + \Delta_2)(\Delta_{e_1}\Delta_2 + \Delta_1(\Delta_{e_2} + \Delta_2))(\Delta_1^2 + \Delta_{e_1}\Delta_2 + \Delta_1(\Delta_{e_2} + \Delta_2)) \\ & \quad + (-\Delta_1^2(\Delta_{e_2} + \Delta_2) + \Delta_1(\Delta_2^2 + 2\Delta_e(\Delta_{e_2} + \Delta_2)) \\ & \quad + \Delta_{d1}(\Delta_2^2 + \Delta_d(2\Delta_{d2} + 3\Delta_2)))\omega_2^2 + (\Delta_{d2} + \Delta_2)\omega_2^4) \\ & \hline & 2((\Delta_{e_1} + \Delta_1)(\Delta_{e_2} + \Delta_2)\omega_1^4 \\ & \quad + (\Delta_{e_2} + \Delta_2)\omega_1^2((\Delta_e + \Delta_1 + \Delta_2)(\Delta_2(\Delta_{e_1} + \Delta_1) + \Delta_{e_2}\Delta_1) \\ & \quad \quad - 2(\Delta_{e_1} + \Delta_1)\omega_2^2) \\ & \quad + (\Delta_{e_1} + \Delta_1)\omega_2^2((\Delta_e + \Delta_1 + \Delta_2)(\Delta_2(\Delta_{e_1} + \Delta_1) + \Delta_{e_2}\Delta_1) \\ & \quad \quad + (\Delta_{e_2} + \Delta_2)\omega_2^2)) \end{aligned} \right] \quad (19)$$

$$\sigma_{a_2}^2 = 2\pi S_0 \left[\begin{aligned} & \omega_1^4((\Delta_{e_2} + \Delta_2)(\Delta_{e_2}^2 + (\Delta_{e_2} + \Delta_2)(\Delta_{e_1} + \Delta_1)) + (\Delta_{e_1} + \Delta_1)\omega_2^2) \\ & + (\Delta_{e_1} + \Delta_1)\omega_2^2((\Delta_2(\Delta_{e_1} + \Delta_1 + \Delta_2) + \Delta_{e_2}\Delta_1)(\Delta_{e_1}\Delta_2 + \Delta_1(\Delta_{e_2} + \Delta_2)) \\ & \quad + (\Delta_1^2 + \Delta_2^2 + \Delta_{e_1}(\Delta_e + \Delta_2) + \Delta_1(2\Delta_e + \Delta_{e_2} + \Delta_2))\omega_2^2 + \omega_2^4) \\ & + \omega_1^2((\Delta_{e_2} + \Delta_2)(\Delta_2(\Delta_{e_1} + \Delta_1 + \Delta_2) + \Delta_{e_2}\Delta_1)(\Delta_{e_1}\Delta_2 + \Delta_1(\Delta_{e_2} + \Delta_2)) \\ & \quad + (\Delta_2(\Delta_{e_1} + \Delta_1)(\Delta_{e_1} + \Delta_1 - \Delta_2) \\ & \quad + (\Delta_1^2 + \Delta_{e_1}(2\Delta_{e_1} + \Delta_2) + \Delta_1(3\Delta_{e_1} + 2\Delta_2))\Delta_{e_2} \\ & \quad + (2\Delta_{e_1} + 3\Delta_1)\Delta_{e_2}^2)\omega_2^2 \\ & \quad - 2(\Delta_{e_1} + \Delta_1)\omega_2^4) \\ & \hline & 2((\Delta_{e_1} + \Delta_1)(\Delta_{e_2} + \Delta_2)\omega_1^4 \\ & \quad + (\Delta_{e_2} + \Delta_2)\omega_1^2((\Delta_e + \Delta_1 + \Delta_2)(\Delta_2(\Delta_{e_1} + \Delta_1) + \Delta_{e_2}\Delta_1) \\ & \quad \quad - 2(\Delta_{e_1} + \Delta_1)\omega_2^2) \\ & \quad + (\Delta_{e_1} + \Delta_1)\omega_2^2((\Delta_e + \Delta_1 + \Delta_2)(\Delta_2(\Delta_{e_1} + \Delta_1) + \Delta_{e_2}\Delta_1) \\ & \quad \quad + (\Delta_{e_2} + \Delta_2)\omega_2^2)) \end{aligned} \right] \quad (20)$$

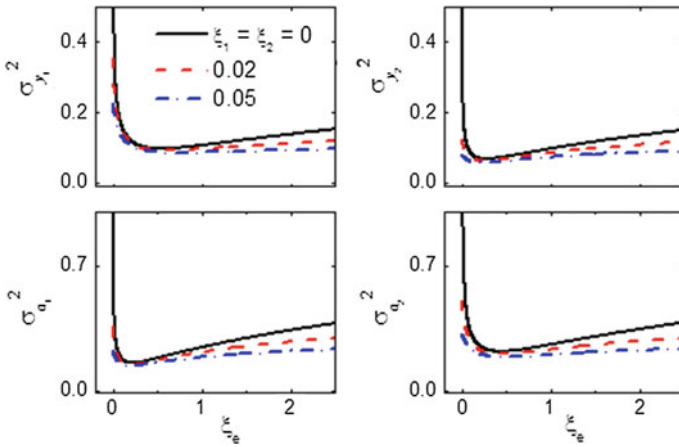


Fig. 3 Variation of mean square responses against equivalent normalized constant ζ_e of the nonlinear damper ($\eta = 1$, $\lambda = 2$ and $S_0 = 0.05$)

Figure 3, shows the variation of mean square displacement and acceleration responses of the two structures against equivalent normalized damping constant ζ_e , considering mass ratio $\eta = 1$, frequency ratio $\lambda = 2$ (i.e. $\omega_1 = \pi$ rad/sec and $\omega_2 = 2\pi$ rad/sec), $S_0 = 0.05$ and different damping ratios of the connected structures (i.e. $\zeta = 0, 0.02$ and 0.05). It is observed that an increase in ζ_e , the mean square displacement and mean square acceleration responses decreases up to certain value and with further increase in ζ_e the mean square responses increases. At the optimum value of ζ_e , the mean square response yield minimum value under stationary white-noise random excitation. Thus, for a given coupled structural system, there exists an optimum value of the normalized equivalent damping coefficient of damper for which the displacement and absolute acceleration response of connected structure attain the minimum value.

To investigate the effect of system parameters like frequency ratio λ and mass ratio η , it requires the α value, decide the type of damper (i.e. $\alpha = 0$ friction damper, $\alpha = 1$ linear viscous damper etc.). Taking $\alpha = 0.25$, the variation of ζ_d^{opt} and corresponding displacement response of both the structures against frequency ratio of connected structure λ for different mass ratios of structures is shown in Fig. 4. It is observed that for higher value of frequency ratio of structure, the optimum damper damping ζ_d^{opt} value is also higher and corresponding response values are reduces. The higher value of frequency ratio of structure, cause larger relative displacement/velocity of damper ends, thus, more dissipation of energy and subsequent response reduction justifies the better performance of the damper for higher frequency ratio. Thus, higher frequency ratio increases the relative displacement and/or velocity between the connected floors, leads damper to be more effective for energy dissipation, results more reduction in mean square displacement responses. It can be concluded that dynamically well-separated structures require higher optimum

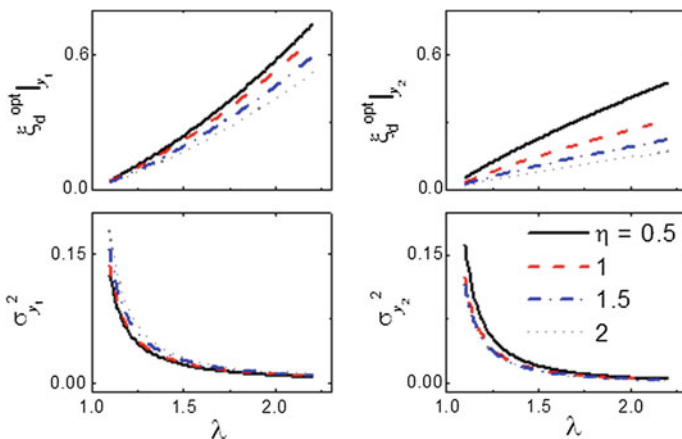


Fig. 4 Variation of optimum damper damping and corresponding mean square displacement response against ζ_d

damping coefficient of damper and result in higher reductions in the responses. Further, the increase in mass ratio reduces the optimum damping of damper. However, the response of soft structure increases, where as that of stiff structure decrease with increase in mass ratio.

Considering $\alpha = 0.25$, the variation of ζ_d^{opt} and corresponding acceleration response of both the structures against frequency ratio λ of the connected structure, for different mass ratios of structures is shown in Fig. 5. It is observed that with increase of frequency ratio, ζ_d^{opt} increases as observed in Fig. 4 and corresponding

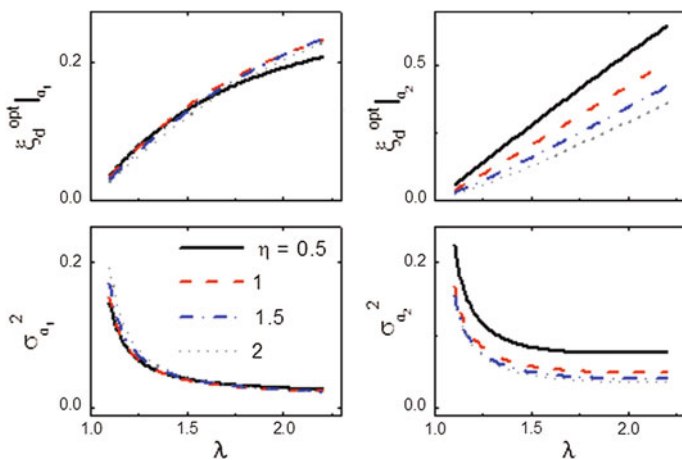


Fig. 5 Variation of optimum damper damping and corresponding mean square acceleration response against ζ_d ($\eta = 1, \lambda = 2$ and $S_0 = 0.05$)

mean square acceleration response decreases. Thus, it can be concluded that nonlinear viscous damper become more effective for acceleration response reduction for dynamically well separated structures. Further it is seen that the increase in mass ratio reduces the optimum damping of damper for acceleration response. However, the acceleration response of soft structure increases, where as that of stiff structure decrease with increase in mass ratio.

From Eqs. (11) and (12), the relation between ξ_d and ξ_e is dependence of the velocity response of the system $\sigma_{\dot{y}_r}$. The mean square relative velocity at damper ends, $\sigma_{\dot{y}_r}^2$ for an undamped connected system subjected to stationary white noise random excitation will be Nigam [15].

$$\sigma_{\dot{y}_r}^2 = \int_{-\infty}^{\infty} \omega^2 |y_r(i\omega)|^2 S_0 d\omega. \tag{21}$$

where $y_r(i\omega) = (y_1(i\omega) - y_2(i\omega))$ is the harmonic transfer function for relative displacement of damper ends, can be calculated by Eqs. (16) and (17). Solving the integral of Eq. (21), using the technique given in Cremer and Heckl [4], results

$$\sigma_{\dot{y}_r}^2 = \frac{\pi S_0 (1 + \eta)^2}{\Delta_e \eta} \tag{22}$$

From Eqs. (11), (12) and (22), the normalized equivalent constant and normalized damping coefficient of nonlinear viscous damper can be expressed as

$$\xi_d = \frac{\xi_e^{\left(\frac{1+\alpha}{2}\right)} \pi^{(1-\frac{\alpha}{2})} \left(\frac{S_0(1+\eta)}{\omega_1 \eta}\right)^{\left(\frac{1-\alpha}{2}\right)}}{2 \Gamma\left(1 + \frac{\alpha}{2}\right)} \tag{23}$$

4 Conclusions

The dynamic response of two adjacent SDOF structures connected by nonlinear viscous damper is investigated. The method of equivalent linearization is used to obtain the dynamic response of the coupled system under stationary white-noise random excitation. It is observed the existence of optimum damping coefficient of damper for minimum value of mean square responses. The effect of system parameter such as frequency ratio and mass ratio on optimum damping coefficient and corresponding response is investigated. The results show the frequency ratio affects the performance of damper and corresponding response significantly, whereas, the effect of mass ratio is marginal.

References

1. Bhaskararao AV, Jangid RS (2006) Seismic analysis of structures connected with friction dampers. *Eng Struct* 28(6):690–703
2. Bhaskararao AV, Jangid RS (2007) Optimum viscous damper for connecting adjacent SDOF structures for harmonic and stationary white-noise random excitations. *Earthq Eng Struct Dyn* 36:563–571
3. Clough RW, Penzien J (1993) *Dynamics of structures*. McGraw Hill, New York
4. Cremer L, Heckl M (1973) *Structure borne sound*, 1st edn. Springer, New York
5. Housner GW, Bergman L, Caughey TK, Chassiakos AG, Claus RO, Masri SF, Skelton RE, Soong TT, Spencer BF, Yao JTP (1997) *Structural control: past, present and future*. *J Eng Mech (ASCE)* 123(9):897–971
6. Iemura H, Igarashi A, Nakita N (2003) Full-scale verification tests of semi-active control of structures using variable joint damper system. In: *Proceedings of 3rd world conference on structural control*, Como, Italy
7. Kasai K, Yaomin Fu, Watanabe A (1998) Passive control systems for seismic damage mitigation. *J Struct Eng (ASCE)* 124(5):501–512
8. Kasai K, Ooki Y, Ishii M, Ozaki H, Ito H, Motoyui S, Hikino T, Sato E (2008a) Valu-added 5-story steel frame and its components: part-1 full-scale damper tests and analysis. In: *The 14th World conference on earthquake engineering*, Beijing, China
9. Kasai K, Nakai M, Nakamura Y, Asai H, Suzuki Y, Ishii M (2008b) Current status of building passive control in Japan. In: *The 14th World conference on earthquake engineering*, Beijing, China
10. Klein RE, Cusano C, Stukel J (1972) Investigation of method to stabilize wind induced oscillations in large structures. In: *ASME winter annual meeting*, New York 72-WA/AUT-H
11. Kunieda M (1976) Earthquake prevent design and earthquake proof design for structures. *JSME (Jpn Soc Mech Eng)* 79(689):86–91 (in Japanese)
12. Luco JE, De Barros FCP (1998) Optimal damping between two adjacent elastic structures. *Earthquake Eng Struct Dyn* 27:649–659
13. Maison BF, Kasai K (1994) Analysis for type of structural pounding. *J Struct Eng (ASCE)* 116(4):957–977
14. Ni Y, Ko J, Ying Z (2001) Random seismic response analysis of adjacent buildings coupled with non-linear hysteretic dampers. *J Sound Vib* 246:403–417
15. Nigam NC (1983) *Introduction to random vibrations*, 1st edn. MIT Press, Cambridge
16. Patel CC, Jangid RS (2010) Seismic response of adjacent structures connected with Maxwell dampers. *Asian J Civ Eng (Build Hous)* 11(5):585–603
17. Patel CC, Jangid RS (2011) Dynamic response of adjacent structures connected by friction damper. *Earthquake Struct Int J* 2:149–169
18. Soong TT, Dargush GF (1997) *Passive energy dissipation system in structural engineering*. John Wiley & Sons, New York
19. Westermo B (1989) The dynamics of inter-structural connection to prevent pounding. *Earthquake Eng Struct Dyn* 18:687–699
20. Zhu H, Iemura H (2000) A study of response control on the passive coupling element between two parallel structures. *Struct Eng Mech* 9:383–396

Comparative Study of Seismically Excited Coupled Buildings with VF Damper and LR Bearing

S.M. Dumne, S.D. Bharti and M.K. Shrimali

Abstract Coupling of adjacent dissimilar buildings connected by semiactive dampers involving base isolation is one of the more viable techniques against seismic hazards mitigation through which counter-acting forces exert one upon another in addition to isolation effect. The proposed study two buildings of dissimilar in dynamic characteristics from these, two coupled building models are considered that is, first model (Model-1) consisting of taller building (Building-1) and shorter building (Building-2) are connected in-line variable friction dampers whereas second model (Model-2) is same as first except taller building is isolated by laminated rubber bearing at base. The seismic response analysis of these two models is compared with normal buildings of same characteristics. The seismic response analysis is carried out by exciting under unidirectional excitation due to Kobe 1995 earthquake. The governing equation of motion of these models and normal buildings are solved by state space method. The dynamic behavior of laminated rubber bearing is studied by Wen's model whereas predictive control law used as control algorithm to predict the dynamic behaviour of variable friction damper. The seismic responses of these buildings are simulated through coding using MATLAB® computing software. The proposed study conclude that seismic performance of coupled building Model-2 work very significantly in reducing seismic response than Model-1 but Model-1 works effectively in avoiding pounding effects by adjacent buildings. Further, there is significant reduction in responses of Building-1 whereas marginal reduction is observed in Building-2.

Keywords Seismic response · Normal buildings · Coupled buildings · Variable friction damper · Laminated rubber bearing · Pounding

S.M. Dumne (✉)

Department of Applied Mechanics, Government Polytechnic, Nashik 422 101, Maharashtra, India

S.D. Bharti · M.K. Shrimali

Department of Civil Engineering, Malaviya National Institute Technology (MNIT), Jaipur 302 017, Rajasthan, India

1 Introduction

The world is living with significant risk to their lives and properties against natural hazards hence, it is necessary to study the performance analysis of seismically excited buildings. In the recent past, many researchers have studied the various strategies for coupled building control using passive, active and semi-active systems or its combinations. Further, research community is focused on adjacent buildings connected by dampers in addition to base isolation systems. The best combination includes semiactive dampers and base isolators because dampers work dissipation of energy which is more prominent to reduce the superstructure acceleration whereas base isolation systems reduce the ground motion to be entered in structure. Moreover, in case of a power failure, passive component of control still offers some degree of protection [1]. The comparative performance of various isolation systems under uniform shear beam in terms of superstructure acceleration and bearing displacement is studied by Su et al. [2]. It is observed that superstructure acceleration is controlled at the expense of bearing displacement and vice versa. The dissipation of seismic energy using friction mechanism for the protection of civil structures has achieved successful gains in recent decades. The friction device has emerged as one of the most promising because this damper remains in continuous slip state by controlling its clamping force in real time during an earthquake and exhibits efficient energy dissipation [3]. Further, friction damper is a displacement-dependent energy dissipation device because its force is independent from velocity and frequency content of excitation input. A semiactive controller is proposed [4] to determine the controllable clamping force of a VF damper, called predictive control law to predict the force from the variable friction damper. Further, controller allows the damper to produce a continuous slip force thus avoiding high frequency response that usually exists in structures with conventional friction dampers. The evaluation of seismic analysis is performed to compute the responses and bearing displacement during impact upon adjacent structures [5]. It is observed that increase in building flexibility causes to increase in superstructure acceleration and decreases in bearing displacement marginally. It is also noted that effects of impact became more severe due to increase in, superstructure flexibility, number of storey and stiffness of adjacent structures. An extensive parametric study on adjacent buildings connected by fluid dampers has been studied by Xu et al. [6]. It has been outlined that joint dampers are more effective for shorter adjacent buildings than taller building but it becomes more effective for adjacent buildings of same height than those of different heights. Further, it was also observed that adjacent buildings of different fundamental frequencies can effectively reduce the earthquake-induced response. The dynamic characteristics and seismic responses of connected building models, namely both buildings isolated and only shorter building is isolated, are connected by discrete linear viscoelastic dampers has been investigated by Matsagar and Jangid [7]. The result implies that this scheme is useful not only in controlling structural response but also reducing large bearing displacement. Moreover, seismic performance is found to be more effective when

one building have isolated base and other fixed base and such scheme is useful in upgrading the seismic performance of existing building adjacent to newly constructed building. The seismic response of connected buildings having different dynamic characteristics in addition, parametric study has been explored by Bhaskararao and Jangid [8]. The study illustrates that passive friction dampers are quite effective in reducing the seismic responses. Also, stated that it is not necessary to connect all floors of adjacent buildings by dampers but lesser dampers at appropriate locations can significantly reduce the earthquake response. The effective study of proposed semiactive controls in addition to parametric study of damper and isolation parameters [9] is performed for connected isolated buildings. It is observed that semiactive hybrid control becomes quite effective in reducing seismic responses, further performance of these controls are influenced by the parameters of dampers and isolators.

In the present study, two adjacent dissimilar buildings of which one is taller (Building 1) and other shorter (Building 2) having same storey height, floor mass and stiffness. For studying the performance analysis of adjacent buildings with proposed controls, two models that is, two adjacent buildings connected by in-line VF dampers at each floor, described as Model-1 whereas second Model-2 in which Building 1 of Model-1 being isolated by laminated rubber bearing. The specific objectives of study are (1) seismic response analysis of normal buildings and coupled building models (2) comparative study on seismic performance of coupled building models with respect to normal buildings (3) investigation of most effective model in reducing the seismic responses and pounding effect of proposed coupled building models.

2 Structural Models of Coupled Buildings

The coupled building models considered in this study are shown in Fig. 1. Each model consisting of two adjacent buildings in which one is taller and another shorter are designated as Building 1 and 2 having dissimilar in characteristics. The adjoining floors of adjacent buildings are connected by inline VF dampers and taller building is isolated by laminated rubber bearing. The models of coupled buildings are idealized as linear shear type building with lateral degrees-of-freedom at their floor levels. The floors of both buildings are at the same level with different storey. For general case, considering the story of Building 1 and 2 equals to m and n respectively. The coupled Building Model 1 will have $(m + n)$ degrees-of-freedom whereas for coupled building Model 2 consisting of isolation system at base of Building 1 therefore, this model will have $(m + n + 1)$ degrees-of-freedom.

The governing equations of motion for the adjacent connected building model involving base isolation is expressed in matrix form as

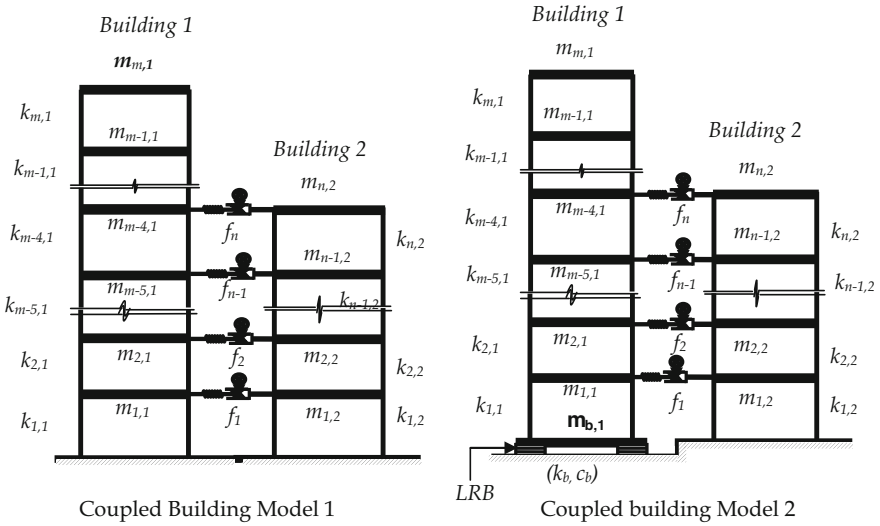


Fig. 1 Structural coupled building models

$$[M]\{\ddot{u}\} + [C]\{\dot{u}\} + [K]\{u\} = [D_p]\{f_d\} + [B_p]\{f_b\} - [M]\{r\}\ddot{u}_g \quad (1)$$

where, $[M]$, $[C]$ and $[K]$ are the matrices of mass, damping and stiffness for model of Coupled Building 2 respectively, $\{u\} = \{u_b, u_1, u_2, u_3, \dots, u_{m+n+1}\}$, $\{\dot{u}\}$ and $\{\ddot{u}\}$ are the vectors of floor displacement, velocity and acceleration respectively with respect to the ground in which response of Building 1 lies in the first $(m + 1)$ positions and that of Building 2 in last (n) positions, u_b is the bearing displacement, $\{r\}$ is the vector of influence coefficient consisting all elements equal to one, \ddot{u}_g is the ground acceleration due to earthquake, $[D_p]$ and $[B_p]$ are the matrices for the position of damper and isolator respectively, $\{f_d\}$ is the damper force vector, and $\{f_b\}$ is the bearing force vector yielded.

In above equation, $[M]$, $[C]$ and $[K]$ are the matrices for mass, stiffness and damping of isolated coupled building respectively of size equal to $(m + n + 1)$ and are explicitly described as

$$[M] = \begin{bmatrix} [M_1] & [O_1] \\ [O_2] & [M_2] \end{bmatrix}, \quad [K] = \begin{bmatrix} [K_1] & [O_1] \\ [O_2] & [K_2] \end{bmatrix} \quad \text{and} \quad [C] = \begin{bmatrix} [C_1] & [O_1] \\ [O_2] & [C_2] \end{bmatrix}$$

where, $[O_1]_{(m+1, m+1)}$ and $[O_2]_{(n, n)}$ are the null matrices of the Building 1 and 2 respectively. The matrices, $[M_1]_{(m+1, m+1)}$ and $[M_2]_{(n, n)}$ of Building 1 and 2 respectively are the mass matrices which has diagonal form and each element of matrix is sum of, half the mass of adjacent storey contributing to a particular node. The classical stiffness and damping matrix may not be suitable since superstructure and substructure have significant difference in stiffness and damping so non-

classical type of matrices are to be constructed. Under which, it is constructed by first evaluating the classical stiffness and damping matrix for building without isolation. Then stiffness and damping matrix for coupled building with isolation is superimposed by assembling matrix due to superstructure and substructure.

The equations of motion (Eq. 1) may be represented in the form of state-space equation as

$$\{\dot{z}(t)\} = [A]\{z(t)\} + [B_d]\{f_d(t)\} + [B_b]\{f_b(t)\} + [E]\ddot{u}_g(t) \quad (2)$$

where, z is the state variable, A is the system matrix composed of structural mass, stiffness and damping, B_d and B_b are the distribution matrices of damper and bearing force respectively and E is the matrix of excitation. The remaining parameters are explicitly given as

$$\dot{z} = \begin{bmatrix} \dot{u} \\ \ddot{u} \end{bmatrix}; \quad z = \begin{bmatrix} u \\ \dot{u} \end{bmatrix}; \quad A = \begin{bmatrix} O & I \\ -M^{-1}K & -M^{-1}C \end{bmatrix}; \quad B_d = \begin{bmatrix} O \\ M^{-1}D_p \end{bmatrix},$$

$$B_b = \begin{bmatrix} O \\ M^{-1}B_p \end{bmatrix} \quad \text{and} \quad E = \begin{bmatrix} O \\ -r \end{bmatrix}$$

where, $[I]$ and $[O]$ are the identity and null matrices respectively; vector $\dot{z}(t)$ represents the state variable of structural system which contains relative velocity and acceleration response of building with respect to ground. Further, the Eq. (2) is further discretized in time domain as

$$z(t + \Delta t) = A_d z(t) + B_{dd} f_d(t) + B_{db} f_b(t) + E_d \ddot{u}_g(t) \quad (3)$$

where, (t) and $(t + \Delta t)$ denotes the time step at which a state variable is evaluated, A_d represents the discrete-time system matrix, B_{dd} , B_{db} and E_d are the constant co-efficient matrices which are the discrete-time counterpart of matrices. The expression of B_d , B_b and E from the equation (Eq. 2) respectively is

$$A_d = e^{A\Delta t}, B_{dd} = A^{-1}(A_d - I)B_d, B_{db} = A^{-1}(A_d - I)B_b, \text{ and } E_d = A^{-1}(A_d - I)E \quad (4)$$

where, I is the identity square matrix of order $2(N + 1) \times 2(N + 1)$ in which N is the degrees-of-freedom of non-isolated building.

3 Computation of VF Damper Force

The cross section and schematic diagram of VF damper is shown in Fig. 2. A friction damper is activated and starts to dissipate energy only if friction force exerted at interface exceeds the maximum friction force otherwise; simply act as a regular bracing [3]. In order to know the dynamic behaviour of VF damper, an

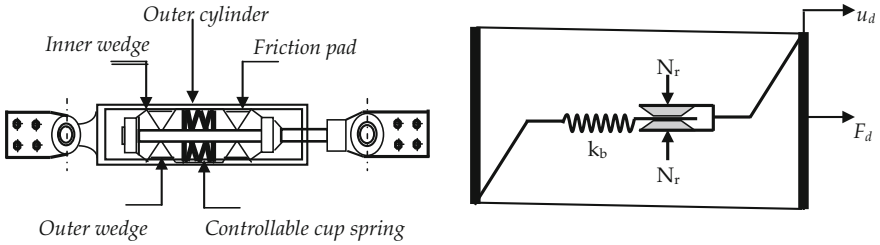


Fig. 2 Cross section and schematic diagram of VF damper

appropriate control algorithm called predictive control law [4] is used. This control law can produce a continuous slip force and also control this slip force slightly lower than the critical force of friction which allows the damper to remain in slip state during an earthquake as a result energy dissipation capacity of damper get improved.

The adjustable clamping force (N_r) using predictive control law is given by

$$N_r(t) = R_f \frac{|f_{cr}(t)|}{\mu} \text{ or } R_f = \frac{\mu N_r(t)}{|f_{cr}(t)|} \text{ in which } 0 \leq R_f < 1 \tag{5}$$

where, R_f is a selectable parameter, called gain multiplier is the ratio of damper force (slip force) to the critical friction force (f_{cr}) which play an important role in enhancing the performance of control law. It is also observed that larger value of R_f lead to higher control force but does not necessary to perform better energy dissipation, f_{cr} is the critical damper force, that is, minimum force of friction to keep the damper in slip state and dissipate the maximum energy. The friction force (f_{cr}) that keeps the variable friction damper in slip state is given by

$$f_{cr}(t) = [G_1 z(t - 1) + G_2 f_d(t - 1) + G_3 \ddot{u}_g(t - 1)] \tag{6}$$

where, G_1 , G_2 and G_3 are the control gain parameters and are described as $G_1 = k_b D_e (A_d - I)$, $G_2 = k_b D_e B_d + I_e$ and $G_3 = k_b D_e E_d$, in which, I_e is the another identity matrix with dimension $(N \times N)$, $[k_b]$ is the bracing stiffness matrix in which diagonal elements equal to $n_b \times k_{br} \times D_e$ in which n_b is the number of bracings provided to each storey, k_{br} be the stiffness of bracings provided and equal to storey stiffness, D_e is a constant matrix composed of damper orientation with size $(N + 1) \times 2(N + 1)$ which is described by a relation between damper displacement and inter-storey drift of floor on which damper installed as $u_d(t) = D_e z(t)$ in which $z(t)$ is the state variable vector over a time step (t), u_d is the damper displacement between floors of adjacent buildings and $\{\dot{u}_d\}$ is the damper velocity which is obtained by following expressions

$$u_{d(m-n+i)} = [u_{(m-n-i)} - u_{(m+n-i)}] \text{ and } \dot{u}_{d(m-n+i)} = [\dot{u}_{(m-n+i)} - \dot{u}_{(m+n-i)}] \quad (7)$$

where, m and n are the degrees-of-freedom for superstructure of Building 1 and 2 respectively, i is the counter ranging, ($i = 1, 2, 3, \dots, n$) and subscript in bracket indicate the damper position at the level of connectivity. The slip force or control force yielded from the VF damper is given by following expressions

$$f_d(t) = R_f [G_1 z(t-1) + G_2 f_d(t-1) + G_3 \ddot{u}_g(t-1)] \quad (8)$$

4 Computation of Laminated Rubber Bearing Force

The laminated rubber bearing (LRB) consisting of alternate layers of natural or synthetic rubber vulcanized between steel shims along with two thick end plates as shown in Fig. 3. The steel plates are strong enough to sustain vertical load while rubber layers imparts horizontal flexibility. Horizontal flexibility of system limits the transmission of ground motions in buildings whereas isolation damping dissipates seismic energy thereby reduces base displacement [2]. The force deformation behaviour of laminated rubber bearing is assumed as linear and its dominant feature is the parallel action of linear spring and damping as shown in Fig. 3.

The bearing force generated by this system is

$$f_b = c_b \dot{u}_b + k_b u_b \quad (9)$$

where, \dot{u}_b and u_b is the velocity and displacement of base isolation floor respectively.

The parameter of elastomeric base isolation system, namely stiffness (k_b) and damping (c_b) are so selected to provide desired value of isolation period (T_b) and damping ratio (ζ_b), respectively using following expressions.

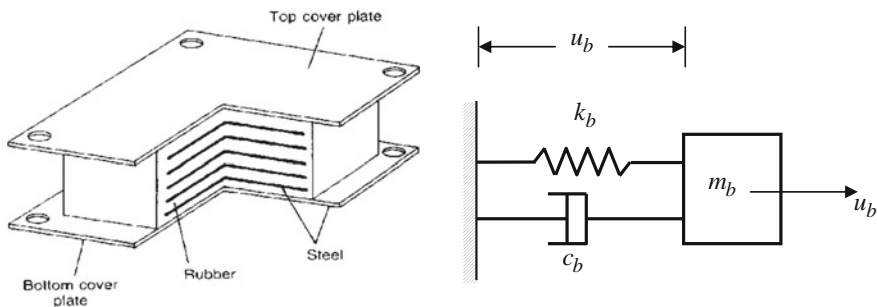


Fig. 3 Cross section and schematic diagram of laminated rubber bearing

$$T_b = 2\pi\sqrt{\frac{M_t}{\alpha_b k_b}} \quad \text{and} \quad \zeta_b = \frac{c_b}{2M_t\omega_b}$$

where, M_t is the total mass of building including isolation floor respectively, ω_b is the natural frequency of bearing, α_b is the ratio of post to pre-yielding stiffness of bearing and its value for LRB system equal to one.

5 Solution Procedure

To compute the response of coupled building models, governing equations of motion (Eq. 1) represented in state space form Eq. (2). Further, the state space equation (Eq. 2) is discretized in time domain in order to compute the state variable (z) from equation (Eq. 3) in which an appropriate value of gain multiplier parameter (R_f) is assumed. The damper force (f_d) and bearing force is obtained from the Eqs. (8) and (9) respectively. The equation of damper and bearing force are solved using 4th order Runge-Kutta method with the help of MATLAB[®] simulation.

6 Numerical Study

This study considered two adjacent RC buildings of ten and eight storey of equal floor height connected by VF dampers in which base of taller building is isolated by elastomeric bearing without lead. The mass and stiffness of each storey is considered as 1,600 tons and 1.2×10^7 kN/m, respectively. Besides, mass of isolation floor is taken as 10 % in excess of superstructure floor mass, that is, equal to 1,760 tons. The mass and stiffness of each storey are considered in order to obtain fundamental time period of Building 1 and 2 as 0.48 and 0.39 s, respectively. The building models are subjected to unidirectional ground motion due to Kobe, 1995 earthquake. The VF damper parameters are considered as $R_f = 0.5$, single bracing with stiffness (k_{br}) equal to storey stiffness (k_s) of building whereas isolation parameters are, $T_b = 2$ s and $\zeta_b = 0.1$. The response parameters of study are: top floor displacement (u_f) and acceleration (a_f), inter-storey drift (u_r), bearing displacement (u_b), normalized storey shear (S_{sy}/W) and normalized base shear (B_{sy}/W). The storey shears (S_{sy}), base shear (B_{sy}), bearing force (f_b) and damper force (f_d) are normalized by weight of Building 2.

The comparison of peak responses of Building 1 and 2 using proposed controls under Kobe 1995 earthquake is shown in Table 1 along with value in parenthesis shows the percentage reduction in response with respect to normal buildings. It is observed that top floor responses of Building 1 of building Model 1 are about 7–12 % whereas for building Model 2 it found as 70–90 %. The base shear of Building 1 of Model 1 becomes slightly increases and of Model 2, it seems to decreases by 70 %. Similarly, top floor responses of Building 2 of building Model 1

Table 1 Comparison of peak top floor responses and base shear of coupled building models with normal buildings under earthquake Kobe, 1995 ($R_f = 0.5$; $T_b = 2$ s, $\zeta_b = 0.1$)

Peak responses	Building 1			Building 2		
	Normal building 1	Building Model-1	Building Model-2	Normal Building 2	Building Model-1	Building Model-2
u_f (cm)	16.645	14.737 (11.46)	1.162 (93.01)	11.498	11.208 (2.52)	9.201 (19.97)
a_f (g)	2.929	2.750 (6.11)	0.928 (68.31)	2.987	2.402 (19.58)	1.530 (48.79)
S_{sy}/W	0.292	0.275 (5.82)	0.092 (68.49)	0.373	0.300 (19.57)	0.191 (48.79)
u_r (cm)	0.370	0.335 (9.46)	0.103 (72.16)	0.374	0.355 (5.08)	0.280 (25.13)
B_{sy}/W	2.100	2.191 (-4.33)	0.645 (69.28)	2.236	1.952 (12.70)	0.924 (58.67)

Note Value in parenthesis represents the percentage reduction in responses of coupled building models with respect to normal Building 1 and 2

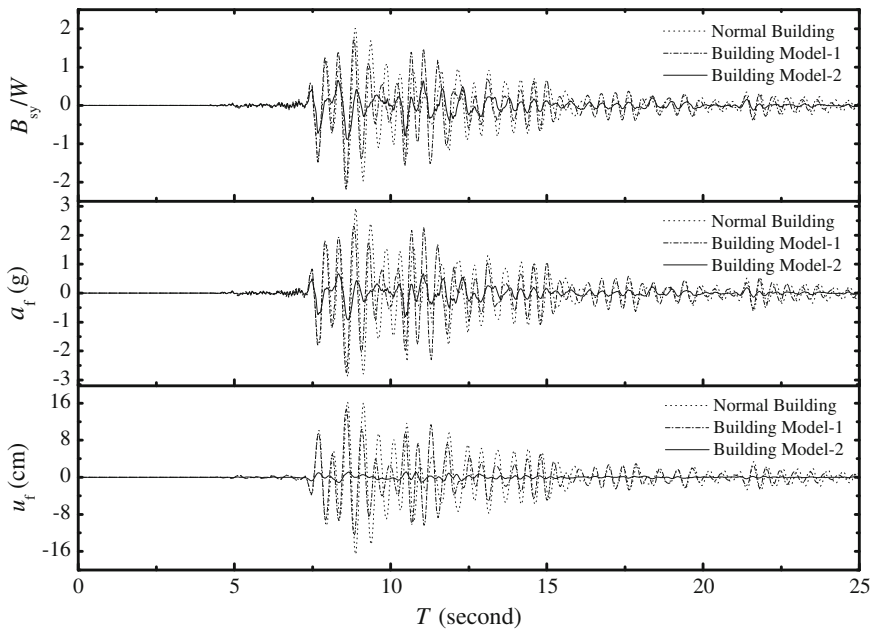


Fig. 4 Time varying response of Building 1 under Kobe 1995 earth quake ($R_f = 0.05$; $T_b = 2$ s, $\zeta_b = 0.1$)

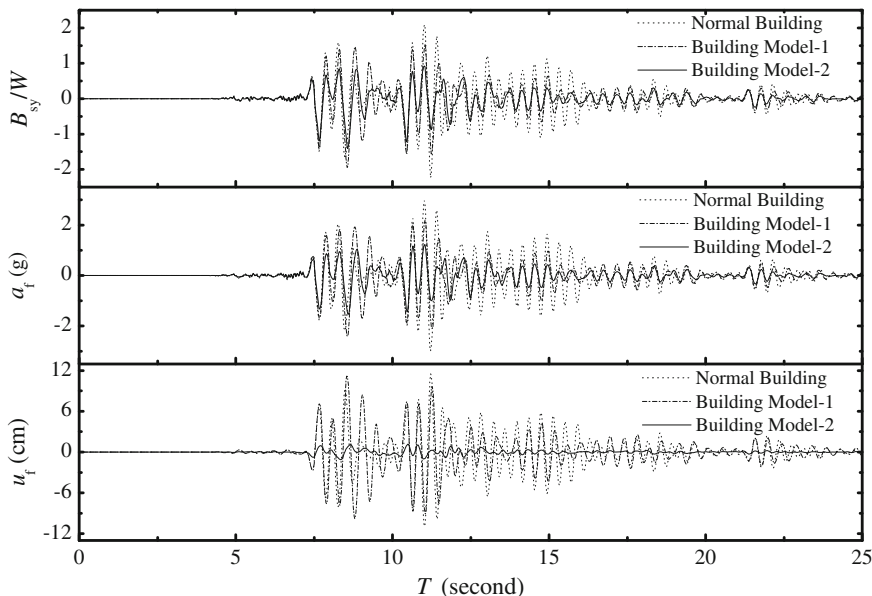


Fig. 5 Time varying response of Building 2 under Kobe, 1995 earthquake ($R_f = 0.05$)

are about 2–15 % whereas for building Model 2 it found as 20–40 %. However, base shear of Building 2 of Model 1 and Model 2 seems to decrease by 10 and 50 % respectively.

The time varying response of top floor displacement, acceleration and base shear for Building 1 and 2 of two coupled building models are compared with respective normal buildings as shown in Figs. 4 and 8. It is observed that significant reduction in response is obtained for Building 1 of Model-2 as compared to normal Building 1 (Fig. 5).

Further, it also seen that marginal reductions in responses are observed in Building 2. Besides that more reduction is noted to upper floors in comparison to lower floors of Building 1.

The hysteretic behaviour of top floor in-line semiactive VF damper which is used for coupled building models 1 and 2 subjected to excitation due to Kobe earthquake are shown in Figs. 6 and 7 respectively. From these energy loops of VF damper, one can note that VF damper is quite effective to dissipate the significant amount of seismic energy input. Further, the force-deformation behaviour of LRB system used at the base of taller building of coupled building Model 2 under Kobe earthquake is depicted in Fig. 8. From this energy loop, it has been observed that LRB isolation system is well capable to deflect the vibration energy to be entered in superstructure.

Fig. 6 Force deformation behaviour of top VF damper under Kobe, 1995 ($R_f = 0.05$; $T_b = 2$ s, $\xi_b = 0.1$)

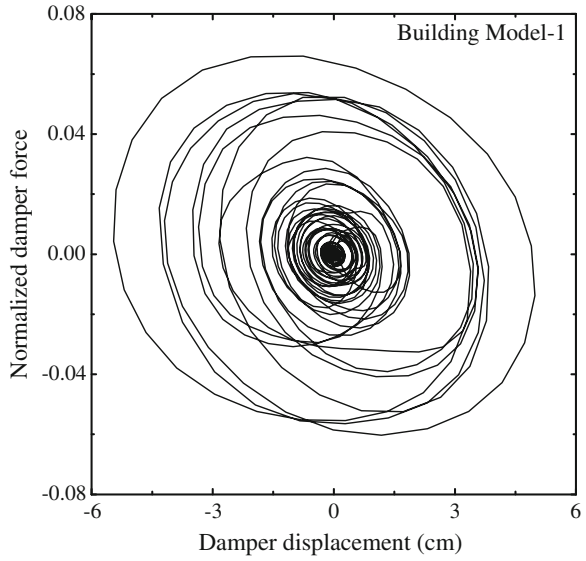


Fig. 7 Force deformation behaviour of top VF damper under Kobe, 1995 ($R_f = 0.05$; $T_b = 2$ s, $x_b = 0.1$)

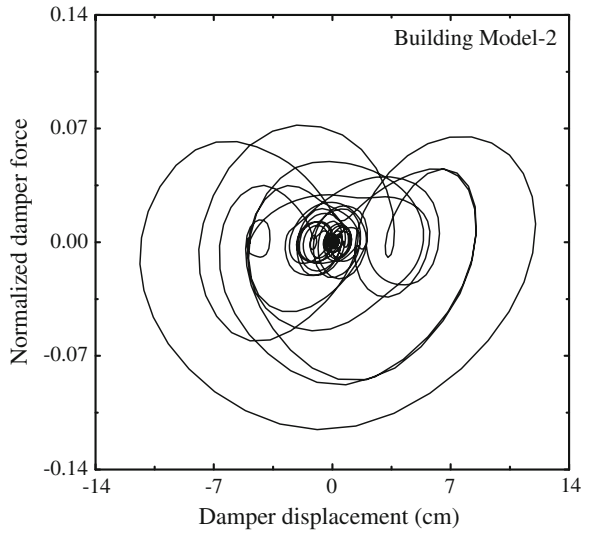
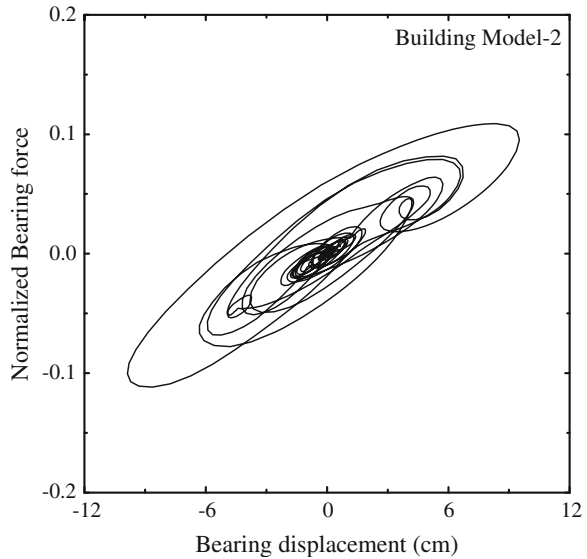


Fig. 8 Force deformation behaviour of laminated rubber bearing under Kobe, 1995 ($R_f = 0.05$; $T_b = 2$ s, $\zeta_b = 0.1$)



7 Conclusion

The comparison of seismic response analysis of two considered coupled building models with respect to normal buildings has been studied using the code in MATLAB[®] 7.0 as computing software. From the performance result, it has been concluded that Building 1 of coupled building Model 2 which is isolated at its base performs significant effective whereas Building 2 of same model perform marginal reduction in seismic responses as compared to respective normal Building 1 and 2. Similarly, coupled building Model-1 responded relatively lesser performance in reducing responses as compared to coupled building Model-2 but perform well in avoiding impact from adjacent buildings. Further, it is also noted that both damper and isolator are functioning well in reducing seismic hazards.

References

1. Housner GW, Bergman LA, Caughey TK, Chassiakos AG, Claus RO, Masri SF, Skelton RE, Soong TT, Spencer BF, Yao JTP (1997) Structural control: past, present and future. *J Eng Mech ASCE* 123(9):897–971
2. Su L, Ahmadi D, Tadjbakhsh IG (1989) Comparative study of performances of various base isolation systems, part I: shear beam structures. *Earthq Eng Struct Dyn* 18:11–32
3. Lu LY (2004) Semi-active model control for seismic structures with variable friction dampers. *Eng Struct* 26:437–454
4. Lu LY (2004) Predictive control of seismic structures with semi-active friction dampers. *Earthq Eng Struct Dyn* 33:647–668

5. Matsagar VA, Jangid RS (2003) Seismic response of base-isolated structures during impact with adjacent structures. *Eng Struct* 25:1311–1323
6. Xu YL, Zhan S, Ko JM, Zhang WS (1999) Experimental investigation of adjacent buildings connected by fluid damper. *Earthq Eng Struct Dyn* 28:609–631
7. Matsagar VA, Jangid RS (2005) Viscoelastic damper connected to adjacent structures involving seismic isolation. *J Civil Eng Manag* 11(4):309–322
8. Bhaskararao AV, Jangid RS (2006) Seismic analysis of structures connected with friction dampers. *Eng Struct* 28:690–703
9. Dumne SM, Shrimali MK Seismic analysis of connected isolated building by VF damper. In: 14th world conference on earthquake engineering (14WCEE). Chinese Association of Earthquake Engineering (CAEE), Beijing, China, pp 1–10

Pounding in Bridges with Passive Isolation Systems Subjected to Earthquake Ground Acceleration

Y. Girish Singh and Diptesh Das

Abstract In recent earthquakes, poundings between the super-structure segments of the elevated bridges have resulted in significant structural damages. The aim of this paper is to study the effect of pounding in bridges which are isolated by elastomeric bearings. Lumped mass models have been developed for the adjacent segments of the bridges and the responses were obtained by solving the governing equation of motion in the state space form. In the present study, the pounding effect has been simulated by applying the nonlinear viscoelastic model. Both near-field as well as far-field earthquakes have been considered as input ground accelerations. The effect of different parameters of elastomeric bearing on pounding has been studied and the performances of bridges with and without isolation systems have been compared.

Keywords Reinforced concrete bridge · Pounding · Seismic isolation · Laminated rubber bearing · NZ bearing · Nonlinear

1 Introduction

Bridges are the main components of any transportation network and as a result of failure of bridges, the entire transportation networks had collapsed during past earthquakes. During recent strong earthquakes, namely, Kobe, Chi, San Fernando earthquakes, pounding between the adjacent decks of bridges were observed. Data records during these earthquakes showed spikes in the magnitudes of acceleration responses which are many times higher than the maximum acceleration value recorded. Investigations revealed that cause behind of these spikes was pounding between the adjacent bridge decks. By using passive isolation system the base shear for bridges is reduced compared to the non-isolated bridges.

Y. Girish Singh (✉) · D. Das
Department of Civil Engineering, National Institute of Technology, Durgapur 713209, India

© Springer India 2015
V. Matsagar (ed.), *Advances in Structural Engineering*,
DOI 10.1007/978-81-322-2193-7_87

1117

There are many studies done on the earthquake induced pounding in bridges. Malhotra [1] investigated about the pounding of bridge at expansion gap. Jankowski et al. [2] used the same model to study pounding of superstructure segments in bridges. The fundamental study on pounding between buildings in series using a linear viscoelastic model of collisions has been conducted by Anagnostopoulos [3]. Jankowski et al. [4] considered also the use of dampers, crushable devices and shock transmission units which provide stiff linking of structural members during earthquakes and do not impose undesired forces resulting from thermal elongation, creep or shrinkage effects. Kim et al. [5] studied about the global behavior of the bridge structures and stated that due to the presence of rigid abutments, poundings occurs. Jankowski [6] proposed a non-linear viscoelastic model of collision which allows more precise simulation of the structural pounding.

The aim of this study is to investigate the effect of seismic isolation in bridges on pounding phenomenon. The bridge is isolated using elastomeric bearings and the pounding effect has been modeled using nonlinear viscoelastic model. Parametric studies are carried out considering the different parameters of the elastomeric bearing. The lumped mass model of the bridge is created and the analysis is done in MATLAB considering earthquake excitation in the longitudinal direction of the bridge.

2 Model of the Elevated Bridge

The bridge considered in this study was used by previous researchers. The bridge consists of 300 m long multi span concrete box girder supported on concrete column and abutment. An intermediate hinge is present at 100 m from the left abutment, the left segment of the box girder is supported on right segment through a set of elastomeric bearings. The separation gap between the two adjacent segments is 5 cm. The assumption considered in this analysis are the bridge and pier are assumed to be in elastic state, lumped mass modeling of the bridge is done in the study. The isolation systems are isotropic, implying the same dynamic properties in two orthogonal directions; additionally, the bearings provided at the piers and abutments have the same dynamic characteristics; and the stiffness of the non-structural part is neglected and the bridge is subjected to unidirectional earthquake.

The equation of motion of the isolated bridge system for unidirectional earthquake considering the pounding is given below:

$$[M]\{\ddot{x}\} + [C]\{\dot{x}\} + [K]\{x\} + [D]\{F\} + [fp] = -[M][r]\{\ddot{x}_g\} \quad (1)$$

where $[M]$, $[C]$ and $[K]$ = mass, damping and stiffness matrix, respectively of the bridge of order $N \times N$; $\{\ddot{x}\}$, $\{\dot{x}\}$ and $\{x\}$ are the acceleration, velocity and displacement responses of the bridge. $[D]$ is the location matrix for the restoring force of the passive system $\{f\}$, the pounding force generated is considered as $[f_p]$, $[r]$ is the influence coefficient matrix and $\{\ddot{x}_g\}$ is the considered earthquake ground acceleration.

3 Modeling of Pounding

When the adjacent structures vibrate in out of phase during a seismic event causing collision between the structures is called pounding. Structural pounding is a complex phenomenon involving plastic deformation at contact points, local cracking, fracturing due to impact, friction, etc. forces created by collisions are applied and removed during a short interval of initiating stress waves which travel away from the region of contact. There are different model of pounding linear viscoelastic model, non-linear elastic model and non-linear viscoelastic [6]. In this paper the pounding has been modeled using non-linear viscoelastic approach. This model overcomes the disadvantages of linear viscoelastic and the non-linear elastic models and it simulates the pounding force accurately than the other. The non-linear viscoelastic model consists of a non-linear spring which follows Hertz Law of contact. The pounding force, $f(t)$, between structures with mass is expressed as

$$f(t) = 0 \tag{2}$$

when $\delta(t) \leq 0$

$$f(t) = \bar{\beta}\delta^{\frac{3}{2}} + \bar{c}(t)\dot{\delta}(t), \tag{3}$$

where $\delta(t) > 0$ and $\dot{\delta}(t) > 0$ (contact-approach period)

$$f(t) = \bar{\beta}\delta^{\frac{3}{2}}, \tag{4}$$

when $\delta(t) > 0$ and $\dot{\delta}(t) \leq 0$ (contact-restitution period)

$$\delta(t) = x1(t) - x2(t) - d \tag{5}$$

where d is the initial separation gap, $\bar{\beta}$ is the impact stiffness parameter depending n material properties and geometry of colliding bodies and $\bar{c}(t)$ is the impact element's damping, which at any instant can be obtained from the formulae

$$\bar{c}(t) = 2\bar{\zeta}\sqrt{\bar{\beta}\sqrt{\delta(t)}\frac{m_1m_2}{m_1 + m_2}} \tag{6}$$

where ζ denotes an impact damping ratio correlated with a coefficient of restitution, e , which accounts for the energy dissipation during collision. The approximate relation between ζ and e in the non-linear viscoelastic model are expressed by the formula

$$\bar{\zeta} = \frac{9\sqrt{5}}{2} \frac{1 - e^2}{e(e(9\pi - 16) + 16)} \tag{7}$$

In this study the value considered to model the pounding are coefficient of restitution is taken as 0.65, value of impact stiffness which is adopted from the literature review is $2.06 \times 10^2 \text{ kN/m}^{3/2}$. Pounding forces are generated on both the adjacent deck when left deck strike right and when right strike left the value of pounding is different.

4 Numerical Modeling of Isolator

Laminated rubber bearing and NZ bearing are used in this model. The laminated rubber bearing is considered to have a linear force deformation behavior. The restoring force exerted by laminated rubber bearing can be expressed as

$$f_b = c_b \dot{x}_b + k_b x_b \quad (8)$$

where c_b is damping constant of the bearing, k_b is stiffness of the bearing and x_b is the relative displacement of the bearing. The two parameters that governed the property of laminated rubber bearing are $t_b = 2\pi\sqrt{M/k_b}$ where t_b is the isolation time period, M = total mass of the super structure and k_b = stiffness of the bearing. $\varepsilon_b = c_b/2M\omega_b$ where ε_b is the damping ratio and ω_b is the fundamental frequency of the bearing.

NZ bearing is a different type of isolation system. It consists of alternative layers of rubber and steel plate, and a lead plug is at the core of the bearing. When the lead core deforms and reaches its yield displacement the bearing exhibit the hysteretic behavior. The hysteretic loop provided by the lead core can be modeled using Bouc-Wen equation.

$$f_b = c_b \dot{x}_b + \alpha k_b x_b + (1 - \alpha) QZ \quad (9)$$

where Q is yield strength of the bearing, α is ratio of post to pre yield stiffness; k_b is the pre yield stiffness; c_b is the viscous damping of the bearing; and Z is the non-dimensional hysteretic displacement component satisfying the following nonlinear first order differential equation expressed as

$$q\dot{z} = -\beta|\dot{x}_b|z|z|^{n-1} - \tau\dot{x}_b|z|^n + A\dot{x}_b \quad (10)$$

where, q is the yield displacement; dimensionless parameters β , τ , A and n are selected such that predicted response from the model closely matches with the experimental results. The parameter n is an integer which controls the smoothness of transition from elastic to plastic response.

The parameters which governed the property of lead rubber bearing are time period of the isolator, damping ratio of the isolator and lastly the normalized yield strength.

Isolation time period $t_b = 2\pi\sqrt{M/\alpha k_b}$, Damping ratio; $\varepsilon_b = c_b/2M\omega_b$ and normalized yield strength Q/W where $W = Mg$ is the total weight of the super structure and g is the ground acceleration. The value of parameters of the hysteresis loop of the LRB are taken as $q = 2.5$ cm, $A = 1$ and $\beta = 1$.

5 Numerical Results

In this study three models of bridges have been considered: (1) non-isolated bridge (2) bridge isolated using laminated rubber bearing and (3) bridge isolated with NZ bearing. The properties of the bridge is presented in Table 1.

For non-isolated bridge, the expansion gap between the two adjacent decks is taken as 5 cm. Figure 1a shows the time history of displacement for both cases considering pounding and without considering pounding when the bridge is subjected to scaled (1.6 times) El Centro earthquake excitation. Figure 1b shows that pounding results in an increase in acceleration. The maximum acceleration observed when pounding occurs is 14.4 m/s^2 which is increased from 7 m/s^2 . When right deck approach the left deck the maximum absolute acceleration is 24 m/s^2 which is increased from 14.4 m/s^2 for El Centro earthquake. Figure 1c shows the pounding time history where the maximum pounding recorded is 20.8 MN and pounding occur 13 times (when right deck approach left). The maximum pounding recorded when left deck approaches to the right deck is 14.4 MN.

6 Effect of Gap Size

From Eqs. (2)–(7), it is evident that the force generated due to pounding between adjacent structures varies with the relative displacement between the colliding structures. The relative displacement in turn depends upon the size of the gap

Table 1 Properties of the bridge

Property bridge segments	Unit	Left segment	Right segment
Mass of the deck	kg	1.2×10^6	2.4×10^6
Span length	M	100	200
Pier stiffness	MN/m	107	94
Pier damping	MN.s/m	1.13	1.5
Damping constant	%	0.05	0.05
Density of the mass	kg/m^3	2.4×10^3	2.4×10^3

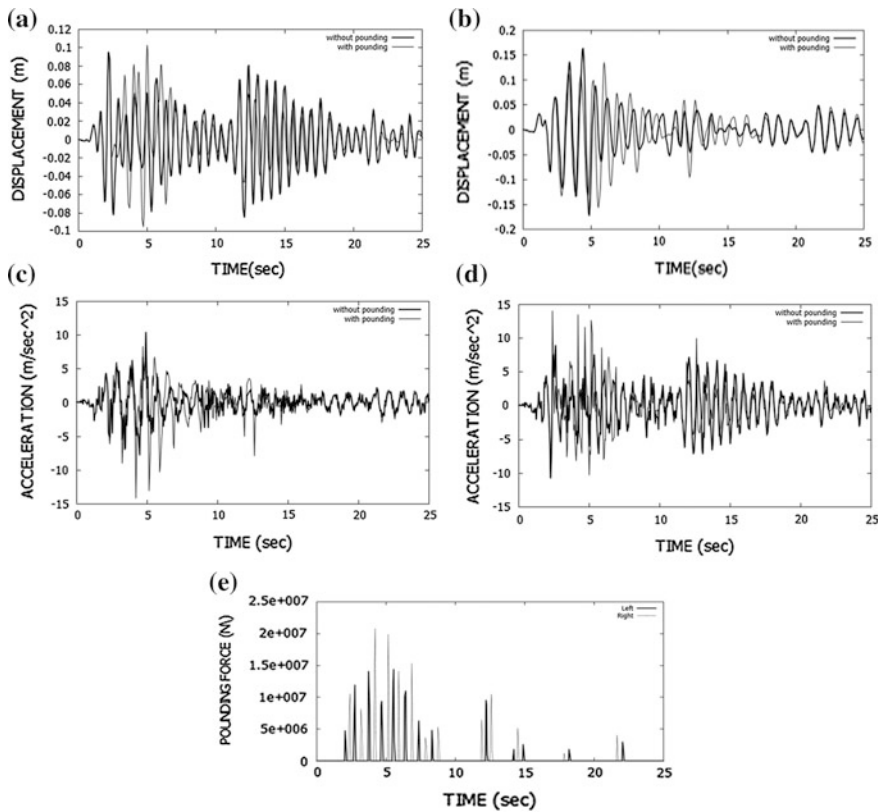


Fig. 1 Time histories of response of non-isolated bridge subjected to El Centro ground motion: **a** left deck displacement; **b** right deck displacement; **c** left deck acceleration; **d** right deck acceleration and **e** pounding force

between the structures. For effective performance of isolation systems, sufficient displacement need to be allowed and some minimum gap between the adjacent structures should be provided in order to cater to this large displacement demand in the isolators. Therefore, as the gap size is reduced, the effectiveness of the isolator in providing isolation is to be reduced. On the other hand, since the gaps between adjacent bridge decks are filled with properly designed expansion joints, larger gaps result in higher installation, maintenance and operational costs. Problems in inspection and maintenance also are more. Hence, it is very important to ascertain the optimum size of the gap. The bridge, isolated with NZ bearing, is subjected to scaled El Centro ground motion and is analyzed with different gap sizes, varying uniformly from 1 to 15 cm. The variation of five quantities, namely, magnitude of maximum pounding force, absolute maximum displacements of left and right decks and absolute maximum acceleration of left and right decks, due to the variation of gap sizes for the non-isolated bridge are shown in Table 2. Figure 2 demonstrates

Table 2 Peak response quantities for non-isolated bridge for El Centro ground motions

Gap size (cm)	Max pounding force (MN)	Absolute maximum displacement of left deck (m)	Absolute maximum displacement of right deck (m)	Absolute maximum acceleration of left deck (m/s^2)	Absolute maximum acceleration of right deck (m/s^2)
1	48.03	0.26	0.32	33.08	25.29
2	48.40	0.26	0.33	34.48	30.98
3	53.75	0.26	0.34	37.68	32.11
4	63.40	0.26	0.35	35.46	31.55
5	57.60	0.26	0.36	31.11	31.79
6	50.57	0.26	0.37	33.66	32.90
7	59.89	0.25	0.36	35.08	33.19
8	61.07	0.25	0.37	32.11	32.53
9	57.22	0.25	0.37	31.06	29.83
10	52.84	0.26	0.37	31.52	29.81
11	51.81	0.25	0.36	36.56	33.18
12	56.45	0.25	0.36	37.95	33.67
13	54.62	0.25	0.36	32.94	32.71
14	59.50	0.24	0.37	40.76	37.69
15	57.00	0.24	0.36	36.23	35.49

the effect of gap size on three response quantities—magnitude of maximum pounding force, number of occurrences of pounding and percentage control of acceleration. The figure indicates that first quantity mentioned above more or less remains constant, the second one decreases but the third one increases as the gap size is increased. The reduction in number of pounding events with increasing gap size can be considered to be more or less uniform in nature (except for gap sizes between 1 and 3 cm) and the acceleration control increase significantly beyond a gap size of 10 cm. In view of the above discussion, it can be concluded that the percentage control of deck acceleration is increased and magnitude of maximum pounding force and number of occurrences of pounding are reduced with increase in the gap size for isolated bridges. These effects are very much pronounce for a gap size more than 10 cm (refer Fig. 2).

7 Effect of Time Period of the Laminated Isolator on Pounding Force

A parametric study is performed on both the LRB and NZ isolated bridge, to study the effect of isolation time period (t_b) and time period value is varied uniformly from 2 to 4 s. Maximum responses for different isolation period for different earthquake for bridge isolated with LRB and NZ system are presented in Tables 3 and 4, respectively.

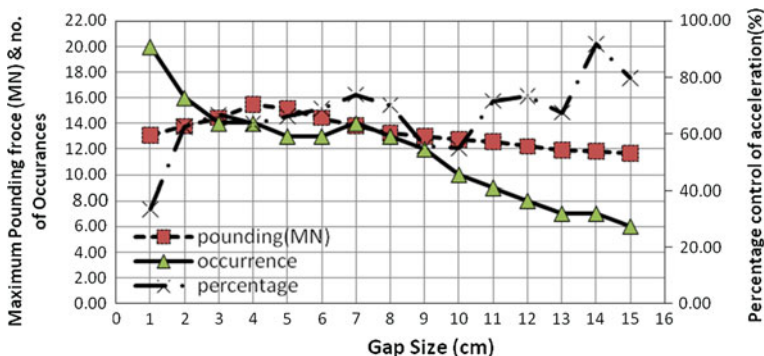


Fig. 2 Variation of number of poundings, maximum pounding force and percentage increase in deck acceleration with gap size

Table 3 Maximum responses for different isolation period for different earthquake for bridge isolated with LRB

t_b (s)	Earthquake	Maximum pounding force			
		Left (MN)	Occurrence of pounding	Right deck (MN)	Occurrence of pounding
2	El Centro (0.5 PGA) scaled	3.823	5	4.15	5
2.5		3.18	6	2.83	6
3		2.22	5	1.685	4
3.5		6.26	2	5.61	2
4		0	0	0	0
2	Kobe	3.08	7	2.7	5
2.5		2	4	2.22	4
3		9.3	2	9.12	2
3.5		0	0	0	0
4		0	0	0	0
2	Chi Chi	10.4	7	10.3	13
2.5		4.56	6	5.66	13
3		2.25	4	2.8	12
3.5		1.8	2	1.4	8
4		1.2	2	1.3	4

The maximum pounding force, along with the number of occurrences of pounding is studied. It is observed that the number of occurrences of pounding and, in general, the magnitude of maximum pounding force reduces as the isolation time period increases. i.e. both these quantities have inverse relationship with the time period of the isolators. However, the results indicate that for certain particular values of time period, which varies from earthquake to earthquake, there magnitude of pounding force suddenly

Table 4 Maximum responses recorded for different isolation period for different earthquake for bridge isolated with NZ bearing

t_b (s)	Earthquake	Maximum pounding force			
		Left deck (MN)	Occurrence of pounding	Right deck (MN)	Occurrence of pounding
2	El Centro (0.5 PGA) scaled	2.85	7	2.97	7
2.5		2.24	3	2.213	4
3		9.28	3	6.73	3
3.5		0	0	0	0
4		0	0	0	0
2	Kobe	1.73	8	1.85	8
2.5		1.67	4	1.67	4
3		0.8	1	4.29	1
3.5		0	0	1.94	1
4		0	0	5.94	1
2	Chi Chi (Taiwan)	0.4	14	9.3	16
2.5		4.22	10	4.6	12
3		2.4	7	2.05	8
3.5		1.8	5	1.57	6
4		9.8	2	0.525	4

increases. Therefore, it can be concluded that the pounding force and the number of poundings reduce in general with increase in isolation period. But in case of pounding force, it cannot be said for certain as there are some cases of exception.

8 Effect of Earthquake Ground Motion on Pounding

All the earthquakes considered in this study are scaled to have the same PGA as that of the San Fernando Earthquake. It is observed that the pounding force is inversely proportional to the isolation time period. Figure 3a, b indicate that the effect of ground motion characteristics on the pounding force developed is predominant for stiffer bridges (i.e. for bridges in which the isolators used have high stiffness values) and this effect becomes less significant for flexible bridges. This becomes evident from the figures which show that at the time period of 1.5 s, variation in magnitudes of the maximum pounding forces is observed to be about 6–7 times. At the time period of 2 s this variation is about 1.5–2 times and at higher time periods this variation becomes negligible. Thus, the effect of earthquake ground motion characteristics on pounding reduces considerably for time period greater than 2.5 s.

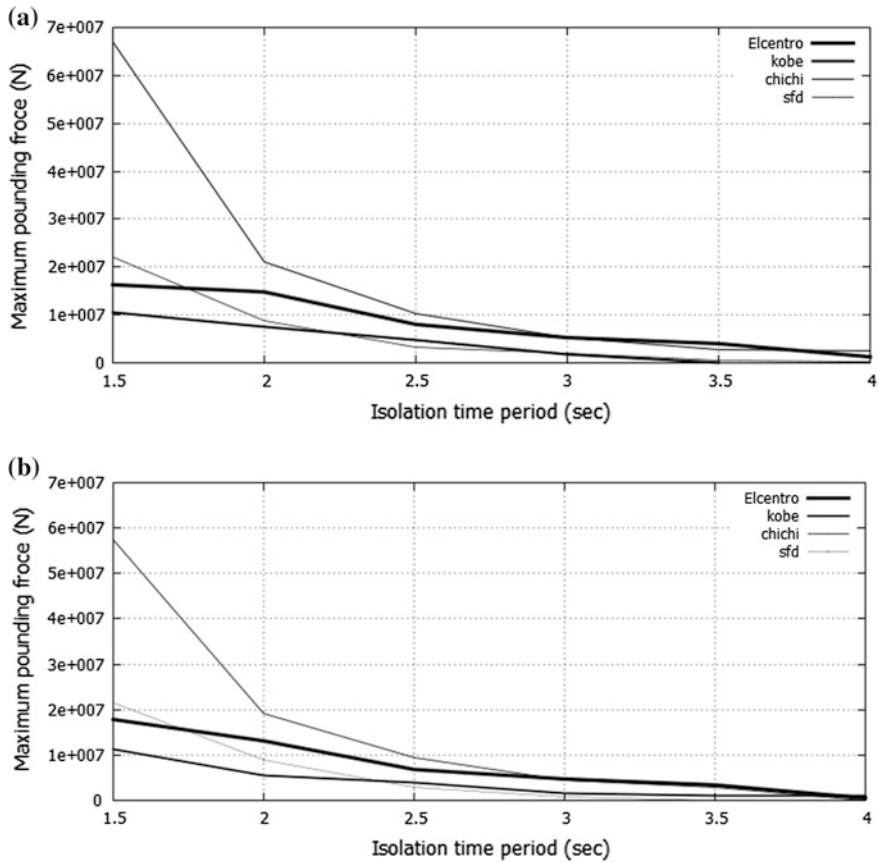


Fig. 3 Maximum pounding force versus isolation time period for different earthquakes: a LRB and b NZ bearing

9 Conclusions

In the present study effect of pounding in isolated bridge is studied. The numerical model of seismically isolated bridge is developed using Laminated-Rubber bearing and NZ bearing. The isolated bridge model is subjected to different earthquake ground motion to study the effect of pounding on it. The pounding force is modeled as nonlinear viscoelastic model. Following are the conclusions of the study:

1. Due to the occurrence of pounding, there is a sudden increase in absolute acceleration of the bridge deck. This affects the performance and behavior of the bridge and hence, the pounding effect needs to be considered in the design of bridges.
2. From the results it has been observed that either very small or large gap size reduces the effect of pounding, but providing a large gap size is not practically

feasible as it creates problems in installation, maintenance and operation. When the gap size is small, the isolators cannot perform effectively. Thus, there exists an optimum range of gap size for desired performance of the isolators.

3. As far as performance of the isolators are concerned, the percentage control of deck acceleration is increased, and the magnitude of maximum pounding force and the number of occurrences of pounding are reduced with increase in the gap size. These effects are very much pronounced after a certain value of gap size, which in the present case is found to be 10 cm.
4. The pounding force and the number of poundings reduce in general with increase in isolation period but in case of the pounding force, this phenomenon cannot be said for certain as there are certain cases of exception.
5. The effect of ground motion characteristics on the pounding force developed is predominant for stiffer bridges (i.e. for bridges in which the isolators used have high stiffness values) and this effect becomes less significant for flexible bridges. For any isolated bridge, this effect of earthquake ground motion characteristics on pounding reduces considerably after a certain value time period, which in the present case is found to be 2.5 s.

References

1. Malhotra PK (1998) Dynamics of seismic pounding at expansion joints of concrete bridges. *J Eng Mech* 124(7):794–802
2. Jankowski R, Wilde K, Fujino Y (1998) Pounding of superstructure segments in isolated elevated bridge during earthquakes. *Earthq Eng Struct Dynam* 27(5):487–502
3. Anagnostopoulos SA (1988) Pounding of building in series during earthquake. *Earthq Eng Struct Dynam* 16(3):443–456
4. Jankowski R, Wilde K, Fujino Y (2000) Reduction of pounding effects in elevated bridges during earthquakes. *Earthq Eng Struct Dynam* 29(2):195–212
5. Kim S, Lee S, Won J, Mha H (2000) Dynamic behaviors of bridges under seismic excitations with pounding between adjacent girders. In: *Proceedings of 12th world conference on earthquake engineering*, 1815. Auckland, New Zealand
6. Jankowski R (2005) Non-linear viscoelastic modelling of earthquake-induced structural pounding. *Earthq Eng Struct Dynam* 34(6):595–611

Random Response Analysis of Adjacent Structures Connected by Viscous Damper

C.C. Patel

Abstract The response of two adjacent single degree-of-freedom (SDOF) structures connected by viscous damper under base excitation, modeled as non-stationary random process is investigated. To study the effect of amplitude non-stationary characteristics of earthquake excitation, the ground motion is modeled as a uniformly modulated stationary Gaussian random process with zero-mean. The non-stationary response of coupled structure is obtained for modulating function having different strong motion duration and compared with the corresponding stationary response. The peak value of root mean square (RMS) response of the connected structures for other model of earthquake excitation such as Kanai-Tajimi and white noise is compared for stationary and two non-stationary conditions. It is observed that stationary response is achieved in a very short time. The peak value of RMS response under non-stationary ground motion is nearly same as that of the stationary response. The result indicates that the peak value of responses for stationary and two non-stationary cases is quite comparable with each other. Thus, the random response of coupled structure can be obtained by considering stationary model of earthquake ground motion.

Keywords Adjacent structures • Dynamic response • Viscous damper • Passive control • Seismic effect

1 Introduction

Significant effort have been given for research and development of various energy dissipation devices and control mechanisms, to increase the safety and reliability of engineering structures against natural disturbances like strong wind and earthquakes.

C.C. Patel (✉)

Department of Civil Engineering, Sir Padampat Singhanian University,
Udaipur 313601, India
e-mail: drccmpatel@gmail.com

The control mechanism can modify dynamically the response of structure in a desirable manner, it termed as protective system for the new structures and the existing structures can be retrofitted effectively for future seismic activity. Structural control paper by Housner et al. [1], state-of-the-art paper by Soong and Spencer [2] focused on passive and other structural control systems, Kasai et al. [3] presented the passive control systems for seismic damage mitigation, Kasai et al. [4] gives full scale damper tests and analysis in 5 storey steel frame, Kasai et al. [5] presents the current status of building passive control in Japan, these studies confirm that the passive control devices are found to be effective for seismic response control of structures. Thus, passive control using energy absorbing devices has received considerable attention in recent years. Significant effort have been given for research and development of various energy dissipation devices and control mechanisms, to increase the safety and reliability of engineering structures against natural disturbances like strong wind and earthquakes. The control mechanism can modify dynamically the response of structure in a desirable manner, it termed as protective system for the new structures and the existing structures can be retrofitted effectively for future seismic activity. Structural control paper by Housner et al. [1], state-of-the-art paper by Soong and Spencer [2] focused on passive and other structural control systems, Kasai et al. [3] presented the passive control systems for seismic damage mitigation, Kasai et al. [4] gives full scale damper tests and analysis in 5 storey steel frame, Kasai et al. [5] presents the current status of building passive control in Japan, these studies confirm that the passive control devices are found to be effective for seismic response control of structures. Thus, passive control using energy absorbing devices has received considerable attention in recent years.

Connecting adjacent structures by passive energy dissipation device when possible is an effective alternate amongst the various structural control techniques. It is developing control mechanism to reduce the excessive structural vibration due to natural disturbances and also helpful to minimize the chances of pounding. The concept of coupling adjacent tall building was proposed by Klein et al. [6] in United States, and by Kunieda [7] coupling multiple structure in Japan. Response control by coupling adjacent structure is working on the concept to allow exerting control forces upon one another to reduce the overall response of the coupled system. However, it alters the dynamic characteristics of the unconnected structures, enhances undesirable torsional response if the buildings have asymmetric geometry, and increase the base shear of the stiffer structure. In certain situations the free space available between adjacent structures can be effectively utilized for installation of control devices. Maison and Kasai [8] have presented a analysis for types of structural pounding; Luco and De Barros [9] have studied connecting low to medium rise structures with passive devices; Zhu and Iemura [10] proposed a new structure-vibration-control approach using passive coupling element between two parallel structures to reduce the seismic response of a system due to earthquake excitation; Yang et al. [11] presented experimental seismic study of adjacent buildings with fluid dampers, Cimellaro and Lepoz [12] studied the seismic response of a pair of linear multistorey building structures connected by nonlinear passive devices; study found the optimal value of the damper exponent depends on

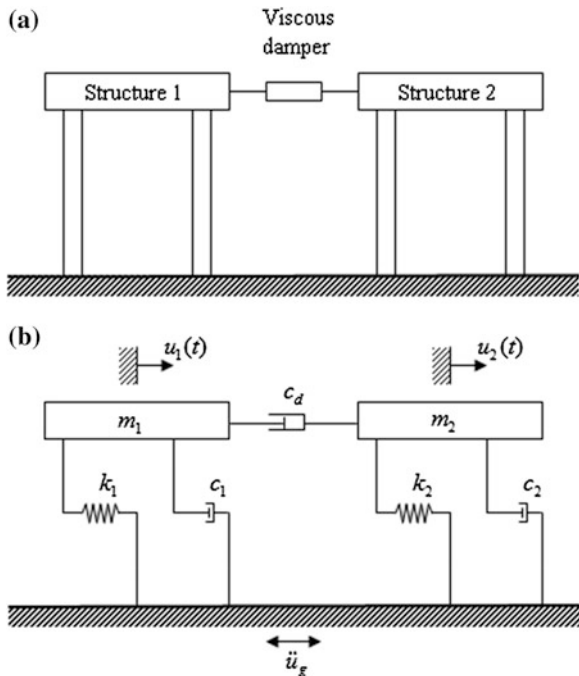
the value of the damper coefficient of damper device, Anunthanakul and Jiansinlapadamrong [13] presented study on structural pounding response mitigation by liquid dampers, found the displacement response of both the building reduced significantly and pulse accelerations were eliminated which reduced the impact forces on the structures.

The response of adjacent structures connected by viscous damper to non-stationary ground motions is studied. The objectives of the present work are to: (1) study the response of adjacent SDOF coupled structures subjected to non-stationary ground motion; (2) study the non-stationary (having different strong motion duration) RMS response of coupled structures and corresponding stationary response; (3) study the RMS response of the connected structures for other model of ground excitation such as Kanai-Tajimi and white noise.

2 Modeling of Adjacent Structures Coupled by Viscous Damper

Consider two adjacent SDOF structures connected with a viscous damper as shown in Fig. 1a and corresponding mathematical model shown in Fig. 1b. Various assumptions made for the structural system under consideration are; (i) the two structures are symmetric with their symmetric planes in the alignment and ground

Fig. 1 Structural model of two SDOF adjacent coupled structures **a** adjacent structures connected by viscous damper, **b** mathematical model



motion is to occur in one direction in the symmetric planes, (ii) both structures are to be of the same height and are connected by viscous damper at their floor level, (iii) both structures are subjected to the same ground motion (iv) the coupled structure remain in linear elastic and (v) effect due to soil-structure interaction is neglected. The adjacent structures are idealized as two SDOF coupled system and referred as structures 1 and 2, respectively.

Let m_1, k_1, c_1 and m_2, k_2, c_2 be the mass, stiffness and damping coefficient of the Structures 1 and 2, respectively. Let $\omega_1 = \sqrt{k_1/m_1}$ and $\omega_2 = \sqrt{k_2/m_2}$ be the natural frequencies and $\zeta_1 = c_1/2m_1\omega_1$ and $\zeta_2 = c_2/2m_2\omega_2$ be the damping ratios of Structures 1 and 2, respectively. Let μ and γ be the mass and frequency ratio of two structures, respectively, expressed as

$$\mu = \frac{m_1}{m_2} \quad (1)$$

$$\gamma = \frac{\omega_2}{\omega_1} \quad (2)$$

The damper force is a function of damper stiffness and damper damping ratio. The damper offer a stiffness and the damper force is affected by damper stiffness also. The past studies shows that the small value of damper stiffness of the damper connecting adjacent structures has no effect on response of the structures and the frequency of both the structures unaltered whereas, the strong damper stiffness reduces the relative displacement and the relative velocity of damper and hence the performance of damper deteriorates; and sometimes maximum displacement and base shear of stiffer structure may increase than unconnected structure. For present study the force in the viscous damper f_d is assumed to be proportional to the relative velocity of damper ends, is given by

$$f_d = c_d \dot{u}_r \quad (3)$$

The damping coefficient of damper c_d , which is expressed in the normalized form as

$$\zeta_d = \frac{c_d}{2m_1\omega_1} \quad (4)$$

where \dot{u}_r is relative velocity of the damper ends and ζ_d is the normalized damping coefficient of damper. The governing equations of motion for the damper connected system can be written as

$$m_1 \ddot{u}_1(t) + c_1 \dot{u}_1(t) + k_1 u_1(t) + c_d (\dot{u}_1(t) - \dot{u}_2(t)) = -m_1 \ddot{u}_g(t) \quad (5)$$

$$m_2\ddot{u}_2(t) + c_2\dot{u}_2(t) + k_2u_2(t) - c_d(\dot{u}_1(t) - \dot{u}_2(t)) = -m_2\ddot{u}_g(t) \quad (6)$$

where $u_1(t)$ and $u_2(t)$ are the displacement response, relative to the ground, of Structures 1 and 2, respectively; and $\ddot{u}_g(t)$ is the ground acceleration. From Eqs. (5) and (6), it can be written as

$$\ddot{u}_1(t) + \ddot{u}_g(t) = -(c_1/m_1)\dot{u}_1(t) - (c_d/m_1)(\dot{u}_1(t) - \dot{u}_2(t)) - (k_1/m_1)u_1(t) \quad (7)$$

$$\ddot{u}_2(t) + \ddot{u}_g(t) = -(c_2/m_2)\dot{u}_2(t) + (c_d/m_2)(\dot{u}_1(t) - \dot{u}_2(t)) - (k_2/m_2)u_2(t) \quad (8)$$

The structural control criteria depend on the nature of dynamic loads and the response quantities of interest. Minimizing the relative displacement or absolute acceleration of the system are always been considered as the control objective. In case of flexible structures, displacements are predominant that need to be mitigated. In case of stiff structures, accelerations which generate higher inertial force in structures, requires to be controlled. In view of this, the study aims to arrive the distinct expressions for optimum parameters of damper for minimizing exclusively displacement as well as acceleration response.

3 Model of Ground Motion Excitation

The purposes of modeling the earthquake ground motion are to represent the frequency content, time dependent frequency content which is due to arrival of different waves at different time, transient nature and duration of earthquake ground motion in translations and rotations of displacement, velocity and acceleration components, spatial variability especially for long span structures, multi-component nature, and various seismological considerations like source mechanism, propagation of waves in geological medium, scattering etc. The various stochastic models for earthquake ground motions are Single component model, Multi-component model, spatially varying load model, Gaussian random process model and Poisson pulse process model. Single component model are stationary random process or non-stationary random process, whereas for multi component and spatially varying load model uses vector random process model.

Earthquake ground motion is transient phenomenon. Generally, structural engineers are interested in maximum response due to ground motion. For small time, the response is non-stationary and depends on initial conditions, whereas for reasonably large time the response become stationary and ground motion can be modeled as stationary.

Non-stationarity in ground motion is non-stationarity in amplitude and frequency content. Non-stationarity in frequency content can be introduced by random pulse process and evolutionary power spectral density function. Power spectral density function is time dependent function, such process is called as evolutionary process. If the evolution of the frequency content with time can be neglected, the ground

motion can be characterized by a matrix of the power spectral density function (PSDF) and intensity envelop function. Amplitude non-stationarity can be introduced by multiply the stationary Gaussian random process with zero mean whose power spectral density by deterministic modulating function (also called envelop function), which captured the non-stationary trend observed in earthquake ground motion. The non-stationary response of a SDOF system to non-stationary earthquake motion for different shapes of modulating functions is investigated and comparison of the non-stationary earthquake response of the SDOF system for different modulating functions having same energy content is studied by Jangid [14]. The earthquake excitation $\ddot{u}_g(t)$ is expressed as

$$\ddot{u}_g(t) = A(t)\ddot{u}_f(t) \quad (9)$$

where $A(t)$ = deterministic modulating function; and $\ddot{u}_f(t)$ stationary random process. The modulating function proposed by Amin and Ang [15] initially increases parabolic (up to time t_1), remains constant between t_1 and t_2 , and then decreases exponentially, is expressed by

$$A(t) = \begin{cases} A_0(t/t_1)^2 & (0 \leq t \leq t_1) \\ A_0 & (t_1 \leq t \leq t_2) \\ A_0 e^{-c(t-t_2)} & (t \geq t_2) \end{cases} \quad (10)$$

A_0 is the scaling factor and c is the constant.

In present study the deterministic modulating function is considered from Amin and Ang [15] with scaling factor A_0 , t_1 and t_2 are time for start and end of strong motion duration, respectively; c = constant; and $T_0 = t_2 - t_1$ strong motion duration of earthquake. The evolutionary PSDF of the earthquake excitation is given by

$$S_{\ddot{u}_g}(\omega) = |A(t)|^2 S_{\ddot{u}_f}(\omega) \quad (11)$$

where $S_{\ddot{u}_g}(\omega)$ = stationary PSDF of the earthquake ground motion. In the present study the PSDF of the earthquake excitation $\ddot{u}_f(t)$ is considered as [16]

$$S_{\ddot{u}_f}(\omega) = S_0 \left(\frac{1 + 4\xi_g^2(\omega/\omega_g)^2}{(1 - (\omega/\omega_g)^2)^2 + 4\xi_g^2(\omega/\omega_g)^2} \right) \left(\frac{(\omega/\omega_f)^4}{(1 - (\omega/\omega_f)^2)^2 + 4\xi_f^2(\omega/\omega_f)^2} \right) \quad (12)$$

where S_0 is the constant PSDF of input white-noise random process, and ω_g , ξ_g , ω_f and ξ_f are the ground filter parameters.

The PSDF of $\ddot{u}_f(t)$ is a nonwhite random process, whereas the state variable method for random response of any system requires that the excitation must be either white noise or sort noise. However, this obstacle can be circumvented by

introducing the shaping filters in which the random process $\ddot{u}_f(t)$ can be considered as the response of two linear filters subjected to white-noise excitation as

$$\ddot{u}_f(t) + 2\zeta_f^2\omega_f\dot{u}_f(t) + \omega_f^2u_f(t) = -(\ddot{u}_g(t) + \ddot{u}_0(t)) \tag{13}$$

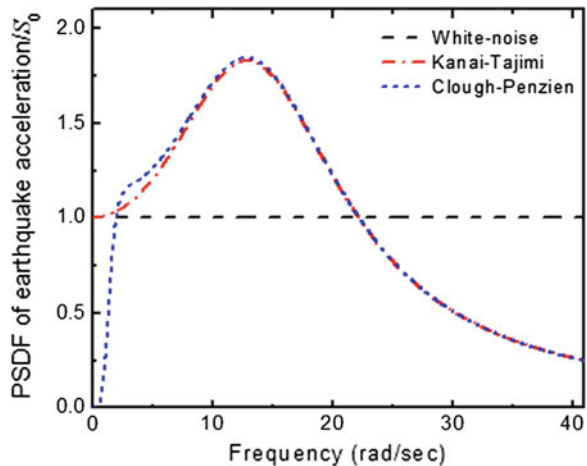
$$\ddot{u}_g(t) + 2\zeta_g^2\omega_g\dot{u}_g(t) + \omega_g^2u_g(t) = -\ddot{u}_0(t) \tag{14}$$

where $\ddot{u}_0(t)$ input white-noise random process with constant intensity of the PSDF as S_0 . Equations (13) and (14) provide the stationary PSDF of the response $\ddot{u}_f(t)$ as that expressed by Eq. (12). The ω_g and ζ_g generally represent the predominant frequency and damping ratio of soil strata, respectively. The value of various parameters considered are $\zeta_g = \zeta_f = 0.6$ moreover, the parameters ω_g and ω_f are varied to model various shape of the PSDF of earthquake excitation such as Kanai-Tajimi (i.e. $\omega_f \rightarrow 0$) [17] and the simple white-noise (i.e. $\omega_f \rightarrow 0$ and $\omega_g \rightarrow \infty$) model. For the Kanai-Tajimi model the ω_f is considered as 10^{-6} rad/s, where as for white-noise model the ω_g and ω_f are taken as 10^6 and 10^{-6} rad/s, respectively. Three models of the PSDF function of earthquake ground motion using Eq. (12) and the above parameters are shown in Fig. 2. The variable values of ω_g and S_0 is used to study the influence of predominant frequency and intensity of excitation on the response of the coupled structural system.

4 Evaluation of Stochastic Response

The stochastic response of base isolated structure through nonlinear time history simulation analysis has been validated by Jangid [18] and many other researchers. Thus, Eqs. (5) and (6) along with (9), (13) and (14) can be rewritten as a system of first-order differential equations as

Fig. 2 Plot of different spectra of earthquake ground motion using Eq. (12)



$$\frac{d}{dt}[Y] = [H][Y] + [W] \tag{15}$$

where $[Y]$ is state vector; $[H]$ is augmented system matrix; and $[W]$ is excitation vector. Vector $[Y]$ and $[W]$ are expressed as

$$[Y] = [u_1(t) \ u_2(t) \ \dot{u}_1(t) \ \dot{u}_2(t) \ u_f(t) \ \dot{u}_f(t) \ u_g(t) \ \dot{u}_g(t)]^T \tag{16}$$

$$[W] = [0 \ 0 \ 0 \ 0 \ 0 \ 0 \ -\ddot{u}_0(t)]^T \tag{17}$$

The augmented response vector $[Y]$ is Markov process and corresponding covariance matrix $[V]$ satisfies the following equation Nigam [19]

$$\frac{d}{dt}[V] = [H][V]^T + [V][H]^T + [P] \tag{18}$$

where superscript T is transpose of matrix.

The elements of matrix $[V]$ and $[P]$ are given by

$$V_{ij} = E[Y_i Y_j] \tag{19}$$

$$P_{ij} = E[W_i W_j] \tag{20}$$

where Y_i and W_i are i th elements of the vector $[Y]$ and $[W]$, respectively. All the elements of matrix $[P]$ are zero except $P(2n + 4, 2n + 4) = 2\pi S_0$, ($n = 2$).

By introduction of modulating function $A(t)$, the augmented system matrix, $[H]$, becomes time dependent. The non-stationary response of the system (i.e. $[V]$ matrix) is obtained by solving the moment Eq. (18) using step-by-step method. The fourth-order Runge-Kutta method is employed for the present study.

5 Numerical Study

The non-stationary response of the system is obtained by solving Eq. (18) and the response quantities of interest are the root mean square (RMS) relative displacement and absolute acceleration of structures 1 and 2. The response of the system is investigated for two types of modulating functions express by Eq. (12), namely, (1) $t_1 = 2$ s, $t_2 = 7$ s and $c = 0.5$ s⁻¹; and (2) $t_1 = 2$ s, $t_2 = 12$ s and $c = 0.5$ s⁻¹. These modulating functions are referred as Types I and II which have the strong motion duration of $T_0 = 5$ s and 10 s, respectively. In addition, the response is also investigated for $A(t) = 1$ for all values of time t . (i.e., this corresponding to a stationary earthquake ground motion) in order to distinguish between the stationary and non-stationary response of the coupled structures. The model of the coupled

structure in this study requires the specifications of parameters, namely: (1) frequency ratio γ ; (2) mass ratio μ ; (3) structural damping ζ_1 and ζ_2 and (4) normalized damping coefficient ζ_d . The earthquake excitation requires the specification of the system parameters ω_g , ω_f and S_0 . Figure 3 shows the time variation of RMS relative displacement and absolute acceleration of Structure 1 and 2 for different types of modulating functions with $\omega_f = \pi/2$ rad/s, $\omega_g = 5\pi$ rad/s, and $S_0 = 0.05 \text{ m}^2/\text{s}^3$. The response is shown for the system parameters: frequency ratio $\gamma = 2$, mass ratio $\mu = 1$, structural damping $\zeta_1 = \zeta_2 = 0.05$, and normalized damping coefficient $\zeta_d = 0.23$. It is observed from the figure that the stationary response is achieved in a very short time (i.e. about 2.0 s). In addition, the peak value of RMS response under non-stationary ground motion is the same as that of the stationary response. This happens mainly due to the relatively large damping due to external damper coupling two structures. In Table 1, the peak value of RMS response of the coupled structure for other models of earthquake excitation such as Kanai-Tajimi and white-noise is compared for stationary and two non-stationary conditions. Table 1 indicates that the peak response for stationary and two non-stationary cases is quite comparable with each other. Thus, the stochastic earthquake response of coupled structure can be obtained by considering stationary model of earthquake ground motion with appropriate frequency variation of PSDF and intensity.

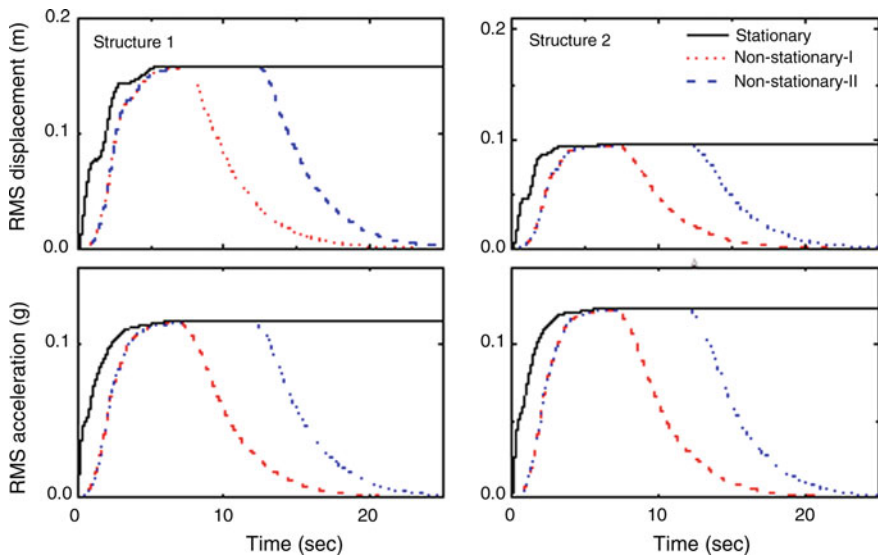


Fig. 3 Comparison of stationary and non-stationary response of adjacent structures connected by viscous damper ($\mu = 1$, $\gamma = 2$, $\zeta_1 = \zeta_2 = 0$, $\zeta_d = 0.23$, $\omega_f = \pi/2$ rad/s, $\omega_g = 5\pi$ rad/s, and $S_0 = 0.05 \text{ m}^2/\text{s}^3$)

Table 1 Comparison of stationary and nonstationary response of adjacent coupled structures ($\gamma = 2$, $\mu = 1$, $\xi_1 = \xi_2 = 0.05$, and $S_0 = 0.05 \text{ m}^2/\text{s}^3$)

Model of PSDF of earthquake excitation	Response quantity	Stationary	Nonstationary-I	Nonstationary-II
Clough-Penzien model with $\omega_f = \pi/2 \text{ rad/s}$ and $\omega_g = 5\pi \text{ rad/s}$	RMS displacement u_1 (mm)	158.83	158.07	158.80
	RMS displacement u_2 (mm)	95.29	94.60	95.28
	RMS acceleration a_1 (g)	0.115	0.114	0.115
	RMS acceleration a_2 (g)	0.124	0.123	0.124
Kanai-Tajimi model with $\omega_g = 5\pi \text{ rad/s}$	RMS displacement u_1 (mm)	155.02	154.18	155.00
	RMS displacement u_2 (mm)	92.40	91.72	92.39
	RMS acceleration a_1 (g)	0.111	0.110	0.111
	RMS acceleration a_2 (g)	0.119	0.119	0.119
White-noise model	RMS displacement u_1 (mm)	148.48	147.62	148.45
	RMS displacement u_2 (mm)	82.76	82.15	82.75
	RMS acceleration a_1 (g)	0.102	0.101	0.102
	RMS acceleration a_2 (g)	0.107	0.106	0.107

6 Conclusions

The response of two adjacent SDOF structures connected by viscous damper under non-stationary earthquake ground motion is investigated. The non-stationary response for two different strong motion duration of various earthquake excitation model is compared with corresponding stationary response of the system. The peak value of RMS response for various earthquake excitation models is calculated. From the trends of the results of present study, the following conclusions may be drawn:

- (1) For non-stationary type excitations, the stationary response is achieved in a very short time.
- (2) The RMS response under non-stationary ground motion is nearly same as that of stationary response.
- (3) The peak value of RMS response for stationary and two non-stationary cases is quite comparable with each other.
- (4) The random response of coupled structure can be obtained by considering stationary model of earthquake ground motion.

References

1. Housner GW, Bergman L, Caughey TK, Chassiakos AG, Claus RO, Masri SF, Skelton RE, Soong TT, Spencer BF, Yao JTP (1997) Structural control: past, present and future. *J Eng Mech (ASCE)* 123(9):897–971
2. Soong TT, Spencer BF (2002) Supplemental energy dissipation: state-of-the-art and state-of-the-practice. *Eng Struct* 24:243–259
3. Kasai K, Yaomin Fu, Atsushi W (1998) Passive control system for seismic damage mitigation. *J Struct Eng (ASCE)* 124(5):501–512
4. Kasai K, Ooki Y, Ishii M, Ozaki H, Ito H, Motoyui S, Hikino T, Sato E (2008) Valu-added 5-storey steel frame and its components: part-1 full-scale damper tests and analysis. In: The 14th world conference on earthquake engineering, Beijing, China
5. Kasai K, Nakai M, Nakamura Y, Asai H, Suzuki Y, Ishii M (2008) Current status of building passive control in Japan. In: The 14th world conference on earthquake engineering, Beijing, China
6. Klein RE, Cusano C, Stukel J (1972) Investigation of method to stabilize wind induced oscillations in large structures. In: ASME winter annual meeting, New York, 72-WA/AUT-H
7. Kunieda M (1976) Earthquake prevent design and earthquake proof design for structures. *J JSME* 79(689):86–91 (in Japanese)
8. Maison BF, Kasai K (1994) Analysis for type of structural pounding. *J Struct Eng (ASCE)* 116(4):957–977
9. Luco, JE, De Barros FCP (1998) Optimal damping between two adjacent elastic structures. *Earthq Eng Struct Dyn* 27:649–659
10. Zhu H, Iemura H (2000) A study of response control on the passive coupling element between two parallel structures. *Struct Eng Mech* 9:383–396
11. Yang Z, Xu YL, Lu XL (2003) Experimental seismic study of adjacent buildings with fluid dampers. *J Struct Eng ASCE* 129(2):197–205
12. Cimellaro GP, Lopez-Garcia D (2007) Seismic response of adjacent buildings connected by nonlinear viscous dampers. *Struct Eng Res Front* 1–12. doi:[10.1061/40944\(249\)64](https://doi.org/10.1061/40944(249)64)
13. Anunthanakul N, Jianinlapadamrong M (2009) Structural pounding response mitigation by liquid dampers. ASCE. doi:[10.1061/41084\(364\)131](https://doi.org/10.1061/41084(364)131)
14. Jangid RS (2004) Response of SDOF system to non-stationary earthquake excitation. *Earthq Eng Struct Dyn* 33:1417–1428
15. Amin M, Ang AHS (1968) Non-stationary stochastic model of earthquake motion. *J Eng Mech ASCE* 94:559–583
16. Clough RW, Penzien J (1993) Dynamics of structures. McGraw Hill, New York
17. Tajimi HA (1960) A statistical method for determining the maximum response of a building structure during an earthquake. In: 2nd world conference on earthquake engineering, vol 3, pp 781–797
18. Jangid RS (2008) Stochastic response of bridges seismically isolated by friction pendulum system. *J Bridge Eng ASCE* 13(4):319–330
19. Nigam NC (1983) Introduction to random vibrations, 1st edn. MIT Press, Cambridge

Part XI
Hydro-Dynamics and Fluid-Structure
Interaction

Dynamic Analysis of a Mega-Float

K.S. Arunraj and R. Panner Selvam

Abstract This paper covers the wave induced hydro-elastic response analysis of a pontoon type very large floating structure (VLFS) or Mega-Float. This coupled Fluid–Structure interaction problem can be solved using modal expansion method in the frequency domain. In this paper, a pontoon type VLFS structure is analyzed for wave responses. HYDRAN software package has been used for the numerical modeling. Vertical displacement of the structure is obtained in regular waves for different wave periods at three different points (bow, mid-ship and stern) of VLFS for 0° wave heading angle. The variation of the vertical displacement for mid-section are also obtained for four different wave headings for various wave periods. Similarly variations of vertical displacements with change in ratio of wavelength to the length of the structure and for two different materials (steel and aluminium) are obtained. Finally, the longitudinal stresses for different wave periods at bow, stern and midship of the structure are compared.

Keywords Very large floating structures · Hydro-elasticity · Dynamic analysis · Mega-float · Modal expansion method · Response amplitude operator

1 Introduction

Owing to an exponential growth in human population the land scarce island countries and countries with long coastline are looking to expand their horizon into ocean environment to reduce the burden on the land. But the land reclamation procedures are time consuming and found to have negative impact on environment, mainly on the ecological systems in continental shelf. In this scenario Very Large Floating Structures (VLFS) are gaining more popularity as these are cost effective, environmental friendly and can be constructed easily and can be easily removed or expanded. VLFS can be used for making Floating Airports, Artificial Islands, and

K.S. Arunraj (✉) · R. Panner Selvam
Department of Ocean Engineering, IIT Madras, Chennai, India

© Springer India 2015
V. Matsagar (ed.), *Advances in Structural Engineering*,
DOI 10.1007/978-81-322-2193-7_89

1143

Mobile Offshore Base etc. VLFSs may be classified into two broad categories according to Watanabe et al. [1], namely, the semi-submersible type and the pontoon-type. The semi-submersible type of VLFSs having their platform raised above the sea level and supported by columns resting on submerged pontoons. In deep seas where the wave elevations are higher, it is advisable to use semi-submersible type VLFS to minimize the effects of waves and to obtain structural stability. The pontoon-type VLFS is a simple flat box structure floating on the sea surface suitable for very calm seas. A pontoon type VLFS commonly referred as Mega-Float by Japanese scientists. A typical Mega-Float has large horizontal dimensions compared to its draft. Given such a small depth to length ratio, a VLFS has relatively small flexural rigidity which makes it behaves almost like an elastic plate on water. In other words, the VLFS has a significant elastic deformation in addition to the rigid body motion under wave actions; these elastic deformations are more crucial than their rigid body motions. When the structure is considered as flexible the equations of motion become coupled and the term hydro-elasticity comes into the picture. Suzuki and Yoshida [2] proposed two conditions that a VLFS must satisfy. These are

- (i) Length of the structure must be greater than the wavelength.
- (ii) Length of the floating structure to be larger than the characteristic length λ_c defined by:

$$\lambda_c = 2\pi \left(\frac{EI}{\rho_w g} \right)^{1/4} \quad (1)$$

where EI is the flexural rigidity per unit length, ρ_w the fluid density, and g is the gravitational acceleration. If the length of the structure is less than characteristic length the response is dominated by rigid body motions, else by elastic deformations ISSC [3].

Hydro-elastic analysis is critical in the VLFS assessment as well as for design improvement. Bishop and Price [4] and Price and Wu [5], did significant contribution in developing 3-D hydro-elasticity theory where the Green function method is used to model the fluid and the finite element method to model the VLFS. HYDRAN software computations are bases on 3D hydro-elasticity theory. A brief description of salient features of the analysis of the Mega-float is presented in the next section. Details of the theoretical formulation of the analysis are given in Ruiping [6].

2 Frequency Domain Analysis

The coordinate system used for the numerical modeling is shown Fig. 1. A Cartesian coordinate system selected with origin at the undisturbed free surface and the z-axis pointing upwards. The seabed is flat and impermeable at $z = -h$ and

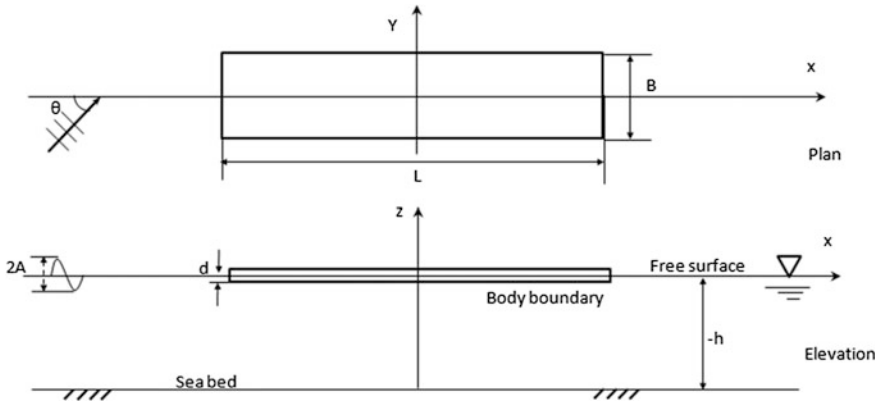


Fig. 1 Schematic diagram of a pontoon type VLFS and coordinate system

assuming an incident wave with a circular frequency ω , height $2A$ (A is the amplitude) and wave angle θ excites the mega-float of length L , beam B and draft d and the deflection, $w(x,y)$, is measured from the still water level.

2.1 Fluid Domain Potential and Boundary Conditions

Since the fluid is ideal and flow is irrotational velocity potential (ϕ) must exist and it should satisfy the Laplace equation,

$$\nabla^2 \phi(x, y, 0) = 0 \tag{2}$$

Time-harmonic motions are considered, with the complex time dependence $e^{i\omega t}$ applied to all first-order oscillatory quantities. The boundary conditions that velocity potential has to be satisfied are

$$\frac{\partial \phi(x, y, 0)}{\partial z} = \frac{\omega^2}{g} \phi(x, y, 0) \quad \text{on free surface} \tag{3}$$

$$\frac{\partial \phi(x, y, -h)}{\partial z} = 0 \quad \text{on bottom boundary} \tag{4}$$

$$\frac{\partial \phi(x, y, -d)}{\partial n} = -i\omega w(x, y) \quad \text{on body boundary} \tag{5}$$

where Eq. (3) is the free surface boundary condition, which is derived from the linearized Bernoulli equation. Equation (4) is the boundary condition at the seabed which expresses impermeability. Equation (5) implies that no gap exists between

the plate and the water-free surface. And w is the vertical complex displacement of the plate, g is the gravitational acceleration and n is the unit normal vector pointing from the fluid domain into the body. The wave velocity potential must also satisfy the Sommerfeld radiation condition

$$\lim_{|x| \rightarrow \infty} \sqrt{|x|} \left(\frac{\partial}{\partial |x|} - ik \right) (\phi - \phi_I) = 0 \quad \text{on far field} \quad (6)$$

where x represents the artificial fluid boundary at infinity, k is the wave number, and ϕ_I is the undisturbed incident wave.

2.2 Deformation of Megafloat

To analyze the deformations of the Mega-Float Modal Expansion method is adapted as detailed in Newman [7]. Here, the coupled equation of motion is decoupled into hydrodynamic problem in terms of the velocity potential and structural problem of a freely vibrating plate with free edges. The deflection of the plate can be expressed by the superposition of the different vibration modes as

$$w(x, y) = \sum_i^n \zeta_i w_i(x, y) \quad (7)$$

where ζ_i is the amplitude of the i -th mode of vibration of plate, and n is the number of modes. The complex equation of motion in frequency domain can be represented by

$$(-\omega^2 [M + M_w] + i\omega [C_w] + [K_s + K_w]) \{w\} = \{F\} \quad (8)$$

where $[K_s]$, $[K_w]$, $[M]$, $[M_w]$, $[C_w]$ are the global flexural stiffness matrix, global restoring force matrix, global mass matrix, global added mass matrix and global added damping matrix, respectively and $\{F\}$ is the excitation force contributed by incident and scattered wave.

3 Numerical Modeling

A pontoon type VLFS i.e. a rectangular box is considered for the analysis. The structure is completely closed. The specification of the Mega-float is provided in Table 1.

Table 1 Specification of the barge

Quantity	Dimension
Length (m)	1,000
Beam (m)	60
Depth (m)	8
Draft (m)	5
Vertical bending stiffness (EI_y, Nm^2)	1.507228×10^{13}
Horizontal bending stiffness (EI_z, Nm^2)	4.269084×10^{14}
Torsion stiffness (GI_t, Nm^2)	1.668054×10^{14}
Young's modulus (E, Gpa)	210
Mass of per unit length (kg/m)	3.075000×10^5

3.1 Structural Modeling

The floating structure has been modeled using SAP2000 software package. The modeled structure is shown in Fig. 2. The box consists of six flat plates: the top deck and the bottom hull, the two sides, and the bow and stern plates made of steel. And these steel plates are having a nominal thickness of 35 mm. To account for the additional bending stiffness associated with stiffeners that are not modeled, the plate thickness is increased by 0.25 m for top and bottom plates. The mass density of steel is taken as $7,850 \text{ kg/m}^3$, and the structural mass is based on the nominal steel volume given the 35 mm plate thickness. To model the non-structural mass, the top and bottom plates are assigned an additional mass density of $81,950 \text{ kg/m}^3$ and structural damping is not considered in the dynamic analysis.

3.2 Hydrodynamic Modeling

Structural modeling data has been imported from SAP2000 to HYDRAN software package. HYDRAN is a three dimensional hydro-elastic code which uses panel

Fig. 2 Structural model of the mega-float using SAP2000

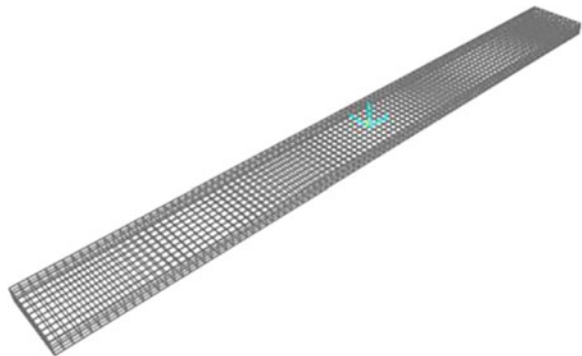


Table 2 Specification of the mesh convergence study

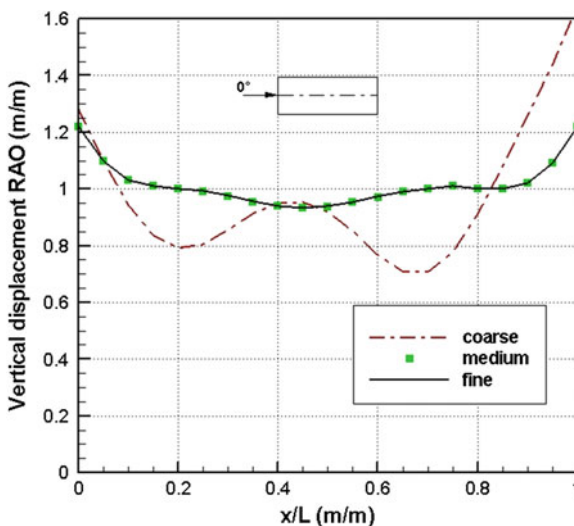
No	Type of mesh	Number of elements in each plane			Total elements
		xy	yz	xz	
1	Coarse	40 × 20	20 × 4	40 × 4	2 × 1,040 = 2,080
2	Medium	100 × 20	20 × 8	100 × 8	2 × 2,960 = 5,920
3	Finer	200 × 20	20 × 8	200 × 8	2 × 5,760 = 11,520

method for the hydrodynamic calculations. A one-to-one mapping between structural elements and fluid panels is used in HYDRAN, which uses a 3-D, shell finite element model. The basic element is a 3-node, flat, triangular element that uses shear-deformable Mindlin plate theory for the out-of-plane bending and a constant strain formulation for the in-plane behavior. The hydrodynamic analysis is based on linear potential theory. The Green function method with constant source strengths over each fluid panel is used to solve the hydrodynamic variables, Riggs et al. [8].

3.3 Convergence Study

Vertical displacement Response Amplitude Operators (RAOs) along the centre line of the structure at salient points along the length of the structure are obtained for a wave period whose wave length (λ) is equal to the length of the structure (L) and for unit wave height. RAO is defined as ratio of structural response to wave height in general. Three different mesh sizes are considered for the convergence study. Rectangular shell elements were used for meshing. The dimensions of the meshes are given in the Table 2.

Fig. 3 Displacement along the centre line of the structure when ($\lambda = L$)



The distribution of vertical displacement along the centre line of the structure for three different meshes is shown in Fig. 3 in terms of RAOs. From this plot, for better computational efficiency medium type mesh has been adopted for further analysis.

4 Results and Discussion

4.1 Natural Periods and Modes

A subset of the dry normal modes is used to form a reduced basis to determine the wave induced motion of the Mega-Float, Riggs et al. [8]. The first six modes correspond to surge, sway, heave, roll, pitch, and yaw, respectively, and of course, the corresponding natural frequencies are zero, so they are not included in the Table 3. These modes, together with the next 12 deformational modes, are used to form the reduced basis. The natural periods and a description of the modes are given in Table 3. The modes are similar to mode shapes of a free-free beam, although they are more complicated than simple beam modes.

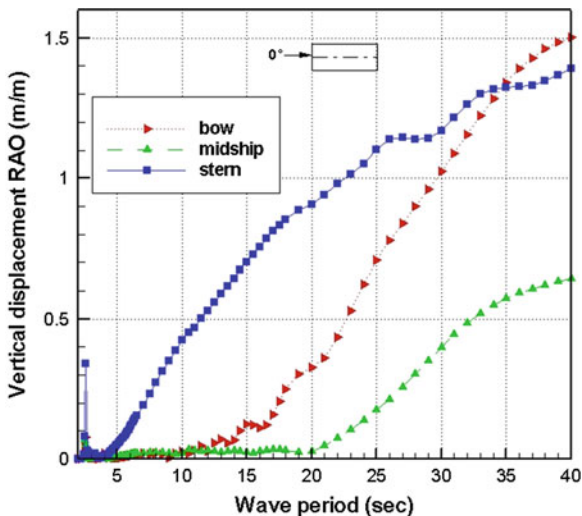
4.2 Wave Induced Responses

The wave-induced response of the structure are determined for wave periods ranging from 2 to 40 s and for wave angles of 0°, 30°, 60° and 90°. The water depth considered at site is 20 m and wave height is 1 m. The variation of vertical displacement at the bow, midship and stern of the structure for different wave periods is shown in Fig. 4 in terms of RAOs.

Table 3 Natural periods and modes

Mode no.	Natural period (s)	Description
7	40.554	Vertical bending 1
8	14.856	Vertical bending 2
9	9.322	Horizontal bending 1
10	7.691	Vertical bending 3
11	4.746	Vertical bending 4
12	4.523	Torsion 1
13	3.473	Horizontal bending 2
14	3.256	Vertical bending 5
15	2.397	Vertical bending 6
16	2.274	Torsion 2
17	1.857	Vertical bending 7
18	1.837	Horizontal bending 3

Fig. 4 Comparison of vertical displacement RAO for 0° wave angle



From this figure it is observed that that the edges of the structure (bow and stern) are found to have larger vertical displacement than that of the mid-ship vertical displacement. Vertical displacements at edges of the structure are found to be 70–80 % more than the mid-ship. Also the vertical displacements of the structure are prominent at higher wave periods or wave lengths.

The vertical displacement RAOs are compared for different wave angle of incidence at the midship of the structure and shown in Fig. 5. The vertical displacements at the midship are negligible for lower wave periods and vertical displacements increases as the angle of attack increases from 0° to 90°.

Fig. 5 Variation of vertical displacement RAO with wave angle

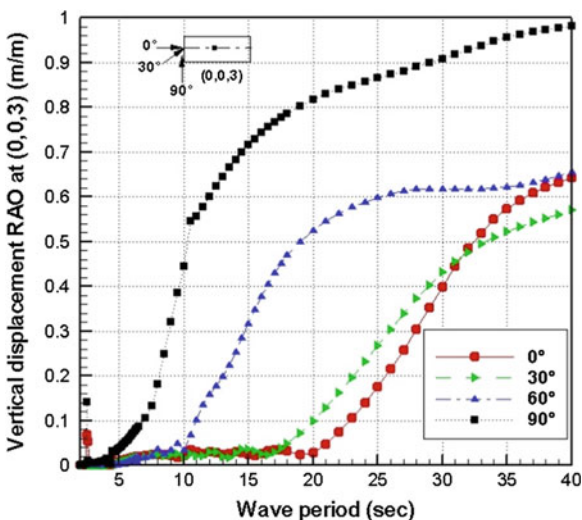
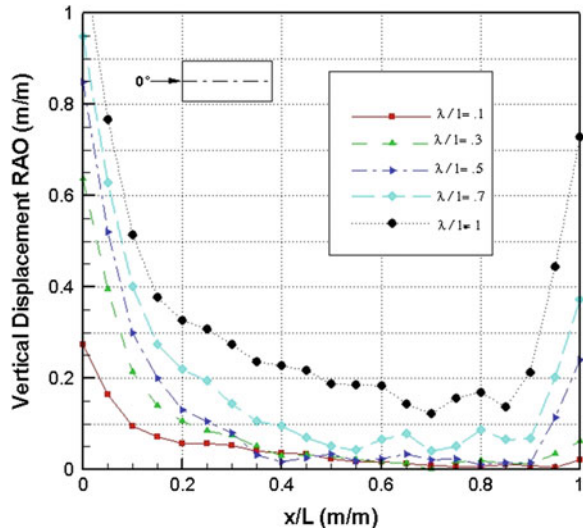


Fig. 6 Variation of vertical displacement RAO with change in λ/L ratio



The variation of vertical displacement on the top plate with change in λ/L ratio is shown in Fig. 6, where λ is the wave length and L is length of the structure. It is observed that the responses of the structure along the longitudinal centerline increases with increase λ/L ratio (i.e. increase in wave period). The variation in response of the structure with λ/L shows that at lower period vertical displacements at center portion of the structure is negligible compared to the edges.

The behavior of the structure with variation of stiffnesses is analyzed assuming two different materials. Steel and Aluminium are considered for this study, where steel is having more stiffness than aluminium. The vertical displacement along the longitudinal length of the structure is compared and is shown in Fig. 7. It shows

Fig. 7 Variation of vertical displacement for steel and aluminium

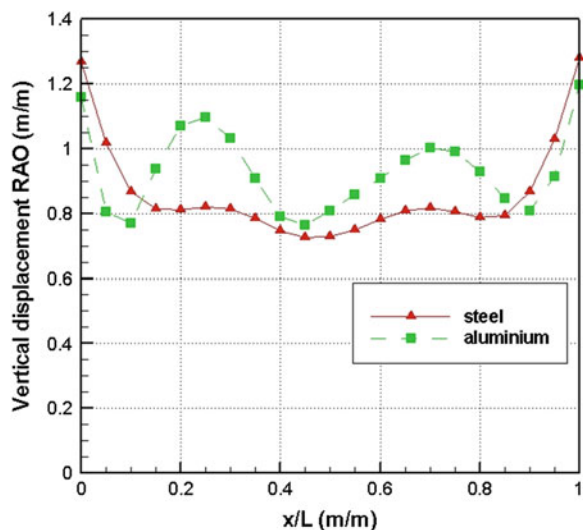
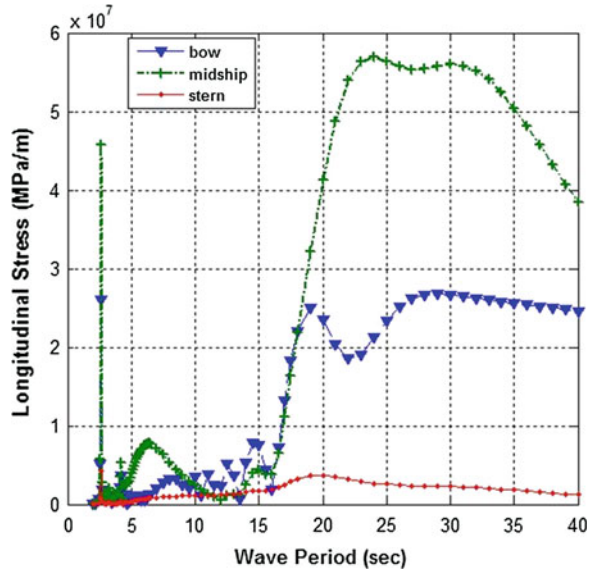


Fig. 8 Comparison of longitudinal stresses for 0° wave angle



that as the flexural rigidity decreases the vertical deflections increases for the Mega-float. The variation in vertical displacement is found to be higher at interior portion of the structure.

Longitudinal stresses for unit wave height are compared at bow, midship, and stern of the Mega-Float modeled with steel material. The stresses were obtained for 0° wave angle and are shown in Fig. 8. The peak near 2 s in the longitudinal stress coincides with the natural period of the structure. The stress is found to be less than 10 MPa for wave periods less than 17 s. The longitudinal stresses are found to be higher at midship of the Mega-Float compared to stern and bow.

5 Summary and Conclusions

A pontoon type VLFS or Mega-Float was analyzed using HYDRAN software and following conclusions were made for unit wave height excitation:

- Vertical displacements at edges of the structure were found to be 70–80 % higher than the midship section.
- Vertical displacements at the midship are negligible for lower wave periods and vertical displacements increases as the angle of attack increases from 0° to 90° .
- The responses of the structure along the longitudinal centerline increases with increase in the ratio of wavelength to structure length.
- With the variation in flexural rigidity the difference in vertical displacement is found to be higher at interior portion of the structure compared to the edges.
- The longitudinal stresses are found to be higher at midship compared to bow and stern of the mega-float.

References

1. Watanabe E, Utsunomiya T, Wang CM (2004) Hydroelastic analysis of pontoon type VLFS: a literature survey. *Eng Struct* 26:245–256
2. Suzuki H, Yoshida K (1996) Design flow and strategy for safety of very large floating structure. In: Proceedings of international workshop on very large floating structures, VLFS'96, Hayama, Japan, pp 21–27
3. ISSC (2006) Report of special task committee VI.2, very large floating structures. In: Proceedings of the 16th international ship and offshore structures congress, Southampton, UK, pp 391–442
4. Bishop RED, Price WG (1983) An introduction to ship hydroelasticity. *J Sound Vib* 87 (3):391–407
5. Price WG, Wu Y (1985) Hydroelasticity of marine structures. In: Niordson FI, Olhoff N (eds) *Theoretical and applied mechanics*. Elsevier Science Publishers B.V., Amsterdam, pp 311–337
6. Ruyin G (2012) Hydroelasticity of VLFS: allowances for flexible connectors, gill cells, arbitrary shapes and stochastic waves. PhD thesis, National university of Singapore
7. Newman JN (1994) Wave effects on deformable bodies. *Appl Ocean Res* 16(1):47–59
8. Riggs HR, Niimi KM, Huang LL (2007) Two benchmark problems for three-dimensional, linear hydroelasticity. *J Offshore Mech Arct Eng* 129:149–157

Coupled Acoustic-Structure Interaction in Cylindrical Liquid Storage Tank Subjected to Bi-directional Excitation

Aruna Rawat, Vasant Matsagar and A.K. Nagpal

Abstract Seismic response of ground-supported cylindrical liquid storage tank subjected to uni-directional harmonic base excitation and bi-directional components of earthquake is investigated using coupled acoustic-structure interaction approach. Finite element (FE) modeling of the liquid storage tank is carried out to evaluate sloshing displacement and base shear responses. Further, the seismic responses evaluated using the coupled acoustic-structure interaction approach are compared with that obtained using lumped mass (LM) model. The responses computed using the coupled acoustic-structure interaction analysis and the lumped mass model for estimating sloshing displacement and base shear are in good agreement.

Keywords Acoustic-structure interaction · Bi-directional earthquake · Finite element · Sloshing

1 Introduction

Liquid storage tanks are one of the lifeline structures used in water supply facilities, fire-fighting system, different industries, nuclear reactors for storage of various forms of liquid. Failure of these liquid storage tanks were reported in past earthquake events in the form of compression stresses due to buckling of tank wall, elephant foot buckling at the bottom of tank wall, sliding of the base, uplifting of base, sloshing of liquid causing damage to the roof and the top of the tank wall, failure of piping systems etc.

A. Rawat (✉) · V. Matsagar · A.K. Nagpal
Indian Institute of Technology (IIT) Delhi, New Delhi, India
e-mail: augupta2001@gmail.com

V. Matsagar
e-mail: matsagar@civil.iitd.ac.in

A.K. Nagpal
e-mail: aknagapal@civil.iitd.ac.in

There are numerous studies carried out on the seismic response of liquid storage tanks. Housner [1, 2] developed analytical model for fixed ground-supported cylindrical tank having rigid wall, using lumped mass approach with two degree-of-freedom. Convective and impulsive components of liquid vibration inside tank were considered. Veletsos [3] investigated flexible anchored tank and found that hydrodynamic pressure is dependent on the flexibility of the tank wall. Haroun and Housner [4] developed a three-mass model of ground-supported cylindrical liquid storage tank having flexible tank walls. Haroun [5] developed design charts to estimate the three lumped mass model and also carried out experiments of full-scale water storage tanks. Haroun and Tayal [6] used finite element method (FEM) for analyzing dynamic response of tanks. Simple procedure was developed for seismic analysis of liquid storage tank by Malhotra et al. [7] considering the first impulsive and convective modes. Virella et al. [8] investigated the dynamic response of cylindrical tanks subjected to horizontal ground excitation using finite element modeling in Abaqus. Mackerle [9] presented a bibliography of references based on fluid-structure interaction (FSI) problems.

The objectives of the present study are: (i) to compare the sloshing and base shear responses of fixed-base cylindrical liquid storage tank with lumped mass (LM) model [4] and three-dimensional (3-D) coupled acoustic-structure finite element (FE) model, (ii) to study the liquid storage tank behavior when it is subjected to uni-directional harmonic base excitation and bi-directional components of earthquake ground motions and (iii) to study seismic response of the tanks with two different aspect ratios, i.e. height of liquid to radius of the tank. The seismic analysis of 3-D liquid storage tank is carried out using the FE modeling in Abaqus® 6.11 [10] using coupled acoustic-structural approach, which considers the FSI.

2 Basic Governing Equations of Motion of Liquid Storage Tanks

According to the theory of fluid dynamics, for the irrotational, inviscid, frictionless liquid, the velocity distribution of liquid $v_x = \frac{\partial\phi}{\partial x}$, $v_y = \frac{\partial\phi}{\partial y}$, $v_z = \frac{\partial\phi}{\partial z}$ may be represented as a gradient of the velocity potential, $\phi(x, y, z, t)$, satisfies the Laplace equation, can be written in general three-dimensional space (x, y, z) as $\frac{\partial\phi^2}{\partial x^2} + \frac{\partial\phi^2}{\partial y^2} + \frac{\partial\phi^2}{\partial z^2} = 0$. The hydrodynamic pressure, p at any point and time is

$$p(x, y, z, t) = -\rho_L \frac{\partial\phi}{\partial t} \quad (1)$$

where ρ_L is the mass density of the liquid and t is time. The boundary condition at the rigid base of tank is given as $\frac{\partial\phi}{\partial z} = 0$ at $z = 0$, thus the liquid velocity in vertical direction is zero. The boundary condition along fluid-structure interface is

$$\frac{\partial p(x, y, z, t)}{\partial n} = -\rho_L a_n(x, y, z, t) \tag{2}$$

where a_n is the acceleration component along the direction vector for an outward pointing normal n , to the fluid region. On the free surface, it is assumed that the liquid forms small amplitude of wave, h , relative to the mean surface [11]. This condition is known as linearized surface wave condition, which accounts for gravity waves to be included in the analysis. The boundary condition at the free surface is

$$\frac{1}{g} \frac{\partial^2 p(x, y, z, t)}{\partial t^2} + \frac{\partial p(x, y, z, t)}{\partial z} = 0 \quad \text{at } z = H_L \tag{3}$$

where g is acceleration due to gravity. By applying the above boundary condition given in Eq. (3) on the free surface of liquid, the convective pressure distribution within the liquid can be calculated. The impulsive component of pressure distribution can be obtained by replacing the boundary condition Eq. (3) at the free surface with the condition $p = 0$ at $z = H_L$.

3 Modeling of Liquid Storage Tank

3.1 Lumped Mass (LM) Model

Lumped mass model is an analytical model proposed by Haroun and Housner [4] and is widely used for the dynamic analysis of flexible cylindrical ground-supported liquid storage tank on a rigid base. In this model the liquid in tank is assumed as three lumped masses as shown in Fig. 1. The top liquid which causes the sloshing phenomenon is called as convective mass (m_c), the middle portion of liquid which

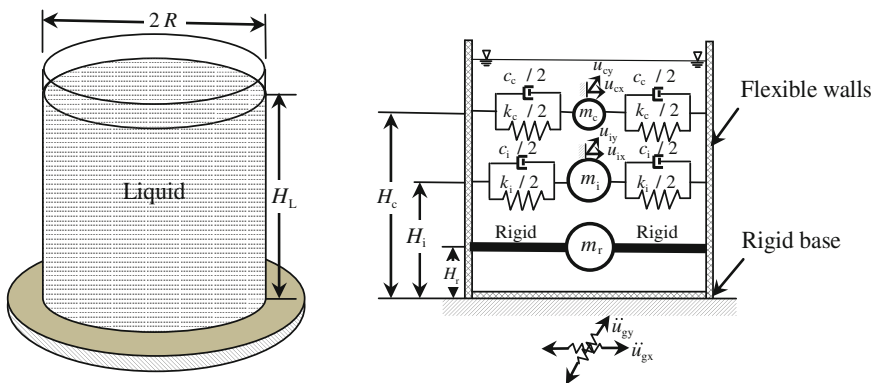


Fig. 1 Lumped mass (LM) model for fixed base cylindrical liquid storage tank [4]

accelerates along with the tank is called as impulsive mass (m_i) and the base liquid that moves rigidly along with the tank wall is rigid mass (m_r). These masses are lumped at the heights H_c , H_i and H_r respectively from bottom of the tank. The effective masses in terms of liquid mass of cylindrical tank are given in graphical form in Haroun [5] and in mathematical form by Shrimali and Jangid [12]. The maximum sloshing displacement of liquid surface as given by [5, 13] is

$$h_L = 0.837 \frac{RA_c}{g} \quad (4)$$

where $A_c = \omega_c^2 x_c$ is convective pseudo-acceleration, R is the radius of tank and ω_c natural frequency of convective mass.

3.2 Finite Element Model

Morand and Ohyan [14] and Wang and Bathe [15] used acoustic-structure interaction problems, in which fluid was modeled using acoustic element. In the present study the coupled acoustic-structure interaction is investigated using finite element method. Boundary impedance condition is used in FE model defined for the free surface of acoustic medium in order to model the sloshing behavior, taking into consideration the linearized wave condition. The impedance boundary condition at any point along an acoustic medium is

$$\dot{u}_{out} = \frac{1}{k_1} \dot{p} + \frac{1}{c_1} p \quad (5)$$

where \dot{u}_{out} is the acoustic particle velocity in the outward normal direction of the acoustic medium surface, p is the acoustic pressure, \dot{p} is the time rate of change of the acoustic pressure, $1/k_1 = 1/(\rho_L g)$ is the proportionality coefficient between the pressure and the displacement in the normal direction to the surface, and $1/c_1$ is the proportionality coefficient between the pressure and the velocity in normal direction to the surface [10]. The parameter ρ_L is the density of the liquid and g is the gravitational acceleration directed normal to the surface. By applying the above boundary condition sloshing or convective pressure distribution within the fluid domain can be obtained. And if only the impulsive component of the fluid response is to be obtained then above boundary condition at free surface of fluid is to be replaced by zero pressure condition.

In coupled acoustic-structure FE model, the liquid is modeled using eight-node three-dimensional continuum acoustic AC3D8R elements with reduced integration and hourglass control. The tank walls are modeled with four-node quadrilateral and triangular three-dimensional shell S4R and S3R element with reduced integration and hourglass control, respectively as shown in Fig. 2. The tank base is modeled using discrete rigid four-node and three-node R3D4 and R3D3 elements,

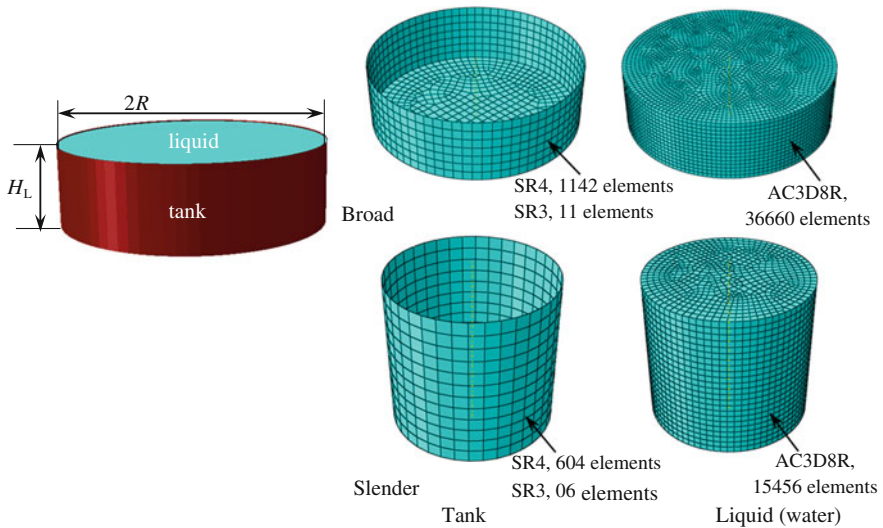


Fig. 2 Coupled acoustic-structure FE model for 3-D cylindrical liquid storage tank

respectively. The interaction between the tank walls and the acoustic medium is defined using a surface-based tie constraint which allows both the surfaces to remain in contact throughout the simulation process [10]. The earthquake ground motion is applied at the base of the tank in the form of acceleration boundary condition. An acoustic element has only pressure degree of freedom at each node. The acoustic pressure is calculated at the top surface of the liquid and the corresponding sloshing wave height h is obtained by $p = \rho_L g h$.

4 Numerical Study

In the present study, ground-supported cylindrical tanks are investigated under uni-directional harmonic base excitations for validation and bi-directional components of three different earthquake ground motions. The tank wall is made up of steel having density, $\rho_s = 7,900 \text{ kg/m}^3$, modulus of elasticity, $E_s = 200 \text{ GPa}$ and Poisson's ratio, $\mu = 0.3$. The liquid in tank is water having density $\rho_w = 1,000 \text{ kg/m}^3$ and bulk modulus, $K = 2,250 \text{ MPa}$. The broad and slender tanks with aspect ratio, i.e. height of liquid in tank to radius of tank ($S = H_L/R$), 0.6 and 1.85, respectively are used for the present study. The height of liquid in tank (H_L) is 14.3 and 11.3 m in broad and slender tanks, respectively. The thickness of tank walls is 0.0973 and 0.0244 m for broad and slender tanks, respectively. The damping ratio 2 % for tank and 0.5 % for liquid, respectively are adopted in the present study.

4.1 Response of Cylindrical Tank to Harmonic Ground Motions

In the present section, both the broad and slender tanks are subjected to uni-directional harmonic ground motion, $\ddot{x}_g = a_o e^{i\omega t}$ where a_o and ω are the amplitude and excitation frequencies, respectively. Amplitude in the range of 0.225–0.375 g and excitation frequency in the range of 1–3 Hz are considered for the study. The mesh convergence study is carried out for FE model and the smallest size in mesh is adopted as 0.09 m.

Figure 3 shows the time history responses of sloshing displacement for broad and slender tanks for FE and LM models. Fourier spectrum of sloshing height in broad tank is shown in Fig. 4. The peak values of the base shear and sloshing displacement of both the tanks using FE model are shown in Table 1 and are compared with the LM model. It is observed from the table that the base shear and sloshing displacement increases with an increase in the peak ground acceleration (PGA).

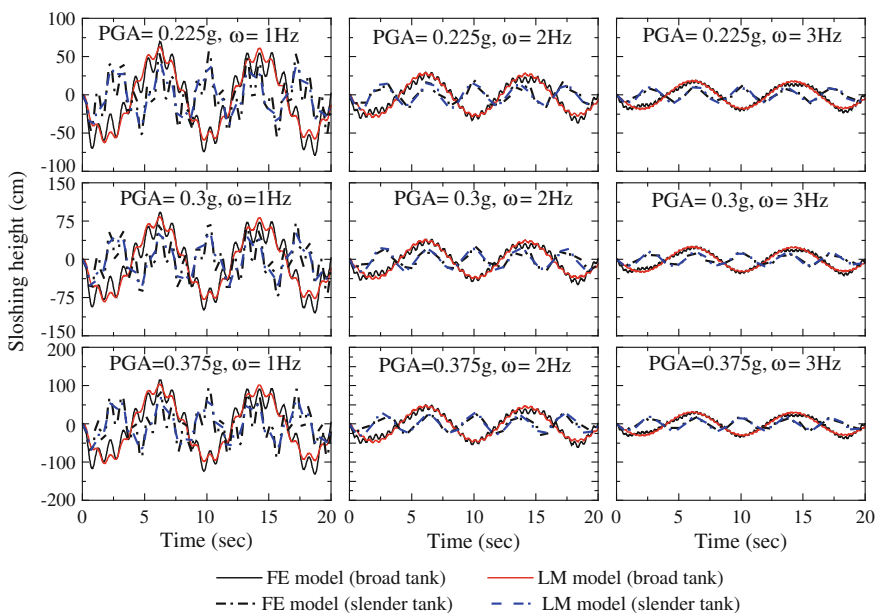


Fig. 3 Sloshing response of broad and slender tanks subjected to harmonic base excitations

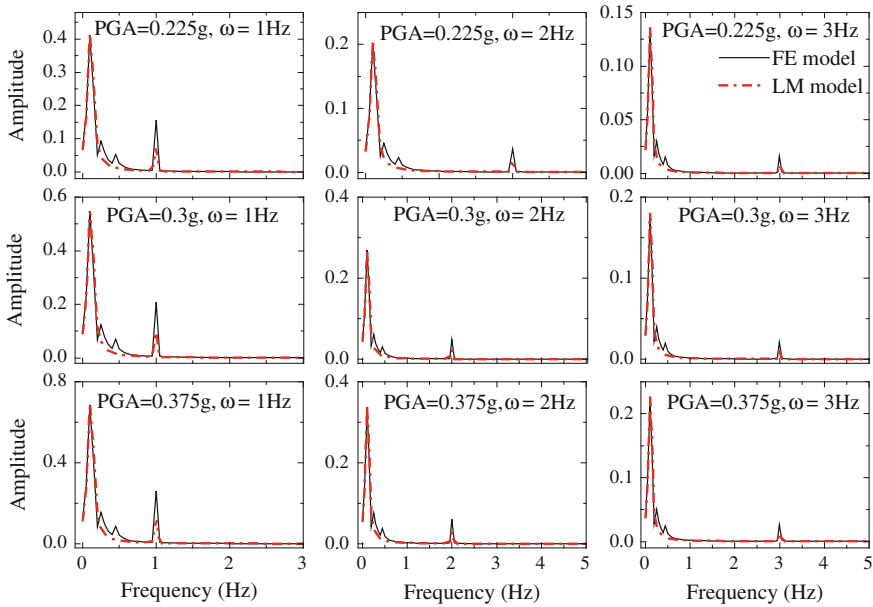


Fig. 4 Fourier spectrum of sloshing height of broad tank subjected to harmonic base excitations

Table 1 Maximum sloshing height and base shear for tank under harmonic base excitations

Aspect ratio (H_L/R)	PGA (g)	Excitation frequency (Hz)	Maximum sloshing height (cm)		Maximum base shear (MN)	
			LM model	FE model	LM model	FE model
0.6	0.225	1	62.41	78.74	50.57	51.22
		2	29.40	36.98	57.38	60.29
		3	19.09	23.42	106.69	119.10
	0.3	1	83.21	104.02	68.3	74.17
		2	39.20	49.31	80.33	80.39
		3	25.46	31.23	110.96	113.43
	0.375	1	104.01	131.23	85.37	91.35
		2	49.00	61.64	100.42	101.69
		3	31.83	39.04	177.81	198.50
1.8	0.225	1	41.91	56.20	4.62	4.88
		2	17.94	18.54	5.34	5.49
		3	11.31	11.33	5.69	6.11
	0.3	1	55.89	74.94	6.15	6.51
		2	23.93	24.72	7.12	7.33
		3	15.08	15.11	7.59	7.96
	0.375	1	69.86	93.68	7.69	8.13
		2	29.91	30.90	8.90	9.35
		3	18.85	18.89	9.49	9.97

4.2 Response to Bi-directional Components of Earthquake Ground Motions

The ground-supported cylindrical tanks are studied for bi-directional components of earthquake ground motion. The earthquake motion selected for the present study are Imperial Valley earthquake of 1940 California recorded at El Centro station, Kobe earthquake of 1995 recorded at Japan Meteorological Agency (JMA) station, Northridge earthquake of 1994 recorded at Sylmar station. The two components of peak ground acceleration (PGA) of Imperial Valley earthquake are 0.348 g and 0.214 g, Kobe earthquake are 0.834 g and 0.629 g and Northridge earthquake are 0.842 g and 0.604 g, respectively.

The acoustic pressure field variable are measured at the two extreme nodes from the centre of the tank in both x -direction ($\theta = 0^\circ$) and y -direction ($\theta = 90^\circ$) and the corresponding sloshing displacements are determined. Figure 5 shows the sloshing displacement time history responses for broad and slender tanks obtained by FE model and compared with LM model in both x -direction ($\theta = 0^\circ$) and y -direction ($\theta = 90^\circ$). The sloshing amplitude is more in case of Northridge earthquake in

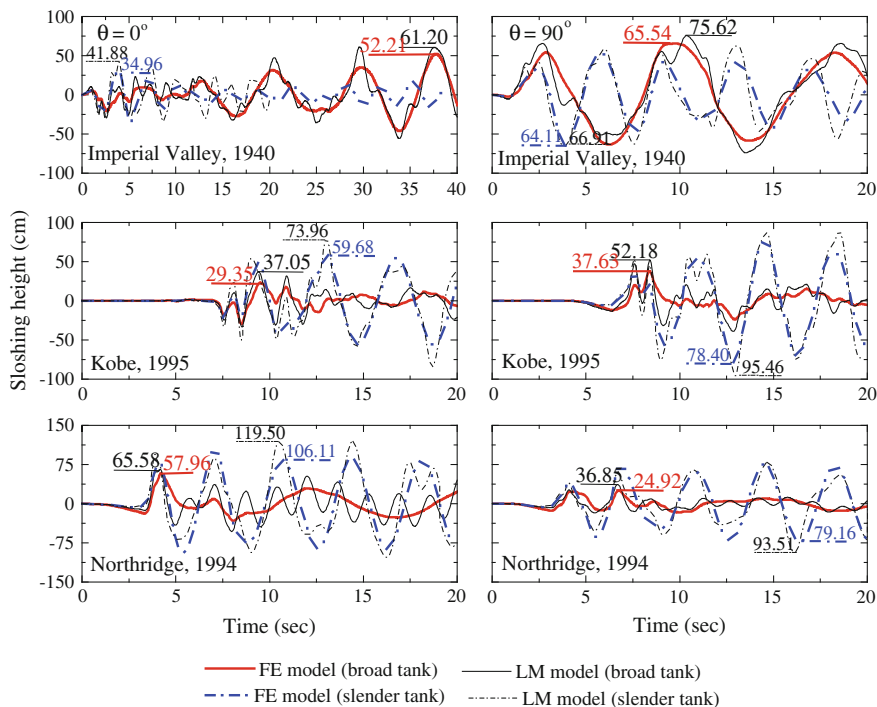


Fig. 5 Sloshing response in x -direction ($\theta = 0^\circ$) and y -direction ($\theta = 90^\circ$) of broad and slender tanks under bi-directional components of earthquake motions

Table 2 Maximum sloshing height for tank subjected to bi-directional components of earthquake ground motion

Aspect ratio (H_L/R)	Earthquake ground motion	Along x -axis ($\theta = 0^\circ$)		Along y -axis ($\theta = 90^\circ$)	
		LM model (cm)	FE model (cm)	LM model (cm)	FE model (cm)
0.6	Imperial Valley, 1940	52.21	61.20	65.54	75.62
	Kobe, 1995	29.35	37.05	37.63	52.18
	Northridge, 1994	57.96	65.58	24.92	36.85
1.8	Imperial Valley, 1940	34.96	41.88	64.11	66.91
	Kobe, 1995	59.68	73.96	78.40	95.46
	Northridge, 1994	106.11	119.50	79.16	93.51

x -direction due to higher PGA. Table 2 summarizes the maximum values of sloshing displacements for broad and slender tanks using FE and LM models. The plot shows the sloshing height in FE model are more by 15–20 % (average) than LM model. The FE model results into higher amplitude of sloshing displacement because it is based on real condition while in the LM model, the sloshing displacement is calculated from the horizontal displacement of convective mass considering its first convective mode only as given in Eq. (4).

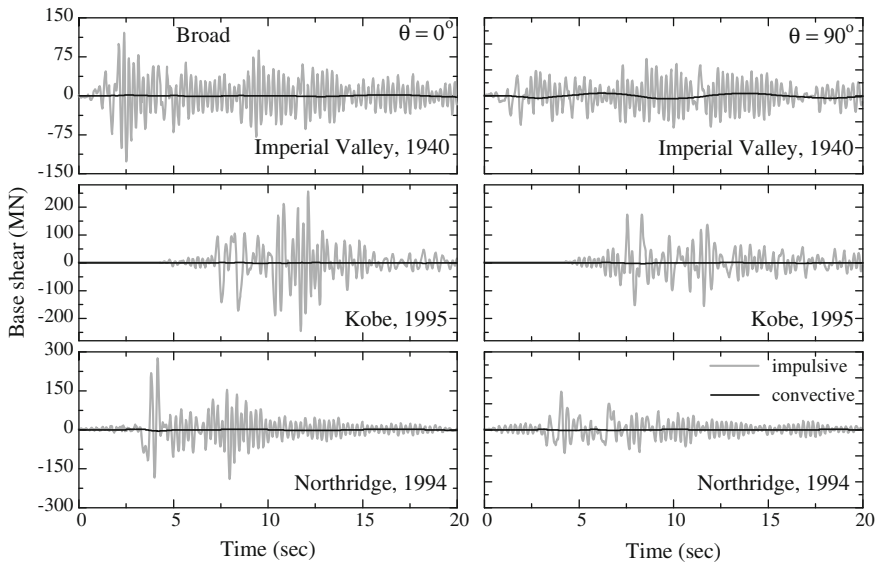


Fig. 6 Base shear time history responses in x -direction ($\theta = 0^\circ$) and y -direction ($\theta = 90^\circ$) for broad tank subjected to bi-directional components of earthquake ground motion using FE model

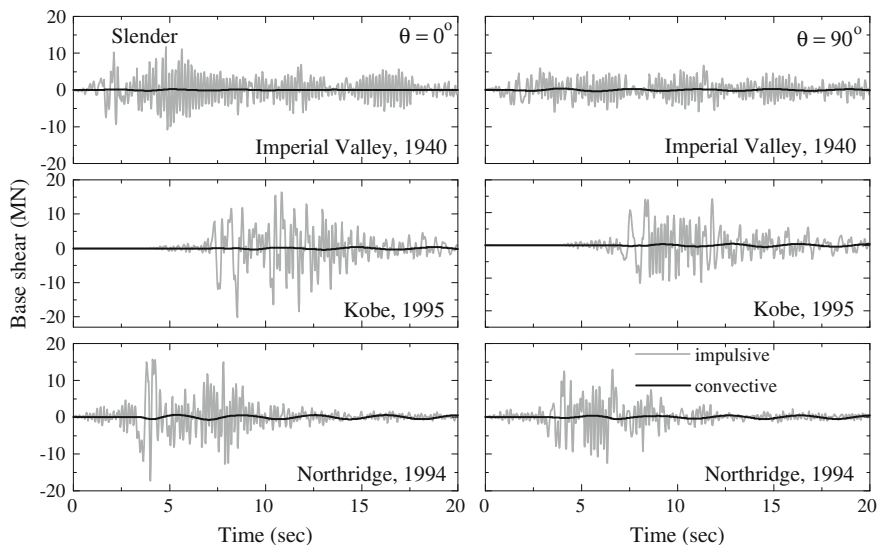


Fig. 7 Base shear time history responses in x - ($\theta = 0^\circ$) and y -directions ($\theta = 90^\circ$) for slender tank subjected to bi-directional components of earthquake ground motion using FE model

The base shear time history responses are shown in Fig. 6 for broad and Fig. 7 for slender tanks using FE model. The base shear values are less in case of slender tank in comparison to the broad tank. The impulsive hydrodynamic pressure has maximum value at the base of the tank and is the major contribution to the base shear occurring in the tank wall in comparison to the convective component. The maximum impulsive component and convective components of base shear in x - and y -directions are summarised in Tables 3 and 4, respectively. The FE model base shear is more by 4–6 % (average) than the LM model.

Table 3 Maximum impulsive component of base shear for tanks subjected to bi-directional components of earthquake ground motion

Aspect ratio (H_i/R)	Earthquake ground motion	Along x -axis ($\theta = 0^\circ$)		Along y -axis ($\theta = 90^\circ$)	
		LM model (MN)	FE model (MN)	LM model (MN)	FE model (MN)
0.6	Imperial Valley, 1940	126	127.08	95	96.05
	Kobe, 1995	256	258.32	171	173.21
	Northridge, 1994	273	274.92	144	145.43
1.8	Imperial Valley, 1940	11.57	12.41	6.53	7.04
	Kobe, 1995	20.21	21.34	14.07	15.62
	Northridge, 1994	17.42	19.03	12.78	14.47

Table 4 Maximum convective component of base shear for tanks subjected to bi-directional components of earthquake ground motion

Aspect ratio (H_t/R)	Earthquake ground motion	Along x -axis ($\theta = 0^\circ$)		Along y -axis ($\theta = 90^\circ$)	
		LM model (MN)	FE model (MN)	LM model (MN)	FE model (MN)
0.6	Imperial Valley, 1940	4.12	5.06	5.17	6.01
	Kobe, 1995	2.32	2.98	2.97	3.18
	Northridge, 1994	4.57	5.62	1.96	2.18
1.8	Imperial Valley, 1940	0.22	0.34	0.41	0.46
	Kobe, 1995	0.38	0.42	0.51	0.56
	Northridge, 1994	0.69	0.72	0.51	0.57

5 Conclusions

The simulation of ground-supported cylindrical liquid storage tanks subjected to uni-directional harmonic base excitations and bi-directional components of earthquake ground motion using coupled acoustic-structure interaction is performed herein and results are compared with lumped mass formulation results. A coupled acoustic-structure finite model has been developed for seismic analysis of ground-supported liquid storage tanks. The model accounts for convective and impulsive components by using appropriate boundary conditions at the top liquid surface. The difference in FE and LM models for maximum sloshing displacement is about 15–20 % (average) and for base shear it is 4–6 % (average). The difference in FE and LM models in sloshing response is due to the assumption that in LM model only the first convective mode has been considered in the analysis.

References

1. Housner GW (1957) Dynamic pressures on accelerated fluid containers. *Bull Seismol Soc Am* 55(1):15
2. Housner HW (1963) The dynamic behavior of water tanks. *Bull of Seismol Soc Am* 53 (2):381–389
3. Veletsos AS (1974) Seismic effects in flexible liquid storage tanks. In: *Proceeding of 5th world conference on earthquake engineering*, vol 1. Rome, Italy, pp 630–639
4. Haroun MA, Housner GW (1981) Seismic design of liquid storage tanks. *J Tech Counc ASCE* 107:191–207
5. Haroun MA (1983) Vibration studies and tests of liquid storage tanks. *Earthq Eng Struct Dyn* 11:179
6. Haroun MA, Tayal M (1985) Response of tanks to vertical seismic excitations. II. *Earthquake Eng Struct Dyn* 13:583–595

7. Malhotra PK, Wenk T, Wieland M (2000) Simple procedure for seismic analysis of liquid storage tanks. *Struct Eng Int* 10(3):197–201. International Association for Bridge and Structural Engineering (IABSE), Zurich, Switzerland
8. Virella J, Suarez L, Godoy L (2008) A static nonlinear procedure for the evaluation of the elastic buckling of anchored steel tanks due to earthquake. *J Earthq Eng* 12:999–1022
9. Mackerel J (1999) Fluid-structure problems, finite element and boundary element approaches: a bibliography (1995–1998). *Finite Elem Anal Des* 31:231–240
10. Abaqus/Implicit User's Manual, Version 6.11 (2011) Dassault Systèmes Simulia Corporation, Providence, Rhode Island, USA
11. Zienkiewicz OC, Taylor RL (2000) *The finite element method, volume 1: the basics*, 5th edn. Butterworth-Heinemann, Oxford
12. Shriali MK, Jangid RS (2002) Seismic response of liquid storage tanks isolated by sliding bearings. *Eng Struct* 24:907–919
13. European Committee for Standardization (2006) Eurocode 8: design of structures for earthquake resistance, part 4: silos, tanks and pipelines
14. Morand H, Ohayon R (1995) *Fluid structure interaction: applied numerical methods*. Wiley, New York
15. Wang X, Bathe K (1997) Displacement/pressure based mixed finite element formulations for acoustic fluid-structure interaction problems. *Int J Numer Meth Eng* 40:2001–2017

Behaviour of Elevated Water Storage Tanks Under Seismic Events

M.V. Waghmare, S.N. Madhekar and Vasant Matsagar

Abstract Liquid storage tanks are lifeline structures and strategically very important. Water tanks, in particular are important to the continued operation of water distribution system in the event of earthquakes. Most of the failures of large tanks after earthquakes are suspected to have resulted from the dynamic buckling caused by overturning moments of seismically induced liquid inertia and surface slosh waves. Recent earthquakes have shown that liquid storage tanks are found to be vulnerable to damage. The dynamic behaviour of liquid containing structures cannot be estimated by the same approach as for normal building structure as the weight of storage tanks varies in time because of variable liquid storage level. Also there exists sloshing of liquid which influences the response of the tank. Current knowledge about the behaviour of liquid storage tank is extensive, but many of the analytical and theoretical results are for tanks ground supported and open tanks. Therefore, appropriate modeling of the liquid storage tanks is essential for dynamic analysis and seismic response evaluation. In most of the research works, the liquid storage tank has been modeled using two mass model or three mass model concepts. The major difference of these two models is the number of lumped masses into which the liquid column is divided. The two-mass model is convenient for designers to use due to ease but the three-mass model predicts the seismic response more accurately. The objective of the study is to investigate the uncontrolled response of Steel and Reinforced Cement Concrete (RCC) Elevated Water reservoirs of different aspect ratio $S = H/R$ (height of the container to its radius) and subjected to different strong ground motion earthquakes. The simulation of water tank using three-mass model concept is carried out through MATLAB. The paper deals with two H/R ratios viz. 0.6 and 1.85. The governing equations of motion are solved by State Space

M.V. Waghmare (✉) · S.N. Madhekar
Department of Civil Engineering, College of Engineering, Pune, India
e-mail: mani_vw@yahoo.co.in

S.N. Madhekar
e-mail: snm.civil@coep.ac.in

V. Matsagar
Department of Civil Engineering, Indian Institute of Technology, Delhi, India
e-mail: vasant.matsagar@gmail.com

Method. In the first phase, the response of the tanks to different real earthquake ground excitations is investigated using simplified three mass model of the tank. In the second phase, characteristics of earthquakes are varied and emphasis is given to study their effect on response of the tanks. The response quantities such as sloshing displacement, impulsive displacement, tower displacement and base shear are measured by varying the characteristics of earthquake time history. It is observed that the sloshing displacement is highly influenced by the characteristics of the time history compared to other response quantities.

Keywords Earthquake · Seismic events · Sloshing · State space · Tank

1 Introduction

In dynamic analysis of structures most often it is assumed that the response of the structure depends upon the magnitude of the earthquake and its peak ground acceleration (PGA). However studies show that the seismic hazard depends upon characteristics of acceleration time history of the particular earthquake. Studies by researchers Anderson and Bertero [1], Uang and Bertero [2], and Bertero et al. [3], JP Singh and Associates, Richmond, California [4], have shown that earthquake ground motion attributes such as frequency content, duration, velocity, displacement, incremental velocity, and incremental displacement can have profound effects on the structural response than the peak ground acceleration. Shoji et al. [5], claimed that among various indices of earthquake ground motions, the maximum amplitude value and frequency content are considered as the most important indices for earthquake engineering. Though rigorous work on multi-storeyed building or ground supported tanks Kianoush and Ghaemmaghami [6], and Shekari et al. [7] is carried out in this area, such work has not been performed and reported in the literature for elevated water reservoir, Jacobsen [8], Epstein [9], Barton and Parker [10], Chen et al. [11], Liu and Schubert [12], Shrimali and Jangid [13], Livaoglu and Dogangun [14], Omidinasab and Shakib [15], Ozdemir et al. [16], Moslemi et al. [17], and Zhang et al. [18]. Due to their special dynamic characteristic, the seismic behaviour of the elevated liquid storage tank is highly complex. Therefore it is interesting to study the effect of characteristics of ground motion on behaviour of RCC and steel elevated water tank.

2 Modeling of Water Tank

In the present study two types of elevated tank materials viz. steel and concrete are considered with aspect ratio $S = H/R$ ratios as 0.6 and 1.85. The tank is modeled as 3 DOF system viz. sloshing displacements (d_1), impulsive displacements (d_2) and

rigid mass displacement or tower drift (d_3). MATLAB code has been written for State Space method to find out the response quantities.

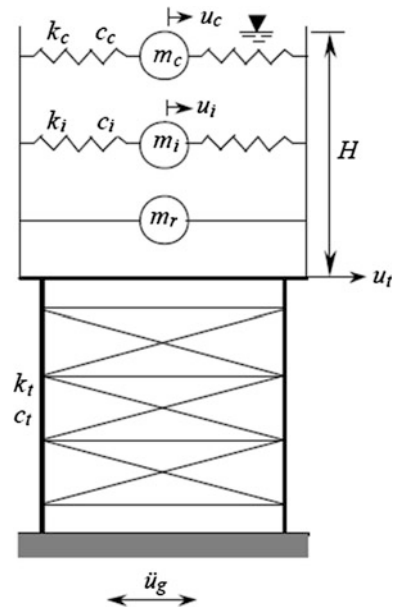
For obtaining the mathematical model of elevated water tank spring mass model for seismic analysis of tanks is considered to take into account fluid structure interaction. In order to include the effect of hydrodynamic pressure in the analysis, tank can be idealized by an equivalent spring mass model, which includes the effect of tank wall-liquid interaction. The sloshing, impulsive and rigid lumped masses are denoted by m_c , m_i and m_r , respectively. The convective and impulsive masses are connected to the tank wall by corresponding equivalent spring having stiffness k_c and k_i , respectively. The damping constant of the convective and impulsive masses are c_c and c_i , respectively. The tank has three-degrees-of-freedom under unidirectional excitation are viz. d_1 , d_2 and d_3 which denote the absolute displacements of convective mass, impulsive mass and tower, respectively. Mathematical model suggested by Shrimali and Jangid [13] is used to study and validate the response. The schematic diagram of the elevated liquid storage tank is shown in Fig. 1.

The equations of motion of elevated liquid storage tank subjected to unidirectional earthquake ground motion are expressed in the matrix form as

$$[m] = \begin{bmatrix} m_c & 0 & m_c \\ 0 & m_i & m_i \\ m_c & m_i & M + m_b \end{bmatrix} \tag{1}$$

$$[c] = \text{diag} [c_c, c_i, c_t] \tag{2}$$

Fig. 1 Elevation of model of elevated water tank, Shrimali and Jangid [13]



$$[k] = \text{diag} [k_c, k_i, k_t] \tag{3}$$

$$\{r\} = \{0, 0, 1\}^T \tag{4}$$

where $M = m_c + m_i + m_r$ is the effective mass of tank and m_b (mass of the tower) is equal to 0.05 m. The stiffness, k_t and damping, c_t of the tower structure based on the assumption of simple single-degree-of-freedom system are defined as

$$k_t = \left(\frac{2\pi}{T_t}\right)^2 (M + 0.05 \text{ m}) \tag{5}$$

$$c_t = 2\xi_t(M + 0.05)\omega_t \tag{6}$$

where T_t and ξ_t are time period and damping ratio of the tower structure [13]

3 Problem Formulation and Numerical Validation

In the first phase the tanks are subjected to time history records of five earthquakes viz. Chi–Chi (1999), Northridge (1994), El-Centro (1940), Kobe (1995), North Palm Spring (1986). In the second phase, the response is studied by considering 80, 90, 100, 110 and 120 % of the acceleration of the real earthquake ground motion. The tanks considered are cylindrical in shape and effective masses and stiffness are computed using Haroun’s model [19]. For comparative studies the properties of these tanks are given in Table 1. The tank is considered as filled to a height H with water. The damping ratio for the convective mass and the impulsive mass is taken as 0.5 and 2 %, respectively. For the tanks with steel wall the modulus of elasticity is taken as $E = 200 \text{ MPa}$ and the mass density, $\rho_s = 7,900 \text{ kg/m}^3$, time period of tower is taken as $T_s = 0.5 \text{ s}$. The results are validated with those of the Shrimali and Jangid [13].

Table 1 Properties of the tank

Material of tank	Type of tank	S = H/R	ω_c (Hz)	ω_i (Hz)
Steel	Broad	0.6	0.123	3.944
	Slender	1.85	0.273	5.963
RCC	Broad	0.6	0.123	2.48
	Slender	1.85	0.273	3.75

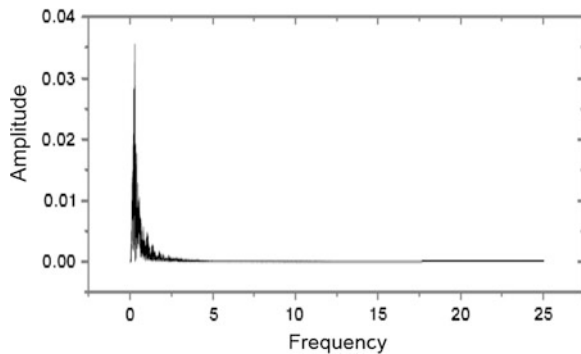
4 Characteristics of Earthquakes

For the present study five earthquakes viz. Chi–Chi (1999), Northridge (1994), El-Centro (1940), Kobe (1995), North Palm Spring (1986) are considered. Fast Fourier transform (FFT) is carried out on the time history of the earthquakes to get the frequency contents of the particular earthquake. The characteristics of these earthquakes are tabulated in Table 2 and are shown in Fig. 2 for Chi–Chi Earthquake.

Table 2 Characteristics of earthquakes

Earthquake	Date	Name of the fault	Magnitude on Richter scale	Number of frequency content (–0.12 to 0.12 Hz)	Number of frequency content (–0.28 to 0.28 Hz)
Chi–Chi	21 September 1999	Chelungpu fault	7.6	24	52
Northridge	17 January 1994	San Andreas or blind thrust fault	6.9	16	34
El-Centro	19 May 1940	–	7.1	14	30
Kobe	16 January 1995	–	6.9	40	86
North Palm Spring	8 July 1986	Banning fault or Garnet Hill fault	6.1	06	12

Fig. 2 FFT analysis—frequency–amplitude variation for Chi–Chi Earthquake



5 Response of the Water Tank

After time history analysis root mean square (RMS) displacements of all masses viz. convective mass (m_c), impulsive mass (m_i) and mass of tower (m_t) are noted and presented. Response of the water tank to all earthquakes is studied by changing the percentage of acceleration of time history records as 80, 90, 100, 110 and 120 %. The results of the time history analysis for response quantities such as RMS Displacements are presented through Fig. 3 for RCC tank with $S = 0.6$, Fig. 4 for Steel tank with $S = 0.6$. Figure 5 show the RMS displacements of RCC and steel tank with $S = 1.85$. Normalized Base shear are presented in Fig. 6.

The results clearly show that the response quantities viz. convective displacements (d_1), impulsive displacements (d_2), tower drift (d_3) and base shear are directly proportional to the percentage of acceleration. It is very interesting to note that frequency content of the earthquakes have played major role in the response. From Figs. 3 and 4, for broad tank it is observed that as for RCC tank sloshing frequency and impulsive frequency is 0.123 and 2.48 Hz respectively, resonance for convective (d_1) and impulsive displacement (d_2) has occurred in case of Chi-Chi earthquake which contains more number of low frequencies falling in this range. However for tower, resonance has occurred under Northridge earthquake which has comparatively more number of frequencies nearer to the natural frequency of the

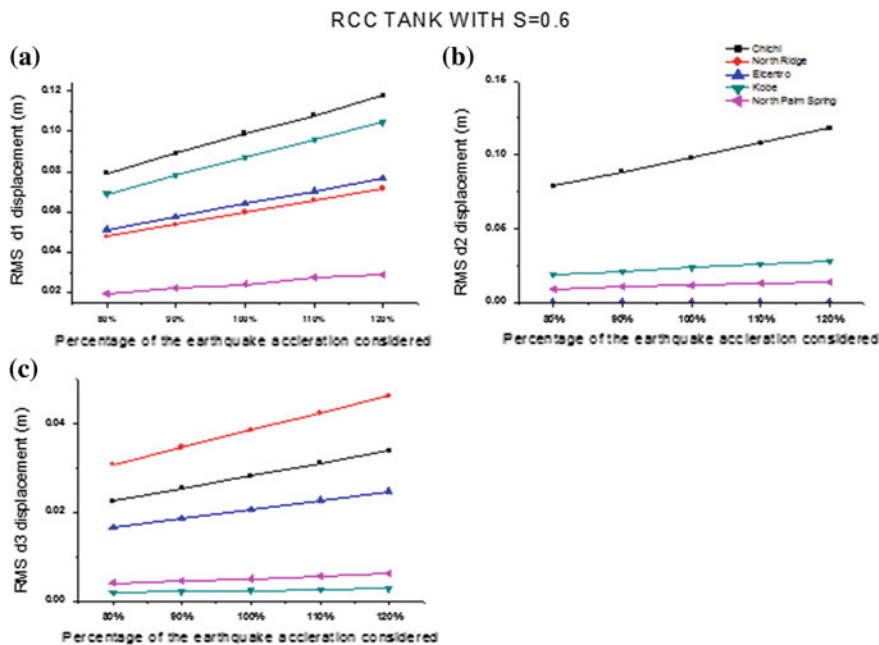


Fig. 3 RMS displacements for RCC tank with $S = 0.6$, **a** d_1 displacements, **b** d_2 displacements, **c** d_3 displacements

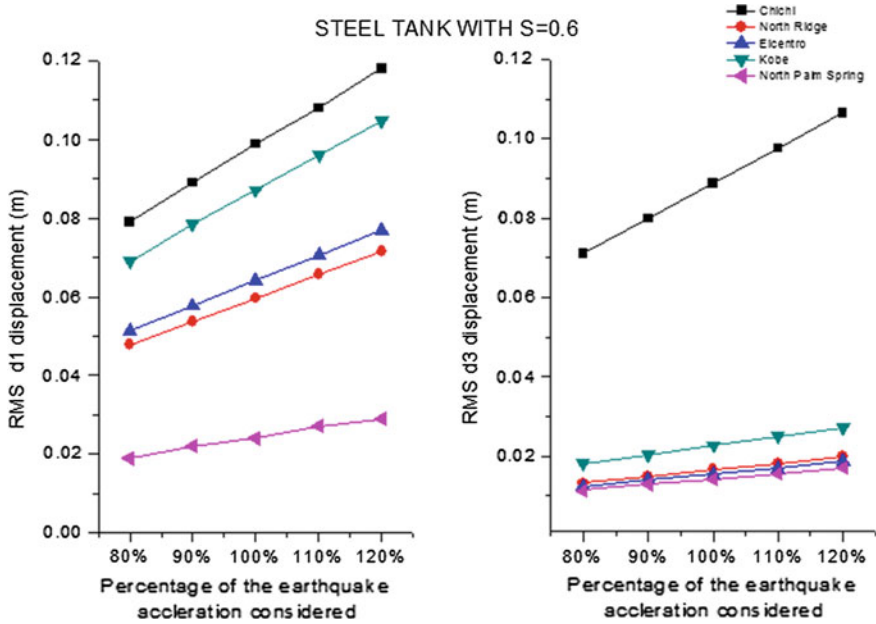


Fig. 4 RMS displacements for steel tank with $S = 0.6$

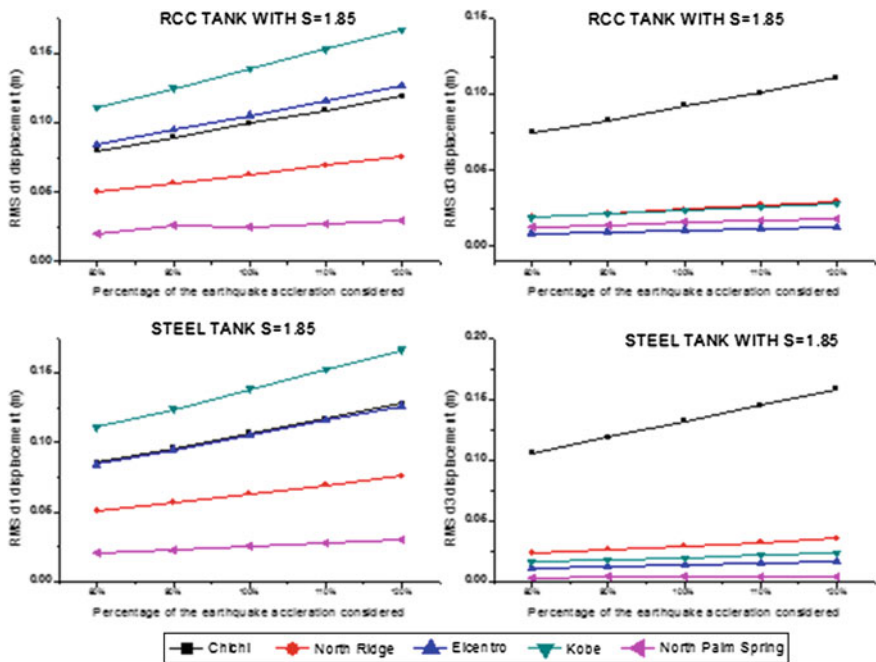


Fig. 5 RMS displacements for RCC and steel tank with $S = 1.85$

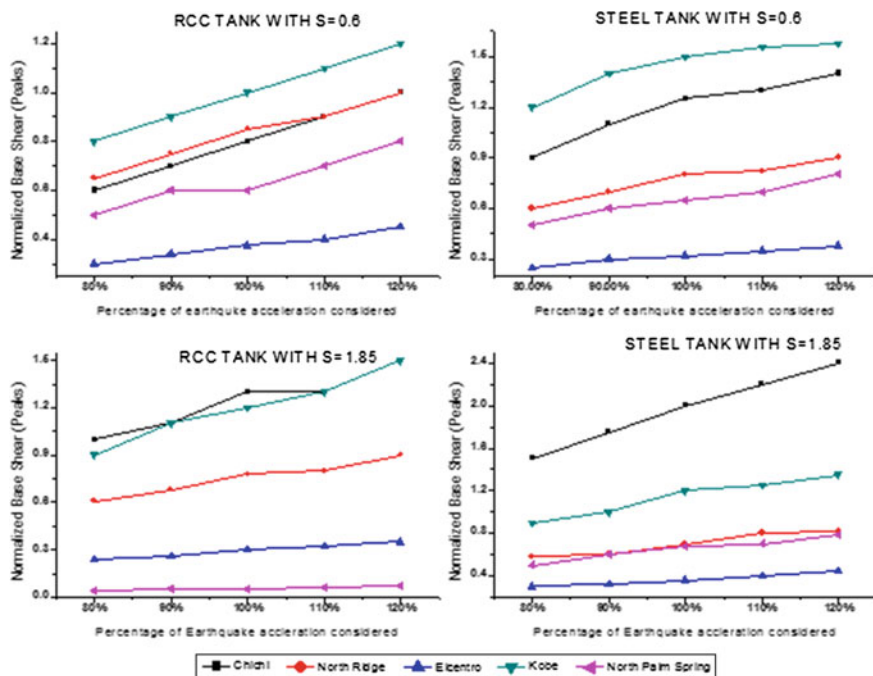


Fig. 6 Normalized base shear for RCC and steel tank with $S = 0.6$ and $S = 1.85$

tower than the other earthquakes. From Fig. 4, for broad steel tank with natural frequencies 0.123 and 3.94 Hz resonance is observed under the Kobe Earthquake for (d_1) and (d_3) displacement however RMS values for impulsive displacement (d_2) is zero. For slender tank with $S = 1.85$ it is seen from the results that only RMS Convective displacements (d_1) and tower drift (d_3) were observed for both RCC and steel elevated tank while RMS impulsive (d_2) displacements were absent. From Fig. 5, for slender RCC and steel tank resonance for sloshing displacement was observed under Kobe earthquake. Hence it is seen that aspect ratio ‘S’ plays a significant role in the analysis of the elevated tanks. It is interesting to note that for towers in most of the cases resonance has occurred under Chi–Chi earthquake except for broad RCC tank Therefore it is concluded that apart from aspect ratio material properties are also important in estimating the response of the elevated tanks subjected to seismic events. As resonance for convective displacement (d_1) has occurred during different earthquakes viz. Chi–Chi earthquake and Kobe earthquake it is observed that the sloshing displacement is highly influenced by the characteristics of the time history compared to other response quantities.

From Fig. 6 it is observed that base shear depends upon the amplitude, magnitude and on number of times the maximum amplitude frequencies hits the surface. Therefore, though in many of the above discussed cases resonance has occurred during Chi–Chi earthquake, as far as base shear is concerned Kobe earthquake governs the base shear of RCC as well as steel water tanks except the slender steel tank.

6 Conclusion

The following observations are based on the results presented in this paper

1. As the percentage of the earthquake considered increases or decreases the response quantities also increase or decrease.
2. Apart from frequency content material properties are also important for response of elevated water tank under seismic events.
3. It is observed that Base shear depends upon the amplitude, magnitude and on number of times the maximum amplitude frequencies hits the surface.
4. The dynamic behaviour of liquid containing structures cannot be estimated by the same approach as for normal building structure as the weight of storage tanks varies in time because of variable liquid storage level also there exists sloshing of liquid which influences the response of the tank.
5. In broad RCC tanks the total mass was divided into three parts giving response quantities viz. convective displacement, impulsive displacement and tower drift. However such response is not observed in case of broad steel tank and slender RCC and steel tanks.
6. Sloshing displacement is highly influenced by the characteristics of the time history compared to other response quantities.

References

1. Anderson JC, Bertero, VV (1987) Uncertainties in establishing design earthquakes. *J Struct Eng* 113(8):1709–1724
2. Uang C-M, Bertero, VV (1988) Implications of recorded earthquake ground motion on seismic design of building structures. *Earthquake Engineering, Research Center, University of California, Berkeley (UCB/EERC-88/13)*
3. Bertero VV, Anderson JC, Krawinkler H, Miranda E (1991) Design guidelines for ductility and drift limits: review of state-of-the-practice and state-of-the-art in ductility and drift-based earthquake-resistant design of tall buildings. *Earthquake Engineering Research Center, University of California, Berkeley (UCB/EERC-91/15)*
4. JP Singh and Associates, Richmond, California (1995) Seismic loading: code versus site specific. Portland regional seminar on seismic engineering issues
5. Shoji Y, Tanii K, Kamiyama M (2004) The duration and amplitude characteristics of earthquake ground motions with emphasis on local site effects. In: 13th world conference on earthquake engineering, Vancouver, B.C., Canada
6. Kianoush MR, Ghaemmaghami AR (2011) The effect of earthquake frequency content on the seismic behavior of concrete rectangular liquid tanks using the finite element method incorporating soil–structure interaction. *Eng Struct* 33(2011):2186–2200
7. Shekari MR, Khaji N, Ahmadi MT (2010) On the seismic behavior of cylindrical base-isolated liquid storage tanks excited by long-period ground motions. *Soil Dyn Earthq Eng* 30 (2010):968–980
8. Jacobsen LS (1949) Impulsive hydrodynamics of fluid inside a cylindrical tank and of fluid surrounding a cylindrical pier. *Bull Seismol Soc Am* 39:189–204

9. Epstein HI (1976) Seismic design of liquid storage tanks. *J Struct Div-ASCE* 102 (ST.9):1659–1673
10. Barton DC, Parker JV (1987) FEM analysis of the seismic response of anchored and unanchored liquid storage tanks. *Earthq Eng Struct Dyn* 15(3):299–322
11. Wei C, Haroun MA, Liu F (1996) Large amplitude liquid sloshing in seismically excited tanks. *Earthq Eng Struct Dyn* 25(7):653–669
12. Liu H, Schubert DH (2001) Effects of nonlinear geometric and material properties on the seismic response of fluid/tank system. American Water Works Association, D100
13. Shrimali MK, Jangid RS (2003) Earthquake response of isolated elevated liquid storage steel tanks. *J Constr Steel Res* 59(2003):1267–1288
14. Livaoglu R, Dogangun A (2006) Simplified seismic analysis procedures for elevated tanks considering fluid–structure–soil interaction. *J Fluids Struct* 22:421–439
15. Omidinasab, F, Shakib H (2008) Seismic vulnerability of elevated water tanks using performance based design. In: 14th world conference on earthquake engineering, Beijing, China
16. Ozdemir Z, Souli M, Fahjan YM (2010) Application of nonlinear fluid-structure interaction methods to seismic analysis of anchored and unanchored tanks. *Eng Struct* 32:409–423
17. Moslemi M, Kianoushi M, Pogorzelski W (2011) Seismic response of liquid-filled elevated tanks. *Eng Struct* 33:2074–2084
18. Zhang R, Weng D, Ren X (2011) Seismic analysis of a LNG storage tank isolated by a multiple friction pendulum system. *Earthq Eng Eng Vib* 10(2):253–262
19. Haroun MA, Housner GW (1982) Dynamic characteristics of liquid storage tanks. *J Struct Div-ASCE* 108(EM5):783–800

Bibliography

1. Asari Falguni P, Vanza MG (2012) Structural control system for elevated water tank. *Int J Adv Eng Res Stud* 1(3):325–328
2. Housner GW (1963) The dynamic behavior of water tanks. *Bull Seismol Soc Am* 53 (2):381–387
3. Tung ATY, Kiremidjian AS (1991) Seismic reliability analysis of elevated liquid-storage vessels. *J Struct Eng* 117:1372–1392

Assessing Seismic Base Isolation Systems for Liquid Storage Tanks using Fragility Analysis

Sandip Kumar Saha, Vasant Matsagar and Arvind K. Jain

Abstract Liquid storage tanks are essential component of petroleum industries, thermal power plants, chemical factories and numerous other important industries along with civil society. Herein, seismic fragility of base-isolated liquid storage tank is evaluated to assess the performance of various base isolation systems in enhancing the seismic protection. The liquid storage tank is modeled using lumped mass mechanical analog. Failure of the liquid storage tank is defined in terms of buckling of the tank wall in elastic range. The maximum displacement at isolation level is also considered in the failure criteria. The equations of motion are solved using Newmark's method to obtain the peak response quantities of the base-isolated liquid storage tank. Two different configurations, i.e. broad and slender, of the base-isolated liquid storage tanks are chosen for the comparison. Monte Carlo (MC) simulation is used to obtain the probability of failure (p_f) at different seismic intensity level. The probability of failure for the slender tank is observed more as compared to the broad tank. The seismic fragility of the base-isolated liquid storage tanks is evaluated considering the randomness in the earthquake ground motion. Seismic performance of fixed-base tanks are compared with the base-isolated tanks in terms of the probability of failure. It is observed that the base isolation enhances the seismic performance of the liquid storage tanks irrespective of the type of isolation system. However, enhancement in the seismic performance of the liquid storage tanks varies significantly for different isolation systems considered in the present study.

Keywords Base isolation · Earthquake · Fragility analysis · Monte Carlo simulation · Non-stationary earthquake · Tank

S.K. Saha (✉) · V. Matsagar · A.K. Jain
Department of Civil Engineering, Indian Institute of Technology (IIT) Delhi,
Hauz Khas, New Delhi 110016, India
e-mail: sandipksh@civil.iitd.ac.in

© Springer India 2015
V. Matsagar (ed.), *Advances in Structural Engineering*,
DOI 10.1007/978-81-322-2193-7_92

1177

1 Introduction

Importance of liquid storage tanks are enormous for several industries such as petroleum, power, chemical, food processing etc., along with civil society. Failure of such a lifeline structures during earthquakes may severely hinder the rescue and rehabilitation operation due to unavailability of power, water, and other basic needs. Various seismic base isolation systems were proposed during last few decades to protect strategically important and lifeline structures against devastating earthquakes around the world [1, 2, 5, 9, 10]. Shrimali and Jangid [16] compared the performance of elastomeric and sliding isolation systems to safeguard the liquid storage tanks against large earthquakes. Later, Seleemah and El-Sharkawy [15] compared the effectiveness of high damping rubber bearing (HDRB), lead-rubber bearing (New Zealand–NZ system) and friction pendulum system (FPS) as the base isolation systems for the liquid storage tanks. However, performance of other isolation systems, which consist of both the elastomeric and sliding components, such as resilient friction base isolator (RFBI) and Electric de France (EDF) system are not reported earlier for base isolation of liquid storage tank. Moreover, all the earlier studies, on the comparison of base isolation systems for liquid storage tank, were carried out considering the deterministic peak response quantities under few recorded earthquake ground motions. Nevertheless, performance of base isolation systems may vary with the randomness in the peak ground acceleration (PGA), frequency content, and duration of the earthquakes. Therefore, the effectiveness of the various isolation systems is required to be established considering the randomness in the earthquake excitation. Herein, performance of six different types of base isolation systems, namely (i) laminated rubber bearing (LRB), (ii) lead-rubber bearing (NZ system), (iii) pure friction (PF) system, (iv) friction pendulum system (FPS), (v) resilient friction base isolator (RFBI) and (vi) Electric de France (EDF) system, are assessed through development of seismic fragility curves for the base-isolated liquid storage tanks

2 Governing Equations of Motion for Base-Isolated Liquid Storage Tank

The mechanical analog proposed by Haroun and Housner [4] for liquid storage tank with flexible wall is adopted here. Figure 1 shows a schematic diagram of the base-isolated liquid storage tank with the three lumped masses and other parameters. The sloshing or convective mass (m_c), acting at a height of H_c , is considered to be in contact with the tank wall through a spring of stiffness, k_c . The impulsive mass (m_i), acting at a height of H_i , is considered to be in contact with the tank wall through a spring of stiffness, k_i . The rigid mass (m_r), acting at a height of H_r , is considered to be rigidly connected with the tank wall. The damping for sloshing component (ξ_c) is taken as 0.5 %, and that for impulsive component (ξ_i) as 2 % of the critical damping [3].

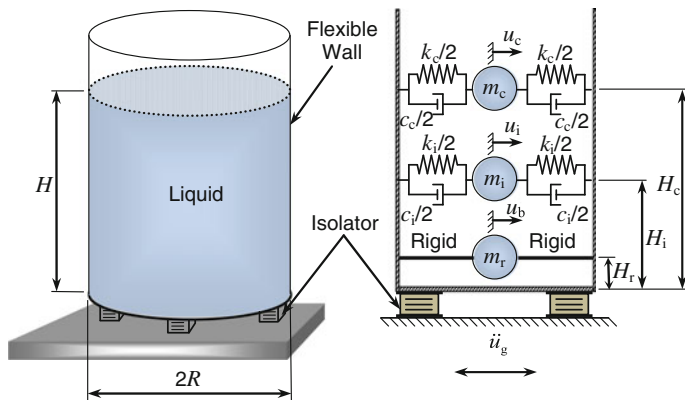


Fig. 1 Schematic diagram of base-isolated liquid storage tank under uni-directional earthquake

Here, the sloshing and impulsive damping coefficients are denoted by c_c and c_i , respectively. The lumped masses (m_c , m_i and m_r) are computed from the total mass of the liquid column ($= \pi \rho_w R^2 H$), neglecting the mass of the tank wall; here H and R denote the liquid column height and radius, respectively and ρ_w is the liquid mass density. The tank wall weight is ignored, as it is less than 5 % of the total weight. The coupled equations of motion under, uni-directional earthquake excitation is expressed as follows for,

$$\text{Sloshing mass :} \quad m_c \ddot{x}_c + c_c \dot{x}_c + k_c x_c = -m_c (\ddot{u}_g + \ddot{x}_b) \tag{1a}$$

$$\text{Impulsive mass :} \quad m_i \ddot{x}_i + c_i \dot{x}_i + k_i x_i = -m_i (\ddot{u}_g + \ddot{x}_b) \tag{1b}$$

$$\text{Rigid mass :} \quad m_c \ddot{x}_c + m_i \ddot{x}_i + F_b = -M (\ddot{u}_g + \ddot{x}_b) \tag{1c}$$

where, $x_c = (u_c - u_b)$ and $x_i = (u_i - u_b)$ are the relative displacements of the sloshing and impulsive masses, respectively, with respect to the isolator; $x_b = (u_b - u_g)$ is the relative displacement of the isolator with respect to the ground; m , c and k are the mass, damping and stiffness, respectively; subscripts c and i denote sloshing and impulsive masses, respectively; F_b is the restoring force developed in the isolations system; \ddot{u}_g is the uni-directional earthquake acceleration. Here, $M = m_c + m_i + m_r$ is the total dynamic mass of the base-isolated liquid storage tank; where, m_r denotes the rigid mass.

Schematic diagrams of the isolation systems considered herein are presented in Fig. 2. The restoring force (F_b) developed in the LRB is expressed as,

$$F_b = c_b \dot{x}_b + k_b x_b. \tag{2}$$

where, c_b and k_b denote the damping and stiffness of the LRB, respectively. The damping and stiffness of the LRB are generally represented in terms of the isolation

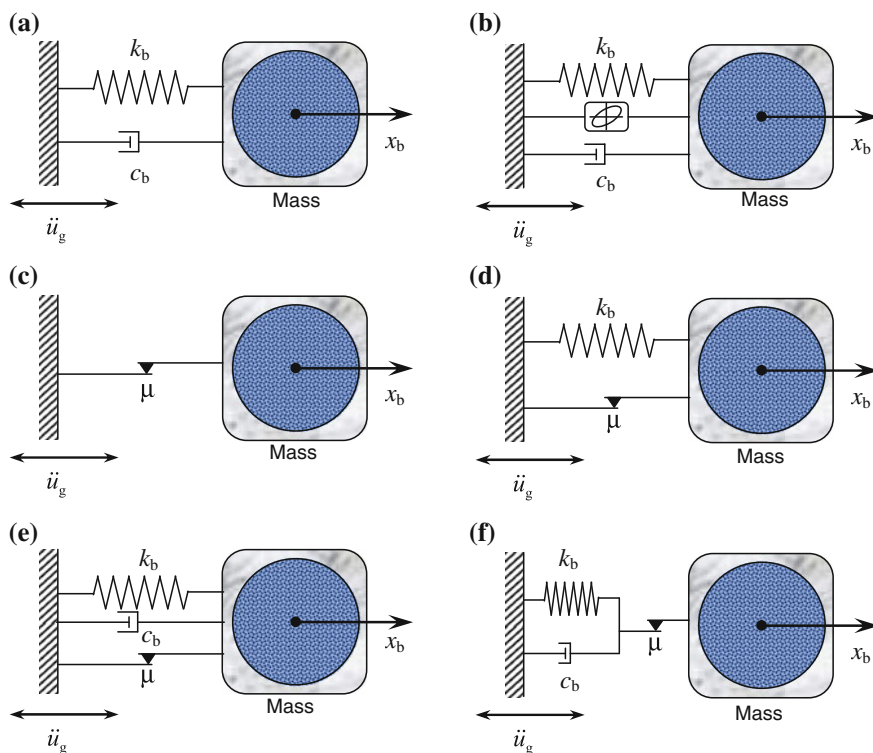


Fig. 2 Schematic diagrams of various isolation systems. **a** Laminated rubber bearing (LRB). **b** Lead-rubber bearing (NZ system). **c** Pure friction (PF) system. **d** Frictional pendulum system (FPS). **e** Resilient friction base isolator (RFBI), **f** Electric de France (EDF) system

damping ratio (ξ_b) and isolation time period (T_b), respectively. The restoring force (F_b) in the NZ system is given by the following equation [18].

$$F_b = c_b \dot{x}_b + k_b x_b + (1 - \alpha) F_y Z. \tag{3}$$

where, α is the post-yield to pre-yield stiffness ratio and Z denotes the non-dimensional hysteretic displacement component satisfying the following non-linear first order differential equation.

$$q\dot{Z} = A\dot{x}_b - \beta|\dot{x}_b Z|Z - \tau\dot{x}_b Z^2. \tag{4}$$

where, the constants A , β and τ define the non-linear hysteretic loop of the isolator. The limiting frictional force (F_s) in the PF system is given by,

$$F_s = \mu Mg \tag{5}$$

where, μ is the frictional coefficient and g is the gravitational acceleration. If the frictional force (F_x) is less than the limiting frictional force (i.e. $F_x < F_s$), then the system remains in non-sliding (stick) phase, and the restoring force (F_b) is given as,

$$F_b = F_x. \quad (6)$$

If the frictional force is more than the limiting frictional force (i.e. $F_x > F_s$), then the system remains in sliding (slip) phase. The restoring force (F_b) is given as,

$$F_b = F_s \text{sgn}(\dot{x}_b). \quad (7)$$

where, $\text{sgn}(\dot{x}_b)$ denotes the sign of the velocity corresponding to the isolation system.

The restoring force developed in FPS is given as,

$$F_b = F_x + k_b x_b. \quad (8)$$

where, k_b is the isolation stiffness provided by virtue of inward gravity action at the concave surface and F_x is the frictional force. The system is characterized by the isolation period (T_b) and friction coefficient (μ) of the concave surface.

The isolation restoring force developed in RFBI is given by,

$$F_b = c_b \dot{x}_b + k_b x_b + F_x. \quad (9)$$

where, c_b and k_b are the isolation damping and stiffness, respectively and F_x is the frictional force. The RFBI is characterized by three parameters, namely isolation time period (T_b), isolation damping ratio (ξ_b) and the friction coefficient of sliding surface (μ).

The force-deformation behavior of the EDF system is distinctly divided into two phases, i.e. stick and slip. Before sliding takes place (stick phase), the restoring force developed in the elastomeric layers is given by,

$$F_b = c_b \dot{x}_b + k_b x_b. \quad (10)$$

where, c_b and k_b are the isolation damping and stiffness, respectively. The sliding phase of the EDF system initiates once the restoring force exceeds the limiting friction force, $F_s = \mu Mg$. The resisting force (F_b) during the sliding phase remains constant, which is given by,

$$F_b = F_s \text{sgn}(\dot{x}_b). \quad (11)$$

The characteristic parameters of the EDF system are isolation time period (T_b), damping ratio (ξ_b) and friction coefficient (μ).

3 Stochastic Ground Motion Model

To address the non-stationary nature of the earthquake ground motion, a stochastic ground motion model, proposed by Rezaeian and Kiureghian [14], is considered here. According to this model, total duration (T_N) of the ground motion is discretized into N steps (i.e. $T_N = \Delta t \times N$). Then the ground acceleration ($\ddot{u}_g(t)$) is given by,

$$\ddot{u}_g(t) = f(t) \sum_{i=1}^k a_i(t) v_i, \quad \text{for } t_k \leq t < t_{k+1} \quad (12)$$

where, k can be any integer between 1 and N ; $f(t)$ denotes the modulation function which defines the variation of the acceleration amplitude; $a_i(t)$ denotes the filter function and v_i is any standard normal variable. Details of the procedure to obtain the distribution of the model parameters and generation of random ground acceleration can be found in Jacob et al. [6].

4 Numerical Solution

Newmark's step-by-step integration procedure is applied to numerically solve the equations of motion for obtaining the peak seismic response quantities. The linear variation of acceleration input is considered between two time steps. The time interval, Δt , is taken such that numerical solution is feasible for the earthquake ground motions in consideration.

5 Seismic Fragility Analysis

Seismic fragility is defined as the probability of failure for a given level of considered seismic intensity measure (IM) parameter. The failure can be expressed as the condition when the seismic demand (load) exceeds the structural capacity (resistance). Therefore, the seismic fragility is expressed in the following simple form.

$$Fragility \approx P[Dem > Cap|IM] \quad (13)$$

where, Dem represents the demand corresponding to specific level of a selected seismic intensity measure (IM), and Cap represents the structural capacity corresponding to a particular failure criterion. Here, the intensity measure parameter is considered as the PGA of the earthquake ground motion.

Two different limit states of failure are considered corresponding to (i) the tank wall buckling and (ii) isolation displacement. The tank wall buckling is defined by the critical base shear ($V_{b,cr}$) and the critical overturning moment ($M_{b,cr}$) corresponding to the elastic buckling of the tank wall. The critical values are computed as [13],

$$V_{b,cr} = \tau_{cr} \pi R t_s \quad (14)$$

and

$$M_{b,cr} = \sigma_{cr} \pi R^2 t_s \quad (15)$$

where, τ_{cr} and σ_{cr} are the elastic shear buckling stress and the elastic bending buckling stress, respectively. The elastic buckling stresses depend on the material and geometrical properties of the tank wall and expressed as,

$$\tau_{cr} = 0.07708 \frac{\pi^2 E_s}{(1 - \nu^2)^{5/8} \sqrt{\frac{H}{R}}} \left(\frac{R}{t_s}\right)^{-5/4} \quad (16)$$

and

$$\sigma_{cr} = \frac{1}{\sqrt{3(1 - \nu^2)}} \frac{E_s t_s}{R} \quad (17)$$

where, E_s and ν are the modulus of elasticity and Poisson's ratio of the tank wall material and t_s is the tank wall thickness. It can be noted here that the radius of the tank wall is almost equal to the radius of the liquid column ($R + t_s/2 \approx R$).

To define the limit state corresponding to the isolation displacement, the maximum design displacement of the isolator is considered. In most of the practical applications of the base isolation systems, the maximum design isolation displacement is considered as 250 mm; however, greater design displacement for the isolation systems is possible [11]. In the present study, the critical isolation displacement (D_{cr}) is considered as 250 mm irrespective of the isolation system. Therefore, to compute the probability of failure for the present study, the peak base shear (V_b) and peak overturning moment (M_b) are compared with the corresponding critical values (i.e. $V_{b,cr}$ and $M_{b,cr}$), and the peak base displacement (x_b) is compared with the critical base displacement (D_{cr}).

Based on the identified probability distribution of the earthquake ground motion model parameters, N_{sim} numbers of artificial earthquake acceleration time histories are generated using MC simulation. All the earthquake time histories are then normalized to a PGA level within the considered range of variation. Afterwards, the liquid storage tank model is analyzed for N_{sim} number of earthquake acceleration time histories, and the peak response quantities are determined. Thereafter, the

seismic demands are compared with the capacities as of the tank. Probability of failure (p_f) is computed for any particular PGA level as,

$$p_f = \frac{N_{\text{fail}}}{N_{\text{sim}}} \quad (18)$$

where, N_{fail} is the number of the cases when any one or all of the limit states are exceeded (i.e., the demand exceeds the corresponding capacity). The probability of failure is plotted against the corresponding PGA level to obtain a failure point. The procedure is then repeated for a range of PGA levels, and the fragility curve is obtained by joining the failure points. For the present study, the number of simulation for the computation of probability of failure is considered as 1,000.

6 Numerical Study

Herein, the seismic fragility of base-isolated liquid storage tank is evaluated for both the broad ($S = 0.6$) and slender ($S = 1.85$) tank configurations, where $S = H/R$. The height of the liquid column in the broad tank is taken as 14.6 m, whereas that for the slender tank is taken as 11.3 m. In both the cases, the tank wall is considered to be made of steel, and the liquid is considered as water. The ratio of the tank wall thickness to the radius (i.e. t_s/R) is taken as 0.001. The critical base shears for the broad and slender tanks are computed as $0.19 W$ and $0.11 W$, respectively, where $W = Mg$ is the total weight of the tank. The critical overturning moments are computed as $14.89 W\text{-m}$ and $3.84 W\text{-m}$ corresponding to the broad and slender tanks, respectively.

6.1 Comparison of Fragility Curves for Different Isolation Systems

The fragility curves for the liquid storage tanks (broad and slender), base-isolated using LRB ($T_b = 2$ s, $\xi_b = 0.1$), NZ system ($T_b = 2.5$ s, $\xi_b = 0.05$, $q = 2.5$ cm and $F_y/W = 0.05$), PF system ($\mu = 0.1$), FPS ($T_b = 2.5$ s and $\mu = 0.05$), RFBI ($T_b = 4$ s, $\xi_b = 0.1$ and $\mu = 0.04$) and EDF system ($\mu = 0.2$ and $q = 5$ cm), are compared. The parameters of the different isolation systems are selected based on commonly used values in practice. Similar range of the isolator parameters were also considered in several earlier studies [7, 12, 17]. Monte Carlo (MC) simulation is used to obtain the probability of failure. The base-isolated liquid storage tanks are analyzed under 1,000 randomly generated earthquake ground motions, scaled to a particular PGA level. Thereafter, the seismic demands (peak response quantities, i.e. V_b , M_b and x_b) are compared with respective capacities (i.e. $V_{b,\text{cr}}$, $M_{b,\text{cr}}$ and D_{cr}) to obtain the probability of failure at each PGA level. Figure 3 shows the comparison of the

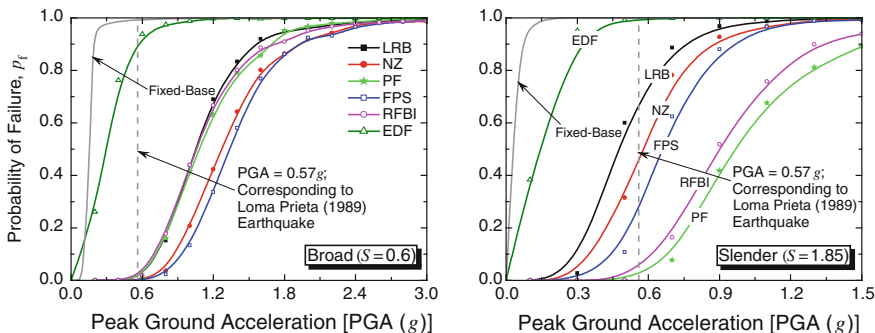


Fig. 3 Fragility curves for fixed-base and base-isolated liquid storage tanks

fragility curves obtained for the broad and slender base-isolated liquid storage tanks. The PGA corresponding to the Loma Prieta (1989) earthquake, recorded at Los Gatos Presentation Centre, (0.57 g) is shown along with the fragility curves to visually compare the probabilities of failure for the broad and slender liquid storage tanks. Significant difference among the seismic fragility curves is observed when the liquid storage tank is isolated using different isolation systems, especially for slender tank configuration. The slope of the fragility curves of liquid storage tanks, isolated using EDF system, is highest for both the tank configurations. It indicates that the EDF system is less effective as compared to other isolation systems considered in the present study. For the chosen parameters of the liquid storage tanks and the isolation systems, the FPS is observed to be the most effective for the broad tank, whereas the PF system is observed as the most effective for the slender tank.

Further, to investigate the predominant failure criterion for different isolation systems, probability of failure for the base-isolated liquid storage tank is obtained separately corresponding to (i) the tanks wall buckling ($V_{b,cr}$ and $M_{b,cr}$) and (ii) the critical isolation displacement (D_{cr}). Figure 4 shows the fragility curves corresponding to tank wall buckling criterion and maximum isolation displacement criterion. It is observed that the tank wall buckling governs in the case of LRB, NZ system, FPS, and EDF system; whereas for PF system and RFBI critical isolator displacement governs the failure for both the broad and slender tank configurations. It can be noted that for PF system, no failure is observed due to the tank wall buckling. It is owing to the fact that the peak base shear (V_b in terms of W) in the tank wall cannot be more than the friction coefficient ($\mu = 0.1$), which is less than the capacities of both the tank configurations. Moreover, mean values of the overturning moment is computed as 0.74 W -m for the broad tank at 3 g PGA, and 0.73 W -m at 2 g PGA, for the slender tank, which are significantly less than the computed capacities. Therefore, the critical isolation displacement criterion governs the failure of the liquid storage tanks base-isolated using the PF system.

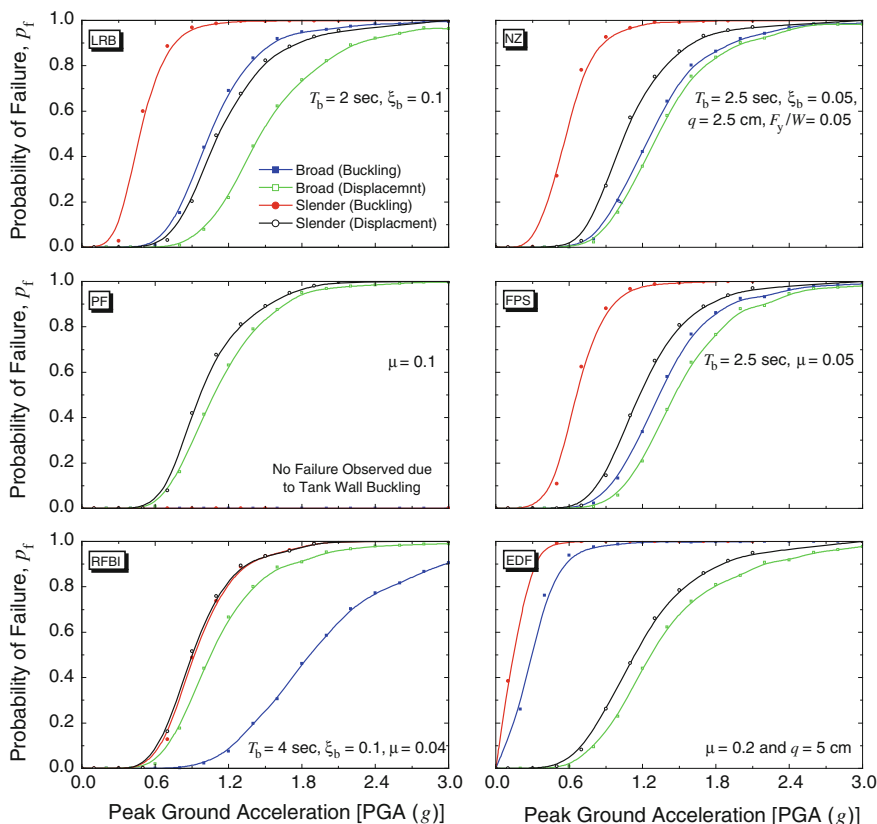


Fig. 4 Fragility curves for liquid storage tanks corresponding to tank wall buckling limit state and isolation displacement limit state

6.2 Effect of Isolator Parameters on Fragility Curves

Herein, the effects of variation in the parameters for different isolation systems (FPS and RFBI) on the seismic fragility of base-isolated liquid storage tanks are studied. Seismic fragility curves of the broad and slender base-isolated liquid storage tanks, corresponding to different isolation time period (T_b), are shown in Figs. 5 and 6 for the FPS and RFBI, respectively. The isolation time period for both the isolation systems is varied from 1 to 4 s with 1 s increment. The friction coefficient (μ) for the FPS is kept constant at 0.05. The friction coefficient (μ) and damping ratio (ξ_b) of the RFBI are kept constant at 0.04 and 0.1, respectively.

For both the isolation systems, slope of the fragility curves decreases with increasing isolation time period. This is because of the fact that the higher isolation time period makes the structure more flexible, which in turn attracts less seismic force. However, for FPS system the fragility curve of the broad tank for $T_b = 4 \text{ s}$,

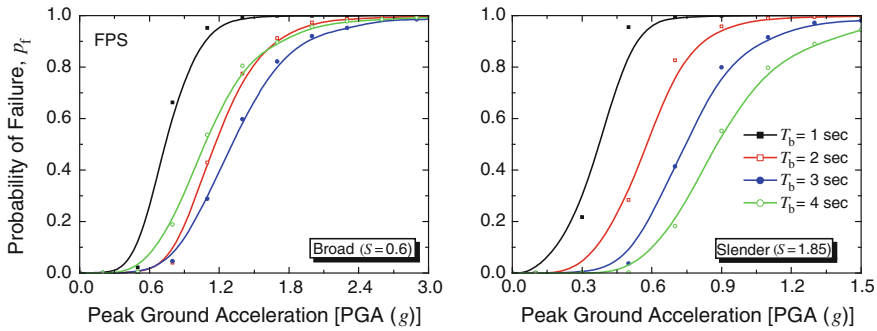


Fig. 5 Effect of the isolation time period variation on the fragility curves for liquid storage tanks, base-isolated using FPS

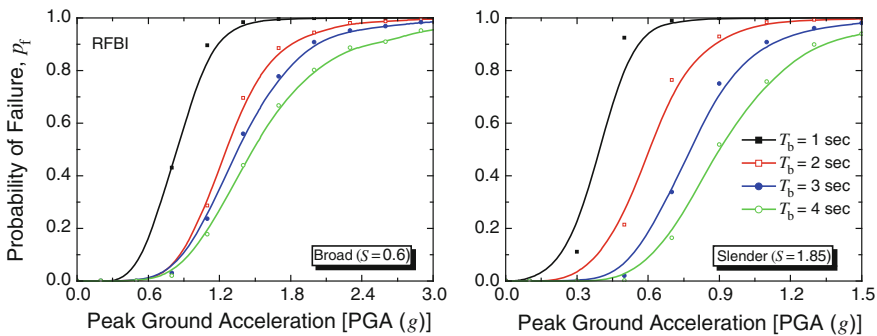


Fig. 6 Effect of the isolation time period variation on the fragility curves for liquid storage tanks, base-isolated using RFBI

shows steeper slope as compared to the curves for $T_b = 2$ s and $T_b = 3$ s. This is owing to the fact that with higher time period of the isolation system, the isolation displacement is also expected to be higher. Therefore, there are higher possibilities that the isolation displacement (x_b) exceeds the critical value (D_{cr}). To investigate this observation, probabilities of failure at various PGA levels, due to exceedance of the tank wall buckling limit and the isolation displacement limit, are presented corresponding to different isolation time period in Table 1 for the FPS. It is clearly seen from Table 1 that the probabilities of failure due to exceedance of the tank wall buckling limit decreases with increasing isolation time period. Nevertheless, the probabilities of failure due to the exceedance of isolation displacement limit increase rapidly with increase in the isolation time period. Further, for the broad tank, the failure occurs due to tank wall buckling at the lower isolation time periods (i.e. 1 and 2 s). However, at higher isolation time periods (i.e. 3 and 4 s) critical isolation displacement exceedance governs the failure. Therefore, the design isolation time period for FPS should be decided judiciously to avoid failure due to excessive isolation displacement.

Table 1 Probability of failure (p_f) with increasing isolation time period (T_b) for FPS

Time period (T_b) (s) \rightarrow	Buckling limit exceedance				Displacement limit exceedance				
	1	2	3	4	1	2	3	4	
Broad ($S = 0.6$)	PGA, $g \downarrow$								
	0.2	0	0	0	0	0	0	0	0
	0.5	0.021	0	0	0	0	0	0	0.005
	0.8	0.662	0.04	0.017	0.004	0	0	0.045	0.188
	1.1	0.952	0.429	0.146	0.052	0.001	0.025	0.288	0.536
	1.4	0.993	0.774	0.392	0.243	0.001	0.216	0.597	0.804
	1.7	0.998	0.912	0.697	0.44	0.028	0.514	0.821	0.896
	2	0.999	0.973	0.817	0.648	0.148	0.758	0.919	0.956
	0.3	0.217	0	0	0	0	0	0	0
	0.5	0.954	0.283	0.037	0.002	0	0	0	0.002
Slender ($S = 1.85$)	0.7	0.995	0.826	0.414	0.182	0	0.002	0.045	0.151
	0.9	0.999	0.958	0.798	0.551	0	0.034	0.28	0.511
	1.1	1	0.989	0.915	0.797	0.003	0.187	0.556	0.763
	1.3	1	0.979	0.971	0.889	0.034	0.455	0.774	0.87
	1.5	1	0.999	0.98	0.944	0.109	0.691	0.877	0.936

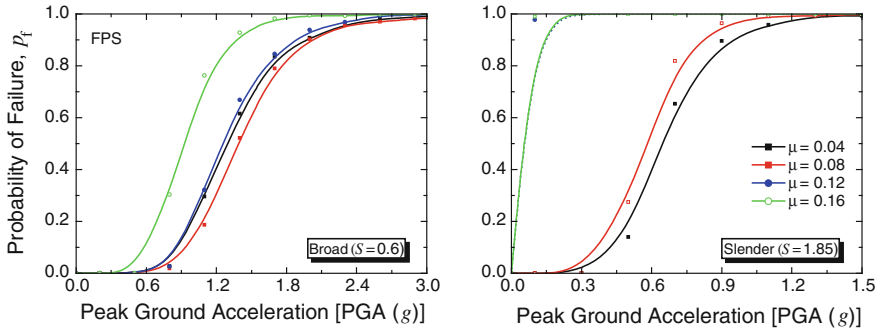


Fig. 7 Effect of the friction coefficient variation on the fragility curves for liquid storage tanks, base-isolated using FPS

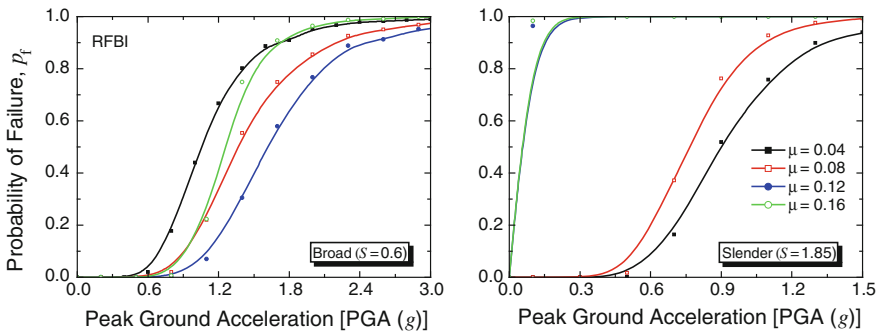


Fig. 8 Effect of the friction coefficient variation on the fragility curves for liquid storage tanks, base-isolated using RFBI

Figures 7 and 8 show the effect of the friction coefficient variation on the seismic fragility of base-isolated liquid storage tanks for the FPS and RFBI, respectively. It is observed that for the slender tank, probability of failure increases with increase in the friction coefficient for both the isolation systems, i.e. FPS and RFBI. Moreover, the probabilities of failure in the slender tank abruptly increase when the friction coefficient is increased from 0.08 to 0.12. This is attributed to the fact that the critical base shear (capacity, i.e. $V_{b,cr}$), which governs the tank wall buckling, lies in this range ($0.11 W$). Therefore, as the friction coefficient overcomes the critical base shear ($V_{b,cr}$ in terms of W) the tank wall buckling governs the failure of the base-isolated liquid storage tank for both the isolation systems, i.e. FPS and RFBI. Therefore, while designing friction coefficient for the FPS and RFBI, the capacity of the tank should be taken into consideration.

For the broad tank, critical base shear ($V_{b,cr} = 0.19 W$) is beyond the range of the considered variation of the friction coefficient. Therefore, effect of the friction coefficient variation on the fragility curves is not similar as compared to the effect of friction coefficient variation on the slender tank. It is observed from Fig. 7 that the

Table 2 Probability of failure (p_f) with increasing friction coefficient (μ) for broad tank ($S = 0.6$)

Friction coefficient (μ) \rightarrow	PGA, $g \downarrow$	Buckling limit exceedance					Displacement limit exceedance					
		0.04	0.08	0.12	0.16	0.20	0.04	0.08	0.12	0.16	0.20	
FPS ($T_b = 2.5$ s)	0.2	0	0	0	0	0	0	0	0	0	0	0
	0.5	0	0	0	0	0	0	0	0	0	0	0
	0.8	0.027	0.018	0.026	0.303	0.001	0.011	0.004	0.001	0	0	0
	1.1	0.295	0.186	0.321	0.762	0.026	0.224	0.026	0.01	0.002	0	0
	1.4	0.615	0.521	0.668	0.928	0.189	0.54	0.189	0.064	0.017	0	0
	1.7	0.835	0.789	0.845	0.982	0.466	0.796	0.466	0.233	0.093	0	0
RFBI ($T_b = 4$ s, $\xi_b = 0.1$)	2	0.908	0.901	0.938	0.994	0.684	0.895	0.684	0.475	0.271	0	0
	0.2	0	0	0	0	0	0	0	0	0	0	0
	0.5	0	0	0	0	0	0.01	0	0	0	0	0
	0.8	0.001	0.002	0.001	0.006	0.019	0.177	0.019	0.001	0.001	0	0
	1.1	0.049	0.027	0.064	0.223	0.22	0.553	0.22	0.068	0.018	0	0
	1.4	0.198	0.176	0.292	0.748	0.553	0.801	0.553	0.299	0.123	0	0
	1.7	0.252	0.404	0.573	0.907	0.749	0.844	0.749	0.559	0.343	0	0
	2	0.586	0.641	0.766	0.964	0.855	0.952	0.855	0.74	0.585	0	0

slope of the fragility curve, for the broad liquid storage tank base-isolated using the FPS, decreases when the friction coefficient (μ) decreases from 0.16 to 0.08. However, the slope of the fragility curve obtained for $\mu = 0.04$ is comparatively more than the same obtained for $\mu = 0.08$. For the broad liquid storage tank, base-isolated using the RFBI, slope of the fragility curve decreases with increase in the friction coefficient from 0.04 to 0.12. However, the slope of the fragility curve suddenly increases for $\mu = 0.16$, especially at the higher PGA level.

The probabilities of failure due to exceedance of the tank wall buckling and critical isolation displacement are presented in Table 2 for the FPS and RFBI, respectively at various PGA levels to investigate these observations further. It is observed that the probabilities of failure corresponding to the critical isolation displacement decrease with increasing friction coefficient for the broad liquid storage tank, base-isolated using the FPS. However, the probabilities of failure due to tank wall buckling decrease initially (for $\mu = 0.04$ to $\mu = 0.08$), then it increase as the friction coefficient increases. Therefore, there exists an optimum value of the friction coefficient in the range of 0.04–0.08, for which probability of failure due to tank wall buckling is the lowest. It can be noted here, that for buildings and bridges, the optimum range of the friction coefficient corresponding to the FPS was reported as 0.05–0.15 [8]. In case of the broad liquid storage tank, base-isolated using the RFBI, it is observed that the dominant mode of failure changes from isolation displacement to tank wall buckling when the friction coefficient vary from 0.08 to 0.12. Moreover, the probability of failure due tank wall buckling increases rapidly as the friction coefficient increases further. Therefore, there exists an optimum range of the friction coefficient in the range of 0.08–0.12 for the RFBI.

7 Conclusions

Seismic fragility of base-isolated liquid storage tank is evaluated to assess the performance of various base isolation systems to enhance the seismic protection level. The liquid storage tank is modeled using lumped mass mechanical analog. Failure of the liquid storage tank is defined in terms of buckling of the tank wall in elastic range and maximum isolation displacement. Two different configurations, i.e. broad and slender, of the base-isolated liquid storage tanks are chosen for the comparison. Following are the major conclusions derived from the present study.

- (i) The buckling of tank wall governs the failure of liquid storage tanks, isolated with elastomeric type isolators (LRB, NZ system etc.). However, exceedance of isolation level displacement governs the failure in the liquid storage tanks base-isolated using the PF system and the RFBI.
- (ii) Effectiveness of the EDF system to enhance the seismic performance of the liquid storage tanks is lesser as compared to other isolation systems considered in the present study. The FPS is observed to be the most effective for the broad tank, whereas the PF system is observed as the most effective for

the slender tank. Moreover, the critical isolation displacement criterion governs the failure of the liquid storage tanks base-isolated using the PF system.

- (iii) If the limiting frictional force is more than the critical base shear, the tank wall buckling governs the failure of the base-isolated liquid storage tank for both the FPS and the RFBI. While designing friction coefficient for the FPS and the RFBI, the capacity of the tank should be taken into consideration.

References

1. Buckle IG, Mayes RL (1990) Seismic isolation: history, application, and performance—a world view. *Earthq Spectra* 6(2):161–202
2. Deb SK (2004) Seismic base isolation—an overview. *Curr Sci* 87(10):1426–1430
3. Haroun MA (1983) Vibration studies and tests of liquid storage tanks. *Earthq Eng Struct Dyn* 11(2):179–206
4. Haroun MA, Housner GW (1981) Seismic design of liquid storage tanks. *J Tech Councils ASCE* 107(TC1):191–207
5. Ibrahim RA (2008) Recent advances in nonlinear passive vibration isolators. *J Sound Vib* 314 (3–5):371–452
6. Jacob CM, Sepahvand K, Matsagar VA, Marburg S (2013) Stochastic seismic response of an isolated building. *Int J Appl Mech* 5(1). doi:[10.1142/S1758825113500063](https://doi.org/10.1142/S1758825113500063)
7. Jadhav MB, Jangid RS (2006) Response of base-isolated liquid storage tanks to near-fault motions. *Struct Eng Mech* 23(6):615–634
8. Jangid RS (2005) Optimum friction pendulum system for near-fault motions. *Eng Struct* 27 (3):349–359
9. Jangid RS, Datta TK (1995) Seismic behavior of base-isolated buildings: a state-of-the-art-review. *Struct Build* 110(2):186–203
10. Kelly JM (1986) Aseismic base isolation: review and bibliography. *Soil Dyn Earthq Eng* 5 (4):202–216
11. Kelly TE, Skinner RI, Robinson WH (2010) Seismic isolation for designers and structural engineers. National Information Centre of Earthquake Engineering (NICEE), Indian Institute of Technology Kanpur, Kanpur
12. Matsagar VA, Jangid RS (2003) Seismic response of base-isolated structures during impact with adjacent structures. *Eng Struct* 25(10):1311–1323
13. Okada J, Iwata K, Tsukimori K, Nagata T (1995) An evaluation method for elastic-plastic buckling of cylindrical shells under shear forces. *Nucl Eng Des* 157(1–2):65–79
14. Rezaeian S, Kiureghian AD (2008) A stochastic ground motion model with separable temporal and spectral nonstationarities. *Earthq Eng Struct Dyn* 37(13):1565–1584
15. Seleemah AA, El-Sharkawy M (2011) Seismic response of base isolated liquid storage ground tanks. *Ain Shams Eng J* 2(1):33–42
16. Shriali MK, Jangid RS (2002) A comparative study of performance of various isolation systems for liquid storage tanks. *Int J Struct Stab Dyn* 2(4):573–591
17. Su L, Ahmadi G, Tadjbakhsh IG (1989) A comparative study of performances of various base isolation systems, part I: shear beam structures. *Earthq Eng Struct Dyn* 18(1):11–32
18. Wen YK (1976) Method for random vibration of hysteretic systems. *J Eng Mech Div ASCE* 102(2):249–263

Hydrodynamic Effects on a Ground Supported Structure

Kuncharapu Shiva and V.S. Phanikanth

Abstract Liquid storage tanks are used for storing water, inflammable liquids and other chemicals. Thus storage structures are very important for public utility and for industries. Such structures shall be designed for lateral loads such as wind loads/ earthquake loads. Earthquake is a sudden movement of the earth caused by the abrupt release of strain that has accumulated over a long time. This dynamic vibration of lateral movement affects structural strength and its behaviour. During the recent past earthquakes, many failures of liquid retaining structures are observed and thus there is a need to understand the behaviour of liquid retaining structures and to consider the latest advances in the design of such structures so that they are not vulnerable under earthquake loads. In the present study, behaviour of a typical ground supported structure under earthquake loads is studied using analytical solutions based on the codes/guidelines prevalent and the same are compared with the detailed dynamic finite element solutions. Both the convective and impulsive mode are captured in the detailed dynamic analysis and the time periods of respective modes of vibration are compared with the available guidelines. Good agreement in results is obtained using the computer based analysis. Behaviour of liquid storage tanks under earthquake loads has been studied as per Draft code Part II of IS 1893: 2002 [1]. A FEM based computer software is used (SAP2000) for seismic analysis of tank and finally their results are compared.

Keywords Liquid storage structures • Hydrodynamic effects • Earthquake load • SAP2000 • Finite element method

K. Shiva (✉)

Civil Engineering Division, Bhabha Atomic Research Centre, Visakhapatnam, India
e-mail: shivabar3@gmail.com

V.S. Phanikanth

Civil Engineering Division, Bhabha Atomic Research Centre,
Trombay, 400085 Mumbai, India
e-mail: vphanikanth@yahoo.com

1 Introduction

1.1 General

Apart from ensuring the design safety of liquid retaining structures, the main purpose of the construction of the facility is to distribute water effectively and efficiently to cater the expected demand. Water is important to human being for their daily usage in residential and commercial services. Considering the importance of such structures, its performance under seismic event, shall be carefully examined and the safety of the same shall be ensured. Time and again Earthquakes proved to cause worst phenomenon that can happen in human life with a lot of damages.

Structures located in seismically active areas have to be designed to resist the lateral forces arising due to earthquake loads in addition to vertical loads due to self weight and live loads etc. Due to rapid urbanisation and to cater for the increase in population demand there is an increase in demand for construction of various kinds of water tanks and other liquid retaining structures built in different parts of the country. Water storage tanks should remain functional in the post-earthquake period to ensure potable water supply to earthquake-affected regions and also to cater the need for fire fighting and hence seismic safety of liquid tanks is of considerable importance. Industrial liquid containing tanks may contain highly toxic and inflammable liquids and this toxic material should remain intact and shall not leak to outside the containment to ensure safety to the population surrounding the affected area.

To perform well in an earthquake the structure needs to have a well defined structural configuration and the structural analysis of the system shall capture all the stiffness and mass of the system in the dynamic analysis. Also it depends on design procedure adopted, the detailing of the structural elements and skilful construction as per the prevalent codes of practices existing in those regions. IS 1893 (Part 2) Draft code [1] has given analytical formulations on the design of liquid storage tanks, for evaluating the hydrodynamic forces due to seismic loading. Using these codal provisions it is possible to evaluate time periods in impulsive and convective modes of vibrations and hydro-dynamic forces for both elevated tanks and ground supported tanks. According to this code a water tank should be modelled as a two degree of freedom system based on the work of Housner [2]. First mass consists tank container and staging and impulsive water. Second mass consists convective water. Housner [2] studied the behaviour of small steel tanks with open roof under dynamic forces. He has given expressions for both impulsive and convective modes of vibrations.

In the present study, an attempt has been made to perform a detailed dynamic FE based analysis of a ground supported structure and the responses so obtained are compared with the analytical formulations described in the code. FE based commercial software SAP2000 is used for the present study. The results obtained from both the methods are found to be in reasonable agreement.

1.2 Some Damages to Storage Tanks During Recent Earthquakes

The behavior of liquid storage tanks during the seismic event has an importance beyond its economic value because of consequences that results from tank failures. The loss of public water supply can have serious consequences as it happened during 1933 long beach, California earthquake because of tank collapses [3].

Failure of tanks containing high inflammable products, combustible products such as gasoline and other petroleum products can lead to extensive, uncontrolled fires, as occurred following the Nigata, japan earthquake 1964 and Alaska earthquake of 1964 [3].

The major damages observed in the liquid storage tanks during past earthquakes are side wall buckling (Elephant foot and Diamond shape buckling), sliding and Uplifting of tank, failure of tank roofs and their junctions and are shown in Fig. 1. Literature shows that, shell buckling is caused by combined action of outward hydrodynamic wall pressures generated by vertical ground motion and axial compressive stresses caused by overturning moment generated by horizontal ground motion. For broad tanks, shell buckling takes the form of an axis-symmetric bulge (elephant Foot). For slender tanks, buckling is in the form of a diamond pattern. Unanchored or partially anchored tanks experience base uplifting. This can cause a break in the inlet/outlet piping connections which are not designed to accommodate the vertical movement. Pipe breaks can also result from horizontal movement (sliding) of the base. Tanks that are not provided with sufficient free-board can be damaged by the sloshing waves.

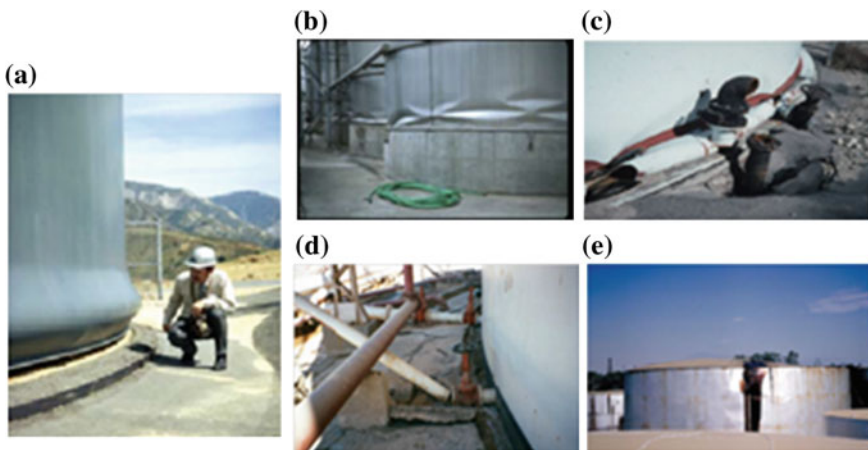


Fig. 1 Damages to liquid storage tanks, **a** elephant foot buckling, **b** diamond shape buckling, **c** pipe inlet-outlet breaking, **d** base sliding, **e** failure of tank roof (Photo courtesy University of California, Berkeley, [4])

2 Seismic Analysis of Liquid Retaining Structures

Hydrodynamic forces exerted by liquid on tank wall shall be considered in the analysis in addition to hydrostatic forces. These hydrodynamic forces are evaluated with the help of spring mass model of tanks.

2.1 Spring Mass Model for Seismic Analysis Using IS 1893 (Part 2) (Draft Code)

When a tank containing liquid with a free surface is subjected to horizontal earthquake ground motion, tank wall and liquid are subjected to horizontal acceleration. The liquid in the lower region of tank behaves like a mass that is rigidly connected to tank wall. This mass is termed as impulsive liquid mass which accelerates along with the wall and induces impulsive hydrodynamic pressure on tank wall and similarly on base. Liquid mass in the upper region of tank undergoes sloshing motion. This mass is termed as convective liquid mass and it exerts convective hydrodynamic pressure on tank wall and base. Thus, total liquid mass gets divided into two parts, i.e., impulsive mass and convective mass. The analysis of liquid storage structures under dynamic condition considers forces induced due to acceleration of tank structure and hydrodynamic forces due to acceleration of liquid. To include these forces, tank can be idealized by an equivalent spring mass model, which includes the effect of tank wall liquid interaction. In spring mass model of tank-liquid system, impulsive and convective masses are to be suitably represented. these two liquid masses and their points of application depends on aspect ratio of tanks and the all parameters of mechanical analogue are obtained from mathematical expressions given in the draft code.

Sometimes, vertical columns and shaft are present inside the tank. These elements cause obstruction to sloshing motion of liquid. In the presence of such obstructions, impulsive and convective pressure distributions are likely to change. At present, no study is available to quantify effect of such obstructions on impulsive and convective pressures. However, it is reasonable to expect that due to presence of such obstructions, impulsive pressure will increase and convective pressure will decrease.

The various steps involved in the analysis include computation of dead load, modelling of liquid (spring mass model parameters), time period calculations, computing design horizontal seismic coefficient, base shear and base moment, hydrodynamic pressure and sloshing wave height and anchorage requirement.

2.2 Ground Supported Rectangular Tank

Ground supported tanks can be idealized as spring-mass model as shown in Fig. 2. The impulsive mass of liquid, m_i is rigidly attached to tank wall at height h_i . Similarly, convective mass, m_c is attached to the tank wall at height h_c by a spring of stiffness K_c .

The spring mass model for ground supported tank is based on work of Housner [2]. In the spring mass model of tank, h_i is the height at which the resultant of impulsive hydrodynamic pressure on wall is located from the bottom of tank wall. On the other hand, h_i^* is the height at which the resultant of impulsive pressure on wall and base is located from the bottom of tank wall. Thus, if effect of base pressure is not considered, impulsive mass of liquid, m_i will act at a height of h_i and if effect of base pressure is considered, m_i will act at h_i^* . The same may be evaluated using above mentioned draft code. Thus, it is possible to evaluate the convective and impulsive masses and also the convective stiffness by knowing height of liquid ‘h’ and tank base dimension ‘L’ parallel to earthquake excitation under consideration as shown in Fig. 3. Also, the height at which these masses act can be evaluated using Fig. 4. Similarly, h_c , is the height at which resultant of convective pressure on wall is located from the bottom of tank wall, while, h_c^* is the height at which resultant of convective pressure on wall and base is located.

The time periods are calculated based on the expressions give in the code. Damping in the convective mode for all types of liquids and for all types of tanks shall be taken as 0.5 % of the critical. Damping in the impulsive mode shall be taken as 2 % of the critical for steel tanks and 5 % of the critical for concrete or masonry tanks. In the calculation of average response acceleration coefficient, if time period is less than 0.1 s, the value of S_d/g shall be taken as 2.5 for 5 % damping and be multiplied with appropriate factor, for other damping. Value of multiplying factor for 0.5 % damping shall be taken as 1.75.

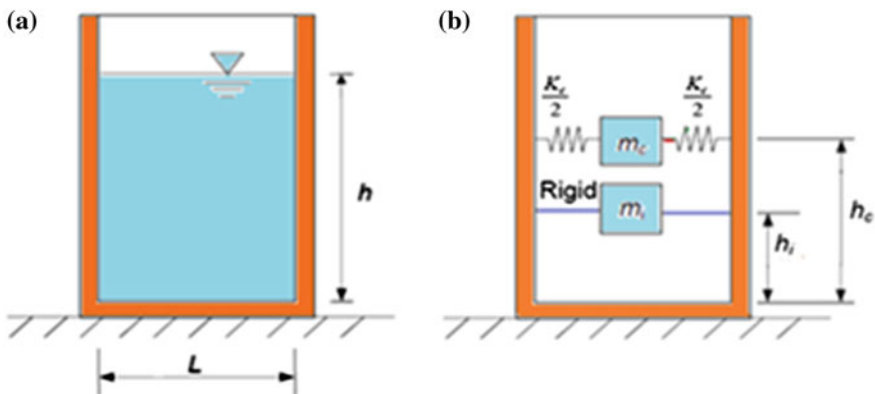


Fig. 2 Spring mass model for ground supported rectangular tank [IS 1893 (Part 2) Draft code]

Fig. 3 Impulsive and convective mass and convective spring stiffness [IS 1893 (Part 2) Draft code]

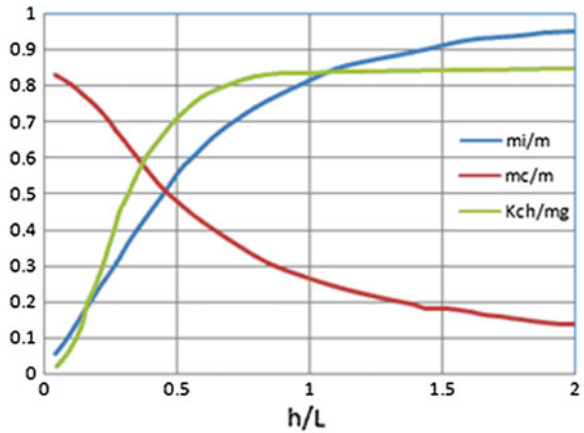
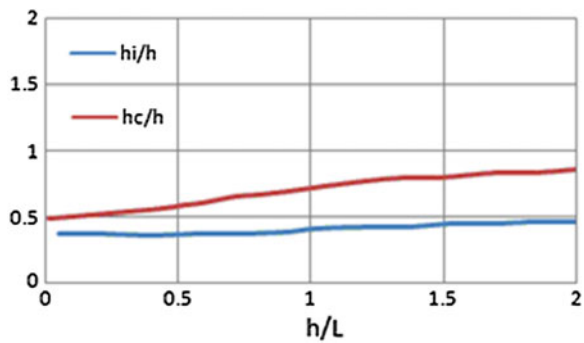


Fig. 4 Heights of impulsive and convective masses [IS 1893 (Part 2) Draft code]



2.3 Spring Mass Model Parameters as per IS 1893 (Part 2) Draft Code, for Rectangular Tank

Based on the Draft code base shear and base moments can be calculated as follows:

In Impulsive mode:

$$V_i = (A_h)_i(m_i + m_w + m_t)g$$

$$M_i = (A_h)_i(m_i h_i + m_w h_w + m_t h_t)g$$

In Convective mode:

$$V_c = (A_h)_c(m_c)g$$

$$M_c = (A_h)_c(m_c h_c)g$$

Where

- $(A_h)_i$ Design horizontal seismic coefficient for impulsive mode,
- $(A_h)_c$ Design horizontal seismic coefficient for convective mode,
- m_i Impulsive mass of water,
- m_t Mass of roof slab, and
- g Acceleration due to gravity.
- h_w Height of centre of gravity of wall mass, and
- h_t Height of centre of gravity of roof mass.

Here, Impulsive and convective stiffness, their masses and respective heights can be calculated by using Figs. 3 and 4. Also, the final shear force, bending moment shall be computed by using SRSS (square root sum of squares) rule for both impulsive and convective values. Design horizontal seismic coefficient can be calculated as $A_h = \frac{Z}{2} \frac{I}{R} \frac{S_a}{g}$, where $\frac{S_a}{g}$ is the average spectral acceleration coefficient which depends upon the time period [5], and shall be computed both for impulsive and convective modes. These time periods are found out by using the mathematical formulations given in above mentioned draft code, wherein convective stiffness can also be calculated by using the Fig. 3.

Final Hydrodynamic pressure includes the Impulsive, convective pressures, pressure due to wall inertia, and pressure on the wall due to vertical ground acceleration. All these pressures should be suitably combined to get final pressure.

When free board (FB), provided is less than the computed slosh height say d_{max} , then roof slab is subjected to contact pressure and Impact force due to fluid sloshing during the earthquake. Such roof slab shall be designed for the contact pressure with an impact factor, IF (IF can be taken as 2).

Pressure can be computed as: $p_{s1} = \gamma_w (d_{max} - FB) \cdot IF$.

3 Case Study of a Ground Supported Structure

A ground supported rectangular RC water tank with plan dimensions of 39.6×30.5 m and height of 4.45 m including a free board of 1.2 m is considered for the present study. The structure has RCC walls all around with wall thickness varying thickness from 700 mm at the base to 300 mm at the top. The thickness of base slab is considered as 250 mm and that of roof slab is taken as 300 mm. There are 12 columns of size 600×600 mm inside the tank and 11 beams (7 of $600 \times 1,000$ mm and 4 of 400×750 mm) in the tank. Grade of concrete is considered as M30. Based on the geotechnical data and using IS 1893 (Part 2) Draft code the structure is resting on medium type soil. The importance factor is taken as 1.5 and response reduction factor is considered as 2 for the purpose of analysis. The structure is in seismic zone II as per IS 1893 (Part 2) Draft code [1] and zone factor is considered as $Z = 0.10$ and DBE level earthquake is considered for the present study.

3.1 Typical Results Using IS 1893 (Part 2) Draft Code

In X(longer) direction:

- Base shear is found to be 1991 kN and is 3.56 % of seismic weight (56004.38 kN) of tank.
- Total Moment at the base of the walls = 5749.9 kN-m.
- Moment per unit length at the base of the wall = 92.72 kN-m/m.
- Overturning moment = 15,685 kN-m.
- Maximum hydrodynamic pressure at base = 4.785 kN/m². It is found to be 15 % of hydrostatic pressure = 31.88 kN/m² (at base).
- Slosh height is found to be 0.25 m and is less than the free board (1.2 m) provided.
- No anchorage required.

In Y(shorter) direction:

- Base shear is found to be 2099.5 kN and is 3.74 % of seismic weight of tank.
- Total Moment at the bottom of the wall = 6246.7 kN-m.
- Moment per unit length at the base of the wall = 78.08 kN-m/m.
- Over turning moment = 13907.65 kN-m.
- Maximum hydrodynamic pressure = 4.772 kN/m² at base. It is found to be 15 % of hydrostatic pressure (31.88 kN/m²).
- Slosh height is found to be 0.25 m and is less than the free board (1.2 m) provided.
- No anchorage required.

3.2 Detailed Dynamic Analysis

The structure is also analysed using detailed dynamic analysis using SAP2000 with the input data described above. The varying wall thickness is approximated to uniform wall thickness instead of tapered wall. Columns masses are lumped at the roof slab and base slab modelling is not considered for simplicity. All RC walls are fixed at the bottom.

Impulsive and convective masses are added as joint masses at the junction of the four springs (two in each direction for each of the masses) which are connected to the walls at different levels. Dynamic analysis has been carried out for earthquake loading in X and Y directions and is compared with the theoretical calculations which are presented in the previous section.

Dynamic analysis is carried out for 100 modes to enable 90 % mass participation in X and Y directions. The typical 3D view of FE model is shown in Fig. 5 and plans at convective and impulsive heights of the FE mode is shown in Fig. 6.

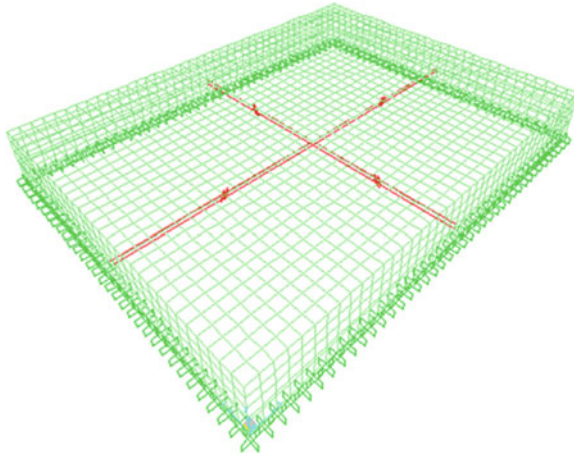


Fig. 5 3D view of FE model

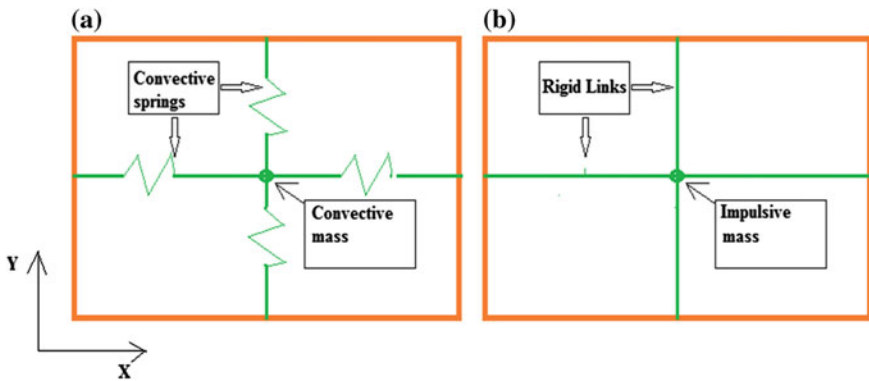


Fig. 6 a Plan @ 1.61 m convective mass and springs, b plan @ 1.21 m impulsive mass and rigid links

The damping value for the R.C. structure is considered as 5 % for all modes, except for first two modes wherein 0.5 % (as per draft code) damping is considered. All the input parameters considered for the FE model is shown in Table 1. It was observed that the first two modes represent convective mass participations in X and Y directions respectively. Response spectrum function is used according to the draft code IS 1893 (Part 2) Draft code. The various seismic input parameters such as zone factor $Z = 0.10$, importance factor = 1.5, and response reduction factor $R = 2$ are considered using IS 1893 (Part 2) Draft code and considering DBR level earthquake as discussed above. Loading function was defined in both X and Y

Table 1 The details of the SAP-FE modelling

Finite element method using shell elements of mesh size 1×1 m	
Material properties	Concrete (M30, $\gamma = 25 \text{ kn/m}^3$)
Section properties	Concrete walls of uniform thickness 0.5 m, concrete roof slab of thickness 0.3 m
Support conditions	Fixed at the base of the walls
Springs used for modeling of liquid	Spring stiffness for impulsive loads = 1×10^{10} kN/m (rigid link); spring stiffness for convective loads = 317.06 kN/m in X and 523.81 kN/m in Y direction respectively
Response spectrum used	As per IS 1893 (Part 2) Draft code [Z = 0.10, I = 1.5, R = 2 and soil type 2]
No of modes considered	100
Damping values for modes	0.5 % for first 2 modes and 5 % for all other modes

Table 2 Comparison of results-analytical solution versus dynamic analysis results

Parameter	IS 1893 (Part 2) (Draft code)		Finite element detailed dynamic analysis using SAP2000 (Mesh size = 1×1 m)	
	X-DIR	Y-DIR	X-DIR	Y-DIR
Time period (S)- impulsive mode	0.01	0.01	0.05	0.06
Mode no	1	1	37	47
Time period (S)- convective mode	14.1	10.92	14.12	10.88
Mode no	2	2	1	2
Base shear (kN)	1991	2099.5	2545.9	2602.4
Unit moment at base of wall (kN-m/m)	92.72	78.08	93.68	73.47

directions individually. The structure is analysed for various forces viz. base shear, bending moment, hydrodynamic pressure based on formulations given in IS 1893 (Part 2) Draft code and the obtained results are presented in Table 2.

4 Conclusions

This paper reviews the earthquake induced forces on ground supported liquid retaining R.C. structures. It is observed that results obtained based on dynamic analysis carried out in FEM based software SAP2000 [6] are in good agreement with the results from the analysis methods of IS 1893 (Part 2) Draft code. The hydrodynamic pressure is observed to be 15 % of the maximum hydrostatic

pressure. The wall bending moments due to hydrodynamic effects are significant compared to hydrostatic effects and thus underlines the importance of consideration of such effects of liquid retaining structures in seismically active areas.

References

1. IS 1893 (Part-2) Draft code, Indian standard criteria for earthquake resistant design of structures: part 2 liquid retaining tanks (Revision of IS 1893)
2. Housner GW (1963) Dynamic analysis of fluids in containers subjected to acceleration. Nuclear reactors and earthquakes, report no. TID 7024, U.S. Atomic Energy Commission, Washington D.C
3. Hanson RD (1964) The university of Michigan, behaviour of liquid-storage tanks, structural engineering page no 331, the great Alaska earthquake of 1964-part 1 by national research council (U.S.)
4. Malhotra PK, Wenk T, Wieland M (2000) Simple procedure for seismic analysis of liquid storage tanks. Structural engineering international 3/2000, reports 197–201
5. IS: 1893 (Part-1): 2002 Indian standard criteria for earthquake resistant design of structures: part 1 general provisions and buildings (Fifth Revision), Bureau of Indian Standards, New Delhi
6. Structural Analysis Program SAP2000 (1999) User's manual. Computers and Structures, Inc., Berkeley

Seismic Behaviour of R/C Elevated Water Tanks with Shaft Stagings: Effect of Biaxial Interaction and Ground Motion Characteristics

Aparna Roy and Rana Roy

Abstract An important lifeline facility such as elevated water tanks with R/C shaft staging has been observed to be potentially damaged during earthquakes in the past. Seismic demand of lateral load-resisting members are seldom evaluated accounting bi-directional interaction. Existing guideline to estimate total response combining 100 % of the maximum response for excitation in one direction and 30 % of the maximum responses for excitation in the other horizontal direction (as per ‘30 % rule’) is evidently deficient at least for systems excited well into inelastic range. Present investigation aims to explore the response of shaft-supported reinforced concrete elevated water tank under bi-directional near-fault records with forward-directive signature. Following detailed review, shaft staging of elevated tank is modelled through distributed plasticity element. Hydrodynamic action is also adequately modeled following established standards. Bi-directional interaction may considerably amplify global response particularly at tank-empty condition. Complex combination of bi-directional load-path may lead to adverse system response. Increase of ground motion characteristics such as mean period, significant duration relative to the impulsive period of the tank, with some scatter, leads to increase interaction effect.

Keywords RC elevated water tanks · Bi-axial interaction · Ground motion · Hydrodynamics

A. Roy

Department of Civil Engineering, University Institute of Technology, University of Burdwan, Burdwan, India

R. Roy (✉)

Department of Aerospace Engineering and Applied Mechanics,
Indian Institute of Engineering Science and Technology, Shibpur,
Botanic Garden, Howrah 711103, West-Bengal, India
e-mail: roybec@yahoo.com

1 Introduction

In the accepted practice, structures are expected to be in linear range only under minor shaking and experiences post-elastic range vibration during moderate to strong earthquakes. Thus, seismic design relies on the ductile behavior of structures in order to ensure safety with limited cost. Such inelastic damage of reinforced concrete (R/C) structures are associated with permanent cracking, spalling of concrete, fracture or buckling of reinforcing bars etc. To comply with the design requirements in the performance based seismic design (PBSD), assessment of behavior at each performance state is essential [1].

Elevated water tanks are important structures in water supply networks. Liquid storage tanks are used extensively by municipalities and industries for storing water, inflammable liquids and other chemicals. Thus these type of structures are very important for public utility and for industrial purpose to secure necessary water supply. Reinforced concrete circular shafts type support (staging) is widely used for elevated tanks of low to very high capacity. It is extremely essential for these systems to remain operational after earthquakes for post-earthquake damage mitigation. The poor seismic performance of these inverted pendulum-type constructions has been reported frequently during major earthquakes [2–8]. Inadequate performance of these tanks also prevented fire-fighting and other emergency activities in the past.

It is well-known that during seismic shaking elevated tanks are usually subjected to bi-directional shaking which is recognized to pose stronger seismic vulnerability. However, principles for capacity estimate primarily bases on the experimental results of uniaxial tests without accounting for simultaneous action along two principal directions [9]. On the other hand, design forces are also evaluated without explicit account of bi-axial interaction (e.g., ASCE/SEI 7-05 [10]). Code only recommends simple combination rule of ‘100 % of the forces for one direction plus 30 % of the forces for perpendicular direction’ for systems with a specific form of irregularity (Type 5). In principle, total response is computed as 100 % of the maximum response for excitation in one direction plus 30 % of the maximum response for excitation in the other horizontal direction; the combination leading to the largest response is considered for design [11]. Responses under uni-directional components separately applied to 100 and 30 % along the principal directions of the structures are often combined by SRSS [12]. The obvious limitation of such simplified approaches are intuitive [12] at least in the post-elastic range.

Relatively simple representation yet severe destructive potential of near-fault earthquakes has been demonstrated during several earthquakes (e.g., 1978 Tabas, Iran; 1995 Kobe, Japan; 1999 Chi-Chi, Taiwan; 2003 Bam, Iran and 2009 L’Aquila, Italy) in the past. Such pulses involving forward-directivity (FD) effect are well-known to bring about havoc in many historical events and also noted in the literatures (for example, [13, 14]). In fact, it is believed that the “near-fault FD fault-normal components of motion are especially severe and potentially destructive” [17]. It may be noted that the existing methods to implicitly consider inelastic

demands by amplifying the design spectra do not provide a reliable basis for representing near-fault ground motions [18].

With these in view, this investigation focuses on the response of shaft supported elevated water tanks in case of bi-directional seismic attack close to a causative ground fault. On close scrutiny of different analytical models, a state-of-the-art numerical scheme is adopted. Response of the elevated tank both at tank-empty and tank-full conditions are analyzed under uni-directional and bi-directional near-field FD records. Seismic behavior under FD near-field events are explained unfolding the impact of bi-directional interaction. The study is believed to be useful to realize the consequence of limitation of current codal provisions.

2 System Idealization

2.1 Hydrodynamic Action

Behaviour of elevated water tank undergoing lateral vibration at the bottom physically induces two different types of vibration in the water of the tank. While a part of the water at the upper portion of tank participates in sloshing motion (convective) with a longer period [19, 20], the rest of the water vibrates rigidly with the tank wall. The former one is recognized as convective mass of water, while the latter is known as impulsive mass of water. The impulsive mass of water experiences the same acceleration as the tank container and contributes predominantly to the base shear and overturning moment [3, 7]. Thus, the behaviour of elevated tanks can be represented by an equivalent two-mass model as suggested in the literature [7]. For the sake of convenience, this two degrees of freedom system is schematically shown in Fig. 1a. The effective structural mass, M_s ; i.e., the mass of the tank

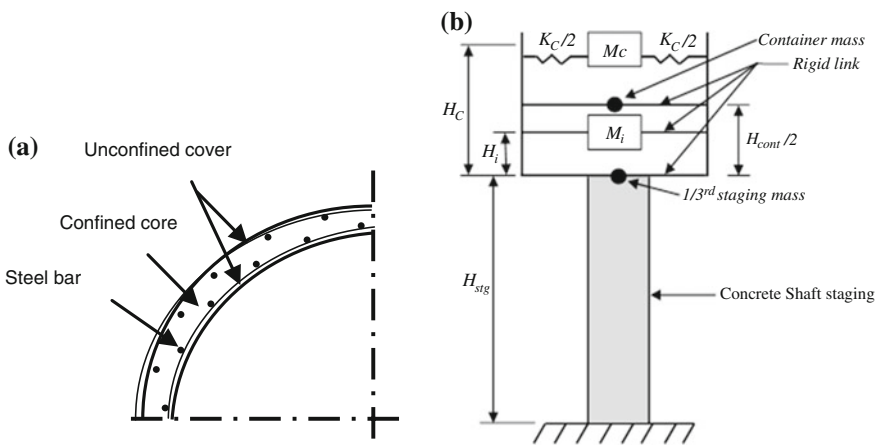


Fig. 1 a Cross-section of concrete model. b Two mass model for lateral vibration as proposed by Housner [17]

container and one-third mass of the staging [3, 5, 7] as well as the equivalent mass of water participating in impulsive mode, M_o ; is considered to be rigidly attached to the tank container. The one-third mass of the staging is located at the top of the staging and the container mass is located at the mid-height of the container ($H_{cont}/2$). The convective mass, M_c ; is attached to the staging through a vertical member of height, H_c ; attached at the top of staging level. The lateral stiffness, K_c ; which is the equivalent stiffness involved in sloshing vibration is attached to M_c . The expressions for these masses and stiffness quantities were originally proposed in a literature [7] and were finally reported further with minor modification in another literature [21]. The expressions for various equivalent mass and stiffness quantities according to the literature [21] are also given here for convenience.

$$M_o = M \frac{\tanh(1.7R/h)}{1.7R/h}; \quad M_c = 0.71M \frac{\tanh(1.8h/R)}{1.8h/R}; \quad K_c = 4.75M_c^2 \frac{gh}{MR^2}$$

In these expressions, M denotes total mass of the water, R represents radius of container and g denotes acceleration due to gravity. The impulsive and convective masses are considered to be located at a height of H_o and H_c , respectively, from the bottom of the tank container. The expressions for these heights according to the same literature [21] are as follows:

$$H_o = \frac{3}{8}H \left\{ 1 + \frac{4}{3} \left(\frac{M}{M_o} - 1 \right) \right\}$$

$$H_c = H \left\{ 1 - 0.21 \frac{M}{M_c} \left(\frac{R}{H} \right)^2 + 1.1 \frac{R}{H} \sqrt{0.15 \left(\frac{RM}{HM_c} \right) - 1} \right\}$$

2.2 Modeling of Shaft Staging

Lateral load resisting staging of the shaft is modeled using distributed inelasticity fiber models that represent the cross-section behavior through uni-axial stress-strain relationship of the discrete fibers. A detailed review of the available models is presented elsewhere [22, 23]. Simplicity of the input data for numerical schemes is also essential as otherwise such models become ‘inaccessible to designers’. Considering pros and cons, the present investigation models RC shaft staging using distributed plasticity elements in the framework of standard finite element software SeismoStruct: Version 6 (Seismo-Soft 2012). Sectional details of the shaft is furnished in Fig. 1b.

Fibre discretization is adopted to represent the member at the section level, where each fibre is associated with a uniaxial stress-strain law. The sectional moment-curvature state is then obtained through the integration of the nonlinear uniaxial stress-strain response of the individual fibers that constitutes the section.

The global inelasticity of the shaft is then obtained by integration of the contribution provided by each controlling section. Cross-section is discretized into three hundred fibers. Shaft is discretized into four sub-elements considering ten Gauss sections (at least six recommended in [24]) per element. The Gauss-Lobatto quadrature rule is used to numerically integrate the forced-based elements [25].

Typical section consisting of unconfined concrete, confined concrete and reinforcing steel are modified using established scheme. It is assumed that once ultimate conditions are reached, R/C members continue to have a residual strength as proposed elsewhere [26]. The concrete constitutive behavior is modeled using non-linear constant confinement concrete model originally proposed by Mander et al. [27] and later modified by Martinez-Rueda and Elnashai [28]. Confinement effect due to lateral reinforcement is taken into account through the definition of the confinement factor of section core [27]. Thus, the loss of member strength due to spalling of concrete cover is accounted. Constitutive behavior for reinforcement steel is modeled using Menegotto-Pinto steel model [29] modified by Filippou et al. [30]. This model assumes a bilinear backbone curve with isotropic strain hardening. The model takes into account the *Bauschinger* effect to adequately represent the stiffness degradation of columns under cyclic loading.

3 Ground Motions, Methodology and System Parameters

Limited studies conducted herein select seven near-fault records with forward directivity signature. Details of the ground motions along with the different important characteristics are presented in Table 1.

Moment magnitude for the ground motions ranges between 5.8 and 6.9. Closest site-to-fault-rupture distance ranges between 4.0 and 8.5 km. Average shear wave velocity in the top 30 m of the site (V_{s30}), by and large, represents a site class D [31]. Under specified ground acceleration histories, standard equations of motion

Table 1 Details of ground motions adopted

Sl. no	Nomen-clature used	Seismic events	Station	Date	Magnitude in Richter	Distance from epicentre (km)
1	A-A1	Chalfant Valley	Zack Brothers ranch	07.20.86	5.8	6.4
2	B-B1	Coyote Lake	Gilroy Array #3	06.08.79	5.7	7.4
3	C-C1	Dinar, Turkey	Dinar	01.10.95	6.4	3.4
4	D-D1	Imperial Valley	El Centro Array #3	10.15.79	6.5	12.9
5	E-E1	Imperial Valley	El Centro Array #5	10.15.79	6.5	4.0
6	F-F1	Imperial Valley	Sahop Casa Flores,	10.15.79	6.5	9.6
7	G-G1	Loma Prieta	Saratoga—Aloha Ave	10.18.89	6.9	8.5

(refer to [11]) of the system are solved in the time domain using Hilber-Hughes-Taylor integration scheme [32]. While Hilber-Hughes-Taylor parameters α , γ and β are chosen respectively as -0.1 , 0.6 and 0.3025 , time step of integration is taken to be sufficiently small to ensure convergence. A tangent-stiffness proportional viscous damping of 5% and displacement/rotation based criterion (tolerance limits: 0.1 mm and 10^{-4} rad) is selected to ensure convergence in analysis.

Elevated water tanks (Fig. 1b) with varying capacities of $380\text{--}1,050\text{ kl}$ with diameter of shaft staging ranging between 7.0 and 12.24 m are chosen as the reference system. Geometric and structural details of the tank stagings and containers are listed in Table 2.

Shell thicknesses of the stagings are taken as 150 mm throughout reinforced with 0.8% steel in both longitudinal and circumferential directions [33, 34]. Capacity curve of the shaft is established by conducting a conventional static pushover analysis where lateral load is applied employing automatic response control algorithm [35] implemented in standard software (SeismoStruct: Version 6). It is important to note that capacity is determined without accounting axial load. Yield capacity (F_y) and yield displacement (u_y) of the structure is estimated from such capacity curve. Subsequently, the ground motion is suitably scaled to simulate a response reduction factor (R) of 2 . Standard response history analysis is then performed for systems so idealized following the methodology outlined.

4 Results and Discussions

Limited studies conducted herein select seven near-fault records with forward directivity signature. With the intent of assessing influence of bi-directional effect, drift is measured from two set of nonlinear response history analysis. In the first, each component of a ground motion is applied separately. Drifts measured under two components of a ground motion are compared and the greater one is regarded as the drift of the pier under uni-directional shaking (Δ_U). In the second, both the components of each ground motion are simultaneously applied along two mutually orthogonal directions and drifts under two orthogonal directions, viz., Δ_θ and $\Delta_{\pi/2+\theta}$ are noted. These are geometrically combined as $[\Delta_\theta^2 + \Delta_{\pi/2+\theta}^2]^{0.5}$ to estimate the drift under bi-directional excitation (Δ_B). Values of Δ_U and Δ_B so computed for each record are plotted in the form of bar chart (Fig. 2). It is observed that the drift tends to consistently increase even to the extent of 50% due to bi-directional interaction. Such increase may generally be greater in tank-empty condition. During tank empty condition, period of the system becomes even stiffer and hence the impact of bi-directional interaction is expected to be more prominent [34, 35]. Similar response in terms of normalized hysteretic energy ductility demand (NHEDD), although not presented, also reveal a parallel trend.

Table 2 Structural details and dynamic characteristics of tanks

Tank	Capacity (m ³)	Mass of container (×103 kg)	Height of shaft staging (m)	Diameter of shaft c/c (m)	Thickness of shaft wall (m)	Mass of staging (×103 kg)	Impulsive mass of water (×103 kg)	Convective mass of water (×103 kg)	Impulsive period (s)		Convective period (s)
									Tank-fullcondition	Tank-empty condition	
1	380	19.60	12.0	7.0	0.15	9.30	249.1	114.4	0.12	0.04	3.3
2	1.050	66.16	27.8	12.24	0.15	40.08	488.6	456.5	0.25	0.10	4.4

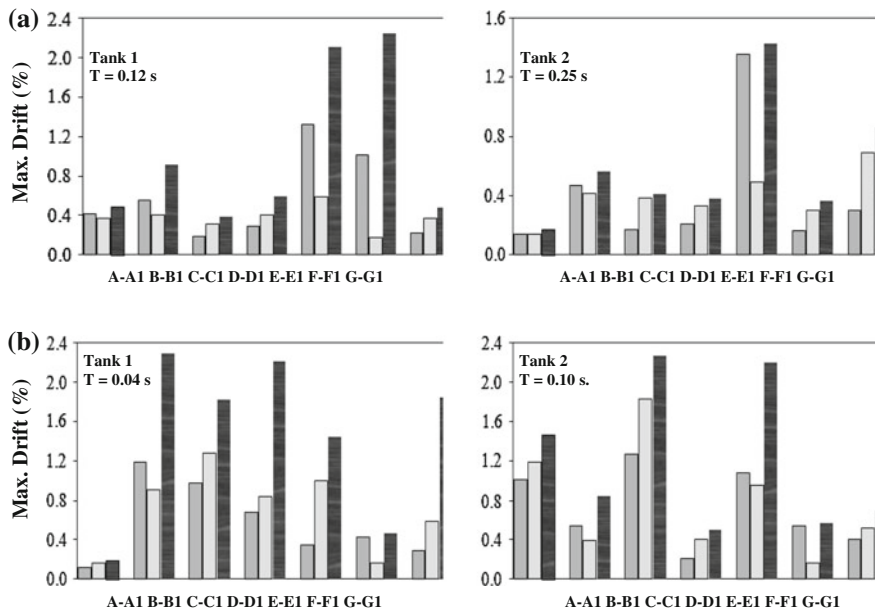


Fig. 2 Change of drift (%) due to bi-directional interaction under different ground motions ($R = 2$)

5 Influence of Ground Motion Characteristics

Dynamic response of structural systems are significantly influenced by the frequency content of earthquake motions (e.g., [38]). Earthquake motions comprised of a range of frequencies are often described by characteristic periods such as mean period (T_m) [38, 39]. Thus, the mean period is derived from the Fourier amplitude spectrum of acceleration-time history as $(\sum_i C_i^2 / f_i) / (\sum_i C_i^2)$ [39] where C_i are the Fourier amplitudes of the accelerogram and f_i the corresponding discrete Fourier transform frequencies between 0.25 and 20 Hz. Significant duration, based on the accumulation of energy in the accelerogram and defined as the interval over which a certain portion (in which the motion is deemed strong taken herein as 5–95 %) of the total Arias intensity is accumulated, is also believed to be an influential parameter. Responses of structures thus are presented as a function of T_m to T ratio and the variation of the similar quantities as a function of T_{sig}/T in Fig. 3. Average values of components T_m and T_{sig} are considered to represent response under bi-directional shaking. Figures display, with some scatter, an increasing trend in response under both uni-directional and bi-directional shaking.

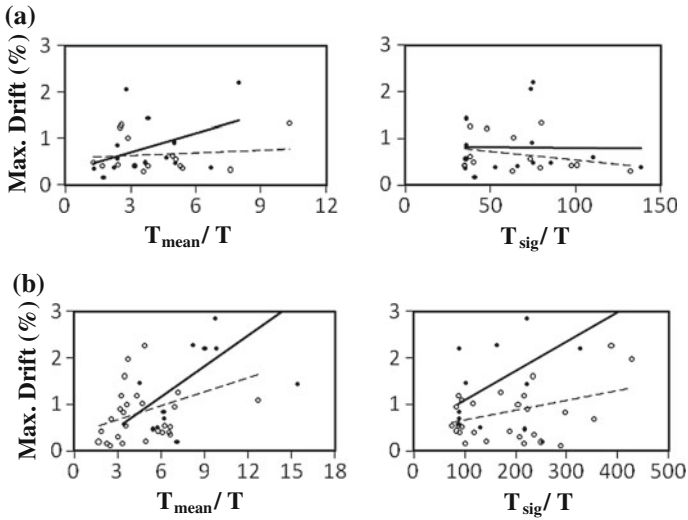


Fig. 3 Change of drift (%) due to bi-directional interaction with respect to mean period and significant duration of ground motions ($R = 2$)

6 Summary and Conclusions

Current design generally evaluates inelastic seismic demand under bi-directional shaking through combining responses under uni-directional excitation using simple empirical rule. This study is an attempt to assess the consequence of bi-directional interaction using under near-fault records with forward directivity. Reviewing the available state-of-the-art analytical models, an appropriate model for RC elements is selected. Subsequently, response of five shaft-supported elevated water tanks are evaluated, at both tank-empty and tank-full conditions, under both uni-directional and bi-directional shaking. The present work thus leads to following conclusions:

1. Bi-axial interaction seems to amplify the peak deformation demand around 50 % for shaft supported elevated water tanks which are dynamically stiff system. Such increase tends to further amplify at tank-empty condition as the system becomes even stiffer under such situation.
2. Increase of relative values of ground motion characteristics such as mean period and significant duration with respect to the period of the tanks, with some scatter, tend to increase the response.

Conclusions above collectively epitomize the significance of bi-directional interaction during near-fault forward directivity events.

References

1. SEAOC Vision 2000 (1995) Performance based seismic engineering of buildings. Conceptual framework, Sacramento (CA), Structural Engineers Association of California, vols I and II
2. Astaneh A, Ghafory-Ashtiany M (1990) The Manjil, Iran, earthquake of June 1990. EERI Special Earthquake Rep, EERI Newslett 24:5–13
3. Jain SK, Murty CVR, Chandak N, Seeber L, Jain NK (1994) The September 29, 1993, M6.4 Killari, Maharashtra, earthquake in central India. EERI Special Earthquake Rep, EERI Newslett 28:1–8
4. Mehraïn M (1990) Reconnaissance report on the Northern Iran earthquake of June 21, 1990. State University of New York at Buffalo, NCEER, Buffalo, New York
5. Rai DC (2003) Performance of elevated tanks in Mw 7.7 Bhuj earthquake of January 26th, 2001. Proc Indian Acad Sci—Earth Planet Sci 112(3):421–429
6. Saffarini HS (2000) Ground motion characteristics of the November 1995 Aqaba earthquake. Eng Struct 22:343–351
7. Steinbrugge KV, Moran DF (1954) An engineering study of the southern California earthquake of July 21, 1952 and its aftershocks. Bull Seismol Soc Am 44:201–462
8. Steinbrugge KV (1970) Earthquake damage and structural performance in the United States. In: Wiegel RL (ed) Earthquake engineering. Prentice-Hall, Englewood Cliffs
9. EN 1998-1 (2003) Design of structures for earthquake resistance, part 1: general rules, seismic actions and rules for buildings. Eurocode 8, European Standard
10. ASCE/SEI 7-05 (2005) Minimum design loads for buildings and structures. American Society of Civil Engineers (ASCE), Reston
11. Clough RW, Penzien J (1993) Dynamics of structures. McGraw-Hill, New York
12. Dutta SC, Kunnath SK (2013) Effect of bi-directional interaction on seismic demand of structures. Soil Dyn Earthq Eng 52:27–39
13. Iwan WD, Huang CT, Guyader AC (2000) Important features of the response of inelastic structures to near-fault ground motion. In: Proceedings of 12th world conference on earthquake engineering, Auckland, New Zealand
14. Singh JP (1985) Earthquake ground motions: implications for designing structures and reconciling structural damage. Earthq Spectra 1:239–270
15. Bray DJ, Marek RA, Gillie LJ (2009) Design ground motions near active faults. Bull NZ Soc Earthq Eng 42(1):1–8
16. Kalkan E, Kunnath SK (2006) Effects of fling step and forward directivity on seismic response of buildings. Earthq Spectra 22(2):367–390
17. Housner GW (1963) Behaviour of inverted pendulum structures during earthquake. Bull Seismol Soc Am 53(2):403–417
18. Newmark NM, Rosenblueth E (1971) Fundamentals of earthquake engineering. Prentice Hall, New Jersey
19. Haroun MA, Ellaihy MH (1985) Seismically induced fluid forces on elevated tanks. J Tech Topic Civil Eng 111(1):1–15
20. CEB (1996) RC frames under earthquake loading: state of the art report Comité euro-international du béton, Thomas Telford, London, England
21. Fardis MN (1991) Member-type models for the nonlinear structure in experimental and numerical methods in engineering D.A.P.M jones. In: Kluwer (ed) Academic publishers, Dordrecht, Netherland
22. Calabrese A, Almeida JP, Pinho R (2010) Numerical issues in distributed inelasticity modelling of R/C frame elements for seismic analysis. J Earthq Eng 14(S1):38–68
23. Alemdar BN, White DW (2005) Displacement, flexibility and mixed beam-column finite element formulations for distributed plasticity analysis. J Struct Eng ASCE 131(12):1811–1819

26. Mpampatsikos V, Nascimbene R, Petrini L (2008) A critical review of the R.C. frame existing building assessment procedure according to Eurocode 8 and Italian seismic code. *J Earthq Eng* 12(SP1):52–58
27. Mander JB, Priestley MJN, Park R (1988) Theoretical stress—strain model for confined concrete. *J Struct Eng ASCE* 114(8):1804–1823
28. Martinez-Rueda JE, Elnashai AS (1997) Confined concrete model under cyclic load. *Mater Struct* 30(197):139–147
29. Menegotto M, Pinto PE (1973) Method of analysis for cyclically loaded RC plane frames including changes in geometry and non-elastic behaviour of elements under combined normal force and bending. In: *Symposium on the resistance and ultimate deformability of structures acted on by well defined repeated loads*, international association for bridge and structural engineering, Zurich, Switzerland, pp 15–22
30. Filippou FC, Popov EP, Bertero VV (1983) Effects of bond deterioration on hysteretic behaviour of reinforced concrete joints. Earthquake engineering research center, University of California, Berkeley, CA, report no. UCB/EERC 83/19
31. FEMA 356 (2000) Prestandard and commentary for the seismic rehabilitation of buildings. Federal emergency management agency (FEMA) report 356, Washington DC, USA
32. Hilber HM, Hughes TJR, Taylor RL (1977) Improved numerical dissipation for time integration algorithms in structural dynamics. *Earthq Eng Struct Dyn* 5(3):283–292
33. Dayaratnam P (1983) Design of reinforced concrete structures. M. Primlani Publisher, New Delhi
34. Krishnaraju N (2003) Advanced reinforced concrete design (IS456-2000). CBS Publishers, New Delhi
35. Izzuddin BA (1991) Nonlinear dynamic analysis of framed structures. Ph.D. thesis, Imperial College, University of London, London, UK
36. Pecknold DA (1974) Inelastic structural response to 2D ground motions. *J Eng Mech Div ASCE* 100(EM5):949–963
37. Nigam N (1967) Inelastic interactions in the dynamic response of structures. Earthquake Engineering Research Laboratory (EERL6764), California Institute of Technology, Pasadena, California
38. Rathje EM, Abrahamson NA, Bray JD (1998) Simplified frequency content estimates of earthquake ground motions. *J Geotech Eng* 124:150–159
39. Dimitrakopoulos E, Kappos AJ, Makris N (2009) Dimensional analysis of yielding and pounding structures for records without distinct pulses. *Soil Dyn Earthq Eng* 29(7):1170–1180

Part XII
Dynamic Vibration Control of Structures

Steel Hysteretic Damper Featuring Displacement Dependent Hardening for Seismic Protection of Structures

Murat Dicleli and Ali Salem Milani

Abstract In this paper, a summary of analytical and experimental studies into the behavior of a new hysteretic damper, designed for seismic protection of structures is presented. The Multi-directional Torsional Hysteretic Damper (MTHD) is a recently-patented invention in which a symmetrical arrangement of identical cylindrical steel cores is so configured as to yield in torsion while the structure experiences planar movements due to earthquake shakings. The new device has certain desirable properties. In this paper, a summary of analytical and experimental studies into the behavior of a new hysteretic damper, designed for seismic protection of structures is presented. The Multi-directional Torsional Hysteretic Damper (MTHD) is a recently-patented invention in which a symmetrical arrangement of identical cylindrical steel cores is so configured as to yield in torsion while the structure experiences planar movements due to earthquake shakings. The new device has certain desirable properties. Notably, it is characterized by a variable and controllable-via-design post-elastic stiffness. The mentioned property is a result of MTHD's kinematic configuration which produces this geometric hardening, rather than being a secondary large-displacement effect. Additionally, the new system is capable of reaching high force and displacement capacities, shows high levels of damping, and very stable cyclic response. The device has gone through many stages of design refinement, multiple prototype verification tests and development of design guidelines and computer codes to facilitate its implementation in practice. Practicality of the new device, as offspring of an academic sphere, is assured through extensive collaboration with industry in its final design stages, prototyping and verification test programs.

Keywords Hysteretic damper · Displacement dependent hardening

M. Dicleli (✉) · A.S. Milani
Middle East Technical University, Ankara, Turkey

© Springer India 2015
V. Matsagar (ed.), *Advances in Structural Engineering*,
DOI 10.1007/978-81-322-2193-7_95

1219

1 Introduction

Major bridge structures when threatened by earthquake hazard, often require especial seismic protection to meet the design objectives of controlled displacement and limited or no damage. This is usually a combination of isolation/dissipation devices integrated into an isolation system for the bridge. While isolators reduce the force demand on superstructure by increasing the effective period and bringing the structure to low-energy region of the design spectrum, energy dissipaters absorb and dissipate part of the energy that has already swept into the structure and reduce the displacement and ductility demand on structural components. However, the added energy dissipation capacity due to addition of energy dissipaters is accompanied by increased effective stiffness owing to the added reaction force of the damper, necessary for it to function. This is an effect in contrast to that of an isolator. Depending on project specifics and design demands, usually an appropriate combination of these two different but complimentary mechanisms is sought to provide an effective design.

The first appearance and application of steel hysteretic dampers during late 60s and early 70s came about as the outcome of a study in the Engineering Seismology Section of the Physics and Engineering Laboratory, DSIR, [1–3]. Ever since, hysteretic dampers have come under increasing attention as an effective and economical means for response control for important structures. Compared to buildings, deployment of hysteretic dampers in bridges encounters the additional difficulties of multidirectional displacements and presence of service-condition temperature-induced displacements, which are not supposed to engage the dampers. Multi-directionality of displacements demands that the device be both mechanically capable of displacement at all planar directions and also providing a uniform response irrespective of displacement direction. Consequently, bridge hysteretic dampers are not as diverse as the building ones. A thorough review of bridge dissipation and isolation devices can be found in [4]. The focus of this paper is a newly developed bridge hysteretic damper, Multi-directional Torsional Hysteretic Damper (MTHD). MTHD is capable of large force/displacement capacities and combination of geometric and material hardening gives it a variable post-elastic stiffness, which is believed to be necessary in displacement control of highway bridges. MTHD has passed most phases of necessary analytical and design optimization studies and a 200 kN, 120 mm-capacity prototype of MTHD has recently been tested in the laboratory of the Institute of Structural Engineering at the University of the German Armed Forces in Munich (UniBwM) and also in the Mechanics Laboratory of Engineering Sciences Department at METU. Further experimental investigations, which focus on low-cycle fatigue endurance of energy dissipaters are currently in progress in the Middle East Technical University.

2 Basic Mechanisms and Working Principle of MTHD

MTHD is designed to dissipate energy by torsionally-yielding cylindrical energy dissipaters, named yielding cores. Eight of these identical yielding cores each attached to a torsion arm are arranged in a symmetric configuration to create the MTHD device, as depicted in Fig. 1. To convert translational motion of the structure to twisting in the cylindrical cores, each arm is coupled with a guiding rail, which through a low-friction slider block guides the motion of the arm. The arms are thus restrained to move along a predetermined path regardless of the direction of the imposed displacement on the rail system relative to the base, creating a guided roller hinge connection. The yielding cores are configured in an upright position around a central column to which they are attached through a thick plate (see Fig. 1c). The plate functions as a diaphragm in transmitting the shear and bending forces imposed by the arms to the top part of the corresponding yielding cores, into the central column, base plate and base anchorage; thus protecting the uniform part of the yielding core below from significant bending and its associated shear force. The uniform part of the yielding cores is where energy dissipation due to torsional yielding occurs.

As a general rule in shape design of a yielding dissipater, dictated by optimized design principle, plasticization and energy dissipation should be obtained at a minimum expense to the device, i.e., damage, i.e., plastic straining. Assuming that the objective is to minimize the largest strain value irrespective of the extent and distribution, this leads to uniform strain criterion. The shape should thus be designed so as to result in uniform strains over the body of the dissipater. For a dissipater working based on pure twist/torsion, this criterion suggests a uniform cylinder as the optimum shape. As the shape is optimized for pure twist/torsion, unwanted bending and shear will upset the desired uniformity in strains and thus the

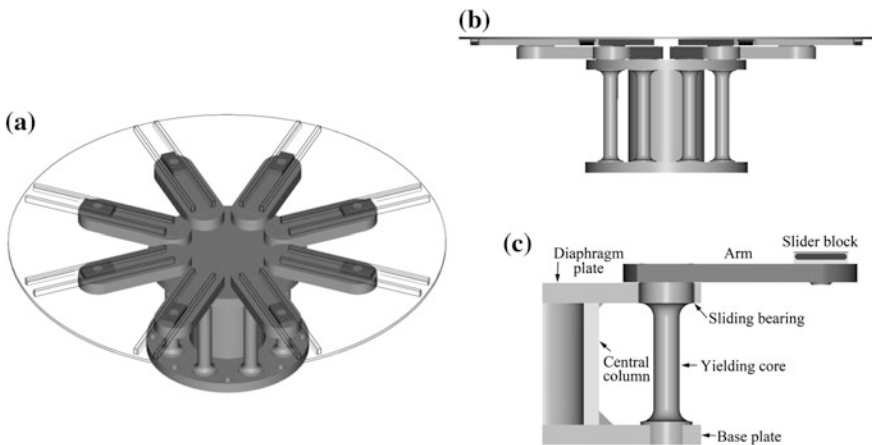


Fig. 1 Multi-directional Torsional Hysteretic damper (MTHD): **a** isometric view showing the rail system and base device underneath; **b** side view; **c** energy dissipation unit of MTHD: a yielding core, as attached to other components of the device

minimum damage objective, as laid out above. Proper functioning of base plate-central column-diaphragm plate as a rigid support for yielding cores against bending is thus crucial to stable and reliable performance of the device. A more detailed description of the system is presented in [5, 6].

3 Force-Displacement Response Features of MTHD

A distinguishing feature in force-displacement response of MTHD is the geometric hardening behavior, which is the outcome of translation-to-rotation motion conversion mechanism in MTHD. As depicted in Fig. 2, this mechanism, working at individual energy dissipater level, magnifies the reaction force required to balance the torque in yielding cores. Reaction force of the device is the sum of projections of all eight forces at slider-rail interface. Since the projection angles are independent of displacement and depend only on orientation of rails, the hardening behavior at eight energy dissipater level directly translates to similar behavior in global response of

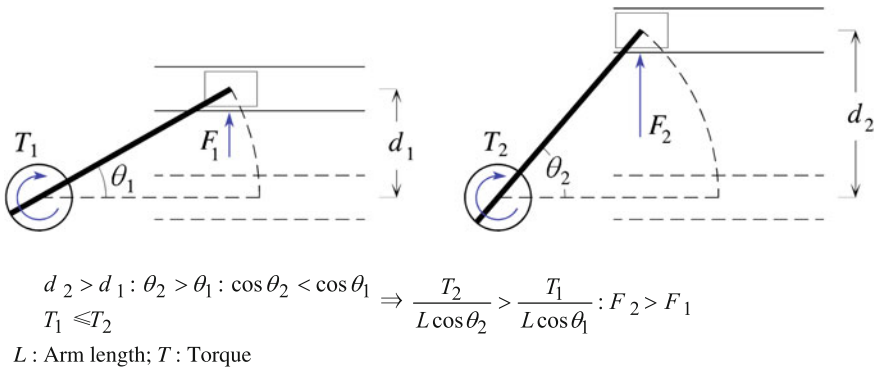


Fig. 2 Working mechanism of MTHD responsible for geometric hardening

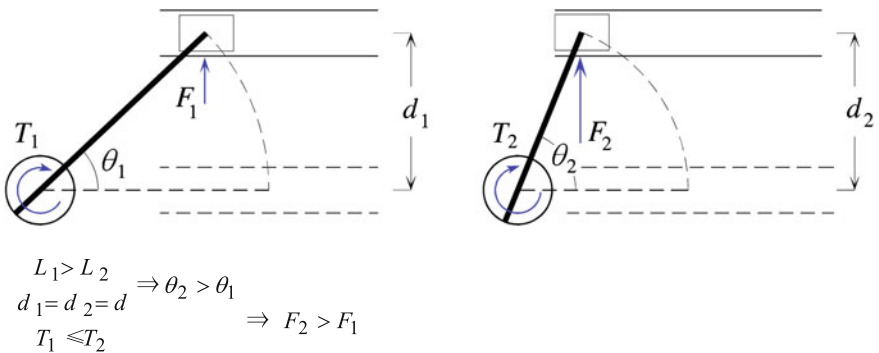


Fig. 3 Target hardening index is obtained by adjusting the arm length

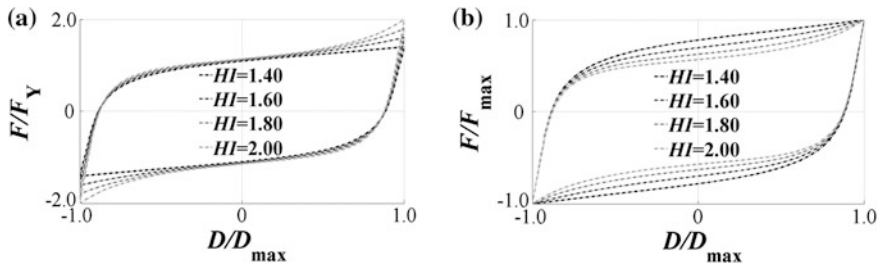


Fig. 4 MTHD response for different design hardening indices ($HI = F_{max}/F_Y$). **a** force values are normalized to F_Y to emphasize variation in F_{max} among loops; **b** force values are normalized to F_{max} to emphasize shape variation of hysteresis loops among MTHDs designed for the same maximum force

the device. The same mechanism also offers the possibility of controlling the desired level of hardening in force-displacement response, through adjustment of the arm length to maximum displacement ratio. This is depicted in Fig. 3. Varying levels of hardening obtained as such, leads to hysteresis loops of different shapes as shown in Fig. 4; As indicated on these graphs, the parameter used to characterize hardening in MTHD is termed ‘Hardening Index’, defined as:

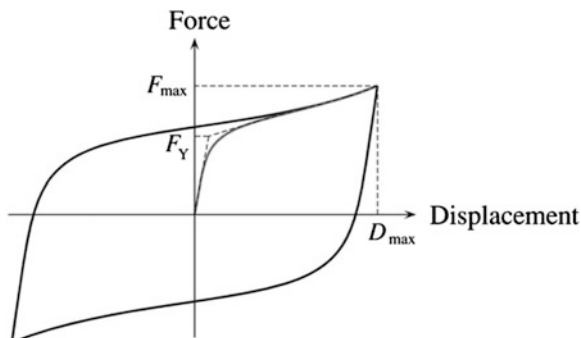
$$HI = \frac{F_{max}}{F_Y} \quad (1)$$

where F_{max} and F_Y stand for maximum force capacity (force at D_{max}) and effective yield force of MTHD, respectively. Analytical formulation of force-displacement response of MTHD leads to complicated equations unfit for hand calculations. Nevertheless, simulations have shown that assuming a certain material model for energy dissipaters (steel grade), properly normalized form of force-displacement curves, categorized by their HI values, are universal and can be established as the scalable response curves for any MTHD with a specific HI , regardless of component dimensions and force/displacement capacity but made of the same steel. Graphs in Fig. 4 represent such curves obtained for C45 steel. Furthermore, component friction is found to have negligible impact on the shape of normalized loops and equations for frictionless MTHD can reliably be used to construct the curves.

4 Characteristic Properties of MTHD as Relevant to Structural Analysis

Three parameters are necessary and enough to characterize force displacement behavior of MTHD: either (F_{max}, F_Y, D_{max}) or (F_{max}, D_{max}, HI) . HI (F_{max}/F_Y) is used to define the normalized curve (see Fig. 4) and F_{max}, D_{max} are used as scale factors. In the parameter sets above, yield displacement could be an alternative to D_{max} ,

Fig. 5 Characteristic properties of MTHD



however, displacement capacity is preferred, being more relevant in design of both the MTHD and the structure, and also a more concretely-defined point on force-displacement curve, as opposed to the effective yield point (see Fig. 5). Once a hardening index is chosen by the structural engineer based on requirements of design, geometric properties of MTHD can be easily adjusted to obtain the demanded level of hardening, as indicated in the preceding section and depicted in Fig. 3. This is done in design phase of the MTHD itself, which follows the structural design of the bridge. The three parameters are therefore enough for the structural engineer to proceed with the design without any knowledge or assumption on design specifics of the device itself.

5 Prototype Testing

A 200 kN, 120 mm capacity MTHD was designed for prototype testing, as shown in Fig. 6. Since design and configuration of the MTHD allows for easy replacement of the yielding cores (energy dissipaters of MTHD), four sets of replaceable yielding cores were produced out of S355J2+N, C45 (two sets), 42CrMo4+QT steel grades. The device is considered a low-capacity version of its kind, as in real practice a much higher force/displacement capacity devices are employed. Experiments on prototype MTHD, consist of fully-reversed cyclic quasi-static displacement-controlled tests at varying amplitudes, consisting of 1/4, 1/2 and 1.0 D_{max} . After completing the test with one steel grade, the eight yielding cores were replaced for the next phase of tests. The most sought-after results in a quasi-static cyclic test on a seismic device are:

- i. General shape of force-displacement response loops, force measurements, effective stiffness and damping of the device,
- ii. Observations on stability of response expressed in terms of the extent of variation in force-displacement response loops, the maximum force and enclosed loop area at a certain displacement range of response,
- iii. Consistency of measured response with theoretical predictions.

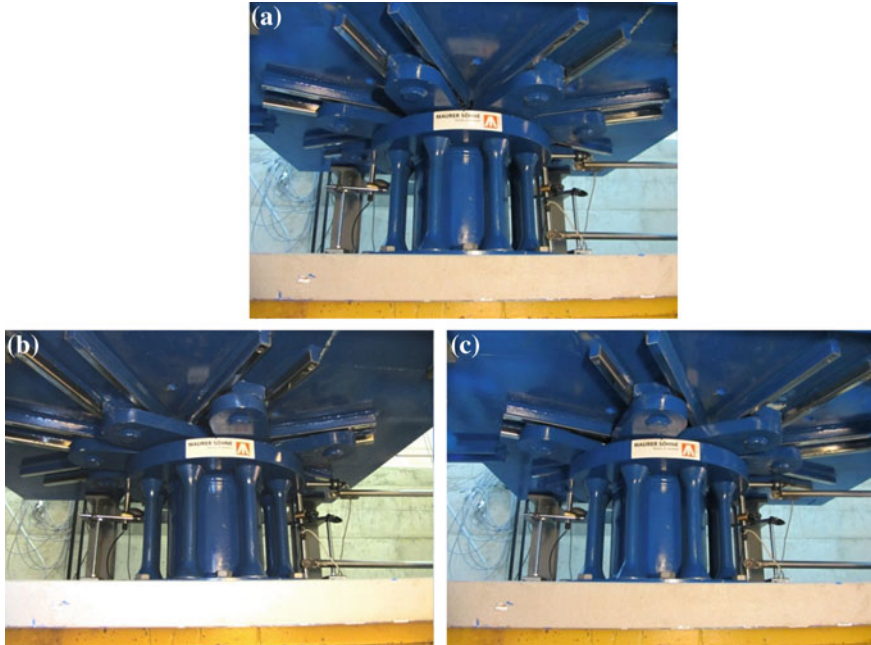


Fig. 6 200 kN, 120 mm-capacity prototype MTHD, as tested at METU: **a** un-displaced position, **b, c** two extreme strokes of ± 120 mm

Force-displacement response loops for nearly all of the tests are plotted in separate figures for each type of steel used as energy dissipaters, in Fig. 7. The graphs show a very stable cyclic response with little variation in force levels not exceeding 4.0 % the mean value at worst which is considerably smaller than 15 % limit prescribed by EN-15129, ASCE 07-05 and ASCE 41-06. Higher hardening in the MTHD with 42CrMo4+QT steel and the second set of C45 steel is clearly attributed to higher material hardening, since the rate of geometric hardening is the same for tests with the same displacement amplitudes. Small segments are seen near (force) zero-crossing points with a sharp drop in stiffness. These appear as sloped lines with lower slope than the main unloading branch of the curve and resemble the behavior characteristics of systems with gap. The cause is attributed to the clearances at certain components of MTHD. Lowering of the manufacturing tolerances will reduce the size of these segments. Table 1 contains the summary of two main properties of the damper, force and effective damping coefficient. The shown values are average of all loops at the described displacement.

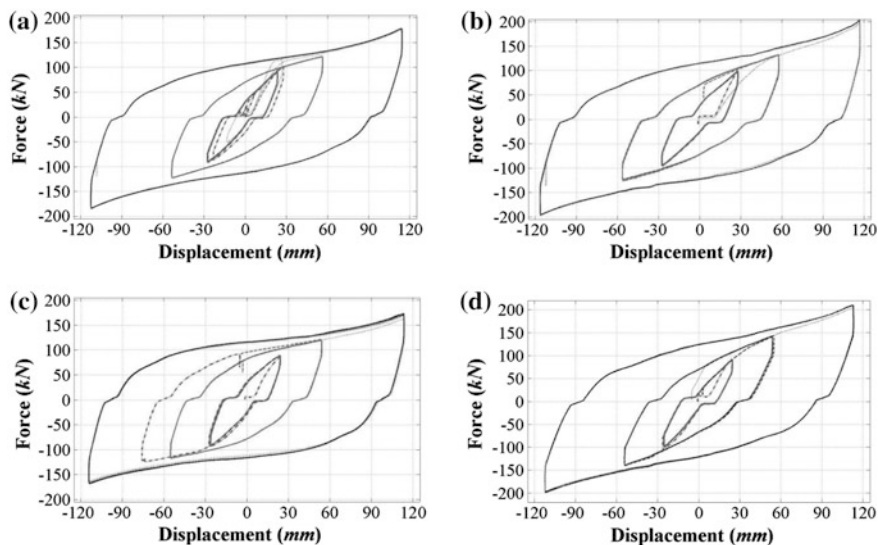


Fig. 7 Cyclic response of prototype MTHD with yielding cores made of three different steels: **a** C45-set 1, **b** C45-set 2, **c** S355J2+N, **d** 42CrMo4+QT

Table 1 Measured maximum force and effective damping coefficient

Steel grade	D_{\max} (mm)	F_{\max} (kN)	β_{eff} at D_{\max}
C45-set 1	-113, +114	-184, +178	0.33
C45-set 2	-116, +117	-196, +204	0.33
S355J2+N	-114, +114	-168, +172	0.38
42CrMo4+QT	-112, +113	-198, +210	0.32

6 Summary and Conclusions

A summary of analytical and experimental studies into the behavior of a new hysteretic damper, Multi-directional Torsional Hysteretic Damper (MTHD) is presented. A 200 kN, 120 mm-capacity version of the device was built and tested in UniBw Munich and also at METU. The new system is capable of reaching high force and displacement capacities, shows high levels of damping, controllable post-elastic stiffness and very stable cyclic response. A design methodology for the device has also been completed recently. The work so far, has demonstrated the prospects of the system. To further establish the new device as a technically proven anti-seismic system, and also to optimize the design process of the device, more tests on larger-capacity MTHDs will be required.

Acknowledgments Full sponsorship of the experimental phase of this work by the international construction firm, MAURER SÖHNE, and provided technical assistance has been instrumental in progress of the research. This contribution is hereby acknowledged. The second author gratefully acknowledges the financial support provided by the Scientific and Technological Research Council of Turkey (TÜBİTAK), under the Ph.D. fellowship program 2215.

References

1. Skinner RI, Robinson WH, McVerry GH (1993) An introduction to seismic isolation. Wiley, Chichester
2. Kelly JM, Skinner RI, Heine AJ (1972) Mechanisms of energy absorption in special devices for use in earthquake resistant structures. *Bull NZ Soc Earthq Eng* 5:63–88
3. Skinner RI, Kelly JM, Heine AJ (1974) Hysteretic dampers for earthquake-resistant structures. *Earthq Eng Struct Dyn* 3:287–296
4. Casarotti C (2004) Bridge isolation and dissipation devices: state of the art review in bridge isolation, structural seismic response and modeling of modern seismic isolation and dissipation devices. MSc dissertation, ROSE School
5. Dicleli M, Salem Milani A (2010) Multi directional hysteretic damper with adaptive post-elastic stiffness for seismic protection of bridges in near fault zones. In: Proceedings of the 5th international conference on bridge maintenance, safety and management (IABMAS2010), Philadelphia, USA. CRC Press, pp 615–615, 11–15 July 2010
6. Dicleli M, Salem Milani A (2011) Multi-directional hysteretic damper with geometrically hardening post-elastic stiffness for seismic protection of bridges. In: 2011 world congress on advances in structural engineering and mechanics (ASEM11+), Seoul, Korea, paper no. 329

Seismic Performance of Shear-Wall and Shear-Wall Core Buildings Designed for Indian Codes

Mitesh Surana, Yogendra Singh and Dominik H. Lang

Abstract The shear-wall and shear-wall cores are the most commonly used lateral load resisting elements in mid-rise to high-rise RC buildings. The present study focusses on estimation of seismic performance of shear-walls and shear-wall core buildings designed for Indian codes using non-linear pushover analysis. The literature review for modelling of shear-walls is carried out and the most commonly used models, i.e. wide column model and shell element model are validated through the experimental results available in literature. It is observed that both the wide column model and shell element model predict nearly the same strength capacity for the shear-walls and shear-wall cores. However, the wide column model underestimates while the shell element model overestimates the ductility capacity of the shear-walls and shear-wall cores. It is also observed that the stiffness obtained from moment-curvature analysis is in close agreement with the experimental results while the shell element model predicts high initial stiffness and after cracking it reduces and matches with experimental results. These validated models are implemented for performance evaluation of “Dual Systems” designed according to Indian code. It has been observed that buildings with shear-walls placed at periphery have better performance than buildings with centrally placed shear-wall core.

Keywords Pushover analysis · Shear-walls · Shear-wall cores · Shell element model · Wide column model

M. Surana (✉) · Y. Singh
Department of Earthquake Engineering, IIT Roorkee, Roorkee, India

D.H. Lang
NORSAR, Kjeller, Norway

1 Introduction

A wall that is subjected to lateral loads in its plane is referred as “Shear-wall”. The extent to which this wall shares the lateral load coming on the structure is governed by the stiffness and strength characteristics of the wall. The shear-wall enhances strength, stiffness and ductility of the frame. The term shear-wall is actually a misnomer as far as high rise building is concerned. The shear-walls are designed to resist lateral forces induced by earthquakes and wind. They may be used as exterior, interior or cores enclosing elevator shafts or stair-case. These shear-walls may be of any shape like rectangular, angle, channel and wide flanges as shown in Fig. 1. The shear-walls are the most commonly used as lateral load resisting elements in frame buildings. The behavior of the shear-walls is dependent on its height to width ratio and according to height to width ratio the shear-wall may be squat or slender. The design of squat shear-walls is governed by shear while the design of slender shear-walls is governed by flexure. The slender walls are most commonly used and primarily deforms in flexure mode like a free standing cantilever as shown in the Fig. 2.

Fig. 1 Shapes of planar and non-planar walls

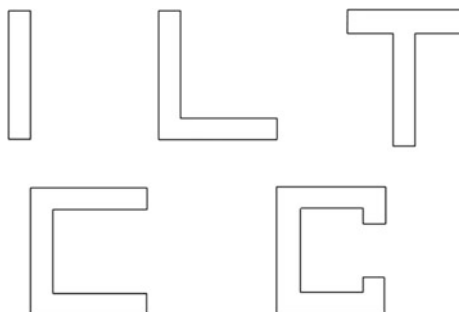
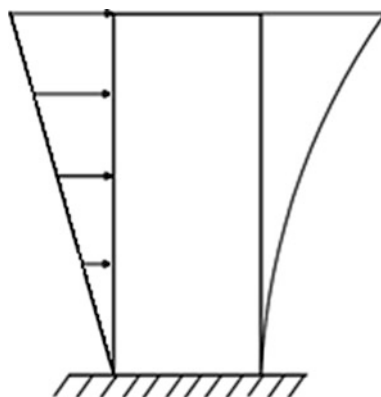


Fig. 2 Deformed shape of shear-wall under lateral load



2 Modelling of Shear-Walls and Shear-Wall Cores

Planar and non-planar walls are the common structural elements providing lateral stiffness and strength in RC buildings. The modelling of walls is necessary in order to predict their force deformation behavior. In this section different techniques of modelling the behavior of planar and non-planar walls under seismic loading are reviewed. The shear-walls can be modelled as either by equivalent frame elements (EFM) or by finite element modelling (FEM). The various models available in literature are discussed in this section.

2.1 Equivalent Frame Models of Shear-Walls

The planar and non-planar walls can be modelled using equivalent frame models. The available equivalent frame models consist of wide column analogy and braced frame analogy. The each of equivalent frame model has certain advantages and limitations. This section summarizes the equivalent frame models.

2.1.1 Wide Column Analogy

The wide column model was initially developed for planar walls by Clough et al. [1]. Later on it was extended for non-planar walls also. The wide column modelling of shear-walls and shear-wall cores consist of assigning the properties of shear-wall to a column, which is assigned at the centroid of the wall section as shown in the Fig. 3. This column is connected through a rigid link which is modelled as rigid in shear and flexure.

The designer needs axial force, bending moments and shear force in order to design the shear-walls; hence wide column model is very easy since only frame analysis is required. The wide column analogy has certain drawbacks also. The first drawback is that in the wide column analogy the shear-walls are subjected to parasitic moments since the continuous shear stresses at the edges of the wall is modelled as equivalent nodal forces as shown in the Fig. 4. This equivalent nodal force leads to development of additional bending moment (parasitic) in shear-walls. This parasitic moment causes the reverse bending of the column element. A large

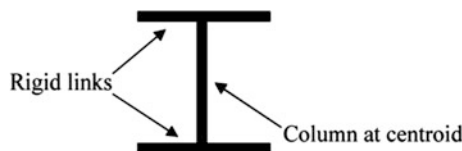
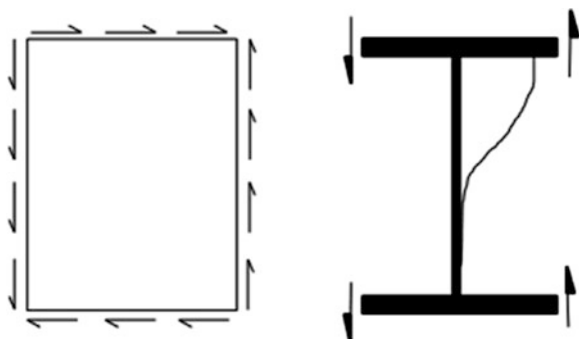


Fig. 3 Wide column analogy

Fig. 4 Parasitic moments in wide column analogy



number of efforts have been made by number of researchers to improve the wide column model and to overcome its shortcomings related to parasitic bending moments. Stafford-Smith and Abate [2], Stafford-Smith and Girgis [3] and Kwan [4] suggested modifying the wide column model by adding bracings to the wide column models in order to avoid the displacements due to parasitic moments.

2.1.2 Braced Frame Analogy

Stafford-Smith and Abate [2], Stafford-Smith and Girgis [3] and Kwan [4] suggested that modifying the wide column model by addition of the braces to the wide column model as shown in the Fig. 5. It can eliminate the displacements induced due to parasitic moments. However, wide column models with braces have several drawbacks. The first drawback is that the stiffness of the braces and the stiffness of the column element need to be determined such that sum of the stiffness is equal to true wall stiffness, so that the column element is no longer the direct model of the wall section.

The second drawback is that the internal forces of the wall can no longer be directly obtained from internal forces of the column element, but equilibrium needs to satisfy on the entire wide column model including braces. The third drawback is that the more number of elements and nodes are required as compared to wide column analogy. The stiffness properties of the column (I_c , moment of inertia of the

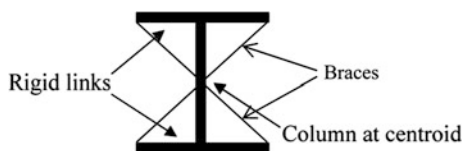


Fig. 5 Braced frame analogy

column and A_c , area of the column and braces A_d , axial area of the diagonal brace) are determined by the following three equations of equilibrium:

$$I_c = \frac{tb^3}{12} \quad (1)$$

$$\frac{12EI_c}{h^3} + \frac{2EA_d \cos^2 \theta}{l} = \frac{btG}{h}, \quad (2)$$

$$\frac{EA_c}{h} + \frac{2EA_d \sin^2 \theta}{l} = \frac{EA_w}{h}. \quad (3)$$

These equations are based on bending, shear and axial stiffness of the corresponding wall section.

where

- t thickness of the shear-wall
- b width of the shear-wall
- E modulus of elasticity
- h height of the shear-wall

The wide column model with bracing is only practical for elastic analysis because it seems very improbable to find an appropriate combination of inelastic properties of the braces and the column element, which represent correctly the bending moment-axial force interaction of the wall section.

2.2 *Finite Element Models of Shear-Walls*

The finite element model is the most widely used in three dimensional analyses of shear-walls and shear-wall cores. The shell element which is a combination of membrane element and plane stress element, with six degrees of freedom is commonly used for modelling of planar as well as non-planar walls. The damage state of an element is dependent on the peak strains in the most critical section; hence shell element makes use of peak strains. The ultimate strain capacity of unconfined concrete is of the order of 0.0050 while it is of the order of 0.02 for confined concrete. The strain capacity of confined concrete depends on a number of factors such as confinement ratio, spacing of confining reinforcement and yield strength of confining reinforcement. It becomes necessary while using the finite element model that suitable strain limits should be used for concrete material model as well as steel material model. Further, accuracy of the results in the finite element analysis is dependent on the mesh size. A very fine meshing may lead to increase the computational efforts while a coarse meshing may lead to erroneous results. In order to get good results first sensitivity analysis should be performed and depending upon the accuracy requirements the mesh size should be selected. A mesh size of $0.2 \text{ m} \times 0.2 \text{ m}$ gives good results for the shear walls.

3 Model Validation

In this study two U-shaped walls which were tested under quasi-static cyclic loading by Beyer et al. [5] are validated using wide column model (equivalent frame model) and shell element model (finite element model). During the testing of the walls the applied axial load was kept constant; the axial load at the base of the wall was 780 kN (including the self-weight of the wall). The axial load was applied at the approximate centre of the gross section. The wall thickness of Test Unit A (TUA) was 150 mm while the wall thickness of Test Unit B (TUB) was 100 mm. The total area of the vertical reinforcement was approximately same for the two test units (TUA: A_s : 3,281 mm², TUB: A_s : 3,224 mm²). The material behavior of the concrete has been modelled as the stress strain relationship by Mander et al. [6] model. The approach by Mander et al. [6] was also used for estimating the strength and strain capacity of the confined concrete regions. The sections and reinforcement details of the walls are as shown in the Fig. 6. The Fig. 7 shows the different directions of loading which consists of loading parallel to web (position A and B) and loading parallel to flanges (position C and D).

3.1 Moment-Curvature Analysis

The moment-curvature curves have been developed for two different directions of loading, i.e. parallel to web and parallel to flanges using the Euler's beam theory through section analysis, without considering any tensile strength of the concrete. All the moments and curvatures have been plotted as positive values. These moment-curvature curves have been converted into equivalent bilinear curves using Caltrans idealized model. From this idealized bilinear curves the effective stiffness is determined. The stiffness modifiers obtained from moment-curvature analysis are shown in Table 1 and used in modelling of U-shaped RC walls which were tested experimentally by Beyer et al. [5]. The Fig. 8 shows moment-curvature curves for TUA and TUB under different directions of loading. From the section analysis it has been observed that when wall is loaded in direction A or B, the wall is symmetric about NS axis; hence same moment-curvature curve has been obtained while when wall is loaded in direction C (web in compression) and D (flanges in compression), the wall is asymmetric about EW axis; hence different moment-curvature curves have been obtained.

3.2 Force Deformation Curves

In order to obtain force deformation curves the pushover analysis has been performed on the wall units TUA and TUB. To perform pushover analysis wide

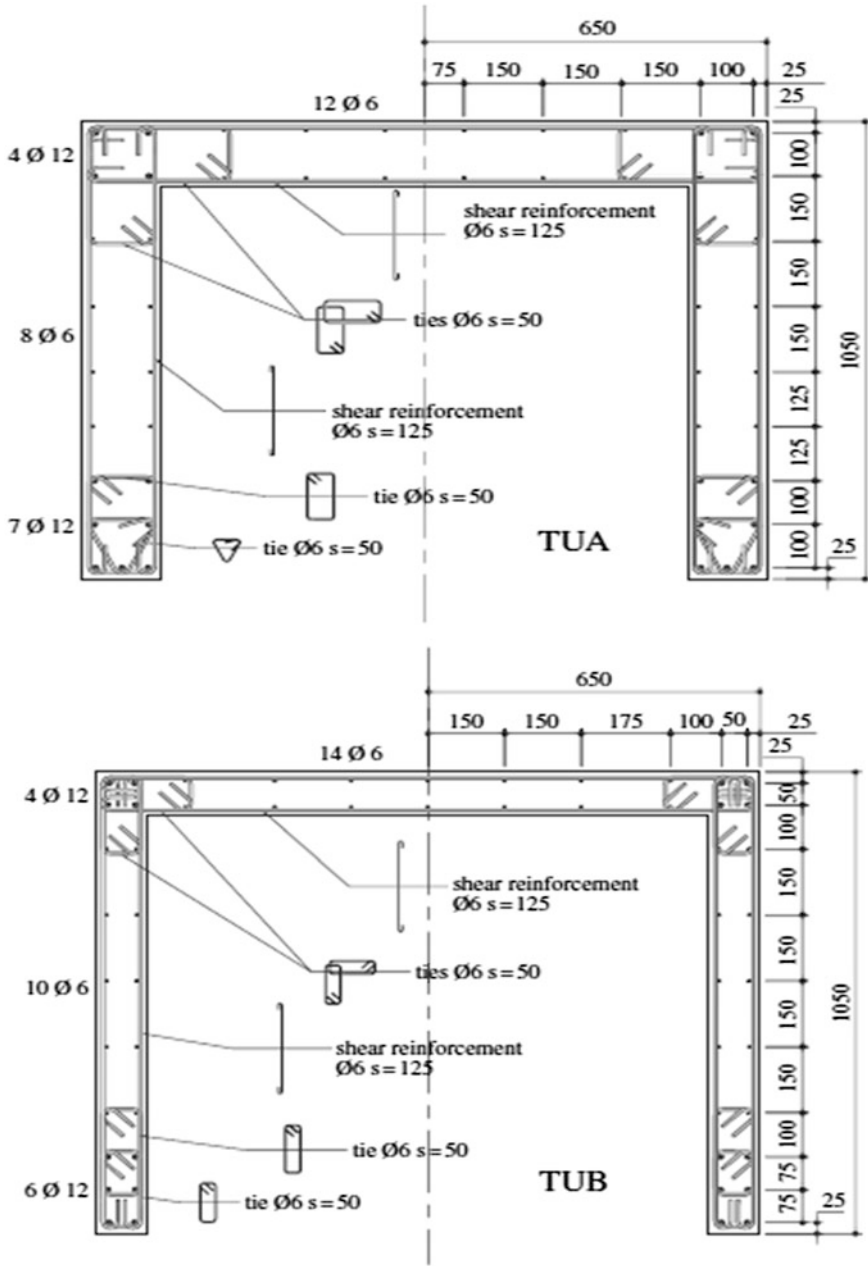


Fig. 6 Sections and reinforcement details of wall TUA and TUB (Beyer et al. [5])

Fig. 7 Direction of loading (Beyer et al. [5])

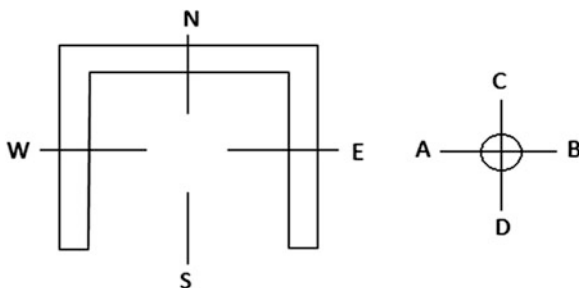


Table 1 Stiffness modifiers for different directions of loading

Position	M_y (kN-m)	ϕ_y (1/m)	$EI_{effective}$ (kN-m ²)	EI_{gross} (kN-m ²)	EI_{eff}/EI_{gross}
TUA A, B	1,500	0.0028	5.36E + 05	3.83E + 06	0.14
TUA C	1,296	0.0049	2.65E + 05	1.65E + 06	0.16
TUA D	1,111	0.0039	2.85E + 05	1.65E + 06	0.17
TUB A, B	1,522	0.0028	5.44E + 05	2.86E + 06	0.19
TUB C	1,335	0.0050	2.67E + 05	1.21E + 06	0.22
TUB D	1,075	0.0039	2.76E + 05	1.21E + 06	0.23

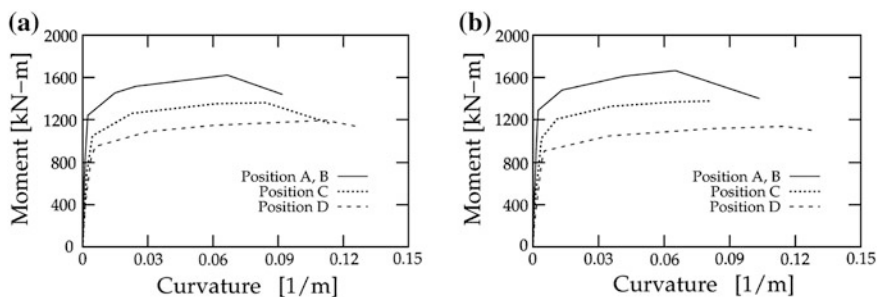


Fig. 8 Moment-curvature curves for different directions of loading. **a** TUA. **b** TUB

column model (EFM) and shell element model (FEM) has been developed in proprietary finite element code SAP 2000, CSI [7]. The pushover analysis has been performed in displacement control domain. The loading has been applied at the shear centre in order to prevent twisting of the wall. The force versus displacement has been monitored at a height of 3.35 and 2.95 m for loading parallel to web and loading parallel to flanges, respectively according to experimental programme. The stiffness modifiers obtained from section analysis has been used in wide column model in order to consider the effect of the cracked section, while in case of shell element model no modifier has been used. The actual pushover curve obtained

from experimental results Beyer et al. [5] was of curvilinear shape but in this study that curvilinear shape is approximated as an equivalent bilinear curve. The Fig. 9 shows the comparison of the force deformation curve for walls TUA and TUB under different direction of loading using the experimental and analytical models. The force deformation curve clearly indicates that both the EFM and FEM predicts the strength capacities in the close agreement with as obtained from the experimental results but the EFM underestimates the ductility capacity while FEM overestimates the ductility capacity of the walls.

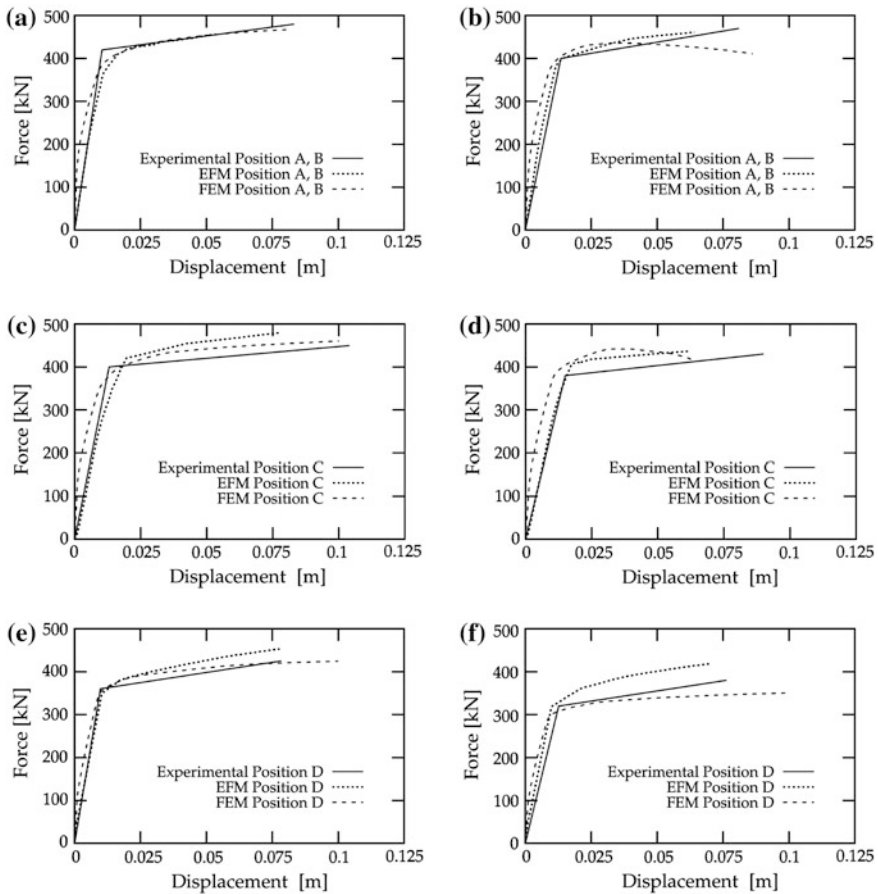


Fig. 9 Comparison of force deformation curves for different directions of loading using analytical models and experimental approach. **a** TUA position A, B **b** TUB position A, B **c** TUA position C **d** TUB position C **e** TUA position D **f** TUB position D

4 Numerical Study and Performance of the Considered Buildings

The buildings considered in this study consists of two artificially generated 15 storied buildings, consisting of shear walls located at the periphery of the building (SW) and the shear wall core located centrally (SWC) with plan as shown in the Fig. 10. The shear-wall building is symmetric about both axes while shear-wall core building is asymmetric about longitudinal axes. These buildings are designed as per Indian standards IS: 1893 Part 1 [8] and IS: 13920 [9] for zone V and soft soil conditions with demand curve as shown in the Fig. 11. The Table 2 presents the section and percentage of longitudinal reinforcement for shear-walls and shear-wall core. The displacement controlled non-linear static analysis has been performed with loading proportional to the fundamental mode as per ATC-40 [10] and the performance has been evaluated using ASCE/SEI 41-06 [11]. The validated models in previous section have been implemented in this study and Fig. 12 represents the capacity curves for the considered buildings. It has been observed that the both EFM and FEM have very close estimate of strength for shear-wall and shear-wall core buildings but the EFM predicts lesser stiffness than FEM for shear-wall cores.

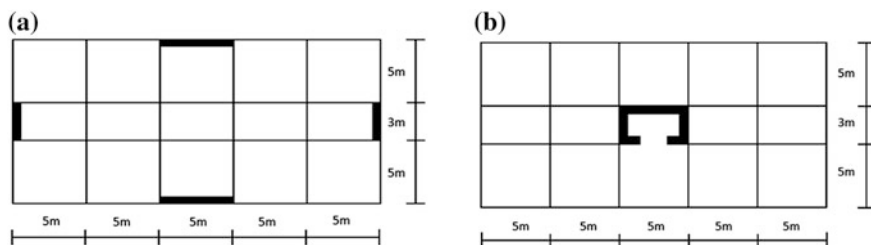


Fig. 10 Plan of the considered buildings. a Shear-wall building (SW) b Shear-wall core building (SWC)

Fig. 11 Demand curves for DBE and MCE (5 % Damping)

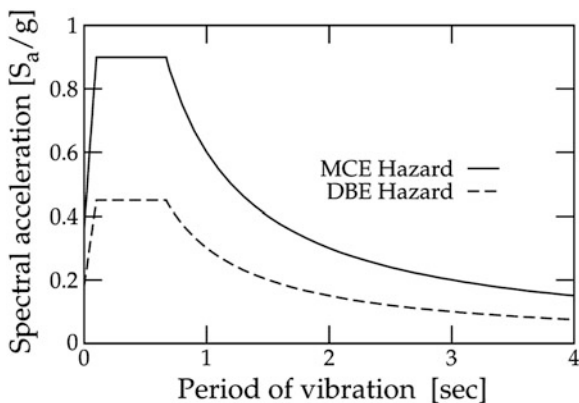


Table 2 Details of shear-walls and shear-wall core

Wall description	Wall thickness (mm)	Longitudinal reinforcement %
5 m long shear-wall	300	1.10
3 m long shear-wall	300	1.10
Shear-wall core	200	1.04

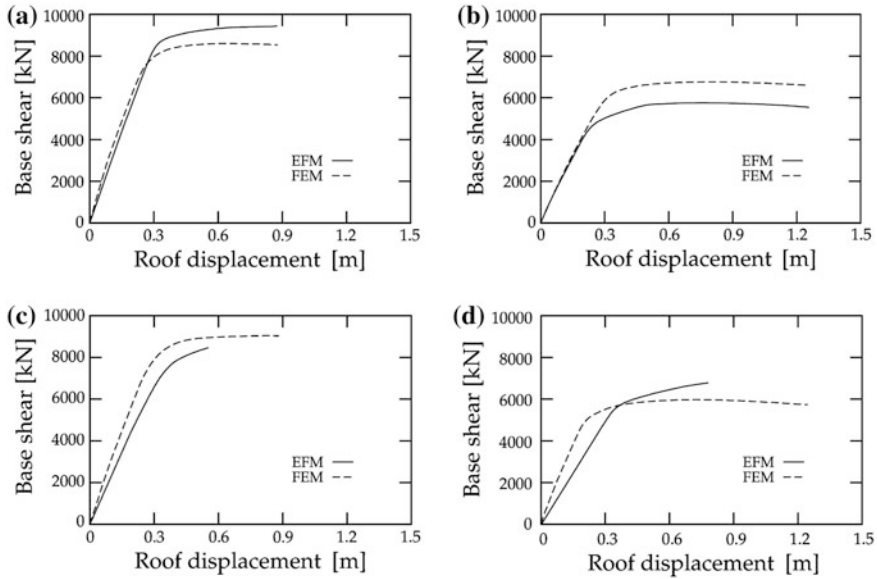


Fig. 12 Capacity curves for the considered buildings. **a** Shear-wall building (Longitudinal) **b** Shear-wall building (Transverse) **c** Shear-wall core building (Longitudinal) **d** Shear-wall core building (Transverse)

The performance of the considered buildings has been evaluated following the displacement modification method (DMM) of ASCE/SEI 41-06 [11]. The DMM consists of modification of the elastic displacement by constant factors which accounts for site class, effective period (T_{eff}) and strength and stiffness degradation characteristics of the structural system. The target displacement is calculated as

$$\Delta_t = C_0 C_1 C_2 S_a \frac{T_e^2}{4\pi^2} g \tag{4}$$

where

- Δ_t target displacement for a given hazard
- C_0 a factor to relate response of single degree of freedom system to multi degree of freedom system

Table 3 Performance of the considered building

Model description	Direction	Performance point (DBE) (mm)	Performance level (DBE)	Performance point (MCE) (mm)	Performance Level (MCE)
SW	Longitudinal	238	IO	476	LS
SW	Transverse	267	IO	534	LS
SWC	Longitudinal	258	IO	516	CP
SWC	Transverse	302	IO	604	CP

Note SW Shear Wall, SWC Shear Core Wall

IO Immediate Occupancy, LS Life Safety and CP Collapse Prevention

C_1 a factor which accounts for site class

C_2 a factor to account strength and stiffness degradation characteristics of structural system

T_e effective period of vibration of system for direction under consideration and

S_a spectral acceleration at the effective period of vibration for direction under consideration

The Table 3 represents the performance of the considered buildings obtained from and it has been observed that for Design Basis Earthquake (DBE) level of seismic demand both shear-wall and shear-wall core buildings have Immediate Occupancy (IO) performance level while for Maximum Considered Earthquake (MCE) level of seismic demand the shear wall building has Life Safety (LS) performance level and shear-wall core building has Collapse Prevention (CP) performance level.

5 Conclusions

The various modelling techniques for shear-walls and shear-wall cores have been discussed with their limitations. The shear-walls and shear-wall cores modelled using the frame elements and finite elements seem to be suitable for static as well as dynamic analysis. The wide column model and shell element model are validated using experimental results available in literature for quasi-static testing of two U-shaped RC walls. These validated models have been implemented for shear-walls and shear-wall cores in the present study. It has been observed that both the wide column model and shell element model predict the strength capacities of the wall in close agreement with the experimental results while the ductility capacity of the walls is slightly underestimated by the wide column model and overestimated by the shell element model. The performance of the shear-wall and shear-wall core buildings for Design Basis Earthquake is Immediate Occupancy (IO), whereas for the Maximum Considered Earthquake, the performance of shear-wall building is Life Safety (LS) and shear-wall core building is Collapse Prevention (CP). Hence, it

can be concluded that shear-wall building has performed slightly better in comparison to the shear-wall core building. Nevertheless, performance of both the buildings designed for Indian code, is satisfactory.

References

1. Clough RW, King IP, Wilson EL (1964) Structural analysis of multi-storey buildings. *J Struct Div ASCE* 90(19):19–34
2. Stafford-Smith B, Abate A (1981) Analysis of non-planar shear wall assemblies by analogous frame. *Proc Inst Civ Eng* 71(2):395–406
3. Stafford-Smith B, Girgis A (1984) Simple analogous frames for shear wall analysis. *J Struct Eng ASCE* 110(11):2655–2666
4. Kwan AKH (1994) Unification of existing frame analogies for coupled shear/core wall analysis. *Comput Struct* 51(4):393–401
5. Beyer K, Dazio A, Priestley MJN (2006) Quasi-static cyclic tests on U-shaped RC walls: test design and preliminary results. In: *Proceedings of the first european conference on earthquake engineering and seismology*, Geneva, Switzerland
6. Mander JB, Priestley MJN, Park R (1988) Theoretical stress-strain model for confined concrete. *ASCE J Struct Eng* 114(8):1804–1826
7. CSI (2010) SAP 2000: integrated software for structural analysis and design, version 14.2.4. Computers and Structures, Inc., Berkeley
8. IS: 1893 Part 1 (2002) Indian standard criteria for earthquake resistant design of structures, part 1: general provisions and buildings (fifth revision). Bureau of Indian Standards, New Delhi
9. IS: 13920 (1993) Indian standard ductile detailing of reinforced concrete structures subjected to seismic forces—code of practice. Bureau of Indian Standards, New Delhi
10. ATC-40 (1996) Seismic evaluation and retrofit of concrete buildings: volume 1. Applied Technology Council, Redwood City
11. ASCE/SEI 41-06 (2007) Seismic rehabilitation of existing buildings. ASCE Standard, American Society of Civil Engineers, Reston

A Study on the Design Parameters of the Compliant LCD for Structural Vibration Control Under Near Fault Earthquakes

Achintya Kumar Roy and Aparna (Dey) Ghosh

Abstract Earthquake ground motions, recorded in near-fault zones, differ from those observed in the far-fault regions. The most important characteristics of the near-fault ground motion is the pulse like nature with high magnitude often found in the velocity time history along with large ground displacement which contribute significantly to the long period content of the resulting ground motions. This impulsive behavior is mostly caused by forward directivity effect and found in the fault normal component of the ground motion. Again, because of the short travel distance the ground motion is rich in high frequencies. Consequently both short period as well as flexible structures have very high damage and collapse potential under near-fault earthquake ground motions. Nowadays, the focus of researchers is seismic protection of structures by the use control devices. Amongst the relatively low-cost but reliable and effective passive control devices, the Liquid Column Damper (LCD) has gained ground but the conventional damper is only applicable to flexible structures. A variation of the LCD, termed the Compliant LCD (CLCD) is found suitable for short-period structures as well. However, both LCD and CLCD have hitherto been studied for suppression of structural vibrations due to far-field earthquakes only. In this paper, an investigation is made into the performance of the CLCD incorporated into a structure, modeled as a SDOF system. A simulation study is carried out with earthquake data specified as near-fault pulse type ground motions. The sensitivity of some of the design parameters of the CLCD to the damper performance has also been examined. The study indicates that the CLCD is capable of acting as a control device for such earthquake vibrations. The results of the parametric study indicate design trends some of which are different from the existing ones for far-field ground motions.

A.K. Roy · A. (Dey) Ghosh (✉)

Department of Civil Engineering, Indian Institute of Engineering Science and Technology, Shibpur (Formerly Bengal Engineering and Science University, Shibpur), Howrah, India
e-mail: aparna@civil.becs.ac.in

A.K. Roy
e-mail: kumarroyachintya@gmail.com

Keywords Liquid column damper (LCD) · Earthquake ground motion · SDOF · Sensitivity · Structural vibration control

1 Introduction

Near-fault ground motions containing strong velocity pulses have been identified as imposing extreme demands on structures [3]. The near-fault earthquakes are also rich in high frequencies because of the short travel distance. The pulse-type motion is particular to the “forward” direction, where the fault rupture propagates towards the site at a velocity close to the shear wave velocity, causing most of the seismic energy to arrive at the site within a short time. The ground shaking near a fault rupture may thus be characterized by a short duration impulsive motion that exposes structures to a high input energy at the beginning of the record. As a result, the structures mainly get damaged by a few large displacements. This was reported by Bertero et al. [6] who were the first to study the effects of near-fault impulse-type ground motion on structures after the 1971 San Fernando earthquake. They also stated that short period structures could experience very high ductility demands when subjected to near-fault ground motions. Since then, several researchers such as Anderson and Bertero [2], Hall et al. [11], Alavi and Krawinkler [1], Ghobarah [7] and others have devoted research to the study of structural response to near-fault seismic excitation. Some researchers including Jangid and Kelly [14] and Shen et al. [17] have investigated the effectiveness of protecting structures from the damaging effects of near-fault ground motion by using base isolation. Ozbulut et al. [15] have studied variable friction dampers for adaptive control of base-isolated structures for protection against near-field earthquakes.

In recent years, considerable efforts have been made to better protect structures from earthquakes by the incorporation of liquid dampers, which rely on the motion of liquid in a rigid container for providing the energy dissipating characteristics. These have gained popularity as they offer the following advantages: (1) simple equipment, arbitrary shapes, and easy handling (2) clear mechanism and (3) near freedom from maintenance (4) multiple uses, e.g., containers may be used as water tanks for drinking and emergency. Specifically, the liquid column damper (LCD) which dissipates the energy through the motion of the liquid mass in a tube-like container fitted with orifice(s), has several more advantages such as high volumetric efficiency with respect to a given amount of liquid, quantitative definiteness of damping and consistent behavior across a wide range of excitation levels. Application of LCD for flexible structures such as cable-stayed bridges, towers and tall buildings for mitigation of wind-induced vibrations has been well-investigated by researchers such as by Xu et al. [19], Balendra et al. [4] and Balendra et al. [5]. Won et al. [18] and Han and Won [12], amongst a few others, studied the seismic performance of LCDs for flexible structures. But the applicability of the damper to stiff or short period structures is restrictive because the fundamental frequency of

the LCD depends only on the length of the liquid column. This results in an infeasible length of the liquid column while tuning the LCD to a short period structure. A variation of the conventional LCD was proposed by Ghosh and Basu [8] which is suitable for the vibration control of short period structures. This device is an LCD connected to the structure by a spring and hence combines the advantages of TMD with LCD. The efficiency of this compliant LCD or CLCD to mitigate the structural response to far-field earthquake is well established [9, 10]. In this work an investigation is made on the effectiveness of the CLCD in the vibration control of structures subjected to near-fault earthquakes.

2 Modelling of Structure-CLCD System

The model of the structure-CLCD system considered is shown in Fig. 1. The CLCD is composed of a U-tube like container with orifice(s) installed in the horizontal portion and is connected to the structure with the help of a spring (k_2) and dashpot (c_2). The tube has cross-sectional area A , horizontal dimension B , and contains liquid of mass density ρ . The coefficient of head loss, controlled by the opening ratio of the orifice(s), is denoted by ζ . The length of the liquid column in the tube is denoted by L . The structure is modeled as a linear single-degree-of-freedom (SDOF) system. The parameters of mass, stiffness and damping for the SDOF system representing the structure are denoted by m , k_1 and c_1 respectively. If M_c

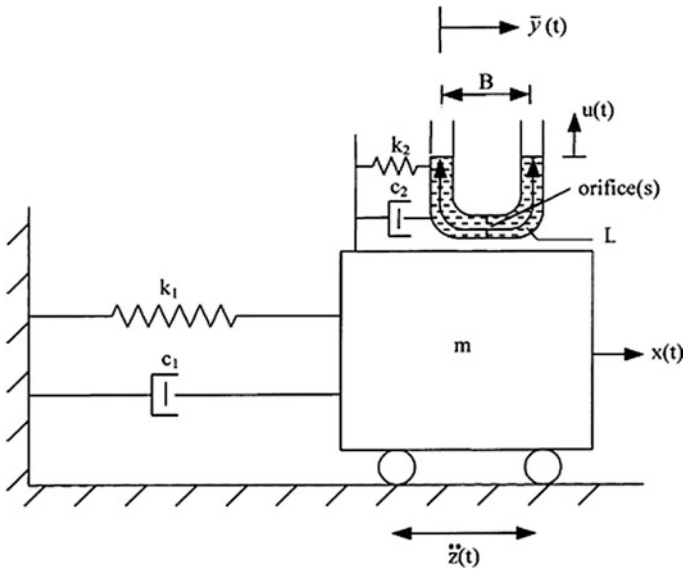


Fig. 1 Structure-CLCD model

denotes the mass of the LCD container excluding the liquid mass then the total mass of the damper system is given by $(M_c + \rho AL)$.

3 Simulation Study

3.1 Equations of Motion

As indicated in Fig. 1, the structure-CLCD system is subjected to a base acceleration $\ddot{z}(t)$. Let $x(t)$ denote the horizontal displacement of the SDOF structural system with respect to the ground, $\bar{y}(t)$ the horizontal motion of the container relative to the SDOF system and $u(t)$ the change in elevation of the liquid column. The equation of motion of the liquid column as given by Sakai et al. [16] can be written as

$$\rho AL \ddot{u}(t) + \frac{1}{2} \rho A \xi |\dot{u}(t)| \dot{u}(t) + 2\rho A g u(t) = -\rho AB \{\ddot{\bar{y}}(t) + \ddot{x}(t) + \ddot{z}(t)\} \quad (1)$$

By adopting an equivalent linearization procedure, the following equivalent linear equation may be written to represent the nonlinear system in Eq. (1) [13]

$$\rho AL \ddot{u}(t) + 2\rho AC_p \dot{u}(t) + 2\rho A g u(t) = -\rho AB \{\ddot{\bar{y}}(t) + \ddot{x}(t) + \ddot{z}(t)\} \quad (2)$$

Here, C_p represents the equivalent linearized damping coefficient and may be obtained by minimizing the mean square value of the error between Eqs. (1) and (2). The expression for the equivalent damping coefficient is given by

$$C_p = \frac{\sigma_{\dot{u}} \xi}{\sqrt{2\pi}} \quad (3)$$

In Eq. (3), $\sigma_{\dot{u}}$ is the standard deviation of the liquid velocity, $\dot{u}(t)$. From Eq. (3) it is clear that as C_p depends on $\sigma_{\dot{u}}$ which is not known previously, an iterative procedure is required to evaluate C_p . On normalizing Eq. (2) with respect to the mass of liquid in the container, ρAL , the following is obtained.

$$\ddot{u}(t) + \frac{2C_p}{L} \dot{u}(t) + \omega_L^2 u(t) = -\alpha \{\ddot{\bar{y}}(t) + \ddot{x}(t) + \ddot{z}(t)\} \quad (4)$$

where, $\omega_L (= \sqrt{2g/L})$ is the natural frequency of the oscillating liquid in the LCD and $\alpha (= B/L)$ is the ratio of the horizontal portion of the damper tube to its total length.

The equation of motion of the mass of the SDOF system is given by

$$m\{\ddot{x}(t) + \ddot{z}(t)\} + c_1 \dot{x}(t) + k_1x(t) = c_2 \dot{\bar{y}}(t) + k_2\bar{y}(t) \tag{5}$$

where, $\{c_2 \dot{\bar{y}}(t) + k_2\bar{y}(t)\}$ denotes the interactive force between the structure and the damper.

The dynamic equilibrium of the whole damper system, comprising the liquid column mass and the container mass, leads to the following equation

$$(M_c + \rho AL)\{\ddot{\bar{y}}(t) + \ddot{x}(t) + \ddot{z}(t)\} + \rho AB \ddot{u}(t) + c_2 \dot{\bar{y}}(t) + k_2\bar{y}(t) = 0 \tag{6}$$

On normalizing Eq. (6) with respect to the total damper mass $(\rho AL + M_c)$, we obtain

$$\{\ddot{\bar{y}}(t) + \ddot{x}(t) + \ddot{z}(t)\} + \frac{\alpha}{(1+\tau)} \ddot{u}(t) + 2\xi_2\omega_2 \dot{\bar{y}}(t) + \omega_2^2\bar{y}(t) = 0 \tag{7}$$

where, $\omega_2(=k_2/(\rho AL + M_c))$ is the natural frequency and $\xi_2(=c_2/2\omega_2(\rho AL + M_c))$ is the damping ratio of the whole damper system considering the liquid in the container to be relatively still. Further, $\tau(=M_c/\rho AL)$ represents the ratio of the container mass to the liquid mass.

Normalizing Eq. (5) with respect to the mass, m , of the structure leads to

$$\{\ddot{x}(t) + \ddot{z}(t)\} + 2\xi_1\omega_1 \dot{x}(t) + \omega_1^2x(t) = \hat{\mu}\{2\xi_2\omega_2 \dot{\bar{y}}(t) + \omega_2^2\bar{y}(t)\} \tag{8}$$

where, ξ_1 and ω_1 represent the damping ratio and natural frequency of the SDOF system, respectively. The ratio of the total damper mass to that of the structure is denoted by $\hat{\mu}(=(\rho AL + M_c)/m)$.

The solution of Eqs. (4), (7) and (8) provide the response of the structure and the damper to a given base acceleration input.

3.2 Description of Example SDOF Structural System and CLCD Parameters

The performance of the CLCD is studied in detail for a short period structure with structural time period, T_n , 0.3 s and equivalent viscous damping ratio, ζ , 2 %. The LCD design parameters may be listed as the mass ratio, $\hat{\mu}$, the length ratio, α , the tuning ratio, ν , the ratio of the container mass to liquid mass, τ , and the ratio of the head loss coefficient to the liquid column length, (ξ/L) . It is very important to examine the damper performance with the variation in these design parameters to arrive at the optimal choice of these parameters. There may be constraints such as practical limitations regarding additional load on the structure, available space and liquid displacement leading to part of the horizontal portion of the damper

becoming empty. In this study, the liquid column length, L , is assumed to be $2m$ and the optimum values of (ξ/L) obtained are checked so that there is no loss of mass coupling for the corresponding values of α . Two different values of $\hat{\mu}$, namely 1 and 3 %, and two values of α , namely 0.5 and 0.7, are considered here. As in Ghosh and Basu [8], the value of τ is initially considered unity. The ν and (ξ/L) values have been numerically optimized for reductions in the peak response quantity, whether displacement or acceleration. The corresponding reductions in rms response quantities are also computed.

3.3 Description of Near-Fault Earthquake Data

Three recorded near-fault earthquake data are considered as the base input. As the intention of the present paper is to examine whether the CLCD can mitigate structural vibrations arising out of near-source ground motions containing strong velocity pulses, the selected data fall into the pulse-type category. The accelerogram data have been accessed from the PEER Ground Motion Database. The details of the earthquake records are shown in Table 1. Specifically, the second data has the fling effect which is the permanent displacement of the ground and is the consequence of excessive tectonic deformations due to large slip on the fault plane. As an illustration, the velocity and displacement time histories of the first and second records respectively are shown in Figs. 2 and 3 respectively.

Table 1 Near-fault earthquake data

SI No.	Event	Station	PGA (g)	PGV (cm/s)	PGD (cm)
1.	Loma Prieta	Saratoga—Aloha	0.32	42.63	27.59
2.	Landers	Lucerne	0.73	146.77	262.73
3.	1971 San Fernando	Pacoima Dam (upper left abut)	1.226	112.5	35.5

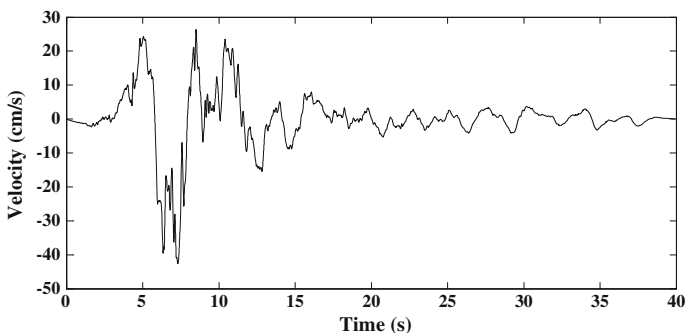


Fig. 2 Velocity time history of Loma Prieta ground motion

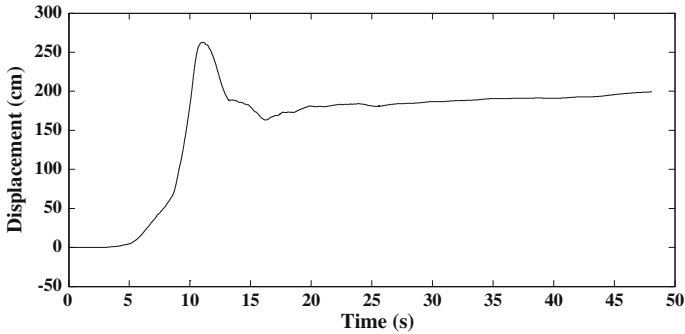


Fig. 3 Displacement time history of Landers ground motion

4 Performance Study of CLCD for Short Period Structure

By solving the equations of motion the response reductions of the example short period SDOF structure considered are evaluated for the different parametric conditions of the CLCD mentioned earlier. The results of reductions in peak and rms displacements for the three earthquake data are presented in Tables 2, 3 and 4. The optimum values of ν and (ξ/L) corresponding to maximum peak displacement reductions have also been indicated in these tables.

The results in Tables 2, 3 and 4 indicate substantial displacement response reductions by the CLCD for all the three cases of earthquake input considered for the study. It is observed that, while in the case of far-field earthquake ground motion, the damper performance always improves with increase in mass ratio, here it may not be always so as seen in Table 4. The improvements in performance with

Table 2 Displacement response reduction by CLCD for Loma Prieta earthquake

Parameters	Mass ratio = 1 %		Mass ratio = 3 %	
	B/L = 0.5	B/L = 0.7	B/L = 0.5	B/L = 0.7
ξ/L	115	162	275	190
Tuning ratio	0.83	0.81	0.84	0.79
Peak reduction (%)	22	18.5	22.82	31
RMS reduction (%)	9.83	18.1	30.61	32.69

Table 3 Displacement response reduction by CLCD for Landers earthquake

Parameters	Mass ratio = 1 %		Mass ratio = 3 %	
	B/L = 0.5	B/L = 0.7	B/L = 0.5	B/L = 0.7
ξ/L	2.5	0.5	72.5	498.5
Tuning ratio	0.9	0.83	1	0.98
Peak reduction (%)	33.46	32.01	45.26	47.23
RMS reduction (%)	10.30	12.19	40.07	45.35

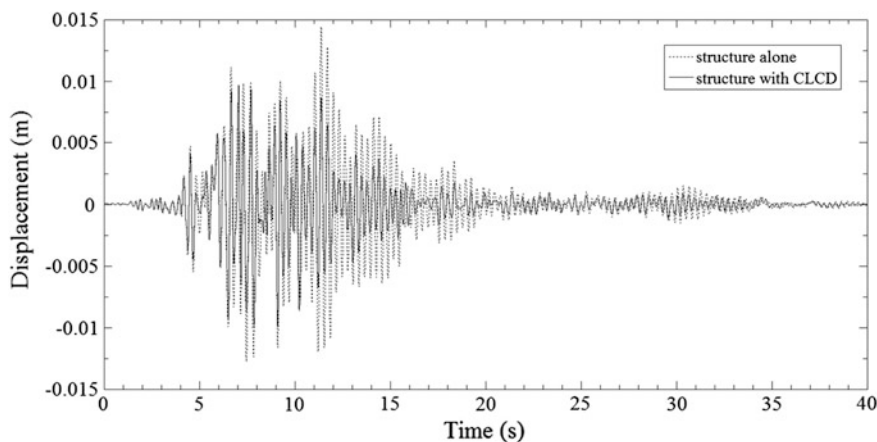
Table 4 Displacement response reduction by CLCD for 1971 San Fernando earthquake

Parameters	Mass ratio = 1 %		Mass ratio = 3 %	
	B/L = 0.5	B/L = 0.7	B/L = 0.5	B/L = 0.7
ξ/L	500	500	345.5	195
Tuning ratio	0.97	0.97	0.99	0.96
Peak reduction (%)	48.45	47.72	37.75	48.3
RMS reduction (%)	43.75	43.55	40.83	46.7

mass ratio for the first two records are more significant in the case of the rms displacement response as compared to the peak displacement response. The displacement time histories of the SDOF structural system, with and without CLCD, for the case corresponding to the last column in Table 2 are shown in Fig. 4.

It is also evident from Table 3 that the CLCD is capable of controlling the vibrations of the SDOF structural system even when subjected to the severe fling effect contained in the Landers earthquake. The time histories corresponding to the third column of Table 3 are presented in Fig. 5.

When the mass ratio is low the damper is effective in controlling the peak displacement response but does not perform well in mitigating the overall response. The latter is achieved when the mass ratio is increased to 3 % when both the peak as well as the rms displacement responses is substantially reduced. The results in Tables 2, 3 and 4 also indicate that higher length ratio does not necessarily ensure better performance of the CLCD. Further, the mass ratio seems to have no effect on the optimum tuning ratio. These observations are in contrast to the trends found in case of far-field earthquake ground motion, where the CLCD performance improves with higher length ratio and the optimum tuning ratio moves away from unity as the mass ratio increases. In case of the near-field ground motion results in Tables 2, 3

**Fig. 4** Displacement time histories of SDOF structure, with and without CLCD with 3 % mass ratio and (B/L) = 0.7 for Loma Prieta input

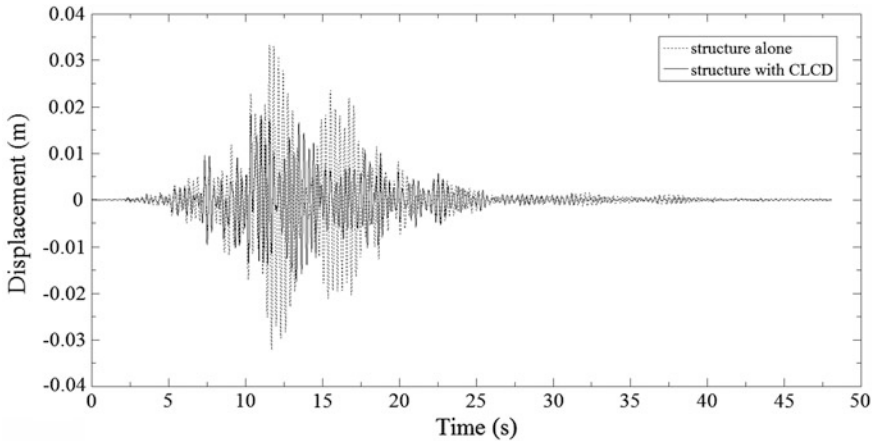


Fig. 5 Displacement time histories of SDOF structure, with and without CLCD with 3 % mass ratio and $(B/L) = 0.5$ for Landers input

and 4, the optimum tuning ratio shows a general trend of moving away from unity for higher length ratio.

Next, a sensitivity study of the damper parameters is carried out. Some representative results for the San Fernando input motion are presented here. Figures 6, 7 and 8 indicate the variation in percent response reduction in peak displacement of the example structural system to (ξ/L) , ν and τ respectively for the specific combinations of μ and α considered earlier.

It is observed from Fig. 6 that the performance of the CLCD is sharply sensitive to ξ/L but only till the optimal value. Figure 7 indicates that proper tuning is important to ensure good performance of the damper. In all cases, the optimal

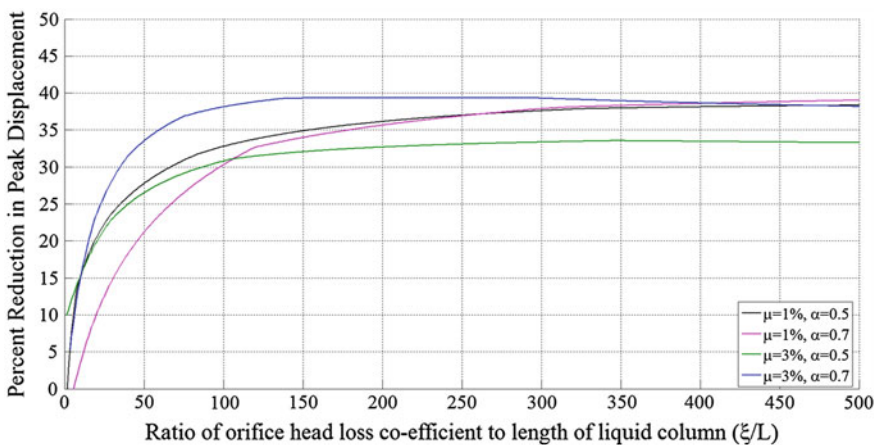


Fig. 6 Sensitivity of peak reduction to ξ/L for San Fernando earthquake

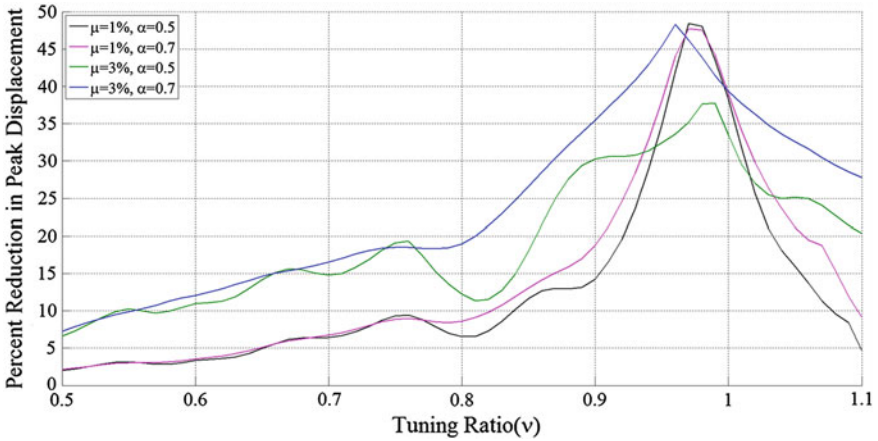


Fig. 7 Sensitivity of Peak reduction to v at optimized ξ/L for San Fernando earthquake

tuning ratio lies between 0.95 and 1.0. Though the sensitivity of the CLCD performance to the tuning ratio generally increases with decrease in the mass ratio, it is again evident that for the same α and τ , higher mass ratio is not ensuring a better performance. In Fig. 8, it is observed that for the higher mass ratio, τ_{opt} is less than unity, while the lower mass ratio shows little sensitivity to τ .

As discussed earlier, the pulse-like ground motions induce very high accelerations in the structure that can lead to sudden shear failure of the structure. Thus the mitigation of the acceleration response of the structure subjected to such type of ground motion is very important. The performance of the CLCD in reducing the acceleration response of the example structure is studied and the results obtained

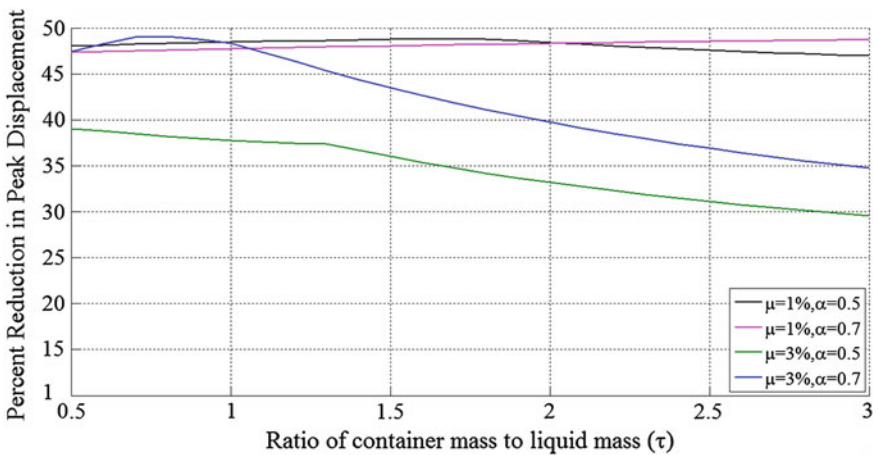


Fig. 8 Sensitivity of peak reduction to τ at optimized ξ/L and v for San Fernando earthquake

Table 5 Acceleration response reduction by CLCD for for Loma Prieta earthquake

Parameters	Mass ratio = 1 %		Mass ratio = 3 %	
	B/L = 0.5	B/L = 0.7	B/L = 0.5	B/L = 0.7
ξ/L	143.50	158.50	498.50	271.50
Tuning ratio	0.84	0.81	0.76	0.80
Peak reduction (%)	20.93	17.70	26.91	30.02
RMS reduction (%)	19.45	17.19	26.33	31.63

have indicated that the CLCD is capable of achieving considerable acceleration response reductions of the structure. Sample results of reductions in peak and rms absolute acceleration responses for the first earthquake data are presented in Table 5. The optimum values of ν and (ξ/L) corresponding to maximum peak acceleration reductions have also been indicated therein.

The performance of the damper is also apparent from the acceleration time histories for the structure alone subjected to the Loma Prieta earthquake and with the CLCD with parameters corresponding to those in the last column of Table 5, as shown in Fig. 9.

In Table 5 significant improvements are registered with the increase in the mass ratio. Again it is noted that the length ratio does not have much of an effect on the response reductions achieved by the damper. Also in contrast with the far-field case, mass ratio does not seem to have any definite effect on the optimum value of the tuning ratio. The overall trends observed in the case of the acceleration response reduction by the CLCD match with those for the displacement response reduction.

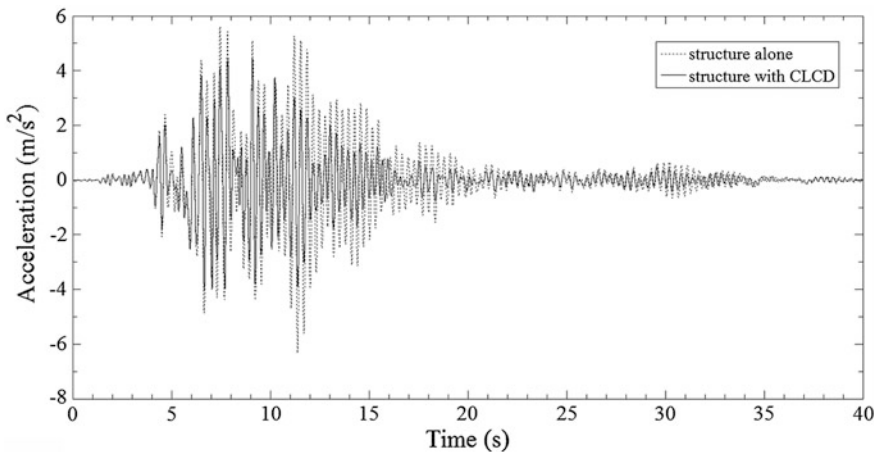


Fig. 9 Acceleration time histories of SDOF structure, with and without CLCD with 3 % mass ratio and $(B/L) = 0.7$ for Loma Prieta input

5 Conclusions

The CLCD, which was hitherto found effective in controlling the vibrations of short period structures subjected to far-field earthquake ground motions was investigated for the possible vibration mitigation of short period structures subjected to pulse-type near-source ground motion. The CLCD was found to achieve substantial reductions in both the displacement as well as the acceleration responses of a short period SDOF structural system. The CLCD was also able to control the severe fling effect that may be present in near fault earthquake ground motions. A study on the damper parameters yielded some observations different from those reported in case of the far field earthquakes. Higher mass ratio does not always ensure better performance. Also the mass ratio has no specific effect on the optimal tuning ratio. Further, an increase in length ratio does not always affect the damper performance positively as in the case of the far-field earthquake excitation. Overall, the CLCD offers to be a very promising control device for structural vibrations due to near-fault ground motions.

Acknowledgments The funding from the Science and Engineering Research Council, Department of Science and Technology, Govt. of India, for the project "Passive control of seismically excited short period structures by the compliant liquid column damper" is gratefully acknowledged.

References

1. Alavi B, Krawinkler H (2000) Consideration of near-fault ground motion effects in seismic design. In: Proceedings of the 12th world conference on earthquake engineering, paper no 2665, Auckland, New Zealand
2. Anderson JC, Bertero VV (1987) Uncertainties in establishing design earthquake. *J Struct Eng ASCE* 113(8):1709–1724
3. Baker JW (2007) Quantitative classification of near-fault ground motions using wavelet analysis. *B Seismol Soc Am* 97(5):1486–1501
4. Balendra T, Wang CM, Cheong HF (1995) Effectiveness of tuned liquid column dampers for vibration control of towers. *Eng Struct* 17(9):668–675
5. Balendra T, Wang CM, Rakesh G (1999) Vibration control of various types of buildings using TLCD. *J Wind Eng Ind Aerodyn* 83(1–3):197–208
6. Bertero VV, Mahin SA, Herrera RA (1978) Aseismic design implications of San Fernando earthquake records. *Earthquake Eng Struct Dynam* 6(1):31–42
7. Ghobarah A (2004) Response of structures to near-fault ground motion. In: Proceedings of the 13th world conference on earthquake engineering, paper no 1031, Vancouver, Canada
8. Ghosh A, Basu B (2004) Seismic vibration control of short period structures using the liquid column damper. *Eng Struct* 26(13):1905–1913
9. Ghosh A, Basu B (2006) Compliant liquid column dampers for control of seismically excited short period structures. In: Proceedings of the first European conference on earthquake engineering and seismology, paper no 45, Geneva, Switzerland
10. Ghosh RK, Ghosh A(D) (2006) Design of a compliant liquid column damper for seismic vibration control of stiff structures. In: Proceedings of the 13th symposium on earthquake engineering, paper no 80, IIT Roorkee, India

11. Hall JF, Heaton TH, Halling MW, Wald DJ (1995) Near-source ground motion and its effect on flexible buildings. *Earthq Spectra* 11(4):569–605
12. Han BK, Won YJ (1998) Stochastic seismic performance of TLCD for the passive control of structures. *KSCE J Civ Eng* 2(3):273–280
13. Iwan WD, Yang JM (1972) Application of statistical linearization techniques to nonlinear multidegree-of-freedom systems. *J Appl Mech* 39(2):545–550
14. Jangid RS, Kelly JM (2001) Base isolation for near-fault motions. *Earthquake Eng Struct Dynam* 30(5):691–707
15. Ozbulut O, Bitaraf M, Hurlebaus S (2011) Adaptive control of base-isolated structures against near-field earthquakes using variable friction dampers. *Eng Struct* 33(12):3143–3154
16. Sakai F, Takaeda S, Tamaki T (1989) Tuned liquid column dampers new type device for suppression of building vibrations. In: *Proceedings of the international conference on high-rise buildings*, vol 2, Nanjing, China
17. Shen J, Tsai M, Chang K, Lee G (2004) Performance of a seismically isolated bridge under near-fault earthquake ground motions. *J Struct Eng* 130(6):861–868
18. Won AYJ, Pires JA, Haroun MA (1997) Performance assessment of tuned liquid column dampers under random seismic loading. *Int J Non-linear Mech* 32(4):745–758
19. Xu YL, Samali B, Kwok KCS (1992) Control of along-wind response of structures by mass and liquid dampers. *J Eng Mech ASCE* 118(1):20–39

Comparison of Performance of Different Tuned Liquid Column Dampers (TLCDs)

Meghana Kalva and Samit Ray-Chaudhuri

Abstract Many of the modern slender and flexible structures are highly susceptible to wind-and earthquake-induced vibrations, which may result in damage to these structures. Of late tuned liquid column dampers (TLCD) has drawn significant attention of researchers. In TLCD, the motion of liquid column in a U-tube container counteracts the forces acting on the structure resulting in reduction of structural response. The advantages of TLCD include low cost and maintenance. There are many varieties of TLCDs proposed for vibration control. In this study, the efficiency in vibration suppression of four different types of passive TLCDs has been compared. These are U-shaped TLCD, liquid column vibration absorber (LCVA), V-shaped TLCD and tuned liquid column ball damper (TLCBD). For this purpose, the response of an SDOF system with and without TLCD is evaluated when subjected to harmonic excitation of varying frequencies and excitation levels. Transfer functions are evaluated for uncontrolled and controlled (i.e., with TLCD) cases by using an equivalent linearization approach for the non-linear TLCD damping. Further, a numerical method is also used for solving equations of motion involving non-linear damping of TLCDs. Results are presented in terms of percentage reduction in SDOF system response. The results of this work demonstrate that TLCBD has better performance when compared to other TLCDs.

Keywords Non-linear damping · TLCD · Transfer function · Tuned mass damper · Vibration control

M. Kalva (✉) · S. Ray-Chaudhuri
Department of Civil Engineering, IIT Kanpur, Kanpur UP-208016, India
e-mail: meghana12103024@gmail.com

S. Ray-Chaudhuri
e-mail: samitrc@iitk.ac.in

© Springer India 2015
V. Matsagar (ed.), *Advances in Structural Engineering*,
DOI 10.1007/978-81-322-2193-7_98

1257

1 Introduction

Tuned systems (such as tuned mass dampers (TMD), tuned liquid dampers (TLD) and tuned liquid column dampers (TLCD)) are used for the vibration control of tall and slender structures. TLCD was first proposed by [1]. TLCD relies on the motion of a column of liquid in a U-tube container to counteract the forces acting on the structure. This device has drawn significant attention of the researchers as one type of secondary systems. The frequency of a TLCD is tuned with the fundamental frequency of the structure by changing the length of the liquid column in the U-tube. Damping is introduced in the oscillating liquid column through an orifice in the liquid passage. Unlike TMDs, the damping in TLCD is amplitude dependent and hence the damping is non-linear. The advantages of TLCD systems include low cost and maintenance. There are several invariants of passive TLCDs proposed by many researchers. They are U-shaped TLCD (U-TLCD) [1], liquid column damper with period adjustment equipment (LCD-PA) [2], liquid column vibration absorber (LCVA) [3], U-shaped TLCD for short period structures [4], V-shaped TLCD (V-TLCD) [3], tuned liquid column ball damper (TLCBD) [5], sealed TLCD [6], tank-pipe damper (T-P damper) [7] and pendulum type liquid column damper (PLCD) [8].

This paper includes the comparison of efficiency of four different types of passive TLCDs (U-TLCD, LCVA, V-TLCD and TLCBD) in vibration suppression. For this purpose, the response of an SDOF system with or without TLCD is evaluated when subjected to harmonic excitation of varying frequencies and excitation levels. Transfer functions are evaluated for uncontrolled and controlled (i.e., with TLCD) cases by using an equivalent linearization approach for the non-linear TLCD damping. Further, a numerical method is also used for solving equations of motion involving non-linear damping of TLCDs. Results are presented in terms of percentage reduction in SDOF system response. The results of this work demonstrate that TLCBD has better performance when compared to other TLCDs.

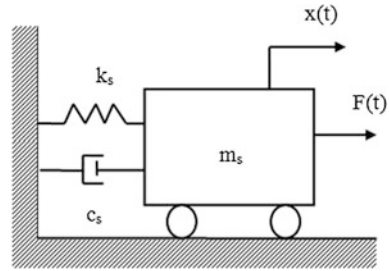
2 Equations of Motion

SDOF System: Let us consider a linear SDOF system as shown in Fig. 1. Let m_s , c_s and k_s denote the mass, damping and stiffness of the system, respectively. The system is subjected to a harmonic excitation, $F(t)$ as shown in Fig. 1. The equation of motion of the system can be written as

$$m_s \ddot{x}(t) + c_s \dot{x}(t) + k_s x(t) = F(t) \quad (1)$$

where $\ddot{x}(t)$, $\dot{x}(t)$, $x(t)$ are the acceleration, velocity and displacement responses of the system, respectively.

Fig. 1 Schematic diagram showing a SDOF system



SDOF System with U-TLCD: Let us consider a U-shaped TLCD installed on a SDOF system. The schematic diagram showing the combined structure-TLCD is provided in Fig. 2. The equations of motion of the structure and the liquid column can be written as [1].

For structure:

$$(m_s + m_d)\ddot{x}(t) + c_s\dot{x}(t) + k_sx(t) + \alpha m_d\ddot{y}(t) = F(t) \tag{2}$$

For liquid column:

$$\alpha m_d\ddot{x}(t) + m_d\ddot{y}(t) + \frac{1}{2}\rho A\zeta|\dot{y}(t)|\dot{y}(t) + k_d y(t) = 0 \tag{3}$$

where m_d and k_d are the mass and stiffness of the TLCD, respectively; ρ represents the density of liquid; ζ is the head loss coefficient; A represents the cross-sectional area of TLCD. In Eq. 3, $\ddot{y}(t)$, $\dot{y}(t)$ and $y(t)$ are the acceleration, velocity and displacement responses of the liquid column, respectively. The ratio of width to the total length of the liquid column is $\alpha (= b/L)$. The nonlinear damping of TLCD is given as $\rho A\zeta|\dot{y}(t)|/2$. All the remaining terms are similar as previously defined.

SDOF System with LCVA: Let us consider a LCVA installed on a SDOF system. The schematic diagram showing the combined structure-LCVA is provided in Fig. 3. The equations of motion of structure and liquid column can be written as [3]

Fig. 2 Schematic diagram showing U-shaped TLCD installed on a SDOF system

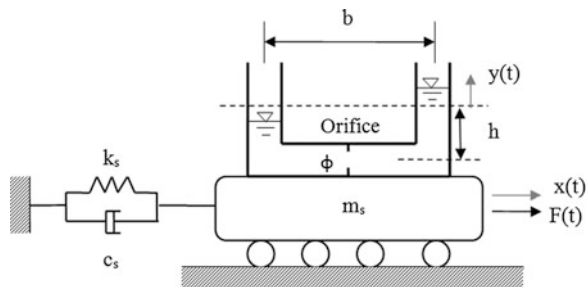
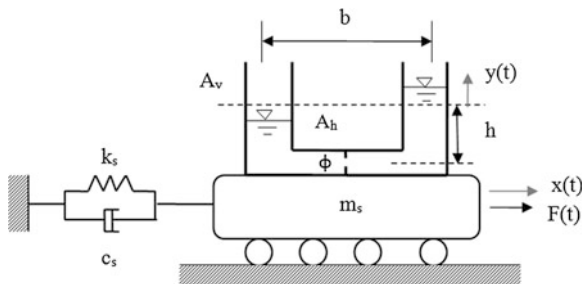


Fig. 3 Schematic diagram showing LCVA installed on a SDOF system



For structure:

$$m_s \ddot{x}(t) + \rho A_h (2\nu L_v + L_h) \ddot{x}(t) + c_s \dot{x}(t) + k_s x(t) + \rho A_h \nu L_h \ddot{y}(t) = F(t) \quad (4)$$

For liquid column:

$$\rho A_h L_h \ddot{x}(t) + \rho A_h L_{ee} \ddot{y}(t) + \frac{1}{2} \rho A_h \zeta |\dot{y}(t)| \dot{y}(t) + 2\rho A_h g y(t) = 0 \quad (5)$$

where A_h and A_v are the cross-sectional areas of horizontal and vertical portions of LCVA, respectively; L_h and L_v are the horizontal and vertical lengths of the liquid column, respectively; g is the acceleration due to gravity; b is the total width of the LCVA; $\nu (= A_v/A_h)$ is the ratio of cross sectional area of vertical and horizontal sections of LCVA; $L_e (= L_h + 2L_v)$ is the total length of the liquid column; $\alpha (= b/L_e)$ is the ratio of width to the actual length of the liquid column; $L_{ee} (= L_e(\frac{\alpha}{\nu} + (1 - \alpha)))$ is the equivalent length of the liquid column with constant cross-sectional area. All the remaining terms are similar as previously defined.

SDOF System with V-TLCD: Let us consider a V-shaped TLCD installed on a SDOF system. The schematic diagram showing the V-shaped TLCD is provided in Fig. 4. The equations of motion of the structure and the liquid column can be written as [3]

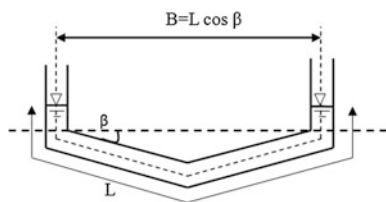


Fig. 4 Schematic diagram showing V-shaped TLCD

For structure:

$$(m_s + \rho AL)\ddot{x}(t) + c_s\dot{x}(t) + k_sx(t) + \frac{m_s\mu(L - |y|)\cos\beta}{L}\ddot{y}(t) = F(t) \quad (6)$$

For liquid column:

$$\rho AL\ddot{y}(t) + \frac{1}{2}\rho A\xi|\dot{y}(t)|\dot{y}(t) + \rho Ag(1 + \sin\beta)y(t) = -\rho A(L - |y|)\cos\beta\ddot{x}(t) \quad (7)$$

where β is the angle of inclination of horizontal portion of TLCD; μ is the ratio of mass of TLCD to that of the structure; L is the length of liquid column; A is the area of cross-section of V-shaped TLCD. All the remaining terms are similar as previously defined.

SDOF System TLCBD: Let us consider a TLCBD installed on a SDOF system. The schematic diagram showing the combined structure-TLCBD model is provided in Fig. 5. The equations of motion of the structure, liquid column and ball can be written as [5]

For structure:

$$(m_s + m_d + \frac{J_c}{R_b^2})\ddot{x}(t) + c_s\dot{x}(t) + k_sx(t) + \alpha m_d\ddot{y}(t) - \frac{J_c}{R_b^2}\ddot{z}(t) = F(t) \quad (8)$$

For liquid column:

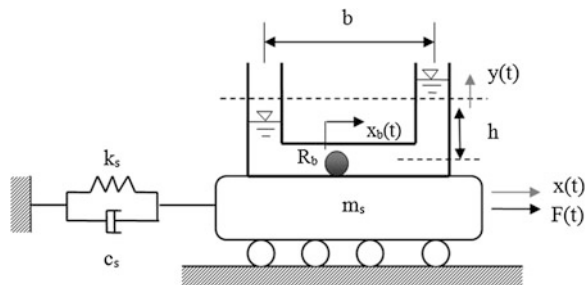
$$m_d\ddot{y}(t) + c_d\dot{y}(t) + 2\rho Agy(t) + \alpha m_d\ddot{x}(t) = 0 \quad (9)$$

For ball:

$$(m_b + \frac{J_c}{R_b^2})\ddot{z}(t) + d_{eq}\dot{z}(t) = \frac{J_c}{R_b^2}\ddot{x}(t) + d_{eq}\dot{y}(t) + 2\rho gA_b y(t) \quad (10)$$

where J_c is the mass moment of inertia of ball about its center of mass; m_b , R_b and A_b are the mass, radius and main cross-sectional area of the coated steel ball, respectively;

Fig. 5 Schematic diagram showing TLCBD installed on a SDOF system



c_d is the damping coefficient of liquid column; d_{eq} is the equivalent damping coefficient; $\ddot{z}(t)$, $\dot{z}(t)$, $z(t)$ are the acceleration, velocity and displacement response of ball, respectively. All the remaining terms are similar as previously defined.

3 Transfer Functions

3.1 Formulation

SDOF System: The equation of motion of SDOF system as shown in Fig. 1 is given in Eq. 1. By taking Fourier transform, Eq. 1 reduces to

$$-\omega^2 x(\omega) + 2\zeta_s \omega_s i \omega x(\omega) + \omega_s^2 x(\omega) = \frac{F(\omega)}{m_s} \quad (11)$$

The transfer function of SDOF system is

$$T_f(\omega) = \frac{x(\omega)}{F(\omega)} = \frac{1}{m_s(-\omega^2 + 2\zeta_s \omega_s i \omega + \omega_s^2)} \quad (12)$$

SDOF system with U-TLCD: The equations of motion of the structure and TLCD system as shown in Fig. 2 are given in Eqs. 2 and 3. The nonlinear damping is replaced by equivalent linear damping C_d . The equivalent linear damping is obtained by minimizing the square of the error between non-linear and equivalent linear damping. Assuming the liquid has a steady state harmonic response, the damping coefficient is obtained as $C_d = (4\rho A \xi \omega_f W_o)/3\pi$. The frequency of external excitation is ω_f ; W_o is a constant and is proportional to intensity of excitation [3]. By taking the Fourier transform, the Eqs. 2 and 3 reduces to

$$-\omega^2(1 + \mu)x(\omega) + 2\zeta_s \omega_s i \omega x(\omega) + \omega_s^2 x(\omega) - \omega^2 \alpha \mu y(\omega) = \frac{F(\omega)}{m_s} \quad (13)$$

$$-\omega^2 \alpha x(\omega) - \omega^2 y(\omega) + \frac{C_d}{m_d} i \omega y(\omega) + \omega_d^2 y(\omega) = 0 \quad (14)$$

By solving the Eqs. 13 and 14 the transfer functions of the structure and TLCD obtained are given as

For structure:

$$T_f(\omega) = \frac{x(\omega)}{F(\omega)} = \frac{\frac{1}{m_s} \left[-\omega^2 + \frac{C_d}{m_d} i \omega + \omega_d^2 \right]}{\left[-\omega^2(1 + \mu) + 2\zeta_s \omega_s i \omega + \omega_s^2 \right] \left[-\omega^2 + \frac{C_d}{m_d} i \omega + \omega_d^2 \right] - \omega^4 \alpha^2 \mu} \quad (15)$$

For liquid column:

$$H_f(\omega) = \frac{y(\omega)}{F(\omega)} = \frac{\frac{1}{m_s} \alpha \omega^2}{[-\omega^2(1 + \mu) + 2\zeta_s \omega_s i \omega + \omega_s^2] \left[-\omega^2 + \frac{C_d}{m_d} i \omega + \omega_d^2\right] - \omega^4 \alpha^2 \mu} \tag{16}$$

SDOF system with LCVA: By considering simplified TLCD system which has equivalent length and area of cross section same as vertical section of LCVA. The equation of motion of the structure and LCVA system are shown in Eqs. 4 and 5. The length of liquid column in equivalent TLCD with uniform cross sectional area A_v having same mass as LCVA is L_{em} ; length of equivalent uniform liquid column with cross sectional area A_v that possess the same energy as TLCD is L_{ee} . By taking the Fourier transform the Eqs. 4 and 5 reduces to

$$-\omega^2(1 + \mu)x(\omega) + 2\zeta_s \omega_s i \omega x(\omega) + \omega_s^2 x(\omega) - \omega^2 \mu \frac{B}{L_{em}} y(\omega) = \frac{F(\omega)}{m_s} \tag{17}$$

$$-\rho A_v L_{ee} \omega^2 y(\omega) + C_d i \omega y(\omega) + 2\rho A_v g y(\omega) = \omega^2 \rho A_v B x(\omega) \tag{18}$$

By solving the Eqs. 17 and 18 the transfer functions of the structure and TLCD are obtained as

For structure:

$$T_f(\omega) = \frac{x(\omega)}{F(\omega)} = \frac{\frac{1}{m_s} (-\rho A_v L_{ee} \omega^2 + C_d i \omega + 2\rho A_v g)}{[-\omega^2(1 + \mu) + 2\zeta_s \omega_s i \omega + \omega_s^2] [-\rho A_v L_{ee} \omega^2 + C_d i \omega + 2\rho A_v g] - \omega^4 \mu \rho A_v \frac{B^2}{L_{em}}} \tag{19}$$

For liquid column:

$$H_f(\omega) = \frac{y(\omega)}{F(\omega)} = \frac{\frac{1}{m_s} \omega^2 \rho A_v B}{[-\omega^2(1 + \mu) + 2\zeta_s \omega_s i \omega + \omega_s^2] [-\rho A_v L_{ee} \omega^2 + C_d i \omega + 2\rho A_v g] - \omega^4 \mu \rho A_v \frac{B^2}{L_{em}}} \tag{20}$$

SDOF system with TLCBD: The equations of motion of structure, liquid column and ball as shown in Fig. 5 are given in Eqs. 8, 9 and 10, respectively. By taking Fourier transforms, of the equations of motion reduces to

For structure:

$$\begin{aligned}
 & -\omega^2(m_s + m_d + \frac{J_c}{R_b^2})x(\omega) + c_s i\omega x(\omega) + k_s x(\omega) - \omega^2 \alpha m_d y(\omega) \\
 & + \frac{J_c}{R_b^2} \omega^2 x_b(\omega) = F(\omega)
 \end{aligned} \tag{21}$$

For liquid column:

$$-\omega^2 m_d y(\omega) + c_t i\omega y(\omega) + 2\rho A g y(\omega) = \omega^2 \alpha m_d x(\omega) \tag{22}$$

For ball:

$$\begin{aligned}
 & -\omega^2(m_b + \frac{J_c}{R_b^2})x_b(\omega) + d_{eq} i\omega x_b(\omega) = -\omega^2 \frac{J_c}{R_b^2} x(\omega) + d_{eq} i\omega y(\omega) + 2\rho A_b g y(\omega)
 \end{aligned} \tag{23}$$

By solving the Eqs. 21–23 the transfer functions of the structure and TLCBD obtained are given as

For structure:

$$H_f(\omega) = \frac{x(\omega)}{F(\omega)} = \frac{(B)(C)}{(A)(B)(C) - \omega^4 \alpha^2 m_d^2 (B) - \omega^4 \frac{J_c^2}{R_b^4} (C) + \omega^4 \alpha m_d \frac{J_c}{R_b^2} (D)} \tag{24}$$

For liquid column:

$$G_f(\omega) = \frac{y(\omega)}{F(\omega)} = \frac{\omega^2 \alpha m_d B}{ABC - \omega^4 \frac{J_c^2}{R_b^4} C - \omega^4 \alpha^2 m_d^2 B + \omega^4 \alpha m_d \frac{J_c}{R_b^2} D} \tag{25}$$

For ball:

$$T_f(\omega) = \frac{x_b(\omega)}{F(\omega)} = \frac{-\omega^2 C \frac{J_c}{R_b^2} + D \omega^2 \alpha m_d}{ABC - \omega^4 \alpha^2 m_d^2 B - \omega^4 \frac{J_c^2}{R_b^4} C + \omega^4 \alpha m_d \frac{J_c}{R_b^2} D} \tag{26}$$

where

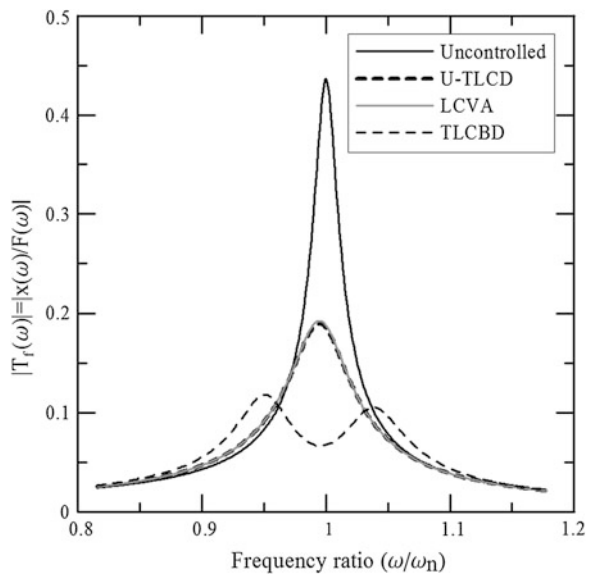
$$\begin{aligned}
 A &= -\omega^2(m_s + m_d + \frac{J_c}{R_b^2}) + c_s i\omega + k_s; & B &= -\omega^2(m_b + \frac{J_c}{R_b^2}) + d_{eq} i\omega; \\
 C &= -\omega^2 m_d + c_t i\omega + 2\rho A g; & D &= d_{eq} i\omega + 2\rho A_b g \quad \text{and} \quad E = (m_s + m_d + \frac{J_c}{R_b^2})
 \end{aligned}$$

3.2 Results and Discussion

The SDOF system considered has mass, $m_s = 1$ kg; stiffness, $k_s = 121.886$ N/m and damping ratio $\zeta = 0.94$ %. The natural frequency of the system is $\omega_n = 11.04$ rad/s (adopted from [9]). For the purpose of comparison, the basic properties of all TLCDs are kept same i.e., mass ratio, length ratio, frequency ratio and head loss coefficient. The mass ratio and length ratio are selected and the frequency ratio and head loss coefficient are obtained from the optimal parameters given by Shum [10]. The mass ratio, length ratio, frequency ratio and head loss coefficient considered for TLCDs are 0.01, 0.8, 0.99066 and 10, respectively. The area ratio for LCVA is considered to be 1.5. The angle of inclination for V-TLCD is considered to be 30° . In TLCBD, a coated steel ball with the density of $8,000\text{-kg/m}^3$ is used.

The comparison of transfer functions of uncontrolled and controlled system with different TLCDs is shown in Fig. 6. The performance of U-TLCD and LCVA is almost similar. From the transfer functions, it can be observed that performance of U-TLCD and LCVA is unimodal type, except that of TLCBD. It can also be observed that for TLCBD, at the frequency ratios of 0.95 and 1.05, the response of the controlled system is more than that of the uncontrolled system. Also, TLCBD is not effective in lower and higher frequency ranges. It can also be observed that there is a significant reduction in the response of the controlled system with different types of TLCDs. The percentage reduction of response at resonance for SDOF system controlled with TLCBD is observed to be 84.47 %. For SDOF system

Fig. 6 Transfer function for uncontrolled and controlled system with different TLCDs



controlled with U-TLCD and LCVA it is found to be 57.45 and 56.85 %. From this it can be observed that at resonance, TLCBD has better performance compared to U-shaped TLCBD and LCVA.

4 Nonlinear Response

In the preceding section, nonlinear damping of TLCBDs is linearized to derive the transfer functions. In this section, for the comparison of variation in the response due to nonlinear damping and equivalent linear damping, the equations of motion are solved using Euler's method. The SDOF system and TLCBDs have the similar parameters as defined in the previous section. The combined systems are subjected to harmonic loading $F(t) = F_o \sin(\omega t)$. The amplitude of excitation is the fraction of weight of the primary system (i.e., $F_o = C m_s g$); C is the dimensionless force intensity factor; $m_s g$ denotes the weight of the primary system. The systems are subjected to the loading with various intensity factors to study the effect of TLCBDs with increasing intensity of loading.

Figure 9 shows the displacement time histories of uncontrolled and controlled systems subjected to excitation frequency $\omega = \omega_n$ and load intensity factor 0.001. It can be observed that there is a significant reduction in the response of the system with different TLCBDs. It can also be observed that TLCBD is more effective in reduction of response as observed from Fig. 8. Figure 7 shows the frequency response curves for the controlled and uncontrolled systems for load intensity factor

Fig. 7 Frequency response curve of SDOF system for $C = 0.001$

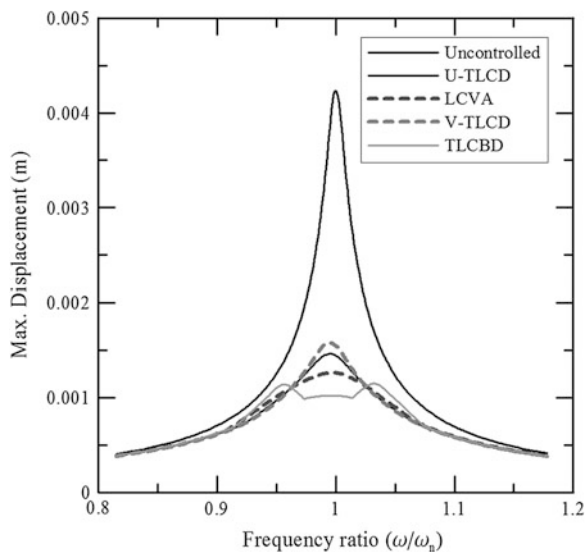
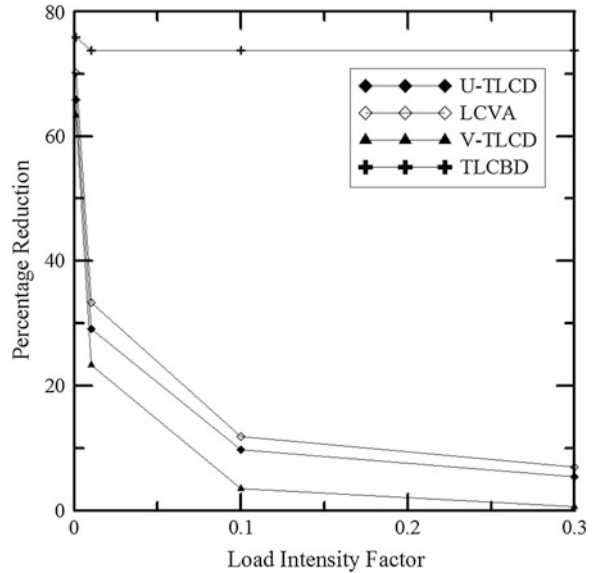


Fig. 8 Percentage reduction of displacement response using different TLCDs with varying intensity of excitation



0.001. It can be observed that there is a significant reduction in response of the system for all the TLCDs. The performance of the U-TLCD, LCVA, V-TLCD are unimodal type, except TLCBD. The response of the system with TLCBD is more than the response of the system with other TLCDs at frequency ratios of 0.95 and 1.05. At the frequency ratio 1, the performance of TLCBD is better compared to other TLCDs. This is because, in TLCBD, there are two dynamic vibration absorbers. The percentage reduction of response at resonance for SDOF system controlled with TLCBD is observed to be 75.87 %. For SDOF system controlled with U-TLCD, LCVA and V-TLCD it is found to be 65.84, 70.2 and 63.4 %, respectively. From this it can be observed that at resonance, TLCBD has better performance compared to U-TLCD, LCVA and V-TLCD. Further, the combined systems are subjected to harmonic excitations with varying load intensity factors ranging from 0.001–0.3. Figure 8 shows the variation of effectiveness of different TLCDs with increasing force intensity factors. The result reveals that for U-TLCD, LCVA and V-TLCD, the effectiveness reduces drastically as the intensity of loading increases. But for TLCBD, the effectiveness of the damper reduces gradually as the intensity of excitation increases. Hence, it can be concluded that compared to all the types of TLCDs, TLCDB is effective at higher intensity of excitations.

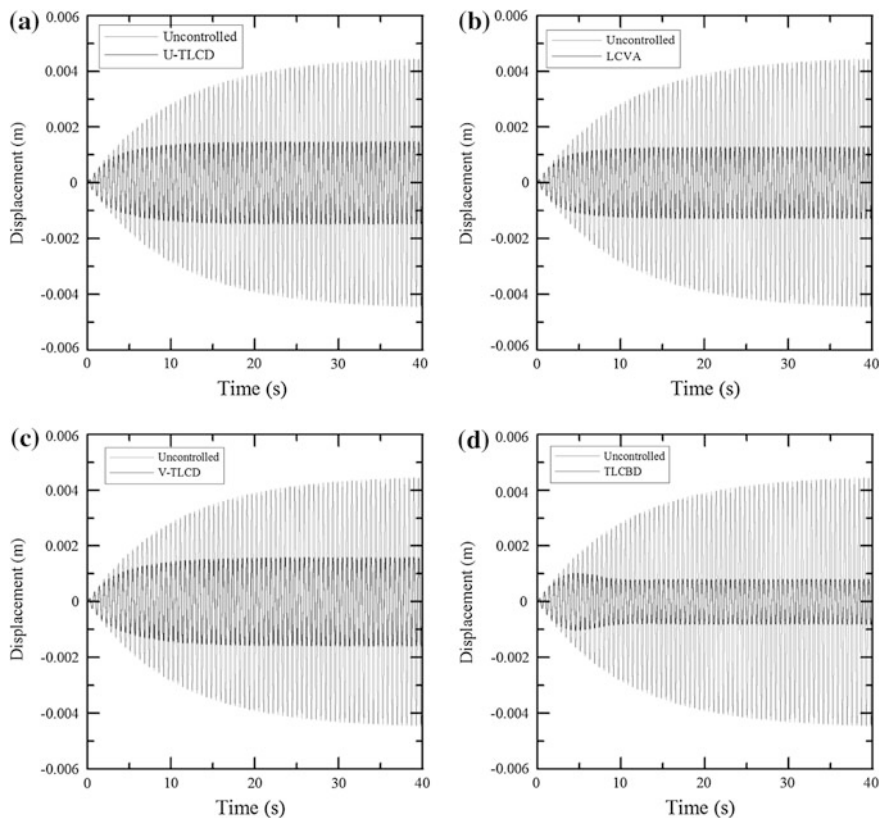


Fig. 9 Displacement time histories of controlled and uncontrolled systems with different TLCDs subjected to excitation frequency $\omega = \omega_n$ and load intensity factor 0.001. **a** U-shaped TLCD. **b** LCVA. **c** V-shaped TLCD. **d** TLCBD

5 Conclusions

The performance of four different types of passive TLCDs namely: U-TLCD, LCVA, V-TLCD and TLCBD is compared. The TLCDs are considered to be installed on a SDOF system subjected to harmonic excitations. From the comparative study, it can be observed that TLCBD has a better performance compared to other TLCDs at resonance. The effectiveness of TLCBD reduces at frequency ratios around 0.95 and 1.05 compared to other TLCDs as observed from the frequency response curves. Numerical study shows that LCVA has better performance compared to U-TLCD. However, the similar performance is not observed from the transfer functions derived due to linearization of nonlinear damping. From the transfer functions, it can be observed that performance of U-TLCD and LCVA are unimodal type, except that of TLCBD. It can also be observed from the transfer

function based approach and numerical study that there is a significant reduction in the response of the controlled system with different types of TLCDS. As the intensity of loading increases, the effectiveness of all the TLCDS reduces, with TLCBD being most effective at higher intensities.

References

1. Sakai F, Takaeda S, and Tamaki T (1989) Tuned liquid column damper-new type of device for suppression of building vibrations. In:Proceedings of international conference on high rise buildings, Nanjing, China
2. Teramura A and Yoshida O (1996) Development of vibration control system using U-shaped water tank. In:11th world conference on earthquake engineering, Acapulco, Mexico
3. Gao H, Kwok KCS, Samali B (1997) Optimization of tuned liquid column dampers. *Eng Struct* 19:476–486
4. Ghosh A, Basu B (2004) Sesimic vibration control of short period structures using the liquid column damper. *Eng Struct* 26:1905–1913
5. Al-Saif KA, Aldakkan KA, Foda MA (2011) Modified tuned liquid column dampers for vibration control of structures. *Int J Mech Sci* 53:505–512
6. Hochrainer MJ, Ziegler F (2005) Control of tall building vibrations by sealed tuned liquid column dampers. *Struct Control and Health Monit* 13:980–1002
7. Ghosh AD and Saha PC (2012) Study of tank-pipe damper system for seismic vibration control of structures. In:15th world conference on earthquake engineering, Lisboa, Portugal
8. Sarkar A, Gudmestad OT (2013) Pendulum type liquid column damper (PLCD) for controlling vibrations of a structure: Theoretical and experimental study. *Eng Struct* 49:221–233
9. Colweli S, Basu B (2008) Experimental and theoretical investigations of equivalent viscous damping of structures with TLCD for different fluids. *J Struct Eng, ASCE* 134:154–163
10. Shum KM (2009) Closed form optimal solution of tuned liquid column damper for suppressing harmonic vibration of structures. *Eng Struct* 31:84–92

Seismic Control of Benchmark Cable-Stayed Bridges Using Variable Friction Pendulum Isolator

Purnachandra Saha

Abstract Earthquake response of phase-II benchmark cable-stayed bridge with variable friction pendulum Isolator (VFPI) is investigated. The performance of this isolator is compared with traditional friction pendulum system (FPS). The seismic response of the bridge is evaluated using the hysteretic model of these sliding isolators. In phase-II benchmark problem, the ground acceleration is applied in any arbitrary direction using both horizontal components of the earthquakes with a specified incidence angle. Multi-support excitations are also considered in this phase. A comparative performance study among these two selected sliding isolators for seismic response of the bridge is carried out. Varying the important parameters of VFPI, evaluation criteria of the benchmark cable-stayed bridge problem are evaluated and optimum values of the parameters are determined. Significant reduction in base shear, base moment and other responses are observed without large deck displacement by using the VFPI. Comparing the evaluation criteria of the benchmark problem, it is observed that the performance of VFPI is better than FPS.

Keywords Benchmark cable-stayed bridge · FPS · VFPI · Seismic response · Sliding base isolation

1 Introduction

Cable stayed bridges have become popular throughout the world and are also very important lifeline structures. The increasing popularity of these bridges among bridge engineers can be attributed to their appealing aesthetics, full and efficient utilization of structural materials and increased stiffness over substructure. However this structure is susceptible to earthquake motions due to its flexibility and low damping. For direct comparison among the different control strategies for a specific type of structure, benchmark problems were developed. Then researchers can

P. Saha (✉)

School of Civil Engineering, KIIT University, Bhubaneswar, Orissa, India
e-mail: dr.purnasaha@gmail.com

compare their various algorithms, devices and sensors for a particular structure through same problem. On the basis of the Bill Emerson Memorial Bridge constructed in Cape Girardeau, Missouri, USA, benchmark problem on cable-stayed bridge have been developed by Dyke et al. [1] in 2003. It specifies some performance objectives from which direct comparison could be made. The control of energy that is transmitted from the ground or foundation to the structure is one of the most effective techniques for seismic design of structures. In recent years, there have been significant studies on the use of frictional isolators to add damping to the isolated structure. The performance of friction isolators is quite insensitive to severe variations in the frequency content of the base excitation, making them very robust [2]. This feature is the most important advantage of the friction type isolators as compared to elastomeric bearings. The benefit of the friction isolators is that it ensures the maximum acceleration transmissibility equal to the maximum limiting frictional force [3, 4].

There are several types of passive control devices used by various researchers to control the seismic response of the civil engineering structures. The sliding isolation system, which is based on the concept of sliding friction, is one of them. Among various friction base isolators, the Friction Pendulum System (FPS) is found to be most attractive due to its ease in installation and simple mechanism of restoring force by gravity action. In this isolator, the sliding and re-centering mechanisms are integrated in single unit. The sliding surface of FPS is spherical so that its time period of oscillation remains constant. Numerous studies had been carried out on behaviour of FPS. Seismic control of bridge using sliding isolation was performed experimentally by Tsopelas et al. [5]. The finite element formulation of the FPS for seismic isolation had been carried out by Tsai et al. [6]. A systematic method for the dynamic analysis of the continuous bridge with sliding isolation is developed by Wang et al. [7]. Jangid [8] investigated the optimum friction coefficient of a sliding system with a restoring force for the minimum acceleration response of a base-isolated structure under earthquake ground motion. The performance of the optimum FPS system for near-fault ground motions has been investigated by Jangid [9] and observed that, for lower values of friction coefficient, significant sliding displacement in the FPS. The seismic response of bridges isolated by elastomeric bearings and the sliding system is investigated by Kunde and Jangid [10]. Soneji and Jangid [11] investigated the effectiveness of elastomeric and sliding isolation systems for the seismic response control of cable-stayed bridge. Comparative performance of isolation systems for benchmark cable-stayed bridge is carried out by Saha and Jangid [12] and noticed that isolator displacement is very large for near-field earthquake (Gebze 1999 earthquake). The FPS had also been practically used for the seismic isolation for bridges such as Benicia-Martinez Bridge, California and American River Bridge, California etc. However, based on the literature survey on FPS, it is observed that the use of spherical sliding surface of the FPS results in several practical disadvantages. One main disadvantage is that FPS needs to be designed for a specific level (intensity) of ground excitation. This is primarily because the maximum intensity of excitation has a strong influence on FPS design, even though the performance of structures isolated by FPS is relatively independent

of the frequency content of ground motion. In general, FPS designed for a particular intensity of excitation may not give very satisfactory performance during earthquakes with much lower or higher intensity. To overcome this problem, variable sliding isolators like VFPI [13] is developed modifying the parameters of the FPS. The success of variable sliding isolators for controlling the seismic forces leads us to study the performance of the different variable sliding isolation systems for phase-II benchmark cable-stayed bridge.

The aim of the present study is (i) to investigate the effectiveness of the VFPI for seismic response control of the phase-II benchmark cable-stayed bridge subjected to specified earthquake ground motions, and (ii) to investigate the influence of variation in important parameters of the isolators on the seismic response of the bridge.

2 Benchmark Cable-Stayed Bridge

Bill Emerson Memorial Bridge crossing the Mississippi River near Cape Girardeau, Missouri (Fig. 1), designed by the HNTB Corporation, is the benchmark cable-stayed bridge used for this study. As the bridge is the primary crossing of river and is in the New Madrid seismic zone, seismic forces were strongly considered in this bridge design.

3 Evaluation Criteria

For each control design, the evaluation criteria should be evaluated for each of the following three earthquake records provided in the benchmark problem [14]: (i) *El Centro*, recorded at the Imperial Valley Irrigation District station in El Centro, California, during the Imperial Valley, California earthquake of 18, May, 1940; (ii) *Mexico City*, recorded at the Galeta de Campos station with site geology of Meta-Andesite Breccia on 19, September, 1985; (iii) *Gebze, Turkey*, the north-south component of the Kocaeli earthquake recorded at the Gebze Tubitak Marmara Arastirma Merkezi on 17, August, 1999.

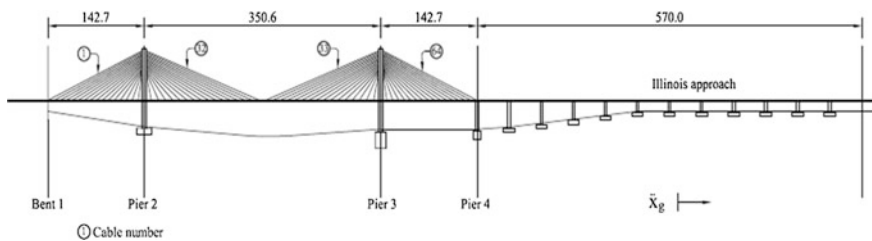


Fig. 1 Bill Emerson memorial bridge crossing the Mississippi River near Cape Girardeau, Missouri

4 Response of Bridge without Control

For a cable-stayed bridge subject to an earthquake in the longitudinal direction of the deck, there are three response variables of interest. Those are (i) the actions on the towers; (ii) the displacement of the deck and (iii) the variations of force in the stays, which should be confined in the range $0.2T_f - 0.7T_f$, (with T_f denoting the failure tension) [1]. The bridge without control can assume two distinct configurations: (a) a configuration in which the deck is restrained longitudinally to the main piers; (b) a configuration in which the deck is not restrained longitudinally to the piers and the tie in this direction is supplied only by the stays. In configuration (a) the bridge shows limited displacements, but a high shear at the base of the towers as well as unacceptable variations of tension in the cables. In particular these are found in the cables anchored in the highest positions on the towers; such cables are those with the greatest tensions. In configuration (b), even though there are maximum values of shear and moment respectively equal to 45.6 and 58.7 % of those of configuration (a), one sees an unacceptable sliding of the deck, with a maximum displacement equal to 0.77 m [1].

5 Friction Pendulum System (FPS)

The FPS is a frictional isolation system that combines a sliding action and a restoring force by geometrical properties. The FPS isolator, shown schematically in Fig. 2, has an articulated slider that moves on a stainless steel spherical surface. As the slider moves over the spherical surface, it causes the supported mass to rise and provides the restoring force for the system. The natural period of the FPS depends on the radius of curvature (r_c) of the concave surface. The natural period vibration (T_b) of a rigid mass supported on FPS connections is determined from the pendulum equation:

$$T_b = 2\pi\sqrt{\frac{r_c}{g}} \quad (1)$$

where, g is the acceleration due to gravity. The isolated period becomes active once the friction force level of the isolator is exceeded. The ideal force-deformation

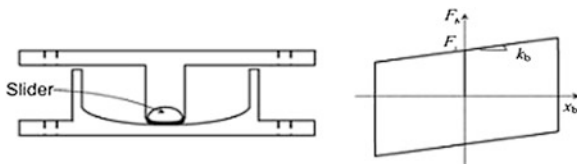


Fig. 2 Friction Pendulum System (FPS)

behavior of FPS is also shown in Fig. 2. The resisting force (f) provided by the FPS is given by:

$$f = k_b x_b + F_x \tag{2}$$

where, k_b is the bearing stiffness provided by virtue of inward gravity action at the concave surface; x_b is the device displacement and F_x is the frictional force.

6 Variable Frequency Pendulum Isolator (VFPI)

A new isolator called the VFPI [15] (refer Fig. 3) incorporates the advantages of both the friction pendulum system (FPS) and Pure-Friction (P-F) isolators. In this isolator, the shape of the sliding surface is non-spherical and its geometry has been derived from the basic equation of an ellipse, with its semi-major axis being a linear function of sliding displacement. This is equivalent to an infinite number of ellipses continuously transforming into one another such that the semi-major axis is larger for larger sliding displacement. The performance of the VFPI is found to be very effective for a variety of excitation and structural characteristics [15]. The most important properties of this system are: (i) its time period of oscillation depends on the sliding displacement and (ii) its restoring force exhibits softening behavior. The isolator geometry is such that its frequency decreases with an increase in the sliding displacement and asymptotically approaches zero at very large displacement. The response of structure with the FPS increases for higher time periods, whereas the response of the VFPI is almost independent of the structural time period [15].

The instantaneous stiffness of the VFPI [15] can be written as:

$$k_b(x_b) = m_d \omega_b^2(x_b) \tag{3}$$

$$\omega_b^2(x_b) = \left[\frac{\omega_t^2}{(1+r)^2 \sqrt{(1+2r)}} \right] \tag{4}$$

$$r = \frac{x_b \operatorname{sgn}(x_b)}{d} \tag{5}$$

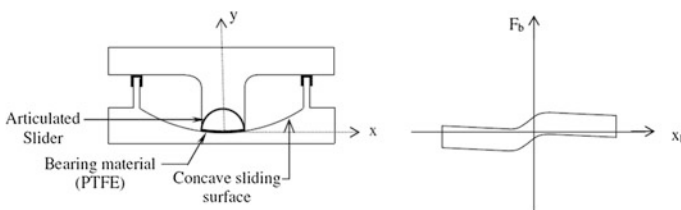


Fig. 3 VFPI

$$\omega_i^2 = \frac{gb}{d^2} \tag{6}$$

$$T_i = 2\pi\sqrt{\frac{d^2}{gb}} \tag{7}$$

where m_d is the total mass of the deck; b and d are semi-minor axis and initial value of the semi-major axis (which is greater than zero) of sliding surface; $\text{sgn}(x_b)$ is incorporated to maintain the symmetry of the sliding surface about the central vertical axis. r is the non-dimensional parameter for the sliding surface; $\omega_b(x_b)$ is the instantaneous frequency of VFPI which depends on the geometry of the sliding surface; ω_i is the initial frequency of VFPI at zero isolator displacement; and T_i is the initial time period of the VFPI.

It can be noticed that the ratio b/d^2 governs the initial frequency of the isolator. Similarly, the value of $1/d$ determines the rate of variation of isolator frequency, and this factor has been defined as frequency variation factor (FVF) [15]. It can also be seen from Eq. (4) that the rate of decrease of isolator frequency is directly proportional to the FVF for a given initial frequency.

The restoring force of the VFPI is expressed by

$$f = k_b(x_b).x_b + F_x \tag{8}$$

where F_x is the frictional force in the VFPI using the hysteretic model, keeping the parameters same as FPS; $k_b(x_b)$ is the stiffness of the VFPI which can be determined by Eq. (3); and x_b is the isolator displacement.

Thus, the modeling of the VFPI is required the specific value of the two parameters, namely frequency variation factor (FVF) and friction coefficient (μ).

7 Governing Equations of Motion

The general equation of motion for a structural system subjected to seismic loads when the excitation has a single component or when the excitation is uniformly applied at all supports of the structure

$$\mathbf{M}\ddot{\mathbf{U}} + \mathbf{C}\dot{\mathbf{U}} + \mathbf{K}\mathbf{U} = -\mathbf{M}\Gamma\ddot{x}_g + \mathbf{A}\mathbf{f} \tag{9}$$

For multiple supports,

$$\mathbf{M}\ddot{\mathbf{U}} + \mathbf{C}\dot{\mathbf{U}} + \mathbf{K}\mathbf{U} = \mathbf{A}\mathbf{f} - (\mathbf{M}\mathbf{R}_s + \mathbf{M}_g)\ddot{\mathbf{U}}_g - (\mathbf{C}\mathbf{R}_s + \mathbf{C}_g)\dot{\mathbf{U}}_g \tag{10}$$

where $\ddot{\mathbf{U}}[m/s^2]$ is the second time derivative of the displacement response vector $\mathbf{U}[m]$, \mathbf{M} , \mathbf{C} , and \mathbf{K} are the mass, damping and stiffness matrices of the structure,

$\mathbf{f}[N]$ is the vector of control force inputs, $\ddot{x}_g[m/s^2]$ is the ground acceleration, Γ is a vector of zeros and ones, relating the ground acceleration to the bridge degrees of freedom (DOF), Λ is a vector relating the force(s) produced by the control device(s) to the bridge DOFs [1]. Matrices \mathbf{M}_g , \mathbf{C}_g and \mathbf{K}_g are the mass, damping and elastic coupling matrices expressing the forces developed in the active DOFs by the motion of the supports. \mathbf{R}_s ($\mathbf{R}_s = -\mathbf{K}^{-1}\mathbf{K}_g$) is the pseudo-static influence vector which describes the influence of support displacements on the structural displacements [14]. Equation (9) is used for phase II benchmark cable-stayed bridge problem.

8 Numerical Study

A set of numerical simulation is performed in MATLAB (2002) and SIMULINK (1997) for the specified three historical earthquakes to investigate the effectiveness of the sliding isolation systems of the phase-II benchmark cable-stayed bridge. The fundamental frequency of the bridge in evaluation model (a) is 3.45 s and that of evaluation model (b) is 6.18 s. To implement the isolation systems, a total numbers of 24 isolators were used in 8 locations between the deck and pier/bent, 3 at each location [3]. Time history analysis is performed for the three earthquake ground motions specified in the benchmark problem [14] to obtain the structural responses of the bridge. For the parametric studies, normal evaluation model 2 with incidence angle 15° has been chosen.

The important parameters of the VFPI are frequency variation factor (FVF) and friction coefficient (μ). A parametric study has been performed to observe the variation and to find out possible optimum value of FVF of the VFPI on the peak seismic responses of the bridge. The study is carried out varying the value of FVF from 0.01 to 100, considering the value of friction coefficient equal to 0.05. Figure 4 shows the variation of the peak seismic responses of the bridge for different values of FVF of VFPI considering all the specified earthquakes.

It is evident from the Figure that response characteristics are changing after FVF equal to 1.0. For Gebze (1999) earthquake, significant increase in peak responses is noticed after that value of FVF. Therefore, frequency variation factor (FVF) of 1.0 has been chosen as optimum value which is good for all the specified earthquakes.

The results of the parametric study performed on VFPI for the effect of (μ) on variation of peak seismic responses of the bridge are presented in Fig. 5. The influence of coefficient of friction on the VFPI over the response of the benchmark bridge is investigated by varying it from 0.05 to 0.15, keeping the value of FVF as optimum one (i.e., FVF = 1.0). From Fig. 5, it is revealed that increase in friction coefficient of VFPI, decreases the bearing displacement and deck moment response of the bridge for all the specified earthquakes. With the increase in friction coefficient,

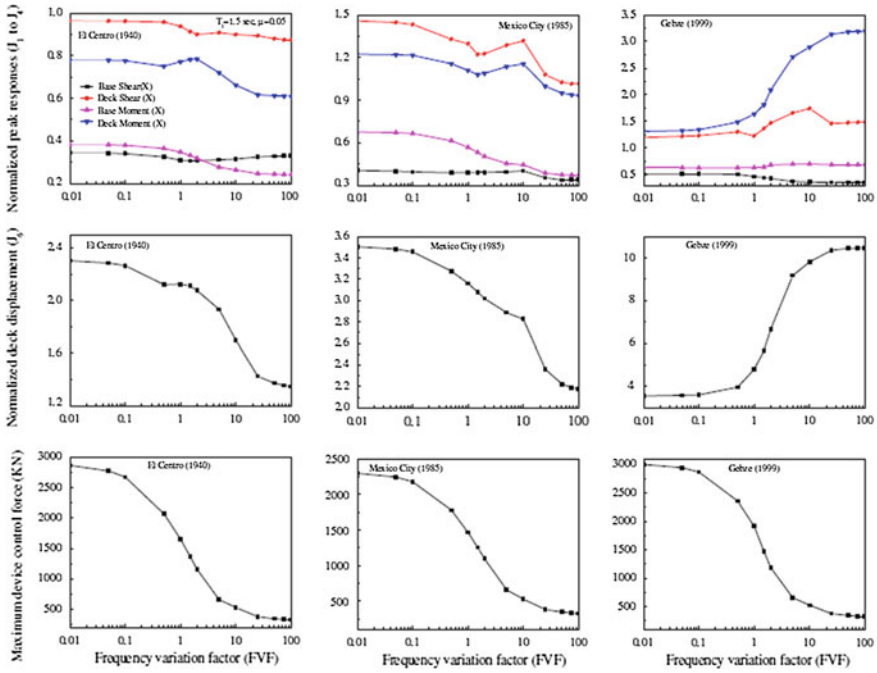


Fig. 4 Effect of frequency variation factor (FVF) of VFPI on normalized peak response of the bridge

base shear response of Mexico City (1985) earthquake increases significantly. It is observed from the Figure that higher value of (μ) is beneficial but for this study (μ) equal to 0.05 which is recommended for conventional FPS is chosen.

The time variation of the base shear response (X direction) at pier 2 of the earthquakes for the optimum parameters value considered above are shown in Fig. 6 for VFPI. From the Fig. 6, it can be observed that around 68 % reduction for El Centro (1940) earthquake, 42–60 % reduction for Mexico City (1985) earthquake and 60–64 % reduction for Gebze (1999) earthquake can be achieved by these isolators. It can be noted that maximum reduction of base shear response in longitudinal direction, for El Centro (1940), Mexico City (1985) and Gebze (1999) earthquakes is achieved by this isolator.

The force-deformation behavior of the VFPI at pier 2 (tower), for the specified earthquakes are shown in Fig. 7.

The evaluation criteria of the bridge considering the above isolation parameters for incidence angle (θ) equals to 15^0 and 45^0 are shown in Table 1 for the maximum values of the evaluation criteria for all the three earthquakes. To investigate the robustness of the control strategies, an alternate model is developed in phase-II problem considering the snow load. The evaluation criteria of the bridge for incidence angle (θ) equals to 15^0 and 45^0 with snow load are shown in Table 1. From

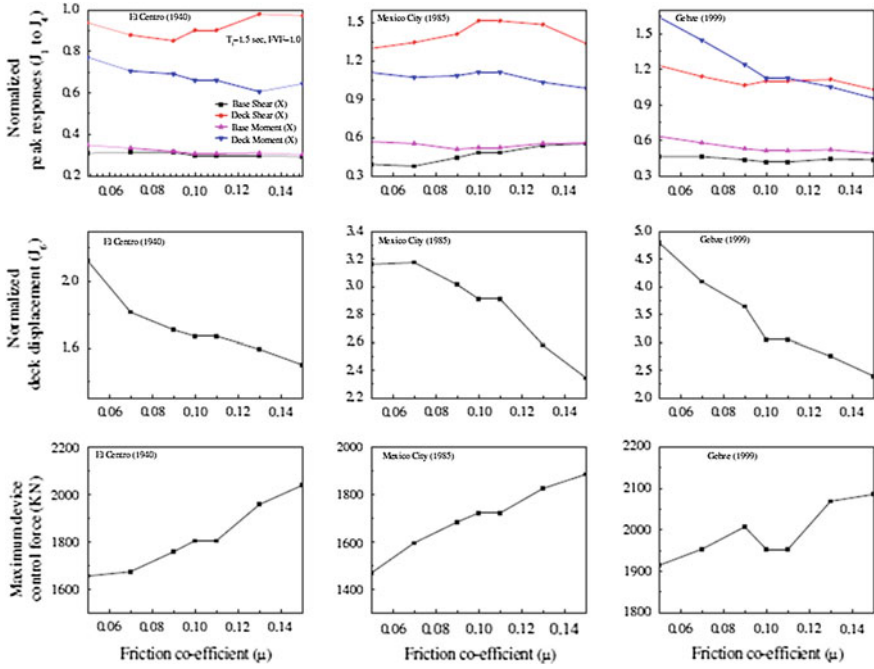


Fig. 5 Effect of friction coefficient of the VFPI on normalized peak response of the bridge

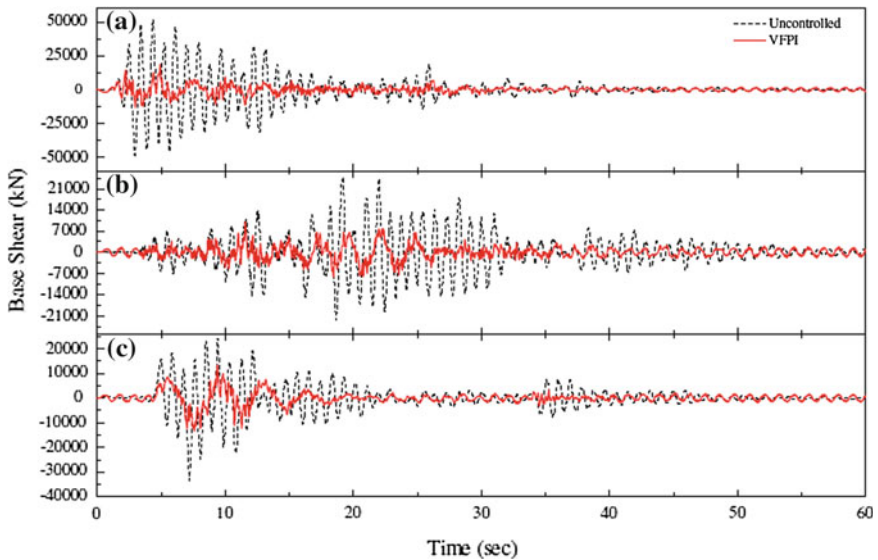


Fig. 6 Uncontrolled and VFPI controlled base shear response for a El Centro (1940), b Mexico city (1985) and c Gebze (1999) earthquakes at pier 2

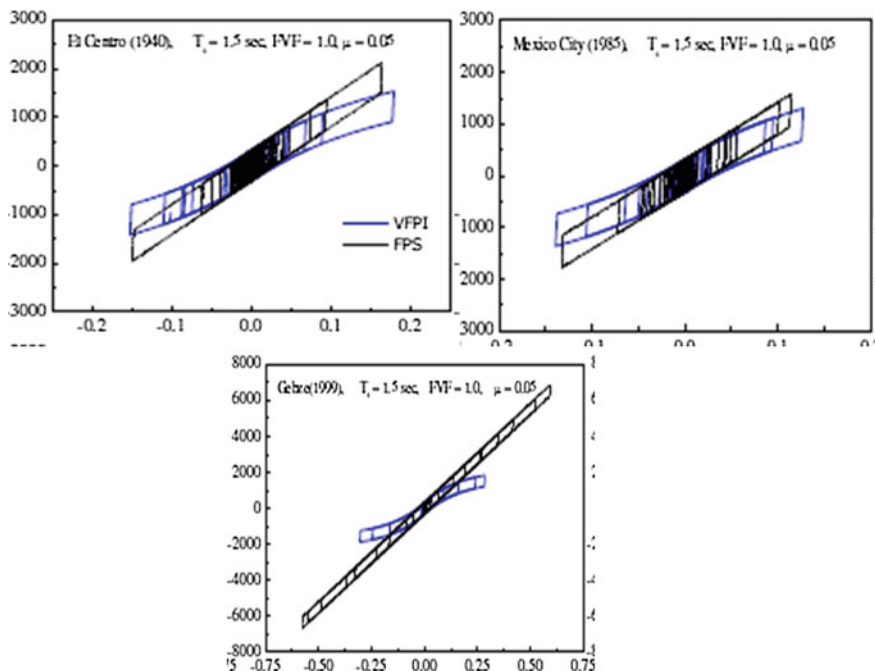


Fig. 7 Force deformation behavior of VFPI for **a** El Centro (1940), **b** Mexico City (1985) and **c** Gebze (1999) earthquakes at pier 2

the results presented in Table 1, it can be deduced that isolation can substantially reduce the seismically induced responses in the bridge. Clinically comparing the evaluation criteria Table 1, it is observed that, VFPI is more effective in reducing the deck displacement for all the three specified earthquake considering all the cases in this study and robust for the conditions without snow loads. The control force produced by this variable sliding isolator to reduce the seismic response bridge is much less than that of FPS. So we can conclude that the performance of VFPI is better than FPS.

The results of the numerical study exhibit that for the flexible structure like cable-stayed bridge, which is already having natural isolation by virtue of its large fundamental period, nevertheless, the variable seismic isolation is found very much effective in reducing seismically induced forces including superstructure displacement. It is also observed that parameters of the isolators have significant effect on the response of the bridge. Higher value of friction coefficient (μ) than the normal is beneficial for securing the displacement and base shear responses of the bridge. VFPI significantly reduces the deck displacement for all the specified earthquakes especially Gebze (1999) earthquake but produce larger base shear than the FPS.

Table 1 Evaluation criteria of bridge

Evaluation criteria		Incidence angle $\theta = 15^0$				Incidence angle $\theta = 45^0$			
		FPS	VFPI	FPS	VFPI	FPS	VFPI	FPS	VFPI
J_1	Peak base shear (X)	0.484	0.463	0.491	0.709	0.608	0.455	0.815	0.754
	Peak base shear (Z)	1.192	1.230	1.049	1.229	1.167	1.109	1.217	1.150
J_2	Peak shear at deck (X)	1.648	1.298	1.370	1.328	1.367	1.273	2.370	1.374
	Peak shear at deck (Z)	1.079	1.100	1.106	1.078	1.089	1.106	1.075	1.029
J_3	Peak base moment (X)	0.885	0.633	0.986	0.790	0.627	0.717	0.736	0.831
	Peak base moment (Z)	1.136	1.172	1.259	1.201	1.364	1.317	1.192	1.230
J_4	Peak moments at deck (X)	2.629	1.638	2.531	1.143	0.886	1.571	0.891	1.069
	Peak moments at deck (Z)	1.137	1.165	1.022	1.113	1.019	1.022	1.028	1.009
J_5	Peak cable tension	0.362	0.279	0.351	0.232	0.276	0.277	0.313	0.266
J_6	Peak deck displacement	9.049	4.800	11.218	3.717	3.041	6.157	2.191	4.348
J_7	norm base shear (X)	0.623	0.538	0.662	1.057	0.541	0.612	1.318	1.283
	norm base shear (Z)	1.132	1.141	1.103	1.221	1.111	1.103	2.098	1.162
J_8	norm shear at deck (X)	2.140	1.441	2.196	1.829	1.553	1.543	2.743	1.858
	norm shear at deck (Z)	1.002	1.003	1.037	1.014	1.035	1.038	1.097	1.019
J_9	norm base moment (X)	1.490	0.786	1.582	0.881	0.653	0.913	1.042	1.053
	norm base moment (Z)	1.100	1.113	1.083	1.154	1.087	1.083	1.850	1.118
J_{10}	norm moments at deck (X)	3.560	1.544	3.771	1.647	0.977	1.799	2.229	1.958
	norm moments at deck (Z)	1.216	1.216	1.048	1.012	1.046	1.049	1.033	1.024
J_{11}	norm of cable tension	0.058	0.033	0.052	0.046	0.028	0.035	0.045	0.046
J_{12}	peak control force (X)	0.014	0.004	0.014	0.007	0.004	0.004	0.007	0.007
	peak control force (Z)	0.000	0.000	0.000	0.000	0.000	0.000	0.000	0.000
J_{13}	max device stroke (X)	3.922	2.081	4.897	2.063	1.363	2.687	1.021	2.025
	max device stroke (Z)	0.000	0.000	0.000	0.000	0.000	0.000	0.000	0.000
J_{16}	number of control device	24	24	24	24	24	24	24	24

9 Conclusions

In this study, an attempt is made to present benchmark cable-stayed bridges with various variable sliding seismic isolators. The performance of the bridge under different sliding isolators is investigated using the hysteretic model and the results are tabulated in the form of evaluation criteria's mentioned in the benchmark problem for direct comparison. Parametric studies have been carried out by varying the important parameters of each isolator to find out the optimum value. Based on the investigation performed on the seismic response control of the bridge, the following conclusions are drawn:

1. Despite being a flexible structure, significant seismic response reduction of the bridge can be achieved by installing VFPI in the benchmark cable-stayed bridge.
2. Reduction in the base shear response of the towers is achieved about 42–68 % for the specified isolators and earthquake ground motion.

3. The reduction of the seismic responses depends on the types of isolator as well as types of earthquake ground motions.
4. Initial isolation time period has a significant effect on the seismic responses and there exist an optimum value for the isolator but that value again depends on the types of earthquake ground motion.
5. Comparing the values of evaluation criteria presented, it can be deduced that VFPI significantly reduces the deck displacement for all the specified earthquakes especially Gebze (1999) earthquake but produce larger base shear than the FPS.

References

1. Dyke SJ, Caicedo JM, Turan G, Bergman LA, Hague S (2003) Phase I benchmark control problem for seismic response of cable-stayed bridges. *J Struct Eng* 129:857–872
2. Mostaghel N, Khodaverdian M (1987) Dynamics of resilient-friction base isolator (R-FBI). *Earthq Eng Struct Dynam* 15:379–390
3. Mostaghel N, Hejazi M, Tanbakuchi J (1983) Response of sliding structures to harmonic support motion. *Earthq Eng Struct Dynam* 11:355–366
4. Mostaghel N, Tanbakuchi J (1983) Response of sliding structures to earthquake support motion. *Earthq Eng Struct Dynam* 11:729–748
5. Tsopelas P, Constantinou C, Okamoto S, Fujji S, Ozaki D (1996) Experimental study of bridge seismic sliding isolation system. *Eng Struct* 18:301–310
6. Tsai CS (1997) Finite element formulations for friction pendulum seismic isolation bearings. *Int J Numer Meth Eng* 40:29–49
7. Wang Y-P, Chung L-L, Liao W-H (1998) Seismic response analysis of bridges isolated with friction pendulum bearings. *Earthq Eng Struct Dynam* 27:1069–1093
8. Jangid RS (2000) Optimum frictional elements in sliding isolation systems. *Comput Struct* 76:651–661
9. Jangid RS (2005) Computational numerical models for seismic response of structures isolated by sliding systems. *Struct Contr Health Monit* 12:117–137
10. Kunde MC, Jangid RS (2006) Effects of pier and deck flexibility on the seismic response of isolated bridges. *J Bridge Eng* 11:109–121
11. Soneji BB, Jangid RS (2006) Effectiveness of seismic isolation for cable-stayed bridge. *Int J Struct Stab Dyn* 6:77–96
12. Saha P, Jangid RS (2008) Comparative performance of isolation systems for benchmark cable-stayed bridge. *Int J Eng Appl Sci* 6:111–139
13. Panchal VR, Jangid RS (2008) Variable friction pendulum system for near-fault ground motions. *Struct Contr Health Monit* 15:568–584
14. Caicedo JM, Dyke SJ, Moon SJ, Bergman LA, Turan G, Hague S (2003) Phase II benchmark control problem for seismic response of cable-stayed bridges. *J Struct Contr* 10:137–168
15. Pranesh M, Sinha R (2000) VFPI: an isolation device for aseismic design. *Earthq Eng Struct Dynam* 29:603–627

Energy Assessment of Friction Damped Two Dimensional Frame Subjected to Seismic Load

Ankit Bhardwaj, Vasant Matsagar and A.K. Nagpal

Abstract Energy based seismic analysis is expected to provide better idea for design and damage assessment of structure subjected to seismic load compared to displacement based analysis as former can take care of repeated plastic deformations. However, the approach based on energy concepts has not been explored in depth. At the same time, use of dampers in structures is also being investigated in order to protect the structures from adverse effects from earthquake. Herein, formulation for energy dissipated by friction damper and energy balance approach has been established for friction damped medium and high-rise buildings. Also, it has been observed that friction dampers not only can reduce the input energy but also dissipate major part of the input energy. The effect of friction damper on kinetic energy and strain energy has also been studied.

Keywords Energy balance · Friction damper · Earthquake resistant design

1 Introduction

Friction dampers (FD) are widely accepted as a means of passive control of structures against seismic hazard. These devices help to reduce the displacement response of the structure during seismic event [1]. Response in terms of top floor acceleration and base shear of the structures coupled with the FDs is also reduced significantly. Moreover, the FDs can be replaced easily when damaged and the

A. Bhardwaj (✉) · V. Matsagar · A.K. Nagpal
Department of Civil Engineering, Indian Institute of Technology (IIT),
Hauz Khas, 110 016 New Delhi, India
e-mail: ank.bhardwaj@gmail.com

V. Matsagar
e-mail: matsagar@civil.iitd.ac.in

A.K. Nagpal
e-mail: aknagpal@civil.iitd.ac.in

structure can retain its strength even after several earthquakes. Moreover, FDs can be used for seismic upgradation of existing structures [2, 3].

The usefulness of the FDs in building frames for seismic response reduction has been reported by several researchers. Pall and Marsh [4] analysed different ten-storey frame models including one moment resisting frame (MRF), one braced frame (BF) and one frictional damped frame (FDF). The researchers found seismic performance of the FDF in terms of top floor displacement, base shear and top floor acceleration better than those of the MRF and BF. Some other studies also found improvement in the seismic performance of the structure while coupled with the FDs [1, 5]. Few experimental study on the FDF were also conducted [6–9]. These studies enforce the idea of using the FD because top floor displacement, base shear and top floor acceleration of the FDF were found to be significantly reduced as compared to the MRF.

These studies established seismic response reduction of structure using the FDF very well. However, little work has been done on the energy balance assessment and energy dissipation characteristics of the FDs. The energy analysis has received attraction of researchers as it can include the effect of hysteretic cycles the structures undergo. Thereby, it can help to assess the performance of structures much better compared to displacement based approaches during earthquake. Hence, there is a need to explore energy based approaches in depth [10–13]. Taking note of such suggestions, few energy assessment studies on various kind of structures also have been conducted [14–18]. Further, energy based design approaches have also been proposed, which aim to reduce the input energy and maximize the energy dissipated by supplementary damping [19, 20].

In the wake of importance of energy assessment and effectiveness of the FDs, energy balance equation for the FDF subjected to earthquakes is established in the present work. Furthermore, the investigation includes assessing the effectiveness of the FDs for energy dissipation, reduction of input energy, and structural damping energy dissipation demand by comparing with the results of the MRF and FDF.

2 Mathematical Modelling

Figure 1 shows models of multi-storey moment resisting frame (MRF), braced frame (BF) and friction damped frame (FDF), which are subjected to the earthquake ground motion. The governing equations of the motion for the MRF are given as:

$$[M]\{\ddot{x}\} + [C]\{\dot{x}\} + [K_c]\{x\} = -[M]\{r\}(\ddot{x}_g) \quad (1)$$

while the governing equations of the motion for BF are given as:

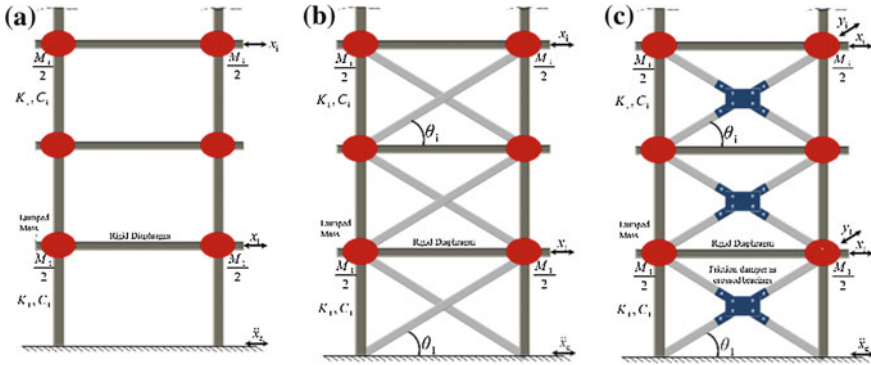


Fig. 1 MRF, BF and FDF models showing lumped mass at each storey while members have been as taken massless

$$[M]\{\ddot{x}\} + [C]\{\dot{x}\} + [K_c + K_b \cos^2 \theta]\{x\} = -[M]\{r\}(\ddot{x}_g) \tag{2}$$

and the governing equations of the motion for FDF are given as:

$$[M]\{\ddot{x}\} + [C]\{\dot{x}\} + [K_c]\{x\} + \{R'\} = -[M]\{r\}(\ddot{x}_g) \tag{3}$$

where $[M]$ is the mass matrix; $[C]$ is the damping matrix; $[K_c]$ is the column stiffness matrix; $[K_c + K_b \cos^2 \theta]$ is effective stiffness matrix due to columns and braces; $\{R'\}$ is the matrix of resisting forces offered by FDs in the horizontal direction on each floor in the FDF; $\{r\}$ is influence coefficient matrix; \ddot{x}_g is ground acceleration for single support excitation; and $\{\ddot{x}\}$, $\{\dot{x}\}$ and $\{x\}$ are acceleration vector, velocity vector and displacement vector, respectively. Acceleration, velocity and displacement of each floor are measured relative to the ground.

Equations (1), (2) and (3) can be solved for obtaining closed form solution for given continuous time history input. However, as the time history available is discrete, Newmark's- β average acceleration method has been used in the present study.

2.1 Energy Balance Equations

For any type of frame, the input energy of the structure must be equal to the sum of the energy stored in the structure at that time/moment and the total energy dissipated by the structure up to that moment. The structure can store energy in two forms as strain energy and kinetic energy, while it can dissipate energy by the means of structural damping, hysteretic damping and provided supplementary damping. However, in the present study, structure is considered to remain in elastic phase only as the FDs are supposed to reduce the response of the structure enough. Hence, hysteretic damping has not been considered. Among the considered frames,

the FDF has structural damping as well as supplementary damping in form of the FDs. While, the MRF and BF can dissipate energy by structural damping only. FEMA-445 [13] suggested energy balance equation for single degree of freedom (SDOF) MRF based on work done by different active forces on the structure at the time of motion. The equation proposed by them is:

$$\int_0^t m \ddot{x} \dot{x} d\tau + \int_0^t c \dot{x}^2 d\tau + \int_0^t f_s \dot{x} d\tau = - \int_0^t m \ddot{x}_g \dot{x} d\tau \tag{4}$$

or

$$\int_0^x m \ddot{x} dx + \int_0^x c \dot{x} dx + \int_0^x f_s dx = - \int_0^x m \ddot{x}_g dx \tag{5}$$

Here, f_s is resisting force in the structure; m , c and k respectively denote mass, damping and stiffness. Equation (4) can be further modified for multi-degree of freedom (MDOF) MRF as:

$$\begin{aligned} & \int_0^x \{dx\}^T [M] \{\ddot{x}\} + \int_0^x \{dx\}^T [C] \{\dot{x}\} + \int_0^x \{dx\}^T [K_c] \{x\} \\ & = - \int_0^x \{dx\}^T [M] \{r\} (\ddot{x}_g) \end{aligned} \tag{6}$$

while the energy balance equation for the MDOF BF can be written as:

$$\begin{aligned} & \int_0^x \{dx\}^T [M] \{\ddot{x}\} + \int_0^x \{dx\}^T [C] \{\dot{x}\} + \int_0^x \{dx\}^T [K_c + K_b \cos^2 \theta] \{x\} \\ & = - \int_0^x \{dx\}^T [M] \{r\} (\ddot{x}_g) \end{aligned} \tag{7}$$

and the energy balance equation for the MDOF FDF can be written as:

$$\begin{aligned} & \int_0^x \{dx\}^T [M] \{\ddot{x}\} + \int_0^x \{dx\}^T [C] \{\dot{x}\} + \int_0^x \{dx\}^T [K_c] \{x\} + \int_0^x \{dx\}^T \{R'\} \\ & = - \int_0^x \{dx\}^T [M] \{r\} (\ddot{x}_g) \end{aligned} \tag{8}$$

where $\{dx\}$ is vector representing change in displacement of each floor.

2.2 Input Energy

Input energy (E_i) can also be termed as the work done by the external forces on the structure. During the seismic event, it is work done by the ground motion on the structure. It plays very crucial role in determining structure’s behaviour during the event. The input energy should be minimized for energy based design, while keeping check on other energies as well. Mathematically, input energy can be computed using several different equations. The equation used for this purpose during the present study has been taken from equation proposed by Zahrah and Hall [14] for single degree of freedom (SDOF). The equation proposed by them is:

$$\frac{E_i}{m} = - \int_0^t \ddot{x}_g \dot{x} dt \tag{9}$$

or
$$\frac{E_i}{m} = - \int_0^x \ddot{x}_g dx \tag{10}$$

The equation can further be modified for multi degree of freedom (MDOF) structure as:

$$E_i = - \int_0^x \{dx\}^T [M] \{r\} (\ddot{x}_g) \tag{11}$$

After the seismic event, the structure comes to rest and no energy is stored in the structure. In other words, all the input energy has to be equal to the total dissipated energy. As the time history available is discrete, Eq. (11) should be modified as:

$$E_i = - \sum_0^{n-1} \{dx\}^T [M] \{r\} (\ddot{x}_g) \tag{12}$$

where n is no. of data points in the input time history.

2.3 Energy Dissipated by Structural Damping

Energy dissipated by structural damping (E_{sd}) can be termed as work done by structural damping force. This force acts against the motion of the structure, thereby the work done causes energy dissipation. In the present study, viscous damping has been considered, so the product of damping coefficient and velocity of the floor ($C \dot{x}$) represents structural damping force. This way, the product of damping force

and change in displacement of floor ($C \dot{x} dx$) represents the energy dissipated by structural damping for SDOF structure. It can be estimated for MDOF as:

$$E_{sd} = \int_0^t \{\dot{x}\}^T [C] \{\dot{x}\} dt \quad (13)$$

$$\text{or} \quad E_{sd} = \int_0^x \{dx\}^T [C] \{\dot{x}\} \quad (14)$$

As the time history available is discrete, Eq. (14) should be modified as:

$$E_{sd} = \sum_1^n \{dx\}^T [C] \{\dot{x}\} \quad (15)$$

2.4 Energy Dissipated by FDs

No energy is dissipated when the FD undergoes stick phase or no-slip phase. On the other hand, when the FD undergoes slip phase, energy is dissipated. In this phase, magnitude of the force of resistance remains constant. This force is equal to the slip load (Q) and always act against the relative motion of the two nodes to which the FD is attached. Therefore, the energy dissipated by the FD is same as the work done by the FD, that is the product of slip force and relative displacement of the nodes to which the FD is attached ($Q \cdot |dy|$). Hence, the energy dissipated by the FDs in a MDOF system can be given as:

$$E_{fd} = \int_0^x \{dx\}^T \{R'\} \quad (16)$$

$$\text{or} \quad E_{fd} = \int_0^y \{dy\}^T \{R\} \quad (17)$$

where $\{R\}$ is a vector of force in individual FD during slip phase.

The energy dissipated by the FD should be maximised for improved performance of the structure. It will not only restrain the structure from high displacements but also reduce base shear significantly. Moreover, due to high rate of dissipation of energy, the structure comes to rest in lesser time as compared to structure without supplementary damping. For discrete time history, Eq. (17) should be modified as:

$$E_{fd} = \sum_1^n \{dy\}^T \{R\} \quad (18)$$

2.5 Strain Energy

Strain energy indicates the drift or deformation in the structure or in turn the displacement of the structure. Therefore, the structure must be designed to minimize the maximum potential energy during the seismic event. The strain energy of a MDOF system can be termed as work done by internal forces ($[K]\{x\}$), and can be estimated as:

$$E_s = \int_0^x \{dx\}^T [K_c] \{x\} \quad (19)$$

$$\text{or} \quad E_s = \frac{1}{2} \{x\}^T [K_c] \{x\} \quad (20)$$

Strain energy is one of the stored energies in the structure and shall be calculated at the time of interest. On the other hand, input energy and dissipated energies, which are computed cumulatively till the time of interest. Hence, irrespective of continuous or discrete time history, Eq. (20) can be used.

2.6 Kinetic Energy

Kinetic energy is measure of energy stored in the structure at any time due to motion of its mass. It can also be defined as the work done by the inertial forces ($[M]\{\ddot{x}\}$), which can be calculated as:

$$E_k = \int_0^x \{dx\}^T [M] \{\ddot{x}\} \quad (21)$$

$$\text{or} \quad E_k = \int_0^t \{\dot{x}\}^T [M] \{\ddot{x}\} dt \quad (22)$$

$$\text{or} \quad E_k = \frac{1}{2} \{\dot{x}\}^T [M] \{\dot{x}\} \quad (23)$$

Similar to strain energy, Eq. (23) can be used for both continuous and discrete time history.

3 Numerical Study

The two dimensional models of the MRF, BF and FDF have been considered for the purpose of numerical study. All the members have been assumed to be weightless and mass of each storey has been assumed to be lumped equally at two ends of the floor (Fig. 1). Sway at each floor has been considered as the only degree of freedom associated with that floor. All diaphragms and joints have been considered to be rigid and bases are considered to be fixed for all the models. Soil-structure interaction has been ignored and the ground motion is considered in the plane of the structure.

Mass at each end of the floor has been taken as 25 kN and column stiffness associated to each storey has been taken 8441.3 kN/m. The selection of these two values ensures that the first natural frequency of the MRF model matches with the first natural frequency of real buildings. Braces have been considered elastic with stiffness of 21,217 kN/m in the BF however rigid in the FDF. The slip load in the FD has been taken as 30 % of the storey weight. This value has been chosen since the optimum slip load for the FD was observed to vary between 20 to 30 % of the storey weight by Kaur et al. [1]. The work conducted by these researchers focused on five-storey to twenty-storey two dimensional FDF models. The hysteretic curve of the FD is shown in Fig. 2. Modal damping for each mode in each case has been taken 2 % of critical damping.

All the three type of models were analysed for different storeys such as 5, 10, 15 and 20. The earthquake motions selected for the study are S00E component of Imperial Valley earthquake, 1940; N00E component of Loma Prieta earthquake, 1989; and N90S component of Northridge earthquake, 1994 with PGA of 0.34, 0.56 and 0.60 g , respectively. Here, g is acceleration due to gravity.

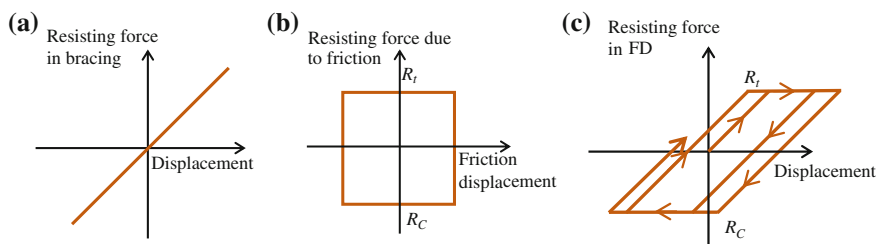


Fig. 2 Elasto-plastic force-deformation behaviour of friction damped cross-bracing **a** No slip phase (bracing action). **b** Response due to FD only. **c** Combined action of bracing and FD

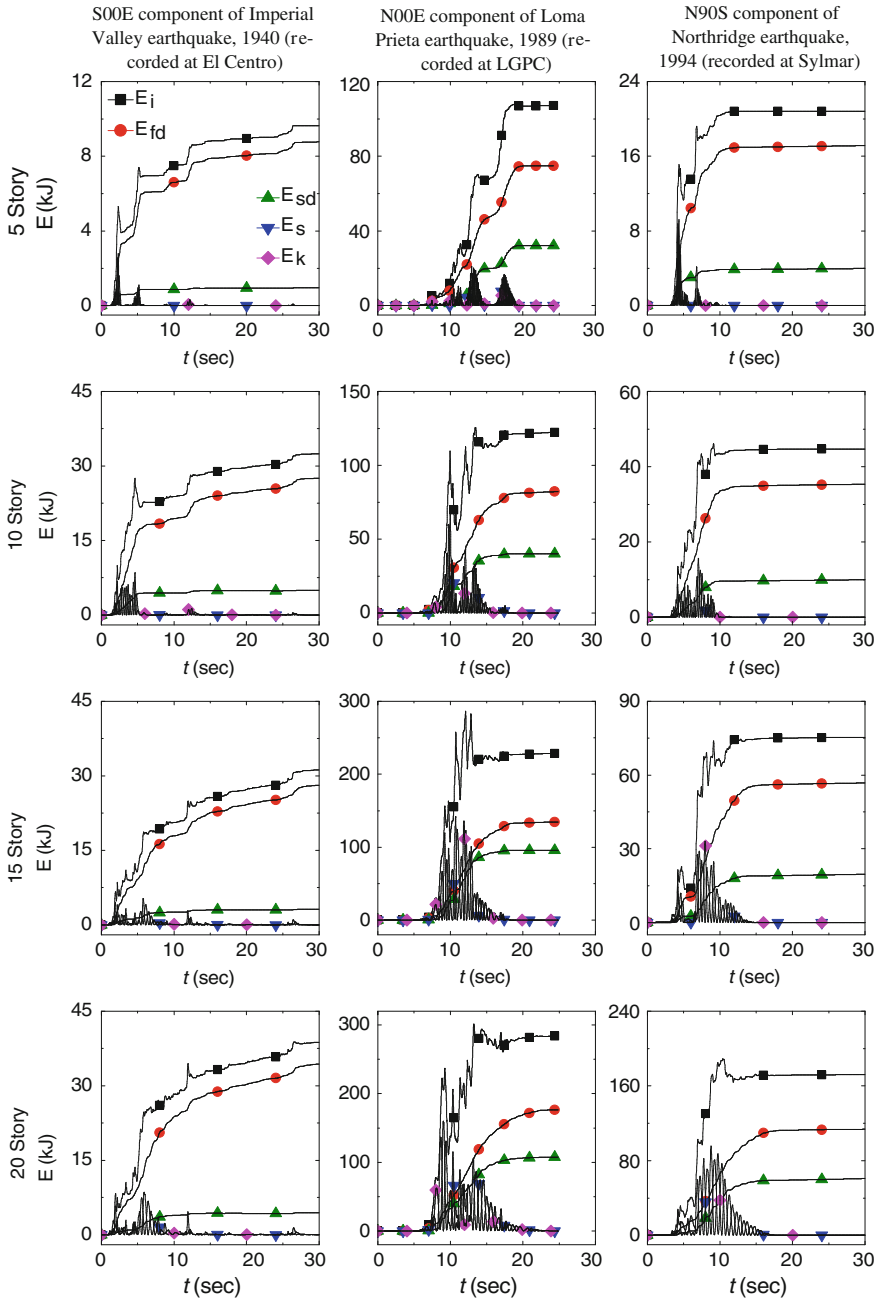


Fig. 3 Input energy and its distribution for the FDF under the considered earthquakes with variation of storeys

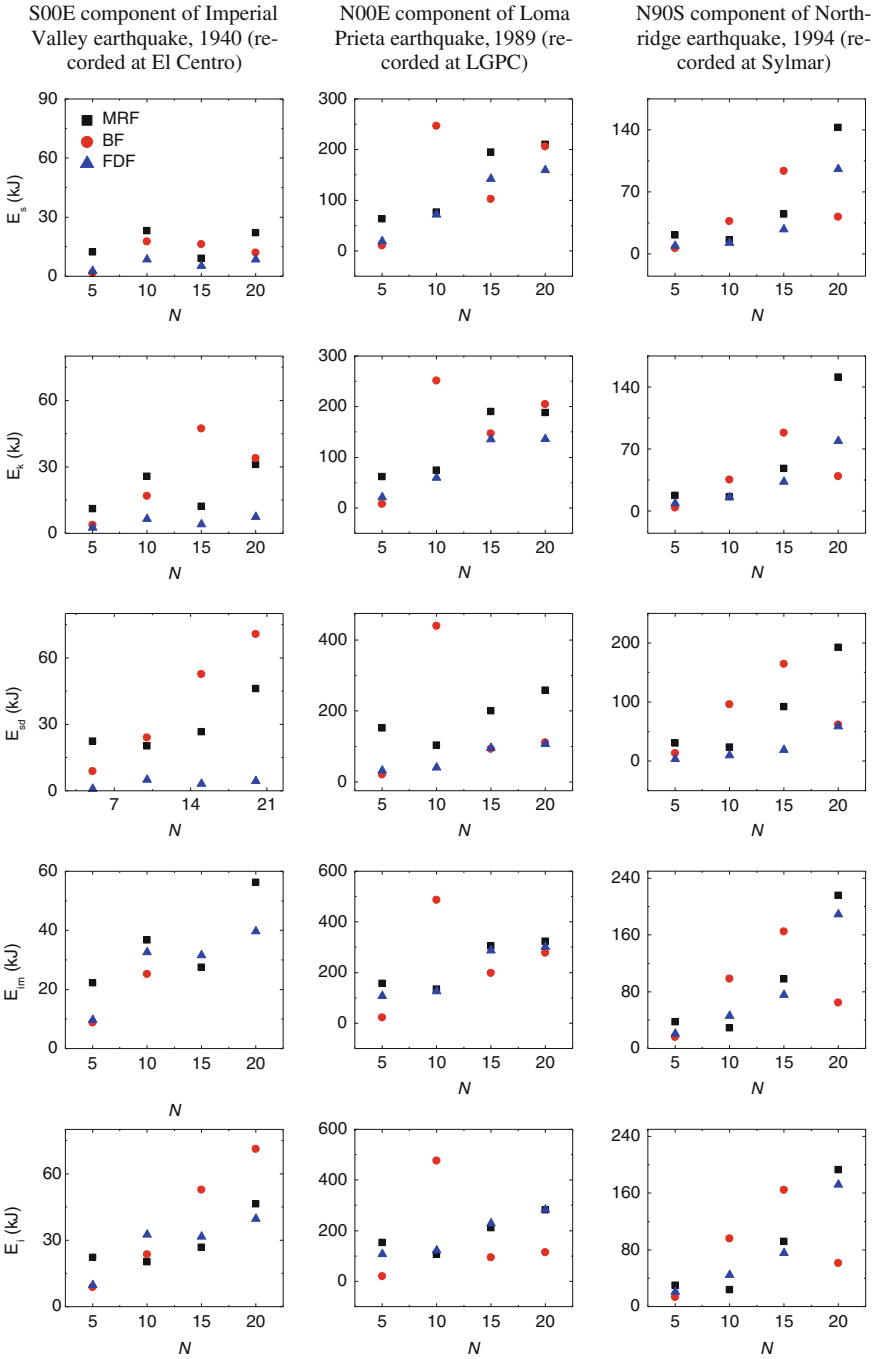


Fig. 4 Variation of various energies in MRF, BF and FDF under the considered earthquakes with variation of storeys

4 Results and Discussion

Figure 3 shows distribution of input energy of the FDF subjected to S00E component of Imperial Valley earthquake, 1940; N00E component of Loma Prieta earthquake, 1989; and N90S component of Northridge earthquake, 1994. The number of storeys taken are 5, 10, 15 and 20. The input energy is either being stored as strain energy and kinetic energy or being dissipated due to the FD and structural damping. It is observed that major part of input energy is being dissipated by the FD while the contribution of structural damping has reduced enormously. On the other hand, in absence of the FD, whole input energy has to be dissipated by the structural damping only. This implies that the structure will dissipate energy at a much higher rate resulting in lesser stored energy.

This way, maximum values of strain energy and kinetic energy are reduced significantly (Fig. 4) when compared to MRF and BF. The reduction in maximum value of strain energy indicates better protection of structure from drift and the reduction in maximum value of kinetic energy indicates lesser panic among the occupants of the structure. Similarly, energy dissipation by structural damping in the FDF reduces substantially. Moreover, it is also clear from Fig. 4 that, maximum input energy and total input energy attracted by the FDF is almost same as that of the MRF, however less than those of the BF for most of the cases.

5 Conclusions

Energy balance equations for the MDOF FDF structures have been established in the present study. Also, various energies have been investigated for the considered FDF models using the same equation. The following conclusions have been arrived at from the trends of the results obtained.

1. The friction damped frame (FDF) and braced frame (BF) attract significantly lesser input energy for taller buildings (15 to 20 storey) as compared to the moment resisting frame (MRF).
2. The stored energy in the FDF is significantly lesser than that in the MRF and BF.
3. Structural damping dissipation energy demand is much lesser in the FDF than that in the MRF and BF.
4. Major part of energy can be dissipated by friction damper, which reduces the chances of damage to the structure.

The study supports the idea of application of the friction dampers (FD) to reduce the seismic hazard to the structure and suggests the use of the energy based designs for better perception of the efficiency of the FD for the given structure for design earthquake.

References

1. Kaur N, Matsagar VA, Nagpal AK (2011) Earthquake response of medium-rise to high-rise buildings with friction dampers. In: 18th international congress on sound and vibration (ICSV 18) Rio-de-Janeiro, Brazil, pp 151–158
2. Pall A, Pall RT (2004) Performance-based design using pall friction dampers—an economical design solution. In: 13th world conference on earthquake engineering, Vancouver, Canada, Paper No. 1955
3. Shao D, Pall A, Soli B (2006) Friction dampers for seismic upgrade of a 14-storey patient tower with a 36-foot tall soft-story. In: 8th national conference on earthquake engineering, San Francisco, USA, Paper No. 90
4. Pall A, Marsh C (1982) Seismic response of friction damped braced frames. *J Struct Div* 108 (6):1313–1323
5. Bhaskararao AV, Jangid RS (2006) Seismic analysis of structures connected with friction dampers. *Eng Struct* 28(5):690–703
6. Aiken ID, Kelly JM, Pall A (1988) Seismic response of a nine-story steel frame with friction damped cross-bracing. In: 9th world conference on earthquake engineering, Tokyo, Japan, pp 156
7. Constantinou MC, Reinhorn AM, Mokha AS, Watson R (1991) Displacement control device for base isolated bridges, *Earthq spectra*. (Earthquake Engineering Research Institute (EERI)) 7(2):179–200
8. Fitzgerald TF, Anagnos T, Goodson M, Zsutty T (1989) Slotted bolted connections in a seismic design of concentrically braced connections, *Earthq spectra*. (Earthquake Engineering Research Institute (EERI)) 5(2):383–391
9. Grigorian CE, Popov EP (1993) Slotted bolted connection energy dissipaters. *Earthq spectra* (Earthquake Engineering Research Institute (EERI)) 9(3):491–504
10. ATC-40 (1996) Seismic evaluation and retrofit of concrete buildings. *Appl Technol Council (ATC)*, Vol. 1, Washington, D.C., USA
11. Bertero RD, Bertero VV and Teran-Gilmore A (1996) Performance-based seismic design based on comprehensive design philosophy and energy approaches. In: 11th world conference of earthquake engineering pp 611
12. Priestley MJN (1997) Displacement-based seismic assessment of reinforced concrete buildings. *J Earthq Eng* 1(1):157–192
13. FEMA-445 (2006) Next generation performance-based seismic design guidelines. *Fed Emerg Manage Agency (FEMA)*, Washington, D.C., USA
14. Zahrah TF, Hall WJ (1984) Earthquake energy absorption in SDOF structures. *J Struct Eng (American Society of Civil Engineering (ASCE))* 110(8):1757–1772
15. Uang CM, Bertero VV (1990) Evaluation of seismic energy in structures. *Earthq Eng Struct Dyn* 19(1):77–90
16. Austin MA, Lin W (2004) Energy balance assessment of base-isolated structures. *J Eng Mech* 130(3):347–358
17. Khashaei P, Mohraz B, Sadek F, Lew HS, Gross JL (2003) Distribution of earthquake input energy in structures. *Building and Fire Research Laboratory, National Institute of Standards and Technology, Gaithersburg, Maryland, USA*
18. Leelataviwat S, Saewon W and Goel SC (2008) An energy based method for seismic evaluation of structures. In: world conference on earthquake engineering, Beijing, China.
19. Akbas B, Shen J, Hao H (2001) Energy approach in performance based seismic design of steel moment resisting frames for basic safety objective. *Struct Des of Tall Buildings* 10 (3):193–217
20. NIST GCR 09-917-2 (2009) Research required to support full implementation of performance-based seismic design. *National Institute of Standard and Technology (NIST), Building and Fire Research Laboratory Gaithersburg, Maryland, USA*

Seismic Response Control of Multi-story Asymmetric Building Installed with Dampers

Snehal V. Mevada

Abstract The seismic response of linearly elastic, four-story asymmetric building installed with various dampers is investigated by numerical simulation study. The governing equations of motion are derived based on the mathematical model of asymmetric building. The seismic response of the system is obtained by numerically solving the equations of motion using state space method. The peak and root mean square response quantities obtained for the study are: lateral and torsional displacements, lateral and torsional accelerations, base shear, base torque as well as the control forces. The responses are obtained corresponding to the four real earthquake ground motions. The comparative performance is investigated for optimally designed dampers namely, semi-active magneto-rheological dampers, semi-active variable dampers, semi-active variable friction dampers, semi-active variable stiffness dampers and non-linear viscous dampers. The parametric studies are carried out to derive the optimum parameters for various control devices. It is observed that there exists an optimum parameters for various control devices such as to have optimum compromise between lateral-torsional displacement and acceleration response reduction as well as the damper capacity. Further, the implemented control devices are quite effective in reducing the lateral-torsional responses and the effectiveness is more in reducing the torsional responses as compared to the lateral responses.

Keywords Seismic response • Multi-story • Asymmetric • Passive • Semi-active

S.V. Mevada (✉)

Structural Engineering Department, Birla Vishvakarma Mahavidyalaya
(Engineering College), Vallabh Vidyanagar 388120, Gujarat, India
e-mail: svmevada@bvmengineering.ac.in

1 Introduction

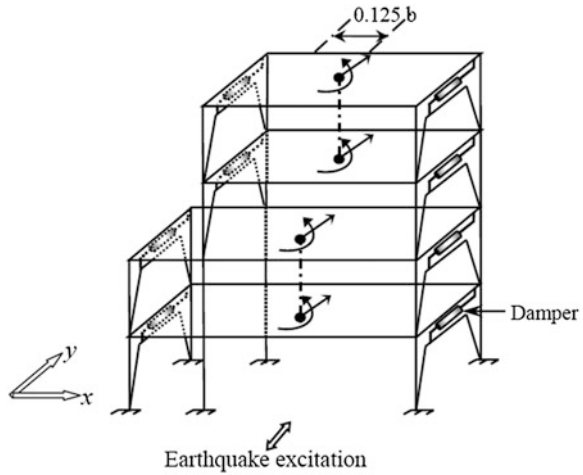
In the past, many researchers have investigated the seismic response of single-story asymmetric buildings. Most of the real civil engineering structures have more than one storey and possess irregularity in plan and/or elevation due to uneven mass and/or stiffness distribution of the structural members. Further, a severe damage and collapse of the multi-story asymmetric buildings has been observed during the earthquakes occurred in past. For example, during Mexico City (1985) earthquake, 42 % of the total collapses of buildings were related to the torsional response of asymmetric buildings [1]. Hence, there is need to reduce the seismic response of multi-story asymmetric buildings using various control techniques. In recent past, some researchers have investigated the seismic response of multi-story asymmetric buildings using passive, active, hybrid and semi-active dampers. For example, effectiveness of passive dampers for multi-story asymmetric building are studied by Jangid and Datta [2], Singh et al. [3], De La Llera and Almazan [4]. Further, effectiveness of semi-active dampers for multi-story asymmetric building are studied by Chi et al. [5], Yoshida and Dyke [6], Li and Li [7] and Shook et al. [8]. Although, above research work shown the effectiveness of some of the passive and semi-active devices for the response reduction of multi-story asymmetric buildings. However, no work has been reported to study the comparative performance of commonly available dampers for multi-story asymmetric buildings. The specific objectives of the study are as follows:

- (i) to derive the optimum parameters for various control devices such as semi-active MR dampers, semi-active variable dampers, semi-active variable friction dampers, semi-active variable stiffness dampers and non-linear viscous dampers installed in multi-story asymmetric building such as to have optimum reduction in various responses, and
- (ii) to study the comparative performance of the above mentioned devices in controlling lateral-torsional displacements as well as their acceleration for multi-story asymmetric building.

2 Structural Model

The building considered for the present study is a four-story building model given by De La Llera and Chopra [9]. The isometric view of the building is shown in Fig. 1. The building is symmetric in x -direction and asymmetric in y -direction and subjected to an earthquake excitation in the y -direction. The building is having infinitely rigid floor diaphragms, where story masses are lumped and the lateral resistance is provided by resisting planes in the x - and y -directions. The most important feature of this structure is its irregularity in height produced by a setback on the third story. This setback produces an offset equal to $0.125b$ (where, b is plan

Fig. 1 Isometric view of building showing lateral-torsional degree-of-freedom and locations of dampers



dimension of building along x -direction, perpendicular to direction of earthquake motion) between the centre of mass of the first two and upper two (3rd and 4th) stories. Because of this offset the building has lateral-torsional coupling despite its stiffness and strength symmetry. The properties of the building are given in Table 1. The natural periods of vibration in first three modes are obtained as 0.745, 0.635 and 0.294 s in the direction of earthquake excitation which is considered along y -direction.

The governing equations of motion of asymmetric building system in the matrix form are expressed as

$$M\ddot{u} + C\dot{u} + Ku = -M\Gamma\ddot{u}_g + \Lambda f \tag{1}$$

Table 1 Properties of four-story building [9]

Parameter	Value	Parameter	Value
Aspect ratio of plan, a/b	0.5	Damping ratio (each mode)	1 %
Lumped mass of 1st floor, m_1	145.72×10^3 kg	Polar moment of inertia, I_{p1}	21659.79×10^3 kg-m ²
Lumped mass of 2nd floor, m_2	145.72×10^3 kg	Polar moment of inertia, I_{p2}	21659.79×10^3 kg-m ²
Lumped mass of 3rd floor, m_3	116.57×10^3 kg	Polar moment of inertia, I_{p3}	16244.84×10^3 kg-m ²
Lumped mass of 4th floor, m_4	116.57×10^3 kg	Polar moment of inertia, I_{p4}	16244.84×10^3 kg-m ²
Lateral stiffness of each column, k_{yi}	5940.87 kN/m	Lateral stiffness of each column, k_{xi}	400.14 kN/m

where M , C and K and are mass, damping and stiffness matrices of the system, respectively; $\mathbf{u} = \{u_{y1} \ u_{y2} \ u_{y3} \ u_{y4} \ u_{\theta1} \ u_{\theta2} \ u_{\theta3} \ u_{\theta4}\}^T$ is the displacement vector representing the relative displacements of the centre of mass (CM) of each floor in y - and θ -directions; $\dot{\mathbf{u}}$ is the velocity vector; $\ddot{\mathbf{u}}$ is the acceleration vector; Γ is the influence coefficient matrix; $\ddot{\mathbf{u}}_g = \{\ddot{u}_{gy} \ \mathbf{0}\}^T$ is the ground acceleration vector; $\ddot{\mathbf{u}}_{gy}$ is the vector containing the component of ground acceleration in y -direction, \mathbf{u}_{gy} is the matrix that defines the location of control devices; $\mathbf{f} = \{f_{dy1} \ f_{dy2} \ f_{dy3} \ f_{dy4} \ f_{d\theta1} \ f_{d\theta2} \ f_{d\theta3} \ f_{d\theta4}\}^T$ is the vector of control forces in which $f_{dy1}, f_{dy2}, f_{dy3}$ and f_{dy4} are the resultant damper forces in y -direction of dampers placed at 1st, 2nd, 3rd and 4th story of building, respectively and $f_{d\theta1}, f_{d\theta2}, f_{d\theta3}$ and $f_{d\theta4}$ are the resultant damper forces in θ -direction of dampers placed at 1st, 2nd, 3rd and 4th story of building, respectively.

The mass matrix, M is a diagonal matrix and can be expressed as,

$$M = \begin{bmatrix} m_1 & & & & & & & \\ & \dots & & & & & & \\ & & m_4 & & & & & \\ & & & I_{p1} & & & & \\ & & & & \dots & & & \\ & & & & & & I_{p4} & \end{bmatrix} \tag{2}$$

where m_i and I_{pi} represents the lumped mass and polar moment of inertia of i th floor respectively, where $i = 1-4$.

The stiffness matrix of the system is obtained as follows,

$$K = \begin{bmatrix} K_y & K_{y\theta} \\ K_{\theta y} & K_{\theta\theta} \end{bmatrix} \tag{3}$$

where,

$$K_y = \begin{bmatrix} K_{y1} + K_{y2} & -K_{y2} & 0 & 0 \\ -K_{y2} & K_{y2} + K_{y3} & -K_{y3} & 0 \\ 0 & -K_{y3} & K_{y3} + K_{y4} & -K_{y4} \\ 0 & 0 & -K_{y4} & K_{y4} \end{bmatrix}, \tag{4}$$

$$K_{y\theta} = K_{\theta y} = \begin{bmatrix} K_{y\theta1} + K_{y\theta2} & -K_{y\theta2} & 0 & 0 \\ -K_{y\theta2} & K_{y\theta2} + K_{y\theta3} & -K_{y\theta3} & 0 \\ 0 & -K_{y\theta3} & K_{y\theta3} + K_{y\theta4} & -K_{y\theta4} \\ 0 & 0 & -K_{y\theta4} & K_{y\theta4} \end{bmatrix} \tag{5}$$

$$K_{\theta\theta} = \begin{bmatrix} K_{\theta1} + K_{\theta2} & -K_{\theta2} & 0 & 0 \\ -K_{\theta2} & K_{\theta2} + K_{\theta3} & -K_{\theta3} & 0 \\ 0 & -K_{\theta3} & K_{\theta3} + K_{\theta4} & -K_{\theta4} \\ 0 & 0 & -K_{\theta4} & K_{\theta4} \end{bmatrix}, \tag{6}$$

$$K_{\theta i} = \sum_i k_{xi}y_i^2 + \sum_i k_{yi}x_i^2 \quad (7)$$

where K_{yi} and $K_{\theta i}$ corresponds to the total stiffness of i th storey in y - and θ -directions, respectively; and k_{xi} and k_{yi} are lateral stiffness of i th column in x - and y -directions, respectively; x_i is the x -coordinate distance of i th element with respect to CM; and y_i is the y -coordinate distance of i th element with respect to CM.

The damping matrix of the system is not known explicitly and it is constructed from the Rayleigh's damping considering mass and stiffness proportional as,

$$C = a_0M + a_1K \quad (8)$$

in which a_0 and a_1 are the coefficients depends on damping ratio of two vibration modes. For the building under consideration, 1 % damping is taken for vibration modes of the system. The governing equations of motion are solved using the state space method.

3 Model of Dampers and Control Laws

The seismic response of linearly elastic, idealized shear type four-story asymmetric building installed with dampers is investigated by numerical simulation study. The comparative performances of various control devices as shown in Fig. 2 are investigated. The control devices which are considered for the investigation are: semi-active MR dampers with clipped optimal control (SAMRDs), semi-active variable dampers with two-step viscous algorithm (SAVDs), semi-active variable friction dampers with predictive control (SAVFDs), semi-active variable stiffness dampers with resetting stiffness control (SAVSDs) and non-linear viscous dampers (NLVDs). The dampers are installed in the building at the edges such as to have maximum torsional resistance. The capacities of dampers are selected based on the optimum damper parameters which are derived separately for each category in the subsequent sections.

The response quantities of interest are lateral and torsional displacements of the floor mass obtained at the CM of respective floors (u_{yi} and $u_{\theta i}$), lateral and torsional accelerations of the floor mass obtained at the CM of respective floors (\ddot{u}_{yi} and $\ddot{u}_{\theta i}$), base shear, base torque as well as the control forces. The peak responses are obtained corresponding to the four earthquake ground motions namely, Imperial Valley (19th May, 1940, El Centro), Loma Prieta (18th October, 1989, LGPC), Northridge (17th January, 1994, Sylmar CS) and Kobe (16th January, 1995, JMA) with corresponding peak ground acceleration values of 0.31, 0.96, 0.89 and 0.82 g. The damper forces are normalized with total seismic weight of building, $W = 5245.8$ kN. The parametric studies are carried out to obtain optimum parameters for individual dampers such as to have optimum reduction in various

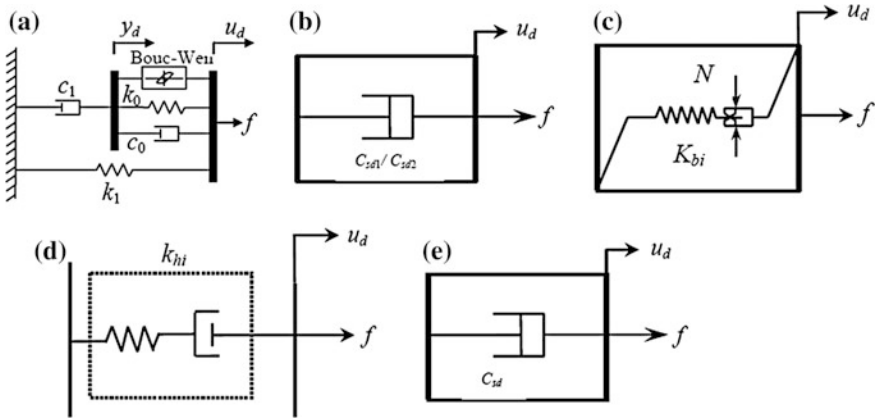


Fig. 2 Mathematical models of various dampers. **a** Model of MRD **b** Model of SAVD **c** Model of SAVFD **d** Model of SAVSD **e** Model of NLVD [11–14]

response quantities. The procedure for determining the optimum values for various damper parameters and the approach of comparing the effectiveness of various dampers by designing them optimally is similar to as used by He et al. [10].

In order to study the effectiveness of various control systems, the responses are expressed in terms of index, R_e defined as follows:

$$R_e = \frac{\text{Peak response of controlled asymmetric system}}{\text{Peak response of corresponding uncontrolled system}} \tag{9}$$

The value of R_e less than unity indicates that the implemented control system is effective in controlling the responses.

3.1 Parametric Study with Semi-active MR Dampers (SAMRDs)

Semi-active clipped-optimal control algorithm based on acceleration feedback is used. The accelerometers (total 08 nos.) are assumed to be fixed at the left and right edges of the floors of the building. For the design of controller, the absolute acceleration of the ground, u_{gy} , is taken to be a stationary white noise. The control force of damper, f is obtained as,

$$f = \alpha_i z_i + c_{0i}(\dot{x}_{di} - \dot{y}_{di}) + k_0(x_{di} - y_{di}) + k_1(x_{di} - x_0) \tag{10}$$

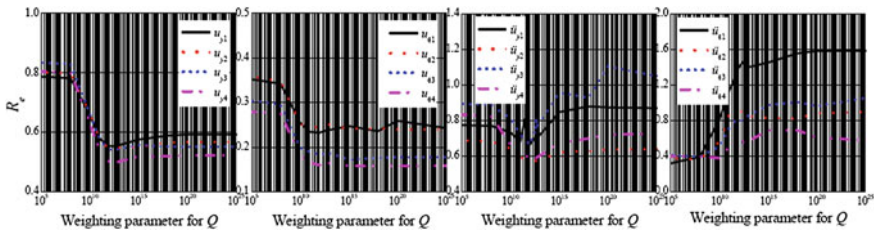


Fig. 3 Effect of weighting parameter Q on response ratio, R_e for displacement and acceleration responses under Imperial Valley earthquake

In the design of controller, Q and R are weighting matrices for the vector of measured responses, $\mathbf{y}_m = \{u_{mL1} \ddot{u}_{mR1} \ddot{u}_{mL2} \ddot{u}_{mR2} \ddot{u}_{mL3} \ddot{u}_{mR3} \ddot{u}_{mL4} \ddot{u}_{mR4}\}^T$ and of control forces, $\mathbf{f} = \{f_{dy1} f_{dy2} f_{dy3} f_{dy4} f_{d\theta1} f_{d\theta2} f_{d\theta3} f_{d\theta4}\}^T$, respectively, u_{mL1} is the acceleration measured by the accelerometer which is placed at the left side edge of 1st story floor and so on. The measurement noise vector, \mathbf{v} is assumed to contain identically distributed, statistically independent Gaussian white noise processes with $S_{u_{gy} \ddot{u}_{gy}} / S_{v_i v_i} = \gamma_g = 50$. The capacity of each MR damper used for this study is 200 kN. In order to determine the optimum coefficients of weighting matrices Q and R , initially, the matrix, R is considered as unity and the matrix, Q is varied by placing higher weightage on the response quantities. The ratios, R_e are obtained for various responses obtained at CM of respective floors such as lateral and torsional displacements of 1st floor (u_{y1} and $u_{\theta1}$), of 2nd floor (u_{y2} and $u_{\theta2}$), of 3rd floor (u_{y3} and $u_{\theta3}$), of 4th floor (u_{y4} and $u_{\theta4}$) as well as their lateral and torsional accelerations counterparts.

The variations of R_e against weighting parameter, Q are shown in Fig. 3 under Imperial Valley earthquake. From the Figure, it can be noticed that initially with the increase in weighting parameter, the ratio, R_e for various responses decreases up to certain limit and then increases with further increase in Q . This means there exists an optimum value of coefficient, Q for which R_e is minimum, which shows the maximum reduction in various displacements and accelerations. Thus, for the present study, to achieve an optimum compromise between reduction in various responses, the suitable optimum value for Q is considered as 10^{11} . Further, trials have been done by keeping Q as constant (i.e. $Q = 10^{11}$) and by varying the coefficient, R . It is observed that the ratio, R_e is minimum corresponding to the value of $R = 1$. Thus, the optimum values of coefficients for the weighting matrices Q and R are considered as 10^{11} and 1, respectively.

3.2 Parametric Study with Semi-active Variable Dampers (SAVDs)

The variable dampers are designed such that the supplemental damping coefficient, C_d can be varied with respect to the displacement and velocity of the damper. The control force of damper, f is obtained as,

$$f = C_d \dot{u}_d \tag{11}$$

The ratio between two supplemental damping coefficients, R is defined as $R = C_{d1}/C_{d2}$ and it plays an important role in effectiveness of damper control system. Normally, for the multi-story buildings, the top floor responses are more significant as compared to the responses of other floors. Hence, in order to derive the suitable and optimum value of the large damping coefficient, C_{d1} for the building under consideration, the response ratio, R_e is obtained for peak values of top floor lateral (u_{y4}) and torsional ($u_{\theta 4}$) displacements, top floor lateral (\dot{u}_{y4}) and torsional ($\dot{u}_{\theta 4}$) accelerations. The variations of ratio, R_e for above mentioned responses against large damping coefficient (C_{d1}) are shown in Fig. 4.

The damping coefficient, C_{d1} is varied from 0 to 3,000 kN.s/m. Figure also shows the variation of normalized peak resultant damper force, $F_{d,total}/W$, (resultant damper force of all (i.e. eight) dampers in lateral direction normalized with total seismic weight of building, $W = 5245.8$ kN) against C_{d1} .

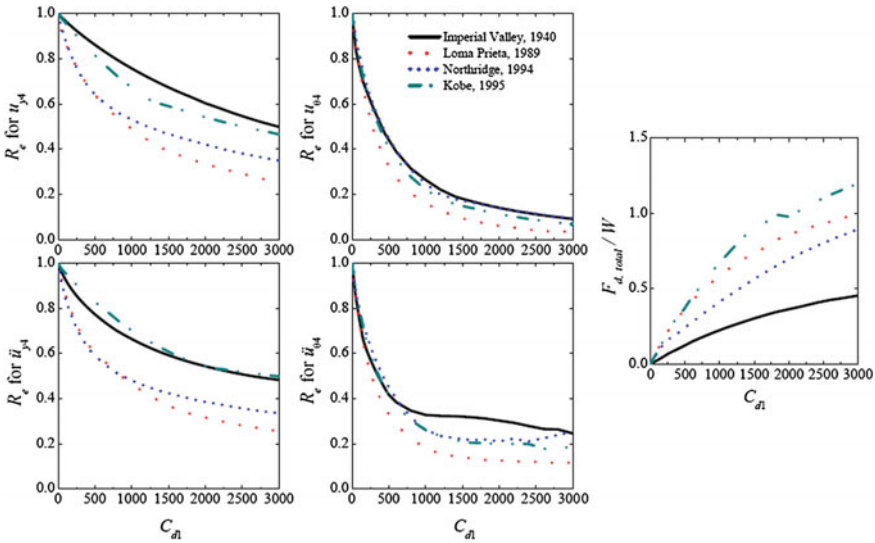


Fig. 4 Effect of supplemental damping coefficient, C_{d1} on response ratio, R_e for various responses and normalized control force under different earthquakes

It is observed from the figure that the ratio, R_e for various response quantities decreases continuously with an increase in values of C_{d1} . On the other hand, the resultant damper force increases with increase in C_{d1} . It is further observed that the decrease in various response quantities is rapid in the beginning and it is gradual for a value of $C_{d1} > 1,000$ kN.s/m. Moreover, beyond the value of $C_{d1} = 1,000$ kN.s/m, increase in damper force is significant which does not affect much on the reduction of various responses. In other words, by increasing the damper capacity beyond certain limit does not help much in improving the reduction in various responses. Hence to achieve the optimum compromise between response reduction and damper capacity, the supplemental damping coefficient ratio is considered as $R = 2$ and the large supplemental damping coefficient (C_{d1}) = 1,000 kN.s/m is considered as optimum parameter.

3.3 Parametric Study with Semi-active Variable Friction Dampers (SAVFDs)

The stiffness of each damper ($k_{b,i}$) is considered as $k_{b,i} = k_{bf,i}$ Horizontal Story Stiffness; where $k_{bf,i}$ is damper stiffness factor for the i th damper. The control force of damper, f is obtained as,

$$f = \alpha_f(G_z z[k - 1] + G_f F[k - 1] + G_g \ddot{u}_g [k - 1]) \tag{12}$$

The control force for the SAVFD depends on the gain matrices, G_z , G_f and G_g as well as gain multiplier (α_f) which in turn depend on the stiffness of the damper (k_b) and damper stiffness factor (k_{bf}). To derive the suitable and optimum value of the damper stiffness factor (k_{bf}), the response ratio, R_e is obtained for peak values of top floor lateral-torsional displacements and top floor lateral-torsional accelerations. The variations of ratio, R_e for peak values of above mentioned responses against k_{bf} are shown in Fig. 5. The damper stiffness factor is varied from 0 to 15. In addition, figure also shows the variation of normalized peak resultant damper force, $F_{d,total}/W$ against k_{bf} . It is observed from the figure that the ratio, R_e for various peak response quantities decreases continuously with an increase in values of k_{bf} . On the other hand, the peak resultant damper force increases with increase in k_{bf} . It is further observed that the decrease in various response quantities is rapid in the beginning and it is gradual for a value of $k_{bf} > 3$. Moreover, beyond the value of $k_{bf} = 3$, the increase in damper force is significant which does not affect much on the reduction of various responses. Hence to achieve the optimum compromise between response reduction and damper capacity, $k_{bf} = 3$ is considered as optimum parameter. Further, the value of gain multiplier is selected as 0.98 for the present study.

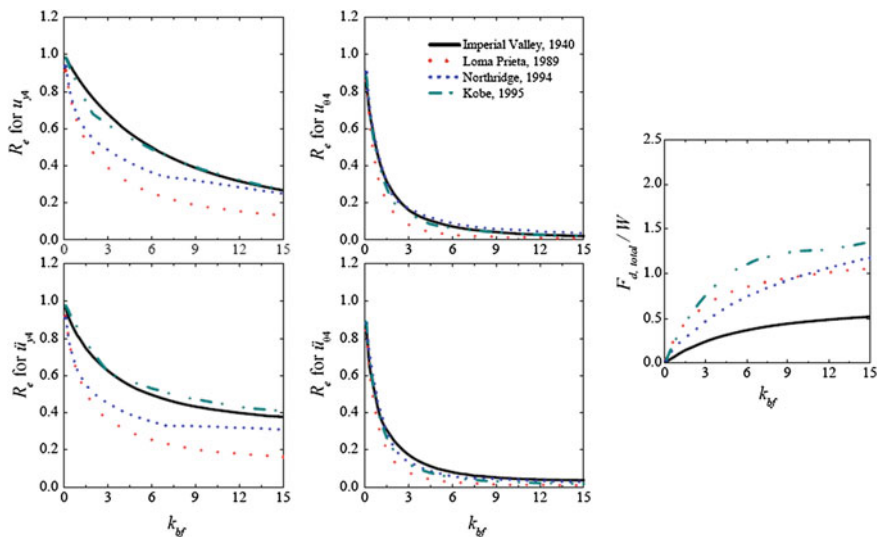


Fig. 5 Effect of damper stiffness factor, k_{bf} on response ratio, R_e for various responses and normalized control force under different earthquakes

3.4 Parametric Study with Semi-active Variable Stiffness Dampers (SAVSDs)

The resetting semi-active stiffness damper (RSASD) is considered as SAVSD. The control force of damper, f is obtained as,

$$f = k_{hi}(u_i - u_{ri}) \tag{13}$$

For the stiffness damper, the effective damper stiffness (k_{hi}) plays an important role while designing the control system. The stiffness ratio is defined as $k_r = k_{hi}/k_{si}$; where k_{si} is the story stiffness. The response ratio, R_e is obtained for peak values of top floor lateral-torsional displacements and lateral-torsional accelerations. The constant parameter, α_L is considered as zero as a special case as proposed by Yang et al. [11]. The variations of ratio, R_e for peak values of above mentioned responses against k_r are shown in Fig. 6. The stiffness ratio (k_r) is varied from 0 to 2. Figure also shows the variation of normalized peak resultant damper force, $F_{d,total}/W$ against k_r . It is observed from the Figure that with the increase in k_r , the ratio, R_e for top floor lateral-torsional displacement responses decreases continuously. This means the effectiveness of control system is more in reducing displacements with higher values of k_r . On the other hand, R_e for top floor lateral-torsional accelerations decreases initially with increase in k_r and then increases with further increase in k_r . This implies that there exists an optimum range of stiffness ratio, k_r in order to achieve the optimum reduction in top floor accelerations. Hence to achieve the

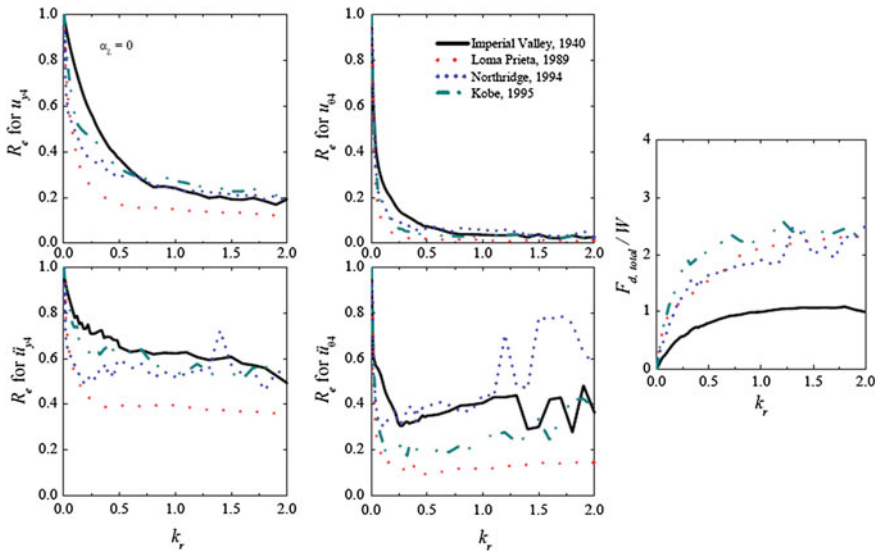


Fig. 6 Effect of stiffness ratio, k_r on response ratio, R_e for various responses and normalized control force under different earthquakes

optimum compromise between displacement and accelerations response reduction and damper capacity, the stiffness ratio, $k_r = 0.5$ is considered as optimum parameter.

3.5 Parametric Study with Non-linear Viscous Dampers (NLVDs)

For the NLVD, two important parameters are responsible for generating the force in damper, namely, damper coefficient (C_{sd}) and damper exponent (α) which is ranging from 0.2 to 1 for seismic applications. The control force of damper, f is obtained as,

$$f = C_{sdi} |\dot{u}_{di}|^\alpha \text{sgn}(\dot{u}_{di}) \tag{14}$$

For the present study, in order to derive the optimum value of damper coefficient (C_{sd}), the parametric study is carried out by varying C_{sd} (i.e. varied from 0 to 3,000 kN.s/m) by taking damper non-linearity exponent, $\alpha = 0.35$. The response ratio, R_e is obtained for peak values of top floor lateral-torsional displacements and lateral-torsional accelerations. The variations of ratio, R_e for above mentioned responses against C_{sd} are shown in Fig. 7. Figure also shows the variation of normalized peak resultant damper force, $F_{d, total} / W$ against C_{sd} . It is observed that with the increase in C_{sd} , the ratio, R_e for top floor displacement responses decreases continuously.

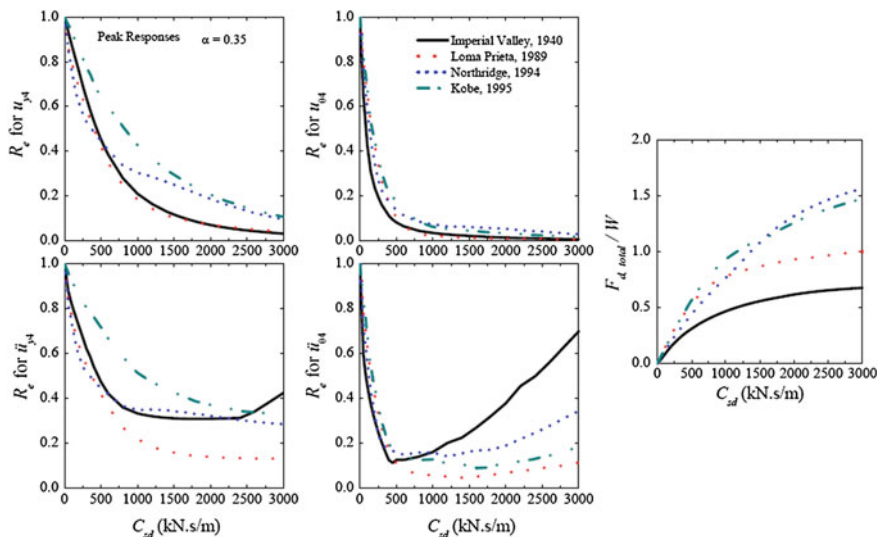


Fig. 7 Effect of damper coefficient, C_{sd} on response ratio, R_e for various responses and normalized control force under different earthquakes

This means the effectiveness of control system is more in reducing displacements with higher values of C_{sd} . On the other hand, R_e for top floor accelerations decreases initially with increase in C_{sd} and then increases with further increase in C_{sd} . This implies that there exists an optimum range of damper coefficient, C_{sd} in order to achieve the optimum reduction in top floor accelerations. With the increase in damping beyond some limit increases the stiffness of dampers and thus, stiffness of the building increases and this result in increased acceleration responses. The optimum coefficient, C_{sd} is found in the range of 500–1,000 N.s/m based on above observations. It is further observed that the decrease in various response quantities is rapid in the beginning and it is gradual for a value of $C_{sd} > 1000$ kN.s/m. Hence, to achieve the optimum compromise between displacement and accelerations response reduction and damper capacity, the damper coefficient, $C_{sd} = 750$ kN.s/m is considered as optimum.

3.6 Comparative Performance of Various Control Devices

In the previous sections, the extensive parametric studies were carried out to derive the optimum parameters for various control devices. Figure 8 represents the variation of uncontrolled and controlled peak lateral and torsional displacements as well as accelerations obtained at each floor level against the story height. In general, it is observed that, the lateral-torsional responses are lesser at ground floor and it increases and maximum at top floor. The significant reductions in lateral-torsional

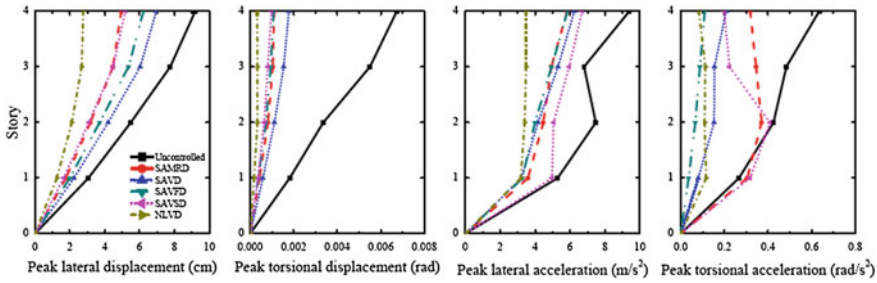


Fig. 8 Comparison of lateral and torsional responses at all floors obtained with different control devices under Imperial Valley earthquake

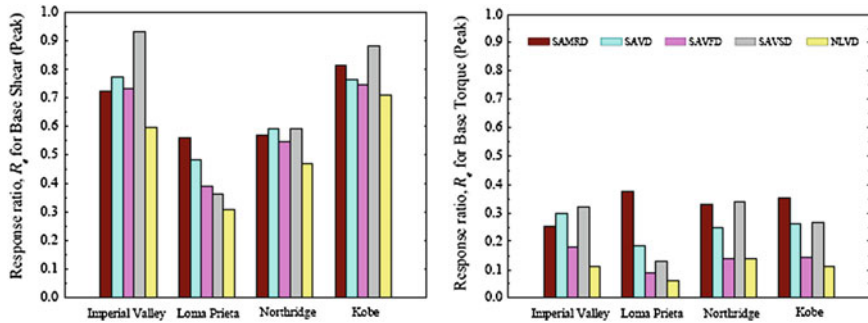


Fig. 9 Variation of response ratio, R_e for base shear and base torque obtained with different control devices under various earthquakes

displacements at all floor levels are observed as compared to uncontrolled case. Further, the SAVSDs and NLVDs proved better than other devices. It is also observed that NLVDs perform better in reducing the peak lateral accelerations at all floor levels as compared to uncontrolled and other dampers cases. On the other hand, SAVFDs are found better as compared to other dampers in reducing the peak torsional accelerations at all floors and SAVSDs are less effective in reducing the torsional acceleration responses. This is due to the fact the SAVFDs always remains in slip state and hence smoothly reduces the response, whereas, the on-off operation in SAVSDs produces the high frequency responses and hence not good for reducing torsional accelerations.

In addition to the various structural responses, the peak values of base shear and base torque are also important quantities. In order to compare the effectiveness of various control devices in reducing the base shear and base torque, the response ratio, R_e is obtained for various cases and its variations are shown in Fig. 9. It is noticed from the bar charts that the ratio, R_e for peak and RMS values of base shear and base torque is minimum for the building installed with NLVDs. Hence, NLVDs are quite effective in reducing base shear and base torque.

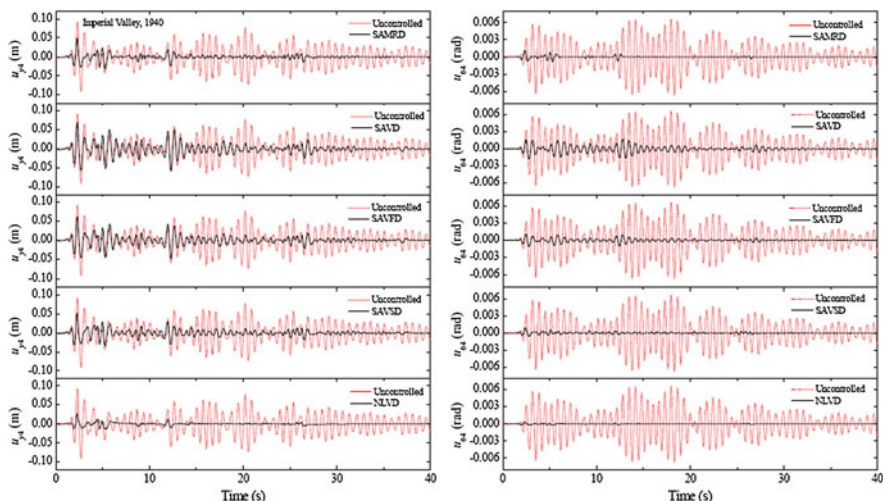


Fig. 10 Time histories of various uncontrolled and controlled top floor lateral-torsional displacements under Imperial Valley earthquake

Figure 10 shows the time histories of uncontrolled and controlled top floor lateral-torsional displacements and accelerations under Imperial Valley (1940) earthquake. It can be seen from the time histories that all the implemented control devices are effective in reducing the lateral-torsional responses.

4 Conclusions

The seismic response of four-story asymmetric building installed with various control devices is investigated. The numerical study is carried out for the building installed with optimally designed dampers. The comparative performance is investigated for dampers namely, semi-active MR dampers (SAMRDs), semi-active variable dampers (SAVDs), semi-active variable friction dampers (SAVFDs), semi-active variable stiffness dampers (SAVSDs) and non-linear viscous dampers (NLVDs). The extensive parametric studies are carried out to derive the optimum parameters for various control devices. The response quantities obtained for the study are: lateral and torsional displacements, lateral and torsional accelerations, base shear as well as base torque. From the trends of the results of the present numerical study, the following conclusions can be drawn:

1. There exists optimum parameters for various control devices such as to have optimum compromise between lateral-torsional displacement and acceleration response reduction as well as the damper capacity.

2. The implemented control devices are quite effective in reducing the lateral-torsional responses and the effectiveness is more in reducing the torsional responses as compared to the lateral responses.
3. The SAVSDs and NLVDs are more effective in controlling the lateral-torsional displacements. However, the control forces are higher for these devices as compared to other considered dampers. Thus, judiciary decision shall be taken while accessing the comparative performance of various dampers.
4. The NLVDs perform better in reducing the lateral accelerations at all floor levels as compared other dampers. On the other hand, SAVFDs are found better as compared to other dampers in reducing the torsional accelerations of all floors and SAVSDs are less effective in reducing the torsional acceleration responses.

References

1. Arturo TC, Jose LEC (2007) Torsional amplifications in asymmetric base-isolated structures. *Eng Struct* 29(2):237–247
2. Jangid RS, Datta TK (1997) Performance of multiple tuned mass dampers for torsionally coupled system. *Earthq Eng Struct Dyn* 26(3):307–317
3. Singh MP, Singh S, Moreschi LM (2002) Tuned mass dampers for response control of torsional buildings. *Earthq Eng Struct Dyn* 31(4):749–769
4. De La Llera JC, Almazan JL (2003) An experimental study of nominally symmetric and asymmetric structures isolated with the FPS. *Earthq Eng Struct Dyn* 32(6):891–918
5. Chi Y, Sain MK, Pham KD, Spencer BF Jr (2000) Structural control paradigms for an asymmetric building. In: Proceedings of the 8th ASCE specialty conference on probabilistic mechanics and structural reliability, PMC2000-152, University of Notre Dame, Notre Dame, Indiana, July 2000
6. Yoshida O, Dyke SJ (2005) Response control of full-scale irregular buildings using magnetorheological dampers. *J Struct Eng (ASCE)* 131(5):734–742
7. Li HN, Li XL (2009) Experiment and analysis of torsional seismic responses for asymmetric structures with semi-active control by MR dampers. *Smart Mater Struct* 18(7):075007
8. Shook DA, Roschke PN, Lin PY, Loh CH (2009) Semi-active control of torsionally-responsive structure. *Eng Struct* 31(1):57–68
9. De La Llera JC, Chopra AK (1995) A simplified model for analysis and design of asymmetric-plan buildings. *Earthq Eng Struct Dyn* 24(4):573–594
10. He WL, Agrawal AK, Mahmoud K (2001) Control of seismically excited cable-stayed bridge using resetting semiactive stiffness dampers. *J Bridge Eng (ASCE)* 6(6):376–384
11. Yang JN, Kim JH, Agrawal AK (2000) Resetting semiactive stiffness damper for seismic response control. *J Struct Eng (ASCE)* 126(12):1427–1433
12. Lu LY (2004) Predictive control of seismic structures with semi-active friction dampers. *Earthq Eng Struct Dyn* 33(5):647–668
13. Ruangrassamee A, Kawashima K (2001) Experimental study on semi-active control of bridges with use of magnetorheological damper. *J Struct Eng* 47A:639–650
14. Spencer BF Jr, Dyke SJ, Sain MK, Carlson JD (1997) Phenomenological model for magnetorheological dampers. *J Eng Mech (ASCE)* 123(3):230–238

Seismic Protection of Soft Storey Buildings Using Energy Dissipation Device

Subhransu Sekhar Swain and Sanjaya K. Patro

Abstract Poor and devastating performance of the soft storey buildings during earthquakes always advocated against the construction of such buildings with soft ground storey. Increasing construction of multistoried buildings with soft ground story however indicates that the practical need of an open space to provide car parking space far overweighs the advice issued by the engineering community. In past, several researchers have addressed the vulnerability of soft storey due to seismic loading. As the conventional local/member level strengthening techniques (steel jacketing, concrete jacketing, steel caging, FRP jacketing, etc.) may not be feasible to enhance the seismic performance of the deficient reinforced concrete structures beyond a certain limit, the improvement of seismic performance of this type of deficient structures by reducing the seismic demand through the supplemental energy dissipation mechanisms has warranted the focus of the researchers. In recent years efforts have been made by researchers to develop the concept of energy dissipation or supplemental damping into a workable technology, and a number of these devices have been installed in structures, throughout the world. The effectiveness of sliding friction damper, in improving the seismic performance of the soft storey reinforced concrete frame building, has been investigated in this paper. The response parameters, such as absolute acceleration, interstorey drift and base shear have been investigated for the example soft storey frame equipped with friction damper. The present study demonstrates the effectiveness of the friction damper in controlling the response behavior of the soft storey frame building due to significant energy dissipation by the friction damper at the soft storey level.

Keywords Seismic protection · Soft storey · Energy dissipation device · Seismic loading · Friction damper

S.S. Swain (✉) · S.K. Patro
School of Civil Engineering, KIIT University, Bhubaneswar, Odisha, India
e-mail: subhransu12930@yahoo.com

S.K. Patro
e-mail: litusanjay@yahoo.com

1 Introduction

Current trends of urbanization is witnessing construction of multi-storeyed buildings with open ground floor reserved for parking or other utility services. These buildings are designed as reinforced concrete frame structures without considering the effect of structural action of the masonry infill walls present in the upper floors. The absence of masonry infill walls at the ground story level of a reinforced concrete building introduces sudden discontinuities in the lateral strength and stiffness along its height, as masonry infill walls in the upper floors make those floors substantially stiffer against lateral load (e.g. earthquake) compared to ground floor rendering these buildings into soft story buildings. As per Indian standard code of practice a soft storey is one in which the lateral stiffness is less than 70 % of that in the storey above or less than 80 % of the average lateral stiffness of the three storeys above [1]. Different national codes differ in considering the role of masonry infill while designing the reinforced concrete frames. A very few codes, e.g. the New Zealand and Russian codes, specifically recommend isolating the masonry infill from the reinforced concrete frames such that the stiffness of masonry infill does not play any role in the overall stiffness of the frame. As a result, masonry walls are not considered in the analysis and design procedure. However, construction of such a building with isolated masonry infill wall requires high construction skill and may not be appropriate for the developing nations, where demand for cheaper housing is very high.

Studies on Bhuj earthquake [2] indicate that about 2350 G+4 and G+10 storey buildings having soft storey at the ground floor suffered structural damage in urban areas within 250 km of the epicenter. A large number of reinforced concrete buildings in urban areas near the epicenter collapsed whereas most of the buildings experienced structural damage resulting in numbers of casualties. Such poor and devastating performance of the soft storey buildings during earthquakes always advocated against the construction of such buildings with soft ground floor. Increasing construction of multistoried buildings with soft ground story however indicates that the practical need of an open space to provide car parking space far outweighs the advice issued by the engineering community. Hence the need for strengthening the buildings with the unavoidable soft storeys has gathered attention of researchers.

Several researchers have addressed the problem of soft storey from different angles in recent past. One approach to address the problem is in (a) increasing the stiffness of the first storey such that the first storey is at least 50 % as stiff as the second storey, i.e., soft first storeys are to be avoided, and (b) providing adequate lateral strength in the first storey. The possible measures to achieve the above are (i) provision of stiffer columns in the first storey, and (ii) provision of a concrete service core in the building. The former is effective only in reducing the lateral drift demand on the first storey columns. However the latter is effective in reducing the drift as well as the strength demands on the first storey columns [3]. Structural behavior of low-to-midrise concrete buildings of various configurations with emphases on

dynamic properties, internal energy, and the magnitude and distribution of seismic load has also been studied [4]. Several idealized models were made to represent different structural configurations including pure frame, frames with fully or partially infilled panels, and frames with a soft story at the bottom level, and comparisons were made on the fundamental periods, base shear, and strain energy absorbed by the bottom level between these structures.

From a seismic point of view, soft story is found to be dangerous, because the lateral response of these buildings is characterized by a large rotation ductility demand concentrated at the extreme sections of the columns of the ground floor, while the superstructure behaves like a quasi-rigid body [5]. Response spectra of elastic SDOF frames with nonlinear infills show that, despite their apparent stiffening effect on the system, infills reduce spectral displacements and forces mainly through their high damping in the first large post-cracking excursion [6].

Indian seismic code requires members of the soft storey to be designed for 2.5 times the seismic storey shears and moments, obtained without considering the effects of masonry infill in any storey. As the local/member level strengthening techniques (e.g. steel jacketing, concrete jacketing, steel caging, FRP jacketing, etc.) may not be economically viable to enhance the seismic performance of the deficient reinforced concrete structures beyond a certain limit, the seismic performance of this type of deficient structures can be improved by reducing the seismic demand through the supplemental energy dissipation mechanisms. In recent years efforts have been made by researchers to develop the concept of energy dissipation or supplemental damping into a workable technology, and a number of these devices, such as friction dampers, viscoelastic dampers, viscous dampers, metallic dampers, aluminium shear links [7] and bracing elements have been installed in structures for passive energy dissipation in the global (i.e., structure-level) modification techniques throughout the world. However, very limited research has been done on strengthening of soft storeyed reinforced concrete framed building using passive energy dissipation devices. The effectiveness of one such passive energy device, i.e. sliding friction damper, in improving the seismic performance of the soft storey reinforced concrete frame building has been investigated in this chapter. The background on the characteristics, working principles and behavior of sliding friction device or friction damper is given below.

2 Background of Sliding Friction Device and Its Modeling

Friction damper dissipates energy through friction forces. These dampers rely on the resistance developed between moving solid interfaces to dissipate a substantial amount of input energy in the form of heat. During severe seismic excitations, the friction damper slips at a predetermined load, providing the desired energy dissipation by friction while at the same time shifting the structural fundamental mode away from the earthquake resonant frequencies.

Pall et al. [8] developed limited slip bolts (LSB) for the seismic control of precast and cast-in-place concrete walls. The LSB incorporates brake lining pads between steel plates. Experimental results have shown [9] that the hysteretic behaviour of the slipping friction joints is reliable and repeatable, and approaches a rectangular hysteretic loop with negligible degradation over many more cycles than encountered in successive earthquakes. Pall and Marsh [9] showed that the friction joints should be tuned in order to optimize seismic performance. However, the study considered only one earthquake record and hence the influence of the seismic excitation on the efficiency of the proposed structural system was not addressed.

Braced frames are an economical solution for the control of lateral deflections due to wind and moderate earthquakes. However, during severe ground motion, these structures do not perform well. Pall [10] has proposed friction devices that can be installed at the intersection of steel bracing. These devices aim at solving the drawbacks encountered in the performance of steel bracing. The device is designed not to slip under normal service loads and moderate earthquakes. During a severe earthquake, the device slips at a predetermined load, before yielding occurs in the other structural elements of the frame. Filiatrault and Cherry [11–13] conducted further experimental and analytical studies on the application of the friction device for cross bracing proposed by Pall. They have developed design spectrum that takes into account the properties of the structure and of the ground motion based on their investigation.

FitzGerald et al. [14] and Grigorian et al. [15] have developed simpler type of friction device referred to as slotted bolted connection (SBC). They have chosen brass as the frictional material and a Belleville washer beneath the nut may be used as a mechanism to counteract wear due to friction, preventing the loss of the clamping force. Martinez-Rueda [16] proposed the geometry of bracing systems that favour the activation of rotational hysteretic devices at discrete locations of the braces. The adopted geometry eliminates the inconvenience due to cross-chevron bracings to the designer.

The investigations by various researchers indicate that the ratio of the initial slip load to the yielding force of corresponding structural storey has significant influence on its ability to reduce seismic response [17]. They noted that in the development of friction dampers, it is important to minimize stick-slip phenomena to avoid introducing high frequency excitation. The effectiveness of these systems mostly relies on the modelling of devices and their implementation in numerical solution process because of its highly nonlinear behaviour. The devices differ in their mechanical complexity and the materials used in the sliding surfaces.

Compatible materials must be employed to maintain a consistent coefficient of friction over the intended life of the device. Most friction devices mounted on bracings utilize sliding interfaces consisting of steel on steel, brass on steel, or graphite impregnated bronze on stainless steel. In general, the systems involving friction has been idealized as Coulomb's friction in frame structures. Numerous efforts have been made by various researchers to arrive at a theoretical explanation of variation of friction forces when relative motion impends in past and at present. The proportionality factor (or friction coefficient) in Coulomb model is considered

to be a constant. The dependence of friction coefficient on slip velocity, normal load, and history of motion, has received considerable attention in the recent past [18–23]. De La Cruz et al. [24] have presented comparison between numerical and experimental dynamic responses of building structures equipped with friction-based supplemental devices for Coulomb's friction model subjected to earthquake loads to access the seismic efficiency of structures. Friction dampers differ in their mechanical property based on the materials used in the sliding surface. These dampers possess good characteristics of structural behavior. For analysis point of view, the idealized Coulomb friction model has been adopted in this study.

2.1 Coulomb Friction Model

This is the most frequently used model, proposed over 200 years ago and is represented in Fig. 1. In this model, the coefficient of friction remains constant and the friction force is expressed as

$$F = \mu F_N \operatorname{sgn}(\dot{u}) \quad (1)$$

where F_N is the normal load on the sliding surface, F is the frictional resistance, which same for both stick and sliding stage, μ is the coefficient of friction, \dot{u} is relative sliding velocity, and $\operatorname{sgn}(\dot{u})$ is the signum function that assumes a value of +1 for positive sliding velocity and -1 for negative sliding velocity. This signum function determines the direction of sliding.

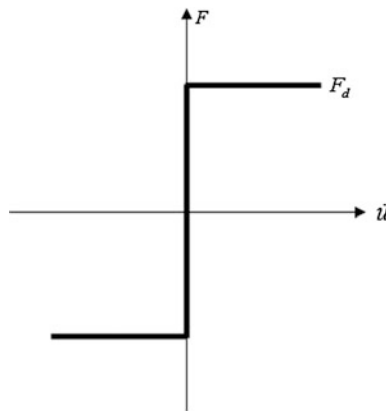


Fig. 1 Friction force variation with sliding velocity for Coulomb friction model

3 Mathematical Formulation

The mathematical formulation of multi-degree-of-freedom (MDOF) frame structure with friction slider mounted on Chevron brace (Fig. 2) has been presented herein [25]. The structure is considered as a two-dimensional (2-D) shear building. Two degrees-of-freedom are present on each floor, corresponding to the horizontal displacement of the storey and the brace with damper relative to the ground, as shown in in Fig. 2a. Simple friction energy-dissipation dampers with slotted bolted connection (SBC) has been considered, where the sliding plate within the vertical plane is connected to the centerline of beam soffit as shown in Fig. 2b. The sliding plate having slotted holes is sandwiched between two clamping plates. The clamping plates are rigidly mounted on the Chevron brace and connected to the sliding plate through prestressing bolts. The slotted holes facilitate the sliding of the sliding plate over the frictional interface at constant controllable prestressing force. In the formulation of the MDOF structure, the structure degrees-of-freedom is denoted with subscript f and the brace with damper degrees-of-freedom with subscript d . Two lumped mass models, one for the free frame structure and another for the brace with damper, are required to idealize the dynamic behavior of the structure.

Through the entire solution process, the equations of motion is split into two subsets with sub-indices st representing the stick phase (non-sliding phase) and sl representing the sliding phase respectively. The motion of any storey of the structure consists of either of two phases: (1) non-sliding or stick phase wherein the stick frictional resistance (F_{st}) between the floor and the damper has not been overcome, and (2) sliding or slip phase in which sliding frictional resistance (F_{sl}) exceeds and the friction force, and acts opposite to the direction of the relative velocity between

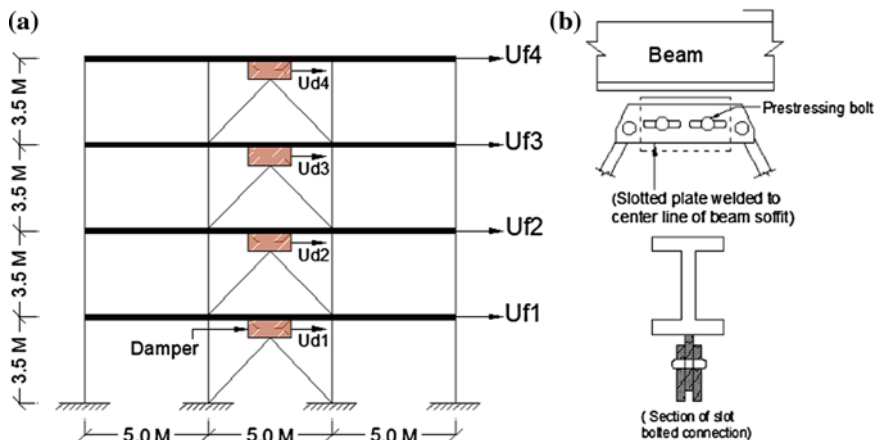


Fig. 2 Schematic diagram of building with supplemental damping systems. **a** Damper added building MDOF system with damper. **b** Details of friction damper

the floor and friction damper. Linear behavior of structure with friction dampers is assumed at both stick and sliding stage of response. The overall response for each storey consists of series of non-sliding and sliding phases. The number of active degree of freedom ranges between N (all the dampers in non-sliding phase) and $2 N$ (all dampers are in sliding phase). If the total number of non-sliding floors are denoted by n_{st} and total number of sliding floors n_{sl} , then the total number of degrees of freedom at any instant of time is equal to $n_{st} + 2 \times n_{sl}$.

The generalized governing equations of motion in matrix form can be given as:

$$\mathbf{M}\ddot{\mathbf{u}}_{st+sl} + \mathbf{C}\dot{\mathbf{u}}_{st+sl} + \mathbf{K}\mathbf{u}_{st+sl} = -\mathbf{M}\mathbf{r}\ddot{u}_g - \mathbf{F}_{f+sl} \tag{2}$$

where \mathbf{M} , \mathbf{C} , and \mathbf{K} are the mass, damping and stiffness matrices, respectively, \mathbf{r} is the force-influence vector, \mathbf{u} represents the displacement degrees of freedom relative to the base of the structure and u_g is the ground displacement. The over dot represent derivatives with respect to time. The friction force vector is represented as \mathbf{F} , and the matrices are given as:

$$\mathbf{M} = \begin{bmatrix} \mathbf{M}_f & 0 \\ 0 & \mathbf{M}_d \end{bmatrix}, \mathbf{C} = \begin{bmatrix} \mathbf{C}_f + \mathbf{C}_{d2} & \mathbf{C}_{d3} \\ (\mathbf{C}_{d3})^T & \mathbf{C}_{d1} \end{bmatrix}, \mathbf{K} = \begin{bmatrix} \mathbf{K}_f + \mathbf{K}_{d2} & \mathbf{K}_{d3} \\ (\mathbf{K}_{d3})^T & \mathbf{K}_{d1} \end{bmatrix}, \tag{3}$$

$$\mathbf{u}_{st+sl} = \begin{Bmatrix} \mathbf{u}_{f,st+sl} \\ \mathbf{u}_{d,st+sl} \end{Bmatrix}, \mathbf{r} = \begin{Bmatrix} \mathbf{r}_f \\ \mathbf{r}_d \end{Bmatrix}, \mathbf{F} = \begin{Bmatrix} +\mathbf{F}_{f+sl} \\ -\mathbf{F}_{f+sl} \end{Bmatrix}, \mathbf{r}_f = \mathbf{1}, \mathbf{r}_d = \mathbf{1}$$

where

$$\mathbf{M}_d = \begin{bmatrix} m_{d1} & 0 & 0 \\ 0 & \ddots & 0 \\ 0 & 0 & m_{dN} \end{bmatrix},$$

$$\mathbf{C}_{d1} = \begin{bmatrix} c_{d1} & 0 & 0 \\ 0 & \ddots & 0 \\ 0 & 0 & c_{dN} \end{bmatrix}, \mathbf{C}_{d2} = \begin{bmatrix} c_{d2} & 0 & 0 \\ 0 & \ddots & c_{dN} \\ 0 & 0 & 0 \end{bmatrix}, \mathbf{C}_{d3} = \begin{bmatrix} 0 & -c_{d2} & 0 \\ 0 & 0 & \ddots & -c_{dN} \\ 0 & 0 & 0 & 0 \end{bmatrix}, \tag{4}$$

$$\mathbf{K}_{d1} = \begin{bmatrix} k_{d1} & 0 & 0 \\ 0 & \ddots & 0 \\ 0 & 0 & k_{dN} \end{bmatrix}, \mathbf{K}_{d2} = \begin{bmatrix} k_{d2} & 0 & 0 \\ 0 & \ddots & k_{dN} \\ 0 & 0 & 0 \end{bmatrix}, \mathbf{K}_{d3} = \begin{bmatrix} 0 & -k_{d2} & 0 \\ 0 & 0 & \ddots & -k_{dN} \\ 0 & 0 & 0 & 0 \end{bmatrix}$$

In the above equations, \mathbf{M}_f , \mathbf{C}_f , and \mathbf{K}_f are the $N \times N$ mass, damping and stiffness matrices of the structure excluding the bracing members, \mathbf{M}_d , \mathbf{C}_{d1} , \mathbf{C}_{d2} , \mathbf{C}_{d3} , \mathbf{K}_{d1} , \mathbf{K}_{d2} and \mathbf{K}_{d3} are $N \times N$ mass, damping and stiffness matrices of the brace with friction damper, respectively. The damping property of the free frame (excluding the brace with damper) structure may be different from the same of the brace with damper. So the complete structure is non-classical damped system. The non-classical damping matrix $[\mathbf{C}]$ for the structure is developed by first evaluating

the classical damping matrix for the free frame, $[C_f]$, based on the damping ratios appropriate for the structure [26].

The structure and the brace DOFs at any storey satisfy the following conditions during the stick phase:

$$\begin{aligned}\ddot{\mathbf{u}}_{f,st} &= \ddot{\mathbf{u}}_{d,st} \\ \dot{\mathbf{u}}_{f,st} &= \dot{\mathbf{u}}_{d,st} \\ \mathbf{u}_{f,st} - \mathbf{u}_{d,st} &= \text{constant}\end{aligned}\quad (5)$$

In Eq. (2), stick or non-sliding phase of a particular floor requires that the corresponding friction force satisfy the equation,

$$|F_{f,st}| < F_{st} \quad (6)$$

where the friction force vector consisting of the friction force in all the dampers is given by:

$$\begin{aligned}\mathbf{F}_{f,st} &= \mathbf{M}_{f,st}\mathbf{u}_{f,st+sl} + \mathbf{M}_{f,st}\mathbf{r}_f\ddot{\mathbf{u}}_g + (\mathbf{C}_{f,st} + \mathbf{C}_{d2,st})\dot{\mathbf{u}}_{f,st+sl} \\ &+ \mathbf{C}_{d3,st}\dot{\mathbf{u}}_{f,st+sl} + (\mathbf{K}_{f,st} + \mathbf{K}_{d2,st})\mathbf{u}_{f,st+sl} + \mathbf{K}_{d3,st}\mathbf{u}_{d,st+sl}\end{aligned}\quad (7)$$

In Eq. (7), $\mathbf{F}_{f,st}$ is the vector of frictional resistance of all friction dampers at stick stage. When the inequality in Eq. (6) is not satisfied for any floor, that floor enters into the sliding phase. Then the corresponding brace degree-of-freedom at the floor level also becomes active in the equations of motion.

The direction of sliding of a brace degree of freedom can be expressed by the following relationship:

$$\text{sgn}(\dot{u}_f - \dot{u}_d) = -\frac{F_{f,st \max}}{|F_{f,st \max}|} \quad (8)$$

The response of the structure always starts in the stick phase. This phase of response continues until the unbalanced frictional resistance of any floor exceeds the maximum frictional resistance of the brace with damper at that floor. It is important to note that the number of storeys experiencing stick and sliding conditions varies continuously through the entire response phase. When the relative sliding velocity ($\dot{u}_f - \dot{u}_d$) at any floor becomes zero or changes its sign during motion, then the brace with damper at that storey may enter the stick phase/or non-sliding phase. It may reverse its direction of sliding or have a momentary halt and continue in the same direction. The status of motion during transition phase can be evaluated from Eq. (6). The equations of motion corresponding to the appropriate stick or sliding are evaluated during the next time-step.

4 Solution Procedure

The complete solution consists of a series of non-sliding and sliding phase at each storey level following one to other which makes the system highly non-linear. These equations can be numerically solved using appropriate non-linear solution techniques. Among the many methods one of the most effective is the step-by-step direct integration method. This problem is solved by modification of step-by-step linear acceleration method. During the solution of such non-linear equations, accuracy of the result is extremely sensitive to the change in phase of motion from non-sliding to sliding and vice versa. This can be taken care by subdividing the chosen time interval whenever change in phase is anticipated. These can possible for single point sliding system. But for multi-point sliding system this will be very complex. In this solution process, the response is evaluated at successive increment Δt (10^{-4} s) of time, usually taken of equal length of time for computational convenience. At the beginning of each interval, the condition of dynamic equilibrium is established.

The equation of motion in matrix form at a particular i th time step can be divided into two equations: (1) equation at the degree-of-freedom on the level of floor, and (2) equation at the degree-of-freedom on the level of damper. The response at $i + 1$ time step can be computed from the known response at the i th time step. It is initially assumed that the sticking-sliding conditions in the damper at instant i are the same at $i + 1$. The complete solution consists of three nested iteration loops with coupling quantities ($\mathbf{u}_{f,i+1}$, $\mathbf{u}_{d,i+1}$, $\dot{\mathbf{u}}_{f,i+1}$, $\dot{\mathbf{u}}_{d,i+1}$ and $\mathbf{F}_{f,i+1}$) and the estimated unbalanced frictional resistance as well as estimated acceleration $\left(\left(\mathbf{F}_{f,st,i+1}\right)_{temp}, \left(\mathbf{u}_{f,i+1}\right)_{temp}, \left(\mathbf{u}_{d,i+1}\right)_{temp}\right)$ at step $i + 1$. Initially at $i + 1$ floor displacement, damper displacement, floor velocity, damper velocity with assumed initial estimated quantities of floor and damper acceleration can be obtained. The new estimated floor acceleration can be obtained from the equation at the degree-of-freedom on the level of floor, which is first iteration loop. In second iteration unbalanced frictional resistance will be found from equation of motion corresponding to degree-of-freedom at the level of damper. Through the third iteration, brace with damper acceleration can be calculated from the equation at the degree-of-freedom on the level of damper. Iterations will continue until the convergence to the tolerance error (10^{-4}) between new and old estimated quantities. Thus, after the fulfillment of the established conditions for the above iteration loops, the sliding-sticking condition Eq. (6) at the each floor level must be checked before going to the next instant.

5 Performance Indices for Structural Response

To characterize the seismic efficiency of friction dampers, three dimensionless performance indices have been considered. All these indices are defined as the ratios between the peak values of a certain response quantity (displacements, acceleration,

base shear, strain energy, input energy, and dissipated energy) of the frame with friction dampers, and the peak value of same responses of the free or braced frame structure. The response quantities in the indices are peak quantities for full time-history of response and among all the floors. Consequently, these indices are dimensionless and always positive with their value range usually between 0 and 1. Values close to zero indicate excellent performance of the friction dampers in reducing the response while values close to 1 or higher indicate ineffectiveness of the friction dampers. In the present formulation by considering stick or sliding frictional resistance (slip load) equals to zero, the response for free frame structure can be obtained. Similarly the response of brace frame structure can be obtained by considering stick or sliding frictional resistance (slip load) as infinite value. The following different indices have been considered for the performance evaluation:

- (i) Drift and acceleration ratio (DAR): This ratio is defined as [27]

$$DARF = \frac{1}{2} \left(\frac{\text{Peak inter-story drift of the structure with friction damper}}{\text{Peak inter-story drift of the free frame structure}} + \frac{\text{Peak absolute acceleration of the structure with friction damper}}{\text{Peak absolute acceleration of the free frame structure}} \right),$$

$$DARB = \frac{1}{2} \left(\frac{\text{Peak inter-story drift of the structure with friction damper}}{\text{Peak inter-story drift of the braced frame structure}} + \frac{\text{Peak absolute acceleration of the structure with friction damper}}{\text{Peak absolute acceleration of the braced frame structure}} \right) \quad (9)$$

It is noted that this parameter gives equal weight age to the deformation and acceleration related responses and represents a combined contribution of the two factors.

- (ii) Base shear ratio (BSR): This ratio is defined as

$$BSRF = \frac{\text{Peak base shear of the structure with friction damper}}{\text{Peak base shear of the freeframe structure}}, \quad (10)$$

$$BSRB = \frac{\text{Peak base shear of the structure with friction damper}}{\text{Peak base shear of the braced frame structure}}$$

The base shear is used as a basic design parameter and low values of BSR indicate corresponding reduction in design earthquake forces.

- (iii) Relative performance index (RPI): This ratio is defined as [13]

$$RPIF = \frac{1}{2} \left(\frac{SEA}{ASEF} + \frac{SEM}{SEMF} \right),$$

$$RPIB = \frac{1}{2} \left(\frac{SEA}{ASEB} + \frac{SEM}{SEMB} \right) \quad (11)$$

where *SEA* = strain energy area, is the area under the strain-energy time history for the system with friction dampers, *ASEF* = strain energy area for free frame structure, *ASEB* = strain energy area for braced frame structure, *SEM* = peak strain energy for the system with friction dampers, *SEMF* = peak strain energy for the free frame structure, and *SEMB* = peak strain energy for the braced frame structure. If *RPIF* or *RPIB* is equal to 1, then the response corresponds to the behavior of a free or braced frame structure.

All the performance indices have been normalized with respect to both the free frame and the braced frame structures. This enables assessment of response reduction and performance enhancement of the structures with friction dampers also including the stiffening influence of the bracing system.

6 Earthquake Ground Motion Records

A total of nine different earthquake ground motions have also been used based on the soil type and their details are given in Table 1. Figure 3 shows the ensemble of the acceleration time-histories of ground motion records. These records are categorized in three groups based on the soil type at the recording stations, and their time-histories are shown in Fig. 4. Three time histories have been selected for each of soft soil (FSR1, FSR2 and FSR3), alluvium or medium soil (FMR1, FMR2 and FMR3) and hard soil or rock (FHR1, FHR2 and FHR3). The evaluations using these ground motions represent the likely response under the likely range of expected ground motion characteristics.

Table 1 Details of nine ground motion records used for numerical simulations

Sl. no	Name of earthquake	Soil type	Designation	Magnitude	PGA (g)	Duration (s)
1	Kobe 1995/01/16	Soft soil	FSR1-(EW)	M6.9	0.345	20
2	Kobe 1995/01/16		FSR2-(NS)	M6.9	0.251	20
3	Imperial Valley 979/10/15		FSR3	M6.5	0.221	20
4	Northridge 1994/01/17	Alluvium soil	FMR1	M6.7	0.364	20
5	Imperial Valley 979/10/15		FMR2	M6.5	0.275	20
6	Chi-Chi Taiwan 1999/09/20		FMR3	M7.6	0.246	70
7	Loma Prieta 1989/10/18	Hard soil/rock	FHR1	M6.9	0.41	20
8	Loma Prieta 1989/10/18		FHR2	M6.9	0.409	20
9	Kocaeli, Turkey 999/08/17		FHR3	M7.4	0.244	20

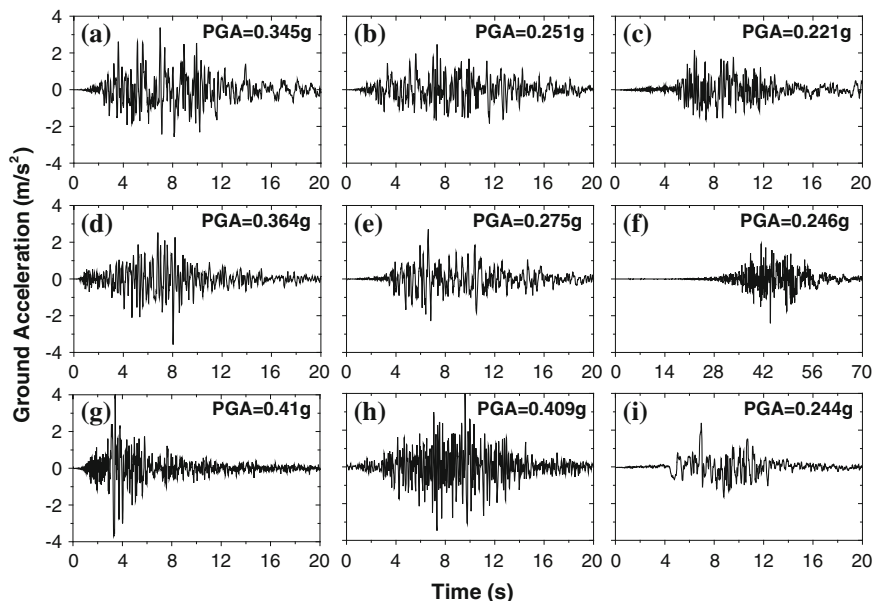


Fig. 3 Ensemble of acceleration time-histories of ground motion records. **a** FSR1, **b** FSR2, **c** FSR3, **d** FMR1, **e** FMR2, **f** FMR3, **g** FHR1, **h** FHR2, **i** FHR3

7 Performance Evaluation of Existing Building

A four-storey reinforced concrete frame building with, (i) Free ground floor (Soft Storey Free Frame), (ii) Braced ground floor (Soft Storey Braced Frame) and (iii) Ground floor with friction damper (Fig. 5) has been considered for evaluating the seismic performance of friction damper based on the above mathematical modeling. Friction joints with slotted holes are positioned in such a manner that sliding plate can be mounted vertically as shown in Fig. 2b. The placement of sliders in vertical plane of the beam ensures that only the prestressing force controls the normal load on the sliding surface. The braces with damping dampers exhibit highly non-linear behavior. The effect of energy dissipation due to viscous damping in the brace members is normally very small compared to the work done by friction sliding. So the viscous damping in the brace has been neglected. The structural damping ratios of the free-frame have been taken as 5 % of its critical damping. The four storey reinforced concrete shear frame building [28] is idealized as four degrees of freedom lumped mass model system. Example building parameters are evaluated as below based on the preliminary data presented in Table 2:

Calculation of Mass of the Floors:

Mass on the Roof: $mf_4 =$

Mass of the infill + Mass of the columns + Mass of the beams in the longitudinal and transverse direction + Mass of the floor + Imposed load of the floor =

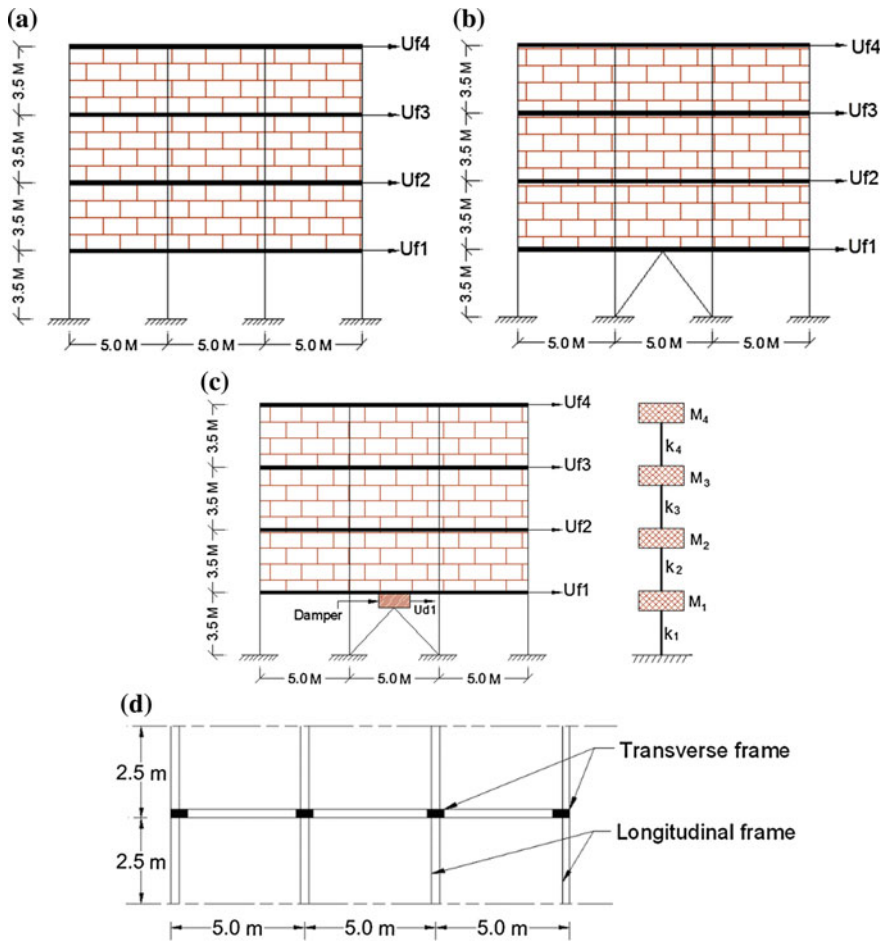


Fig. 4 Schematic diagram of example soft storey frame building with supplemental damping system. **a** Soft storey free frame. **b** Soft storey braced frame. **c** Soft storey frame with friction damper **d** Plan showing columns and beams at floor level for the example soft storey frame building

$$\{ (0.25 \times 15 \times 3.5/2) + (0.15 \times 20 \times 3.5/2) \} \times 20 + 0.25 \times 0.45 \times 3.5/2 \times 4 \times 25 + (0.25 \times 0.40 \times 15 + 0.25 \times 0.35 \times 20) \times 25 + 5 \times 15 \times 0.10 \times 25 + 0 = 524.6875 \text{ kN} = 53485 \text{ kg}$$

Mass of the 2nd and 3rd floor: mf_2 and mf_3

Mass of the infill + Mass of the columns + Mass of the beams in the longitudinal and transverse direction + Mass of the floor + Imposed load of the floor =

$$\{ (0.25 \times 15 \times 3.5) + (0.15 \times 20 \times 3.5) \} \times 20 + 0.25 \times 0.45 \times 3.5 \times 4 \times 25 + (0.25 \times 0.40 \times 15 + 0.25 \times 0.35 \times 20) \times 25 + 5 \times 15 \times 0.10 \times 25 + 5 \times 15 \times 3.5 \times 0.5$$

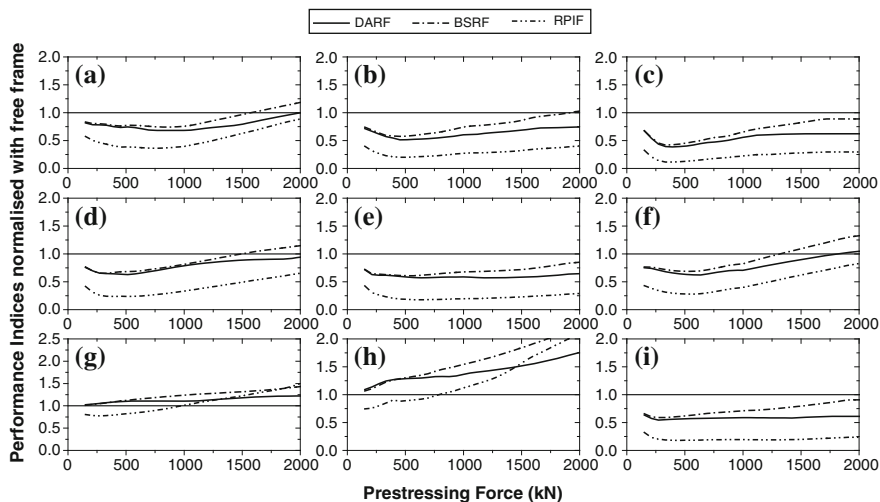


Fig. 5 Performance Indices of example structure with friction damper subjected to different ground motions normalized with free frame response. **a** FSR1, **b** FSR2, **c** FSR3, **d** FMR1, **e** FMR2, **f** FMR3, **g** FHR1, **h** FHR2, **i** FHR3

Table 2 Assumed Preliminary data required for analysis of example soft storey building

Sl. no.	Details	Assumed in current problem
1.	Type of structure	Multi storey rigid jointed plane frame (Special RC moment resisting frame)
2.	Number of stories	Four (G + 3)
3.	Floor height	3.5 m
4.	Infill wall	250 mm thick including plaster in longitudinal and 150 mm in transverse direction
5.	Imposed load	3.5 kN/m ²
6.	Materials	Concrete (M 20) and reinforcement (Fe 415)
7.	Size of columns	250 mm × 450 mm
8.	Size of beams	250 mm × 400 mm in longitudinal and 250 mm × 350 mm in transverse direction
9.	Depth of slab	100 mm
10.	Specific weight of RCC	25 kN/m ³
11.	Specific weight of infill	20 kN/m ³
12.	Elastic modulus of concrete	22,360 N/mm
13.	Elastic modulus of mortar	13,800 N/mm

$$= 911.875 \text{ kN} = 92954 \text{ kg}$$

Mass of the first floor: m_{f1}

$$\begin{aligned} &\text{Mass of the infill} + \text{Mass of the columns} + \text{Mass of the beams in the longitudinal} \\ &\text{and transverse direction} + \text{Mass of the floor} + \text{Imposed load of the floor} = \\ &\{(0.25 \times 15 \times 3.5/2) + (0.15 \times 20 \times 3.5/2)\} \times 20 + 0.25 \times 0.45 \times 3.5/ \\ &2 \times 4 \times 25 + (0.25 \times 0.40 \times 15 + 0.25 \times 0.35 \times 20) \times 25 + 5 \times 15 \times 0.10 \times 25 + \\ &5 \times 15 \times 3.5 \times 0.5 \\ &= 675.625 \text{ KN} = 68871 \text{ kg} \end{aligned}$$

Calculation of stiffness of the Floors:

$$\text{Column stiffness of the storey} = \frac{12EI}{l^3}$$

$$= \frac{12 \times (22360 \times 10^3) \times \left(\frac{0.25 \times 0.45^3}{12}\right)}{3.5^3} = 11880.79 \text{ KN/m}$$

$$\begin{aligned} \text{Total lateral stiffness of each storey} &= 4 \times \text{Column stiffness of the storey} \\ &= 4 \times 11880.79 \\ &= 47523.16 \text{ kN/m} \end{aligned}$$

Stiffness of the infill: (Considering Diagonal strut Model):

$$\text{Width of the strut (W)} = \frac{1}{2} \times \sqrt{\alpha_h^2 + \alpha_t^2}$$

$$\text{where, } \alpha_h = \frac{\pi}{2} \times \left[\frac{E_f I_c h}{2 E_m t \sin 2\theta} \right]^4 \text{ and}$$

$$\alpha_t = \pi \times \left[\frac{E_f I_b l}{E_m t \sin 2\theta} \right]^4$$

$$\theta = \tan^{-1} \frac{h}{l} = \tan^{-1} \frac{3.5}{5} = 35^\circ$$

$$I_c = \frac{1}{12} \times (0.25 \times 0.45^3) = 1.8984 \times 10^{-3} \text{ m}^4$$

$$I_b = \frac{1}{12} \times (0.25 \times 0.40^3) = 1.3333 \times 10^{-3} \text{ m}^4$$

$$\alpha_h = \frac{\pi}{2} \times \left[\frac{22360 \times 1.8984 \times 10^{-3} \times 3.5}{2 \times 13800 \times 0.25 \times \sin 70} \right]^4 = 0.611$$

$$\alpha_l = \pi \times \left[\frac{22360 \times 1.3333 \times 10^{-3} \times 5}{13800 \times 0.25 \times \sin 70} \right]^4 = 1.455$$

$$\text{Width of the strut (W)} = \frac{1}{2} \times \sqrt{0.611^2 + 1.455^2} = 0.789 \text{ m}$$

Cross Sectional area of the diagonal strut = $W \times t = 0.789 \times 0.25 = 0.19725 \text{ m}^2$

Diagonal length of the strut = $ld = \sqrt{h^2 + l^2} = 6.103 \text{ m}$

Hence, stiffness of the infill = $\left[\frac{AE_m}{ld} \right] \cos^2 \theta = 299171.72 \text{ KN/m}$

So, for a frame of 3 bays there are 3 struts participating in one direction, the total stiffness of each storey hence =

$4 \times \text{stiffness of columns} + 3 \times \text{stiffness of infill}$

$= 4 \times 11880.79 + 3 \times 299171.72$

$= 945038.31 \text{ KN/m} = k_2 = k_3 = k_4$

And for frames having no infill, total stiffness of storey

$= 4 \times \text{stiffness of columns} = 47523.15 \text{ KN/m} = k_1$

Mass of bracings and friction dampers: $m_{bdi} = 50.0 \text{ kg}$

Stiffness of bracing members: $k_{di} = 95446.30 \text{ KN/m}$

The presence of two friction interfaces doubles the frictional resistance. The total normal load (F_N) on the sliding surface is equal to $2n_b F_{Ni}$, where n_b is the number of prestressing bolts, and F_{Ni} is the prestressing force in a single bolt. All the bolts in a particular friction damper are assumed to have the same prestressing force. It may be noted that the structure weight does not have any effect to the normal load (F_N). In this investigation, the coefficients of sliding friction (sliding stage, μ_d) and (stick stage, μ_s) are taken as 0.5 as this coefficient resembles with the coefficient values for different surfaces such as (i) Surfaces blasted with short or grit with any loose rust removed, no pitting (ii) Sand blasted surface, after light rusting (iii) Surface blasted with shot or grit and spray metallized with aluminium (thickness $>50 \mu\text{m}$) and (iv) Sand blasted surface [29].

The floor mass, floor stiffness and total weight calculated above for the lumped mass model of the structural frame has been considered to be the same for all three models, i.e. for (i) Soft storey free frame (considering stick or sliding frictional resistance (slip load) equals to zero) (ii) Soft storey braced frame (considering stick or sliding frictional resistance (slip load) as infinite value) and (iii) Soft storey frame with friction damper.

7.1 Performance Indices

In this investigation, various performance indices of the example structure have been evaluated for the ensemble of nine earthquake records. The peak inter-storey drift (IDF/IDB), the peak absolute acceleration of floor mass (AAF/AAB), and the peak

base shear (BSF/BSB), the total strain energy (area of strain energy time history, ASEF/ASEB), the peak strain energy (SEMF/SEMB), and the total input energy (area of input energy time history, IEF/IEB) for the example free frame and braced frame buildings subjected to ensemble of ground motions are presented in Table 3.

The performance of the friction damper has been evaluated for the range of prestressing forces from 5 % ($F_N = 151$ kN) to 72 % ($F_N = 2,147$ kN) of total floor weight (3,024 kN) of structure. Figure 5 represents the performance indices of example structure with friction damper subjected to ensemble of nine earthquake ground motions normalized with free frame response, where as in Fig. 6 evaluation is carried out for response normalized with fixed braced frame response. Optimum structural performance can be obtained for a prestressing force of 375–625 kN, if the RPI or BSR is to be minimized, 500–1,000 kN, if the DAR is to be minimized for the example structure. The investigation implies that the friction dampers are most effective to reduce absolute acceleration as compared to fixed braced frame response, whereas the dampers are more effective to reduce inter-storey drift as compared to

Table 3 Peak responses of 4 storey example structure subjected to ensemble of ground motions

<i>Free frame response</i>						
Ground motion	IDF (m)	AAF (m/s ²)	BSF (kN)	ASEF (kNms)	SEMF (kNm)	IEF (kNms)
FSR1	0.0346	5.5005	1653.253	33.07815	29.73667	1096.375
FSR2	0.0311	4.9885	1487.812	36.36090	24.04857	970.958
FSR3	0.0303	4.7880	1448.111	23.82963	22.84704	644.896
FMR1	0.0338	5.4084	1614.313	44.53183	28.29310	1330.899
FMR2	0.0415	6.6238	1984.360	71.21273	42.82050	1945.814
FMR3	0.0275	4.3911	1314.519	45.49677	18.77373	2902.345
FHR1	0.0319	5.0909	1527.376	13.83174	25.26704	630.196
FHR2	0.0184	3.0375	881.1019	13.75743	8.395696	872.522
FHR3	0.0333	5.3288	1590.924	50.50276	27.50161	1332.844
<i>Braced frame response</i>						
Ground motion	IDB (m)	AAB (m/s ²)	BSB (kN)	ASEB (kNms)	SEMB (kNm)	IEB (kNms)
FSR1	0.0241	12.0277	3444.324	70.967	47.283	2168.650
FSR2	0.0113	5.6487	1610.352	15.459	10.341	388.347
FSR3	0.0090	4.5487	1286.208	7.251	6.603	225.645
FMR1	0.0255	12.8796	3647.251	90.040	53.075	2881.789
FMR2	0.0135	6.5394	1931.123	24.979	14.823	609.089
FMR3	0.0162	8.0352	2309.735	60.513	21.251	3639.230
FHR1	0.0255	13.1599	3643.121	31.959	53.034	1105.406
FHR2	0.0271	13.5753	3869.354	81.177	59.706	4062.577
FHR3	0.0101	4.9056	1442.706	8.759	8.278	285.075

IDF/IDB Peak Inter-storey drift, *AAF/AAB* Peak absolute acceleration of floor mass, *BSF/BSB* Peak Base shear, *ASEF/ASEB* Total strain energy, *SEMF/SEMB* Peak strain energy, *IEF/IEB* Total input energy

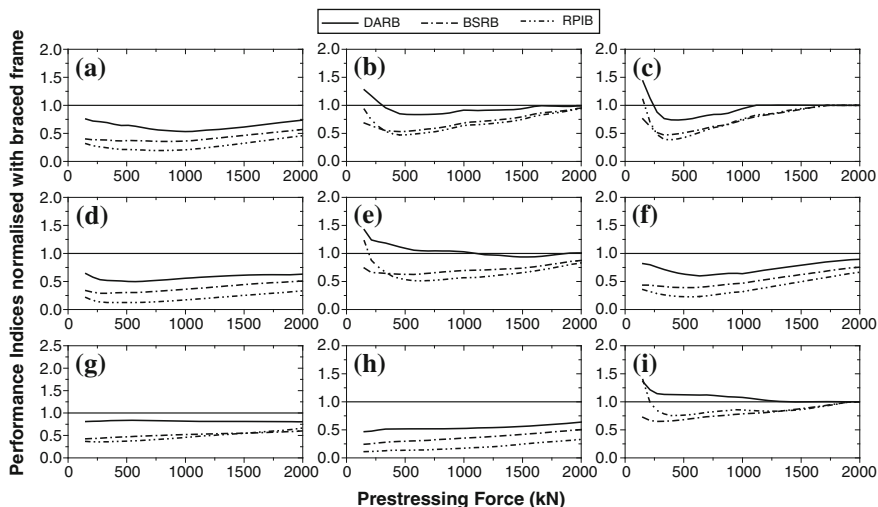


Fig. 6 Performance indices of example structure with friction damper subjected to different ground motions normalized with braced frame response. **a** FSR1, **b** FSR2, **c** FSR3, **d** FMR1, **e** FMR2, **f** FMR3, **g** FHR1, **h** FHR2, **i** FHR3

free frame response in most ground motions. The reduction of inter-storey drift and acceleration of the structure with friction dampers when compared to the braced frame and free frame structures for other ground motions is a demonstration of the effectiveness of these dampers in dissipating energy and thereby reducing the response.

The peak responses of 4 storey example structure subjected to ensemble of nine ground motions i.e. Peak Inter-storey drift, Peak Absolute acceleration of floor mass, Peak Base shear, Total strain energy, Peak Strain energy, Total input energy for both free frame and braced frame response are tabulated as shown in Table 3. The optimal values of the performance indices, normalized with free or braced frame, and the corresponding prestressing force are presented in Tables 4 and 5. It can be seen that different performance indices are minimized for different prestressing forces. It is also seen in Tables 4 and 5 that the optimum prestressing force for indices involving absolute floor accelerations differs significantly from those involving floor displacements and inter-storey drifts. The optimum structural performance of the example structure can be obtained for a prestressing force of 300–550 kN if the AAR, DAR, BSR or the RPI are to be minimized in majority of ground motions in Soft and Medium soil. The performance indices can be minimized for hard soil for a prestressing force of 150–300 kN. It can also be observed that the optimal prestressing force range corresponding to DAR is close to the optimal prestressing force ranges corresponding to BSR. Determination of the prestressing force, however, resulting in optimal reduction of all responses is not possible. The optimal performance indices given in Tables 4 and 5 are compared with the performance indices obtained for prestressing force of 500 kN as shown in

Table 4 Optimal values of Performance indices of 4-storey example structure with friction damper through bracing normalized with peak response of free frame structure

Index	Ground motion									
	FSR1	FSR2	FSR3	FMR1	FMR2	FMR3	FHR1	FHR2	FHR3	
DARF	Prestressing force (kN)	756.018	453.611	393.129	514.092	1179.387	635.055	151.204	151.2035	272.166
	Response index	0.6796	0.5144	0.3856	0.6307	0.5713	0.6218	1.0241	1.0929	0.5445
BSRF	Prestressing force (kN)	876.980	453.611	332.648	332.648	574.573	514.092	151.204	151.2035	272.166
	Response index	0.7438	0.5770	0.4183	0.6526	0.6079	0.6878	1.0120	1.0666	0.5895
RPIF	Prestressing force (kN)	756.018	453.611	393.129	514.092	635.055	514.092	272.166	151.2035	453.611
	Response index	0.3620	0.2019	0.1148	0.2391	0.1782	0.2790	0.7767	0.7448	0.1808

Table 5 Optimal values of Performance indices of 4-storey example structure with friction damper through bracing normalized with peak response of braced frame structure

Index	Ground motion									
	FSR1	FSR2	FSR3	FMR1	FMR2	FMR3	FHR1	FHR2	FHR3	
DARB	Prestressing force (kN)	997.943	574.573	453.611	574.573	1542.276	635.055	1965.645	151.2035	1421.313
	Response index	0.5325	0.8355	0.7384	0.4981	0.9366	0.6004	0.8057	0.4668	0.9963
BSRB	Prestressing force (kN)	876.980	453.611	332.648	332.648	574.573	514.092	151.204	151.2035	272.166
	Response index	0.3570	0.5331	0.4710	0.2889	0.6246	0.3914	0.4243	0.2429	0.6500
RPB	Prestressing force (kN)	756.018	453.611	393.129	514.092	635.055	574.573	272.166	151.2035	393.129
	Response index	0.1936	0.4723	0.3858	0.1239	0.5123	0.2271	0.3564	0.1122	0.7556

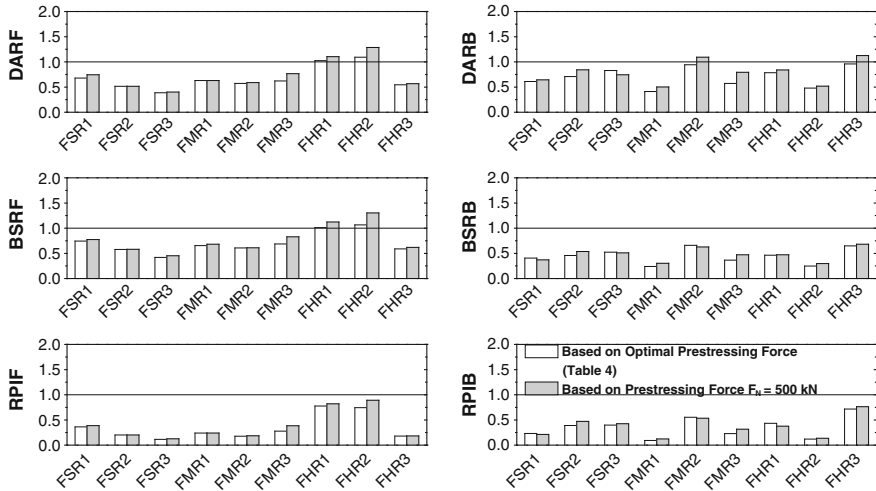


Fig. 7 Optimal performance indices of example structure with friction damper subjected to different ground motions normalized with free frame and braced frame structure response

Fig. 7. In these figures it can be observed that other than very few ground motions the use of prestressing force of 500 kN gives similar reduction in response with reference to the optimal prestressing force. It can also be seen that significant reduction in response is observed for nearly all ground motions thereby demonstrating the robustness of the friction dampers for aseismic design. This indicates that the use of friction dampers with prestressing force of 500 kN will provide good performance for a wide range of expected ground motions.

7.2 Maximum Responses

The maximum inter-storey drift and the maximum absolute acceleration for the example structure is evaluated at each storey level subjected to the ensemble of nine (9) different ground motions and shown in Figs. 8 and 9. The maximum inter-storey drifts and absolute accelerations are evaluated for soft-storey free frame structure, soft-storey braced frame structure, and soft-storey frame with friction damper. The optimal slip-load corresponding to each performance index of the example structure subjected to different ground motions discussed earlier, indicates that the performance indices are optimized at a nearly optimal prestressing force, F_N , equal to 500 kN. Hence the response behavior of the example structure has been investigated for prestressing force, F_N , equal to 500 kN. Since the prime objective of the frame buildings with friction-based energy dissipation system is to reduce the peak responses, the investigations of maximum responses enable one to evaluate the effectiveness of the friction damper.

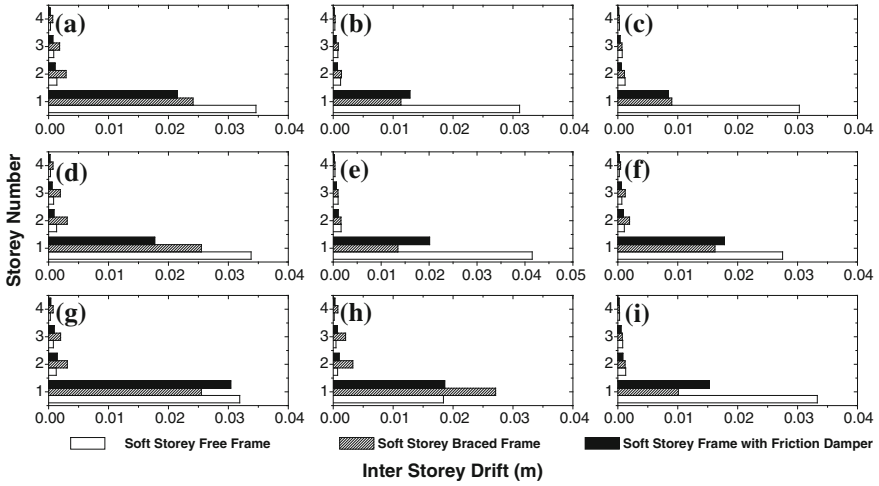


Fig. 8 Maximum inter-storey drift response of example structure for prestressing force of 500 kN and different ground motions. **a** FSR1, **b** FSR2, **c** FSR3, **d** FMR1, **e** FMR2, **f** FMR3, **g** FHR1, **h** FHR2, **i** FHR3

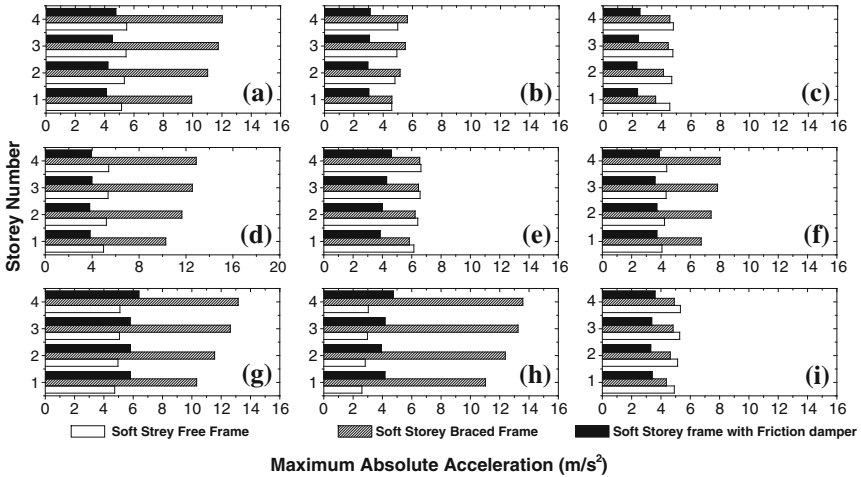


Fig. 9 Maximum absolute acceleration response of example structure for prestressing force of 500 kN and different ground motions. **a** FSR1, **b** FSR2, **c** FSR3, **d** FMR1, **e** FMR2, **f** FMR3, **g** FHR1, **h** FHR2, **i** FHR3

Figure 8 shows that the inter-storey drift of structure with friction damper can be reduced by 35–70 % of the peak inter-storey drift of free frame structure at first floor level, i.e. the soft storey level and 15–50 % at other floors of the structure. Similarly inter-storey drift of structure with friction damper can be reduced by 6–30 % of the peak inter-storey drift of braced frame structure at first floor level, and 30–70 % at other floors of the structure. It can also be observed that the friction damper do not reduce the maximum inter-storey drift at some floor levels for FHR1 and FHR2 ground motions when compared to free frame structure and FSR2, FMR2, FMR3, FHR1 and FHR3 ground motions when compared to braced frame structure. This result is expected since the use of friction damper results in smaller bracing stiffness than that of the braced frame resulting in larger drifts. The reduction of inter-storey drift of the structure with friction damper when compared to the braced frame structures for other ground motions is a demonstration of the effectiveness of these dampers in dissipating energy and thereby reducing the response.

The maximum absolute acceleration of the structure as observed in Fig. 9 with friction damper can be reduced by over 10–50 % of the peak absolute acceleration of free frame structure and 30–70 % with reference to braced frame structure response. It is also seen that the maximum absolute acceleration has been reduced at every floor level. It can also be observed that the friction damper do not reduce the maximum absolute acceleration at some floor levels for FHR1 and FHR2 ground motions when compared to free frame structure. However the reduction in the absolute acceleration response of structure with friction damper in each storey in comparison to the free frame and brace frame indicates the effectiveness of the damper in filtering the absolute acceleration of the system thus by reducing the energy into the system.

7.3 Time-History Responses

The typical time-history responses i.e. absolute acceleration, inter-storey drift and base shear time history of example structure subjected to ensemble of nine ground motions are shown in Figs. 10, 11 and 12. Each time-history response is evaluated for braced frame structure, free frame structure and structure with friction damper with prestressing force of 500 kN.

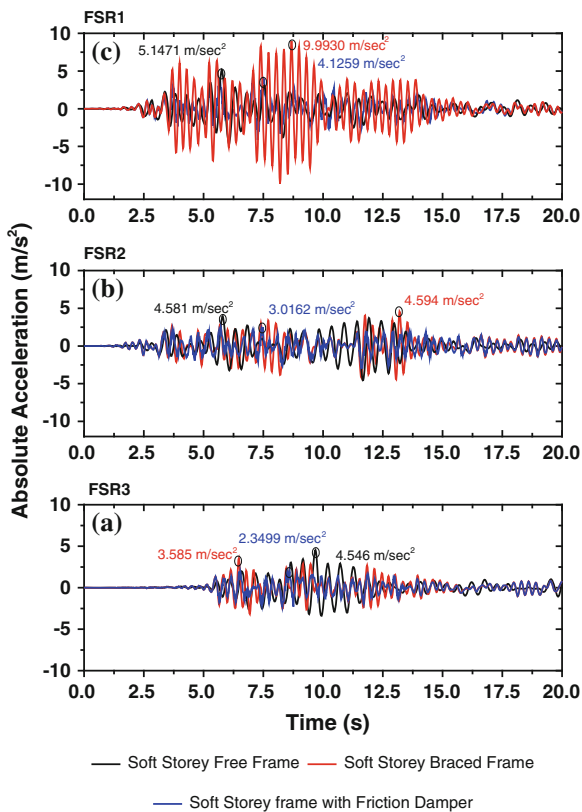


Fig. 10 Absolute acceleration at soft storey level of example structure subjected to FSR1, FSR2 and FSR3 ground motions for prestressing force = 500 kN

The higher acceleration in the response may significantly affect the performance of equipment and also other secondary systems mounted on the structure. It will also affect the behavior of non-structural members of structures. Figure 10 shows the effectiveness of the friction damper in reducing the absolute acceleration of the system when compared to free frame and braced frame model. It shows 20–50 %

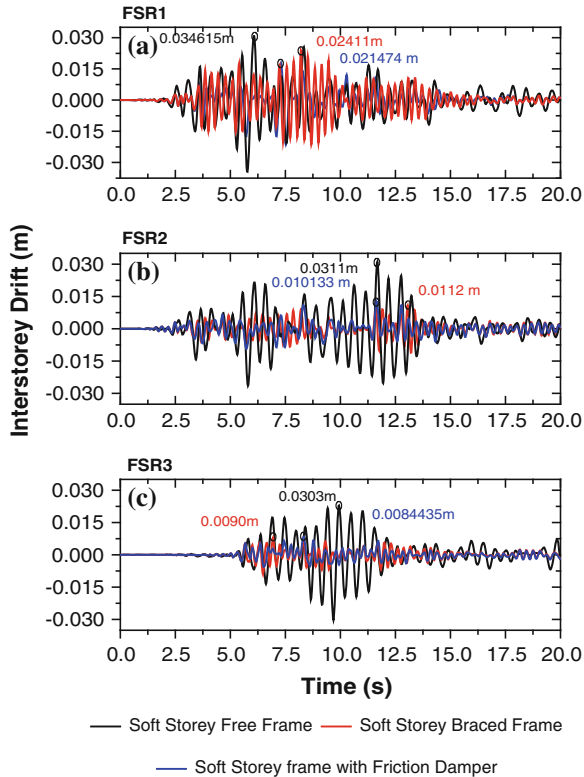


Fig. 11 Inter-storey drift at soft storey level of example structure subjected to FSR1, FSR2 and FSR3 ground motions for prestressing force = 500 KN

reduction in absolute acceleration in the frame with friction damper in comparison to braced frame and free frame. Response reduction is also observed in the response parameters such as inter-storey drift (Fig. 11) and base shear (Fig. 12) in the example structure. It is observed the all the response parameters have been reduced, by 40–50 % in the frame with friction damper when compared to braced frame and free frame, at all floor levels.

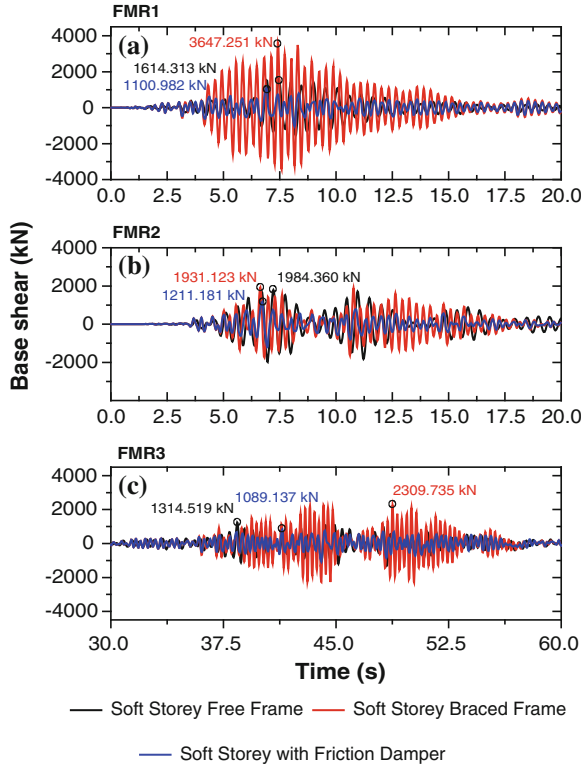


Fig. 12 Base Shear of example structure subjected to FMR1, FMR2 and FMR3 ground motions for prestressing force = 500 KN

8 Conclusions

The effectiveness of friction-based energy dissipation systems in controlling the response parameters when compared to free frame and braced frame structure has been investigated in this paper for the example 4-storey frame structure. Coulomb friction model is adopted for the mathematical modeling. Based on the investigations presented in this paper, the following main conclusions can be drawn:

1. The response parameters of soft storey free frame as obtained from the time history analysis indicates the reinforced concrete frames with soft storey have very poor seismic performance due to their inadequate stiffness, drift capacity & energy dissipation potential.
2. Adding stiffness to the frames by mean of bracings doesn't always solve the purpose of seismic strengthening of soft stories. As by introduction of bracings in the frames the drift response parameters are controlled, whereas the absolute acceleration and responses observed to be increased, affecting the frames adversely.

However, it is observed that that strain energy is reduced by introduction of bracings in the soft story frame, when compared to soft story free frame.

3. Supplemental sliding friction damper as passive energy dissipation device showed excellent seismic behavior, in terms of enhanced stiffness hence strength, and controlled inter-storey drift (reduced by 35–70 % that of free frame response and 6–30 % that of braced frame response), absolute acceleration (reduced by 10–50 % that of free frame response and 30–70 % that of braced frame response) and base shear (reduced by 40–50 %). The damage level of the frame has been controlled as the supplemental energy dissipation due to frictional work done (nearly 70 %) by the friction damper reduced the lateral load demand. It is also observed that that strain energy is reduced due to introduction of friction damper in the soft story frame, when compared to soft story free frame and braced frame.
4. Though the optimum prestressing force for the friction damper is highly related to characteristics of ground motion and its required performance index, the optimum prestressing force of 500 kN for the example structure proves to be effective in controlling all the response parameters.
5. Friction based energy dissipation systems with prestressing force of 500 kN are proved to be most effective for soft soil and the effectiveness reduces with change of soil from soft soil to medium soil and from medium soil to hard soil.

References

1. IS:1893 (2002) Indian standard criteria for earthquake resistant design of structures part I general provisions of buildings (Fifth Revision). Bureau of Indian Standards, New Delhi
2. Shaw R, Sinha R, Goyal A, Saita J, Arai H, Choudhury M, Jaiswal K, Pribadi K (2001) The Bhuj earthquake of January 2001, Indian Institute of Technology Bombay and Earthquake Disaster Mitigation Research Center, Japan Joint Publication, pp 90–97
3. Arlekar JN, Jain SK, Murty CVR (1997) Proceedings of the CBRI Golden jubilee conference on natural hazards in Urban Habitat, New Delhi
4. Huang S (2005) Seismic behaviors of reinforced concrete structures with soft story. In: Proceedings of the 3rd international conference on structural stability and dynamics, Kissimmee, Florida, 19–22 June 2005
5. Mezzi M (2004) Architectural and structural configurations of buildings with innovative aseismic systems. In: Proceedings of the 13th World conference on earthquake engineering, (Paper No. 1318), Vancouver, B.C., Canada
6. Fardis MN, Panagiotakos TB (1997) Seismic design and response of bare and masonry-infilled reinforced concrete buildings, part II: infilled structures. *J Earthq Eng* 1(3):475–503
7. Sahoo DR, Rai DC (2013) Design and evaluation of seismic strengthening techniques for reinforced concrete frames with soft ground storey. *Eng Struct* 56:1933–1944
8. Pall AS, Marsh C, Fazio P (1980) Friction joints for seismic control of large panel structures. *J Prestress Concr Instit* 25(6):38–61
9. Pall AS, Marsh C (1981) Friction damped concrete shear walls. *J Am Concr Inst* 78:187–193
10. Pall AS (1983) Friction devices for aseismic design of buildings. In: Proceedings of the 4th Canadian conference on earthquake engineering, pp 475–484
11. Filiatrault A, Cherry S (1987) Performance evaluation of friction damped braced steel frames under simulated earthquake loads. *Earthq Spectra* 3(1):57–78

12. Filiatrault A, Cherry S (1988) Comparative performance of friction-damped systems and base isolation systems for earthquake retrofit and aseismic design. *Earthq Eng Struct Dyn* 16 (3):389–416
13. Filiatrault A, Cherry S (1990) Seismic design spectra for friction-damped structures. *J Struct Eng* 116(5):1334–1355
14. FitzGerald TF, Anagnos T, Goodson M, Zsutty T (1989) Slotted bolted connection in aseismic design for concentrically braced connections. *Earthq Spectra* 5(2):383–391
15. Grigorian CE, Yang TS, Popov EP (1993) Slotted bolted connection energy dissipators. *Earthq Spectra* 9(3):491–504
16. Martinez-Rueda JK (2002) On the evolution of energy dissipation devices for seismic design. *Earthq Spectra* 18(2):309–346
17. Housner GW, Bergman LA, Caughey TK, Chassiakos AG, Claus RO, Masri SF, Skelton RE, Soong TT, Spencer BF, Yao JTP (1997) Structural control: past, present, and future. *J Eng Mech* 123(9):897–971
18. Ibrahim RA (1994) Friction-induced vibration, chatter, squeal, and chaos; Part 1: Mechanics of contact and friction, part 2: dynamics and modeling. *Appl Mech Rev* 47(7):209–274
19. Armstrong-Helouvry B (1991) Control of machines with friction. Kluwer Academic Publishers, Boston
20. Armstrong-Helouvry B, Dupont P, Canudas de Wit C (1994) A survey of models, analysis tools and compensation methods for the control of machines with friction. *Automatica* 30 (7):1083–1138
21. Oden JT, Martins JAC (1985) Models and computational methods for dynamic friction phenomena. *Comput Methods Appl Mech Eng* 52:527–634
22. Feeny B, Guran A, Hinrichs N, Popp K (1998) A historical review on dry friction and stick-slip phenomena. *Appl Mech Rev* 51(5):321–341
23. Berger EJ (2002) Friction modeling for dynamic system simulation. *Appl Mech Rev* 55 (6):535–577
24. De La Cruz S, Lopez-Almansa F, Taylor C (2004) Shaking table tests of steel frames equipped with friction dissipators and subjected to earthquake loads. In: 13th World conference on earthquake engineering, Vancouver, B. C., Canada, Paper no. 1525
25. Patro SK (2006) Vibration control of frame buildings using energy dissipation devices. Ph.D thesis, Indian Institute of Technology Bombay, Mumbai
26. Chopra AK (2001) Dynamics of structures: theory and applications to earthquake engineering, 2nd edn. Prentice Hall, New Delhi, pp 731–755
27. Moreschi LM (2000) Seismic design of energy dissipation systems for optimal structural performance. Ph.D. thesis, Virginia Polytechnic Institute and State University, Blacksburg, Virginia
28. Agarwal P, Shrikhande M (2006) Earthquake resistant design of structures. Prentice Hall India, New Delhi
29. IS:800 (2007) Indian standard general construction in steel—code of practice (Third Revision). Bureau of Indian Standards, New Delhi

Significance of Elastomeric Bearing on Seismic Response Reduction in Bridges

E.T. Abey, T.P. Somasundaran and A.S. Sajith

Abstract The seismic design of conventionally framed bridges relies on the dissipation of earthquake-induced energy through inelastic response in selected components of the structural frame. Such response is associated with structural damage that produces direct loss, indirect loss and perhaps casualties. For bridge construction, the typical design goals associated with the use of seismic isolation are, (a) reduction of forces (accelerations) in the superstructure and substructure, and (b) force redistribution between the piers and the abutments. For minimising the effect of increased displacement response in such bridges, damping is typically introduced in the isolator. The paper discusses the importance of elastomeric bearings in the design of seismic resistant bridges with an overview of the present IRC code recommendations. The response modifications of such bridges are also included to strengthen the theoretical implications through parametric studies on the same.

Keywords Bridges · Elastomeric bearings · Energy dissipation · Performance evaluation · Seismic design · Seismic response

1 Introduction

Bridges are the most vulnerable components of the transportation system and a vital component, the disruption of which would pose a threat to emergency response and recovery as well as serious economic losses after a strong earthquake. Increased knowledge on seismic engineering with the occurrences of the past major earthquakes like Northridge, California (1994), Kobe, Japan (1995), Bhuj, India (2001) has led to serious discussions in the international community regarding the need for seismic resistant design in structures. Major portion of the research were confined to buildings and there retrofit, with a slower but steady improvement in bridges also.

E.T. Abey (✉) · T.P. Somasundaran · A.S. Sajith
Civil Engineering Department, NIT, Calicut, India

These researches pointed out the main issues relating to the widely accepted force-based design methodology and emphasised the need for using a displacement-based design approach, which brings out the now highly discussed performance-based methodology.

Among the various methods for reducing the seismic impact on bridge decks, isolation bearings were greatly accepted. This helps in decoupling the superstructure from the substructure and hence from the damaging effects of ground accelerations. One of the goals of the seismic isolation is to shift the fundamental frequency of a structure away from the dominant frequencies of earthquake ground motion. The other purpose of an isolation system is to provide an additional means of energy dissipation, thereby reducing the transmitted acceleration into the superstructure. A variety of isolation devices including elastomeric bearings (with and without lead core), frictional/sliding bearings and roller bearings have been developed and used practically for the seismic design of bridges during the last few decades in many countries.

The present study discusses the implications of elastomeric bearings in seismic resistant design of precast prestressed box-girder bridges through code review and analytical evaluation of bridge models with and without bearings for varied parameters. Nonlinear static or pushover analysis using SAP2000 NL is used for assessing the performance of the bridge models considered.

2 Seismic Isolation

For the last few decades, various retrofit techniques are being used, one of which is the use of seismic isolation. It has received increased attention from the designers for seismic hazard mitigation. The isolation system does not absorb the earthquake energy, but rather deflects it through the dynamics of the system [1]. In this manner, a building is isolated from its foundations, and the superstructure of a bridge is isolated from its piers.

The first dynamic mode of the isolated structure involves deformation only in the isolation system and the structure above is assumed to behave as rigid. The higher modes that produce deformation in the structure are orthogonal to the first mode and consequently to the ground motion and do not participate in the motion. And, the energy in the ground motion related to these frequencies cannot be transmitted into the structure. Hence, the lengthening of the first-mode period results into the reduction of the earthquake-induced forces in the structure. But, this technique is more significant for short period structures than long period ones.

The objective of isolating a bridge structure differs from that of a building. A bridge is typically isolated immediately below the superstructure. This helps in reducing the shear forces transmitted from the superstructure to the piers by shifting the natural period of the bridge away from the frequency range where the energy content of earthquakes is high. As a result, the superstructure motion is decoupled from the piers motion during the earthquake, thus, producing an effect of the

reduction of inertia forces. At the same time, the seismic energy demand of the bridge is also reduced as a consequence of the energy dissipation concentrated in isolators, which are suitably designed for this purpose. The articulation provided in the bridge will additionally help it to resist significant service lateral loads, displacements from wind and traffic loads and from creep, shrinkage and thermal movements.

The suitability of a particular arrangement and type of isolation system will depend on many factors including the span, number of continuous spans, seismicity of the region, frequencies of vibration of the relatively severe components of the earthquake, maintenance and replacement facilities. Various parameters to be considered in the choice of an isolation system, apart from its general ability of shifting the vibration period and adding damping to the structure are: (i) deformability under frequent quasi-static load (i.e. initial stiffness), (ii) yielding force and displacement, (iii) capacity of self-centering after deformation, and (iv) vertical stiffness.

3 Review of Elastomeric Bearings

Elastomeric bearings are formed of horizontal layers of natural or synthetic rubber in thin layers bonded between steel plates. The steel plates prevent the rubber layers from bulging and thus increasing the ability of bearing to support higher vertical loads with only small deformations. Under a lateral load the bearing is flexible. Plain elastomeric bearings provide flexibility but do not have significant damping and will move under service loads.

The laminated rubber bearing (LRB) is the most commonly used base isolation system. The basic components of LRB system are steel and rubber plates built in alternate layers. Generally, the LRB system exhibits high-damping capacity, horizontal flexibility and high vertical stiffness. The damping constant of the system varies considerably with the strain level of the bearing (generally of the order of 10 %) [1]. These devices can be manufactured easily and are quite resistant to environmental effects.

The second category of elastomeric bearings is lead-rubber bearings [2]. This system provides the combined features of vertical load support, horizontal flexibility, restoring force and damping in a single unit. These bearings are similar to the laminated rubber bearing but a central lead core is used to provide an additional means of energy dissipation. The energy absorbing capacity by the lead core reduces the lateral displacements of the isolator.

Important specifications which can be referred to for elastomeric bearings are listed below:

- i. UIC 772-2R 1989
- ii. BS:5400 Part 9.1
- iii. IRC 83 Part II
- iv. AASHTO specifications
- v. IS:3400 Part I to XXIV.

3.1 Behaviour of Elastomeric Bearings

In order to carry out successful design and installation of elastomeric bearings, it is necessary to understand the behaviour of elastomeric bearings against various imposed loads. The elastomer being practically incompressible, the total volume of the pad in loaded and unloaded conditions remains unchanged. If the elastomer is bonded between two layers, the lateral expansion is prevented at the interfaces and bulging is controlled. The compressive stiffness of the bearing, therefore, depends upon the ratio of loaded area to the area of the bearing free to bulge. This is essentially quantified by Shape Factor 'S' which is a dimensionless parameter defined as,

$$S = \frac{\text{Plan area loaded in compression}}{\text{Perimeter area free to bulge}}$$

Greater compressive stiffness is, therefore, obtained by dividing elastomer into many layers by introducing very thin, usually 1–3 mm, steel reinforcement plates between the elastomer layers and bonding the plates firmly with the elastomer to prevent any relative movement. This has the effect of decreasing the area free to bulge without any change in the loaded area. Hence, higher the shape factor, stiffer is the bearing under compressive load. Since the elastomer expands laterally, shear stresses are set up in the elastomer by the bond forces. The steel plate, in turn, is subjected to pure tensile stresses for which its thickness is to be designed.

The elastomeric bearing provides horizontal translation by shear strains and rotation by differential compression. Elastomeric bearings can accommodate horizontal movements to an extent of 125 mm, while, it is claimed that each 13 mm thickness of the pad could accommodate one degree of rotation [3].

3.2 Design Considerations

Shape factor, S should be maintained in between 6 and 12 for proper vertical stiffness [4]. For preventing slip of the bearing, minimum vertical pressure which is the ratio of dead load and plan area of the bearing should be kept above 2 MPa or else provide 'Anti Creep Devise'. The maximum vertical pressure on bearing which is the ratio of total vertical load including impact and plan area of bearing, should be maintained well below 10 MPa. Total shear in elastomer due to compression, horizontal load and rotation should be limited to $5G$ or 5 MPa, considering the shear modulus $G = 1\text{MPa}$.

3.3 Bearing Properties for Modelling

The properties of elastomeric bearings used at both the abutments and bents are kept the same. The bearing stiffness values used in the analysis are as follows [5],

Translation vertical, $U_1 = 2,055,499$ kN/m
Translation normal to layout line, $U_2 = 9,899$ kN/m
Translation along layout line, $U_3 = 9,899$ kN/m
Rotation about vertical, $R_1 = 61,869$ kN/m
Rotation about normal to layout line, $R_2 = 109,627$ kN/m
Rotation along layout line, $R_3 = 83,933$ kN/m.

4 Effect of Elastomeric Bearing in Seismic Response Reduction

4.1 Preamble

PSC box-girder bridges are becoming the most commonly used type of structural form for Highway and Railway bridges in India. The improved stiffness and serviceability, increased shear capacity and improved resilience to dynamic and fatigue loading led to a widespread interest in prestressed technologies for the last few decades. Box-girder bridges became common due to its possibility for longer spans i.e., beyond 40 m, where I-girders are not promising. The increased moment of inertia per unit weight of this structural form substantially reduced the self weight of the superstructure deck and hence proves to perform well in seismic action. The better torsional resistance particularly for curved spans make it a better option for structural engineers. All the advantages of precast construction along with the suitability of segmental construction further improve its place as a widely regarded structural form. Difficulty of maintenance and expensiveness of fabrication are the two main limitations highlighted for this structural form.

Various parameters affecting the seismic design and behaviour of PSC box-girder bridges are analytically investigated with reference to the bearing stiffness values provided at the bents and or abutments for improving the overall structural flexibility. The bearing pad-bridge girder interface defines support boundary conditions and may affect the seismic performance of the bridge. SAP2000 NL is used to evaluate the performance of the bridge models considered through non-linear static or pushover analysis. The parameters considered in the present study include span length, deck support condition and slenderness ratio of piers.

4.2 Model Details and Description of Parameters

Twin celled, three span PSC box-girder bridges with rectangular piers are taken for the present study. Dimension and geometry detail of the bridge deck is shown in Fig. 1. M50 concrete and Fe 415 steel for nominal reinforcement is used for all the

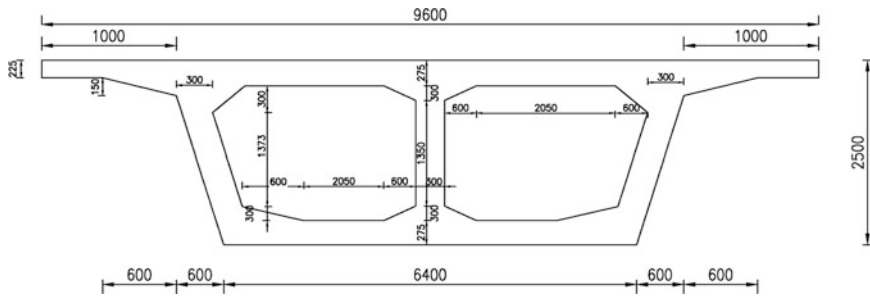


Fig. 1 Details of geometry and dimension of the deck (All dimension in mm)

models analysed. The prestressing steel used for post tensioning the segments conforms to IS: 14268. Foundations are assumed to be fixed and soil structure interaction is neglected. A super imposed dead load (SIDL) of 2 kN/m^2 is also added to include the weight of wearing course and other secondary elements which did not contribute to the structural stiffness directly.

Three cases are studied in the parameter 'Deck Support Condition', which includes simply supported (SS), semi-integral (SI) and integral bridges (IN). Semi-integral bridges are those with their piers as integral and abutments resting on elastomeric bearings, whereas for integral bridges both the bents and abutments are monolithic.

The second parameter taken for comparison of bearing stiffness value is the slenderness ratio (λ) of piers. As the pier height is taken as a separate parameter, in this study the radius of gyration will be varied and hence changing the plan dimension, keeping an aspect ratio of *two* and pier height 8 m. The λ values considered are 15, 20 and 25, correspondingly the pier dimensions adopted were $4.8 \times 2.4 \text{ m}$, $3.6 \times 1.8 \text{ m}$ and $2.9 \times 1.45 \text{ m}$. The percentage of longitudinal reinforcement is taken as 0.6, 0.8 and 1, while the confinement reinforcement percentage is kept as 0.07, 0.09, 0.12 for $\lambda = 15, 20$ and 25 respectively.

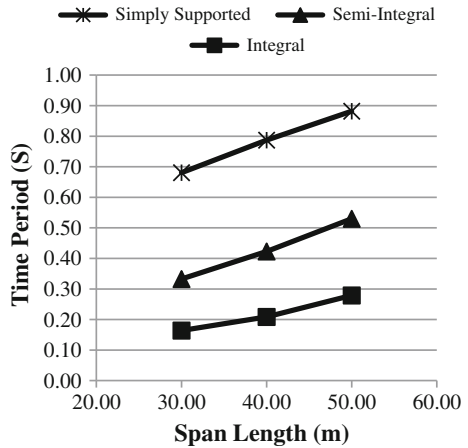
4.3 Modal Analysis Results

The seismic forces exerted on a bridge are due to the response of cyclic motions at the base of a bridge causing accelerations and hence inertia force, which is essentially dynamic in nature. The dynamic properties of the structure such as natural period, damping and mode shape play a crucial role in determining the response of a bridge.

4.3.1 Deck Support Condition

The selection of the optimum structural system for bridges is influenced by structural methods, traffic requirements and also by site-specific conditions [6].

Fig. 2 Influence of deck support condition and span length on fundamental time period



The seismic response of bridges is often proven to be a decisive parameter for the selection of the resisting system and critical for the selection and the design of individual structural members, for which the seismic action is proven to be critical.

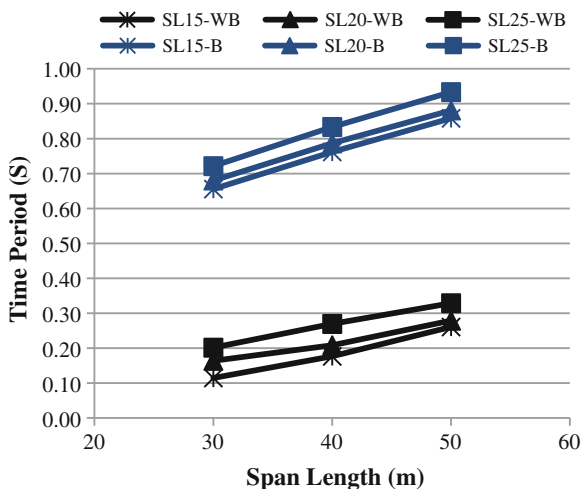
Figure 2 clearly shows the improvement in structural stiffness as the support condition got varied from simply supported to semi-integral to integral, which resulted in an overall decrease in the fundamental time period. It should be noted that, the percentage decrease in time period of integral bridges compared to simply supported bridges got reduced from nearly 76–68 % when the span length got increased from 30 to 50 m. This reduction may be attributed to the overall reduction in flexural stiffness along with the effect of torsional component at longer spans in SI and IN bridges. Also, there is a 15 % increase in fundamental time period for SS bridge models as the span length increases by 10 m and 27 % increase in case of SI and IN bridge models.

4.3.2 Slenderness Ratio

Classical buckling defined as, sudden failure due to instability of perfectly axially loaded members without horizontal load does not usually occur in practical reinforced/prestressed concrete members. However, long slender members at ultimate load exhibit large and disproportionate increase of deflections due to combined effect of geometric non-linearity (P-Δ effect) and non-linear structural response due to material non-linearity, progressive cracking and local plasticity. This reduces the ultimate load carrying capacity as compared to short members of identical cross-section and steel ratio. Thus slenderness ratio is an important criterion to be checked in the design of bridge structures.

From Fig. 3, it is obvious that, as the slenderness ratio increases regardless of span length, fundamental time period of the structure increases, which shows the relation between slenderness and structural bending stiffness. The percentage

Fig. 3 Influence of slenderness ratio and span length on fundamental time period. Legend: *SL* slenderness ratio, *WB* without bearing, *B* with bearing



increase in time period is more for integral bridge models than simply supported models due to the monolith construction of integral bridges without bridge deck isolation along with an overall reduction in structural stiffness. Figure 3 gives a comprehensive idea about the influence of slenderness ratio and span length on *T* for both SS and IN bridge models.

4.4 Pushover Analysis Results

Nonlinear static or pushover analysis is the simplest technique by which the designer can assess the capacity and corresponding performance of a structure subjected to seismic excitation. Here, the capacity spectrum method as discussed in ATC 40 is used to determine the performance level of the models generated. Default PMM Hinge is used in bents to incorporate nonlinearity in structural models. In this study, transverse pushover analysis is only done as the models were found least stiff in that direction particularly for IN bridge models. For brevity, span lengths of 30 and 40 m were considered in this section.

4.4.1 Deck Support Condition

Figure 4 shows the capacity curve of the bridge models in the transverse direction. It is obvious from the figure that, bridge models that are simply supported will have more deformation capacity than integral bridges, without much reduction in their overall structural stiffness. Table 1 further substantiate the above point through the

Fig. 4 Capacity curve in transverse direction. Legend: *S* span, *R* rectangular

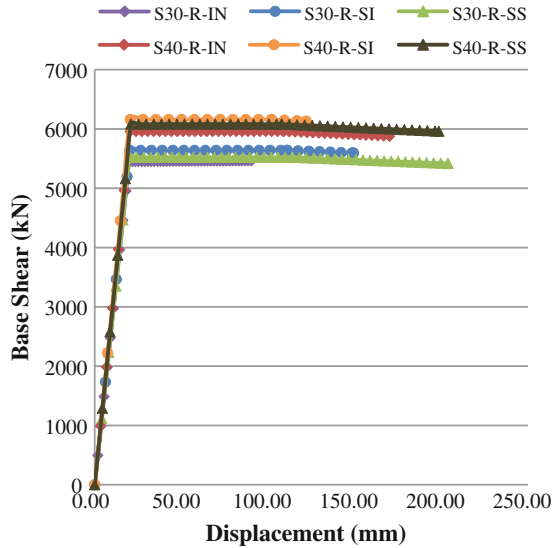


Table 1 Ductility and energy dissipation capacity

Span length	Deck support condition	Pier deformation		Ductility factor	Base shear (kN)	Energy dissipation (J)
		Yield (mm)	Ultimate (mm)			
30	IN	19.8	90.1	4.55	5444.1	1,530,881
	SI	19.9	148.6	7.47	5661.36	2,914,468
	SS	20.4	202.8	9.94	5543.1	4,044,246
40	IN	19.8	169.5	8.56	5979.66	3,580,620
	SI	20	121.3	6.07	6,179	2,503,731
	SS	20.1	198	9.85	6,100	4,340,760

increased ductility factor and energy dissipation capacity of the SS bridge models. Ductility and Energy Dissipation Capacity (obtained from capacity curve) are two important criteria which the designers normally rely on for better seismic resistance of any structures. This indicates the significance of proper isolation through bridge bearings. It is to be noted that, as the span length increases the ductility and energy dissipation capacity of IN bridge models are improving and is comparable with SS bridge models. This is mainly due to the greater flexibility attained by the IN bridge models at longer spans which can be well understood from the modal analysis results. Thus, it can be summarized that bridge bearings are more significant for short span bridges i.e. below 40 m, from the seismic resistance point of view.

The performance level of the bridge models considered was assessed for both maximum considered earthquake (MCE) and design basis earthquake (DBE) in the transverse direction. From Tables 2 and 3, it is apparent that the performance of

Table 2 Performance evaluation for MCE in transverse direction

Span length	Deck support condition	Time period (T_{eff}), S	Damping (B_{eff})	Base shear (kN)	Pier deformation (mm)	Performance level
30	IN	NIL	NIL	NIL	NIL	C
	SI	1.654	0.324	5639.77	108	CP
	SS	1.634	0.324	5522.1	107	CP
40	IN	1.95	0.335	5935.2	125	C
	SI	NIL	NIL	NIL	NIL	C
	SS	1.914	0.333	6061.1	124	C

Note NIL indicates demand and capacity spectrum doesn't meet or no performance point obtained and performance levels are, *C* collapse, *CP* collapse prevention, *LS* life safety, *IO* immediate occupancy and *O* operational

Table 3 Performance evaluation for DBE in transverse direction

Span length	Deck support condition	Time period (T_{eff}), S	Damping (B_{eff})	Base shear (kN)	Pier deformation (mm)	Performance level
30	IN	0.959	0.235	5452.85	36	O
	SI	0.959	0.231	5639.77	36	O
	SS	0.95	0.232	5522.1	36	O
40	IN	1.114	0.249	5957.17	41	O
	SI	1.113	0.247	6160.44	41	IO
	SS	1.097	0.244	6081.9	41	O

integral bridge models are almost the same as that of simply supported bridge models for DBE irrespective of span length. But, for MCE, integral bridge models are not preferable for shorter spans below 40 m.

4.4.2 Slenderness Ratio

From Fig. 5 and Tables 4 and 5, it is evident that, for the same slenderness ratio considered SS bridge models are far superior than IN bridge models in its ductility and energy dissipation capacity particularly for shorter spans (below 40 m). Also, it can be deduced that a slenderness ratio of 20 is best suitable for the span lengths considered, for better seismic resistance. The performance levels at MCE and DBE (Tables 6, 7, 8 and 9) further reinforce the above suggestion.

Fig. 5 Capacity curve in transverse direction. Legend: *S* span, *R* rectangular, *SL* slenderness ratio

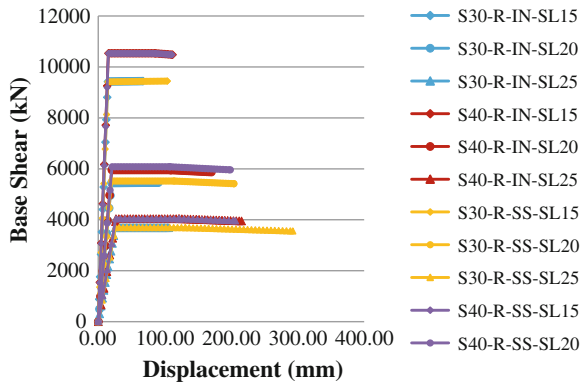


Table 4 Ductility and energy dissipation capacity for ‘IN’ bridges

Span length	Slenderness ratio (λ)	Pier deformation		Ductility factor	Base shear (kN)	Energy dissipation (J)
		Yield (mm)	Ultimate (mm)			
30	15	14.4	66.92	4.65	9435.6	1,982,231
	20	19.99	90.1	4.51	5444.1	1,526,743
	25	25.52	105.83	4.15	3687.46	1,184,560
40	15	14.9	111.3	7.47	10589.8	4,083,438
	20	20.3	169	8.33	5959.32	3,544,604
	25	26.1	214.9	8.23	4044.4	3,054,331

Table 5 Ductility and energy dissipation capacity for ‘SS’ bridges

Span length	Slenderness ratio (λ)	Pier deformation		Ductility factor	Base shear (kN)	Energy dissipation (J)
		Yield (mm)	Ultimate (mm)			
30	15	14.5	103.5	7.14	9403.4	3,347,610
	20	20.4	203.4	9.97	5524.1	4,043,641
	25	25.6	291.5	11.39	3,700	3,935,320
40	15	14.9	110.6	7.42	10552.5	4,039,497
	20	20.6	198	9.61	6,100	4,328,560
	25	26.6	205.7	7.73	4058.3	2,907,366

Table 6 Performance evaluation for MCE in transverse direction for 'IN' bridges

Span length	Slenderness ratio (λ)	Time period (T_{eff}), S	Damping (B_{eff})	Base shear (kN)	Pier deformation (mm)	Performance level
30	15	NIL	NIL	NIL	NIL	C
	20	NIL	NIL	NIL	NIL	C
	25	NIL	NIL	NIL	NIL	C
40	15	1.172	0.321	10536.7	77	CP
	20	1.95	0.335	5935.2	125	C
	25	2.814	0.345	3988.9	180	CP

Table 7 Performance evaluation for DBE in transverse direction for 'IN' bridges

Span length	Slenderness ratio (λ)	Time period (T_{eff}), S	Damping (B_{eff})	Base shear (kN)	Pier deformation (mm)	Performance level
30	15	0.617	0.223	9432.4	24	O
	20	0.959	0.235	5452.85	36	O
	25	1.35	0.245	3690.65	50	O
40	15	0.698	0.232	10536.7	27	O
	20	1.114	0.249	5957.17	41	O
	25	1.575	0.256	4043.46	57	IO

Table 8 Performance evaluation for MCE in transverse direction for 'SS' bridges

Span length	Slenderness ratio (λ)	Time period (T_{eff}), S	Damping (B_{eff})	Base shear (kN)	Pier deformation (mm)	Performance level
30	15	1.027	0.315	9435.4	68	IO
	20	1.634	0.324	5522.1	107	CP
	25	2.372	0.334	3675.39	154	C
40	15	1.172	0.321	10532.9	77	CP
	20	1.914	0.333	6061.1	124	C
	25	2.813	0.345	3986.26	179	C

Table 9 Performance evaluation for DBE in transverse direction for ‘SS’ bridges

Span length	Slenderness ratio (λ)	Time period (T_{eff}),S	Damping (B_{eff})	Base shear (kN)	Pier deformation (mm)	Performance level
30	15	0.616	0.222	9421.46	24	O
	20	0.95	0.232	5522.1	36	O
	25	1.347	0.245	3694.21	50	O
40	15	0.697	0.232	10532.9	27	O
	20	1.097	0.244	6081.9	41	IO
	25	1.575	0.256	4040.01	57	IO

5 Conclusion

Seismic isolation is a simple structural design approach to mitigate or reduce the earthquake damage potential. Elastomeric bearings became a common isolation device for bridges owing to its high vertical stiffness and horizontal flexibility, enabling the structure to move horizontally during strong ground motion. The present study emphasises the significance of elastomeric bearing through a parametric study. The parameters considered were span length, deck support condition and slenderness ratio. For all the above parameters, it is unanimously proven that bearings play a significant role in seismic response reduction. The modal analysis results prove the relevance of the above parameters selected through the variation in the dynamic properties obtained. The study on ductility, energy dissipation capacity and performance level reveals that, it is always better to go for simply supported bridges than integral bridges particularly for shorter span below 40 m. Based on the evaluation of the influence of slenderness ratios selected for simply supported and integral bridge models for different span length, it can be deduced that, using a slenderness ratio of 20 will be more effective in seismic response reduction.

References

1. Kelly JM (1997) Earthquake design with rubber. Springer, New York
2. Robinson WH (1982) Lead-rubber hysteretic bearings suitable for protecting structures during earthquakes. Earthq Eng Struct Dynam 10:593–604
3. Bridge bearings-Indian Railways Institute of Civil Engineering, Pune, March 2006
4. IRC (1987) IRC 83 (Part II): 1987-standard specifications and code of practice for road bridges. Indian Roads Congress, New Delhi
5. Mitoulis SA, Tegos IA, Stylianidis KC (2010) Cost-effectiveness related to the earthquake resisting system of multi-span bridges. J Eng Struct 32:2658–2671
6. Kunde MC, Jangid RS (2006) Effects of pier and deck flexibility on the seismic response of isolated bridges. J Bridge Eng 11:109–121
7. Nielson BG, Desroches R (2007) Seismic performance assessment of simply supported and continuous multispan concrete girder highway bridges. J Bridge Eng 12:611–620

8. Abeyasinghe RS, Gavaise E, Rosignoli M, Tzaveas T (2002) Pushover analysis of inelastic seismic behaviour of Greveniotikos bridge. *J Bridge Eng* 7:115–126
9. IRC (2010) IRC 6: 2010-standard specifications and code of practice for road bridges section: II, loads and stresses. Indian Roads Congress, New Delhi
10. IRC (2011) IRC 112: 2011-code of practice for concrete road bridges. Indian Roads Congress, New Delhi

Performance of Seismic Base-Isolated Building for Secondary System Protection Under Real Earthquakes

P.V. Mallikarjun, Pravin Jagtap, Pardeep Kumar
and Vasant Matsagar

Abstract Damages due to earthquake can be reduced by controlling the seismic response of structure. For the structures containing expensive equipments such as nuclear power plants, computer centers and hospitals reduction of seismic response of secondary system (SS) is as important as reduction in seismic response of primary structures (PS) since damage to secondary system (SS) leads to significant social chaos. This paper provides the investigation of effectiveness of base isolation technology for secondary system. A three storied reinforced cement concrete (RCC) building is modeled as a PS in this study. Laminated plug bearing is adopted for base isolation of PS. Secondary system is housed at first floor level of the PS. SS is isolated with elastomeric bearing from the supporting PS floor. The earthquake ground motions recorded at Myanmar border region recording station location 25°N 95°E having PGA 0.003 and 0.0021 g are used as input ground accelerations. Seismic responses of SS with and without isolation are evaluated and the effect of interaction between PS and SS is also studied. A remarkable reduction in seismic response of SS is observed when it is isolated.

Keywords Base-isolation • Earthquake • Elastomeric bearing • Primary structure • Secondary system • Seismic response

P.V. Mallikarjun (✉) · P. Kumar
Civil Engineering Department, NIT Hamirpur (HP), Hamirpur, India
e-mail: mallikarjun.10692@gmail.com

P. Kumar
e-mail: pardeepkumar.nit@gmail.com

P. Jagtap · V. Matsagar
Department of Civil Engineering, Indian Institute of Technology (IIT) Delhi, Hauz Khas,
New Delhi 110 016, India
e-mail: jagtap@civil.iitd.ac.in

V. Matsagar
e-mail: matsagar@civil.iitd.ac.in

1 Introduction

Secondary systems are those systems and elements, which are attached to the wall or floor of PS. These are named as secondary however, not secondary in importance. Hence, the SS are widely recognised due to their necessity to provide essential emergency and recovery services after occurrence math of an earthquake event. During an earthquake, the primary structures containing expensive equipment excites the installed SS through floor motions induced in PS. Due to tuning effects SS get significantly damaged even in low intensity earthquakes. In numerous cases structural damage is caused to installed secondary systems, while the primary structure survives the earthquake. Various studies have shown drastic reduction in peak accelerations and deflections in structure by using properly designed base isolation systems [1]. Several analytical and numerical schemes for calculating peak response of SS have been developed [2, 3]. A state of art review on response of secondary systems has been presented by Chen and Soong [4].

Present study aims at investigation of base isolation for SS and numerical study of interaction between PS and SS. For PS, Lead plug bearing whose behaviour is represented by bilinear force deformation is used. Earthquake ground motions recorded on 6th November, 2006 at Myanmar 25°N 95°E station having an earthquake magnitude of 5.2. The peak acceleration responses of SS with and without isolation are evaluated and the effect of SS interaction with PS is studied. Seismic response of the fixed-base and base-isolated SS are compared and remarkable reductions in seismic response of SS is observed when those are base isolated.

2 Mathematical Formulations

Elastomeric bearing is widely used as base isolator, which consists of alternate layers of steel shims and hard rubber. Major function of elastomeric bearing is to reduce the transmission of shear force to super structure by augmenting the vibration period of the entire super structure. Figure 1 represents a mathematical model of base isolated secondary structure with the assumption that the superstructure is rigid compared to stiffness of elastomeric bearing. The equation of motion of the entire system is given as, (x and x_b are with respect to fixed support) [5],

$$\begin{aligned} & \begin{pmatrix} m & 0 \\ 0 & m_b \end{pmatrix} \begin{Bmatrix} \ddot{x} \\ \ddot{x}_b \end{Bmatrix} + \begin{pmatrix} c & -c \\ -c & c_b + c \end{pmatrix} \begin{Bmatrix} \dot{x} \\ \dot{x}_b \end{Bmatrix} + \begin{pmatrix} k & -k \\ -k & k_b + k \end{pmatrix} \begin{Bmatrix} x \\ x_b \end{Bmatrix} \\ & = - \begin{pmatrix} m & 0 \\ 0 & m_b \end{pmatrix} \begin{Bmatrix} 1 \\ 1 \end{Bmatrix} \ddot{x}_g \end{aligned} \quad (1)$$

The mathematical model of a base isolated primary and fixed base secondary system is shown in Fig. 2. Equation of motion for the base isolated primary

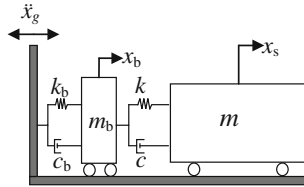


Fig. 1 Mathematical model for base-isolated PS

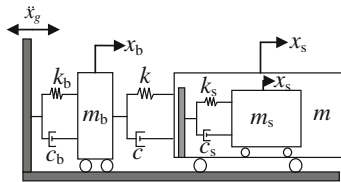


Fig. 2 Mathematical model for base-isolated PS housing fixed-base SS

structure housing secondary system when it is subjected to ground motion is given by

$$\begin{pmatrix} m_s & 0 & 0 \\ 0 & m & 0 \\ 0 & 0 & m_b \end{pmatrix} \begin{Bmatrix} \ddot{x}_s \\ \ddot{x} \\ \ddot{x}_b \end{Bmatrix} + \begin{pmatrix} c_s & -c_s & 0 \\ -c_s & c + c_s & -c \\ 0 & -c & c + c_b \end{pmatrix} \begin{Bmatrix} \dot{x}_s \\ \dot{x} \\ \dot{x}_b \end{Bmatrix} + \begin{pmatrix} k_s & -k_s & 0 \\ -k_s & k + k_s & -k \\ 0 & -k & k + k_b \end{pmatrix} \begin{Bmatrix} x_g \\ x \\ x_b \end{Bmatrix} = - \begin{pmatrix} m_s & 0 & 0 \\ 0 & m & 0 \\ 0 & 0 & m_b \end{pmatrix} \begin{Bmatrix} 1 \\ 1 \\ 1 \end{Bmatrix} \ddot{x}_g \tag{2}$$

where, m represents mass, c represents damping coefficient and k represents stiffness of the system. Also, the subscript s and b are associated with secondary and base respectively. The corresponding equation of motion for the base mass under earthquake ground acceleration x_g can be given by,

$$m_b \ddot{x}_b + F_b - kx - c\dot{x} = -m_b \ddot{x}_g \tag{3}$$

Restoring force developed in the elastomeric bearing F_b is given by [6],

$$F_b = c_b \dot{x}_b + k_b x_b \tag{4}$$

where, c_b and k_b are damping and stiffness of elastomeric bearing respectively. The restoring force (F_b) developed in isolation system depends upon the type of isolation system considered.

3 Description of Numerical Model

Fixed-base and base isolated building, constructed at IIT Guwahati are considered as primary structures. A plan of the fixed-base and the base-isolated building is shown in Fig. 3 with the position of the isolators marked in the isolated building. As seen from Fig. 3, both buildings are rectangular in plan having dimension $4.5\text{ m} \times 3.3\text{ m}$. The cross sectional dimension of columns is $400\text{ mm} \times 300\text{ mm}$, with the larger oriented along the longer span of the buildings. Beams along both sides of the buildings are 250 mm wide, while the depth varies as 450 mm along the longer span and 350 mm along the shorter span. Masonry infill walls are 125 mm thick and slab thickness is 150 mm . SS (Fig. 4) consists of two steel plates of $450\text{ mm} \times 580\text{ mm}$ with 10 mm diameter steel rods placed at four corners between ground and first floor of SS. SS is housed at first floor of the PS. PS is isolated with laminated plug bearing ($480\text{ mm} \times 400\text{ mm}$) under each column [7]. Secondary system is placed on elastomeric bearing ($80\text{ mm} \times 60\text{ mm}$) with mass of 53 kg and has having horizontal stiffness of 52 N/mm with damping ratio of 0.1 , time period 0.283 s . Different properties of materials and isolators used in primary and secondary system are given in Tables 1 and 2.

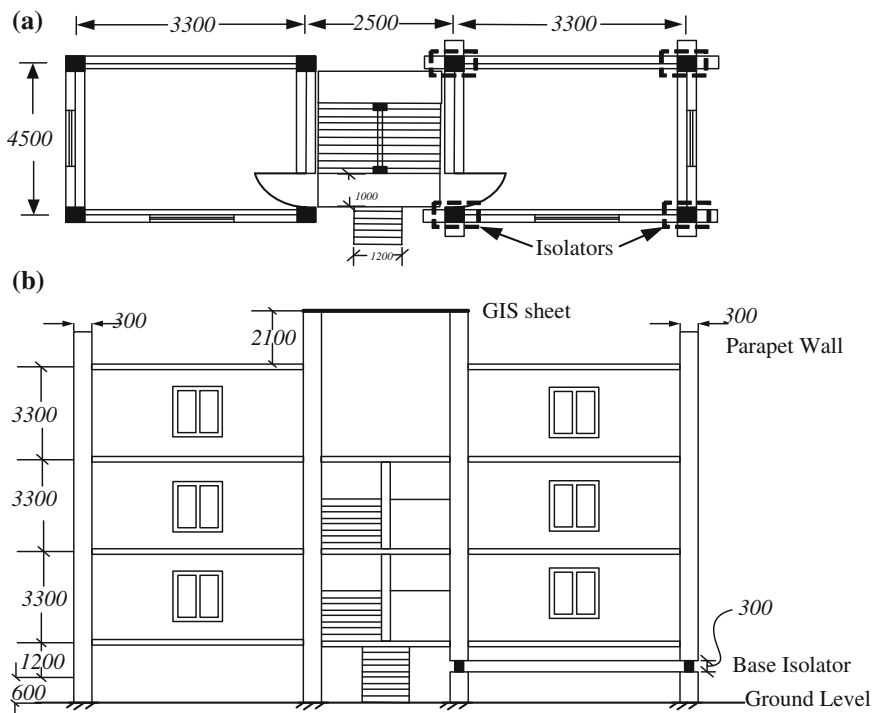


Fig. 3 a Plan of fixed-base and base-isolated RCC building showing the position of isolators, b front elevation of the building (all the dimensions are in millimeter)

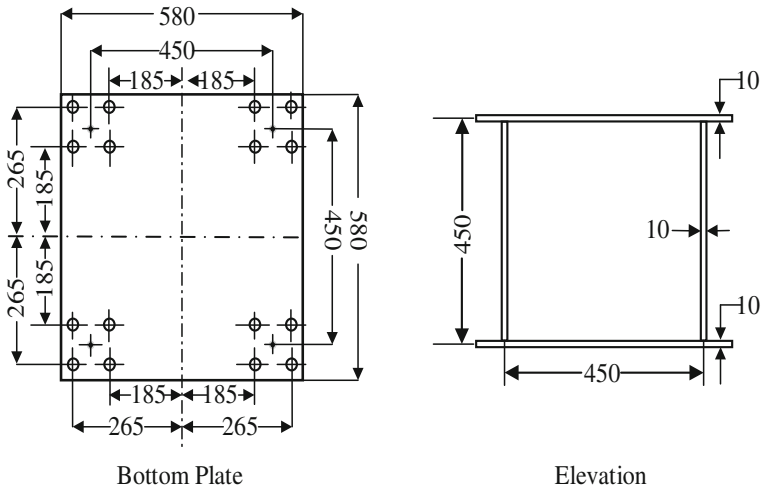


Fig. 4 Plan and elevation of secondary system

Table 1 Material properties used for PS and SS

Model	Material	Properties	Explanation
Primary structure	Concrete	2548.42 kg/m ³	Density
		$E = 25,000$ MPa	Young's modulus
		$\nu = 0.2$	Poisson's ratio
		M25	Grade of concrete
Secondary system	Steel	7846.37 kg/m ³	Density
		$E = 2 \times 10^5$ MPa	Young's modulus
		$\nu = 0.3$	Poisson's ratio
		Fe250	Grade of steel

Table 2 Properties of isolator used for PS and SS

Model	Property	Value
Primary structure (lead plug bearing)	Mass	0.5 T
	Vertical stiffness	188,960 kN/m
	Post yield stiffness	796 kN/m
	Ratio of post to pre yield stiffness	0.0463
	Effective damping	0.1056
	Yield strength	25.38 kN
	Effective horizontal stiffness	1292.085 kN/m
Secondary system (elastomeric bearing)	Effective horizontal stiffness	52 kN/m
	Effective damping	0.1

4 Numerical Analysis

The assumptions made in this model are: (i) superstructure is assumed to be linear elastic throughout the analysis, (ii) torsional effects are neglected (iii) effect of soil-structure interaction is not taken into consideration. Seismic response of secondary system with elastomeric bearing are investigated under bi-directional earthquake excitation of real ground motions [7]. The seismic response is studied considering SS as fixed-base and base-isolated. The seismic event recorded is on the 6th of November, 2006. The event, measured 5.2 on the Richter scale, with epicenter located at latitude 25°N and longitude 95°E at Myanmar border region having a focal depth of 33 km. The peak ground acceleration (PGA) recorded in fixed base primary structure at site in the longer direction of the building was 0.0021 g while that in the shorter direction was 0.003 g as shown in Fig. 5. Classical modal superposition method cannot be used in the solution of Eqs. (1) and (2) since the system is non-classically damped and the force deformation behaviour of isolators used for primary structure is non-linear. Newmark's direct integration method of step by step time integration is used in SAP 2000 [8] with time interval 0.005 s using linear variation of acceleration.

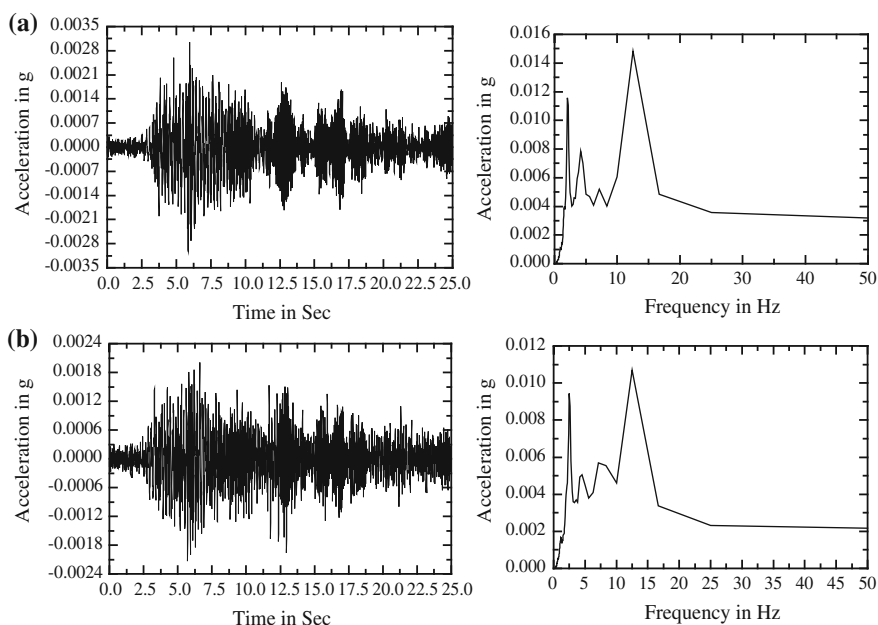


Fig. 5 **a** Ground motion and ground acceleration spectrum in X-direction. **b** Ground motion and ground acceleration spectrum in Y-direction for the earthquake event on 6th November, 2006

4.1 Seismic Response of Fixed-Base with and Without PS Interaction

Seismic response of fixed base PS and SS is studied here for both the cases by considering and not considering their interactions. In the first case without considering interaction between fixed-base PS and fixed-base SS the seismic ground acceleration is applied at the base of the fixed-base PS. From the seismic analysis the floor response at the first floor of fixed-base PS is obtained. This obtained response is applied as a seismic excitation to the fixed-base SS. In the second case for considering the interaction between fixed-base PS and fixed-base SS they are modeled together i.e. fixed-base SS is attached at the first floor of the fixed-base PS. The response recorded taken from fixed-base SS automatically considers the interaction between fixed-base PS and fixed-base SS. The difference between seismic response of SS with and without interaction is observed in Fig. 6.

4.2 Seismic Response of Fixed-Base and Base-Isolated SS Without PS Interaction

Seismic response of fixed-base SS and base-isolated SS is studied here without considering their interaction with PS. From the seismic analysis the floor response is obtained at the first floor of fixed-base PS is obtained. This obtained response is applied as an input to the fixed-base SS and base-isolated SS separately. The comparison of response of fixed-base and base isolated SS for the earthquake event recorded on 6th November, 2006 is shown in Fig. 7. The trend of results obtained from this study shows the seismic response reduction when SS is base isolated with elastomeric bearing. This reduction in seismic response of SS prevents the damages after earthquake event.

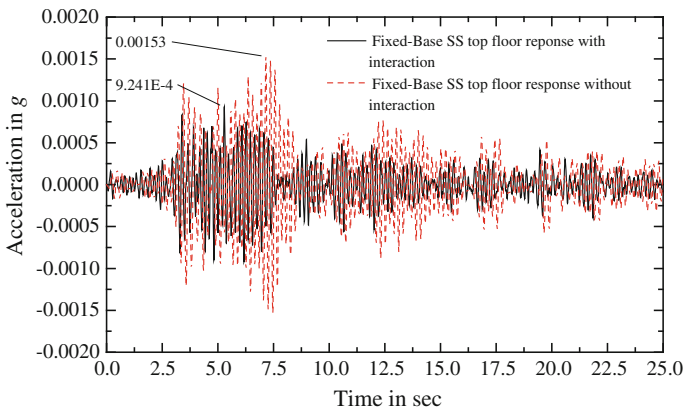


Fig. 6 Comparison of top floor acceleration of fixed base SS considering primary and secondary system interaction for the earthquake event on 6th November, 2006

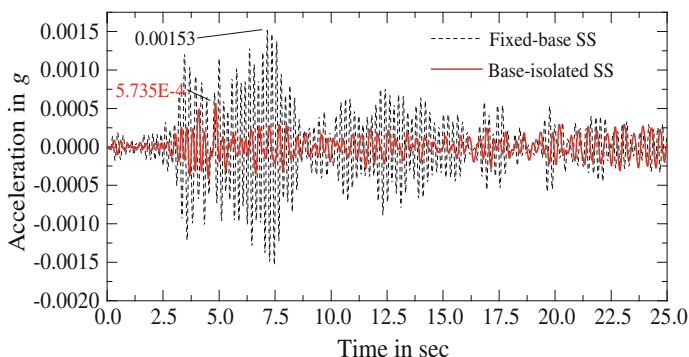


Fig. 7 Comparison of top floor acceleration time history plots for the earthquake event on 6th, November, 2006 of fixed-base SS and base-isolated SS ($T_b = 0.22$ s, $\beta_{\text{eff}} = 0.1$, $q = 3$ mm) without interaction

4.3 Seismic Response of Fixed-Base and Base-Isolated SS with PS Interaction

In this study base-isolated and fixed-base SS are modeled in fixed base PS. Response of fixed-base SS and base-isolated SS modeled in fixed-base PS is studied with interaction effect. Comparison of time history plots of top floor acceleration for the earthquake event on 6th November, 2006 of fixed-base SS and base isolated SS housed in fixed-base PS is shown in Fig. 8. Peak response of fixed-base SS reduces drastically with the provision of isolation to SS.

4.4 Response of Fixed-Base SS Housed in Base-Isolated PS

In this part of study the fixed base SS is housed at first floor of the base-isolated PS and the top floor acceleration response of the fixed-base SS are investigated. Lead plug bearing is used for isolation of PS. Different properties of lead plug bearing used are given in Table 2. Ground motion accelerations for the earthquake event on 6th November, 2006 is applied as input at the base of base-isolated PS housing fixed-base SS modeled at the first floor. Comparisons of peak response of fixed-base SS placed in base-isolated PS are made in Fig. 9. The provision of isolation in primary structure does not have remarkable variation in reduction of peak response in secondary system as is clear from comparison of Figs. 8 and 9. Thus it can be concluded that the influence of isolation provide to PS is comparatively less effective than providing isolation to the SS. Thus, base isolation in secondary system ensures more reliable earthquake mitigation technology for secondary system protection.

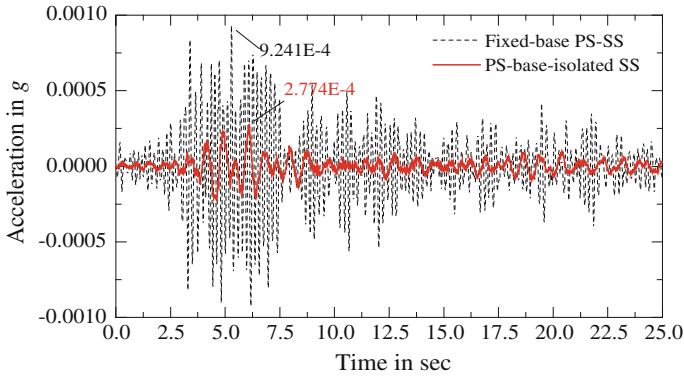


Fig. 8 Comparison of top floor acceleration time history plots for the earthquake event on 6th, November, 2006 of fixed-base SS and base-isolated SS ($T_b = 0.22$ s, $\beta_{eff} = 0.1$, $q = 3$ mm) with interaction

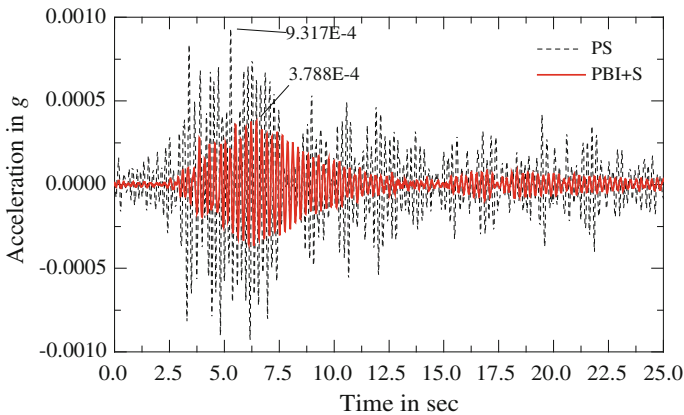


Fig. 9 Comparison of top floor acceleration time history plots for the earthquake event on 6th, November, 2006 of fixed-base PS and primary base-isolated SS

4.5 Comparison of Floor Responses of Primary and Secondary System

An initial analysis of the floor responses of SS for the event on 6th November, 2006 show magnification in the roof acceleration for the fixed-base SS while significant reduction in roof acceleration has been observed for the isolated SS. It is observed from the time history plots in Fig. 8, that there is reduction of the roof response for the base-isolated SS as compared to the fixed-base SS. The floor response of fixed-base SS attached to primary structure reduces reasonably, when mutual interaction between primary and secondary systems is considered. From Fig. 7 it is evident that

the elastomeric bearing isolation system is effective in reducing the roof response of SS, with reduction of as much as 63.1 % is achieved when interaction effect is ignored. Only 37.9 % of the ground motion is getting transferred to the roof. Hence, the isolated buildings can be designed for lesser magnitude of earthquake forces compared to the conventional buildings.

When SS is housed in base-isolated primary system, a considerable reduction in the roof acceleration of SS is observed in comparison to when it is housed in fixed-base PS. It is seen from the time history plots of Fig. 9, that there is reduction of peak value of the roof response for the base-isolated PS as compared to the SS housed in fixed-base PS and from Fig. 8, it is evident that the lead plug bearing isolation system is very effective in reducing the roof response of the isolated structure, with reduction of as much as 40.9 % achieved when mutual interaction between primary and secondary is considered. Hence, the isolated system can be effectively used for the seismic protection of secondary systems.

5 Concluding Remarks

Preliminary investigation of the recorded earthquake events and the structural responses from both buildings has shown the effectiveness of the isolation systems. As much as 70 % reduction in roof response for the isolated secondary structure has been achieved with the elastomeric bearing isolation system. The fixed base secondary system, on the other hand, has shown structural behavior typical of such structures, with more amplification in the floor response as compared to base isolated secondary system. This aspect of the behavior of elastomeric bearing needs to be investigated further.

Acknowledgments Prof. S. K. Deb of Indian Institute of Technology (IIT) Guwahati and Dr. G. R. Reddy of Bhabha Atomic Research Centre (BARC) Mumbai are gratefully acknowledged for providing the necessary data required to accomplish the herewith presented research study.

References

1. Kelly JM (1986) Aseismic base isolation: review and bibliography. *Soil Dyn Earthq Eng* 5 (4):202–216
2. Sackman JL, Kelly JM (1979) Seismic analysis of internal equipment and components in structures. *Eng Struct* 1(4):179–190
3. Singh MP (1980) Seismic design input for secondary systems. *J Struct Div ASCE* 106 (2):505–517
4. Chen Y, Soong TT (1988) State-of-the-art- review: seismic response of secondary systems. *Eng Struct* 10:218–228
5. Chopra AK (2002) *Dynamics of structures: theory and applications to earthquake engineering*, 2nd edn. Prentice-Hall of India Pvt. Ltd., Delhi

6. Matsagar VA, Jangid RS (2004) Influence of isolator characteristics on the response of base-isolated structures. *Eng Struct* 26:1735–1749
7. Dubey PN, Reddy GR, Vaze KK, Ghosh AK, Kushwaha HS, Deb SK (2008) Performance of base-isolated RCC framed building under actual earthquake. *J Struct Eng* 35(3):195–201
8. SAP (2000) Linear and non-linear static and dynamic analysis of 3D-structure. CSI Computers and Structures, Inc., California

Part XIII
Bridge Engineering and Seismic
Response Control

Nonstationary Response of Orthotropic Bridge Deck to Moving Vehicle

Prasenjit Paul and S. Talukdar

Abstract In the present paper, an orthotropic bridge deck has been analyzed to find out non-stationary response statistics when subject to moving vehicle at variable velocity. The solution strategy adopted is Monte Carlo simulation technique after properly developing system equations and dynamic excitation. The governing partial differential equation of the orthotropic plate is first discretized using mode superimposition technique and then combined with equation of motions of the rigid vehicle model. Exact mode shape functions and natural frequencies are used in the discretization of the equations of motion. Bridge deck roughness has been modeled by generalized power spectral density (PSD) function. As the vehicle traverses with variable velocity over the uneven surface, the wheel input becomes nonstationary which renders the second order statistics of the bridge dynamic response, a time dependent stochastic process. The response statistics of the mid span displacement have been presented and effects of vehicle speed/acceleration on the dynamic amplification factors (DAF) are discussed.

Keywords Dynamic amplification factor • Mode superimposition • Nonstationary • Orthotropic bridge deck • Power spectral density

1 Introduction

Bridge construction is one of the most important applications of orthotropic plate structures. Orthotropy is understood as a special case of anisotropy in which the material properties are different in two mutually perpendicular directions. Orthotropy in bridges is usually achieved by means of transversal and longitudinal ribs resulting in different stiffness in direction parallel and perpendicular to the bridge axis. The decks are modeled as equivalent orthotropic plates with elastic properties

P. Paul · S. Talukdar (✉)

Department of Civil Engineering, Indian Institute of Technology, Guwahati 781039, India
e-mail: staluk@iitg.ernet.in

equal to the average properties of various components evenly distributed across the plates [1].

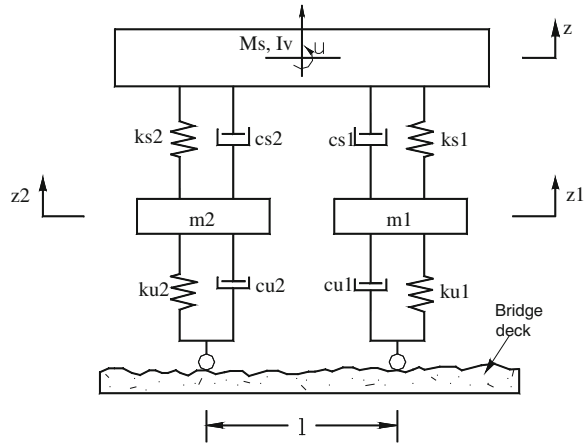
Theoretical studies on bridge-vehicle dynamic interaction have drawn considerable attention among the researchers. Veletsos and Huang [2] and Fryba [3] have solved the bridge-vehicle interaction problems with simple beam or continuous beam model incorporating inertial reaction of the moving weight over the bridge. Mulcahy [4] utilized an orthotropic plate model of a single span bridge to obtain dynamic response of a three-axle tractor-trailer vehicle. The effect of rough pavement on the bridge-vehicle dynamic system was considered by Inbanathan and Wieland [5]. Jayaraman et al. [6] and Gorman [7] presented the results of free vibration of rectangular orthotropic plate with different edge conditions. A study on transverse vibration of non homogeneous orthotropic plate of non uniform thickness using spline technique has been conducted by Lal and Dhanpati [8]. Vehicle interaction with orthotropic bridge model incorporating random surface roughness are not readily available in literature except for few simplified cases of quarter car model of vehicle or constant moving mass [9–11]. In the present paper, dynamic analysis of orthotropic bridge deck subjected to moving load has been presented. Vehicle model considered has heave and pitch motion with forward velocity variable in time. Because of variable velocity of the vehicle the bridge roughness, though homogeneous in space, renders to be a temporal nonstationary process. The study takes the help of modal superposition techniques to develop bridge-vehicle system equations, which are then numerically solved for stochastic dynamic input resulted from deck unevenness. Statistics of the responses are presented and Dynamic Amplification Factor (DAF) for constant velocity and variable velocity has been discussed.

2 Model of Bridge-Vehicle System

2.1 Vehicle Model

The vehicle body is assumed as rigid beam and it is subjected to heave motion (z) in the vertical direction and pitch rotation (θ), which is assumed positive in anti-clockwise direction. The mass of the vehicle body is lumped at its center of gravity, which is termed as ‘sprung mass (M_s)’. The mass of the axle with wheels are also assumed to be lumped at the center of the axle and ‘unsprung mass’. The vertical displacements of the unsprung masses (m_1 and m_2) of front axle and rear axle are z_1 and z_2 , respectively. The vehicle body and the front and rear unsprung masses are connected by front and rear suspension system comprising of spring elements of stiffness ks_1 and ks_2 and dashpots with damping constants cs_1 and cs_2 , respectively. Tire stiffness and damping of front and rear axle locations are ku_1 , cu_2 and ku_2 , cu_2 respectively. The model has been presented in Fig. 1. The equation of motion for sprung mass is

Fig. 1 Heave and pitch model of the vehicle



$$M_s \ddot{z} + cs_1 (\dot{z} + l_1 \dot{\theta} - \dot{z}_1) + cs_2 (\dot{z} - l_2 \dot{\theta} - \dot{z}_2) + ks_1 (z + l_1 \theta - z_1) + ks_2 (z - l_2 \theta - z_2) = 0. \tag{1}$$

Pitching motion of the rigid beam is given by the following equation as

$$I_v \ddot{\theta} + cs_1 (\dot{z} + l_1 \dot{\theta} - \dot{z}_1) l_1 - cs_2 (\dot{z} - l_2 \dot{\theta} - \dot{z}_2) l_2 + ks_1 (z + l_1 \theta - z_1) l_1 - ks_2 (z - l_2 \theta - z_2) l_2 = 0. \tag{2}$$

The front and rear wheel bounce can be represented by Eqs. (3) and (4) respectively as

$$m_1 \ddot{z}_1 - cs_1 (\dot{z} + l_1 \dot{\theta} - \dot{z}_1) - ks_1 (z + l_1 \theta - z_1) + cu_1 [\dot{z}_1 - \dot{h}(x_1, y_1) - \dot{w}(x_1, y_1, t)] + ku_1 [z_1 - h(x_1, y_1) - w(x_1, y_1, t)] = 0, \tag{3}$$

and

$$m_2 \ddot{z}_2 - cs_2 (\dot{z} - l_2 \dot{\theta} - \dot{z}_2) - ks_2 (z - l_2 \theta - z_2) + cu_2 [\dot{z}_2 - \dot{h}(x_2, y_2) - \dot{w}(x_2, y_2, t)] + ku_2 [z_2 - h(x_2, y_2) - w(x_2, y_2, t)] = 0 \tag{4}$$

where $w(x, y, t)$ denotes transverse displacement of the plate at time instant t .

2.2 Orthotropic Plate Equations and Discretization

A bridge deck (Fig. 2) has been modeled as a thin orthotropic rectangular plate of uniform thickness h and of dimension a and b with two sides ($x = 0, x = a$) simply supported and opposite two edges as free (Levy’s condition). The governing partial differential equation of the orthotropic plate of uniform thickness is given by [12]

$$D_x \frac{\partial^4 w(x, y, t)}{\partial x^4} + 2D_{xy} \frac{\partial^4 w(x, y, t)}{\partial x^2 \partial y^2} + D_y \frac{\partial^4 w(x, y, t)}{\partial y^4} + \rho h \frac{\partial^2 w(x, y, t)}{\partial t^2} = p(x, y, t) \tag{5}$$

where D_x and D_y are flexural rigidities of the plate in x and y direction, respectively and D_{xy} is torsional rigidity of the plate per unit width of. These are given as

$$D_x = \frac{E_x h^3}{12(1 - \nu_{xy} \nu_{yx})}; D_y = \frac{E_y h^3}{12(1 - \nu_{xy} \nu_{yx})} \quad D_{xy} = \frac{1}{2} (\nu_{yx} D_x + \nu_{xy} D_y + 4D_k) \tag{6}$$

$$D_k = \frac{G_{xy} h^3}{12}$$

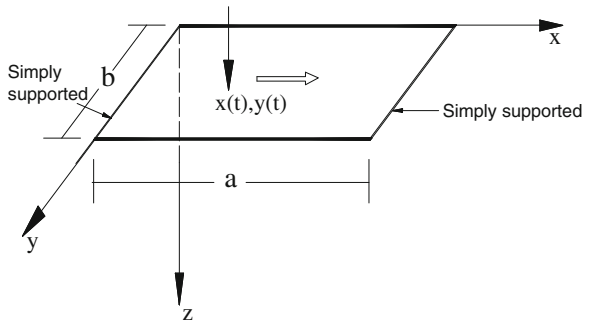
where E_x and E_y are elastic moduli of the orthotropic plate in x and y direction, respectively; ν_{xy} or ν_{yx} is Poisson’s ratio associated with a strain in the y or x direction for a load in the x or y direction. G_{xy} is the shear modulus. The impressed force, $p(x, y, t)$ can be written as

$$p(x, y, t) = \{cu_1 [\dot{z}_1 - \dot{h}(x_1, y_1) - \dot{w}(x_1, y_1, t)] + ku_1 [z_1 - h(x_1, y_1) - w(x_1, y_1, t)]\} \delta(x - x_1)(y - y_1) + \{cu_2 [\dot{z}_2 - \dot{h}(x_2, y_2) - \dot{w}(x_2, y_2, t)] + ku_2 [z_2 - h(x_2, y_2) - w(x_2, y_2, t)]\} \delta(x - x_2)(y - y_2) \tag{7}$$

where $\delta(\cdot)$ represents Dirac delta function

The displacement of the plate is represented by the summation of normal mode function in the x and y co-ordinates as

Fig. 2 Bridge deck plate modeled as orthotropic plate with Levy’s condition



$$w(x, y, t) = \sum_{ij} \varphi_{ij}(x, y)q_{ij}(t) = \sum_i \sum_j \psi_i(x)\phi_j(y)q_{ij}(t) \tag{8}$$

where ψ_i and ϕ_j are normal modes of the plate under appropriate boundary conditions in x and y directions respectively ($i = 1, 2, \dots, m; j = 1, 2, \dots, n$). q_{ij} are corresponding normal coordinates. Adopting Levy's boundary conditions with other opposite edges free, the natural frequencies and mode shapes for different wave numbers ($m = 1, 2, 3 \dots; n = 1, 2, 3 \dots$) have been found [13] which are used along with orthogonality condition of mode shape function to discretize the plate equations of motion. The discretized plate equations are given as

$$M_{ij} \ddot{\eta}_{ij}(t) + C_{ij} \dot{\eta}_{ij}(t) + K_{ij} \eta_{ij}(t) = \int_0^a \int_0^b p(x, y, t) \psi_i(x) \phi_j(y) dx dy \tag{9}$$

$$\text{where } M_{ij} = \int_0^a \int_0^b \rho h \psi_i^2(x) \phi_j^2(y) dx dy \tag{10}$$

$$C_{ij} = \int_0^a \int_0^b c \psi_i^2(x) \phi_j^2(y) dx dy \tag{11}$$

$$K_{ij} = \int_0^a \int_0^b \left[D_x \psi_i^{IV}(x) \psi_i(x) \phi_j^2(y) + 2D_{xy} \psi_i''(x) \phi_j''(y) \psi_i(x) \phi_j(y) \right] dx dy \tag{12}$$

Here, $i = 1, 2, \dots, m; j = 1, 2, \dots, n; m$ and n are wave numbers corresponding to normal mode of vibration.

3 Response Statistics and DAF

The response of the bridge-vehicle coupled system can be found by solving simultaneously Eqs. (1) to (4) and Eqs. (9). To solve the system of equations, the input has to be specified. Here, the input to wheel of the vehicle is the random surface roughness, which has been digitally simulated from the generalized power spectral density function [14]. In the formulation, vehicle velocity is assumed to vary with time which renders the input to be nonstationary process. In order to find out response statistics, response samples are generated corresponding to each input sample and ensemble averages are considered to calculate mean and standard deviation of the bridge response. Newmark's Beta Method [15] has been adopted for numerical integration of the system equations. For the illustration of the present

approach, a simply supported bridge composed of five steel I-girders and concrete deck has been considered whose details are given below and illustrated in Fig. 3. The dimensions and material properties are chosen with minor variation as appropriate to an orthotropic bridge [16].

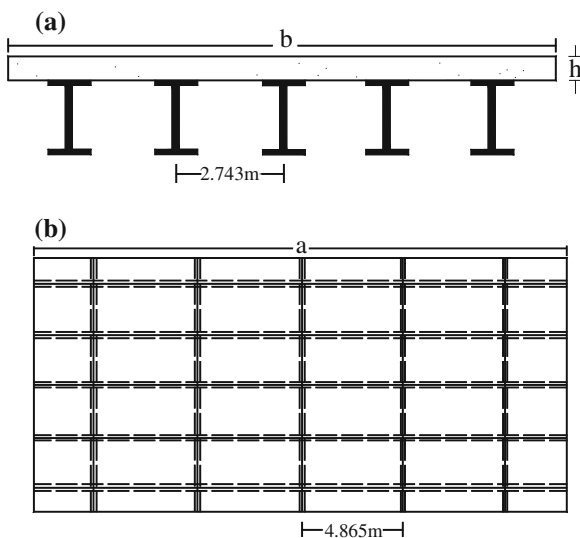
The parameters of the bridge deck are listed as follows: length of the bridge (a) = 24.5 m, width of the bridge (b) = 13.7 m, deck thickness (h) = 0.225 m, $E_x = 4.2 \times 10^{10}$ N/m², $E_y = 2.9 \times 10^{10}$ N/m², mass per unit area, (ρ_h) = 675 kg/m². For the steel I-beam: web thickness = 0.012 m, web height = 1.5 m, flange width = 0.410 m, flange thickness = 0.032 m. The damping ratio of the bridge is taken as 0.02 for all the vibration modes.

The equivalent orthotropic plate parameters are: aspect ratio = 1.78, $D_x = 2.415 \times 10^9$ N-m; $D_y = 2.1813 \times 10^7$ N-m and $D_{xy} = 2.2195 \times 10^8$ N-m; principal vehicle parameters: sprung masse $M = 36,000$ kg; pitch moment of inertia = 144×10^3 kg m²; unsprung masses $m_1 = m_2 = 2,000$ kg; wheel base = 2.0 m; suspension stiffnesses $ks_1 = ks_2 = 0.9 \times 10^7$ N/m; suspension damping: $C_{s1} = C_{s2} = 7.2 \times 10^4$ N/ms⁻¹.

Figures 4 and 5 show the effect of increased speed of the vehicle on the mean deflection and standard deviation at the center of the bridge for constant speed of the vehicle. It is found that deflection is slightly increased with speed but increase of speed has caused the shifting of the peak towards left indicating the increase of excitation frequency. However, standard deviation does not reflect the change of excitation frequency with increasing speed but peak magnitude is considerably higher at higher speed.

Effect of accelerated run of the vehicle on the response statistics are presented in Figs. 6 and 7. Entry velocity of the vehicle is taken as 60 km/h. It is found that consideration of nonstationarity due to variable velocity does not affect the

Fig. 3 Orthotropic bridge model, **a** cross section, **b** plan



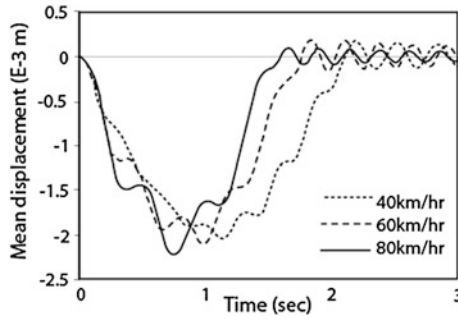


Fig. 4 Mean deflection of the center of the bridge for constant velocity runs of the vehicle

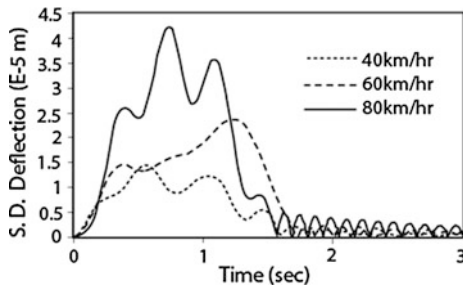
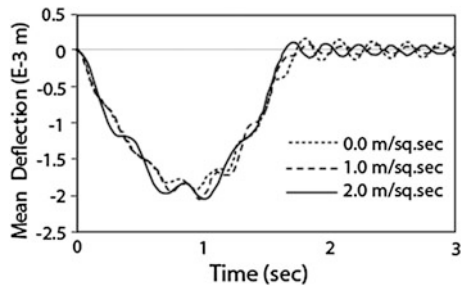


Fig. 5 Standard deviation (S.D) of the deflection at the center of the bridge for constant velocity runs

Fig. 6 Mean deflection of at the centre of the bridge for accelerated run of the vehicle



maximum values of mean and standard deviation, however, response characteristics due to passage of moving load can change the location of peak response because of change in excitation frequency.

The Dynamic Amplification Factor (DAF) has been evaluated and shown in Figs. 8 and 9 for different velocities and accelerations of the vehicle respectively. In the present paper, DAF is calculated based on the ratio of maximum mean plus standard deviation of the deflection to the maximum static deflection.

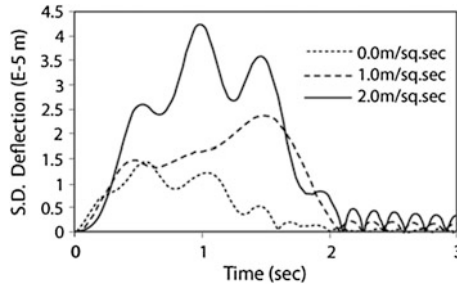


Fig. 7 Standard deviation (S.D) of the deflection at the center of the bridge for accelerated run of the vehicle

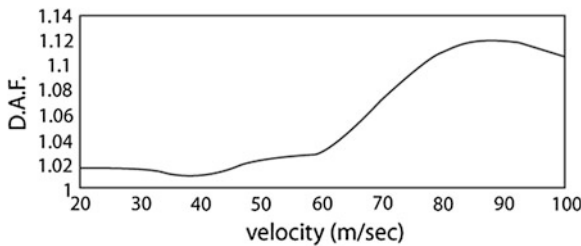


Fig. 8 Effect of vehicle velocity on DAF Dynamic amplification factor

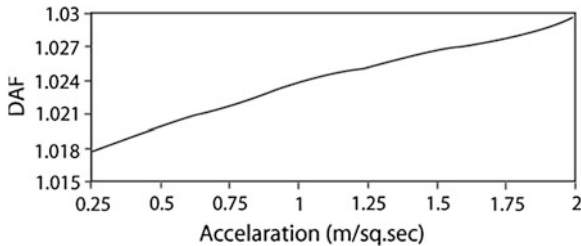


Fig. 9 Effect of vehicle acceleration on DAF Dynamic amplification factor

It has been observed in the results that DAF slowly increases up to a speed of 60 km/h, thereafter, increases at higher rate and tends to stabilize beyond 80 km/h and found to reduce after 85 km/h. This may be attributed to the fact that at some critical speed of the vehicle, the excitation imposed from spatial disturbance along the bridge may approach the system’s fundamental natural frequency. However, this behavior is not observed in case of the accelerated run of the vehicle, as the

bridge has shorter time of interaction with the vehicle. The DAF, is however found to increase with the vehicle forward acceleration. No linear dependence is found in any one of the cases.

4 Conclusions

The dynamic response of the orthotropic deck slab subjected to nonstationary excitation induced by moving vehicle has been studied. Nonstationary excitation has been resulted from the uneven pavement surface traversed by the vehicle at variable speed. Monte Carlo simulation technique is adopted to find the response statistics. Increase of vehicle speed does not cause much increase in the mean response but the time period of mean time history is significantly affected by the change in vehicle speed. Standard deviation of the response in both constant velocity and accelerated run of the vehicle is higher when the speed parameter or forward acceleration increases. DAF for the various vehicle velocities shows that there exists a critical speed of the vehicle when bridge may undergo excessive deformation, and therefore, vehicle should ply sufficiently lower than the critical speed for bridge safety. The DAF is found to increase with the increasing magnitude of vehicle forward acceleration.

References

1. Szilard R (1974) Theory and analysis of plates: classical and numerical methods. Prentice Hall, New Jersey
2. Veletsos AS, Huang T (1970) Analysis of dynamic response of highway bridge. *J Eng Mech* 96:593–620
3. Fryba L (1972) Vibration of solids and structures under moving loads. Noordhoff International Publishing, Groningen
4. Mulcahy NL (1983) Bridge response with tractor trailer vehicle loading. *Earthq Eng Struct Dynam* 11:649–665
5. Inbanthan MJ, Wieland M (1987) Bridge vibrations due to vehicle moving over rough surface. *J Struct Eng* 113:1994–2008
6. Jayaraman G, Chen P, Synder VW (1990) Free vibration of rectangular orthotropic plates with a pair of parallel edges simply supported. *Comput Struct* 34:203–214
7. Gorman DJ (1990) Accurate free vibration analysis of clamped orthotropic plates by the method of superposition. *J Sound Vib* 140:391–411
8. Lal R, Dhanpati (2007) Transverse vibration of non homogeneous orthotropic plate of non uniform thickness: a spline technique. *J Sound Vib* 306:203–214
9. Humar JL, Kashif JL (1995) Dynamic response analysis of slab-type bridges. *J Struct Eng* 121:48–62
10. Gbadeyan JA (1995) Dynamic behavior of beams and rectangular plates under moving loads. *J Sound Vib* 182:677–695
11. Zhu XQ, Law SS (2003) Dynamic behavior of orthotropic rectangular plates under moving loads. *J Eng Mech* 129:79–87

12. Soedel W (1993) *Vibration of Shell and Plates*. Marcel Dekker, New York
13. Prasenjit Paul (2004) *Fatigue analysis of orthotropic bridge deck*. Dissertation, Indian Institute of Technology Guwahati
14. Eui-Seung H, Nowak AS (1991) Simulation of dynamic load for bridges. *J Struct Eng* 117:1413–1434
15. Bathe KJ, Wilson E (1987) *Numerical methods in finite element analysis*. Prentice Hall, New Delhi
16. Zhu XQ, Law SS (2003) Time domain identification of moving loads on bridge deck. *J Vib Acoust* 125:187–198

Seismic Performance of Benchmark Highway Bridge Installed with Passive Control Devices

Suhasini N. Madhekar

Abstract Major earthquakes of the last few decades have generated a great deal of interest in structural control systems, to mitigate seismic hazards to lifeline structures—in particular, bridges. The vast destruction and economic losses during earthquakes underscore the importance of finding more rational and substantiated solutions for protection of bridges. One of the most promising devices, considered as a structural control system, is a passive device. Although, there has been substantial work in the recent past in the development of seismic isolators and structural control systems, their effectiveness could not be compared by a systematic study, because they were applied to different types of structures subjected to different types of loadings. A benchmark problem on highway bridges has been developed to compare the performance and effectiveness of different control systems in protecting bridges from earthquakes. In the present study, seismic response of the Benchmark Highway Bridge, with passive controllers is investigated. The problem is based on the 91/5 highway over-crossing at Southern California, USA. In the first phase, the deck is fixed to the outriggers, and in the second phase, the deck is isolated from the outriggers. Using an analytical frame work, a thorough investigation of the isolation devices has been carried out to evaluate their effectiveness under different earthquakes. The response of the bridge to six different real earthquake ground excitations is investigated using simplified lumped mass finite element model of the bridge. The optimum device parameters are investigated to improve response of the benchmark highway bridge. The study explores the use of seismic isolators, namely, Friction Pendulum System (FPS), Double Concave Friction Pendulum System (DCFPS), Variable Friction Pendulum System (VFPS) and Variable Frequency Pendulum Isolator (VFPI). The governing equations of motion are solved by Newmark-beta solver in MATLAB and SIMULINK toolbox. The effectiveness of the devices is explored in terms of reduction of the specified evaluation criteria, considering maximum and norm values. The analytical simulation results demonstrate that these isolators, under optimum parameters are quite effective and can be practically implemented for the vibration control of bridges.

S.N. Madhekar (✉)

Department of Civil Engineering, College of Engineering Pune, Pune 411 005, India
e-mail: suhasinimadhekar@gmail.com

Keywords Benchmark highway bridge · Friction pendulum system · Double concave friction pendulum system · Variable friction pendulum system · Variable friction pendulum isolator

1 Introduction

Seismic design of highway bridges draws great significance since bridges come under the category of *lifeline structures*. Strong near-fault ground motions such as Northridge, Kobe and Chi-Chi earthquake have caused severe effects on the stability of bridges. Kobe earthquake in Japan (17th January, 1995) and Chi-Chi earthquake in Taiwan (20th September, 1999) have demonstrated that the strength alone would not be sufficient for the safety of bridges during an earthquake. Extensive damage to highway and railway bridges occurred in the Kobe earthquake, including the 18-span bridge at Fukae, Hanshin Expressways. In view of the extensive damage of bridge during earthquake, the current research is focused on finding out more rational and substantiated solutions for their protection.

Seismic isolators significantly reduce the deck acceleration and consequently the force transmitted to the piers and abutments. The performance of friction isolators is quite insensitive to severe variations in the frequency content of the base excitation, making them more robust. However, the sliding displacement might be unacceptably large and there may be some residual displacement after an earthquake. Jangid [4] investigated the seismic response of three-span continuous deck bridge isolated with the FPS under near-fault ground motions and concluded that there exists an optimum value of the friction coefficient. Kim and Yun [5] presented the Double Concave Friction Pendulum System (DCFPS) with tri-linear behavior. Panchal and Jangid [8] proposed an advanced friction base isolator called Variable Friction Pendulum System (VFPS), for near-fault ground motions. The effectiveness of friction isolator is enhanced thereby reducing the residual displacements to manageable levels. Pranesh and Sinha [9] proposed an advanced base isolator, Variable Frequency Friction Isolator (VFPI), which is found to be effective for a wide range of earthquake excitations.

To compare the performance and effectiveness of various control systems in protecting bridges from earthquakes, a benchmark problem on Highway Bridge has been developed by Agrawal and Tan [1]. Tan et al. [10] presented sample passive, semi-active and active control system designs for the seismically excited benchmark highway bridge. The benchmark highway bridge, isolated with the lead rubber bearings (LRBs) is subjected to the prescribed ground motions. In case of near-fault motions, large size isolators are required to accommodate large displacements, demanding for more space. Moreover, an inadequate seismic gap provided to accommodate such large isolator displacement, may lead to pounding of girders and pounding of deck with abutments [7]. In the present study, the response of benchmark Highway Bridge seismically isolated with different friction

isolators is investigated. The specific objectives of the study are summarized as: (i) to study the dynamic behaviour of benchmark Highway Bridge isolated with friction isolators; viz. FPS, DCFPS, VFPS, and VFPI; and (ii) to compare the seismic response of the bridge isolated with friction isolators in terms of the defined performance criteria.

2 The Benchmark Highway Bridge Model

The bridge model used for the benchmark study is that of the 91/5 highway overcrossing in Southern California. A brief description of the benchmark bridge and its model is presented herein and the detailed information can be found in Agrawal et al. (2009) [12]. The superstructure of the bridge consists of a two-span continuous, cast-in situ pre-stressed concrete 3-cell box-girder; and the substructure is in the form of pre-stressed concrete outriggers. Each span of the bridge is 58.5 m long, spanning a four-lane highway, with two skewed abutments. The width of the deck is 12.95 m along east and 15 m along west direction. The total mass of the benchmark bridge is 4,237,544 kg and the mass of the deck is 3,278,404 kg. The deck is supported by a 31.4 m long and 6.9 m high pre-stressed concrete outrigger, resting on pile foundation. In the actual bridge, four conventional elastomeric bearings are provided at each abutment and four passive fluid dampers are installed between each abutment and the deck-end. In the evaluation model used for numerical simulations, lead rubber bearings (LRB) are used in place of the elastomeric bearings.

The uncontrolled structure, used as a basis of comparison for the controlled system, corresponds to the model, isolated with four LRBs at each deck-end. The model resulting from the finite-element formulation has a large number of degrees-of-freedom. To make it manageable for dynamic simulation, while retaining the fundamental behaviour of the bridge, an extensive evaluation model of the bridge with 430 (N) degrees-of-freedoms (DOFs) has been developed in ABAQUS. Figure 1 shows the Elevation and plan view of the 91/5 highway over-crossing. Transverse (referred as x -direction) is the North-South and the longitudinal (referred as y -direction) is the East-West.

The bridge superstructure is represented by three dimensional beam elements. Rigid links are used to connect the control devices between the deck-end and abutments. The effects of soil-structure interaction at the abutments and approach embankments are taken into consideration [6]. The pre-yield shear stiffness of bearings (k_{b1}) is 4,800 kN/m and the post-yield shear stiffness (k_{b2}) is 600 kN/m. The yield displacement of bearing (y_p) is 0.015 m and the yield force of the lead core versus weight of the deck (Q_d/W_d) ratio is 0.05. In phase I of the benchmark highway bridge problem, the bridge deck is fixed to the outriggers whereas in phase II, the bridge deck is isolated from the outriggers. The present study is focused on the phase I bridge problem.

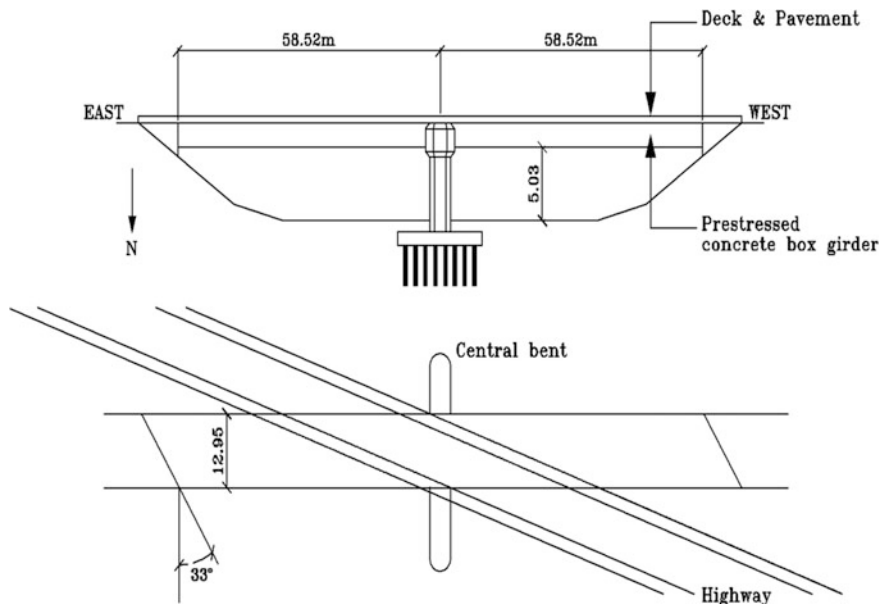


Fig. 1 Elevation and plan view of the 91/5 highway over-crossing

3 Friction Pendulum System

Among various friction base isolators, the Friction Pendulum System (FPS) is most attractive due to its ease in installation and simple mechanism of restoring force by gravity action. The sliding surface of FPS is spherical so that its time period of oscillation remains constant [11]. A continuous model of frictional force of a sliding system presented by Constantinou et al. [2] is used for the present study. The rigid-plastic behaviour of the frictional force of the sliding systems is modeled by nonlinear differential equations. The restoring force of the FPS is considered as linear (i.e. proportional to relative displacement) and is expressed by

$$F_b = k_b x_b + F_x \tag{1}$$

where F_x is the frictional force in the FPS in the x -direction; and k_b is the stiffness of the FPS provided by the curvature of the spherical surface through inward gravity action. The FPS is designed in such a way as to provide the specific value of the isolation period, T_b expressed as

$$T_b = 2\pi \sqrt{\frac{m_d}{\sum k_b}} \tag{2}$$

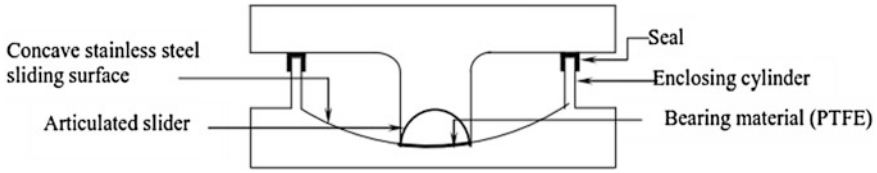


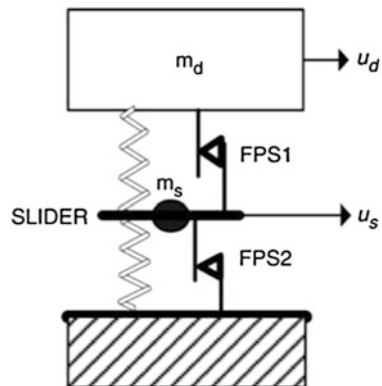
Fig. 2 Schematic diagram of typical curved sliding-surface isolator

where $\sum k_b$ is the total horizontal stiffness of the FPS provided by its curved surface. Figure 2 shows the schematic diagram of FPS. The most effective FPS for the benchmark highway bridge is designed by taking the friction coefficient as 0.1 and selecting the curvature of the spherical surface ($R = 1$ m) that provides the isolation period of 2 s.

4 Double Concave Friction Pendulum System (DCFPS)

The Double Concave Friction Pendulum System (DCFPS) is an adaptation of the traditional, well-proven single concave FPS, which allows for significantly larger displacements. The principal benefit of the DCFPS is its capacity to accommodate substantially larger displacements compared to the traditional FPS of identical plan dimensions. Moreover, there is the capability to use sliding surfaces with varying radii of curvature and coefficients of friction, offering the designer greater flexibility to optimize performance. The DCFPS consists of two sliding surfaces with different friction coefficients and radii of curvature. The effects of DCFPS with various friction values and restoring properties on a bridge are investigated under various earthquake excitations. The characteristic of an FPS can be made more effective by introducing a second sliding surface. Theoretical modeling of DFPS has been studied by Fenz and Constantinou [3]. A double concave friction pendulum can be modeled as a serial combination of two FPS as shown in Fig. 3.

Fig. 3 Bilinear model of DCFPS



Owing to the series nature and neglecting the inertial effect of the small mass (m_s) of slider, the reaction force at two friction pendulum systems (FPS₁ and FPS₂) became identical, from which the reaction force of the DFPS can readily be obtained. Parameters of DCFPS are suggested by Constantinou (2004) [13] as Radius of FPS₁ ($R_1 = 1.074$ m), Radius of FPS₂ ($R_2 = 1.074$ m), and the corresponding coefficient of friction are $\mu_1 = 0.03$ and $\mu_2 = 0.06$. These are used for the application of DCFPS to the benchmark highway bridge.

5 Variable Friction Pendulum System

The Variable Friction Pendulum System (VFPS) proposed by Panchal and Jangid [8] is an advanced friction base isolator similar to the FPS in terms of geometry. The difference between the FPS and the VFPS is that the friction coefficient of FPS remains constant whereas the friction coefficient of VFPS is varied in the form of a curve. This feature of the VFPS makes it more robust and superior friction isolator device. Figure 4 illustrates the comparison between the friction coefficient of FPS and VFPS. The selected variation of the friction coefficient is such that up to a certain value of isolator displacement, the frictional force increases and then it decreases with further increase in the displacement. A mathematical idealization is used for the variation of the friction coefficient. The equation adopted to define the curve for friction coefficient, μ of VFPS is as follows

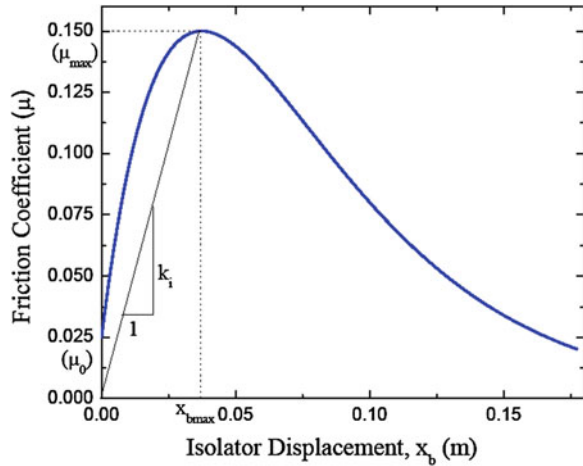
$$\mu = (\mu_0 + a_1|x_b|)e^{-a_2|x_b|} \quad (3)$$

where μ_0 is the initial value of friction coefficient; a_1 and a_2 are the parameters that describe the variation of friction coefficient along the sliding surface of VFPS; and x_b is the isolator displacement. To find parameters a_1 and a_2 , a straight line can be drawn from the origin up to the peak value of the friction coefficient which is generally kept in the range of 0.15–0.2. The slope of the line gives the initial stiffness of the VFPS which controls its initial time period. Referring to the Fig. 4, the initial stiffness of the VFPS is given by

$$k_i = \frac{\mu_{\max} W}{x_{b\max}} \quad (4)$$

In Eq. (4), μ_{\max} is the peak friction coefficient of the VFPS; $x_{b\max}$ is the isolator displacement corresponding to maximum value of friction coefficient; and W is the weight supported by the VFPS. The term $\mu_0 + a_1|x_b|$ in the Eq. (3) represents linear increase of friction coefficient and the term $e^{-a_2|x_b|}$ represents exponential decrease in friction coefficient. The initial time period, T_i of the VFPS is given by

Fig. 4 Variation of coefficient of friction



$$T_i = 2\pi \sqrt{\frac{m_d}{\sum k_i}} \tag{5}$$

where $\sum k_i$ is the total initial stiffness of VFPS isolators. The initial value of friction coefficient μ_0 is assumed as 0.025. The total force of VFPS consists of two main components i.e. (i) the force due to the component of the self-weight tangent to sliding surface and (ii) the frictional force opposing the sliding. The self-weight always contributes towards the restoring mechanism and is directed towards the initial position. The direction of friction force is opposite to the direction of sliding and may contribute or resist the restoring mechanism. Thus, the forces due to the component of the self-weight and frictional force are additive or subtractive depending on the direction of sliding.

$$F_s = \mu W \tag{6}$$

The limiting value of the frictional force F_s to which the VFPS can be subjected before sliding, is expressed by Eq. (6), where μ is the coefficient of friction of the VFPS controlled by Eq. (3) which can be defined by two parameters, namely the initial time period, T_i and the peak friction coefficient μ_{max} . The stiffness, of the VFPS is designed so as to provide the specific value of the isolation period, T_b given by Eq. (2), where $\sum k_b$ is the total stiffness of the VFPS isolators provided by its spherical surface. The results of the analytical parametric study performed on VFPS suggest following parameters for the present study. $T_i = 1.2$ s, $T_b = 2$ s and $\mu_{max} = 0.20$.

6 Variable Frequency Pendulum Isolator (VFPI)

The Variable Frequency Pendulum Isolator (VFPI) proposed by Pranesh and Sinha [9] is an advanced base isolator, effective for a wide range of earthquake excitations. The essential characteristics of VFPI include its ability to change the fundamental time period of isolated structure with sliding displacement and its ability to limit the maximum lateral force transmitted to the structure due to ground motions. Its performance is found to be stable during low-intensity excitations and fail-safe during high intensity excitations. The geometry of the sliding surface of isolator can be chosen to achieve a progressive period shift at different response levels such that its frequency decreases with increase in sliding displacement and asymptotically approaches zero at very large displacement.

The oscillation frequency continuously varies, even for high level of excitation and the isolation always remains effective. The restoring force decreases for larger sliding displacement and thereby provides force-softening mechanism. It gives performance similar to that of FPS for low levels of excitation and similar to that of PF system for high level of excitation. The geometry of sliding surface of VFPI can be represented as:

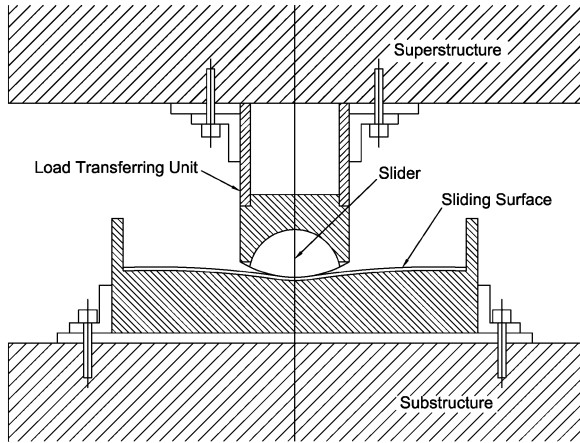
$$y = b \left[1 - \frac{\sqrt{d^2 + 2dx \operatorname{sgn}(x)}}{d + x \operatorname{sgn}(x)} \right] \quad (7)$$

where b and d are the geometrical parameters defining the profile of the sliding surface and y is the vertical displacement. The signum function $\operatorname{sgn}(x)$ has been incorporated to maintain symmetry of the sliding surface about the central vertical axis. It assumes a value of $+1$ for positive sliding displacement and -1 for negative sliding displacement. The instantaneous isolator frequency $\omega_b(x)$, at any sliding displacement is expressed as

$$\omega_b^2(x) = \frac{\omega_1^2}{(1+r)^2 \sqrt{1+2r}} \quad (8)$$

where r is a non-dimensional parameter, given by $r = x \operatorname{sgn}(x)/d$, ω_1 is the initial frequency of the isolator when displacement x is zero, defined as $\omega_1^2 = gb/d^2$. In Eq. (7), the parameters b and d completely define the isolator properties. The ratio bd^2 decides the initial frequency of the isolator and the value of d decides the rate of variation of the isolator frequency. The factor $1/d$ is termed as *frequency variation factor* (FVF). The isolator frequency $\omega_b(x)$ depends solely on geometry of the sliding surface, which is selected such that $\omega_b(x)$ continuously decreases; increasing the isolation period of the structure. The rate of decrease of isolator frequency is directly proportional to the FVF for a given initial frequency. A very low value of FVF results in a performance similar to FPS, with almost constant isolator period, while a very high value results in performance similar to PF system [9].

Fig. 5 Attachment of VFPI to bridge



$$F_b = k_b x_b + F_x \tag{9}$$

The restoring force of VFPI is given by given by Eq. (9), where $\omega_b(x)$ varies according to Eq. (8). The results of the analytical parametric study performed on VFPI suggest frequency variation factor (FVF) = 5, $T_1 = 2.25$ s and $\mu = 0.07$, which yield a considerable reduction in the displacement of the deck and abutment bearings of the bridge, without hampering the gain achieved in the base shear response. Schematic details of the VFPI and its attachment mechanism for bridge are shown in Fig. 5.

7 Governing Equations of Motion

For the benchmark highway bridge, the governing equations of motion are obtained by considering equilibrium of forces at the location of each degree of freedom during seismic excitations. The nonlinear finite element model of the bridge is considered excited under two horizontal components of earthquake ground motion, applied along the two orthogonal directions, acting simultaneously at all supports. The responses in both directions are considered to be uncoupled and there is no interaction between frictional forces. The equations of motion of the evaluation model are expressed in the following matrix form:

$$[M]\{\ddot{u}(t)\} + [C]\{\dot{u}(t)\} + [K(t)]\{u(t)\} = -[M]\{\eta\}\left\{\ddot{u}_g(t)\right\} + [b]\{F(t)\} \tag{10}$$

$$\{u(t)\} = \{x_1, x_2, x_3, \dots, x_N, y_1, y_2, y_3, \dots, y_N\}^T \quad (11)$$

$$\{\ddot{u}_g\} = \left\{ \begin{matrix} \ddot{x}_g \\ \ddot{y}_g \end{matrix} \right\} \quad (12)$$

where $[M]$, $[C]$ and $[K(t)]$ are the mass, damping and stiffness matrix, respectively of the bridge structure of the order $2N \times 2N$; a $\{\ddot{u}(t)\}$, $\{\dot{u}(t)\}$ and $\{u(t)\}$ are structural acceleration, structural velocity and structural displacement vectors, respectively of size $N \times 1$; $\{\ddot{u}_g(t)\}$ is the vector of earthquake ground accelerations acting in two horizontal directions; representing the earthquake ground accelerations (m/s^2) in the transverse and longitudinal directions, respectively; x_i and y_i denote displacements of the i th node of the bridge in transverse and longitudinal directions, respectively; $\{F(t)\}$ is the vector of control force inputs; $\{\eta\}$ is the influence coefficient vector; and $\{b\}$ is the vector defining how the forces produced by the control devices enter the structure. The governing differential equations of motion of the bridge are solved by Newmark- β iterative method of step-by-step integration. The time interval for solving the equations of motion is taken as 0.002 s.

8 Numerical Study

The seismic response of benchmark highway bridge is investigated for the six specified earthquake ground excitations, namely (i) North Palm Springs (1986), (ii) TUC084 component of Chi-Chi earthquake, Taiwan (1999), (iii) El Centro component of 1940 Imperial Valley earthquake, (iv) Rinaldi component of Northridge (1994) earthquake, (v) Bolu component of Duzce, Turkey (1999) earthquake and (vi) Nishi-Akashi component of Kobe (1995) earthquake. To control the response, at each junction of deck and abutment, four isolators of 1,000 kN capacity each are installed. All isolators contribute equally in carrying the deck-mass. To facilitate direct comparison and to evaluate the capabilities of various protective devices and algorithms, evaluation criteria have been developed, as shown in Table 1. The value of performance criteria = 1 indicates uncontrolled response. It is seen from the table that all most for all earthquakes, FPS, DCFPS, VFPS and VFPI are most effective in reducing the response of the benchmark highway bridge. Bold numbers indicate the least response. Hysteresis loops of FPS and VFPI for Chi Chi earthquake are shown in Fig. 6. Larger area under the loop indicates greater energy dissipation.

Table 1 Comparison of response by different passive devices

Isolator	North Palm Springs	Chichi	El Centro	Rinadi	Turk Bolu	Kobe
<i>J₁</i> (Peak base shear)						
FPS	1.059	0.822	0.755	0.891	0.940	0.885
DFPS	1.090	0.800	0.680	0.870	0.930	0.870
VFPS	1.019	0.789	0.795	0.847	0.895	0.894
VFPI	1.023	0.891	0.845	0.930	0.939	0.902
<i>J₂</i> (Peak base moment)						
FPS	0.728	0.981	0.720	0.978	0.990	0.668
DFPS	0.670	0.980	0.650	0.980	0.980	0.670
VFPS	0.737	0.983	0.738	0.973	0.982	0.673
VFPI	0.786	0.982	0.803	0.983	0.987	0.768
<i>J₃</i> (Peak midspan displacement)						
FPS	0.761	0.939	0.798	0.865	0.847	0.753
DFPS	0.700	0.910	0.720	0.820	0.800	0.750
VFPS	0.768	0.887	0.821	0.790	0.768	0.757
VFPI	0.815	0.964	0.878	0.915	0.897	0.764
<i>J₄</i> (Peak midspan acceleration)						
FPS	1.147	1.044	1.049	0.996	1.000	1.039
DFPS	1.270	1.080	1.000	1.020	1.010	1.140
VFPS	1.374	1.032	1.174	0.957	0.984	1.074
VFPI	1.018	0.997	1.025	0.969	0.984	1.034
<i>J₅</i> (Peak bearing deformation)						
FPS	0.647	0.898	0.436	0.834	0.800	0.428
DFPS	0.580	0.860	0.380	0.770	0.740	0.350
VFPS	0.526	0.840	0.444	0.749	0.711	0.351
VFPI	0.683	0.939	0.492	0.899	0.852	0.534
<i>J₉</i> (Normed base shear)						
FPS	0.944	0.860	0.554	0.811	0.855	0.717
DFPS	0.970	0.830	0.530	0.780	0.830	0.730
VFPS	0.916	0.823	0.545	0.768	0.812	0.715
VFPI	0.879	0.899	0.556	0.859	0.914	0.714
<i>J₁₀</i> (Normed base moment)						
FPS	0.668	0.820	0.420	0.840	0.756	0.629
DFPS	0.620	0.820	0.350	0.800	0.670	0.560
VFPS	0.678	0.800	0.501	0.789	0.581	0.631
VFPI	0.726	0.853	0.520	0.878	0.934	0.674
<i>J₁₁</i> (Normed midspan displacement)						
FPS	0.692	0.821	0.436	0.807	0.659	0.656
DFPS	0.650	0.770	0.360	0.760	0.540	0.590
VFPS	0.699	0.746	0.520	0.734	0.546	0.660

(continued)

Table 1 (continued)

Isolator	North Palm Springs	Chichi	El Centro	Rinadi	Turk Bolu	Kobe
VFPI	0.748	0.876	0.535	0.866	0.725	0.699
<i>J</i> ₁₂ (Normed midspan acceleration)						
FPS	1.009	0.937	0.824	0.923	0.995	1.014
DFPS	1.020	0.930	0.780	0.920	1.010	1.050
VFPS	0.975	0.915	0.756	0.896	0.981	1.029
VFPI	0.977	0.940	0.795	0.924	0.959	0.933
<i>J</i> ₁₃ (Normed bearing deformation)						
FPS	0.531	0.794	0.272	0.780	0.476	0.257
DFPS	0.390	0.740	0.210	0.720	0.360	0.220
VFPS	0.513	0.711	0.325	0.699	0.369	0.247
VFPI	0.460	0.860	0.337	0.851	0.522	0.317

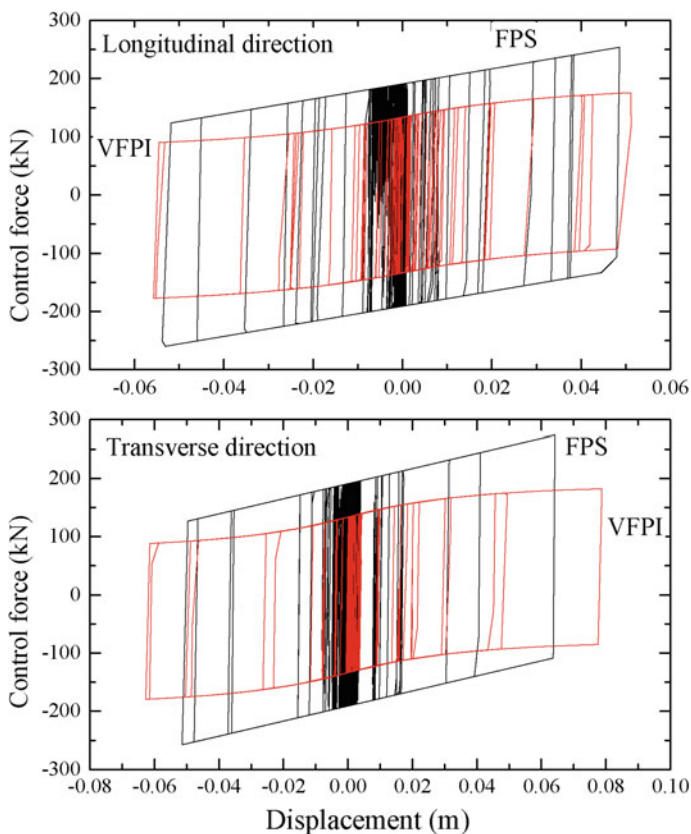


Fig. 6 Hysteresis loops for FPS and VFPI

9 Conclusions

The analytical seismic response of a simplified benchmark model of 91/5 highway bridge at Southern California with friction isolators, viz. FPS, DCFPS, VFPS and VFPI is investigated under two horizontal components of the six recorded earthquake ground motions. The seismic response of the bridge with isolators is evaluated using standard numerical technique and SIMULINK models. The effectiveness of the isolators is studied under different system parameters for assessment of their comparative performance. From the trend of the results of the present study, the following conclusions are drawn:

1. With the installation of friction isolators in the benchmark highway bridge, the base shear and isolator displacement under near-fault ground motions can be controlled within a desirable range.
2. The most appropriate parameters of each device have been decided through large number of numerical simulations. It is found that isolators with these parameters substantially reduce the overall repose of the benchmark highway bridge.
3. The isolators maintain the potential benefits of base isolation as well as reduce the isolator displacement and pier base shear thereby proving their effectiveness in controlling the response of the benchmark highway bridge.
4. The isolators are found to be significantly controlling the peak displacement response of the deck and abutment bearings, while simultaneously limiting the pier base shear response. Average reduction in the peak bearing displacement is substantial, as compared to the uncontrolled repose.

References

1. Agrawal AK, Tan P (2005) Benchmark structural control problem for a seismically excited highway bridge, Part II: Sample control designs. <http://www-ce.engr.cny.cuny.edu/People/Agrawal>
2. Constantinou MC, Mokha AS, Reinhorn AM (1990) Teflon bearings in base isolation II: modeling. *J Struct Eng (ASCE)* 116:455–474
3. Fenz DM, Constantinou MC (2006) Behaviour of the double concave friction pendulum bearing. *Earthq Eng Struct Dynam* 35:1403–1424
4. Jangid RS (2005) Optimum friction pendulum system for near-fault motions. *Eng Struct* 27:349–359
5. Kim Y-S, Yun CB (2007) Seismic response characteristics of bridges using double concave friction pendulum bearings with tri-linear behavior. *Eng Struct* 29(11):3082–3093
6. Makris N, Zhang J (2002) Seismic response analysis of highway overcrossings including soil-structure interaction. *Earthq Eng Struct Dynam* 31(11):1967–1991
7. Nagarajaiah S, Sun X (2001) Base-isolated FCC building: impact response in Northridge earthquake. *J Struct Eng ASCE* 127:1063–1075
8. Panchal VR, Jangid RS (2008) Variable friction pendulum system for near-fault ground motions. *Struct Control Health Monit* 15:568–584

9. Pranesh M, Sinha R (2000) VFPI: an isolation device for aseismic design. *Earthq Eng Struct Dynam* 29(5):603–627
10. Tan P, Agrawal AK, Nagarajaiah S, Zhang J (2005) Benchmark structural control problem for a seismically excited highway bridge, Part II: Sample control designs. <http://www-ce.engr.ccnycunyu.edu/People/Agrawal>
11. Zayas VA, Low SS, Mahin SA (1990) A simple pendulum technique for achieving seismic isolation. *Earthq Spectra* 6(2):317–333
12. Agrawal A & Tan P (2009) “Benchmark structural control problem for a seismically excited highway bridge-Part II: phase I sample control designs”, *Struct Control Health Monit* 16:530–548
13. Constantinou MC (2004) *Friction pendulum double concave bearing*. State university New York. Buffalo

Estimation of Seismic Capacity of Reinforced Concrete Skew Bridge by Nonlinear Static Analysis

E. Praneet Reddy and Kaustubh Dasgupta

Abstract Skew bridges are constructed in situations where the supports need to be aligned in a non-orthogonal orientation with the direction of traffic. During strong earthquake shaking, the non-orthogonal orientation of deck leads to rotation in the deck and significant overall torsional response of the deck. Finally, this rotation may lead to unseating of the deck and failure in pier as observed during several past earthquakes. Based on a representative skewed bridge thirty five models of bridges with varying angle of skew and varying soil conditions having similar dimensions are modeled and analyzed using nonlinear static analysis. The bridges are modeled using the computer program SAP2000. Lumped plasticity model is adopted by assigning flexural plastic hinges at appropriate sections of the piers. The rotation of the deck, torsion in the piers, lateral force in bearings, lateral shear and displacement capacities of the various RC skew bridge are estimated and compared with each other and with those of a non-skew bridge with similar dimensions. The effect of soil structure interaction on the behavior of the bridge is also studied. It is observed that the rotation in the skew bridge with a smaller skew angle begins earlier either in the case of a seat type abutment or the case where there is a deterioration in the lateral capacity of the bearings at the abutment. The consideration of soil structure interaction shows that softer soils provide for greater deck rotations and smaller torsion in the pier. Comparison of various pushover curves with bearings fixed at abutments in the direction along the abutment, shows the trend in the contribution of the abutment with the skew angle and the effect of soil structure interaction in the longitudinal and transverse pushover cases.

Keywords Skew bridge · Soil structure interaction · Nonlinear static analysis · Pounding

E.P. Reddy (✉) · K. Dasgupta (✉)
Department of Civil Engineering, Indian Institute of Technology, Guwahati, India
e-mail: epraneet@gmail.com

K. Dasgupta
e-mail: kd@iitg.ac.i

1 Introduction

Skew bridges are ones where the supports are not orthogonal to the direction of traffic. They are not chosen willingly but are necessitated due to site considerations such as alignment constraints, land acquisitions problems etc. The behaviour of skew slabs is complicated and there is a tendency to avoid or reduce the skew effects. As seen in past research, it was reported by Maragakis and Jennings [4] that the planar rigid body rotation of the deck was the main cause of extensive damage in the bridges which was a result of skewness of the deck. Priestly et al. [6], Watanabe and Kawashima [9] suggested that the planar rigid body rotation was a result of the pounding of the deck with the abutment. This rotation took place in the direction of decreasing skew such that the length supported by the abutment decreases, creating a tendency of the deck to drop off the support at the acute corners.

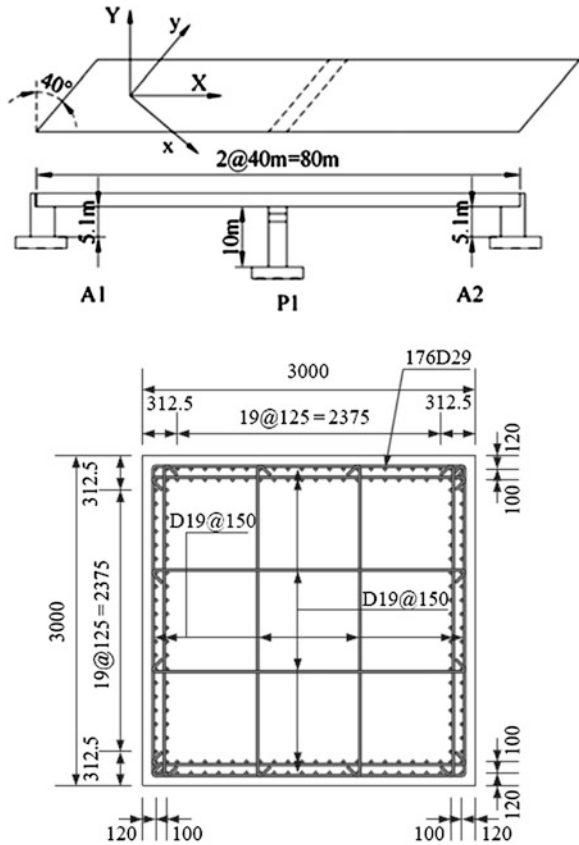
Hsu and Wang [3] and Tirasit and Kawashima [7] investigated the behaviour of reinforced concrete members subjected to bending and torsion, it was concluded that major reductions in flexural strength of the member were exhibited when moderate degrees of torsion was applied. Tirasit and Kawashima [8] suspected the skewed bridge piers to be susceptible to seismic torsion because of the in plane rotation of skewed bridge deck caused by the collision of the deck with the abutments and adjacent spans. The large eccentric impact force due to the locking of bearing movement after failure sharply increases seismic torsion in skewed bridge piers.

This paper presents a parametric study of skewed bridges with varying skew angle and soil condition. Pushover analysis is conducted on varying skew angles of 15°, 30°, 45° and 60° with soft, medium, stiff and rocky soil conditions. Gazetas [2] proposed a set of algebraic formulas to easily compute the stiffness of foundations in a homogeneous half space. The influence of the skew angle and soil condition on the initial stiffness, lateral displacement capacity, maximum base shear, rotation of the deck and torsion in the pier are investigated.

2 Representative Bridge and Modeling

A two-span continuous skewed bridge (skew angle 40°) is chosen to be the representative bridge for the parametric study, similar to the one selected for analysis. The skewed bridge consists of a composite deck with a mass of 1.25 tons supported by 2 reinforced concrete abutments and 1 reinforced concrete pier. The pier denoted by P1 is 10 m high and has a square section of dimensions 3 m × 3 m. The abutments denoted by A1 and A2 are 5.1 m high and have a 2 m × 15.66 m wall section. The compressive strength of concrete used in the piers and abutments is 21 MPa. 29 and 19 mm deformed bars are used in the longitudinal and transverse reinforcement of SD295 grade having a yield strength of 295 MPa. The deck is

Fig. 1 Representative skew bridge and square pier section reinforcement detail [6]



supported by 5 bearings at each of the abutments and pier. The bearings are of 2 types, fixed bearing denoted by FB and movable bearing denoted by MB. The fixed bearing is locked in the longitudinal and transverse direction where as the movable bearing is free in the longitudinal but restrained in the transverse direction. The FB is located at pier and the MB located at both the abutments. The pier is resting on a shallow footing. Figure 1 shows representative diagram of skew bridge and square pier section reinforcement detail [5]. Figure 2 show an idealized figure of skew bridge.

Using the above mentioned base bridge as reference, 5 similar bridges with skew angles of 0°, 15°, 30°, 45°, 60° were appropriately modelled to study the effect of skew angle. The global “X” axis is in the direction joining the abutments and the global “Y” axis perpendicular to the X axis in the plane of the deck, the Z axis is the vertical direction of the bridge. The skew angle is the angle between the normal to the centreline of the bridge and the centreline of the abutment or pier cap. The skewed axis “x” axis and “y” axis is obtained by rotating the global coordinates by the skew angle about the vertical axis. The length and width of the bridge deck was

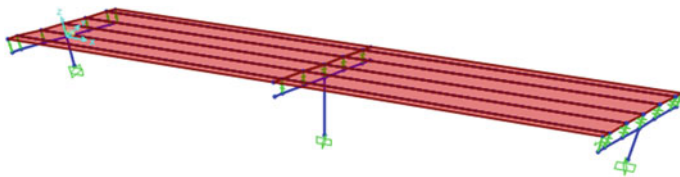


Fig. 2 Representative skew bridge idealization

kept constant while varying the skew angle. The pier, pier cap, abutment and bearings were aligned appropriately to the skewed angle of the deck.

The objective of the modelling is to accurately predict the response of the bridge using a mathematical formulation. The computer program SAP2000 V14.0.1 [1] was used to model the bridges and carry out the required analysis. The modulus of elasticity of the concrete used is 23,000 MPa, the strain at unconfined compressive strength is 0.002 and the ultimate unconfined strain capacity is 0.005. The confined compressive strength is 47.6 MPa at a strain of 0.01. The reinforcing steel used is as per JIS G 3112 having elastic modulus of 200,000 MPa with a yield stress of 295 MPa and an ultimate tensile stress of 440 MPa.

The pier, pier cap, girders and abutment are modelled using frame elements and the deck slabs using shell elements. The bridge superstructure consisting of the pier cap, girder and deck are assumed to remain in the elastic range under seismic force input whereas the pier and abutments under the seismic force input may enter the nonlinear range. The deck modelled as a shell element is given the material properties of concrete and a thickness of 235 mm. The steel girders are I sections of 2.2 m depth and 40 m long which are continuous at the pier. The deck and the girder are discretized to ensure displacement compatibility between the girder and deck at intermediate points. The cap beam is modelled as a frame element with a rectangular cross section and is connected to the deck section through the bearing elements.

The bearings are of 2 types; movable bearing (MB) which is free in the longitudinal direction but restrained in the transverse direction and fixed bearings (FB) which is restrained in both the longitudinal and transverse direction. The bearings are expected to have rupture strength of 574.7 kN with a failure displacement of 1 mm, the stiffness of the bearings are given accordingly.

The pounding between the deck and the abutment is represented by a link element with the corresponding stiffness given

$$k_l = \gamma nEA/L \quad (1)$$

where, EA and L are the axial stiffness and the length of the bridge deck respectively; n is the total number of beam elements on the length L and γ is the stiffness ratio which is equal to 1. EA is 1.217×10^5 MN, L is 80 m and n is 8. The stiffness of the pounding spring is 12,174 MN/m.

The pier is modelled using the frame element in the Section Designer module. Discretization helps approximate the lumped masses at the center of each element to help increase the accuracy of analysis. A similar modelling is carried out for modelling the abutment section.

The pier and abutment are expected to enter the nonlinear range and hence hinge must be defined for each of abutments and pier to account for the plastic deformation in the structure. The length of the plastic hinge is determined using the following expression

$$L_p = 0.08L + 0.022f_{ye}d_{bl} > 0.044f_{ye}d_{bl} \quad (2)$$

where f_{ye} is the yield stress and d_{bl} is the diameter of the rebar used. The length of the plastic hinge for the pier is computed as 1 m and for the wall section is 0.3 m. The lumped plasticity model is adopted for analysis; the hinge is located at the section which is at center of the plastic hinge length.

A user defined interacting P-M-M hinge which is deformation controlled is adopted. The corresponding interaction surface and the moment curvature plots given as input for various axial force values close to the one obtained during analysis.

To account for the soil structure interaction the foundation of the pier is also modelled based on the set of algebraic formulae proposed by Gazetas [2]. Seven different soil conditions; very soft clay, soft clay, medium clay, stiff clay, very stiff clay, hard clay and rocky are adopted to study the effect of soil structure interaction.

Parameters ϕ , γ and σ of the various soil are kept constant where as the c and E of the soil is varied to obtain the different soil conditions. Based on the soil properties and the axial force in the column, bearing strength and dimension of the footing required is calculated. Finally the values of K_x , K_y , K_z , K_{rx} , K_{ry} and K_t are calculated. The corresponding linear springs are assigned at the base of the pier.

3 Analysis and Results

The bridges modeled are analyzed using displacement controlled non linear static analysis or pushover analysis in the longitudinal and transverse direction. The analysis is performed in a load control manner to apply all gravity loads on the structure and then a lateral pushover analysis in a displacement control manner starting at the end of the gravity load case.

As seen in past literature it is reported by Maragakis and Jennings [4] that the planar body rotation of deck due to pounding of deck with abutment is a major source of damage in skew bridges and reported by Ngoc et al. [5] that the bearings of skewed bridges suffer extensive damage resulting in deterioration of the lateral capacity. To study the behavior of the skewed bridge where in there is extensive damage in the bearing leading to deterioration of lateral capacity, the bearings at the abutments are made free to translate in the direction along the abutment that is

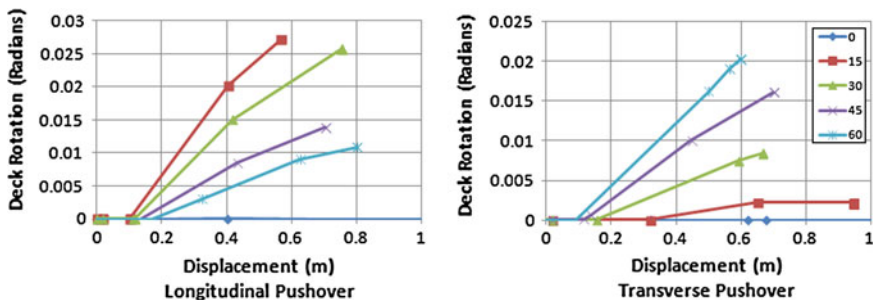


Fig. 3 Deck rotation for 0°, 15°, 30°, 45°, 60° with rocky soil condition

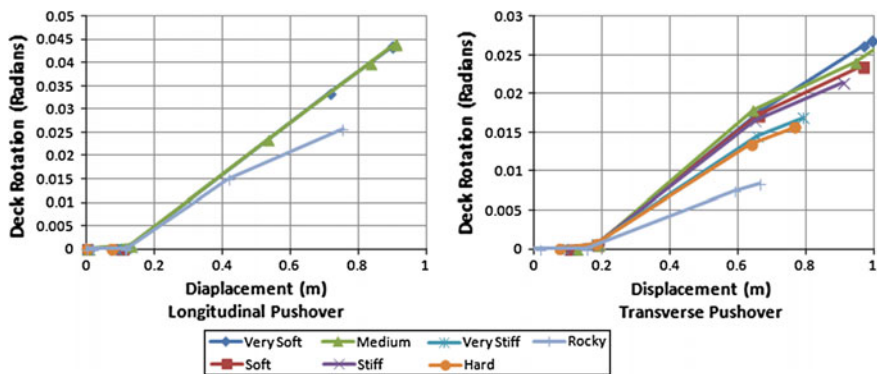


Fig. 4 Deck rotations for 30° skew with varying soil condition

the “y” axis as well, this is also the case for seat type abutments where the deck is not rigidly connected to the abutments.

Figures 3 and 4 show the rotation of the deck for varying skew angles and varying soil conditions. It is observed that the rotation of the deck for a given displacement of the deck in the longitudinal direction decreases with increasing skew. The rotation is highest in the case of 15° and decreases for 30°, 45°, 60°, the rotation is zero for the case of 0° skew angle. The reverse is true in the case of rotation of the deck for transverse pushover with the 60° having the greatest rotation for a given displacement followed by 45°, 30°, 15° and zero in the case of 0° skew angle.

The pounding gap is set as 100 mm, when this gap closes pounding occurs which causes rotation in the deck. In longitudinal pushover the pounding gap first closes in the case of 0° skew angle bridge at a displacement of 100 mm but this does not cause any rotation as there is no contribution of the pounding spring in the transverse direction of the bridge. The pounding gap next closes in the case of 15° skew angle bridge at a displacement of 103.53 mm (100/cos15° mm) then followed by 30°, 45° and 60° skew angle bridge at 115.47, 141.42 and 200 mm respectively. Hence we

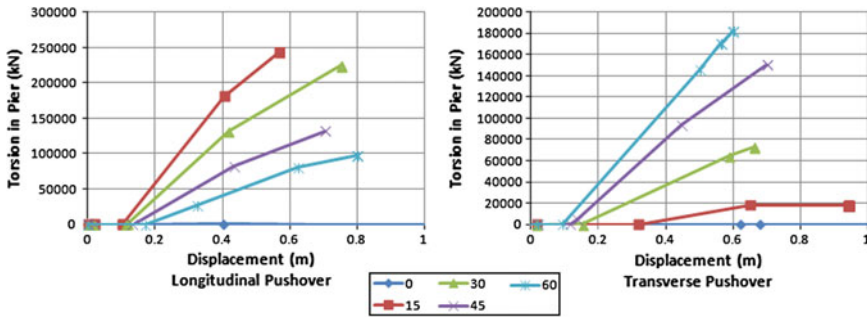


Fig. 5 Torsion in pier for rocky soil condition with varying skew angle

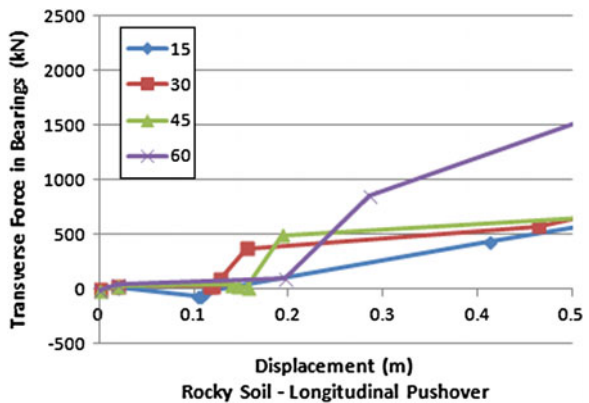
observe that the rotation starts first in the case of 15° followed by 30°, 45° and 60°. In the transverse pushover the order is reversed as the first to close would be 60° skew angle at a displacement of 115.47 mm ($100/\cos(90^\circ - 60^\circ)$ mm) followed by 45°, 30° and 15° at 141.42, 200 and 386.37 mm. Similar trends are observed for the various soil conditions.

The soil condition allows some of the rotation in the deck to be transferred to the foundation through the pier allowing for greater rotation of the deck in softer soils. As the stiffness of the soil increases the resistance of the foundation to rotate increases, providing greater resistance to the rotation of the deck. Hence we observe that deck rotation is the least in the case of rocky foundation and increases as the stiffness of the soil decreases.

Figure 5 compares the torsion developed in the piers for various skew angles for the rocky soil condition. The torsion in the piers is a direct result of the rotation of the deck and hence follows a similar trend for the various skew angles with varying soil condition.

Assuming that there is no deterioration in the lateral strength of the bearings, the bearings at the abutments are fixed in the transverse direction. Figure 6 shows the transverse force in the bearings encountered during the longitudinal pushover. Here

Fig. 6 Transverse force in bearings for varying skew angle in rocky soil condition



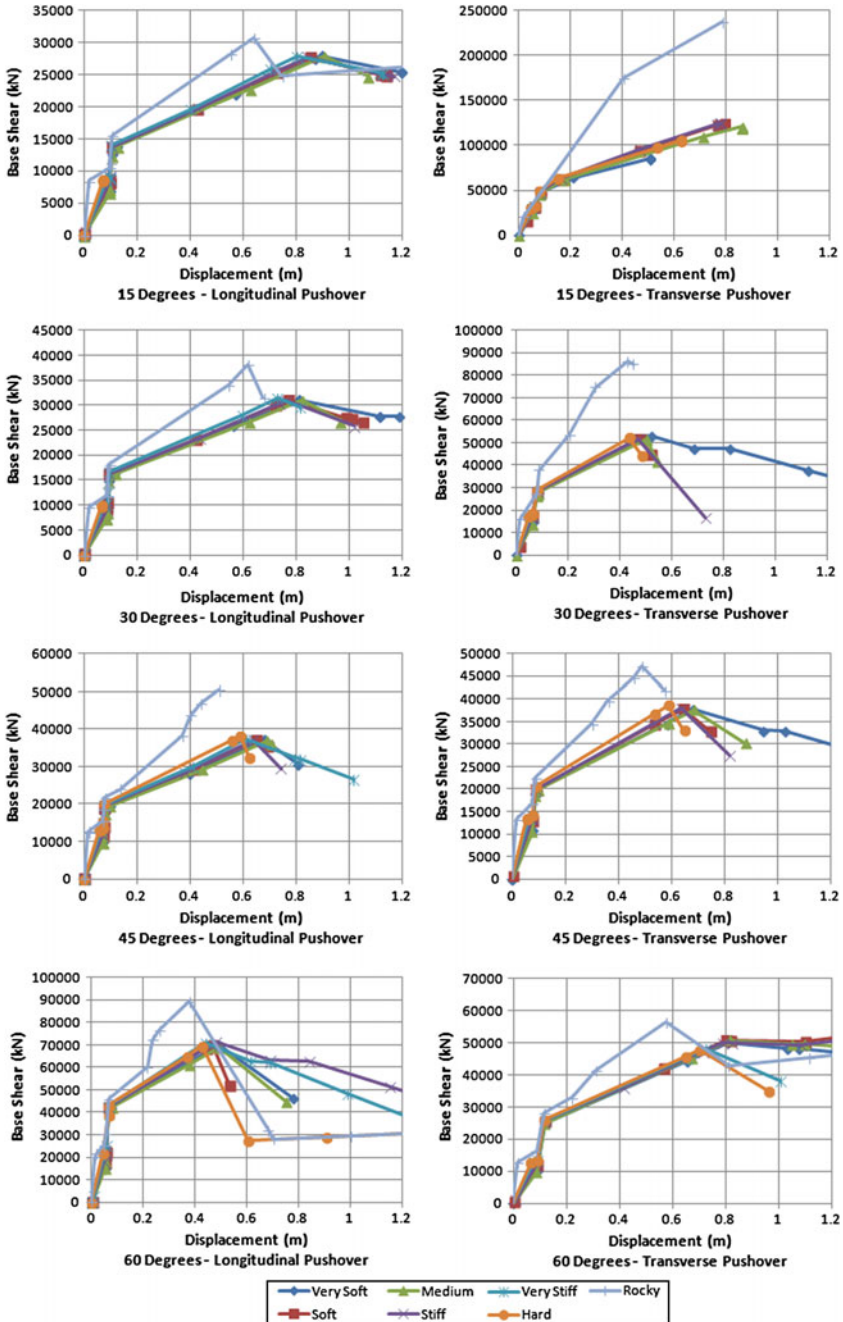


Fig. 7 Longitudinal and Transverse Pushover curves for 15°, 30°, 45°, 60° with varying soil conditions

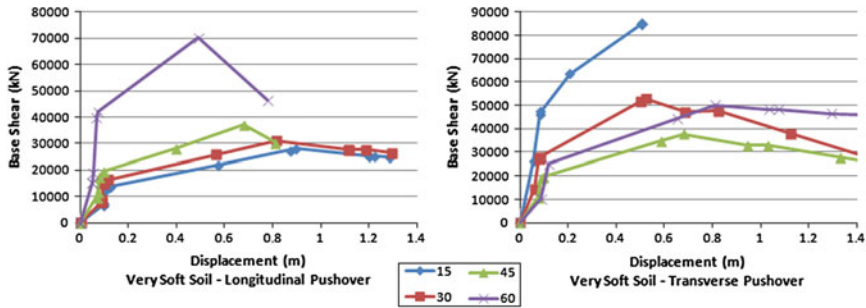


Fig. 8 Pushover curves for very soft soil with varying skew angle

it is observed that the transverse force is not significant until the rotation in the deck takes place. This curve gives us a magnitude of the transverse force that the bearing must be able to sustain based on the level of displacement expected.

The pushover curves for a given skew angle with varying soil conditions are compared in Fig. 8. It is observed here that in the longitudinal pushover when the skew angle is small; the soil condition plays a major role in determining the initial stiffness of the structure, with increasing skew angle this contribution significantly diminishes. The reverse is true in the case of transverse pushover where the soil condition has a greater contribution in the initial stiffness of the structure when the skew angle is high. This behavior may be attributed to the significant contribution of the abutment to the initial stiffness of the structure due to the restraint of the movable bearing along the length of the abutment, at high skew angle during longitudinal pushover and at low skew angles during transverse pushover. It is also observed that in these cases the abutment is entering the plastic zone and displaying plastic rotation by formation of plastic hinge before the pier, supporting the fact that the initial stiffness is governed by the abutment.

The maximum base shears for the various soil conditions are close with an exception of the rocky soil condition. The displacement corresponding to the maximum base shear has a direct relation to the soil condition. For shallow foundations with close dimensions this displacement decreases with the increasing stiffness of the soil. When the dimensions of the foundation vary the displacement depends on the dimension of the foundation and the corresponding elastic spring stiffness obtained i.e. greater the spring stiffness lesser the displacement. This explains the trend when we have shallow footings with close dimensions.

From the pushover curves in Fig. 7, it is also observe that the post maximum base shear stiffness increases in magnitude as the stiffness of the soil increases. The drop is more sudden in the case of rocky and gradual in the case of very soft soil.

In Fig. 8, the pushover curves for very soft soil condition with varying skew angle are compared for longitudinal and transverse pushover. It is observed that during the pushover the case where the abutment has the maximum contribution has the higher initial stiffness and the greatest peak base shear. In the case of transverse pushover the length of the abutment is significantly higher in the case 60° skew

angle and is the reason that it has a higher peak base shear as compared to 45° skew angle. With the decreasing contribution of the abutment the displacement corresponding to maximum base shear increases and the post peak stiffness is more gradual. Similar trends are observed for all the soil conditions.

4 Conclusions

The following salient conclusions are drawn from the present study:

- (1) When the bearing at the abutments have insufficient lateral capacity or get ruptured leading to deterioration in the lateral capacity the rotation in the deck is significant imposing greater torsional demand on the pier. This leads to rotation of the deck at a smaller displacement in case of bridges with smaller skew angles.
- (2) The stiffer the soil condition the greater its capacity to resist rotation of the pier. This induces higher force demand in bridge piers on soft soils.
- (3) The rotation of the deck due to pounding and the soil condition must be taken into account for bearing design for skewed bridges.
- (4) In general for a given skew angle and given soil condition the transverse stiffness is greater for skew angle below 45° and is the reverse when skew angle is greater than 45°.

Acknowledgments The support and resources provided by Department of Civil Engineering, Indian Institute of Technology Guwahati and Ministry of Human Resources and Development, are gratefully acknowledged by the authors.

References

1. CSI (2011) SAP2000 structural analysis program V14.0. Computers and Structures Inc., California, USA
2. Gazetas G (1991) Formulas and charts for impedances of surface and embedded foundations. *J Geotech Eng ASCE* 117(9):1363–1381
3. Hsu H-L, Wang C-L (2000) Flexural-torsional behavior of steel reinforced concrete members subjected to repeated loading. *Earthq Eng Struct Dyn* 29:667–682
4. Maragakis EA, Jennings PC (1987) Analytical models for the rigid body motions of skew bridges. *Earthq Eng Struct Dyn* 15:923–944
5. Ngoc LA, Tirasit P, Kawashima K (2008) Seismic performance of a skewed bridge considering flexure and torsion interaction. In: *Proceedings of the 14th world conference on earthquake engineering*, 12–17 Oct 2008, Beijing, China
6. Priestley MJN, Seible F, Calvi GM (1996) *Seismic design and retrofit of bridges*. Wiley, New York
7. Tirasit P, Kawashima K (2007) Seismic performance of square reinforced concrete columns under combined cyclic flexural and torsional loadings. *J Earthq Eng* 11:425–452

8. Tirasit P, Kawashima K (2008) Effect of nonlinear seismic torsion on the performance of skewed bridge piers. *J Earthq Eng* 12:980–998
9. Watanabe G, Kawashima K (2004) Effectiveness of cable-restrainer for mitigating rotation of a skewed bridge subjected to strong ground shaking. In: 13 WCEE, Vancouver, B.C., Canada, p 789 (CD-ROM)

Part XIV
Wind Induced Vibration Response
of Structures

Shape Memory Alloy-Tuned Mass Damper (SMA-TMD) for Seismic Vibration Control

Sutanu Bhowmick and Sudib K. Mishra

Abstract Tuned-Mass-Damper (TMD) is a passive control device for vibration control of structures. However, the requirement of higher mass ratio restricts its applicability for seismic excitations. The improved performance of TMD is attempted herein by supplementing it with nonlinear restoring devices made of Shape-Memory-Alloy (SMA) (hence referred as SMA-TMD), motivated by its energy dissipation capability through micro-structural phase transitional hysteresis under cyclic loading. Extensive numerical simulations are conducted based on nonlinear random vibration analysis. A design optimization based on minimizing the root mean square displacement of the main structure is also carried in search for the optimal design parameters, latter validated through its performance under recorded ground motions. Significant improvements of the control efficiency and reduction of TMD displacement at a much reduced mass ratio is achieved by the SMA-TMD.

Keywords Tuned mass damper · Shape memory alloy · Vibration control · Earthquake · Optimization

1 Introduction

The potential of Tuned Mass Damper (TMD) in reduction of vibration effects of structures under various type of excitations is well established [1] and was successfully implemented to many well known structures, such as the Citicorp Center (New York), John Hancock Tower (Boston), Funade Bridge Tower (Osaka), CN Tower (Toronto) and Taipei 101 (Taipei) are to mention a few. A summary of these applications is illustrated by Lee et al. [2].

S. Bhowmick · S.K. Mishra (✉)
Department of Civil Engineering, Indian Institute of Technology,
Kanpur 208016, Uttar Pradesh, India
e-mail: smishra@iitk.ac.in

The TMD is composed of a mass, damping device and a restoring mechanism with which it is attached to the primary structure intended for vibration control. The frequency of the TMD is tuned to the fundamental mode of the structure, so that at the exciting frequency the TMD will resonate out of phase with respect to the structural motion. This allows transferring the kinetic energy from the main structure to the TMD which is subsequently dissipated through viscous damping. Although the frequency and damping ratio of TMD are important parameters to influence the controlled response of the structure, the mass ratio also play significant role.

The studies on optimal design of TMD with linear spring and viscous damping are well established. Neglecting damping of structures, Den Hartog stipulates formulas for choosing the optimum damping and stiffness for the TMD for given mass ratio [3]. A single-degree-of-freedom-system (SDOF) with a linear TMD subjected to white-noise base excitation was analyzed by Crandall and Mark [4]. Design formulas for optimum parameters for linear TMD were derived by Fujino and Abe [5]. Bakre and Jangid [6] has studied the optimum damping and tuning ratio of a linear TMD attached to a SDOF system subjected to both external loads and base excitations. Noting that a single TMD can only be optimally tuned to the fundamental mode of a structure, multiple TMDs have been proposed [7–10] to suppress higher modes of vibration.

It is relatively recent that the TMD has been supplemented by nonlinear hysteretic damper for enhanced dissipation of vibration energy. Inaudi and Kelly [11] proposed friction dampers as a mean of energy dissipation in TMD. Performance and design optimization of TMD with nonlinear viscous damper under random white noise excitation has been studied by Rudinger [12]. Unlike linear TMD, the optimal characteristics of nonlinear TMDs depend on the intensity of excitations. The effectiveness of TMD supplemented by elasto-plastic restoring mechanism is investigated by Jaiswal et al. [13]. It is demonstrated that such TMD shows frequency-sensitive characteristics and are found to be more effective than the conventional TMD only in certain range of the exciting frequencies.

TMDs have been proven effective in suppressing vibrations induced by narrow band excitations such as wind loads in tall buildings and traffic loads in bridges. In fact, the applicability of TMDs in tall buildings is primarily in view of the response control under wind loading. The effectiveness of TMD in suppressing broadband excitations, such as earthquake induced motion is still debated [14, 15]. A general observation is that the mass ratio of the TMD needs to be much higher (5–8 %) for being effective in seismic environment [16]. However, the requirement of such higher mass ratio restricts its applicability for seismic vibration control of civil engineering structures. In this regard, the ability of Shape Memory Alloy (SMA) in dissipating the input energy through hysteretic phase transformation of its micro-structure under cyclic loading is notable [17–19]. Thus, a TMD system supplemented with SMA is expected to be more effective in seismic vibration control. Moreover, the relative motion of TMD with respect to main mass is also an important aspect in view of restraining the extended physical limits of TMD [20–22]. A penalty is imposed on the control effort to obtain controllers for a range of

displacement amplitudes for system with space constraint [20–22]. It is also expected that due to its force-deformation characteristic, the SMA-spring might reduce the displacement of the TMD largely, which could be much lesser than that experienced by the conventional linear-TMD.

With above in view, an attempt has been made in the present study to explore the improved performance possible to achieve by TMD system supplemented with SMA in controlling earthquake induced vibration of structures in passive mode. This is also compared with the conventional linear TMD through extensive numerical simulations.

2 Force-Deformation Behavior of SMA

The property of SMA that is indeed of interest is the super-elasticity. This property is discussed with reference to the plot in Fig. 1a, b. The SMA remains in Austenite phase (OA) above certain range of temperature. While loaded, the Austenite SMA starts transforming into Martensite (AB), resulting in a stress-plateau (AB). The force required to trigger the Austenite to Martensite phase transition, corresponding to point A is called the (forward)-transformation strength, denoted as F_{ys} . This is an important parameter to govern the behavior of SMA-based system. The gradual transition in its microstructure from the Austenite to Martensite phase is completed at the end of this plateau (B). At any instant, the fraction of Martensite is denoted as ξ (Fig. 1b). On further loading, fully transformed Martensite again shows evidence of further hardening (BC). During unloading (CD), the Martensite SMA recovers its deformation by gradual backward transformation from the Martensite to Austenite (DE), which is accompanied by decreasing fraction of Martensite (ξ). The saturation and depletion of the Martensite is attained on completion of phase transition, indicated by point B and E. It is noted that no residual displacement is left after completion of the back-transformation through unloading. Two important characteristics of the flag-shaped hysteresis of SMA are (1) the hysteresis loop is fat

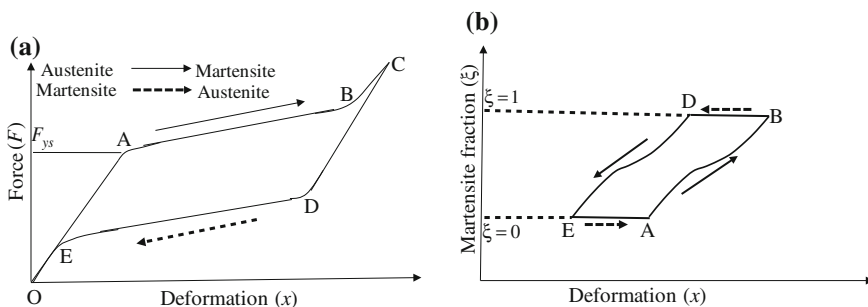


Fig. 1 Schematic **a** load-deformation behavior of superelastic SMA and **b** respective phase transition in its microstructure

enough to dissipate the input seismic energy and (2) the loop leaves no residual displacement on unloading.

The hysteresis of SMA has been characterized by the Graesser-Cozzarelli model [23, 24] expressed as

$$\dot{F}_{sh} = k_s \left[\dot{x}_s - |\dot{x}_s| \left| \frac{F_{sh} - \beta}{F_{ys}} \right|^{\eta-1} \left(\frac{F_{sh} - \beta}{F_{ys}} \right) \right] \quad (1)$$

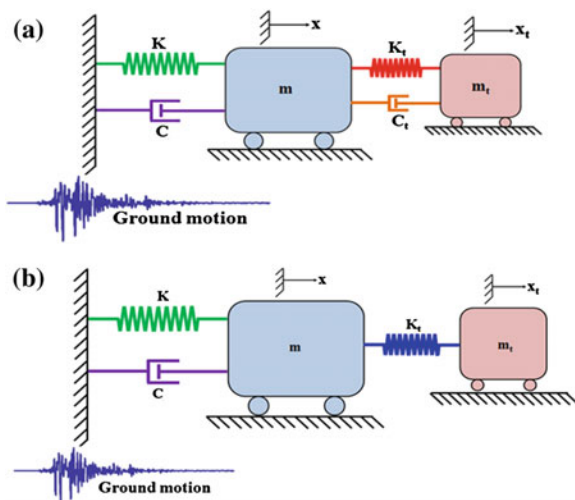
$$\beta = k_s \alpha_s \left[x_s - \frac{F_{sh}}{k_s} + f_T |x|^{c'} \operatorname{erf}(a' x_s) \right] \quad (2)$$

in which F_{sh} is the restoring force, x_s is the displacement, k_s is the initial stiffness of SMA in the Austenite phase (OA), F_{ys} is the force triggering the forward-transformation from the Austenite to Martensite (point A in Fig. 1a) i.e. the transformation strength. The force required for transformation can be viewed as equivalent to the ‘yield’ force in elasto-plastic hysteresis. The parameter α_s is a constant determining the ratio of post (AB) to pre (OA) transformation stiffness. This is analogous to the post to pre-yield stiffness in bilinear hysteretic system, which is referred as rigidity ratio. The parameter a' controls the amount of recovery through backward transformation from Martensite to Austenite by unloading. The parameter η controls the sharpness of the forward and reverse transition. The parameter c' decides the slope of unloading path (DE) which is parallel to the force plateau (AB). The dot over a symbol denotes its time derivative. The quantity $|x_s|$ is the absolute value of x_s and $\operatorname{erf}(x_s)$ is the error function with argument x_s , parameter β is one-dimensional back stress given by Eq. (2). The quantity f_T controls the type and size of hysteresis. For $f_T = 0$, the Graesser-Cozzarelli model merges to the Bouc-Wen model.

3 Dynamic Analysis of SMA-TMD System

A structure, idealized as a SDOF system and equipped with the SMA-TMD is adopted for analysis, as shown in Fig. 2b. The same structure with conventional TMD is also shown in Fig. 2a. As the control strategy reduces the response of the structure substantially, the behavior of the controlled structure is reasonably assumed to be linear. The equation of motion of the structure-linear TMD is well established and can be obtained from the literature [6, 16, 20, 21] and is not presented herein. However, the formulation for the structure supplemented with SMA-TMD is presented. The equations of motion of a linear SDOF system assisted by the SMA-TMD (Fig. 2b) are written as

Fig. 2 SDOF model equipped with **a** linear TMD and **b** SMA-TMD



$$m \ddot{x} + c \dot{x} + kx - F_s(x_t, x, \dot{x}_t, \dot{x}) = -m \ddot{x}_g \tag{3a}$$

$$m_t \ddot{x}_t + F_s(x_t, x, \dot{x}_t, \dot{x}) = -m_t \ddot{x}_g \tag{3b}$$

where m, m_t are the mass of the structure and TMD respectively. The elastic stiffness of the structure and viscous damping are denoted by k and c respectively. The relative displacement of the structure and TMD with respect to the ground is given by x, x_t respectively. Respective velocities and accelerations are denoted as \dot{x}, \dot{x}_t and \ddot{x}, \ddot{x}_t . The ground acceleration of earthquake is denoted by \ddot{x}_g . The restoring force developed in the SMA spring attached to the TMD is given by $F_s(x_t, x, \dot{x}_t, \dot{x})$. Due to nonlinearity of the SMA spring, the restoring force is a nonlinear function of the relative displacement and velocity of the TMD with respect to the structure. Adopting stochastic linearization of SMA, this can be simplified as

$$F(x_t, x, \dot{x}_t, \dot{x}) = \alpha_s k_s (x_t - x) + (1 - \alpha_s) \{ C_{es} (\dot{x}_t - \dot{x}) + K_{es} (x_t - x) \} \tag{4}$$

where the equivalent stiffness and damping parameters are obtained by minimizing the mean square error between the actual model and its linearized version, details of which can be obtained from Yan and Nie [25].

On substituting Eq. (4) in the Eqs. (3a) and (3b), the equations becomes

$$[M] \{\ddot{u}\} + [C] \{\dot{u}\} + [K] \{u\} = -[M] \{r\} \ddot{x}_g \tag{5}$$

where $[M], [C]$ and $[K]$ are the combined mass, damping and stiffness matrix for the structure-TMD system. The vector of displacement is given by $\{u\} = \{x \quad x_t\}^T$

and so is the vector of velocity and acceleration. The system properties are conveniently normalized as

$$\mu = m_t/m; \quad \gamma = \omega_t/\omega \quad (6a)$$

where μ, γ are the mass and frequency ratio of the TMD. The transformation strength of SMA spring (F_s) is also normalized w.r.t its weight ($m_t g$) as

$$F_0 = F_{ys}/(m_t g) \quad (6b)$$

The frequency of the structure (ω) and the TMD (ω_t) are expressed as

$$\omega = \sqrt{k/m} \quad (7a)$$

$$\omega_t = \sqrt{\alpha_s k_s/m_t} \quad (7b)$$

The pre-transformation stiffness of the SMA-spring is determined as

$$k_s = F_0 m_t g / u_{ys} \quad (8)$$

where u_{ys} is the displacement corresponds to the forward phase transition in the SMA spring.

A widely adopted model for stationary ground motion (\ddot{x}_g) is obtained by filtering a white noise process acting at the bed rock through a linear filter representing the ground. This is the well-known Kanai-Tajimi stochastic model [26, 27] for the input frequencies of earthquakes for wide range of practical situations. The filter equations are expressed as

$$\ddot{x}_f + 2\zeta_f \omega_f \dot{x}_f + \omega_f^2 x_f = -\ddot{w} \quad (9)$$

$$\ddot{x}_g = -2\zeta_f \omega_f \dot{x}_f - \omega_f^2 x_f \quad (10)$$

in which \ddot{w} is the white noise intensity at the rock bed with power spectral density S_0 . The parameter ω_f and ζ_f are the frequency and damping of the soil strata respectively. \ddot{x}_f , \dot{x}_f and x_f are the acceleration, velocity and displacement response of the filter. The Kanai-Tajimi model of seismic motion is introduced by substituting expression of \ddot{x}_g from Eq. (10) in Eq. (5). The state vector $\{Y\}$ for the system is then defined as

$$\{Y\} = \{ \{u\} \quad x_f \quad \{\dot{u}\} \quad \dot{x}_f \}^T \quad (11)$$

This is in order to write the equations of motions in the state space form as

$$\frac{d}{dt}\{Y\} = [A]\{Y\} + \{w\} \quad (12)$$

where $[A]$ is the augmented system matrix and $\{w\} = \{ \{0\} \quad 0 \quad \{0\} \quad -\ddot{w} \}^T$ is a vector containing the terms of the intensity of the rock bed white noise. The evolution equation for the covariance matrix $[C_{YY}]$ of the state vector $\{Y\}$ is given by Tajimi [28]

$$\frac{d}{dt}[C_{YY}] = [A][C_{YY}]^T + [C_{YY}][A]^T + [S_{ww}] \quad (13)$$

$[S_{ww}]$ is the input matrix of the rock bed excitations. Following the structure of the vector $\{w\}$, the matrix $[S_{ww}]$ has all terms zero except the last diagonal as $2\pi S_0$. The RMS response are obtained from the covariance of the response as

$$\sigma_{Y_i} = \sqrt{C_{Y_i Y_i}} \quad (14)$$

Quite often the RMS response of the controlled structure (σ_x) is conveniently normalized with respect to the respective response of the uncontrolled structure (σ_x^{uc}).

4 Optimization of SMA-TMD System

It is known that for a conventional linear TMD with a given mass ratio (μ), the frequency ratio (γ) and the damping of the TMD $\{\xi_t\}$ are the two important parameters to control the efficiency of vibration reduction [5], expressed in terms of the normalized response. The associated optimization problem is stated as

$$\text{Find } [\gamma \quad \xi_t]^T \text{ to minimize } \bar{\sigma}_x \quad (15)$$

For SMA-TMD these design parameters are replaced by the frequency ratio (γ) and the normalized transformation strength (F_0) of the SMA spring. This leads to an optimization problem, stated as

$$\text{Find } [\gamma \quad F_0]^T \text{ to minimize } \bar{\sigma}_x \quad (16.a)$$

In the present study, the Unconstrained Optimization is solved to obtain the optimal characteristics of the SMA-TMD system. The displacement of the TMD is shown to reduce to a large extent from the conventional linear TMD.

The consistency of optimal response behavior of SMA-TMD, as addressed in the previous section is further studied by evaluating their performance under recorded ground motions of real earthquakes. A set of recorded accelerations are selected to evaluate the nonlinear time history responses. This involves integrating the dynamic equations of motions (Eq. 5) for the structure-TMD system. The Newmark beta method with average acceleration is employed in order to integrate the equations of motion. The scheme efficiently incorporates the flag shape hysteresis of the SMA spring. The time steps adopted is sufficiently low (0.0001 s) to ensure stability and accuracy of the scheme. The time histories of the displacement and acceleration of the structure and the displacement of the TMD are obtained as the response quantities of interest from this analysis.

5 Numerical Illustration

A typical configuration of the structure-TMD system is considered for numerical elucidation of the improved performance of the proposed SMA-TMD. The adopted system properties and the ground motion parameters are listed in Table 1.

The response behavior and the optimal choice of TMD parameters are presented in this section. The comparison among the performances of the SMA-TMD and conventional linear TMD is also presented. The variation of responses for different frequency ratio of the TMD is shown in Fig. 3a, b. It is observed that, as in linear TMD, an optimal frequency ratio minimizes the controlled displacement of the structure to maximize the control efficiency. Comparing the RMS displacement of the structure (Fig. 3a) corresponding to optimal frequency ratio, it is clearly observed that the SMA-TMD leads to much higher control efficiency than the conventional linear TMD. This could be as high as 40 %. Comparison among the RMS displacements of the TMD (Fig. 4b) also implies that the SMA-TMD largely reduces the displacement of the TMD than the linear TMD, which is around 20 %. Thus, it appears that the proposed SMA-TMD not only improve the control efficiency but also helps in reducing the TMD-displacement. The optimal frequency ratio also corresponds to the maximum displacement of the TMD, which implies

Table 1 Forensic metadata in network video analytics

Properties of the structure	Properties of the TMD		Ground motion parameters
	Linear TMD	SMA-TMD	
Time period = 1.5 s Damping ratio = 3 %	Tuning ratio = 0.96 Damping ratio = 7 % Mass ratio = 2.5 %	Tuning ratio = 0.885 Transformation strength = 0.35 Mass ratio = 2.5 % Hysteresis of SMA $\alpha_s = 0.10$; $a = 0.005\text{m}$ $f_T = 0.07$; $c' = 0.001$; $a' = 2500$; $\eta = 3$	$\omega_f = 9\pi \text{ rad/s}$ $\xi_f = 0.6$ $S_0 = 0.05 \text{ m}^2/\text{s}^3$

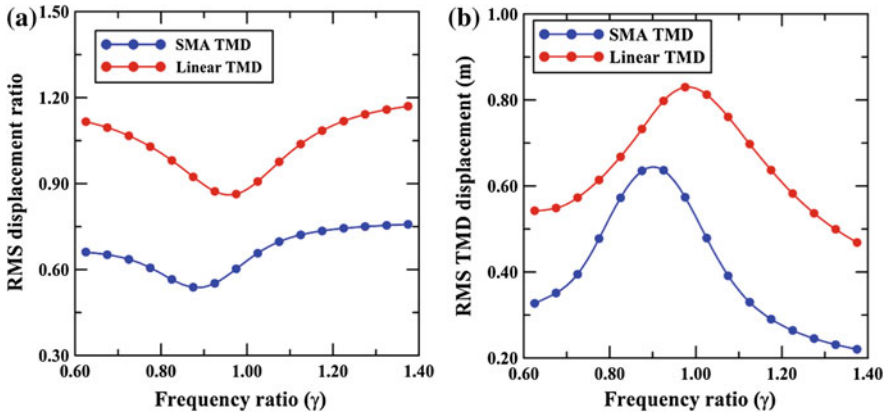


Fig. 3 a Normalized displacement of structure and b displacement of the conventional TMD and SMA-TMD under different frequency ratios

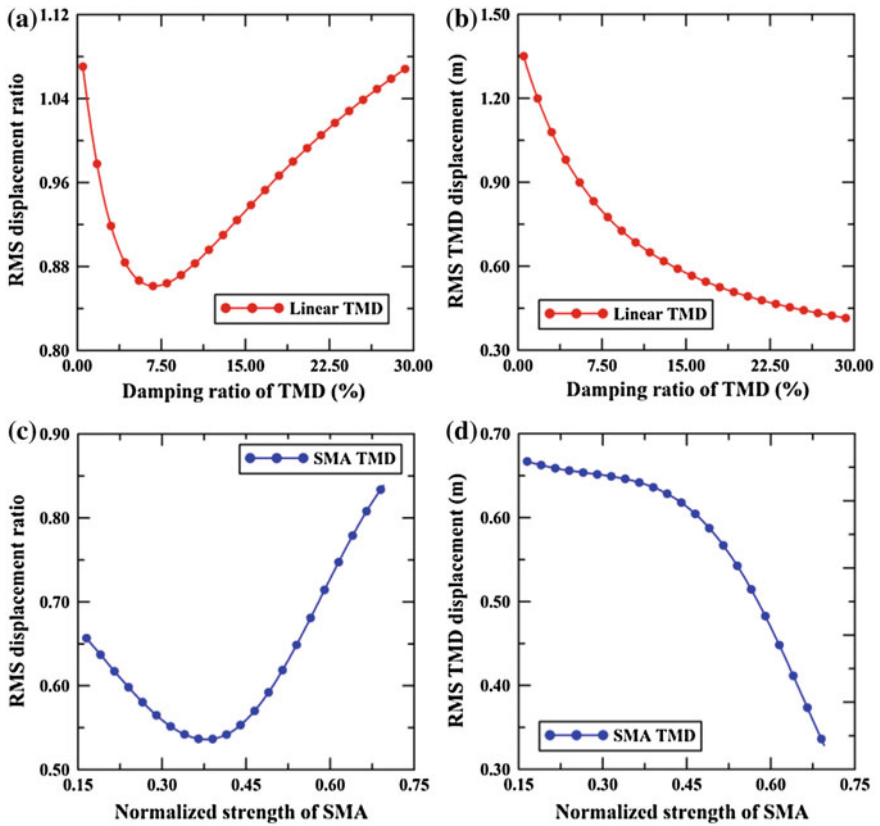


Fig. 4 a Normalized displacement of structure and b displacement of the linear TMD for different damping ratios. The variations of the normalized displacement of the c structure and d SMA-TMD under varying transformation strength of the SMA spring

that better control efficiency is achieved only at the expense of larger displacement of the TMD. Therefore, the displacement of the structure and the TMD consists two mutually conflicting objectives in optimizing such system. However, the latter criterion is often overruled [17–19].

Similar to the effect of frequency ratio; the effect of damping of linear TMD and transformation strength of the SMA-TMD is assessed on the performance of the structure-TMD system. The viscous damping in linear TMD is characterized by its damping ratio. It is mentioned that the transformation strength (which is analogous to the yield strength in the hysteretic damper) of the SMA spring dictates the hysteretic damping in the SMA-TMD. This is because the hysteresis in SMA is induced by the micro-structural phase transition, which is governed by its transformation strength. The variation of responses with varying viscous damping in linear TMD is shown in Fig. 4a, b and similar variations for the SMA-TMD for different values of its transformation strengths are shown in Fig. 4c, d.

Similar to the optimal frequency ratio, the optimal damping ratio maximizes the control efficiency for linear TMD as shown in Fig. 4a. As shown in Fig. 4c, the role of optimum damping ratio is analogously switched to the optimal transformation strength of the SMA spring in order to maximize the control efficiency of the SMA-TMD. Comparing the respective responses of the controlled structure and the TMD, it can be pointed out that the SMA-TMD increases the control efficiency to a large extent and also simultaneously reduces the displacement of the TMD. The existence of the optimal damping ratio/transformation strength can be explained from the variations of the respect PSDF with different damping/transformation strength.

The preceding discussions clearly indicate that, whereas the optimal parameters for the conventional TMD are the frequency ratio and viscous damping of the TMD, the SMA-TMD is dictated by the frequency ratio and the transformation strength of the SMA spring. An important factor to affect these values is the mass ratio of the TMD. Therefore the optimal choices of the frequency ratio, damping ratio for the linear TMD and the frequency ratio, transformation strength for the SMA-TMD are presented for different mass ratios of the TMD along with the optimal response behavior in Table 2. It can be observed from here that almost identical efficiency can be achieved with a mere 1 % mass ratio in SMA-TMD,

Table 2 Comparison of optimal responses for varying mass ratios

Mass ratios (%)	Displacement ratio of structure (m)			TMD displacement (m)		
	SMA-TMD	Linear TMD	Response reduction (%)	SMA-TMD	Linear TMD	Response reduction (%)
1.25	0.6374	1.0022	36.4	1.025	1.523	32.7
2.50	0.566	0.9075	37.6	0.642	0.802	19.9
3.75	0.527	0.8492	37.9	0.479	0.600	20.1
5.0	0.503	0.8073	37.7	0.386	0.504	23.4
6.25	0.489	0.7754	36.9	0.324	0.448	27.7

whereas the conventional TMD would require more than 6 %. The SMA-TMD seems to show potential for practical application in seismic control of civil engineering structure.

The viability of the facts established through the previous stochastic analysis is also verified by subjecting the structure-TMD system to a set of real recorded earthquake motions. A set of real earthquake motions listed in Table 3 are employed for the transient response analysis. The salient characteristics of the motions, such as peak ground acceleration (PGA), dominant periods (frequency content) are shown in this Table. These parameters primarily govern the dynamic response behavior. Also, these motions pertain to widely varying geological fault conditions. The characteristic variability of these motions can be visualized from their respective acceleration response spectra, not shown herein.

A typical time history responses of the structure-TMD system is shown under the 1989 Loma Prieta earthquake motion (GM3). The displacement time history of the structure and TMDs are shown in Fig. 5a, b respectively. These responses are also compared with the responses of the uncontrolled structure. The hysteretic force-deformation characteristic for both the SMA-TMD and linear TMD are shown in Fig. 5a, c. These show that the SMA-TMD largely reduces the structural displacement than the linear TMD. The displacement of TMD is also observed to be largely reduced. It is important to note that, even though the reduction of displacement in SMA-TMD was signaled in stochastic analysis, it was not that significant magnitude, which might be attributed to the error in stochastic linearization. Additionally, comparison among the force-deformation behavior under earthquake loading in Fig. 5c clearly indicates to the enhanced hysteretic dissipation through the micro structural phase transition of SMA, which is key to the better control efficiency of the SMA-TMD over linear TMD. It is also important to note that unlike many other nonlinear TMDs, such as nonlinear viscous, friction TMD, the SMA-TMD does not leave any residual displacement after the loading cycles [8–10]. This is an important aspect of the flag-shaped hysteresis offered only by SMA.

Table 3 Set of ground motion time histories selected for response evaluation

Serials	Earthquake	Year	Station	PGA (g)	Dominant period (s)
GM1	Imperial valley	10/15/1979	El Centro array 5, 230	0.379	0.39
GM2	Kocaeli	08/17/1999	Yarimca 060 (Koeri)	0.268	0.45, 0.54, 0.60
GM3	Loma Prieta	10/18/1989	LGPC, 000	0.563	0.47, 0.64, 0.70
GM4	Northridge Sylmar	01/17/1994	Sylmar-Converter	0.897	0.59, 0.84
GM5	Superstition hills	11/24/1987	PTS, 225	0.455	0.28, 0.64
GM6	Erzikan	03/13/1992	Erzikan N-S comp	0.515	0.29
GM7	Duzce	11/12/1999	Duzce, 180 (ERD)	0.348	0.41

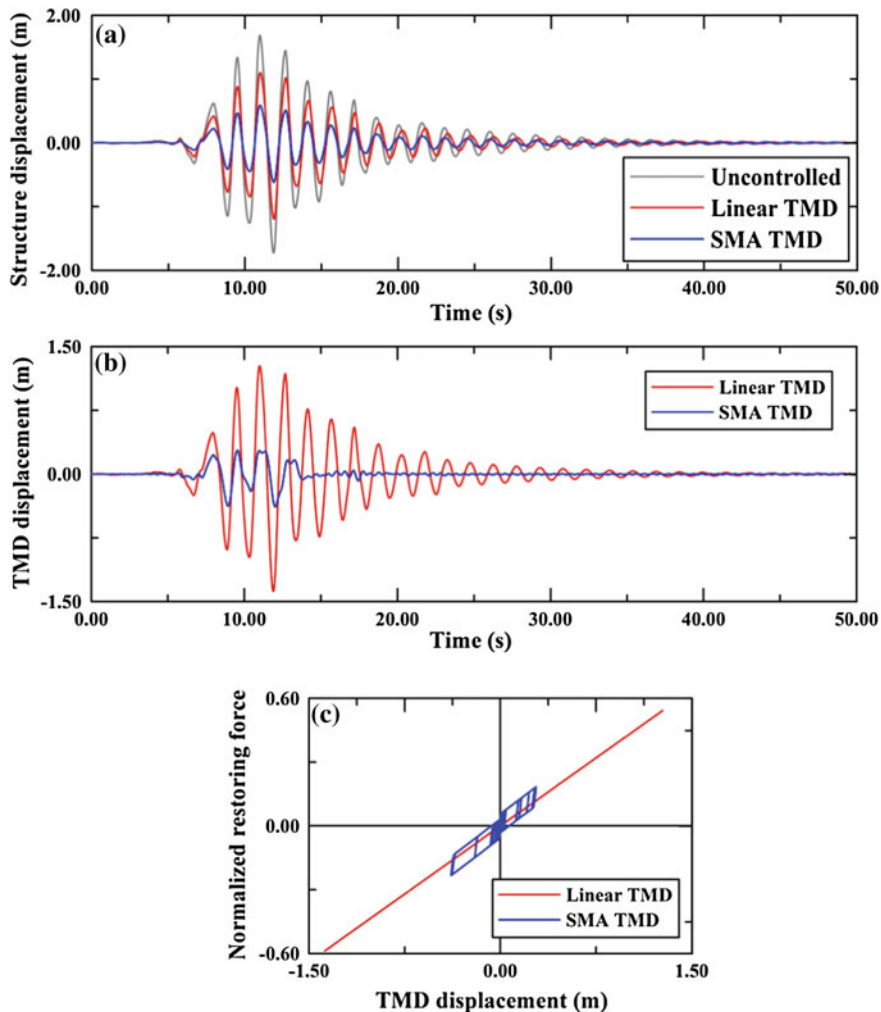


Fig. 5 Time history of displacement of the **a** structure **b** TMD and respective **c** force-deformation hysteresis of the linear TMD and the SMA-TMD controlled structure

6 Conclusion

An improved version of the conventional linear TMD has been presented in this work by replacing the linear spring and viscous damper with a spring made of SMA, referred as SMA-TMD. The superior performance of the SMA-TMD over the conventional linear TMD is established through simulations. The proposed SMA-TMD is shown to significantly enhance the control efficiency and simultaneously

reduce the displacement of the TMD itself. For identical control efficiency, the required mass ratio in SMA-TMD is also shown to be much less than the linear TMD. The important parameters affecting the performance of the SMA-TMD are identified as the frequency ratio and the transformation strength of the SMA-spring. A design optimization is also carried out in order to propose the optimal choice of these parameters to ensure best performance. The superiority of the SMA-TMD is also verified under real earthquakes by nonlinear dynamic analysis of the structures equipped with the optimal TMD. Due to unique hysteresis behavior of SMA, the SMA-TMD almost eliminates the residual displacement of the TMD.

Acknowledgments The financial support provided through the Fast Track Research Grant (SR/FTP/ETA-35/2012) for young investigators by the Department of Science and Technology, under Ministry of Science and Technology, Government of India is greatly acknowledged.

References

1. Ormondroyd J, Den Hartog JP (1928) The theory of the vibration absorber. *Trans Am Soc Mech Eng* 49:9–22
2. Lee CL, Chen YT, Chung LL, Wang YP (2006) Optimal design theories and applications of tuned mass dampers. *Eng Struct* 28:43–53
3. Den Hartog JP (1934) *Mechanical vibrations*. McGraw Hill, The Maple Press Company, New York, pp 93–105
4. Crandall SH, Mark WD (1973) *Random vibration in mechanical systems*. Academic Press, New York
5. Fujino Y, Abe M (1993) Design formulas for mass dampers based on a perturbation technique. *Earthq Eng Struct Dynam* 22:833–854
6. Bakre SV, Jangid RS (2007) Optimum parameters of tuned mass damper for damped main system. *Struct Control Health Monit* 14:448–470
7. Bandivadekar TP, Jangid RS (2013) Optimization of multiple tuned mass dampers for vibration control of system under external excitation. *J Vib Control*. doi:[10.1177/1077546312449849](https://doi.org/10.1177/1077546312449849)
8. Lin CC, Wang JF, Lien CH, Chiang HW, Lin CS (2010) Optimum design and experimental study of multiple tuned mass dampers with limited stroke. *Earthq Eng Struct Dynam* 39:1631–1651
9. Soheili S, Farshidianfar A (2013) Ant colony optimization of tuned mass dampers for earthquake oscillations of high-rise structures including soil-structure interaction. *Soil Dynam Earthq Eng* 51:14–22
10. Bekdaş G, Nigdeli SM (2011) Estimating optimum parameters of tuned mass dampers using harmony search. *Eng Struct* 33:2716–2723
11. Inaudi JA, Kelly JM (1995) Mass damper using friction-dissipating devices. *J Eng Mech ASCE* 121:142–149
12. Rudinger F (2006) Optimal vibration absorber with nonlinear viscous power law damping and white noise excitation. *J Eng Mech* 132:46–53
13. Jaiswal OR, Chaudhari JV, Madankar NH (2008) Elasto-plastic tuned mass damper for controlling seismic response of structures. In: *The 14th world conference on earthquake engineering*, Beijing, China
14. Hoang N, Fujino Y, Warnitchai P (2008) Optimal tuned mass damper for seismic applications and practical design formulas. *Eng Struct* 30:707–715

15. Casciati F, Giuliani F (2009) Performance of multi-TMD in the towers of suspension bridges. *J Vib Control* 15:821–847
16. Adam C, Furtmuller T (2010) Seismic performance of tuned mass dampers In: *Mechanics and model-based control of smart materials and structures*, Springer, Vienna, pp 11–18
17. Ozbulut OE, Hurlbaeus S, Desroches R (2011) Seismic response control using shape memory alloys a review. *J Intell Mater Syst Struct* 22:1531–1549
18. Dolce M, Cardone D, Marnetto R (2000) Implementation and testing of passive control devices based on shape-memory alloys. *Earthq Eng Struct Dynam* 29:945–968
19. Dolce M, Cardone D (2001) Mechanical behavior of shape memory alloys for seismic applications 2 austenite NiTi wires subjected to tension. *Int J Mech Sci* 43:2657–2677
20. Kasturi P, Dupont P (1998) Constrained optimal control of vibration dampers. *J Sound Vib* 215:499–509
21. Son YK, Savage GJ (2007) Optimal probabilistic design of the dynamic performance of a vibration absorber. *J Sound Vib* 307:20–37
22. Chakraborty S, Debbarma R, Marano GC (2012) Performance of tuned liquid dampers considering maximum liquid motion in seismic vibration control of structures. *J Sound Vib* 331:1519–1531
23. Graesser EJ, Cozzarelli FA (1991) Shape memory alloys as new materials for a seismic isolation. *J Eng Mech ASCE* 117:2590–2608
24. Tiseo B, Concilio A, Ameduri S, Gianvito A (2010) A shape memory alloys based tunable dynamic vibration absorber for vibrational control. *J Theor Appl Mech* 48:135–153
25. Yan X, Nie J (2000) Response of SMA superelastic systems under random excitation. *J Sound Vib* 238:893–901
26. Kanai K (1957) Semi-empirical formula for the seismic characteristics of the ground. *Bull Earthq Res Inst Univ Tokyo* 35:309–325
27. Tajimi HA (1960) Statistical method of determining the maximum response of a building structure during an earthquake In: *Proceedings of the 2nd world conference on earthquake engineering*, vol 11, pp 781–798
28. Graesser EJ, Cozzarelli FA (1994) A proposed three-dimensional constitutive model for shape memory alloys. *J Intell Mater Syst Struct* 5:78–89

Wind Analysis of Suspension and Cable Stayed Bridges Using Computational Fluid Dynamics

B.G. Birajdar, A.D. Shingana and J.A. Jain

Abstract In the present work, Computational Fluid Dynamic analysis of a suspension bridge is carried out using ANSYS 13.0 and FLOTRAN module has been used for initial analysis. Validation of CFD analysis is carried out by comparing wind aerodynamic coefficients such as drag, lift and moment coefficients obtained from wind tunnel test, which are available in the earlier literature. After validation, the same Computational Fluid Dynamics approach is used to perform wind analysis of two different types of long span cable stayed bridges and the results are compared with the wind tunnel test results available in the literature. One is having novel twin box girder section and other is having streamlined box girder section. FLUENT module is used to perform wind analysis of cable stayed bridges. Further, the effect of consideration of cables in analysis is studied for cable stayed bridge structure.

Keywords Computational fluid dynamics · Drag coefficient · Lift coefficient · Moment coefficient

1 Introduction

Suspension and Cable Stayed bridges are more vulnerable to vibrations produced due to wind. As the history tells there are many failures of suspension bridge structures across the world due to wind vibrations like Angers bridge, France (1850), Tacoma Narrows (1940) etc. Therefore, the study of aerodynamic properties becomes

B.G. Birajdar (✉) · A.D. Shingana · J.A. Jain
Department of Civil Engineering, College of Engineering, Pune 411 005, India
e-mail: bgb.civil@coep.ac.in

A.D. Shingana
e-mail: shinganaamol@yahoo.com

J.A. Jain
e-mail: Jayjain244@gmail.com

important. The conventional approach of aerodynamic analysis of such structures is wind tunnel testing. However, these tests are very expensive and time consuming. By using Computational Fluid Dynamics approach, we can perform same simulations as those performed in wind tunnel. Moreover, by using CFD approach we can model the geometry with some changes at any instant of time during execution of project very, quickly which is sometimes difficult in wind tunnel tests.

2 CFD Analysis

1. Governing Equation:

The governing equations represent mathematical statement of the conservation law of physics, where following laws are adopted:

A. The Continuity Equation: Mass Conservation

Law of conservation of mass states that matter may be neither created nor destroyed. Conservation of mass can be expressed in mathematical form as,

$$\rho, t + (\rho u), x + (\rho v), y + (\rho w), z = 0 \quad (1)$$

B. The Momentum Equation: (Navier-Stokes Equation)

$$u, t + (u)u, x + (v)u, y = (1/\rho)P, x + (v)u, xx + (v)u, yy \quad (2)$$

$$v, t + (u)v, x + (v)v, y = (1/\rho)P, y + (v)v, xx + (v)u, yy \quad (3)$$

Equations (2) and (3) are derived from Newton's second law of motion, where ν is kinematic viscosity, describes the conservation of momentum of fluid flow and are also known as the Navier-Stokes equations

2. Boundary Conditions.

The various boundary conditions used to solve the above governing differential equations are,

- a. No-slip condition to walls and surfaces of bridge deck section.
- b. Velocity inlet to the inlet wall.
- c. Pressure outlet to outlet wall.

3. Domain size.

Adopted from a literature by Shirai and Ueda [1], from Journal of Wind Engineering and Industrial Aerodynamics.

Dimensions of domain are $16B \times 7B \times 7B$. Where 'B' is the width of the bridge deck.

3 Analysis of Bridges

1. Wind analysis of Tacoma Narrows suspension bridge.

Tacoma Narrows suspension bridge was analyzed in wind tunnel and the results are reported in a report titled ‘Failure of Tacoma Narrows’. The same bridge section is modeled in ANSYS 13.0 and CFD analysis is carried out and aerodynamic coefficients are determined and are compared with the wind tunnel test results

Problem Statement

The Tacoma Narrows bridge was located in Washington. The main span for the Tacoma Narrows bridge is 853.44 m. All components of superstructure are made up of steel material. The deck section is made up of plate girder section. The velocity at deck height is 45 m/s. Figures 1 and 2 show the overall configuration of Tacoma Narrows bridge.

Results

The results from the Tables 1, 2 and 3 indicate increase in drag and lift coefficients with increase in angle of attack. The increment is verified by results of both CFD and wind tunnel tests. Also, increment in moment coefficient is observed with increase in angle of attack.



Fig. 1 Elevation of Tacoma Narrows

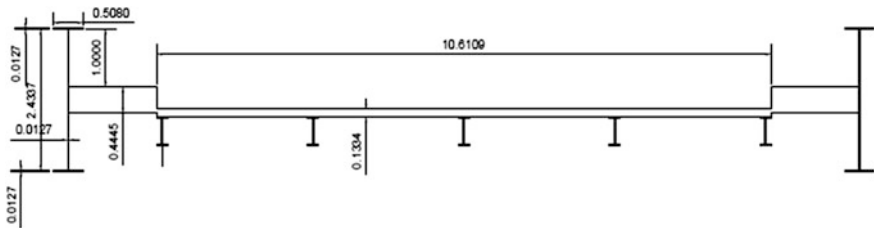


Fig. 2 Cross section of Tacoma Narrows

Table 1 Drag coefficient variation with angle of attack for Tacoma Narrows

Angle of attack (in degree)	Cd (wind tunnel)	Cd (CFD)
0	0.310	0.303
+1	0.313	0.305
+2	0.320	0.306
+3	0.327	0.312
+4	0.335	0.313
+5	0.3467	0.316
+7	0.367	0.335

Table 2 Lift coefficient variation with angle of attack for Tacoma Narrows

Angle of attack (in degree)	C_L (wind tunnel)	C_L (CFD)
0	0.13	0.124
+1	0.92	0.891
+2	1.47	1.382
+3	1.64	1.538
+4	1.81	1.697
+5	1.91	1.783
+7	2.12	1.976

Table 3 Moment coefficient variation with angle of attack for Tacoma Narrows

Angle of attack (in degree)	C_M (wind tunnel)	C_M (CFD)
0	-0.014	-0.0132
+1	-0.022	-0.0206
+2	-0.034	-0.0316
+3	-0.044	-0.041
+4	-0.054	-0.0502
+5	-0.058	-0.0524
+7	-0.063	-0.0586

Pressure contours

The pictorial representation of pressure contours (refer Figs. 3, 4, 5 and 6) on top and bottom of the bridge deck indicates that reduction in positive pressure on top of the deck accompanied with increase in negative pressure on bottom side of the deck as angle of attack increases there is.

Fig. 3 Pressure contour for 0 angle

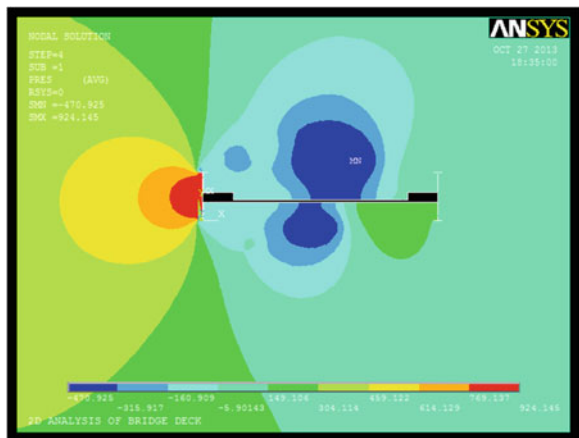


Fig. 4 Pressure contour for +1 angle

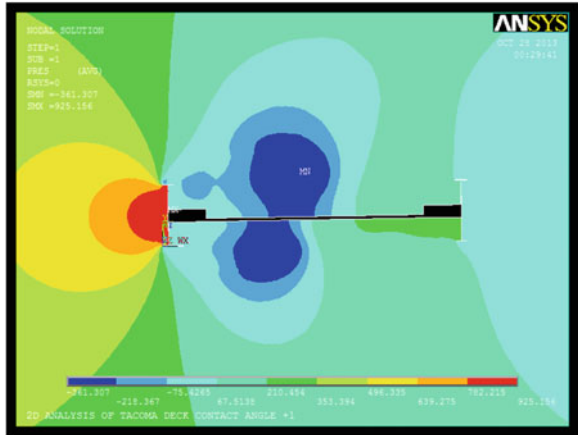


Fig. 5 Pressure contour for +3 angle

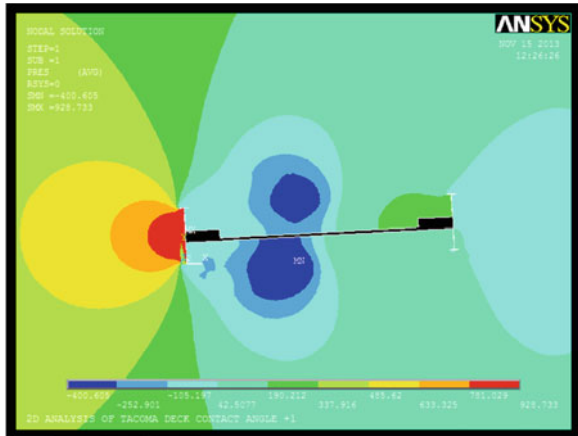
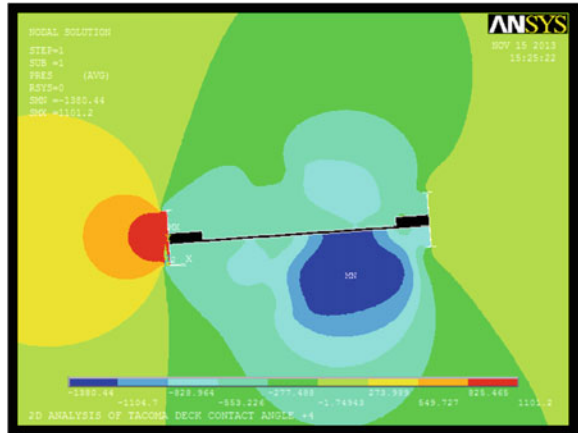


Fig. 6 Pressure contour for +4 angle



2. Wind analysis of Stonecutters cable stayed bridge.

The Stonecutters bridge is located in China. The main span for the Stonecutters bridge is 1,018 m. All components of superstructure are made up of steel material. The deck section is of novel twin box type. The velocity at deck height is 55 m/s.

The geometry of the bridge section is as presented in Figs. 7 and 8.

Results

The results from the Tables 4, 5 and 6 indicate increase in drag and lift coefficients with increase in angle of attack. The increment is verified by results of both CFD and wind tunnel tests. In addition, increment in moment coefficient is observed with increase in angle of attack. Streamlines showing flow over the Stonecutters cable stayed bridge section is presented in Fig. 9.

The pictorial representation of velocity contours shoes that flow get properly separated over the deck section.

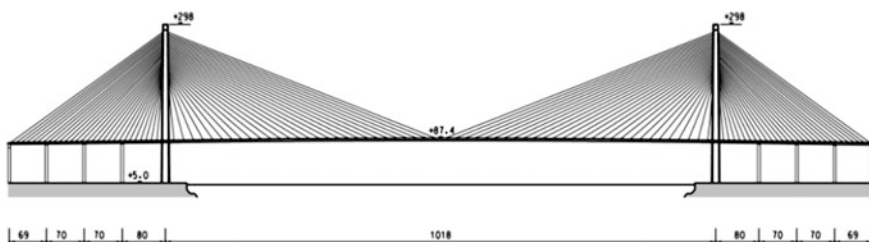


Fig. 7 Elevation of Stonecutters bridge

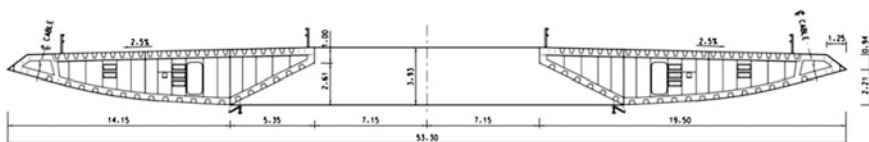


Fig. 8 Cross section of Stonecutters bridge

Table 4 Drag coefficient variation with angle of attack for Stonecutters bridge

Angle of attack (in degree)	C _d (CFD)	C _d (wind tunnel)
-3	1.2148	1.28
-2	1.1402	1.20
-1	1.1214	1.18
0	1.1194	1.16
1	1.0795	1.12
2	1.1288	1.18
3	1.1592	1.22

Table 5 Lift coefficient variation with angle of attack for Stonecutters bridge

Angle of attack (in degree)	C_L (CFD)	C_L (wind tunnel)
-3	-0.2668	-0.3
-2	-0.2261	-0.25
-1	-0.1732	-0.19
0	-0.1101	-0.12
+1	-0.8209	-0.9
+2	0.091	0.1
+3	0.627	0.7

Table 6 Moment coefficient variation with angle of attack for Stonecutters bridge

Angle of attack (in degree)	C_M (CFD)	C_M (wind tunnel)
-3	-0.0228	-0.025
-2	-0.0137	-0.015
-1	-0.0046	-0.005
0	0.0097	0.01
+1	0.0139	0.015
+2	0.037	0.04
+3	0.0508	0.055

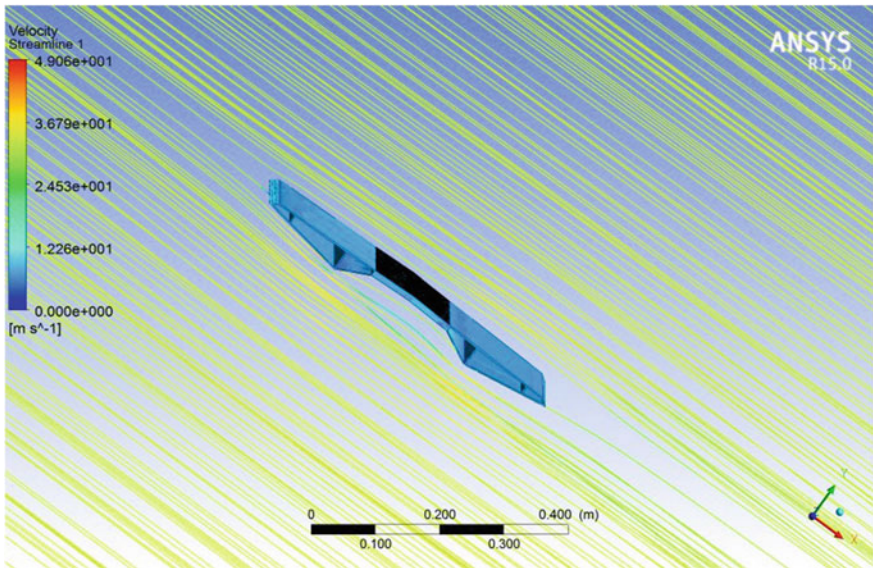


Fig. 9 Streamlines showing flow over the Stonecutters cable stayed bridge section

3. Wind analysis of Sutong cable stayed bridge.

The Sutong Bridge is located in China. The main span for the Sutong bridge is 1,088 m. All components of superstructure are made up of steel material. The deck section is of streamlined box type. The velocity at deck height is 45 m/s.

The geometry of the bridge section is presented in Figs. 10 and 11.

Results

The results from the Tables 7, 8 and 9 indicate increase in drag and lift coefficients with increase in angle of attack. The increment is verified by results of both CFD and wind tunnel tests. But for moment coefficient there is increase in value with positive angle of attack and the value decreases with negative angle of attack. Streamlines showing flow over the Sutong cable stayed bridge section is presented in Fig. 12.

The pictorial representation of velocity contours shoes that flow get properly separated over the deck Section.

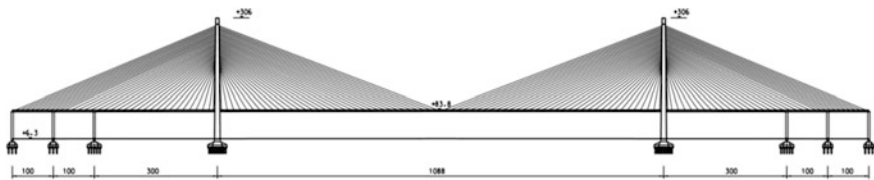


Fig. 10 Elevation of Sutong bridge

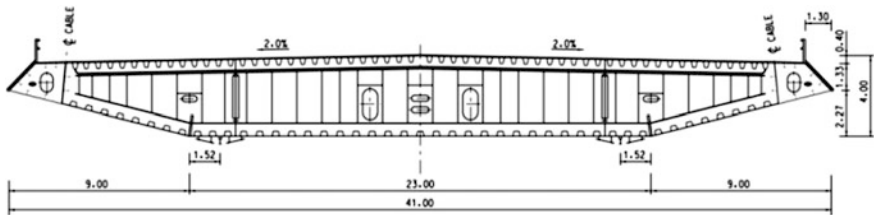


Fig. 11 Cross section of Sutong bridge

Table 7 Drag coefficient variation with angle of attack for Sutong bridge

Angle of attack (in degree)	Cd (wind tunnel)	Cd (CFD)
-3	0.78	0.7131
-2	0.76	0.7093
-1	0.74	0.7143
0	0.70	0.6798
1	0.74	0.7108
2	0.78	0.7308
3	0.82	0.7623

Table 8 Lift coefficient variation with angle of attack for Sutong bridge

Angle of attack (in degree)	C_L (CFD)	C_L (wind tunnel)
-3	-0.3162	-0.36
-2	-0.2587	-0.29
-1	-0.1996	-0.22
0	-0.1109	-0.12
+1	-0.018	-0.02
+2	0.071	0.08
+3	0.1592	0.18

Table 9 Moment coefficient variation with angle of attack for Sutong bridge

Angle of attack (in degree)	C_M (CFD)	C_M (wind tunnel)
-3	-0.026	-0.030
-2	-0.0044	-0.005
-1	0.0182	0.020
0	0.0369	0.04
+1	0.0608	0.065
+2	0.0792	0.085
+3	0.096	0.105

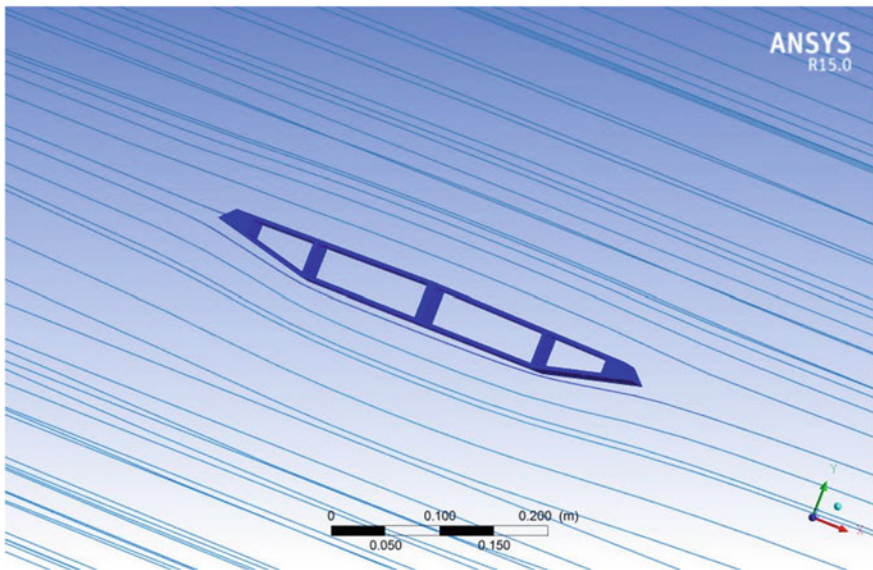


Fig. 12 Streamlines showing flow over the Sutong cable stayed bridge section

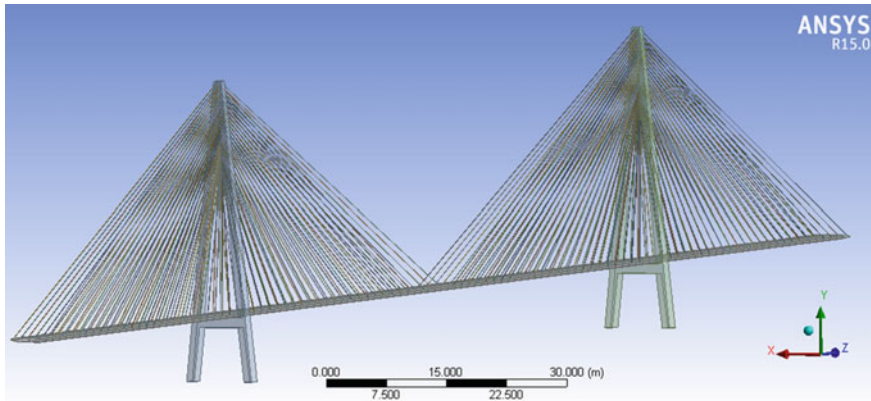


Fig. 13 ANSYS model of Sutong bridge with cables

Table 10 Comparison of drag coefficient with considering effect of cables

Angle of attack (in degree)	Cd (wind tunnel)	Cd (CFD) W/O cables	Cd (CFD)With cables
-3	0.78	0.7131	0.728
-2	0.76	0.7093	0.716
-1	0.74	0.7143	0.7192
0	0.70	0.6798	0.6827
1	0.74	0.7108	0.7186
2	0.78	0.7308	0.7521
3	0.82	0.7623	0.776

4. Wind analysis of Sutong bridge considering effect of cables.

ANSYS model of Sutong bridge with cables, used for the wind analysis is presented in Fig. 13. The results are presented in Table 10.

Results

It is observed from above table that the values obtained with consideration of cables and without cables are very close.

4 Conclusions

The following findings are reported based on the results obtained from CFD analysis,

- i. After CFD analysis of Tacoma Narrows bridge deck section, it is observed that due to greater depth of section provided to satisfy the serviceability criteria, which in turn increase the projected area, this result in large pressure on the

upstream side and also suction on the downstream side. Hence, it is observed that for long span bridges plate girder section need to be avoided, as reported elsewhere.

- ii. As the secondary effects due to distortion are neglected in CFD analyses, it is observed that pressure coefficients obtained using CFD analyses are smaller than the wind tunnel test.
- iii. It can be concluded that, as the CFD results are closer to wind tunnel test results, the variance is by maximum 12 %. Therefore, CFD can be used for preliminary design stage of suspension and cable stayed bridges.
- iv. In CFD analysis of long span suspension and cable stayed bridges, the effect of cables on values of derived results of C_d , C_L and C_M is insignificant (max 5 %), which may be ignored in modeling to save the computational efforts and time while performing CFD analysis.

Bibliography

1. Shirai S, Ueda T (2003) Aerodynamic simulation by CFD on flat box girder of super-long-span suspension bridge. *J Wind Eng Ind Aerodyn* 91:279–290
2. Ding Q, Lee PKK (2000) Computer simulation of buffeting actions of suspension bridges under turbulent wind. *Comput Struct* 76:787–797
3. Zhang X, Xiang H, Sun B (2002) Nonlinear aerostatic and aerodynamic analysis of long-span suspension bridges considering wind-structure interactions. *J Wind Eng Ind Aerodyn* 90:1065–1080
4. Sepe V, D’Asdia Piero (2003) Influence of low-frequency wind speed fluctuations on the aeroelastic stability of suspension bridges. *J Wind Eng Ind Aerodyn* 91:1285–1297
5. Chen SR, Cai CS (2003) Evolution of long-span bridge response to wind-numerical and discussion. *Comput Struct* 81:2055–2066
6. Jeong UY, Kwon S-D (2003) Sequential numerical procedures for predicting flutter velocity of bridge sections. *J Wind Eng Ind Aerodyn* 91:291–305
7. Cheng J, Cai CS, Xiao R, Chen SR (2005) Flutter reliability analysis of suspension bridges. *J Wind Eng Ind Aerodyn* 93:757–777
8. Zhang X (2007) Influence of some factors on the aerodynamic behavior of long span suspension bridges. *J Wind Eng Ind Aerodyn* 95:149–164

Improved ERA Based Identification of Flutter Derivatives of a Thin Plate

M. Keerthana and P. Harikrishna

Abstract In this paper, improved Eigensystem Realization Algorithm (ERA/DC—Eigensystem Realization Algorithm with Data Correlation) from literature has been applied for the identification of flutter derivatives of a thin plate section under free decay (transient) responses, to overcome the problem of poor noise handling capability of original Eigen Realization Algorithm (ERA). A thin plate section has been considered in the present study as theoretical solutions of flutter derivatives are available for it from Theodorsen's functions and also most of the bridge deck cross-sections have large side ratio. The 2-DOF (heave and pitch) aeroelastic responses of thin plate section have been numerically simulated using Newmark-beta time integration method for various reduced wind speeds (U/fB ; U —oncoming wind speed, f —frequency of oscillation, B —width of the plate), using flutter derivatives obtained from Theodorsen's theoretical solution. Then, ERA and ERA/DC, have been applied towards identification of frequencies and damping ratios for the chosen range of reduced wind speeds and for 5, 10 and 20 % noise levels. Further, flutter derivatives have also been identified and compared with theoretical values to prove the robustness of the improved Eigen Realization Algorithm (ERA/DC) in identification of flutter derivatives and in handling noise.

Keywords Eigensystem realization algorithm · Plate section · Theodorsen's theoretical solution · Bridges · Wind

M. Keerthana (✉) · P. Harikrishna
CSIR-Structural Engineering Research Centre (SERC), Chennai, India
e-mail: keerthana@serc.res.in

P. Harikrishna
e-mail: hari@serc.res.in

M. Keerthana · P. Harikrishna
Academy of Scientific and Innovative Research (AcSIR), New Delhi, India

1 Introduction

Bridges are indispensable part of civil infrastructure of a country. Bridges with longer unsupported spans are being designed or envisioned for the future to fully utilize the efficiency of the structure in connecting/crossing obstacles, viz, wide rivers and sea straits, etc. Such long span bridges, which are mostly suspension/cable-stayed, are highly wind sensitive owing to their flexibility and low damping characteristics. The interaction and feedback mechanism between oncoming wind and the structural motion results in aeroelastic forces, which can potentially cause diverging oscillations. Flutter is one such phenomenon that needs to be addressed in the early stages of design of such long span bridges to ensure safety. The effect of motion induced aeroelastic forces is realized through aerodynamic stiffness and damping, characterized by non-dimensional “flutter derivatives”, which are functions of wind speeds, geometry and frequency of vibrations [9].

Experimental assessment of these flutter derivatives involves either forced or free vibration studies on sectional models of bridges under simulated wind conditions. Though evaluation of flutter derivatives from forced vibration studies are simpler, they involve very complex experimental set up to force the motion of the bridge model in wind tunnel. Hence, free vibration studies are preferred owing to their simplicity in execution of the experiment and closeness to the actual behavior. However, identification of flutter derivatives from wind tunnel testing of scaled down sectional models of bridges using free vibration studies require application of improved system identification procedures, with better noise handling capability [1]. Some of the recently used system identification techniques for the aforementioned purpose include frequency modulated empirical modal decomposition [13], stochastic subspace identification methods [1, 11] and non-linear least squares technique [10]. It has been observed that these techniques have clearly exhibited better identification capabilities in comparison with conventionally used Ibrahim time domain (ITD) method, least squares method and ARMA (Autoregressive moving average) method, etc.

In the present study, one of the most commonly used multi input multi output (MIMO) system identification algorithms in structural engineering, namely Eigensystem Realization Algorithm (ERA) proposed by Juang and Pappa [5], which is highly effective in identification of lightly damped structures has been chosen towards identification of flutter derivatives. One of the main limitation of ERA as reported in literature is its inability to handle noise in the data. Hence, an improved version of the algorithm was proposed [6] and was termed as Eigensystem Realization Algorithm with Data Correlation (ERA/DC), which uses the concept of data correlations to reduce the effect of noise in the data. This technique has been used towards identification of modal parameters from ambient vibration measurements [2]. Zhu et al. [14] have identified flutter derivatives of a thin plate system with FERA/DC (Fast Eigensystem Realization Algorithm with Data Correlation) to overcome the limitation of ERA. However, researchers have also used

random decrement technique (RD) [4], natural excitation technique (NExT) [12] in conjunction with ERA to overcome the problem of noise interference.

In the present study, ERA and ERA/DC have been applied towards identification of flutter derivatives of a thin plate section using the simulated 2-DOF aeroelastic responses. The 2-DOF (heave and pitch) aeroelastic responses of thin plate section have been numerically simulated using Newmark-beta time integration method for various reduced wind speeds (U/fB ; U —oncoming wind speed, f —frequency of oscillation, B —width of the plate), using flutter derivatives obtained from Theodorsen’s theoretical solution. The modal parameters, namely, vertical and torsional frequencies and damping ratios obtained from both the methods have been compared for the chosen range of reduced wind speeds and for 5, 10 and 20 % noise levels. Further, flutter derivatives have also been identified and compared with theoretical values to assess the robustness of the improved Eigen Realization Algorithm (ERA/DC) in identification of flutter derivatives and in handling noise.

2 Numerical Simulation of Aeroelastic Response of a Thin Plate

The dynamic equations of motions for a typical 2-DOF bridge deck system with the degrees of freedom (Fig. 1) being heave/vertical (h) and pitch/torsion (α) under smooth flow is given by

$$\begin{aligned}
 m(\ddot{h} + 2\omega_h \zeta_h \dot{h} + \omega_h^2 h) &= L_{se} \\
 I(\ddot{\alpha} + 2\omega_\alpha \zeta_\alpha \dot{\alpha} + \omega_\alpha^2 \alpha) &= M_{se}
 \end{aligned}
 \tag{1}$$

L_{se} and M_{se} are the self-excited forces acting on the bridge deck system, defined in terms of the responses

$$\begin{aligned}
 L_{se} &= \frac{1}{2} \rho U^2 B \left[KH_1 \frac{\dot{h}}{U} + KH_2 \frac{\dot{\alpha} B}{U} + K^2 H_3 \alpha + K^2 H_4 \frac{h}{B} \right] \\
 M_{se} &= \frac{1}{2} \rho U^2 B^2 \left[KA_1 \frac{\dot{h}}{U} + KA_2 \frac{\dot{\alpha} B}{U} + K^2 A_3 \alpha + K^2 A_4 \frac{h}{B} \right]
 \end{aligned}
 \tag{2}$$

K is the defined as $\frac{\omega B}{U}$

U is the oncoming wind speed

ρ is the density of air (=1.2 kg/m³)

H_i and A_i are the flutter derivatives ($i = 1, 2, 3$ and 4).

m mass of the plate per unit length = 11.94 kg/m

I mass moment of inertia of the plate per unit length = 0.532 kg m²/m

B width of the plate = 0.45 m

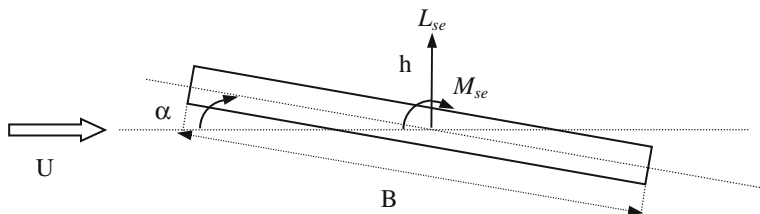


Fig. 1 Two degree of freedom system of the thin plate

ω_h frequency of the mechanical system for heave/vertical mode (under still wind) = 9.349 rad/s

ω_α frequency of the mechanical system for pitch/torsional mode (under still wind) = 18.824 rad/s

ζ_h damping ratio of the mechanical system for heave/vertical mode (under still wind) = 0.007

ζ_α damping ratio of the mechanical system for pitch/torsional mode (under still wind) = 0.002

In the present study, the theoretical values of flutter derivatives H_i and A_i [8, 9] have been obtained based on the concept of forced oscillation of a flat plate in uniform stream [3]. Substituting Eq. (2) in Eq. (1), and grouping like terms,

$$\ddot{x} + C^e \dot{x} + K^e x = 0 \tag{3}$$

where C^e and K^e are the damping and stiffness matrices modified by the aeroelastic interaction. In state space representation, the Eq. (3) can be written as

$$\begin{bmatrix} \dot{x} \\ \ddot{x} \end{bmatrix} = \begin{bmatrix} O_d & I_d \\ -K^e & -C^e \end{bmatrix} \begin{bmatrix} x \\ \dot{x} \end{bmatrix} \tag{4}$$

$$Y = A_d X$$

where O_d and I_d are zero and unit matrices. X and Y are state and output vectors. A_d is the state matrix.

Based on Eq. (3), free decay responses of the flat plate system have been numerically simulated for wind speeds of 0–18 m/s (in increments of 2 m/s) using Newmark-beta time integration method with sampling frequency of 150 Hz. The time histories of heaving and pitching responses for wind speeds of 0 and 6 m/s are shown in Figs. 2 and 3, respectively. Further, Gaussian white noise of 5, 10 and 20 % have been added to the simulated responses. Noise of 5 % means that, the standard deviation of noise added is 5 % of the standard deviation of original signal. The time histories of responses with noise of 5 and 10 % for wind speed of 10 m/s are shown in Figs. 4 and 5, respectively.

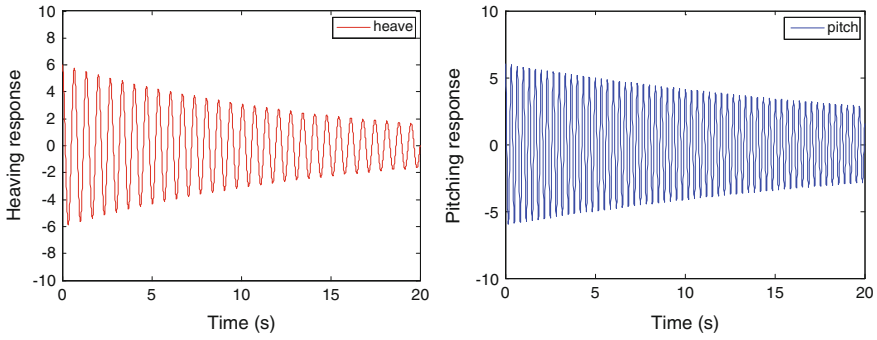


Fig. 2 Generated time histories of responses for still wind (0 m/s)

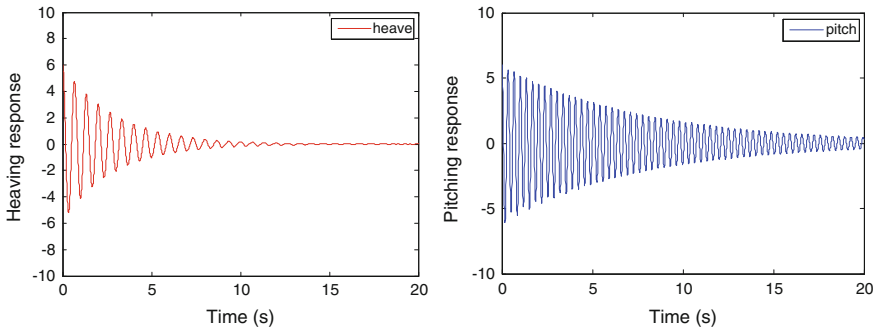


Fig. 3 Generated time histories of responses for wind speed of 6 m/s

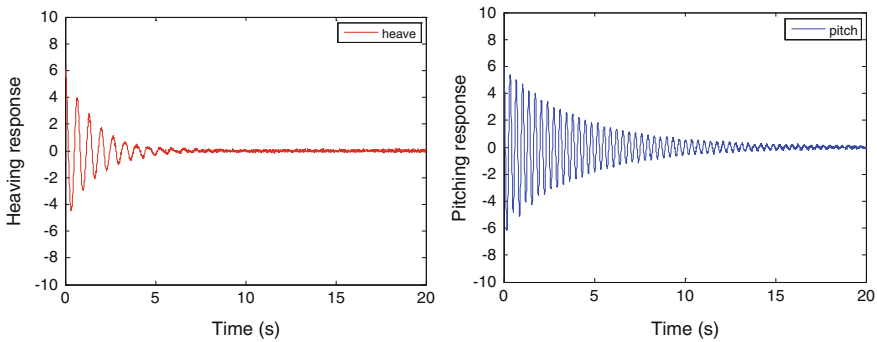


Fig. 4 Generated time histories of responses for wind speed of 10 m/s with 5 % noise

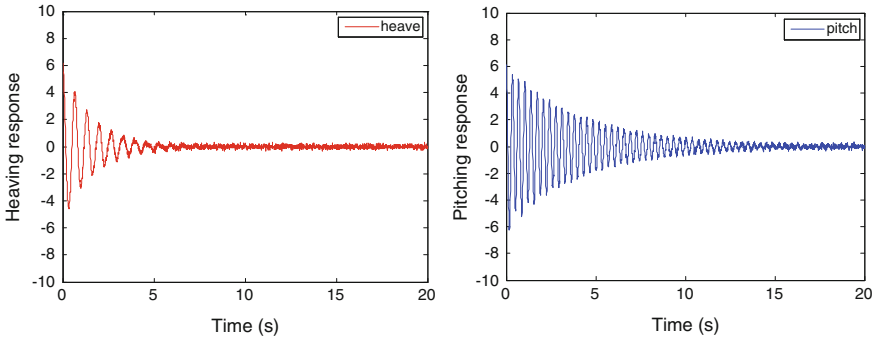


Fig. 5 Generated time histories of responses for wind speed of 10 m/s with 10 % noise

3 ERA and ERA/DC Algorithms for System Identification

ERA as proposed by [5] uses the concept of minimum system realization in control theory towards identification of modal and system parameters from the system response. Consider a state space system given by

$$\begin{aligned} x[k + 1] &= A_d x[k] + B_d u[k] \\ y[k] &= C_d x[k] + D_d u[k] \end{aligned} \tag{5}$$

where A_d , B_d , C_d and D_d are state matrix, input matrix, output matrix and feed forward matrix. x , y and u are state, output and input vectors. k is the index. The impulse response of the system is given by

$$y[k] = \begin{cases} D_d & \text{for } k = 0 \\ C_d A_d^{k-1} B_d & \text{for } k > 0 \end{cases} \tag{6}$$

The term $C_d A_d^{k-1} B_d$ is called Markov parameters of the system. Given the values of $y[k]$, the system matrices A_d , B_d and C_d are to be identified. The algorithm involves construction of block Hankel matrix (of size $r \times s$) given by Eq. (7) from the impulse response time histories.

$$H_{rs}[k] = \begin{bmatrix} Y[k] & Y[k + t_1] & \dots & Y[k + t_{s-1}] \\ Y[j_1 + k] & Y[j_1 + k + t_1] & \dots & Y[j_1 + k + t_{s-1}] \\ \vdots & \vdots & \dots & \vdots \\ Y[j_{r-1} + k] & Y[j_{r-1} + k + t_1] & \dots & Y[j_{r-1} + k + t_{s-1}] \end{bmatrix} \tag{7}$$

where j_i and t_i are time shifts among the entries of Hankel matrix. The size of Hankel matrix is an important parameter in the identification process. Guidelines

for selection of the same are available [7]. Singular value decomposition of Hankel matrix is then carried out as in Eq. (8).

$$H_{rs}[0] = PDQ^T \tag{8}$$

where D is the diagonal matrix with non negative diagonal elements in decreasing order; P and Q are orthogonal matrices. Matrices P , D and Q have to be reduced to matrices P_n , Q_n and D_n with ‘ n ’ number of rows. The number ‘ n ’ also called system order is arrived at by observing the variation in neighboring singular values.

Defining $E_p^T = [I_p, 0_p, \dots, 0_p]$ and $E_m^T = [I_m, 0_m, \dots, 0_m]$, the system matrices for linear time invariant system can be obtained as

$$\begin{aligned} A_d &= D_n^{-1/2} P_n^T H_{rs}[1] Q_n D_n^{-1/2} \\ B_d &= D_n^{1/2} Q_n^T E_m \\ C_d &= E_p^T P_n D_n^{1/2} \end{aligned} \tag{9}$$

where $H_{rs}[1]$ is time-shifted Hankel matrix.

In case of ERA-DC, the block correlation Hankel matrix ($U[q]$) given by Eq. (11) is formed with correlative records of the impulse response records through correlation matrix $R(q)$, instead of actual impulse response records of data.

$$R(q) = H_{rs}(q) H_{rs}^T(0) \tag{10}$$

$$U[q] = \begin{bmatrix} R[q] & R[q + \gamma] & \dots & R[q + \beta\gamma] \\ R[q + \gamma] & R[q + 2\gamma] & \dots & \vdots \\ \vdots & \vdots & \dots & \vdots \\ \vdots & \vdots & \dots & \vdots \\ R[q + \alpha\gamma] & Y[j_{r-1} + k + t_1] & \dots & R[q + (\alpha + \beta)\gamma] \end{bmatrix} \tag{11}$$

This is followed by the singular value decomposition of the matrix $U[0]$. The rest of the procedure remains same as that of ERA. MATLAB programs have been developed for ERA and ERA/DC. These techniques have been applied on the simulated responses to obtain the state matrix ‘ A_d ’. Eigen value decomposition of the A_d matrix has been carried out to obtain eigen values (Λ) and eigen vectors (Ψ). From the eigen values, the vertical and torsional frequencies (ω_i) and damping ratios (ξ_i) have been evaluated as follows [7].

$$\begin{aligned} \frac{1}{\Delta t} \ln(\Lambda) &= \text{diag}(a_i \pm ib_i) \\ \xi_i &= -\frac{a_i}{\sqrt{a_i^2 + b_i^2}} = -\frac{\text{real}(\ln(\Lambda)/\Delta t)}{\text{abs}(\ln(\Lambda)/\Delta t)} \\ \omega_i &= -\text{abs}(\text{imag}(\ln(\Lambda)/\Delta t)) \end{aligned} \tag{12}$$

where a_i and b_i are real and imaginary parts of the natural logarithm of eigen values of state matrix, divided by the sampling time. Defining $\Phi = C\Psi$, the stiffness and damping matrices as in Eq. (4) have been evaluated based on Eq. (13) [14].

$$[K^e C^e] = -M [\Phi\Lambda^2 \Phi^*(\Lambda^*)^2] \begin{bmatrix} \Phi & \Phi^* \\ \Phi^*\Lambda & \Phi^*\Lambda^* \end{bmatrix}^\dagger \quad (13)$$

where \dagger is the operation defined by Moore-Penrose pseudo-inverse of the matrix.

The flutter derivatives have been evaluated from the difference in stiffness and damping matrices corresponding to the system with (K^e and C^e) and without (K^0 and C^0) aeroelastic effects.

$$\begin{aligned} H_1(K_h) &= -\frac{2m}{\rho B^2 \omega_h} (\bar{C}_{11}^e - \bar{C}_{11}); & A_1(K_h) &= -\frac{2I}{\rho B^3 \omega_h} (\bar{C}_{21}^e - \bar{C}_{21}) \\ H_2(K_x) &= -\frac{2m}{\rho B^3 \omega_x} (\bar{C}_{12}^e - \bar{C}_{12}); & A_2(K_x) &= -\frac{2I}{\rho B^4 \omega_x} (\bar{C}_{22}^e - \bar{C}_{22}) \\ H_3(K_x) &= -\frac{2m}{\rho B^3 \omega_x^2} (\bar{K}_{12}^e - \bar{K}_{12}); & A_3(K_x) &= -\frac{2I}{\rho B^4 \omega_x^2} (\bar{K}_{22}^e - \bar{K}_{22}) \\ H_4(K_h) &= -\frac{2m}{\rho B^3 \omega_h^2} (\bar{K}_{11}^e - \bar{K}_{11}); & A_4(K_h) &= -\frac{2I}{\rho B^3 \omega_h^2} (\bar{K}_{21}^e - \bar{K}_{21}) \end{aligned} \quad (14)$$

$$\begin{aligned} \bar{C}^e &= M^{-1} C^e; & \bar{K}^e &= M^{-1} K^e \\ \bar{C} &= M^{-1} C^0; & \bar{K} &= M^{-1} K^0 \end{aligned}$$

4 Results and Discussions

The identified vertical and torsional frequencies based on ERA and ERA/DC have been presented in Figs. 6 and 7 for various oncoming wind speeds and for various noise levels. The corresponding vertical and torsional damping ratios have been presented in Figs. 8 and 9. For the 0 % noise case, i.e., the response without any noise, the identified frequencies and damping ratios corresponding to ERA and ERA/DC have been observed to match. Identification of torsional frequencies have been observed to be insensitive to the noise in the responses for entire range of wind speeds studied, as can be seen in Fig. 7.

The identified vertical frequency, vertical and torsional damping ratios corresponding to ERA has been observed to deviate from the trend of literature in proportion to noise level, especially for wind speeds greater than 10 m/s. The maximum deviation of 5 % has been observed in case of vertical frequency for ERA with 20 % noise. Even though the difference might seem marginal, this may be contributing significantly to the deviation in the evaluated flutter derivatives as squares of these frequencies appear in Eq. (14). However, the frequencies and damping ratios identified from ERA/DC are found to be more robust even with

Fig. 6 Identified vertical frequencies using ERA and ERA/DC for various levels of noise

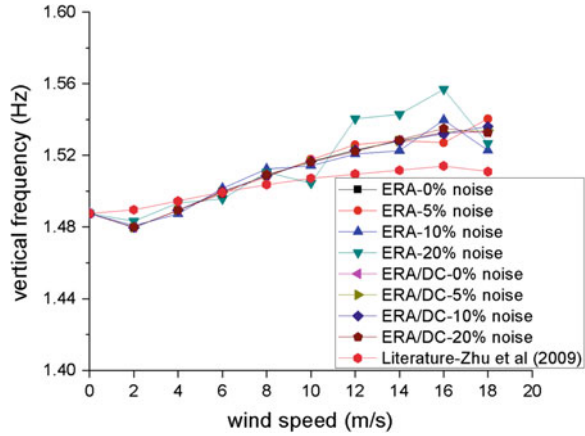


Fig. 7 Identified torsional frequencies using ERA and ERA/DC for various levels of noise

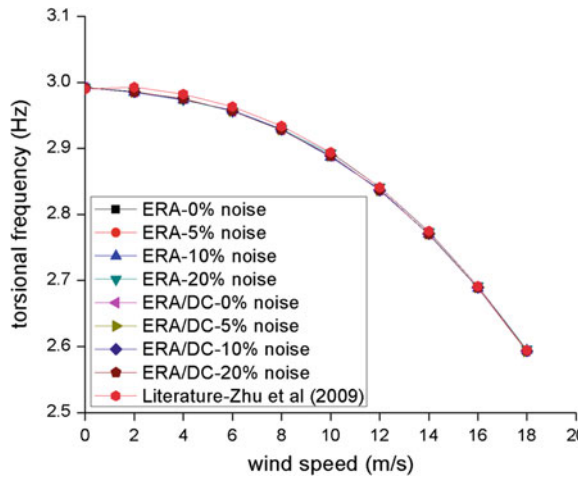


Fig. 8 Identified vertical damping ratios using ERA and ERA/DC for various levels of noise

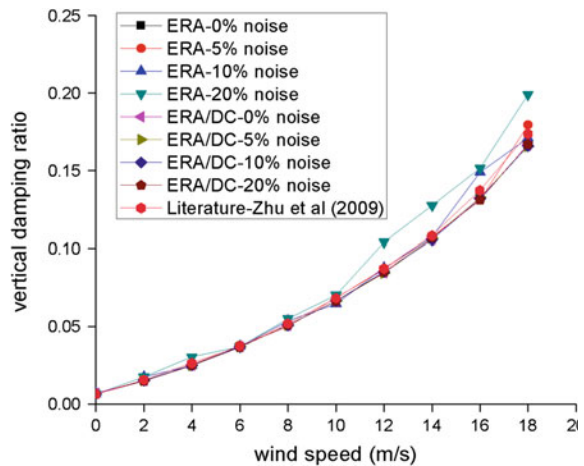


Fig. 11 Identified flutter derivative H_4 for flat plate under various noise levels

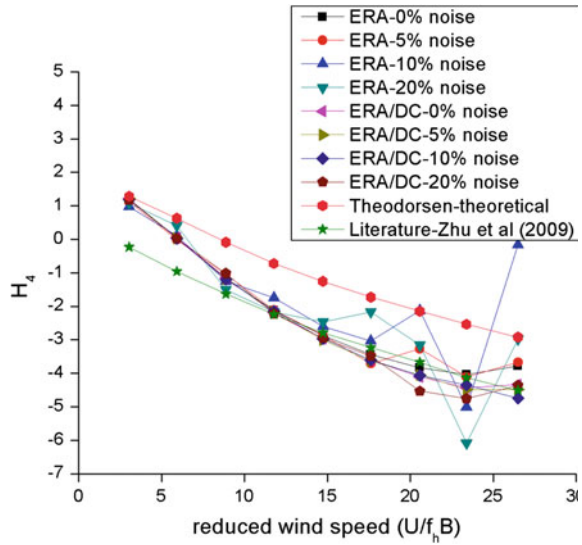
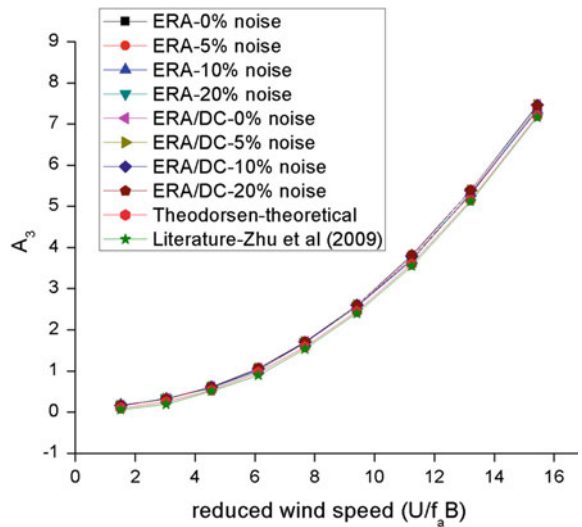
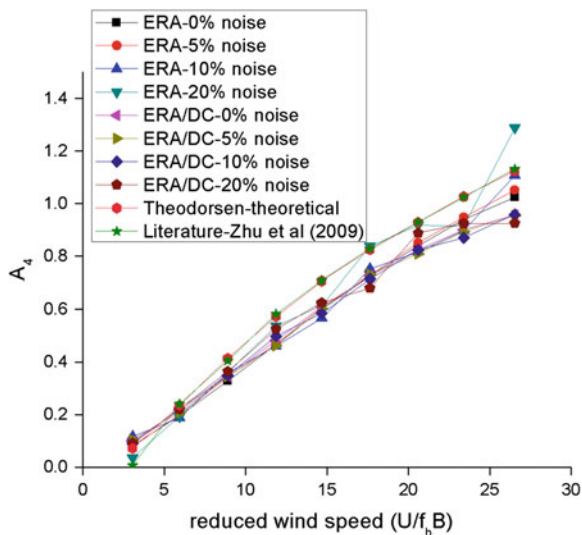


Fig. 12 Identified flutter derivative A_3 for flat plate under various noise levels



ERA/DC for various levels of noise compare well with the theoretical solution. Beyond this reduced wind speed of 17, the evaluated values of H_1 from both ERA and ERA/DC deviate from the theoretical solution with ERA showing significantly high deviation of 45 % with theoretical solution, for the response with 20 % noise level at reduced wind speed of 26.

Fig. 13 Identified flutter derivative A_4 for flat plate under various noise levels



The flutter derivative H_4 evaluated from the present study as well as from literature [14] have been observed to deviate from theoretical solutions for all reduced wind speeds, with maximum deviations at higher reduced wind speeds. However, the values obtained from the present study have been observed to be comparable with those reported by Zhu et al. [14]. The magnitudes of H_4 evaluated from ERA for data with 10 and 20 % noise levels have been observed to show scatter beyond reduced wind speed of 17. This scatter has been completely eliminated with use of ERA/DC.

5 Summary and Conclusions

The effectiveness and accuracy of ERA/DC, an improved system identification algorithm over ERA in handling noise in response has been studied with the numerically simulated response of thin plate aeroelastic system for various wind speeds/reduced wind speeds and various noise levels of 5, 10 and 20 %. The identification of vertical and torsional frequencies, and damping ratios from ERA/DC have been observed to be satisfactory in comparison with ERA, even with data contaminated with high density noise of 20 %. The evaluation of flutter derivatives using ERA/DC has been observed to be advantageous over ERA in terms of handling noise in data. However, the magnitudes of the derivatives evaluated from ERA/DC, especially at higher reduced wind speeds have been observed to deviate with the theoretical values. The reason for this deviation needs to be further studied by applying the system identification technique to another aeroelastic system with different dynamic characteristics.

Acknowledgments This paper is being published with the kind permission of Director, CSIR-Structural Engineering Research Centre, Chennai, India.

References

1. Boonyapinyo V, Janesupasaeree T (2010) Data-driven stochastic subspace identification of flutter derivatives of bridge decks. *J Wind Eng Ind Aerodyn* 98:784–799
2. Chiang DY, Lin CS, Su FH (2010) Identification of modal parameters from ambient vibration data by modified eigensystem realization algorithm. *J Aeronaut Astronaut Aviat Ser A* 42 (2):79–86
3. Fung YC (1969) An introduction to the theory of aeroelasticity. Dover Publications, New York
4. Gurung CB, Yamaguchi H, Yukino T (2003) Identification and characterization of galloping of Tsuruga test line based on multi-channel modal analysis of field data. *J Wind Eng Ind Aerodyn* 91:903–924
5. Juang JN, Pappa R (1985) An eigensystem realization algorithm for modal parameter identification and modal reduction. *J Guid Control Dyn* 8(5):620–627
6. Juang JN, Cooper JE, Wright JR (1988) An eigensystem realization algorithm using data correlations (ERA/DC) for modal parameter identification. *Control Theory Adv Technol* 4 (1):5–14
7. Nayeri RD, Tasbihgoo F, Wahbeh M, Caffrey JP, Masri SF, Conte JP, Elgamal A (2009) Study of time-domain techniques for modal parameter identification of a long suspension bridge with dense sensor arrays. *ASCS J Eng Mech* 135(7):669–683
8. Scanlan RH, Jones NP, Singh L (1997) Inter-relations among flutter derivatives. *J Wind Eng Ind Aerodyn* 69–71:829–837
9. Scanlan RH, Tomko JJ (1971) Airfoil and bridge deck flutter derivatives. *J Eng Mech ASCE* 97(6):1171–1737
10. Wei H (2010) A method for identification of flutter derivatives of bridge decks. In: Proceedings of the 3rd international congress on image and signal processing (CISP2010), China, pp 2946–2950
11. Xu FY, Chen XZ, Cai CS, Chen AR (2012) Determination of 18 flutter derivatives of bridge decks by an improved stochastic search algorithm. *ASCE J Bridge Eng* 17(4):576–588
12. Ye X, Yan Q, Wang W, Yu X, Zhu T (2011) Output-only modal identification of Guangzhou New TV Tower subject to different environment effects. In: Proceedings of the 6th international workshop on advanced smart materials and smart structures technology (ANCRiSST-2011), China
13. Zhang X, Du X, Brownjohn J (2012) Frequency modulated empirical modal decomposition method for the identification of instantaneous modal parameters of aeroelastic systems. *J Wind Eng Ind Aerodyn* 101:43–52
14. Zhu ZW, Chen ZQ, Li YX (2009) Identification of flutter derivatives of bridges with ERA and its modifications. In: Proceedings of the seventh Asia-Pacific conference on wind engineering, Taiwan

Along and Across Wind Effects on Irregular Plan Shaped Tall Building

Biswarup Bhattacharyya and Sujit Kumar Dalui

Abstract This paper presents detailed study of force and pressure coefficients of an unsymmetrical 'E' plan shaped tall building under wind excitation. The building is unsymmetrical about both direction (along and across wind direction) in plan. Experimental and numerical study is carried out by wind tunnel test in boundary layer wind tunnel and Computational Fluid Dynamics (CFD) technique using ANSYS CFX software respectively to study the above model under wind excitation. Two different types of models were used for force and pressure measurements in wind tunnel. Rigid model was used at a model scale of 1:300 for both the cases. Force measurement model was tested under three different wind speeds of 6, 8, 10 m/s whether pressure measurement model was tested under wind speed of 10 m/s in wind tunnel. Wind flow pattern around the building model is studied by CFD technique for both wind flow direction which predicts about the nature of pressure distribution on different surfaces. Some dynamic nature of wind flow is observed at the rear side in case of across wind effects. Maximum positive force and pressure coefficients noticed in case of along wind effects as the surface area is maximum and maximum wind energy dissipates on frontal surface. Same mean pressure occurred on similar faces in case of along wind effects. Pressure contours are symmetrical about vertical axis on frontal faces for both directions of flow and pressure fluctuation noticed at the rear side face due to dynamic effects of flow pattern in case of across wind effect. A comparative study is carried out between experimental and numerical study and results found from these two methods have good agreement to each other.

Keywords ANSYS · Tall building · Computational fluid dynamics · Wind tunnel

B. Bhattacharyya (✉) · S.K. Dalui
Indian Institute of Engineering Science and Technology, Shibpur, Howrah 711103, India
e-mail: biswarupb6@gmail.com

S.K. Dalui
e-mail: sujit_dalui@rediffmail.com

1 Introduction

Tall buildings are constructed more in recent decades which may regular or irregular in plan shaped. Regular plan shaped buildings are more stable as compared to irregular plan shaped buildings. Less torsional force is acted generally in regular plan shaped buildings but, due to larger surface area more wind pressure occurred on these types of buildings. Irregular plan shaped tall buildings may susceptible to torsional effect but wind pressure on these types buildings are lesser than regular plan shaped buildings.

Wind loads acts on buildings generally in two ways i.e., statically and dynamically. Static nature noticed in case of low rise buildings whether dynamic nature noticed in case of high rise buildings. Critical pressure occurs at perpendicular wind angles in case of regular plan shaped buildings whether critical pressure may occur at skew wind angles in between perpendicular angles in case of irregular plan shaped buildings. Also variation of pressure on different faces of irregular plan shaped buildings may different in nature from regular plan shaped buildings. So, it is desirable to study of pressure coefficient due to wind effects before designing the irregular plan shaped tall buildings. Pressure coefficients and force coefficients (i.e., drag and lift coefficients) of some regular plan shaped buildings are given in relevant codes [1–4] but there are no such provisions for calculating pressure or force coefficients of irregular plan shaped tall buildings. Pressure and force coefficients could be found from experimental method (i.e., wind tunnel test) and numerical method (Computational Fluid Dynamics technique). Many research works have been carried out earlier in the field of wind engineering based on wind tunnel test and Computational Fluid Dynamics (CFD) technique. The effect of wind on L and U plan shape structures in wind tunnel [5] was studied in 2005. A multi-channel pressure measurement system was used to measure mean values of loads on 1:100 scale model. The models were experimented with angle of wind flow varying from 0° to 180°. The influence of additional wing transforming the L into the U-shaped model was noticeable on the pressure distribution. Amin and Ahuja [6] presented experimental results of wind tunnel model tests to evaluate wind pressure distributions on different faces having the same plan area and height but varying plan shapes (“L” and “T”) at a geometric scale of 1:300 under boundary layer flow in 2008. Wind pressure was measured in the range of wind directions from 0° to 180° with an interval of 15°. It was noticed that a large variation of pressure along the height as well as along the width of different faces of models and it was also observed that changing the plan dimensions considerably affects the wind pressure distributions on different faces of the building models. An experimental results on the aerodynamic behavior with square cylinders with rounded corners [7] was also studied earlier. Global force and surface pressure was measured for different Reynolds numbers and it was found that critical angle of incidence decreases corresponding to flow reattachment as radius of rounded corners increases. Some of

the researchers also compared experimental as well as numerical results for adequacy of both the techniques [8–13]. The requirement of both the experimental as well as numerical techniques is noticed from the above mentioned previous studies.

Present study describes about force and pressure variation on different faces of an unsymmetrical ‘E’ plan shaped tall building under wind excitation. Both along and across wind effects is considered for this case. Experimental as well as numerical study is carried out to achieve acceptable results for this case. Experimental study has been carried out in boundary layer wind tunnel whether numerical study has been carried out by Computational Fluid Dynamics (CFD) technique using ANSYS CFX software.

2 Experimental Study

Experimental study was carried out in open circuit boundary layer wind tunnel at Department of Civil Engineering, IIT Roorkee, India. The cross section of the wind tunnel was 2 m (width) × 2 m (height) with a length of 38 m. The experimental work has been carried out under terrain category-II as per IS 875 (Part 3)-1987 [1] and the terrain category was formed by using square cubes of different sizes at inlet region. Force and pressure were measured by two different models made of wood board of thickness 6 mm and Perspex sheet of thickness 4 mm respectively (Fig. 1). Both drag (C_D) and lift (C_L) coefficients were measured by force measurement model whereas pressure coefficient (C_p) of different faces was measured by pressure measurement model. The models were scaled at 1:300. Different faces along with

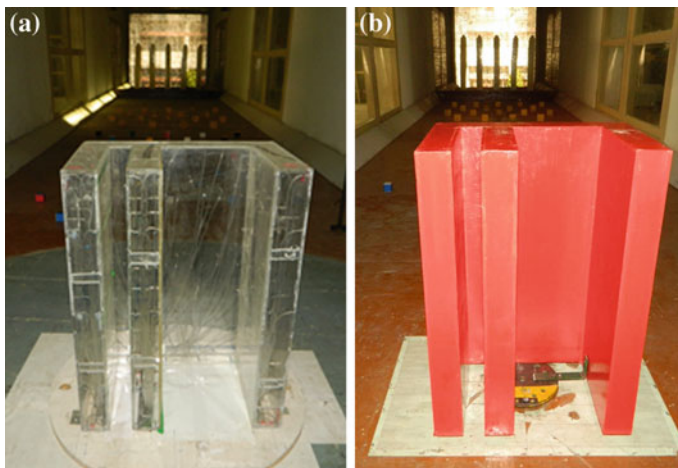
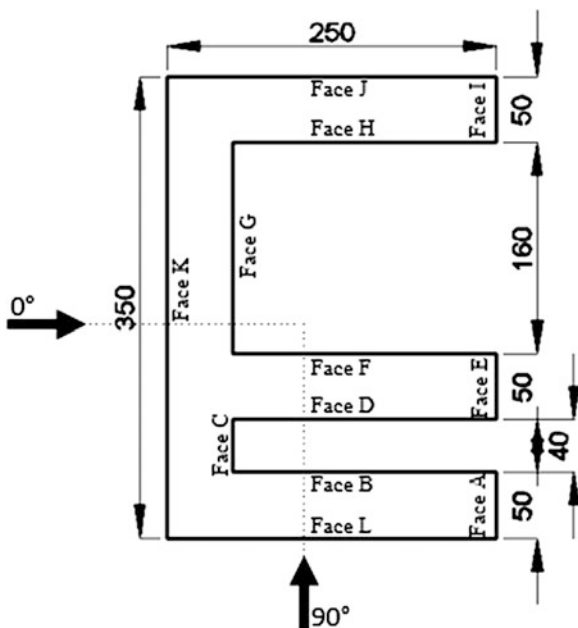


Fig. 1 Unsymmetrical ‘E’ plan shaped tall building model placed in wind tunnel, **a** pressure measurement model, **b** force measurement model

Fig. 2 Different faces of unsymmetrical ‘E’ plan shaped tall building along with detail dimension and wind angles (*plan view*) [all dimensions are in ‘mm’]



detail dimensions of the model are shown in Fig. 2. Pressure was measured by pressure tapings of internal diameter 1 and 15–20 mm long installed at every faces.

The velocity of wind in the wind tunnel was considered as 10 m/s and turbulence intensity was 10 % in the wind tunnel. Boundary layer flow was generated by vortex generator and cubic blocks placed in the upstream side of the wind tunnel. The power law index (α) for the velocity profile inside the wind tunnel was 0.133. Force measurement model was tested under three different wind velocity of 6, 8 and 10 m/s.

3 Numerical Study

Numerical study was carried out by Computational Fluid Dynamics (CFD) method by using ANSYS CFX software package. Two equations k- ϵ turbulence model was used for modelling as they offers a good compromise between numerical effort and computational accuracy. The k- ϵ model use the gradient diffusion hypothesis to relate the Reynold stresses to the mean velocity gradients and turbulent viscosity. ‘k’ is turbulence kinetic energy and is defined as the variance of fluctuations in velocity and ‘ ϵ ’ is the turbulence eddy dissipation (the rate at which the velocity fluctuation dissipate).

So, modified continuity and momentum equation after incorporating two new variables i.e., k and ϵ are

$$\frac{\partial \rho}{\partial t} + \frac{\partial}{\partial x_j} (\rho U_j) = 0 \tag{1}$$

$$\frac{\partial \rho U_i}{\partial t} + \frac{\partial}{\partial x_j} (\rho U_i U_j) = -\frac{\partial p'}{\partial x_i} + \frac{\partial}{\partial x_j} \left[\mu_{eff} \left(\frac{\partial U_i}{\partial x_j} + \frac{\partial U_j}{\partial x_i} \right) \right] + S_M \tag{2}$$

where S_M is the sum of body forces, μ_{eff} is the effective viscosity accounting for turbulence and p' is the modified pressure. The k-ε model, like the zero equation model, is based on the eddy viscosity concept, so that

$$\mu_{eff} = \mu + \mu_t \tag{3}$$

where μ_t is the turbulence viscosity. The k-ε model assumes that the turbulence viscosity is linked to the turbulence kinetic energy and dissipation via the relation

$$\mu_t = C_\mu \rho \frac{k^2}{\varepsilon} \tag{4}$$

where C_μ is a constant.

The values of k and ε come directly from the differential transport equations for the turbulence kinetic energy and turbulence dissipation rate:

$$\frac{\partial(\rho k)}{\partial t} + \frac{\partial}{\partial x_j} (\rho U_j k) = \frac{\partial}{\partial x_j} \left[\left(\mu + \frac{\mu_t}{\sigma_k} \right) \frac{\partial k}{\partial x_j} \right] + P_k - \rho \varepsilon + P_{kb} \tag{5}$$

$$\begin{aligned} \frac{\partial(\rho \varepsilon)}{\partial t} + \frac{\partial}{\partial x_j} (\rho U_j \varepsilon) &= \frac{\partial}{\partial x_j} \left[\left(\mu + \frac{\mu_t}{\sigma_\varepsilon} \right) \frac{\partial \varepsilon}{\partial x_j} \right] \\ &+ \frac{\varepsilon}{k} (C_{\varepsilon 1} P_k - C_{\varepsilon 2} \rho \varepsilon + C_{\varepsilon 1} P_{\varepsilon b}) \end{aligned} \tag{6}$$

P_k is turbulence production due to viscous forces, which is modeled using:

$$P_k = \mu_t \left(\frac{\partial U_i}{\partial x_j} + \frac{\partial U_j}{\partial x_i} \right) \frac{\partial U_i}{\partial x_j} - \frac{2}{3} \frac{\partial U_k}{\partial x_k} \left(3\mu_t \frac{\partial U_k}{\partial x_k} + \rho k \right) \tag{7}$$

C_μ is k-ε turbulence model constant of value 0.09. $C_{\varepsilon 1}$, $C_{\varepsilon 2}$ are also k-ε turbulence model constant in ANSYS CFX of values 1.44, 1.92 respectively. σ_k is the turbulence model constant for k equation of value 1.0 and σ_ε is the turbulence model constant for ε equation of value 1.3. ρ is the density of air in ANSYS CFX taken as 1.224 kg/m³. μ and μ_t are dynamic and turbulent viscosity respectively. The other notations having their usual meanings. The building was considered as bluff body in ANSYS CFX and the flow pattern around the building was studied.

The domain size (Fig. 3) was taken as referred by Franke et al. [14] and Revuz et al. [15].

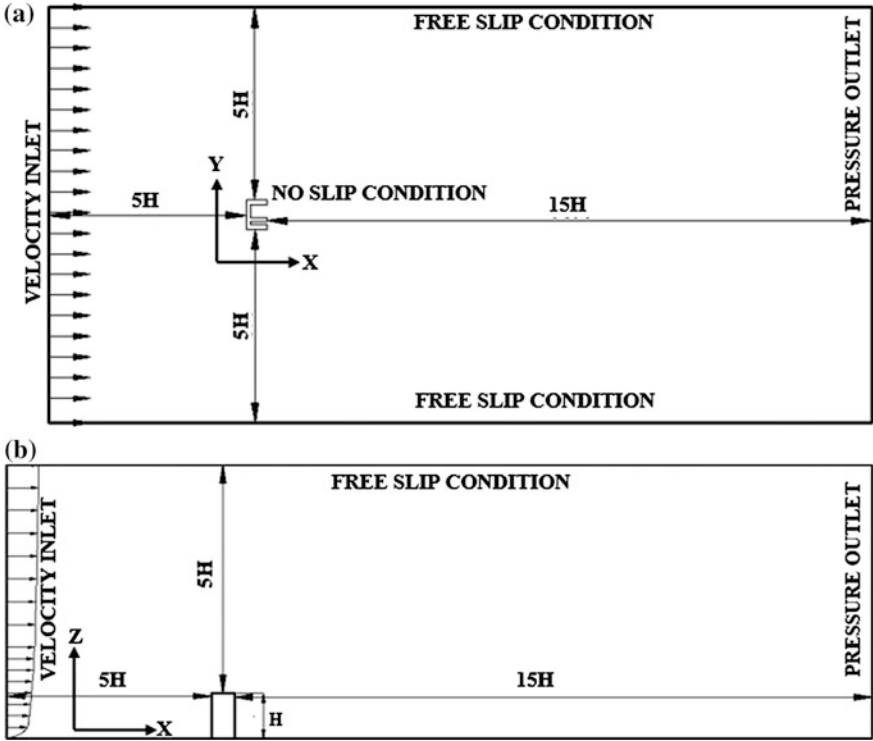


Fig. 3 Details of domain with boundary conditions, **a** plan, **b** elevation

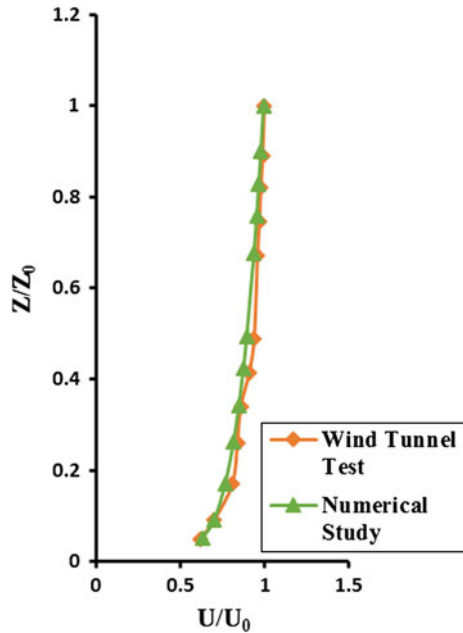
The upstream side was taken as 5H from the face of the building, downstream side was taken as 15H from the face of the building, two side distance of the domain was taken as 5H from the face of the building and top clearance was taken as 5H from the top surface of the building. Such large size of domain helps in vortex generation in the leeward side of the flow and backflow of wind also be prevented. Tetrahedron meshing was done throughout the domain with tetrahedral element and it was inflated near the model with hexagonal meshing for uniform wind flow near the surfaces of the ‘E’ plan shaped tall building.

The boundary conditions were taken as the same in the wind tunnel test such that the results found from the experiment can validate the results obtained from the numerical analysis.

Boundary layer wind flow near the windward side was generated in the inlet of the domain using Power law:

$$\frac{U}{U_0} = \left(\frac{z}{z_0}\right)^\alpha \tag{8}$$

Fig. 4 Velocity profile in inlet by experimental and analytical technique



where U_0 is the basic wind speed was taken as 10 m/s, z_0 is the boundary layer height was considered as 1 m as same as the wind tunnel and power law index α was taken as 0.133. The velocity profile for experiment and numerical study is shown in Fig. 4. Relative pressure at outlet was considered as 0 Pa. The velocity in all other directions was set to zero. Side surfaces and top surfaces of the domain were taken as free slip condition so that no Shear stress should generate there whereas, all surfaces of the body and ground of the domain were considered as no slip condition to measure the pressure contour accurately.

4 Results and Discussions

4.1 Wind Flow Pattern

Wind flow pattern around the building were studied for along wind (0°) and across wind (90°) direction by Computational Fluid Dynamics (CFD) technique. Plan view of both flow pattern are shown in Fig. 5. Flow pattern is almost symmetrical about central axis for along wind direction but it is very much asymmetrical about central axis for across wind direction. So, it is expected to get similar pressure on similar faces for along wind action before wind flow separation and pressure distribution on rear side faces may differ due to unsymmetrical plan shape but, pressure distribution may differ on each face in case of across wind action due to

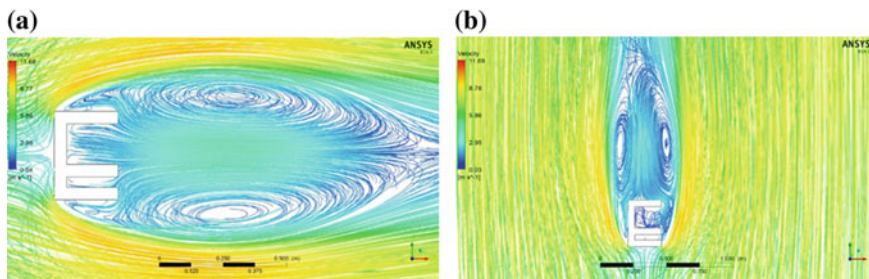


Fig. 5 Flow pattern around unsymmetrical ‘E’ plan shaped tall building shown in plan, **a** at 0° wind angle, **b** at 90° wind angle

unequal plan shape and irregular eddies formation due to interference effects of the limbs of unsymmetrical ‘E’ plan shape tall building. Pressure distribution on frontal face may symmetrical about vertical axis for both the wind directions because, wind is perpendicularly hitting the frontal surfaces in each case. Frictional suction force may occur at the sidewalls in both the cases, so that negative pressure may generate on these side faces. Also negative pressure may occur at the rear side faces due to suction force of vortex generated at the rear side faces.

4.2 Variation of Drag and Lift Coefficients

Drag and lift coefficients are found from experimental study of force measurement model in the wind tunnel. Force was measured in two directions (i.e., X and Y direction) for each wind incidence angle. Forces measured along X direction are termed as drag coefficients whereas forces measured along Y direction are termed as lift coefficients. Drag and lift coefficients are measured for three different wind speed of 6, 8, 10 m/s. Variation of drag and lift coefficients with different wind speed are shown in Fig. 6.

Variation of drag and lift coefficients with wind speed is almost linear with vertical axis which indicates that drag and lift coefficients are almost constant for a particular wind incidence angle which implies the accuracy of the experiment. Drag coefficients are more than corresponding lift coefficients for each wind angles because less suction effect occurred in perpendicular to wind direction when the frontal face is perfectly perpendicular to wind flow direction. A large variation of drag coefficients occurred between both wind incidence angles but lift coefficients are almost equal for both wind incidence angles. Maximum drag coefficient (0.95) occurred at 0° wind angle for wind speed of 10 m/s. Maximum wind dissipate on the frontal face due to maximum frontal area in case of 0° wind incidence angle so that maximum drag coefficient occurred at 0° wind incidence angle. Maximum lift coefficient (0.10) is occurred at both 0° and 90° wind incidence angles.

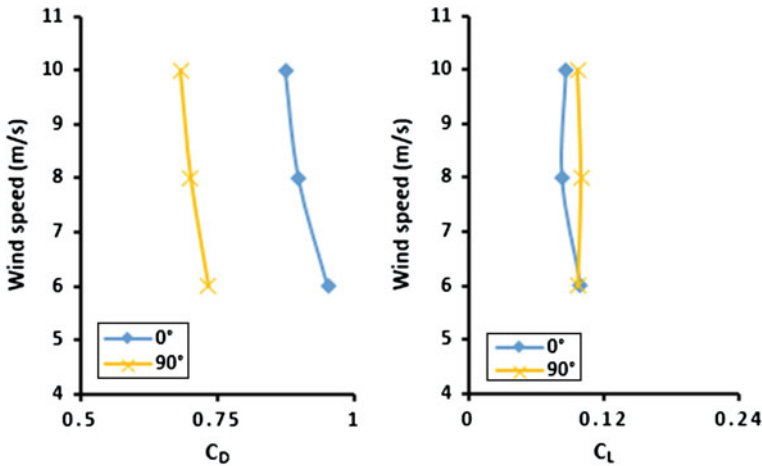


Fig. 6 Variation of drag coefficients (C_D) and lift coefficients (C_L) with wind speeds

4.3 Variation of Pressure Coefficients

Pressure coefficients (C_p) on different surfaces of the model were measured by experimental as well as numerical method. Also pressure contours on different surfaces of the model are plotted for along and across wind direction of flow. After that a comparative study between experimental and numerical method has carried out to justify the compatibility of both the method.

4.3.1 Pressure Contours

Pressure contour on different faces of unsymmetrical ‘E’ plan shape tall building are plotted for 0° as well as 90° wind action. Both experimentally predicted (Fig. 7) and numerically predicted (Fig. 8) pressure contours are plotted. Pressure contour on face A, C and on face B, I, L are plotted for 0° and 90° wind incidence angle respectively by both experimental as well as numerical technique. Pressure contour on face L is symmetrical about vertical axis due to symmetrical flow pattern about this face (Fig. 5). Also only positive pressure occurred on face L at 90° wind incidence angle because wind is directly hitting on this surface. Maximum negative pressure occurred on face B at 90° wind incidence angle due to high suction force of separated out flow lines after separation from face A. Negative pressure contours occurred on face A and C at an wind incidence angle 0° due to vortices generated at the rear side of the model. Pressure contour is almost symmetrical about vertical axis on face C for along wind direction due to small vortex inside the limbs and uniformity of vortex formation between the small limbs.

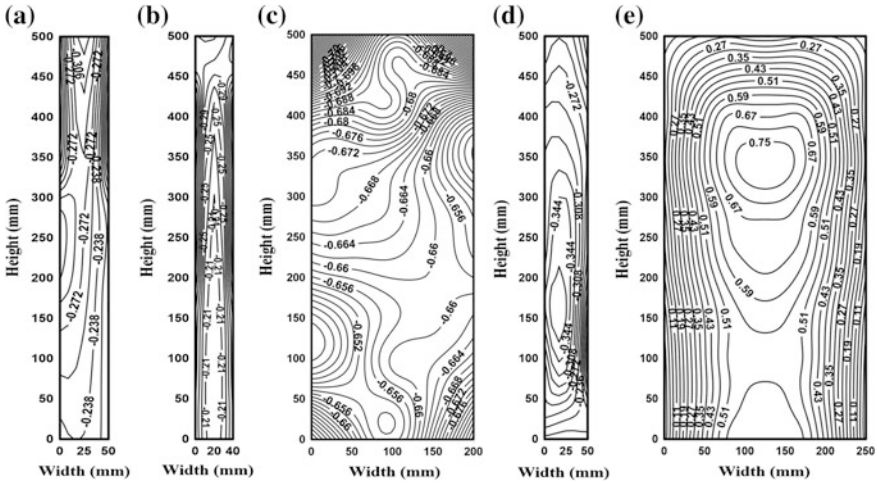


Fig. 7 Pressure contour on different faces of unsymmetrical ‘E’ plan shaped tall building by wind tunnel test, a face A at 0°, b face C at 0°, c face B at 90°, d face I at 90°, e face L at 90°

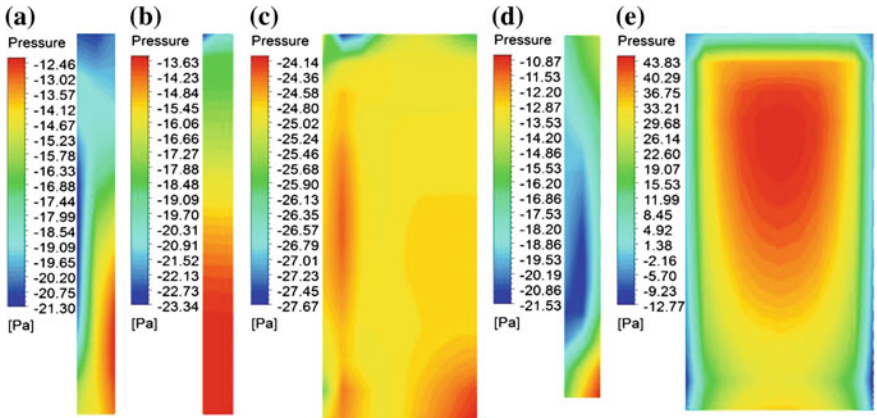


Fig. 8 Pressure contour on different faces of unsymmetrical ‘E’ plan shaped tall building by numerical technique, a face A at 0°, b face C at 0°, c face B at 90°, d face I at 90°, e face L at 90°

4.3.2 Mean Pressure Coefficients

Mean pressure coefficients of all the surfaces of unsymmetrical ‘E’ plan shaped tall building are given in Table 1. Similar mean pressure occurred on similar faces (face J and L) for 0° wind incidence angle as wind is perpendicularly hitting the frontal surface and separation of flow through the faces J and L are same in nature. Positive pressure occurred on frontal faces with respect to the flow direction of 0° (face K) and 90° (face L) wind action. Negative mean pressure occurred on rear side faces

Table 1 Mean pressure coefficients on different faces of unsymmetrical 'E' plan shaped tall building for different wind angles

Wind angles (θ)	Results category	Mean pressure coefficients of different faces											
		A	B	C	D	E	F	G	H	I	J	K	L
0°	Wind tunnel	-0.26	-0.24	-0.25	-0.34	-0.29	-0.29	-0.22	-0.23	-0.3	-0.51	0.55	-0.51
	k-ε model	-0.28	-0.26	-0.26	-0.29	-0.25	-0.24	-0.22	-0.23	-0.29	-0.43	0.57	-0.43
	Difference (%) of k-ε model w. r.t. wind tunnel	8	8	4	-15	-14	-17	0	0	-3	-16	4	-16
90°	Wind tunnel	-0.64	-0.67	-0.54	-0.66	-0.55	-0.41	-0.37	-0.36	-0.28	-0.19	-0.56	0.44
	k-ε model	-0.58	-0.56	-0.47	-0.54	-0.45	-0.35	-0.34	-0.32	-0.29	-0.21	-0.46	0.5
	Difference (%) of k-ε model w. r.t. wind tunnel	-9	-16	-13	-18	-18	-15	-8	-11	4	11	-18	14

due to vortices generated at the rear side faces and suction force occurred due to these vortices. A small vortex generated between the limbs of 'E' plan shaped building (Fig. 5) due to interference effect of the 50 mm width limbs and suction force generated in between these faces such that negative pressure occurred in between these faces for 0° as well as 90° wind angle. Also the intensity of mean pressure coefficients of these faces (face F, G, H) are almost same at 90° wind angle due to almost similar suction pressure. Maximum positive pressure occurred on face K in along wind action (0°) due to maximum force dissipation on that surface. Pressure intensity on face B, C and G, H are almost same in case of along wind action because stream lines are washed out of these zones in same nature with same intensity (Fig. 5). Mean pressure coefficients of face B, C, D are almost same for across wind direction of flow due to almost equal suction force occurred on these faces.

4.4 Comparative Study

A comparative study between results obtained from experimental and numerical study is carried out to justify the adequacy of both the methods. Mean pressure coefficients, pressure variation of some faces along vertical centerline and pressure variation along horizontal centerline are obtained by both the methods to compare the above two procedure.

Mean pressure coefficients of each face along with percentage of error of numerical study with respect to experimental study are given in Table 1. Positive and negative sign indicates the increment and decrement of magnitude with respect to experimental study. Positive pressure is almost equal for along wind action (0°) by both methods whether some discrepancy noticed in case of across wind direction (90°) due to less number of pressure tapping points installed in experimental model but this could be improved by providing more number of pressure tappings. Negative mean pressures on all faces are almost equal for both experimental as well as numerical method in case of 0° wind angle but some discrepancy occurred in case of 90° wind angle by numerical technique due to mesh pattern and mesh size. This discrepancy could further be improved by improving mesh sizes with higher efficient computational technique.

Pressure variation along vertical centerline of some faces (face D, G, H, K at 0° wind incidence angle and face F, G, I, L at 90° wind incidence angle) are plotted in Fig. 9 by both experimental as well as numerical technique. This variation can also be called as point to point variation of pressure along vertical centerline of different faces.

It is seen from the figure (Fig. 9) the results obtained from both methods are almost merging with each other for each face. Almost parabolic nature is noticed on face K and L in case of 0° and 90° wind incidence angles respectively due to

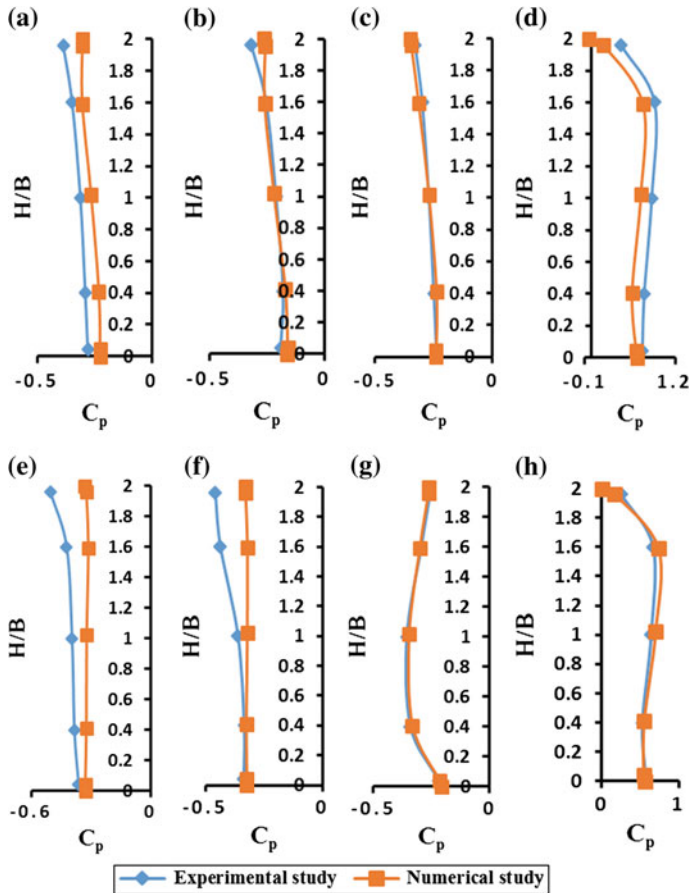


Fig. 9 Variation of pressure coefficients along vertical centerline on different faces of unsymmetrical ‘E’ plan shaped tall building, **a** face D at 0° , **b** face G at 0° , **c** face H at 0° , **d** face K at 0° , **e** face F at 90° , **f** face G at 90° , **g** face I at 90° , **h** face L at 90°

boundary layer wind flow in inlet region. Almost zero pressure occurred at the top portion in both the cases due to upwash of wind flow at this region. Pressure variation is almost convective from vertical line of face D, G, H in case of 0° wind incidence angle and the magnitudes are increasing with height.

Variation of pressure coefficients along horizontal centerline on all the faces are plotted in Figs. 10 and 11 for 0° and 90° wind angles respectively. Pressure variation is almost symmetrical about face K at 0° wind angle but not such symmetry occurred in case of 90° wind angle. However, a good agreement of results obtained by numerical method with wind tunnel test results are noticed.

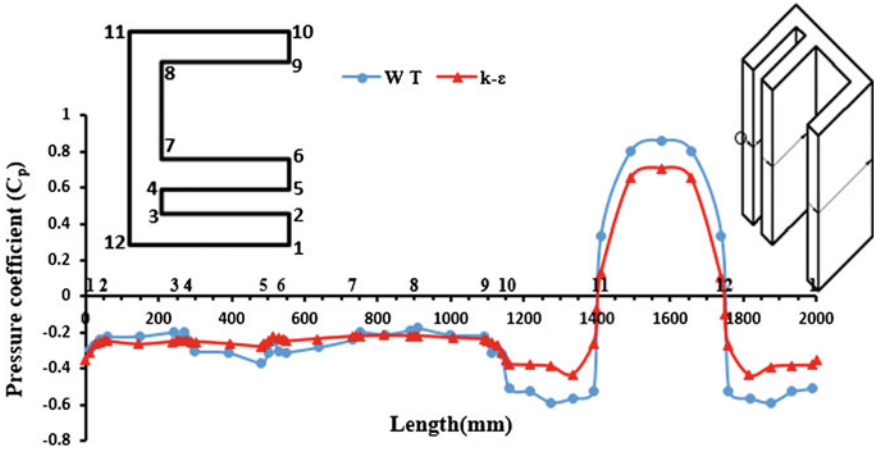


Fig. 10 Comparison of pressure coefficients along horizontal centerline for 0° wind angle

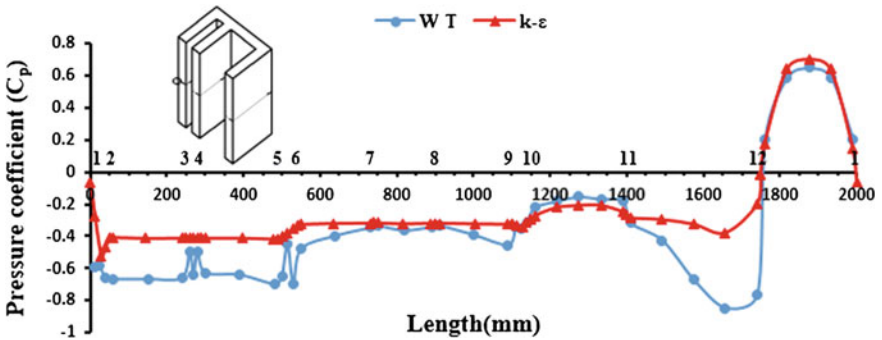


Fig. 11 Comparison of pressure coefficients along horizontal centerline for 90° wind angle

5 Conclusion

Present study mainly focussed on force and pressure variation on different faces of an unsymmetrical 'E' plan shaped tall building under 0° and 90° wind angle. In spite of perpendicular wind incidence angles, the building behaves in different nature under wind excitation from the rectangular building due to interference effects of the three limbs of 'E' plan shaped building. The most important outcomes are summarized below:

1. Wind flow pattern is noticeably changed after separation at 90° wind angle due to interference effect of the limbs ($200\text{ mm} \times 50\text{ mm}$ in plan) of 'E' plan shaped building.
2. Maximum drag coefficient occurred at 0° wind angle but maximum lift coefficient occurred at both 0° and 90° wind angles.
3. Symmetrical pressure contour about vertical axis occurred on face K and L at 0° and 90° wind incidence angle respectively due to perpendicular wind flow directions in both the cases with respect to the faces. Also pattern of pressure variation is parabolic (positive) in nature on both the faces due to boundary layer wind flow.
4. Negative pressure contour occurred on rear side faces with respect to wind flow direction. Also negative pressure experienced by the faces in between the limbs of 'E' plan shaped building due to irregular vortices formed in between the limbs.
5. Maximum positive mean C_p (0.57) occurred on face K at 0° wind angle due to direct wind force dissipation on this face.
6. Maximum negative mean C_p (-0.67) occurred on face B at 90° wind incidence angle due to high suction force of flow after separated out from face A and irregular eddies formation inbetween the limbs caused by interference effect of limb and turbulence.
7. Mean pressure coefficients on face A to face I are comparatively higher in case of 90° wind incidence angle with respect to 0° wind angle due to more irregular wind flow pattern at 90° wind angle. Also high suction force occurred in between these faces after separation of flow and interference effects highly occurred due to the limbs of 'E' plan shaped building.
8. A good agreement of numerically predicted results noticed with wind tunnel results by three comparisons (mean pressure coefficients, variation of pressure coefficients along horizontal and vertical centerline on the faces).

Acknowledgments The work described in this paper was fully supported by Wind Engineering Centre (WEC) of IIT Roorkee, India. Financial supports for this experimental study from Department of Science & Technology (DST) of India is gratefully appreciated.

References

1. IS: 875 (Part 3)-1987 (1987) Indian standard code of practice for design wind load on building and structures. Second Revision, New Delhi, India
2. AS/NZS 1170.2: 2011 (2011) Structural design action, part 2: wind actions. Australian/New-Zealand Standard, Sydney, Wellington
3. BS 6399-2: 1997 (1997) Loading for buildings—part 2: code of practice for wind loads. British Standard, London, UK
4. ASCE 7-10 (2010) Minimum design loads for buildings and other structures, 2nd edn. American Society of Civil Engineering, ASCE Standard, Reston, Virginia
5. Gomes MG, Rodrigues AM, Mendes P (2005) Experimental and numerical study of wind pressures on irregular-plan shapes. *J Wind Eng Ind Aerodyn* 93(10):741–756

6. Amin JA, Ahuja AK (2008) Experimental study of wind pressures on irregular plan shape buildings. In: BBAA VI International colloquium on: bluff bodies aerodynamics and applications, Milano, Italy, 20–24 July 2008
7. Carassale L, Freda A, Brunenghi MM (2014) Experimental investigation on the aerodynamic behavior of square cylinders with rounded corners. *J Fluids Struct* 44:195–204
8. Huang S, Li QS, Xu S (2007) Numerical evaluation of wind effects on a tall steel building by CFD. *J Constr Steel Res* 63:612–627
9. Mendis P, Ngo T, Haritos N, Hira A, Samali B, Cheung J (2007) Wind loading on tall buildings. *EJSE Spec Issue Load Struct* 3:41–54
10. Dalui SK (2008) Wind effects on tall buildings with peculiar shapes. Ph.D. thesis, Department of Civil Engineering, IIT Roorkee, India
11. Fu JY, Li QS, Wu JR, Xiao YQ, Song LL (2008) Field measurements of boundary layer wind characteristics and wind-induced responses of super-tall buildings. *J Wind Eng Ind Aerodyn* 96(8–9):1332–1358
12. Kim YC, Kanda J (2013) Wind pressures on tapered and set-back tall buildings. *J Fluids Struct* 39:306–321
13. Chakraborty S, Dalui SK, Ahuja AK (2013) Experimental and numerical study of surface pressure on ‘+’ plan shape tall building. *Int J Constr Mater Struct* 1(1):45–58
14. Franke J, Hirsch C, Jensen AG, Krüs HW, Schatzmann M, Westbury PS, Miles SD, Wisse JA, Wright NG (2004) Recommendations on the use of CFD in wind engineering. In: Proceedings of the international conference on Urban wind engineering and building aerodynamics: COST C14: impact of wind and storm on city life and built environment. Rhode, Saint-Genève
15. Revuz J, Hargreaves DM, Owen JS (2012) On the domain size for the steady-state CFD modelling of a tall building. *J Wind Struct* 15(4):313–329

Seismic and Wind Response Reduction of Benchmark Building Using Viscoelastic Damper

Praveen Kumar and Barun Gopal Pati

Abstract In the last three decades, there has been great deal of interest in the use of control systems to mitigate the effects of dynamic environmental hazards like earthquake and strong winds on the civil engineering structures. A variety of control systems have been considered for these applications that can be classified as passive, semi-active active or hybrid. In the present study, Viscoelastic damper as a structural protective system has be implemented to mitigate the damaging effects from the seismic and wind forces acting on the benchmark building. The dynamic behavior of the structural system supported on viscoelastic damper, the optimum parameters of the damper and effect of damper properties on the free vibration characteristics of the structure subjected to seismic and wind forces are investigated. The seismic force considered for study is El-Cento and wind force as simulated onsite wind velocity from the results obtained from the wind tunnel test. It is observed from the study that vicoelastic damper is very effective in reducing the reposes of benchmark building due to seismic and wind forces with respect to uncontrolled structure.

Keywords Benchmark building · Seismic · Viscoelastic damper · Wind tunnel

1 Introduction

An engineer's ability to reduce a city's damage caused by earthquakes and wind excitation is crucial to the economy and human life. Earthquake and wind excitation can claim the lives of many people cause millions of Rupees in damages and also reduce building longevity. Recent advances in civil structures such as high-rise buildings, towers and long span bridges go with an additional flexibility and

P. Kumar (✉) · B.G. Pati
Architectural and Structural Engineering Division, Bhabha Atomic Research Centre,
Trombay, Mumbai 400 085, India
e-mail: pra_veen74@rediffmail.com

© Springer India 2015
V. Matsagar (ed.), *Advances in Structural Engineering*,
DOI 10.1007/978-81-322-2193-7_112

1461

insufficient inherent damping, which lead to increase in their susceptibility to external excitation. Therefore, these flexible structures are susceptible to be exposed to excessive levels of vibration under the actions of a strong wind or earthquake motion. The protection of such structures from natural hazards puts an important task for engineers and researchers. To ensure the functional performance of flexible structures against such undesirable vibrations, various design alternatives have been developed, ranging from alternative structural systems to modern control systems with the use of various types of control devices.

In general, we could classify modern control systems into four categories, namely passive, active, semi-active and hybrid control system. A passive controller is a system that does not require power to operate and directly damps vibration or movement. Active control requires significant power to run and applies a force directly into the system to damp vibration. Semi-active control requires minimal power and it applies a force that changes the system's physical properties, therefore damping the vibration.

Among the various control devices Passive Viscoelastic Damper is proposed in the study to reduce the seismic and wind effects on the structure. Viscoelastic (VE) damper is a modification from the fluid viscous dampers. This VE damper usually consists of an orifice and piston moving in a hollow cylinder filled with highly viscous fluid, the gap between the piston and cylinder filled with viscoelastic material. These dampers have been successfully incorporated in a number of tall buildings as a viable energy dissipating system to suppress wind and earthquake induced motion of building structures. This type of damper dissipates the building's mechanical energy by converting it into heat. Several factors such as ambient temperature and the loading frequency will affect the performance and hence the effectiveness of the damper system. VE dampers have been able to increase the overall damping of the structure significantly, hence improving the overall performance of dynamically sensitive structures. The twin towers of the World Trade Center Buildings in New York City and the Columbia Seafirst Building in Seattle, Washington, are among the first buildings, which benefited from the installation of VE dampers. In seismic applications, the VE dampers can be incorporated either into new construction or as a viable candidate for the retrofit of existing buildings, which adds to the versatility of VE dampers.

Mahmoodi initiated the preliminary work and proposal for use of visco-elastic dampers in the year 1972 [1]. Tsai [2] presented innovative design, which he claimed was superior to the dampers proposed by Mahmoodi and Keel [3]. The experimental and analytical work on piping systems controlled using these devices is reported from Kunieda et al. [4] and Chiba and Kobayashi [5]. Recent studies on optimal design of visco-elastic dampers are reported by Shukla and Datta [6] and Park et al. [7].

The main objective of the present study is to develop: Optimum design parameter of the benchmark building equipped with VE damper; To investigate numerically the feasibility and efficiency of VE damper in comparison to uncontrolled structure; To investigate the response of benchmark building equipped with VE damper under the seismic and wind forces.

2 Modelling of Benchmark Building with VE Damper

A six storied benchmark building with passive viscoelastic damper is shown in Fig. 1. This system is a simple representation of the scaled, six-storied, test structure that is being used for experimental control studies at the Washington University Structural control and Earthquake Engineering Laboratory by Jansen and Dyke [8]. This, six storied benchmark building having mass of each floor, M_i as $0.227 \text{ N}/(\text{cm}/\text{s}^2)$ [22.7 kg], the stiffness of each floor K_i as 297 N/cm (29,700 N/m) and a damping ratio for each mode of 2 %. The seismic force considered is NS component of the El-Centro 1940 as the input ground motion to the structure. The time history of El-Centro 1940 earthquake is shown Fig. 2. Wind force considered for analysis is the stipulated wind velocity at Mumbai, India site from the wind tunnel test performed at University of technology Sydney, Australia by Samali et al. [9]. The wind velocity as wind excitation to the structure is shown in Fig. 3.

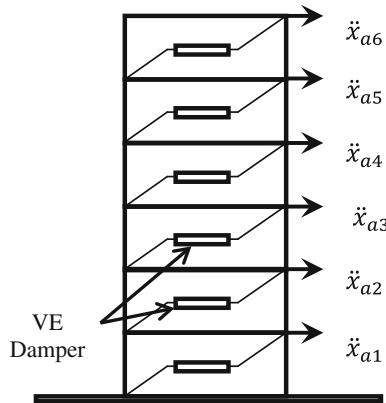


Fig. 1 Six storied benchmark building with VE dampers in all stories

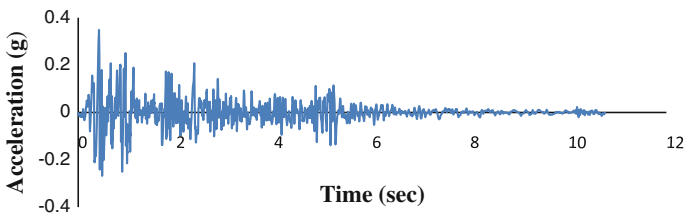


Fig. 2 NS component of El-Centro 1940 ground motion

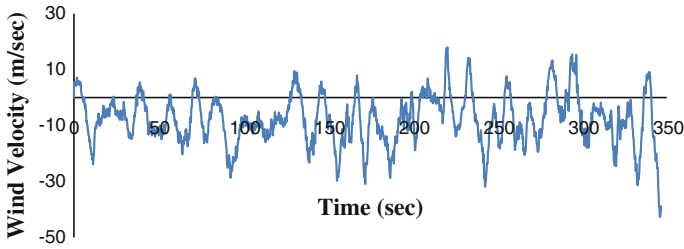
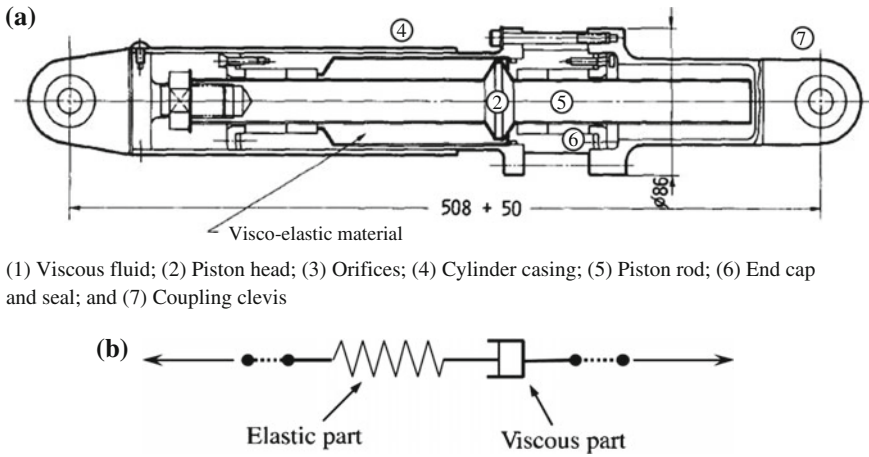


Fig. 3 Scaled wind velocity data



(1) Viscous fluid; (2) Piston head; (3) Orifices; (4) Cylinder casing; (5) Piston rod; (6) End cap and seal; and (7) Coupling clevis

Fig. 4 a Schematic model of viscoelastic damper; b Maxwell model for the viscoelastic damper

Figure 4a shows a schematic diagram of a typical viscoelastic damper proposed by Kunieda et al. [4]. Figure 4b shows the generalized Maxwell Model. According to Maxwell, the resistance of the damper is dependent upon both velocity and displacement. The damper has two part; elastic (represented by spring) and viscous (represented by damper). Here Spring and damper connected in series.

The equations of motion of the structure equipped with viscoelastic damper, under the ground motion are expressed in the following matrix form:

$$[M]\{\ddot{u}\} + [C]\{\dot{u}\} + [K]\{u\} = -[M]\{r\} \ddot{u}_g \tag{1}$$

$$\{u\} = \{x_1, y_1, z_1, \theta_{x1}, \theta_{y1}, \theta_{z1}, x_2, y_2, z_2, \theta_{x2}, \theta_{y2}, \theta_{z2}, \dots, x_N, y_N, z_N, \theta_{xN}, \theta_{yN}, \theta_{zN}\}^T \tag{2}$$

where $[M]$, $[C]$ and $[K]$ represents the mass, damping and stiffness matrix, respectively of the structural system with VE damper of order $6 N \times 6 N$, where N is the number of nodes; $\{\ddot{u}\}$, $\{\dot{u}\}$ and $\{u\}$ represent acceleration, velocity and displacement vectors, respectively; $\{r\}$ is the influence coefficient vector; \ddot{u}_g is the earthquake ground acceleration; and x_i , y_i and z_i are the displacements of the i th node in the structural system in X -, Y - and Z -directions, respectively. A lumped mass matrix is obtained by ignoring the masses in the rotational degrees-of-freedom and it has a diagonal form. The stiffness matrix of the structures with VE damper is constructed separately as given below and then static condensation is carried out to eliminate the rotational degrees-of-freedom.

$$[K] = \sum_{p=1}^{n_d} [K_b] + [u_f^p] K_d^p \tag{3}$$

where $[K_b]$ is the stiffness matrix of the structure alone; n_d is the total number of VE dampers provided in the structure; $[u_f^p]$ is the location matrix of the p th damper and K_d^p is the stiffness of the p th VE damper.

The damping matrix of the overall system (i.e. structure with dampers) is obtained by adding the inherent structure damping matrix $[C_b]$ and the damping contribution from the dampers and is expressed by

$$[C] = \sum_{p=1}^{n_d} [C_b] + [u_f^p] c_d^p \tag{4}$$

where $[C_b]$ is the damping matrix of the structure alone; $[u_f^p]$ is the location matrix of the p th damper and c_d^p is the damping coefficient of the p th damper. With the first two natural frequencies of the structural system known and the damping ratio, the damping matrix is obtained by using Rayleigh’s method.

3 Numerical Study of Structure with Viscoelastic Dampers

The seismic and wind response of the benchmark building with visco-elastic damper is investigated for El-Centro earthquake stipulated and wind velocity for Mumbai site, India. Dynamic analysis of six storied benchmark structure under seismic and wind excitation has been performed with different configuration of VE dampers placement.

It is observed that there are two parameters, c_d and K_d that affects the performance of a VE damper. To numerically search for design parameters of individual damper is computationally time-consuming. Therefore, firstly, it is assumed that the dampers are having constant damping ratios (i.e. $c_d = c_{d1}, c_{d2}$). Then, to obtain the design parameters of the VE dampers, the seismic responses of the controlled

structures are noted for different values of damping ratios in the dampers in the practical range of ratio $c_d/c_b = 0-20$, where c_b is the first mode damping coefficient of the uncontrolled structure expressed as

$$c_b = 2\xi_b m_1 \omega_1 \tag{5}$$

in which, ξ_b is the damping ratio; ω_1 is the fundamental natural frequency and m_1 is the corresponding modal mass of the structural system. Similarly for the design parameters for VE dampers attached to the structure, the seismic responses of the structure are noted for different values of both K_d and c_d . Keeping the range of variation of c_d , the responses of the structural system are noted for different values of the ratio K_d/K_b in the practical range of $=0.01-0.4$, where K_b is first mode stiffness of the structural system and expressed as

$$K_b = m_1 \omega_1^2 \tag{6}$$

The variation of displacements and acceleration are studied with respect to different c_d and K_d values and are shown in Figs. 5 and 6. From the Figs. 5 and 6, the ratios $c_d/c_b = 12$ and $K_d/K_b = 0.1$ are selected as optimum value. The optimum

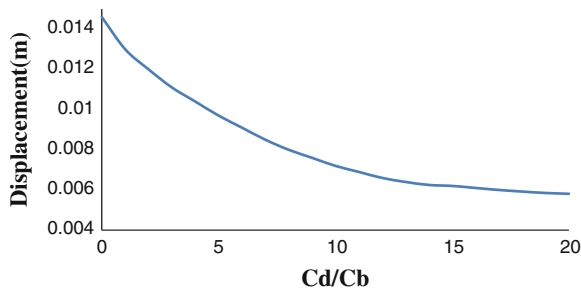


Fig. 5 Peak displacement of 6th floor for passive viscoelastic damper

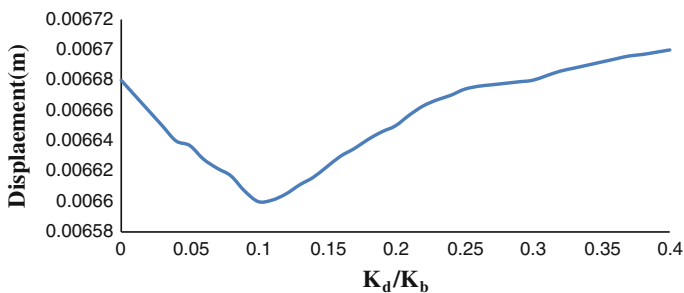


Fig. 6 Peak displacement of each floor for passive viscoelastic damper

values of stiffness and damping of the damper are obtained for the seismic case and the same optimum values of VE damper are used in the structure excited by wind.

The first fundamental frequency of the benchmark building obtained from the experiment is 8.61 rad/s, which are near to value calculated in present analysis and is 8.72 rad/s in the first mode.

Peak responses of displacement and acceleration by the seismic excitation are shown in Figs. 7 and 8 with different configuration of the damper placements. It is observed that as the number of damper increased, the peak displacement of each floor in general reduces. However, for displacement controlled systems it is observed that dampers continuously starting with first damper between 1st and ground floor and subsequent damper should be connected on subsequent stories without leaving any intermediate story without any damper can be noticed from the

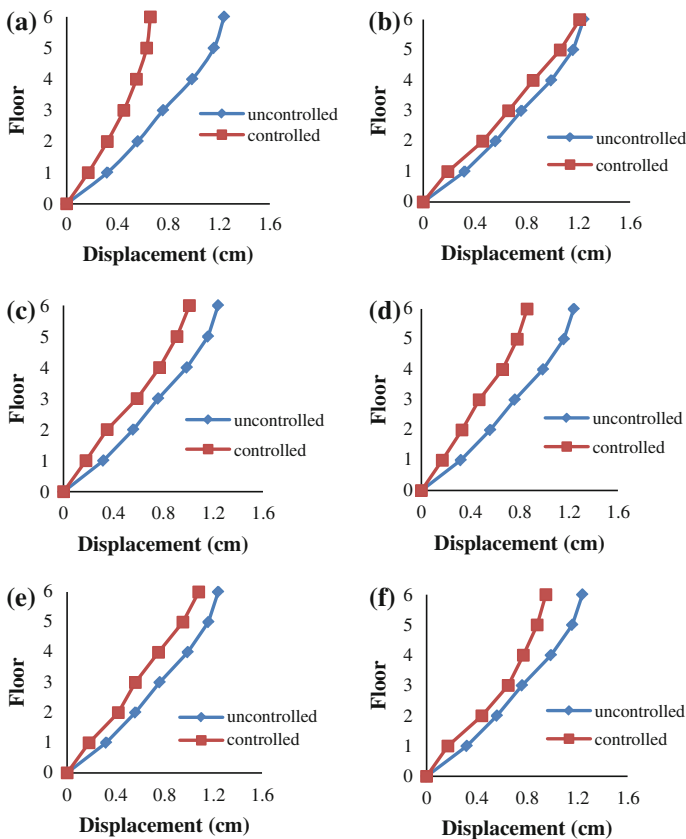


Fig. 7 Peak displacement of each floor for passive viscoelastic damper **a** all stories, **b** 1st story, **c** 1st and 2nd stories, **d** 1st, 2nd and 3rd stories, **e** 1st and 3rd stories, **f** 1st, 3rd and 5th stories, subjected to earthquake

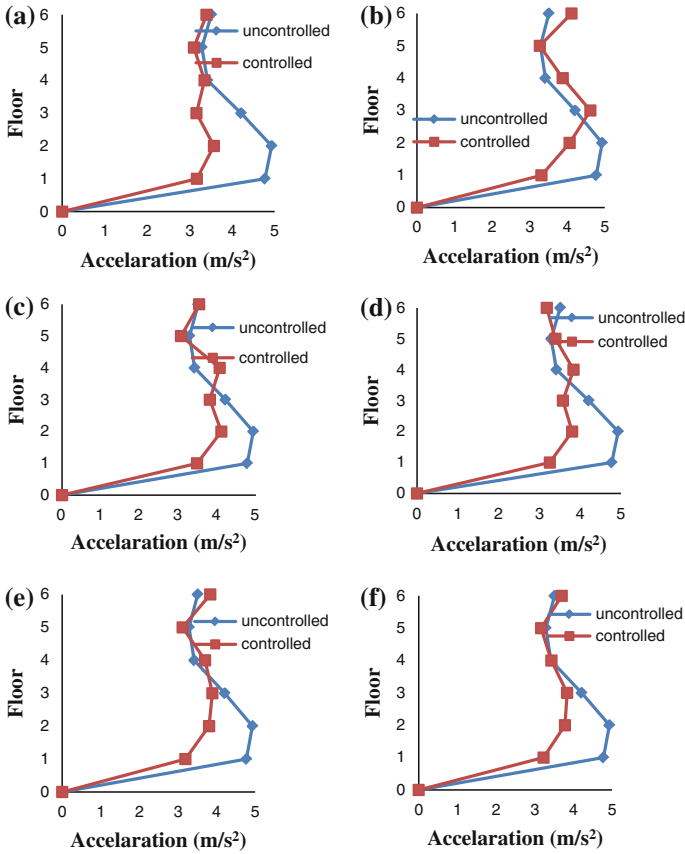


Fig. 8 Peak acceleration of each floor for passive viscoelastic damper **a** all stories, **b** 1st story, **c** 1st and 2nd stories, **d** 1st, 2nd and 3rd stories, **e** 1st and 3rd stories, **f** 1st, 3rd and 5th stories, subjected to earthquake

results of dampers in 1st, 3rd and 5th stories. For maximum reduction in peak displacements, the VE Dampers in all stories should be employed. The peak values of inter-story drifts also get reduced by introduction of VE dampers. From Fig. 8, it is observed that numbers of dampers are increased, the peak acceleration of each floor, in general, reduces. It is notice from the Fig. 8 that reduction of displacement is predominately at the first three floors and the upper floor acceleration reduction is not substantial. Hence, for maximum reduction in peak acceleration VE dampers is placed on all stories. Figure 9 shows the displacement-time, acceleration-time variation at 6th floor and base shear-time variation for VE damper at all stories subjected to earthquake excitation. It observed from the Fig. 9 that responses reduction in term of displacement, acceleration and base shear is substantial.

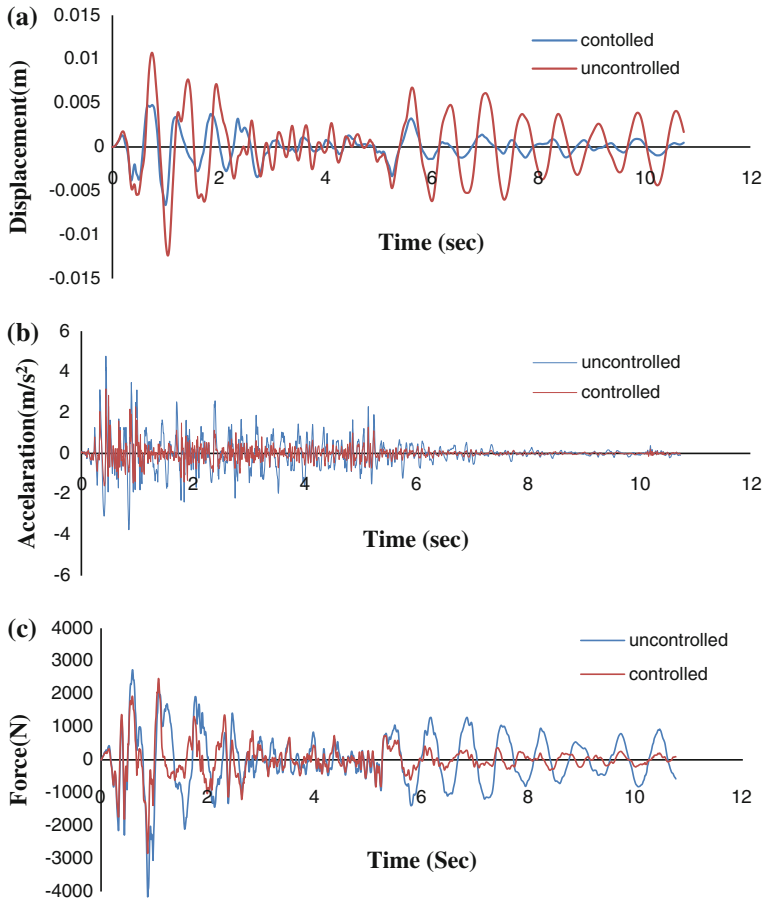


Fig. 9 a Displacement-time, b acceleration-time graph (6th floor) and c base shear-time graph for passive viscoelastic damper at all stories subjected to earthquake excitation

Peak responses of displacement and acceleration by the wind excitation are shown in Figs. 10 and 11 with different configuration of the damper placements. It is observed that as the number of damper increased, the peak displacement of each floor in general reduces. Figure 12 shows the displacement-time and acceleration-time variation at 6th floor for VE damper at all stories subjected to wind excitation. It observed from the Fig. 12 that responses reduction in term of displacement, acceleration and base shear is substantial.

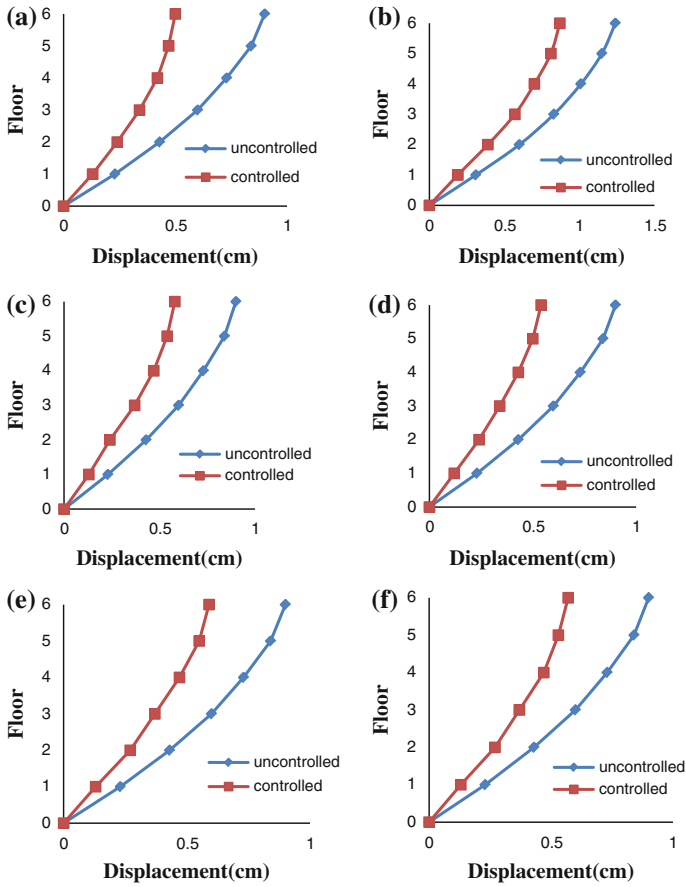


Fig. 10 Peak displacement of each floor for passive viscoelastic damper **a** all stories, **b** 1st story, **c** 1st and 2nd stories, **d** 1st, 2nd and 3rd stories, **e** 1st and 3rd stories, **f** 1st, 3rd and 5th stories, subjected to wind excitation

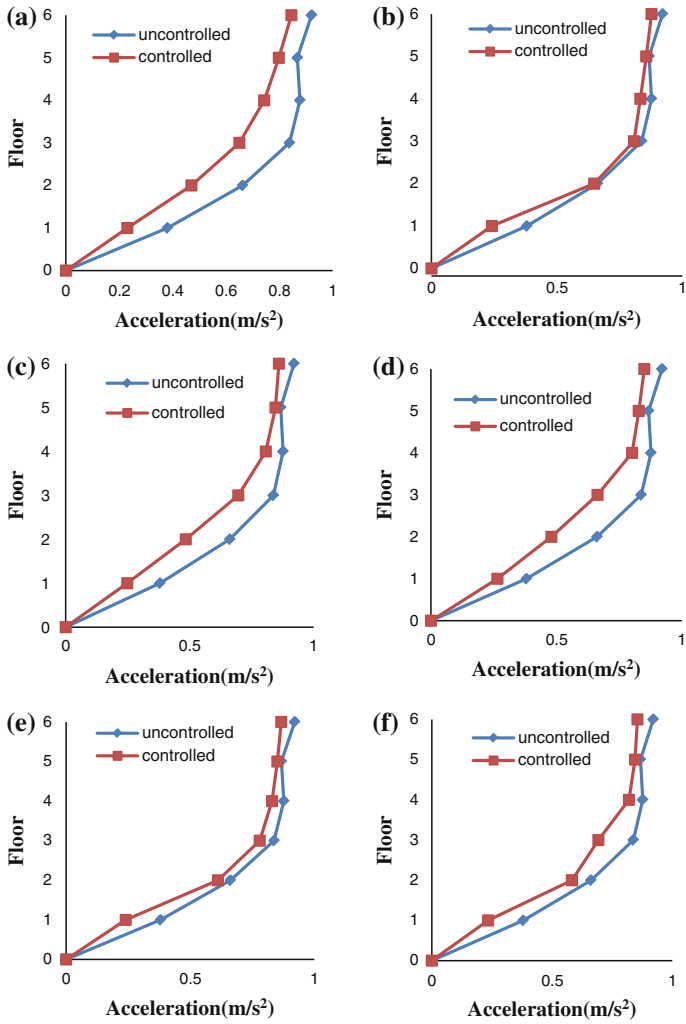


Fig. 11 Peak acceleration of each floor for passive viscoelastic damper **a** all stories, **b** 1st story, **c** 1st and 2nd stories, **d** 1st, 2nd and 3rd stories, **e** 1st and 3rd stories, **f** 1st, 3rd and 5th stories, subjected to wind excitation

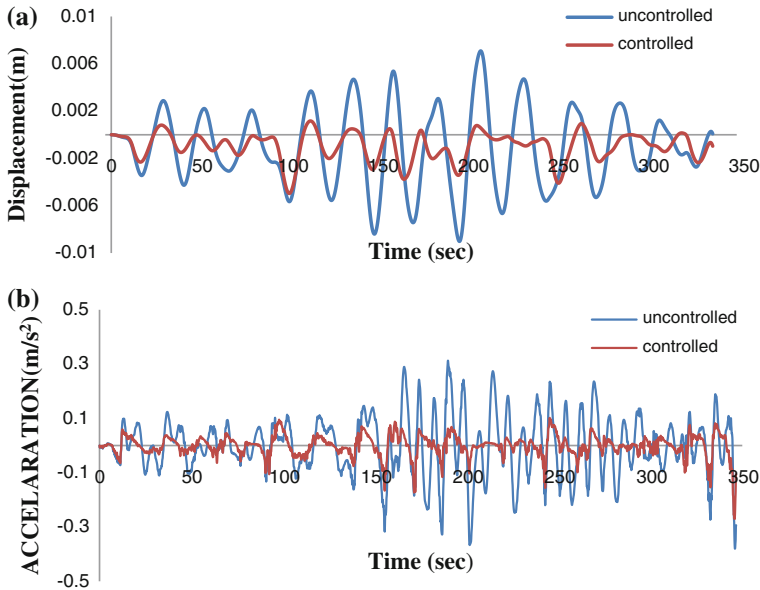


Fig. 12 a Displacement-time graph (6th floor), b acceleration-time graph (1st floor) for passive viscoelastic damper at all stories under wind excitation

4 Conclusions

The effectiveness and performance of VE damper in six storied benchmark building subjected to El-Centro earthquake motion and simulated wind data at Mumbai, India with configuration of damper placement in the structure has been investigated and presented. From that optimum damper parameters, performance of VE damper are studied at different configurations of damper in the benchmark building. From numerical investigation for the structural system with VE dampers as a protective control system, the following conclusions are drawn:

1. Numerical studies show that the VE dampers are effective in reducing the seismic and wind responses of the structural system with respect to uncontrolled structure. It is very effective in reducing displacement and acceleration; almost 45 % in case of displacement, 35 % in case of acceleration and base-shear; about 20 % reduction can be seen.
2. From the parametric study it is seen that with increase in damping value of the VE damper, the peak displacements, accelerations and base-shear are reducing but after certain value the amount of reduction becomes very less. From this point of view optimum damper parameters are selected.
3. By studying the effect of various damper placement configurations it has been found that for obtaining best results, VE dampers must be installed in consecutive floors rather than alternate floors for same number of dampers.

Also preferably damper installation should start from ground floor for the significant reduction in acceleration.

4. Desire response reduction at particular floor can be achieved by applying VE damper at the particular floors only.
5. High percentage of reduction in displacement of top floor of the building can be greatly effective where the space between two buildings is less.

References

1. Mahmoodi P (1972) Structural dampers. *J Struct Div, ASCE* 95(8):1661–1672
2. Tsai CS (1993) Innovative design of viscoelastic dampers for seismic mitigation. *Nucl Eng Des* 139:165–182
3. Mahmoodi P, Keel CJ (1986) Performance of viscoelastic structural dampers for the Columbia Center building. *Build Motion Wind ASCE* 21:66–82
4. Kunieda M, Chiba T, Kobayashi H (1987) Positive use of damping devices for piping systems—some experiences and new proposals. *Nucl Eng Des* 104(2):107–120
5. Chiba T, Kobayashi H (1990) Response characteristics of piping system supported by viscoelastic and elasto-plastic dampers. *J Press Vessel Technol* 112(1):34–38
6. Shukla AK, Datta TK (1999) Optimal use of viscoelastic dampers in building frames for seismic force. *J Struct Eng ASCE* 125:401–409
7. Park J-H, Kim J, Min K-W (2004) Opti design of added visco-elastic dampers and supporting braces. *Earthq Eng Struct Dyn* 33:465–484
8. Jansen LM, Dyke SJ (1999) Semiactive control strategies for MR Dampers: comparative study. *J Eng Mech* 126(8):795–803
9. Samali B, Kwok KCS, Wood GS, Yang JN (2004) Wind tunnel tests for wind-excited benchmark building. *J Eng Mech ASCE* 15(5):447–450

Optimum Tuned Mass Damper for Wind and Earthquake Response Control of High-Rise Building

Said Elias and Vasant Matsagar

Abstract The effectiveness of optimal single tuned mass damper (STMD) for wind and earthquake response control of high-rise building is investigated. Two buildings one 76-storey benchmark building and one 20-storey benchmark building are modeled as shear type structure with a lateral degree-of-freedom at each floor, and STMD is installed at top or different floors. The structure is controlled by installing STMD at different locations. The modal frequencies and mode shapes of the buildings are determined. Several optimal locations are identified based on the mode shapes of the uncontrolled and controlled benchmark building. The STMD is placed where the mode shape amplitude of the benchmark building is the largest/larger in the particular mode and each time tuned with the corresponding modal frequency, while controlling up to first five modes. The coupled differential equations of motion for the system are derived and solved using Newmark's step-by-step iteration method. The variations of buildings responses under wind and earthquake forces are computed to study the effectiveness of the STMD. In addition the optimum mass ratios for STMD are obtained. It is observed that the STMD is effective to control the responses of structures subjected to wind and earthquake. Further, STMD tuned to higher modal frequencies will be effective to reduce the responses of the building significantly.

Keywords High-rise building · Modal frequency/shape · Optimal STMD · Tuned mass damper

S. Elias (✉) · V. Matsagar
Indian Institute of Technology (IIT), Delhi, India
e-mail: eliasrahimi959@gmail.com

V. Matsagar
e-mail: matsagar@civil.iitd.ac.in

1 Introduction

At present the cities are growing fast, as their populations are increasing, the low rise building spaces are not enough. Needs for the increasing population is resulted to construction of tall buildings and increasing the bridges for network facilities. Natural hazard such as earthquake and wind causes damages for the buildings and bridges. The concern of structural engineers is to bring safety and make people to feel safe and comfortable. Energy dissipation of the natural hazard with the help of passive, semi-active and active structural control devices are reported to be better than relying on the inelastic deformation of the structure. Significant progress has been made in the area of structural control in the past by using analytical and experimental study on various different buildings and bridges. Wind and earthquake vibrations in structures are principally controlled by usage of single tuned mass damper (STMD). The concept of a TMD has been originated since the attempt made by Frahm [1]. He tried to use spring absorber to control rolling motion in ships, and undamped mass-spring absorber shown ability to set the amplitude of main system to zero for a single frequency. Thus, Frahm's design has been improved by Ormondroyd and Den Hartog [2]. They designed damped vibration absorber for broadband attenuation. In addition they introduced the system of invariant points which has evolved as the path for analytical optimal solution which could control the response of the main structure, and its own motion. The detailed theory of the TMD system attached to undamped main structure was discussed by Den Hartog [3]. Optimal linear vibration absorber for linear damped primary system was determined by Randall et al. [4] using graphical solution. The optimum control of absorbers continued over the years and different approaches have been proposed by investigators. Abe and Igusa [5] investigated the effectiveness of TMD structures with closely spaced natural frequencies. They have concluded that the number of TMDs must be equal or larger than the number of closely spaced modes and the spatial placement of the TMDs must be such that a certain matrix rank is satisfied. In addition they also reported that for widely spaced natural frequencies, the response is the same as that of an equivalent single degree of freedom (SDOF) structure/TMD system. The TMDs are most effective when the first mode contribution to the response is dominant is reported by Soong and Dargush [6]. This is generally the case for tall and slender structural systems. Nagarajaiah [7] introduced the concept of adaptive passive tuned mass dampers (APTMD). In addition, the new adaptive length pendulum stiffness tuned mass damper's (PSTMD) were introduced. He observed that the TMD loses its effectiveness even with just 5 % mistuning, whereas PSTMD retunes, and reduces the response effectively. The PSTMD and APTMD offer a number of new possibilities for response control of flexible structures, such as tall buildings, and long span bridges, under wind and earthquake loading. Pisal and Jangid [8] had shown the effectiveness of the semi-active tuned mass friction damper. The study shown that new system produces continuous and smooth slip force and eliminates the frequency response of the structure usually occurs in case of passive tuned mass friction damper. However, no study is conducted on earthquake response control of structure

wherein placement and tuning of the TMD in structures are made in accordance with the modal properties of the structures.

The objective of this study, therefore, is to study effective placement of STMD based on the mode shapes and frequencies of the main structure. The STMD placed where the mode shape amplitudes of the structure is the largest or larger in the particular modes and tuning of the STMD to higher modal frequencies while controlling first five modes for mitigation of structures vibration under wind forces and earthquake ground excitations.

2 Theory

In present study, two buildings are considered for wind and earthquake response control. For wind response control a 76-storey benchmark building is considered, having 306.1 m height and 42 m \times 42 m plan dimensions. It is sensitive to wind because the aspect ratio (height to width ratio) is 7.3. The first storey is 10 m high; stories from 2–3, 38–40 and 74–76 are 4.5 m high; all other stories are having typical height of 3.9 m. Yang et al. [9] have given detailed description of the benchmark building and its model. The rotational degrees of freedom have been removed by the static condensation procedure, only translational degrees of freedom, one at each floor of the building is considered. Figure 1a through Fig. 1e show mathematical model of the benchmark building installed with STMD at different locations. In addition, the heights of various floors and configuration of the STMD have also been depicted.

For earthquake response control a 20-storey benchmark building is considered, having 80.77 m height and 30.48 m \times 36.58 m plan dimension. Figure 2a, b show the plan and elevation of benchmark building installed with STMD at different locations. The benchmark building [10] is having of five bays in north–south (N–S) direction and six bays in east–west (E–W) direction with each bay width of 6.10 m. The lateral load of the building is resisted by steel perimeter moment resisting frames (MRFs) in both directions. The floor to floor height is 3.96 m for 19 upper floors, 5.49 m for first floor and 3.65 m for both basements. Splices are used for the columns after every three floors. The columns are assumed to be pinned. In addition it is assumed that the horizontal displacement is to be restrained at first floor. The seismic mass, including both N–S MRFs, are 5.323105, 5.633105, 5.523105 and 5.843105 kg of the ground level, first level, second level to 19th, and 20th level respectively. The seismic mass of the above ground levels of the entire structure is 1.113107 kg. The beams and columns of the structures are modeled as plane-frame elements, and a mass and stiffness matrix for each of the structure is determined. The damping matrix is determined based on an assumption of Rayleigh damping. The first 10 natural frequencies of the 20-storey benchmark evaluation model are: 0.261, 0.753, 1.30, 1.83, 2.40, 2.44, 2.92, 3.01, 3.63, and 3.68 Hz. Floors are assumed to be rigid in the horizontal plane because they provide diaphragm action. It is assumed that floor diaphragm carries the inertial effects of each level to each perimeter MRF, hence,

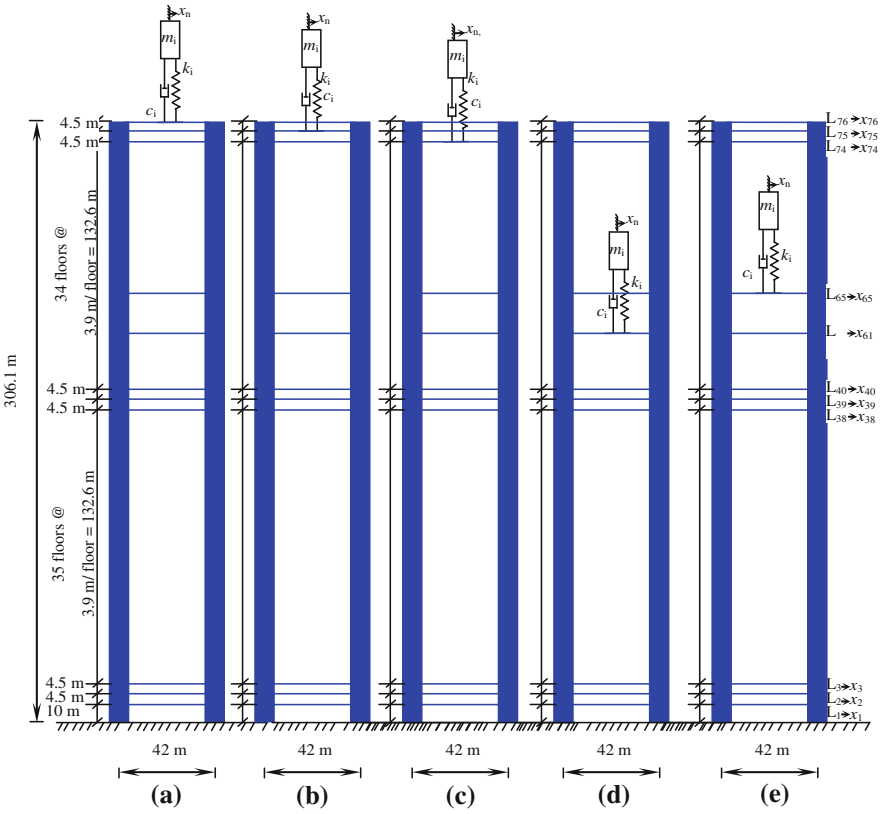


Fig. 1 a Through e mathematical model of the benchmark building installed with STMD at different locations

each frame resists one-half of the seismic mass associated with the entire structure. Further, the following assumptions are made for analytical formulation.

1. The benchmark buildings are considered to remain within the elastic limit under wind and earthquake forces.
2. These systems are subjected to single horizontal (uni-directional) components of the forces.
3. The effect of the soil-structure interaction are not taken into consideration.

In general the governing equations of motion for the structures installed with STMD are obtained by considering the equilibrium of forces at the location of each degree of freedom as follows.

$$[M_s]\{\ddot{x}_s\} + [C_s]\{\dot{x}_s\} + [K_s]\{x_s\} = f(t) + \{G_s\} \quad (1)$$

where $[M_s]$, $[C_s]$, and $[K_s]$ are the mass, damping, and stiffness matrices of the building, respectively of order $(N + n) \times (N + n)$. Here, N indicates degrees of

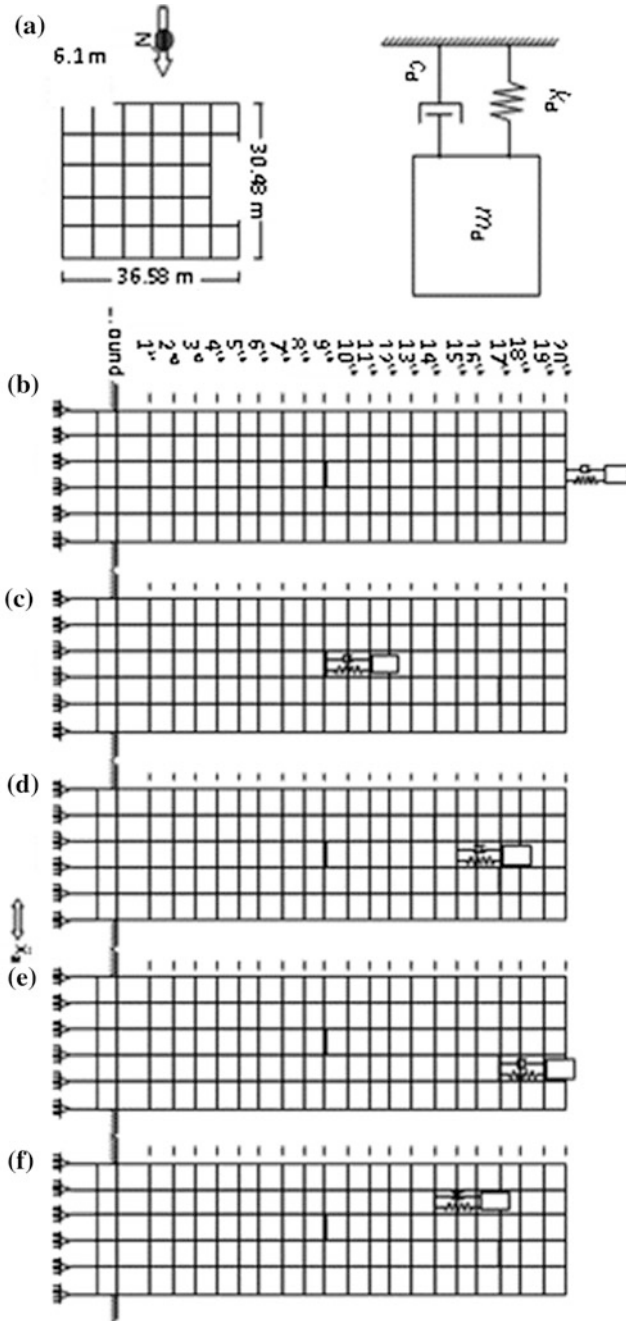


Fig. 2 Model of 20-storey benchmark building. **a** Plan of the building and schematics of STMD, **b** elevation with STMD at top, **c** elevation with STMD at 9th, **d** elevation with STMD at 15th, **e** elevation with STMD at 17th and **f** elevation with STMD at 14th floor

freedom (DOF) for the building and n indicates degrees of freedom for STMD ($n = 1$).

$\{x_s\} = \{x_1, x_2, \dots, x_N, \dots, x_n\}^T$, $\{\dot{x}_s\}$, and $\{\ddot{x}_s\}$ are the unknown relative node displacement, velocity, and acceleration vectors, respectively. $f(t)$ is the force. The force can be wind load and it is considered acting on the N floors of the building, however not on the STMD. The earthquake force is given by $[-M_s]\{r\}\{\ddot{x}_g\}$ where the earthquake ground acceleration vector, $\{\ddot{x}_g\}$ and $\{r\}$ is the vector of influence coefficients. The $\{G_s\}$ is a vector size of $(N \times n)$ where all elements are zero except the element where the STMD is placed. The value for the element is given by:

$$c_i(\dot{x}_n - \dot{X}_N) + k_i(x_n - X_N) \tag{2}$$

where c_i is the damping of the STMD and k_i is the stiffness of the STMD. The modal frequencies and mode shapes of the structures are determined by conducting free vibration analysis solving eigen value problem for tuning STMD and deciding the placement. The STMD is placed where the mode shape amplitude of the structure is the largest/larger in the particular mode and each time tuned to the corresponding modal frequency, while controlling up to first five modes. In all cases, the mass matrix is of order $(N + n) \times (N + n)$ with acceleration vector $\{\ddot{x}_s\}$ as given in Eq. 3.

$$[M_s]\{\ddot{x}_s\} = \begin{bmatrix} [M_N]_{N \times N} & 0 \\ 0 & [M_n]_{n \times n} \end{bmatrix} \begin{Bmatrix} \{\ddot{X}_i\}_{N \times 1} \\ \{\ddot{x}_i\}_{n \times 1} \end{Bmatrix} \tag{3}$$

The condensed stiffness matrix of the NC Building is $[K_N]$. This matrix $[K_N]$ is calculated by removing the rotation degrees of freedom of the building by static condensation. The damping matrix ($[C_N]$) is not explicitly known but can be defined with the help of the Rayleigh’s approach using damping ratio ($\zeta_s = 0.05$) for first five modes. For the building installed with the STMD, stiffness and damping of the STMD were input in the generic stiffness matrix $[K_s]$ and damping matrix $[C_s]$ shown with the help of Eqs. 4 and 5.

$$[K_s]\{x_s\} = \begin{bmatrix} [K_N]_{N \times N} & [0]_{N \times n} \\ [0]_{n \times N} & [0]_{n \times n} \end{bmatrix} \begin{Bmatrix} \{X_i\}_{N \times 1} \\ \{x_j\}_{n \times 1} \end{Bmatrix} + \begin{bmatrix} [K_n]_{N \times N} & -[K_n]_{N \times n} \\ -[K_n]_{n \times N} & [K_n]_{n \times n} \end{bmatrix} \begin{Bmatrix} \{X_i\}_{N \times 1} \\ \{x_i\}_{n \times 1} \end{Bmatrix} \tag{4}$$

$$[C_s]\{\dot{x}_s\} = \begin{bmatrix} [C_N]_{N \times N} & [0]_{N \times n} \\ [0]_{n \times N} & [0]_{n \times n} \end{bmatrix} \begin{Bmatrix} \{\dot{X}_i\}_{N \times 1} \\ \{\dot{x}_j\}_{n \times 1} \end{Bmatrix} + \begin{bmatrix} [C_n]_{N \times N} & -[C_n]_{N \times n} \\ -[C_n]_{n \times N} & [C_n]_{n \times n} \end{bmatrix} \begin{Bmatrix} \{\dot{X}_i\}_{N \times 1} \\ \{\dot{x}_j\}_{n \times 1} \end{Bmatrix} \tag{5}$$

In which $[K_n]$ and $[C_n]$ are the stiffness and damping matrices corresponding to the DOF of the TMDs.

3 Numerical Study

Wind and earthquake response of high-rise buildings controlled with the STMD is investigated. The time histories of across wind loads are available on internet [11] and the detailed description of the wind tunnel tests conducted at the University of Sydney is given by Samali et al. [12, 13]. Seismic response of high-rise building is investigated under N00S component of 1995 Kobe earthquake recorded at JMA. The peak ground acceleration (PGA) of Kobe ground motion is 0.86 g. Five STMD are chosen and placed at different location to control the wind and earthquake response of the selected buildings. The first, second, third, fourth and fifth modal frequencies decided to be controlled by STMD₁–STMD₅ respectively.

3.1 Wind Response Control

The effectiveness of optimum STMD for wind response control of 76-storey benchmark building is presented. In order, to find the optimum STMD, it is placed at different location and tuned to the higher modal frequencies of the building. In addition, the mass of the STMD is varied to find the optimum mass ratio of the STMD. In the present study, the performance of the dampers is studied only up-to the duration of 900 s. To simplify the direct comparisons and to show the performance of various devices a set of 12 performance criteria are proposed. To measure the reduction in root mean square (RMS) response quantities of the wind excited benchmark building, the performance criteria J_1 – J_4 are defined. These quantities are to measure the controlled by normalizing them by the response quantities of the uncontrolled building. To find the peak response of controlled structure normalized by the peak response of the uncontrolled building, the performance criteria J_7 – J_{10} are defined. Because the study is passive system of control, thus there is no need to consider the other four performance criteria J_5 , J_6 , J_{11} , and J_{12} which represent the performance of the actuator. However, Yang et al. [9] defined all these performance criteria, for the wind excited benchmark building. In this study first five modal frequencies of the building are considered to be controlled. Figure 3 shows the effectiveness of the STMD located at different location and in each location tuned to different modal frequencies. It is observed that placing STMD at topmost floor and tuning to first modal frequency of the building will have the maximum wind response reduction. In addition, it is observed that with increasing the mass ratio the wind response reduction also will increase. Further, STMD tuned to higher modal frequencies will have improved performance if they are placed accordance to mode shapes amplitude. The Figure also shows that only up to three modes control are significant in response reduction of the benchmark building. The reduction due to STMD tuned above third frequency can be address to the background effect of the wind. It is concluded that for wind response control of 76-benchmark building higher mass ratios have more effect comparing to light STMD. In order to improve the performance of the system and easy installation the distributed multiple tuned mass dampers (d-MTMDs) are recommended.

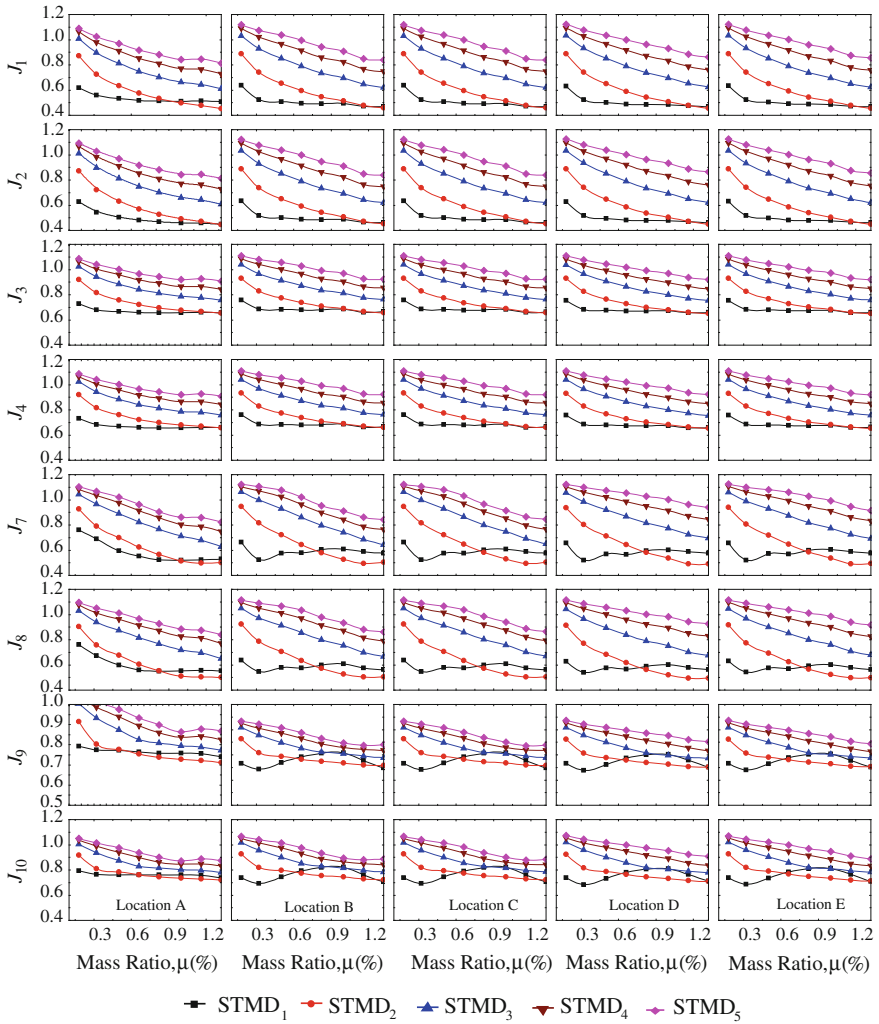


Fig. 3 Variation of wind response of 76-benchmark building installed with STMD at different locations

3.2 Earthquake Response Control

In this section the effectiveness of optimum STMD for earthquake response control of 20-storey benchmark building is investigated. Location, tuning and mass ratio are the parameters to be optimized. The location is chosen as per maximum amplitude of mode shapes. The first five modal frequencies of the building are considered. The STMD placed at five different floors and in each placement the STMD is tuned to the first five modal frequencies of the benchmark building. In order to compare

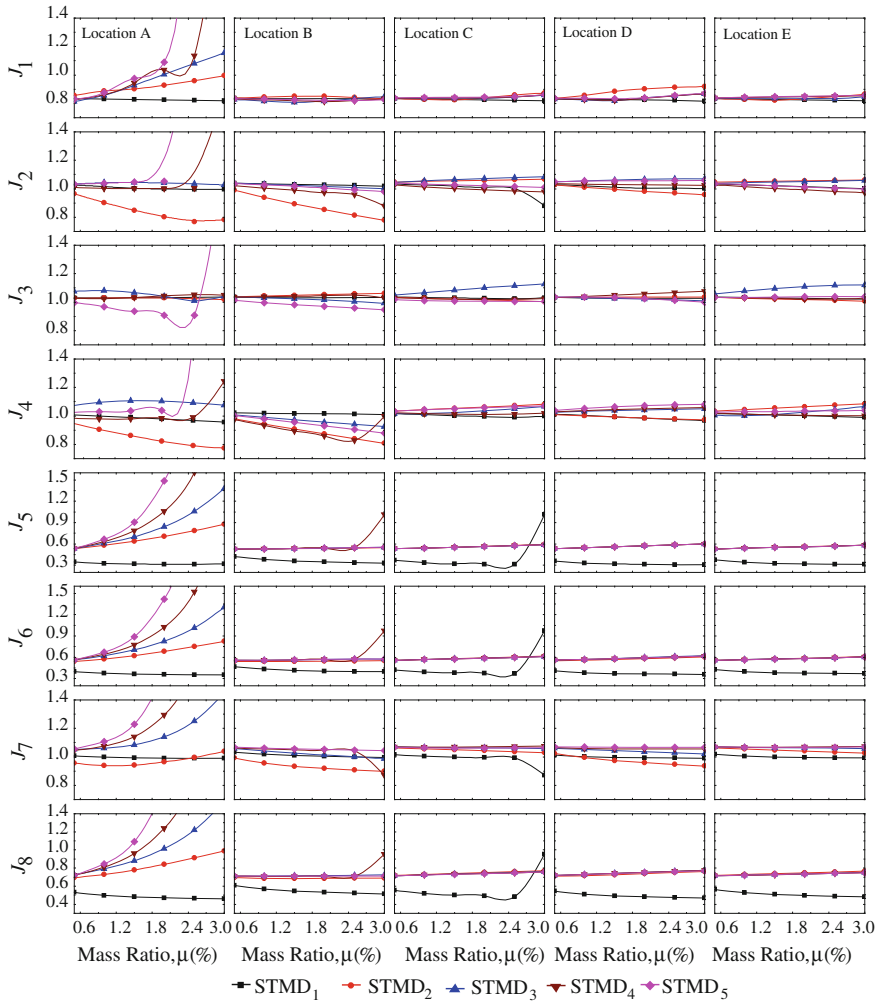


Fig. 4 Variation of earthquake response of 20-benchmark building installed with STMD at different locations

different control systems performance criteria was defined for the 20-storey benchmark building [10]. The performance criteria for maximum displacement, drift, acceleration and base shear are $J_1, J_2, J_3,$ and J_4 respectively. To obtain insight into the performance of the controlled structural system that may not be provided by the maximum response evaluation criteria, four evaluation criteria correspond to normed measures of the structural responses are considered. The performance criteria for normed displacement, drift, acceleration and base shear are $J_5, J_6, J_7,$ and J_8 respectively. Figure 4 shows the effectiveness of STMD located at different locations and effect of tuning to different modal frequencies. It is observed that tuning and

placement of STMD is playing the important role in seismic response control of buildings. It is also observed that the STMD tuned to first modal frequency will be the most effective among all. In addition, it is observed that all the STMD tuned to higher modal frequencies are effective when they are effectively placed. As shown in figure if they are not placed effectively even the response of the building may increase under ground motion. As much the mass ratio increased the performance criteria improved in most of the cases.

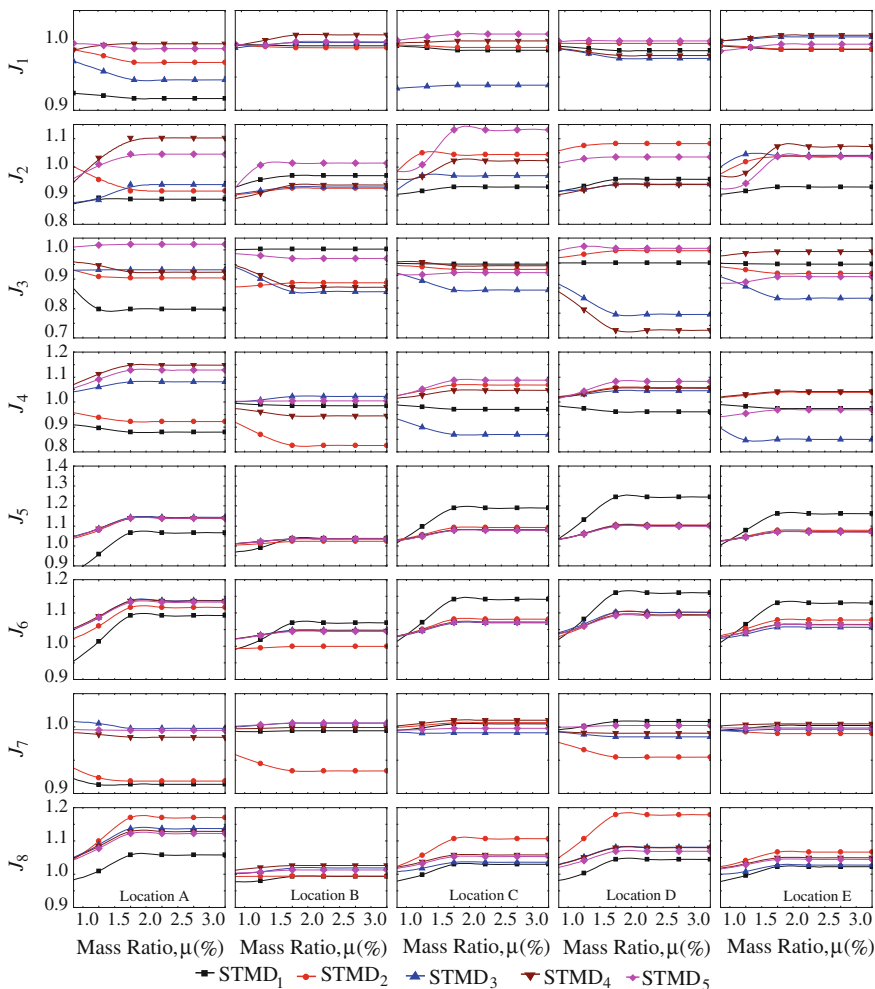


Fig. 5 Variation of earthquake response of 20-benchmark pre-earthquake building installed with STMD at different locations

3.3 Effect of Miss-Tuning

In this section the robustness of the STMD is checked in earthquake response of buildings. The check for robustness of the STMD in wind response of the building is neglected because the wind tunnel tests were not available for the two new buildings. In order to find out the effect of the miss-tuning, the effect of the changes of the dynamic properties of building from before (pre-earthquake) to after (post-earthquake) strong motion is considered. The first 5 natural frequencies of the

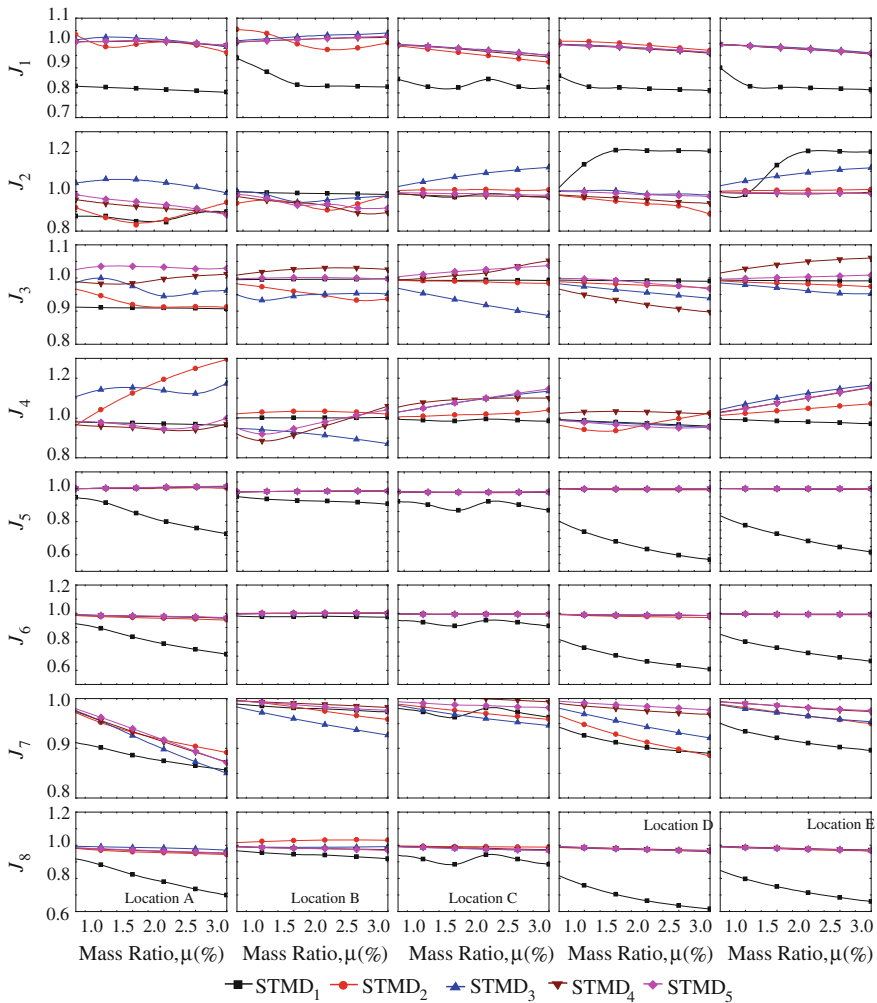


Fig. 6 Variation of earthquake response of 20-benchmark post-earthquake building installed with STMD at different locations

pre-earthquake model are: 0.29, 0.83, 1.43, 2.01 and 2.64 Hz. The first 5 natural frequencies of the post-earthquake model are: 0.24, 0.68, 1.17, 1.65 and 2.16 Hz. The STMD is tuned to the first 5 natural frequencies of the 20-storey benchmark evaluation model and they are: 0.261, 0.753, 1.30, 1.83 and 2.40.

The pre-earthquake damping is determined using this increased stiffness and the post-earthquake damping is determined using this decreased stiffness. Figures 5 and 6 show the effectiveness of STMD for response control of pre-earthquake and post-earthquake models.

It is observed from both figures that the STMD1 is more sensitive in miss-tuning effect comparing the other STMD. The reason can be larger shift in frequency. In addition, it is observed that STMD are more robust in acceleration control of the building comparing to displacement response control of the building. Figure 6 shows that STMD are more robust in post-earthquake model.

4 Conclusion

The effectiveness of optimal single tuned mass damper (STMD) for wind and earthquake response control of high-rise building is investigated. Further, the optimum STMD are identified based the effective placement and tuning. The following conclusions are drawn from the trends of the results shown in present study:

1. Displacement, drift, acceleration and base share are reduced when STMD₁–STMD₅ are placed effectively.
2. The robust problem is more visible in case of STMD₁ comparing to other STMD.
3. Increasing the mass ratio of STMD will help the performance criteria to be improved.
4. STMD tuned to higher modal frequencies will have improved performance if they are placed accordance to mode shapes amplitude.

References

1. Frahm H (1909) Device for damping vibration of bodies. US Patent 989958
2. Ormondroyd J, Den Hartog JP (1928) The theory of the dynamic vibration absorber. *Trans Am Soc Mech Eng* 50:A9–A22
3. Den Hartog JP (1956) *Mechanical vibrations*, 4th edn. McGraw-Hill Book Company, New York
4. Randall SE, Halsted DM, Taylor DL (1981) Optimum vibration absorbers for linear damped systems. *Mech Des* 103(12):908–913
5. Abe M, Igusa T (1995) Tuned mass dampers for structures with closely spaced natural frequencies. *Earthq Eng Struct Dyn* 24(2):247–261

6. Soong TT, Dargush GF (1997) *Passive energy dissipation systems in structural engineering*, 1st edn. Wiley, Chichester
7. Nagarajaiah S (2009) Adaptive passive semi active smart tuned mass dampers identification and control using empirical mode decomposition Hilbert transform and short-term Fourier transform. *Struct Control Health Monitor* 16(3):800–841
8. Pisal AY, Jangid RS (2013) Dynamic response of structure with semi-active tuned friction damper. *Int J Struct Civil Eng Res* 2(1):17–31
9. Yang JN, Agrawal AK, Samali B, Wu JC (2004) Benchmark problem for response control of wind-excited tall buildings. *J Eng Mech ASCE* 130(4):437–446
10. Spencer BF, Christenson RE, Dyke SJ (1998) Next generation benchmark control problem for seismically excited building. In: *Proceedings of the second world conference on structural control (2WCSC)*, Kyoto, Japan, 28th June–1st July, vol 2, pp 1351–1360
11. Smart Structures Technology Laboratory (SSTL) (2002) Structural control: benchmark comparisons. <http://sstl.cee.illinois.edu/benchmarks/index.html>
12. Samali B, Kwok KCS, Wood GS, Yang JN (2004) Wind tunnel tests for wind-excited benchmark building. *J Eng Mech ASCE* 130(4):447–450
13. Samali B, Mayol E, Kwok KCS, Mack A, Hitchcock P (2004) Vibration control of the wind-excited 76-storey benchmark building by liquid column vibration absorber. *J Eng Mech ASCE* 130(4):478–485

Part XV
Statistical, Probabilistic and Reliability
Approaches in Structural Dynamics

Tuned Liquid Column Damper in Seismic Vibration Control Considering Random Parameters: A Reliability Based Approach

Rama Debbarma and Subrata Chakraborty

Abstract The present study deals with reliability based optimization of tuned liquid column damper (TLCD) parameters in seismic vibration control considering uncertainties in the properties of primary structure and ground motion parameters. In doing so, the conditional second order information of the response quantities is obtained in random vibration framework using state space formulation. Subsequently, the total probability theorem is used to evaluate the unconditional response of the primary structures considering random system parameters. The unconditional root mean square displacement (RMSD) of the primary structures is considered as the performance index to define the failure of the primary system which is used as the objective function to obtain the optimum TLCD parameters. Numerical study is performed to elucidate the effect of parameters uncertainties on the optimization of TLCD parameters and system performance. As expected, the RMSD of the primary system is quite significantly reduced with increasing mass ratio and damping ratio of the structure. However, when the system parameters uncertainties are considered, there is a definite change in the optimal tuning ratio and head loss coefficient of the TLCD yielding a reduced efficiency of the system. It is observed that though the randomness in the seismic events dominates, the random variations of the system parameters have a definite and important role to play in affecting the design. In general, the advantage of the TLCD system tends to reduce with increasing level of uncertainty. However, the efficiency is not completely eliminated as it is seen that the probability of failure of the primary structure is still remains much lower than that of the unprotected system.

Keywords Tuned liquid column dampers • Stochastic earthquake • Vibration control • Optimization • Parameter uncertainty • Reliability based approach

R. Debbarma (✉)

Department of Civil Engineering, National Institute of Technology, Agartala, India
e-mail: ramadebbarma@gmail.com

S. Chakraborty

Department of Civil Engineering, Indian Institute of Engineering Science and Technology, Shibpur, Howrah 711103, India
e-mail: schak@civil.beecs.ac.in

1 Introduction

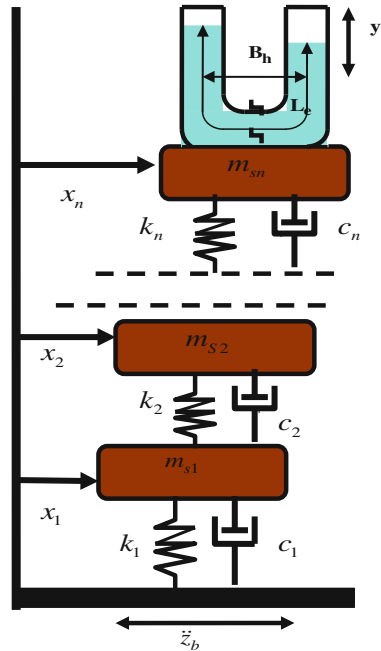
The tuned liquid column damper (TLCD) is an effective passive vibration control device due to its easy installation procedure and flexibility in liquid frequency adjustment capability. In such system, the damper dissipates the vibration energy by a combined action of the movement of the liquid in a U-shaped container, damping effect through an orifice with inherent head loss characteristics and the restoring force on the liquid due to gravity. The applicability of liquid damper to mitigate the effect of wind and seismic induced vibration is studied extensively [1–3]. In fact, the optimal design of passive control devices like tuned mass damper (TMD) and TLCD assuming deterministic system parameters is well established [4–6].

The deterministic approach as mentioned above cannot include the effects of system parameter uncertainty in the optimization process. Recently, the studies on the effect of system parameter uncertainty have attracted lot of interests [7–12]. These studies are based on minimizing the unconditional expected value of the mean square response and a notable different optimal TMD parameters are obtained than that of obtained by considering deterministic parameters. The performance of TLCD considering uncertainties in the stiffness of the primary system and earthquake load parameters was studied in [13, 14]. The optimization of liquid damper system under uncertain system parameters is very limited. The present study deals with reliability based design optimization (RBDO) of TLCD parameters in seismic vibration control considering uncertainties in the properties of primary structure and ground motion parameter. In doing so, the conditional second order information of the response quantities is obtained in random vibration framework using state space formulation. Subsequently, the total probability theorem is used to evaluate the unconditional response of the primary structures considering random system parameters. The unconditional RMSD of the primary structures is considered as the performance index to define the failure of the primary system which is used as the objective function to obtain the optimum TLCD parameters. Numerical study is performed to elucidate the effect of parameters uncertainties on the optimization of TLCD parameters and system performance.

2 Stochastic Dynamic Response Analysis of TLCD—Structure System

A TLCD is a U-shaped liquid column tube attached to a primary structure. A simplified TLCD structure system is shown in Fig. 1. The cross sectional area, length of the horizontal portion, vertical height of the liquid inside the tube and the density of the liquid mass are denoted by A , B_h , h and ρ , respectively. The total length of liquid column is, $L_e = (2h + B_h)$. Assuming that the mass of the liquid container is included in the mass of the primary structure, the mass of the TLCD can be expressed as: $m_l = (\rho A L_e)$. The structure-damper system is subjected to a

Fig. 1 The structure and TLCD system



base acceleration, \ddot{z} . If x and y represents the time dependent horizontal displacement of the primary system relative to the ground and the displacement of liquid surface respectively, the equation of motion of the liquid column can be expressed as,

$$\rho AL_e \ddot{y} + \frac{1}{2} \rho A \xi |\dot{y}| \dot{y} + 2 \rho g A y = -\rho A B_h \{ \ddot{x} + \ddot{z} \} \tag{1}$$

The constant ξ is the coefficient of head loss controlled by the opening ratio of the orifice. Normalizing Eq. (2) with respect to m_l and applying equivalent linearization techniques [15] above non-linear equation can be expressed in linearized form as

$$\ddot{y} + 2c_p/L_e \dot{y} + 2g/L_e y + p \ddot{x} = -p \ddot{z} \tag{2}$$

where, c_p represents the equivalent linearization damping co-efficient and this can be expressed as: $c_p = \sigma_{\dot{y}} \xi / \sqrt{2\pi}$, where, $\sigma_{\dot{y}}$ is the standard deviation of the liquid velocity. In the above $B_h/L_e = p$ is the ratio of the horizontal portion of the liquid column to its total length. Following notations are also introduced: tuning ratio, $\gamma = \omega_l/\omega_0$ where, ω_0 is the frequency of the primary structure and $\omega_l = \sqrt{2g/L_e}$ is the frequency of liquid. It can be further noted that c_p depends on the liquid response,

σ_y of the liquid column which is not known a priori and required an iterative solution procedure.

The equation of motion of the mdof structure attached with TLCD as shown in Fig. 1 can be expressed as,

$$\mathbf{M}\ddot{\mathbf{Y}} + \mathbf{C}\dot{\mathbf{Y}} + \mathbf{K}\mathbf{Y} = -\mathbf{M}\tilde{\mathbf{r}}\ddot{z}_b \tag{3}$$

where, $\mathbf{Y} = [y, x_n, x_{n-1}, \dots, x_1]^T$ is the relative displacement vector, and $\tilde{\mathbf{r}} = [0 \ \mathbf{I}]^T$, where \mathbf{I} is an unit vector of size n. \mathbf{M} , \mathbf{C} , and \mathbf{K} represent the mass, damping and stiffness matrix of the combined system (details will be discussed during presentation). Introducing the state space vector, $\mathbf{Y}_s = (y, x_n, x_{n-1}, \dots, x_1, \dot{y}, \dot{x}_n, \dot{x}_{n-1}, \dots, \dot{x}_1)^T$, Eq. (3) can be expressed as:

$$\dot{\mathbf{Y}}_s = \mathbf{A}_s\mathbf{Y}_s + \tilde{\mathbf{r}}\ddot{z}_b \tag{4}$$

where, $\mathbf{A}_s = \begin{bmatrix} 0 & \mathbf{I} \\ \mathbf{H}_k & \mathbf{H}_c \end{bmatrix}$ in which $\mathbf{H}_k = \mathbf{M}^{-1}\mathbf{K}$ and $\mathbf{H}_c = \mathbf{M}^{-1}\mathbf{C}$, $\tilde{\mathbf{r}} = [0, \mathbf{I}]^T$ with \mathbf{I} and 0 is the $(n+1) \times (n+1)$ unit and null matrices, respectively.

The system experienced load due to random seismic acceleration \ddot{z}_b that excites the primary structure at base. The well-known Kanai-Tajimi stationary stochastic process model [16] which is able to characterize the input frequency content for a wide range of practical situations is adopted here. The process of excitation at the base can be described as

$$\begin{aligned} \ddot{x}_f(t) + 2\zeta_f\omega_f\dot{x}_f + \omega_f^2x_f &= -W(t) \\ \ddot{z}_b(t) = \ddot{x}_f(t) + \omega(t) &= 2\zeta_f\omega_f\dot{x}_f + \omega_f^2x_f \end{aligned} \tag{5}$$

where, $W(t)$ is a stationary Gaussian zero mean white noise process, representing the excitation at the bed rock, ω_f is the base filter frequency and ζ_f is the filter or ground damping. Defining the global state space vector as: $Z = (y, x_n, x_{n-1}, \dots, x_1, x_f\dot{y}, \dot{x}_n, \dot{x}_{n-1}, \dots, \dot{x}_1, \dot{x}_f)^T$, Eqs. (4) and (5) leads to an algebraic matrix equation of order six i.e. the so called Lyapunov equation [17]:

$$\mathbf{A}\mathbf{R} + \mathbf{R}\mathbf{A}^T + \mathbf{B} = 0 \tag{6}$$

Where, the details of the state space matrix \mathbf{A} and \mathbf{B} are given as below.

$$[\mathbf{A}] = \begin{bmatrix} 0 & \mathbf{I} \\ \mathbf{H}_k & \mathbf{H}_c \end{bmatrix}$$

$$\begin{aligned}
 \bar{\mathbf{H}}_k &= \begin{bmatrix} \vdots & 0 \\ -\mathbf{M}^{-1}\mathbf{K} & \omega_f^2 \\ \vdots & \omega_f^2 \\ \vdots & \vdots \\ \dots & \dots \\ 0 & 0 \dots 0 & \vdots & -\omega_f^2 \end{bmatrix} \bar{\mathbf{H}}_c \\
 &= \begin{bmatrix} \vdots & 0 \\ -\mathbf{M}^{-1}\mathbf{C} & 2\xi_f\omega_f \\ \vdots & \vdots \\ \vdots & 2\xi_f\omega_f \\ \dots & \dots \\ 0 & 0 & 0 & 0 & \vdots & -2\xi_f\omega_f \end{bmatrix} \text{ and } \mathbf{B} \\
 &= \begin{bmatrix} 0 & \dots & \dots & \dots & \dots & 0 \\ \vdots & \dots & \dots & \dots & \dots & \vdots \\ \vdots & \dots & \dots & \dots & \dots & \vdots \\ \vdots & \dots & \dots & \dots & \dots & \vdots \\ \vdots & \dots & \dots & \dots & \dots & \vdots \\ \vdots & \dots & \dots & \dots & \dots & \vdots \\ 0 & \dots & \dots & \dots & \dots & 2\pi S_o \end{bmatrix}
 \end{aligned}$$

The state space covariance matrix \mathbf{R} is obtained as the solution of the above Lyapunov equation and can be described as:

$$\mathbf{R} = \begin{bmatrix} \mathbf{R}_{zz} & \mathbf{R}_{z\dot{z}} \\ \mathbf{R}_{\dot{z}z} & \mathbf{R}_{\dot{z}\dot{z}} \end{bmatrix} \tag{7}$$

In which, R_{zz} , $R_{z\dot{z}}$, $R_{\dot{z}z}$ and $R_{\dot{z}\dot{z}}$ are the sub-matrices of \mathbf{R} . The rmsd of the liquid and that of the i -th storey of the primary structure can be obtained as:

$$\sigma_y = \sqrt{R_{zz}(1, 1)} \quad \text{and} \quad \sigma_{xi} = \sqrt{R_{zz}(p, p)} \quad \text{where, } p = (n + 1) - (i - 1) \tag{8}$$

3 Conventional Reliability Based Optimization of TLCD Parameters

The TLCD parameters optimization involves determination of the tuning ratio of damper system (defined as the ratio of the liquid frequency ω_L to the primary system frequency, ω_0 and the coefficient of linear equivalent damping C_p). The design vector (DV) can be thus defined as: $\bar{b} = (\gamma \xi)^T$. The conventional optimization problem so defined for system subject to stochastic load can be transformed into a standard nonlinear programming problem [18] and the design vector is obtained for a known frequency, damping ratio of the primary structure. One of the much used approaches is to minimize the mean square response of the primary structure. In this regard, it can be noted that minimizing the mean square response does not necessarily correspond to the optimal design in terms of reliability [8]. The exceedance of some predefined serviceability or strength limit state by the primary structure are more important to minimize in connection with optimum design of TLCD parameters. Thus, the probability of failure of the primary system is used as the objective function to obtain the optimum TLCD parameters in the present study. The failure is associated with a threshold crossing failure. It is determined by the first crossing of any structural response x_i through a given threshold value β_i . For a system subjected to stochastic load, the first time bilateral crossing of any response x_i to barrier level β_i can be expressed as: $F_i = \{|x_i(t)| > \beta_i\}; t \in [0, T]$. The conditional failure probability $P(F_i/\mathbf{u})$ with regard to response x_i based on the structural and the excitation model specified by \mathbf{u} can be estimated following classical Rice's formulation:

$$P(F_i/\mathbf{u}) \cong 1 - \exp[-\alpha_{\beta_i}(\mathbf{u})T] \quad (9)$$

where, $\alpha_{\beta_i}(\mathbf{u})$ is the conditional threshold-crossing rate for i th failure mode and T is the duration of earthquake motion. For stationary stochastic Gaussian process with zero mean, the conditioned threshold crossing rate can be written as [17]:

$$\alpha_{\beta_i}(\mathbf{u}) = \frac{\dot{\sigma}_{x_i}}{\pi\sigma_{x_i}} \exp\left(-\frac{\beta_i^2}{2\sigma_{x_i}^2}\right) \quad (10)$$

where, σ_{x_i} and $\dot{\sigma}_{x_i}$ are the rms of x_i and \dot{x}_i . For multiple failure events, $F = \sum_{i=1}^{N_q} F_i$ i.e. the system fails if any $|x_i|$ exceeds its threshold β_i . Since the mean out-crossing rate of the system can be approximated by: $\alpha = \sum_{i=1}^{N_q} \alpha_{\beta_i}(\mathbf{u})$, the probability of failure $P(F/\mathbf{u})$ of the controlled structural system can be approximated by:

$$P(F/\mathbf{u}) \approx 1 - \exp\left[-\sum_{i=1}^{N_q} \alpha_{\beta_i}(\mathbf{u})T\right] \quad (11)$$

The optimization approach involving mechanical systems subject to random load can be transformed into a standard nonlinear optimization problem as [1]

$$\text{Find } \bar{b} = \begin{pmatrix} \gamma \\ \xi \end{pmatrix} \quad \text{to minimize: } f = P_f = P(F/\mathbf{u}) \approx 1 - \exp \left[- \sum_{i=1}^{N_q} \alpha_{\beta_i}(\mathbf{u}) T \right] \tag{12}$$

The standard gradient based techniques of optimization can be used to solve the problem. In present study, the MATLAB routine is used.

4 The Parameter Uncertainty and Evaluation of Response Sensitivity

The response statistic evaluation as discussed in previous section intuitively assumes that these parameters are completely known. Thus, evaluation of stochastic response using Eq. (8) and subsequent solution of the optimization problem to obtain the optimum TLCD parameters are conditional. To include the effect of parameter uncertainty, the total probability concept is used in the present study to evaluate the unconditional stochastic response of the structure. The uncertain system parameters as mentioned above are denoted by a vector \mathbf{u} . To obtain the sensitivity of responses, the first order derivative of basic Lyapunov equation can be obtained by differentiating Eq. (6) with respect to k -th parameter u_k :

$$\mathbf{A} \frac{\partial \mathbf{R}}{\partial u_k} + \frac{\partial \mathbf{A}}{\partial u_k} \mathbf{R} + \frac{\partial \mathbf{R}}{\partial u_k} \mathbf{A}^T + \mathbf{R} \frac{\partial \mathbf{A}^T}{\partial u_k} + \frac{\partial}{\partial u_k} (\mathbf{B}) = 0 \text{ i.e. } \mathbf{A} \mathbf{R}_{,u_k} + \mathbf{R}_{,u_k} \mathbf{A}^T + \mathbf{B}_1 = 0 \tag{13}$$

$$\text{Where, } \mathbf{B}_1 = \mathbf{A}_{,u_k} \mathbf{R} + \mathbf{R} \mathbf{A}_{,u_k}^T + \frac{\partial}{\partial u_k} (\mathbf{B}) \tag{14}$$

The sensitivity of response (RMSD as considered here) can be obtained directly by differentiating the corresponding expression of Eq. (8) with respect to k -th random variable u_k as following:

$$\frac{\partial}{\partial u_k} (\sigma_{x_i}) \text{ i.e. } \sigma_{x_i, u_k} = \frac{1}{2} \frac{\mathbf{R}_{,u_k}(j, j)}{\sqrt{\mathbf{R}(j, j)}}, \quad j = (n + 1) - (i - 1) \tag{15}$$

In which, $\mathbf{R}_{,u_k}(j, j)$ is obtained by solving Eq. (13). Now, taking the second derivative with respect to l -th parameter, one can further obtain the following:

$$\mathbf{A}\mathbf{R}_{,u_k u_l} + \mathbf{R}_{,u_k u_l} \mathbf{A}^T + \mathbf{B}_2 = 0$$

where, $\mathbf{B}_2 = 2[\mathbf{A}_{,u_k} \mathbf{R}_{,u_k} + \mathbf{R}_{,u_k} \mathbf{A}_{,u_k}^T] + [\mathbf{A}_{,u_k u_l} \mathbf{R} + \mathbf{R} \mathbf{A}_{,u_k u_l}^T]$ (16)

The second order sensitivity of rmsd can be obtained by differentiating Eq. (15) with respect to l-th random variable u_l as following:

$$\sigma_{x_i, u_k u_l} = \frac{1}{2\sqrt{\mathbf{R}(2, 2)}} \left\{ \mathbf{R}_{,u_k u_l}(j, j) - \frac{1}{2} \frac{[\mathbf{R}_{,u_k}(j, j)]^2}{\mathbf{R}(j, j)} \right\}$$
 (17)

It can be noted that the equations need to be solved for each random variable involve in the problem to obtain the first and second order sensitivities of the covariance matrix.

5 Uncertain Parameters and Unconditional Optimization

Any response quantity x is function of the system parameters \mathbf{u} . The random design parameter u_k can be viewed as the superposition of the deterministic mean component (\bar{u}_k) with a zero mean deviatoric component (Δu_k). Now the Taylor series expansion of rmsd about its mean value is,

$$\sigma_{x_i} = \sigma_{x_i(\bar{u}_k)} + \sum_{i=1}^{nv} \frac{\partial \sigma_{x_i}}{\partial u_k} \Delta u_k + \frac{1}{2} \sum_{k=1}^{nv} \sum_{l=1}^{nv} \frac{\partial^2 \sigma_{x_i}}{\partial u_k \partial u_l} \Delta u_k \Delta u_l + \dots$$
 (18)

In above, nv is the total number of random variables involve in the problem. Assuming uncertain variables \mathbf{u} are uncorrelated, the quadratic approximation provides the expected value as:

$$\sigma_{x_i} = \sigma_{x_i(\bar{u}_k)} + \frac{1}{2} \sum_{i=1}^{nv} \frac{\partial^2 \sigma_{x_i}}{\partial u_k^2} \sigma_{u_k}^2$$
 (19)

Where, σ_{u_k} is the standard deviation of i th Gaussain random parameter. It can be thus noted that the parameter optimization as described by Eq. (12) in Sect. 3 was conditional due to the fact that the structural and excitation model specified by \mathbf{u} were assumed to be known a priori. Based on this assumption, the threshold crossing rate was computed using Eq. (10) and subsequently the probability of failure was evaluated from Eq. (11). However, knowing the conditional second order information of response quantities, the unconditional response can be obtained by Taylor series expansion as described in Eq. (19). And, this unconditional response can be now used to evaluate the unconditional crossing rate using Eq. (10) and subsequently the unconditional probability of failure using Eq. (11).

6 Numerical Study

A three storey building with an attached TLCD is undertaken to study the proposed unconditional reliability based TLCD parameters optimization procedure for MDOF system. The primary structure has the following mean mass and stiffness values: $m_{s1} = m_{s2} = 5.0 \times 10^5$ kg, $m_{s3} = 4.0 \times 10^5$ kg, $k_1 = k_2 = k_3 = 11.0 \times 10^7$ N/m. Unless mentioned otherwise, the following nominal values are assumed for various parameters: structural damping, $\zeta_0 = 3\%$, mass ratio, $\mu = 3\%$ and length ratio $p = 0.7$. The threshold value (β) is taken as 1% of the storey height. The storey heights are taken as 3.5 m. The power spectral density (PSD) of the white noise process at bed rock, S_0 is related to the standard deviation σ_z of ground acceleration [19] by: $S_0 = \frac{2\xi_f \sigma_z^2}{\pi(1+4\xi_f^2)\omega_f}$. For numerical study, the peak ground acceleration is taken as, $PGA = 0.2$ g, where ‘g’ is the acceleration due to gravity. It is assumed that $PGA = 3\sigma_{z_b}$. The mean value of the filter frequency (ω_f) and damping (ξ_f) are taken as 9rad/s and 0.6, respectively. The uncertainties are considered in k , ξ_0 , ω_f , ξ_f and S_0 and assumed to be independent Gaussian random variables. The probability of failure computed for unprotected structure (i.e. without TLCD) considering deterministic system parameters is 0.98.

The variations of optimum tuning ratio and head loss coefficient with increasing level of randomness of the system parameters represented by respective coefficient of variation (cov) are shown in Figs. 2 and 3. The associated probability of failure is depicted in Fig. 4.

The variations of optimum tuning ratio and head loss coefficient with increasing level damping ratio of the primary structure and for different level of cov of system parameters are shown in Figs. 5 and 6. The associated probability of failure is depicted in Fig. 7. It can be observed from these plots that there is a definite and noticeable change in the damper parameters considering cov of system parameters with respect to that of a deterministic system. The probability of failure increases as

Fig. 2 The optimum tuning ratio with varying cov of parameters for different mass ratio

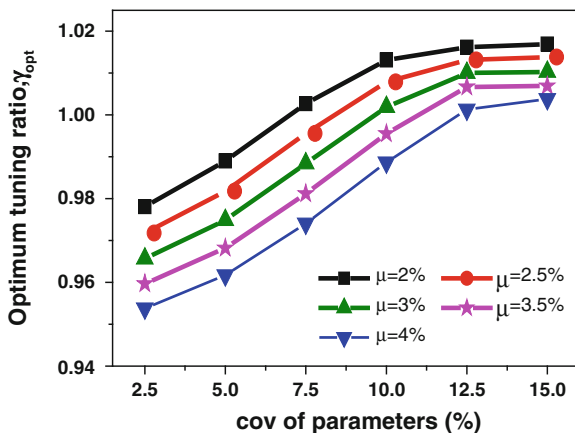


Fig. 3 The optimum head loss coefficient with varying cov of parameters for different mass ratio

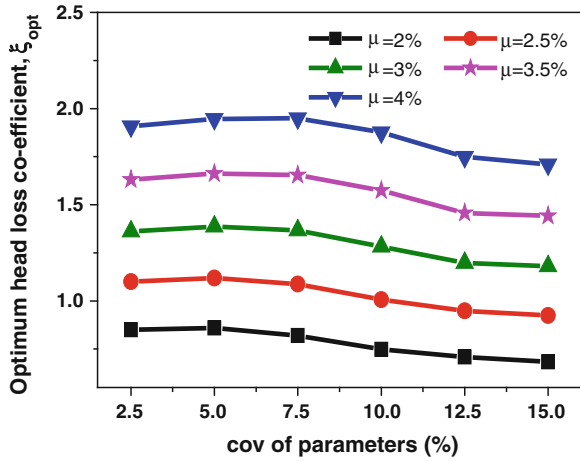


Fig. 4 The probability of failure with varying cov of parameters for different mass ratio

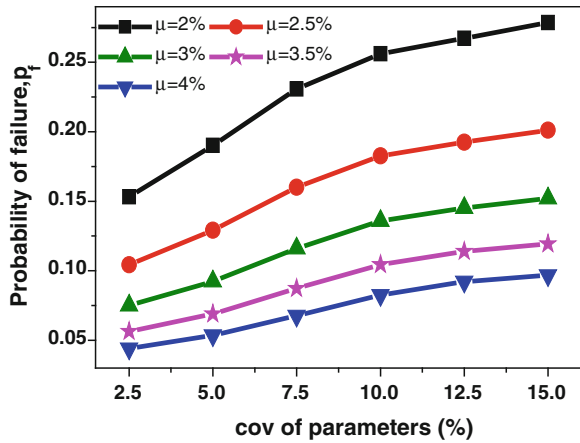


Fig. 5 The optimum tuning ratio with varying damping ratio for different uncertainty range

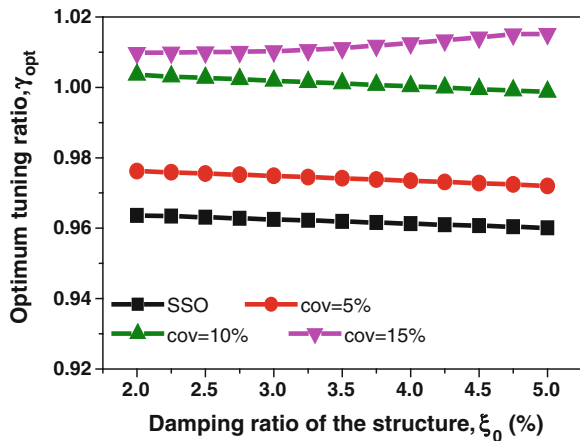


Fig. 6 The optimum head loss coefficient with varying damping ratio for different uncertainty range

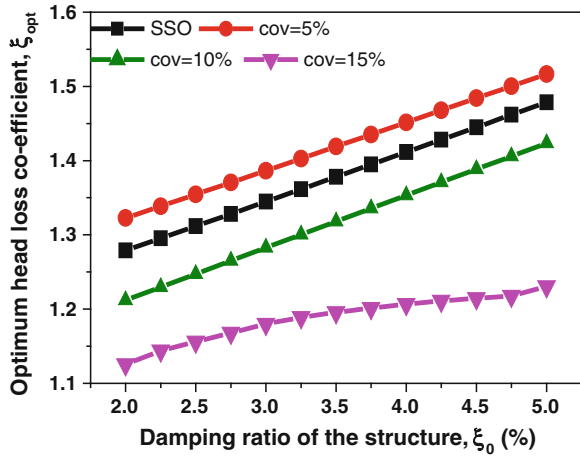
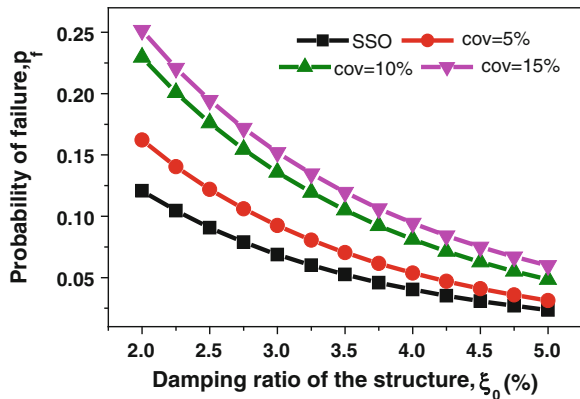


Fig. 7 The probability of failure with varying damping ratio for different uncertainty range



the cov increases which indicates that the efficiency of TLCD reduced. It is also observed that the damper performance is overestimated. It may be observed from the plots that the effect of uncertainty on damper performance is more for comparatively lower structural damping. It may be pointed here that the control devices are applied typically to mitigate the vibration level of flexible structure having smaller structural damping. Thus the effect of uncertainty will be a critical issue in such cases. It can be noted that the response of the structure is comparatively higher considering parameters uncertainty with respect to deterministic value.

The variation of optimum TLCD parameters and probability of failure with changing length ratio are shown in Figs. 8, 9, and 10. The changes in the optimum TLCD parameters and probability of failure are notable for different level of uncertainty.

Fig. 8 The optimum tuning ratio with varying length ratio for different uncertainty range

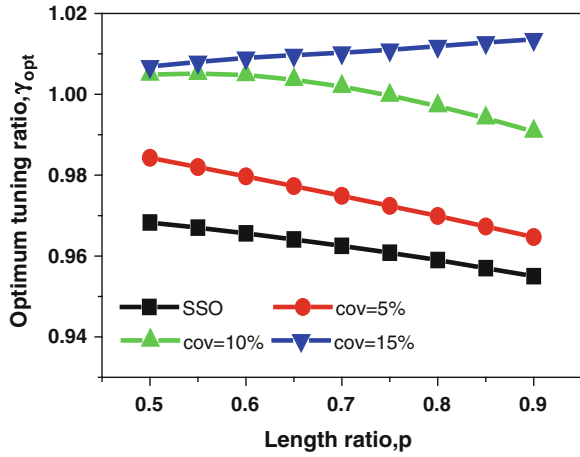


Fig. 9 The optimum head loss coefficient with varying length ratio for different uncertainty range

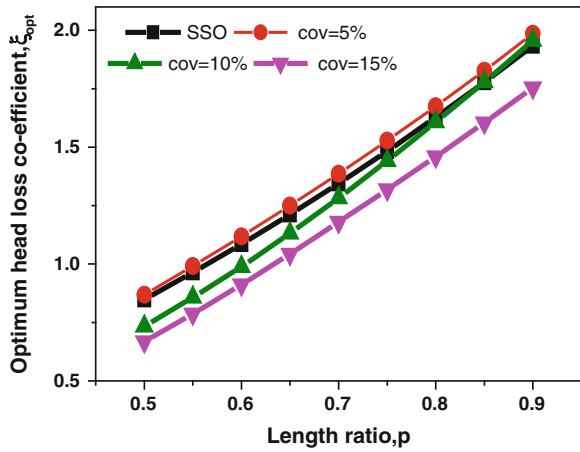
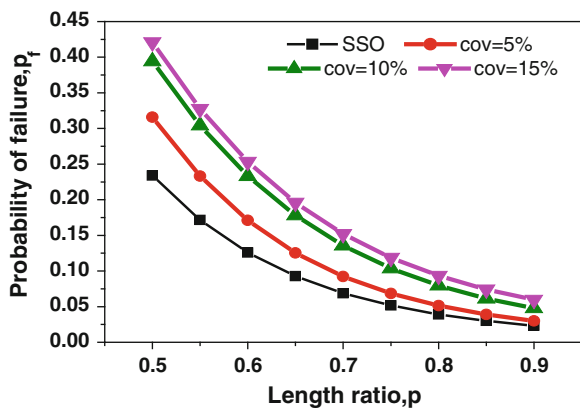


Fig. 10 The probability of failure with varying length ratio for different uncertainty range



7 Conclusions

The effect of parametric uncertainties in the reliability based design of TLCD system for control of vibration level of building frame structure subjected to earthquake loading is presented. The random variability in the design process is incorporated in the stochastic optimization framework through the total probability theorem. As expected, the RMSD of the primary system is quite significantly reduced with increasing mass ratio and damping ratio of the structure. However, when the system parameters uncertainties are considered, there is a definite change in the optimal tuning ratio and head loss coefficient of the TLCD yielding a reduced efficiency of the system. It is clearly demonstrated that though the randomness in the seismic events dominates, the random variations of the system parameters has a definite and important role to play in affecting the design. In general, the advantage of the TLCD system tends to reduce with increasing level of uncertainties. However, the efficiency is not completely eliminated as it is seen that the probability of failure of the primary structure is still remains much lower than that of the unprotected system. In general, the advantage of the TLCD tends to reduce with increasing level of uncertainties.

References

1. Won AYJ, Piers JA, Haroun MA (1996) Stochastic seismic performance evaluation of tuned liquid column dampers. *Earthq Eng Struct Dyn* 2, 5:1259–1274
2. Chang CC, Hsu CT (1998) Control performance of liquid column vibration absorbers. *Eng Struct* 20(7):580–586
3. Lee HH, Wong S-H, Lee R-S (2006) Response mitigation on the offshore floating platform system with tuned liquid column damper. *Ocean Eng* 33:1118–1142
4. Gao H, Kwok KCS, Samali B (1997) Optimization of tuned liquid column dampers. *Eng Struct* 19(6):476–486
5. Yalla SK, Kareem A (2000) Optimum absorber parameters for tuned liquid column dampers. *J Struct Eng* 1268:906–915
6. Hoang N, Warnitchai P (2005) Design of multiple tuned mass dampers by using a numerical optimizer. *Earthq Eng Struct Dyn* 34:125–144
7. Jensen H, Setareh M, Peek R (1992) TMDs for vibration control of system with uncertain properties. *J Struct Eng* 18(2):3285–3296
8. Papadimitriou C, Katafygiotis LS, Au SK (1997) Effects of structural uncertainties on TMD design: a reliability based approach". *J Struct Control* 4(1):65–88
9. Son YK, Savage GJ (2007) Optimal probabilistic design of the dynamic performance of a vibration absorber. *J Sound Vib* 307:20–37
10. Marano GC, Sgobba S, Greco R, Mezzina M (2008) Robust optimum design of tuned mass dampers devices in random vibrations mitigation. *J Sound Vib* 313:472–492
11. Taflanidis AA, Scruggs JT, Beck JL (2008) Reliability-based performance objectives and probabilistic robustness in structural control applications. *J Eng Mech* 134(4):291–301
12. Chakraborty S, Roy BK (2011) Reliability based optimum design of tuned mass damper in seismic vibration control of structures with bounded uncertain parameters. *Probab Eng Mech* 26:215–221

13. Taflanidis AA, Beck JL, Angelides DC (2007) Robust reliability-based design of liquid column mass dampers under earthquake excitation using an analytical reliability approximation. *Eng Struct* 29:3525–3537
14. Debbarma R, Chakraborty S, Ghosh S (2010) Optimum design of tuned liquid column dampers under stochastic earthquake load considering uncertain bounded system parameters. *Int J Mech Sci* 52:1385–1393
15. Iwan WD, Yang IM (1972) Application of statistical linearization techniques to non-linear multi-degree of freedom systems. *J Appl Mech* 39:545–550
16. Lutes LD, Sarkani S (1997) *Stochastic analysis of structural and mechanical vibrations*. Prentice Hall, NJ
17. Nigam NC (1972) Structural optimization in random vibration environment. *AIAA J* 10 (4):551–553
18. Tajimi H (1960) A statistical method of determining the maximum response of a building during earthquake. In: *Proceedings of the 2nd world conference on earthquake engineering*, Tokyo, Japan
19. Crandall SH, Mark WD (1963) *Random vibration in mechanical systems*. Academic Press, New York

Robust Design of TMD for Vibration Control of Uncertain Systems Using Adaptive Response Surface Method

Amit Kumar Rathi and Arunasis Chakraborty

Abstract The effect of randomness in system parameters on robust design of tuned mass damper (TMD) is examined in this work. For this purpose, mean and standard deviation based robust design optimization (RDO) scheme is suggested. The performance of TMD is evaluated using the percentage reduction of the root mean square (RMS) of the output displacement. Adaptive response surface method (ARSM) is used for the optimization and for the estimation of first two moments. In this context, moving least square (MLS) based regression technique is used for better fitting of the response surface. A comparative numerical study is conducted to show the effectiveness of the proposed method to improve the reliability of the controller.

Keywords Moving least square • Response surface method • Tuned mass damper • Vibration control • Uncertain systems

1 Introduction

TMD is a popular passive vibration control mechanism for improving serviceability of the structure. Generally, it constitutes a spring-mass-damping secondary system positioned at the desired degree of freedom (DOF) of a main system to absorb the vibration energy by tuning at the desired natural frequency of the main system. Initially, for tuning or design of TMD, a two-point method was suggested by Den Hartog [1] for an undamped system where the frequency response function of system with TMD invariably passes through two points. Later, studies proposed

A.K. Rathi (✉) · A. Chakraborty
Department of Civil Engineering, Indian Institute of Technology Guwahati,
Guwahati 781039, Assam, India
e-mail: ak.rathi@iitg.ernet.in

A. Chakraborty
e-mail: arunasis@iitg.ernet.in

tuning criteria based on standard deviation of time response, frequency response function, dissipation energy in time response etc. [2]. Also, theoretical close-form solutions for varying input and tuning criteria were derived for single DOF (SDOF) with TMD [3, 4].

Once the parameters of the TMD are optimized, the device is left alone to absorb the vibration energy during operation. However, almost every structure see a deviation of the parameters (viz. geometric, material, loading etc.) during its construction and service life due to uncertainties. This causes detuning of the TMD once designed for a particular set of design values of the above mentioned parameters [5, 6]. Hence, optimization of TMD parameters demands to consider uncertainties associated with system parameters and loading. Papadimitriou et al. [7] proposed reliability based TMD design for level crossing. They suggested incorporation of the random variables in tuning of TMD for better performance. Marano et al. [8] proposed RDO with multiple objective functions based on minimizing mean and standard deviation of the performance function. Their study shows that objective functions based on mean and standard deviation lead to conflicting results. Hoang et al. [9] conducted a sensitivity study and concluded that higher mass of TMD is relatively less sensitive to detuning by system uncertainties. Chakraborty and Roy [10] proposed reliability based design of TMD for varying levels of uncertainties. In their study, probability distribution function (PDF) of random variables were not incorporated. However, they used perturbation approach to study the sensitivity of the TMD parameters.

From the previous studies, one can conclude that reliability based design of TMD parameters considering the uncertainties need further research as this ensures the optimal performance of the controller to avoid detuning in presence of randomness. Although, previous studies have shown the effect of uncertainties on the performance of TMD, proper modelling of randomness through their PDF and correlation, if any, demands further attentions. With this is view, present study aims to investigate RDO of TMD for vibration control of a dynamical system with uncertain parameters. For this purpose, ARSM is proposed in a MLS framework for optimization. A SDOF-TMD system with uncertain parameters is considered to demonstrate the performance of the proposed RDO.

2 Dynamic System and Performance Function

Figure 1 shows the SDOF system attached with a TMD. Here, m , c and k are mass, damping and stiffness of the system while subscripts $.s$ and $.D$ represents the primary system and the controller. The displacement u is relative to the support. Input excitation to the system is through the base acceleration $\ddot{u}_g(t)$. The dynamic behaviour of the model is represented by

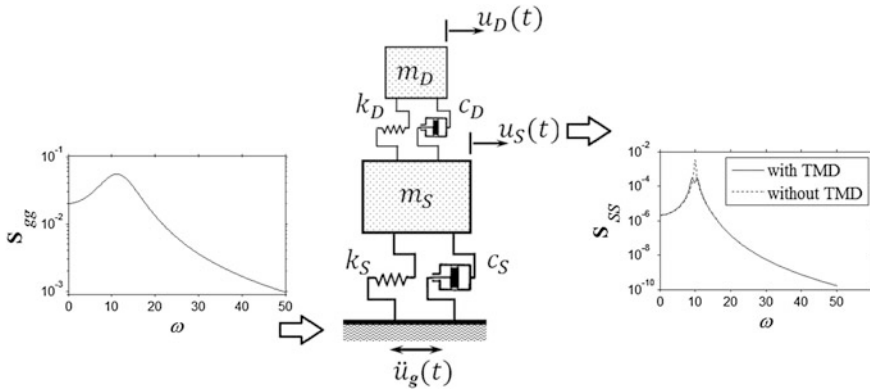


Fig. 1 Schematic diagram of SDOF-TMD system with input-output power spectral density function

$$\mathbf{M} \ddot{\mathbf{u}}(t) + \mathbf{C} \dot{\mathbf{u}}(t) + \mathbf{K} \mathbf{u}(t) = \mathbf{M} \mathbf{I} \ddot{u}_g(t) \tag{1}$$

In Eq. 1, mass matrix \mathbf{M} , damping matrix \mathbf{C} and stiffness matrix \mathbf{K} represent the complete system. Overdot in Eq. 1 represents differentiation with respect to time t and \mathbf{I} is the influence vector. On pre-multiplying both sides of Eq. 1 by \mathbf{M}^{-1} and simplifying one can show that

$$\begin{aligned} & \begin{bmatrix} 1 & 0 \\ 0 & 1 \end{bmatrix} \begin{Bmatrix} \ddot{u}_S(t) \\ \ddot{u}_D(t) \end{Bmatrix} + \begin{bmatrix} 2(\eta_S \omega_S + m_r \eta_D \omega_D) & -2m_r \eta_D \omega_D \\ -2\eta_D \omega_D & 2\eta_D \omega_D \end{bmatrix} \begin{Bmatrix} \dot{u}_S(t) \\ \dot{u}_D(t) \end{Bmatrix} \\ & + \begin{bmatrix} \omega_S^2 + m_r \omega_D^2 & -m_r \omega_D^2 \\ -\omega_D^2 & \omega_D^2 \end{bmatrix} \begin{Bmatrix} u_S(t) \\ u_D(t) \end{Bmatrix} = \begin{bmatrix} 1 & 0 \\ 0 & 1 \end{bmatrix} \begin{Bmatrix} 1 \\ 1 \end{Bmatrix} \ddot{u}_g(t) \end{aligned} \tag{2}$$

where, ω_S and η_S are the natural frequency and the damping ratio of the primary system without TMD. Similarly, ω_D and η_D are the natural frequency and the damping ratio of the TMD unit. Parameters m_r and ω_r in Eq. 2 are the mass ratio (i.e. m_D/m_S) and the frequency ratio (i.e. ω_D/ω_S), respectively. The frequency response function \mathbf{H} of the system described in Eq. 2 is given by

$$\begin{aligned} \mathbf{H}(\omega) = & - \left[\begin{bmatrix} 1 & 0 \\ 0 & 1 \end{bmatrix} \omega^2 - \begin{bmatrix} 2(\eta_S \omega_S + m_r \eta_D \omega_D) & -2m_r \eta_D \omega_D \\ -2\eta_D \omega_D & 2\eta_D \omega_D \end{bmatrix} i \omega \right. \\ & \left. - \begin{bmatrix} \omega_S^2 + m_r \omega_D^2 & -m_r \omega_D^2 \\ -\omega_D^2 & \omega_D^2 \end{bmatrix} \right]^{-1} \end{aligned} \tag{3}$$

where, $i = \sqrt{-1}$. In this study, the base excitation $\ddot{x}_g(t)$ is modeled as a filtered white noise whose power spectral density function (PSDF) is given by [11, 12]

$$\mathbf{S}_{gg}(\omega) = S_o \frac{1 + \left(2\eta_g \frac{\omega}{\omega_g}\right)^2}{\left\{1 - \left(\frac{\omega}{\omega_g}\right)^2\right\}^2 + \left(2\eta_g \frac{\omega}{\omega_g}\right)^2} \quad (4)$$

The parameters in the above equation S_o , ω_g and η_g are intensity of the white noise at bedrock level, ground natural frequency and damping ratio of soil. The output PSDF $\mathbf{S}_{uu}(\omega)$ of the model is given by

$$\mathbf{S}_{uu}(\omega) = \mathbf{H}^*(\omega) \mathbf{S}_{gg}(\omega) \mathbf{H}(\omega) \quad (5)$$

Here, superscript $*$ denotes the conjugate transpose. Since input to the system is a zero mean process, the output of the linear system will also have zero mean. Moreover, the RMS value of the response can be evaluated from the PSDF $\mathbf{S}_{uu}(\omega)$. The RMS value of primary response is given by the area under the auto PSDF as

$$r = \sqrt{2 \int_0^{\infty} \mathbf{S}_{uu}(\omega) d\omega} \quad (6)$$

Equation 6 may be used to evaluate the RMS value of the primary system with and without TMD by adequately adjusting the respective terms in Eq. 1. Let r_S and r_O be the RMS value of the primary system with and without TMD, respectively. For optimal performance of the TMD, the ratio of the two RMS values (i.e. $J = r_S/r_O$) is minimized to obtain ω_r and η_D for a given m_r . However, a deterministically designed TMD is exposed to detuning as the system parameters are often random. Therefore, the optimal design of TMD parameters needs to include the uncertainty present in the system. This sets the objective for the present study.

3 Response Surface Method

In this study, response surface is used to solve the optimization problem. Generally, meta-modelling is performed by surrogating the original function $r(\mathbf{x})$ by a quadratic polynomial that is often referred as response surface $\hat{r}(\mathbf{x})$. A typical illustration of the response surface can be expressed as

$$\hat{r}(\mathbf{x}) = a_0 + a_1x_1 + a_2x_2 + a_{11}x_1^2 + a_{22}x_2^2 + a_{12}x_1x_2 \quad (7)$$

where, $a_0, a_1, a_2, a_{11}, a_{22}$ and a_{12} are unknown coefficients of the response surface. Number of these unknown coefficients n_c can be evaluated as $\{1 + n + n(n + 1)/2\}$. Where, n is the number of variables. Estimation of the unknown coefficients are preformed by solving adequate experimental points in the desired vicinity. Number of

experimental points n_e are selected optimally based on n_c and for better fitting of $\hat{r}(\mathbf{x})$. Different schemes are proposed in the literature [13] to select n_e which is also called as design of experiment (DOE). In this study, central composite design (CCD) [14] is used as DOE where $n_e = 1 + 2n + 2^n$. The matrix representation of Eq. 7 can be expressed as

$$\mathbf{X} \mathbf{a} = \mathbf{r} \tag{8}$$

where,

$$\mathbf{X} = \begin{bmatrix} 1 & x_{1,1} & x_{2,1} & x_{1,1}^2 & x_{2,1}^2 & x_{1,1}x_{2,1} \\ 1 & x_{1,2} & x_{2,2} & x_{1,2}^2 & x_{2,2}^2 & x_{1,2}x_{2,2} \\ \vdots & \vdots & \vdots & \vdots & \vdots & \vdots \\ 1 & x_{1,n_e} & x_{2,n_e} & x_{1,n_e}^2 & x_{2,n_e}^2 & x_{1,n_e}x_{2,n_e} \end{bmatrix}, \mathbf{a} = \left\{ \begin{matrix} a_0 \\ a_1 \\ \vdots \\ a_{12} \end{matrix} \right\} \text{ and}$$

$$\mathbf{r} = \left\{ \begin{matrix} r(\mathbf{x})_1 \\ r(\mathbf{x})_2 \\ \vdots \\ r(\mathbf{x})_{n_e} \end{matrix} \right\}.$$

Further in this study, estimation of \mathbf{a} is carried out by moving least square (MLS) based linear regression analysis which is given by [13]

$$\mathbf{a} = (\mathbf{X}^T \Delta \mathbf{X})^{-1} \mathbf{X}^T \Delta \mathbf{r} \tag{9}$$

where, Δ is the diagonal matrix containing the weight function (δ) which is given by [13]

$$\delta(d) = \begin{cases} \frac{\bar{\delta}(d)}{\sum_{i=1}^{n_e} \bar{\delta}(d)}, & \text{if } d \leq \beta \\ 0, & \text{if } d > \beta \end{cases} \tag{10}$$

In the above equation, d is the Euclidean distance of the experiment points from an assumed center point and β is the influence radius. Furthermore, the individual weight function is given by

$$\bar{\delta}(d) = \frac{\left(\left(\frac{d}{\beta} \right)^2 + \varepsilon \right)^{-2} - (1 + \varepsilon)^{-2}}{\varepsilon^{-2} - (1 + \varepsilon)^{-2}} \tag{11}$$

In the above equation, ε is assumed as 10^{-5} . Using this MLS based adaptive response surface, the robust design of TMD is performed in this study which is described below.

4 Robust Design Optimization Scheme

Traditionally, TMD is tuned by minimizing different objective functions like H_∞ norm, H_2 norm, RMS value of the primary response among many others. However, every structural system is exposed to uncertainties not only during its design and construction phase but also during its entire service life. Therefore, deterministic design of TMD parameters does not necessarily ensure optimal tuning during operations. To ensure optimal tuning, present study advocates RDO of TMD parameters considering the uncertainties associated to the system parameters and loading. This is achieved by the following constrained robust optimization which is given as

$$\begin{aligned} \text{Minimize : } & J(\mathbf{x}) \\ \text{Subjected to : } & \mu_J + \vartheta\sigma_J \leq 1.0 \\ & \vartheta \geq \vartheta_{\text{assumed}} \end{aligned} \quad (12)$$

where, μ_J and σ_J are the mean and the standard deviation of J and ϑ is the sigma level that ensures the reliability. In the above equation, robustness of the design is addressed by constraint that is evaluated from the first two moments of the objective function J . In this context, it may be noted that $J = 1.0$ represents complete detuning of the controller as r_S is equal to r_O . The sigma level in the constraint equation ensure that area in the failure region (i.e. $J \geq 1.0$) is less. The mean and standard deviation at each design point are evaluated from the adaptive response surface that is fitted by CCD as discussed above. The MLS based ARSM thus helps in both optimization as well as robustness evaluation. Besides this, the proposed meta-model based approach does not impose any restriction of the distribution of random variables as well as the correlation among themselves. The algorithm of the proposed ARSM based RDO is as follows

- Step 1 Generate initial design point \mathbf{x}^* .
- Step 2 Generate n_e points using CCD in the vicinity of \mathbf{x}^* fit $\hat{r}(\mathbf{x})$ using MLS.
- Step 3 At each experiment points generated in Step 2, perform simulation to evaluate μ_J and σ_J .
- Step 4 Using the $\hat{r}(\mathbf{x})$ in Step 2 and the first two moments (i.e. μ_J and σ_J^2) perform gradient based optimization to identify the new design point \mathbf{x}^* .
- Step 5 Repeat Step 2–4 with the new design point \mathbf{x}^* and reducing the search domain by 20 % until convergence is achieved. The convergence criteria is $|J(\mathbf{x}^*)_{it-1} - J(\mathbf{x}^*)_{it}| \leq e$, where it is current iteration and e is permissible error, generally considered as 0.1 %.

Using the above mentioned algorithm, a numerical analysis is performed to study the robust design of TMD.

5 Results and Discussion

The robust optimization of TMD parameters in presence of uncertainty is considered in this section for numerical analysis. Three different cases of optimization are solved to compare the efficiency of the proposed RDO of TMD. These are—(a) minimizing $J(\mathbf{x})$ where there is no uncertainty (i.e. conventional design of TMD), (b) minimizing mean of $J(\mathbf{x})$ when system parameters are random and (c) constrained RDO as in Eq. 12 when system parameters are random. The natural frequency of the primary system and ground are assumed to be uniformly distributed random variables with mean values 10 and 4π rad/s, respectively. Three different levels of variations are considered with coefficient of variation (COV) 10, 20 and 30 %. Although, the random variables are assumed to be uncorrelated uniform, the formulation does not impose any restriction on the type and nature of the random variables. The other parameters of the primary system and Kanai-Tajimi spectrum are assumed to be $\eta_s = 2\%$, $\eta_g = 40\%$ and $S_0 = 0.020 \text{ m}^2/\text{s}^3$. The mass ratio is varied from 1 to 5 % for all the cases while the search domain for optimal parameters ω_r and η_D are restricted to [0.6 1.2] and [0 0.4], respectively to avoid computation cost in infeasible domain. To ensure improvement in reliability of the system, the sigma level $\vartheta_{\text{assumed}}$ in the constraint function (in Eq. 12) is considered to be 3.0. Using these values, optimization for three different models are carried out using ARSM as described in the previous section. For this purpose, β in Eq. 10 is considered to be 0.7211. The experiment points for ARSM are generated using CCD. The distance between the extreme points are reduced by 20 % in each successive iterations to achieve faster convergence.

The optimized design results are presented in Figs. 2 and 3, where conventional design optimization, RDO by minimizing mean and the proposed constraint RDO are presented. In Fig. 2, the design value of ω_r as per conventional optimization decreases with increase in m_r . This is caused by decrease in natural frequency of the two DOF model in Fig. 1 due to increase in mass of TMD thereby decreasing the tuning value of ω_r . Similar observations can be noticed for the design value ω_r from the other two models. The effect of uncertainty is evident in the RDO design as the design value shifts from the conventional design. With increase in level of uncertainties (i.e. COV = 20 and 30 %) the difference between the designs widen with increase in m_r . However, the design point optimized by the proposed RDO has fixed reliability factor. Consequently, this makes the design point sensitive to the amount of uncertainties. Figure 2a shows less significant change in the design value of ω_r for all the three optimization cases. This phenomenon is obvious as the uncertainty is low and the design is likely to be deterministic. When the level of uncertainties are increased to 20 and 30 % (see Fig. 2b, c, respectively), the difference in the design points is observed as the ϑ attained is more compared to that achieved by the conventional optimization and the mean minimizing RDO (refer Tables 1 and 2). Again for the case of COV = 20 % and above, the design points as per the proposed RDO shows an initial rise in ω_r with increase in m_r . Furthermore increase in mass

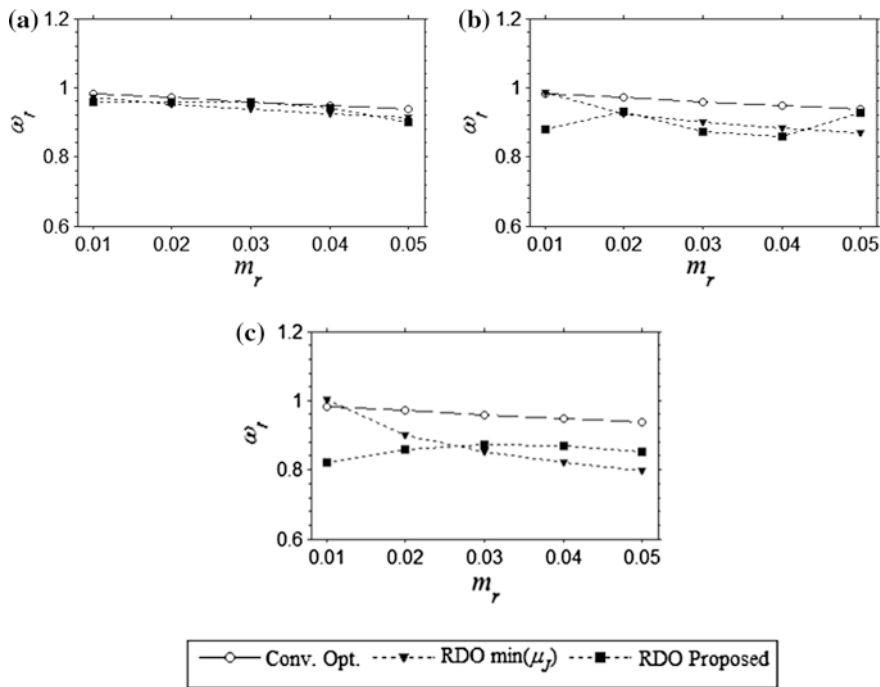


Fig. 2 Comparison of the design frequency ratio value by different optimizations with uncertainties a 10 %, b 20 % and c 30 %

improves the reliability and thus, the design point follows the trend of the other designs.

In Fig. 3, the deterministic design shows a gentle increase with increasing mass of TMD and the RDO design obtained by minimizing mean has increasing trend too. But the effect of uncertainties causes higher optimal η_D up to 24.5 %. On comparing these two designs, it is obvious that the η_D is sensitive to uncertainty in the system variables. The proposed RDO improves the reliability of TMD performance which influences the design of η_D . In Fig. 3, the design points with lower m_r (say 1 and 2 %) corresponding to the proposed RDO is higher as compared to the other design values. The proposed optimization is governed by the constraint function to achieve desired reliability. Further increase in m_r shows a decreased difference in the designs of the proposed one and the others because desired reliability can be achieved at lower η_D value. Similar trend is followed under all the three different COV. But in case of uncertainty of 30 %, the demand increases up to 3 % of m_r and then decreases as per the aforementioned reasons. It is clear from the above discussion that the design value of TMD parameters ω_r and η_D are sensitive when uncertainty is present.

Figure 4 shows the mean of TMD performance function at the design points presented in Figs. 2 and 3. Obviously, μ_j is least for the mean minimizing robust

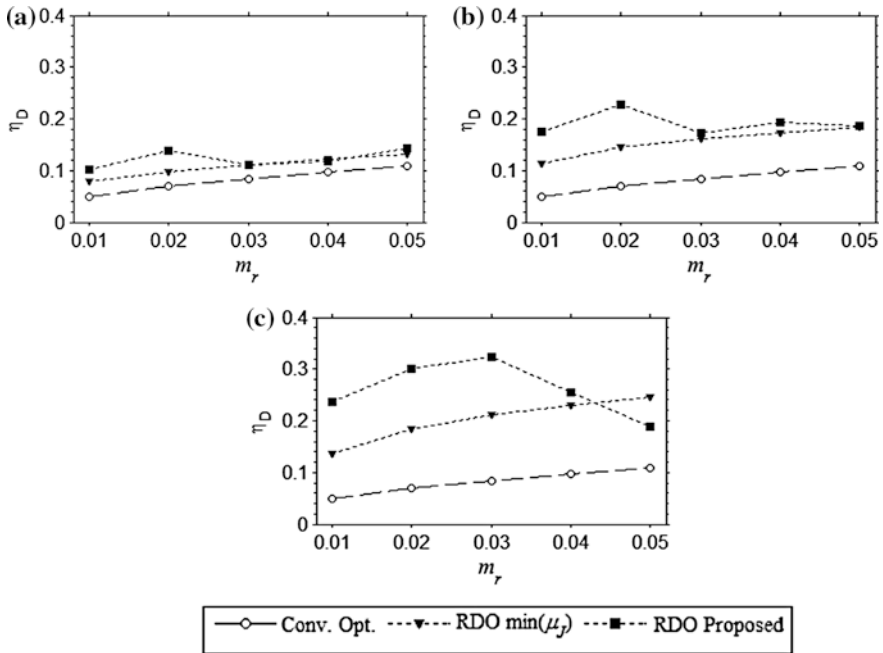


Fig. 3 Design value of TMD damping ratio evaluated by different optimizations with uncertainties **a** 10 %, **b** 20 % and **c** 30 %

Table 1 Comparison of sigma level ϑ by three different design optimizations for uncertainties = 20 %

m_r^a	Conv. opt.	RDO min (μ_J)	RDO proposed
0.01	1.4052	1.9759	4.1613
0.02	1.8897	2.9493	4.7698

^a For cases where either Conv. Opt. or RDO min (J) have achieved ϑ more or equal to the assumed is not included in results

Table 2 Improvement in sigma level ϑ for uncertainties = 30 %

m_r^a	Conv. Opt.	RDO min (μ_J)	RDO proposed
0.01	0.9870	1.4261	3.5509
0.02	1.2533	1.9925	3.7075
0.03	1.4518	2.4211	4.0190
0.04	1.6127	2.7892	3.7188

^a For cases where either Conv. Opt. or RDO min (J) have achieved ϑ more or equal to the assumed is not included in results

design. Increase in uncertainties gives higher difference in mean by the proposed robust design and conventional design with respect to the minimized mean. But the overall variation is not significant. Hence, the design points from all the three optimizations have less significant effect on the mean μ_J as shown in Fig. 4.

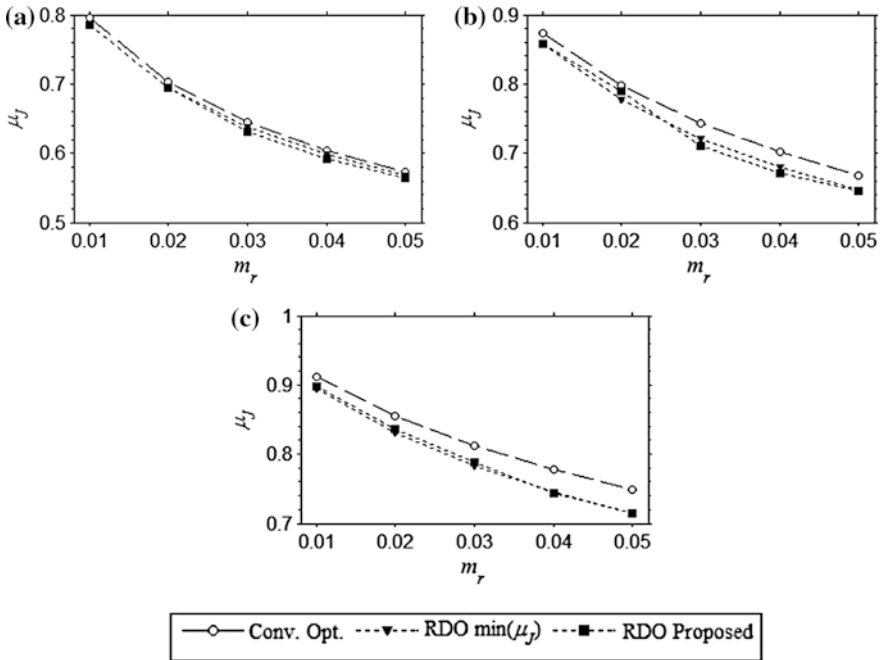


Fig. 4 Mean of TMD performance function with uncertainties **a** 10 %, **b** 20 % and **c** 30 % at the optimized designs

On the contrary, standard deviation is sensitive to the design (refer Fig. 5). Standard deviation of performance function, σ_J from the conventional design has the highest value because the probability distribution of the output (i.e. J) is widest as compared to the two robust designs. The effect on σ_J is more severe when uncertainties are high, see Fig. 5b, c. The mean minimizing RDO reduces σ_J by decreasing ω_r and increasing η_D , thus making the PDF narrower that eventually improves sigma level (see Tables 1 and 2). It is also worth noticing that in this two DOF model, the mean and standard deviation of the TMD performance function cannot be minimized simultaneously. For an nearly invariant mean μ_J , the shape of the PDF of J is governed by σ_J . Thus, making its implementation critical during the operation which is described in the Eq. 12. This helps to attain relatively lower σ_J under the proposed RDO. The improvement of σ_J is prominent due to higher η_D where the detuning effect is low. The same can be reflected for ϑ in Tables 1 and 2. Thus from the above discussion one can notice the role of damping of TMD is vital in overall performance of controller especially under random system parameters. The proposed RDO of TMD parameter helps to avoid detuning during its operation as the sigma level of the performance is increased significantly.

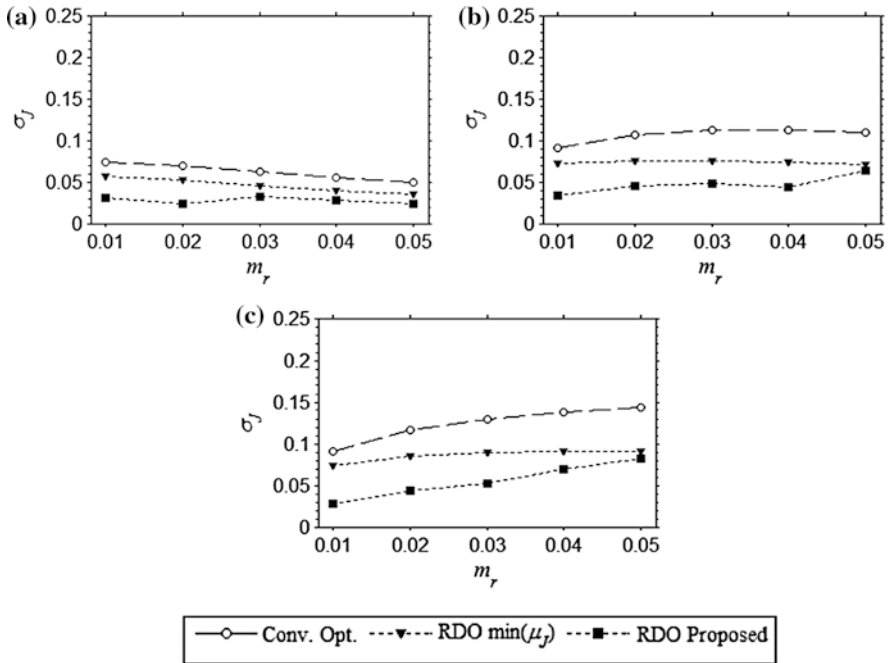


Fig. 5 Variation in standard deviation of TMD performance from different optimizations with varying uncertainties—a 10 %, b 20 % and c 30 %

6 Conclusions

A two-level ARSM based RDO of the TMD is proposed in this study. Where the optimization and the effect of randomness of the system parameters are dealt separately by fitting response surfaces. The optimization of the TMD parameters (viz. natural frequency and damping ratio) is solved iteratively by ARSM which then satisfies the constraint condition to ensure robustness. To illustrate its application, a SDOF-TMD model is solved. A comparative study is conducted between deterministic design where the performance function is minimized without considering uncertainties and robust design by minimizing the mean and the standard deviation of the performance function. Based on the numerical study following observations are made

- The TMD parameters (i.e. frequency ratio and damping) are significantly affected by the uncertainties in the system. In this context, the proposed RDO of TMD ensures the reliability in response reduction by achieving the desired sigma level in optimization.
- Mass ratio significantly affect the overall performance of the TMD. Increase in mass ratio reduces the adverse effect of detuning due to uncertainty as it absorbs more energy.

- The role of damping in TMD is critical on overall performance of controller. Increase in TMD damping reduces the effect of uncertainties by decreasing the variance of performance function.
- As the uncertainty level increases, conventional optimization shows significant detuning of the controller which is reflected in the variance of the primary response. Hence, it justifies the use of RDO in tuning the controller in presence of uncertainties. The modified tuning parameters show significant decrease in variance thereby increasing the effectiveness of the controller.
- Use of meta-modelling in optimization and estimating of statistical moments (mean and standard deviation) helps in significant reduction in number of performance function evaluations. For complex finite element (FE) models, this will reduce the overall cost of computation and thus, justifies the use of ARSM.
- The proposed method is applicable to any probability distribution or correlation of random variables. It can be adopted for RDO based tuning of other passive control devices.

References

1. Den Hartog J (1985) *Mechanical vibrations*, 4th edn. Dover Publications, New York
2. Wang YZ, Cheng SH (1989) The optimal design of dynamic absorber in the time domain and the frequency domain. *Appl Acoust* 28(1):67–78
3. Asami T, Nishihara O, Baz AM (2002) Analytical solutions to H_{∞} and H_2 optimization of dynamic vibration absorbers attached to damped linear systems. *J Vib Acoust* 124(2):284–295
4. Fujino Y, Abé M (1993) Design formulas for tuned mass dampers based on a perturbation technique. *Earthq Eng Struct Dyn* 22(10):833–854
5. Kenarangi H, Rofooei FR (2010) Application of tuned mass dampers in controlling the nonlinear behavior of 3-D structural models, considering the soil-structure interaction. In: *Proceedings of 5th national congress on civil engineering*, Iran, 4–6 May 2010
6. Roffel A, Lourenco R, Narasimhan S, Yarusevych S (2011) Adaptive compensation for detuning in pendulum tuned mass dampers. *J Struct Eng* 137(2):242–251
7. Papadimitriou C, Katafygiotis LS, Au SK (1997) Effects of structural uncertainties on TMD design: a reliability-based approach. *J Struct Control* 4(1):65–88
8. Marano GC, Greco R, Sgobba S (2010) A comparison between different robust optimum design approaches: application to tuned mass dampers. *Probab Eng Mech* 25(1):108–118
9. Hoang N, Fujino Y, Warnitchai P (2008) Optimal tuned mass damper for seismic applications and practical design formulas. *Eng Struct* 30(3):707–715
10. Chakraborty S, Roy B (2011) Reliability based optimum design of tuned mass damper in seismic vibration control of structures with bounded uncertain parameters. *Probab Eng Mech* 26(2):215–221
11. Kanai K (1957) Semi-empirical formula for the seismic characteristics of the ground. *Bull Earthq Res Inst Japan* 35:309–324
12. Tajimi H (1960) A statistical method of determining the maximum response of a building structure during an earthquake. In: *Proceedings of the 2nd world conference on earthquake engineering*, Japan, 11–18 July 1960

13. Roos D, Adam U (2006) Adaptive moving least square approximation for the design reliability analysis. In: Proceedings of Weimar optimization and stochastic days 3.0, Germany
14. Box GEP, Wilson KB (1951) On the experimental attainment of optimum conditions. *J Roy Stat Soc Ser B (Methodol)* 13(1):1–45

A Hybrid Approach for Solution of Fokker-Planck Equation

Souvik Chakraborty and Rajib Chowdhury

Abstract Quantification of response statistics of non-linear systems subjected to harmonic, parametric and random excitation is of great importance in the field of stochastic dynamics. It is a well-known fact that probability density function of the stochastic response of non-linear systems subjected to white and coloured noise excitation is governed by both forward Fokker-Planck (FP) and backward Kolmogorov equations. This paper presents a novel approach, referred here as recursive decomposition method (RDM), for the solution of FP equation. The proposed approach decomposes the solution into number of component functions and determines the component functions in a recursive way. Unlike some of the traditional techniques, where the solutions are obtained at grid points, RDM yields the solution in a series form. Three examples illustrate the proposed approach for the solution of FP equation.

Keywords Backward Kolmogorov equation · Fokker-Planck equation · Hybrid approach · Recursive decomposition

1 Introduction

Response of dynamic systems subjected to stochastic excitation has been a topic of interest for a number of years. It is a well-known fact that if the system is linear and the excitation is Gaussian, the output is also Gaussian [1–3]. Solution of such dynamic system is comparatively easier. Even for linear systems subjected to non-Gaussian excitation, the response can be approximated as Gaussian. Conversely,

S. Chakraborty (✉) · R. Chowdhury
IIT Roorkee, Roorkee 247667, India
e-mail: csouvik41@gmail.com

R. Chowdhury
e-mail: rajibfce@iitr.ac.in

nonlinear systems give rise to non-Gaussian responses [4, 5], solution of which is non-trivial and complicated.

It is well-known that the response statistics of dynamical systems subjected to Gaussian white noise may be calculated by solving the appropriate Fokker-Planck (FP) equation [6–9]. However, exact solutions for the FP equation are available for few linear systems [10, 11], scalar systems [12] and some multi-dimensional conservative systems [4]. For this reason several approximate techniques have been developed such as finite element method [6, 13], finite difference method [6], weighted residuals scheme [14–16], maximum entropy based methods [17] and the path integral methods [9, 18–20]. However all the method require large computational resources, specifically for computing the tail probabilities [21, 22].

Another class of approximation method, known as Moment Closure Method (MCM) [23–25], is based on the theory of diffusion process and on Ito stochastic differential calculus which predicts probability density function (PDF) of response based on moments or equivalent terms, known as cumulants and quasi-moments. In order to overcome the infinite hierarchy of coupled moment equations, various closure approximations are introduced. However, with increase in the order of closure, the complexity of the moment equations increases drastically.

The above limitations are not shared by equivalent linearization method (EQL) [26–28], making it a popular choice among researchers. In this method, the original non-linear system is replaced by an equivalent linear system. Parameters of the linear system are determined by minimizing the difference between the two systems, i.e., the original and the equivalent linear system, in some statistical sense. The main advantage of ELM lies in its versatility and applicability. However, ELM yields accurate results only for system having a low degree of nonlinearity. Other methods for non-linear stochastic dynamic includes Monte Carlo simulation (MCS) [29], first-order reliability method [30–32], Bayesian emulators [33], neural network [34], etc.

This paper presents a novel approach, referred here as recursive decomposition method (RDM) [35], for solution of the FP equations for some nonlinear systems subjected to stochastic excitation. Compared to other available techniques, RDM has several advantages. Firstly, it can handle both linear and nonlinear FP equation without the need for any linearization or discretization. Secondly, unlike some conventional method which provide solution at nodal points, RDM provides an explicit solution. Thirdly, it avoids perturbation in order to find solution if given equations are nonlinear. Furthermore, the calculations for RDM is minimal.

The paper is presented in five sections including this introductory section. Section 2 provides the problem set up for nonlinear stochastic dynamic problems. The basic idea of RDM is presented in Sect. 3. Section 4 illustrates the RDM in solution of FP equations. Finally the paper is concluded in Sect. 5.

2 Problem Setup

Let us consider a N degree of freedom system with the nodal displacement $\mathbf{u}(t) = [u_1(t), u_2(t), \dots, u_N(t)]^T: \Omega \rightarrow \mathbf{R}^N$. Assuming a state vector $\mathbf{Z}(t) = [\mathbf{u}(t)^T, \dot{\mathbf{u}}(t)^T]^T$, where $\dot{}$ denotes time derivation. The equation of motion of the above described system can be written as

$$\dot{\mathbf{Z}}(t) = \mathbf{b}(\mathbf{Z}(t)) + \mathbf{G}(\mathbf{Z}(t))\mathbf{W}(t) \tag{1}$$

where, \mathbf{Z} is an \mathbf{R}^N valued stochastic process. $\mathbf{b}(\mathbf{Z}(t))$ and $\mathbf{G}(\mathbf{Z}(t))$ are the drift and diffusion matrix, respectively. $\mathbf{W}(t)$ represents the random excitation which is often modelled as white noise, i.e.,

$$\begin{aligned} \langle W_i(t) \rangle &= \langle W_j(t) \rangle = 0, & \langle W_i(t_1)W_j(t_2) \rangle &= 2\sigma_i\delta(\tau) \\ \langle W_i(t)W_j(t) \rangle &= 0 & \text{and } \tau &= t_2 - t_1 \end{aligned} \tag{2}$$

where, $\langle \bullet \rangle$ denotes expectation operator. σ_i is the spectral density of i th excitation and $\delta(\tau)$ is Dirac delta function. The FP equation for aforementioned system is given as [36]

$$\frac{\partial p}{\partial t} = - \sum_{i=1}^N \frac{\partial [b_i(\mathbf{Z})p]}{\partial z_i} + \sum_{i=1}^N \sum_{j=1}^N \frac{\partial^2 [h_{ij}(\mathbf{Z})p]}{\partial z_i \partial z_j} \tag{3}$$

where, h_{ij} is the ij th element of the matrix $\mathbf{H}(\mathbf{Z}) = \mathbf{G}(\mathbf{Z}(t)) \cdot \sigma \cdot \mathbf{G}^T(\mathbf{Z}(t))$ and p is the transition PDF of $\mathbf{Z}(t)$.

3 Recursive Decomposition Method

Let us introduce an operator L such that

$$L_r = \frac{\partial}{\partial t} \tag{4}$$

and

$$L_{FP} = - \sum_{i=1}^N \frac{\partial}{\partial z_i} b_i(\mathbf{Z}) + \sum_{i=1}^N \sum_{j=1}^N \frac{\partial^2 h_{ij}(\mathbf{Z})}{\partial z_i \partial z_j}. \tag{5}$$

Rewriting Eq. (3) in operator form, we obtain

$$L_t(p) = L_{FP}(p). \quad (6)$$

Now assuming that there exists an inverse operator L_t^{-1} such that

$$L_t^{-1} = \int_0^t (\bullet) d\tau. \quad (7)$$

We can write

$$L_t^{-1}L_t(p) = L_t^{-1}L_{FP}(p). \quad (8)$$

Now considering initial value to be $p(0)$, we obtain

$$p - p(0) = L_t^{-1}L_{FP}(p) \quad (9)$$

and thus

$$p = p(0) + L_t^{-1}L_{FP}(p). \quad (10)$$

We next decompose p as

$$p = p(0) + \lim_{n \rightarrow \infty} \sum_{i=1}^n p_i. \quad (11)$$

Replacing p from Eq. (11) in Eq. (10), we obtain

$$p = p(0) + L_t^{-1}L_{FP} \left(p(0) + \lim_{n \rightarrow \infty} \sum_{i=1}^n p_i \right). \quad (12)$$

From Eq. (12), we obtain

$$p_{n+1} = L_t^{-1}L_{FP}(p_n), \quad n \geq 0. \quad (13)$$

Remark 1 RDM yields a close form solution if there exists an exact solution for the FP equation under consideration.

Remark 2 RDM yields a solution of FP equation based on the initial condition only. Unlike other traditional techniques which provide result at grid points only, RDM yields an explicit solution.

Remark 3 If determination of exact values of the components become impossible, we resort to numerical methods to determine the components.

4 Numerical Examples

Implementation of proposed approach have been illustrated with three examples. The first example is a simple FP equation with known analytical solution. This provides a definite overviews of the proposed approach. The second and third example illustrates the applicability of proposed approach for solving nonlinear stochastic dynamic problems. Result obtained compare well with MCS.

4.1 An Analytical Problem

In this example we consider the FP equation described in Eq. (3) with $n = 2$ and $b_1 = u_1, b_2 = 5u_2, h_{11} = u_1^2, h_{12} = h_{21} = 1$ and $h_{22} = u_2^2$. We further consider the initial condition to be $p(0) = u_1$.

Using RDM we have

$$p_{n+1} = L_t^{-1}L_{FP}(p_n), \quad n \geq 0. \tag{14}$$

We, therefore, have

$$p_1 = L_t^{-1}L_{FP}(p_0) = u_1 t \tag{15}$$

$$p_2 = L_t^{-1}L_{FP}(p_1) = u_1 \frac{t^2}{2!} \tag{16}$$

⋮

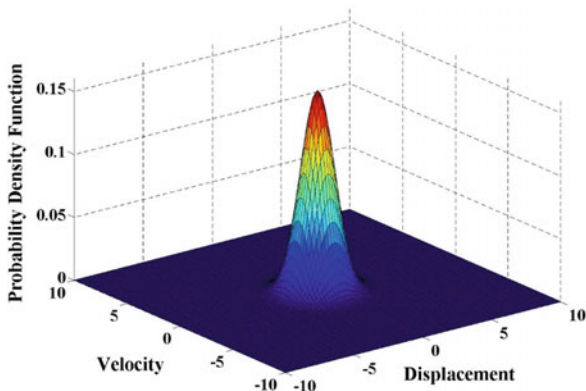
$$p_n = u_1 \frac{t^n}{n!}. \tag{17}$$

Combing Eqs. (14)–(17), we obtain

$$\begin{aligned} p &= \lim_{n \rightarrow \infty} \left(u_1 + u_1 t + u_1 \frac{t^2}{2!} + \dots + u_1 \frac{t^n}{n!} \right) \\ &= u_1 \lim_{n \rightarrow \infty} \left(1 + t + \frac{t^2}{2!} + \dots + \frac{t^n}{n!} \right) \\ &= u_1 e^t \end{aligned} \tag{18}$$

Equation (18) represents the closed form solution of FP equation under discussion.

Fig. 1 Stationary PDF of linear oscillator obtained using RDM



4.2 Linear Oscillator

In this example, we have considered a linear oscillator of the following form:

$$d\mathbf{x}_t = b(\mathbf{x}_t)dt + \mathbf{K}d\mathbf{W}_t \tag{19}$$

where,

$$b(\mathbf{x}_t) = \begin{bmatrix} x_2 \\ -2\eta\omega_0x_2 - \omega_0x_1^2 \end{bmatrix}. \tag{20}$$

We assume $\eta = 0.05$, $\omega_0 = 1$ and $\mathbf{K} = [0 \ 1]^T$. \mathbf{W} is modelled as Gaussian white noise with spectral density $D = 0.1$. The initial condition is assumed to be binormal with $\mu_{x_1} = \mu_{x_2} = 5$ and $\sigma_{x_1} = \sigma_{x_2} = \frac{1}{3}$.

Figure 1 shows the stationary joint PDF of response as obtained from RDM. As expected the PDF is binormal. Figure 2 shows a cross section of stationary PDF at $x_2 = 0$. It is observed that the result obtained are in excellent agreement with exact solution.

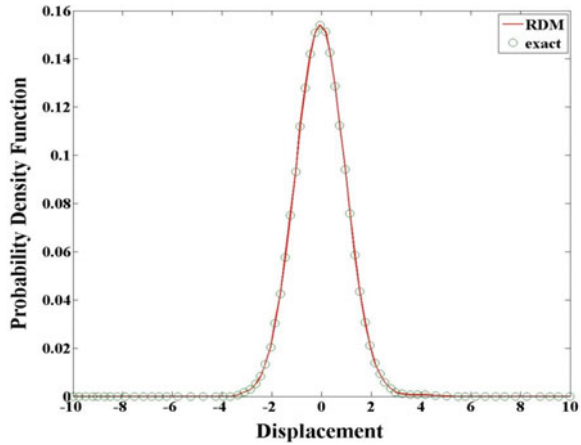
4.3 Bouc-Wen Oscillator [37]

Bouc-Wen oscillator is a hysteretic oscillator governed by the differential equation

$$\begin{aligned} m\ddot{u}(t) + c\dot{u}(t) + k[\alpha\dot{u}(t) + (1 - \alpha)Z(t)] &= F(t) \\ \dot{Z}(t) &= -\delta|\dot{u}(t)||Z(t)|^{r-1}Z(t) - \gamma|Z(t)|^r\dot{u}(t) + A\dot{u}(t) \end{aligned} \tag{21}$$

where, m , c and k are mass, damping and stiffness respectively. While the parameters r, A, γ and δ controls the shape of hysteresis loop, α controls the degree of hysteresis.

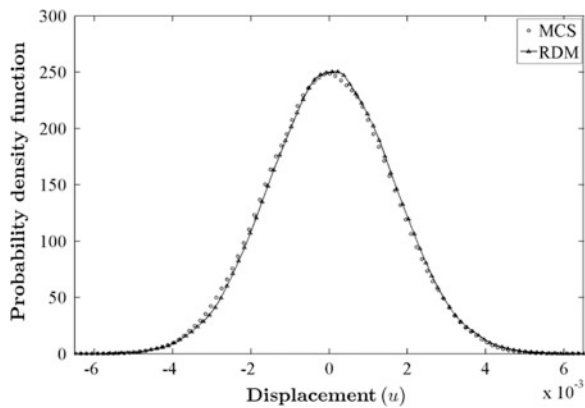
Fig. 2 Marginal PDF of displacement obtained using RDM. The result is in excellent agreement with exact solution



The external excitation $F(t)$ is considered to be the force generated due to acceleration $a_g(t)$ and is defined as $F(t) = -ma_g(t)$, where $a_g(t)$ is modelled as Gaussian white noise. We consider $m = 3 \times 10^5$ kg, $c = 1.5 \times 10^2$ kNs/m and $k = 2.1 \times 10^4$ kN/m. Considering mean square response of the linear system, obtained at $\alpha = 1$, to be $\sigma_0 (= m^2 \pi S / ck)$, δ and γ are defined as $1/2\sigma_0$. We further consider $\alpha = 0.5$, $r = 3$, $A = 1$ and $\mathbf{H} = 0.1$. The result obtained is benchmarked against MCS result.

Figure 3 shows the PDF of response as obtained RDM and MCS with $N_s = 10^5$, where N_s denotes number of realizations. Excellent agreement among results obtained from RDM and MCS is observed.

Fig. 3 PDF of displacement response of Bouc-Wen oscillator [36] obtained using RDM



5 Conclusion

A novel approach, referred here as recursive decomposition method (RDM), for solution of Fokker-Planck equation has been presented. RDM determines an exact solution of the FP equation based on initial condition only. Unlike traditional methods, this method does not require any discretization and requires minimal calculation. Furthermore, RDM is implemented directly without the need for any linearization or perturbation.

Implementation of the proposed approach has been illustrated with three examples. Results obtained are in excellent agreement with other results. In fact, the proposed approach yields exact solution for problems having a closed form solution as shown in the first problem. Moreover, the amount of calculation requirement is also minimal.

References

1. Newland DE (1996) An introduction to random vibrations, spectral and wavelet analysis. Prentice Hall, Longman, London
2. Nigam NC (1983) Introduction to random vibrations. The MIT Press, London
3. Grigoriu M (1995) Applied non-gaussian processes. Prentice-Hall, Englewood Cliffs
4. Caughey TK (1971) Non linear theory of random vibrations. In: Advances in applied Mechanics. Academic Press, New York
5. Kliemann W, Namachchivaya S (1995) Nonlinear dynamics and stochastic mechanics (mathematical modeling). CRC Press, London
6. Kumar P, Narayanan S (2006) Solution of Fokker-Planck equation by finite element and finite difference methods for nonlinear systems. *Sadhana-Acad Proc Eng Sci* 31:445–461
7. Kumar P, Narayanan S (2009) Numerical solution of multidimensional Fokker-Planck equation for nonlinear stochastic dynamical systems. *Adv Vib Eng* 8:153–163
8. Narayanan S, Kumar P (2012) Numerical solutions of Fokker-Planck equation of nonlinear systems subjected to random and harmonic excitations. *Probab Eng Mech* 27:35–46
9. Kumar P, Narayanan S (2010) Modified path integral solution of Fokker-Planck equation: response and bifurcation of nonlinear systems. *J Comput Nonlinear Dyn*. doi:[10.1115/1.4000312](https://doi.org/10.1115/1.4000312)
10. Wang MC, Uhlenbeck G (1945) On the theory of Brownian motion II. *Rev Mod Phys* 17:323–342
11. Soize C (1994) The Fokker-Planck equation for stochastic dynamical system and its explicit steady state solution. World Scientific Publishing Co Pte Ltd, Singapore
12. Caughey TK, Dienes JK (1962) The behaviour of linear systems with white noise input. *J Math Phys* 32:2476–2479
13. Cho WST (2013) Stochastic structural dynamics: application of finite element methods. Wiley, New York
14. Cai GQ, Lin YK (1988) A new approximate solution technique for randomly excited nonlinear oscillators. *Int J Non Linear Mech* 23:409–420
15. Spencer BF, Bergman LA (1993) On the numerical solution of the Fokker-Planck equation for nonlinear stochastic systems. *Nonlinear Dyn* 4:357–372. doi:[10.1007/BF00120671](https://doi.org/10.1007/BF00120671)
16. Wen Y-K (1975) Approximate method for nonlinear random vibration. *J Eng Mech Div* 101:389–401

17. Liu Q, Davies HG (1990) The non-stationary response probability density functions of non-linearly damped oscillators subjected to white noise excitations. *J Sound Vib* 139:425–435. doi:10.1016/0022-460X(90)90674-O
18. Kougioumtzoglou IA, Spanos PD (2012) An analytical Wiener path integral technique for non-stationary response determination of nonlinear oscillators. *Probab Eng Mech* 28:125–131
19. Alibrandi U, Di Paola M, Ricciardi G (2007) Path integral solution solved by the kernel density maximum entropy approach. In: International symposium on recent advance mechanical system on probability theory
20. Feng GM, Wang B, Lu YF (1992) Path integral, functional method, and stochastic dynamical systems. *Probab Eng Mech* 7:149–157
21. Johnson EA, Wojthiewicz SF, Spencer BFJ, Bergman LA (1997) Finite element and finite difference solutions to the transient Fokker–Planck equation, Technical note. The Deutsches Elektronen-Synchrotron (DESY-97:161), pp 290–306
22. Schuller GI, Pradlwarter HJ, Pandey MD (1993) Methods for reliability assessment of nonlinear system under stochastic dynamic loading—a review. In: Proceedings of second european conference on structural dynamics EURODYN'93, Balkema, Rotterdam, pp 751–759
23. Muscolino G, Ricciardi G, Cacciola P (2003) Monte Carlo simulation in the stochastic analysis of non-linear systems under external stationary poisson white noise input. *Int J Nonlinear Mech* 38:1269–1983
24. Paola MD, Vasta M (1997) Stochastic integro-differential and differential equations of non-linear systems excited by parametric Poisson pulses. *Int J Nonlinear Mech* 32:855–862
25. Zeng Y, Li G (2013) Stationary response of bilinear hysteretic system driven by Poisson white noise. *Probab Eng Mech* 33:135–143
26. Chu C (1985) Random vibration of non-linear building-foundation systems, Ph.D. Thesis, Illinois
27. Lutes LD, Sarkani S (2004) Random vibrations: analysis of structural and mechanical systems. Elsevier, Burlington (MA)
28. Roberts JB, Spanos PD (1990) Random vibration and statistical linearization. Wiley, New York
29. Rubinstein RY (1981) Simulation and the Monte Carlo method. Wiley, New York
30. Alibrandi U (2011) A response surface method for nonlinear stochastic dynamic analysis. In: 11th international conference on applications of statistics and probability in civil engineering (ICASP 11), pp 1–7
31. Der Kiureghian A (2000) The geometry of random vibrations and solutions by FORM and SORM. *Probab Eng Mech* 15:81–90
32. Alibrandi U, Der Kiureghian A (2012) A gradient-free method for determining the design point in nonlinear stochastic dynamic analysis. *Probab Eng Mech* 28:2–10
33. DiazDelaO FA, Adhikari S, Flores EIS, Friswell MI (2013) Stochastic structural dynamic analysis using Bayesian emulators. *Comput Struct* 120:24–32
34. Beer M, Spanos PD (2009) A neural network approach for simulating stationary stochastic processes. *Struct Eng Mech* 32:71–94
35. Adomian G (1997) Explicit solutions of nonlinear partial differential equations. *Appl Math Comput* 88:117–126
36. Risken H (1996) The Fokker-Planck equation: methods of solution and applications, 2nd edn. Springer, Berlin
37. Wen Y-K (1976) Method for random vibration of hysteretic systems. *J Eng Mech Div* 102:249–263

On Parameter Estimation of Linear Time Invariant (LTI) Systems Using Bootstrap Filters

Anshul Goyal and Arunasis Chakraborty

Abstract In this paper, sequential Markov Chain Monte Carlo (MCMC) simulation based algorithm (aka Particle Filter) is used for parameter estimation of a three storied shear building model subjected to recorded earthquake ground motions with different non-stationary features (i.e. pga, strong motion durations, amplitude and frequency content). The forward problem is solved using time integration schemes and synthetic measurements are generated by adding simulated zero mean Gaussian noise. Using these synthetic data, stiffness and damping values are identified at different degrees of freedom (dof). Initially, random values (i.e. particles) of these parameters are generated from a pre-selected probability distribution function (e.g. uniform distribution). Each particle is then passed through the model equation and the state is updated using the measurement at each time step. A weight is then assigned to each particle by evaluating their likelihood to the measurement. Once the likelihoods for all particles are evaluated, the new samples for the next iteration are drawn from the simulated initial pool of particles as per the estimated likelihoods. For this purpose, four different re-sampling strategies (e.g. simple, wheel, systematic and stratified) are used to test their relative performance. The performances of the re-sampling algorithms are compared on the basis on number of convergence steps, computational time and the accuracy of the identified parameters. The efficiency of the Bootstrap identification algorithm is also discussed in the light of noise contamination of different intensity.

Keywords Bootstrap filters · Likelihood function · Markov chain · Monte Carlo simulation · Particle filter

A. Goyal (✉) · A. Chakraborty
Department of Civil Engineering, Indian Institute of Technology Guwahati,
Guwahati, Assam 781039, India
e-mail: anshul.goyal@iitg.ernet.in

A. Chakraborty
e-mail: arunasis@iitg.ernet.in

1 Introduction

Assessment of structural health primarily involves developing a mathematical model of the structure whose parameters are to be estimated from the measurements. This constitute an important class of problem known as the “inverse problem”, where the task is to estimate the structural parameters based on the recorded vibration measurement of structure using sensors placed at appropriate locations. This is broadly known as System identification. Its main application is in structural vibration control and health monitoring [1]. The first step of system identification is to determine an appropriate form of model which is typically a differential equation of certain order. The next step is to estimate the unknown parameters using several statistical approaches. The model thus obtained is tested to determine whether it is an appropriate representation of the actual system. If the model fails, a more complex model is chosen and the process is repeated. There are several methods used for identification of structural systems [2]. The present paper discusses the application of Bootstrap Filter (BF) for parameter estimation of a three story shear building model. It starts with a background on dynamic state estimation and recursive Bayesian model updating. After this mathematical formulation, the algorithm for Bootstrap filter is given. The paper ends with numerical results and conclusions.

1.1 Recursive Bayesian Filtering

State estimation is the process of using dynamic data from a system to estimate the quantities that give a complete description of the state according to some representative model of it. The ability to estimate the system state in real time is useful for efficient monitoring and control of the structures. However, models of physical system always have uncertainties associated with them. These may be due to the approximations while modeling the system or due to the noisy measurements by the sensors. Hence, obtaining the parameters of the system optimally out of the limited noise corrupted data is a challenge. The governing equation of the system can be written as

$$x(t) = q(P(t), t) \quad (1)$$

where, $x(t)$ is the response of the structure when an input force $P(t)$ is applied to the system and $q(\cdot)$ relates the input to the output. Since the measurements are available at discrete time steps, it becomes obvious to discretize the above model equation as

$$X_{k+1} = q_k(x_k, w_k) \quad (2)$$

where, x_k represents the state of the system at time $t = k$; x_{k+1} represents predicted state at time $t = k + 1$ and w_t represents the zero mean Gaussian model noise. The discretized measurement equation can be written as

$$y_k = h_k(x_k, v_k) \tag{3}$$

where, y_k is the measurement at time $t = k$ corresponding to the state x_k and v_k is the measurement noise similar to the model noise. The model and the measurement noise are assumed to be uncorrelated. The measurements from the sensors are sampled at a particular rate and can be denoted as a vector

$$\mathbf{M}_k = [y_1, y_2, \dots, y_k] \tag{4}$$

The objective of this formulation is to estimate the true hidden discrete states x_k of the system based on the observed states y_k . Due to the presence of uncertainties in the model and measurement, this determination is probabilistic with an aim of estimating the statistics of the true state x_k given as

$$\mu = \int x_k p(x_k | \mathbf{M}_k) dx_k \tag{5a}$$

$$\sigma = \int (x_k - \mu)^T (x_k - \mu) p(x_k | \mathbf{M}_k) dx_k \tag{5b}$$

where, μ and σ are the first and the second moment of the pdf of $p(x_k | \mathbf{M}_k)$ respectively. The next task is to estimate the pdf $p(x_k | \mathbf{M}_k)$ which is done using sequential Bayesian filtering. Bayesian filtering uses the prior knowledge of the system to generate the posterior distribution of the states at the next time instance once the measurement data becomes available. The recursive relationship between the pdf of the present state and the previous estimate can be expressed as

$$p(x_{0:k} | y_{0:k}) = q[p(x_{0:k-1} | y_{0:k-1}), y_k]. \tag{6}$$

In this process, two assumptions are made to derive the recursive Bayesian relation. The first one is that the states follow the first order Markov process (i.e. the next state depends only upon the current state rather than on the entire history of the state).

$$p(x_k | x_{0:k-1}) = p(x_k | x_{k-1}). \tag{7}$$

The second assumption is that the current observation depends upon the current state only

$$p(y_k | x_k, \dots) = p(y_k | x_k). \tag{8}$$

Now using Bayes' rule one gets

$$p(x_{0:k}|y_{0:k}) = \frac{p(y_{0:k}|x_{0:k})p(x_{0:k})}{p(y_{0:k})}. \quad (9)$$

Using Eqs. 7 and 8 in the above equation, the recursive relation for Bayesian filtering is given by

$$p(x_{0:k}|y_{0:k}) = \frac{p(x_k|x_{k-1})p(y_k|x_k)}{p(y_k|y_{0:k-1})}p(x_{0:k-1}|y_{0:k-1}). \quad (10)$$

Here, $p(x_k|x_{k-1})$ can be derived from the process Eq. 2. In presence of model uncertainty w_k

$$p(x_k|x_{k-1}) = \int p(x_k|x_{k-1}, w_{k-1})p(w_{k-1}|x_{k-1})dw_{k-1}. \quad (11)$$

Since, w_k is independent of the state, it can be written as

$$p(w_{k-1}|x_{k-1}) = p(w_{k-1}). \quad (12)$$

Therefore, the normalizing pdf in Eq. 10 are given by

$$p(y_k|y_{0:k-1}) = \int p(y_k|x_k)p(x_k|y_{k-1})dx_k \quad (13a)$$

$$p(y_k|x_k) = \int p(y_k|x_k, v_k)p(v_k)dv_k. \quad (13b)$$

1.2 Particle Filter

Particle filtering is a general Monte Carlo sampling method for performing inference in state-space models where the state of a system evolves in time. Information about the state is obtained from noisy measurements made at each time step. The method has advantage as it is not subjected to the constraints of linearity and Gaussianity [3, 4]. It also has appealing convergence properties. Several variants of particle filters are available in the literature e.g. Sequential Importance Sampling (SIS), Sequential Importance Resampling (SIR) and Bootstrap Filter (BF). This paper discusses the Bootstrap filter and implementation of several resampling strategies for tackling degeneracy of the algorithm due to skewness of particle weights.

Particle filter generate a set of samples that approximate the filtering distribution $p(x_k|y_0, y_1, \dots, y_k)$ also known as the posterior distribution. Therefore, the expectation with respect to this posterior distribution can be approximated by N number of discrete particles as

$$\int q(x_k)p(x_k|y_0, y_1, \dots, y_k)dx_k \approx \frac{1}{N} \sum_{i=1}^N q(x_k^i). \tag{14}$$

However, it may not be easy and beneficial to sample each time from the posterior distribution and hence samples from an importance distribution is chosen such that

$$\int q(x_k)p(x_k|y_0, y_1, \dots, y_k)dx_k \approx \sum_{i=1}^N q(x_k^i)w_k^i \tag{15}$$

where, x_k^i is simulated from the importance distribution with w_k^i as the weight of the corresponding i th particle. This is known as Importance Sampling. The importance weights are can be written as the ratio of $\frac{p(x_{0:k}|y_{0:k})}{q(x_{0:k}|y_{0:k})}$. Therefore, from Eq. 10 it can be written as

$$w_k^i \propto \frac{p(y_k|x_k^i)p(x_k^i|x_{k-1}^i)p(x_{0:k-1}^i|y_{1:k-1})}{q(x_{0:k}^i|y_{1:k})} \tag{16}$$

where, $q(x_{0:k}^i|y_{1:k})$ is the proposal importance density function and w_k^i is the importance weight of the i th particle at the k th time instant. Thus the recursive importance weights can be written as

$$w_k^i \propto \frac{p(y_k|x_k^i)p(x_k^i|x_{k-1}^i)}{q(x_k^i|x_{0:k-1}^i, y_{1:k})} w_{k-1}^i. \tag{17}$$

Equation 17 forms the basis of SIS, SIR and BF. One of the major problems associated with SIS filter is the degeneracy where all the particles have negligible weight except one particle after few iterations. The variance of the importance weights increases with time and it becomes impossible to control the degeneracy phenomenon. A suitable measure of the degeneracy of the algorithm is the effective sample size as proposed by Gordon [3]. There are two ways to counter this problem:

1. Good choice of Importance density: This involves choosing the importance density such that the variance in importance weights can be reduced and the value of effective sample size increases.
2. Resampling: It is incorporated exclusively in Bootstrap Filter. Here, multiple copies of the best particles are formed while the sample size remains same in

each iteration. Resampling ensures that particles with larger weights are more likely to be preserved than particles with smaller weights. Although the resampling solves the degeneracy, but it introduces sample impoverishment. The present study provides a comparative study among the traditional resampling algorithms viz. simple, wheel, systematic and stratified. The details of these algorithm is omitted here. However, one may refer Haug [4] for the details of these resampling strategy and their numerical implementation.

2 Problem Formulation

We consider the problem of identifying the stiffness and damping at each of the floor levels of a three story shear building model using the Bootstrap Particle filter algorithm. The natural frequency is calculated by solving the eigen value problem involving mass and stiffness matrix. Assuming the structure to be linear, the equation of motion is given by

$$\mathbf{m}\ddot{z}(t) + \mathbf{c}\dot{z}(t) + \mathbf{k}z(t) = \mathbf{F}(t). \quad (18)$$

where, \mathbf{m} is the mass matrix, \mathbf{c} is the damping matrix, \mathbf{k} is the stiffness matrix, $\mathbf{F}(t)$ is the time varying excitation and $z(t)$, $\dot{z}(t)$ and $\ddot{z}(t)$ are respectively the displacement, velocity and acceleration of the floors. The discretized model and the measurement equations can be written as

$$\psi_{k+1} = \psi_k + \mathbf{w}_k \quad (19a)$$

$$\mathbf{Y}_k = h_k(\psi_k) + \mathbf{v}_k \quad (19b)$$

where, ψ_k is the augmented state vector with parameters to be identified. Using these models, following algorithm is adopted for parameter estimation:

1. It starts with simulating N samples for all the parameters to be identified (ψ_0), from the assumed pdf of ψ_0 at the time instant $t = 0$. The random particles are generated in a suitable domain identified by the upper and the lower bounds. These are also known as the prior estimates.
2. The next step involves solving N linear forward problems, using Eq. 19a corresponding to each of the prior estimate ψ_{k-1} . The forward problems are solved using the direct time integration scheme.
3. The predicted values obtained from step 2 are compared to the measurement values. The measurements are either available through sensor recordings or generated synthetically. We have considered synthetic measurements in the present study.
4. The comparison between the predicted values and the measurement is made using the likelihood function $p(y_k|x_k)$ at time $t = k$. The likelihood function is

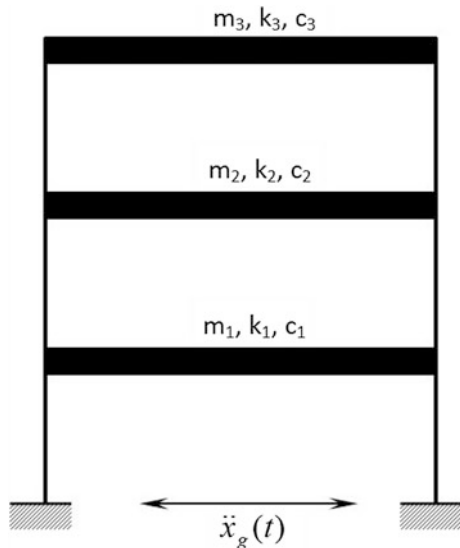
- modeled as the normal distribution centered about the measurement with a small value of standard deviation. Thus, each particle propagated at $t = k$ is weighted.
5. The weights are normalized and then passed through the resampling algorithms. Thus, these normalized weights constitute the discrete probability mass function for the next iteration.
 6. The mean and standard deviation of the estimates are calculated over the ensemble and the process is repeated for the next time step, $t = k + 1$.

3 Numerical Results and Discussions

Figure 1 shows the schematic diagram of a three story shear building model used in this study. The mass at each floor is assumed to be 15.2 kg while the stiffness at those levels are 41987, 76842 and 74812 N/m respectively. Using these values one can estimate the natural frequencies which are 4.1565, 12.8093 and 19.8511 Hz. Figure 2 shows the recorded ground motions of El-Centro and Loma Prieta earthquake used in this study. Using these ground motions, forward problems are simulated and the responses are shown in Fig. 3. These response serve as the synthetic measurement in this study. Using these synthetic data, BF algorithm as describe in the previous section is used for identification.

The inverse problem starts with simulating random values from the uniform distribution for the parameters to be identified. Here, we simulate random values for stiffness and damping at all the floor levels. The domain over which the stiffness values are simulated is between 10,000–90,000 N/m and the damping values are

Fig. 1 Schematic 3DOF system



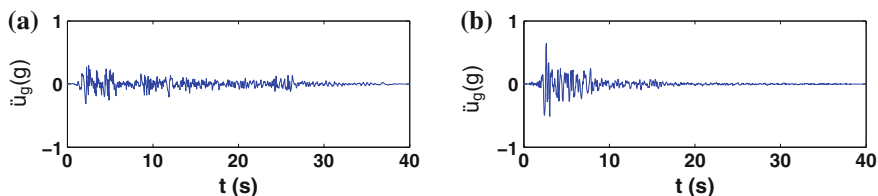


Fig. 2 Ground motions **a** El-Centro and **b** Loma Prieta

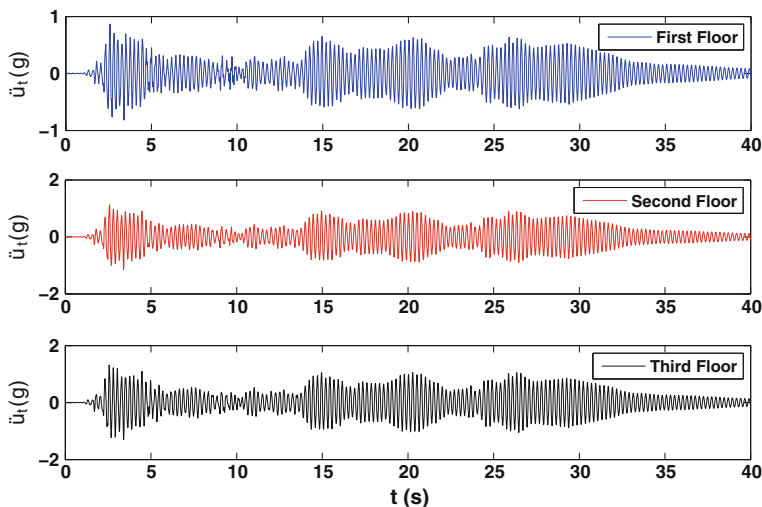


Fig. 3 Response of the model due to El-Centro earthquake

between 0–50 N-s/m. The number of values generated at $t = 0$ are 100. This number remains constant for each and every iteration of the algorithm. Using these samples, forward problem as described in Eq. 19a are solved for the next time step and the likelihood with respect to measurement are evaluated. Normal distribution has been used to calculate the likelihoods (i.e. the weights) of the particles with error covariance been chosen as 0.001. Using the weights, new particles are resampled from the initial generated pool. The process is continued till the end. Figure 4 shows the identified values of parameters using Bootstrap Filter. It may be observed that different resampling strategies converge as more and more measurement are available that helps to upgrade the likelihood. Figure 5 shows the standard deviation of the samples at different time. As the stiffness and damping parameters converge to their respective values, the standard deviation of the samples reduced to zero. The statistical fluctuations die out once the parameters are identified and the standard deviation becomes zero. Figure 6 shows the estimated state of the system. It may be observed that the two states match closely with each other indicating the convergence of the Bootstrap algorithm. In this context, mean value of the

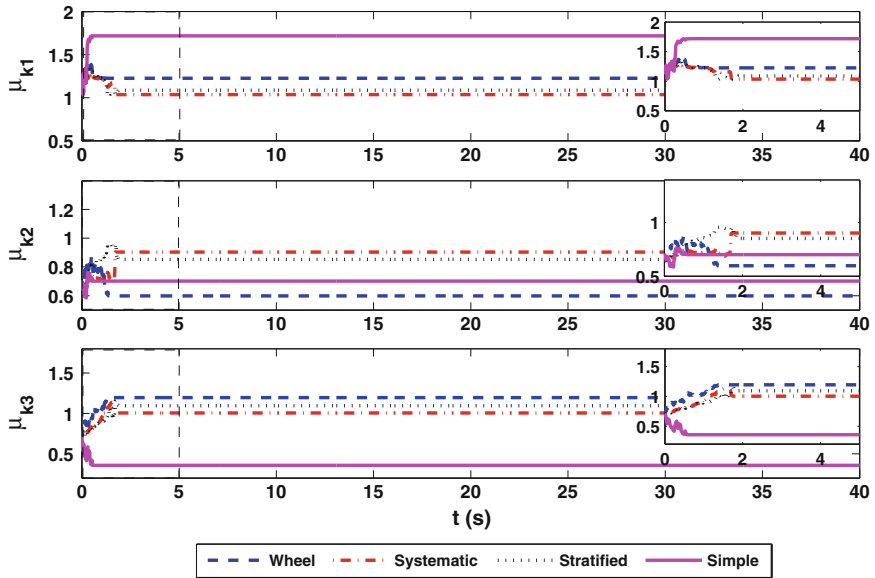


Fig. 4 Ratio of mean value of identified stiffness to original stiffness for El-Centro earthquake

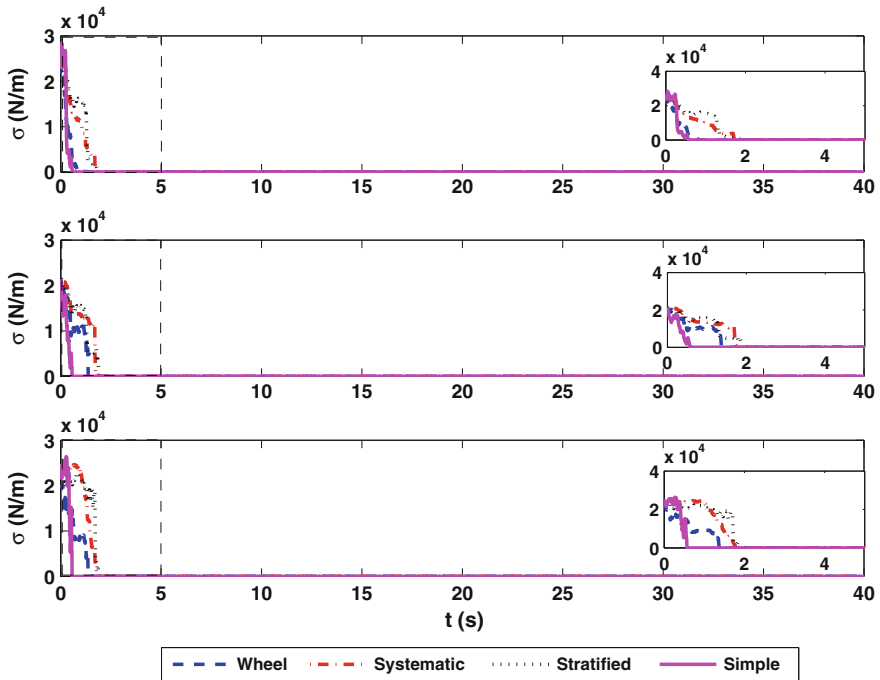


Fig. 5 Standard deviation of stiffness for El-Centro earthquake

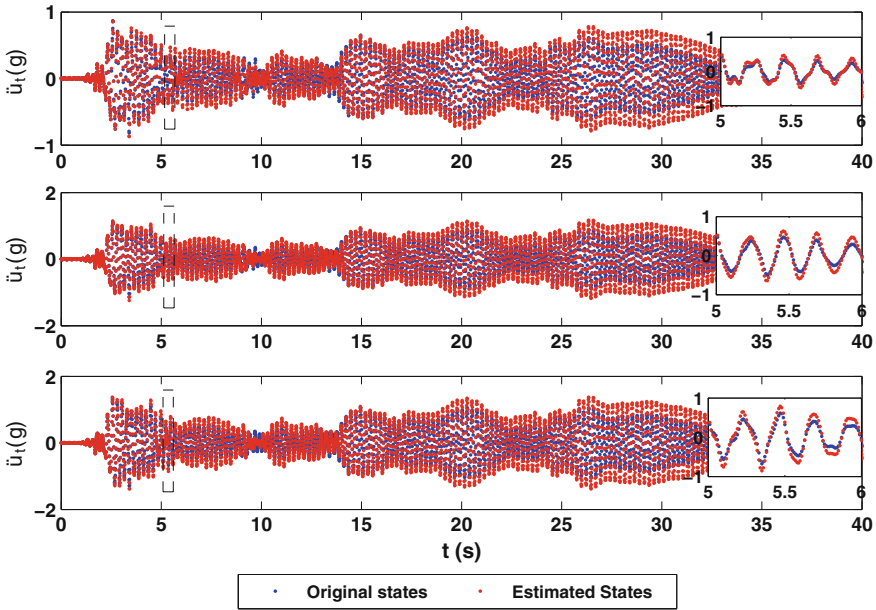


Fig. 6 Original and estimated states for El-Centro earthquake

identified parameters are used to estimate the state of the systems. Figure 7 shows the mode shapes in first three modes of the original and the identified systems. A close match is observed in all three cases which, in turn, proves the accuracy of the Bootstrap based identification strategy. Table 1 shows the ratio of the original values and identified values of the stiffness and damping at different dof for different particle size. It also shows the estimated natural frequency in these modes for each case. The estimation of parameters becomes more accurate by increasing the number of particles but the computational time increases. Several resampling algorithms have been compared based on the percentage error in the values identified as well as the time steps required to attain the convergence. These are simple, wheel, systematic and stratified. The robustness of the algorithm is clearly depicted in Tables 2, 3 and 4, for different earthquakes. Table 1 shows the effect on ratio of identified values to original values by increasing the number of particles from 100 to 1,000. Here, it is noteworthy to mention that the computational time also increases with particle size. However, with generation of more and more samples the probability of obtaining near accurate values increases. The sensitivity analysis for different SNR (signal to noise ratio) has been performed for both El-Centro and Loma Prieta earthquake as shown in Table 2. The results show that Bootstrap filter is robust even for low SNR values. Tables 3 and 4 show the accuracy of the different resampling strategies to identify the parameters. The results in these two

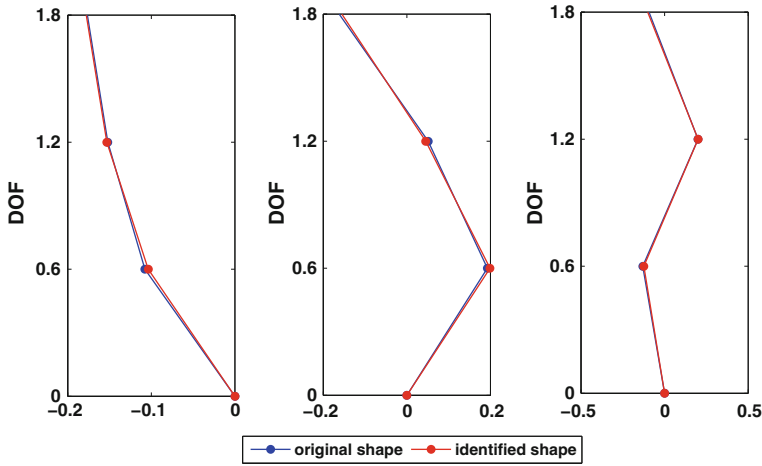


Fig. 7 Mode shape of the original and identified system for El-Centro earthquake

Table 1 Effect on number of particles on estimation of parameters and frequency

No. of particles	Ratio of identified to original value						Identified frequency (Hz)		
	k_1	k_2	k_3	c_1	c_2	c_3	f_1	f_2	f_3
100	1.04	0.90	1.00	0.30	0.78	1.21	4.16	12.72	19.37
500	1.00	0.95	1.01	0.45	0.75	1.02	4.14	12.78	19.66
1,000	1.03	0.96	1.01	1.93	1.32	0.70	4.18	12.95	19.86

Table 2 Sensitivity analysis due to addition of noise with different SNR

Earthquake	SNR	Ratio of identified parameters to original					
		k_1	k_2	k_3	c_1	c_2	c_3
El-Centro	No noise	1.036	0.904	1.004	0.300	0.771	1.205
	0.005	1.036	0.904	1.004	0.300	0.771	1.205
	0.050	1.036	0.904	1.004	0.300	0.771	1.205
	0.010	1.036	0.904	1.004	0.300	0.771	1.205
Loma Prieta	No noise	1.036	0.904	1.004	0.300	0.771	1.205
	0.005	1.036	0.904	1.004	0.300	0.771	1.205
	0.050	1.036	0.904	1.004	0.300	0.771	1.205
	0.010	1.036	0.904	1.004	0.300	0.771	1.205

tables suggest that systematic and stratified resampling algorithms give better estimate of the parameters. However, the other two resampling algorithms (i.e. wheel and simple) converge at a much faster rate.

Table 3 Comparison of different resampling algorithms on the basis of identified values of natural frequency

Earthquake	Resampling	Identified natural frequency (Hz)			% error		
		f_1	f_2	f_3	e_1	e_2	e_3
El-Centro	Simple	4.400	12.804	19.454	5.847	-0.039	-2.002
	Wheel	4.280	13.157	19.993	2.978	2.918	0.716
	Stratified	4.187	12.669	19.748	0.729	-1.093	-0.520
	Systematic	4.187	12.669	19.748	0.729	-1.093	-0.520
Loma Prieta	Simple	4.529	13.746	17.980	8.953	7.309	-9.423
	Wheel	4.081	12.984	20.307	-1.824	1.362	2.296
	Stratified	4.203	12.863	19.496	1.110	0.417	-1.788
	Systematic	4.187	12.669	19.748	0.729	-1.093	-0.520

Table 4 Ratio of identified value of parameters to original value and comparison on the basis of convergence steps

Earthquake	Resampling	Ratio of identified to original parameters						Steps
		k_1	k_2	k_3	c_1	c_2	c_3	
El-Centro	Simple	1.21	0.96	0.92	0.33	1.30	0.19	150
	Wheel	1.10	0.94	1.10	2.13	0.55	1.06	150
	Stratified	1.02	1.02	0.94	0.79	0.55	1.34	200
	Systematic	1.02	1.02	0.94	0.79	0.55	1.34	200
Loma Prieta	Simple	1.96	0.57	1.00	0.52	1.03	0.85	150
	Wheel	0.93	1.04	1.06	1.72	0.61	0.93	150
	Stratified	1.07	0.89	1.04	0.52	1.08	1.30	250
	Systematic	1.02	1.02	0.94	0.79	0.55	1.34	250

4 Conclusions

In this paper, implementation of Bootstrap algorithm to identify linear time invariant (LTI) systems subjected to a non-stationary earthquake signal has been discussed. The advantage of using the particle based approach is that it is robust to pick the best value among the samples generated at $t = 0$. The comparative study of the resampling algorithms clearly suggests that stratified and systematic resampling algorithms give better estimates than simple and wheel. However, the number of convergence steps for them are more. With increase in number of particles, the algorithm may provide better estimates. Besides this, the algorithm is robust for low SNR values. Theoretically the algorithm can be extended to n unknowns but the computational cost increases as more particles are needed for simulations. This demand further research on the implementation Bootstrap filter for large scale structural systems like building and bridges.

References

1. Housner GW, Bergman LA, Caughey TK, Chassiakos AG, Claus RO, Masri SF, Skelton RE, Soong TT, Spencer BF, Yao JTP (1997) Structural control: past, present, and future. *J Eng Mech* 123(9):897–971
2. Sirca GF Jr, Adeli H (2012) System identification in structural engineering. *Sci Iranica* 19 (6):1355–1364
3. Gordon NJ, Salmond DJ, Smith AFM (1993) Novel approach to nonlinear/non-gaussian bayesian state estimation. In: *IEE Proceedings F (Radar and Signal Processing)*, vol 140, IET, pp 107–113
4. Haug AJ (2005) A tutorial on bayesian estimation and tracking techniques applicable to nonlinear and non-gaussian processes. Mitre Corporation, McLean

Seismic Analysis of Weightless Sagging Elasto-flexible Cables

Pankaj Kumar, Abhijit Ganguli and Gurmail S. Benipal

Abstract There exists considerable literature which deals with the dynamic response of cables with distributed self-weight and some lumped masses, if any. Seismic response of single weightless cable structures has not yet been sufficiently investigated. In this Paper, seismic response of a single weightless planer elasto-flexible sagging cable with lumped nodal masses is studied. This investigation is informed by the appreciation that weightless flexible cables lack unique natural state. Rate-type constitutive equation and third order differential equations of motion have been derived earlier. Using these equations, the dynamic response of such cables subjected to harmonic excitation has also been studied by the Authors. Configurational response is distinguished from the elastic response. The scope of the present Paper is limited to prediction of vibration response of a weightless sagging planer two-node cable structure with lumped masses and sustained gravity loads subjected to horizontal and vertical seismic excitations in the presence of sustained gravity loads. The horizontal and vertical seismic excitations are predicted to cause predominantly configurational and elastic displacements from the equilibrium state. Also, the tensile forces in the inclined and horizontal segments are caused predominantly by these excitations respectively. Cross effects due to mode coupling are predicted. No empirical validation of the theory is attempted. The theoretical predictions are validated by comparing with the seismic response of heavy cable nets predicted by other researchers. The theoretical significance of the approach followed here is critically evaluated.

Keywords Weightless cables • Seismic response • Loading rate • Horizontal and vertical excitations • Configurational and elastic modes

P. Kumar (✉) · A. Ganguli · G.S. Benipal
Department of Civil Engineering, IIT, Delhi, India

© Springer India 2015
V. Matsagar (ed.), *Advances in Structural Engineering*,
DOI 10.1007/978-81-322-2193-7_118

1543

1 Introduction

Because of their versatility, cables are employed in diverse areas of structural engineering. It is well-known that flexible sagging cables lack definite natural reference configuration in their passive state. Generally, the analysts assume the equilibrium configuration under self-weight, dead load of the bridge deck, etc., as the reference configuration. Quite sophisticated analytical and computational techniques have been developed for obtaining the static and dynamic response of cable structures. Presence of self-weight renders the response of the cable to additional loads nonlinear. Linear modal frequencies of single sagging cables have been found to depend upon elasto-geometrical parameters [2]. This approach is extended to arbitrarily-oriented cables supporting uniform as well as concentrated loads [3]. A complementary energy principle has also been formulated [8]. Continuous catenary as well as discrete elements have been formulated [1]. Well-known stability functions and equivalent elastic modulus method are used to simulate respectively the geometric stiffness and the effect of self-weight on the constitutive relations of the cables [9]. A spatial two-node catenary cable element with derived tangent stiffness matrix is proposed for conducting nonlinear seismic analysis of cable structures under self-weight and concentrated loads [10]. Such a popular approach involving elastic and geometric stiffness matrices for dynamic analysis of essentially nonlinear cables has been criticized [11]. Internal resonances as well as subharmonic resonances have been predicted for these nonlinear structures [5].

The main point of departure of the Authors' approach is the assumed weightlessness of the cables and the lack of their unique natural configuration. Static and dynamic response of a single weightless elasto-flexible sagging planer cable carrying lumped masses and applied nodal loads has earlier been investigated by the Authors. Rate-type constitutive equations and third order differential equations of motion for these two-node 4-DOF cable structures have been derived. The dynamic response of such structures to harmonic nodal force is determined for different sustained nodal forces, axial elastic stiffness and sag/span ratios. Subharmonic resonances as well as jump and beat phenomena are predicted for elastic and inextensible cables [6]. The incremental equation of motion involving tangent stiffness matrix employed by other researchers is equivalent to the third order equation of motion proposed by the Authors [10].

Further, it has been established by the Authors that elasto-flexible cables exhibit elasto-configurational static and dynamic response. A clear distinction is made between the configurational and elastic response of these structures. In contrast to the elastic structures which are capable of exhibiting purely elastic response, the inextensible flexible cables can exhibit purely configurational static and dynamic response under load variations. The tangent constitutive matrices D_{ij} , f_{ij} and N_{ij} respectively relate the configurational, elastic and elasto-configurational nodal velocities (\dot{x}_i , \dot{u}_i and \dot{y}_i respectively) with the applied nodal rates of loading. The coefficients of these constitutive matrices depend upon the instantaneous magnitudes of the nodal resistive forces P_i . Clearly, the configurational nonlinearity is

also distinct from the conventional geometric nonlinearity associated with the finite or large nodal elastic displacements [6].

Using these constitutive equations and equations of motion, the seismic response of a particular sagging planer cable structure is determined in this Paper. The cable material is assumed to be linear elastic in tension, while both the geometrical and configurational nonlinearities are considered here. As determined by the equation of motion, the time-derivative of the two well-known seismic excitations is obtained. Dynamic response is determined under horizontal and vertical seismic excitations applied separately as well as simultaneously. The theoretical contribution of the Paper is critically evaluated. No attempt is made to validate the predictions with empirical evidence.

2 Theoretical Formulation

Consider a two-node 4-DOF weightless planer sagging elasto-flexible cable as shown in Fig. 1. Let x_i and y_i denote the nodal co-ordinates in the undeformed and deformed state while u_i denote the nodal elastic displacements of the cable carrying sustained nodal loads F_{0i} .

The following third order coupled nonlinear differential equations of motion are derived for such cables carrying lumped masses M_{ij} :

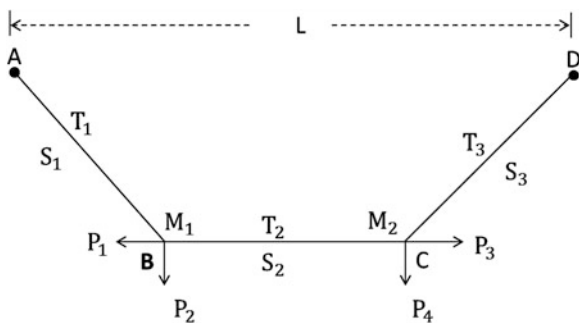
$$M_{ij} \ddot{\dot{y}}_j + C_{ij} \ddot{y}_j + K_{ij} \dot{y}_i = \dot{F}_i(t) \tag{1}$$

The instantaneous internal resistive nodal forces P_i are obtained as

$$P_i = F_i(t) - C_{ij} \dot{y}_i - M_{ij} \ddot{y}_j \tag{2}$$

The rate-type constitutive equations relating these internal nodal forces P_i and the nodal velocities \dot{y}_i are stated as

Fig. 1 Planer cable system



$$\begin{aligned}
 y_i &= x_i + u_i & \dot{y}_i &= \dot{x}_i + \dot{u}_i & \dot{x}_i &= D_{ij}\dot{P}_i & \dot{u}_i &= f_{ij}\dot{P}_i \\
 \dot{y}_i &= N_{ij}\dot{P}_i & N_{ij} &= D_{ij} + f_{ij} & K_{ij} &= N_{ij}^{-1}
 \end{aligned}
 \tag{3}$$

When the elastic displacements are assumed to be small, the nodal coordinates x_i of the undeformed cable, elastic displacements u_i , coefficients D_{ij} and coefficients f_{ij} are functions homogeneous of order 0, 1, -1 and 0 respectively of the nodal resistive forces P_i . Explicit expressions for x_i , u_i , y_i , D_{ij} , f_{ij} and N_{ij} are reported elsewhere [6].

The nonlinear cable structure is assumed to be instantaneously classically damped with the instantaneous damping matrix C_{ij} being determined as

$$C_{ij} = a_0 M_{ij} + a_1 K_{ij} \tag{4}$$

Here, K_{ij} represents the instantaneous tangent elasto-configurational stiffness matrix.

3 Structural and Loading Details

The seismic behavior of a plane cable net has been investigated earlier [10]. The particular single planer sagging cable structure investigated in this Paper obtained from this cable net by idealization is shown in Fig. 1. Its structural details are as below:

$$\begin{aligned}
 E &= 1.21 \times 10^7 \text{ N/m}^2 & L &= 91.44 \text{ m} & H &= 0 \\
 F_0 &= (0, 17.793, 0, 17.793) \text{ kN}
 \end{aligned}$$

Two equal masses ($M = 4,380 \text{ kg}$) are lumped at the two nodes. Self-weight of the cable is ignored. The equilibrium state response is presented below:

$$\begin{aligned}
 x_1 &= 30.48 \text{ m} & x_2 &= 9.144 \text{ m} & x_3 &= 60.96 \text{ m} & x_4 &= 9.144 \text{ m} \\
 u_1 &= -0.069 \text{ m} & u_2 &= 0.708 \text{ m} & u_3 &= 0.069 \text{ m} & u_4 &= 0.708 \text{ m} \\
 y_1 &= 30.409 \text{ m} & y_2 &= 9.85 \text{ m} & y_3 &= 61.029 \text{ m} & y_4 &= 9.85 \text{ m} \\
 T_1 &= 57.71 \text{ kN} & T_2 &= 54.90 \text{ kN} & T_3 &= 57.71 \text{ kN}
 \end{aligned}$$

The linear modal frequencies given by eigenvalues of the matrix $M_{ij}^{-1}K_{ij}$ are determined as

$$\omega_{n1} = 1.07 \text{ rad/s} \quad \omega_{n2} = 2.38 \text{ rad/s} \quad \omega_{n3} = 9.16 \text{ rad/s} \quad \omega_{n4} = 16.17 \text{ rad/s}$$

The characteristic damping ratios for the cable structures are of the order of 0.01 [4]. However, for ease of comparison with published literature [10], the modal

damping ratios for the lowest two modes are assumed to be as 0.05 for the determination of instantaneous damping matrix.

In the presence of seismic excitation, the nodal force vector is obtained as

$$F_i(t) = F_{0i} + E_i(t) \tag{5}$$

Here, $E_i(t)$ denote the time-dependent seismic forces. Dynamic forces introduced by the earthquakes and acting on the lumped modal masses are considered here to be lying in the plane of the cable. These forces depend upon the horizontal and vertical components \ddot{y}_h, \ddot{y}_v of the seismic acceleration. When only horizontal seismic forces are considered,

$$E_h(t) = (-M_1 \ddot{y}_h, 0, -M_2 \ddot{y}_h, 0) \tag{6}$$

Similarly, in the case of vertical seismic forces acting alone,

$$E_v(t) = (0, -M_1 \ddot{y}_v, 0, -M_2 \ddot{y}_v) \tag{7}$$

Of course, the horizontal and vertical components of the seismic forces act simultaneously and can be obtained by adding the above horizontal and vertical seismic load vectors. Here, \ddot{y}_h and \ddot{y}_v represent the absolute horizontal and vertical components of the ground accelerations. In this Paper, the vertical component of the ground acceleration is obtained by scaling down the horizontal component to its two-third value at all instants without changing its frequency content. The equation of motion demands the evaluation of applied rate of loading vector $\dot{F}(t)$ which in the present case equals $\dot{E}(t)$. In the case of horizontal and vertical seismic accelerations, the loading rate vectors are specified as follows:

$$\begin{aligned} \dot{F}(t) &= \dot{E}_h(t) = (-M_1 \dddot{y}_h, 0, -M_2 \dddot{y}_h, 0) \\ \dot{F}(t) &= \dot{E}_v(t) = (0, -M_1 \dddot{y}_v, 0, -M_2 \dddot{y}_v) \end{aligned} \tag{8}$$

Here, \dddot{y}_h and \dddot{y}_v represent respectively the rates of change of horizontal and vertical components of ground acceleration. In this Paper, \dddot{y}_h and \dddot{y}_v , components are evaluated from the available ground acceleration components \ddot{y}_h and \ddot{y}_v respectively as shown in Eq. (9).

$$\dddot{y}_{h(t_i+\Delta t)} = \frac{\ddot{y}_{h(t_i+\Delta t)} - \ddot{y}_{h(t_i)}}{\Delta t} \quad \dddot{y}_{v(t_i+\Delta t)} = \frac{\ddot{y}_{h(t_i+\Delta t)} - \ddot{y}_{h(t_i)}}{\Delta t} \tag{9}$$

Figure 2a, b show the El Centro earthquake records of the horizontal ground acceleration components and the deduced rate of acceleration normalized with

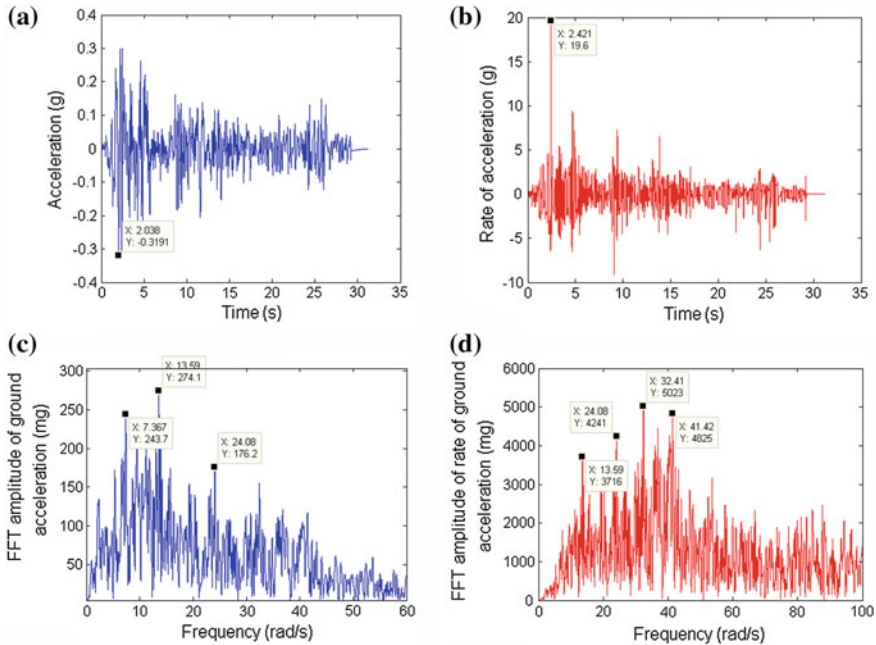


Fig. 2 a El Centro ground acceleration, b time rate of El centro ground acceleration, c FFT of El Centro ground acceleration, d FFT of El centro rate of ground acceleration

respect to acceleration due to gravity. The seismic response of structures depends upon their modal frequencies as well as the frequency content of the earthquake. Numerical methods like Newton Raphson method and Runge Kutta method are used on MATLAB platform. For ease of interpretation of the dynamic response predicted later, the fast Fourier transform (FFT) plot of the same ground acceleration as well as the rate of ground acceleration is presented in Fig. 2c, d.

Similar characteristics of the Loma Prieta earthquake are shown in Fig. 3a, b, c, d respectively. The peak ground acceleration (PGA) of the El Centro and the Loma Prieta earthquakes are 0.319 and 0.529 g respectively. Here, g represents the acceleration due to gravity. It can be observed that the dominant frequency ranges for the El Centro and the Loma Prieta seismic accelerations are identified as 5–45 and 4–25 rad/s respectively. The corresponding frequency ranges for of the dominant rate of seismic accelerations are 13–42 and 17–52 rad/s².

Initial conditions are deduced from the assumption that the system is in static equilibrium with the sustained vertical nodal forces in the form of self-weight of the nodal masses. The predicted response presented later involves total elasto-configurational, configurational and elastic displacements (z_i , z_{ic} and z_{ie}) from the equilibrium configuration. Thus,

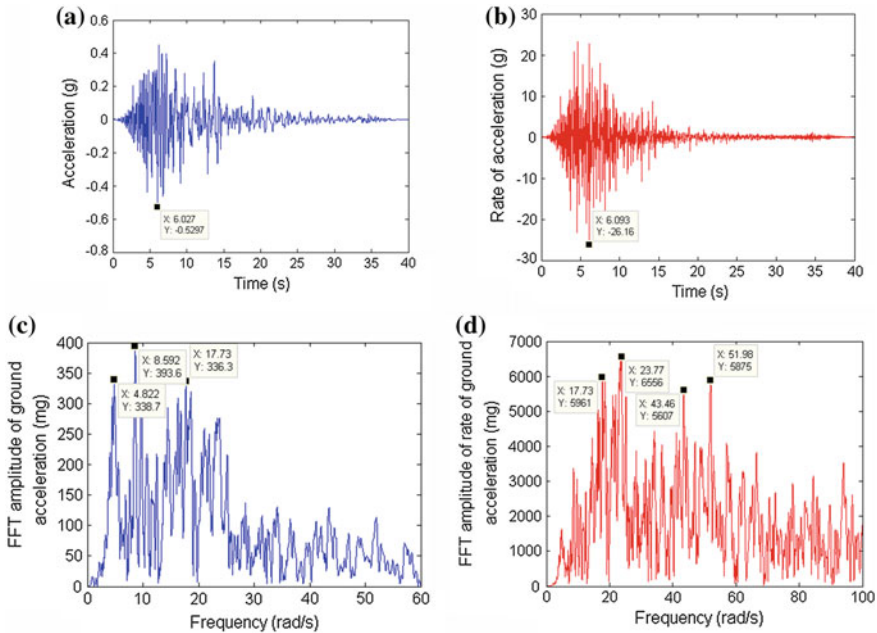


Fig. 3 **a** Loma prieta ground acceleration, **b** time rate of Loma Prieta ground acceleration, **c** FFT of Loma Prieta ground acceleration, **d** FFT of Loma Prieta rate of ground acceleration

$$z_i(t) = y_i(t) - y_i(0) \quad z_{ic}(t) = x_i(t) - x_i(0) \quad z_{ie}(t) = u_i(t) - u_i(0) \quad (10)$$

Here, initial values $y_i(0)$, $x_i(0)$ and $u_i(0)$ correspond to the equilibrium state are tabulated above.

4 Predicted Seismic Response: El Centro Earthquake

The predicted seismic behavior of the cable system to El Centro ground acceleration is presented below: The dynamic response of the cable structure is investigated for horizontal excitation, vertical excitation and combination of both horizontal and vertical excitations. Under horizontal ground motion, the seismic responses are similar for all (z_1 , z_2 , z_3 and z_4) degrees of freedom. For space constraints, only z_2 -response is presented here.

The peak elasto- configurational z_2 -response at time 2.038 s for horizontal ground motion plotted in the Fig. 4a comes out to be 0.2255 m. Also, at the same instant, the peak elastic response is 0.0310 m, while the peak configurational response is 0.1945 m. Obviously, the total nodal elasto- configurational response is mainly due to configurational nodal displacements. Figure 4b shows that the configurational and

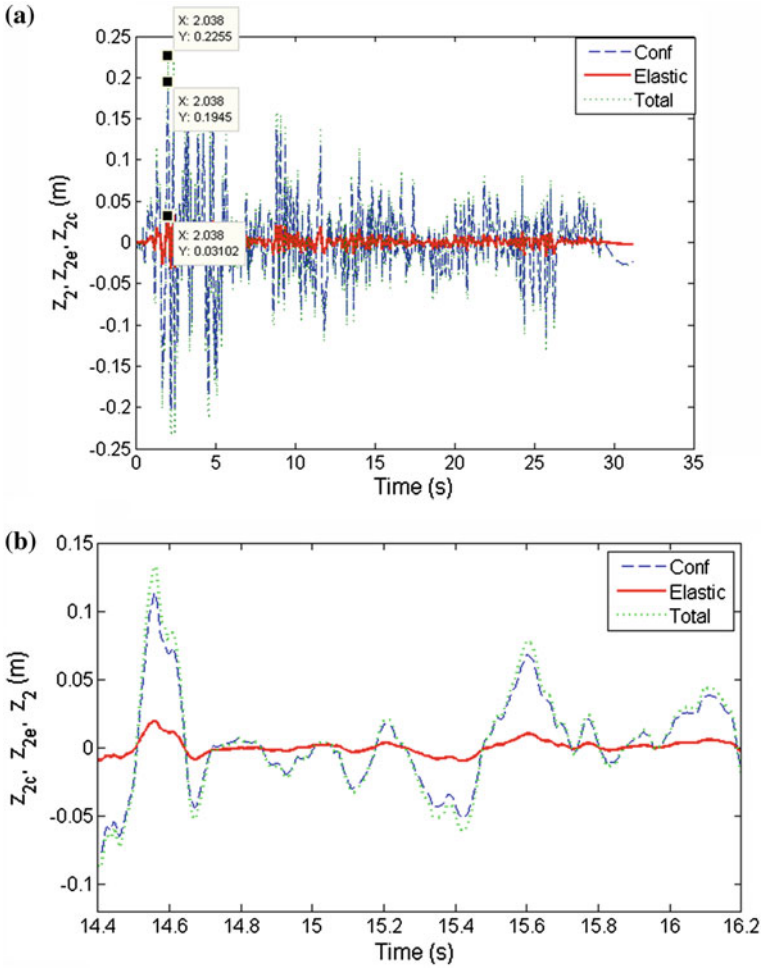


Fig. 4 **a** Typical z_2 -response for horizontal ground acceleration, **b** magnified z_2 -response for horizontal ground acceleration

elastic response waveforms are in phase. The peak elasto- configurational z_2 -response (0.0975 m) at time 2.443 s for vertical ground motion shown in the Fig. 5a is mainly-elastic. The peak configurational response at same instant is almost negligible (-4.493×10^{-7} m). Due to very small configurational response in vertical ground excitation as shown in Fig. 5b, the phase sense of elastic and configurational response is not clear.

In the dynamic response for combined horizontal and vertical ground motion as shown in Fig. 6a, the configurational and elastic components of the peak total nodal response are of the same order. The peak z_2 -elasto-configurational response (0.1475 m) at time 2.038 s is the summation of configurational response (0.2305 m)

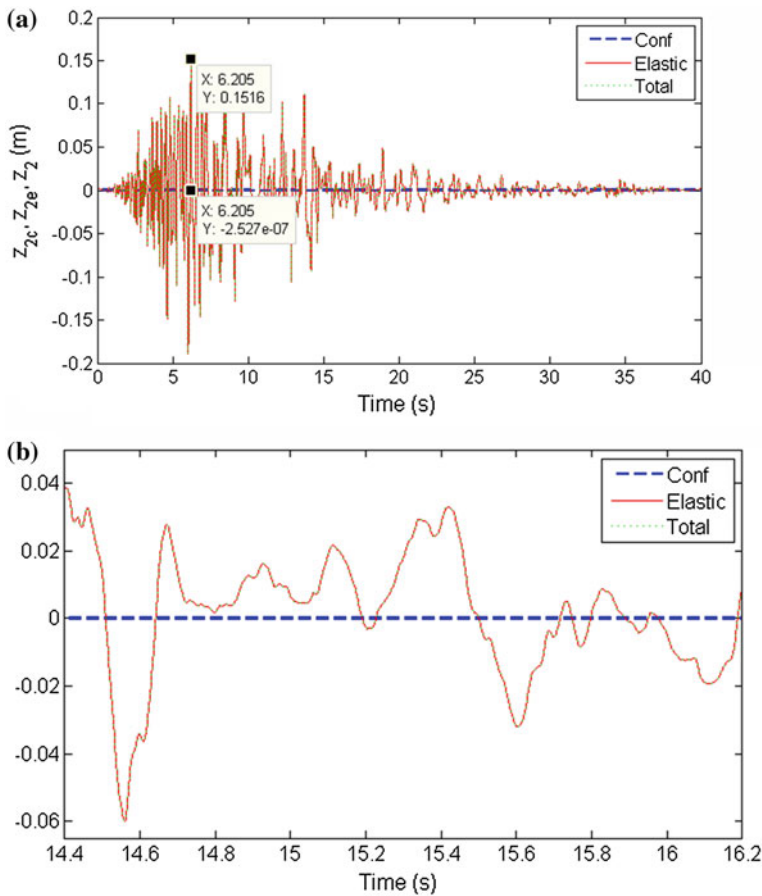


Fig. 5 **a** Typical z_2 -response for vertical ground acceleration, **b** magnified z_2 -response for vertical ground acceleration

and elastic response (-0.0830 m). The configurational and elastic z_2 -responses are out of phase as shown in Fig. 6b. It has been verified, though not presented here, both the configurational and elastic responses are in phase for other degrees of freedom.

The FFT plots of the seismic response to horizontal, vertical and combined ground motion are shown in Fig. 7a, b, c respectively. The dominant frequencies for seismic response are 0.9896, 7.367 and 13.59 rad/s for horizontal ground motion, 2.34, 7.367 and 13.59 rad/s for vertical ground motion and 0.9896, 2.34, 7.367 and 13.59 rad/s for combined ground motion. To recapitulate, the dominant frequencies of the applied El Centro ground motion are 7.367, 13.59 and 24.08 rad/s and the linear modal frequencies of the system are 1.07, 2.38, 9.16 and 16.17 rad/s. It can be observed that the higher two response frequencies (7.367 and 13.59 rad/s)

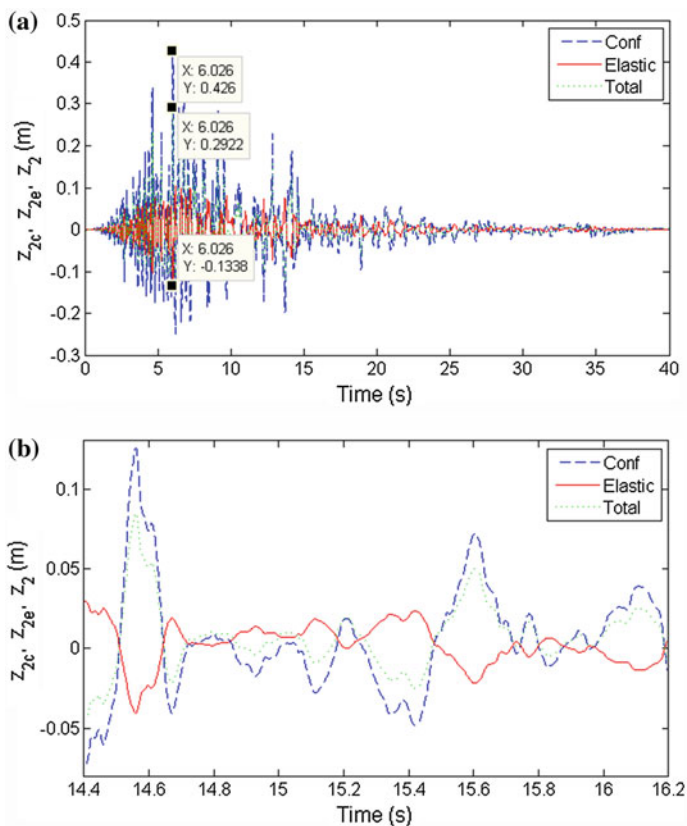


Fig. 6 **a** Typical z_2 -response for combined ground acceleration, **b** magnified z_2 -response for combined ground acceleration

coincide with the dominant frequencies of the ground motion, while the lower two response frequencies (0.9896 and 2.34 rad/s) coincide with the lower two modal frequencies of the system.

Due to symmetry of the structure and loading, the tensile forces T_1 and T_3 in cable segments AB and CD show same pattern of temporal variation. The change in the tensions due to ground excitation is plotted for all three cases, viz., horizontal, vertical and combination of both horizontal and vertical ground motion. Figure 8a shows that, in the antisymmetric vibration mode due to the horizontal excitation alone, the maximum change introduced in the tensile forces T_1 and T_3 is much more than that in the tensile force T_2 in segment BC. In contrast, the symmetric mode vibration caused by the vertical excitation is associated with very high change in tensile force T_2 relative to both T_1 and T_3 as shown in Fig. 8b. Thus, under combined horizontal-vertical seismic excitation, the change in tension T_1 of segment AB is mainly due to horizontal ground motion, while in tension T_2 of segment BC is mainly due to vertical ground motion. The magnitude of change of tension T_1

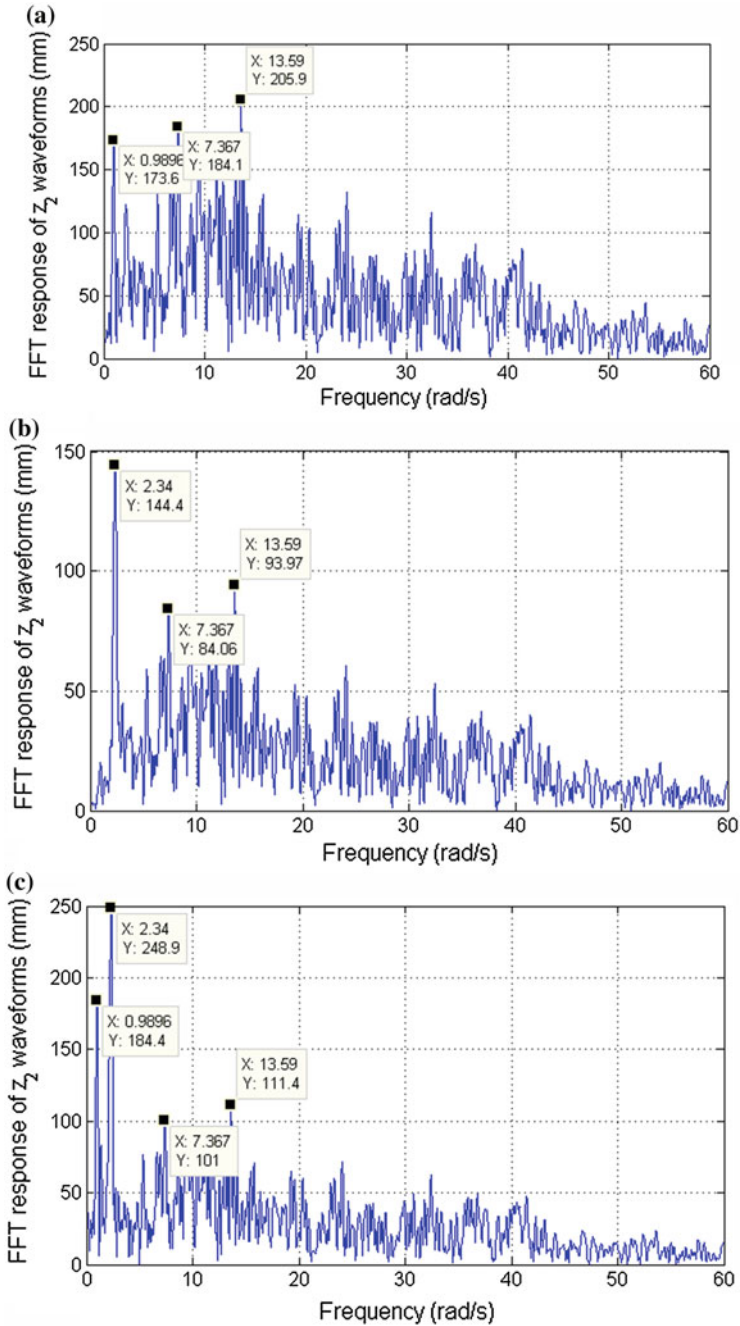


Fig. 7 a FFT response for z_2 -response for horizontal ground acceleration, b FFT response for z_2 -response for vertical ground acceleration, c FFT for z_2 -response for combined ground acceleration

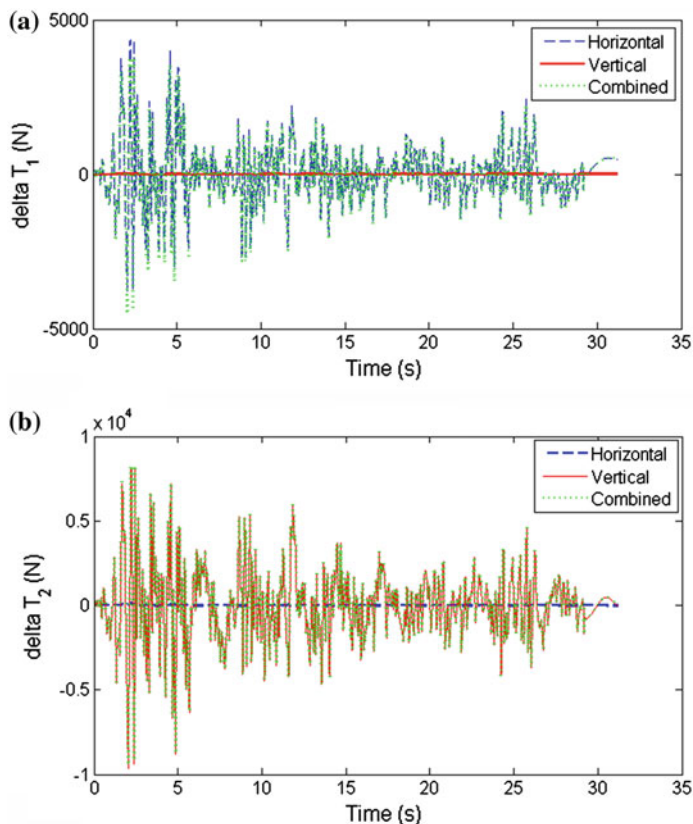


Fig. 8 **a** ΔT_1 plot for all three cases of ground motion, **b** ΔT_2 plot for all three cases of ground motion

in segment AB is about 4 kN, while the change in tension T_2 in segment BC is about 8 kN. It is interesting to note that the higher total peak response (0.2255 m) due to horizontal ground motion introduces lesser maximum change in the tensile forces than the lower total peak response (0.0975 m) due to vertical ground motion. However, the elastic components, 0.0310 and 0.0975 m respectively, for the horizontal the vertical ground excitations are qualitatively consistent with the magnitudes of the predicted corresponding maximum changes in the tensile forces.

5 Predicted Seismic Response: Loma Prieta Earthquake

The z_2 -response as shown in Fig. 9a has peak elasto-configurational response of 0.3754 m at time 6.026 s to horizontal excitation. The configurational and elastic responses are 0.3206 and 0.0548 m respectively. Figure 9b shows the configurational

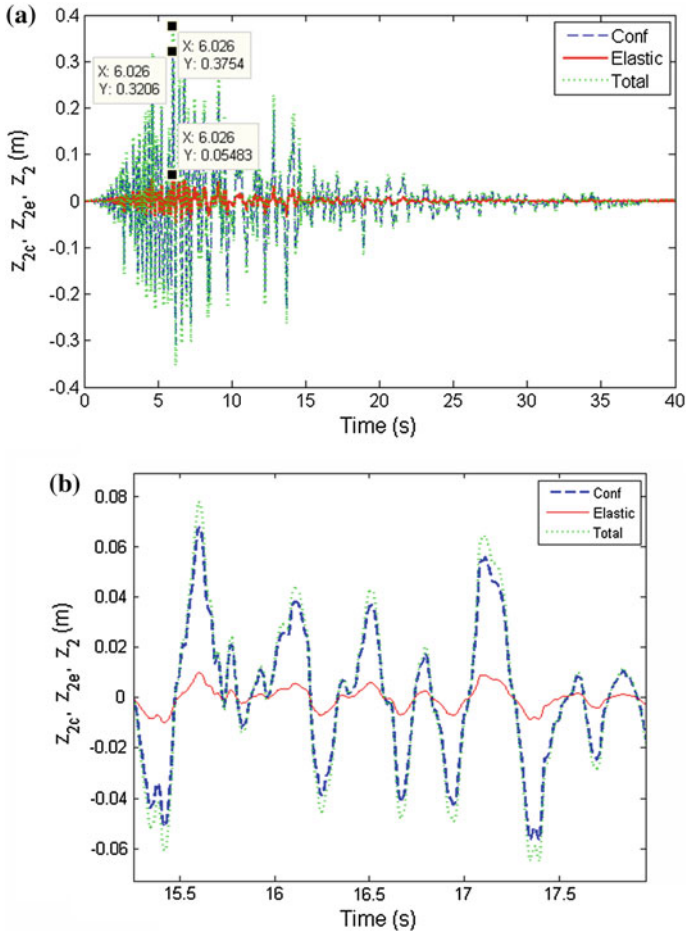


Fig. 9 **a** Typical z_2 -response for horizontal ground acceleration, **b** magnified z_2 -response for horizontal ground acceleration

and elastic responses to be in phase. The configurational and elastic responses at time 6.205 s shown in Fig. 10a to vertical ground acceleration respectively are -2.527×10^{-7} and 0.1516 m. The magnified view presented in Fig. 10b show these responses to be out of phase. Figure 11a depicts the relative magnitudes of elastic and configurational z_2 -response waveform at time 6.026 s to simultaneously acting horizontal and vertical excitations. The peak configurational, elastic and elasto- configurational responses respectively are 0.4260, -0.1338 and 0.2922 m. Figure 11b shows the elastic and configurational responses to be out of phase. A comparison of FFT plots shows similar characteristics of the response of typical nodal displacements in all three cases of horizontal, vertical and combined action of ground acceleration are shown in Fig. 12a, b, c respectively. It can be observed that, like in the case of El

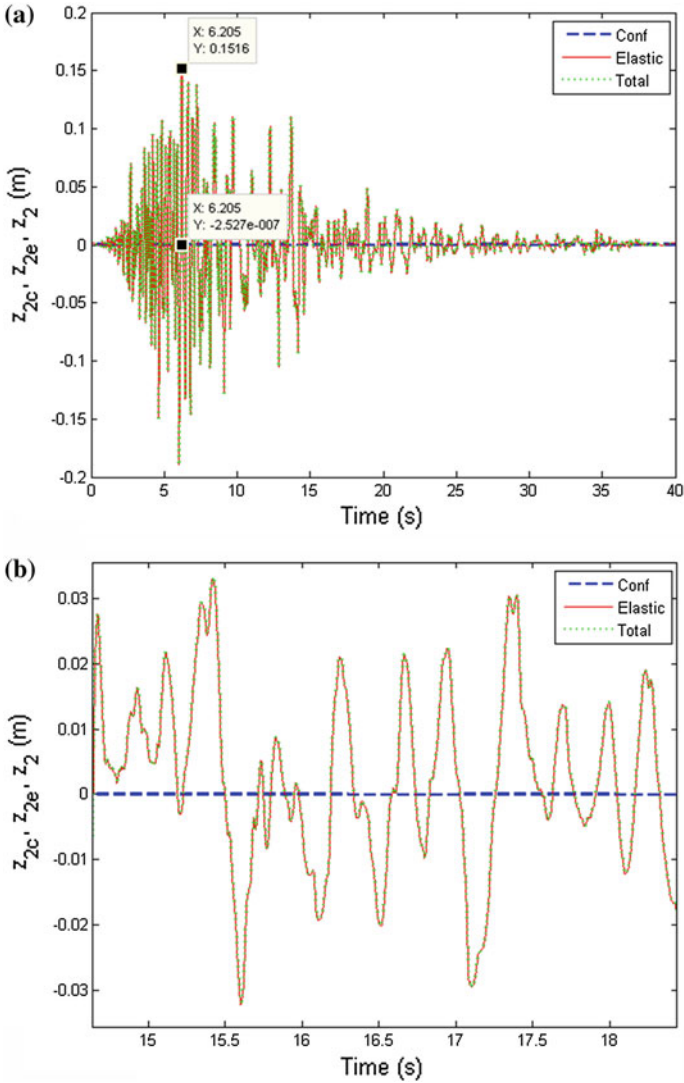


Fig. 10 **a** Typical z_2 -response for vertical ground acceleration, **b** magnified z_2 -response for vertical ground acceleration

Centro earthquake, the frequency content of these responses contains the dominant frequencies as in the corresponding ground excitations apart from the linear modal frequencies of the structure.

Change in tension T_1 of segment AB and tension T_2 of segment BC is shown in Fig. 13a, b respectively for three different situation of horizontal, vertical and combined action of ground acceleration. The change in tension T_1 of segment AB

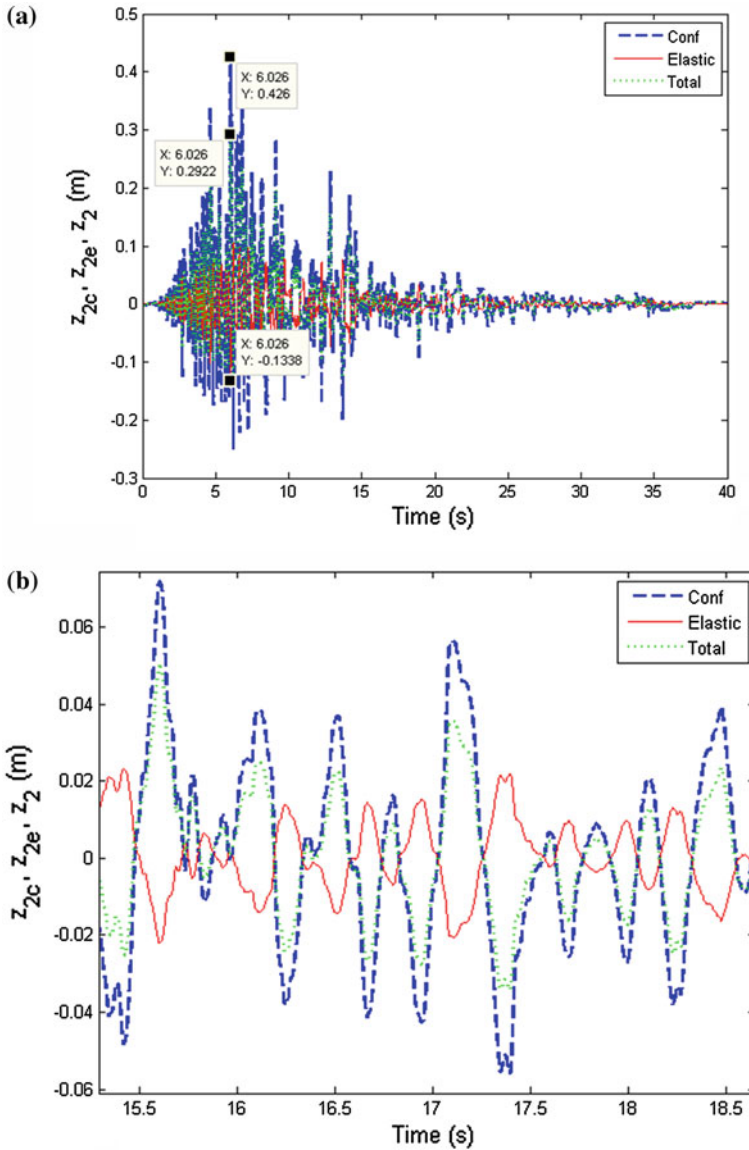


Fig. 11 **a** Typical z_2 -response for combined ground acceleration, **b** magnified z_2 -response for combined ground acceleration

results only due to horizontal action of ground acceleration while the change in tension T_2 of segment BC is only due to vertical ground acceleration. An interesting point is that, change (5.425 kN) in tension T_1 due to combined excitation is only marginally less than change (6.742 kN) due to horizontal excitation alone.

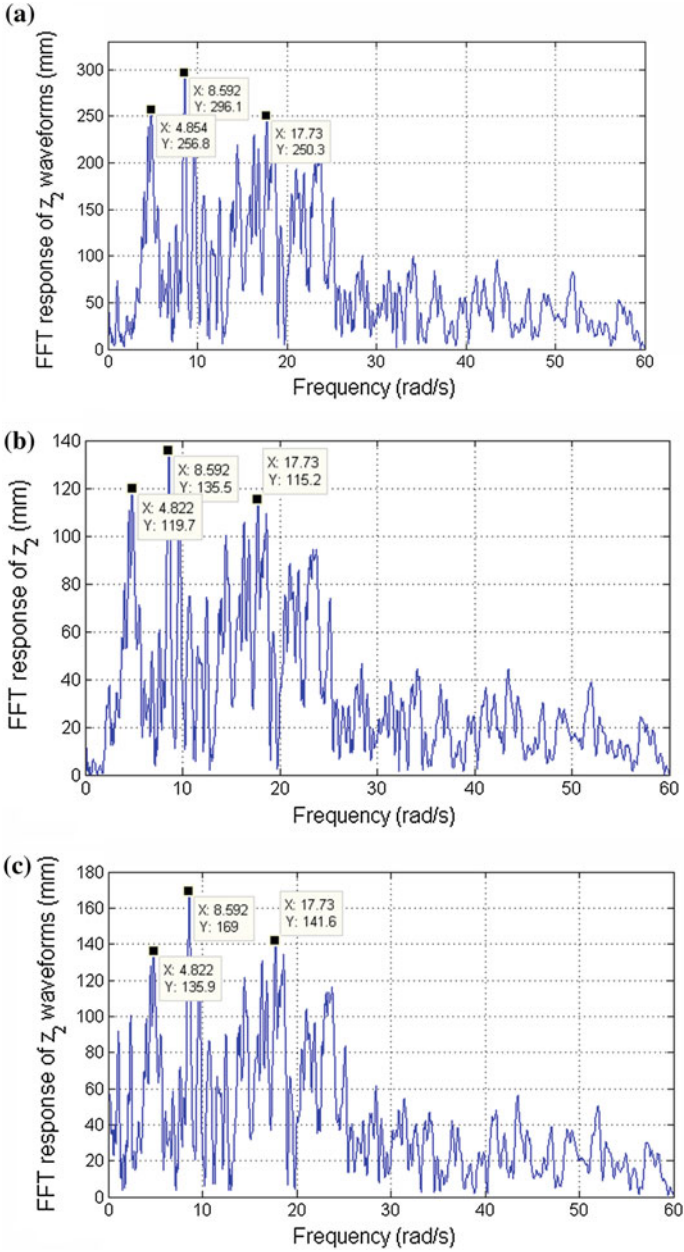


Fig. 12 **a** FFT for z_2 -response for horizontal ground acceleration, **b** FFT for z_2 -response for vertical ground acceleration, **c** FFT for z_2 -response for combined ground acceleration

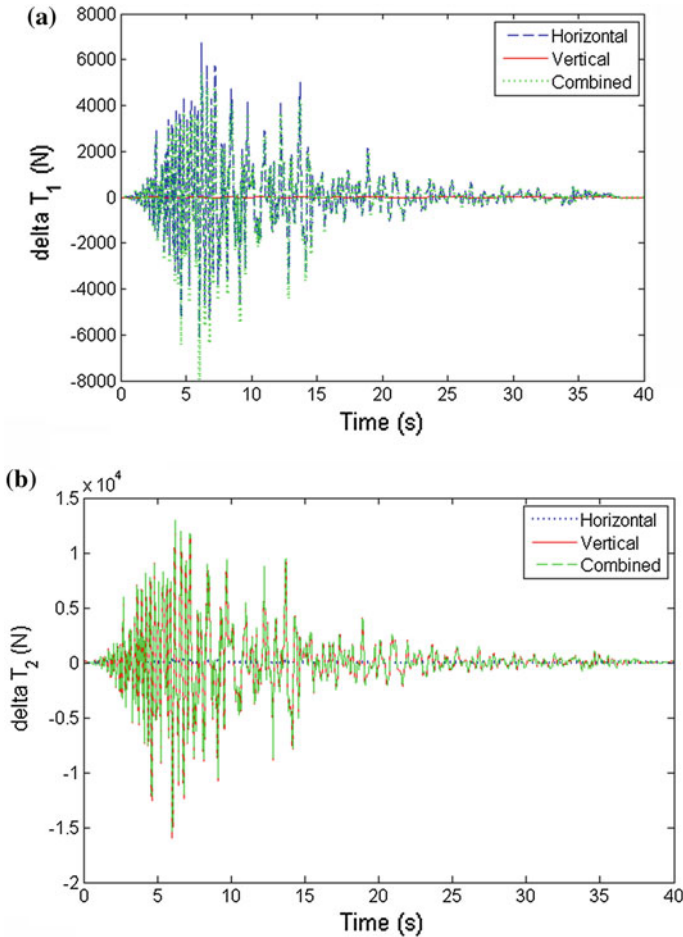


Fig. 13 a ΔT_1 plot for all three cases of ground motion, b ΔT_2 plot for all three cases of ground motion

Similarly, the main contribution (12.77 kN) to the change (13.02 kN) in T_2 due to combined excitation is by the vertical excitation.

To recapitulate, the PGA of Loma Prieta earthquake (0.529 g) is considerably higher than the El Centro earthquake (0.319 g). Despite this fact, it can be observed that the seismic responses of the structure to these earthquakes are qualitatively similar. However, the peak nodal displacements (0.2255, 0.0975 and 0.1475 m) to horizontal, vertical and combined El Centro ground excitations respectively are considerably lower than those (0.3754, 0.1516 and 0.4260 m) for the Loma Prieta ground excitation. Similarly, the changes (4 and 8 kN) in tensile forces in the inclined and horizontal segments due to El Centro earthquake are smaller than those (5.42 and 13.02 kN) for Loma Prieta earthquake.

6 Discussion

It has also been established by the Authors that the eigenvector corresponding to the sole non-zero eigenvalue of the symmetric singular tangent configurational matrix D_{ij} represents the sole mode of vibration of the inextensible cables. Apart from the other eigenvectors, this antisymmetric eigenvector is also orthogonal to the loading rate vector collinear with the instantaneous resistive nodal force vector P_i . This latter proportionate loading vector approximately corresponds to the symmetric elastic mode of displacements and vibrations of the elasto-flexible cables. The antisymmetric mode generally has the lowest modal frequency and corresponds to the configurational vibration mode. On the other hand, the symmetric mode with higher modal frequency corresponds to the elastic vibration mode of elasto-flexible cables. For small vibration amplitudes, these linear modal frequencies and the corresponding mode shapes can be considered to depend upon the sustained load vector F_0 in place of the instantaneous internal resistive nodal force vector P_i [6].

A closer look at the sustained load vector F_0 and the applied horizontal and vertical seismic force vectors, E_h and E_v , reveals that the vertical seismic force vector remains parallel to the sustained load vector. Since the relative magnitudes of the applied nodal forces remain unaltered for the duration of the earthquakes, the vertical seismic force vector represents the proportionate load vector. In contrast, the horizontal seismic force vector can be observed to remain orthogonal to the sustained load vector. Thus, under horizontal seismic forces, the cable vibrates in the antisymmetric mode, while it vibrates in the symmetric mode under vertical seismic forces. In view of the above discussion, horizontal and vertical seismic forces are expected to elicit respectively predominantly configurational and elastic responses from the elasto-flexible cable structures. Such indeed happens to be the case. As discussed in the preceding section, the elastic component of the total horizontal seismic response and the configurational component of the vertical seismic response indeed are vanishingly small.

It is generally assumed that the dynamic response of the structures under multi-directional seismic forces can be obtained just by adding the responses to seismic excitations in different directions. This assumption is not justified in the presence of cross effects associated with mode-coupling [7]. Such cross effects are observed to play a significant role in the seismic response of cable structures investigated here. As discussed above, the mainly-configurational modal displacements caused by horizontal excitation are out of phase with the mainly-elastic modal displacements associated with the vertical excitation. Thus, the peak nodal displacement response under simultaneous horizontal and vertical excitations is different from those caused by the excitations acting separately. Even the principle of superposition is not valid. The same holds true for the maximum magnitudes of the tensile forces in the cable segments.

The seismic response of the conventional elastic structures is represented in terms of the peak nodal elastic displacements. This is because of the fact that the higher nodal displacements of such structures imply higher internal elastic forces introduced by seismic forces. However, it is established by the Authors [6] that such

a direct relation between the nodal displacements and internal forces does not hold for these elasto-flexible structures. Only the elastic component of the total elasto-configurational nodal displacements determines the tensile forces in the cable segments. However, for the same elastic nodal displacements, these tensile forces depend upon the current configuration which is characterized by the configurational nodal displacements from the reference configuration.

No attempt has been made for empirical validation of the seismic response predictions presented in this Paper. However, these theoretical predictions are compared with those of other investigators' predictions for the seismic response of a similar structure. Recently, Thai and Kim have determined the dynamic response of a cable net to horizontal components of El Centro and Loma Prieta earthquakes [10]. Here, a part of this essentially spatial cable net is idealized as a planer cable, but all the other structural and loading details are kept same. The only exception is that a part of the self-weight of the cable is lumped at the nodes. The nodal coordinates of the elasto-flexible cable in its passive state are predicted to be same. The predicted in-plane horizontal and vertical nodal displacements (-0.069 and 0.708 m) are considerably higher than those (-0.040 and 0.446 m) predicted by Thai and Kim. Similarly, the predicted tensile forces (54.90 and 57.71 kN) in the horizontal and inclined segments far exceed those (24.283 and 23.687 kN) estimated by these investigators.

The vertical nodal peak displacements to horizontal components of El Centro and Loma Prieta earthquakes predicted in this Paper respectively are 0.2255 and 0.3754 m. The corresponding predictions of these investigators respectively are estimated from figures are 0.196 and 0.186 m. The dominant response frequencies in the later parts of the waveforms for both the seismic excitations as estimated from these figures are about 2.38 rad/s. It is surmised here that dominant frequencies of the initial and later parts of the seismic response equal respectively the dominant seismic forcing frequencies and lowest modal frequencies of the structure. To recapitulate, the lowest linear modal frequencies of the cable under sustained loads are 1.07 and 2.38 rad/s. It can be observed that the second lowest frequency predicted here is quite close to those predicted by these investigators. Thus, the static response predicted here differs considerably from that predicted by these investigators. This could be due to the assumed planer cable idealization of the essentially spatial cable net. Despite this fact, the predicted seismic response is similar, though quantitatively different, in both the investigations. It should be noted that the seismic response of cable structures predicted in this Paper is based on entirely new constitutive equations and equations of motion proposed earlier by the Authors.

7 Conclusions

Using the Authors' rate- type constitutive equations and third order differential equations of motion, the response of weightless sagging planer cables to El Centro and Loma Prieta earthquakes is investigated in this Paper. Vertical ground

acceleration is obtained by reducing the horizontal ground acceleration to its two-thirds value. In addition to the ground accelerations, their time rate of variation required as per the theoretical formulation in the equations of motion is also computed.

In both the earthquakes, the horizontal excitation is predicted to excite the antisymmetric mainly-configurational vibration mode and introduce the tensile forces in the side inclined segments of the cable. In contrast, mainly-elastic symmetric mode and the tensile forces in the central horizontal segment are associated with the vertical excitation component. Due to strong mode coupling, in some cases, the nodal displacements as well as tensile forces due to simultaneous horizontal and vertical excitations are lesser than those caused by the separately acting horizontal and vertical excitations. However, planer cable idealization of essentially spatial cable nets attempted here turned out to be unsatisfactory for predicting their seismic response. Even though, the qualitatively similar response predictions using an entirely different formulation based upon rate-type constitutive equations and third order differential equations of motion confirm basic soundness of the Authors' proposed vibration theory of elasto-flexible cables.

References

1. Abad MSA, Shooshtari A, Esmaeili V, Riabi AN (2013) Nonlinear analysis of cable structures under general loadings. *Finite Elem Anal Des* 73:11–19
2. Irvine HM, Caughey TK (1974) The linear theory of free vibrations of a suspended cable. *Math Phys Sci* 341(1626):299–315
3. Impollonia N, Ricciardi G, Saitta F (2011) Vibrations of inclined cables under skew wind. *Int J Nonlinear Mech* 46:907–918
4. Johnson E, Baker GA, Spencer B, Fujino Y (2007) Semiactive damping of stay cables. *J Eng Mech ASCE* 133(1):1–11
5. Kamel MM, Hamed YS (2010) Nonlinear analysis of an elastic cable under harmonic excitation. *Acta Mech Springer-Verlag* 214:135–325
6. Kumar P, Ganguli A, Benipal G (2014) Theory of weightless sagging elasto-flexible cables. *J Eng Mech*
7. Lee GC, Liang Z (1998) On cross effects of seismic response of structures. *Eng Struct* 20(4–6): 503–509
8. Santos HAFA, Paulo CIA (2011) On a pure complementary energy principle and a force-based finite element formulation for non-linear elastic cable. *Int J Non-Linear Mech* 46:395–406
9. Thai HT, Kim SE (2008) Second-order inelastic dynamic analysis of three-dimensional cable-stayed bridges. *Steel Struct* 8:205–214
10. Thai HT, Kim SE (2011) Nonlinear static and dynamic analysis of cable structures. *Finite Elem Anal Des* 47:237–246
11. Volokh KY, Vilnay O, Averbuh I (2003) Dynamics of cable structures. *J Eng Mech* 129 (2):175–180

Damage Detection in Beams Using Frequency Response Function Curvatures Near Resonating Frequencies

Subhajit Mondal, Bidyut Mondal, Anila Bhutia
and Sushanta Chakraborty

Abstract Structural damage detection from measured vibration responses has gain popularity among the research community for a long time. Damage is identified in structures as reduction of stiffness and is determined from its sensitivity towards the changes in modal properties such as frequency, mode shape or damping values with respect to the corresponding undamaged state. Damage can also be detected directly from observed changes in frequency response function (FRF) or its derivatives and has become popular in recent time. A damage detection algorithm based on FRF curvature is presented here which can identify both the existence of damage as well as the location of damage very easily. The novelty of the present method is that the curvatures of FRF at frequencies other than natural frequencies are used for detecting damage. This paper tries to identify the most effective zone of frequency ranges to determine the FRF curvature for identifying damages. A numerical example has been presented involving a beam in simply supported boundary condition to prove the concept. The effect of random noise on the damage detection using the present algorithm has been verified.

Keywords Structural damage detection · Frequency response function curvature · Finite element analysis

1 Introduction

Damage detection, condition assessment and health monitoring of structures and machines are always a concern to the engineers. For a long time, engineers have tried to devise methodology through which damage or deterioration of structures can be detected at an earliest possible stage so that necessary repair and retrofitting

S. Mondal · B. Mondal · A. Bhutia · S. Chakraborty (✉)
Department of Civil Engineering, Indian Institute of Technology Kharagpur,
Kharagpur, India
e-mail: sushanta@civil.iitkgp.ernet.in

© Springer India 2015
V. Matsagar (ed.), *Advances in Structural Engineering*,
DOI 10.1007/978-81-322-2193-7_119

1563

can be carried out. Recently, due to the rapid expansion of infrastructural facilities as well as deterioration of the already existing infrastructures, the magnitude of the problem has become enormous to the civil engineering community. Detection of damages using various local and global approaches has been explored in current literature. The measured dynamical properties have been used effectively for detecting damages. The dynamical responses of structures can be very precisely measured using modern hardware and a large amount of data can be stored for further post processing to subsequently detect damages. The damage detection problem can be classified as identification or detection of damage, location of damage, severity of damage and at the last-estimation of the remaining service life of a structure and its possible ultimate failure modes. During the last three decades significant research has been conducted on damage detection using modal properties (frequencies, mode shapes and damping etc.). The mostly referred paper on damage detection using dynamical responses is due to Deobling et al. [1] which give a vivid account of all the methodologies of structural damage detection using vibration signature until 90 s. Damage detection using changes in frequency has been surveyed by Salawu and Williums [2]. The main drawback of detecting damages using only frequency information is the lack of sensitivity for the small damage cases. The main advantage of this method is that, frequency being a global quantity it can be measured by placing the response sensor such as an accelerometer at any position. Mode shapes can also be effectively used along with frequency information to locate damage [3, 4], but the major drawback is that mode shape is susceptible to the environment noise much more than the frequency. Moreover, mode shapes being a normalized quantity is less sensitive to the localized changes in stiffness. The random noise can be averaged out to some extent but systematic noise cannot be fully eliminated. Furthermore, in vibration based damage detection methodologies, depending upon the location the damage may or may not be detected if it falls on the node point of that particular mode. Lower modes sometimes remain less sensitive to localized damages and measurement of higher modes are almost always necessary which is more difficult in practice.

In contrast with frequency and mode shape based damage detection, methodologies using mode shape curvature, arising from the second order differentiation of the measured displacement mode shape is considered more effective for detecting cracks in beams [5]. Wahab and Roeck [6] showed that damage detection using modal curvature is more accurate in lower mode than the higher mode. Whalen [7] also used higher order mode shape derivatives for damage detection and showed that damage produce global changes in the mode shapes, rendering them less effective at locating local damages. Curvature mode shapes also have a noticeable drawback of susceptibility to noise, caused by these second order differentiation of mode shapes. This differentiation process may amplify lower level of noise to such an extent to produce noise-dominated curvature mode shapes [8] with obscured damage signature. Most recently, Cao et al. [9] identified multiple damages of beams using a robust curvature mode shape based methodology.

In recent years, many methods of damage detection based on changes in dynamical properties have been developed and implemented for various

complicated structural forms. Wavelet transformation is one of the recent popular techniques for damage detection in local level, although its performance to detect small cracks is questioned [10, 11].

A structure vibrates on its own during resonance at high amplitude and therefore the FRFs become very sensitive to noise. Ratcliffe [12] explored the frequency response function sensitivities at all frequencies rather than at just the resonant frequencies to define a suitable damage index which can be used in a robust manner in presence of inevitable experimental noise. Sampaio et al. [13] have given an account of the frequency response function curvature methods for damage detection. Pai and Young [14] detected small damages in beams employing the operational deflected shapes (ODS) using a boundary effect detection method. Scanning laser vibrometer was used for measuring the mode shapes. Bhutia [15] and Mondal [16] have also investigated damage detection using operational deflected shapes and using FRFs at frequencies other than natural frequencies respectively.

Therefore, it appears that at frequencies slightly away from the natural frequency (either above or below), it may be somewhat less affected by measurement noise. But, it is to be also remembered that the sensitivity of FRFs to damage will also fall down at the frequencies other than the natural frequencies. Hence, the FRFs at frequencies other than natural frequencies, although less noise prone is less sensitive to damage as well. With all probability, there might exist an optimum location in FRF curve nearer to the resonant peaks where the measured FRFs still have enough sensitivity towards damage yet have substantial less sensitivity to noise. It must also be noted that most of the existing damage detection algorithm works well when the damage is severe, because the level of stiffness changes will be substantial for such damages and will be easily detectable. Such damages can be detected easily by other means such as direct visual observations. The real challenge in the research field of structural damage detection is to test the damage indicator's sensitivity for small damages in presence of inevitable measurement noise. Most algorithms are observed to give spurious indications of damage when the noise level becomes somewhat higher.

In this paper FRF curvature is used at frequencies different than the natural frequencies to detect damage. Thus the fundamental principle behind this damage detection methodology is to exploit the relative gain in terms of lower noise sensitivity, sacrificing a bit in terms of resonant response magnitude. Although the concept appears to be attractive, the current literature does not provide enough guidance in this regard. The present paper tries to explore the same through an example beam in simply supported condition.

The present study concentrates on a forward problem of simulating damage scenarios, considering the FRF curvatures as the damage indicators to see if it performs better than the methods employing FRFs at natural frequencies. The key question is the robustness of the algorithm, i.e. whether the results obtained will remain unique in the presence of real experimental noise, especially under the condition of modal and coordinate sparsity. Finite element analysis using ABAQUS [17] has been used to generate the required vibration responses for this simulated study. Simulated noises into the data are added as a percentage of FRF magnitude.

2 Theoretical Background of the Present Methodology

The mass, stiffness and damping properties of a linear vibrating structure are related to the time varying applied force by the second order differential force equilibrium equations involving the displacement, velocity and acceleration of a structure. The corresponding homogenized equation can be written in discretized form-

$$[M]\{\ddot{x}(t)\} + [C]\{\dot{x}(t)\} + [K]\{x(t)\} = \{0\} \quad (1)$$

where $[M]$, $[K]$ and $[C]$ are the mass, stiffness and viscous damping matrices with constant coefficients and $\{\ddot{x}(t)\}$, $\{\dot{x}(t)\}$ and $\{x(t)\}$ are the acceleration, velocity and displacement vectors respectively as functions of time. The eigensolution of the undamped homogenized equation gives the natural frequencies and mode shapes.

If the damping is small, the form of FRF can be expressed by the following equation [18].

$$H_{jk}(\omega) = \frac{X_j}{F_k} = \sum_{r=1}^N \frac{rA_{jk}}{\lambda_r^2 - \omega^2} \quad (2)$$

Here, $H_{jk}(\omega)$ is the frequency response functions, rA_{jk} is the modal constant, λ_r is the natural frequency at mode r and ω is the frequency.

The individual terms of the Frequency Response Functions (FRF) are summed taking contribution from each mode [18]. At a particular natural frequency, one of the terms containing that particular frequency predominates and sum total of the others form a small residue. But for a FRF at frequency just slightly away from the natural frequency, the other terms also starts contributing somewhat significantly, thereby remaining sensitive to stiffness changes of the structure. For localizing the damage, FRF curvature method can more effectively be used than the FRFs themselves.

3 Numerical Investigation

In this current investigation a simply supported aluminum beam has been modeled using the C3D20R element (20 noded solid brick element). Eigensolutions have been found out using the Block Lanczos algorithm with appropriately converged mesh sizes for the modes under consideration. The material properties of beam are assumed to be $E = 70$ GPa and $\nu = 0.33$. Then, damage has been inflicted with a deep narrow cut of width 2.5 mm thick and 5 mm deep as shown in Fig. 1. The FRFs are computed at 21 evenly spaced locations as shown in Fig. 2.

Figure 3 shows the natural frequencies and the corresponding mode shapes of the 'undamaged' beam and damaged beam.

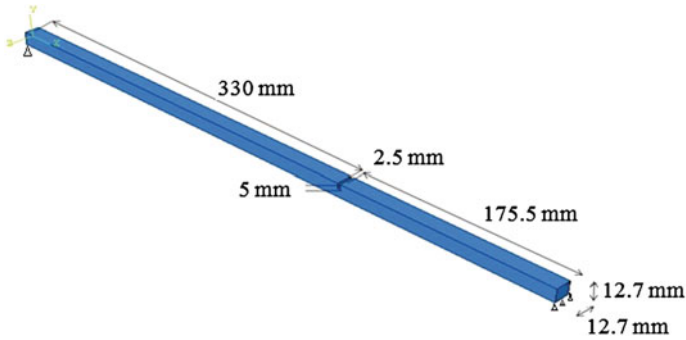


Fig. 1 Dimension and damage location of simply supported beam

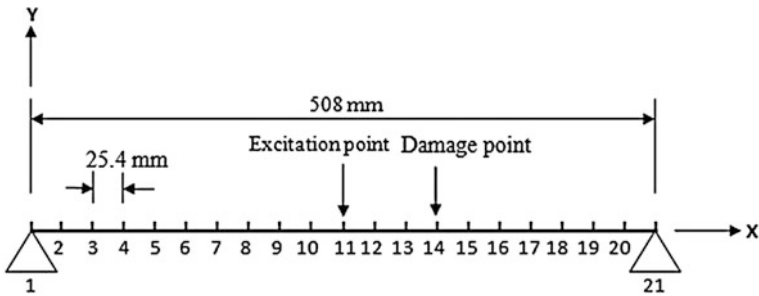


Fig. 2 Location of FRF measurement along the center line of beam

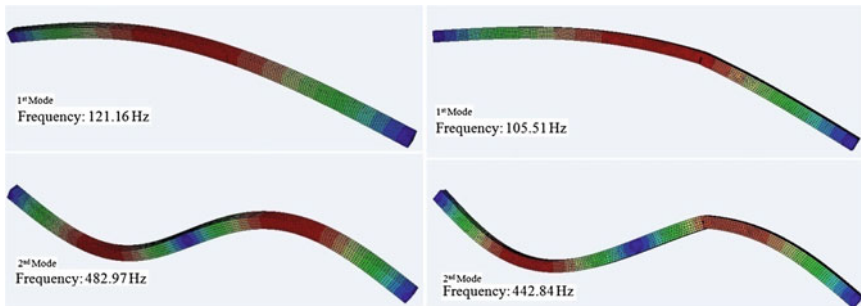


Fig. 3 Mode shape and frequency of undamaged and damaged beam

The FRFs of the undamaged and the damaged beam has been overlaid in Fig. 4. The difference is noticeable in some modes, indicating more damage sensitivity.

Curvature of FRFs, i.e. the rate of change of FRFs measured at twenty one locations and at different frequency (lies in between 90 and 110 % of the natural

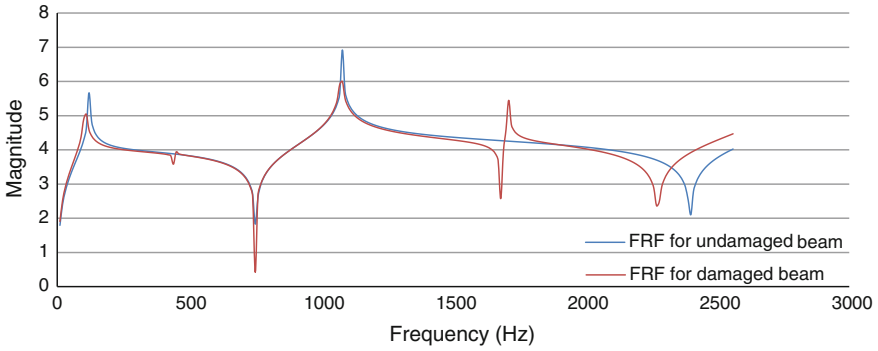


Fig. 4 Comparisons of point FRFs (point 11) of undamaged and damaged beam

frequencies) for undamaged and damage cases are determined. The procedure to compute the FRF curvature is a central difference scheme and is given below

$$H''_{ij}(\omega) = \frac{H_{(i+1)j}(\omega) - 2H_{ij}(\omega) + H_{(i-1)j}(\omega)}{(\Delta h)^2} \tag{3}$$

For example, as shown in the Fig. 5 FRF curvature was taken at 90, 95, and 98 % of 1st natural frequency for both the undamaged and damaged cases and this process was continued for twenty one different location of the beam. The difference was taken as absolute difference of the curvature. Since there is a frequency ‘shift’ due to damage, a mapping scheme has been adopted as shown. Many references just directly compare FRFs without accounting for such frequency shifts and may not truly represent the effect of FRF changes due to damage.

Figure 5 shows the absolute change in FRFs at different frequencies around the first natural frequency without considering the noise.

3.1 Damage Detection Using FRF Curvature Near the First Fundamental Mode

Figure 6 shows the FRF curvatures at various locations along the beam length for different values of frequencies away from the natural frequencies as a percentage of the resonant frequency. Thereafter, random noise is added to the FRFs and the same methodology is applied to determine the sensitivities. Figure 7a–f shows that as the noise level increases the FRF curvatures show pseudo peaks of much higher magnitudes to obscure the actual damages, however the effect is minimum around FRF curvature computed at 95 % of natural frequency.

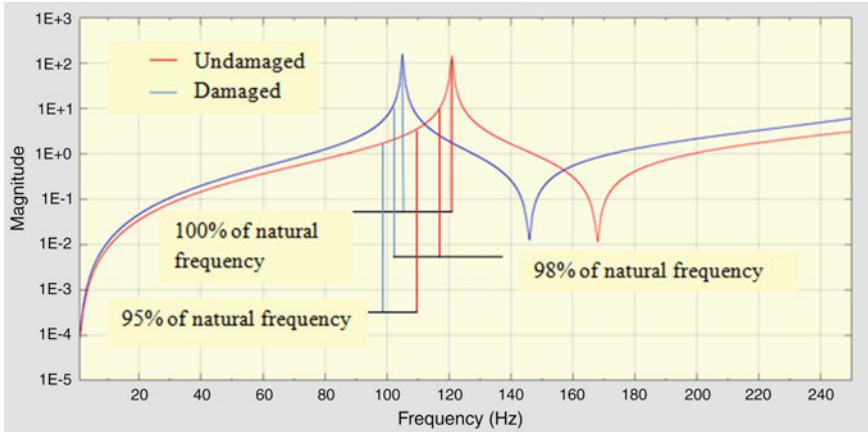


Fig. 5 Mapping of FRF for undamaged and damaged beam at different frequency

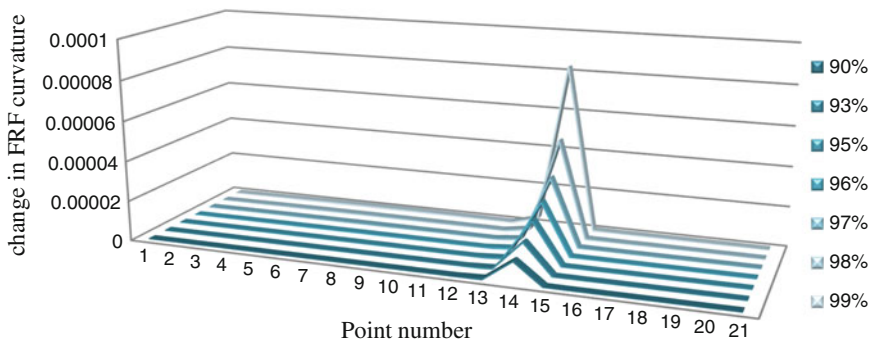


Fig. 6 FRF curvature beam without noise

Figure 7a shows the effect of noise on the damage localization using the FRF curvature at around 1st natural frequency. With 1 % noise, false peaks appear in addition to peak at 14th number point, so the localization sensitivity reduces. Addition of 2 % noise gives pseudo peaks at other points having much higher magnitudes which are however actually not damaged. Thus addition of noise has caused more and more false detection of damages as compared to the noise-free case. Addition of 3 % noise gives an even more unacceptable result with substantial increase in false detections apart from the actual damage at point 14.

Figure 7b which is the plot of FRF curvature at 98 % of 1st natural frequency shows similar kind of result with very little improvement towards the noise resistance. However when curvature differences at 96 and 95 % of 1st natural frequency are explored, they show substantial increase in resistance towards the added random noise as is evident from Fig. 7c, d. It can be easily observed that the small peaks are

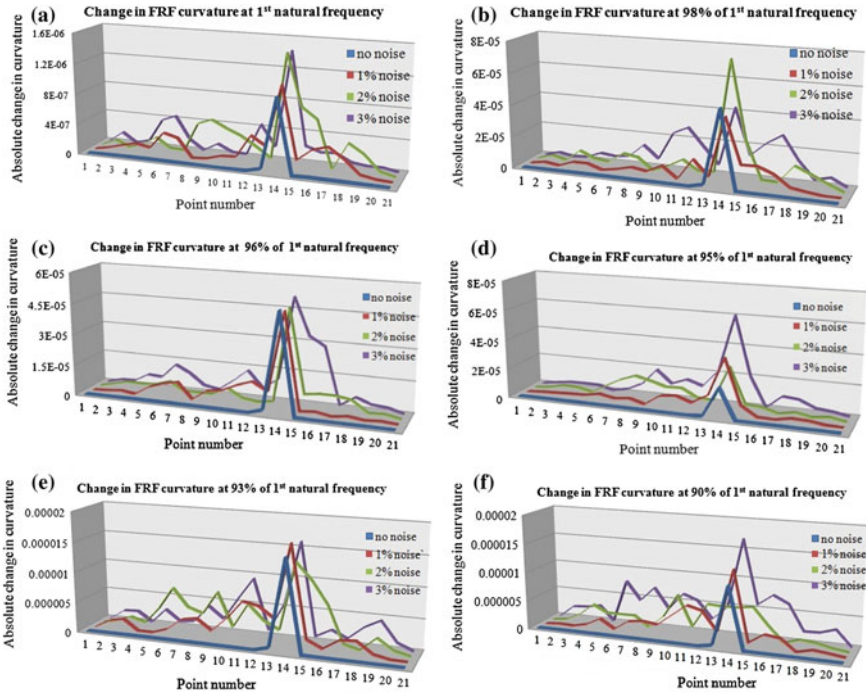


Fig. 7 Difference between curvatures of FRFs of undamaged and damaged (point 14) Simply supported beam for **a** 1st natural frequency **b** 98 %, **c** 96 %, **d** 95 %, **e** 93 % and **f** 90 % of 1st natural frequency for different percentage of noise. Input force at mid point

relatively suppressed, thereby locating the damage much more uniquely at the designated point number 14. Further downward movement along frequency scale however could not fetch any benefit and in fact shows reduction in damage detection capacity. At 93 and 90 % of 1st natural frequency false peaks again started to predominate. Hence, Curvature difference away from 1st natural frequency shows very distinct damage localization capability, even with substantial level of added random noise. The peaks at the actual damage location are distinct enough to pin-point the actual damage location. Overall damage identification capability in presence of noise increases as we move away from resonant peak of FRF and damage detection is most robust within certain range of frequency, very close to the natural frequency.

Similar phenomenon on other side of the FRF peak at natural frequency have been observed and are presented in Fig. 8.

From Fig. 9a–f it is clear that damage detection can be done better between 104 and 105 % of natural frequency in noisy environment than the usual practice of using FRFs at resonant frequency.

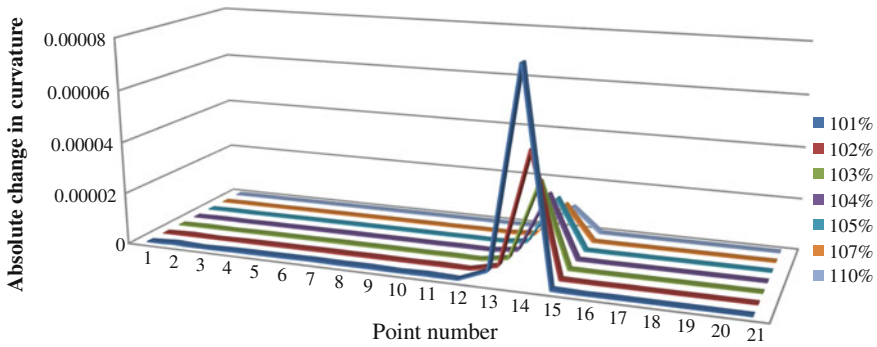


Fig. 8 Difference between curvatures of FRFs of undamaged and damaged (point 14) simply supported beam for different percentage (100–110 %) 1st natural frequency. Input force at mid point

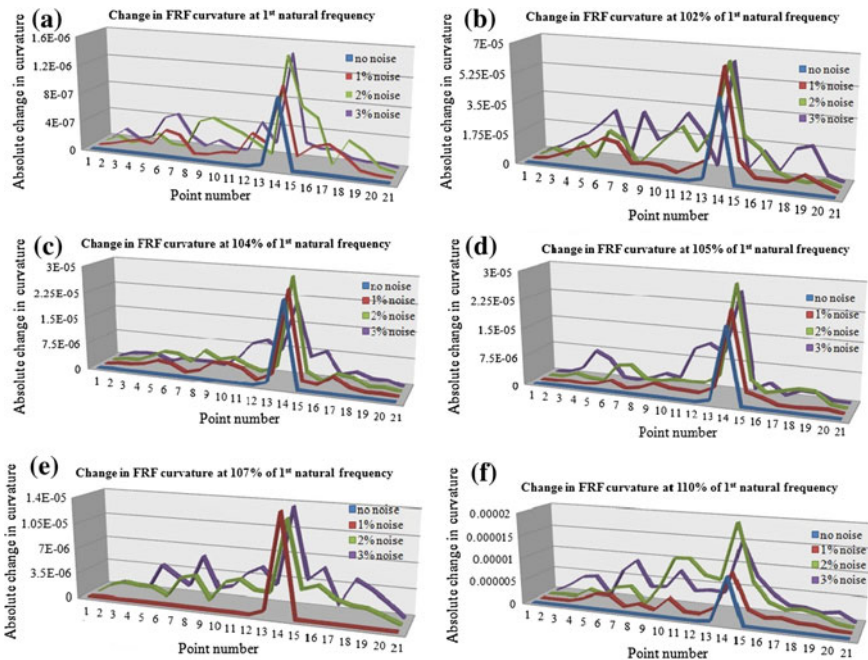


Fig. 9 Difference between curvatures of FRFs of undamaged and damaged (point 14) simply supported beam for **a** 1st natural frequency **b** 102 %, **c** 104 %, **d** 105 %, **e** 107 % and **f** 110 % of 1st natural frequency for different percentage of noise. Input force at mid point

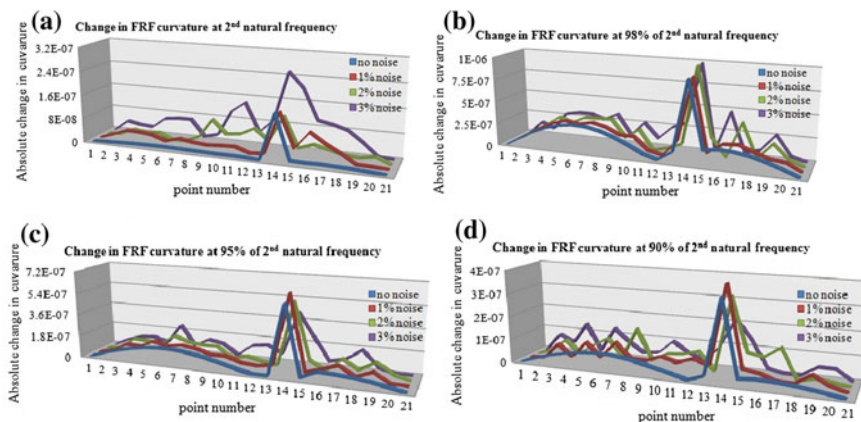


Fig. 10 Difference between curvatures of FRFs of undamaged and damaged (point 14) Simply supported beam for **a** 2nd natural frequency, **b** 98 %, **c** 95 % and **d** 90 % of 2nd natural frequency for different percentage of noise. Input force at mid point

3.2 Damage Detection Using FRF Curvature Near the Second Mode

The investigation is extended further to include the second mode also and similar results are obtained and are presented in Fig. 10. Most effective zone to detect damage is again found to be at 95–96 % of the resonant frequency (so also at 100–110 % of the second natural frequency) and is not presented here for brevity.

4 Conclusions

An attempt has been made to detect the location of damage in a simply supported aluminum beam using FRF curvatures at frequencies other than natural frequencies and is found to be more robust as compared to method using FRFs at resonant frequencies when random noise are present in data. Upto 2–3 % of random noise in observed FRF data are tried. An optimum frequency zone at around 95–96 % (or 105–106 %) of the natural frequency has been identified as ideal to locate damage as they maintain the required sensitivity for damage detection yet being slightly offset from the peak value. Keeping all the above observations, we can conclude that damage detection using FRF curvature at other than natural frequency may be a better option if considerable measurement noise is present into the data. The method needs to be further explored with appropriate model of noise actually present in real modal testing of structures in various boundary conditions.

References

1. Doebling SW, Farrar CR, Prime MB (1998) A summary review of vibration based damage identification methods. *Shock Vib Dig* 30(2):91–105
2. Salawu OS, Williams C (1994) Damage location using vibration mode shapes. In: *Proceedings of the SPIE, Proceedings of the 12th international modal analysis conference*, vol 2251, pp 933–941
3. Chen J, Garba JA (1988) On-orbit damage assessment for large space structures. *AIAA J* 26(9):1119–1126
4. Pandey AK, Biswas M (1994) Damage detection in structures using changes in flexibility. *J Sound Vib* 169:3–17
5. Pandey AK, Biswas M, Samman MM (1991) Damage detection from changes in curvature mode shapes. *J Sound Vib* 145:321–332
6. Waheb MMA, Roeck GDE (1999) Damage detection in bridges using modal curvature: application to real world scenario. *J Sound Vib* 226(2):217–235
7. Whalen TM (2008) The behavior of higher order mode shape derivatives in damaged beam like structures. *J Sound Vib* 309(3–5):426–464
8. Cao MS, Cheng L, Su ZQ, Xu H (2012) A multi-scale pseudo-remodeling wavelet domain for identification of damage in structural components. *Mech Syst Signal Process* 28:638–659
9. Cao M, Radziński M, Xu W, Ostachowicz W (2014) Identification of multiple damage in beams based on robust curvature mode shapes. *Mech Syst Signal Process* 46:268–280
10. Lee YY, Liew KM (2001) Detection of damage locations in a beam using the wavelet analysis. *Int J Struct Stab Dyn* 01(03):455–465
11. Liew KM, Wang Q (1998) Application of wavelets for crack identification in structures. *J Eng Mech ASCE* 124(2):152–157
12. Ratcliffe CP (2000) A frequency and curvature based experimental method for locating damage in structures. *ASME J Vib Acoust* 122(3):324–329
13. Sampaio RPC, Maia NMM, Silva JMM (1999) Damage detection using the frequency-response-function curvature method. *J Sound Vib* 226(5):1029–1042
14. Frank Pai P, Leyland G (2001) Young, damage detection of beams using operational deflection shapes. *Int J Solids Struct* 38:3161–3192
15. Bhutia A (2013) Damage detection using operational deflection shapes. M.Tech thesis, Department of Civil Engineering, IIT Kharagpur
16. Mondal B (2014) Damage detection of structures using frequency response functions at frequencies other than natural frequencies. M.Tech thesis, Department of Civil Engineering, IIT Kharagpur
17. ABAQUS/CAE 6.10-1, Dassault Systèmes Simulia Corp., Providence, RI, USA
18. Ewins DJ (2000) *Modal testing: theory, practice and application*. Research Studies Press Ltd, England

Dynamic Response of Block Foundation Resting on Layered System Under Coupled Vibration

Renuka Darshyamkar, Bappaditya Manna and Ankesh Kumar

Abstract In the present study, the effect of various soil-rock and rock-rock foundation system on dynamic response of block foundations of different mass and equivalent radius under coupled mode of vibration are investigated. The dynamic response characteristics of foundation resting on the layered system considering soil-rock and weathered rock-rock combination are evaluated using finite element program with transmitting boundaries. The procedure to determine the frequency amplitude response of soil-rock and weathered rock-rock system is discussed in details and the equations are proposed for the same. The variation of natural frequency and resonant amplitude with shear wave velocity are investigated for different top layer thickness. It has been observed that the natural frequency increases and the peak displacement amplitude decreases with increase in shear wave velocity ratio. The variation of natural frequency and peak displacement amplitude are also studied for different top layer thickness and eccentric moments.

Keywords Block foundation · Soil-rock · Rock-rock · Coupled vibration · Frequency amplitude response

1 Introduction

Due to the diverse nature of Earth's geology, the homogeneity of soil or rock is rare on the earth surface. These days, engineers and geologist frequently encounter non-homogeneity in surface and sub-surface strata because of presence of bedding planes of varying strengths, fissures, joints and faults, due to this the dynamic behavior of machine foundation on such type of strata is very complex. The layered systems commonly available are soil-rock and rock-rock system and the dynamic force experienced by these systems are mainly due to the rotating type of machines. In case of rotating type machines, horizontal load acts on the complete system of

R. Darshyamkar (✉) · B. Manna · A. Kumar
Department of Civil Engineering, Indian Institute of Technology (IIT), Delhi, India

block foundation leading to the coupled vibration. Due to the complexity of the problem in machine induced coupled vibration there is a need of research addressing these issues.

The basic mathematical model used for foundation resting on soil is of a lumped mass with a spring and dashpot. Many researchers have used this model to study the dynamic response of footing, in this model soil medium was replaced by a vertical independent springs and the dissipation of energy from the vibrating system was represented by a dashpot.

Reissner [1] used elastic half-space as the mathematical model and proposed an analytical solution for dynamic analysis. Further, the elastic half-space theory is extended by Arnold et al. [2] to incorporate other modes of vibrations. Lysmer and Kuhlemeyer [3], and Veletsos and Wei [4] introduced the finite element and boundary element solutions. Some researchers [5] considered cone idealization for modeling foundation on a homogeneous half-space for the dynamic loading condition.

Many researchers [6–11] reproduced stiffness and damping parameters for embedded and surface footing on a viscoelastic half-space or layered medium by considering different modes of vibration. The problem is quite complex because of the mixed boundary conditions on the surface of the half-space. Displacements at the contact area between the rigid plate and half-space are uniform or linearly varying depending on the mode of vibration (translational or rotational). Veletsos and Wei [4] used analytical method and presented numerical data for the steady-state rocking and sliding response of a rigid, circular, massless disk.

In previous investigations, researchers studied numerous factors on which natural frequency of the block foundation soil system depends and these factors are shape and size of the foundation, depth of embedment, dynamic soil properties, nonhomogeneities in the soil, frequency of vibration etc. Nonhomogeneities in soil system are one of the important factors which have not been studied effectively in the past. Some researchers [12–14] investigated the effect of footing resting on layered soil. Many researchers studied the dynamic response of foundations considering the heterogeneities of the soil [14–16].

Numerical solutions for the response of foundations on a finite stratum over a half-space have been reported by Hadijan and Luco [15], and Gazetas and Roesset [17]. Dynamic response of rigid footings on the surface of homogenous, isotropic, and elastic or viscoelastic layered media has been studied by Kausel [18] and Lysmer et al. [19], using the finite element technique.

A solution is developed by Baidya [20] to find the stiffness of the i th layer of a multilayered system and this theory has been verified by model block vibration tests conducted by Baidya and Muralikrishna [21], Baidya and Rathi [22], and Baidya et al. [23]. Kumar et al. [24] studied the effect of soil-rock and rock-rock systems on dynamic response of block foundation under vertical excitation by using the finite element program for two different foundation systems.

In present paper, the block foundation on layered soil-rock and weathered rock-rock system are analyzed for frequency amplitude behavior. The layered combinations have been assumed as composite medium. The variation of dimensionless

natural frequency and resonant amplitude with shear wave velocity ratio for soil-rock and weathered rock-rock system is shown graphically and different equations are proposed for the same.

2 Theoretical Study

In the present study, the behavior of soil-rock and weathered rock-rock system are analyzed using finite element method (FEM) based formulation and computer program developed by Kausel [18]. The dynamic analysis of axisymmetric foundation resting on viscoelastic soil layers underlain by rock of infinite horizontal dimension were presented in a numerical method form by Kausel [18]. The technique used for the analysis of axisymmetric systems subjected to arbitrary non-axisymmetric loading was an extension of the solution technique proposed by Lysmer and Waas [25] using Fourier expansion method developed by Wilson [26]. The strains in finite element formulation are given in terms of the displacement.

$$\varepsilon = Bu_o \tag{1}$$

where $B = A\Phi^T$ in which ε = strain vector and A = partitioned matrix operator.

Principle of virtual displacement to define Eigen-value problem for the visco-elastic energy absorbing boundary is given as,

$$\sum \delta u_o^T \left\{ \iiint (B^T DB - \rho\Omega^2 \Phi\Phi^T) u_o r dr dz \right\} - \int \Phi Pr ds = 0 \tag{2}$$

where D = constitutive matrix containing material propertied, ρ = density of soil, Ω = frequency, r = equivalent radius.

And from the arbitrariness of the virtual displacement,

$$(-\rho\Omega^2 m + K)u = P \tag{3}$$

where u, P stand now for the total nodal displacement and load vector. The total stiffness and mass matrices K, m and the load vector P are assembled from the element matrices.

In the formulation of far-field core region is removed and substituted by equivalent distributed forces corresponding to the actual internal stresses as given by continuum theory. The displacement at the boundary is uniquely defined in terms of these fictitious boundary stresses. The displacement in the far-field region is expressed in terms of Eigen functions corresponding to the natural modes of wave propagation in the stratum and this displacement is related to the stresses by means of dynamic stiffness function.

Table 1 Properties of soil and rock

Type of soil and weathered rock	Shear wave velocity (m/s)	Unit weight (N/m ³)
Soil	185	16,000
Weathered rock	1,680	20,810
Sandstone	1,110	22,000

Defining the system dynamic stiffness matrix (K_d) as,

$$K_d = -\rho\Omega^2 m + K + R \tag{4}$$

$$P^* = DY^* \tag{5}$$

where D = dynamic stiffness matrix depends on the displacement pattern of wave propagation, P = forces at lateral boundary causes system to vibrate.

$$\Delta P = -R(Y - Y^*) \tag{6}$$

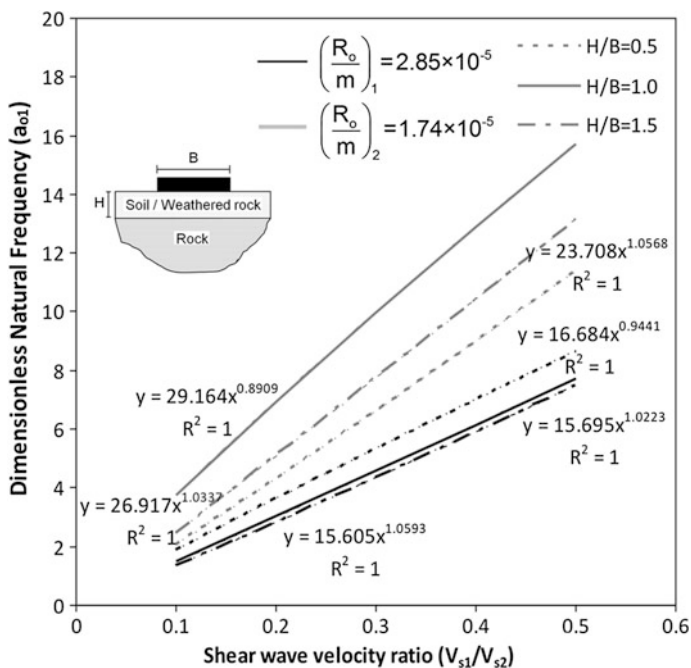


Fig. 1 Variation of dimensionless natural frequency (first peak, a_{o1}) with shear wave velocity ratio (V_{s1}/V_{s2}) for $(R_o/m)_1$ and $(R_o/m)_2$

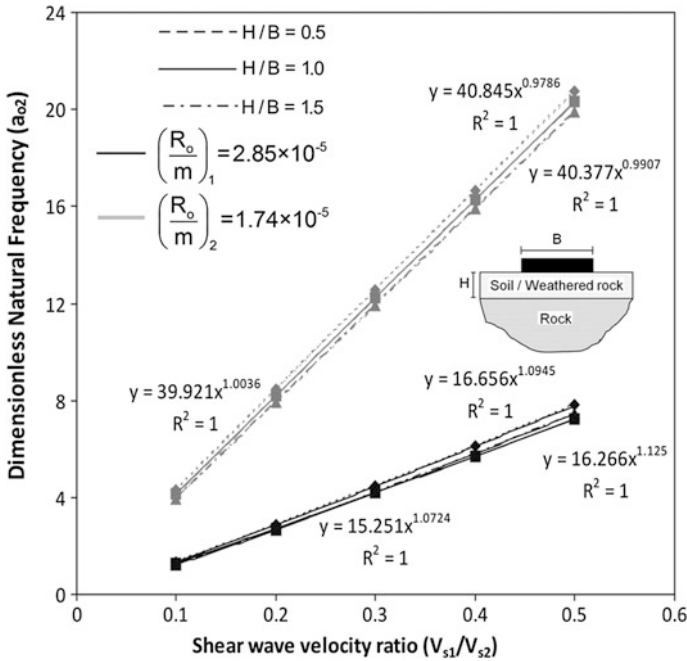


Fig. 2 Variation of dimensionless natural frequency (second peak, a_{o2}) with shear wave velocity ratio (V_{s1}/V_{s2}) for $(R_o/m)_1$ and $(R_o/m)_2$

Here, ΔP is nodal forces necessary to balance secondary forces at finite element boundary, $(Y - Y^*)$ represents deviation of the displacements produced by the secondary wave train, and R is the stiffness matrix of far-field.

$$(-\Omega^2 m + K + R)Y = (D + R)Y^* \tag{7}$$

Yields finally,

$$K_d Y = (D + R)Y^* + P \tag{8}$$

$Y^* = \{y_i\}$, y_i stands for either u_i or v_i .

Finally, load displacement is given as,

$$P_1^* = D_1 Y_1^* \tag{9}$$

which can be solved by the conventional numerical techniques for arbitrary dynamic loading, it must be solved in the frequency domain, as the dynamic stiffness matrix is a function of the driving frequency. Time histories are then obtained using the well-known Fourier transformation procedures.

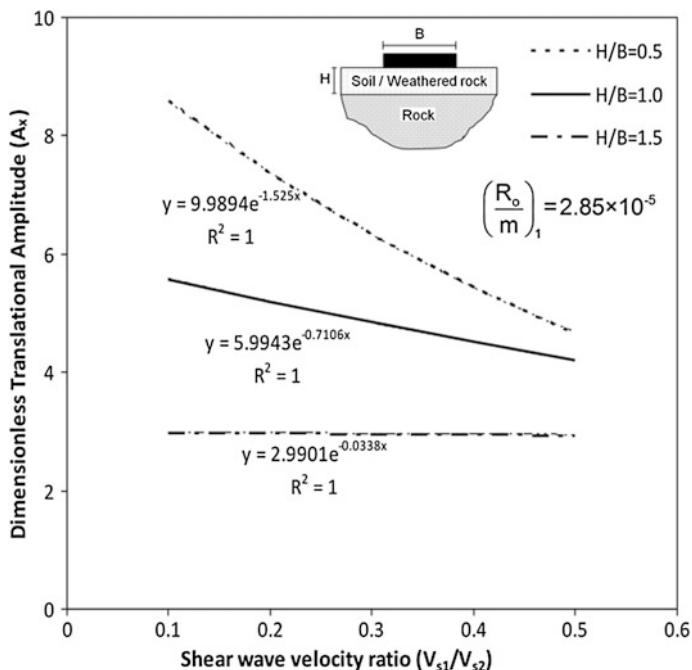


Fig. 3 Variation of dimensionless translational amplitude (A_x) with shear wave velocity ratio (V_{s1}/V_{s2}) for $(R_o/m)_1$

Novak et al. [27] formulated the computer program DYNA 5 which contains the above methodology. This program is used to present the dynamic behavior of block foundation as frequency response curves for coupled displacement, stiffness, and damping constants for layered system.

In the present analysis, two different ratios of equivalent radius of block foundation with mass of block foundation are considered as $(R_o/m)_1 = 2.85 \times 10^{-5}$ and $(R_o/m)_2 = 1.74 \times 10^{-5}$ to study the effect of mass and size of foundation on the dynamic response of block foundation, where R_o is equivalent radius of footing in meter and m is total mass of footing in kN. The properties of soil and rocks [24] considered for the analysis are shown in Table 1.

3 Results and Discussions

To study the effect of depth of layer on frequency amplitude response, the ratio of depth of top layer (H) with width of footing (B) is taken as $(H/B) = 0.5, 1.0,$ and 1.5 . In the present investigation, three different eccentric moment ($m_e = 0.028, 0.037,$ and 0.045 kg m) are used. The results so obtained in analysis are plotted in the form

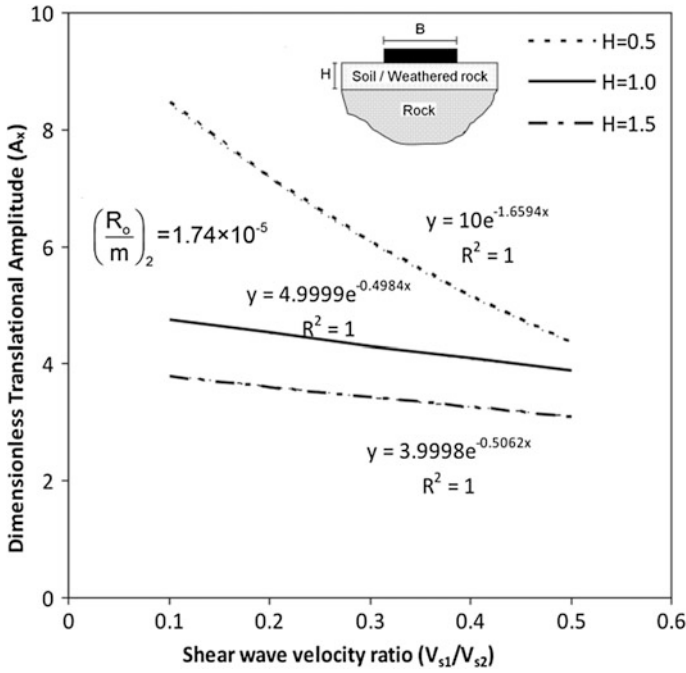


Fig. 4 Variation of dimensionless translational amplitude (A_x) with shear wave velocity ratio (V_{s1}/V_{s2}) for $(R_o/m)_2$

of dimensionless parameters, i.e. dimensionless frequency a_o , dimensionless amplitude A_x and A_ψ .

$$\text{Dimensionless translational amplitude, } A_x = \frac{x \cdot m}{m_e e} \tag{10}$$

$$\text{Dimensionless rotational amplitude, } A_\psi = \frac{I_\psi}{m_e e Z_e} \tag{11}$$

$$\text{Dimensionless frequency, } a_o = \frac{\omega r_o}{v_s} \tag{12}$$

The analysis is carried out for three different shear wave velocity ratios of 0.8, 0.6, and 0.3, respectively. The variation of natural frequency and resonant amplitude of translational and rotational mode of vibration are obtained for H/B ratio = 0.5, 1.0, and 1.5. The trend lines are then obtained for the graphs between (i) natural frequency and shear wave velocity, and (ii) resonant amplitude and shear wave velocity ratios. The graphs are extended for the lower values of shear wave velocity ratios ($V_{s1}/V_{s2} < 0.5$; where V_{s1} is the shear wave velocity of top layer, and

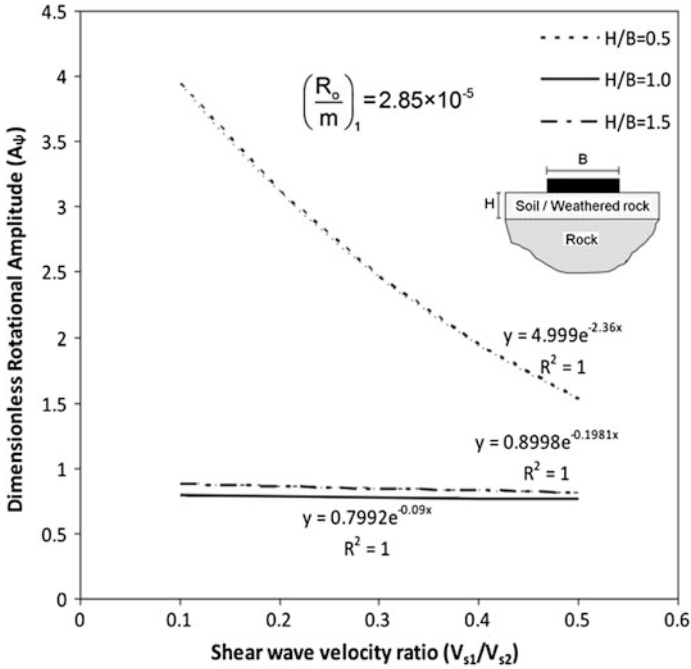


Fig. 5 Variation of dimensionless rotational amplitude (A_ψ) with shear wave velocity ratio (V_{s1}/V_{s2}) for $(R_o/m)_1$

V_{s2} is the shear wave velocity of half space) by using trend line equations, which indicate the different soil-rock and weathered rock-rock combination systems.

The variation of dimensionless natural frequency for first peak with shear wave velocity ratio is shown in Fig. 1 for both $(R_o/m)_1$ and $(R_o/m)_2$. Similarly, the variation of dimensionless natural frequency for second peak with shear wave velocity ratio is shown in Fig. 2 for both $(R_o/m)_1$ and $(R_o/m)_2$. The trend line shown in graphs are the variation of first and second peak of natural frequency (due to the effect of coupled vibration) with shear wave velocity ratios. It is observed from Figs. 1 and 2 that the dimensionless natural frequency decreases with the decrease in shear wave velocity ratios due to the properties of weathered rock or soil.

The variation of dimensionless translational amplitude with shear wave velocity ratio is shown in Figs. 3 and 4 for $(R_o/m)_1$ and $(R_o/m)_2$, respectively. The trend line equation given in the graphs shows the variation of dimensionless rotational amplitude with shear wave velocity for different H/B ratios.

Similarly, the variation of dimensionless rotational amplitude with shear wave velocity ratio is shown in Figs. 5 and 6 for $(R_o/m)_1$ and $(R_o/m)_2$, respectively. It can be seen from Figs. 3, 4, 5, and 6 that as H/B ratio increases the dimensionless rotational and translational amplitude decreases. It is observed that both the dimensionless amplitude decreases with increase in shear wave velocity ratio. It is

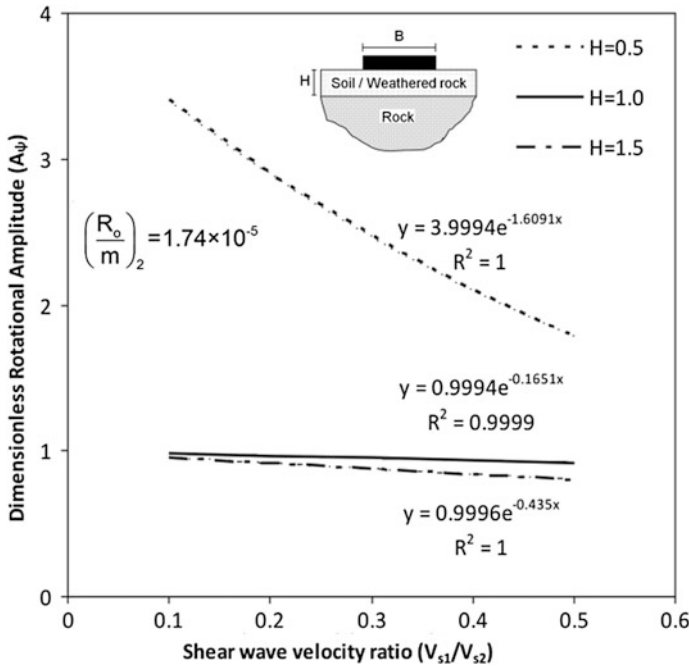


Fig. 6 Variation of dimensionless rotational amplitude (A_ψ) with shear wave velocity ratio (V_{s1}/V_{s2}) for $(R_o/m)_2$

also observed that the value of dimensionless rotational amplitude of $(R_o/m)_1$ ratio is higher than that of $(R_o/m)_2$ ratio, due to the mass and size effect of the two footings. It is also noted that trend lines are approaching to a constant value and that value can be obtained at shear wave velocity ratio of 1.

4 Conclusions

In the present work, the procedure to predict the dynamic response is described in details for soil-rock and weathered rock-rock system for different R_o/m ratios under coupled vibration. Different equations are proposed to calculate the dimensionless natural frequency and resonant amplitudes (translational and rotational) for soil-rock and weathered rock-rock system for different H/B ratios which depend on shear wave velocity ratio. In case of layered media, the response is usually dominated by the first resonant peak and the second peak is entirely suppressed for the translational case and reverse character can be seen in case of rotational.

It is observed that dimensionless resonant amplitudes (translational and rotational) decrease and natural frequency (both first and second peak) increases with increase in shear wave velocity ratio. It is further observed that with increase in H/B

ratio the dimensionless resonant amplitudes (translational and rotational) and natural frequency (both first and second peak) decreases. Also, it is observed that the value of dimensionless translation amplitude is higher for $(R_o/m)_1$ ratio which represents small foundation as compared to $(R_o/m)_2$ ratio. It can be seen that the natural frequency (both first and second peak) is higher in the case of $(R_o/m)_1$ as compared to $(R_o/m)_2$ ratio.

The best option as foundation medium for the construction of block foundation in layered system is the one with high value of shear wave velocity of top layer, due to the high natural frequency and low resonant amplitudes values of the system. The normalized graphs proposed for the coupled dynamic behavior of block foundations resting on soil-rock system, can be useful for practicing engineers and academicians.

References

1. Reissner E (1936) Stationäre, Axialsymmetrische Durch Eine Schut-telnde Masse Erregte Schwingungen Eines Homogenen Elastischen Halbraumes. Ingenieur Archive, Berlin, Germany, vol 7, no 6, pp 381–396
2. Arnold RN, Bycroft GN, Warburton GB (1955) Forced vibrations of a body on an infinite elastic solids. J Appl Mech Trans ASME 77:391–401
3. Lysmer J, Kuhlemeyer RL (1969) Finite-dynamic model for infinite media. J Eng Mech Div 95(4):859–877
4. Veletsos AS, Wei YT (1971) Lateral and rocking vibration of footings. J Soil Mech Found Div ASCE SM9:1227–1248
5. Meek J, Wolf J (1992) Cone models for soil layer on rigid rock. II. J Geotech Eng 118(5):686–703
6. Beredugo YO, Novak M (1972) Coupled horizontal and rocking vibration of embedded footings. Can Geotech J 9(4):477–497
7. Luco JE (1976) Vibrations of a rigid disc on a layered viscoelastic medium. Nucl Eng Des 36:325
8. Lysmer J (1980) Foundation vibrations with soil-structure damping. Civil engineering nuclear power, ASCE, II, 10/4/1-18
9. Novak M, Sachs K (1973) Torsional and coupled vibrations of embedded footings. Earthq Eng Struct Dyn 2(11):33
10. Veletsos AS, Verbic B (1973) Vibration of viscoelastic foundation. Earthq Eng Struct Dyn 2:87–102
11. Veletsos AS, Nair VVD (1974) Torsional vibration of viscoelastic foundation. J Geotech Div ASCE 100(GT3):225–246
12. Gazetas G, Roesset JM (1979) Vertical vibration of machine foundations. J Geotech Eng ASCE 105(12):1435–1454
13. Kausel E, Roesset JM, Waas G (1976) Dynamic analysis of footings on layered media. J Eng Mech ASCE 101(5):679–693
14. Kagawa T, Kraft LM (1981) Machine foundations on layered soil deposits. In: 10th international conference on soil mechanics and foundation engineering, Stockholm, vol 3, pp 249–252
15. Hadijan AH, Luco JE (1977) On the importance of layering on impedance functions. In: Proceedings of 6th world conference on earthquake engineering (WCEE), New Delhi
16. Warburton GB (1957) Forced vibrations of a body on an elastic stratum. J Appl Mech ASME 1A:55–58

17. Gazetas G, Roesset JM (1976) Forced vibrations of strip footings on layered soil. *Meth Struct Anal ASCE* 1:115–131
18. Kausel E (1974) Forced vibrations of circular foundations on layered media. Ph.D. thesis, Massachusetts Institute of Technology, USA
19. Lysmer J, Udaka T, Seed HB, Hwang R (1974) LUSH a computer program for complex response analysis of soil-structure systems, Report No. EERC 74-4, University of California, Berkeley, USA
20. Baidya DK (1992) Dynamic response of footings resting on layered and nonhomogeneous soils. Ph.D. thesis, Indian Institute of Science (IISc), Bangalore, India
21. Baidya DK, Muralikrishna G (2000) Dynamic response of foundation on finite stratum—an experimental investigation. *Indian Geotech J* 30(4):327–350
22. Baidya DK, Rathi A (2004) Dynamic response of footings resting on a sand layer of finite thickness. *J Geotech Geoenviron Eng* 130(6):651–655
23. Baidya DK, Muralikrishna G, Pradhan PK (2006) Investigation of foundation vibrations resting on a layered soil system. *J Geotech Geoenviron Eng* 132(1):116–123
24. Kumar A, Manna B, Rao KS (2013) Dynamic response of block foundations resting on soil-rock and rock-rock system under vertical excitation. *J Indian Geotech* 43(1):83–95
25. Lysmer T, Waas G (1972) Shear waves in plane infinite structure. *J Eng Mech Div ASCE* 98:85–105
26. Wilson E (1965) Structural analysis of axisymmetric solids. *AIAA J* 3(12):2269
27. Novak M, El-Naggar MH, Sheta M, El-Hifnawy L, El-Marsafawi H, Ramadan O (1999) DYNAS—a computer program for calculation of foundation response to dynamic loads. Geotechnical Research Centre, University of Western Ontario, London

Interior Coupled Structural Acoustic Analysis in Rectangular Cabin Structures

Sreyashi Das (Pal), Sourav Chandra and Arup Guha Niyogi

Abstract The structural acoustic problem, wherein an acoustic domain is confined within a partly flexible laminated composite enclosure, subjected to harmonic excitation, is presented. From the finite element free vibration analysis of the laminated composite folded plate structure, a mobility relation is derived that relates the acoustic pressure and structural velocity normal to the containing structure. A boundary element solver for the Helmholtz equation with 8 noded quadratic isoparametric elements is developed using pressure-velocity formulation. Velocity is specified over the rigid part of the boundary, the rest being the interactive boundary, where the mobility relation correlates nodal pressures and velocities, neither being explicitly known. The pressure boundary values are solved from the boundary element equations coupled with the mobility relations, while the velocity at flexible boundary is computed from mobility relationship. New results presented here reveal the effects of the variation in thickness of the wall, damping ratio, different stacking sequences and length of the enclosure on acoustic pressure.

Keywords Cabin · Coupled · Acoustic · Vibration · Laminated · Composites

1 Introduction

The noise produced within the flexible pulsating walls of a cabin-type structure, forming an acoustic cavity is of particular importance in vehicular and aviation industries. Typical examples include cabin noise inside vehicles, aircraft fuselages

S. Das (Pal) (✉) · A.G. Niyogi
Department of Civil Engineering, Jadavpur University, Kolkata-32, India
e-mail: palsreyashi@gmail.com

A.G. Niyogi
e-mail: agn_ju@yahoo.com

S. Chandra
Department of Civil Engineering, JIS College of Engineering, Kalyani, India
e-mail: chandra.sourav2009@gmail.com

and control rooms etc., which are usually modeled by a cavity enclosed inside a flexible composite structure. High level of interior noise in cabin structure is a negative factor in the assessment of vehicle quality. Uncontrolled sound leads to various health hazards like hearing damage along with other ailments like mental stress, physiological, endocrinal and cardiovascular damages and even fetal disorders. Being thin, flexible and light, the interaction of a cabin structure undergoing vibration with the enclosed and/or surrounding acoustic field can considerably modify the acoustic response compared to the case where the cabin is thick and acoustically rigid. The problem is complicated as the enclosure is laminated composite in nature, having their own unique behavior pattern. This situation has resulted in low frequency noise (upto about 200 Hz) which creates uneasiness. An interior coupled structural acoustic (ICSA) study can assess this response pattern and can help to design a quiet ambience within aircrafts, vehicles, auditoria, control rooms, machine rooms, and the like. Thus knowledge of the dynamic behavior and sound pressure level of an enclosed structure is essential for the design of structures in different thicknesses, damping conditions and stacking sequences.

Seybert et al. [1] discussed a coupled Finite Element-Boundary Element (FE-BE) analysis where, the two system matrices, the structural (obtained by using FEM) and the acoustic (obtained by using BEM), were solved simultaneously. Ohayon et al. [2] provide a detail discussion on methodologies of fluid-structure analysis, mainly based on finite element technique. Suzuki et al. [3, 4] solved coupled interior structural acoustic problems using constant boundary elements and modal methods, where the boundary integral equations and the structural equations in uncoupled modal form were solved simultaneously. Recently, Morand and Ohayon [5] and Ohayon and Soize [6] provided detail discussions on methodologies of fluid-structure analysis, mainly based on finite element technique. Deu et al. [7] computed the vibro-acoustic interior problems with interface damping. Gaul and Wenzel [8] conducted a coupled symmetric FE-BE method of linear acoustic fluid-structure interaction in time and frequency domain using hybrid boundary element method (HBEM). He et al. [9] used 3 noded triangular meshes to couple edge-based smooth FEM with BEM in fluid-structure interaction problem. Li and Cheng [10] developed a fully coupled vibro-acoustic model to characterize the structural and acoustic coupling of a flexible panel backed by a rectangular cavity with a tilted wall. Niyogi et al. [11] accounted for coupled interior vibro-acoustic problem inside laminated composite enclosure where multiple surfaces of the enclosure can be defined to interact with the interior acoustic domain.

In this study, coupled finite element—boundary element (FE-BE) method is used for the analysis. The mobility approach has been adopted to undertake the coupled analysis. The structure containing the acoustic fluid is an assemblage of flat plates forming a sort of closed folded plate compartment and analyzed using FEM, considering transverse shear deformation and rotary inertia. Appropriate transformations are applied to modify the element matrices from local to global coordinates before assembly. In the BEM analysis of the acoustic cavity, pressure and velocity at the surfaces are the primary variables. The mobility relation derived from the structural analysis is used to eliminate the nodal velocity terms in the zone of

interaction, and only the nodal pressures are solved in the acoustic BE analysis. The present research addresses this problem using graphite/epoxy laminated composite as the cabin building material. Parametric studies, conducted by incorporating variation in fibre angles, thicknesses, damping ratios and length of cabin, are provided. If a cabin built of epoxy matrix is found to remain quiet in the intended range of working frequency, the degree of passive control gained with a cheap matrix would render the cabins extremely cost-effective.

2 Mathematical Formulation

2.1 Finite Element Analysis of Structure

The mathematical model is complicated by the orthotropic nature of the material. First order transverse shear deformation based on Yang-Norris-Stavsky (YNS) theory [12] is used along with rotary inertia of the material. The displacement field related to mid plane displacement as

$$u = u_0 + z\theta_y, \quad v = v_0 - z\theta_x, \quad w = w_0, \quad \varphi_x = \theta_y + w_{,x}, \quad \varphi_y = -\theta_x + w_{,y} \quad (1)$$

where displacement and rotations follow right hand cork screw rule with z direction upward. The notations have their usual meaning. φ_x and φ_y are shear rotation about x and y axis respectively.

The stiffness matrix of the plate element assume the form

$$[K]_e = \int [B]^T [D] [B] dA \quad (2)$$

$$\text{where,} \quad \{\varepsilon\} = [B] \{\delta_i\} \quad (3)$$

$\{\varepsilon\}$ being the strain vector, and $\{\delta_i\}$ the nodal displacement vector. $[B]$ is the strain displacement matrix and $[D]$ is the stiffness matrix given by

$$[D] = \begin{bmatrix} A_{ij} & B_{ij} & 0 \\ B_{ij} & D_{ij} & 0 \\ 0 & 0 & A_{lm} \end{bmatrix} \quad (4)$$

$$\text{where,} \quad A_{ij}, B_{ij}, D_{ij} = \sum_{k=1}^N \int_{z_{k-1}}^{z_k} (Q_{ij})^k (q, z, z^2) dz, \quad i, j = 1, 2, 6$$

$$\text{and} \quad A_{ij} = \sum_{k=1}^N \int_{z_{k-1}}^{z_k} \alpha (Q_{ij})^k dz, \quad l, m = 4, 5$$

α is a shear correction factor, taken as 5/6, to take account of the non-uniform distribution of the transverse shear strain across the thickness of the laminate. The mass matrix of the plate element is given by

$$[M]_e = \int_{A_e} [N]^T [\rho] [N] dA \quad (5)$$

$[\rho]$ being the density matrix functions.

Eight-noded isoparametric plate elements with 6 degrees of freedom per node have been implemented in the present computations. The stiffness matrix and the mass matrix of the element are derived by using the principle of minimum potential energy. The detail of transformation to relate local and global displacements are already discussed in [13]. Finally, the governing equation can be written as

$$([K'] - \omega_n^2 [M]) = 0 \quad (6)$$

The Eigen problem is solved using the subspace iteration technique so that desired number of eigenvalues and eigenvectors can be expected. The impedance relation is obtained from the time derivative of the response relationship of a damped multi-degree of freedom (MDOF) system under harmonic loading as presented below [14]:

$$\{v\} = \left[\Omega [\varphi] \text{diag} \left(\frac{2\Omega\omega_k\zeta_k + i(\omega_k^2 - \Omega^2)}{(\omega_k^2 - \Omega^2)^2 + 4(\Omega\omega_k\zeta_k)^2} \right) [\varphi]^T \right] \{f\} e^{i(\Omega t)} \quad (7)$$

Here, Ω is the forcing frequency in rad/s. $[\varphi]$ denotes the matrix of mass-normalized mode shapes, ω_k is the k th natural frequency of the multi-degree of freedom structure and ζ_k is the modal damping ratio of mode k . Only the normal-to-the-boundary components of the velocity and forces however are used while coupling the structural and acoustic domains.

2.2 Boundary Element Analysis of Structure

The governing equation of a time harmonic acoustic problem is given by the reduced wave (Helmholtz) equation,

$$\nabla^2 p + k^2 p = 0 \quad (8)$$

Here, p is the acoustic pressure and k is the wave number.

Assuming the surface is discretized into M number of eight-noded surface elements, the discretized form of boundary integral equation [11] is given as

$$\begin{aligned}
 C(p)p(P) + \sum_{m=1}^M \sum_{l=1}^8 \int_{-1}^{+1} \int_{-1}^{+1} \frac{\partial p^*}{\partial n}(P, Q)N_1(\xi_1, \xi_2)p_1J\xi_1, \xi_2)d\xi_1d\xi_2 \\
 = \sum_{m=1}^M \sum_{l=1}^8 \int_{-1}^{+1} \int_{-1}^{+1} [-i\omega\rho p^*(P, Q)]N_1(\xi_1, \xi_2)v_1j\xi_1, \xi_2)d\xi_1d\xi_2
 \end{aligned}
 \tag{9}$$

Each node of the BE mesh is used once as an observation point and a boundary element equation is generated. Upon assembly of these equations the system equation for the acoustic enclosure is found in the form of a set of linear algebraic equations.

$$[H]\{p\} = [G]\{v\} \tag{10}$$

Combining Eqs. (9) and (10), and selecting only the normal velocity and pressure components on the interacting zone, the final mobility relation is derived as

$$\{v\} = [Q]\{p\} \tag{11}$$

where, $[Q]$ is the desired mobility matrix, while $\{[v]\}$ and $\{p\}$ are the nodal velocities and pressures, respectively at the interactive boundary.

3 Numerical Results

A FORTRAN program has been developed for the present analysis. The main program has two modules; FEM tools to generate the mobility relation from free vibration analysis, and a BEM solver for the acoustic cavity.

3.1 Study on Mesh Convergence

In order to verify the convergence of results with the refinement of finite element mesh, the first four natural frequencies are computed for a graphite/epoxy (0/90/0/90) laminated composite box, idealized as a folded plate structure (Fig. 1), using different mesh sizes. This 3 mm thick laminated composite box structure will be used as an acoustic container with the left wall acting as a rigid piston. The top and the right walls are assumed to be flexible, and the remaining walls are assumed to be rigid. The material properties are as follows: $E1 = 130 \text{ GPa}$, $E2 = 9.5 \text{ GPa}$, $G23 = 0.5$, $G12 = 0.5$, $G13 = 3 \text{ GPa}$, $\nu12 = 0.3$, $\rho = 1,600 \text{ kg/m}^3$. From Table 1, it is observed that a $6 \times 2 \times 2$ mesh can be used for all future analyses.

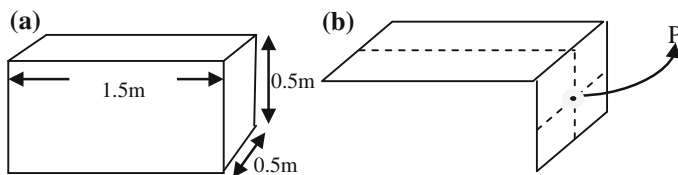


Fig. 1 a Acoustic enclosure. b Flexible membrane of acoustic cavity

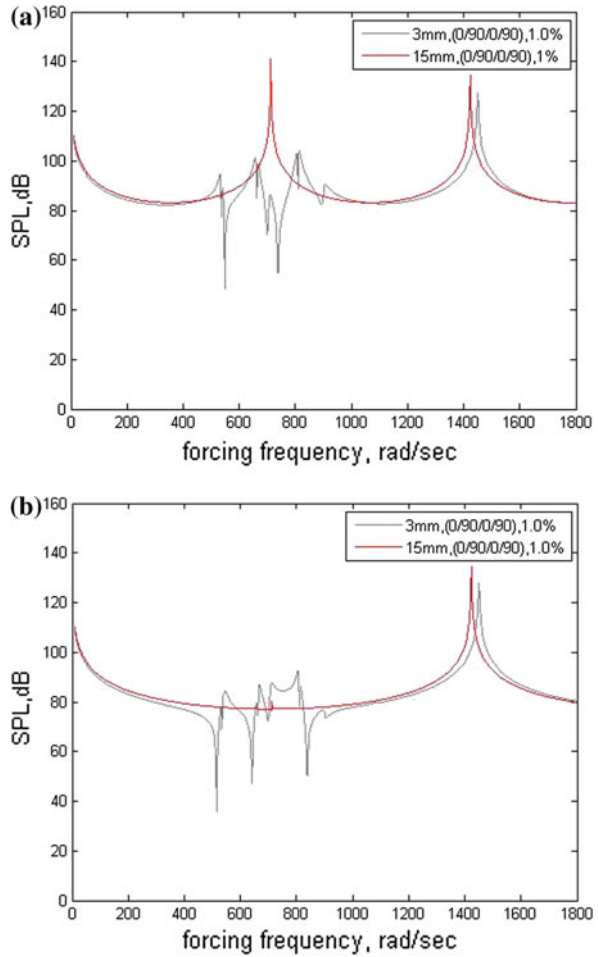
Table 1 Natural frequency (Hz) for different mesh size

Mode	Mesh size		
	$5 \times 2 \times 2$	$6 \times 2 \times 2$	$8 \times 2 \times 2$
1	83.47	83.61	83.00
2	91.77	92.41	92.03
3	110.00	112.19	110.48
4	115.06	116.16	118.01

3.2 Validation Problem

To validate the ICSA code, a passive, but quite a revealing approach has been adopted. The interior structural acoustic problem within the box structure, shown in Fig. 1a, with flexible top and right walls, is adopted for this study. The remaining four walls are assumed to be acoustically rigid, i.e., their wall thicknesses and stiffness's are too high to be influenced by the force that creates acoustic excitement within the cavity. Two set of numeric tests have been carried out here by varying wall thicknesses of the flexible walls. The first trial is made with 3 mm thick flexible walls and next with 15 mm flexible walls. The damping co-efficient is taken as 1 %. The response of a rigid acoustic cavity is very regular with a wide trough and regular resonances at an interval of $\Omega = nc\pi/l = 1 \times 340 \text{ m/s} \times \pi/1.5 \text{ m} = 712.4 \text{ rad/s}$ at the right hand side wall and twice of that at the centre of the domain [15]. Twenty contributing modes have been taken into account to compute the mobility relation for 3 mm thick cavity in the ICSA problems. The forcing frequency is limited to 1,800 rad/s computed at an interval of 2 rad/s. The left hand wall is set to execute simple harmonic motion where the velocity amplitude is set at 0.001 m/s. The material properties are used as in previous study. The SPL at the boundary and at domain are plotted in Fig. 2a, b. From the figures it is observed that when the thickness of the box is increased upto 15 mm, the behaviour is perfectly rigid [15]. For 3 mm thick cavity, the interaction spikes comes into picture, which matches quite well with the general understanding. Hence our program works well and can be used for further study.

Fig. 2 a Variation of SPL (dB) at the boundary point P. **b** Variation of SPL (dB) at domain (0.75, 0.25, 0.25)



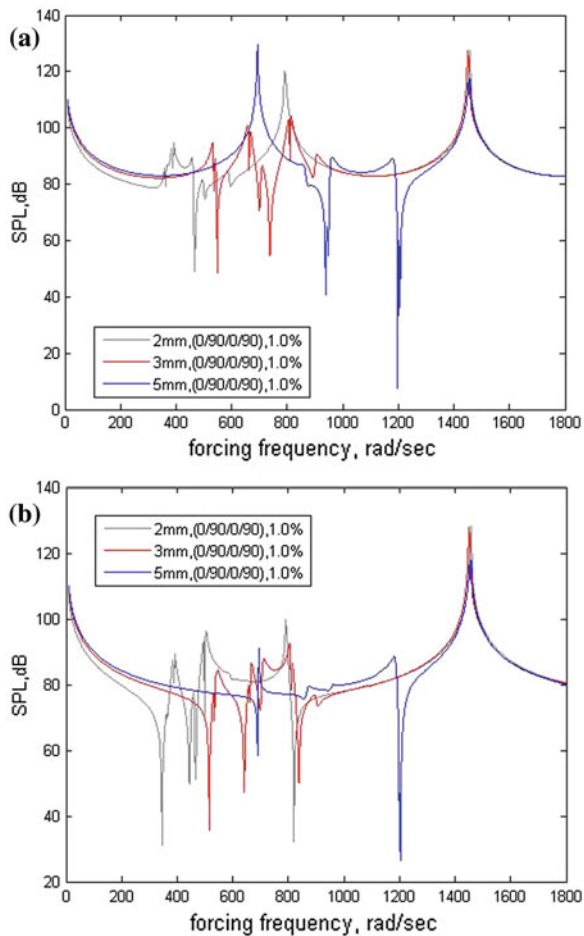
3.3 Case Study 1: Variation of Sound Pressure Level for Different Thickness of Wall of an Enclosed Acoustic Cavity

In this study, the variation of SPL (dB) is shown in an enclosed cavity with wall thickness of 2, 3 and 5 mm made up of graphite/epoxy laminate (0°/90°)₂. The damping ratio is kept constant (1 %) in this case. Table 2 shows the first six natural frequencies for different wall thickness. The variation of SPL for the above mentioned three cases is shown graphically at point P on the right wall (1.5, 0.25 and 0.25 m) and at the centre of the domain (0.75, 0.25 and 0.25 m), respectively, in Fig. 3a, b.

Table 2 First six natural frequencies (rad/s) of cabin for different wall thickness

Mode	2 mm	3 mm	5 mm	Mode	2 mm	3 mm	5 mm
1	352.642	525.571	867.659	4	489.955	730.449	1206.254
2	393.414	580.864	948.533	5	608.640	903.664	1468.482
3	480.733	705.357	1130.936	6	737.562	1102.516	1819.749

Fig. 3 a Variation of SPL (dB) at the boundary point P for different wall thickness. **b** Variation of SPL (dB) at domain (0.75, 0.25, 0.25) for different wall thickness



That with increase in thickness, the stiffness of the box structure increases is clearly evident from Table 2. Due to change in stiffness, the nature of variation of SPL, also changes. For rigid acoustics, the resonances at the right wall should appear at 0 rad/s, and would repeat after every $(\pi \times \text{sound speed in air}/\text{length})$ 712.4 rad/s increment of forcing frequency [15].

From Table 2 we see that the first three dry structural natural frequency of 2 mm thick cavity is 352.642, 393.414 and 480.733 rad/s. Here in Fig. 3a, the first spike is developed at 384 rad/s with SPL 92.6 dB, not exactly at their first natural frequency but slightly higher than that since the contained air adds to the dry structural stiffness. For 3 mm thick cavity, the fundamental frequency is 525.6 rad/s. here, upto nearly 450 rad/s rigid acoustic nature comes. After that interaction curves started. Similar nature is observed for 5 mm thick cavity. A sharp drop in SPL (8 dB) is observed near 1,200 rad/s for 5 mm thick cavity. The highest peak is present near 694 rad/s with 129 dB for this case. In Fig. 3b, the SPL at the domain starts deviating from rigid acoustic behavior just after first natural frequency. In general 5 mm thick cavity gives higher SPL level at the boundary compared to others.

3.4 Case Study 2: Variation of SPL for Symmetric and Anti-symmetric Cross Ply in an Enclosed Acoustic Cavity

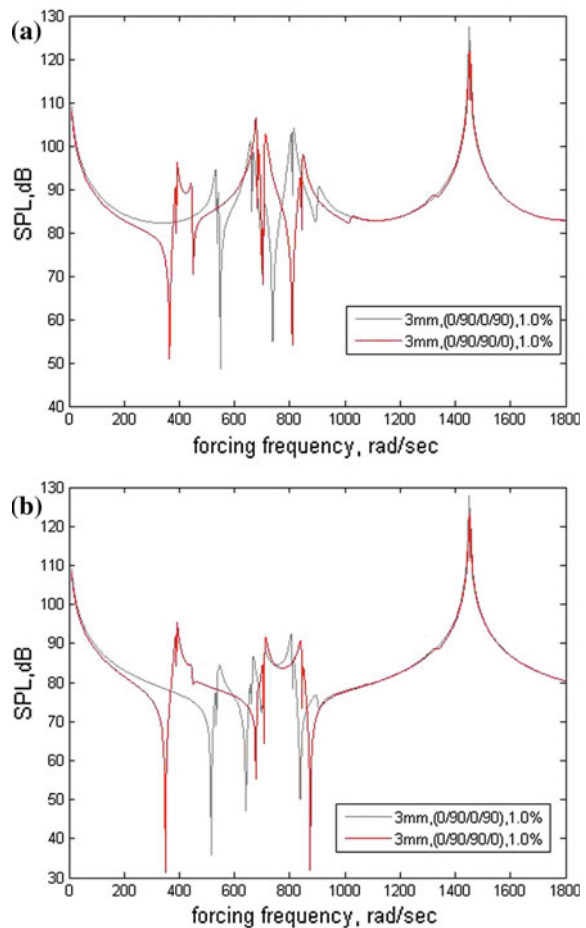
In this case, the same box structure as used in case study 1, is taken for analysis. The SPL (dB) at the boundary and at domain, are compared for symmetric and anti-symmetric cross ply laminates, namely (0/90)₂ and (0/90)_s. Table 3 gives the first six natural frequencies of laminated composite structure of above mentioned fiber arrangements.

From Table 3 we can see that (0/90/90/0) gives the lowest natural frequency at 356.389 rad/s whereas (0/90/0/90) gives the highest natural frequency at 525.571 rad/s. This indicates that composite structure with (0/90/0/90) fibre angle is stiffer compared to (0/90/90/0). As a result there is a sharp change in pattern of SPL (Fig. 4a, b). (0/90/0/90) laminates give rigid acoustic behavior upto its first natural frequency. There is no sharp peak near first acoustic mode. This is due to presence of third natural frequency near 712.4 rad/s which is its first acoustic mode. In Fig. 4b, in the domain also similar behavior is observed.

Table 3 First six natural frequencies (rad/s) for an enclosed cavity for different stacking sequence, 3 mm, $\xi = 1.0 \%$

Mode	0/90/0/90	0/90/90/0	Mode	0/90/0/90	0/90/90/0
1	525.571	356.389	4	730.449	796.606
2	580.864	471.595	5	903.664	1032.072
3	705.357	708.636	6	1102.516	1346.837

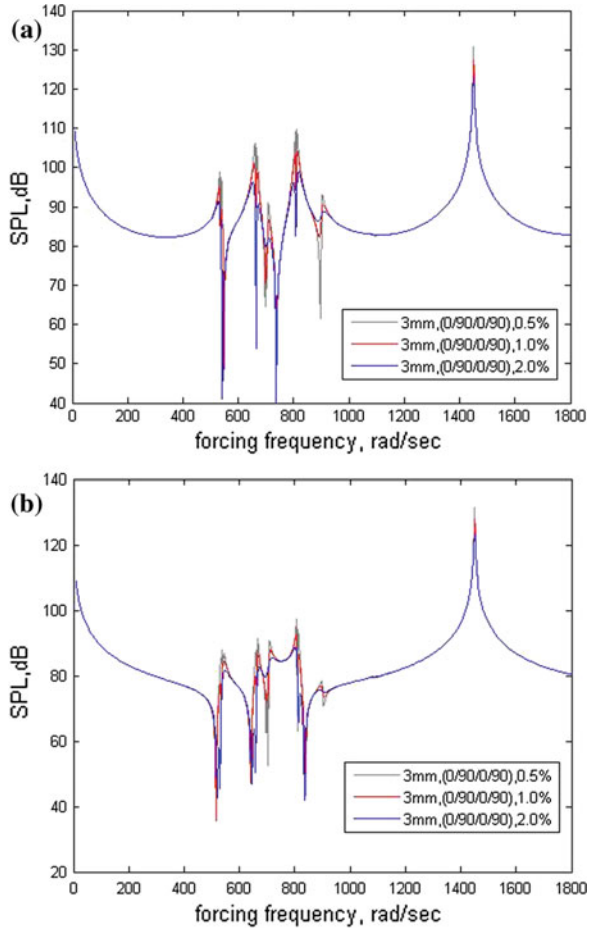
Fig. 4 a Variation of SPL (dB) at boundary point P. **b** Variation of SPL (dB) at (0.75, 0.25, 0.25)



3.5 Case Study 3: Variation of Sound Pressure Level for Different Damping Ratio in an Enclosed Acoustic Cavity

In this study, the variation of SPL (dB) is obtained due to variation in modal damping ratio. The damping ratio ξ is varied from 0.5 to 1 to 2 %. The variation of SPL is shown graphically at point P on the right wall in Fig. 5a, b. The box thickness taken as 3 mm for the experiment. The lay-up sequence is taken as (0/90/0/90). From Fig. 5a, b it is evident that there is no change in stiffness when the damping ratio changes. Only the peak value reduces with increased damping ratio both for SPL at the boundary and at the domain. For example, near 660 rad/s, the SPL for 0.5 % damping ratio is 106.3 dB whereas for 1 % damping ratio the SPL reduces to 101 dB and for 2 % damping the SPL reduces to 96.2 dB Similar nature

Fig. 5 a Variation of SPL (dB) at boundary point P for different damping ratios.
b Variation of SPL (dB) at domain (0.75, 0.25, 0.25) for different damping ratios



is obtained in domain analysis also. From Fig. 5a, b, it can be observed that higher damping ratio truncates the peaks to render the overall response patterns smoother generating a narrower response band. But they do not influence the response when the response pattern is smooth and spikes are absent.

3.6 Case Study 4: Variation of Sound Pressure Level for Variation of Length of an Enclosed Acoustic Cavity

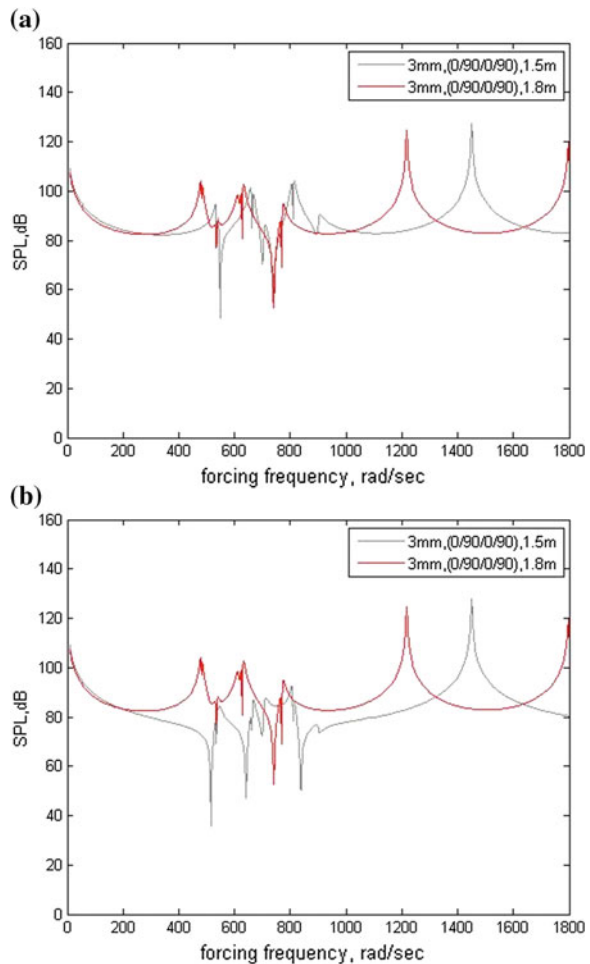
In this study the box length has been changed from 1.5 to 1.8 m. As a result, the stiffness of the box structure changes. First eight natural frequencies are given in Table 4. From the table it is observed that the stiffness of the box structure reduces with increase in length. The SPL at the boundary and at the domain also changes

Table 4 First eight natural frequencies (rad/s) for an enclosed cavity for different box dimension, 3 mm, $\xi = 1.0 \%$

Mode	1.5 m × 0.5 m × 0.5 m	1.8 m × 0.5 m × 0.5 m	Mode	1.5 m × 0.5 m × 0.5 m	1.8 m × 0.5 m × 0.5 m
1	525.571	519.300	5	903.664	742.386
2	580.864	551.538	6	1102.516	864.736
3	705.357	628.347	7	2268.522	2194.132
4	730.449	721.348	8	5582.344	3210.505

considerably as observed from Fig. 6a, b. Between 300 and 1,100 rad/s, a clear interaction graph is visible. This is due to interaction between its structural and acoustic modes. But the 7th mode frequency is observed to be above 2,000 rad/s. Hence, after 1,100 rad/s the SPL curve becomes smooth showing only the rigid acoustic mode.

Fig. 6 a Variation of SPL (dB) at boundary point P for different box length.
b Variation of SPL (dB) at domain (0.75, 0.25, 0.25) for different box length



4 Conclusion

The present study offers a very general FE-BE procedure to deal with interior acoustic problems coupled with partly flexible laminated composite enclosures. In mobility method of ICSA, the mobility relation is drawn from free vibration analysis of the cabin and plugging it in the pressure-velocity boundary element formulation of the interior acoustic domain in frequency domain. A thicker acoustic cavity, in general, produces higher acoustic response near the rigid acoustic modes compared to a thinner cavity. The cavities with thicker walls manifest interactions at higher forcing frequencies. Till such forcing frequency is attained, the effect of structural damping too is not visible. If the cavity damping is increased, the kinks visible in the SPL plot are truncated in amplitude at either end making the overall response pattern appear smoother. Thus, higher damping coefficient generates an acoustic response restricted within a narrow decibel band. Damping does not influence the response of SPL when the sound pressure level is passing through a saddle and spikes are absent. Fibre angle also plays an important role in the SPL in an acoustic cavity.

References

1. Seybert AF, Wu TW, Li WL (1990) Applications of the FEM and BEM in structural acoustics. In: Tanaka M, Brebbia CA, Honma T (eds) *Boundary elements BE XII*, vol -2, Applications in fluid mechanics and field problems. CMP-Springer, Berlin, pp 171–182
2. Ohayon R, Soize C (1998) *Structural acoustics and vibration: mechanical models, variational formulations and discretization*. Academic Press, San Diego
3. Suzuki S, Imai M, Ishihara S (1984) Boundary element analysis of structural-acoustic problems. In: Brebbia CA (ed) *Boundary elements-VI. Proceedings of the 6th international conference*. CML Publications, Southampton, NY, pp (7–27) – (7–35)
4. Suzuki S, Imai M, Ishihara S (1986) ACOUST/BOOM—a noise level predicting and reducing computer code. In: Tanaka M, Brebbia CA (eds) *Boundary elements-VIII, vol.-1. Proceedings of the 8th international conference*. CMP, Springer, pp 105–114
5. Morand HJP, Ohayon R (1995) *Fluid structure interaction, applied numerical methods*. Wiley, Masson
6. Ohayon R, Soize C (1998) *Structural acoustics and vibration: mechanical models, variational formulations and discretization*. Academic Press, London
7. Deu JF, Larbi W, Ohayon R (2008) Vibration and transient response of structural-acoustic interior coupled systems with dissipative interface. *Comput Methods Appl Mech Eng* 197:4894–4905
8. Gaul L, Wenzel W (2002) A coupled symmetric BE–FE method for acoustic fluid-structure interaction. *Eng Anal Boundary Elem* 26(7):629–636
9. He ZC, Liu GR, Zhong ZH, Zhang GY, Cheng AG (2011) A coupled ES-FEM/BEM method for fluid-structure interaction problems. *Eng Anal Boundary Elem* 35(1):140–147
10. Li YY, Cheng L (2007) Vibro-acoustic analysis of a rectangular-like cavity with a tilted wall. *Appl Acoust* 68(7):739–751
11. Niyogi AG, Laha MK, Sinha PK (2000) A coupled FE-BE analysis of acoustic cavities confined inside laminated composite enclosures. *Aircr Eng Aerosp Technol-An Int J* 72:345–357

12. Yang PC, Norris CH, Stavsky Y (1966) Elastic wave propagation in heterogeneous plates. *Int J Solids Struct* 2:665–684
13. Pal S, Guha Niyogi A (2008) Application of folded plate formulation in analyzing stiffened laminated composite and sandwich folded plate vibration. *J Reinf Plast Compos* 27(7):693–710
14. Utku S (1984) Analysis of multi-degree of freedom systems. In: Wilson JF (ed) Ch-9 of dynamics of offshore structures. Wiley-Interscience Publication, New York
15. Jayachandran V, Hirsch SM, Sun JQ (1998) On the numerical modelling of interior sound fields by the modal function expansion approach. *J Sound Vib* 210(2):243–254

Experimental and Numerical Analysis of Cracked Shaft in Viscous Medium at Finite Region

Adik R. Yadao and Dayal R. Parhi

Abstract The present investigation is an attempt to evaluate the dynamic behaviors of cantilever cracked shaft with attached mass at the end of the shaft in viscous medium at finite region. In this work we focused on the theoretical expression which is developed for finding the fundamental natural frequency and amplitude of the shaft with attached mass using influence co-efficient method. External fluid forces are analyzed by the Navier Stoke's equation. Viscosity of fluid and relative crack depth is taken as main variable parameters. In this investigation, the presence of transverse crack in the shaft has been considered. After that the suitable theoretical expressions are considered, and coding is done using Matlab. Further experimental verification have also done to prove the validity of the theory which is developed so far.

Keywords Crack location • Crack depth • Viscous medium • Influence coefficient method

Nomenclature

A_1	Shaft cross-sectional area
a_1	Crack depth
D	Diameter of the shaft
δ	Whirling radius of the shaft
i	Modulus of elasticity of shaft material
ε	Eccentricity
F_x, F_y	Fluid forces on shaft in x and y direction, respectively
β	Relative crack depth (a_1/D)
α	Relative crack position (L_1/L)

A.R. Yadao (✉) · D.R. Parhi
Department of Mechanical Engineering, National Institute of Technology (NIT) Rourkela,
Rourkela 769008, Orissa, India
e-mail: adik.mech@gmail.com

D.R. Parhi
e-mail: dayalparhi@yahoo.com

I	Section moment of inertia of the shaft
L	Total length of the shaft
L_1	Cracked position from left side of shaft
M_s	Mass of the shaft per unit length
M	Fluid mass displaced by the shaft per unit length
P	Pressure
R_1	Radius of the shaft
R_2	Radius of the cylinder
u	Radial flow velocity
v	Tangential flow velocity
ν	Coefficient of viscosity
μ	Poisson's ratio
ρ	Fluid density
ω	Rotating speed
ω_0	Natural angular frequency of the shaft
Ω	Angular velocity of whirling
44-Dim	Direction perpendicular to crack
55-Dim	Direction along the crack

1 Introduction

Dynamic analysis of rotating shaft has been given at most importance in field of vibration because of frequent failure of such shaft in industrial application as crack on such shaft aggravates the failure, investigation for dynamic analysis of rotor with crack is essential for safe design. Moreover when a shaft rotates in a viscous medium with crack on it. The dynamic analysis of such system becomes more complicated and difficult. Mario et al. [1] have developed a hybrid-mixed stress finite element model for the dynamic analysis of structure assuming a physically and geometrically linear behavior. Wang et al. [2] have studied the methodical approach sort out the confines of wind turbine models in analyzing the complex dynamic response of tower blade interaction. Hashemi et al. [3] have studied a finite element formulation for vibration analysis of rotating thick plate. Plate modeling developed by utilizes the Mindlin plate theory combine with second order strain-displacement. Juna and Gadalab [4] have analyzed the dynamic behavior of cracked rotor by using the additional slope and bending moment at crack position. Penacchi [5] have analyzed the shaft vibrations of a 100 MW for that proposed a model based diagnostic methodology which is help full to identified a crack in a load coupling of a gas turbine before happening a serious failure problem. Sino et al. [6] have studied the dynamic analysis of an internally damped rotating composite shaft. Nerantzaki et al. [7] have proposed the boundary element method

meant for the nonlinear free and force vibration of circular plates with varying thickness undergoing large deflection. Zhou et al. [8] have studied the experimental authentication of the theoretical results is required, particularly for the nonlinear dynamic behavior of the cracked rotor. The crack in the rotor was replicated by a real fatigue crack, as a substitute of a narrow slot. Nandi [9] have presented a simple method of reduction for finite element model of non-axisymmetric rotors on no isotropic spring support in a rotating frame.

In this investigation, an organized analysis for the vibrational behavior of a cantilever cracked shaft in viscous medium at finite region is obtainable. Damping effect due to viscous fluid is determined with the help of Navier Stoke’s equation. Natural frequency of the shaft used for finding the critical speed of the system is determined using the influence coefficients method.

2 Theoretical Analysis

2.1 Equation of Motion

The Navier-Stoke equation for fluid velocity is expressed in the polar co-ordinate system $r-\theta$ as follows,

$$\frac{\partial u}{\partial t} = -\frac{1}{\rho} \frac{\partial p}{\partial r} + v \left(\frac{\partial^2 u}{\partial r^2} + \frac{1}{r} \frac{\partial u}{\partial r} - \frac{u}{r^2} + \frac{1}{r^2} \frac{\partial^2 u}{\partial \theta^2} - \frac{2}{r^2} \frac{\partial v}{\partial \theta} \right) \tag{1a}$$

$$\frac{\partial v}{\partial t} = -\frac{1}{\rho r} \frac{\partial p}{\partial \theta} + v \left(\frac{\partial^2 v}{\partial r^2} + \frac{1}{r} \frac{\partial v}{\partial r} - \frac{v}{r^2} + \frac{1}{r^2} \frac{\partial^2 v}{\partial \theta^2} + \frac{2}{r^2} \frac{\partial u}{\partial \theta} \right) \tag{1b}$$

where u and v denote flow velocities in radial and tangential directions, respectively, and p means a pressure. Rewriting the above equation with the help of a stream function $\Psi(r, \theta, t)$ the above equation can be written as,

We obtain,

$$\nabla^4 \psi - \left(\frac{1}{v} \right) \frac{\partial}{\partial t} (\nabla^2 \psi) = 0 \tag{2}$$

When the shaft is immersed in a fixed circular cylindrical fluid region with radius R_2 , The boundary conditions for $r = R_2$ are,

$$u_{r=R_2} = v_{r=R_2} = 0 \tag{3}$$

The non-stationary components of flow velocities induced by the whirling motion of a shaft are given as follows

$$ud = -\frac{1}{r} \frac{\partial \varphi}{\partial \theta} = j\delta\omega \left[\begin{array}{l} A\left(\frac{R_1}{r}\right)^2 + B + C\left(\frac{R_1}{r}\right)I_1(kr) \\ + D\left(\frac{R_1}{r}\right)K_1(kr) \end{array} \right] e^{j(\omega t - \theta)} \tag{4a}$$

$$vd = \frac{\partial \varphi}{\partial r} = \delta\omega \left[\begin{array}{l} -A\left(\frac{R_1}{r}\right)^2 + B + C\left\{-\left(\frac{R_1}{r}\right)I_1(kr) + kR_1I_0(kr)\right\} + \\ D\left\{-\left(\frac{R_1}{r}\right)K_1(kr) - kR_1K_0(kr)\right\} \end{array} \right] e^{j(\omega t - \theta)} \tag{4b}$$

2.2 Analysis of Fluid Forces

Substitute the flow velocities given by Eq. (4a, 4b) into Eq. (1a, 1b), the non-stationary component of pressure p can be written as

$$p = \int \frac{\partial p}{\partial \theta} \partial \theta = \delta\rho\omega^2 \left\{ \frac{-A}{r} R_1^2 + Br \right\} e^{j(\omega t - \theta)} \tag{5}$$

The coordinates of the center of the shaft are $x = \delta \cos \omega t$ and $v = \delta \sin \omega t$

$$F_x = -m \operatorname{Re}(H) \frac{d^2x}{dt^2} + m\omega \operatorname{Im}(H) \frac{dx}{dt} \tag{6a}$$

$$F_y = -m \operatorname{Re}(H) \frac{d^2y}{dt^2} + m\omega \operatorname{Im}(H) \frac{dy}{dt} \tag{6b}$$

2.3 Analysis of Cracked Cantilever Shaft with Mass at Free End

In the current analysis a lumped mass at the free end of the cantilever rotating cracked shaft submerged in finite fluid region is considered. If a disk with mass M_{s1} is attached with the end span of the shaft, a total lumped mass of the shaft is given by the expression

$$M_1M_s = M_{s1} + \alpha_{eq1}M_{s2} \quad \text{and} \quad M_2M_s = M_{s1} + \alpha_{eq2}M_{s2} \tag{7}$$

$$\{1 + M_1^* \operatorname{Re}(H)\} \frac{d^2 \zeta_2}{d\tau_1} - M_1^* \omega_1^* \operatorname{Im}(H) \frac{d\zeta}{d\tau_1} + \zeta = \varepsilon_1^* (\omega_1^*)^2 \cos(\omega_1^* \tau_1) \quad (8a)$$

$$\{1 + M_2^* \operatorname{Re}(H)\} \frac{d^2 \eta_2}{d\tau_2} - M_2^* \omega_2^* \operatorname{Im}(H) \frac{d\eta}{d\tau_2} + \eta = \varepsilon_2^* (\omega_2^*)^2 \cos(\omega_2^* \tau_2) \quad (8b)$$

The total dimensionless deflection in ‘X’ and ‘Y’ direction, when the 44-dirⁿ (perpendicular to crack) and 55-dirⁿ (along the crack) coincide with X-axis and Y-axis respectively is,

$$\delta_{n=1}^* = \delta_{44}^* = \zeta_{44} + \zeta_{55} \quad \text{and} \quad \delta_{n=2}^* = \delta_{55}^* = \eta_{44} + \eta_{55} \quad (9)$$

In this investigation, consider the dimensionless deflection in 44-dirⁿ (perpendicular to crack).

3 Numerical Results and Discussion

In the current investigation, the mild steel cantilever cracked shaft with a disc attached at the free end in viscous fluid at finite region has the following specification.

- (1) Density of material $\rho = 7,830 \text{ kg/m}^3$
- (2) Modulus of elasticity $E = 2.1 \times 10^{11} \text{ N/m}^2$
- (3) Length of the shaft $L = 1.3 \text{ m}$
- (4) Radius of the shaft $R_1 = 0.01 \text{ m}$
- (5) Radius of disc $R_D = 0.035 \text{ m}$
- (6) Length of disc $L_D = 0.035 \text{ m}$
- (7) Damping coefficient of viscous fluid ‘ ν ’ = 2.3/0.427/0.0633 Stokes.
- (8) Equivalent mass of fluid displaced ‘ M^* ’ = 0.158/0.1534/0.144
- (9) Gap ratio $q = (R_2 - R_1)/R_1 = 20$

Illustrations the effect of varying the viscosity of the fluid and crack depth at constant location on the frequency and amplitude of the cantilever cracked shaft with additional mass. In Figs. 1, 2 and 3 the graph are plotted between dimensionless amplitude ratio and frequency ratio. It is observed that as the crack depth increase the resonance frequency decreases. It is also found that as the viscosity of the fluid increase the amplitude of vibration decrease, due to increase in crack depth the corresponding amplitude of vibration under same condition decreases.

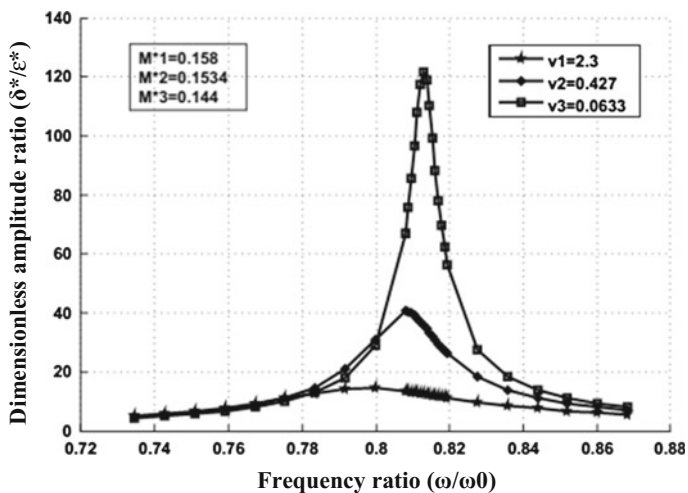


Fig. 1 Frequency ratio vs. Dimensionless amplitude ratio. Mild steel shaft ($R_1=0.01m$, $L=1.3m$, $q=20$, $\beta=0.28$, $\alpha =0.185$)

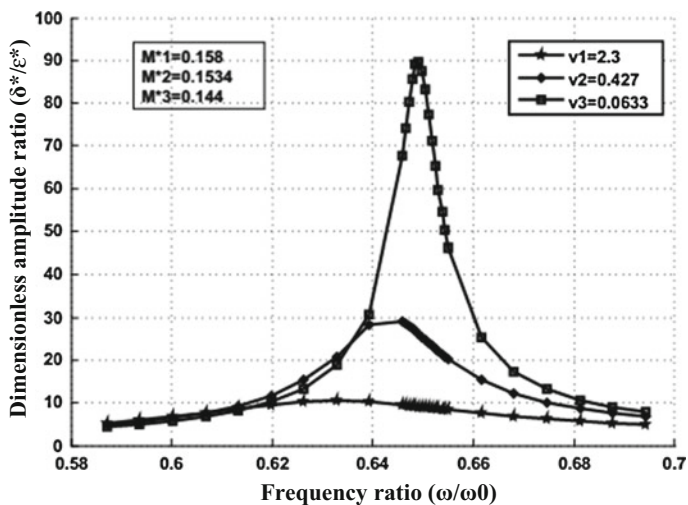


Fig. 2 Frequency ratio vs. dimensionless amplitude ratio. Mild steel shaft ($R_1 = 0.01 m$, $L = 1.3 m$, $q = 20$, $\beta = 0.38$, $\alpha = 0.185$)

4 Experimental Analysis

The experiment are accompanied by cantilever cracked shaft with additional mass at the free end which is rotating in viscous medium for determining the amplitude of vibration by varying damping coefficient of viscosity of fluid and crack depth of

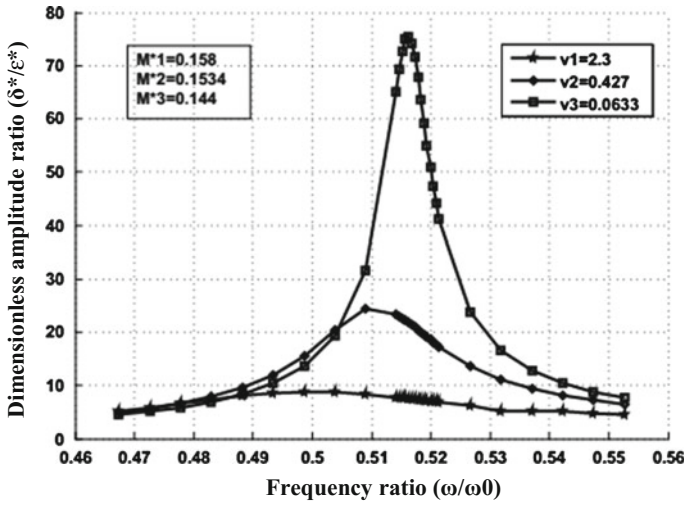


Fig. 3 Frequency ratio vs. dimensionless amplitude ratio. Mild steel shaft ($R_1 = 0.01$ m, $L = 1.3$ m, $q = 20$, $\beta = 0.48$, $\alpha = 0.185$)

Fig. 4 Schematic diagram of experimental Setup

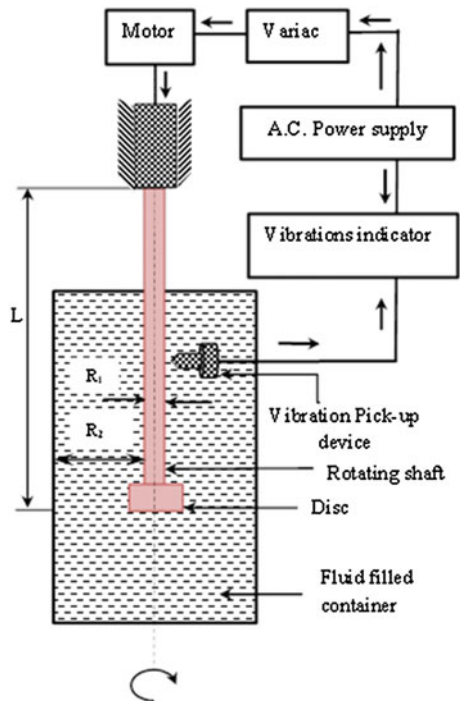


Table 1 Influence of crack depth on the amplitude ratio

Serial no.	Theoretical			Experimental			%Error		
	V = 0.0633 (stokes)			V = 0.0633 (stokes)			V = 0.0633 (stokes)		
	β_1	β_2	β_3	β_1	β_2	β_3	β_1	β_2	β_3
	0.25	0.35	0.45	0.25	0.35	0.45	0.25	0.35	0.45
1	4.41	4.46	4.50	4.59	4.62	4.66	4.2	3.8	3.6
2	12.90	10.22	8.36	13.41	10.64	8.76	4.0	4.2	4.9
3	67.12	67.75	19.28	70.40	69.71	20.03	4.9	2.9	3.9
4	96.67	85.61	69.34	99.76	89.61	72.52	3.2	4.8	4.6
5	121.64	89.79	75.46	125.77	94.49	77.57	3.4	5.3	2.8
6	110.26	83.21	67.82	114.22	86.37	71.55	3.6	3.8	5.5
7	88.04	71.25	54.93	91.38	74.10	57.23	3.8	4.8	4.2
8	62.25	54.64	44.04	65.17	56.88	45.88	4.7	4.1	4.2
9	18.28	25.31	12.80	18.81	26.27	13.41	2.9	3.8	4.8
10	8.02	7.84	7.72	8.32	8.26	8.09	3.8	5.4	4.9

Table 2 Influences of varying viscosity of fluid on the amplitude ratio

S.N	Theoretical			Experimental			%Error		
	V = 0.0633 (stokes)			V = 0.0633 (stokes)			V = 0.0633 (stokes)		
	v_1	v_2	v_3	v_1	v_2	v_3	v_1	v_2	v_3
	2.3	0.427	0.0633	2.3	0.427	0.0633	2.3	0.427	0.0633
1	5.01	4.68	4.41	5.26	4.87	4.59	5.1	4.2	4.2
2	9.28	8.91	12.90	9.51	9.23	13.41	2.9	3.7	4.0
3	14.26	21.00	67.12	14.74	21.56	70.4	3.4	2.7	4.9
4	13.38	40.54	96.67	14.08	42.20	99.76	5.3	4.1	3.2
5	13.08	38.24	121.64	13.62	40.07	125.77	4.2	4.8	3.4
6	12.45	34.64	110.26	12.83	35.99	114.22	3.1	3.9	3.6
7	11.96	29.58	88.04	12.48	30.43	91.38	4.4	2.9	3.8
8	11.48	27.28	62.25	11.91	28.31	65.17	3.8	3.8	4.7
9	7.62	13.92	18.28	7.89	14.53	18.81	3.6	4.4	2.9
10	5.64	7.16	8.02	5.83	7.46	8.31	3.4	4.3	3.8

shaft. The speed is controlled by a variac which is connected to the motor shaft from the fixed end of the cantilever shaft. From the free end of shaft the amplitude of the vibration was measured with the help of vibration pick-up device and vibration indicator for cantilever cracked shaft rotating in different viscous fluid and with the different crack depth. The experimental setup is shown in Fig. 4. The experimental and theoretical values are compared in Tables 1 and 2.

5 Conclusion

In this article, dynamic behavior of spinning cantilever cracked shaft with attached mass at the free end in viscous medium at finite area has been evaluated numerically which have authenticated by the experimentally. From above we conclude that as the viscosity of external fluid increases there is a decreases in the amplitude of vibration of shaft also it is establish that as the crack depth increase with constant location the natural frequency and amplitude of vibration of cracked shaft are decrease and the rate of decrease is faster with increase in crack depth. This investigation can also be used for rotating shaft in viscous medium such as long rotating shafts used in drilling rigs, high speed centrifugal and high speed turbine rotor etc.

References

1. Arruda MRT, Castro LMS (2012) Structural dynamic analysis using hybrid and mixed finite element models. *Finite Elem Anal Des* 57:43–54
2. Wang J, Qin D, Lim TC (2010) Dynamic analysis of horizontal axis wind turbine by thin-walled beam theory. *J Sound Vib* 329:3565–3586
3. Hashemi SH, Farhadi S, Carra S (2009) Free vibration analysis of rotating thick plates. *J Sound Vib* 323:366–384
4. Juna OS, Gadalab MS (2008) Dynamic behavior analysis of cracked rotor. *J Sound Vib* 309:210–245
5. Pennacchi P, Vania A (2008) Diagnostics of a crack in a load coupling of a gas turbine using machine model and the analysis of the shaft vibrations. *Mech Syst Signal Process* 22:1157–1178
6. Sino R, Baranger TN, Chatelet E, Jacquet G (2008) Dynamic analysis of a rotating composite shaft. *Compos Sci Technol* 68:337–345
7. Nerantzaki MS, Katsikadelis JT (2007) Nonlinear dynamic analysis of circular plates with varying thickness. *Arch Appl Mech* 77:381–391
8. Zhou T, Sun Z, Xu J, Han W (2005) Experimental analysis of cracked rotor. *J Dyn Syst Measur Control* 127:313–320
9. Nandi R (2004) Reduction of finite element equations for a rotor model on non-isotropic spring support in a rotating frame. *Finite Elem Anal Des* 40:935–952

Bibliography

10. Van Kadyrov SG, Wauer J, Sorokin SV (2001) A potential technique in the theory of interaction between a structure and a viscous, compressible fluid. *Arch Appl Mech* 71:405–417

Author Index

A

Abey, E. T., 1339
Arunraj, K. S., 1143

B

Baqi, Abdul, 1001
Benipal, Gurmail S., 1543
Bhanja, Santanu, 831
Bhardwaj, Ankit, 1283
Bharti, S. D., 933, 1103
Bhat, Subzar Ahmad, 869
Bhattacharyya, Biswarup, 1445
Bhaumik, Subhayan, 955
Bhowmick, Sutanu, 1405
Bhutia, Anila, 1563
Birajdar, B. G., 1419

C

Chakraborty, Arunasis, 1505, 1529
Chakraborty, Souvik, 1519
Chakraborty, Subrata, 1491
Chakraborty, Sushanta, 1563
Chandra, Sourav, 1587
Chowdhury, Rajib, 1519

D

Dalui, Sujit Kumar, 1445
Daniel, Joshua, A., 1027
Darshyamkar, Renuka, 1575
Dasgupta, Kaustubh, 1391
Das, Diptesh, 1117
Das (Pal), Sreyashi, 1587
Das, Prithwish Kumar, 955, 977
Das, Sanjib, 831
Debbarma, Rama, 1491
Devi, Kanchana, 885
(Dey) Ghosh, Aparna, 1243

Dicleli, Murat, 1219
Dubey, R. N., 1027
Dumne, S. M., 1103

E

Elias, Said, 1475
El-Khoriby, Saher, 1073
Elwardany, Hytham, 1073

G

Ganguli, Abhijit, 1543
Ghowsi, Ahmad Fayeeg, 841
Girish Singh, Y., 1117
Goswami, Rupen, 933
Goyal, Anshul, 1529
Goyal, Sudhanshu, 1015

H

Haldar, Putul, 1055
Halder, Lipika, 1039
Harikrishna, P., 1431
Hora, M. S., 789

J

Jagtap, Pravin, 1353
Jain, Arvind K., 1177
Jain, D. K., 789
Jain, J. A., 1419
Jangid, R. S., 817
Jankowski, Robert, 1073

K

Kalva, Meghana, 1257
Kanchana Devi, A., 909
Kasar, Arnab Anuj, 933
Keerthana, M., 1431
Khadiranaikar, R. B., 803

Kumar, Ankesh, 1575
 Kumar, P. C. Ashwin, 855
 Kumar, Pankaj, 1543
 Kumar, Pardeep, 1353
 Kumar, Praveen, 817, 1461
 Kumar, Ratnesh, 963

L

Lang, Dominik H., 1229

M

Madhekar, S. N., 945, 1167
 Madhekar, Suhasini N., 1377
 Mallikarjun, P. V., 1353
 Manna, Bappaditya, 1575
 Masali, Arif, 803
 Matsagar, Vasant, 1155, 1167, 1177,
 1283, 1353, 1475
 Mevada, Snehal V., 1295
 Milani, Ali Salem, 1219
 Mishra, Sudib K., 1405
 Mohammad, Zaid, 1001
 Mondal, Bidyut, 1563
 Mondal, Subhajit, 1563

N

Nagpal, A. K., 779, 1155, 1283
 Niyogi, Arup Guha, 1587

P

Pallav, Kumar, 751
 Panner Selvam, R., 1143
 Parhi, Dayal R., 1601
 Patel, C. C., 1091, 1129
 Pati, Barun Gopal, 1461
 Patro, Sanjaya K., 1311
 Paul, D. K., 1055
 Paul, Pradip, 977
 Paul, Prasenjit, 1367
 Phanikanth, V. S., 1193
 Prabhu, Muthuganeisan, 765
 Pujari, P. D., 945

R

Raghukanth, S. T. G., 751, 765
 Ramana, G. V., 779
 Ramanjaneyulu, K., 885, 909
 Rathi, Amit Kumar, 1505

Rawat, Aruna, 1155
 Ray-Chaudhuri, Samit, 1257
 Reddy, E. Praneeet, 1391
 Roy, Achintya Kumar, 1243
 Roy, Aparna, 1205
 Roy, Rana, 1205

S

Saha, Purnachandra, 1271
 Saha, Sandip Kumar, 1177
 Sahoo, Dipti Ranjan, 841, 855
 Sajith, A. S., 1339
 Sarkar, Abhijit, 1039
 Sarkar, Pradip, 977
 Sarkar, Rajib, 1015
 Sasmal, Saptarshi, 885, 909
 Satish Kumar, S. R., 989
 Sehgal, V. K., 869
 Seleemah, Ayman, 1073
 Sen, Subhajit, 897
 Senthil Kumar, R., 989
 Setia, Saraswati, 869
 Sharma, Richi Prasad, 1039
 Shingana, A. D., 1419
 Shiva, Kuncharapu, 1193
 Shrimal, Devendra, 1015
 Shrimali, M. K., 933, 1103
 Shrivastava, Hemant, 779
 Singhal, Abhishek, 921
 Singh, Konjengbam Darunkumar, 751
 Singh, Yogendra, 897, 921, 1055, 1229
 Smita, Chande, 963
 Somasundaran, T. P., 1339
 Surana, Mitesh, 1229
 Swain, Subhransu Sekhar, 1311

T

Talha, S. M., 1001
 Talukdar, S., 1367

V

Vishnu Pradeesh, L., 885

W

Waghmare, M. V., 1167

Y

Yadao, Adik R., 1601

Subject Index

A

Acoustic, 1587–1599
Acoustic-structure, 1156, 1158, 1165
Adjacent structures, 1092, 1093, 1095, 1130, 1131, 1137
ANSYS, 1447–1449
Asymmetric, 1296, 1297, 1299, 1308
Asymmetric structures, 955, 956

B

Backward Kolmogorov equation, 1519
Base isolation, 1178, 1183, 1191, 1354, 1360
Beam-column, 919
Beam-column joint, 886, 889, 892, 894, 977–979, 981, 987
Beam-to-column connections, 934
Benchmark building, 1462, 1465, 1472
Benchmark cable-stayed bridge, 1272, 1273, 1277, 1281
Benchmark highway bridge, 1377–1379, 1381, 1382, 1385, 1386, 1389
Bi-axial interaction, 1206, 1213
Bi-directional, 1156, 1159, 1162–1164
Block foundation, 1576, 1580, 1584
Bootstrap filters, 1530, 1532, 1533, 1536, 1540
Braced, 855–858, 861, 863, 867
Braces, 841, 848
Brick masonry building, 1028–1030, 1032, 1037
Bridges, 1339, 1340, 1343–1347, 1351, 1432
Building frame, 1001, 1003, 1009, 1013, 1014

C

Cabin, 1587–1589, 1594, 1599
Capacity curve, 1040, 1047–1051
Capacity demand, 947
Chevron, 841, 842, 847–853
Code, 898, 900, 906
Column forces, 795, 797, 800

Composite, 989–991, 993, 994, 996, 998, 999, 1588, 1589, 1591, 1595, 1599
Computational fluid dynamics, 1420, 1446–1448, 1451
Configurational and elastic modes, 1544, 1546, 1548, 1554, 1555, 1561
Construction sequence, 1060, 1061, 1063–1066, 1068
Contact surfaces, 1086
Control law, 824, 826, 827, 829
Coupled, 1588, 1599
Coupled buildings, 1105
Coupled vibration, 1576, 1582, 1583
Crack depth, 1605, 1606, 1608, 1609
Crack location, 1605, 1609
Critical joint, 978, 986, 988

D

Damage, 1040, 1042, 1044, 1049, 1050, 1052
Deformation, 934–936, 939
Delhi region, 779–782, 786
Design, 898, 900, 901, 905
Displacement dependent hardening, 1222
Double concave friction pendulum system, 1377, 1378, 1381
Drag coefficient, 1421, 1424, 1426, 1428
Drift, 841, 842, 847–849, 852
Dynamic, 855, 861–863, 865
Dynamic amplification factor, 1367, 1368, 1371, 1373–1375
Dynamic analysis, 1028, 1030, 1032, 1037, 1147, 1148
Dynamic response, 1092, 1101, 1130, 1133

E

Earthquake, 751–753, 756, 758, 762, 779, 780, 782, 783, 785, 786, 841, 846, 886, 889, 898, 955, 956, 959, 1001, 1002, 1012, 1155, 1156, 1159, 1162–1164,

- 1168–1170, 1172, 1174, 1178, 1179,
1182–1185, 1353–1355, 1358–1362,
1406, 1409, 1415
- Earthquake excitation, 1179
- Earthquake ground motion, 1249, 1250, 1254
- Earthquake load, 1194, 1200
- Earthquakes, 842, 849, 1073, 1084, 1086,
1088, 1411, 1417
- Eccentrically braced frames, 922, 925, 930
- Eigensystem realization algorithm, 1432
- Elastomeric bearing, 1340–1342, 1344, 1351,
1353–1358, 1362
- Energy balance, 1284–1286, 1293
- Energy dissipation, 1340, 1341, 1347–1349,
1351
- Energy dissipation device, 1313, 1336
- Experimental data, 1027
- F**
- Faults, 753
- FEMA, 946, 948, 949
- Finite element, 1156, 1158
- Finite element analysis, 1565
- Finite element method, 1202
- Finite element model, 1029, 1030
- Flat slab, 898–900, 902–907
- Fokker-Planck equation, 1526
- Fragility analysis, 1182
- Fragility curve, 1040, 1049, 1050, 1052
- Fragility functions, 974
- Frame, 989, 990, 992–996, 999
- Frequency amplitude response, 1580
- Frequency response function curvature, 1565
- Friction damper, 1283–1286, 1288, 1290,
1293, 1313–1324, 1326–1331,
1333–1336
- Friction pendulum system, 1272–1276, 1278,
1280–1282, 1377, 1378, 1380–1382,
1384, 1386, 1387
- G**
- Gravity load design, 909–911, 914, 919
- Ground acceleration, 751
- Ground motion, 1207, 1209–1213
- H**
- High-rise building, 1481, 1486
- Horizontal and vertical excitations, 1549, 1555,
1560, 1562
- Hydrodynamic effects, 1203
- Hydrodynamics, 1207
- Hydro-elasticity, 1144
- Hysteretic damper, 1220, 1221, 1226
- I**
- Infilled frame, 1056–1059, 1061, 1063–1066,
1068
- Infill stiffness, 869, 872, 881, 882
- Influence coefficient method, 1603
- In-plane behaviour, 1039
- IS code, 1019–1021, 1023
- Interaction, 1156, 1158, 1159, 1165
- Interstorey, 848
- J**
- Joint shear, 977, 980–982, 985–988
- K**
- Kinking of column, 934, 935, 938
- L**
- Laminated, 1588, 1589, 1591, 1595, 1599
- Laminated rubber bearing, 1105, 1109–1121
- Least square, 1509
- Lift coefficient, 1421, 1422, 1425, 1427
- Likelihood function, 1534
- Linear elastic analysis, 793
- Liquid column damper (LCD), 1244–1247
- Liquid storage structures, 1196
- Loading rate, 1547, 1560
- M**
- Main boundary thrust, 766, 768, 769
- Main central thrust, 766, 768, 769
- Markov chain, 1531
- Masonry, 1040–1042, 1044
- Mega-float, 1144, 1146, 1147, 1149, 1152
- Modal expansion method, 1146
- Modal frequency/shape, 1480, 1481, 1484
- Mode superimposition, 1367
- Moment coefficient, 1422, 1424–1427
- Monolithic, 1001, 1002
- Monte Carlo simulation, 1183, 1184, 1532
- Multi-flue chimney, 1015
- Multi-story, 1296, 1302
- N**
- Near fault, 779–782, 784
- Near-fault motion, 955, 960
- Non-linear, 855, 861–863, 865, 1118, 1120,
1126
- Non-linear analysis, 900, 902, 926
- Non-linear damping, 1258
- Non-linear static analysis, 1391
- Non-stationary, 1367, 1371, 1375
- Non-stationary earthquake, 1182
- Normal buildings, 1105, 1110, 1112, 1114

- Numerical analysis, 1086
 NZ bearing, 1120, 1122, 1125, 1126
- O**
 Open ground storey, 869–873, 875, 876, 878, 880–882
 Optimal STMD, 1477–1482, 1486
 Optimization, 1405, 1406, 1411, 1417, 1492, 1497–1499, 1503
 Orthotropic bridge deck, 1367, 1368
- P**
 Panel zone shear strength, 935, 937, 938
 Parameter uncertainty, 1492, 1497
 Particle filter, 1532, 1534
 Passive, 1296
 Passive and semi-active supplemental devices, 817, 819, 828
 Passive control, 1092, 1130
 Performance, 989, 990, 993, 995, 998, 999
 Performance based, pushover, 946, 950, 952, 953
 Performance evaluation, 1348, 1350, 1351
 Performance point, 948, 950
 Piping systems, 817–819
 Plastic hinges, 933
 Plate section, 1433
 Pounding, 1105, 1117–1121, 1123–1126, 1392, 1394–1396, 1400
 Power spectral density, 1367, 1371
 Primary structure, 1353–1362
 Probabilistic seismic hazard, 765, 772, 776
 Pushover analysis, 965, 974, 1234, 1236
- R**
 RC elevated water tanks, 1206, 1207, 1210, 1213
 RC frame, 1056–1063, 1068
 RC frame buildings, 963
 Recursive decomposition, 1520, 1521, 1526
 Reinforce concrete, 886, 892, 893, 955, 956, 958–960, 977, 978, 1001
 Reliability based approach, 1492, 1499, 1503
 Response amplitude operator, 1148
 Response spectrum, 784, 785, 831–833, 835–839
 Response spectrum analysis, 872, 875
 Response surface method, 1508
 Rock-rock, 1575, 1576, 1582, 1583
- S**
 SAC, 846
 SAP 2000, 945, 948, 949, 951, 1203
 SDOF, 1245–1247, 1249–1251, 1253, 1254
 Secondary system, 1353, 1354, 1356–1362
 Seismic, 817–819, 821, 824, 828, 989–991, 993, 994, 996, 998, 999, 1462, 1465, 1472
 Seismic analysis, 1016
 Seismic design, 1340, 1343
 Seismic design codes, 1057
 Seismic effect, 1091, 1092, 1130
 Seismic events, 1174, 1175
 Seismic isolation, 1118
 Seismic loading, 1311, 1313
 Seismic performance, 804, 805, 809, 900, 926, 928, 965, 967, 974
 Seismic response, 1104, 1105, 1114, 1272, 1273, 1277, 1280–1282, 1296, 1299, 1308, 1343, 1345, 1351, 1353, 1354, 1358–1360, 1545, 1548, 1549, 1551
 Semi-active, 1296, 1299, 1300, 1302–1304, 1308
 Semi-rigid, 989–994, 999
 Sensitivity, 1251, 1252
 Series of structures, 1073, 1075, 1088
 Shape memory alloy, 1405–1410, 1412, 1413, 1417
 Shear strength, 886, 888, 889, 894
 Shear-wall, 791–795, 797, 800, 1230, 1231, 1233, 1238–1240
 Shear-wall cores, 1231, 1233, 1238–1241
 Shell element model, 1234, 1236, 1240
 Shock loading, 1029, 1032
 Signed, 833, 836–839
 Site response, 753, 756, 762, 763
 Skew bridge, 1391–1394
 Sliding base isolation, 1272, 1273, 1277
 Sloping ground, 803–809, 811
 Sloshing, 1155–1158, 1160, 1163, 1165, 1168, 1169, 1172, 1175
 Soft storey, 1312, 1313, 1322–1324, 1326, 1332–1334, 1336
 Soft storey effect, 869, 873, 881, 882
 Soil investigation, 754
 Soil-rock, 1575, 1576, 1582–1584
 Soil structure interaction, 1391, 1395
 Special concentric, 867
 Split-X, 841
 Staircase, 1003–1006
 State space, 1169
 Steel design code, 922
 Step back building, 803–806, 809, 810–812
 Step back set back building, 804, 805, 810–812
 Stiffness irregularities, 870, 871, 876
 Stiffness ratio, 827
 Stochastic, 753, 756, 757, 762

Stochastic earthquake, [1492](#), [1496](#), [1497](#), [1503](#)
Structural damage detection, [1564](#), [1565](#)
Structural pounding, [1074](#)
Structural vibration control, [1245](#)

T

Tall building, [1446–1448](#), [1450](#), [1452–1454](#),
[1457](#), [1458](#)
Tank, [1168–1170](#), [1172](#), [1174](#), [1175](#), [1178](#),
[1179](#), [1183–1187](#), [1189–1192](#)
Theodorsen's theoretical solution, [1433](#)
Transfer function, [1258](#), [1262–1266](#), [1268](#)
Tuned liquid column dampers (TLCD),
[1258–1263](#), [1265–1269](#), [1492](#)
Tuned mass damper, [1258](#), [1405–1409](#),
[1411–1414](#), [1416](#), [1476](#), [1481](#), [1486](#),
[1505](#)

U

Uncertain systems, [1506](#)
URM infills, [1056](#)

V

Variable friction damper, [1104](#), [1108](#)

Variable friction pendulum isolator, [1273](#),
[1275–1282](#), [1380](#)
Variable friction pendulum system, [1377](#),
[1378](#), [1382](#), [1383](#), [1387](#)
Velocity pulse, [779–786](#)
Very large floating structures, [1143](#)
Vibration, [1588](#), [1591](#), [1599](#)
Vibration control, [1258](#), [1405](#), [1406](#), [1492](#),
[1505](#), [1506](#)
Viscoelastic damper, [1462](#), [1463](#)
Viscous damper, [1091–1094](#), [1099](#), [1101](#),
[1131](#), [1132](#)
viscous damper, [1137](#), [1138](#)
Viscous medium, [1602](#), [1603](#), [1606](#), [1609](#)
Vulnerability assessment, [965](#), [967](#)

W

Watch tower, [833–835](#)
Weightless cables, [1544](#), [1545](#), [1561](#)
Wide column model, [1231–1234](#), [1236](#), [1240](#)
Wind, [1432–1435](#), [1438](#), [1441](#)
Wind tunnel, [1446](#), [1447](#), [1450–1452](#), [1454](#),
[1457](#), [1459](#), [1463](#)